

Special Issue in Honor of Professor Nick Hadjiliadis' Retirement

Guest Editors: Evy Manessi-Zoupa and Spyros P. Perlepes





**Special Issue in Honor of Professor
Nick Hadjiliadis' Retirement**

Bioinorganic Chemistry and Applications

**Special Issue in Honor of Professor
Nick Hadjiliadis' Retirement**

Guest Editors: Evy Manessi-Zoupa and Spyros P. Perlepes



Copyright © 2010 Hindawi Publishing Corporation. All rights reserved.

This is a special issue published in volume 2010 of "Bioinorganic Chemistry and Applications." All articles are open access articles distributed under the Creative Commons Attribution License, which permits unrestricted use, distribution, and reproduction in any medium, provided the original work is properly cited.

Editorial Board

Triantafillos Albanis, Greece
Patrick Bednarski, Germany
Ivano Bertini, Italy
Viktor Brabec, Czech Republic
Ian S. Butler, Canada
Luigi Casella, Italy
Zhe-Sheng Chen, USA
Zheng Dong, USA
Nicholas P. Farrell, USA
Igor O. Fritsky, Ukraine
Cláudio M. Gomes, Portugal
Nick Hadjiliadis, Greece
Gerard Jaouen, France

Nick Katsaros, Greece
Bernhard Klaus Keppler, Austria
Anastasios Keramidis, Cyprus
Dimitris P. Kessissoglou, Greece
Concepción López, Spain
Luigi Marzilli, USA
Guillermo Mendoza-Diaz, Mexico
Albrecht Messerschmidt, Germany
E. R. Milaeva, Russia
Virtudes Moreno, Spain
Govindasamy Mugesh, India
Giovanni Natile, Italy
Akihiro Nawa, Japan

Ebbe Nordlander, Sweden
Lorenzo Pellerito, Italy
Spyros P. Perlepes, Greece
Claudio Pettinari, Italy
Enrico Rizzarelli, Italy
Tracey A. Rouault, USA
Imre Sovago, Hungary
Marie Stiborova, Czech Republic
Konstantinos Tsipis, Greece
Takeshi Uchiumi, Japan
Takao Yagi, USA

Contents

Special Issue in Honor of Professor Nick Hadjiliadis' Retirement, Evy Manessi-Zoupa and Spyros P. Perlepes
Volume 2010, Article ID 136485, 2 pages

Low-Power Ultrasounds as a Tool to Culture Human Osteoblasts inside Cancellous Hydroxyapatite, Lorenzo Fassina, Enrica Saino, Maria Gabriella Cusella De Angelis, Giovanni Magenes, Francesco Benazzo, and Livia Visai
Volume 2010, Article ID 456240, 8 pages

Niobium Uptake and Release by Bacterial Ferric Ion Binding Protein, Yanbo Shi, Ian Harvey, Dominic Campopiano, and Peter J. Sadler
Volume 2010, Article ID 307578, 11 pages

Effect of Common Buffers and Heterocyclic Ligands on the Binding of Cu(II) at the Multimetal Binding Site in Human Serum Albumin, Magdalena Sokołowska, Krystyna Pawlas, and Wojciech Bal
Volume 2010, Article ID 725153, 7 pages

The Zn- or Cu-Thionein Character of a Metallothionein Determines Its Metal Load When Synthesized in Physiological (Metal-Unsupplemented) Conditions, Mercè Capdevila, Òscar Palacios, and Silvia Atrian
Volume 2010, Article ID 541829, 6 pages

The $\Delta 33-35$ Mutant α -Domain Containing β -Domain-Like M_3S_9 Cluster Exhibits the Function of α -Domain with M_4S_{11} Cluster in Human Growth Inhibitory Factor, Qingui Bao, Zhichun Ding, Zhong-Xian Huang, and Xiangshi Tan
Volume 2010, Article ID 294169, 8 pages

Molecular Architectures Derived from Metal Ions and the Flexible 3,3'-Bipyridine Ligand: Unexpected Dimer with Hg(II), Anupam Khutia, Pablo J. Sanz Miguel, and Bernhard Lippert
Volume 2010, Article ID 169054, 8 pages

Synthesis and Characterization of Novel Ruthenium(III) Complexes with Histamine, Jakob Kljun, Saša Petriček, Dušan Žigon, Rosana Hudej, Damijan Miklavčič, and Iztok Turel
Volume 2010, Article ID 183097, 6 pages

Synthesis and Structural Characterization of a Metal Cluster and a Coordination Polymer Based on the $[Mn_6(\mu_4-O)_2]^{10+}$ Unit, Eleni E. Moushi, Anastasios J. Tasiopoulos, and Manolis J. Manos
Volume 2010, Article ID 367128, 7 pages

pH-Potentiometric Investigation towards Chelating Tendencies of *p*-Hydroquinone and Phenol Iminodiacetate Copper(II) Complexes, Marios Stylianou, Anastasios D. Keramidis, and Chryssoula Drouza
Volume 2010, Article ID 125717, 8 pages

"Lantern-Shaped" Platinum(III) Complexes with Axially Bound 9-Ethylguanine or 1-Methylcytosine (L) of General Formula $[Pt_2\{HN=C(Bu^t)O\}_4L_2](NO_3)_2$, Concetta Pacifico, Francesco Paolo Intini, Fiorentin Nushi, and Giovanni Natile
Volume 2010, Article ID 102863, 8 pages

Antioxidative Activity of Ferrocenes Bearing 2,6-Di-*Tert*-Butylphenol Moieties, E. R. Milaeva, S. I. Filimonova, N. N. Meleshonkova, L. G. Dubova, E. F. Shevtsova, S. O. Bachurin, and N. S. Zefirov
Volume 2010, Article ID 165482, 6 pages

Studies of the Antiproliferative Activity of Ruthenium (II) Cyclopentadienyl-Derived Complexes with Nitrogen Coordinated Ligands, Virtudes Moreno, Julia Lorenzo, Francesc X. Aviles, M. Helena Garcia, João P. Ribeiro, Tânia S. Morais, Pedro Florindo, and M. Paula Robalo
Volume 2010, Article ID 936834, 11 pages

Measuring the Cytochrome *c* Nitrite Reductase Activity—Practical Considerations on the Enzyme Assays, Célia M. Silveira, Stéphane Besson, Isabel Moura, José J. G. Moura, and M. Gabriela Almeida
Volume 2010, Article ID 634597, 8 pages

Antineoplastic Activity of New Transition Metal Complexes of 6-Methylpyridine-2-carbaldehyde-N(4)-ethylthiosemicarbazone: X-Ray Crystal Structures of [VO₂(mpETSC)] and [Pt(mpETSC)Cl], Shadia A. Elsayed, Ahmed M. El-Hendawy, Sahar I. Mostafa, Bertrand J. Jean-Claude, Margarita Todorova, and Ian S. Butler
Volume 2010, Article ID 149149, 11 pages

Computational Modeling of the Mechanism of Urease, Håkan Carlsson and Ebbe Nordlander
Volume 2010, Article ID 364891, 8 pages

Structural Properties, Cytotoxicity, and Anti-Inflammatory Activity of Silver(I) Complexes with tris(*p*-tolyl)Phosphine and 5-Chloro-2-Mercaptobenzothiazole, L. Kyros, N. Kourkoumelis, M. Kubicki, L. Male, M. B. Hursthouse, I. I. Verginadis, E. Gouma, S. Karkabounas, K. Charalabopoulos, and S. K. Hadjikakou
Volume 2010, Article ID 386860, 12 pages

Synthesis, Solution, and Structural Characterization of Tetrahydrofuran-2,2-Bisphosphonic Acid Disodium Salt, Elena Maltezou, Marios Stylianou, Sudeshna Roy, Chryssoula Drouza, and Anastasios D. Keramidas
Volume 2010, Article ID 563875, 7 pages

Organotin Compound Derived from 3-Hydroxy-2-formylpyridine Semicarbazone: Synthesis, Crystal Structure, and Antiproliferative Activity, Joanna Wiecek, Dimitra Kovala-Demertzi, Zbigniew Ciunik, Joanna Wietrzyk, Maria Zervou, and Mavroudis A. Demertzis
Volume 2010, Article ID 718606, 7 pages

Synthesis and Characterization of a Linear [Mn₃(O₂CMe)₄(py)₈]²⁺ Complex, Eleni E. Moushi, Christos Kizas, Vassilios Nastopoulos, and Anastasios J. Tasiopoulos
Volume 2010, Article ID 932569, 7 pages

Synthesis and Supramolecular Structure of a (5-(3-(1*H*-tetrazol-5-yl)phenyl)-1*H*-tetrazole) Cobalt Complex, George E. Kostakis, Christopher E. Anson, and Annie K. Powell
Volume 2010, Article ID 104329, 5 pages

Diorganotin Complexes of a Thiosemicarbazone, Synthesis: Properties, X-Ray Crystal Structure, and Antiproliferative Activity of Diorganotin Complexes, Joanna Wiecek, Dimitra Kovala-Demertzi, Zbigniew Ciunik, Maria Zervou, and Mavroudis A. Demertzis
Volume 2010, Article ID 867195, 9 pages

Synthesis and Biological Evaluation of New CRH Analogues, Spyridon Papazacharias, Vassiliki Magafa, Nicole Bernad, George Pairas, Georgios A. Spyroulias, Jean Martinez, and Paul Cordopatis
Volume 2010, Article ID 252348, 8 pages

Mononuclear and Dinuclear Manganese(II) Complexes from the Use of Methyl(2-pyridyl)ketone Oxime,
Constantinos G. Efthymiou, Vassilios Nastopoulos, Catherine Raptopoulou, Anastasios Tasiopoulos,
Spyros P. Perlepes, and Constantina Papatriantafyllopoulou
Volume 2010, Article ID 960571, 9 pages

Kinetic Studies and Mechanism of Hydrogen Peroxide Catalytic Decomposition by Cu(II) Complexes with Polyelectrolytes Derived from L-Alanine and Glycylglycine, Spyridon Skounas,
Constantinos Methenitis, George Pneumatikakis, and Michel Morcellet
Volume 2010, Article ID 643120, 9 pages

Zinc(II) and Nickel(II) Benzoate Complexes from the Use of 1-methyl-4,5-diphenylimidazole,
Konstantina A. Kounavi, Manolis J. Manos, Anastasios J. Tasiopoulos, Spyros P. Perlepes,
and Vassilios Nastopoulos
Volume 2010, Article ID 178034, 7 pages

Tetramic and Tetrionic Acids as Scaffolds in Bioinorganic and Bioorganic Chemistry, G. Athanasellis,
O. Igglessi-Markopoulou, and J. Markopoulos
Volume 2010, Article ID 315056, 11 pages

Biofunctional Characteristics of Lignite Fly Ash Modified by Humates: A New Soil Conditioner,
Konstantinos Chassapis, Maria Roulia, Evangelia Vrettou, Despina Fili, and Monica Zervaki
Volume 2010, Article ID 457964, 8 pages

Kinetics and Mechanism of the Reaction between Chromium(III) and 2,3-Dihydroxybenzoic Acid in Weak Acidic Aqueous Solutions, Athinoula L. Petrou, Vladimiro Thoma, and Konstantinos Tampouris
Volume 2010, Article ID 348692, 8 pages

Synthesis, Characterization, DNA Binding, and Photocleavage Activity of Oxorhenium (V) Complexes with α -Diimine and Quinoxaline Ligands, Christiana A. Mitsopoulou and Constantinos Dagas
Volume 2010, Article ID 973742, 9 pages

Synthetic Peptides as Structural Maquettes of Angiotensin-I Converting Enzyme Catalytic Sites,
Zinovia Spyraanti, Athanassios S. Galanis, George Pairas, Georgios A. Spyroulias, Evy Manessi-Zoupa,
and Paul Cordopatis
Volume 2010, Article ID 820476, 13 pages

A Synthetic Approach of New Trans-Substituted Hydroxylporphyrins, Dimitra Daphnomili,
Maria Grammatikopoulou, Catherine Raptopoulou, George Charalambidis, Theodore Lazarides,
and Athanasios G. Coutsolelos
Volume 2010, Article ID 307696, 6 pages

Interactions of Trivalent Lanthanide Cations with a New Hexadentate Di-Schiff Base: New Lanthanide(III) Complexes from (NE,N'E)-2,2'-(ethane-1,2-diylbis(oxy))bis(N-(pyridin-2-ylmethylene)ethanamine), Mantha Tsiouri, Konstantina Skorda, Christos Papadimitriou, Yang Li, J. Derek Woollins,
and John C. Plakatouras
Volume 2010, Article ID 613140, 7 pages

In Search for Titanocene Complexes with Improved Cytotoxic Activity: Synthesis, X-Ray Structure, and Spectroscopic Study of Bis(η^5 -cyclopentadienyl)difluorotitanium(IV), Elias Koleros,
Theocharis C. Stamatatos, Vassilis Psycharis, Catherine P. Raptopoulou, Spyros P. Perlepes,
and Nikolaos Klouras
Volume 2010, Article ID 914580, 6 pages

The Catalytic Function of Nonheme Iron (III) Complex for Hydrocarbon Oxidation, Giorgos Bilis and Maria Louloudi

Volume 2010, Article ID 861892, 9 pages

Zinc Binding Properties of Engineered RING Finger Domain of Arkadia E3 Ubiquitin Ligase,

Christos T. Chasapis, Ariadni K. Loutsidou, Malvina G. Orkoulou, and Georgios A. Spyroulias

Volume 2010, Article ID 323152, 7 pages

Hydrogen-Bonded Networks Based on Cobalt(II), Nickel(II), and Zinc(II) Complexes of

N,N'-Diethylurea, Labrini Drakopoulou, Catherine P. Raptopoulou, Aris Terzis, and Giannis S. Papaefstathiou

Volume 2010, Article ID 618202, 12 pages

Structurally Diverse Metal Coordination Compounds, Bearing Imidodiphosphinate and Diphosphinoamine Ligands, as Potential Inhibitors of the Platelet Activating Factor,

Alexandros B. Tsoupras, Maria Roulia, Eleftherios Ferentinos, Ioannis Stamatopoulos, Constantinos A. Demopoulos, and Panayotis Kyritsis

Volume 2010, Article ID 731202, 8 pages

Kinetics and Mechanisms of the Chromium(III) Reactions with 2,4- and 2,5-Dihydroxybenzoic Acids in Weak Acidic Aqueous Solutions,

Kimon Zavitsanos and Athinoula L. Petrou

Volume 2010, Article ID 832768, 10 pages

Use of the 2-Pyridinealdoxime/N,N'-Donor Ligand Combination in Cobalt(III) Chemistry: Synthesis and Characterization of Two Cationic Mononuclear Cobalt(III) Complexes,

Konstantis F. Konidaris, Catherine P. Raptopoulou, Vassilis Psycharis, Spyros P. Perlepes, Evy Manessi-Zoupa, and Theodoros C. Stamatatos

Volume 2010, Article ID 159656, 7 pages

Synthesis, Structure, and Antiproliferative Activity of Three Gallium(III) Azole Complexes,

Stergios Zanas, Giannis S. Papaefstathiou, Catherine P. Raptopoulou, Konstantinos T. Papazisis, Vasiliki Vala, Dimitra Zambouli, Alexandros H. Kortsaris, Dimitrios A. Kyriakidis, and Theodoros F. Zafiroopoulos

Volume 2010, Article ID 168030, 10 pages

Synthesis, X-Ray Structure, and Characterization of *Catena*-bis(benzoate)bis{*N,N*-bis(2-hydroxyethyl)glycinate}cadmium(II),

Eugenia Katsoulakou, Konstantis F. Konidaris, Catherine P. Raptopoulou, Vassilis Psycharis, Evy Manessi-Zoupa, and Spyros P. Perlepes

Volume 2010, Article ID 281932, 8 pages

Synthesis, Crystal Structures, and DNA Binding Properties of Zinc(II) Complexes with 3-Pyridine Aldoxime,

Konstantis F. Konidaris, Rigini Papi, Eugenia Katsoulakou, Catherine P. Raptopoulou, Dimitrios A. Kyriakidis, and Evy Manessi-Zoupa

Volume 2010, Article ID 803424, 7 pages

Editorial

Special Issue in Honor of Professor Nick Hadjiliadis' Retirement

Evy Manessi-Zoupa and Spyros P. Perlepes

Department of Chemistry, University of Patras, 26504 Patras, Greece

Correspondence should be addressed to Evy Manessi-Zoupa, e.manesi@chemistry.upatras.gr and Spyros P. Perlepes, perlepes@patreas.upatras.gr

Received 28 November 2010; Accepted 28 November 2010

Copyright © 2010 E. Manessi-Zoupa and S. P. Perlepes. This is an open access article distributed under the Creative Commons Attribution License, which permits unrestricted use, distribution, and reproduction in any medium, provided the original work is properly cited.

We are more than happy to see the completion of this special issue. The idea for this issue came from the recognition that bioinorganic chemistry research in Greece has been tremendously developed over the last three decades or so. The obvious reason is that this period has seen significant changes to the Greek chemistry community. New Laws permitted independent research by all the members of the academic staff, especially at the Lecturer and Assistant Professor positions. Nowadays, all five chemistry departments in Greek Universities (Athens, Thessaloniki, Patras, Ioannina, Crete) have strong research programs in bioinorganic chemistry. Bioinorganic chemistry was also developed in a brilliant way at three institutes in the National Center of Scientific Research "Demokritos," located in Athens. Many appointments by the universities and "Demokritos" created new generations of scientists with their own research ideas and directions, and they are currently helping to shape the future of bioinorganic chemistry in Greece. Another important reason for the progress of bioinorganic chemistry in Greece has been the scientific impact and personality of *Professor Nick Hadjiliadis*, the scientist who undoubtedly introduced bioinorganic chemistry to and pioneered research in this field in Greece. This special issue is devoted to him.

Professor Nick Hadjiliadis retired in September 2008 (he is currently Emeritus Professor) after a brilliant academic career, mainly at the University of Ioannina, Ioannina, Greece. However, he continues to be involved in research and other academic activities. His scientific and professional achievements are numerous. He has carried out excellent research in at least four interesting areas of contemporary bioinorganic chemistry, holding an outstanding publication record in peer-review journals and thematic books. Many

of his former Ph.D. students occupy academic or research positions in Greece. He has received international awards and organized international conferences and meetings in Greece and abroad, including the very successful 5th International Symposium on Applied Bioinorganic Chemistry. He has established and directed for more than 10 years the prestigious interuniversity graduate programme "Bioinorganic Chemistry" in Greece. Finally, he was Editor-in-Chief of Bioinorganic Chemistry and Applications and other bioinorganic chemistry books. His impact on the scientific community goes far beyond the just mentioned aspects. Nick had the ability to inspire many Greek inorganic chemists to try bioinorganic chemistry projects, often giving smart ideas to them. In addition to being an excellent scientist, Nick is also a friendly and broadly educated person (but strict with his collaborators when he was seeing them relaxing and being out of the schedule) with whom it was a privilege for us to be associated for the last 25–30 years.

This issue contains 42 papers. There are contributions from some of the scientists with whom Nick has been collaborating and from his old students. However, there are many contributions from researchers who gladly accepted our invitation to participate as a means to show their respect for the scientist and the man. Seventeen (17) papers are entirely from Greece, fifteen (15) contributions come from foreign laboratories, and the rest (10) describe research resulting from collaboration between Greek and foreign universities and institutes.

We have attempted as far as possible to have this special issue reflect research activities on currently "hot" topics of bioinorganic chemistry [1] and the respect that Professor Hadjiliadis commands through the scientific community

in our country and internationally. The “hot” areas of bioinorganic chemistry covered in the issue include—among others—metal entry into cells and active sites, understanding metalloenzymes, biomimetic chemistry (success in this endeavor has the potential not only to provide insights in the working mechanisms of the enzymes but also to produce new chemical catalysts for promoting difficult reactions under mild conditions), probing metal ions in cells (this topic has been important for therapeutic, toxic, and pathological aspects of medicinal applications of bioinorganic chemistry), and biomaterials. It can be seen from the contributions of this special issue that elucidating the structures and reactivities of metallobiomolecules, mimicking and utilizing molecular and macromolecular systems at the interface of biology and inorganic chemistry continue to be fertile research areas which promise new discoveries.

On behalf of all the authors, and indeed the Greek chemical community as a whole, we wish Professor Nick Hadjiladis a happy retirement, good health, and many more years of scientific success.

Last, but not least, we would like to express our gratitude to (i) the reviewers of the papers for their time to study the submitted manuscripts and for their valuable comments, (ii) Dr. Konstantis F. Konidaris for his every day help in many scientific and practical problems concerning our correspondence with the authors, and (iii) the officials, journal developers, and editorial assistants of Bioinorganic Chemistry and Applications (we have met such perfect professionals for the first time in our job!) for their great help during the organization of the special issue.

*Evy Manessi-Zoupa
Spyros P. Perlepes*

References

- [1] S. J. Lippard, “The interface of inorganic chemistry and biology,” *Journal of the American Chemical Society*, vol. 132, no. 42, pp. 14689–14693, 2010.

Research Article

Low-Power Ultrasounds as a Tool to Culture Human Osteoblasts inside Cancellous Hydroxyapatite

Lorenzo Fassina,^{1,2} Enrica Saino,^{2,3} Maria Gabriella Cusella De Angelis,^{2,4}
Giovanni Magenes,^{1,2} Francesco Benazzo,^{2,5} and Livia Visai^{2,3}

¹ *Dipartimento di Informatica e Sistemistica, University of Pavia, 27100 Pavia, Italy*

² *Centre for Tissue Engineering (C.I.T.), University of Pavia, 27100 Pavia, Italy*

³ *Dipartimento di Biochimica, University of Pavia, 27100 Pavia, Italy*

⁴ *Dipartimento di Medicina Sperimentale, University of Pavia, 27100 Pavia, Italy*

⁵ *Dipartimento SMEC, IRCCS San Matteo, University of Pavia, 27100 Pavia, Italy*

Correspondence should be addressed to Lorenzo Fassina, lorenzo.fassina@unipv.it

Received 4 January 2010; Accepted 30 January 2010

Academic Editor: Spyros Perlepes

Copyright © 2010 Lorenzo Fassina et al. This is an open access article distributed under the Creative Commons Attribution License, which permits unrestricted use, distribution, and reproduction in any medium, provided the original work is properly cited.

Bone graft substitutes and cancellous biomaterials have been widely used to heal critical-size long bone defects due to trauma, tumor resection, and tissue degeneration. In particular, porous hydroxyapatite is widely used in reconstructive bone surgery owing to its biocompatibility. In addition, the *in vitro* modification of cancellous hydroxyapatite with osteogenic signals enhances the tissue regeneration *in vivo*, suggesting that the biomaterial modification could play an important role in tissue engineering. In this study, we have followed a tissue-engineering strategy where ultrasonically stimulated SAOS-2 human osteoblasts proliferated and built their extracellular matrix inside a porous hydroxyapatite scaffold. The ultrasonic stimulus had the following parameters: average power equal to 149 mW and frequency of 1.5 MHz. In comparison with control conditions, the ultrasonic stimulus increased the cell proliferation and the surface coating with bone proteins (decorin, osteocalcin, osteopontin, type-I collagen, and type-III collagen). The mechanical stimulus aimed at obtaining a better modification of the biomaterial internal surface in terms of cell colonization and coating with bone matrix. The modified biomaterial could be used, in clinical applications, as an implant for bone repair.

1. Introduction

One of the key challenges in reconstructive bone surgery is to provide living constructs that possess the ability to integrate in the surrounding tissue. Bone graft substitutes, such as autografts, allografts, xenografts, and porous biomaterials have been widely used to heal critical-size long bone defects due to trauma, tumor resection, and tissue degeneration. The biomaterials used to build 3D scaffolds for bone tissue engineering are, for instance, the hydroxyapatite [1], the partially demineralized bone [2], biodegradable porous polymer-ceramic matrices [3], and bioactive glasses [4, 5].

The preceding osteoinductive and osteoconductive biomaterials are ideal in order to follow a typical approach of the tissue engineering, an approach that involves the seeding

and the *in vitro* culturing of cells within a cancellous scaffold before the implantation.

The tissue-engineering method is of great importance. In order to overcome the drawbacks associated with the standard culture systems *in vitro*, such as limited diffusion and inhomogeneous cell-matrix distribution, several bioreactors have been designed to provide different physical stimuli: a rotating vessel bioreactor [6], a perfusion bioreactor [7], or an electromagnetic bioreactor [8], for instance. The ideal feature of a bioreactor is the supplying of suitable levels of oxygen, nutrients, cytokines, growth factors, and appropriate physical stimuli, in order to populate, with living bone cells and mineralized extracellular matrix, the volume of a porous biomaterial for reconstructive bone surgery: this living and biocompatible tissue-engineering construct could

be implanted together with the insertion of a vascular pedicle [9].

Gorna and Gogolewski [10, 11] have drawn attention to the ideal features of a bone graft substitute: it should be porous with interconnected pores of adequate size (at least $200\ \mu\text{m}$) allowing for the ingrowth of capillaries and perivascular tissues; it should attract mesenchymal stem cells from the surrounding bone and promote their differentiation into osteoblasts; it should avoid shear forces at the interface between bone and bone graft substitute; it should be biodegradable.

In this study, following the preceding “golden rules” of Gorna and Gogolewski, we have elected porous hydroxyapatite [12–14] as cancellous bone graft substitute and, using an ultrasonic stimulation [15], we have attempted to populate it with extracellular matrix and osteoblasts, of which cell function can be ultrasonically modulated [15].

Hydroxyapatite is widely used in reconstructive bone surgery owing to its biocompatibility. The *in vitro* modification of porous hydroxyapatite, with osteogenic signals of the transforming growth factor- β superfamily and with bone morphogenetic proteins, enhances the tissue regeneration *in vivo* [16], suggesting that the modification of hydroxyapatite could play an important role in tissue engineering.

As consequence, aiming, in a future work, at accelerated and enhanced bone regeneration *in vivo*, in the present study of tissue engineering, we show a particular “biomimetic strategy” that consists in the *in vitro* modification of porous hydroxyapatite with proliferated osteoblasts and their extracellular matrix produced *in situ*. In other words, applying an ultrasonic wave [15], our aim was to enhance a bone cell culture inside cancellous hydroxyapatite, that is, to coat the hydroxyapatite internal surface with physiological and biocompatible cell-matrix layers. Using this approach, the *in vitro* cultured material could be theoretically used, in clinical applications, as an osteointegrable implant.

2. Materials and Methods

2.1. Hydroxyapatite Disks. Porous Orthoss bovine hydroxyapatite disks (diameter, 8 mm; height, 4 mm) were kindly provided by Geistlich Pharma AG (Wolhusen, Switzerland) [12–14]. The biomaterial had the following characteristics: internal surface area of $97\ \text{m}^2/\text{g}$, average porosity equal to 60%, crystal dimensions of $10\div 60\ \text{nm}$, and Ca/P ratio equal to 2.03, as in normal human cancellous bone (Figure 1).

2.2. Cells. The human osteosarcoma cell line SAOS-2 was obtained from the American Type Culture Collection (HTB85, ATCC, Rockville, MD). The cells were cultured in McCoy’s 5A modified medium with L-glutamine and HEPES (Cambrex Bio Science Baltimore, Inc., Baltimore, MD), supplemented with 15% fetal bovine serum, 2% sodium pyruvate, 1% antibiotics, $10^{-8}\ \text{M}$ dexamethasone, and 10 mM β -glycerophosphate (Sigma-Aldrich, Inc., Milwaukee, WI). Ascorbic acid, another osteogenic supplement, is a component of McCoy’s 5A modified medium. The cells were cultured at 37°C with 5% CO_2 , routinely trypsinized

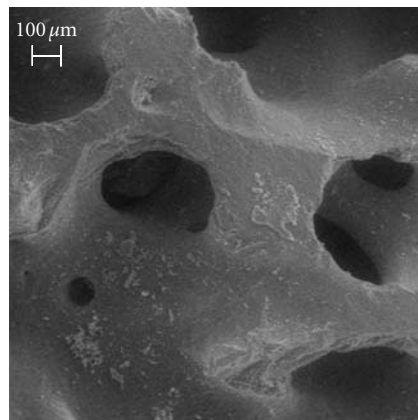


FIGURE 1: SEM image of unseeded hydroxyapatite, bar equal to $100\ \mu\text{m}$.

after confluency, counted, and seeded onto the hydroxyapatite disks.

2.3. Cell Seeding. In order to anchor the hydroxyapatite disks to two standard well-plates, 3% (w/v) agarose solution was prepared and sterilized in autoclave, and during cooling, at 45°C , $100\ \mu\text{L}$ of agarose solution were poured inside the wells to hold the placed hydroxyapatite disks and to fix them after completed cooling.

The well-plates with the biomaterial disks were sterilized by ethylene oxide at 38°C for 8 hours at 65% relative humidity. After 24 hours of aeration in order to remove the residual ethylene oxide, the disks were ready inside the two culture systems: the “static,” that is, the control well-plate without external stimulus and the “ultrasonic,” that is, the ultrasonically stimulated well-plate.

A cell suspension of 10×10^6 cells in $400\ \mu\text{L}$ was added onto the top of each disk and, after 0.5 hour, $600\ \mu\text{L}$ of culture medium was added to cover the disks. Cells were allowed to attach overnight, then the static culture was continued in the standard well-plate and the ultrasound stimulation was applied for the first time.

2.4. Ultrasound Stimulation. An ultrasound stimulus [15] was applied through the culture medium by a FAST ultrasound generator (Igea, Carpi, Italy) to the seeded hydroxyapatite disks. The mechanical wave had the following characteristics: signal frequency equal to $1.5 \pm 0.03\ \text{MHz}$, duty cycle of $200 \pm 4\ \mu\text{s}$, repetition rate equal to $1 \pm 0.02\ \text{kHz}$, and temporal average power of $149 \pm 3\ \text{mW}$. Low-intensity ultrasound stimulus accelerates the fracture healing in clinical studies [17].

The ultrasonic culture was placed into a standard cell culture incubator with an environment of 37°C and 5% CO_2 , and it was stimulated 20 min/day for a total of 22 days. The culture medium was changed on days 4, 7, 10, 13, 16, and 19.

2.5. Standard Well-Plate Culture. The static culture was placed into a standard cell culture incubator. The duration

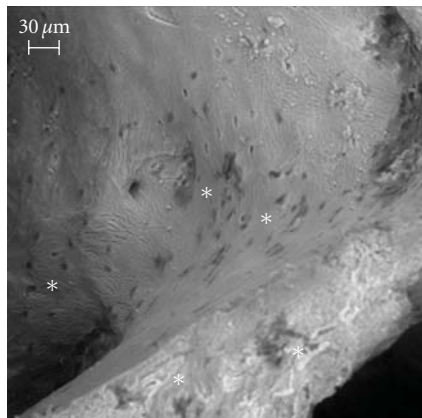


FIGURE 2: SEM image of the static culture, bar equal to 30 μm. The osteoblasts are in the “backscattered depressions” near the juxtaposed asterisks: at the end of the culture period, statically cultured cells were few and, essentially, not surrounded by extracellular matrix; therefore, wide biomaterial regions remained devoid of cell-matrix complexes.

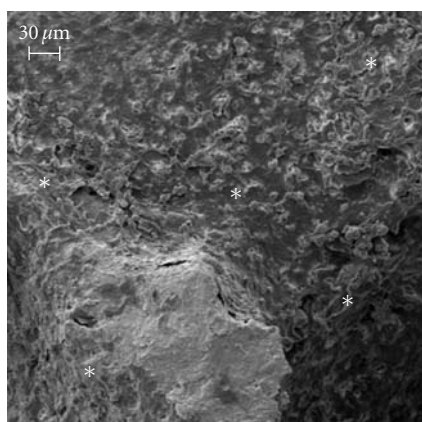


FIGURE 3: SEM image of the ultrasonic culture, bar equal to 30 μm. During the culture period, the physical stimulus caused a wide-ranging coat of the internal surface of the biomaterial: several osteoblasts proliferated and the biomaterial was tending to be hidden by cell-matrix layers (asterisks).

of the static culture was 22 days and the culture medium was changed on days 4, 7, 10, 13, 16, and 19.

2.6. Scanning Electron Microscopy (SEM) Analysis. At the end of the culture period, the disks were fixed with 2.5% (v/v) glutaraldehyde solution in 0.1 M Na-cacodylate buffer (pH = 7.2) for 1 hour at 4°C, washed with Na-cacodylate buffer, and then dehydrated at room temperature in a gradient ethanol series up to 100%. The samples were kept in 100% ethanol for 15 minutes, and then critical point-dried with CO₂. The specimens were mounted on aluminum stubs, sputter coated with gold (degree of purity equal to 99%), and then observed with a Leica Cambridge Stereoscan microscope (Leica Microsystems, Bensheim, Germany).

2.7. DNA Content. At the end of the culture period, the cells were lysed by a freeze-thaw method in sterile deionized distilled water and the released DNA content was evaluated with a fluorometric method (PicoGreen, Molecular Probes, Eugene, OR). A DNA standard curve [15], obtained from a known amount of osteoblasts, was used to express the results as cell number per disk.

2.8. Set of Rabbit Polyclonal Antisera. Fisher et al. (<http://csdb.nidcr.nih.gov/csdb/antisera.htm>, National Institutes of Health, National Institute of Dental and Craniofacial Research, Craniofacial and Skeletal Diseases Branch, Matrix Biochemistry Unit, Bethesda, MD) presented us, generously, with the following rabbit polyclonal antibody immunoglobulins G: antiosteocalcin, anti-type-I collagen, anti-type-III collagen, antidecorin, and antiosteopontin (antiseraum LF-32, LF-67, LF-71, LF-136, and LF-166, respectively) [18].

2.9. Set of Purified Proteins. Decorin [19], osteocalcin (immunoenzymatic assay kit, BT-480, Biomedical Technologies, Inc., Stoughton, MA), osteopontin (immunoenzymatic assay kit, 900-27, Assay Designs, Inc., Ann Arbor, MI), type-I collagen [20], and type-III collagen (Sigma-Aldrich) were used.

2.10. Confocal Microscopy. At the end of the culture period, the disks were fixed with 4% (w/v) paraformaldehyde solution in 0.1 M phosphate buffer (pH = 7.4) for 8 hours at room temperature and washed with PBS (137 mM NaCl, 2.7 mM KCl, 4.3 mM Na₂HPO₄, 1.4 mM KH₂PO₄, pH = 7.4) three times for 15 minutes. The disks were then blocked by incubating with PAT (PBS containing 1% [w/v] bovine serum albumin and 0.02% [v/v] Tween 20) for 2 hours at room temperature and washed.

L. Fisher’s antidecorin, antiosteocalcin, antiosteopontin, anti-type-I collagen, and anti-type-III collagen rabbit polyclonal antisera were used as primary antibodies with a dilution equal to 1 : 1000 in PAT. The incubation with the primary antibodies was performed overnight at 4°C, whereas the negative controls were based upon the incubation, overnight at 4°C, with PAT instead of the primary antibodies. The disks and the negative controls were washed and incubated with Alexa Fluor 488 goat antirabbit IgG (H+L) (Molecular Probes) with a dilution of 1 : 500 in PAT for 1 hour at room temperature.

At the end of the incubation, the disks were washed in PBS, counterstained with Hoechst solution (2 μg/mL) to target the cellular nuclei, and then washed. The images were taken by blue excitation with a confocal microscope (TCS SPII, Leica Microsystems) equipped with a digital image capture system at 100× magnification.

2.11. Extraction of the Extracellular Matrix Proteins from the Cultured Disks and Enzyme-Linked Immunosorbent Assay (ELISA). At the end of the culture period, in order to evaluate the amount of the extracellular matrix constituents over the internal and external hydroxyapatite surfaces, the disks

were washed extensively with sterile PBS (137 mM NaCl, 2.7 mM KCl, 4.3 mM Na₂HPO₄, 1.4 mM KH₂PO₄, pH = 7.4) in order to remove the culture medium, and then incubated for 24 hours at 37°C with 1 mL of sterile sample buffer (1.5 M Tris-HCl, 60% [w/v] sucrose, 0.8% [w/v] sodium dodecyl sulphate, pH = 8.0). At the end of the incubation period, the sample buffer aliquots were removed, and then the disks were centrifuged at 4000 rpm for 15 minutes in order to collect the sample buffer entrapped into the pores. The total protein concentration in the two culture systems was evaluated by the BCA Protein Assay Kit (Pierce Biotechnology, Inc., Rockford, IL). The total protein concentration was $749 \pm 108 \mu\text{g/mL}$ in the static culture and $1527 \pm 274 \mu\text{g/mL}$ in the ultrasonic culture ($P < .05$). After matrix extraction, the disks were incubated, once again, for 24 hours at 37°C with 1 mL of sterile sample buffer, and no protein content was detected.

Calibration curves to measure decorin, osteocalcin, osteopontin, type-I collagen, and type-III collagen were performed. Microtiter wells were coated with increasing concentrations of each purified protein, from 1 ng to 2 μg , in coating buffer (50 mM Na₂CO₃, pH = 9.5) overnight at 4°C. Some of the wells were coated with bovine serum albumin (BSA) as a negative control. In order to measure the extracellular matrix amount of each protein by an ELISA, microtiter wells were coated, overnight at 4°C, with 100 μL of the extracted extracellular matrix (20 $\mu\text{g/mL}$ in coating buffer). After three washes with PBST (PBS containing 0.1% [v/v] Tween 20), the wells were blocked by incubating with 200 μL of PBS containing 2% (w/v) BSA for 2 hours at 22°C. The wells were subsequently incubated for 1.5 hours at 22°C with 100 μL of the L. Fisher's antidecorin, antiosteocalcin, antiosteopontin, anti-type-I collagen, and anti-type-III collagen rabbit polyclonal antisera (1 : 500 dilution in 1% BSA). After washing, the wells were incubated for 1 hour at 22°C with 100 μL of HRP-conjugated goat anti-rabbit IgG (1 : 1000 dilution in 1% BSA).

The wells were finally incubated with 100 μL of development solution (phosphate-citrate buffer with *o*-phenylenediamine dihydrochloride substrate). The color reaction was stopped with 100 μL of 0.5 M H₂SO₄ and the absorbance values were measured at 490 nm with a microplate reader (Bio-Rad Laboratories, Inc., Hercules, CA). The amount of extracellular matrix constituents inside the disks is expressed as $\text{fg}/(\text{cell} \times \text{disk})$.

2.12. Statistics. The disks number was 24 in each repeated experiment (12 disks in the control culture and 12 disks in the ultrasonic culture). The experiment was repeated 4 times. Results are expressed as mean \pm standard deviation. In order to compare the results between the two culture systems, one-way analysis of variance (ANOVA) with *post hoc* Bonferroni test was applied, electing a significance level of 0.05.

3. Results

The human SAOS-2 osteoblasts were seeded onto porous hydroxyapatite disks, and then cultured without or with

an ultrasonic stimulus for 22 days. These culture methods permitted the study of the SAOS-2 cells as they modified the biomaterial through the proliferation and the coating with extracellular matrix. The cell-matrix distribution was compared between the two culture systems.

3.1. Microscope Analysis. In comparison to control condition, SEM images revealed that, due to the ultrasound stimulus, the osteoblasts proliferated and built their extracellular matrix over the available internal hydroxyapatite surface (Figures 2 and 3). At the end of the culture period, statically cultured cells were few and, essentially, not surrounded by extracellular matrix, therefore wide biomaterial regions remained devoid of cell-matrix complexes (Figure 2). In contrast, the physical stimulus caused a wide-ranging coat of the internal surface of the biomaterial: several osteoblasts proliferated and the biomaterial was tending to be hidden by cell-matrix layers (Figure 3).

The immunolocalization of type-I collagen and decorin with the counterstaining of the cellular nuclei showed the stimulation effects in terms of higher cell proliferation and more intense building of the extracellular matrix (Figures 4 and 5). The immunolocalization of osteocalcin, osteopontin, and type-III collagen revealed similar results (data not shown).

These observations were confirmed by the measure of the DNA content at the end of the culture period: in the static culture, the cell number per disk grew to $22.1 \times 10^6 \pm 3.2 \times 10^4$ and in the ultrasonic culture to $34.7 \times 10^6 \pm 3.9 \times 10^4$ with $P < .05$.

3.2. Extracellular Matrix Extraction. In order to evaluate the amount of bone extracellular matrix inside the hydroxyapatite disks, an ELISA of the extracted matrix was performed: at the end of the culture period, in comparison with the static culture, the ultrasound stimulation significantly increased the internal surface coating with decorin, osteocalcin, osteopontin, type-I collagen, and type-III collagen ($P < .05$) (Table 1).

4. Discussion

The aim of this study was the *in vitro* modification of a porous hydroxyapatite with extracellular matrix and osteoblasts to make the biomaterial more biocompatible for the bone repair *in vivo*.

A discussion about the concept of "biocompatibility" is necessary. When a biomaterial is implanted in a biological environment, a nonphysiologic layer of adsorbed proteins mediates the interaction of the surrounding host cells with the material surface. The body interprets this protein layer as a foreign invader that must be walled off in an avascular and tough collagen sac. Therefore, the biomedical surfaces must be developed so that the host tissue can recognize them as "self". Castner and Ratner think the "biocompatible surfaces" of the "biomaterials that heal" as the surfaces with the characters of a "clean, fresh wound" [21]: these "self-surfaces" could obtain a physiological inflammatory reaction

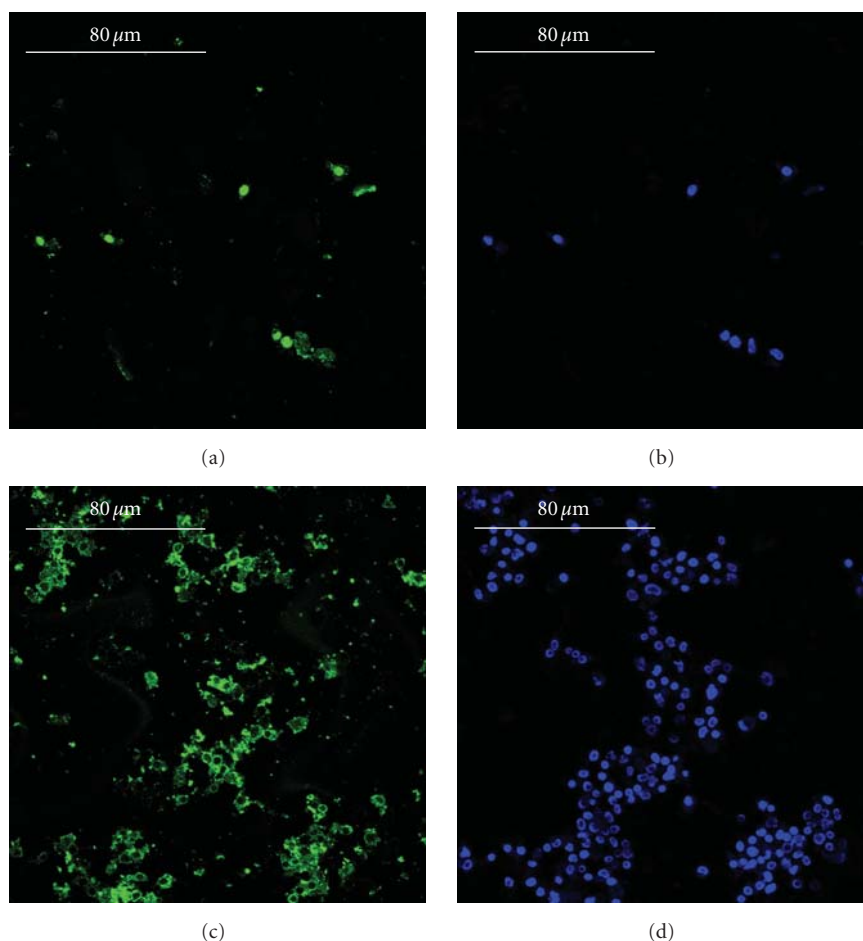


FIGURE 4: Immunolocalization of type-I collagen (panels a and c, green) and cellular nuclei (panels b and d, blue) in the static culture (panels a and b) and in the ultrasonic culture (panels c and d), bars equal to 80 μm . During the culture period, in the control (panels a and b), the osteoblasts built a scanty amount of bone matrix, whereas, in the stimulated culture (panels c and d), the osteoblasts secreted a wide amount of matrix. The immunolocalization of osteocalcin, osteopontin, and type-III collagen revealed similar results.

TABLE 1: Amount of extracellular matrix constituents inside hydroxyapatite.

	Matrix protein total coating after 22 days of culture in fg/(cell \times disk)		
	Static culture	Ultrasonic culture	Ultrasonic /Static
Decorin	5.58 ± 0.22	15.25 ± 0.42	2.73-fold
Osteocalcin	1.79 ± 0.33	5.76 ± 0.39	3.22-fold
Osteopontin	1.75 ± 0.73	3.04 ± 0.47	1.74-fold
Type-I collagen	3.72 ± 0.49	16.85 ± 0.95	4.53-fold
Type-III collagen	4.59 ± 0.13	11.04 ± 0.71	2.40-fold

Table note: $P < .05$ in all "Static" versus "Ultrasonic" comparisons.

leading to normal healing. In this study, we have followed a biomimetic strategy where the seeded osteoblasts built a biocompatible surface made of bone matrix [15, 22].

To enhance the coating of the biomaterial internal surface, an ultrasonic wave was applied to the seeded biomaterial [15]. The ultrasound stimulus increased the cell proliferation around 1.6-fold. Furthermore, the ultrasonic wave significantly enhanced the synthesis of type-I collagen, decorin, osteopontin, osteocalcin, and type-III collagen,

which are fundamental constituents of the physiological bone matrix: in particular, type-I collagen is the most important and abundant structural protein of the bone matrix; decorin is a proteoglycan considered a key regulator for the assembly and the function of many extracellular matrix proteins with a major role in the lateral growth of the collagen fibrils, delaying the lateral assembly on the surface of the fibrils; osteopontin is an extracellular glycosylated bone phosphoprotein secreted at the early stages

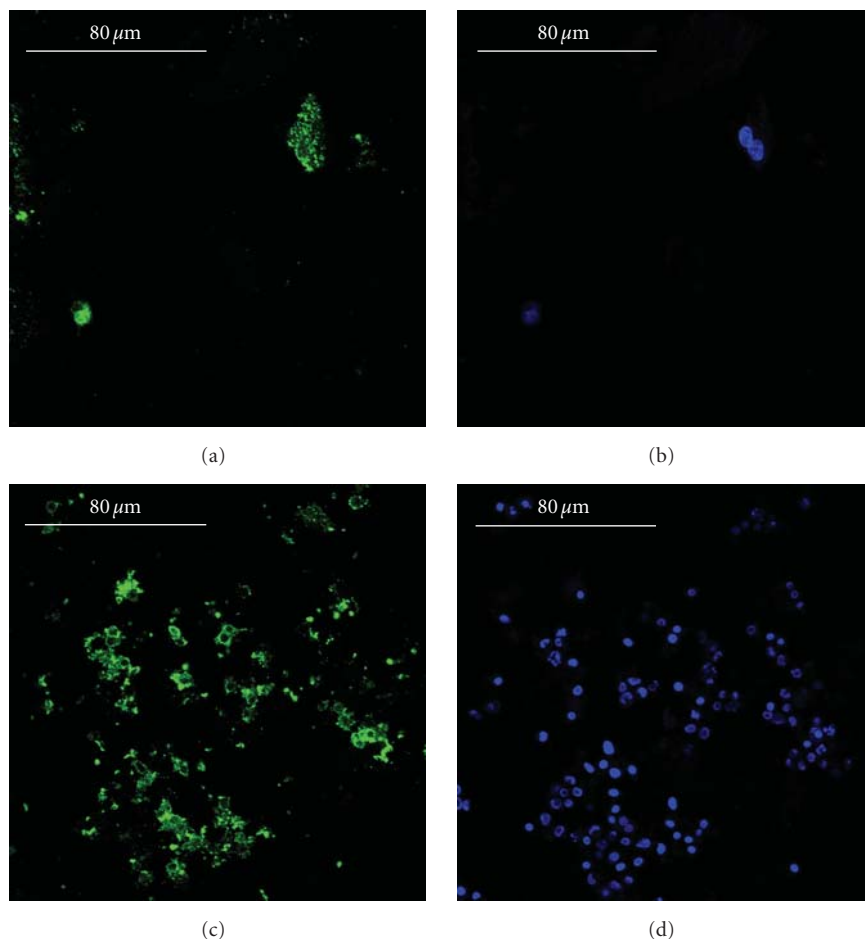


FIGURE 5: Immunolocalization of decorin (panels a and c, green) and cellular nuclei (panels b and d, blue) in the static culture (panels a and b) and in the ultrasonic culture (panels c and d), bars equal to $80\ \mu\text{m}$. During the culture period, in the control (panels a and b), the osteoblasts produced a very little amount of decorin, a key regulator for matrix spatial organization, whereas, in the stimulated culture (panels c and d), the osteoblasts secreted a larger amount of 3D organized bone matrices.

of the osteogenesis before the onset of the mineralization, it binds calcium, it is likely to be involved in the regulation of the hydroxyapatite crystal growth, and, through specific interaction with the vitronectin receptor, it promotes the attachment of the cells to the matrix; osteocalcin is secreted after the onset of mineralization and it binds to bone minerals.

The preceding results could be explained with a signaling model. The ultrasound stimulation raises the net Ca^{2+} flux in the osteoblast cytosol and the release of the intracellular Ca^{2+} [23–25]. According to Pavalko's signaling model, the increase of the cytosolic Ca^{2+} concentration is the starting point of signaling pathways, which cause the secretion of prostaglandins enhancing the osteoblast proliferation, and which target specific bone matrix genes [23].

Consistent with Pavalko's model, mechanically stimulated osteoblasts produce autocrine and paracrine prostaglandin signal for cell proliferation; the same mechanically stimulated osteoblasts produce bone extracellular matrix. Prostaglandins are released in the culture medium, whereas the proteins are deposited onto the biomaterial. Even if

prostaglandins and proteins have partially common biochemical pathways [23], they have a different geometrical destination: the medium and the material surface, respectively. For that reason, the efficiency in prostaglandin action (cell proliferation enhancement of 1.6-fold) was different from the efficiency of matrix deposition (biomaterial coating enhancement of $1.7\div 4.5$ -fold as in Table 1).

In this study, the ultrasonic stimulus was a physical method to obtain the biomimetic modification of the material, whose internal surface was coated by osteoblasts and by a layer of bone matrix. The use of a cell line showed the potential of the ultrasound stimulation; nevertheless, appropriately tuning the parameters of the ultrasonic wave, the stimulus duration, and the culture time, a better result could be obtained with autologous bone marrow stromal cells instead of SAOS-2 osteoblasts for total immunocompatibility with the patient. In addition, after the *in vivo* implantation of the cultured cancellous hydroxyapatite, an ultrasound therapy could be applied with the same wave parameters [15] to enhance the patient healing [17].

In conclusion, we theorize that the cultured “self-surface” could be used fresh, that is, rich in autologous cells and matrix, or after sterilization with ethylene oxide, that is, rich only in autologous matrix. In future work, we intend to use our constructs, which are rich in autologous matrix, as a simple, storable, tissue-engineering product for the bone repair [22].

Acknowledgments

The authors thank L. W. Fisher, K. Martin, S. Setti, R. Cadossi, A. Mortara, D. Piconi, and P. Vaghi. Hydroxyapatite disks were kindly provided by Geistlich Pharma (Wolhusen, Switzerland). The FAST ultrasound generator was a gift from Igea (Carpi, Italy). This work was supported by Fondazione Cariplo Grants (2004.1424/10.8485 and 2006.0581/10.8485) to Francesco Benazzo, by PRIN Grant (2006) from Italian Ministry of Education, University and Research to Livia Visai, and by FIRB Grant (RBIP06FH7J) from Italian Ministry of Education, University and Research to Maria Gabriella Cusella De Angelis.

References

- [1] M. Nishikawa, A. Myoui, H. Ohgushi, M. Ikeuchi, N. Tamai, and H. Yoshikawa, “Bone tissue engineering using novel interconnected porous hydroxyapatite ceramics combined with marrow mesenchymal cells: quantitative and three-dimensional image analysis,” *Cell Transplantation*, vol. 13, no. 4, pp. 367–376, 2004.
- [2] J. R. Mauney, J. Blumberg, M. Pirun, V. Volloch, G. Vunjak-Novakovic, and D. L. Kaplan, “Osteogenic differentiation of human bone marrow stromal cells on partially demineralized bone scaffolds in vitro,” *Tissue Engineering*, vol. 10, no. 1–2, pp. 81–92, 2004.
- [3] J. E. Devin, M. A. Attawia, C. T. Laurencin, et al., “Three-dimensional degradable porous polymer-ceramic matrices for use in bone repair,” *Journal of Biomaterials Science, Polymer Edition*, vol. 7, no. 8, pp. 661–669, 1996.
- [4] S. Deb, R. Mandegaran, and L. Di Silvio, “A porous scaffold for bone tissue engineering/45S5 Bioglass® derived porous scaffolds for co-culturing osteoblasts and endothelial cells,” *Journal of Materials Science: Materials in Medicine*, vol. 21, no. 3, pp. 893–905, 2010.
- [5] L. Francis, D. Meng, J. C. Knowles, I. Roy, and A. R. Boccacini, “Multi-functional P(3HB) microsphere/45S5 Bioglass®-based composite scaffolds for bone tissue engineering,” *Acta Biomaterialia*. In press.
- [6] E. A. Botchwey, S. R. Pollack, E. M. Levine, and C. T. Laurencin, “Bone tissue engineering in a rotating bioreactor using a microcarrier matrix system,” *Journal of Biomedical Materials Research*, vol. 55, no. 2, pp. 242–253, 2001.
- [7] L. Fassina, L. Visai, L. Asti, et al., “Calcified matrix production by SAOS-2 cells inside a polyurethane porous scaffold, using a perfusion bioreactor,” *Tissue Engineering*, vol. 11, no. 5–6, pp. 685–700, 2005.
- [8] L. Fassina, L. Visai, F. Benazzo, et al., “Effects of electromagnetic stimulation on calcified matrix production by SAOS-2 cells over a polyurethane porous scaffold,” *Tissue Engineering*, vol. 12, no. 7, pp. 1985–1999, 2006.
- [9] S. Akita, N. Tamai, A. Myoui, et al., “Capillary vessel network integration by inserting a vascular pedicle enhances bone formation in tissue-engineered bone using interconnected porous hydroxyapatite ceramics,” *Tissue Engineering*, vol. 10, no. 5–6, pp. 789–795, 2004.
- [10] K. Gorna and S. Gogolewski, “Biodegradable polyurethanes for implants. II. In vitro degradation and calcification of materials from poly(ϵ -caprolactone)-poly(ethylene oxide) diols and various chain extenders,” *Journal of Biomedical Materials Research*, vol. 60, no. 4, pp. 592–606, 2002.
- [11] K. Gorna and S. Gogolewski, “Preparation, degradation, and calcification of biodegradable polyurethane foams for bone graft substitutes,” *Journal of Biomedical Materials Research*, vol. 67, no. 3, pp. 813–827, 2003.
- [12] E. B. Stephan, D. Jiang, S. Lynch, P. Bush, and R. Dziak, “Anorganic bovine bone supports osteoblastic cell attachment and proliferation,” *Journal of Periodontology*, vol. 70, no. 4, pp. 364–369, 1999.
- [13] R. E. Cohen, R. H. Mullarky, B. Noble, R. L. Comeau, and M. E. Neiders, “Phenotypic characterization of mononuclear cells following anorganic bovine bone implantation in rats,” *Journal of Periodontology*, vol. 65, no. 11, pp. 1008–1015, 1994.
- [14] Z. Artzi, C. E. Nemcovsky, and H. Tal, “Efficacy of porous bovine bone mineral in various types of osseous deficiencies: clinical observations and literature review,” *International Journal of Periodontics and Restorative Dentistry*, vol. 21, no. 4, pp. 395–405, 2001.
- [15] L. Fassina, E. Saino, M. S. Sbarra, et al., “Ultrasonic and electromagnetic enhancement of a culture of human SAOS-2 osteoblasts seeded onto a titanium plasma-spray surface,” *Tissue Engineering*, vol. 15, no. 2, pp. 233–242, 2009.
- [16] U. Ripamonti, C. Ferretti, and M. Heliotis, “Soluble and insoluble signals and the induction of bone formation: molecular therapeutics recapitulating development,” *Journal of Anatomy*, vol. 209, no. 4, pp. 447–468, 2006.
- [17] J. D. Heckman, J. P. Ryaby, J. McCabe, J. J. Frey, and R. F. Kilcoyne, “Acceleration of tibial fracture-healing by non-invasive, low-intensity pulsed ultrasound,” *Journal of Bone and Joint Surgery. American*, vol. 76, no. 1, pp. 26–34, 1994.
- [18] L. W. Fisher, J. T. Stubbs III, and M. F. Young, “Antisera and cDNA probes to human and certain animal model bone matrix noncollagenous proteins,” *Acta Orthopaedica Scandinavica, Supplement*, vol. 66, no. 266, pp. 61–65, 1995.
- [19] K. G. Vogel and S. P. Evanko, “Proteoglycans of fetal bovine tendon,” *Journal of Biological Chemistry*, vol. 262, no. 28, pp. 13607–13613, 1987.
- [20] A. Rossi, L. V. Zuccarello, G. Zanaboni, et al., “Type I collagen CNBr peptides: species and behavior in solution,” *Biochemistry*, vol. 35, no. 19, pp. 6048–6057, 1996.
- [21] D. G. Castner and B. D. Ratner, “Biomedical surface science: foundations to frontiers,” *Surface Science*, vol. 500, no. 1–3, pp. 28–60, 2002.
- [22] L. Fassina, L. Visai, M. G. Cusella De Angelis, F. Benazzo, and G. Magenes, “Surface modification of a porous polyurethane through a culture of human osteoblasts and an electromagnetic bioreactor,” *Technology and Health Care*, vol. 15, no. 1, pp. 33–45, 2007.
- [23] F. M. Pavalko, S. M. Norvell, D. B. Burr, C. H. Turner, R. L. Duncan, and J. P. Bidwell, “A model for mechanotransduction in bone cells: the load-bearing mechanosomes,” *Journal of Cellular Biochemistry*, vol. 88, no. 1, pp. 104–112, 2003.

- [24] Y. Khan and C. T. Laurencin, "Fracture repair with ultrasound: clinical and cell-based evaluation," *Journal of Bone and Joint Surgery. American*, vol. 90, supplement 1, pp. 138–144, 2008.
- [25] J. K. Li, J. Lin, H. C. Liu, et al., "Comparison of ultrasound and electromagnetic field effects on osteoblast growth," *Ultrasound in Medicine and Biology*, vol. 32, no. 5, pp. 769–775, 2006.

Research Article

Niobium Uptake and Release by Bacterial Ferric Ion Binding Protein

Yanbo Shi,¹ Ian Harvey,² Dominic Campopiano,¹ and Peter J. Sadler³

¹ School of Chemistry, University of Edinburgh, King's Buildings, West Mains Road, Edinburgh EH9 3JJ, UK

² CLRC Daresbury Laboratory, Warrington WA4 4AD, UK

³ Department of Chemistry, University of Warwick, Coventry CV4 7AL, UK

Correspondence should be addressed to Peter J. Sadler, p.j.sadler@warwick.ac.uk

Received 25 January 2010; Accepted 11 February 2010

Academic Editor: Spyros Perlepes

Copyright © 2010 Yanbo Shi et al. This is an open access article distributed under the Creative Commons Attribution License, which permits unrestricted use, distribution, and reproduction in any medium, provided the original work is properly cited.

Ferric ion binding proteins (Fbps) transport Fe^{III} across the periplasm and are vital for the virulence of many Gram negative bacteria. Iron(III) is tightly bound in a hinged binding cleft with octahedral coordination geometry involving binding to protein side chains (including tyrosinate residues) together with a synergistic anion such as phosphate. Niobium compounds are of interest for their potential biological activity, which has been little explored. We have studied the binding of cyclopentadienyl and nitrilotriacetato Nb^V complexes to the Fbp from *Neisseria gonorrhoeae* by UV-vis spectroscopy, chromatography, ICP-OES, mass spectrometry, and Nb K-edge X-ray absorption spectroscopy. These data suggest that Nb^V binds strongly to Fbp and that a dinuclear Nb^V centre can be readily accommodated in the interdomain binding cleft. The possibility of designing niobium-based antibiotics which block iron uptake by pathogenic bacteria is discussed.

1. Introduction

Following the therapeutic success of cisplatin, a large number of complexes of other metals have been studied. Nonplatinum complexes are of particular interest since they may display a lack of cross-resistance with cisplatin, bringing significant benefits for chemotherapy. Metallocene dihalides and pseudohalides of general formula [Cp₂MX₂] (M = Ti, V, Nb, Mo; X = F, Cl, Br, I, CN, SCN; Figure 1(a)), have attracted significant interest since they have shown activity towards a wide variety of murine and human tumors [1–9]. Titanocene dichloride [Cp₂TiCl₂] was the first non-platinum metal complex to enter clinical trials but was eventually abandoned owing to its high reactivity in aqueous solution which gives rise to formulation difficulties [10, 11].

Vanadocene-, molybdenocene-, and niobocene dichlorides also exhibit good activities. Niobocene dichloride (Cp₂NbCl₂) is an extremely potent cancerostatic agent against the Ehrlich ascites tumour in CFI mice [12, 13]. Oxidation to Nb^V reduces the tumor inhibiting properties [14] but potentially could also reduce toxic effects. Hence there is interest in further investigation of the biological chemistry of niobium complexes [15].

Iron is the single most important micronutrient for bacterial survival; it plays important roles in both pathogen virulence and host antimicrobial resistance [16–18]. Numerous pathogenic bacteria such as *Neisseria gonorrhoeae* and *Haemophilus influenzae* have evolved a specific protein-dependent iron-uptake system which can obtain iron from the host transferrin (Tf) and lactoferrin (Lf). The three-component system is a member of the ABC-transporter super-family (FbpABC) and critical for iron uptake is a ferric ion-binding protein (FbpA, referred to here as Fbp, a single-chain 34 kDa protein) which shuttles Fe^{III} across the periplasmic space, transporting Fe^{III} from the outer membrane to the cytoplasmic membrane [19]. This essentiality for virulence makes Fbp an ideal drug target and provides a basis for the design of novel metal-based antibiotics which combat resistance to widely used organic antibiotics.

Structural analysis of the Fe^{III} binding site in Fbp from various bacteria has shown several different classes (Figure 1(b) shows the best characterised). All have a pair of highly conserved Tyr residues in the active site and the other metal binding residues are composed of amino acid side chains (glutamate and histidine) and anions (e.g., phosphate). These tyrosines are critical for strong metal

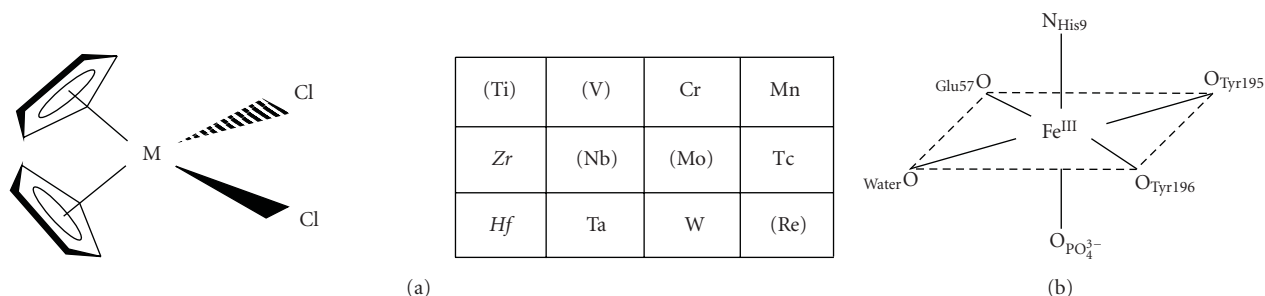


FIGURE 1: (a) Metallocene dihalides with antitumor activity. Key: (M) = maximum activity; M = sporadic activity; M = no activity. (b) Fe^{III} binding sites in bacterial ferric ion-binding proteins (*Neisseria gonorrhoeae* or *Haemophilus influenzae*).

ion binding, as confirmed by site-directed mutagenesis and crystal structures of reconstituted Fbp protein complexes with Fe^{III}. These bacterial Fbps display an extremely high affinity for ferric iron ($K_D \sim 1 \times 10^{-20}$ M) but they also have the capacity to bind other metals. We discovered that *N. gonorrhoeae* Fbp could bind Ti, Zr^{IV}, or Hf^V in the metal binding cleft [20–22]. Moreover, besides binding a single metal ion we observed various metal clusters bound in an adaptable active site which appears to be able to accommodate a wide range of metals ions and anions. To further probe the specificity of this site we report for the first time studies of the binding of Nb^V complexes to Fbp, using a wide variety of techniques including UV-visible spectroscopy, inductively coupled plasma atomic emission spectroscopy (ICP-AES), electropray mass spectrometry, and EXAFS. These studies are important not only for exploring a potential mechanism for niobium transport but also as a basis for the possible design of novel metalloantibiotics.

2. Experimental/Materials and Methods

2.1. Materials. [Cp₂NbCl₂] (Arcos), monosodium citrate (Aldrich), nitrilotriacetic acid (H₃NTA, 99%, Aldrich, N840-7), NaH₂PO₄ and Na₂HPO₄ (BDH), Hepes (Aldrich), Tris (Aldrich), and cetyltrimethylammonium bromide (CTAB, Aldrich) were used as received. Atomic absorption standard solutions of Fe (Aldrich, cat: 30595-2), Nb (1000 ppm, niobium(V) chloride in 4% hydrofluoro, VWR international Ltd. Cat: 1026410100), and P (Aldrich, cat: 20735-7) were used as supplied.

All other chemicals were reagent grade and used as provided.

Stock solutions of [Fe^{III}(NTA)₂]³⁻ and [Nb^V(NTA)_n] were prepared from iron and niobium atomic absorption standard solutions and stoichiometric amounts of H₃NTA. The pH values of the solutions were raised slowly to ~5.6 and 5.26, respectively, with microliter amounts of NaOH (1 M).

The [Cp₂Nb(OH)Cl₂] stock solution was freshly prepared by sonication of [Cp₂NbCl₂] (2.9 mg, 0.099 mmol) in D₂O (0.5 mL) until no solid remained (typically 0.5–1 h). As [Cp₂NbCl₂] is insoluble in water, oxygen was required [22] to effect oxidation to the water-soluble niobium(V) complex [Cp₂Nb(OH)Cl₂] [14]. Finally a yellow solution of [Cp₂Nb(OH)Cl₂] was obtained. This solution

may also contain other hydrolysed Cp₂Nb^V species as well as small amounts of hydrolysed Nb^{IV} species such as [Cp₂NbCl(H₂O)]⁺.

Electrophoresis was carried out using a Bio-Rad ProteinII Minigel system (protein) and Invitrogen H5 system (DNA). GE Healthcare AKTA equipment and columns were used for chromatographic separations of proteins. Precast SDS-PAGE gels (10% bis-Tris) were purchased from Invitrogen and used according to the manufacturer's instructions.

2.2. Overexpression and Purification of Fbp. Fbp was overexpressed in *E. coli* TOP10 One Shot or DH5α cells (Invitrogen) transformed with the plasmid pTrc99A/Fbp/Ng. A single colony from freshly transformed cells was used to inoculate 5 mL of 2YT broth which contained 100 μg/mL ampicillin in a sterile 10 mL vial. This culture was shaken overnight at 310 K and used to inoculate 3 liters of 2YT broth with 100 μg/mL ampicillin in sterile 500 mL flasks. After the flasks were shaken overnight at 310 K, a pink cell pellet was harvested by centrifugation at 10,000 × g for 15 minutes at 277 K and stored at 253 K until use.

Fbp was purified by a modification of the method reported previously [20, 22, 23]. The pink pellet (~15 g) was defrosted at room temperature and resuspended in 150 mL of 50 mM Tris (pH 8.0) containing 2% cetyl trimethylammonium bromide (CTAB), sonicated for 5 minutes (30 second on, 30 s off), followed by stirring slowly overnight at 310 K. The white insoluble material was removed by centrifugation at 10,000 × g for 15 minutes at 277 K. The supernatant (cell-free extract) was dialysed against 5000 mL 10 mM Tris (pH 8.0) at room temperature overnight, followed by the dialysis for another 3 hours to remove CTAB and then filtered using Whatman paper (0.2 μm, Fisher). The cell-free extract was applied to a RESOURCE S strong cation exchange column (6 mL, Amersham Biosciences); the column was equilibrated with 10 mM Tris buffer (pH 8.0). Unbound proteins were removed by extensive washing with low salt buffer. The target protein (Fbp) was then eluted with a linear NaCl gradient of low-to-high salt (0–1 M NaCl) over 20 column volumes in 10 mM Tris buffer. Pink fractions were collected and were analyzed by SDS-PAGE. Fbp was desalted by dialysis and concentrated by ultrafiltration (10 kDa cut-off, Amicon concentrator). The concentration of purified iron-bound, holo-Fbp protein was determined

by UV absorption using $\epsilon_{481} = 2,430 \text{ M}^{-1} \text{ cm}^{-1}$, or $\epsilon_{280} = 48,900 \text{ M}^{-1} \text{ cm}^{-1}$ [24]

2.3. Preparation of Apo-Fbp. Iron-free, apo-Fbp was prepared by treatment of holo-Fbp solutions with 250 mM sodium citrate (pH 4.5) at room temperature for 5 hours, followed by elution with 250 mM sodium citrate (pH 4.5) on a PD-10 column (GE Healthcare), so as to give negligible absorbance at 481 nm. The apo-Fbp was then washed 6 times with 0.1 M KCl in a Centricon YM-30 microconcentrator (Amicon), and the stock solution was stored at 4°C before use. apo-Fbp concentration was determined with $\epsilon_{280} = 44,270 \text{ M}^{-1} \text{ cm}^{-1}$ [24].

2.4. UV-Visible Spectroscopy. All UV experiments were performed with 1 cm cuvettes on a computer-controlled Cary 300 spectrometer with temperature control at 298 or 310 K. For kinetic experiments, the time courses for the reactions of apo-Fbp (10 μM) with 2 mol equivalent of $[\text{Cp}_2\text{Nb}(\text{OH})\text{Cl}_2]$ or $[\text{Nb}(\text{NTA})_2]^-$ were recorded for solutions in Hepes buffer (10 mM, pH 7.4) at 310 K. UV/Vis spectra were recorded at 5 minutes intervals against the same buffer solution containing the same amount of $[\text{Cp}_2\text{Nb}(\text{OH})\text{Cl}_2]$ or $[\text{Nb}(\text{NTA})_2]^-$ in the reference cuvette.

First-order rate constants, k_{obs} , were calculated by fitting plots of absorbance at 245 nm versus time to (1) using the program Origin7.5, where A , A_0 , and A_∞ are the absorbances at time t , time zero, and after infinite time:

$$\log(A_\infty - A) = -k_{\text{obs}}t + \log(A_\infty - A_0). \quad (1)$$

For titration experiments, solutions were prepared by diluting aliquots of a stock apo-Fbp solution to $\sim 10 \mu\text{M}$ with 10 mM Hepes buffer, 5 mM phosphate, pH 7.4. Aliquots of metal complex (0.5–10 μl) were added, and each solution was allowed to equilibrate at 310 K for 1 hour before the spectrum was recorded.

The displacement of metal ions from the protein was also monitored by adding aliquots of 1:50 Nb:NTA to (iron-bound) holo-Fbp in the above buffer at 310 K. UV-visible spectra were recorded half an hour after each addition. Buffers containing the same amount of 1:50 Nb:NTA were used as references. The binding or release of Fe^{III} was monitored by the increase or decrease in absorbance at 481 nm.

2.5. Chromatographic Analysis. For chromatographic analysis, the Nb-Fbps were prepared by reacting apo Fbp with 20 mol equiv of freshly prepared Cp_2NbCl_2 (bubbled with air, as oxygen is required to effect oxidation to the water soluble niobium(V) complex $\text{Cp}_2\text{Nb}(\text{OH})\text{Cl}_2$) or $[\text{Nb}(\text{NTA})_2]^-$ for 48 hours at 310 K in 10 mM Hepes buffer, pH 7.4. Small molecules (<30 kDa) were removed by ultrafiltration using 0.1 M KCl, and then the sample was applied to a Mono S HR5/5 column equilibrated with Hepes buffer (10 mM, pH 7.4, 25 mL), followed by gradient elution with 0.1 M KCl in Hepes (10 mM; pH 7.4) flow rate 0.5 mL min^{-1} . Peak fractions were collected and pooled, and then subjected to

ultrafiltration (Centricon, 30 kDa cut off, YM-30, Millipore) to remove NaCl.

2.6. ICP-OES Analysis. ICP-OES was performed on Perkin Elmer Optical Emission Spectrometer Optima 5300DV using standard methods. Metal-loaded proteins were prepared using the same chromatographic procedures as for holo-Fbp isolation, collected and purified by using Centricon 30 (Amicon) ultrafiltration and washing six times with ultrapure water followed by ultrafiltration after each washing. The protein solution was finally diluted with ultrapure water. The contents of Nb and S were measured, after digestion of the samples, using the emission lines of 309.418 nm and 181.975 nm for Nb and S, respectively.

2.7. Mass Spectrometry. Samples Nb-Fbps for ESI-MS were prepared by reacting a 20-fold molar excess of $[\text{Cp}_2\text{Nb}(\text{OH})\text{Cl}_2]$ or $[\text{Nb}^{\text{V}}(\text{NTA})_2]$ with apoFbp (ca. 0.5 mM) in 10 mM HEPES buffer pH 7.5 in a water bath at 310 K for 48 hours. Unbound Nb^{V} complexes were removed from the protein by ultrafiltration (Centricon 30, cut-off 30 kDa, Amicon) washing with 0.1 M KCl and H_2O three times, respectively, and then exchanged into a 10 mM NH_4Ac buffer (pH 8.0) by using a PD-10 column.

Positive-ion electrospray mass spectrometry was performed on a Micromass Platform II quadrupole mass spectrometer equipped with an electrospray ion source. The purified holo-Fbp, apo-Fbp, or recombinant Nb-Fbp samples in 10 mM NH_4Ac buffer (pH 8.0) were diluted with $\text{CH}_3\text{CN}/\text{H}_2\text{O}$ (1:1, v/v) to a final concentration of 25 μM . Each sample was infused at 50 $\mu\text{L}/\text{minute}$ directly into the mass spectrometer, and the ions were produced in an atmospheric pressure ionization (API)/ESI ion source. The spray voltage was 3.50 kV. The cone voltage was varied from 20 to 60 V as required. The capillary temperature was 338 K for direct infusion, with a 450 L h^{-1} flow of nitrogen drying gas. The quadrupole analyzer, operated at a background pressure of $5.9 \times 10^{-5} \text{ mBar}$, was scanned at 200 Da s^{-1} for direct infusion. Data were collected (for 10 scans during the direct infusion assays) and analyzed on a Mass Lynx (ver.3.5). The deconvoluted average molecular mass was determined using the MaxEnt and Transform algorithms of massLynx software.

2.8. X-Ray Absorption Spectroscopy. X-ray spectra were recorded at the niobium K edge on EXAFS station 16.1 at Daresbury Laboratory Synchrotron Radiation Source (operating at 2 GeV) using an Si (220) double crystal monochromator and vertically focusing mirror for harmonic rejection. Data for apo-Fbp loaded with Nb^{V} were collected at 13 K (using a liquid helium cryostat) in fluorescence mode using a 13-element solid state germanium detector. Data were collected in k space using a k^3 -weighted regime for counting time with a total scan time of 40 minutes. 40 scans were collected from each sample. The edge positions were calibrated against an Nb foil. Samples were prepared as follows. Purified native Fbp was concentrated to 5 mM by ultrafiltration and washed six times with 0.1 M KCl. Nb-Fbp

(1 mM) was prepared by reacting apo-Fbp with 10 mol eq of $\text{Cp}_2\text{Nb}(\text{OH})\text{Cl}_2$ in Hepes buffer (pH 7.4). The excess of $[\text{Cp}_2\text{Nb}(\text{OH})\text{Cl}_2]$ was removed from the yellowish solution by ultrafiltration, washing three times with 0.1 M KCl and then ultrapure water.

Data were processed using EXCALIB and SPLINE (modified for use with EXCURV) [25]. The EXAFS data were converted into k space and analyzed using the fast curved wave (or Rehr-Albers) theory [26] including up to third-order multiple scattering contributions in EXCURV98 [27]. Phase shifts were calculated using Hedin-Lundquist exchange and correlation potentials [28, 29] and tested against the EXAFS data for $[\text{Cp}_2\text{NbCl}_2]$ and NbCl_5 . All the data analysis was conducted on raw EXAFS data (without Fourier filtering) weighted by k^3 to compensate for diminishing amplitude at high k .

3. Results and Discussion

3.1. Characterization of Fbp. Since Fbp contains an N-terminal signal sequence that directs Fbp to the periplasmic space, the overexpressed protein was located in the periplasm of *E. coli*. The molecular masses of holo-Fbp and apo-Fbp determined by electrospray mass spectrometry were 33,640 Da, in good agreement with the amino acid sequence (309 amino acids, without iron or phosphate theoretical mass of 33639.39 Da). This suggests that, under the conditions used for mass spectrometry, neither holo-Fbp nor apo-Fbp had iron or synergistic anion bound to the protein and that the Fbp signal sequence had been cleaved at Asp23 upon translocation to the periplasm. The presence of iron in holo-Fbp was evident from the ligand-to-metal charge-transfer (LMCT) (tyrosinate-to- Fe^{III}) band of Fe^{III} -Fbp (*vide infra*). For metal binding experiments, iron was efficiently removed by incubation with excess citrate to generate apo-Fbp with no detectable iron remaining.

3.2. Rate and Stoichiometry of Nb Binding to ApoFbp. The time-courses of reactions between apoFbp and $[\text{Nb}^{\text{V}}(\text{NTA})_2]^-$ (we use this formulation for solutions containing Nb^{V} and 2 mol equiv of NTA) or $[\text{Cp}_2\text{Nb}^{\text{V}}(\text{OH})\text{Cl}_2]$ were studied using UV/Vis spectroscopy. Two molar equivalents of $[\text{Nb}^{\text{V}}(\text{NTA})_2]^-$ or $[\text{Cp}_2\text{Nb}^{\text{V}}(\text{OH})\text{Cl}_2]$ were added to a solution of apoFbp ($\sim 10 \mu\text{M}$, in 500 μL 10 mM Hepes buffer, 5 mM phosphate, pH 7.4) at 310 K.; typical spectra are shown in Figures 2 and 3, respectively. In the case of $[\text{Nb}^{\text{V}}(\text{NTA})_2]^-$, the reaction produced a UV difference spectrum which is similar to reactions of other metal ions with apoFbp [20, 30]; two new positive bands appeared at ca. 245 and 295 nm, and increased in intensity over a period of 60 minutes (Figures 2(a) and 2(b)). These bands are assignable to $\pi\text{-}\pi^*$ transitions of Tyr residues deprotonated by binding to Nb^{V} . Similar bands are seen when both bacterial and serum transferrins bind to a wide variety of metal ions [31–33]. This suggests that Nb^{V} ions can occupy specific Fe^{III} binding sites. Best fits to the data were obtained using first-order kinetics equations, although the rate law was not investigated. The first-order rate constant, k_{obs} , was

$3.03 \pm 0.01 \text{ h}^{-1}$ (310 K), and the extinction coefficient ($\Delta\epsilon_{245}$) reached ca. $15200 \text{ M}^{-1} \text{ cm}^{-1}$ (Figure 2(c)).

In the case of $[\text{Cp}_2\text{Nb}^{\text{V}}(\text{OH})\text{Cl}_2]$, the reaction produced two new bands in the UV/Vis spectra; one broad band is centred at around 320 nm. The other sharp band is at ca. 244 nm (Figure 3(a)). The reaction was complete in ca. 2 hours (Figures 3(a), 3(b) and 3(c)). Kinetic studies revealed k_{obs} of $1.24 \pm 0.03 \text{ h}^{-1}$ (310 K), and the extinction coefficient ($\Delta\epsilon_{244}$) reached ca. $16700 \text{ M}^{-1} \text{ cm}^{-1}$ (Figure 3(d)). These data indicate that the reactions occur in two kinetic phases; however, the initial phases of the reactions of apoFbp with $[\text{Nb}(\text{NTA})_2]^-$ and $[\text{Cp}_2\text{Nb}^{\text{V}}(\text{OH})\text{Cl}_2]$ were fast (within 1 hour and 2 hours, resp.).

Analysis of the titration curves for the reaction of apoFbp with $[\text{Nb}(\text{NTA})_2]^-$ and $[\text{Cp}_2\text{Nb}(\text{OH})\text{Cl}_2]$ (Figures 2(d) and 3(e)) suggests that about two Nb^{V} ions bind strongly to Fbp in both cases. In these experiments, each sample was allowed to equilibrate for 2 hours after each addition and then UV difference spectra were recorded. The absorptivity $\Delta\epsilon_{244/245}$ increased linearly with increase in molar ratio $r_{[\text{Nb}]/[\text{apoFbp}]}$ until a value of ca. $r = 2$. Beyond $r = 2$, the titration curve reached a plateau (Figures 2(d) and 3(e)). Titration studies suggested that a niobium : protein molar ratio of 2 : 1 is sufficient to deprotonate both Tyr 195 and Tyr 196 when phosphate is present as the synergistic anion; phosphate is known to bind in the interdomain cleft of the apo-protein and may prepare the cleft for metal entry [34]. Beyond a 2 : 1 $[\text{Nb}] : [\text{apoFbp}]$ ratio there was little increase in the absorption at 244 or 245 nm (Figures 2(d) and 3(e)). These data suggest that the initial reaction with apo-Fbp involves Nb^{V} binding to Tyr 195 and Tyr 196 either initially as a mononuclear niobium centre binding to one of the Tyr side-chains followed by subsequent binding of the second niobium to the second Tyr and formation of an oxo-niobium dinuclear center or perhaps by direct uptake of a dinuclear species which may involve one Nb^{V} binding to both Tyr residues or one to each. Hence there is little increase in the absorption at 241 nm beyond a 2 : 1 $[\text{Nb}] : [\text{apoFbp}]$ ratio. In particular, the mobility of Tyr 196 (as observed in crystals of oxo- Fe^{III} -Fbp) [22] may be important for capturing Nb^{V} ions at the protein surface and delivering them into the binding cleft. In our previous studies of the binding of trinuclear Fe^{III} , Hf^{IV} (also pentanuclear Hf^{IV}), and Zr^{IV} oxo-clusters to Fbp, we have observed anchoring of these centres via these tyrosinates with each binding to different metals (or in the case of one Fe^{III} cluster, anchoring via a single Tyr) [20, 22, 35]. It appears that the other two protein ligands, His 9 and Glu 57 are not essential for the initial steps of metal binding in vitro.

3.3. Displacement of Fe^{III} from Fe-Fbp by Nb^{V} . To confirm that Nb^{V} binds to the specific Fe^{III} -binding sites of Fbp/Ng, we investigated the displacement of Fe^{III} from holo-Fbp (Fe^{III} -phosphate-Fbp) by Nb^{V} . Holo-Fbp was saturated with Fe^{3+} by incubating apoFbp (100 μM) with 10 mol equivalent 1 : 2 Fe : NTA in 10 mM Hepes, 5 mM phosphate, pH 7.4, 310 K for 24 hours. After removing unbound Fe and diluting the Fe-Fbp solution to 25 μM , 1.0 mol equivalent

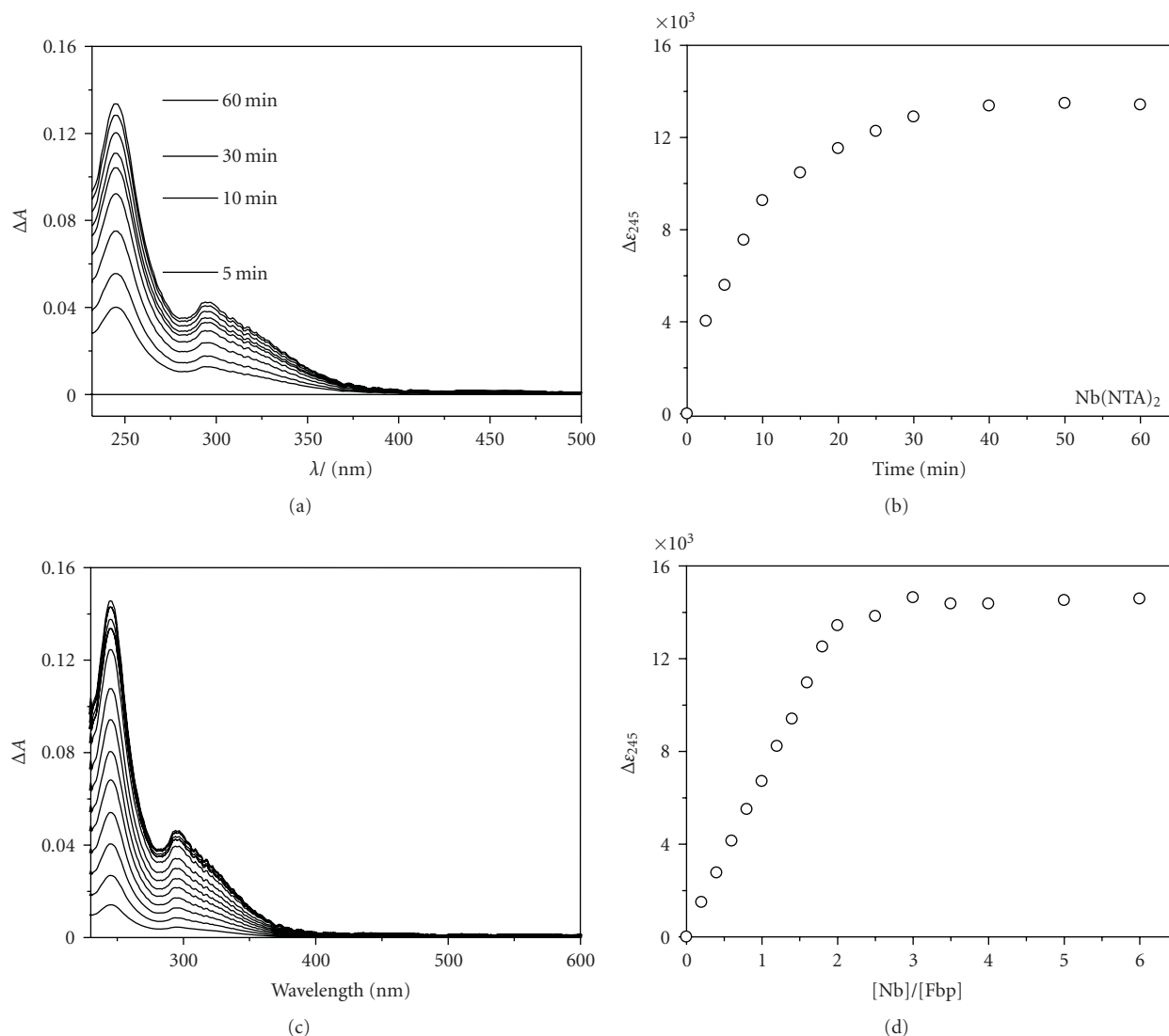


FIGURE 2: (a) UV difference UV/Vis spectra recorded at various times during the reaction of apoFbp (10 μM) with 2.0 mol equivalents of [Nb(NTA)₂]⁻ in 10 mM Hepes buffer, 5 mM phosphate, pH 7.4, 310 K. (b) Time course for reactions of apo-Fbp (ca. 10 μM) with 2 mol equivalents of [Nb(NTA)₂]⁻ in the 10 mM Hepes buffer, 5 mM phosphate, pH 7.4, 310 K, as a plot of molar absorptivity versus time for reaction. (c) Difference UV/Vis spectra for the titration of apoFbp (10 μM) with [Nb(NTA)₂]⁻ in 10 mM Hepes buffer, 5 mM phosphate, pH 7.4, 310 K (1 h equilibration). Molar ratios of Nb-complexes: apo-Fbp from bottom to top: are 0–2.0 in 0.2 mol equivalent steps, then 2.5, 3.0, 3.5, 4.0. (d) Titration curve for the reaction in (C), and Δε is the absorbance at 245 nm divided by the Fbp concentration.

of [Nb(NTA)₂]⁻ was added to the holo-Fbp solution in physiological buffer at 310 K. There was no obvious change to the LMCT band of Fe^{III}-Fbp at 465 nm (Figure 4, insert). In contrast, with the addition of 1 : 50 Nb : NTA, this band decreased in intensity to about half of its original value at the mol ratio of $r_{[\text{Nb}]/[\text{Fe-Fbp}]}$ of 10, and to about 21% when $r_{[\text{Nb}]/[\text{Fe-Fbp}]}$ is 33 (Figure 4). It can be seen from the graph that the wavelength of the absorption maximum of the LMCT band shifted from 480 nm to 465 nm during this titration. This suggests that under these conditions phosphate is displaced from iron [30] and that Nb^V can compete with Fe^{III} for binding to Fbp, perhaps with initial formation of mixed-metal oxo-Fe/Nb species in the binding cleft.

3.4. Displacement of Nb^V from Nb₂-Fbp by Fe^{III}. We also investigated the displacement of Nb^V from Nb-Fbp by Fe^{III}. Nb-Fbp was prepared by incubating apo-Fbp (100 μM) with 10 mol equiv equivalent 1 : 2 Nb : NTA in 10 mM Hepes, 5 mM phosphate⁻, pH 7.4, 310 K for 24 hours, and Fe^{III}-binding was monitored by the appearance of the Fe^{III}-Fbp LMCT band at 465–480 nm. Nb-Fbp was titrated with 0.2–10 mol equiv 1 : 2 Fe : NTA in the same buffer solution at the same temperature. UV difference spectra were recorded 0.5 hours after each addition of Fe^{III}. A peak centred at ca. 465 nm appeared and increased after 1.2 mol equiv of 1 : 2 Fe : NTA had been added, at which point it had almost reached its final intensity and no further increase occurred with 10 mol equiv Fe^{III} present (Figure 5). Therefore, under

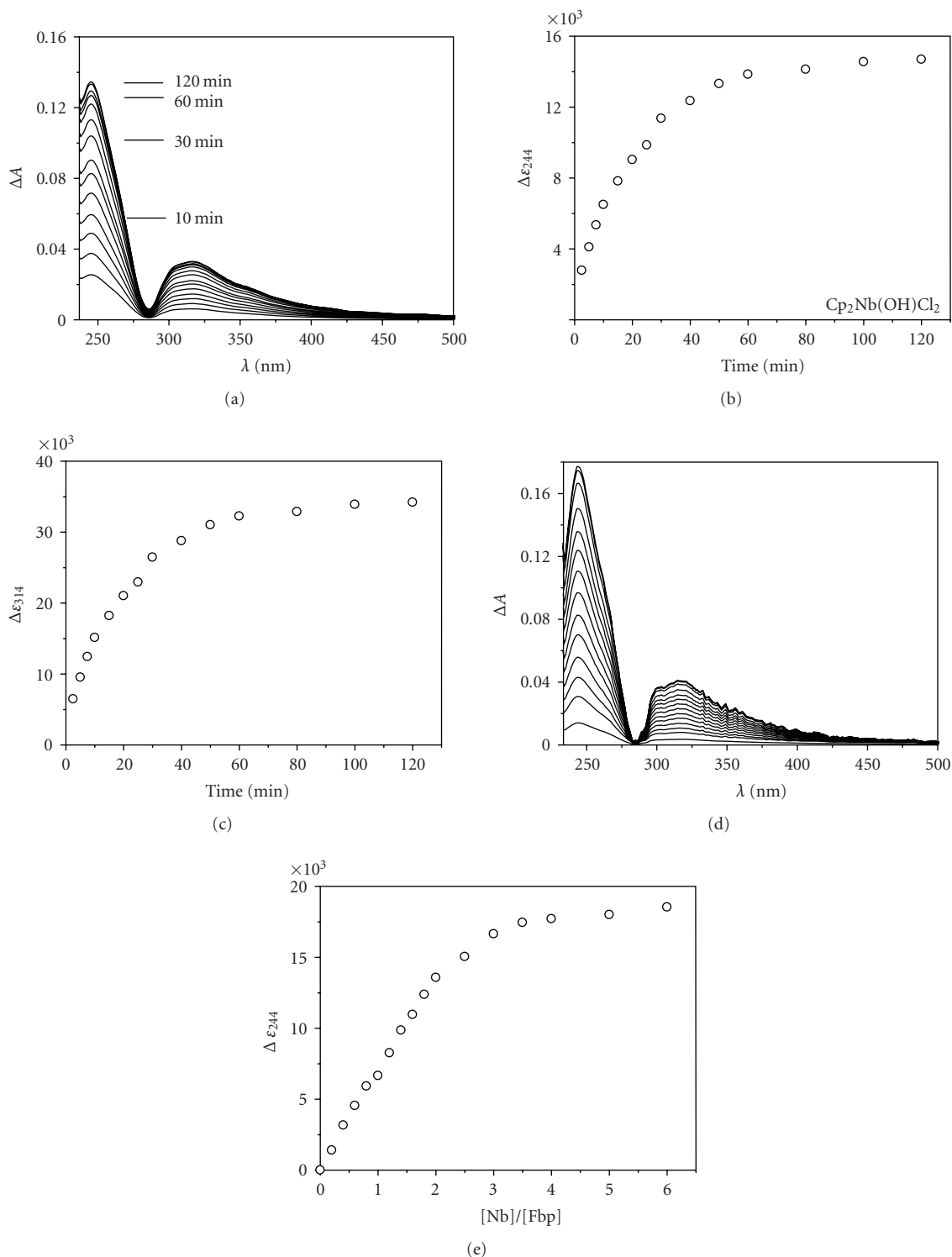


FIGURE 3: (a) Difference UV/Vis spectra recorded at various times during the reaction of apoFbp ($9.8 \mu\text{M}$) with 2.0 mol equivalents of $[\text{Cp}_2\text{Nb}(\text{OH})\text{Cl}_2]$ in 10 mM HEPES buffer, 5 mM phosphate, pH 7.4 (b) Time course for reactions of apo-Fbp (ca. $9.8 \mu\text{M}$) with 2 mol equivalents of $[\text{Cp}_2\text{Nb}(\text{OH})\text{Cl}_2]$ in 10 mM HEPES buffer, 5 mM phosphate, pH 7.4, 310 K, as a plot of molar absorptivity versus time of reaction. (c) Time course for reactions of apo-Fbp (ca. $9.8 \mu\text{M}$) with 2 mol equivalents of $[\text{Cp}_2\text{Nb}(\text{OH})\text{Cl}_2]$ in the 10 mM HEPES buffer, 5 mM phosphate, pH 7.4 at 310 K as a plot of molar absorptivity versus time of reaction. (d) Difference UV/Vis spectra for the titration of apoFbp ($9.8 \mu\text{M}$) with $[\text{Cp}_2\text{Nb}(\text{OH})\text{Cl}_2]$ in 10 mM HEPES buffer, 5 mM phosphate, pH 7.4, 310 K (2 h equilibration). Molar ratios of Nb-complexes: apo-Fbp from bottom to top: are 0–2.0 in 0.2 mol equivalent steps, then 2.5, 3.0, 3.5, 4.0. (e) Titration curve for the reaction in (D), $\Delta \epsilon$ is the absorbance at 244 nm divided by the Fbp concentration.

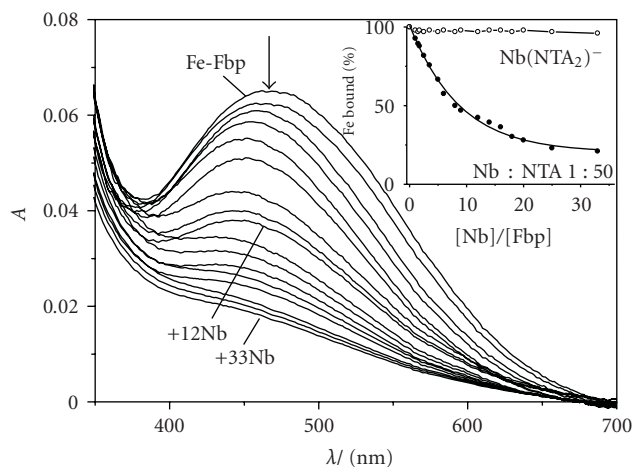


FIGURE 4: Displacement of Fe^{III} from holoFbp ($25 \mu\text{M}$) by 1:50 Nb:NTA under the same conditions as Figure 2(a). Molar ratio of Nb/Fbp (from top to bottom) is 0, 2, 4, 6, 8, 10, 15, 20, 25, 30, and 33. insert shows the percentage of Fe^{III} bound to the protein calculated from the LMCT band at 465 nm. Little Fe^{III} is displaced by $[\text{Nb}(\text{NTA})_2]^-$ (open circles) whereas 1:50 Nb:NTA gives rise to almost complete displacement of Fe^{III} from holoFbp (filled circles).

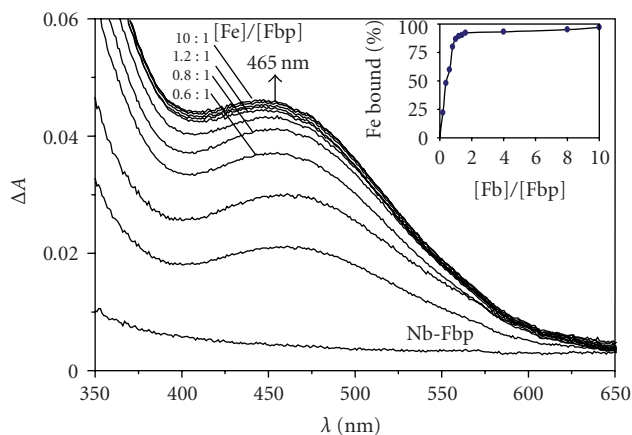


FIGURE 5: Displacement of Nb^{V} from $\text{Nb}_2\text{-Fbp}$ (prepared by incubating apoFbp ($100 \mu\text{M}$) with 10 mol equiv 1:2 Nb:NTA under the same conditions as Figure 2(a)) by 1:2 Fe:NTA in the same buffer at 310 K. the band at ca.465 nm increases in intensity with the addition of Fe^{III} . Molar ratios $r_{[\text{Fe}]/[\text{Fbp}]}$ from bottom to top: are 0, 0.2, 0.4, 0.6, 0.8, 1.0, 1.2, 1.4, 1.6, 4, 8, and 10. Insert shows variation in percentage of Fe^{III} bound to the protein calculated from the LMCT band at 465 nm with the amount of added Fe^{III} .

the conditions studied here, Fe^{III} can displace Nb^{V} from the protein.

3.5. Characterization of Nb-Fbp by Ion Exchange Chromatography and ICP-OES Analysis. The products from reaction of apoFbp with 20 molar equiv of freshly prepared $[\text{Cp}_2\text{NbCl}_2]$ (bubbled with air (oxygen) to obtain the water soluble niobium(V) complex $[\text{Cp}_2\text{Nb}(\text{OH})\text{Cl}_2]$ or $[\text{Nb}(\text{NTA})_2]^-$ are at 310 K in Hepes buffer (10 mM, pH 7.4) for 48 hours. Unbound Nb was removed by extensive ultrafiltration

and the sample was applied to a cation exchange Mono S HR5/5 column equilibrated with Hepes (10 mM; pH 7.4, 25 mL), followed by gradient elution with 0-1 M KCl in Hepes (10 mM; pH 7.4) flow rate 0.5 mL min^{-1} . The chromatograms are shown in Figure 6. We observed two peaks that elute at different KCl concentrations which we assume to be the different forms of Nb-Fbp with different charges. It seems likely that the products from these loading reactions contain different multinuclear forms of Nb-Fbp.

Reaction of Fbp with 1 and 20 mol equivalents of $[\text{Cp}_2\text{Nb}(\text{OH})\text{Cl}_2]$ gave products containing an average of 0.86 and 2.23 mol Nb per mol protein, respectively (ICP-OES data; see Table 1). In the case of reactions with 1 and 20 mol equivalents of $[\text{Nb}(\text{NTA})_2]^-$ under the same conditions, the products contained ca. 0.91 and 2.41 mol Nb per mol protein.

3.6. Electrospray Ionization Mass Spectroscopy (ESI-MS). The recombinant protein, prepared as described in experimental section, was further studied by electrospray ionization mass spectrometry. The products were investigated as dilute solutions in 10 mM NH_4Ac , pH 8.0. For the reaction of $[\text{Cp}_2\text{Nb}(\text{OH})\text{Cl}_2]$ with apoFbp, peaks centred at mass 34813, 34829, 34842, 34871, and 34890 are tentatively assigned to $[\text{aFbp} + 4\text{Cp}_2\text{NbCl}_2]$, $[\text{aFbp} + 4\text{Cp}_2\text{NbCl}_2 + \text{OH}^-]$, $[\text{aFbp} + 4\text{Cp}_2\text{NbCl}_2 + 2\text{OH}^-]$, $[\text{aFbp} + 4\text{Cp}_2\text{NbCl}_2 + 3\text{OH}^-]$, and $[\text{aFbp} + 4\text{Cp}_2\text{Nb}(\text{OH})\text{Cl}_2]$, respectively. Another sample prepared from apoFbp and $[\text{Nb}(\text{NTA})_2]^-$ gave peaks centred at mass 34655, 34837, and 34965 corresponding to $[\text{aFbp} + \text{NH}_4^+]$, $[\text{aFbp} + 2\text{Nb}(\text{NTA})_2 + \text{CH}_3\text{COO}^-]$, $[\text{aFbp} + 3\text{Nb}(\text{NTA})_2 + \text{NTA}]$. Table 2 contains a list of the species observed by ESI-MS assays of Nb-Fbp. These results indicate that apoFbp binds Nb^{V} tightly under the conditions used and suggests that the binding cleft can accommodate not only a single metal ion but also multinuclear Nb species, as observed previously for iron, zirconium and hafnium. However, these data alone do not rule out the possible presence of Nb binding sites elsewhere on the protein and the formulations require further verification before they can be fully interpreted.

3.7. EXAFS Experiment. To obtain more detailed structural information, Nb K-edge X-ray absorption near-edge structure (XANES) and extended X-ray absorption fine structure (EXAFS) studies (Figure 7) were carried out. For these studies, Nb-Fbp was prepared by treating apo-Fbp with $[\text{Cp}_2\text{Nb}(\text{OH})\text{Cl}_2]$ (see experimental section).

The XANES edge position confirms the oxidation state of the Nb as 5+. The Fourier transform shows two intense, overlapping peaks at ca. 1.94 Å and 2.12 Å, and a broader peak at 3.3 Å. The 1.94 Å and 2.12 Å peaks were simulated with six oxygen atoms as back-scatters at two distances (2 atoms at 1.94 Å, and 4 atoms at 2.12 Å). These result from scattering from the atoms directly coordinated to the Nb^{V} center and are likely to include tyrosinate, histidine, glutamate, hydroxide, and oxo groups. ICP measurements showed that phosphate was not present in this sample (data not shown). Niobium-aryloxide bonds of 1.730–1.985 Å have

TABLE 1: Analysis of the products from reactions of apo-Fbp with $[\text{Cp}_2\text{Nb}(\text{OH})\text{Cl}_2]$ and $[\text{Nb}(\text{NTA})_2]^-$.

Reaction mixture ^(a)	Product ^(b)	Reaction mixture	Product
$[\text{Cp}_2\text{Nb}(\text{OH})\text{Cl}_2]/[\text{Fbp}]$	$[\text{Nb}]/[\text{Fbp}]$	$[\text{Nb}(\text{NTA})_2]^-/[\text{Fbp}]$	$[\text{Nb}]/[\text{Fbp}]$
1 : 1	$0.86 \pm 0.10 : 1$	1 : 1	$0.91 \pm 0.10 : 1$
20 : 1	$2.23 \pm 0.10 : 1$	20 : 1	$2.41 \pm 0.10 : 1$

^(a) Reactions carried out for 48 hours in 10 mM HEPES buffer, pH 7.4, 310 K.

^(b) Fbp concentration determined from A_{280} .

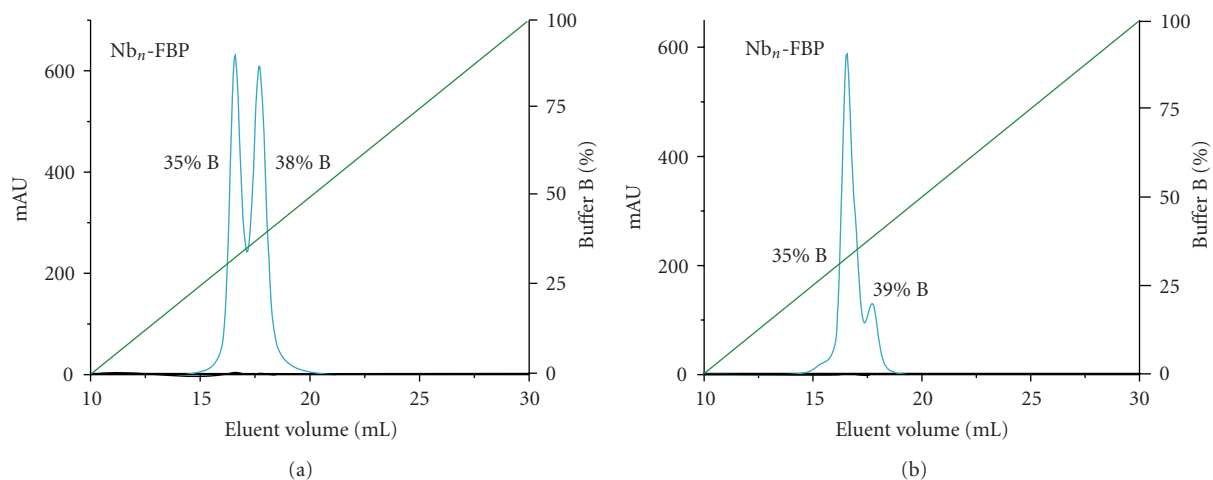


FIGURE 6: Characterization of $\text{Nb}_n\text{-Fbp}$ (apo-Fbp reloaded with $[\text{Cp}_2\text{Nb}(\text{OH})\text{Cl}_2]$ (a) or $[\text{Nb}(\text{NTA})_2]^-$ (b)) by chromatography on a MonoS HR 5/5 column. The left axis shows the absorption profile at 280 nm, and the right axis is the percentage of buffer B (10 mM Hepes, 1 M NaCl, pH7.5). Green line: gradient of the buffer B applied during the elution process; cyan line: absorbance at 280 nm.

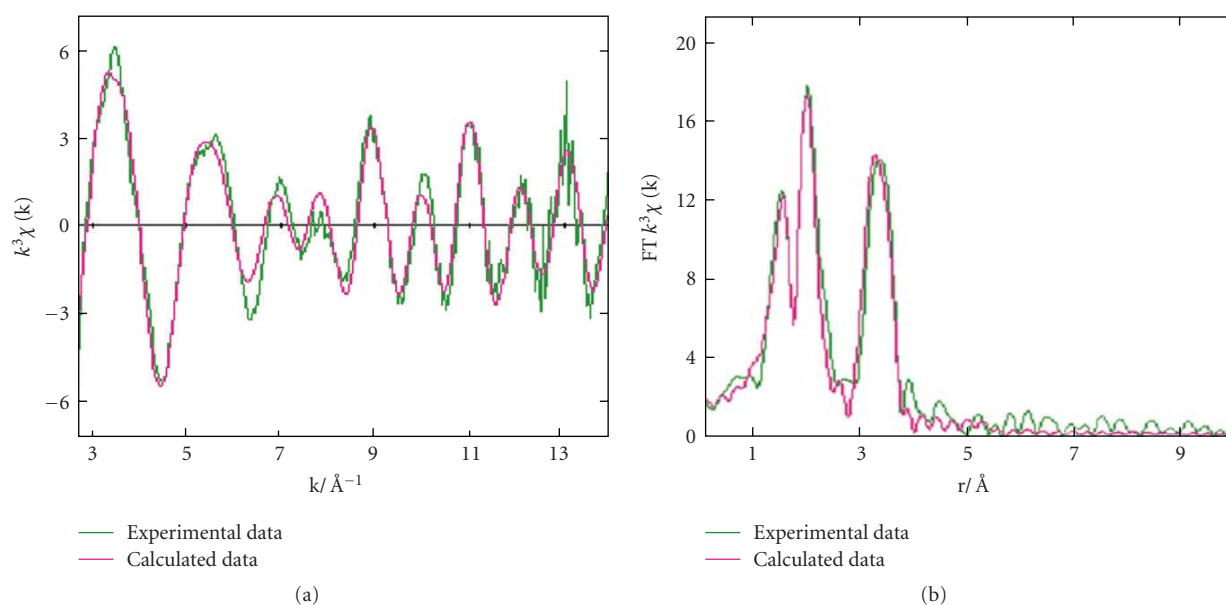


FIGURE 7: Nb K-edge X-ray absorption data. (a) EXAFS spectra, and (b) Fourier transform data for Nb-Fbp (prepared from 10 : 1 $[\text{Cp}_2\text{Nb}(\text{OH})\text{Cl}_2] : \text{apoFbp}$ reaction). Green line: experimental data; red line: calculated data.

TABLE 2: Species detected by ESI-MS assay of products from the reaction of $[\text{Nb}(\text{NTA})_2]^-$ or $[\text{Cp}_2\text{Nb}(\text{OH})\text{Cl}_2]$ with apo-Fbp.

	Calcd/Da ^(a)	Obsd/Da
Recombinant apo-Fbp with $[\text{Cp}_2\text{Nb}(\text{OH})\text{Cl}_2]$		
[a-Fbp]	(33640)	33648
[aFbp + 4Cp ₂ NbCl ₂]	(34816)	34813
[aFbp + 4Cp ₂ NbCl ₂ +OH ⁻]	(34833)	34829
[aFbp + 4Cp ₂ NbCl ₂ +2OH ⁻]	(34850)	34842
[aFbp + 4Cp ₂ NbCl ₂ +3OH ⁻]	(33867)	34871
[aFbp + 4Cp ₂ Nb(OH)Cl ₂]	(34884)	34890
Recombinant apo-Fbp with $[\text{Nb}(\text{NTA})_2]^-$		
[aFbp + NH ₄ ⁺]	(33657)	33655
[aFbp + 2Nb(NTA) ₂ + NTA + CH ₃ COO ⁻]	(34835)	34837
[aFbp + 3Nb(NTA) ₂ + NTA]	(34966)	34965

^(a)The formulations are merely those which give reasonable fits to the observed masses and cannot be interpreted as giving structural information about the nature of the bound complexes. For example some sites could be on the exposed surface of the protein as well as in the interdomain cleft.

previously been reported, including Nb-O_{phenolate} distances of ca. 1.872 Å [36]. Thus the two shorter inner-sphere Nb-O bonds in Nb-Fbp (1.94 Å) are within the range of typical Nb-O bonds assignable to the Nb-tyrosinate bonds but may also be due to Nb=O double bonds and a possible bridging oxo group. The Nb-O bond lengths are also similar to those in known compounds such as (C₂H₆NO₂)₂[NbOF₅] and (C₃H₈-NO₂)₂[NbOF₅]·2H₂O [37], LiNbO(O-2,6-PhMe₂)₄P·3THF, LiNbCl₃(O-2,6-PhMe₂)₂P·2THF [38], NbCl₃(3-[2,2'-methylenebis(4,6-di-*tert*-butylphenol)-5-*tert*-butylsalicylidene-(2,6-diisopropyl)phenylimine]) [34] and the [(Nb₆Cl₈O₄)Cl₆] cluster. The Nb-Nb peak at 3.3 Å is similar to that reported for the single Nb neighbor at 3.3 Å in a niobium-peroxo-citrato complex [39]. The EXAFS data may be consistent with the presence of a dinuclear Nb-O-Nb centre in the adduct. No attempt was made to include Cp ligands in a fit to the EXAFS data.

The EXAFS data do not allow an unambiguous assignment of a structure to the bound niobium(V) dinuclear centre since only averaged Nb-N/O bond lengths are obtained and oxygen ligands cannot be distinguished from nitrogen donors. One possibility is that the dinuclear centre is anchored to the protein only by coordination to the two active site Tyr residues, as are the clusters in previously characterised Fe, Zr, and Hf complexes. The other ligands for Nb^V may be oxygens from water or hydroxide without coordination to the His or Glu sidechains which are ligands in the mononuclear Fe^{III} site.

4. Conclusions

Previous work has shown that efficient iron acquisition is required for the virulence of pathogenic bacteria and that Fbp is one of the iron-uptake virulence genes [22, 30, 35, 40–43]. The di-tyrosyl metal-binding motif in Fbp is highly conserved and shows a strong binding ability with some metals. Targeting this protein with an unnatural metal ion

such as niobium(V) which might block iron(III) uptake therefore becomes a potential strategy for the design of novel antibiotics.

Since the size of the binding cleft in Fbp is thought to be matched to Fe^{III} (ionic radius 0.69 Å), previous studies have shown similar tight binding between apoFbp and various other metal ions such as Ti^{IV} (ionic radius 0.75 Å), Zr^{IV} (ionic radius 0.86 Å) and Hf^V (ionic radius 0.85 Å). Hence it seemed reasonable to suppose that Nb^V (ionic radius 0.78 Å) might behave in a similar manner to these other metal ions. As we expected, Nb^V from the $[\text{Nb}(\text{NTA})_2]^-$ and antitumor complex $[\text{Cp}_2\text{NbCl}_2]/[\text{Cp}_2\text{Nb}(\text{OH})\text{Cl}_2]$ were readily taken up into the specific iron sites of ferric iron binding protein. The tight binding was confirmed by ICP-OES and ESI-MS studies. Interestingly, kinetic studies showed that the uptake of Nb^V by apo-Fbp is relatively rapid in vitro under the conditions used, and titration studies monitored using UV/vis also show that Nb^V can be displaced by Fe^{III}, although suggesting weaker binding of Nb^V. Structural studies using EXAFS suggest the presence of a dinuclear Nb(V) centre possibly with an Nb-O-Nb bridge, but further studies are needed to define the conditions under which the Cp ligands are displaced from Nb on binding to the protein. These properties may allow Nb^V to bind strongly to Fbp under certain environmental conditions. It would also be interesting to investigate potential catalytic properties of such a protein-bound dinuclear niobium centre. The recent novel use of the metal complex desferrioxamine-gallium (DFO-Ga) that targets *P. aeruginosa* iron metabolism and stops biofilm formation [44], coupled with our work, suggests that Nb^V complexes should be explored as potential novel metalloantibiotics.

Acknowledgments

The authors thank the Wellcome Trust (Travelling Research Fellowship awarded to Y. Shi) and Edinburgh Protein Interaction Centre, the BBSRC, EPSRC, for their support for this work. This paper is dedicated to Professor Nick Hadjiliadis (University of Ioannina) on the occasion of his retirement.

References

- [1] H. Köpf and P. Köpf-Maier, "Titanocene dichloride—the first metallocene with cancerostatic activity," *Angewandte Chemie International Edition*, vol. 18, no. 6, pp. 477–478, 1979.
- [2] P. Köpf-Maier, "Development of necroses, virus activation and giant cell formation after treatment of Ehrlich ascites tumor with metallocene dichlorides," *Journal of Cancer Research and Clinical Oncology*, vol. 103, no. 2, pp. 145–164, 1982.
- [3] P. Köpf-Maier, "Stage of pregnancy-dependent transplacental passage of 195mPt after cis-platinum treatment," *European Journal of Cancer and Clinical Oncology*, vol. 19, no. 4, pp. 533–536, 1983.
- [4] P. Köpf-Maier, "Tumor inhibition by titanocene complexes: influence upon two xenografted human lung carcinomas," *Journal of Cancer Research and Clinical Oncology*, vol. 113, no. 4, pp. 342–348, 1987.

- [5] P. Köpf-Maier, "Tumor inhibition by titanocene complexes: influence on xenografted human adenocarcinomas of the gastrointestinal tract," *Cancer Chemotherapy and Pharmacology*, vol. 23, no. 4, pp. 225–230, 1989.
- [6] P. Köpf-Maier, "Antitumor activity of titanocene dichloride in xenografted human renal-cell carcinoma," *Anticancer Research*, vol. 19, no. 1A, pp. 493–504, 1999.
- [7] P. Köpf-Maier and H. Köpf, "Antitumor metallocenes: new developments and toxicologic features," *Anticancer Research*, vol. 6, no. 2, pp. 227–233, 1986.
- [8] P. Köpf-Maier and H. Köpf, "Tumor inhibition by titanocene complexes. Activity against B16 melanoma and colon 38 carcinoma," *Arzneimittel-Forschung*, vol. 37, no. 5, pp. 532–534, 1987.
- [9] P. Köpf-Maier, M. Leitner, R. Voigtländer, and H. Köpf, "Molybdocen-dichlorid als antitumor-agens," *Zeitschrift für Naturforschung C*, vol. 34, no. 12, pp. 1174–1176, 1979.
- [10] N. Kröger, U. R. Kleeberg, K. Mross, L. Edler, G. Saß, and D. K. Hossfeld, "Phase II clinical trial of titanocene dichloride in patients with metastatic breast cancer," *Onkologie*, vol. 23, no. 1, pp. 60–62, 2000.
- [11] M. M. Harding and G. Mokdsi, "Antitumour metallocenes: structure-activity studies and interactions with biomolecules," *Current Medicinal Chemistry*, vol. 7, no. 12, pp. 1289–1303, 2000.
- [12] P. Köpf-Maier and T. Kapötke, "Antitumor activity of ionic niobocene and molybdocene complexes in high oxidation states," *Journal of Cancer Research and Clinical Oncology*, vol. 118, no. 3, pp. 216–221, 1992.
- [13] P. Köpf-Maier and H. Köpf, "Non-platinum-group metal antitumor agents: history, current status, and perspectives," *Chemical Reviews*, vol. 87, no. 5, pp. 1137–1152, 1987.
- [14] P. Köpf-Maier, M. Leitner, and H. Köpf, "Tumor inhibition by metallocenes: antitumor activity of niobocene and tungstocene dichlorides," *Journal of Inorganic and Nuclear Chemistry*, vol. 42, no. 12, pp. 1789–1791, 1980.
- [15] M. M. Harding, M. Prodigalidad, and M. J. Lynch, "Organometallic anticancer agents. 2. Aqueous chemistry and interaction of niobocene dichloride with nucleic acid constituents and amino acids," *Journal of Medicinal Chemistry*, vol. 39, no. 25, pp. 5012–5016, 1996.
- [16] C. Ratledge, "Iron metabolism and infection," *Food and Nutrition Bulletin*, vol. 28, no. 4, supplement, pp. S515–S523, 2007.
- [17] U. E. Schaible and S. H. E. Kaufmann, "Iron and microbial infection," *Nature Reviews Microbiology*, vol. 2, no. 12, pp. 946–953, 2004.
- [18] I. J. Schalk, "Metal trafficking via siderophores in Gram-negative bacteria: specificities and characteristics of the pyoverdine pathway," *Journal of Inorganic Biochemistry*, vol. 102, no. 5–6, pp. 1159–1169, 2008.
- [19] A. J. Nowalk, S. B. Tencza, and T. A. Mietzner, "Coordination of iron by the ferric iron-binding protein of pathogenic *Neisseria* is homologous to the transferrins," *Biochemistry*, vol. 33, no. 43, pp. 12769–12775, 1994.
- [20] W. Zhong, D. Alexeev, I. Harvey, et al., "Assembly of an oxo-zirconium(IV) cluster in a protein cleft," *Angewandte Chemie International Edition*, vol. 43, no. 44, pp. 5914–5918, 2004.
- [21] W. Zhong, J. A. Parkinson, M. Guo, and P. J. Sadler, "Unusual features for zirconium(IV) binding to human serum transferrin," *Journal of Biological Inorganic Chemistry*, vol. 7, no. 6, pp. 589–599, 2002.
- [22] H. Zhu, D. Alexeev, D. J. B. Hunter, D. J. Campopiano, and P. J. Sadler, "Oxo-iron clusters in a bacterial iron-trafficking protein: new roles for a conserved motif," *Biochemical Journal*, vol. 376, no. 1, pp. 35–41, 2003.
- [23] M. Guo, I. Harvey, D. J. Campopiano, and P. J. Sadler, "Short oxo-titanium(IV) bond in bacterial transferrin: a protein target for metalloantibiotics," *Angewandte Chemie International Edition*, vol. 45, no. 17, pp. 2758–2761, 2006.
- [24] C. Ferreirós, M. T. Criado, and J. A. Gómez, "The neisserial 37 kDa ferric binding protein (FbpA)," *Comparative Biochemistry and Physiology B*, vol. 123, no. 1, pp. 1–7, 1999.
- [25] P. Ellis, *Studies of metalloproteins using EXAFS and XPD*, Ph.D. thesis, University of Sydney, Sydney, Australia, 1995.
- [26] J. J. Rehr and R. C. Albers, "Scattering-matrix formulation of curved-wave multiple-scattering theory: application to X-ray-absorption fine structure," *Physical Review B*, vol. 41, no. 12, pp. 8139–8149, 1990.
- [27] N. Binsted, *EXCURV98: CCLRC Daresbury Laboratory Computer Program*, CCLRC Daresbury Laboratory, Warrington, UK, 1998.
- [28] L. Hedin, A. Johansson, Bi. Lundqvist, S. Lundqvist, and V. Samathiy, "Effects of electron-electron interaction on one-electron properties of atoms and solids," *Arkiv för Fysik*, vol. 39, no. 2, p. 97, 1969.
- [29] J. J. Rehr, J. M. de Leon, S. I. Zabinsky, and R. C. Albers, "Theoretical X-ray absorption fine structure standards," *Journal of the American Chemical Society*, vol. 113, no. 14, pp. 5135–5140, 1991.
- [30] M. Guo, I. Harvey, W. Yang, et al., "Synergistic anion and metal binding to the ferric ion-binding protein from *Neisseria gonorrhoeae*," *Journal of Biological Chemistry*, vol. 278, no. 4, pp. 2490–2502, 2003.
- [31] G. M. Then, H. Appel, J. Duffield, D. M. Taylor, and W.-G. Thies, "In vivo and in vitro studies of hafnium-binding to rat serum transferrin," *Journal of Inorganic Biochemistry*, vol. 27, no. 4, pp. 255–270, 1986.
- [32] M. Guo, H. Sun, H. J. McArdle, L. Gambling, and P. J. Sadler, "Ti(IV) uptake and release by human serum transferrin and recognition of Ti(IV)-transferrin by cancer cells: understanding the mechanism of action of the anticancer drug titanocene dichloride," *Biochemistry*, vol. 39, no. 33, pp. 10023–10033, 2000.
- [33] H. Sun, H. Li, and P. J. Sadler, "Transferrin as a metal ion mediator," *Chemical Reviews*, vol. 99, no. 9, pp. 2817–2842, 1999.
- [34] C. M. Bruns, D. S. Anderson, K. G. Vaughan, et al., "Crystallographic and biochemical analyses of the metal-free *Haemophilus influenzae* Fe³⁺-binding protein," *Biochemistry*, vol. 40, no. 51, pp. 15631–15637, 2001.
- [35] D. Alexeev, H. Zhu, M. Guo, et al., "A novel protein-mineral interface," *Nature Structural Biology*, vol. 10, no. 4, pp. 297–302, 2003.
- [36] D. Homden, C. Redshaw, J. A. Wright, D. L. Hughes, and M. R. J. Elsegood, "Early transition metal complexes bearing a C-capped tris(phenolate) ligand incorporating a pendant imine arm: synthesis, structure, and ethylene polymerization behavior," *Inorganic Chemistry*, vol. 47, no. 13, pp. 5799–5814, 2008.
- [37] A. V. Gerasimenko, M. A. Pushilin, and R. L. Davidovich, "Disordering of the [NbOF₅]²⁻ complex anions in bis(glycinium) pentafluoridooxidoniobate(V) and bis(β-alaninium) pentafluoridooxidoniobate(V) dihydrate," *Acta Crystallographica C*, vol. 64, part 11, pp. m358–m361, 2008.

- [38] S. K. Park, S. M. Koo, and Y. E. Lee, "Heterometallic lithium niobium complexes: synthesis and molecular structures of $\text{LiNbO}(\text{O}-2,6\text{-PhMe}_2)_4 \cdot 3\text{TTHF}$ and $[\text{LiNbCl}_3(\text{O}-2,6\text{-PhMe}_2)_2 \cdot 2\text{TTHF}]_2$," *Polyhedron*, vol. 19, no. 9, pp. 1037–1041, 2000.
- [39] M. K. Van Bael, I. Arcon, K. Van Werde, D. Nelis, J. Mullens, and L. C. Van Poucke, "Structure determination by EXAFS of Nb-peroxo-citrato complexes in aqueous solution-gel systems," *Physica Scripta*, vol. T115, pp. 415–417, 2005.
- [40] M. Pintor, L. Ferrón, J. A. Gómez, A. Gorringe, M. T. Criado, and C. M. Ferreirós, "Blocking of iron uptake by monoclonal antibodies specific for the *Neisseria meningitidis* transferrin-binding protein 2," *Journal of Medical Microbiology*, vol. 45, no. 4, pp. 252–257, 1996.
- [41] C. Ferreirós, M. T. Criado, and J. A. Gómez, "The neisserial 37 kDa ferric binding protein (FbpA)," *Comparative Biochemistry and Physiology B*, vol. 123, no. 1, pp. 1–7, 1999.
- [42] H. Boukhalfa, D. S. Anderson, T. A. Mietzner, and A. L. Crumbliss, "Kinetics and mechanism of iron release from the bacterial ferric binding protein nFbp: exogenous anion influence and comparison with mammalian transferrin," *Journal of Biological Inorganic Chemistry*, vol. 8, no. 8, pp. 881–892, 2003.
- [43] J. A. Gómez, M. T. Criado, and C. M. Ferreirós, "Bactericidal activity of antibodies elicited against the *Neisseria meningitidis* 37-kDa ferric binding protein (FbpA) with different adjuvants," *FEMS Immunology and Medical Microbiology*, vol. 20, no. 1, pp. 79–86, 1998.
- [44] E. Banin, A. Lozinski, K. M. Brady, et al., "The potential of desferrioxamine-gallium as an anti-*Pseudomonas* therapeutic agent," *Proceedings of the National Academy of Sciences of the United States of America*, vol. 105, no. 43, pp. 16761–16766, 2008.

Research Article

Effect of Common Buffers and Heterocyclic Ligands on the Binding of Cu(II) at the Multimetal Binding Site in Human Serum Albumin

Magdalena Sokołowska,¹ Krystyna Pawlas,¹ and Wojciech Bal^{2,3}

¹ Department of Hygiene, Wrocław Medical University, Mikulicza-Radeckiego 7, 50-345 Wrocław, Poland

² Institute of Biochemistry and Biophysics, Polish Academy of Sciences, Pawińskiego 5a, 02-106 Warsaw, Poland

³ Central Institute for Labour Protection-National Research Institute, Czerniakowska 16, 00-701 Warsaw, Poland

Correspondence should be addressed to Wojciech Bal, wbal@ibb.waw.pl

Received 16 December 2009; Accepted 16 February 2010

Academic Editor: Spyros Perlepes

Copyright © 2010 Magdalena Sokołowska et al. This is an open access article distributed under the Creative Commons Attribution License, which permits unrestricted use, distribution, and reproduction in any medium, provided the original work is properly cited.

Visible-range circular dichroism titrations were used to study Cu(II) binding properties of Multimetal Binding Site (MBS) of Human Serum Albumin (HSA). The formation of ternary MBS-Cu(II)-Buffer complexes at pH 7.4 was positively verified for sodium phosphate, Tris, and Hepes, the three most common biochemical buffers. The phosphate > Hepes > Tris order of affinities, together with strong spectral changes induced specifically by Tris, indicates the presence of both Buffer-Cu(II) and Buffer-HSA interactions. All complexes are strong enough to yield a nearly 100% ternary complex formation in 0.5 mM HSA dissolved in 100 mM solutions of respective buffers. The effects of warfarin and ibuprofen, specific ligands of hydrophobic pockets I and II in HSA on the Cu(II) binding to MBS were also investigated. The effects of ibuprofen were negligible, but warfarin diminished the MBS affinity for Cu(II) by a factor of 20, as a result of indirect conformational effects. These results indicate that metal binding properties of MBS can be modulated directly and indirectly by small molecules.

1. Introduction

Human serum albumin (HSA) is the most abundant protein of blood serum, at a concentration of ca. 0.6 mM (~4%). It is a versatile carrier protein, involved in the transport of hormones, vitamins, fatty acids, xenobiotics, drugs and metabolites [1]. HSA also carries metal ions, including physiological Ca^{2+} , Zn^{2+} , Co^{2+} , and Cu^{2+} , as well as toxic Cd^{2+} and Ni^{2+} [1–3]. Four distinct metal binding sites have been characterized so far in HSA. Cys-34, the only free thiol in HSA, is located at the bottom of a hydrophobic pocket. It selectively binds hydrophobic complexes of heavy metal ions, such as Pt^{2+} and Au^+ [4–7]. Three other sites are more accessible and more versatile. The N-terminal binding site (NTS, also called the ATCUN motif) has been characterized particularly well. It is composed of the first three amino acid residues of the HSA sequence, Asp-Ala-His. This sequence is

not confined sterically, as evidenced by the absence of trace of these residues in X-ray structures of HSA [1, 2] and has a conformational freedom to wrap around a metal ion. The resulting square-planar complex exhibits a rare coordination mode with deprotonated amide nitrogens of Ala and His residues, in addition to the N-terminal amine and the His-3 imidazole donor [8–10]. It provides the primary binding site for Cu(II) and Ni(II) ions and the tertiary site for Co(II) ions [10, 11]. We recently demonstrated that the conditional dissociation constant for Cu(II) binding at the NTS is as low as 1 pM [12]. The studies of short peptide models of similar His-3 sites performed in our and other laboratories, for example, by Hadjilidiadis et al., uniformly indicated their very high affinities for Cu(II), and also Ni(II) ions [13–15]. There is abundant experimental evidence for the complete saturation of the coordination sphere of the Cu(II) ion bonded to NTS and model peptides [9, 11–16].

Another site is composed of side chains of His67, His247, Asn99 i Asp249. It is located at the interface of domains I and II of HSA. We named it multimetal binding site (MBS) in our previous study, because we demonstrated that it can bind Cu(II), Ni(II), Zn(II), Cd(II), as well as Co(II) ions with comparable affinities [10, 11]. This site is identical with cadmium site B (CdB) characterized by NMR spectroscopy [17–19]. Recent studies on Zn(II) binding at MBS provided crucial data about its spatial arrangement [18]. The location of the third site, called cadmium site A (CdA), remains unknown. It is the primary site for Cd(II) and Co(II) ions but does not participate in Cu(II) binding [11].

The structure of MBS was analyzed by NMR and molecular modeling of the Zn(II) complex [18]. The Zn(II) ion is pentacoordinate in a square pyramidal geometry, with equatorial coordination provided by two imidazole nitrogens (His67 and His247), a carboxylate oxygen (Asp249) and a carbonyl oxygen (Asn99). The axial site in this structure is occupied by a water molecule. This fact suggests that the MBS binding site may be modified by external ligands, forming hypothetical ternary species.

In this work we attempted to find out whether common buffers may interact with the Cu(II) ion bonded at MBS. We also tested whether occupation of hydrophobic pockets, which are used for transportation of endogenous and exogenous aromatic molecules [20–23], may affect the coordination properties of MBS.

2. Experimental

2.1. Materials. Homogeneous, high purity defatted HSA was obtained from Sigma. CuCl₂, Hepes, Tris, sodium phosphate, and NaCl were obtained from Aldrich. Stock solution of CuCl₂ was standardized complexometrically. CuCl₂ solutions were calibrated as described in [15]. NaOH and HCl were purchased from Merck.

2.2. Methods. The CD spectra were recorded at 25°C on a Jasco J-715 spectropolarimeter (JASCO, Japan Spectroscopic Co., Hiroshima, Japan), over the range of 300–800 nm, using a 1 cm cuvette. The spectra are expressed in terms of $\Delta\epsilon = \epsilon_l - \epsilon_r$, where ϵ_l and ϵ_r are molar absorption coefficients for left and right circularly polarized light, respectively. In buffer experiments the solutions contained 100 mM Hepes, Tris, Sodium Phosphate, or NaCl, at pH 7.4.

HSA was dissolved at 0.3–0.5 mM in either a 100 mM Hepes, Tris, Sodium Phosphate buffers, pH 7.4, or in an unbuffered 100 mM NaCl solution. The pH of both types of samples was controlled to remain in the 7.38–7.42 corridor and adjusted with submicroliter amounts of concentrated HCl or NaOH when necessary. Concentrations of stock solutions of HSA were estimated spectrophotometrically at 279 nm [9] and by Cu(II) titrations. The fractional abundance of NTS in HSA was measured by careful CD titrations using calibrated Cu(II) solutions. The average value of 0.73 was obtained, in agreement with the previous studies [10–12, 15, 24].

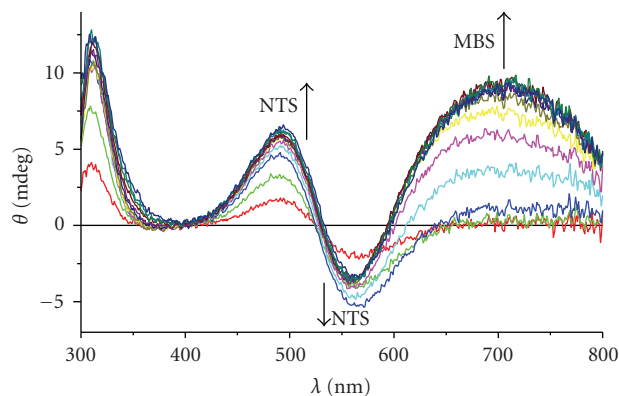


FIGURE 1: CD spectra of Cu(II) titration of HSA (0.5 mM in 0.1 M NaCl, pH 7.4), from 0 to 3 mol equivalents, at a 0.25 mol equivalent step.

3. Results and Discussion

3.1. The Effect of Buffers on the Binding of Cu(II) Ions at MBS.

We chose sodium phosphate, Tris and Hepes as the most common substances used for buffering protein solutions at pH 7.4. Their effect on Cu(II) binding to HSA was studied at a 0.1 M concentration stage versus unbuffered 0.1 M NaCl, used as a control solution. The choice of the latter was dictated by the presence of 0.1 M chloride in the blood serum [25]. The pH of the NaCl samples was controlled by additions of small quantities of concentrated HCl or NaOH solutions, when necessary. This was achieved thanks to the self-buffering properties of HSA, based on the presence of multiple His residues on its surface [9, 26]. The titrations were monitored by CD spectroscopy, analogously to our previous studies [10, 15].

A typical titration is presented on Figure 1. Figure 2 shows titration curves, obtained from titration experiments by plotting the changes of ellipticity ($\Delta\theta$) at λ_{\max} of Cu(II) complexes at MBS (665 nm for Tris and 695 nm for remaining solutions). The changes of ellipticities of transitions related to Cu(II) complexes at NTS, at 492 and 565 nm, were linear up to the NTS saturation, in accordance with a very high affinity of this site [12].

The pure spectra of NTS and MBS complexes in individual solutions, calculated by extrapolation of titration data, are shown in Figures 3 and 4, respectively. The shapes and intensities of NTS bands were not affected by buffers studied. In contrast, the presence of Tris altered the appearance of the characteristic MBS band considerably, compared to the NaCl reference. The effects of phosphate and Hepes were less pronounced, but still significant.

Apparent binding constants (K_{app}) for Cu(II)-MBS complexes in the presence of buffers were obtained from titrations presented in Figure 2. These constants, calculated on a technical assumption of the formation of binary species only, are presented in Table 1. Table 1 contains also further constants, calculated relative to the Cu(II)-MBS interaction in NaCl, taken as corresponding to a 100% binary complex formation. These calculations were prompted by spectral

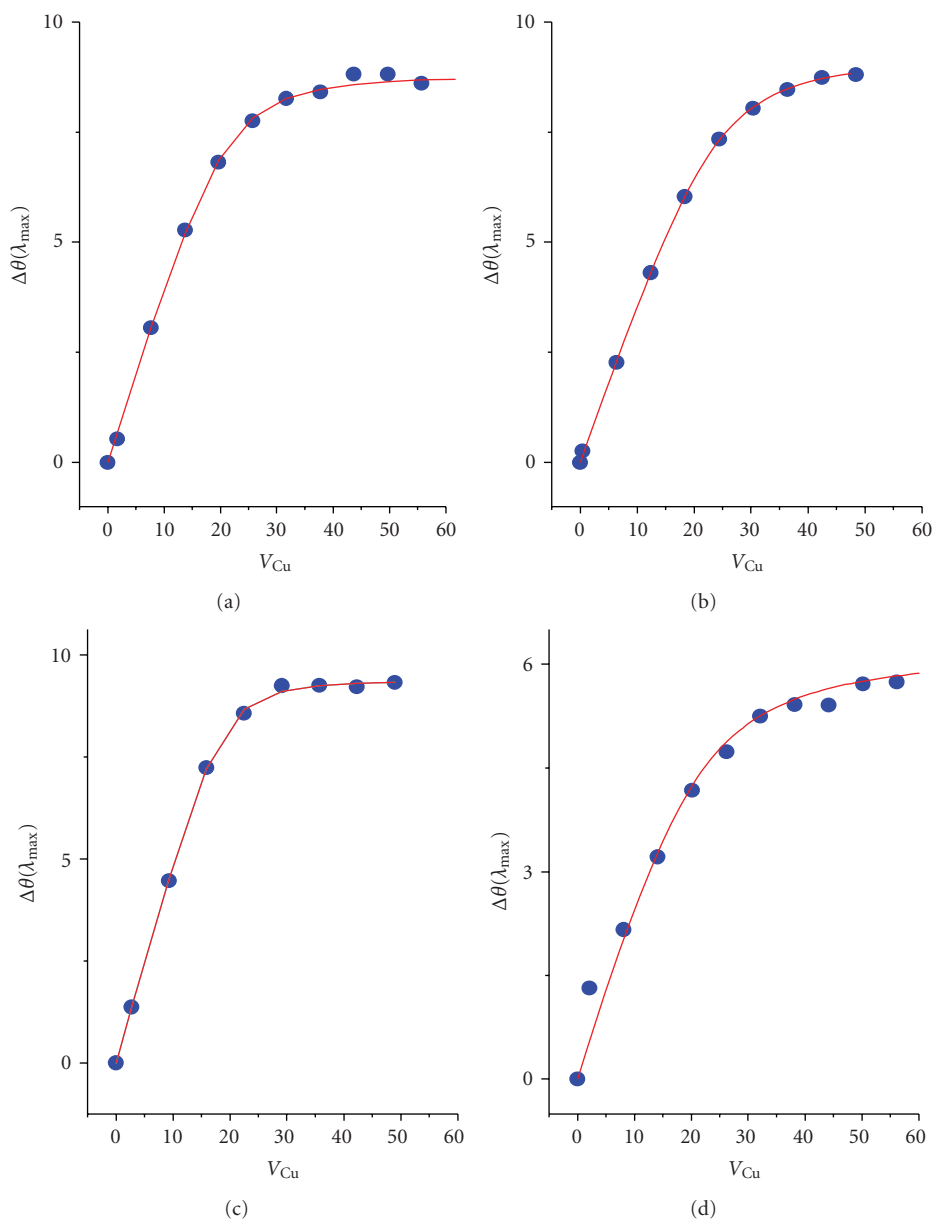


FIGURE 2: Titration curves (experimental points, ●, and fits to the K_{app} formula, —) for Cu(II) binding at MBS in four solutions studied: (a) NaCl; (b) Hepes; (c) sodium phosphate; (d) Tris.

effects described above and by significant differences among $\log K_{app}$ values.

First, the effects of competition of buffers for Cu(II) were accounted for Literature protonation and Cu(II) binding constants of Hepes [27], Tris [28], and phosphate ions [29] were used in these calculations. The competition-only model of interaction, could not, however, reproduce the titration curves, and it was necessary to include ternary complex formation. Figure 5 illustrates this issue for the case of Hepes buffer. The shift of the MBS $d \rightarrow d$ band to higher energies by 30 nm, from 695 on 665 nm, also provided an unequivocal piece of evidence in favor of ternary complex formation with Tris. Calculations based on this assumption, performed for all three buffers, yielded equilibrium constants, given in

Table 1. The reactions defining these constants are provided in the footnotes of Table 1.

Briefly, K_{111} describes the overall formation of a ternary species, K_{11} is the literature binding constant of the Cu(II) complex of a buffer, K_e corresponds to the ternary complex formation by addition of buffer-complexed Cu(II) to MBS, and K_T is the equilibrium constant of the formation of the ternary complex in the reaction of two binary complexes, thus featuring the tendency of binary components to form a ternary species [33]. All these constants, except for K_{11} , are conditional in respect to the pH value of 7.4.

Calculations of titrations in these buffers demonstrated that the observed spectra were practically pure spectra of mixed complexes. The participation of the binary MBS

TABLE 1: Quantitative description of ternary complexes formed by Cu(II) ions at MBS of HSA at pH 7.4. Standard deviations of significant values of experimental logarithms constants on the last digits are given in parentheses.

Ligand (L)	$\log K_{app}$	$\log K_{111}^a$	$\log K_{11}^b$	$\log K_e^c$	$\log K_T^d$	CI ^e
[L] =						0.5 mM 100 mM
NaCl	4.60(3)					7.62
Hepes	4.45(5)	7.54(5)	3.22	4.32	-0.28	7.71 9.27
Tris	4.23(6)	8.22(5)	4.05	4.17	-0.43	7.74 9.42
Phosphate	5.17(7)	8.2(1)	3.20	5.00	+0.40	8.04 10.13

^a K_{111} is the equilibrium constant of the reaction $\text{Cu}^{2+} + \text{L} + \text{MBS} = \text{Cu}(\text{MBS})(\text{L})$.

^b K_{11} is the equilibrium constant of the reaction $\text{Cu}^{2+} + \text{L} = \text{Cu}(\text{L})$; literature values [30–32].

^c K_e is the equilibrium constant of the reaction $\text{MBS} + \text{Cu}(\text{L}) = \text{Cu}(\text{MBS})(\text{L})$; $\log K_{111} = \log K_{11} + \log K_e$.

^d K_T is the equilibrium constant of the reaction $\text{Cu}(\text{MBS}) + \text{Cu}(\text{L}) = \text{Cu}(\text{MBS})(\text{L}) + \text{Cu}^{2+}$.

$\log K_T = \log K_{111} - \log K_{11} - \log K_{app}(\text{NaCl})$.

^e CI is the competitiveness index (description in text), calculated for following total concentrations: Cu(II) and Z = 1 μM , HSA = 0.5 mM, buffer = 0.5 mM, or 100 mM.

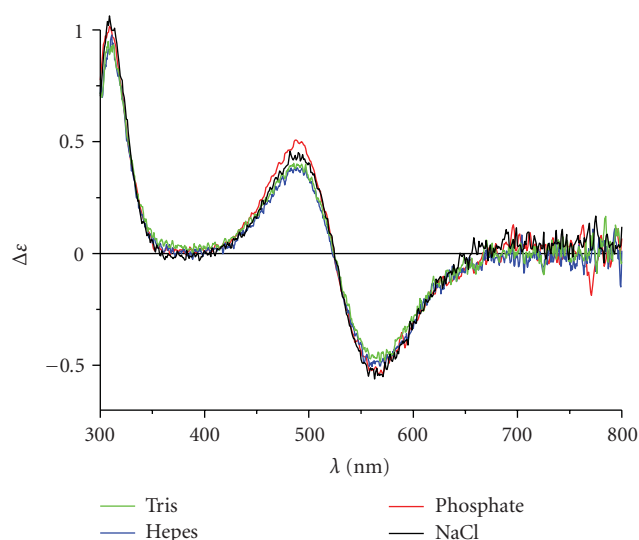


FIGURE 3: Spectra of pure forms of NTS-Cu(II) complexes obtained by extrapolation of titration data.

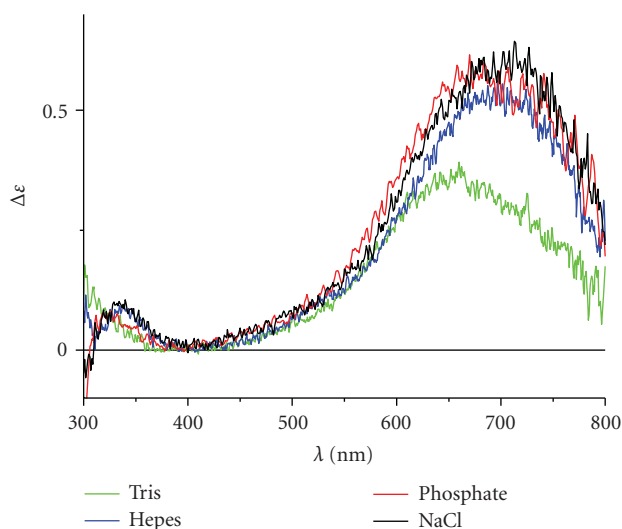


FIGURE 4: Spectra of pure forms of MBS-Cu(II) complexes obtained by extrapolation of titration data.

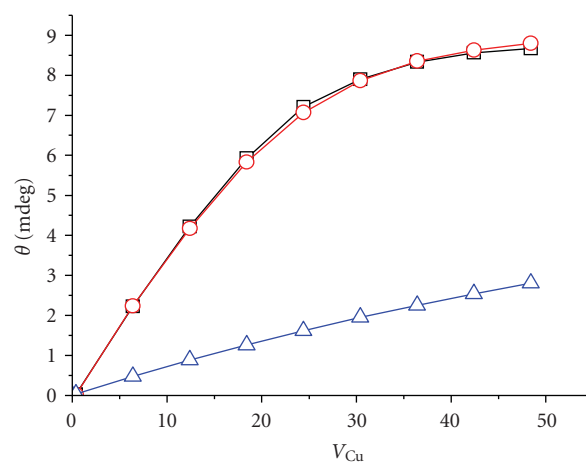


FIGURE 5: Comparison of experimental data (\square), the best fit to the ternary complex model (\circ), and the simulation of titration in the absence of ternary complex formation (\triangle) for the titration of MBS in 0.1 M Hepes, pH 7.4.

complex was less than 1.5% at all titration points. This feature allowed us to speculate about the binding modes in ternary complexes. The spectra for Hepes and phosphate were practically identical with those of the binary complex, but the titration curves demonstrated the significant quantitative deviation from the binary complex-only binding. Therefore, the most likely binding mode for these two substances is that based on a substitution of the axial water molecule with a buffer oxygen donor. The comparatively high binding constants for ternary complexes, in relation to binary complexes, demonstrated the creation of accessory interactions between HSA and the ligand. The blueshift and change of the band intensity for Tris suggests a substitution of an equatorial oxygen, perhaps that of Asn99.

CI values presented in the last column of Table 1 were calculated for total concentrations for Cu(II) and the formal competitor $Z = 1 \mu\text{M}$ and for HSA = 0.5 mM at pH = 7.4. These calculations were done in two versions—for L (buffer) concentrations of 0.5 mM and 100 mM. These concentrations of HSA and Cu(II) ions corresponded to

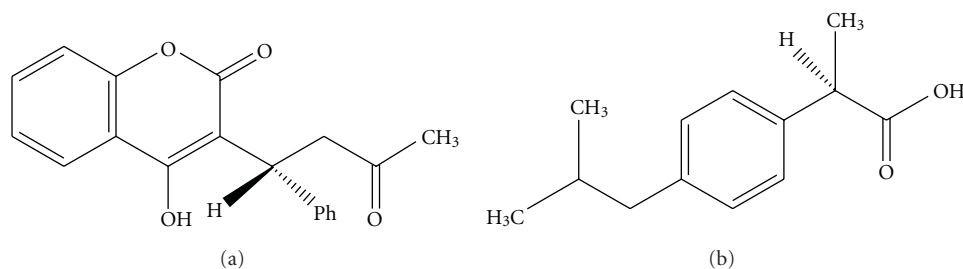


FIGURE 6: Chemical structures of warfarin (War, left) and ibuprofen (Ibu, right).

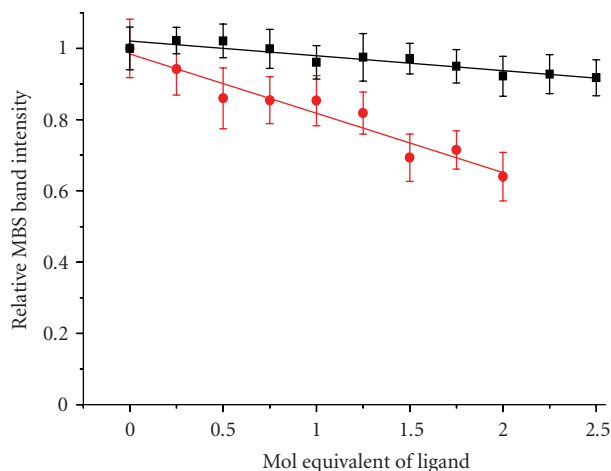


FIGURE 7: Titrations of HSA in the presence of 1.75 mol equivalents of Cu(II) with War (A) and Ibu (B) from 0 to 2.5 mol equivalents in 0.25 mol equivalent steps. The titration of War was terminated at 2 mol equivalents due to the loss of solution transparency. The solid lines represent linear fits to the data.

physiological values, the latter to the exchangeable pool of Cu(II) in blood plasma [32]. From these calculations, one can infer that the formation of ternary complexes with buffers had a relatively small impact on the affinity of Cu(II) ions to MBS. The values of K_T demonstrated that HEPES and Tris buffers somewhat destabilized this interaction, and phosphate ion showed a stabilizing effect. However, their effects on Cu(II) binding were significant at practically used buffer concentrations of 100 mM. HEPES was applied in successive investigations, because this buffer showed the smallest interference with Cu(II) binding parameters of MBS.

3.2. Interaction between MBS and Hydrophobic Pockets for Aromatic Molecules. It was interesting to find out whether the binding of warfarin (War) and ibuprofen (Ibu) (Figure 6, exogenous ligands characteristic for hydrophobic pockets (Sudlow's sites) I and II in HSA, respectively, could influence Cu(II) binding at NTS, and, in particular MBS.

In these experiments we used HSA samples containing 1.75 mol equivalents of Cu(II) ions. According to the results and discussion presented above, these samples contained fully saturated NTS and one mole equivalent of Cu(II) in an equilibrium with MBS, at about 80% saturation. The samples

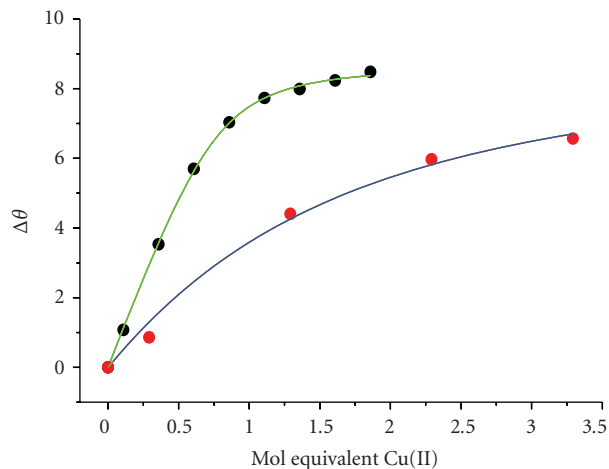


FIGURE 8: Comparison of titration curves for Cu(II) binding at MBS obtained in the presence of 1 mol equivalents of Ibu (experimental points, ●, and fits to the K_{app} formula, —) and War (experimental points, ●, and fits to the K_{app} formula, —).

were titrated separately with War and Ibu. None of these two substances possesses donor groups, which would can effectively bind Cu(II) ions in solution. This notion was confirmed by the absence of complex formation fingerprints in UV-vis spectroscopy and circular dichroism (CD) spectra (data not shown), and by the literature [20–22, 34, 35].

The HSA binding constants for War ($3.3 \times 10^5 \text{ M}^{-1}$) and Ibu ($2.7 \times 10^6 \text{ M}^{-1}$) [30, 36–38] are sufficiently high to assure stoichiometric binding to their respective binding pockets in 0.5 mM HSA solutions—the addition of one equivalent of ligand yields a 93% saturation for War and a 99% saturation for Ibu. Figure 7 shows the titrations of 0.5 mM HSA with War and Ibu in the presence of 1.75 mol equivalents of Cu(II) ions. In the course of these titrations, we observed a specific decrease of intensity of the MBS band. The band position remained unchanged. The effect of Ibu was very subtle, but that of War was clearly pronounced. Interestingly, the linearity of the band intensity decrease was similar before and after the stoichiometric binding point for both HSA ligands.

Figure 8 presents titrations of HSA with Cu(II) ions in the presence of stoichiometric (1 mol equivalent) amounts of War and Ibu, performed in a 100 mM HEPES buffer, pH 7.4. The Ibu titration yielded the $\log K_{app}$ value of 4.49(5), identical within the experimental error with that obtained in

100 mM Hepes in the absence of Ibu (4.45(5), Table 1). The presence of War had however a pronounced effect on Cu(II) binding. A very low log K_{app} value of 3.2(2) was obtained. Therefore, the binding of War decreased the affinity of MBS for Cu(II) by a factor of 20. The Cu(II) binding at NTS was unaffected in both cases.

The effects presented in Figures 7 and 8 can be interpreted by taking into account the locations of hydrophobic pockets. War binds specifically at site I, which is located in subdomain IIA of HSA, while Ibu binds specifically at site II, which is located in subdomain IIIA [1, 2, 31]. MBS is located at the interface of domains IB and IIA, much closer to site I than to site II, which is separated from MBS by a very large crevice [32]. Based on the present data, we can speculate that the binding of warfarin induced a conformational change which decreased the accessibility of MBS. The absence of CD spectral changes of the Cu(II)-MBS complex indicated, however, that the geometry of the site itself was not affected.

4. Conclusion

The results presented above clearly indicate that the Cu(II) binding properties of MBS of HSA can be influenced by external ligands. The order of buffer affinities for the formation of ternary MBS-Cu(II)-Buffer complexes, phosphate > Hepes > Tris, indicates that the interaction is not limited to the binding with the metal ion. This notion is supported by strong spectral changes induced specifically by Tris, which clearly indicate the addition of the Tris nitrogen atom to the coordination sphere of MBS-bound Cu(II) ion. The indirect effect of warfarin indicates a specific negative control of MBS binding of metal ions by site I ligands.

MBS is unlikely to carry Cu(II) physiologically but is considered as a major transport site for Zn(II) ions in blood plasma [18]. The interactions described in this paper are very likely to be shared by MBS occupied by a Zn(II) ion, because Cu(II) and Zn(II) binding modes are thought to be very similar. Therefore, Zn(II) binding properties of MBS may be modulated directly and indirectly by small molecules. This physiologically important issue will be investigated in our future studies.

Acknowledgments

The authors wish to acknowledge the skilled and competent technical assistance of Mrs. Lidia Januszewska M. C. This work was sponsored by the Polish Ministry of Education and Science and supported by the Medical University of Wrocław-Statute Investigations no. 30-ST30.

References

- [1] D. C. Carter and J. X. Ho, "Structure of serum albumin," *Advances in Protein Chemistry*, vol. 45, pp. 153–203, 1994.
- [2] X. M. He and D. C. Carter, "Atomic structure and chemistry of human serum albumin," *Nature*, vol. 358, no. 6383, pp. 209–215, 1992.
- [3] T. Peters Jr., "Serum albumin," *Advances in Protein Chemistry*, vol. 37, pp. 161–245, 1985.
- [4] O. M. N. Dhuhghaill, P. J. Sadler, and A. Tucker, "Drug-induced reactions of bovine serum albumin: ^1H NMR studies of gold binding and cysteine release," *Journal of the American Chemical Society*, vol. 114, no. 3, pp. 1118–1120, 1992.
- [5] J. Christodoulou, P. J. Sadler, and A. Tucker, " ^1H NMR of albumin in human blood plasma: drug binding and redox reactions at Cys34," *FEBS Letters*, vol. 376, no. 1–2, pp. 1–5, 1995.
- [6] J. Talib, J. L. Beck, and S. F. Ralph, "A mass spectrometric investigation of the binding of gold antiarthritic agents and the metabolite $[\text{Au}(\text{CN})_2]^-$ to human serum albumin," *Journal of Biological Inorganic Chemistry*, vol. 11, no. 5, pp. 559–570, 2006.
- [7] A. I. Ivanov, J. Christodoulou, J. A. Parkinson, et al., "Cisplatin binding sites on human albumin," *Journal of Biological Chemistry*, vol. 273, no. 24, pp. 14721–14730, 1998.
- [8] J.-P. Laussac and B. Sarkar, "Characterization of the copper (II)- and nickel(II)-transport site of human serum albumin. Studies of copper(II) and nickel(II) binding to peptide 1–24 of human serum albumin by ^{13}C and ^1H NMR spectroscopy," *Biochemistry*, vol. 23, no. 12, pp. 2832–2838, 1984.
- [9] P. J. Sadler, A. Tucker, and J. H. Viles, "Involvement of a lysine residue in the N-terminal Ni^{2+} and Cu^{2+} binding site of serum albumins. Comparison with Co^{2+} , Cd^{2+} and Al^{3+} ," *European Journal of Biochemistry*, vol. 220, no. 1, pp. 193–200, 1994.
- [10] W. Bal, J. Christodoulou, P. J. Sadler, and A. Tucker, "Multi-metal binding site of serum albumin," *Journal of Inorganic Biochemistry*, vol. 70, no. 1, pp. 33–39, 1998.
- [11] M. Sokołowska, M. Wszelaka-Rylik, J. Poznański, and W. Bal, "Spectroscopic and thermodynamic determination of three distinct binding sites for Co(II) ions in human serum albumin," *Journal of Inorganic Biochemistry*, vol. 103, no. 7, pp. 1005–1013, 2009.
- [12] M. Rózga, M. Sokołowska, A. M. Protas, and W. Bal, "Human serum albumin coordinates Cu(II) at its N-terminal binding site with 1 pM affinity," *Journal of Biological Inorganic Chemistry*, vol. 12, no. 6, pp. 913–918, 2007.
- [13] M. Mylonas, J. C. Plakatouras, and N. Hadjiliadis, "Interactions of Ni(II) and Cu(II) ions with the hydrolysis products of the C-terminal -ESHM-Motif of histone H2A model peptides. Association of the stability of the complexes formed with the cleavage of the -E-S-bond," *Dalton Transactions*, no. 24, pp. 4152–4160, 2004.
- [14] M. Mylonas, J. C. Plakatouras, N. Hadjiliadis, K. D. Papavasileiou, and V. S. Melissas, "An extremely stable Ni(II) complex derived from the hydrolytic cleavage of the C-terminal tail of histone H2A," *Journal of Inorganic Biochemistry*, vol. 99, no. 2, pp. 637–643, 2005.
- [15] M. Sokołowska, A. Krezel, M. Dyba, Z. Szweczek, and W. Bal, "Short peptides are not reliable models of thermodynamic and kinetic properties of the N-terminal metal binding site in serum albumin," *European Journal of Biochemistry*, vol. 269, no. 4, pp. 1323–1331, 2002.
- [16] M. Valko, H. Morris, M. Mazur, J. Telser, E. J. L. McInnes, and F. E. Mabbs, "High-affinity binding site for copper(II) in human and dog serum albumins (an EPR study)," *The Journal of Physical Chemistry B*, vol. 103, pp. 5591–5597, 1999.
- [17] P. J. Sadler and J. H. Viles, " ^1H and ^{113}Cd NMR investigations of Cd^{2+} and Zn^{2+} binding sites on serum albumin: competition with Ca^{2+} , Ni^{2+} , Cu^{2+} , and Zn^{2+} ," *Inorganic Chemistry*, vol. 35, no. 15, pp. 4490–4496, 1996.
- [18] A. J. Stewart, C. A. Blindauer, S. Berezenko, D. Sleep, and P. J. Sadler, "Interdomain zinc site on human albumin,"

- Proceedings of the National Academy of Sciences of the United States of America*, vol. 100, no. 7, pp. 3701–3706, 2003.
- [19] E. O. Martins and T. Drakenberg, “Cadmium(II), zinc(II), and copper(II) ions binding to bovine serum albumin. A ^{113}Cd NMR study,” *Inorganica Chimica Acta*, vol. 67, pp. 71–74, 1982.
- [20] O. J. M. Bos, J. P. M. Remijn, M. J. E. Fischer, J. Wilting, and L. H. M. Janssen, “Location and characterization of the warfarin binding site of human serum albumin. A comparative study of two large fragments,” *Biochemical Pharmacology*, vol. 37, no. 20, pp. 3905–3909, 1988.
- [21] N. A. Kratochwil, W. Huber, F. Müller, M. Kansy, and P. R. Gerber, “Predicting plasma protein binding of drugs: a new approach,” *Biochemical Pharmacology*, vol. 64, no. 9, pp. 1355–1374, 2002.
- [22] F. Zsila, Z. Bikádi, and M. Simonyi, “Molecular basis of the cotton effects induced by the binding of curcumin to human serum albumin,” *Tetrahedron Asymmetry*, vol. 14, no. 16, pp. 2433–2444, 2003.
- [23] J. Wilting, W. F. Van der Giesen, L. H. M. Janssen, M. M. Weideman, M. Otagiri, and J. H. Perrin, “The effect of albumin conformation on the binding of warfarin to human serum albumin. The dependence of the binding of warfarin to human serum albumin on the hydrogen, calcium, and chloride ion concentrations as studied by circular dichroism, fluorescence, and equilibrium dialysis,” *Journal of Biological Chemistry*, vol. 255, no. 7, pp. 3032–3037, 1980.
- [24] B. Chan, N. Dodsworth, J. Woodrow, A. Tucker, and R. Harris, “Site-specific N-terminal auto-degradation of human serum albumin,” *European Journal of Biochemistry*, vol. 227, no. 1–2, pp. 524–528, 1995.
- [25] N. Fogh-Andersen, P. J. Bjerrum, and O. Siggaard-Andersen, “Ionic binding, net charge, and Donnan effect of human serum albumin as a function of pH,” *Clinical Chemistry*, vol. 39, no. 1, pp. 48–52, 1993.
- [26] P. J. Sadler and A. Tucker, “pH-induced structural transitions of bovine serum albumin. Histidine pK(a) values and unfolding of the N-terminus during the N to F transition,” *European Journal of Biochemistry*, vol. 212, no. 3, pp. 811–817, 1993.
- [27] M. Sokołowska and W. Bal, “Cu(II) complexation by “non-coordinating” N-2-hydroxyethylpiperazine-N’-2-ethanesulfonic acid (HEPES buffer),” *Journal of Inorganic Biochemistry*, vol. 99, no. 8, pp. 1653–1660, 2005.
- [28] B. E. Fischer, U. K. Häring, R. Tribolet, and H. Sigel, “Metal ion/buffer interactions. Stability of binary and ternary complexes containing 2-amino-2(hydroxymethyl)-1,3-propanediol (Tris) and adenosine 5’-triphosphate (ATP),” *European Journal of Biochemistry*, vol. 94, no. 2, pp. 523–530, 1979.
- [29] D. Banerjee, T. A. Kaden, and H. Sigel, “Enhanced stability of ternary complexes in solution through the participation of heteroaromatic N bases. Comparison of the coordination tendency of pyridine, imidazole, ammonia, acetate, and hydrogen phosphate toward metal ion nitrilotriacetate complexes,” *Inorganic Chemistry*, vol. 20, no. 8, pp. 2586–2590, 1981.
- [30] S. F. Sun, S. W. Kuo, and R. A. Nash, “Study of binding of warfarin to serum albumins by high performance liquid chromatography,” *Journal of Chromatography*, vol. 288, no. 2, pp. 377–388, 1984.
- [31] G. Sudlow, D. J. Birkett, and D. N. Wade, “The characterization of two specific drug binding sites on human serum albumin,” *Molecular Pharmacology*, vol. 11, no. 6, pp. 824–832, 1975.
- [32] J. Ghuman, P. A. Zunszain, I. Petitpas, A. A. Bhattacharya, M. Otagiri, and S. Curry, “Structural basis of the drug-binding specificity of human serum albumin,” *Journal of Molecular Biology*, vol. 353, no. 1, pp. 38–52, 2005.
- [33] M. Jezowska-Bojczuk, W. Bal, and K. S. Kasprzak, “Copper(II) interactions with an experimental antiviral agent, 1-deoxynojirimycin, and oxygen activation by resulting complexes,” *Journal of Inorganic Biochemistry*, vol. 64, no. 4, pp. 231–246, 1996.
- [34] V. K. Cheruvallath, C. M. Riley, S. R. Narayanan, S. Lindenbaum, and J. H. Perrin, “A quantitative circular dichroic investigation of the binding of the enantiomers of ibuprofen and naproxen to human serum albumin,” *Journal of Pharmaceutical and Biomedical Analysis*, vol. 15, no. 11, pp. 1719–1724, 1997.
- [35] A. M. L. Zátón and J. P. Villamor, “Study of heterocycle rings binding to human serum albumin,” *Chemico-Biological Interactions*, vol. 124, no. 1, pp. 1–11, 2000.
- [36] J. P. Tillement, R. Zini, P. d’Athis, and G. Vassent, “Binding of certain acidic drugs to human albumin: theoretical and practical estimation of fundamental parameters,” *European Journal of Clinical Pharmacology*, vol. 7, no. 4, pp. 307–313, 1974.
- [37] J. Flarakos, K. L. Morand, and P. Vouros, “High-throughput solution-based medicinal library screening against human serum albumin,” *Analytical Chemistry*, vol. 77, no. 5, pp. 1345–1353, 2005.
- [38] U. Kragh-Hansen, “Molecular aspects of ligand binding to serum albumin,” *Pharmacological Reviews*, vol. 33, no. 1, pp. 17–53, 1981.

Research Article

The Zn- or Cu-Thionein Character of a Metallothionein Determines Its Metal Load When Synthesized in Physiological (Metal-Unsupplemented) Conditions

Mercè Capdevila,¹ Òscar Palacios,¹ and Sílvia Atrian²

¹ *Departament de Química, Facultat de Ciències, Universitat Autònoma de Barcelona, 08193 Cerdanyola del Vallès (Barcelona), Spain*

² *Departament de Genètica, Facultat de Biologia, Universitat de Barcelona, Institut de Biomedicina de la Universitat de Barcelona (IBUB), 08028 Barcelona, Spain*

Correspondence should be addressed to Mercè Capdevila, merce.capdevila@uab.cat

Received 11 December 2009; Accepted 26 February 2010

Academic Editor: Spyros Perlepes

Copyright © 2010 Mercè Capdevila et al. This is an open access article distributed under the Creative Commons Attribution License, which permits unrestricted use, distribution, and reproduction in any medium, provided the original work is properly cited.

The present work comprises the recombinant synthesis of four metallothioneins (MTs) in metal-unsupplemented cultures and the characterization of the recovered metal complexes by means of analytical and spectrometric techniques. The four MTs are two *Drosophila* (MtnA and MtnB), one yeast (Crs5), and one mouse (mMT1) metallothionein isoforms. These four MTs exhibit distinct metal binding preferences, from a clear Cu-thionein character to a definite Zn-thionein nature, respectively. Although in all cases, the only metal ion present in the purified complexes is Zn²⁺, our results highlight an inherently different behaviour of those two types of MTs, in conditions that would mimic their synthesis in physiological environments. Therefore, intrinsically different roles can be hypothesized for the constitutively-produced MT peptides in the absence of any metal overload, depending on their Zn- or Cu-thionein character.

1. Introduction

Metallothioneins (MTs) are a superfamily of small proteins, ubiquitous and probably polyphyletic, which coordinate heavy-metal ions through metal-thiolate bonds established by their highly abundant cysteine residues [1]. Currently, and since they were first reported in 1957 [2], MTs biological structure and their contribution to a variety of physiological processes in the most diverse organisms still remain a matter of debate [3]. Besides their detoxifying properties, MTs appear to be involved in Zn and Cu homeostasis, while additionally they seem to participate in a myriad of processes specific to each different group of organisms considered.

Apo-MTs (also called thioneins) are random coil polypeptides, which only fold onto a definite 3D structure upon metal coordination. This implies that MTs adopt different 3D structures—the main determinant of protein functionality—depending on the nature and number of the metal ions that they coordinate in a given metal complex.

This is especially noteworthy because although the level of expression of *MT* genes remains generally low in the absence of metal induction, the possibility exists that some organisms or tissues accumulate demetalated (without metal ions) thionein peptides under definite conditions. In fact, some years ago, it was claimed that the levels of thionein in mammalian tissues under physiological conditions could be significantly high enough to harbour important implications for MT functionality in zinc and redox metabolism [4, 5]. However, native MT synthesis is extremely low unless the corresponding gene is induced by the presence of a specific metal ion or other stress conditions. This, in turn, practically precludes the purification of native apo-forms, produced in physiological conditions. This serious drawback can be avoided by means of recombinant synthesis. Remarkably, although this strategy has been widely used by many authors to obtain metal-MT complexes of the most diverse organisms, it has seldom been used to study MT synthesis in physiological environments in the absence of metal surplus.

Several years ago we set up an *E. coli* expression system that enabled the biosynthesis of Zn²⁺-, Cd²⁺-, and Cu⁺-MT complexes, equivalent to those natively synthesized, of sufficient quantity and purity to permit analytical, spectrometric, and spectroscopic characterization, by growing the corresponding recombinant bacteria in metal supplemented media [6, 7]. In this work, we have adapted the same synthesis rationale to study the metal binding abilities of different MTs when produced in bacteria grown in standard (i.e., nonmetal supplemented media), particularly in order to determine the features of the zinc-complexes biosynthesized in these conditions.

To perform this study we selected four Metallothioneins, belonging to a broad spectrum of organisms: two *Drosophila* (MtnA and MtnB), a yeast (Crs5), and a mouse (mMT1) isoform (Table 1), because they exhibit distinct metal binding preferences when considered in accordance with our classification as Zn-thionein versus Cu-thionein [8]. We have recently revised this first classification scheme, based on two discrete MT groups, and we now propose a stepwise gradation between extreme Zn-thioneins and Cu-thioneins that holds a continuum of intermediate forms in terms of metal binding properties [9]. The results we include in this paper clearly demonstrate, first, that all MTs are able to some extent to capture and coordinate Zn²⁺ ions present in standard (nonsupplemented) bacterial growth medium (LB). But, secondly, it is worth noting how our results show that the average zinc content and the precise Zn-MT complexes recovered for a given MT peptide depend on its situation in our gradate classification, in other words, on its Zn- versus Cu-thionein character. Therefore, on the one hand this work sheds light on the behaviour of MT polypeptides when there is no metal surplus in the surrounding environment; and on the other hand, it adds a new criterion to support our classification of MTs according to their metal handling abilities.

2. Experimental

2.1. Synthesis of the Recombinant Metal-MT Complexes. Recombinant syntheses of MTs (primarily as GST-MT fusions) were achieved through expression of the corresponding cDNAs cloned in pGEX vectors. Construction of these plasmids is reported in detail in [7] for the mouse MT1 isoform, [10] for the yeast *S. cerevisiae* Crs5 MT, and [11, 12] for the *D. melanogaster* Mtn (or MtnA) and Mto (or MtnB) isoforms, respectively. All the metal-MT complexes analyzed in this work were purified from 1L cultures of BL21 *E. coli* cells transformed with the corresponding pGEX-MT plasmid, grown in standard LB (Luria-Bertani) broth with 100 mg mL⁻¹ ampicillin and no metal supplement, except for the control condition, when 300 μM ZnCl₂ was added to the LB medium. GST-MT synthesis was induced with isopropyl-1-thio-β-D-galactopyranoside (IPTG) at a final concentration of 100 mM. After 2.5-hour induction, cells were harvested by centrifugation. To prevent oxidation of the metal-MT complexes, argon was bubbled in all the steps of the purification following cell disruption. For protein

purification, cells were resuspended in ice-cold PBS (1.4 M NaCl, 27 mM KCl, 101 mM Na₂HPO₄, and 18 mM KH₂PO₄) 0.5% v/v β-mercaptoethanol, disrupted by sonication, and centrifuged at 12,000 g for 30 minutes. The GST-MT fusions were purified from the recovered supernatant by glutathione-Sepharose 4B (GE Healthcare) batch affinity chromatography incubating the mixture with gentle agitation for 60 minutes at room temperature. After three washes in PBS, and due to the fact that the GST-MT constructs include a thrombin recognition site, this protease was added (10 U per mg of protein) and digestion was carried out overnight at 23–25°C. This allowed separation of the GST portion—which remained bound to the gel matrix—from the MT moiety (that eluted together with thrombin). Subsequently, this eluate was concentrated using Centriprep Concentrators (Amicon) (Millipore, Billerica, MA, USA) with a cut-off of 3 kDa and fractionated using FPLC, through a Superdex-75 column (GE Healthcare) equilibrated with 50 mM Tris-HCl, pH 7.0, and run at 1 mL min⁻¹. Fractions were collected, and analysed for protein content by their absorbance at 254 nm. Aliquots of the protein-containing FPLC fractions were analysed by 15% SDS-PAGE and stained by Coomassie Blue. MT-containing samples were pooled and stored at –70°C until further characterization.

2.2. Inductively Coupled Plasma Atomic Emission Spectroscopy (ICP-AES). The recombinantly expressed MT complexes were analyzed for element composition (S, Zn, Cd, and Cu) by inductively coupled plasma atomic emission spectroscopy (ICP-AES) on a Polyscan 61E spectrometer (Thermo Jarrell Ash Corporation, Franklin, MA, USA) at appropriate wavelengths (S, 182.040 nm; Zn, 213.856 nm; Cd, 228.802 nm; Cu, 324.803 nm). Samples were prepared either at “conventional” (dilution with 2% HNO₃ (v/v)) [13] or at “acidic” (incubation in 1 M HCl at 65°C for 5 minutes) conditions [14]. MTs concentration in the recombinant preparations was calculated assuming that the only contribution to their S content was that made by the MT peptides.

2.3. Mass Spectrometry. Molecular mass determination was performed by electrospray ionization mass spectrometry equipped with a time-of-fly analyzer (ESI-TOF MS) using a Micro Tof-Q Instrument (Bruker Daltonics GmbH, Bremen, Germany) calibrated with NaI (200 ppm NaI in a 1:1 H₂O:isopropanol mixture), interfaced with a Series 1100 HPLC pump (Agilent Technologies) equipped with an autosampler, both controlled by the Compass Software. The experimental conditions for analyzing MT samples were: 20 μL of the sample was injected through a PEEK long tube (1.5 m × 0.18 mm i.d.) at 40 μL/min under the following conditions: capillary-counter electrode voltage, 5.0 kV; desolvation temperature, 90–110°C; dry gas, 6 L/min. Spectra were collected throughout an m/z range from 800 to 2000. The liquid carrier was a 90:10 mixture of 15 mM ammonium acetate and acetonitrile, pH 7.0. All the samples were injected at least in duplicate to ensure reproducibility. In all cases, molecular masses were calculated according to the reported method [15].

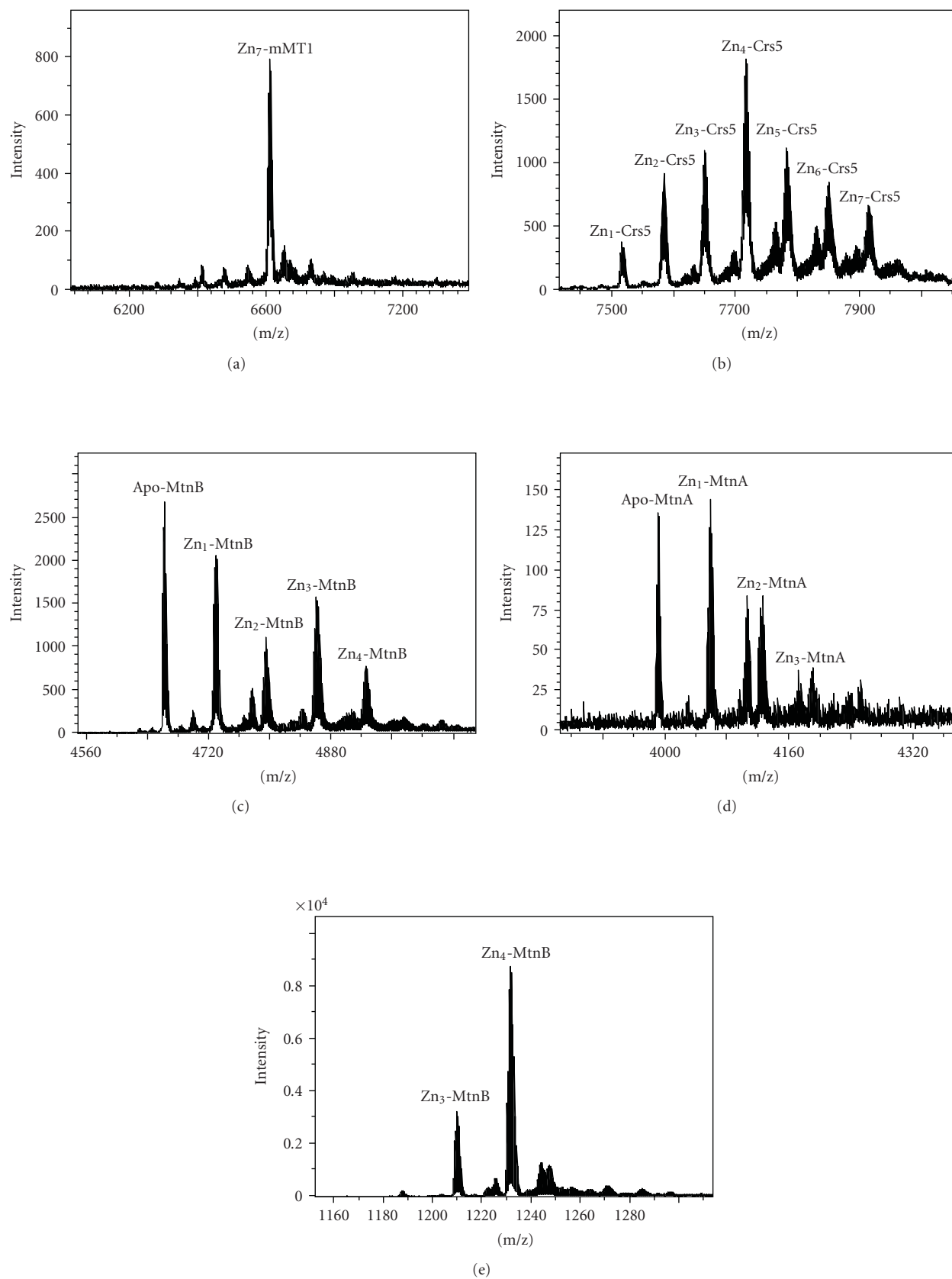


FIGURE 1: Deconvoluted ESI-TOF MS spectra of the recombinant Zn(II)-MT complexes obtained from the pGEX-MT expression system with no zinc supplementation to the culture: (a) mouse MT1; (b) yeast Crs5; (c) *D. melanogaster* MtnB and (d) *D. melanogaster* MtnA. (e) MtnB was also synthesized in zinc-enriched medium, to be used as a control.

TABLE 1: Amino acid sequences of the four MT isoforms analyzed in this work. MtnA and MtnB are two *Drosophila melanogaster* isoforms. Crs5 is a *Saccharomyces cerevisiae* MT and mMT1 is the mouse MT isoform 1. The GST-based expression system used for recombinant synthesis added two N-terminal residues to these sequences (GS), which was previously shown not to influence the binding properties of MT peptides [7], but it has to be considered for the calculation of their theoretical molecular masses (Table 2, Figure 1).

MtnA	MPCPGSGCKCASQATKGSNCGSDCKCGGDKKSACGCSE
MtnB	MVCKGCGTNCQCSAQKCGDNCACNKDCQCVCKNGPKDQCCSNK
Crs5	MTVKICDCEGECCKDSCHCGSTCLPSSGGEKCKKDHSTGSPQCKSCGEEKCKCETTCTCEKSKCNCCEKC
mMT1	MDPNCSCATGGSCTCTGSCCKCKECKCNSCKKSSCCPMSCAKCAQGCICKGASEKCSCCA

3. Results and Discussion

The four MTs studied in this work (Table 1) cover a broad spectrum of organisms: from vertebrates—the mouse mMT1 peptide—to invertebrates—two *Drosophila* (MtnA and MtnB) peptides—and, unicellular eukaryotes—the yeast Crs5 MT. Besides, they exhibit differential metal binding abilities towards Zn^{2+} and Cu^{+} , as evidenced by their position in our Zn- versus Cu-thionein gradated classification [9]. The overall results of this study are presented in a comprehensive table (Table 2) for the sake of easy comparison, but they are discussed independently below. One of the MTs, Mtn-B, was also synthesised under excess zinc conditions ($300\ \mu M$ in the culture medium), as a positive control in relation to the nonsupplemented experiments. It is extremely important to highlight that in all cases, the Cd and Cu content of the preparations was also measured, but the obtained values were always not significant. This is consistent with the metal ion content reported for the intracellular environment of *E. coli* cells, which has been estimated to be about $0.1\ mM$ for zinc while only in the 10 -to- $100\ \mu M$ range for copper [16], so Zn^{2+} ions are indeed the only ones available for the nascent MT peptides.

The mMT1 isoform, one of the four encoded in the mouse (mammalian) genomes, has for a long time been the paradigm of divalent-metal binding MTs. Accordingly, it is in the third position out of sixteen in our gradate classification of Zn-thioneins, as shown in Table 3. This means that the corresponding polypeptide has a high ability to form complexes with divalent metal ions (Zn^{2+} and Cd^{2+}) so that these complexes are well folded and remain steady in physiological conditions. Strikingly, recombinant synthesis of mMT1 renders unique Zn_7 -mMT1 complexes (Figure 1(a), Table 2), regardless of whether the bacterial culture has been supplemented with zinc ($300\ \mu M$) [7] or not. This suggests an extreme proficiency of mMT1 not only to form well-structured Zn-complexes when these metal ions are in surplus, but also to capture the Zn^{2+} ions present in a standard environment, which may be of significant importance when considering its potential functions in physiological conditions.

Crs5 is a *Saccharomyces cerevisiae* MT, nonhomologous to the paradigmatic Cu-thionein Cup1 present in the same yeast species. Despite initially being considered a secondary copper-resistance agent, we showed that it determines survival under zinc overload, and furthermore, all the data concerning its metal-binding abilities converged to define

the partial Zn-thionein character of Crs5 [10]. In fact, it is located in a rather intermediate position in our Zn-versus Cu-thionein ranking (10th position out of 16 MTs, Table 3). When this MT is synthesized in the absence of Zn overload, not only does the mean Zn-per-MT ratio diminish from 5.7 to 4.2 (Table 2), but there is also a huge variety of Zn-Crs5 species produced, as revealed by the ESI-MS spectrum of the sample (Figure 1(b)). Besides the major Zn_4 -Crs5 species, the preparation included other complexes, exhibiting a wide range of stoichiometries, from the highest value observed under zinc supplementation (Zn_7 -Crs) to the major species recovered then [10] (Zn_6 - and Zn_5 -Crs5), as well as other undermetalated (without metals) complexes, from Zn_3 - to Zn_1 -Crs5. It is therefore clear that this MT is able to coordinate some zinc ions from normal physiological environments, but in this case, more than half of the polypeptides encompass a zinc load lower than they would in excess zinc conditions.

Finally, the two *Drosophila* MTs, MtnA and MtnB, served to study the behaviour of Cu-thioneins, since they have been characterized as the animal MTs that are most similar to the paradigmatic Cup1 Cu-thionein [9]. Consequently both polypeptides have been able to render homonuclear Cu(I)-complexes upon recombinant synthesis in copper-supplemented media [11, 12]. Despite these properties, Cu-thioneins are able to fold into Zn^{2+} -containing complexes when produced under excess zinc as observed in the control experiment (Figure 1(e), Table 2) and literature data [11, 12]. However, our current results provide evidence that this is not the case in nonsupplemented media, since both MtnA and MtnB are recovered mostly as apo-forms or Zn_1 -Mtn complexes (Table 2). MS spectra of these preparations (Figures 1(c) and 1(d)) reveal that both MT polypeptides are severely undermetalated (without metals), with a high abundance of complexes exhibiting a metal content far below that they can attain as fully loaded species (Table 3). Therefore, it has to be assumed that should these MTs be present in a normal environment (i.e., with no metal ion surplus), they would coordinate very few Zn^{2+} ions, if any.

The joint observation of these results leads to important considerations. First, it is obvious that the levels of Zn(II) concentrations normally present in the cell cytoplasm (estimated in $0.1\ mM$ for *E. coli* [16]) enable the building of Zn-MT complexes, even in the absence of zinc overload. This is extremely important for predicting the fate of the native MT peptides translated in uninduced conditions, and it would be in full agreement with the hypothesis that in basal

TABLE 2: Metal-to-protein ratios and molecular masses of the recombinant Zn(II)-MT, complexes obtained from the pGEX expression system with no metal supplementation to the culture, except in the Zn-MtnB used as a control (see Section 2). All the measurements have been performed at least twice, from independently obtained samples.

MT protein	Zn/MT ^(a) (ICP-AES)	Zn/MT ^(a) (acidic ICP-AES)	Zn-MT species ^(b) (ESI-MS)	m_{exp} ^(c)	m_{th} ^(d)
mMT1	6.95	7.40	Zn₇-mMT1	6605.5	6605.96
			Zn₄-Crs5	7715.5	7718.92
Crs5	4.20	4.61	Zn ₃ -Crs5 · Zn ₅ -Crs5	7654.5 · 7780.5	7655.53 · 7782.31
			Zn ₂ -Crs5 · Zn ₆ -Crs5	7590.4 · 7844.5	7592.13 · 7845.70
			Zn ₁ -Crs5 · Zn ₇ -Crs5	7525.0 · 7907.5	7528.75 · 7909.09
			apo-MtnB	4667.2	4669.34
			Zn ₁ -MtnB	4733.8	4732.73
MtnB	2.04	2.40	Zn ₃ -MtnB	4857.0	4859.51
			Zn ₂ -MtnB	4795.0	4796.12
			Zn ₄ -MtnB	4920.8	4922.9
			apo-MtnA · Zn₁-MtnA	3996.4 · 4059.4	3997.49 · 4060.88
MtnA	1.70	1.94	Zn ₂ -MtnA	4121.2	4124.27
			Zn ₃ -MtnA	4186.4	4187.66
			Zn₄-MtnB	4922.0	4922.90
Zn-MtnB ^(e)	3.95	5.10	Zn ₃ -MtnB	4850.2	4859.51

ICP-AES inductively coupled plasma atomic emission spectroscopy, ESI-MS electrospray ionization mass spectrometry.

^(a)In all experiments Cd and Cu contents were also measured but their amount was always under detection limits.

^(b)Species proposed according to the mass difference between holo-protein and apo-protein. Species in bold are the major components of the preparation.

^(c)Experimental molecular masses. Measurements were always performed in duplicate. All corresponding standard deviations were always less than 1%.

^(d)Theoretical molecular mass of the corresponding species.

^(e)Control experiment: MtnB synthesized in Zn(II)-supplemented medium.

TABLE 3: Comparison of the Zn-MT complexes recovered from recombinant syntheses in Zn- and nonsupplemented culture media.

MT protein	Zn-MT species recovered when synthesized in Zn-supplemented media	Zn-MT species recovered when synthesized in nonsupplemented media ^(a)	Mean Zn : MT molar ratio, when synthesized in Zn-supplemented media	Mean Zn : MT molar ratio, when synthesized in nonsupplemented media ^(b)	Situation in the Zn-/Cu-thionein gradation ^(c)
mMT1	Zn ₇ -mMT1 [7]	Zn ₇ -mMT1	7.3 [7]	6.95	3/16
Crs5	Zn ₆ -Crs5 · Zn ₅ -Crs5 [10]	Zn ₄ -Crs5	5.7 [10]	4.20	10/16
MtnA	Zn ₄ -MtnA [11]	Apo-MtnA · Zn ₁ -MtnA	3.5 [11]	1.70	14/16
MtnB	Zn ₄ -MtnB [12]	Apo-MtnB	3.7 [12]	2.04	15/16

^(a)In this work, only major species identified by ESI-MS are indicated.

^(b)In this work, the mean Zn : MT value corresponding to the conventional ICP-AES value is indicated.

^(c)The study in [9] includes 16 MT isoforms, classified from the most extreme Zn-thionein to the most extreme Cu-thionein character.

conditions, MTs exhibiting a clear Zn-thionein character are synthesized inside cells as Zn²⁺-complexes, which undergo the corresponding exchange reaction in the presence of an excess of other metal ions [17]. However, the Zn-MT species yielded by the synthesis in nonsupplemented media, and their relation with those obtained from conventional zinc-supplemented cultures, are highly dependent on the type of MT considered, and precisely, on its Zn-thionein character. Hence, the mouse MT1 isoform, a genuine Zn-thionein, yields exactly the same result in both culture conditions, showing its extreme ability to capture Zn²⁺ ions from its physiological environment. On the other hand, the genuine Cu-thioneins analyzed are almost unable to yield Zn²⁺-containing complexes unless they are synthesized

under excess zinc, even rendering apo-forms or Zn₁-MT as major products (cf. results for MtnA and MtnB, Figure 1, Table 2). Comparison of the synthesis in normal and zinc-enriched media (Table 3), both regarding the mean Zn : MT content ratio and the Zn²⁺-containing species recovered, highlights that the higher the Zn-thionein character of a MT peptide, the more similar will be the results of the synthesis of Zn-MT complexes in both conditions. And, on the contrary, the greater the Cu-thionein character, the more different will be the species resulting from these syntheses, to the point that Cu-thioneins are characterized by an inherent incapacity to coordinate Zn²⁺ ions when present at physiological concentrations. This means that Cu-thioneins, if synthesized as the result of the constitutive expression of

their genes (i.e., under no metal surplus), would remain mainly as apo-peptides inside cells, but never as basal Zn^{2+} -containing complexes.

4. Conclusion

Comprehensive consideration of our data suggests that the result of synthesizing different MTs in nonmetal-supplemented media is highly dependent on their Zn- versus Cu-thionein character. Although in all cases Zn^{2+} -containing complexes are produced, the former practically yields the same Zn-MT species when recombinantly produced in zinc-supplemented and in normal (nonsupplemented) medium, while the latter is almost unable to coordinate Zn^{2+} unless these metal ions are in clear surplus (300 μ M in culture media). These results may reflect an intrinsically different role of these two types of MTs in physiological conditions, as well as their well-assumed different role when they are natively synthesized as a protective response to the corresponding cognate-metal overload.

Acknowledgments

This work was supported by Spanish Ministerio de Ciencia y Tecnología grants BIO2009-12513-C02-01 to S. Atrian and BIO2009-12513-C02-02 to M. Capdevila. The authors of this work are recognized as a “Grup de Recerca” by the “Generalitat de Catalunya”, reference 2009SGR-1457. The authors thank the Serveis Científic-Tècnics de la Universitat de Barcelona and the Servei d'Anàlisi Química (SAQ) de la Universitat Autònoma de Barcelona for allocating ICP-AES and ESI-MS instrument time, respectively. They are also grateful to Miriam Romagosa for MT syntheses and to Ayelen Pagani for her technical guidance.

References

- [1] A. Sigel, H. Sigel, and R. K. O. Sigel, Eds., *Metal Ions in Life Sciences*, vol. 5 of *Metallothioneins and related chelators*, Royal Society of Chemistry, Cambridge, UK, 2009.
- [2] M. Margoshes and B. L. Vallee, “A cadmium protein from equine kidney cortex,” *Journal of the American Chemical Society*, vol. 79, no. 17, pp. 4813–4814, 1957.
- [3] R. D. Palmiter, “The elusive function of metallothioneins,” *Proceedings of the National Academy of Sciences of the United States of America*, vol. 95, no. 15, pp. 8428–8430, 1998.
- [4] Y. Yang, W. Maret, and B. L. Vallee, “Differential fluorescence labeling of cysteinyl clusters uncovers high tissue levels of thionein,” *Proceedings of the National Academy of Sciences of the United States of America*, vol. 98, no. 10, pp. 5556–5559, 2001.
- [5] A. Krezel and W. Maret, “Different redox states of metallothionein/thionein in biological tissue,” *Biochemical Journal*, vol. 402, no. 3, pp. 551–558, 2007.
- [6] M. Capdevila, N. Cols, N. Romero-Isart, R. Gonzalez-Duarte, S. Atrian, and P. Gonzalez-Duarte, “Recombinant synthesis of mouse Zn_3 - β and Zn_4 - α metallothionein 1 domains and characterization of their cadmium(II) binding capacity,” *Cellular and Molecular Life Sciences*, vol. 53, no. 8, pp. 681–688, 1997.
- [7] N. Cols, N. Romero-Isart, M. Capdevila, et al., “Binding of excess cadmium(II) to Cd7-metlothionein from recombinant mouse Zn7-metlothionein 1. UV-VIS absorption and circular dichroism studies and theoretical location approach by surface accessibility analysis,” *Journal of Inorganic Biochemistry*, vol. 68, no. 3, pp. 157–166, 1997.
- [8] M. Valls, R. Bofill, R. Gonzalez-Duarte, P. Gonzalez-Duarte, M. Capdevila, and S. Atrian, “A new insight into metallothionein (MT) classification and evolution. The in vivo and in vitro metal binding features of *Homarus americanus* recombinant MT,” *Journal of Biological Chemistry*, vol. 276, no. 35, pp. 32835–32843, 2001.
- [9] R. Bofill, M. Capdevila, and S. Atrian, “Independent metal-binding features of recombinant metallothioneins convergently draw a step gradation between Zn- and Cu-thioneins,” *Metallomics*, vol. 1, no. 3, pp. 229–234, 2009.
- [10] A. Pagani, L. Villarreal, M. Capdevila, and S. Atrian, “The *Saccharomyces cerevisiae* Crs5 metallothionein metal-binding abilities and its role in the response to zinc overload,” *Molecular Microbiology*, vol. 63, no. 1, pp. 256–269, 2007.
- [11] M. Valls, R. Bofill, N. Romero-Isart, et al., “*Drosophila* MTN: a metazoan copper-thionein related to fungal forms,” *FEBS Letters*, vol. 467, no. 2-3, pp. 189–194, 2000.
- [12] J. Domenech, O. Palacios, L. Villarreal, P. Gonzalez-Duarte, M. Capdevila, and S. Atrian, “MTO: the second member of a *Drosophila* dual copper-thionein system,” *FEBS Letters*, vol. 533, no. 2, pp. 72–78, 2003.
- [13] J. Bongers, C. D. Walton, D. Richardson, and J. U. Bell, “Micromolar protein concentrations and metalloprotein stoichiometries obtained by inductively coupled plasma. Atomic emission spectrometric determination of sulfur,” *Analytical Chemistry*, vol. 60, no. 24, pp. 2683–2686, 1988.
- [14] M. Capdevila, J. Domenech, A. Pagani, L. Tío, L. Villarreal, and S. Atrian, “Zn- and Cd-metlothionein recombinant species from the most diverse phyla may contain sulfide (S^{2-}) ligands,” *Angewandte Chemie International Edition*, vol. 44, no. 29, pp. 4618–4622, 2005.
- [15] D. Fabris, J. Zaia, Y. Hathout, and C. Fenselau, “Retention of thiol protons in two classes of protein zinc ion coordination centers,” *Journal of the American Chemical Society*, vol. 118, no. 48, pp. 12242–12243, 1996.
- [16] L. A. Finney and T. V. O'Halloran, “Transition metal speciation in the cell: insights from the chemistry of metal ion receptors,” *Science*, vol. 300, no. 5621, pp. 931–936, 2003.
- [17] F. Haq, M. Mahoney, and J. Koropatnick, “Signaling events for metallothionein induction,” *Mutation Research*, vol. 533, no. 1, pp. 211–226, 2003.

Research Article

The $\Delta 33-35$ Mutant α -Domain Containing β -Domain-Like M_3S_9 Cluster Exhibits the Function of α -Domain with M_4S_{11} Cluster in Human Growth Inhibitory Factor

Qingui Bao,¹ Zhichun Ding,² Zhong-Xian Huang,² and Xiangshi Tan^{1,2}

¹Institute of Biomedical Science, Fudan University, 220 Handan Road, Shanghai 200433, China

²Department of Chemistry, Fudan University, Shanghai 200433, China

Correspondence should be addressed to Xiangshi Tan, xstan@fudan.edu.cn

Received 30 December 2009; Accepted 4 March 2010

Academic Editor: Spyros Perlepes

Copyright © 2010 Qingui Bao et al. This is an open access article distributed under the Creative Commons Attribution License, which permits unrestricted use, distribution, and reproduction in any medium, provided the original work is properly cited.

Neuronal growth inhibitory factor (GIF), also known as metallothionein (metallothionein-3), impairs the survival and neurite formation of cultured neurons. It is known that the α - β domain-domain interaction of hGIF is crucial to the neuron growth inhibitory bioactivity although the exact mechanism is not clear. Herein, the β (MT3)- β (MT3) mutant and the hGIF-truncated $\Delta 33-35$ mutant were constructed, and their biochemical properties were characterized by pH titration, EDTA, and DTNB reactions. Their inhibitory activity toward neuron survival and neurite extension was also examined. We found that the $\Delta 33-35$ mutant α -domain containing β -domain-like M_3S_9 cluster exhibits the function of α -domain with M_4S_{11} cluster in hGIF. These results showed that the stability and solvent accessibility of the metal-thiolate cluster in β -domain is very significant to the neuronal growth inhibitory activity of hGIF and also indicated that the particular primary structure of α -domain is pivotal to domain-domain interaction in hGIF.

1. Introduction

The pathological pattern of Alzheimer's disease (AD) is characterized by the progressive loss of neurons accompanied by the formation of intraneural neurofibrillary tangles and extracellular amyloid plaques [1]. One hypothesis postulated that these symptoms are caused by an imbalance of neurotrophic factors [2]. In 1988, Uchida and coworkers established that brain extracts from AD patients stimulate the neuron survival to a greater degree than normal brain extracts, due to the loss of a human growth inhibitory factor (hGIF) [3, 4]. It has also been reported that the metallothionein-3 (MT3) level decreases in astrocytes in lesioned areas of degenerative diseases such as Parkinson's disease, amyotrophic lateral sclerosis, and progressive supranuclear palsy [5]. Because of the high homogeneity in primary structure with MT1/MT2, hGIF was classified as a member of MT family and was also named hMT3 [6].

Metallothioneins (MTs) are low molecular weight, cysteine-rich, and metal ion binding proteins. In mammals, four MT isoforms (MT1, MT2, MT3, and MT4) have been identified [7]. The two major isoforms MT1 and MT2 are found in most organs and can be rapidly induced by a wide range of stimuli, such as metal ions and cytokines [8, 9]. However, MT3 and MT4 are specifically expressed in the central nervous system (CNS) and stratified squamous epithelia, respectively, and have no response to these inducers [7]. All of the mammalian MTs display two domains, and each domain contains a metal-thiolate cluster: the N-terminal β -domain contains a cluster of three metals coordinated with nine cysteines; the C-terminal α -domain contains a cluster of four metals coordinated with eleven cysteines. The cluster structure, where the metal ions are tetrahedrally coordinated by bridging and terminal cysteines, is important for the function of MTs [10]. Unlike most other metalloproteins, metallothionein can bind metals with a high thermodynamic stability [11–13]. These properties

are believed to enable MTs also to function in essential trace metal homeostasis, detoxification of heavy metal ions and oxidative stress response [14, 15], and so forth. Despite the high similarities between the primary structures of MT-3 and mammalian MT-1/MT-2, the biological properties of these three proteins differ. The most conspicuous feature is that MT-3 but not MT-1/MT-2 exhibits a neuron growth inhibitory activity in neuronal cell culture studies. This activity of MT-3 has been reported for the native Cu_4Zn_3 -hGIF and recombinant Zn_7 -hGIF [16]. Further studies have established that the inhibitory activity is mainly related to the N-terminal β -domain, whereas the C-terminal α -domain alone is found to be inactive [17, 18]. According to our previous studies, it is indicated that the neuronal growth inhibitory bioactivity of hMT3 is regulated by various factors. For examples, both the single amino acid insert (Thr) close to the N-terminus and a glutamate-rich hexapeptide insert close to the C-terminus are pivotal to the bioactivity of hGIF [6]. The CPCP motif is also key to the bioactivity; maybe this motif is the specific binding site of hMT3 with other biological molecules [17–19], the solvent accessibility of the metal-thiolate cluster, which is closely associated with the structure of the protein, and mutual accessibility of metal-thiolate clusters with biologically sensitive small molecules [20–23]. Moreover, domain-domain interactions maybe play important roles in modulating the stability of the metal-thiolate cluster and the conformation of the β -domain, and so forth.

The earlier research showed that α -domain is very significant to the biological function of the protein. We proposed that the α -domain has a stabilizing effect to β -domain in hGIF. However, the mechanism of this stabilizing effect remains unclear. In 2003, Dr. Wenhao Yu in our lab constructed C34M and C35S mutants of monkey metallothionein and discovered that the newly formed α -domain (residue 32 to 61) was able to combine with up to fourfold of metal ions, although the domain had only nine cysteines [24]. Besides, the number of cysteine in the α -domain of sheep metallothionein (sGIF), which was found in 2002, is nine, two less than other species which contain eleven cysteines. Hence, by comparing the primary structure of hGIF with sGIF, we constructed an hGIF $\Delta 33$ -35 mutant ($\Delta 33$ -35 mutant, the fragment of $^{33}\text{SCC}^{35}$ in hGIF was removed, and it contains two M_3S_9 clusters as same as sGIF) and a $\beta(\text{MT}3)$ - $\beta(\text{MT}3)$ mutant. The biochemical properties of the mutants were characterized by pH titration, EDTA, and DTNB reaction, and their bioactivity toward neuron survival and neurite extension was also examined. We found that in hGIF $\Delta 33$ -35 mutant the truncated α -domain (also named as β' -domain in this paper) contains M_3S_9 cluster which is similar to the wild type hGIF β -domain, while it exhibits the functions of α -domain with M_4S_{11} cluster in human growth inhibitory factor. The experimental results showed that the stability and solvent accessibility of the metal-thiolate cluster in the β -domain is very significant to the neuronal growth inhibitory activity of hGIF and also indicated that the particular primary structure of the α -domain of hGIF is pivotal to domain-domain interaction in hGIF.

2. Experimental

2.1. Reagents. Fusion expression vector pGEX-4T-2, Escherichia coli strain BL21, glutathione Sepharose 4B, Superdex-75, and Sephadex G-25 were purchased from Amersham Pharmacia Biotech. The (deoxy-ribonucleoside triphosphate) dNTP, T4 DNA ligase, and restriction enzymes, *BamH I* and *EcoR I*, were purchased from New England Biolabs. Pfu DNA polymerase, cell culture reagents, isopropyl β -D-thiogalactoside (IPTG), and Triton-100 were purchased from Sangon (Shanghai, China). The DNA gel extraction kit was purchased from Qiagen. 2,2'-dithiodipyridine, 5,5'-dithiobis-(1-nitrobenzoic acid) (DTNB), ethylenediamine tetraacetic acid (EDTA), and thrombin were from Sigma (St. Louis, MO, USA). Neurobasal-A medium and B27 serum-free supplements were purchased from GIBCO-BRL (Gaithersburg, MD, USA). The other reagents were of analytic grade.

2.2. Cloning, Expression, and Purification of hMT3 and Its Variants. Human MT3 (hMT3) cDNA was prepared from cells by reverse transcription followed by polymerase chain reaction (PCR). The genes of the $\beta(\text{MT}3)$ - $\beta(\text{MT}3)$ mutant, the hGIF $\Delta 33$ -35 mutant, and the single β -domain of hMT3 were amplified by PCR method [25]. Each segment was digested and cloned into vector pGEX-4T-2 as a *BamH I/EcoR I* fragment and verified by DNA sequencing. The expression and purification procedure for hMT3 and its mutants were carried out as described in the instructions for Glutathione-Sepharose 4B (GE healthcare life science) with some modifications. Briefly, cultures of cells (50 mL) were grown overnight in LB medium containing 100 mg mL^{-1} of ampicillin at 37°C . This start culture was diluted 100-fold into 500 mL of fresh 2 \cdot YTA, and the cells were induced with 0.1 mM IPTG when an absorbance of 0.6 – 0.8 at 600 nm was attained, followed by 1-hour growth before addition of 0.2 mM ZnSO_4 . The cells were harvested at OD_{600} value of 2.5, which was generally reached 3–4 hours after induction. Then, under protection of mercaptoethanol, the GST fusion protein was separated by affinity column of Glutathione Sepharose 4B, which was washed by PBS until the absorbance at 280 nm was less than 0.02. Then the fusion protein was digested by thrombin for 14 hours at 25°C in a cleavage buffer (50 mM Tris-HCl, 150 mM NaCl, and 2.5 mM CaCl_2 , pH 8.0). The elute containing thrombin and recombinant hMT3 (tagged Gly-Ser in the N-terminus) cleaved from the fusion protein was pooled, concentrated, and further separated by a Superdex-75 gel filtration column equilibrated with 10 mM Tris-HCl, 50 mM NaCl, pH 8.0. The main eluted peak was concentrated, desalted, lyophilized, and stored at -80°C .

2.3. Protein Characterization and Reconstitution. The apo-form of hMT3 and its variants were generated according to literature [26] and fully Cd^{2+} - or Zn^{2+} -loaded proteins were prepared by reconstitution under the protection of nitrogen [26]. The concentration of MTs was assessed by reacting with 2, 2'-dithiodipyridine in 10 g L^{-1} SDS, 1 mM EDTA, and 12 mL L^{-1} acetate (pH 4.0), using $\epsilon_{224} = 19,800 \text{ M}^{-1}\text{cm}^{-1}$

[27]. The content of metal ions in each protein was analyzed by flame atomic absorption spectrophotometry (WFX-110, BRAIC, Beijing, China). Electrospray ionization mass spectrometry (ESI-MS) was used to measure the molecular weights of hMT3 and its variants. Each protein was dissolved in 1% formic acid (v/v) at a concentration of 10 mg mL^{-1} . The measurement was carried out on a Bruker Esquire 3000 electrospray mass spectrometer (Bruker Daltonics, Bremen, Germany). The instrumental conditions were capillary volt, 4 kV; dry gas, 5 L min^{-1} ; nebulizer gas, 15 PSI; and infusion flow rate, $3 \mu\text{L min}^{-1}$.

2.4. UV-Vis and Circular Dichroism Spectra. The UV-vis absorption spectra were scanned from 200 to 400 nm on a HP8453 UV-vis spectrophotometer (Hewlett-Packard, Palo Alto, CA, USA) at room temperature using a 1.0 cm quartz cuvette. CD spectra were measured in the range of 200–300 nm on a Jasco J-715 spectropolarimeter at room temperature in phosphate buffer (10 mM Tris-HCl, 100 mM KCl, pH 8.0).

2.5. pH Titration. The spectrophotometric pH titration was performed according to the method of Winge and Miklossy [10]. Briefly, $6\text{--}7 \mu\text{M Cd}^{2+}$ -reconstituted proteins were dissolved in 10 mM Tris-HCl, pH 8.0, containing 100 mM KCl and titrated with increasing amounts of 1 M HCl. The progress of acidification was monitored at 250 nm on the HP8453 UV spectrophotometer.

2.6. Reaction with EDTA and DTNB. The reactions of Cd^{2+} -reconstituted hMT3 and its mutants with EDTA were investigated at 25°C according to the method of Li et al. [28]: $9 \mu\text{M}$ protein was reacted with 1.2 mM EDTA in 10 mM Tris-HCl, pH 8.0, containing 100 mM KCl. To avoid the absorbance of EDTA, the reaction was monitored at 265 nm on the HP8453 UV spectrophotometer at 20-second intervals for 100 minutes. The reactions of Cd^{2+} -reconstituted hMT3 and its mutants with DTNB were studied according to the method of Shaw et al. [29]: $3.5 \mu\text{M}$ protein was reacted with 1 mM DTNB in 10 mM Tris-HCl, pH 8.0, containing 100 mM KCl at 25°C . The reaction was monitored at 412 nm ($\epsilon_{412} = 13,600 \text{ mol}^{-1} \text{ cm}^{-1}$) on an HP8453 UV spectrophotometer at 20-second intervals for 60 minutes.

2.7. Preparation of Rat Brain Extract. Rat brain extracts were prepared as described previously [3]. Briefly, the whole brain from adult male Hooded Wistar rat ($\sim 200 \text{ g}$) was removed and homogenized in one volume of Hanks buffer, followed by centrifugation at $100\times g$. The supernatant was filter-sterilized ($0.22 \mu\text{m}$ filter, Millipore, Billerica, MA, USA). The total protein concentration of freshly prepared rat brain extract was determined by the Bradford method, and brain extracts were used immediately at a concentration of $150 \mu\text{g mL}^{-1}$ [30].

2.8. Culture of Cerebral Cortical Cells. Cultures of cerebral cortical cells were prepared as described previously [30, 31] with slight modification. Briefly, cerebral cortices of Wistar

rat fetuses (day 18) were removed and cells were dissociated mechanically by passing coarsely minced cortical tissues gently and repeatedly through a pipette. Tissue debris was removed by gently passing through a filter. Cells were washed and suspended in a specific culture medium developed for selective neuronal growth, consisting of Neurobasal-A medium (GIBCO), 0.1% (f/c) B-27 supplement (GIBCO), and 0.1 mM (f/c) L-glutamine (Sigma). Then the cells were seeded on polylysine-coated 24-well culture plates at a density of 1×10^5 cells/well. Cultures were maintained in a 37°C chamber under an atmosphere of humidified air containing 5% CO_2 . Four hours later, the culture medium was replaced with fresh medium containing with $150 \mu\text{g mL}^{-1}$ rat brain extract and $10\text{--}20 \mu\text{g mL}^{-1}$ proteins. Cultures were maintained under the same conditions for three days. To visualize neuronal cells, cultures were fixed in 4% paraformaldehyde and then stained with trypan blue. Finally, the neuron neurite length was determined by measuring the distance between the end of the neurite and the cell surface using the Leica Qwin program (Rueil Malmaison, France) and at least 60 neurons with more than 100 neurites were recorded in each individual experiment.

3. Results and Discussion

DNA sequencing showed that all mutation genes were successfully constructed, and the primary structure of hMT3 and its mutants were shown in Figure 1. After expression and purification, the yields of recombinant proteins were about 9 mg L^{-1} culture. Since these proteins were cleaved from GST fusion proteins by thrombin, they had an additional Gly-Ser dipeptide in the N-terminus. However, the existence of the additional dipeptide does not obviously affect the structure and properties of the protein [31]. Their molecular weights were confirmed by ESI-MS, and the measured molecular weights were in good match with the theoretical values (Table 1). According to previous studies, Cd^{2+} is considered to be a useful probe of Zn^{2+} binding sites in MTs [32, 33], providing a wealth of structural information on the Zn^{2+} -substituted MTs. Furthermore, the Cd^{2+} -substituted MTs show a number of advantages over the Zn^{2+} -substituted MTs, including a tendency toward higher oxidation stability, pronounced and thus easier to detect and quantify LMCT band, as well as the use of the ^{111}Cd or ^{113}Cd isotopes for NMR experiments, and so forth. Thus, Cd^{2+} has frequently been used as a substitute for Zn^{2+} in structural studies of hMT3 [20, 23, 34, 35]. In the present studies, Cd^{2+} -reconstituted MTs were adopted in both spectroscopic and metal-binding studies, while Zn^{2+} -reconstituted MTs were only used in bioassays, because Cd^{2+} -MT is cytotoxic to the neurons in the bioassays [17]. The metal contents of hMT3 and its variants were determined by flame atomic absorption spectrophotometry and are listed in Table 1.

Figure 2(a) shows the UV-vis spectra of Cd^{2+} -reconstituted hMT3 and its mutants, dissolved in 10 mM Tris-HCl, pH 8.0, containing 100 mM KCl. All the spectra showed an absorption shoulder at about 250 nm, which is the character of ligand-to-metal charge transfer (LMCT) of Cd-S bond [36]. The absorption at 280 nm was pretty low because

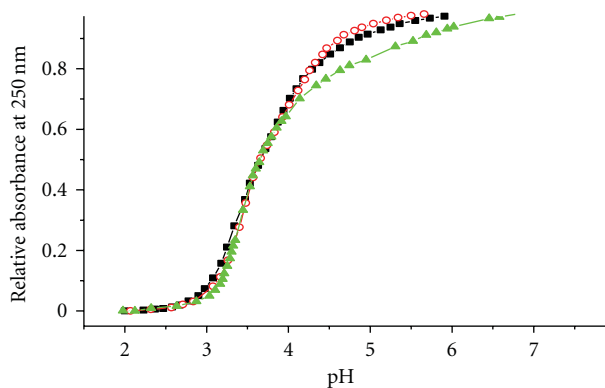


FIGURE 3: UV absorbance at 250 nm of pH titration of Cd^{2+} -reconstituted hGIF (solid squares), the $\Delta 33-35$ mutant (open circles), and the $\beta(\text{MT3})-\beta(\text{MT3})$ mutant (solid triangles). All proteins are dissolved in 10 mM Tris-HCl, 100 mM KCl, and pH 8.0.

the single β -domain, which demonstrates some discrepancy existed in the β' -domain of the $\Delta 33-35$ mutant and the β -domain of hGIF. Maybe the different distribution of the cysteine in the peptide chain leads to the change of protein folding patterns and the structure of metal-thiolate cluster, eventually causing the change of CD spectrum.

In the experiment of pH titration, the concentration of protons would increase with the decrease of pH. So, protons would compete with thiolate ligand for binding to Cd^{2+} , which leads to the release of Cd^{2+} from the Cd^{2+} -thiolate cluster, causing the declining of the characteristic absorption at 250 nm. Hence, the UV absorbance at 250 nm was recorded during the pH titration in order to investigate the stability of the Cd-S clusters. According to our previous study, the titration curve of hMT3 was not clearly divided into two independent stages as it is difficult to tell one stage from the other in the pH titration plot. It is indicated that there is no sharp stability difference between the two Cd-S clusters. According to Figure 3, there is an obvious distinction between the pH titration curves of the $\beta(\text{MT3})-\beta(\text{MT3})$ mutant and hGIF. Due to lacking in α -domain in the $\beta(\text{MT3})-\beta(\text{MT3})$ mutant, the stability of Cd_3S_9 in the $\beta(\text{MT3})-\beta(\text{MT3})$ mutant begins to decrease from neutral pH, while the stability of Cd_3S_9 begins to decrease from pH 5 in $\Delta 33-35$ mutant and hGIF. This further proves that α -domain can stabilize the β -domain effectively in hGIF. Compared the pH titration curves of the $\Delta 33-35$ mutant to the curves of hGIF, we found that the deletion of two cysteines in α -domain did not influence the stability of the Cd_3S_9 cluster to any obvious degree in hGIF. As we all know, both the $\Delta 33-35$ mutant β' -domain and the $\beta(\text{MT3})-\beta(\text{MT3})$ mutant β -domain contain a Cd_3S_9 cluster, while there is a Cd_4S_{11} cluster in the hGIF α -domain. Interestingly, the stabilizing function of Cd_3S_9 in β' -domain is more similar to the Cd_4S_{11} cluster in hGIF α -domain. This result becomes reasonable when the primary structures of the β' -domain and the hGIF α -domain are considered since they have the same primary structure except for the removed fragment ($^{33}\text{SCC}^{35}$). Thus, we suggest that probably it is

due to the particular primary structure of the α -domain they contain, which stabilized the β -domain through the hydrogen bond or hydrophobic interaction, that play an important role in the domain-domain interaction as we described in the previous study [21].

The reaction of MTs with EDTA reflects competition between the sulfhydryl group and the exogenous ligand in the binding of metal ions and is also used to investigate the stabilities of metal-thiolate cluster [35]. Under pseudofirst-order conditions (concentration of EDTA is 300 times that of the MTs), this reaction for hMT3 and its mutants is obviously biphasic, with a fast phase and a slow phase. The observed rate constants were obtained by plotting $\ln(A_t - A_\infty)$ versus time and are listed in Table 2. As shown in the table, the velocity of $\beta(\text{MT3})-\beta(\text{MT3})$ two-phase reaction increased obviously, while that of the $\Delta 33-35$ mutant and hGIF is similar in magnitude, which means that the stability of the metal-thiolate cluster of the $\Delta 33-35$ mutant has no considerable change compared to that of hGIF. This result is consistent with the pH titration experiment result. Unlike EDTA, DTNB can react with the nucleophilic sulfhydryl groups in MTs. This reaction is closely related to the solvent accessibility of the metal-thiolate cluster and usually is biphasic for MTs [29]. According to Winge and coworkers, the fast and slow phases may correspond to the reaction of DTNB with the β -domain and the α -domain of MTs, respectively [17]. The observed rate constants were obtained by plotting $\ln(A_\infty - A_t)$ versus time and these are also listed in Table 2. As indicated, the fast reaction rate constant of the $\beta(\text{MT3})-\beta(\text{MT3})$ mutant was almost twice that of hMT3, showing that the solvent accessibility of the Cd_3S_9 cluster in the β -domain of the $\beta(\text{MT3})-\beta(\text{MT3})$ mutant was greatly enhanced. However, the fast reaction velocity of the $\Delta 33-35$ mutant with DTNB is closer to that of hGIF, as well as the slow reaction velocity. This means that the solvent accessibility of the two Cd_3S_9 clusters in the $\Delta 33-35$ mutant is similar to its counterpart in hGIF. In regards with the results of EDTA and DTNB reactions, the Cd_3S_9 cluster in the β' -domain of the $\Delta 33-35$ mutant, has the same stability and solvent accessibility as the Cd_4S_{11} cluster in the hGIF α -domain. That means the structure of metal-thiolate cluster in hGIF α -domain will not change dramatically after removing two cysteines. Besides, compared to hGIF, the metal-thiolate cluster in $\beta(\text{MT3})-\beta(\text{MT3})$ mutant shows lower stability and higher solvent accessibility. The most conspicuous difference between the $\beta(\text{MT3})-\beta(\text{MT3})$ mutant and the $\Delta 33-35$ mutant is that there is no particular amino acids sequence in the $\beta(\text{MT3})-\beta(\text{MT3})$ mutant as that in hGIF α -domain. Thus, it once again proved that the primary structure of its hGIF α -domain is important to the function, which is quite in consistence with our pH titration experiment.

As mentioned above, Cd^{2+} recombinant protein is toxic to nerve cells. Thus, Zn^{2+} -recombinant protein is adopted to test the physiological function. The nerve grow inhibiting function of hMT3, the $\beta(\text{MT3})-\beta(\text{MT3})$ mutant, and $\Delta 33-35$ mutant was tested. As shown in Figure 4, the average total length of hMT3-treated neurites at three days was $203 \pm 8 \mu\text{m}$. hMT3 significantly reduced the average neurite length to $94 \pm 4 \mu\text{m}$. The average neurite lengths of $\beta(\text{MT3})-\beta(\text{MT3})$

TABLE 2: Observed rate constants of reaction of MTs with EDTA and DTNB.

Protein	Observed rate constants of reaction of MTs with EDTA		Observed rate constants of reaction of MTs with DTNB	
	k_f ($\times 10^{-4}$ s $^{-1}$)	k_s ($\times 10^{-5}$ s $^{-1}$)	k_f ($\times 10^{-3}$ s $^{-1}$)	k_s ($\times 10^{-4}$ s $^{-1}$)
hGIF	12.1 \pm 0.3	4.2 \pm 0.2	2.4 \pm 0.1	9.1 \pm 0.2
$\Delta 33-35$	12.5 \pm 0.2	3.8 \pm 0.2	2.5 \pm 0.1	8.8 \pm 0.2
$\beta(\text{MT3})-\beta(\text{MT3})$	28.7 \pm 0.3	5.8 \pm 0.3	4.4 \pm 0.2	15.6 \pm 0.2

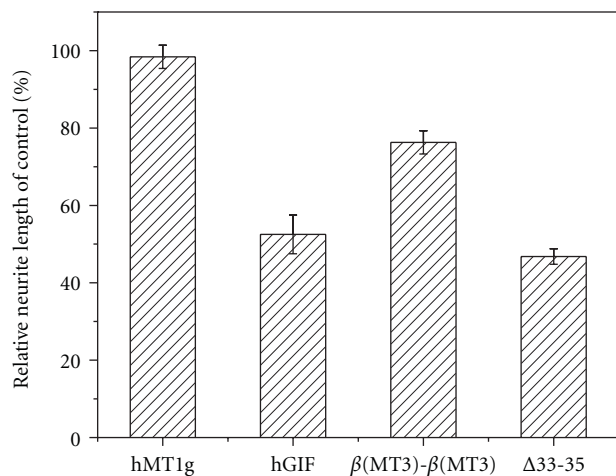


FIGURE 4: Effect of Zn^{2+} -reconstituted hGIF, the $\Delta 33-35$ mutant, and the $\beta(\text{MT3})-\beta(\text{MT3})$ mutant on neurite extension in the presence of adult rat brain extract (150 $\mu\text{g}/\text{mL}$) after 3 days, determined by the average neurite length of 60 neurons. As a comparison, the result of hMT1g (a human MT1 isoform where the segment is $^{20}\text{KCK}^{22}$) under the same conditions was also shown. Error bars represent standard error values.

and $\Delta 33-35$ mutant-treated neurons were 150 ± 5 and 92 ± 3 μm , respectively (the \pm value represents the standard error value). The neuronal growth inhibitory activity of hMT1g and hMT3 well agrees with that reported previously [31, 35]. Moreover, the $\beta(\text{MT3})-\beta(\text{MT3})$ mutant has apparent lower inhibiting activity than that of hGIF. It would be much lower, if taking the concentration of β -domain into account that, the $\beta(\text{MT3})-\beta(\text{MT3})$ mutant protein is two times more active than that of equal molar hMT3 in the nerve growth inhibition. However, the $\Delta 33-35$ mutant is similar to the hGIF in neuronal growth inhibitory activity.

It has been reported that the neuronal growth inhibitory activity of hMT3 mainly arises from its β -domain, while the α -domain is not directly involved in neuronal growth inhibitory activity [17]. However, the α -domain can affect the function of β -domain though domain-domain interactions do exist in MTs [21, 37–39], and it has been proved in our previous work [21, 37]. Taking all the experimental results together, for hGIF and its mutants, the stability and solvent accessibility of the metal-thiolate cluster in N-terminal β -domain are in good line with the bioactivity of the whole protein; so they may be very important to the neuronal growth inhibitory activity of hMT3. Probably, α -domain can influence the stability and solvent accessibility

of the metal-thiolate cluster in β -domain through domain-domain interaction, eventually effecting the bioactivity of the whole protein.

4. Conclusion

Considering the experimental result of EDTA, DTNB reaction, and pH titration together with the neuronal growth inhibitory activity, we proposed that the stability and solvent accessibility of the metal-thiolate cluster in β -domain is very significant to the neuronal growth inhibitory activity in hGIF. Comparing the β -domain of the $\beta(\text{MT3})-\beta(\text{MT3})$ mutant and the β -domain of the $\Delta 33-35$ mutant, these two mutants have different biological activities. It is precisely because the $\Delta 33-35$ mutant has the β' -domain which is similar to hGIF α -domain. This further demonstrates that α -domain stabilizes β -domain via the domain-domain interaction in hGIF, thus to regulate the physiological activity. Moreover, in the present study, we found that there was an obvious difference between the $\Delta 33-35$ mutant and the $\beta(\text{MT3})-\beta(\text{MT3})$ in spectroscopy and biochemical properties. The β' -domain of the $\Delta 33-35$ mutant, which contains M_3S_9 cluster, has the same metal-thiolate cluster as the β -domain of $\beta(\text{MT3})-\beta(\text{MT3})$ mutant and still reserves the function of the M_4S_{11} cluster of the hGIF α -domain. This indicated that the removing of two conservative cysteines does not lead to great changes of the metal-thiolate cluster in the hGIF α -domain. Meanwhile, the β' -domain of the $\Delta 33-35$ mutant is obviously different from the β -domain of the $\beta(\text{MT3})-\beta(\text{MT3})$ mutant in the stabilizing effect, of which the most conspicuous difference is that the β' -domain of the $\Delta 33-35$ mutant contains the primary structure of the hGIF α -domain. But the β -domain of $\beta(\text{MT3})-\beta(\text{MT3})$ mutant contains the primary structure of the hGIF β -domain. That indicated that the particular primary structure of α -domain is pivotal to domain-domain interaction in hGIF. We believe that our results will provide a step further toward better understanding of the relationship between the structure of metal-thiolate cluster and the bioactivity of this group of fascinating molecules.

Acknowledgments

This work is supported in part by Shanghai Pujiang Talent Project (08PJ14017), the National Natural Science Foundation of China (no. 29281005 and no. 20771029), Shanghai Leading Academic Discipline Project (B108), and the Program for the Platform of new medicine creation (no. 2009ZX09301-011). The authors would also like to thank Professor P. Y. Yang and Dr. Y. Wang from the Institute of

Biomedical Sciences of Fudan University for their help in the measurement of ESI mass spectra.

References

- [1] D. J. Selkoe, "The molecular pathology of Alzheimer's disease," *Neuron*, vol. 6, no. 4, pp. 487–498, 1991.
- [2] S. H. Appel, "A unifying hypothesis for the cause of amyotrophic lateral sclerosis, Parkinsonism, and Alzheimer disease," *Annals of Neurology*, vol. 10, no. 6, pp. 499–505, 1981.
- [3] Y. Uchida, Y. Ihara, and M. Tomonaga, "Alzheimer's disease brain extract stimulates the survival of cerebral cortical neurons from neonatal rats," *Biochemical and Biophysical Research Communications*, vol. 150, no. 3, pp. 1263–1267, 1988.
- [4] Y. Uchida and M. Tomonaga, "Neurotrophic action of Alzheimer's disease brain extract is due to the loss of inhibitory factors for survival and neurite formation of cerebral cortical neurons," *Brain Research*, vol. 481, no. 1, pp. 190–193, 1989.
- [5] Y. Uchida, "Growth-inhibitory factor, metallothionein-like protein, and neurodegenerative diseases," *Biological Signals*, vol. 3, no. 4, pp. 211–215, 1994.
- [6] Y. Uchida, K. Takio, K. Titani, Y. Ihara, and M. Tomonaga, "The growth inhibitory factor that is deficient in the Alzheimer's disease brain is a 68 amino acid metallothionein-like protein," *Neuron*, vol. 7, no. 2, pp. 337–347, 1991.
- [7] P. A. Binz and J. H. R. Kagi, "Metallothionein: molecular evolution and classification," in *Metallothionein IV*, C. Klaassen, Ed., pp. 7–13, Birkhäuser, Basel, Switzerland, 1999.
- [8] D. H. Hamer, "Metallothionein," *Annual Review of Biochemistry*, vol. 55, pp. 913–951, 1986.
- [9] R. D. Palmiter, "Molecular biology of metallothionein gene expression," *Experientia. Supplementum*, vol. 52, pp. 63–80, 1987.
- [10] D. R. Winge and K. A. Miklossy, "Domain nature of metallothionein," *Journal of Biological Chemistry*, vol. 257, no. 7, pp. 3471–3476, 1982.
- [11] S. K. Krezoski, J. Villalobos, C. F. Shaw III, and D. H. Petering, "Kinetic lability of zinc bound to metallothionein in Ehrlich cells," *Biochemical Journal*, vol. 255, no. 2, pp. 483–491, 1988.
- [12] D. G. Nettesheim, H. R. Engeseth, and J. D. Otvos, "Products of metal exchange reactions of metallothionein," *Biochemistry*, vol. 24, no. 24, pp. 6744–6751, 1985.
- [13] M. J. Stillman, W. Cai, and A. J. Zelazowski, "Cadmium binding to metallothioneins. Domain specificity in reactions of α and β fragments, apometallothionein, and zinc metallothionein with Cd^{2+} ," *Journal of Biological Chemistry*, vol. 262, no. 10, pp. 4538–4548, 1987.
- [14] J. H. R. Kagi and A. Schäffer, "Biochemistry of metallothionein," *Biochemistry*, vol. 27, no. 23, pp. 8509–8515, 1988.
- [15] C. Jacob, W. Maret, and B. L. Vallee, "Control of zinc transfer between thionein, metallothionein, and zinc proteins," *Proceedings of the National Academy of Sciences of the United States of America*, vol. 95, no. 7, pp. 3489–3494, 1998.
- [16] S. Tsuji, H. Kobayashi, Y. Uchida, Y. Ihara, and T. Miyatake, "Molecular cloning of human growth inhibitory factor cDNA and its down-regulation in Alzheimer's disease," *EMBO Journal*, vol. 11, no. 13, pp. 4843–4850, 1992.
- [17] A. K. Sewell, L. T. Jensen, J. C. Erickson, R. D. Palmiter, and D. R. Winge, "Bioactivity of metallothionein-3 correlates with its novel β domain sequence rather than metal binding properties," *Biochemistry*, vol. 34, no. 14, pp. 4740–4747, 1995.
- [18] Y. Uchida and Y. Ihara, "The N-terminal portion of growth inhibitory factor is sufficient for biological activity," *Journal of Biological Chemistry*, vol. 270, no. 7, pp. 3365–3369, 1995.
- [19] P. Faller and M. Vašák, "Distinct metal-thiolate clusters in the N-terminal domain of neuronal growth inhibitory factor," *Biochemistry*, vol. 36, no. 43, pp. 13341–13348, 1997.
- [20] D. W. Hasler, L. T. Jensen, O. Zerbe, D. R. Winge, and M. Vašák, "Effect of the two conserved prolines of human growth inhibitory factor (metallothionein-3) on its biological activity and structure fluctuation: comparison with a mutant protein," *Biochemistry*, vol. 39, no. 47, pp. 14567–14575, 2000.
- [21] F.-Y. Ni, B. Cai, Z.-C. Ding, et al., "Structural prediction of the β -domain of metallothionein-3 by molecular dynamics simulation," *Proteins: Structure, Function and Genetics*, vol. 68, no. 1, pp. 255–266, 2007.
- [22] M. P. Williamson, "The structure and function of proline-rich regions in proteins," *Biochemical Journal*, vol. 297, no. 2, pp. 249–260, 1994.
- [23] B. Cai, Q. Zheng, X.-C. Teng, et al., "The role of Thr5 in human neuron growth inhibitory factor," *Journal of Biological Inorganic Chemistry*, vol. 11, no. 4, pp. 476–482, 2006.
- [24] W.-H. Yu, B. Cai, Y. Gao, D. Chen, and Z.-X. Huang, "Effect of mutation of Cys33 and Cys34 in the α -domain of monkey metallothionein-1 on the protein stability," *Chemical Journal of Chinese Universities*, vol. 24, no. 4, pp. 569–575, 2003.
- [25] R. Higuchi, B. Krummel, and R. K. Saiki, "A general method of in vitro preparation and specific mutagenesis of DNA fragments: study of protein and DNA interactions," *Nucleic Acids Research*, vol. 16, no. 15, pp. 7351–7367, 1988.
- [26] M. Vašák, "Metal removal and substitution in vertebrate and invertebrate metallothioneins," *Methods in Enzymology*, vol. 205, pp. 452–458, 1991.
- [27] D. R. Grasseti and J. F. Murray Jr., "Determination of sulfhydryl groups with 2,2'- or 4,4'-dithiodipyridine," *Archives of Biochemistry and Biophysics*, vol. 119, pp. 41–49, 1967.
- [28] T. Y. Li, A. J. Kraker, C. F. Shaw III, and D. H. Petering, "Ligand substitution reactions of metallothioneins with EDTA and apo-carbonic anhydrase," *Proceedings of the National Academy of Sciences of the United States of America*, vol. 77, no. 11, pp. 6334–6338, 1980.
- [29] C. F. Shaw III, M. M. Savas, and D. H. Petering, "Ligand substitution and sulfhydryl reactivity of metallothionein," *Methods in Enzymology*, vol. 205, pp. 401–414, 1991.
- [30] R. S. Chung, J. C. Vickers, M. I. Chuah, B. L. Eckhardt, and A. K. West, "Metallothionein-III inhibits initial neurite formation in developing neurons as well as postinjury, regenerative neurite sprouting," *Experimental Neurology*, vol. 178, no. 1, pp. 1–12, 2002.
- [31] J. C. Erickson, A. K. Sewell, L. T. Jensen, D. R. Winge, and R. D. Palmiter, "Enhanced neurotrophic activity in Alzheimer's disease cortex is not associated with down-regulation of metallothionein-III (GIF)," *Brain Research*, vol. 649, no. 1–2, pp. 297–304, 1994.
- [32] M. Vašák, "Application of ^{113}Cd NMR to metallothioneins," *Biodegradation*, vol. 9, no. 6, pp. 501–512, 1998.
- [33] G. Öz, D. L. Pountney, and I. M. Armitage, "NMR spectroscopic studies of $I = 1/2$ metal ions in biological systems," *Biochemistry and Cell Biology*, vol. 76, no. 2–3, pp. 223–234, 1998.
- [34] N. Romero-Isart, L. T. Jensen, O. Zerbe, D. R. Winge, and M. Vašák, "Engineering of metallothionein-3 neuroinhibitory activity into the inactive isoform metallothionein-1," *Journal of Biological Chemistry*, vol. 277, no. 40, pp. 37023–37028, 2002.

- [35] Z.-C. Ding, X.-C. Teng, B. Cai, et al., "Mutation at Glu23 eliminates the neuron growth inhibitory activity of human metallothionein-3," *Biochemical and Biophysical Research Communications*, vol. 349, no. 2, pp. 674–682, 2006.
- [36] M. Vašák, J. H. R. Kägi, and H. A. O. Hill, "Zinc(II), cadmium(II), and mercury(II) thiolate transitions in metallothionein," *Biochemistry*, vol. 20, no. 10, pp. 2852–2856, 1981.
- [37] Z.-C. Ding, Q. Zheng, B. Cai, et al., "Effect of α -domain substitution on the structure, property and function of human neuronal growth inhibitory factor," *Journal of Biological Inorganic Chemistry*, vol. 12, no. 8, pp. 1173–1179, 2007.
- [38] L.-J. Jiang, M. Vašák, B. L. Vallee, and W. Maret, "Zinc transfer potentials of the α - and β -clusters of metallothionein are affected by domain interactions in the whole molecule," *Proceedings of the National Academy of Sciences of the United States of America*, vol. 97, no. 6, pp. 2503–2508, 2000.
- [39] P. Faller, D. W. Hasler, O. Zerbe, S. Klauser, D. R. Winge, and M. Vašák, "Evidence for a dynamic structure of human neuronal growth inhibitory factor and for major rearrangements of its metal-thiolate clusters," *Biochemistry*, vol. 38, no. 31, pp. 10158–10167, 1999.

Research Article

Molecular Architectures Derived from Metal Ions and the Flexible 3,3'-Bipyridine Ligand: Unexpected Dimer with Hg(II)

Anupam Khutia, Pablo J. Sanz Miguel, and Bernhard Lippert

Fakultät Chemie, Technische Universität Dortmund, 44221 Dortmund, Germany

Correspondence should be addressed to Pablo J. Sanz Miguel, pablo.sanz@tu-dortmund.de and Bernhard Lippert, bernhard.lippert@tu-dortmund.de

Received 4 March 2010; Accepted 12 March 2010

Academic Editor: Spyros Perlepes

Copyright © 2010 Anupam Khutia et al. This is an open access article distributed under the Creative Commons Attribution License, which permits unrestricted use, distribution, and reproduction in any medium, provided the original work is properly cited.

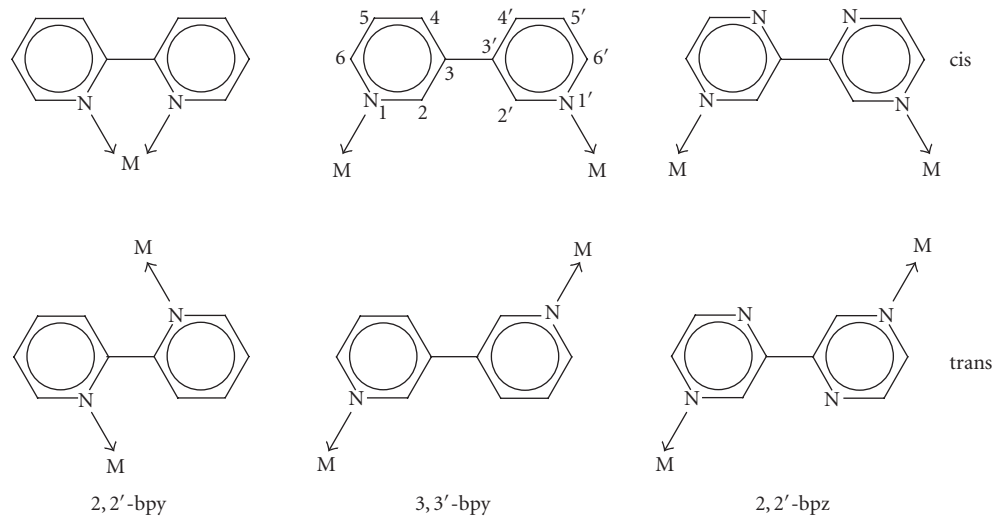
The flexible ditopic ligand 3,3'-bipyridine (3,3'-bpy) has been reacted with a series of transition metal species (Ag^+ , Hg^{2+} , $\text{cis-}a_2\text{M}^{2+}$ ($a = \text{NH}_3$ or $a_2 = \text{en}$; $\text{M} = \text{Pt}, \text{Pd}$), $\text{trans-}a_2\text{Pt}^{2+}$ ($a = \text{NH}_3$)) in an attempt to produce discrete cyclic constructs. While Ag^+ gave a polymeric structure $\{[\text{Ag}(3,3'\text{-bpy})](\text{ClO}_4) \cdot \text{H}_2\text{O}\}_n$ (**1**), with all other metal entities cyclic structures were formed. Interestingly, $\text{Hg}(\text{CH}_3\text{COO})_2$ produced a dinuclear complex $[\text{Hg}(3,3'\text{-bpy})(\text{CH}_3\text{COO})_2]_2 \cdot 3\text{H}_2\text{O}$ (**2**), in which the two 3,3'-bpy ligands adopt a cis-orientation of the coordinating pyridyl entities. With $\text{cis-}(\text{NH}_3)_2\text{Pt}^{2+}$, a cyclic complex **4** was isolated in crystalline form which, according to HRMS, is a trimer. With $\text{trans-}(\text{NH}_3)_2\text{Pt}^{2+}$, different species are formed according to ^1H NMR spectroscopy, the nature of which was not established.

1. Introduction

The “molecular library” concept has proven highly efficient in designing discrete supramolecular metal complexes by combining di- or multitopic metal entities with rigid di- or multitopic ligands [1, 2]. It is less straightforward if ligands are flexible and can adopt, in principle, different rotamer states. In its simplest form, this is the case when two N-heterocyclic ligands are connected via a C–C bond. Examples are, among others, 2,2'-bipyridine (2,2'-bpy), 3,3'-bipyridine (3,3'-bpy) and, 2,2'-bipyrazine (2,2'-bpz) (Scheme 1). While 2,2'-bpy, in the overwhelming number of structures, acts as a chelating ligand with the two ring N atoms in a cis-orientation, there are also rare cases of 2,2'-bpy adopting a bridging mode, hence being in a transconfiguration or half-way between cis and trans- [3]. It depends on the conformation of the ligand and the geometry of the metal, what kind of construct/s is/are formed. With 2,2'-bpz, we have studied this question in more detail and have characterized a number of discrete molecular entities, which include a flat triangular structure, 3D triangular entities of different shapes (prism, vase), as well as a tetranuclear open box [4, 5]. In all these cases the N4/N4' positions are involved in metal

coordination, occasionally complemented by addition of metal chelation via N1/N1', and influenced by counter anions.

In principle, 3,3'-bipyridine (3,3'-bpy) metal complexes should be able to reveal analogous topologies as 2,2'-bpz, with the advantage of higher basicities of the N donor atoms (Figure 1). There are several reports in the literature on polymeric structures containing cis- [6] and in particular trans-arranged 3,3'-bpy ligands [7], yet none with a discrete molecular metallacycle. The only related examples are those of trinuclear cycles containing three $\text{cis-}a_2\text{M}^{\text{II}}$ units ($a_2 = \text{diamine}$; $\text{M} = \text{Pd}$ or Pt) and three 4,7-phenanthroline ligands, which can be considered rigid analogous of 3,3'-bpy ligands with the two pyridine entities fixed in a cis-orientation [8, 9]. Our interest in discrete cationic metallacycles stems, among others, from their potential of interacting noncovalently with DNA [10] or particular DNA secondary structures such as DNA quadruplexes [11], as well as their ability to act as hosts for anions [12, 13]. In the present study, we have employed different transition metal ions and metal entities which previously have been shown by others and ourselves to produce discrete cyclic complexes, namely $\text{Ag}(\text{I})$, $\text{Hg}(\text{II})$, $\text{enPd}(\text{II})$, $\text{cis-}(\text{NH}_3)_2\text{Pt}(\text{II})$ as well as $\text{trans-}a_2\text{Pt}(\text{II})$ ($a = \text{NH}_3$) [14–16].



SCHEME 1: cis- and trans-orientation of pyridine and pyrazine rings in 2,2'-bpy, 3,3'-bpy, and 2,2'-bpz.

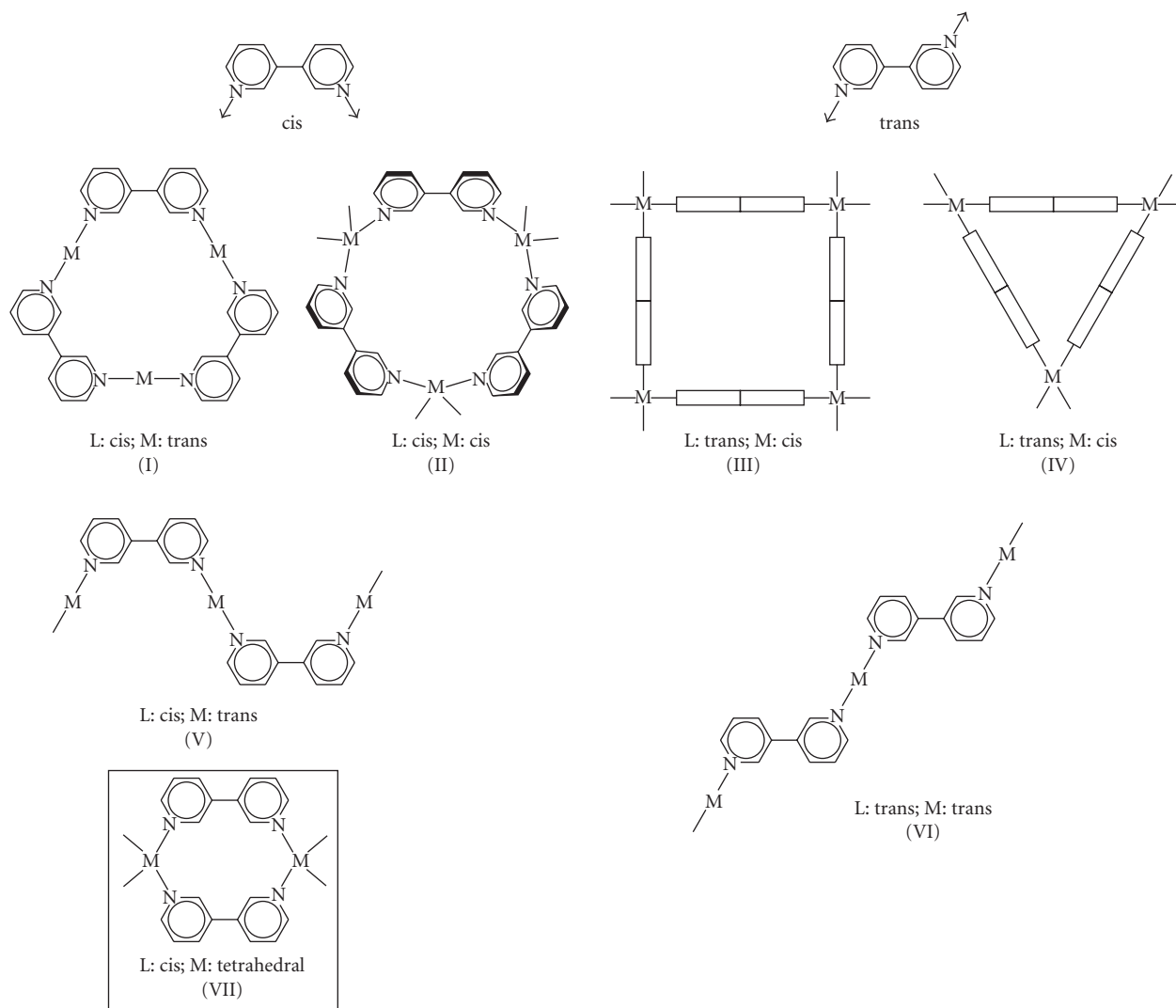


FIGURE 1: Feasible discrete (I–IV) and polymeric (V, VI) structures of 3,3'-bpy metal complexes, and novel dinuclear complex (VII) observed in the Hg^{II} complex 2.

2. Experimental

2.1. Synthesis Procedures. AgClO_4 and $\text{Hg}(\text{CH}_3\text{COO})_2$ were of commercial origin. 3,3'-bpy [17], $\text{PdCl}_2(\text{en})$ [18], $\text{cis-PtCl}_2(\text{NH}_3)_2$ [19], and $\text{trans-PtCl}_2(\text{NH}_3)_2$ [20] were prepared according to known literature procedures.

$\{\text{[Ag}(3,3'\text{-bpy})](\text{ClO}_4)_2 \cdot \text{H}_2\text{O}\}_n$ (**1**). To a solution of 3,3'-bpy (15.6 mg, 0.1 mmol) in water (3 mL), an aqueous solution (2 mL) of AgClO_4 (20.7 mg, 0.1 mmol) was added. The white precipitate which formed immediately was centrifuged off and recrystallized from water (4 mL, 40°C). Colorless crystals were obtained after 2 d at room temperature. Yield: 30.5 mg (80%). Anal. Calcd (%) for $\text{C}_{10}\text{H}_{10}\text{AgClN}_2\text{O}_5$: C, 31.5; H, 2.6; N, 7.3. Found: C, 31.4; H, 2.6; N, 7.5.

$\{\text{[Hg}(3,3'\text{-bpy})(\text{CH}_3\text{COO})_2\}_2 \cdot 3\text{H}_2\text{O}$ (**2**). An aqueous solution (4 mL) of 3,3'-bpy (15.6 mg, 0.1 mmol) and $\text{Hg}(\text{CH}_3\text{COO})_2$ (31.9 mg, 0.1 mmol) was stirred at room temperature for 12 h. The solution is filtered and kept at room temperature. After 3 d, colorless crystals were obtained. Yield: 37.1 mg (74%). **2** was characterized by X-ray analysis.

$\{\text{[Pd}(\text{en})(3,3'\text{-bpy})](\text{NO}_3)_2 \cdot \text{H}_2\text{O}\}_n$ (**3**). An aqueous suspension (15 mL) of $\text{PdCl}_2(\text{en})$ (47.4 mg, 0.2 mmol) and AgNO_3 (68 mg, 0.4 mmol) was stirred in dark for 12 h. The resultant AgCl precipitate was filtered off and 3,3'-bpy (31.2 mg, 0.2 mmol) was added to the filtrate. The solution was stirred at 40°C for 1 day and then concentrated to a volume of 4 mL by rotary evaporator. The solution was filtered and kept at room temperature. After 4 d, light yellow powder was recovered. Yield: 61 mg (66%). Anal. Calcd (%) for $(\text{C}_{12}\text{H}_{18}\text{N}_6\text{O}_7\text{Pd})_n$ (1-hydrate): C, 31.0; H, 3.9; N, 18.1. Found: C, 30.8; H, 4.0; N, 18.0.

$\text{cis-}\{\text{[Pt}(\text{NH}_3)_2(3,3'\text{-bpy})](\text{PF}_6)_2 \cdot \text{H}_2\text{O}\}_n$ (**4**). An aqueous suspension (20 mL) of $\text{cis-PtCl}_2(\text{NH}_3)_2$ (60 mg, 0.2 mmol) and AgNO_3 (68 mg, 0.4 mmol) was stirred in dark for 12 h. The resultant AgCl precipitate was filtered off and 3,3'-bpy (31.2 mg, 0.2 mmol) was added to the filtrate. The solution was stirred at 60°C for 3 d, then solid NH_4PF_6 (65.2 mg, 0.4 mmol) was added to it and the solution was stirred at 60°C for another day. The solution was concentrated to a volume of 5 mL (pD = 3.20) and kept in an open beaker at 4°C. After 5 d, colorless crystals were obtained. According to MS, **4** represents a cyclic trimer, hence $n = 3$. Yield: 73 mg (54%). Anal. Calcd (%) for $\text{C}_{30}\text{H}_{48}\text{N}_{12}\text{O}_3\text{P}_6\text{F}_{36}\text{Pt}_3$: C, 17.3; H, 2.3; N, 8.1. Found: C, 17.5; H, 2.6; N, 7.9.

2.2. X-Ray Crystal Structure Determination. X-ray crystal data for **1** and **2** (Table 1) were recorded at 150 K with an Xcalibur diffractometer equipped with an area detector and graphite monochromated $\text{Mo K}\alpha$ radiation (0.71073 Å). Data reduction was done with the CrysAlisPro software [21]. Both structures were solved by direct methods and refined by full-matrix least-squares methods based on F^2 using SHELXL-97 [22]. All nonhydrogen atoms were refined anisotropically. Hydrogen atoms (including water

molecules) were positioned geometrically and refined with isotropic displacement parameters according to the riding model. All calculations were performed using the SHELXL-97 and WinGX programs [22, 23]. CCDC 763713 and 763714 contain the crystallographic data for compounds **1** and **2**.

2.3. Instruments. Elemental (C, H, N) analysis data were obtained on a Leco CHNS-932 instrument. The ^1H NMR spectra were recorded in D_2O with tetramethylammonium chloride (TMA) and sodium-3-(trimethylsilyl)-1-propanesulfonate (TSP) as internal reference, on Bruker AC 200 and Bruker AC 300 spectrometers.

2.4. Electrospray Mass Spectrometry. The mass spectrum of **4** was recorded with an LTQ orbitrap (high resolution mass spectrometer) coupled to an Accela HPLC-system (consisting of Accela pump, Accela autosampler, and Accela PDA detector), from Thermo Electron. The parameters for HPLC were as follows: (i) Eluent A (0.1% formic acid in H_2O) and eluent B (0.1% formic acid in acetonitrile) with mobile phase consisting of 50% A and 50% B, (ii) Flow rate 250 $\mu\text{L}/\text{min}$, (iii) injection volume 5 μL , (iv) scan of wavelength range from 200 to 600 nm. The parameters for MS were as follows: (i) ionisation mode ESI (electrospray ionization), (ii) source voltage 3.8 kV, Capillary voltage 41 V, Capillary temperature 275°C, tube lens voltage 140 V, (iii) scanned mass range 150 m/z to 2000 m/z with resolution set to 60000. Analysis was done by flow injection (without any column).

2.5. Determination of pK_a Values. The pK_a values of 3,3'-bpy ligand were determined by evaluating the changes in chemical shifts of bipyridine protons at different pD values. pD values were measured by use of a glass electrode and addition of 0.4 units to the uncorrected pH meter reading (pH^*). The graphs (chemical shifts versus pD) were evaluated with a nonlinear least-squares fit according to Newton-Gauss method [24] and the acidity constants (calculated for D_2O) were converted to values valid for H_2O [25].

3. Results and Discussion

^1H NMR Spectra of 3,3'-Bipyridine. Figure 2 displays a typical ^1H NMR spectrum of the free ligand at pD 6.8. The individual resonances show the expected coupling patterns [17]. In the D_2O spectrum, all resonances show splitting due to long-range coupling. For example, the H2 signal is split into a doublet due to coupling with H4 (1.5 Hz) and additionally displays coupling with H5 (0.7 Hz). Upon protonation, all resonances are downfield shifted, with H6 affected most. pK_a values for $[\text{3,3'-bpyH}]^+$ and $[\text{3,3'-bpyH}_2]^{2+}$, as determined by pD dependent ^1H NMR spectroscopy, are 4.58 ± 0.1 and 2.71 ± 0.1 (values converted to H_2O), respectively. These values compare with 4.3 and ca. 0.3 for 2,2'-bpy, and 0.45 and -1.35 for 2,2'-bpz, and reflect the higher basicity of 3,3'-bpy as compared to two other ligands.

TABLE 1: Crystallographic data for compounds $\{[\text{Ag}(3,3'\text{-bpy})](\text{ClO}_4) \cdot \text{H}_2\text{O}\}_n$ (**1**) and $[\text{Hg}(3,3'\text{-bpy})(\text{CH}_3\text{COO})_2]_2 \cdot 3\text{H}_2\text{O}$ (**2**).

	1	2
Formula	$\text{C}_{10}\text{H}_{10}\text{Ag}_1\text{Cl}_1\text{N}_2\text{O}_5$	$\text{C}_{28}\text{H}_{34}\text{Hg}_2\text{N}_4\text{O}_{11}$
Formula weight (g mol^{-1})	381.52	1003.77
Crystal color and habit	colorless prisms	colorless prisms
Crystal size (mm)	$0.20 \times 0.20 \times 0.10$	$0.15 \times 0.10 \times 0.05$
Crystal system	monoclinic	triclinic
Space group	$P2_1/c$	$P-1$
a (Å)	9.7606(10)	8.5635(5)
b (Å)	7.3145(8)	9.2096(6)
c (Å)	19.572(2)	11.3262(6)
α (°)	90	74.746(5)
β (°)	119.148(9)	84.183(4)
γ (°)	90	63.221(6)
V (Å ³)	1220.4(2)	769.21(8)
Z	4	1
$D_{\text{calcd.}}$ (g cm^{-3})	2.077	2.167
$F(000)$	752	478
μ (mm^{-1})	1.888	10.034
No. reflections collected	2333	3572
No. reflections observed	1557	2969
R_{int}	0.0317	0.0359
No. parameters refined	172	208
$R [I > 2\sigma(I)]$	0.0331	0.0270
wR (all reflections)	0.0572	0.0453
Goodness-of-fit (GOF)	1.041	0.911
$\Delta\rho_{\text{max}}$ and $\Delta\rho_{\text{min}}$ ($e \text{ \AA}^{-3}$)	0.941 and -0.517	1.078 and -1.283

$$\text{GOF} = [\Sigma w(F_o^2 - F_c^2)^2 / (N_o - N_v)]^{1/2}; R = \Sigma |F_o| - |F_c| / \Sigma |F_o|; wR = [\Sigma (w(F_o^2 - F_c^2)^2) / \Sigma w(F_o^2)^2]^{1/2}.$$

¹H NMR resonances of 3,3'-bpy in D₂O display a moderate sensitivity on concentration, which is consistent with intermolecular stacking. For example, when going from 0.0125 M to 0.125 M, upfield shifts are 0.06 ppm (H2), 0.03 ppm (H4), 0.05 ppm (H6), and 0.04 ppm (H5).

Ag⁺ and Hg²⁺ Coordination. Addition of Ag⁺ ions to an aqueous solution of 3,3'-bpy in D₂O expectedly does not reveal resonances due to individual species, but rather gives only averaged signals of the free ligand and the various Ag complexes as a consequence of fast exchange.

A similar situation applies to mixtures of 3,3'-bpy and Hg(II) acetate. The spectrum of the dinuclear Hg(II) complex **2** has its ¹H resonances (δ , ppm; D₂O, pD 5.2) at 8.97, 8.73, 8.44, and 7.88 as well as 2.02 (acetate). No coupling of any of the 3,3'-bpy resonances with the ¹⁹⁹Hg isotope is observed as in a previously reported case [26], and a comparison of the shifts of **2** with those of the free ligand at the same pD (downfields shifts of H2, 0.06 ppm; H4, 0.06 ppm; H6, 0.09 ppm; H5, 0.13 ppm) does not permit any conclusions regarding the bonding situation in solution.

The crystal structure of $\{[\text{Ag}(3,3'\text{-bpy})](\text{ClO}_4) \cdot \text{H}_2\text{O}\}_n$ (**1**) reveals a polymeric structure rather than a discrete cyclic

structure as we had hoped for. The silver atom (Ag1) shows a distorted octahedral coordination sphere (Figure 3(a)), with two 3,3'-bpy ligands at the apical positions (Ag1-N1, 2.181(3) Å; Ag1-N11, 2.189(3) Å). The equatorial coordination is completed by a water molecule (Ag1-O1w, 2.722(3) Å), two perchlorate counter anions (Ag1-O13, 2.773(4) Å; Ag1-O13', 2.861(4) Å), and an argentophilic interaction [27, 28] with a neighbor silver atom (Ag ··· Ag, 3.3751(8) Å). Angles and distances involving the coordination sphere of Ag1 are listed in Table 2. The polymeric structure is assembled by coordination of additional silver units to the bridging 3,3'-bpy ligands of the apical positions, with a $-\text{Ag}-[\text{N}11-3,3'\text{-bpy}-\text{N}21]-\text{Ag}-$ basic motif, which extends along the [1 0 1] direction (Figure 3(b)). The 3,3'-bpy ligands adopt transconformations with a twist angle of 27.9(1)° between pyridine halves. The dihedral angle between two pyridyl rings coordinated to Ag1 is 7.2(1)°. The crystal packing is based on $\pi-\pi$ stacking and argentophilic interactions between polymer strands. An upper view of the ac plane evidences the presence of voids in the structure (Figure 4(a)). They are essentially rectangular tunnels along the b axis, which house two sets of hydrogen bond-based perchlorate-water polymers. These polymers are built by connecting water molecules of crystallization and perchlorate anions.

TABLE 2: Selected bond distances (Å) and angles (°) for compound 1.

Ag1-N1, 2.181(3)	N1-Ag1-N11, 174.37(13)	N11-Ag1-Ag1', 76.06(9)
Ag1-N11, 2.189(3)	O13-Ag1-Ag1, 157.52(8)	N11-Ag1-O13, 87.31(11)
Ag1-Ag1, 3.3751(8)	O1w-Ag1-O13, 168.17(10)	N11-Ag1-O13', 92.86(11)
Ag1-O1w, 2.722(3)	N1-Ag1-Ag1', 108.03(9)	N11-Ag1 O1W 95.33(11)
Ag1-O13, 2.773(4)	N1-Ag1-O13, 84.58(11)	Ag1'-Ag1-O1w, 78.60(7)
Ag1-O13', 2.861(4)	N1-Ag1-O13', 87.48(11)	O1w-Ag1-O13, 83.13(10)
Bpy-rings, 27.86(7)	N1-Ag1-O1w, 89.35(11)	O13-Ag1-O13', 85.22(10)
py-Ag-py', 7.19(10)		O13-Ag1-Ag1', 113.22(7)

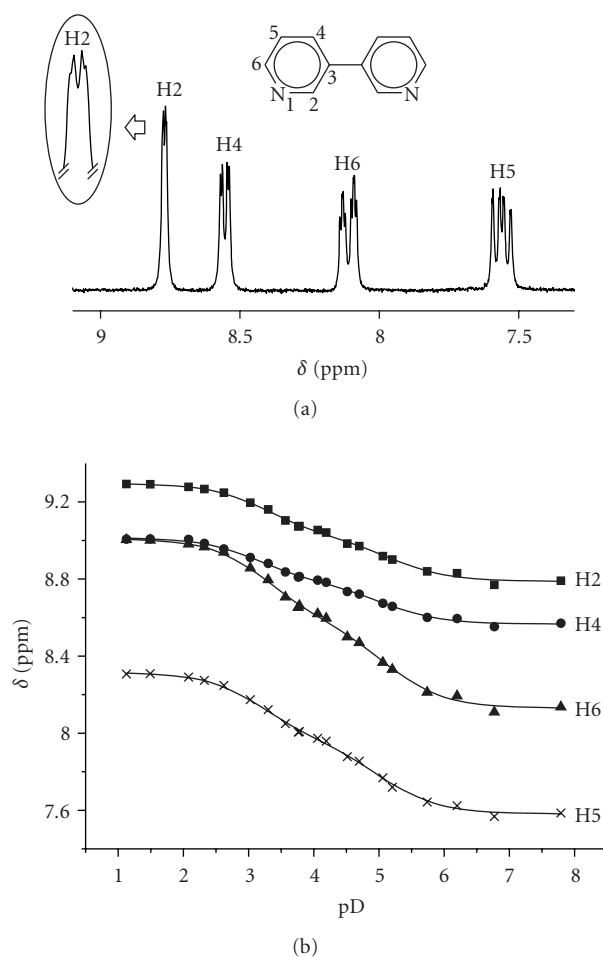


FIGURE 2: (a) Low field section of ^1H NMR spectrum of 3,3'-bpy (D_2O , $\text{pD} = 6.8$) and pD dependence of individual resonances, focusing splitting of the H2 resonances. (b) pD dependence of H2, H4, H6, and H8 resonances of free 3,3'-bipyridine.

Each O1w forms two hydrogen bonds with two perchlorate anions: $\cdots \text{O14}-\text{Cl1}-\text{O12} \cdots (\text{H1w})\text{O1w}(\text{H2w}) \cdots \text{O14}-\text{Cl1}-\text{O12} \cdots$ (Figure 4(b)). Distances and angles involving O1w are $\text{O1w} \cdots \text{O12}$, 2.969(5) Å; $\text{O1w} \cdots \text{O14}$, 2.886(5) Å; $\text{O12} \cdots \text{O1w} \cdots \text{O14}$, 119.5(2)°.

The crystal structure of the dinuclear species $[\text{Hg}(3,3'\text{-bpy})(\text{CH}_3\text{COO})_2]_2 \cdot 3\text{H}_2\text{O}$ (2) is given in Figure 5. Unlike

in 1, in 2 the 3,3'-bpy ligands adopt a cis-conformation of the two pyridyl rings, with a twist angle of 30.4(2)°, and act as bridges between two mercury centers. The coordination geometry of the Hg ion (Table 3) is distorted tetrahedral, enclosing two 3,3'-bpy entities ($\text{Hg1}-\text{N1a}$, 2.274(3) Å; $\text{Hg1}-\text{N1b}$, 2.263(3) Å), and two chelating/semichelating acetates ($\text{Hg1}-\text{O11}$, 2.490(3) Å; $\text{Hg1}-\text{O12}$, 2.392(3) Å; and $\text{Hg1}-\text{O21}$, 2.286(3) Å; $\text{Hg1}-\text{O22}$, 2.762(3) Å). Selected distances and angles around mercury are listed in Table 3. Both 3,3'-bpy ligands and their bonded mercury atoms are almost coplanar with a tendency towards a boat conformation (distance from Hg1 to the plane defined by N1a, N1b, N1a', N1b' is 0.58 Å).

The disposition of the acetate ligands is worthy to be discussed in more detail. Both ligands form a dihedral angle of 79.23(16)° with each other. The ligand containing O11, O12 is roughly coplanar with the pyridyl rings (7.27(27)°, 23.28(23)°), whereas the ligand A2 (with O21, O22) is roughly perpendicular (78.33(15), 72.81(14)°). Both are asymmetrically coordinated to Hg1, displaying significant longer bond distances of those oxygen atoms involved in hydrogen bonding: $\text{O1w} \cdots \text{O11}$, 2.802(5) Å ($\text{Hg1}-\text{O11}$, 2.490(3) Å versus $\text{Hg1}-\text{O12}$, 2.392(3) Å) and $\text{O1w} \cdots \text{O22}$, 2.757(4) Å ($\text{Hg1}-\text{O21}$, 2.286(3) Å versus $\text{Hg1}-\text{O22}$, 2.762(3) Å). Further hydrogen bonding includes a twofold $\text{O1w} \cdots \text{O2w}$ (2.785(10) Å) connection. Besides hydrogen bonding, the crystal packing includes $\pi-\pi$ - and anion- π -interactions. N1a-pyridyl rings are pairwise $\pi-\pi$ stacked (3.5 Å), and both rings are involved in an additional anion- π -interaction with O11 ($\text{O11} \cdots$ centroid, 3.47 Å). Considering the latter, the formation of staggered rows is observed, in which each molecule displays four anion- π -interactions with neighbor molecules. Rows are interconnected by $\pi-\pi$ -stacking and hydrogen bonding.

Complexes with enPd^{II} and $\text{cis}-(\text{NH}_3)_2\text{Pt}^{\text{II}}$. Reactions of 3,3'-bpy with $[\text{Pd}(\text{en})(\text{H}_2\text{O})_2](\text{NO}_3)_2$ and $\text{cis}-[\text{Pt}(\text{NH}_3)_2(\text{H}_2\text{O})_2](\text{NO}_3)_2$ (1 : 1 ratio) give products of 1 : 1 stoichiometry $[\{\text{Pd}(\text{en})(3,3'\text{-bpy})\}(\text{NO}_3)_2]_n$ (3) and $\text{cis}-[\{\text{Pt}(\text{NH}_3)_2(3,3'\text{-bpy})\}(\text{PF}_6)_2]_n$ (4) which, according to ^1H NMR spectroscopy, are pure materials. Only single sets of 3,3'-bpy resonances are observed in both compounds, indicating that both compounds must be cyclic. Chemical shifts (δ , ppm; D_2O , TMA as internal reference) are as follows: 3, 9.15, 8.84, 8.27, 7.69 ppm (3,3'-bpy) and 2.98 (en); 4, 8.99, 8.95, 8.23, 7.67 (3,3'-bpy). When TSP was used

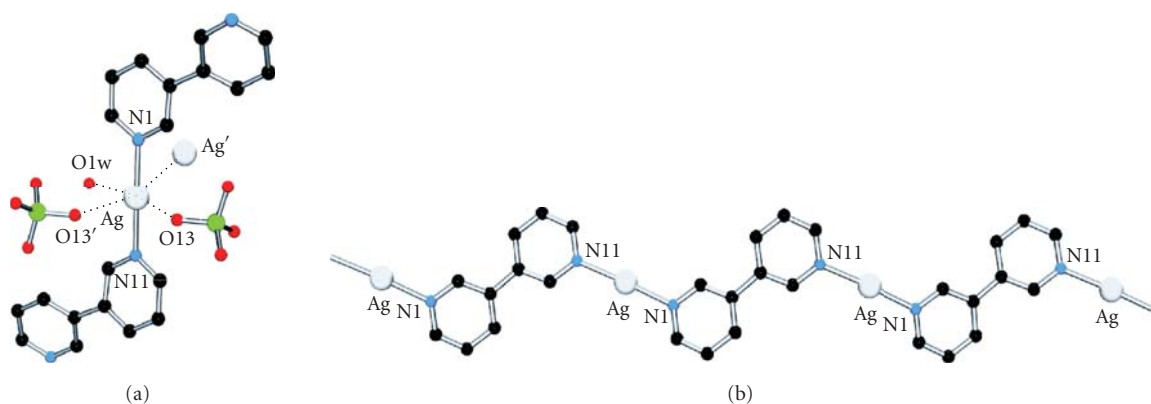


FIGURE 3: (a) Detail of the coordination sphere of the silver atom in **1**. (b) Polymeric motif between AgI and 3,3'-bpy bridging ligands in **1**.

TABLE 3: Selected bond distances (Å) and angles (°) for compound **2**.

Hg1-N1a, 2.274(3)	N1a-Hg1-N1b, 114.74(11)	N1b-Hg1-O21, 115.85(11)
Hg1-N1b, 2.263(3)	N1a-Hg1-O11, 88.58(11)	O11-Hg1-O12, 53.82(11)
Hg1-O11, 2.490(3)	N1a-Hg1-O12, 140.71(12)	O11-Hg1-O21, 93.87(10)
Hg1-O12, 2.392(3)	N1a-Hg1-O21, 103.25(12)	O12-Hg1-O21, 91.53(11)
Hg1-O21, 2.286(3)	N1b-Hg1-O11, 134.38(12)	Bpy-rings, 30.43(16)
Hg1-O22, 2.762(3)	N1b-Hg1-O12 89.72(12)	py-Hg-py', 30.43(16)

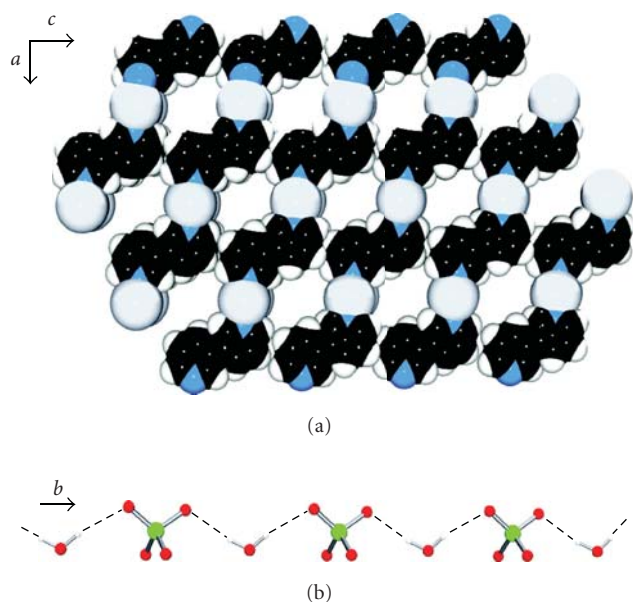


FIGURE 4: (a) Section of the packing pattern in **1** (excluding H₂O and ClO₄⁻), including voids along the *b* direction. (b) Water-perchlorate hydrogen bonded polymer inserted along the packing tunnels of **1**.

as a reference, shifts differed by 0.1 ppm (**3**) and 0.09 ppm (**4**), suggesting that the TSP anion interacts with the cations of **3** and **4** [29]. Although **4** was isolated in microcrystalline form, an X-ray structure determination proved impossible.

The high resolution MS of a sample of **4** was carried out and confirmed a triangular structure (see (II) or (IV) in Figure 1). The mass spectrum displayed peaks due to [M-(PF₆)⁺]: 1880.08114 (calcd. 1880.07904), [M-(PF₆)₂]²⁺: 867.55844 (calcd. 867.55828), and [M-(PF₆)₄]⁴⁺: 361.29666 (calcd. 361.29621). The HRMS spectrum of [M-(PF₆)₄]⁴⁺ is given in Figure 6 and compared with the simulated spectrum.

Reaction with trans-[Pt(NH₃)₂(H₂O)₂]²⁺. Reaction of 3,3'-bpy with trans-[Pt(NH₃)₂(D₂O)₂](NO₃)₂ was carried out with different ratios between 3,3'-bpy and the Pt species (10 : 1, 2 : 1, 1 : 1, 1 : 10) on the ¹H NMR scale in D₂O. Without exception, the spectra displayed time-dependent changes, but within 2-3 d at 50°C, constant spectra were obtained. Even then, however, resonances due to multiple products were present. In the case of a large excess of ligand over Pt (10 : 1), the spectrum reveals the presence of a major species attributed to trans-[Pt(NH₃)₂(3,3'-bpy)₂]²⁺ and excess 3,3'-bpy (Figure 7). The resonances of the free 3,3'-bpy (L) were unambiguously identified by adding solid 3,3'-bpy to the NMR sample. The two sets of pyridine resonances of the coordinated 3,3'-bpy ligands of the 1 : 2 complex are assigned on the basis of their relative intensities. What strikes is that the H2 and H4 resonances of the free ligand are very much broadened (cf. Figure 2(a)) and that H2, H4, and H6 are upfield shifted by *ca.* 0.2, 0.08, and 0.14 ppm, respectively. As these shifts cannot be interpreted with a pD effect, we propose that the presence of the 1 : 2-Pt complex has an effect on the rotamer equilibrium of the

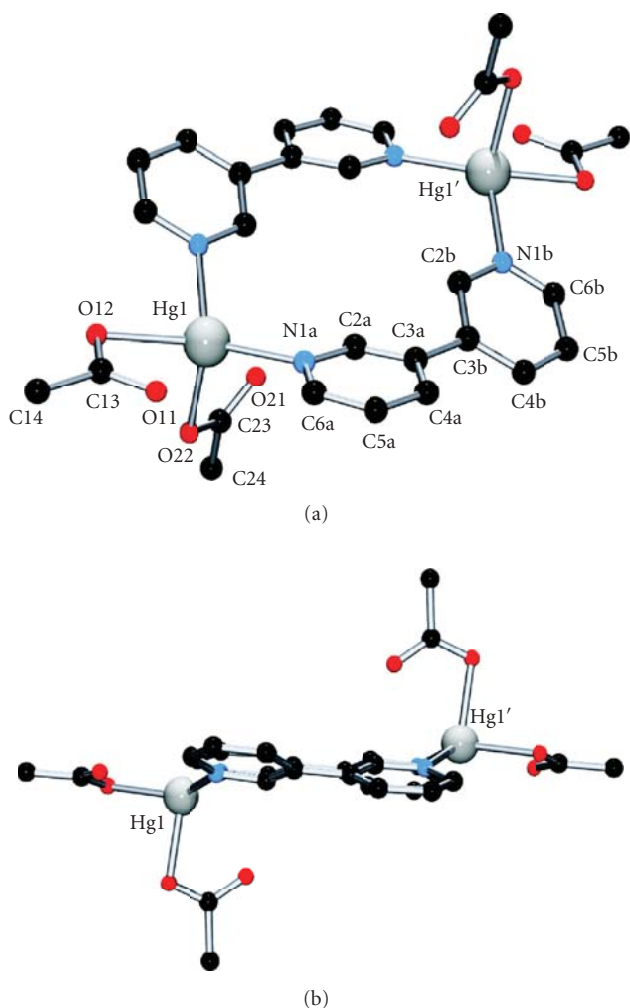


FIGURE 5: (a) View of **2** with atom numbering scheme. (b) Side view of **2**, evidencing a boat conformation of the mercury atoms with respect to the 3,3'-bpy ligands.

free ligand. Consistent with this proposal, the two resonances closest to the C3–C3 bond, hence H2 and H4, become quite broad. Stacking interactions between free and coordinated 3,3'-bpy could possibly account for this feature.

The ^1H NMR spectrum of a 1 : 1 mixture of $\text{trans}[\text{Pt}(\text{NH}_3)_2(\text{D}_2\text{O})_2]^{2+}$ and 3,3'-bpy displays four H2 (H2') singlets of different relative intensities at lowest field, and at least for the H6 (H6') resonances also four components can be differentiated. Free 3,3'-bpy is not detectable. It is obvious that the self-assembly process of $\text{trans}(\text{NH}_3)_2\text{Pt}^{\text{II}}$ and 3,3'-bpy does not lead to a preferred single product, unlike in the case of enPd^{II} and $\text{cis}(\text{NH}_3)_2\text{Pt}^{\text{II}}$.

4. Summary

The flexible ditopic ligand 3,3'-bipyridine forms with $\text{Hg}(\text{CH}_3\text{COO})_2$ and $\text{cis}[\text{Pt}(\text{NH}_3)_2(\text{H}_2\text{O})_2](\text{PF}_6)_2$ discrete di- and trinuclear cycles **2** and **4**, respectively. The solid state structure of the Hg(II) complex **2** is unique in that it

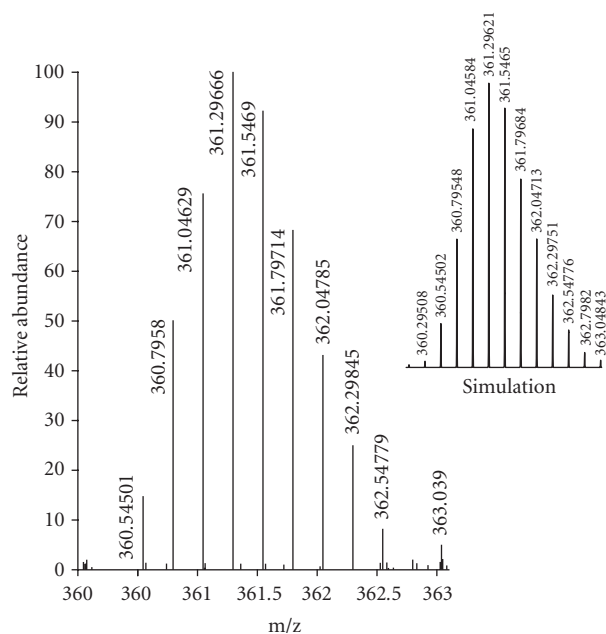


FIGURE 6: HRMS spectrum of complex **4**: Observed and calculated pattern for $[\text{M}-(\text{PF}_6)_4]^{4+}$.

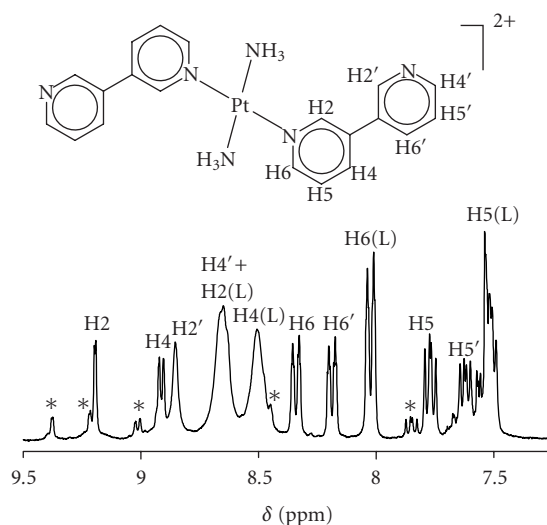


FIGURE 7: ^1H NMR spectrum of mixture of $\text{trans}[\text{Pt}(\text{NH}_3)_2(\text{D}_2\text{O})_2]^{2+}$ and 3,3'-bpy (L) in ratio 1 : 10 after 2 d, 50°C, D_2O , pD = 6.65. Main resonances are assigned to 1 : 2 complex and free ligand; minor resonances (*) are not assigned.

represents the smallest possible entity of any cyclic complex. It appears that the opening of the N1a–Hg–N1b angle to *ca.* 115° allows the dinuclear to be formed. A similar structure, with the two 3,3'-bpy ligands approximately coplanar, is not to be expected for $\text{cis-}a_2\text{Pt}^{\text{II}}$ with its 90° bonding angle. Consequently, **4** is a cyclic trinuclear compound. On the NMR time scale, **2** is kinetically labile in aqueous solution, but **4** is inert. We plan to further study **4** with regard to its host-guest chemistry and its noncovalent interaction with DNA.

Acknowledgments

This work was supported by the Deutsche Forschungsgemeinschaft and the “International Max-Planck Research School in Chemical Biology” in Dortmund (fellowship to Anupam Khutia). The authors thank Mr. Andreas Brockmeyer (MPI Dortmund) for recording the mass spectrum.

References

- [1] S. Leininger, B. Olenyuk, and P. J. Stang, “Self-assembly of discrete cyclic nanostructures mediated by transition metals,” *Chemical Reviews*, vol. 100, no. 3, pp. 853–908, 2000.
- [2] E. Zangrando, M. Casanova, and E. Alessio, “Trinuclear metallacycles: metallatriangles and much more,” *Chemical Reviews*, vol. 108, no. 12, pp. 4979–5013, 2008.
- [3] A. Klein and R. Lepski, “2,2′-bipyridine as bridging and terminal ligand in the binuclear palladium complex $[(\mu - \eta^1, \eta^1\text{-bpy})\{\text{Pd}(\text{Me})(\text{bpy})\}_2](\text{SbF}_6)_2$ —structure and spectroscopic properties,” *Zeitschrift für Anorganische und Allgemeine Chemie*, vol. 635, no. 6–7, pp. 878–884, 2009.
- [4] J. A. R. Navarro and B. Lippert, “Simple 1:1 and 1:2 complexes of metal ions with heterocycles as building blocks for discrete molecular as well as polymeric assemblies,” *Coordination Chemistry Reviews*, vol. 222, no. 1, pp. 219–250, 2001.
- [5] B. Lippert, to be published.
- [6] R. L. LaDuca, M. P. Desciak, R. S. Rarig Jr., and J. A. Zubieta, “Hydrothermal synthesis, solid state structure, and thermal properties of a family of isomorphous 1-D coordination polymers aggregated by extensive hydrogen bonding: $\{[\text{M}(3,3' - \text{bpy})(\text{H}_2\text{O})_4](\text{SO}_4) \cdot 2\text{H}_2\text{O}\}$ (M = Co, Ni, Zn),” *Zeitschrift für Anorganische und Allgemeine Chemie*, vol. 632, no. 3, pp. 449–453, 2006.
- [7] R. S. Rarig Jr., R. Lam, P. Y. Zavalij, et al., “Ligand influences on copper molybdate networks; the structures and magnetism of $[\text{Cu}(3,4' - \text{bpy})(\text{MoO}_4)]$, $[\text{Cu}(3,3' - \text{bpy})_{0.5}(\text{MoO}_4)]$ and $[\text{Cu}(4,4' - \text{bpy})_{0.5}(\text{MoO}_4)] \cdot 1.5\text{H}_2\text{O}$,” *Inorganic Chemistry*, vol. 41, no. 8, pp. 2124–2133, 2002.
- [8] M. A. Galindo, J. A. R. Navarro, M. A. Romero, and M. Quiros, “Mononucleotide recognition by cyclic trinuclear palladium (II) complexes containing 4,7-phenanthroline N,N bridges,” *Dalton Transactions*, no. 10, pp. 1563–1566, 2004.
- [9] S.-Y. Yu, H. Huang, H.-B. Liu, Z.-N. Chen, R. Zhang, and M. Fujita, “Modular cavity-tunable self-assembly of molecular bowls and crowns as structural analogues of calix[3]arenes,” *Angewandte Chemie International Edition*, vol. 42, no. 6, pp. 686–690, 2003.
- [10] M. A. Galindo, D. Olea, M. A. Romero, et al., “Design and non-covalent DNA binding of platinum (II) metallocalix[4]arenes,” *Chemistry A European Journal*, vol. 13, no. 18, pp. 5075–5081, 2007.
- [11] R. Kiełtyka, P. Englebienne, J. Fakhoury, C. Autexier, N. Moitessier, and H. F. Sleiman, “A platinum supramolecular square as an effective G-quadruplex binder and telomerase inhibitor,” *Journal of the American Chemical Society*, vol. 130, no. 31, pp. 10040–10041, 2008.
- [12] M. Roitzsch and B. Lippert, “Inverting the charges of natural nucleobase quartets: a planar platinum-purine quartet with pronounced sulfate affinity,” *Angewandte Chemie International Edition*, vol. 45, no. 1, pp. 147–150, 2005.
- [13] R.-D. Schnebeck, E. Freisinger, and B. Lippert, “A novel highly charged (+12) anion receptor that encapsulates simultaneously NO_3^- and PF_6^- ions,” *Angewandte Chemie International Edition*, vol. 38, no. 1–2, pp. 168–171, 1999.
- [14] A. Houlton, “New aspects of metal-nucleobase chemistry,” *Advances in Inorganic Chemistry*, vol. 53, pp. 87–158, 2002.
- [15] J. A. R. Navarro, E. Barea, M. A. Galindo, et al., “Soft functional polynuclear coordination compounds containing pyrimidine bridges,” *Journal of Solid State Chemistry*, vol. 178, no. 8, pp. 2436–2451, 2005.
- [16] S. Verma, A. K. Mishra, and J. Kumar, “The many facets of adenine: coordination, crystal patterns, and catalysis,” *Accounts of Chemical Research*, vol. 43, no. 1, pp. 79–91, 2010.
- [17] M. Tiecco, L. Testaferri, M. Tingoli, D. Chianelli, and M. Montanucci, “A convenient synthesis of bipyridines by nickel-phosphine complex-mediated homocoupling of halopyridines,” *Synthesis*, pp. 736–738, 1984.
- [18] B. J. McCormick, E. N. Jaynes Jr., and R. I. Kaplan, “Dichloro(ethylenediamine) palladium (II) and (2,2′-bipyridine)dichloro palladium (II),” *Inorganic Syntheses*, vol. 13, pp. 216–218, 1972.
- [19] S. C. Dhara, “A rapid method for the synthesis of $[\text{Pt}(\text{NH}_3)_2\text{Cl}_2]$,” *Indian Journal of Chemistry*, vol. 8, pp. 193–194, 1970.
- [20] G. B. Kauffman and D. O. Cowan, “Cis- and trans-dichlorodiammine-platinum(II),” *Inorganic Syntheses*, vol. 7, pp. 239–245, 1963.
- [21] CrysAlisPro, “Oxford Diffraction (Poland),” 2009.
- [22] G. M. Sheldrick, *SHELXS97 and SHELXL97*, University of Göttingen, Göttingen, Germany, 1997.
- [23] L. J. Farrugia, *WinGX*, University of Glasgow Press, Glasgow, UK, 1998.
- [24] R. Tribolet and H. Sigel, “Self-association and protonation of adenosine 5′-monophosphate in comparison with its 2′- and 3′-analogues and tubercidin 5′-monophosphate (7-deaza-AMP),” *European Journal of Biochemistry*, vol. 163, no. 2, pp. 353–363, 1987.
- [25] R. B. Martin, “Deuterated water effects on acid ionization constants,” *Science*, vol. 139, no. 3560, pp. 1198–1203, 1963.
- [26] M. Krumm, E. Zangrando, L. Randaccio, et al., “Mixed platinum(II)-mercury(II) cytosine nucleobase complexes with metal-metal bonds,” *Inorganic Chemistry*, vol. 32, no. 10, pp. 2183–2189, 1993.
- [27] G. Meyer, M. Sehabi, and I. Pantenburg, “Coordinative flexibility of monovalent silver in $[\text{Ag}^+ - \text{L1}]\text{L2}$ complexes,” in *Design and Construction of Coordination Polymers*, M. C. Hong and L. Chen, Eds., pp. 1–23, John Wiley & Sons, New York, NY, USA, 2009.
- [28] A. J. Blake, N. R. Champness, P. Hubberstey, W.-S. Li, M. A. Withersby, and M. Schröder, “Inorganic crystal engineering using self-assembly of tailored building-blocks,” *Coordination Chemistry Reviews*, vol. 183, no. 1, pp. 117–138, 1999.
- [29] J. A. R. Navarro, M. B. L. Janik, E. Freisinger, and B. Lippert, “[$(\text{Ethylenediamine})\text{Pt}(\text{uracilate})_4$], a metal analogue of calix[4]arene. Coordination and anion host-guest chemistry related to its conformational dynamics,” *Inorganic Chemistry*, vol. 38, pp. 426–432, 1999.

Research Article

Synthesis and Characterization of Novel Ruthenium(III) Complexes with Histamine

Jakob Kljun,¹ Saša Petriček,¹ Dušan Žigon,² Rosana Hudej,^{1,3}
Damijan Miklavčič,³ and Iztok Turel¹

¹ Faculty of Chemistry and Chemical Technology, University of Ljubljana, Aškerčeva 5, 1000 Ljubljana, Slovenia

² Department of Environmental Sciences, Jožef Stefan Institute, Jamova c. 39, 1000 Ljubljana, Slovenia

³ Faculty of Electrical Engineering, University of Ljubljana, Tržaška 25, 1000 Ljubljana, Slovenia

Correspondence should be addressed to Iztok Turel, iztok.turel@fkk.uni-lj.si

Received 30 December 2009; Accepted 9 March 2010

Academic Editor: Spyros Perlepes

Copyright © 2010 Jakob Kljun et al. This is an open access article distributed under the Creative Commons Attribution License, which permits unrestricted use, distribution, and reproduction in any medium, provided the original work is properly cited.

Novel ruthenium(III) complexes with histamine [RuCl₄(dmsO-S)(histamineH)]·H₂O (**1a**) and [RuCl₄(dmsO-S)(histamineH)] (**1b**) have been prepared and characterized by X-ray structure analysis. Their crystal structures are similar and show a protonated amino group on the side chain of the ligand which is not very common for a simple heterocyclic derivative such as histamine. Biological assays to test the cytotoxicity of the compound **1b** combined with electroporation were performed to determine its potential for future medical applications in cancer treatment.

1. Introduction

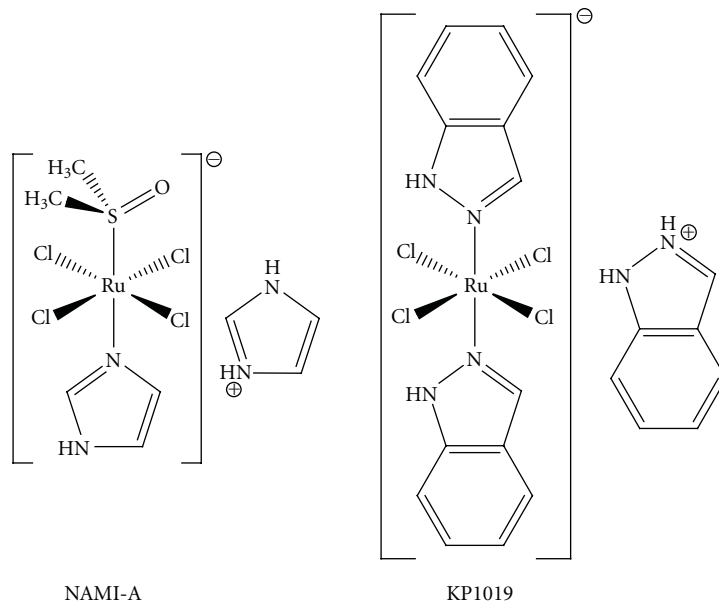
Before the discovery of cisplatin and its successful use as an anticancer agent in the 70s, metal complexes were rarely considered useful for medical applications. Afterwards, new cisplatin analogues (carboplatin, oxaliplatin) were developed and introduced into clinical use [1–3]. The development of platinum-drug resistance in cancer patients, the general toxicity and severe side effects of platinum drugs however required a different approach in the research of anticancer metal complexes [2].

Complexes of different metals were prepared and tested. Two ruthenium compounds, NAMI-A and KP1019 [4–6], are currently among the most successful candidates to enter the clinical practice. These two ruthenium(III) complexes have an octahedral geometry and contain four in-plane chlorido ligands as well as one dimethylsulfoxido and one imidazole (NAMI-A) or two indazole ligands (KP1019) in trans positions. The aforementioned compounds are the chosen representatives of two larger classes of compounds bearing nitrogen-bound aromatic heterocycles developed by the Alessio and Keppler research groups, respectively [4, 7, 8].

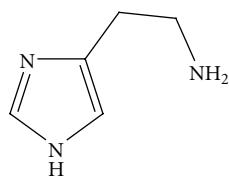
Histamine (4-(2-Aminoethyl)-1H-imidazole, see Scheme 2) is a molecule that performs various functions in the body, the most important being the gastric acid secretion and the triggering of the symptoms of an allergic reaction such as vasodilatation, bronchoconstriction, bronchial muscle contraction, pain, and itching.

Most of the metal complexes in use in current cancer treatment have an intracellular target and the plasma membrane can represent a considerable barrier. Electroporation or electropermeabilization is a process where exposing cells to specific electrical pulses results in temporary formation of hydrophilic pores in the cell membrane. Thus temporally increased cell permeability enables extracellular molecules with otherwise hampered transmembrane transport to enter the cells. Electroporation is used in a variety of biotechnological and medical applications. It has been proven that combining electroporation with chemotherapy potentiates the cytotoxicity of drugs when the drugs' efficacy is limited by its uptake in the cell [9–13].

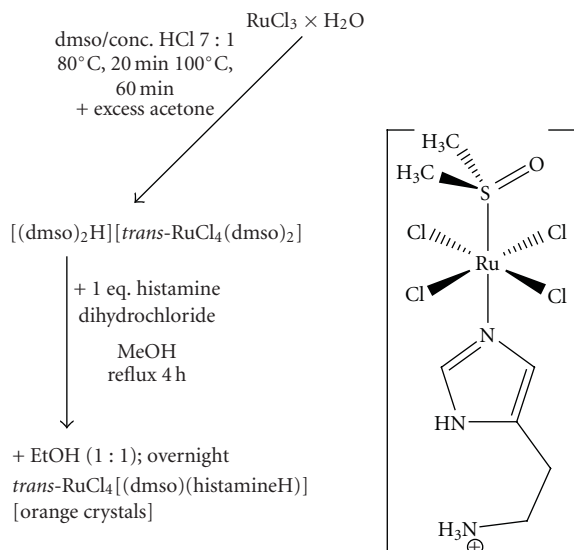
The aim of this study was to prepare and characterize new ruthenium NAMI-type compounds, to test their *in vitro* cytotoxicity and study the influence of electroporation on the cytotoxic activity of the synthesized compounds.



SCHEME 1: NAMI-A and KP1019.



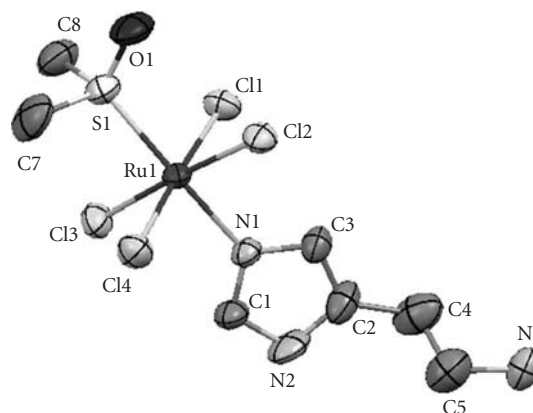
SCHEME 2: Histamine.



SCHEME 3: Two step synthesis and structure of the novel ruthenium complex with histamine.

2. Experimental

2.1. Materials and Instruments. Ruthenium(III) chloride hydrate, histamine dihydrochloride, and the solvents

FIGURE 1: Asymmetric unit of the crystal structure of complex **1b**. The ellipsoids are shown at 50% probability.

(dimethylsulfoxide, concentrated hydrochloric acid, methanol, ethanol, and acetone) were purchased by Sigma-Aldrich and used without further purification.

2.1.1. Infrared Spectroscopy. Infrared spectra (ATR) were recorded on a Perkin-Elmer Spectrum 100 spectrometer. The measurements were made in the range from 4000 to 600 cm^{-1} .

2.1.2. Electrospray Ionization Mass Spectrometry. Mass measurements were run on a hybrid quadrupole time of flight mass spectrometer Q-ToF Premier (Waters Micromass, Manchester, UK), equipped with an orthogonal Z-spray electrospray (ESI) interface.

Water sample solution was introduced directly through syringe pump at a flow rate 5 $\mu\text{L}/\text{min}$. Compressed nitrogen

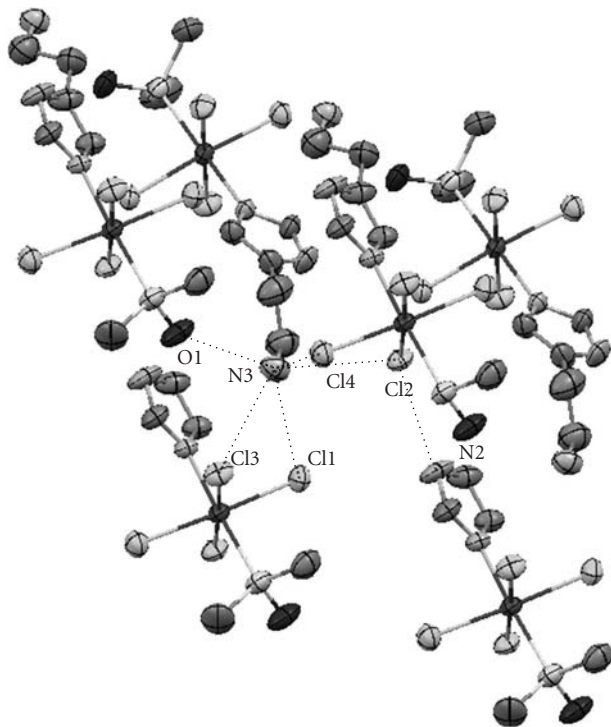


FIGURE 2: The hydrogen bonds in the crystal structure of compound **1b**. The ammonioethyl groups of the lower two asymmetric units are omitted for clarity.

(99.999%, Messer Slovenia) was used as both the drying and the nebulizing gas. The nebulizer gas flow rate was set to approximately 20 L/h and the desolvation gas flow rate to 600 L/h. A cone voltage of 30 V and a capillary voltage of 2.9 kV were used in positive ion mode. The desolvation temperature was set to 150 °C and the source temperature to 100 °C. The mass resolution of approximately 9500 fwhm was used for determination of elemental composition with TOF mass spectrometer. MS and MS/MS spectra were acquired in centroid mode over an m/z range of 50–1000 in scan time 1 s and inter scan time 0.1 s. The detector potential was set to 1850 V. Reproducible and accurate mass measurements at approximate 10000 mass resolution were obtained using an electrospray dual sprayer with leucine enkephalin ($[MH]^+ = 556.2771$) as a reference compound, introduced into the mass spectrometer alternating with a sample solution.

The data station operating software was Mass Lynx v. 4.1 (Micromass, Manchester).

Interpretation of peaks in mass spectra and identification of particular fragment ions were confirmed with elemental composition mass measurements of these ions at high resolution.

2.1.3. CHN Elemental Analysis. Elemental analyses were performed on a Perkin-Elmer Elemental analyzer 2400 CHN.

2.1.4. X-Ray Structure Analysis. X-ray diffraction data were collected on a Nonius Kappa CCD diffractometer at 150 K for compound **1a** and at room temperature for compound

1b using graphite monochromated Mo- K_α radiation and processed using DENZO [14] program. The structures were solved using SIR92 [15]. A full-matrix least-squares refinement on F magnitudes with anisotropic displacement factors for all nonhydrogen atoms using SHELXL [16] was employed. The drawings were prepared with the Mercury program [17]. Hydrogen atoms were placed in geometrically calculated positions and were refined using a riding model.

The crystallographic data for compounds **1a** and **1b** have been deposited with the CCDC as supplementary material with the deposition numbers CCDC 759890 and 759818, respectively (see Supplementary Material available online at doi:10.1155/2010/183097).

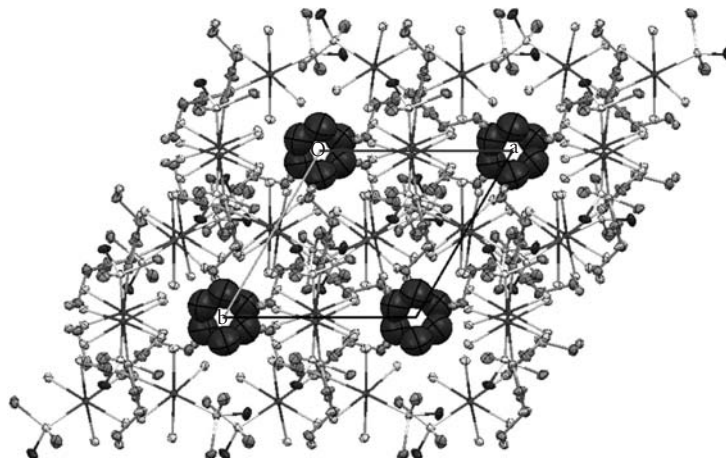
2.2. Syntheses. Syntheses of $[RuCl_4(dms\text{-}S)(\text{histamine-H})] \cdot H_2O$ (**1a**) and $[RuCl_4(dms\text{-}S)(\text{histamineH})]$ (**1b**): the synthesis of compounds **1a** and **1b** consists of two steps (see Scheme 3). The first step is the preparation of a ruthenium precursor **P1** ($dms\text{-}S$)[*trans*- $RuCl_4(dms\text{-}S)_2$]. This compound was prepared according to the literature [18]. 200 mg of **P1** and 70 mg of histamine dihydrochloride were dissolved in 15 mL of methanol and refluxed for 4 hours. After a slow evaporation of the solvent, only a few red crystals of **1a** were obtained. The X-ray structure analysis showed the presence of a solvate water in a molecule. Despite considerable effort, we were not able to obtain such crystals again. Crystals of compound **1b** were later obtained by adding 15 mL of ethanol to the reaction mixture and the solution was left to stand in an open flask. Overnight snowflake-like crystalline orange solid formed. The crystals were washed with cold acetone and diethylether and dried at 50 °C for 30 minutes. Similar crystals although of lower quality were obtained by addition of isopropanol, n-pentanol or ethyl acetate, instead of ethanol, to the reaction mixture.

IR (ATR): 3226 (sh), 3115 (s), 2923 (w), 1597 (w), 1578 (w), 1504 (sh), 1480 (m), 1402 (m), 1231 (w), 1111 (sh), 1082 (s), 1016 (s), 968 (s), 934 (s), 928 (sh), 840 (s), 684 (w), 658 (m) cm^{-1} .

CHN (only **1b**): Calc. C 19,41%, H 3,72%, N 9,70%; Found: C 19,78%, H 3,67%, N 9,49%.

ESI-MS (in H_2O solution): m/z 361, 325, 299, 264.

2.3. Biological Activity Assays. Murine melanoma cell line B16F1 (European Collection of Cell Cultures, UK) was tested *in vitro* to determine cytotoxic effect of compound **1b** in combination with or without electroporation. B16F1 cell suspension ($22 \cdot 10^6$ cells/mL) was prepared in low conductive electroporation buffer (10 mM (Na_2HPO_4/NaH_2PO_4 , pH 7.4) with 1 mM $MgCl_2$ and 250 mM sucrose). Different concentrations of compound **1b** were added to cell suspension to reach final concentrations of 0.01, 0.1, and 1 mM. Immediately after incubation (<0.5 min), a drop of cell suspension was placed between two flat parallel stainless-steel electrodes 2 mm apart and a train of electric pulses (8 pulses, 800 V/cm, 100 μs , 1 Hz) was applied with an electroporator Cliniporator (Igea, Carpi, Italy). The same procedure without electric pulses was used for cells exposed to different concentrations of **1b** without electroporation.

FIGURE 3: The packing in the crystal structure of compound **1a** along the *z* axis.TABLE 1: Crystal data and structure refinement for compounds **1a** and **1b**.

	Compound 1a	Compound 1b
Empirical formula	C ₇ H ₁₆ Cl ₄ N ₃ O ₂ RuS	C ₇ H ₁₆ Cl ₄ N ₃ ORuS
Formula weight	449.16 g/mol	433.16 g/mol
Temperature	150(2) K	293(2) K
Wavelength	0.71073 Å	0.71073 Å
Crystal system	Triclinic	Monoclinic
Space group	<i>P</i> 31 2 1	<i>C</i> 2/ <i>c</i>
Unit cell dimensions	<i>a</i> = 8.233 Å <i>b</i> = 8.233 Å <i>c</i> = 38.9269(3) Å α = 90° β = 90° γ = 120°	<i>a</i> = 14.4860(8) Å <i>b</i> = 7.8741(3) Å <i>c</i> = 27.3464(15) Å α = 90° β = 91.457(2)° γ = 90°
Volume	2284.943(18) Å ³	3118.2(3) Å ³
<i>Z</i>	6	8
Density (calculated)	1.959 g/cm ³	1.845 g/cm ³
Absorption coefficient	1.864 mm ⁻¹	1.813 mm ⁻¹
<i>F</i> (000)	1338	1720
Crystal size	0.1 × 0.1 × 0.1 mm	0.08 × 0.05 × 0.05 mm
Theta range for data collection	3.26 to 28.71°	3.22 to 27.49°
Reflections collected	7263	5747
Independent reflections	3830 [<i>R</i> (int) = 0.0166]	3501 [<i>R</i> (int) = 0.0290]
Refinement method	Full-matrix least-squares on <i>F</i> ²	Full-matrix least-squares on <i>F</i> ²
Data/restraints/parameters	3830/0/166	3501/0/172
Goodness-of-fit on <i>F</i> ²	1.068	1.080
Final <i>R</i> indices [<i>I</i> > 2 sigma(<i>I</i>)]	<i>R</i> ₁ ^a = 0.0236, <i>wR</i> ₂ ^b = 0.0571	<i>R</i> ₁ = 0.0500, <i>wR</i> ₂ = 0.1120
<i>R</i> indices (all data)	<i>R</i> ₁ = 0.0261, <i>wR</i> ₂ = 0.0583	<i>R</i> ₁ = 0.0761, <i>wR</i> ₂ = 0.1229
Largest diff. peak and hole	1.229 and -0.686 e·Å ⁻³	1.098 and -0.560 e·Å ⁻³

$$^a R_1 = \sum(|F_o| - |F_c|) / \sum |F_o|; \quad ^b wR_2 = \{[\sum(w(F_o^2 - F_c^2)^2) / \sum wF_o^2]\}^{1/2}$$

In addition, we tested cytotoxic effect of **1b** after prolonged incubation time (60 min, without electroporation). Cell viability was measured 72 h after treatment using the MTS-based Cell Titer 96 AQ_{ueous} One Solution Cell Proliferation Assay (Promega, Madison, WI, USA). Absorption at 490 nm

wavelength (*A*₄₉₀) was measured with a spectrophotometer Tecan infinite M200 (Tecan, Switzerland). Cell viability (C.V.) of treated cells (tr) was calculated using the formula: C.V. = (*A*₄₉₀)_{tr} / (*A*₄₉₀)_c × 100[%], taking the cell viability of the control I as 100%. Statistical analysis was performed

using One-Way ANOVA test and SigmaStat statistical software (SPSS, Chicago, USA).

3. Results and Discussion

3.1. Synthesis and Crystal Structure. Several complexes of the NAMI and KP families bearing nitrogen-bound simple heterocycles or smaller biologically active molecules were already synthesized and investigated for biological applications [4, 7, 19, 20]. Most of the NAMI analogues were synthesized by mixing a suspension of **P1** in acetone and adding the equivalent amount of the ligand and then recrystallizing the product either from hot acetone or other solvents. In our case this synthetic route was not appropriate due to the low solubility of compound **1b** in acetone or other solvents except in water and methanol. The reaction was thus performed in methanol and another less volatile and less polar solvent was added later. Similar crystals although of lower quality were obtained by addition of isopropanol, n-pentanol, or ethyl acetate instead of ethanol to the reaction mixture. The crystals were cut and were suitable for X-ray structure analysis. The experimental data is shown in Table 1.

The asymmetric unit of compound **1b** is shown in Figure 1. Selected bond lengths and hydrogen bond short contact distances are presented in Tables 2 and 3, respectively.

The crystal structure of compounds **1a** and **1b** does not differ significantly from the other NAMI-type compounds. Compounds **1a** and **1b** have a distorted octahedral geometry with four in-plane chloride anions surrounding the Ru(III) ion in addition to a sulfur atom from an S-bonded dimethylsulfoxide molecule and a nitrogen atom from the histamine molecule in axial positions. The main difference to most of the NAMI-type compounds which are anionic complexes is the protonated amino group on the side chain of the histamine moiety (hence histamineH is used in the formula) that gives compounds **1a** and **1b** a neutral charge. This structural feature is however more common in NAMI-type compounds with a purine derivative as the nitrogen ligand [21]. The hydrogen atoms on the amino group (H3A, H3B and H3C) form hydrogen bonds with the four chloride atoms and the dmsu oxygen. The Cl2 chloride atom forms an additional hydrogen bond with the hydrogen on the imidazole moiety (H2) which results in a slightly longer Ru-Cl2 distance (see Tables 2 and 3 and Figures 1 and 2). Compound **1a** exhibits an additional hydrogen bond between the water molecule and one of the chloride anions. It was not possible to locate the positions of two hydrogen atoms bonded to oxygen in a water molecule of the complex **1a** by difference Fourier maps.

Another interesting feature of the crystal structure of compound **1a** is the formation of channels along z axis where the water molecules are located (see Figure 3).

3.2. Electrospray Ionization Mass Spectrometry. Compound **1b** was also characterized by electrospray ionization mass spectrometry. The peaks in the mass spectrum and their

TABLE 2: Selected bond lengths in compounds **1a**, **1b** and NAMI [22](Na[RuCl₄(S-dmsu)(imidazole)]).

	1a	1b	NAMI
Ru-Cl ₁	2.355 (2)	2.359 (2)	2.3403 (9)
Ru-Cl ₂	2.364 (2)	2.364 (2)	2.3227 (8)
Ru-Cl ₃	2.356 (2)	2.343 (2)	2.3588 (9)
Ru-Cl ₄	2.358 (2)	2.356 (2)	2.3447 (8)
Ru-S	2.300 (2)	2.298 (2)	2.2956 (6)
Ru-N	2.096 (2)	2.097 (2)	2.081 (2)

TABLE 3: Selected hydrogen bond short contact distances in compound **1b**.

D-H...A	D-A (Å)	angle DHA (°)
N ₂ -H ₂ ...Cl ₂	3.218 (6)	151
N ₃ -H _{3A} ...Cl ₂	3.331 (6)	138
N ₃ -H _{3A} ...Cl ₄	3.306 (6)	140
N ₃ -H _{3B} ...Cl ₁	3.308 (6)	149
N ₃ -H _{3B} ...Cl ₃	3.349 (6)	131
N ₃ -H _{3C} ...O ₁	2.889 (6)	172

TABLE 4: Main peaks in the ESI-MS spectrum of compound **1b** and respective assignments.

m/z	fragment
264	RuCl(histamine)(OH)
299	RuCl ₂ (histamine)(OH)
325	RuCl(dmsu)(histamine)
361	RuCl ₂ (dmsu)(histamine)

respective assignments are presented in Table 4. The data confirm a partial hydrolysis of the compound in water solution. Such behavior is usual for the NAMI-type compounds which undergo a rather quick dissociation of two of the chloride ligands and/or the dmsu molecule [23].

3.3. Biological Activity. Previous studies have shown that while NAMI-A is inactive against B16F1 cells *in vitro*, it shows remarkable activity at relatively low concentrations when combined with electroporation [24]. On the other hand compound **1b** shows no activity at any of the tested concentrations (up to 1 mM) either by itself or in combination with electroporation.

As Dyson and Sava suggest [25], the cytotoxicity of a compound as one of the main criteria in the preliminary screenings when looking for a potential drug candidate should be considered with some caution. NAMI-A for example, showed remarkable antimetastatic properties despite very low cytotoxicity. Further investigations of the biological activity of the histaminic analogue and the study of the interactions with different proteins are being planned.

Acknowledgments

Financial support from the Slovenian Research Agency (ARRS) through projects P1-0175, P2-0249, and J1-0200-0103-008 is gratefully acknowledged. This work was performed within the framework of COST Action D39. Jakob Kljun is grateful to ARRS for funding through a junior researcher grant. Jakob Kljun would also like to thank Marta Kasunič for her aid and advice on crystal structure solving.

References

- [1] E. Wiltshaw, "Cisplatin in the treatment of cancer: the first metal anti-tumour drug," *Platinum Metals Review*, vol. 23, no. 3, pp. 90–98, 1979.
- [2] L. Kelland, "The resurgence of platinum-based cancer chemotherapy," *Nature Reviews Cancer*, vol. 7, no. 8, pp. 573–584, 2007.
- [3] T. W. Hambley, "Developing new metal-based therapeutics: challenges and opportunities," *Dalton Transactions*, no. 43, pp. 4929–4937, 2007.
- [4] E. Alessio, G. Mestroni, A. Bergamo, and G. Sava, "Ruthenium antimetastatic agents," *Current Topics in Medicinal Chemistry*, vol. 4, no. 15, pp. 1525–1535, 2004.
- [5] C. G. Hartinger, S. Zorbas-Seifried, M. A. Jakupec, B. Kynast, H. Zorbas, and B. K. Keppler, "From bench to bedside—preclinical and early clinical development of the anticancer agent indazolium *trans*-[tetrachlorobis(1*H*-indazole)ruthenate(III)] (KP1019 or FFC14A)," *Journal of Inorganic Biochemistry*, vol. 100, no. 5–6, pp. 891–904, 2006.
- [6] C. G. Hartinger, M. A. Jakupec, S. Zorbas-Seifried, et al., "KP1019, a new redox-active anticancer agent—preclinical development and results of a clinical phase I study in tumor patients," *Chemistry and Biodiversity*, vol. 5, no. 10, pp. 2140–2155, 2008.
- [7] E. Reisner, V. B. Arion, A. Eichinger, et al., "Tuning of redox properties for the design of ruthenium anticancer drugs—part 2: syntheses, crystal structures, and electrochemistry of potentially antitumor $[\text{Ru}^{\text{III}}\text{Cl}_{6-n}(\text{Azole})_n]^{2-}$ ($n = 3, 4, 6$) complexes," *Inorganic Chemistry*, vol. 44, no. 19, pp. 6704–6716, 2005.
- [8] I. Bratsos, S. Jedner, T. Gianferrara, and E. Alessio, "Ruthenium anticancer compounds: challenges and expectations," *Chimia*, vol. 61, no. 11, pp. 692–697, 2007.
- [9] E. H. Serpersu, K. Kinoshita Jr., and T. Y. Tsong, "Reversible and irreversible modification of erythrocyte membrane permeability by electric field," *Biochimica et Biophysica Acta*, vol. 812, no. 3, pp. 779–785, 1985.
- [10] J. Teissie, M. Golzio, and M. P. Rols, "Mechanisms of cell membrane electropermeabilization: a minireview of our present (lack of?) knowledge," *Biochimica et Biophysica Acta*, vol. 1724, no. 3, pp. 270–280, 2005.
- [11] M. Pavlin and D. Miklavčič, "Theoretical and experimental analysis of conductivity, ion diffusion and molecular transport during cell electroporation—relation between short-lived and long-lived pores," *Bioelectrochemistry*, vol. 74, no. 1, pp. 38–46, 2008.
- [12] S. Orłowski, J. Belehradek Jr., C. Paoletti, and L. M. Mir, "Transient electroporation of cells in culture: increase of the cytotoxicity of anticancer drugs," *Biochemical Pharmacology*, vol. 37, no. 24, pp. 4727–4733, 1988.
- [13] G. Serša, M. Čemažar, and D. Miklavčič, "Antitumor effectiveness of electrochemotherapy with *cis*-diamminedichloroplatinum(II) in mice," *Cancer Research*, vol. 55, no. 15, pp. 3450–3455, 1995.
- [14] Z. Otwinowski and W. Minor, "Processing of X-ray diffraction data collected in oscillation mode," *Methods in Enzymology*, vol. 276, pp. 307–326, 1997.
- [15] A. Altomare, M. C. Burla, M. Camalli, et al., "SIR97: a new tool for crystal structure determination and refinement," *Journal of Applied Crystallography*, vol. 32, no. 1, pp. 115–119, 1999.
- [16] G. M. Sheldrick, "A short history of SHELX," *Acta Crystallographica Section A*, vol. 64, no. 1, pp. 112–122, 2008.
- [17] C. F. Macrae, P. R. Edgington, P. McCabe, et al., "Mercury: visualization and analysis of crystal structures," *Journal of Applied Crystallography*, vol. 39, no. 3, pp. 453–457, 2006.
- [18] E. Alessio, G. Balducci, M. Calligaris, G. Costa, W. M. Attia, and G. Mestroni, "Synthesis, molecular structure, and chemical behavior of hydrogen *trans*-bis(dimethyl sulfoxide)tetrachlororuthenate(III) and *mer*-trichlorotris(dimethyl sulfoxide)ruthenium(III): the first fully characterized chloride-dimethyl sulfoxide-ruthenium(III) complexes," *Inorganic Chemistry*, vol. 30, no. 4, pp. 609–618, 1991.
- [19] D. Griffith, S. Cecco, E. Zangrando, A. Bergamo, G. Sava, and C. J. Marmion, "Ruthenium(III) dimethyl sulfoxide pyridine-hydroxamic acid complexes as potential antimetastatic agents: synthesis, characterisation and *in vitro* pharmacological evaluation," *Journal of Biological Inorganic Chemistry*, vol. 13, no. 4, pp. 511–520, 2008.
- [20] I. Turel, M. Pečanac, A. Golobič, et al., "Solution, solid state and biological characterization of ruthenium(III)-DMSO complexes with purine base derivatives," *Journal of Inorganic Biochemistry*, vol. 98, no. 2, pp. 393–401, 2004.
- [21] A. García-Raso, J. J. Fiol, A. Tasada, et al., "Ruthenium complexes with purine derivatives: syntheses, structural characterization and preliminary studies with plasmidic DNA," *Inorganic Chemistry Communication*, vol. 8, no. 9, pp. 800–804, 2005.
- [22] E. Alessio, G. Balducci, A. Lutman, G. Mestroni, M. Calligaris, and W. M. Attia, "Synthesis and characterization of two new classes of ruthenium(III)-sulfoxide complexes with nitrogen donor ligands (L): $\text{Na}[\text{trans-RuCl}_4(\text{R}_2\text{SO})(\text{L})]$ and *mer*, *cis*- $\text{RuCl}_3(\text{R}_2\text{SO})(\text{R}_2\text{SO})(\text{L})$. The crystal structure of $\text{Na}[\text{trans-RuCl}_4(\text{DMSO})(\text{NH}_3)] \cdot 2\text{DMSO}$, $\text{Na}[\text{trans-RuCl}_4(\text{DMSO})(\text{Im})] \cdot \text{H}_2\text{O}$, $\text{Me}_2\text{CO}(\text{Im} = \text{imidazole})$ and *mer*, *cis*- $\text{RuCl}_3(\text{DMSO})(\text{DMSO})(\text{NH}_3)$," *Inorganica Chimica Acta*, vol. 203, no. 2, pp. 205–217, 1993.
- [23] G. Mestroni, E. Alessio, G. Sava, S. Pacor, M. Coluccia, and A. Boccarelli, "Water-soluble ruthenium(III)-dimethyl sulfoxide complexes: chemical behaviour and pharmaceutical properties," *Metal-Based Drugs*, vol. 1, no. 1, pp. 41–63, 1993.
- [24] A. Bicek, I. Turel, M. Kanduser, and D. Miklavčič, "Combined therapy of the antimetastatic compound NAMI-A and electroporation on B16F1 tumour cells *in vitro*," *Bioelectrochemistry*, vol. 71, no. 2, pp. 113–117, 2007.
- [25] P. J. Dyson and G. Sava, "Metal-based antitumour drugs in the post genomic era," *Dalton Transactions*, no. 16, pp. 1929–1933, 2006.

Research Article

Synthesis and Structural Characterization of a Metal Cluster and a Coordination Polymer Based on the $[\text{Mn}_6(\mu_4\text{-O})_2]^{10+}$ Unit

Eleni E. Moushi, Anastasios J. Tasiopoulos, and Manolis J. Manos

Department of Chemistry, University of Cyprus, 1678 Nicosia, Cyprus

Correspondence should be addressed to Manolis J. Manos, emmanouil.manos@ucy.ac.cy

Received 24 February 2010; Accepted 9 March 2010

Academic Editor: Spyros Perlepes

Copyright © 2010 Eleni E. Moushi et al. This is an open access article distributed under the Creative Commons Attribution License, which permits unrestricted use, distribution, and reproduction in any medium, provided the original work is properly cited.

A new 1-D coordination polymer $\{[\text{Mn}_6\text{O}_2(\text{O}_2\text{CMe})_{10}(\text{H}_2\text{O})_4] \cdot 2.5\text{H}_2\text{O}\}_\infty (1 \cdot 2.5\text{H}_2\text{O})_\infty$ and the cluster $[\text{Mn}_6\text{O}_2(\text{O}_2(\text{O}_2\text{CPh})_{10}(\text{py})_2(\text{MeCN})(\text{H}_2\text{O})) \cdot 2\text{MeCN} (2 \cdot 2\text{MeCN})$ are reported. Both compounds were synthesized by room temperature reactions of $[\text{Mn}_3(\mu_3\text{-O})(\text{O}_2\text{CR})_6(\text{L})_2(\text{L}')]$ (R = Me, L = L' = py, $(1 \cdot 2.5\text{H}_2\text{O})_\infty$; R = Ph, L = py, L' = H₂O, $2 \cdot 2\text{MeCN}$) in the presence of 3-hydroxymethylpyridine (3hmpH) in acetonitrile. The structures of these complexes are based on hexanuclear mixed-valent manganese carboxylate clusters containing the $[\text{Mn}_4^{\text{II}}\text{Mn}_2^{\text{III}}(\mu_4\text{-O})_2]^{10+}$ structural core. $(1 \cdot 2.5\text{H}_2\text{O})_\infty$ consists of zigzag chain polymers constructed from $[\text{Mn}_6\text{O}_2(\text{O}_2\text{CMe})_{10}(\text{H}_2\text{O})_4]$ repeating units linked through acetate ligands, whereas $2 \cdot 2\text{MeCN}$ comprises a discrete Mn₆-benzoate cluster.

1. Introduction

The synthesis of Mn clusters has attracted significant interest due to their relevance to many areas including molecular magnetism, catalysis, and bioinorganic chemistry [1, 2]. In the bioinorganic area, extensive work has been carried out to model the structure and catalytic activity of a tetranuclear Mn cluster, which is present in the water oxidizing centre (WOC) of Photosystem II [3–7]. As a result, a number of oligonuclear high oxidation state Mn-carboxylate clusters have been prepared [3, 5], some of which have been studied for their ability to oxidize H₂O to molecular O₂ [3, 6, 7]. Furthermore, considerable effort has been expended in order to prepare structural and reactivity models of other Mn-containing enzymes, such as Mn catalases. These studies have resulted in a number of oligonuclear Mn complexes with oxo/alkoxo/hydroxo or carboxylate bridges, some of which have proven to be very efficient catalytic scavengers of H₂O₂ [8]. The synthesis of oligonuclear Mn model compounds often involves preformed Mn carboxylate clusters and coordination polymers as starting materials, with the most popular ones being complexes based on the $[\text{Mn}_3\text{O}]^{6+/7+}$ and the $[\text{Mn}_6\text{O}_2]^{10+}$ units [3, 9–11]. Since the

various characteristics of the starting materials including their structural core, carboxylate bridges, and terminal ligation have a significant influence on the identity of the reaction product, there is always a need for new additions in the list of known metal precursor compounds.

Herein, we report the syntheses and the crystal structures of the 1D coordination polymer $\{[\text{Mn}_6\text{O}_2(\text{O}_2\text{CMe})_{10}(\text{H}_2\text{O})_4] \cdot 2.5\text{H}_2\text{O}\}_\infty (1 \cdot 2.5\text{H}_2\text{O})_\infty$ and the discrete cluster $[\text{Mn}_6\text{O}_2(\text{O}_2\text{CPh})_{10}(\text{py})_2(\text{MeCN})(\text{H}_2\text{O})] \cdot 2\text{MeCN} (2 \cdot 2\text{MeCN})$, which both contain the $[\text{Mn}_4^{\text{II}}\text{Mn}_2^{\text{III}}(\mu_4\text{-O})_2]^{10+}$ structural core. Compound $2 \cdot 2\text{MeCN}$ is a new addition in the family of structurally-characterized Mn₆-benzoate clusters [12, 13], whereas $(1 \cdot 2.5\text{H}_2\text{O})_\infty$ represents one of the few coordination polymers based on hexanuclear Mn clusters [14–17].

2. Experimental

2.1. Materials. All manipulations were performed under aerobic conditions using materials (reagent grade) and solvents as received; water was distilled in-house. $[\text{Mn}_3\text{O}(\text{O}_2\text{CMe})_6(\text{py})_3] \cdot \text{py}$ and $[\text{Mn}_3\text{O}(\text{O}_2\text{CPh})_6(\text{py})_2(\text{H}_2\text{O})] \cdot 0.5\text{CH}_3\text{CN}$ were prepared as described elsewhere [18].

2.2. Compound Preparation. $\{[\text{Mn}_6\text{O}_2(\text{O}_2\text{CMe})_{10} \cdot (\text{H}_2\text{O})_4] \cdot 2.5\text{H}_2\text{O}\}_\infty$ ($1 \cdot 2.5\text{H}_2\text{O}$) $_\infty$: $[\text{Mn}_3\text{O}(\text{O}_2\text{CMe})_6(\text{py})_3] \cdot \text{py}$ (0.2 g, 0.24 mmol) was dissolved in MeCN (10 mL), and then 3 hmpH (0.05 g, 0.46 mmol) was added to the dark brown solution. The resulting red-brown solution was left under magnetic stirring for ~ 50 minutes, filtered off, and the filtrate was left undisturbed at room temperature. After a few weeks, brown crystals of $(1 \cdot 2.5\text{H}_2\text{O})_\infty$ suitable for X-ray crystallography were formed. The crystals were collected by filtration, washed with MeCN (10 mL), and Et_2O (2×10 mL) and dried *in vacuo*. The yield was $\sim 27\%$ based on total Mn content. *Anal. Calc.* for $\text{C}_{20}\text{H}_{43}\text{Mn}_6\text{O}_{28.5}(1 \cdot 2.5\text{H}_2\text{O})_\infty$: C, 22.47; H, 4.05. Found: C 22.29; H 4.25%. IR data (KBr pellet, cm^{-1}): $\tilde{\nu} = 3404$ (m,br), 1582 (s), 1421 (s), 1371 (w), 1028 (m), 667 (s), 619 (s).

$[\text{Mn}_6\text{O}_2(\text{O}_2\text{CPh})_{10}(\text{py})_2(\text{MeCN})(\text{H}_2\text{O})] \cdot 2\text{MeCN}$ ($2 \cdot 2\text{MeCN}$): $[\text{Mn}_3\text{O}(\text{O}_2\text{CPh})_6(\text{py})_2(\text{H}_2\text{O})] \cdot 0.5\text{CH}_3\text{CN}$ (0.27 g, 0.24 mmol) was dissolved in MeCN (10 mL) and then, 3 hmpH (0.05 g, 0.46 mmol) was added to the dark brown solution. The resulting red-brown solution was left under magnetic stirring for ~ 45 minutes, filtered off and the filtrate was left undisturbed at room temperature. After a few weeks, brown crystals of $(2 \cdot 2\text{MeCN})$ suitable for X-ray crystallography were formed. The crystals were collected by filtration, washed with MeCN (10 mL) and Et_2O (2×10 mL) and dried *in vacuo*. The yield was $\sim 20\%$ based on total Mn content. *Anal. Calc.* for $\text{C}_{86}\text{H}_{71}\text{Mn}_6\text{N}_5\text{O}_{23}(2 \cdot 2\text{MeCN})$: C, 55.17; H, 3.82; N, 3.74. Found: C 54.98; H 3.91; N, 3.53%. IR data (KBr pellet, cm^{-1}): $\tilde{\nu} = 3398$ (m,br), 1607 (s), 1570 (s), 1430 (s) 720 (s), 691 (m), 676 (m), 614 (m).

2.3. X-Ray Crystallography. Data were collected on an Oxford-Diffraction Xcalibur diffractometer, equipped with a CCD area detector and a graphite monochromator utilizing Mo-K α radiation ($\lambda = 0.71073$ Å). Suitable crystals were attached to glass fibers using paratone-N oil and transferred to a goniostat where they were cooled for data collection. Unit cell dimensions were determined and refined by using 4714 ($3.14 \leq \theta \leq 30.42^\circ$) and 23078 ($3.07 \leq \theta \leq 31.25^\circ$) reflections for $(1 \cdot 2.5\text{H}_2\text{O})_\infty$ and $2 \cdot 2\text{MeCN}$, respectively. Empirical absorption corrections (multiscan based on symmetry-related measurements) were applied using CrysAlis RED software [19]. The structures were solved by direct methods using SIR92 [20] and refined on F^2 using full-matrix least squares with SHELXL97 [21]. Software packages used: CrysAlis CCD [19] for data collection, CrysAlis RED [19] for cell refinement and data reduction, WINGX for geometric calculations [22], and DIAMOND [23] and MERCURY [24] for molecular graphics. The non-H atoms were treated anisotropically, whereas the aromatic and methyl-hydrogen atoms were placed in calculated, ideal positions and refined as riding on their respective carbon atoms. The H atoms of water molecules could not be located. Unit cell data and structure refinement details are listed in Table 1.

2.4. Physical Measurements. Elemental analyses (C, H, N) were performed by the in-house facilities of the University of Cyprus, Chemistry Department. IR spectra were recorded

TABLE 1: Crystallographic data for complexes $(1 \cdot 2.5\text{H}_2\text{O})_\infty$ and $(2 \cdot 2\text{MeCN})$.

	1	2
Formula ^a	$\text{C}_{40}\text{H}_{86}\text{Mn}_{12}\text{O}_{57}$	$\text{C}_{86}\text{H}_{71}\text{Mn}_6\text{N}_5\text{O}_{23}$
M_w	2138.33	1872.13
Crystal System	Orthorhombic	Triclinic
Space group	P b c a	P $\bar{1}$
$a/\text{Å}$	13.615(2)	14.4690(8)
$b/\text{Å}$	21.274(3)	15.8172(7)
$c/\text{Å}$	30.459(4)	18.636(2)
$\alpha/^\circ$	90	83.861(4)
$\beta/^\circ$	90	86.750(4)
$\gamma/^\circ$	90	83.463(4)
$V/\text{Å}^3$	8822(2)	4208.8(4)
Z	4	2
T/K	100(2)	100(2)
λ^b , Å	0.71073	0.71073
D_c , g/cm^{-3} ^a	1.610	1.477
$\mu(\text{Mo-K}\alpha)/\text{mm}^{-1}$	1.750	0.950
Reflections collected/unique(R_{int})	38727/7727(0.1214)	46797/11574(0.0493)
Obs. refl. [$I > 2\sigma(I)$].	3263	8550
$R1\%$ ^c	0.0474	0.0656
$wR2^d$	0.0931	0.1608
Goodness of fit on F^2	0.807	0.974
$\Delta\rho$ max/min/ $e \text{ Å}^{-3}$	0.891/−0.409	1.434/−1.333

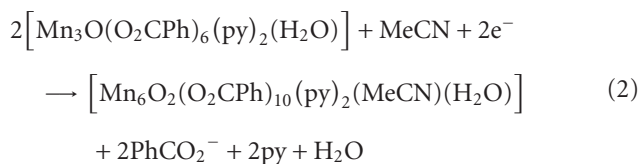
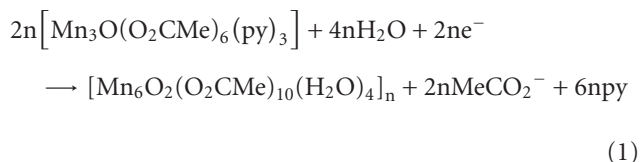
^aIncluding solvent molecules and all hydrogen atoms (even the H atoms of H_2O). ^bGraphite monochromator. ^c $R1 = \Sigma|F_o| - |F_c|/\Sigma|F_o|$. ^d $wR2 = [\Sigma[w(F_o^2 - F_c^2)^2]/\Sigma[wF_o^2]^2]^{1/2}$, $w = 1/[\sigma^2(F_o^2) + (m \cdot p)^2 + n \cdot p]$, $p = [\max(F_o^2, 0) + 2F_c^2]/3$, and m and n are constants.

on KBr pellets in the 4000–400 cm^{-1} range using a Shimadzu Prestige-21 spectrometer.

3. Results and Discussion

3.1. Syntheses. The goal of the described research is the synthesis of multidimensional coordination polymers composed of polynuclear Mn carboxylate clusters with the use of hydroxymethyl-pyridine derivatives [e.g., 4-hydroxymethyl-pyridine (4hmpH), 3-hydroxymethyl-pyridine (3hmpH)] as bridging ligands. The initial result from these investigations was a new hexanuclear Mn complex $[\text{Mn}_6\text{O}_2(\text{O}_2\text{CPh})_{10}(4\text{hmpH})_3(\text{MeCN})]$, which contains the $[\text{Mn}_6\text{O}_2]^{10+}$ structural core and terminal 4 hmpH ligands [12]. This compound was prepared from a reaction of $[\text{Mn}(\text{O}_2\text{CPh})_2] \cdot 2\text{H}_2\text{O}$ with 4hmpH in MeCN. Various modifications of this reaction system that were performed involved the use of preformed Mn clusters as precursor compounds together with 3hmpH. Thus, the reaction of $[\text{Mn}_3(\mu_3\text{-O})(\text{O}_2\text{CR})_6(\text{L})_2(\text{L}')]$ ($\text{R} = \text{Me}$, $\text{L} = \text{L}' = \text{py}$, $(1 \cdot 2.5\text{H}_2\text{O})_\infty$; $\text{R} = \text{Ph}$, $\text{L} = \text{py}$, $\text{L}' = \text{H}_2\text{O}$, $2 \cdot 2\text{MeCN}$) with 3hmpH in acetonitrile resulted in the isolation of compounds $(1 \cdot 2.5\text{H}_2\text{O})_\infty$ and $2 \cdot 2\text{MeCN}$, which however

did not contain the 3hmpH ligands. The formation of $(\mathbf{1})_\infty$ and $\mathbf{2}$ is summarized in equations 1 and 2, respectively:



As it will be discussed in detail below, the structures of $(\mathbf{1}\cdot 2.5\text{H}_2\text{O})_\infty$ and $\mathbf{2}\cdot 2\text{MeCN}$ are very similar with one major difference between them being the fact that $(\mathbf{1}\cdot 2.5\text{H}_2\text{O})_\infty$ is a coordination polymer, whereas $\mathbf{2}\cdot 2\text{MeCN}$ is a discrete metal cluster. A possible explanation for this is that the bulky PhCO_2^- groups that are present in $\mathbf{2}\cdot 2\text{MeCN}$ prevent the polymerization of the Mn_6 clusters, whereas in $(\mathbf{1}\cdot 2.5\text{H}_2\text{O})_\infty$ there are only acetate ligands that are more flexible and thus can easily bridge Mn_6 units leading to a polymeric species. We also note that the average oxidation state of the final products (2.33) of the two reactions is lower than that of the starting materials (2.66). Such a reduction could be explained assuming that a disproportionation reaction of the Mn_3 starting materials takes place upon their dissolution in MeCN in the presence of 3hmpH. Then, the reduced species are aggregated to form $(\mathbf{1}\cdot 2.5\text{H}_2\text{O})_\infty$ or $\mathbf{2}\cdot 2\text{MeCN}$ and the products with Mn ions in higher oxidation states remain in the solution. Similar reactions as those leading to the isolation of $(\mathbf{1}\cdot 2.5\text{H}_2\text{O})_\infty$ or $\mathbf{2}\cdot 2\text{MeCN}$ were performed using 4hmpH or pyridine instead of 3hmpH in the reaction mixtures. These reactions resulted in the isolation of microcrystalline products that have not been completely characterized so far, but seem to be different than compounds $(\mathbf{1}\cdot 2.5\text{H}_2\text{O})_\infty$ and $\mathbf{2}\cdot 2\text{MeCN}$ (by comparisons of infrared spectra). Reactions were also carried out by us in the past, where no other reagent (e.g., pyridine or triethylamine) was used besides the $[\text{Mn}_3\text{O}(\text{O}_2\text{CMe})_6(\text{py})_3]$ precursor compound and the solvent. In that case, an 1D coordination polymer based on Mn_3 -carboxylate cluster linked by Mn^{2+} ions was isolated [25]. Therefore, 3hmpH seems to play an important role in the formation of compounds $(\mathbf{1}\cdot 2.5\text{H}_2\text{O})_\infty$ and $\mathbf{2}\cdot 2\text{MeCN}$, since different compounds are isolated in the absence of 3hmpH. However, the exact role of 3hmpH in the assembly of these compounds is yet unidentified.

3.2. Crystal Structures. The structure of the repeating unit of $(\mathbf{1}\cdot 2.5\text{H}_2\text{O})_\infty$ is very similar to that of compound $\mathbf{2}\cdot 2\text{MeCN}$ (with the main differences between the two compounds being the terminal ligation and the type of carboxylate ligands) and thus, only the first one will be discussed in detail. Selected interatomic distances for $(\mathbf{1}\cdot 2.5\text{H}_2\text{O})_\infty$ and $\mathbf{2}\cdot 2\text{MeCN}$ are given in Tables 2 and 3, respectively.

Compound $(\mathbf{1}\cdot 2.5\text{H}_2\text{O})_\infty$ crystallizes in the orthorhombic space group *Pbca*. Its repeating unit comprises the

TABLE 2: Selected interatomic distances (Å) for complex $(\mathbf{1}\cdot 2.5\text{H}_2\text{O})_\infty$.

Bond distances (Å)			
Mn1···Mn2	3.138(2)	Mn3–O26	2.186(4)
Mn2···Mn6	2.798(2)	Mn3–O24	2.195(4)
Mn2···Mn5	3.164(2)	Mn3–O12	2.201(4)
Mn3···Mn6	3.131(2)	Mn4–O19	2.138(5)
Mn4···Mn6	3.187(2)	Mn4–O22	2.160(5)
Mn1–O7	2.130(5)	Mn4–O6	2.173(5)
Mn1–O24	2.162(4)	Mn4–O9	2.191(5)
Mn1–O3	2.164(5)	Mn4–O25	2.240(4)
Mn1–O21	2.172(4)	Mn4–O8	2.313(5)
Mn1–O1	2.176(4)	Mn5–O20	2.125(5)
Mn1–O5	2.293(5)	Mn5–O11	2.142(5)
Mn2–O25	1.883(4)	Mn5–O18	2.193(5)
Mn2–O24	1.891(4)	Mn5–O14	2.193(4)
Mn2–O4	1.943(4)	Mn5–O23	2.207(4)
Mn2–O17	1.962(5)	Mn5–O25	2.265(4)
Mn2–O5	2.229(4)	Mn6–O24	1.892(4)
Mn2–O14	2.257(4)	Mn6–O25	1.894(5)
Mn3–O2	2.143(4)	Mn6–O10	1.931(4)
Mn3–O15	2.155(5)	Mn6–O16	1.973(5)
Mn3–O13	2.163(5)	Mn6–O8	2.202(4)
		Mn6–O12	2.232(4)

TABLE 3: Selected interatomic distances (Å) for complex $(\mathbf{2}\cdot 2\text{MeCN})$.

Bond Distances (Å)			
Mn1···Mn2	3.133(2)	Mn3–O22	2.206(3)
Mn2···Mn6	2.8134(9)	Mn3–N1	2.263(4)
Mn2···Mn5	3.130(2)	Mn3–O12	2.317(3)
Mn3···Mn6	3.162(2)	Mn4–O6	2.124(3)
Mn4···Mn6	3.167(2)	Mn4–O20	2.131(3)
Mn1–O1	2.121(3)	Mn4–O9	2.154(3)
Mn1–O7	2.121(3)	Mn4–O23	2.186(3)
Mn1–O3	2.145(3)	Mn4–N2	2.287(4)
Mn1–O22	2.190(3)	Mn4–O8	2.302(3)
Mn1–N3	2.250(5)	Mn5–O19	2.155(3)
Mn1–O5	2.281(3)	Mn5–O18	2.158(3)
Mn2–O22	1.872(3)	Mn5–O23	2.176(3)
Mn2–O23	1.894(3)	Mn5–O11	2.197(3)
Mn2–O17	1.936(3)	Mn5–O21	2.226(3)
Mn2–O4	1.972(4)	Mn5–O14	2.237(4)
Mn2–O5	2.239(3)	Mn6–O22	1.889(3)
Mn2–O14	2.241(3)	Mn6–O23	1.893(3)
Mn3–O2	2.127(4)	Mn6–O10	1.951(4)
Mn3–O13	2.146(3)	Mn6–O16	1.954(3)
Mn3–O15	2.151(3)	Mn6–O12	2.202(3)
		Mn6–O8	2.232(3)

hexanuclear cluster $[\text{Mn}_6\text{O}_2(\text{O}_2\text{CMe})_{10}(\text{H}_2\text{O})_4]$ (Figure 1) and totally 2.5 H_2O molecules of crystallization. Charge

TABLE 4: Bond valence sum (BVS)^{a,b} calculations for complexes $(1 \cdot 2.5\text{H}_2\text{O})_\infty$ and $2 \cdot 2\text{MeCN}$

	Complex 1			Complex 2		
	Mn ^{II}	Mn ^{III}	Mn ^{IV}	Mn ^{II}	Mn ^{III}	Mn ^{IV}
Mn1	1.96	1.79	1.88	2.03	1.87	1.94
Mn2	3.20	2.92	3.07	3.21	2.94	3.08
Mn3	1.99	1.82	1.91	1.94	1.79	1.85
Mn4	1.86	1.70	1.79	1.96	1.81	1.87
Mn5	1.93	1.76	1.85	1.90	1.74	1.83
Mn6	3.21	2.94	3.09	3.22	2.94	3.09

^aThe bold value is the one closest to the charge for which it was calculated.

^bThe oxidation state is the nearest whole number to the bold value.

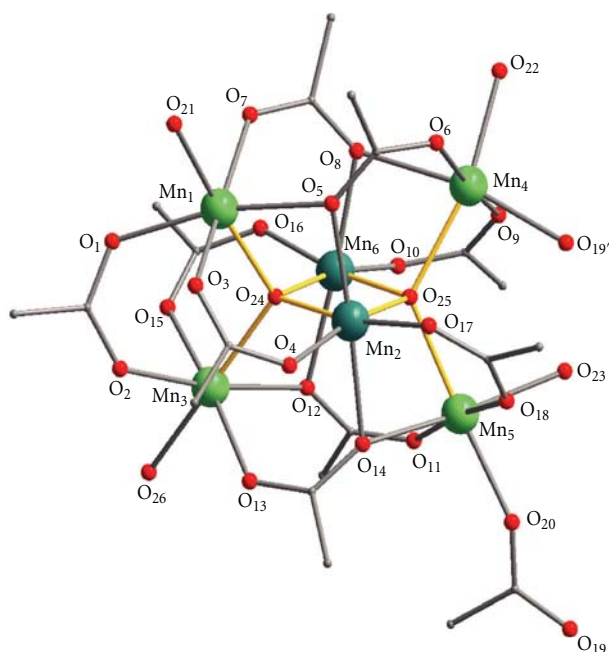


FIGURE 1: A partially labeled plot of the repeating unit of $(1)_\infty$. The yellow lines emphasize the $[\text{Mn}_4^{\text{II}}\text{Mn}_2^{\text{III}}(\mu_4\text{-O})_2]^{10+}$ core. Color code: Mn^{II}, green; Mn^{III}, dark green; O, red; C, grey. H atoms are omitted for clarity.

considerations, bond valence sum calculations (Table 4) and inspection of metric parameters indicate that the cluster is mixed-valent containing four Mn^{II} and two Mn^{III} ions. The $[\text{Mn}_4^{\text{II}}\text{Mn}_2^{\text{III}}(\mu_4\text{-O})_2]^{10+}$ core of **1** has appeared several times in the literature as will be discussed in detail below and can be described as consisting of two edge-sharing $(\mu_4\text{-O})\text{Mn}_4$ tetrahedra. Such units are defined as anti-T1 tetrahedra (T1 is a structural unit having a cation at the center and four anions at the apices of the tetrahedron) [26]. The common edge of the two anti-T1 tetrahedra is formed by the two Mn^{III} ions, whereas the four Mn^{II} ions occupy the corners of the $[\text{Mn}_4^{\text{II}}\text{Mn}_2^{\text{III}}(\mu_4\text{-O})_2]^{10+}$ core. The peripheral ligation of the Mn atoms is completed by 4 terminal H₂O molecules (ligated to the four Mn^{II} atoms) and 10 acetate ligands.

All Mn atoms are in distorted octahedral geometries. Five of the intra-cluster acetate groups are μ_2 with each of their

carboxylate oxygen atoms acting as terminal ligand for a Mn center. Four acetate ligands are coordinated in $\eta^1 : \eta^2 : \mu_3$ fashion. The remaining carboxylate ligand bridges two Mn^{II} atoms (Mn \cdots Mn distance = 4.7914(2) Å) of adjacent Mn₆ clusters, thus resulting in the formation of a zigzag chain structure (Figure 2). The chains are interacting through hydrogen bonds (O \cdots O distances 2.7–2.9 Å) involving the coordinated water molecules and carboxylate O atoms. Thus, a two-dimensional hydrogen-bonded polymer with a 4-connected topology is formed (Figure 3). The hydrogen bonds involving the lattice water molecules cannot be identified with accuracy due to the positional disorder of these molecules and thus, are not discussed here.

A representation of the structure of $2 \cdot 2\text{MeCN}$ is given in Figure 4. The structure of $2 \cdot 2\text{MeCN}$ is very similar to that of $(1 \cdot 2.5\text{H}_2\text{O})_\infty$ with the main differences between them being (i) the type of terminal ligands [4H₂O for $(1 \cdot 2.5\text{H}_2\text{O})_\infty$; 2 py, one MeCN and one H₂O for $2 \cdot 2\text{MeCN}$] (ii) the type of carboxylate groups (acetate for $(1 \cdot 2.5\text{H}_2\text{O})_\infty$; benzoate for $2 \cdot 2\text{MeCN}$) and (iii) their dimensionality [$(1 \cdot 2.5\text{H}_2\text{O})_\infty$ is a coordination polymer, whereas $2 \cdot 2\text{MeCN}$ is a discrete metal cluster]. Regarding point (iii) we note that examination of the packing of $2 \cdot 2\text{MeCN}$ revealed the existence of intermolecular hydrogen bonding interactions (O \cdots O distances 2.792(4) and 2.809(4) Å) involving the terminal H₂O molecule and two O_{benzoate} atoms of two neighboring Mn₆ molecules resulting in the formation of a dimeric $(2 \cdot 2\text{MeCN})_2$ aggregate.

The Mn₆ unit that appears in $(1 \cdot 2.5\text{H}_2\text{O})_\infty$ and $2 \cdot 2\text{MeCN}$, that is, the cluster $[\text{Mn}_6\text{O}_2(\text{O}_2\text{CR})_{10}(\text{L})_2(\text{L}')(\text{L}'')]$ (R = Me, L = L' = L'' = H₂O, **1**; R = Ph, L = py, L' = H₂O, L'' = MeCN, **2**), has a structural motif found in several hexanuclear Mn clusters and coordination polymers [9, 12–16]. For example, we have recently reported the discrete cluster $[\text{Mn}_6\text{O}_2(\text{O}_2\text{CPh})_{10}(4\text{hmpH})_3(\text{MeCN})]$ containing the $[\text{Mn}_4^{\text{II}}\text{Mn}_2^{\text{III}}(\mu_4\text{-O})_2]^{10+}$ core and also three terminal 4hmpH groups linked through their N_{pyridine} atom and a MeCN molecule [12]. In addition, compound $(1 \cdot 2.5\text{H}_2\text{O})_\infty$ is closely related to compound $\{[\text{Mn}_6\text{O}_2(\text{O}_2\text{CEt})_{10}(\text{H}_2\text{O})_4] \cdot 2\text{EtCO}_2\text{H}\}_\infty$ (**3**·2EtCO₂H)_∞, recently published [14]. The main structural differences between them lie in the type of carboxylate ligands in these compounds, being acetate groups in $(1 \cdot 2.5\text{H}_2\text{O})_\infty$ and propionate ligands in $(3 \cdot 2\text{EtCO}_2\text{H})_\infty$ and also in the type of the crystallization solvent molecules. Other related examples to $(1 \cdot 2.5\text{H}_2\text{O})_\infty$ comprise the chain polymers $[\text{Mn}_6\text{O}_2(\text{O}_2\text{CCMe}_3)_{10}(\text{thf})_2(\text{NIT-Me})]$ $[\text{Mn}_6\text{O}_2(\text{O}_2\text{CCMe}_3)_{10}(\text{thf})(\text{CH}_2\text{Cl}_2)(\text{NIT-Me})]$ (thf = tetrahydrofuran, NIT-Me = 4,5-dihydro-1H-imidazolyl-3-oxide-1-oxyl) [15] and $[\text{Mn}_6\text{O}_2(\text{O}_2\text{CCMe}_3)_{10}(\text{HO}_2\text{CCMe}_3)_2(\text{bpy})]$ (bpy = 4,4'-bipyridine) [16].

4. Conclusions

We reported the syntheses and the crystal structures of compounds $(1 \cdot 2.5\text{H}_2\text{O})_\infty$ and $2 \cdot 2\text{MeCN}$, which are based on the well-known $[\text{Mn}_6(\mu_4\text{-O})_2]^{10+}$ structural core. Both compounds were prepared serendipitously in our

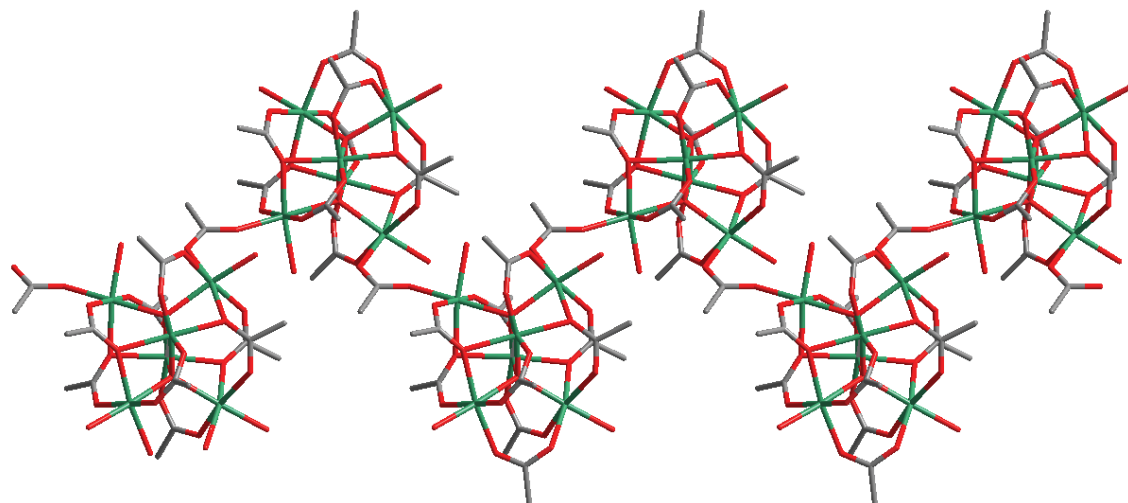


FIGURE 2: Wireframe representation of the zigzag chain of $(1)_{\infty}$ viewed along a -axis. Mn, green; O, red; C, grey. H atoms are omitted for clarity.

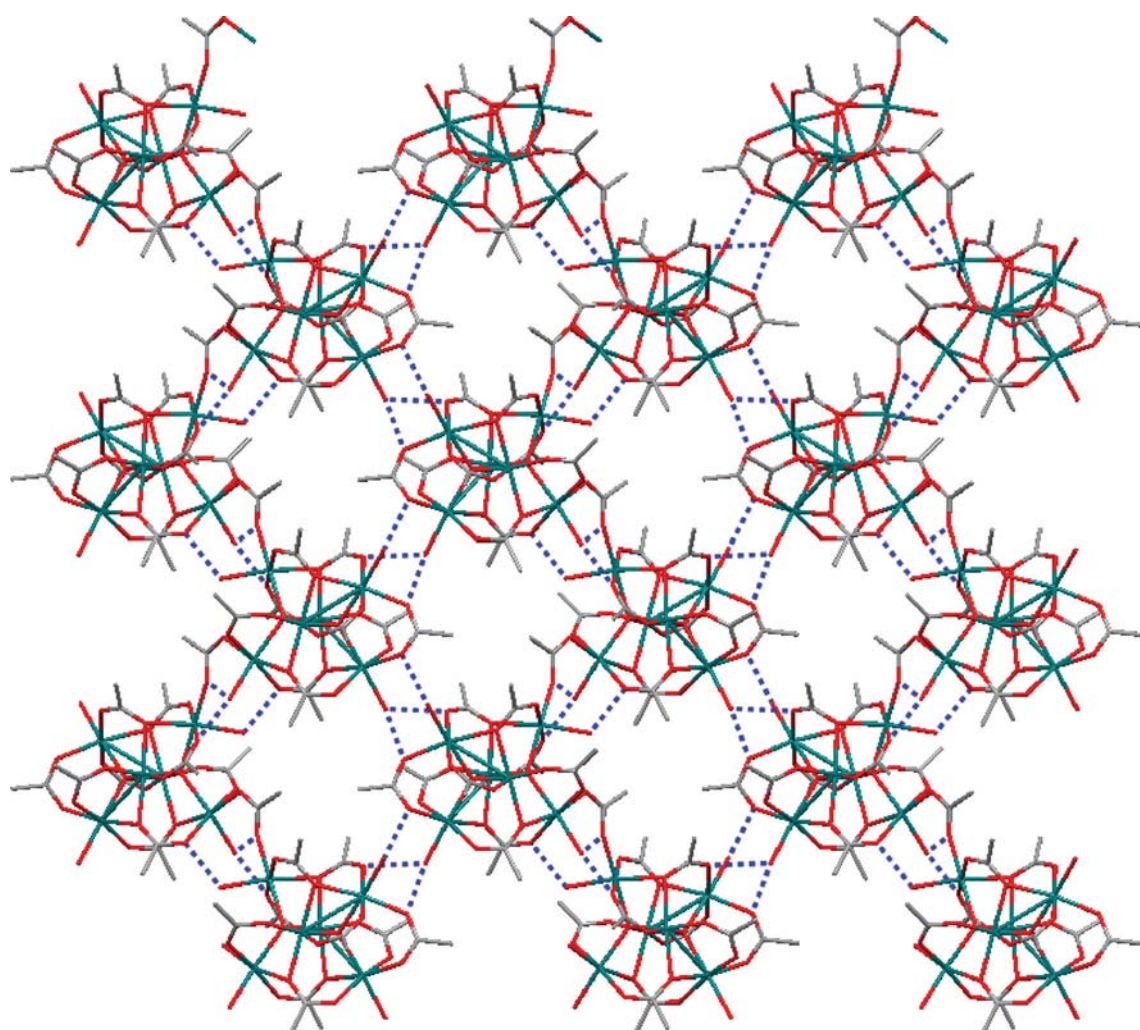


FIGURE 3: Wireframe representation of the layer formed by interchain hydrogen bonds in $(1)_{\infty}$. The hydrogen bonds are shown as dotted blue lines. Mn, green; O, red; C, grey. H atoms are omitted for clarity.

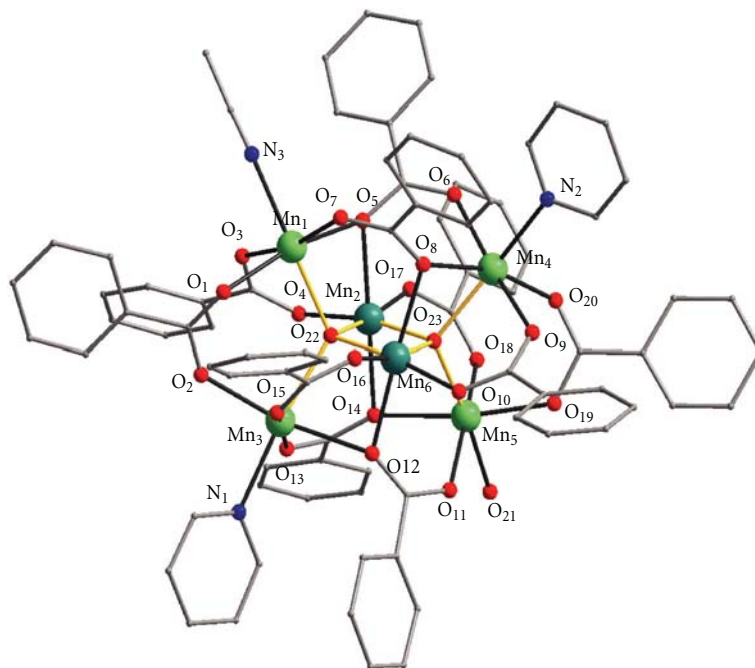


FIGURE 4: A partially labeled plot of **2**. The yellow lines emphasize the $[\text{Mn}_4^{\text{II}}\text{Mn}_2^{\text{III}}(\mu_4\text{-O})_2]^{10+}$ core. Color code: Mn^{II} , green; Mn^{III} , dark green; O, red; N, blue; C, grey. H atoms are omitted for clarity.

attempt to prepare polymeric species consisting of polynuclear Mn clusters linked through 3 hmpH. Compound $(1 \cdot 2.5\text{H}_2\text{O})_\infty$ features a zigzag chain structure formed by $[\text{Mn}_6(\mu_4\text{-O})_2(\text{O}_2\text{CMe})_{10}(\text{H}_2\text{O})_4]$ clusters linked via bridging acetate ligands. This compound joins a family of coordination polymers based on the $[\text{Mn}_6(\mu_4\text{-O})_2]^{10+}$ unit, which numbers only a few members. Furthermore, compound **2**·2MeCN represents a new addition in the growing family of Mn_6 -benzoate clusters. Further work may involve replacement of the terminal solvent molecules in $(1 \cdot 2.5\text{H}_2\text{O})_\infty$ or **2**·2MeCN by various bridging polytopic ligands, in order to isolate higher dimensionality (2D, 3D) polymers. Multidimensional coordination polymers consisting of oligonuclear Mn clusters would be potential candidates for various applications including gas storage and catalysis.

Acknowledgments

The authors thank the Cyprus Research Promotion Foundation (Grant: ΔΙΑΚΤΩΡ/ΔΙΣΕΚ/0308/22), for financial support of this research. Crystallographic data in CIF format have been deposited at the Cambridge Crystallographic Data Centre with CCDC no. 767225 $[(1 \cdot 2.5\text{H}_2\text{O})_\infty]$ and 767226 (**2**·2MeCN). Copies of this information can be obtained free of charge on application to CCDC, 12 Union Road, Cambridge CB2 1EZ, UK (fax: +44-1223-336033; e-mail: deposit@ccdc.cam.ac.uk). This work is dedicated to Professor Nick Hadjiliadis in recognition of his great contribution for the advancement of Bioinorganic and Inorganic Chemistry, both in Greece and internationally, and for his retirement

References

- [1] R. H. Holm, P. Kennepohl, and E. I. Solomon, "Structural and functional aspects of metal sites in biology," *Chemical Reviews*, vol. 96, no. 7, pp. 2239–2314, 1996.
- [2] R. Bagai and G. Christou, "The *Drosophila* of single-molecule magnetism: $[\text{Mn}_{12}\text{O}_{12}(\text{O}_2\text{CR})_{16}(\text{H}_2\text{O})_4]$," *Chemical Society Reviews*, vol. 38, no. 4, pp. 1011–1026, 2009.
- [3] S. Mukhopadhyay, S. K. Mandal, S. Bhaduri, and W. H. Armstrong, "Manganese clusters with relevance to photosystem II," *Chemical Reviews*, vol. 104, no. 9, pp. 3981–4026, 2004.
- [4] J. Barber, "Photosynthetic energy conversion: natural and artificial," *Chemical Society Reviews*, vol. 38, no. 1, pp. 185–196, 2009.
- [5] A. Mishra, W. Wernsdorfer, K. A. Abboud, and G. Christou, "The first high oxidation state manganese-calcium cluster: relevance to the water oxidizing complex of photosynthesis," *Chemical Communications*, no. 1, pp. 54–56, 2005.
- [6] W. Ruttiger and G. C. Dismukes, "Synthetic water-oxidation catalysts for artificial photosynthetic water oxidation," *Chemical Reviews*, vol. 97, no. 1, pp. 1–24, 1997.
- [7] R. Brimblecombe, G. F. Swiegers, G. C. Dismukes, and L. Spiccia, "Sustained water oxidation photocatalysis by a bioinspired manganese cluster," *Angewandte Chemie International Edition*, vol. 47, no. 38, pp. 7335–7338, 2008.
- [8] A. J. Wu, J. E. Penner-Hahn, and V. L. Pecoraro, "Structural, spectroscopic, and reactivity models for the manganese catalases," *Chemical Reviews*, vol. 104, no. 2, pp. 903–938, 2004.
- [9] J. Kim and H. Cho, "Reductive coupling of trinuclear $[\text{Mn}^{\text{II}}\text{Mn}^{\text{III}}_2\text{O}]$ core to form hexanuclear $[\text{Mn}_4^{\text{II}}\text{Mn}_2^{\text{III}}\text{O}_2]$ cluster," *Inorganic Chemistry Communications*, vol. 7, no. 1, pp. 122–124, 2004.
- [10] C. Benelli, M. Murrie, S. Parsons, and R. E. P. Winpenny, "Synthesis, structural and magnetic characterisation of a new

- Mn-Gd pivalate: preparation from a pre-formed hexanuclear cluster," *Dalton Transactions*, no. 23, pp. 4125–4126, 1999.
- [11] R. Manchanda, G. W. Brudvig, and R. H. Crabtree, "High-valent oxomanganese clusters: structural and mechanistic work relevant to the oxygen-evolving center in photosystem II," *Coordination Chemistry Reviews*, vol. 144, pp. 1–38, 1995.
- [12] T. C. Stamatatos, D. Foguet-Albiol, S. P. Perlepes, et al., "4-(hydroxymethyl)pyridine and pyrimidine in manganese benzoate chemistry: preparation and characterization of hexanuclear clusters featuring the $\{\text{Mn}_4^{\text{II}}\text{Mn}_2^{\text{III}}(\mu_4 - \text{O})_2\}^{10+}$ core," *Polyhedron*, vol. 25, no. 8, pp. 1737–1746, 2006.
- [13] A. R. Schake, J. B. Vincent, Q. Li, et al., "Preparation, structure, and magnetochemistry of hexanuclear manganese oxide complexes: chemically and thermally induced aggregation of $\text{Mn}_3\text{O}(\text{O}_2\text{CPh})_6(\text{py})_2(\text{H}_2\text{O})$ forming products containing the $[\text{Mn}_6\text{O}_2]^{10+}$ core," *Inorganic Chemistry*, vol. 28, no. 10, pp. 1915–1923, 1989.
- [14] C.-B. Ma, M.-Q. Hu, H. Chen, C.-N. Chen, and Q.-T. Liu, "Aggregation of hexanuclear, mixed-valence manganese oxide clusters linked by propionato ligands to form a one-dimensional polymer $[\text{Mn}_6\text{O}_2(\text{O}_2\text{Cet})_{10}(\text{H}_2\text{O}_4)]_n$," *European Journal of Inorganic Chemistry*, no. 33, pp. 5274–5280, 2008.
- [15] V. Ovcharenko, E. Fursova, G. Romanenko, and V. Ikorskii, "Synthesis and structure of heterospin compounds based on the $[\text{Mn}_6\text{O}_2\text{piv}_{10}]$ -cluster unit and nitroxide," *Inorganic Chemistry*, vol. 43, no. 11, pp. 3332–3334, 2004.
- [16] K. Nakata, H. Miyasaka, K. Sugimoto, T. Ishii, K.-I. Sugiura, and M. Yamashita, "Construction of a one-dimensional chain composed of Mn_6 clusters and 4,4'-bipyridine linkers: the first step for creation of "nano-dots-wires"," *Chemistry Letters*, no. 7, pp. 658–659, 2002.
- [17] J. W. Choi, J. J. Park, M. Park, D. Y. Moon, and M. S. Lah, "A 2D layered metal-organic framework constructed by using a hexanuclear manganese metallamacrocycle as a supramolecular building block," *European Journal of Inorganic Chemistry*, no. 35, pp. 5465–5470, 2008.
- [18] J. B. Vincent, H.-R. Chang, K. Folting, J. C. Huffman, G. Christou, and D. N. Hendrickson, "Preparation and physical properties of trinuclear oxo-centered manganese complexes of the general formulation $[\text{Mn}_3\text{O}(\text{O}_2\text{CR})_6\text{L}_3]^{0,+}$ (R = Me or Ph; L = a neutral donor group) and the crystal structures of $[\text{Mn}_3\text{O}(\text{O}_2\text{CMe})_6(\text{pyr})_3](\text{pyr})$ and $[\text{Mn}_3\text{O}(\text{O}_2\text{CPh})_6(\text{pyr})_2(\text{H}_2\text{O})] \cdot 0.5\text{MeCN}$," *Journal of the American Chemical Society*, vol. 109, no. 19, pp. 5703–5711, 1987.
- [19] Oxford Diffraction, *CrysAlis CCD and CrysAlis RED, Version 1.171.32.15*, Oxford Diffraction Ltd, Abingdon, Oxford, UK, 2008.
- [20] A. Altomare, G. Cascarano, C. Giacovazzo, et al., "SIR92—a program for automatic solution of crystal structures by direct methods," *Journal of Applied Crystallography*, vol. 27, p. 435, 1994.
- [21] G. M. Sheldrick, *SHELXL97-A Program for the Refinement of Crystal Structure*, University of Göttingen, Göttingen, Germany.
- [22] L. J. Farrugia, "WinGX suite for small-molecule single-crystal crystallography," *Journal of Applied Crystallography*, vol. 32, no. 4, pp. 837–838, 1999.
- [23] K. Brandenburg, *DIAMOND. Version 3.1d*, Crystal Impact GbR, Bonn, Germany, 2006.
- [24] C. F. Macrae, P. R. Edgington, P. McCabe, et al., "Mercury: visualization and analysis of crystal structures," *Journal of Applied Crystallography*, vol. 39, no. 3, pp. 453–457, 2006.
- [25] S. Zartilas, E. E. Moushi, V. Nastopoulos, A. K. Boudalis, and A. J. Tasiopoulos, "Two new coordination polymers containing the triangular $[\text{Mn}_3\text{O}(\text{O}_2\text{CR})_6]^{0/+}$," *Inorganica Chimica Acta*, vol. 361, no. 14–15, pp. 4100–4106, 2008.
- [26] X. Bu, N. Zheng, and P. Feng, "Tetrahedral chalcogenide clusters and open frameworks," *Chemistry: A European Journal*, vol. 10, no. 14, pp. 3356–3362, 2004.

Research Article

pH-Potentiometric Investigation towards Chelating Tendencies of *p*-Hydroquinone and Phenol Iminodiacetate Copper(II) Complexes

Marios Stylianou,¹ Anastasios D. Keramidas,¹ and Chryssoula Drouza²

¹ Department of Chemistry, University of Cyprus, 1678 Nicosia, Cyprus

² Agricultural Production and Biotechnology and Food Science, Cyprus University of Technology, P.O. Box 50329, 3603 Lemesos, Cyprus

Correspondence should be addressed to Chryssoula Drouza, chryssoula.drouza@cut.ac.cy

Received 27 January 2010; Accepted 23 March 2010

Academic Editor: Spyros P. Perlepes

Copyright © 2010 Marios Stylianou et al. This is an open access article distributed under the Creative Commons Attribution License, which permits unrestricted use, distribution, and reproduction in any medium, provided the original work is properly cited.

Copper ions in the active sites of several proteins/enzymes interact with phenols and quinones, and this interaction is associated to the reactivity of the enzymes. In this study the speciation of the Cu^{2+} with iminodiacetic phenolate/hydroquinonate ligands has been examined by pH-potentiometry. The results reveal that the iminodiacetic phenol ligand forms mononuclear complexes with Cu^{2+} at acidic and alkaline pHs, and a binuclear $\text{O}_{\text{phenolate}}$ -bridged complex at pH range from 7 to 8.5. The binucleating hydroquinone ligand forms only 2 : 1 metal to ligand complexes in solution. The pK values of the protonation of the phenolate oxygen of the two ligands are reduced about 2 units after complexation with the metal ion and are close to the pK values for the copper-interacting tyrosine phenol oxygen in copper enzymes.

1. Introduction

Copper ions in the active sites of proteins/enzymes mediate a broad scope of chemical processes including electron transfer, dioxygen uptake, storage, and transport and catalytic conversions [1]. When surveying the known copper enzymes and their functions, it is striking that their reactivity is typically linked to dioxygen or compounds directly synthesized from O_2 -like phenols and quinones [2–7].

For example, copper proteins are involved in reversible dioxygen binding in hemocyanin [8], two-electron reduction to peroxide coupled to oxidation of substrates in amine and galactose oxidases [9], biogenesis of novel metalloenzyme cofactors (e.g., topaquinone in amine oxidases) [10], activation of hydroxylation in tyrosinase [11], and proton pumping in cytochrome c oxidase [12].

Detailed study of the solid and solution chemistry of Cu^{2+} phenolate/hydroquinonate complexes is essential for better understanding of the coordination of the metal ion in the enzymes and the mechanisms of the enzymatic catalysis. Derivatives of phenol or hydroquinone containing nitrogen

[13–22] as donor atoms are the vast majority of the ligands used to model the active site of the copper enzymes. Despite the importance of phenolate/hydroquinonate chelating ligands as models of copper enzymes, ligands with other than nitrogen donor atoms such as aminocarboxylate derivatives of phenols, have been much less studied. These ligands exhibit very attractive features for modelling metal enzymes, such as the highly solubility in aqueous solution, forming stable complexes with metal ions and the similarity of the donor groups to those in biological systems. In addition, the one-electron oxidized *p*-semiquinone radical of the ligand 2,5-bis[N,N-bis(carboxymethyl)aminomethyl] hydroquinone (H_6bicah) has been stabilized in aqueous solution by ligation to metal ions [23] and thus serves as model for the enzymes that operate via a *p*-semiquinone radical, acting in one-electron transfer reactions, including cytochrome c and copper amine oxidases. In previous pH-potentiometric studies [24] of Cu^{2+} with the phenol iminodiacetate ligand HBIDA (Scheme 1) the equilibrium calculations have been performed assuming that all the species of Cu^{2+} with HBIDA in solution at various pHs are mononuclear 1 : 1 and 1 : 2

metal to ligand complexes. A recent detailed crystallographic study [25] of the Cu^{2+} -phenol iminodiacetate H_4cacp , H_4cah and H_6bicah (Scheme 1) complexes isolated at a pH range 2.0–9.0 has shown that binuclear $\text{O}_{\text{phenolate}}$ -bridged Cu^{2+} complexes (Scheme 2) are also present in solution. It is apparent that previous pH-potentiometric studies of these systems should be repeated including also the dinuclear species in the calculations.

Herein, we describe the pH-potentiometric studies of Cu^{2+} with the iminodiacetate phenolate tripod ligands H_4cacp and H_6bicah . In contrast to H_4cacp , H_6bicah exhibits two metal ion binding sites bridged through the hydroquinone moiety. The potentiometric study showed that only the H_4cacp ligand forms in solution $\text{O}_{\text{phenolate}}$ -bridged binuclear complexes, which is also in agreement with the previous crystallographic study [25]. The pK values of the protonation of the phenolate oxygen of the two ligands reduced about 2 units after complexation with the metal ion are close to the pK values for the copper-interacting tyrosine phenol oxygen in copper enzymes, such as glyoxal oxidase [26].

2. Experimental Section

2.1. Materials. Copper(II) acetate monohydrate, *p*-hydroquinone, 4-hydroxybenzoic acid, iminodiacetic acid, paraformaldehyde, potassium chloride, and potassium hydrogen phthalate were obtained from Aldrich. Sodium hydroxide and hydrogen chloride were purchased from Merck. All chemicals were reagent grade and used without further purification.

2.2. Ligand Preparation. The ligands referred to this study 2,5-bis[*N,N'*-bis(carboxymethyl)aminomethyl]-hydroquinone (H_6bicah) and 2-[*N,N'*-bis(carboxymethyl)aminomethyl]-4-carboxyphenol (H_4cacp) were synthesized based on the Mannich type reaction reported in the literature [27, 28]. The synthesis of the organic ligands (Scheme 1) was performed under inert nitrogen atmosphere and their purity was checked and confirmed by means of $^1\text{H-NMR}$ spectroscopy. $^1\text{H-NMR}$ spectra were recorded on a 300.13 MHz Avance Bruker spectrometer.

2.3. Potentiometric Studies and Computational Data Analysis. The potentiometric equilibrium measurements of H_4cacp and H_6bicah ligands in the absence and in the presence of metal ions were carried out with a JENWAY 3020 pH meter fitted with an Ag-AgCl reference electrode in saturated KCl solution. A glass electrode was calibrated as a hydrogen concentration probe by titrating known amounts of HCl with CO_2 -free NaOH solution, and the equivalence point was determined by Gran's method which yields the standard potential E° of the electrode, using the GLEE computational program [29]. The actual concentration of NaOH ($0.157 \text{ mol dm}^{-3}$) was standardized by titration with potassium hydrogen phthalate, and the HCl solution ($0.111 \text{ mol dm}^{-3}$) was standardized by titration of the standard NaOH solution. The temperature was maintained at

298 K and the ionic strength of each experimental sample was adjusted to $0.100 \text{ mol dm}^{-3}$ with the addition of KCl-supporting electrolyte. Typical concentrations of experimental solutions were $5.00 \text{ mmol dm}^{-3}$ in ligand with molar concentration of copper (II) ion half, equivalent, and twice to that of the ligand. Degassed distilled water was used for the preparation of the solutions and the oxygen and carbon dioxide contamination of the reaction mixtures from the atmosphere was avoided by continuous passing of purified nitrogen gas in the reaction cell.

The proton association constants of H_4cacp and H_6bicah ligands and the formation constants of 1:1 ($\text{H}_4\text{cacp}:\text{Cu}^{2+}$) and 1:2 ($\text{H}_6\text{bicah}:2\text{Cu}^{2+}$) metal-ligand systems were obtained using the program TIRMET which is a computational program based on mass-balance and charge-balance equations, written in our laboratory according to the basic principles first reported by Martell and Motekaitis [30, 31]. In this program the input consists of the components and their concentrations, the initial values of the equilibrium constants for each species considered to be present, the potentiometric equilibrium data determined experimentally, and conditions of the potentiometric experimental procedure (E° , $\text{pK}_w = 13.78$ at 298 K, $\gamma = 0.78$). The program sets up simultaneous mass-balance equations for all components at each neutralization value involving the concentration of acid added to the assay and solves for each species present in the pH region 2.00–10.0. Then, equilibrium constants are varied in order to minimize the differences between the calculated and observed values, resulting in the fitting of the calculated results to the experimental curves. The concentration stability constants, $\beta_{pqr} = [\text{M}_p\text{L}_q\text{H}_r]/[\text{M}]^p[\text{L}]^q[\text{H}]^r$, were considered to be estimated according to the model proposed by the computational program PSEQUAD [32]. The species considered present in the assays are those expected to be formed according to established principles of coordination chemistry including the formation of deprotonated and protonated metal chelates, respectively [24, 33–35]. All potentiometric titrations were performed three times for each system (about 100 data points each) in the pH range 2.00–10.0 without significant variation.

3. Results and Discussion

3.1. Ligands. Potentiometric titrations of phenol (H_4cacp) and *p*-hydroquinone (H_6bicah) iminodiacetate derivatives indicate stepwise protonation steps arising from their characteristic functional groups, amine, carboxylates, and phenolate, in the measurable pH range. The protonation constants (overall stability protonation constants $\log \beta$) are listed in Tables 1 and 2, respectively, and their distribution speciation diagrams are illustrated in Figure 1.

The pH-metric titration curve of H_4cacp indicates three major protonation steps due to the phenolate or the benzoic-carboxylate oxygen group, the carboxylate oxygen group, and the amino group with pK_a values 8.47, 4.84, and 2.42, respectively (Table 1). The low pK_a (2.42) value attributed to the amine nitrogen atom demonstrates intramolecular hydrogen bonding between the deprotonated amino group

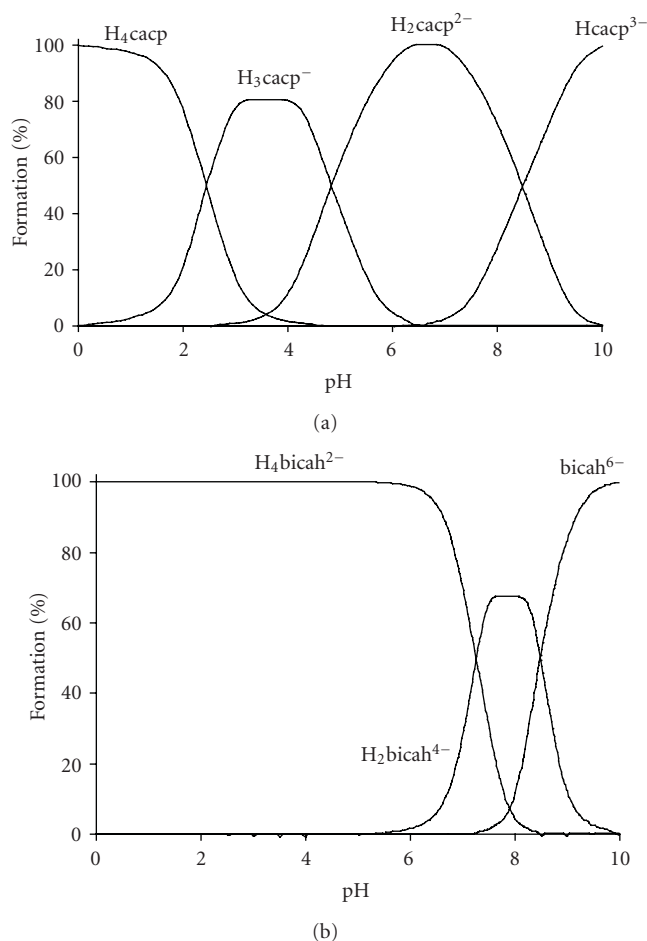


FIGURE 1: Species distribution (% formation) for the phenol (a) and *p*-hydroquinone (b) iminodiacetate ligands as a function of pH over the range 2.00–10.0 at molar concentration 5.00 mol dm^{-3} (25°C , $I = 0.10 \text{ mol dm}^{-3}$ KCl, $\text{p}K_w = 13.78$, and $\gamma = 0.78$).

TABLE 1: Compositions, overall stability formation constants ($\log \beta$), and acidity constants ($\text{p}K_a$) for the species formed in $H_4\text{cacp}$ and $\text{Cu(II)}-H_4\text{cacp}$ system, over the pH range 2.00–10.0 thus obtained from the potentiometric study (25°C , $I = 0.10 \text{ mol dm}^{-3}$ KCl, $\text{p}K_w = 13.78$, and $\gamma = 0.78$).

(p, q, r)	Species	$\log \beta$	$\text{p}K_a$
(0, 1, 1)	$[\text{H}_2\text{cacp}]^{2-}$	8.40 ± 0.01	8.47^a
(0, 1, 2)	$[\text{H}_3\text{cacp}]^-$	13.18 ± 0.04	4.84^b
(0, 1, 3)	$[\text{H}_4\text{cacp}]$	15.56 ± 0.02	2.42^c
(1, 1, -1)	$[\text{Cu}(\text{Hcacp})(\text{OH})]^{2-}$	8.17 ± 0.01	
(2, 2, 0)	$[\text{Cu}_2(\text{Hcacp})_2]^{2-}$	11.26 ± 0.02	
(1, 1, 0)	$[\text{Cu}(\text{Hcacp})(\text{H}_2\text{O})]^-$	14.58 ± 0.02	
(1, 2, 2)	$[\text{Cu}(\text{H}_2\text{cacp})_2]^{2-}$	17.62 ± 0.02	
(1, 1, 1)	$[\text{Cu}(\text{H}_2\text{cacp})(\text{H}_2\text{O})]$	22.94 ± 0.01	

^aPhenolate or aromatic carboxylate oxygen group, ^bcarboxylate oxygen group, ^camine nitrogen group.

and the phenolic hydrogen. Such bonding stabilizes the deprotonated form of the nitrogen and thus facilitates loss of the hydrogen ion as shown by the lower $\text{p}K_a$ value which

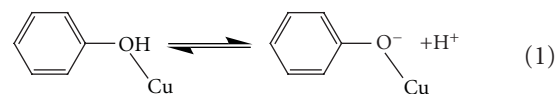
is similar to that found for an analogue ligand [*N*-(*o*-hydroxybenzyl)iminodiacetic acid] [24] (HBIDA, Scheme 1) (2.34) while for the nonphenolic, iminodiacetic acid (ida) the corresponded value is 2.94 [33]

The pH-metric titration of the symmetric bis-substituted iminodiacetate *p*-hydroquinone derivative $H_6\text{bicah}$ gave two steps each one corresponding to two successive protonation of the two phenolate oxygens and the two carboxylate groups with $\text{p}K_a$ values 8.47 and 7.26, respectively (Table 2). It was not possible to determine the $\text{p}K_a$ value for the amine nitrogen group because this value was very low.

3.2. $\text{Cu(II)}-H_4\text{cacp}$. The $\text{Cu(II)}-H_4\text{cacp}$ titration curves were evaluated on the assumption of the formation of various 1:1, 1:2 and 2:1 metal to ligand species with different protonation steps. The extensive crystallographic study of the isolated complexes from solutions of $\text{Cu(II)}-H_4\text{cacp}$ at various pHs reported by Stylianou et al. [25] was also used for the better suggestion of the species in solution (Scheme 2). The best fit with the experimental data (Figure 2(a)) was obtained with the speciation model listed in Table 1. Species distribution curves for the complexes formed in the $\text{Cu(II)}-H_4\text{cacp}$ system as a function of pH are depicted in Figure 3.

Cu(II) ion forms with $H_4\text{cacp}$ three major mononuclear species, the protonated $[\text{Cu}(\text{H}_2\text{cacp})(\text{H}_2\text{O})]$ at pH below 5.0, the deprotonated $[\text{Cu}(\text{Hcacp})(\text{H}_2\text{O})]^-$ at pH between 5.0 and 6.5 the mono-hydroxo species $[\text{Cu}(\text{Hcacp})(\text{OH})]^{2-}$ at pH above 9.0 and a minor 1:2 metal to ligand $[\text{Cu}(\text{H}_2\text{cacp})_2]^{2-}$ species at pH 5.

The process from the deprotonated mononuclear species to the protonated one, which corresponds to the consumption of one H^+ per molecule of complex equation (1), is accompanied by a color change from green to blue attributed to the protonation of the phenolic oxygen. The protonation of the phenolic oxygen will result in weakening or non-bonding of the $\text{Cu}-\text{OH}(\text{phenol})$ bond which is in agreement with the color change (the mononuclear nonphenolic amino acetate complexes of Cu^{2+} at acidic pHs exhibit blue color). The crystallographic data of the complex isolated at pH 3.2 [25] confirm the weak interaction between the protonated phenol oxygen atom and the metal ion [$\text{Cu}-\text{OH}(\text{phenol})$, 2.529(2) Å]:



The estimated $\text{p}K_a$ involved in this protonation step is 5.22 ± 0.02 and is comparable to that calculated by UV-vis spectroscopic studies and was found to be 5.91 ± 0.05 [25]. The overall stability formation constants of complexes $[\text{Cu}(\text{Hcacp})^-]$ and $[\text{Cu}(\text{H}_2\text{cacp})(\text{H}_2\text{O})]$ are greater than those of the iminodiacetate copper (II) complexes $[\text{Cu}(\text{ida})]$ ($\log \beta$ 10.42) and $[\text{Cu}(\text{H})(\text{ida})]$ ($\log \beta$ 12.35) [33]. The higher stability is ascribable to the coordination of the phenolate oxygen atom. This is also supported by the X-ray crystallographic studies which show that the deprotonated form, even at low pHs, strongly interacts with the metal ion. In addition, the planar configuration of the phenyl ring fixes

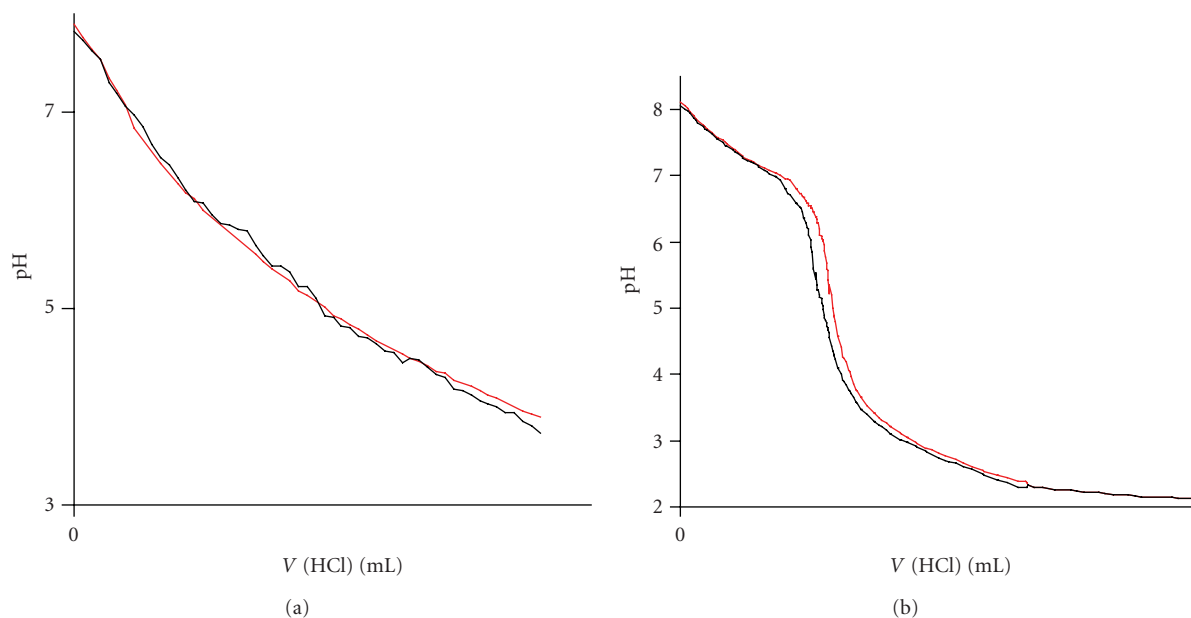


FIGURE 2: Potentiometric titrations for the Cu(II)-H₄cacp (1 : 1) and Cu(II)-H₆bicah (2 : 1) systems (a) and (b), respectively) as a function of pH over the range 2.00–10.0 at molar concentration 2.50 mmol dm⁻³ based on ligand (25°C, *I* = 0.10 mol dm⁻³ KCl, p*K_w* = 13.78, *γ* = 0.78, and HCl = 0.111 mmol dm⁻³). The line denoted with black colour refers to the experimental titration curve while the red refers to the computational fitting of the obtained experimental data.

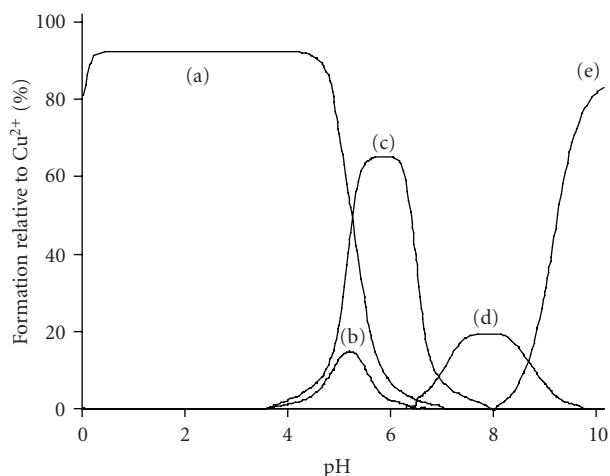


FIGURE 3: Species distribution (% formation relative to Cu²⁺) in the Cu(II)-H₄cacp system at equimolar concentration (5.00 mmol dm⁻³) as a function of pH over the range 2.00–10.0 (25°C, *I* = 0.10 mol dm⁻³ KCl, p*K_w* = 13.78, *γ* = 0.78). The Cu(II) species are as follows: (a) [Cu(H₂cacp)(H₂O)], (b) [Cu(H₂cacp)₂]²⁻, (c) [Cu(Hcacp)(H₂O)]⁻, (d) [Cu₂(Hcacp)₂]²⁻, and (e) [Cu(Hcacp)(OH)]²⁻.

the orientation of the flexible carboxylate groups in positions favorable to chelating, especially in the case of the copper(II) ion which forms stable complexes in an octahedral/or square pyramidal coordination geometry pattern [36].

One very significant result of this potentiometric titration study is the detection of the dimeric species

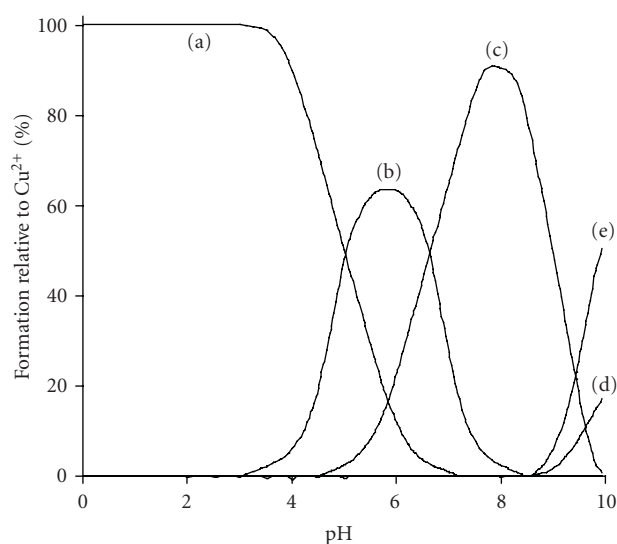
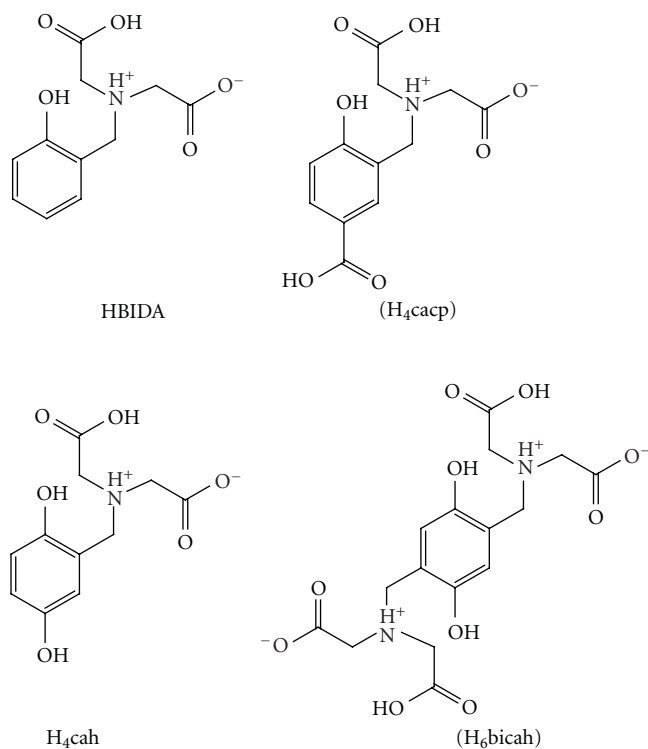
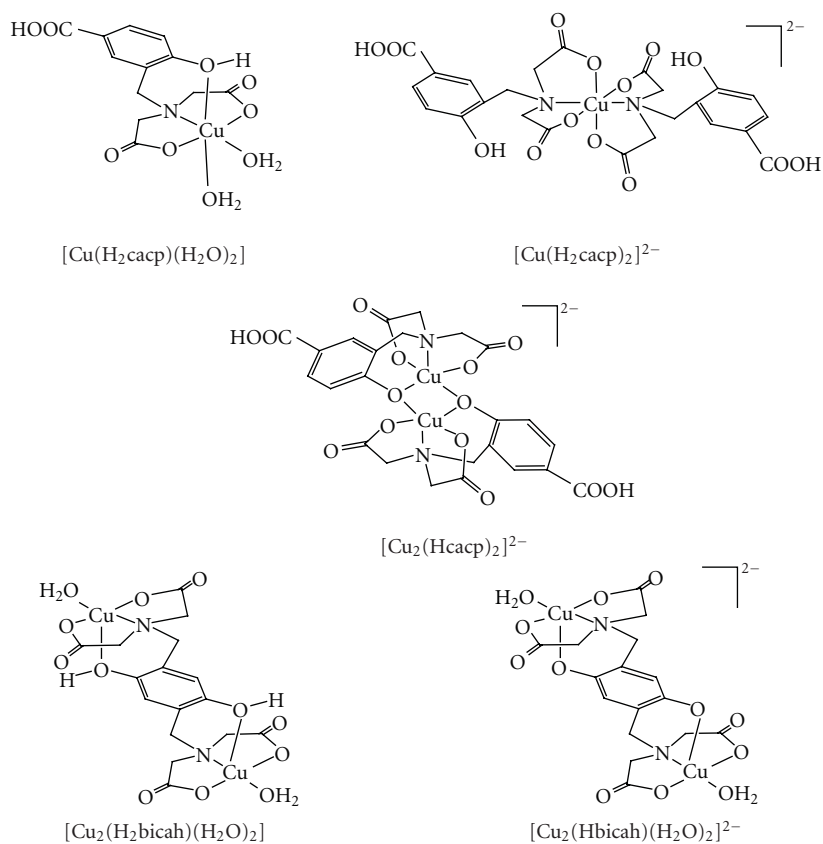


FIGURE 4: Species distribution (% formation relative to Cu²⁺) in the Cu(II)-H₆bicah system with metal-to-ligand molar ratio 1 : 2 concentration (H₆bicah 5.00 mmol dm⁻³) as a function of pH over the range 2.00–10.0 (25°C, *I* = 0.10 mol dm⁻³ KCl, p*K_w* = 13.78, and *γ* = 0.78). The Cu(II) species are as follows: (a) [Cu₂(H₂bicah)(H₂O)₂], (b) [Cu₂(Hbicah)(H₂O)₂]⁻, (c) [Cu₂(bicah)(H₂O)₂]²⁻, (d) [Cu₂(bicah)(OH)(H₂O)]³⁻, and (e) [Cu₂(bicah)(OH)₂]⁴⁻.

[Cu₂(Hcacp)₂]²⁻. Previous potentiometric studies have postulated that the dimeric complexes are not favored in solution because of steric effects and electrostatic destabilization which do not allow a dimerization process [35]. Harris et



SCHEME 1: Iminodiacetic derivatives of phenol/*p*-hydroquinone ligands with their abbreviations. The ligands referred to the potentiometric/stability studies are denoted in parentheses.



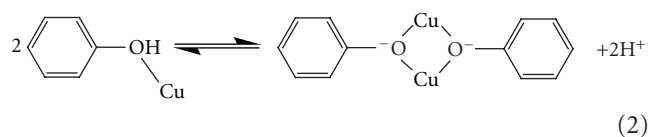
SCHEME 2: Molecular drawings of the structures of the phenol and *p*-hydroquinone iminodiacetate copper(II) complexes, isolated at a pH range 2.0–9.0 according to a recent detailed crystallographic study [25].

TABLE 2: Compositions, overall stability formation constants ($\log \beta$), and acidity constants ($\text{p}K_a$) for the species formed in $H_6\text{bicah}$ and $\text{Cu(II)}-H_6\text{bicah}$ system, over the pH range 2.00–10.0 thus obtained from the potentiometric study (25°C , $I = 0.10 \text{ mol dm}^{-3}$ KCl, $\text{p}K_w = 13.78$, and $\gamma = 0.78$).

(p, q, r)	Species	$\log \beta$	$\text{p}K_a$
(0, 1, 0)	$[\text{H}_2\text{bicah}]^{4-}$	8.41 ± 0.02	8.47^a
(0, 1, 2)	$[\text{H}_4\text{bicah}]^{2-}$	13.40 ± 0.01	7.26^b
(2, 1, -2)	$[\text{Cu}_2(\text{bicah})(\text{OH})_2]^{4-}$	11.57 ± 0.15	
(2, 1, -1)	$[\text{Cu}_2(\text{bicah})(\text{H}_2\text{O})(\text{OH})]^{3-}$	15.72 ± 0.11	
(2, 1, 0)	$[\text{Cu}_2(\text{bicah})(\text{H}_2\text{O})_2]^{2-}$	32.90 ± 0.16	
(2, 1, 1)	$[\text{Cu}_2(\text{Hbicah})(\text{H}_2\text{O})_2]^-$	39.33 ± 0.16	
(2, 1, 2)	$[\text{Cu}_2(\text{H}_2\text{bicah})(\text{H}_2\text{O})_2]$	45.52 ± 0.12	

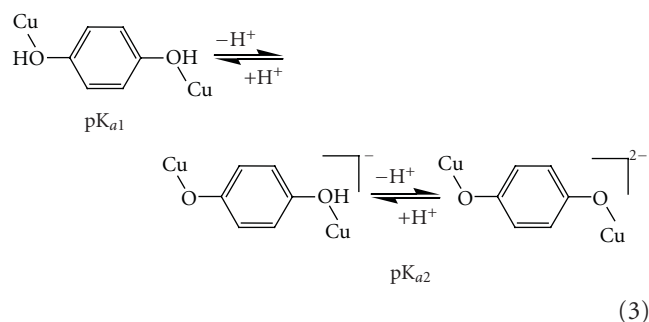
^a Phenolate oxygen group, ^b carboxylate oxygen group.

al. had suggested the formation of a mononuclear phenolate complex of Cu^{2+} and the phenol iminodiacetate ligand HBIDA at pH above 6.0 (Scheme 1), but they have not mentioned the possibility of dimeric binuclear species in solution [24]. However, recently Stylianou et al. [25] have isolated and crystallographically characterized the dimeric species $[\text{Cu}_2(\text{Hcaccp})_2]^{2-}$ from aqueous solution at alkaline pHs 8.0–9.0, indicating that such species are present in solution. In this complex the two Cu^{2+} are bridged through the deprotonated phenolate oxygen (Scheme 2). The speciation diagram of $\text{Cu(II)}-H_4\text{caccp}$ system in Figure 3 shows that $[\text{Cu}_2(\text{Hcaccp})_2]^{2-}$ is the major complex at pH range 7.0–8.5 reaching a maximum of 20% of the total metal ion concentration at pH 8.0 and an overall stability formation constant 11.26 ± 0.02 equation (2).



3.3. $\text{Cu(II)}-H_6\text{bicah}$. The $\text{Cu(II)}-H_6\text{bicah}$ titration curves were evaluated on the assumption of the formation of various 1:1 and 2:1 metal chelates with different protonation steps. The best fit between the simulated curves and the experimental data (Figure 2(b)) was obtained by the speciation model listed in Table 2. Species distribution curves for the complexes formed in the $\text{Cu(II)}-H_6\text{bicah}$ system as a function of pH are depicted in Figure 4. In contrast to $H_4\text{caccp}$, $H_6\text{bicah}$ exhibits two metal binding sites, thus, the ligand may ligate up to two metal ions. The potentiometric study shows that the 1:1 species are unstable and the equilibrium is favoured only to the formation of 2:1 metal to ligand complexes. In addition, the binucleating ligand, $H_6\text{bicah}$, exhibits larger steric hindrance than $H_4\text{caccp}$ and thus does not form $\text{O}_{\text{phenolate}}$ -bridged complexes with Cu^{2+} in solution or in solid state. At pH above 9.5 the di- and mono-hydroxo complexes $[\text{Cu}_2(\text{bicah})(\text{OH})_2]^{4-}$ and $[\text{Cu}_2(\text{bicah})(\text{OH})(\text{H}_2\text{O})]^{3-}$ are the major species with stability formation constants 11.57 ± 0.15 and 15.72 ± 0.11 , respectively. The brown $[\text{Cu}_2(\text{bicah})(\text{H}_2\text{O})_2]^{2-}$ is the major

species between pH 7.0 and 9.5 and the green monoprotonated $[\text{Cu}_2(\text{Hbicah})(\text{H}_2\text{O})_2]^-$ at pH range 5.0 to 7.0. The second phenol is protonated at pH below 5.0 resulting in the formation of the blue neutral $[\text{Cu}_2(\text{H}_2\text{bicah})(\text{H}_2\text{O})_2]$ which has been previously characterized by single crystal X-ray crystallography (Scheme 2) [25]. The two $\text{p}K_a$ values for the two equilibriums of the stepwise protonation of the two phenolate oxygen atoms equation (3) have been calculated as 5.89 ± 0.10 and 6.43 ± 0.10 for $\text{p}K_{a1}$ and $\text{p}K_{a2}$, respectively. These values are close to the values 6.25 ± 0.08 and 7.19 ± 0.08 for $\text{p}K_{a1}$ and $\text{p}K_{a2}$, respectively, found by spectrophotometric studies [25]. These differences are observed because the model used for the calculations in the spectrophotometric studies was incomplete (only the equilibriums in (3) were taken into account):



The fact that there is almost 0.5 pK unit difference between the two deprotonation steps indicates that the electronic interaction between the two metal centres through the hydroquinone bridge is significant.

A comparison between the overall stability constants of the two ligands in this study shows that the bifunctional ligand $H_6\text{bicah}$ forms more stable complexes than $H_4\text{caccp}$ in solution. This extra stabilization is attributed to the larger increase of entropy expected for the formation of the binuclear $\text{Cu}^{2+}-H_6\text{bicah}$ complexes compared to the mononuclear $\text{Cu}^{2+}-H_4\text{caccp}$.

4. Conclusions

The speciation of Cu^{2+} with the iminodiacetic phenol/hydroquinone ligands $H_4\text{caccp}/H_6\text{bicah}$ in aqueous solution was investigated by pH-potentiometry. Ligand $H_4\text{caccp}$, at pH below 5.0 forms with Cu^{2+} the mononuclear 1:1 and 1:2 complexes. At higher pH the phenol proton is deprotonated and at pH range 5.0–7.0 the major species is the mononuclear 1:1 complex. However at pH 7.0–8.0 the formation of a binuclear complex takes place and it is attributed to a $\text{O}_{\text{phenolate}}$ -bridged complex. The binucleating ligand $H_6\text{bicah}$ forms only 2:1 metal to ligand complexes in the pH range 2.0 to 9.0. The major species are the complete phenol protonated complex at pH below 4.5, the monoprotonated at pH range 4.5 to 7.0, and the complete phenol deprotonated species between pHs 7.0 and 9.0. The $H_6\text{bicah}$ did not form binuclear $\text{O}_{\text{phenolate}}$ -bridged complex in solution probably due to steric hindrance originated from the binucleating nature of the ligand. On the other hand, this solution study shows that binuclear $\text{O}_{\text{phenolate}}$ -bridged species

must also be considered in speciation studies of Cu^{2+} ions with mononucleating phenolate ligands such as H_4cacp .

Acknowledgments

The authors thank the Research Promotion Foundation of Cyprus for the financial support of this work with the proposal ANABATHMISH/PAGIO/0308/32. This work dedicated to Professor Nick Hadjiliadis for his retirement.

References

- [1] I. Bento, M. A. Carrondo, and P. F. Lindley, "Reduction of dioxygen by enzymes containing copper," *Journal of Biological Inorganic Chemistry*, vol. 11, no. 5, pp. 539–547, 2006.
- [2] J. L. DuBois and J. P. Klinman, "Mechanism of post-translational quinone formation in copper amine oxidases and its relationship to the catalytic turnover," *Archives of Biochemistry and Biophysics*, vol. 433, no. 1, pp. 255–265, 2005.
- [3] L. Q. Hatcher and K. D. Karlin, "Oxidant types in copper-dioxygen chemistry: the ligand coordination defines the Cu-O₂ structure and subsequent reactivity," *Journal of Biological Inorganic Chemistry*, vol. 9, no. 6, pp. 669–683, 2004.
- [4] M. Mure, "Tyrosine-derived quinone cofactors," *Accounts of Chemical Research*, vol. 37, no. 2, pp. 131–139, 2004.
- [5] S. M. Janes, D. Mu, D. Wemmer, et al., "A new redox cofactor in eukaryotic enzymes: 6-hydroxydopa at the active site of bovine serum amine oxidase," *Science*, vol. 248, no. 4958, pp. 981–987, 1990.
- [6] E. I. Solomon, P. Chen, M. Metz, S.-K. Lee, and A. E. Palmer, "Oxygen binding, activation, and reduction to water by copper proteins," *Angewandte Chemie International Edition*, vol. 40, no. 24, pp. 4570–4590, 2001.
- [7] L. M. Mirica, X. Ottenwaelder, and T. D. P. Stack, "Structure and spectroscopy of copper-dioxygen complexes," *Chemical Reviews*, vol. 104, no. 2, pp. 1013–1045, 2004.
- [8] E. I. Solomon, F. Tuczek, D. E. Root, and C. A. Brown, "Spectroscopy of binuclear dioxygen complexes," *Chemical Reviews*, vol. 94, no. 3, pp. 827–856, 1994.
- [9] J. W. Whittaker, "Free radical catalysis by galactose oxidase," *Chemical Reviews*, vol. 103, no. 6, pp. 2347–2363, 2003.
- [10] J. P. Klinman, "Mechanisms whereby mononuclear copper proteins functionalize organic substrates," *Chemical Reviews*, vol. 96, no. 7, pp. 2541–2561, 1996.
- [11] E. I. Solomon, U. M. Sundaram, and T. E. Machonkin, "Multicopper oxidases and oxygenases," *Chemical Reviews*, vol. 96, no. 7, pp. 2563–2605, 1996.
- [12] G. T. Babcock and M. Wikstrom, "Oxygen activation and the conservation of energy in cell respiration," *Nature*, vol. 356, no. 6367, pp. 301–309, 1992.
- [13] Z. He, S. B. Colbran, and D. C. Craig, "Could redox-switched binding of a redox-active ligand to a copper(II) centre drive a conformational proton pump gate? A synthetic model study," *Chemistry—A European Journal*, vol. 9, no. 1, pp. 116–129, 2003.
- [14] C. L. Foster, X. Liu, C. A. Kilner, M. Thornton-Pett, and M. A. Halcrow, "Complexes of 2-hydroxy-5-methyl-1,4-benzoquinone as models for the 'TPQ-on' form of copper amine oxidases," *Journal of the Chemical Society, Dalton Transactions*, no. 24, pp. 4563–4568, 2000.
- [15] P. Li, N. K. Solanki, H. Ehrncbrg, et al., "Copper(n) complexes of hydroquinone-containing Schiff bases. Towards a structural model for copper amine oxidases," *Journal of the Chemical Society, Dalton Transactions*, no. 10, pp. 1559–1565, 2000.
- [16] J. A. Halfen, B. A. Jazdzewski, S. Mahapatra, et al., "Synthetic models of the inactive copper(II)-tyrosinate and active copper(II)-tyrosyl radical forms of galactose and glyoxal oxidases," *Journal of the American Chemical Society*, vol. 119, no. 35, pp. 8217–8227, 1997.
- [17] D. G. Lonnon, S. T. Lee, and S. B. Colbran, "Valence tautomerism and coordinative lability in copper(II)-imidazolyl-semiquinonate anion radical models for the CuB center in cytochrome c oxidases," *Journal of the American Chemical Society*, vol. 129, no. 18, pp. 5800–5801, 2007.
- [18] F. Michel, F. Thomas, S. Hamman, E. Saint-Aman, C. Bucher, and J.-L. Pierre, "Galactose oxidase models: solution chemistry, and phenoxy radical generation mediated by the copper status," *Chemistry—A European Journal*, vol. 10, no. 17, pp. 4115–4125, 2004.
- [19] K. D. Karlin, M. S. Nasir, B. I. Cohen, R. W. Cruse, S. Kaderli, and A. D. Zuberbühler, "Reversible dioxygen binding and aromatic hydroxylation in O₂-reactions with substituted xylyl dinuclear copper(I) complexes: syntheses and low-temperature kinetic/thermodynamic and spectroscopic investigations of a copper monooxygenase model system," *Journal of the American Chemical Society*, vol. 116, no. 4, pp. 1324–1336, 1994.
- [20] K. Kamaraj, E. Kim, B. Galliker, et al., "Copper(I) and copper(II) complexes possessing cross-linked imidazole-phenol ligands: structures and dioxygen reactivity," *Journal of the American Chemical Society*, vol. 125, no. 20, pp. 6028–6029, 2003.
- [21] R. C. Pratt and T. D. P. Stack, "Mechanistic insights from reactions between copper(II)-phenoxy complexes and substrates with activated C-H bonds," *Inorganic Chemistry*, vol. 44, no. 7, pp. 2367–2375, 2005.
- [22] B. A. Barry and O. Einarsdottir, "Insights into the structure and function of redox-active tyrosines from model compounds," *Journal of Physical Chemistry B*, vol. 109, no. 15, pp. 6972–6981, 2005.
- [23] C. Drouza and A. D. Keramidas, "Solid state and aqueous solution characterization of rectangular tetranuclear VIV/V-p-semiquinonate/hydroquinonate complexes exhibiting a proton induced electron transfer," *Inorganic Chemistry*, vol. 47, no. 16, pp. 7211–7224, 2008.
- [24] W. R. Harris, R. J. Motekaitis, and A. E. Martell, "New Multidentate ligands. XVII. Chelate tendencies of *N*-(*o*-Hydroxybenzyl)iminodiacetic acid (H_3L)," *Inorganic Chemistry*, vol. 14, p. 974, 1975.
- [25] M. Stylianou, C. Drouza, Z. Viskadourakis, J. Giapintzakis, and A. D. Keramidas, "Synthesis, structure, magnetic properties and aqueous solution characterization of *p*-hydroquinone and phenol iminodiacetate copper(ii) complexes," *Dalton Transactions*, no. 44, pp. 6188–6204, 2008.
- [26] M. M. Whittaker, P. J. Kersten, N. Nakamura, J. Sanders-Loehr, E. S. Schweizer, and J. W. Whittaker, "Glyoxal oxidase from *Phanerochaete chrysosporium* is a new radical-copper oxidase," *Journal of Biological Chemistry*, vol. 271, no. 2, pp. 681–687, 1996.
- [27] C. Drouza and A. D. Keramidas, "Synthesis and aqueous solution properties of multinuclear oxo-bridged vanadium(IV/V) complexes," *Journal of Inorganic Biochemistry*, vol. 80, no. 1–2, pp. 75–80, 2000.
- [28] C. Drouza, V. Tolis, V. Gramlich, et al., "*p*-hydroquinone-metal compounds: synthesis and crystal structure of two novel

- V^V-*p*-hydroquinonate and V^{IV}-*p*-semiquinonate species,” *Chemical Communications*, no. 23, pp. 2786–2787, 2002.
- [29] P. Gans and B. O’Sullivan, “GLEE, a new computer program for glass electrode calibration,” *Talanta*, vol. 51, no. 1, pp. 33–37, 2000.
- [30] A. E. Martell and R. J. Motekaitis, “Potentiometry revisited: the determination of thermodynamic equilibria in complex multicomponent systems,” *Coordination Chemistry Reviews*, vol. 100, pp. 323–361, 1990.
- [31] A. E. Martell and R. J. Motekaitis, *Determination and Use of Stability Constants*, Wiley-VCH, New York, NY, USA, 2nd edition, 1992.
- [32] L. Zekany and I. Nagypal, Eds., *Computational Methods for the Determination of Stability Constants*, Plenum, New York, NY, USA, 1985.
- [33] R. P. Bonomo, R. Cali, F. Riggi, E. Rizzarelli, S. Sammartano, and G. Siracusa, “Thermodynamic and spectroscopic properties of mixed complexes in aqueous solution. Copper(II) complexes of 2,2’-bipyridyl and iminodiacetic or pyridine-2,6-dicarboxylic acid,” *Inorganic Chemistry*, vol. 18, no. 12, pp. 3417–3422, 1979.
- [34] F. L’Eplattenier, I. Murase, and A. E. Martell, “New multidentate ligands. VI. Chelating tendencies of N,N’-di (2-hydroxybenzyl) ethylenediamine-N,N’-diacetic acid,” *Journal of the American Chemical Society*, vol. 89, no. 4, pp. 837–843, 1967.
- [35] R. L. Gustafson and A. E. Martell, “Hydrolytic tendencies of metal chelate compounds. V. Hydrolysis and dimerization of copper(II) chelates of 1,2-diamines,” *Journal of the American Chemical Society*, vol. 81, no. 3, pp. 525–529, 1959.
- [36] R. M. Tichane and W. E. Bennett, “Coordination compounds of metal ions with derivatives and analogs of ammoniadiacetic acid,” *Journal of the American Chemical Society*, vol. 79, no. 6, pp. 1293–1296, 1957.

Research Article

“Lantern-Shaped” Platinum(III) Complexes with Axially Bound 9-Ethylguanine or 1-Methylcytosine (L) of General Formula $[\text{Pt}_2\{\text{HN}=\text{C}(\text{Bu}^t)\text{O}\}_4\text{L}_2](\text{NO}_3)_2$

Concetta Pacifico, Francesco Paolo Intini, Fiorentin Nushi, and Giovanni Natile

Dipartimento Farmaco-Chimico, Università degli Studi di Bari, Via E. Orabona 4, 70125 Bari, Italy

Correspondence should be addressed to Giovanni Natile, natile@farmchim.uniba.it

Received 27 January 2010; Accepted 4 March 2010

Academic Editor: Spyros Perlepes

Copyright © 2010 Concetta Pacifico et al. This is an open access article distributed under the Creative Commons Attribution License, which permits unrestricted use, distribution, and reproduction in any medium, provided the original work is properly cited.

The synthesis, NMR characterization, and X-ray crystallography of “lantern-shaped” platinum(III) complexes with four pivaloamidate bridging ligands and two 9-ethylguanines (9-EtG) or 1-methylcytosines (1-MeC) in axial positions are reported: $cis\text{-N}^2\text{O}^2\text{-}[\text{Pt}_2\{\text{HN}=\text{C}(\text{Bu}^t)\text{O}\}_4(9\text{-EtG})_2](\text{NO}_3)_2$ and $cis\text{-N}^2\text{O}^2\text{-}[\text{Pt}_2\{\text{HN}=\text{C}(\text{Bu}^t)\text{O}\}_4(1\text{-MeC})_2](\text{NO}_3)_2$. The last complex is, to the best of our knowledge, the first dinuclear compound of platinum(III) with axially bound 1-MeC.

1. Introduction

The interest in dinuclear platinum(III) complexes is steadily increasing because of their very interesting chemical properties. They contain a metal-metal single bond which is generally supported by two or four bridging ligands (the latter generally indicated as “lantern shaped” complexes) ([1–3] and references therein). Only few exceptions with three bridging ligands [4], or unsupported by covalent bridges [5, 6], have been so far reported. Usually the bridging ligands form five-member rings comprising the two platinum centers and a set of three atoms providing a suitable bite, for example, NCO [6–23] (including pyrimidine nucleobases), NCS, NCN, SCS, OXO (X = C, S, P), or PXP (X = O, C) [24–29]. Some of these dinuclear platinum(III) complexes have antitumor activity [30–32] or have shown to act as catalysts for the oxidation of olefins [2, 33, 34]. Dinuclear platinum(III) complexes have equatorial and axial ligands [35]; these latter are invariably more weakly bound, due to the strong *trans* labilizing influence exerted by the intermetallic bond [5, 22]. In previous works we have reported the synthesis and structural characterization of “lantern-shaped” platinum(III) complexes with acetamidate and pivaloamidate ($\text{HN}=\text{C}(\text{R})\text{O}^-$, R = Me or Bu^t) bridging ligands and chloride, phosphine or water axial ligands [22, 23]. We have now extended the

investigation to the case of axial ligands being purine and pyrimidine nucleobases. In this paper we report the synthesis and NMR characterization of pivaloamidate “lantern-shaped” platinum(III) complexes with 9-ethylguanine (9-EtG) and 1-methylcytosine (1-MeC). The two complexes, $cis\text{-N}^2\text{O}^2\text{-}[\text{Pt}_2\{\text{HN}=\text{C}(\text{Bu}^t)\text{O}\}_4(9\text{-EtG})_2](\text{NO}_3)_2$ and $cis\text{-N}^2\text{O}^2\text{-}[\text{Pt}_2\{\text{HN}=\text{C}(\text{Bu}^t)\text{O}\}_4(1\text{-MeC})_2](\text{NO}_3)_2$, have also been characterized by X-ray crystallography.

2. Experimental

Physical Measurements. Elemental analyses were obtained with an Elemental Analyzer mod. 1106 Carlo Erba instrument. ^1H , ^{13}C , and ^{195}Pt NMR spectra were recorded with a DPX 300 Avance Bruker instrument. ^1H and ^{13}C chemical shifts are referenced to TMS and ^{195}Pt chemical shifts to K_2PtCl_4 (1 M in water, $\delta = -1614$ ppm).

2.1. Synthesis

2.1.1. Starting Materials. Reagent grade chemicals were used as received. $cis\text{-N}^2\text{O}^2\text{-}[\text{Pt}_2\{\text{HN}=\text{C}(\text{Bu}^t)\text{O}\}_4](\text{NO}_3)_2$ was prepared as already described in a previous work [23].

2.1.2. *cis-N²O²-[Pt₂{HN=C(Bu^t)O}₄(9-EtG)₂](NO₃)₂ (1).* *cis-N²O²-[Pt₂{HN=C(Bu^t)O}₄(NO₃)₂]* (50.4 mg, 0.055 mmol) and 9-EtG (20.0 mg, 0.11 mmol) were dissolved in methanol (40 mL) and the reaction solution stirred at 25 °C for 6 hours. The solution was then taken to dryness under reduced pressure and the obtained solid was triturated with chloroform in order to remove unreacted reagents. The suspension was centrifuged and the solid was separated from the solution and dried in a stream of dry air. *Anal.* calc. for C₃₄H₅₈N₁₆O₁₂Pt₂·CHCl₃·CH₃OH: C, 30.35; H, 4.46; N, 15.73. Found: C, 30.87; H, 4.60; N, 16.18. ¹H-NMR (CD₃OD, ppm): 8.20 (s, H8), 4.31 (q, CH₂), 1.52 (t, CH₃), and 1.22 (s, Bu^t). The compound was obtained in crystalline form (green crystals) from a methanol solution layered under tetrahydrofuran (THF).

2.1.3. *cis-N²O²-[Pt₂{HN=C(Bu^t)O}₄(1-MeC)₂](NO₃)₂ (2).* *cis-N²O²-[Pt₂{HN=C(Bu^t)O}₄(NO₃)₂]* (129.0 mg, 0.14 mmol) and 1-MeC (35.3 mg, 0.28 mmol) were dissolved in methanol (30 mL). The reaction mixture was stirred at 25 °C for 6 hours. The green solution was taken to dryness under reduced pressure and the solid dried in a stream of dry air. *Anal.* calc. for C₃₀H₅₄N₁₂O₁₂Pt₂·H₂O·CH₃OH: C, 30.64; H, 4.98; N, 13.83. Found: C, 30.64; H, 4.65; N, 13.81. ¹H-NMR (CD₃OD, ppm): 7.83 (d, H6), 5.95 (d, H5), 3.45 (s, CH₃), and 1.23 (s, Bu^t). The compound was obtained in crystalline form (yellow crystals) from an ethanol solution layered under 1,4-dioxane.

2.2. *X-Ray Crystallography.* Selected crystals of compounds **1** and **2** were mounted on a Bruker AXS X8 APEX CCD system equipped with a four-circle Kappa goniometer and a 4K CCD detector (radiation MoK α). For data reduction and unit cell refinement the SAINT-IRIX package was employed [36].

For compound **1**, that crystallizes from CH₃OH/tetrahydrofuran incorporating a molecule of tetrahydrofuran per molecule of compound (**1**·C₄H₈O), a total of 42660 reflections ($\Theta_{\max} = 25.18^\circ$) were collected. For compound **2**, that crystallizes from CH₃CH₂OH/1,4-dioxane incorporating two molecules of 1,4-dioxane per molecule of compound (**2**·2C₄H₈O₂), a total of 43490 reflections ($\Theta_{\max} = 34.11^\circ$) were collected. All reflections were indexed, integrated, and corrected for Lorentz, polarization, and absorption effects using the program SADABS [37].

The unit cell dimensions were calculated from all reflections and the structures were solved using direct methods technique in the *P* 2₁/*c* space group.

The model was refined by full-matrix least-square methods. All non-hydrogen atoms were refined anisotropically, except for atoms of *tert*-butyl group (disordered in the case of **2**) and of solvent of crystallization (disordered tetrahydrofuran for **1** and disordered 1,4-dioxane for **2**) that required isotropic treatment in order to maintain satisfactory thermal displacement parameters.

In the case of complex **1**, the hydrogen atoms were located by Fourier difference and refined isotropically except for the hydrogen atoms of the *tert*-butyl groups that were placed at calculated positions and refined given isotropic

parameters equal to 1.5 times the *U*(eq) of the atom to which they are bound.

In the case of complex **2**, all hydrogen atoms were placed at calculated positions and refined given isotropic parameters equivalent to 1.5 (methyl groups) or 1.2 (other groups) times those of the atom to which they are attached.

All calculations and molecular graphics were carried out using SIR2002 [38], SHELXL97 [39], PARST97 [40, 41], WinGX [42], and ORTEP-3 for Windows packages [43]. Details of the crystal data are listed in Table 1. Selected bond lengths and angles are listed in Table 2.

CCDC-762181 (**1**) and CCDC-762182 (**2**) are available. These data can be obtained free of charge via <http://www.ccdc.cam.ac.uk/conts/retrieving.html>, or from the Cambridge Crystallographic Data Centre, 12 Union Road, Cambridge CB2 1EZ, UK; fax: (+44) 1223-336-033; or e-mail: deposit@ccdc.cam.ac.uk.

3. Results and Discussion

3.1. *Synthesis and Characterization.* 9-EtG and 1-MeC both react with lantern shaped [Pt₂{HN=C(Bu^t)O}₄(NO₃)₂] (which has a *cis-N²O²* configuration on both platinum subunits), in methanol, giving, respectively, compounds **1** and **2** in almost quantitative yields. The new formed complexes exhibit single ¹⁹⁵Pt NMR signals (−69.8 and 28.2 ppm for **1** and **2**, respectively, solvent CD₃OD + 10% H₂O), which are indicative of dinuclear Pt(III) species with symmetrical capping of the axial sites (the precursor complex, [Pt₂{HN=C(Bu^t)O}₄(NO₃)₂], resonates at −4.41 ppm in CD₃OD). The ¹H-NMR spectrum in CD₃OD + 10% H₂O of complex **1** exhibits a single set of signals for 9-EtG with frequencies at 11.32, 8.17, 6.71, 4.29, and 1.51 ppm assigned, respectively, to NH, H(8), NH₂, CH₂, and CH₃ protons (corresponding signals of free 9-EtG fall at 10.85, 7.78, 6.30, 4.07, and 1.40 ppm, respectively). The 0.40 ppm downfield shift of the 9-EtG H8 proton suggests that the coordination occurs through N7. One set of signals is also observed for the pivaloamidate ligands with resonance peaks at 8.66 and 1.23 ppm assigned, respectively, to NH and *tert*-butyl protons (the corresponding protons in the precursor complex [Pt₂{HN=C(Bu^t)O}₄(NO₃)₂] resonate at 7.54 and 1.22 ppm, respectively). The deshielding of about 1 ppm observed for the amidic protons of the pivaloamidate ligands may be attributed to the interaction with the guanine base in apical position (see following discussion).

The ¹H-NMR spectrum of compound **2** in CD₃OD + 10% H₂O exhibits one set of signals for 1-MeC with resonance peaks at 8.82 and 6.82 (these first two peaks exhibiting a strong exchange peak in the 2D NOESY experiment), 7.83, 5.95, and 3.45 ppm assigned, respectively, to the two unequivalent aminic protons and to H(6), H(5), and methyl group (corresponding signals of free 1-MeC fall at 7.18 (broad singlet), 7.55, 5.85, and 3.35 ppm). The unequivalence of the aminic protons in coordinated 1-MeC is due to the partial double bond character of the C4–N4 linkage, which is reinforced by the metal coordination to N3 [44, 45]. The average deshielding of the aminic protons

TABLE 1: Crystal data and structure refinement parameters for $[\text{Pt}_2\{\text{HN}=\text{C}(\text{Bu}^t)\text{O}\}_4(9\text{-EtG})_2](\text{NO}_3)_2 \cdot \text{tetrahydrofuran}$ ($1 \cdot \text{C}_4\text{H}_8\text{O}$) and $[\text{Pt}_2\{\text{HN}=\text{C}(\text{Bu}^t)\text{O}\}_4(1\text{-MeC})_2](\text{NO}_3)_2 \cdot 2(1,4\text{-dioxane})$ ($2 \cdot 2\text{C}_4\text{H}_8\text{O}_2$).

Crystal	$1 \cdot \text{C}_4\text{H}_8\text{O}$	$2 \cdot 2\text{C}_4\text{H}_8\text{O}_2$
Empirical formula	$\text{C}_{38}\text{H}_{66}\text{N}_{16}\text{O}_{13}\text{Pt}_2$	$\text{C}_{38}\text{H}_{70}\text{N}_{12}\text{O}_{16}\text{Pt}_2$
Formula weight	1345.24	1341.24
Temperature (K)	293(2)	293(2)
Wavelength (Å)	0.71073	0.71073
Crystal system	monoclinic	monoclinic
Space group	$P 2_1/c$	$P 2_1/c$
a (Å)	9.7776(3)	10.6566(5)
b (Å)	14.8367(5)	15.8137(6)
c (Å)	18.8734(7)	15.5868(6)
β (°)	98.54(1)	102.51(1)
Volume (Å ³)	2707.5(2)	2564.5(3)
Z	2	2
Density (calculated) (Mg/m ³)	1.650	1.737
Absorption coefficient (mm ⁻¹)	5.231	5.524
$F(000)$	1332	1332
Crystal size (mm ³)	$0.300 \times 0.150 \times 0.080$	$0.240 \times 0.210 \times 0.075$
θ range for data collection (°)	1.75 to 25.18	2.34 to 34.11
Index ranges	$-11 \leq h \leq 11, -17 \leq k \leq 17, -22 \leq l \leq 22$	$-16 \leq h \leq 16, -24 \leq k \leq 24, -23 \leq l \leq 23$
Reflections collected	42660	43490
Independent reflections	4843 [$R(\text{int}) = 0.0917$]	10083 [$R(\text{int}) = 0.0639$]
Refinement method	Full-matrix least-squares on F^2	Full-matrix least-squares on F^2
Data/restraints/parameters	4843/0/301	10083/0/291
Goodness-of-fit on F^2	1.046	1.003
Final R indices [$I > 2\sigma(I)$]	$R1 = 0.0398, wR2 = 0.0906$	$R1 = 0.0469, wR2 = 0.1117$
R indices (all data)	$R1 = 0.0614, wR2 = 0.1014$	$R1 = 0.0968, wR2 = 0.1390$
Largest diff. peak and hole ($e \text{ \AA}^{-3}$)	1.372 and -0.751	2.571 and -0.766

of 1-MeC, as a consequence of coordination to platinum, is 0.64 ppm. However, while one proton, presumably that pointing towards platinum, undergoes a very large deshielding (1.64 ppm), the other proton undergoes a slight upfield shift (0.36 ppm). The pivaloamidate ligands exhibit one signal for the iminic proton at 8.05 ppm and one signal for the *tert*-butyl groups at 1.23 ppm. The cross peak between the signals at 8.05 and 1.23 ppm, observed in the 2D NOESY spectrum, supports this assignment. Coordination of 1-MeC in apical position causes a deshielding of the amidic protons of the pivaloamidate ligands which is less than half that observed for coordination of 9-EtG (0.51 as compared to 1.12 ppm).

3.2. X-Ray Diffraction Analysis

3.2.1. $[\text{Pt}_2\{\text{HN}=\text{C}(\text{Bu}^t)\text{O}\}_4(9\text{-EtG})_2](\text{NO}_3)_2$ (**1**). Complex **1** crystallizes incorporating one molecule of THF per molecule of complex. The asymmetric unit comprises half molecule of complex and half molecule of THF and the structure is generated by inversion at the midpoint of the Pt–Pt bond (Figure 1). Each platinum(III) atom has distorted octahedral

geometry with the N7 of 9-EtG and the second platinum subunit in axial positions.

The Pt–Pt distance (2.4512(5) Å) is closer to that of the analogous complex with axial chlorides ($[\text{Pt}_2\{\text{HN}=\text{C}(\text{Bu}^t)\text{O}\}_4\text{Cl}_2]$, 2.448(2) Å) than to that of the complexes with one or two axial triphenylphosphine ligand(s) ($[\text{Pt}_2\{\text{HN}=\text{C}(\text{Bu}^t)\text{O}\}_4(\text{PPh}_3)(\text{H}_2\text{O})](\text{NO}_3)_2$, 2.468(1) Å; $[\text{Pt}_2\{\text{HN}=\text{C}(\text{Bu}^t)\text{O}\}_4(\text{PPh}_3)_2](\text{NO}_3)_2$, 2.504(1) Å) [22, 23]. Thus the Pt–Pt distance is influenced by the nature of the axial ligands and an N7-coordinated guanine appears to exert a *trans* influence similar to that of a chloride. The platinum coordination squares are perfectly eclipsed (maximum twist angle 1.5°); such a conformation allows the greatest separation between the platinum atoms. The platinum atoms are displaced from the equatorial coordination planes by 0.087 Å towards the axial 9-EtG, such a displacement being a measure of the strength with which the four bridging ligands pull together the two metal centers.

The equatorial Pt–N [1.993(7)–1.996(6) Å] and Pt–O distances [2.019(5)–2.035(5) Å] are in the range of those reported for doubly and quadruply bridged dinuclear platinum(III) [17, 22, 23, 46], four-coordinate platinum(II), and six-coordinate platinum(IV) complexes [4].

TABLE 2: Bond lengths [Å] and angles [°] for $[\text{Pt}_2\{\text{HN}=\text{C}(\text{Bu}^t)\text{O}\}_4 \cdot (9\text{-EtG})_2](\text{NO}_3)_2 \cdot \text{tetrahydrofuran} (1 \cdot \text{C}_4\text{H}_8\text{O})$ and $[\text{Pt}_2\{\text{HN}=\text{C}(\text{Bu}^t)\text{O}\}_4 (1\text{-MeC})_2](\text{NO}_3)_2 \cdot 2(1,4\text{-dioxane}) (2 \cdot 2\text{C}_4\text{H}_8\text{O}_2)$.

Crystal	$1 \cdot \text{C}_4\text{H}_8\text{O}$	$2 \cdot 2\text{C}_4\text{H}_8\text{O}_2$
Pt–N1	1.993(7)	1.967(5)
Pt–N2	1.996(6)	1.982(5)
Pt–O2	2.019(5)	2.025(4)
Pt–O1	2.035(5)	2.011(4)
Pt–Pt ^{a,b}	2.4512(5)	2.4523(4)
Pt–N7g	2.200(5)	
Pt–N3c		2.230(5)
N1–Pt–N2	90.6(3)	92.0(2)
N1–Pt–O2	90.4(3)	88.2(2)
N2–Pt–O1	90.4(2)	88.4(2)
O1–Pt–O2	88.1(2)	90.9(2)
N1–Pt–N7g	97.7(2)	
N2–Pt–N7g	94.3(2)	
O1–Pt–N7g	87.4(2)	
O2–Pt–N7g	90.4(2)	
Pt ^a –Pt–N7g	177.2(1)	
N1–Pt–N3c		95.3(2)
N2–Pt–N3c		95.4(2)
O1–Pt–N3c		89.9(2)
O2–Pt–N3c		89.8(2)
Pt ^b –Pt–N3c		179.0(1)

Symmetry transformations used to generate equivalent atoms: (a) $-x, -y, -z + 1$ for crystal $1 \cdot \text{C}_4\text{H}_8\text{O}$ and (b) $-x, -y, -z$ for crystal $2 \cdot 2\text{C}_4\text{H}_8\text{O}_2$.

As expected, the axial Pt(III)–N7 bond length (2.200(5) Å in **1**) is longer than those typically seen in 4-coordinate platinum(II) and 6-coordinate platinum(IV) guanine complexes (~1.96–2.11 Å) [47–51]. The lengthening can be ascribed to the strong *trans* influence exerted by the Pt–Pt bond. We also notice that the Pt(III)–N7 bond is slightly longer in **1** than in analogous dinuclear Pt(III) species (e.g., 2.189(6) Å in *ht-cis*- $[\text{Pt}_2(\text{NH}_3)_4(1\text{-Mec-N3,N4})_2(9\text{-EtG})_2](\text{ClO}_4)_4 \cdot 5\text{H}_2\text{O}$ (*ht* indicates the head-to-tail arrangement of the two bridging 1-Mec ligands) [52], 2.187(6) and 2.181(7) Å in *ht-cis*- $[\text{Pt}_2(\text{NH}_3)_4(1\text{-Mec-N3,N4})_2(9\text{-EtG})_2](\text{NO}_3)_4 \cdot 9\text{H}_2\text{O}$) [53]. We believe that the longer Pt(III)–N7 bond observed in **1** can be ascribed to a stronger *trans* influence exerted by the Pt–Pt bond, that in **1** is shorter (2.4511(4) Å) than in the latter two complexes (2.587(1) and 2.586(1) Å in *ht-cis*- $[\text{Pt}_2(\text{NH}_3)_2(1\text{-Mec-N3,N4})_2(9\text{-EtG})_2](\text{ClO}_4)_4 \cdot 5\text{H}_2\text{O}$) [52] and in *ht-cis*- $[\text{Pt}_2(\text{NH}_3)_4(1\text{-Mec-N3,N4})_2(9\text{-EtG})_2](\text{NO}_3)_4 \cdot 9\text{H}_2\text{O}$, respectively) [53].

The guanine is nearly coplanar with a pivaloamidate (C5g–N7g–Pt–N1 torsion angle of 16.4(7)°); this allows the formation of a strong hydrogen bond between the NH of the amidate ligand and the O6 of guanine (N1···O6g = 2.80(1) Å, (N1)H1···O6g = 2.07(9) Å, N1–H1···O6g = 166(9)°). The resulting seven-member ring motif can be defined as S(7) by Etter’s graph-set notation [54].

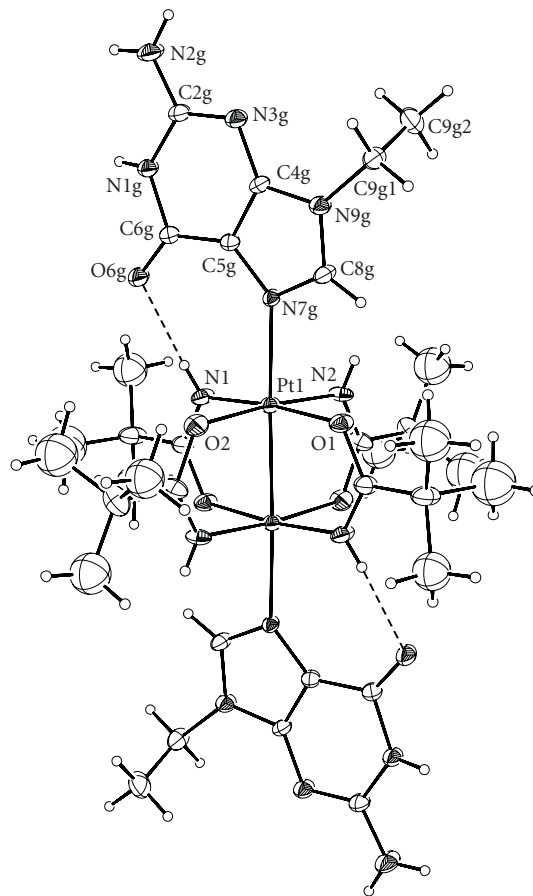


FIGURE 1: View of the $[\text{Pt}_2\{\text{HN}=\text{C}(\text{Bu}^t)\text{O}\}_4(9\text{-EtG})_2]^{2+}$ complex showing the atomic numbering scheme of most important atoms. Displacement ellipsoids are drawn at 20% probability level.

The orientation of the guanine in **1** is very similar to that found in the tetrabridged dirhodium(II) complex $[\text{Rh}_2\{\text{O}=\text{C}(\text{CH}_3)\text{O}\}_2\{\text{HN}=\text{C}(\text{CF}_3)\text{O}\}_2(9\text{-EtG})_2]$ [55] also containing a strong H-bond (N···O6g = 2.94(2) Å, (N1)H1···O6g = 2.20(9) Å, N1–H1···O6g = 158(1)°). It appears that a pivaloamidate ligand is as good as the trifluoroacetamidate ligand in forming such an H-bond.

The crystal packing is mainly governed by two symmetrical hydrogen bonds involving N2 and N3 of two adjacent guanines ($\text{N2g} \cdots \text{N3g}^{ii} = 3.07(1)$ Å, $(\text{N2g})\text{H21g} \cdots \text{N3g}^{ii} = 2.22(1)$ Å, $\text{N2g} \cdots \text{H21g} \cdots \text{N3g}^{ii} = 175(1)^\circ$; $ii = -x + 1, -y + 1, -z + 1$), forming a centrosymmetric eight-member ring. This ring motif can be defined as $\text{R}_2^2(8)$ by Etter’s graph-set notation (Figure 2). These H-bonds allow the formation of chains of complexes extending, alternatively, parallel to the (110) and to the $(1\bar{1}0)$ directions. The angle between adjacent chains is 66°.

Different chains are linked by nitrate anions. The nitrate anion is anchored to the guanine base through two strong H-bonds ($\text{N1g} \cdots \text{O5} = 2.81(1)$ Å, $(\text{N1g})\text{H1g} \cdots \text{O5} = 1.99(8)$ Å, $\text{N1g} \cdots \text{H1g} \cdots \text{O5} = 173(7)^\circ$; $\text{N2g} \cdots \text{O4} = 2.87(1)$ Å, $(\text{N2g})\text{H22g} \cdots \text{O4} = 2.02(8)$ Å, $\text{N2g} \cdots \text{H22g} \cdots \text{O4} = 171(1)^\circ$) forming an eight-member ring ($\text{R}_2^2(8)$) according

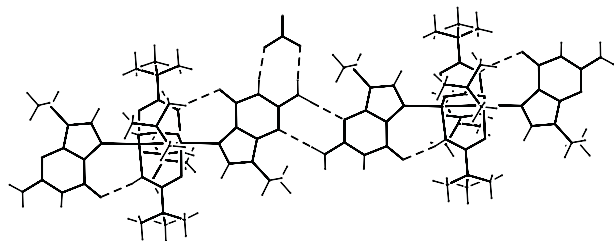


FIGURE 2: View of the H-bonds along the chains of $[\text{Pt}_2\{\text{HN}=\text{C}(\text{Bu}^t)\text{O}\}_4(9\text{-EtG})_2]^{2+}$ complexes.

to Etter's graph-set notation). The same nitrate anion forms a third hydrogen bond with the amidic NH of an adjacent complex ($\text{N}2^i \cdots \text{O}3 = 3.18(1) \text{ \AA}$, $(\text{N}2)^i\text{H}2^i \cdots \text{O}3 = 2.49(8) \text{ \AA}$, $\text{N}2^i\text{-H}2^i \cdots \text{O}3 = 157(8)^\circ$; $i = x, -y + 1/2, z - 1/2$) with an Etter's graph-set motif of type D.

The THF solvent molecule is disordered, the oxygen atom of 50% of the molecules pointing in the direction opposite to that of the other 50% molecules. As a consequence THF appears as a flat 1,4-dioxane-type molecule with the two oxygens having occupancy factor 0.5 and the carbons occupancy factor 1. The accuracy of the X-ray data is not allowed to distinguish between carbon atoms belonging to the differently oriented THF molecules.

3.2.2. $[\text{Pt}_2\{\text{HN}=\text{C}(\text{Bu}^t)\text{O}\}_4(1\text{-MeC})_2](\text{NO}_3)_2$ (**2**). Compound **2** crystallizes incorporating two molecules of 1,4-dioxane per molecule of complex. The asymmetric unit comprises half molecule of complex and one of dioxane and the structure is generated by inversion at the midpoint of the Pt–Pt linkage (Figure 3). Each Pt(III) atom has a distorted octahedral geometry with the N3 of 1-MeC and the second platinum subunit in axial positions.

The Pt–Pt distance ($2.4523(4) \text{ \AA}$) is very similar to the analogous distance observed in compound **1**. As for **1**, the platinum coordination squares are perfectly eclipsed (maximum twist angle of 0.8°), and the platinum atoms are displaced from the equatorial coordination planes by 0.090 \AA towards the axial cytosine. Also the equatorial Pt–N [$1.967(5)$ and $1.982(5) \text{ \AA}$] and Pt–O distances [$2.011(4)$ and $2.025(4) \text{ \AA}$] are in the range of those observed in **1** and reported for four-coordinate platinum(II) and six-coordinate platinum(IV) complexes [4].

As expected, the axial Pt(III)–N3c bond length ($2.230(5) \text{ \AA}$) is longer than that observed in 4-coordinate platinum(II) and 6-coordinate platinum(IV) complexes with cytosine ($\sim 2.025\text{--}2.082 \text{ \AA}$) [45, 47, 56–58]. It is to be noted that the Pt–N3c distance is slightly longer than the Pt–N7g distance observed in compound **1**. The cytosine plane bisects the angle between two adjacent pivaloamidate planes forming a C2c–N3c–Pt–N1 torsion angle of 44° . This allows the formation of bifurcated hydrogen bonds between N4 of 1-MeC and the O atoms of two amidate ligands ($\text{N}4\text{c} \cdots \text{O}1 = 2.92(1) \text{ \AA}$, $(\text{N}4\text{c})\text{H}41\text{c} \cdots \text{O}1 = 2.30(1) \text{ \AA}$, $\text{N}4\text{c}\text{-H}41\text{c} \cdots \text{O}1 = 130(1)^\circ$; $\text{N}4\text{c} \cdots \text{O}2 = 2.93(1) \text{ \AA}$, $(\text{N}4\text{c})\text{H}41\text{c} \cdots \text{O}2 = 2.31(1) \text{ \AA}$, $\text{N}4\text{c}\text{-H}41\text{c} \cdots \text{O}2 = 130(1)^\circ$)

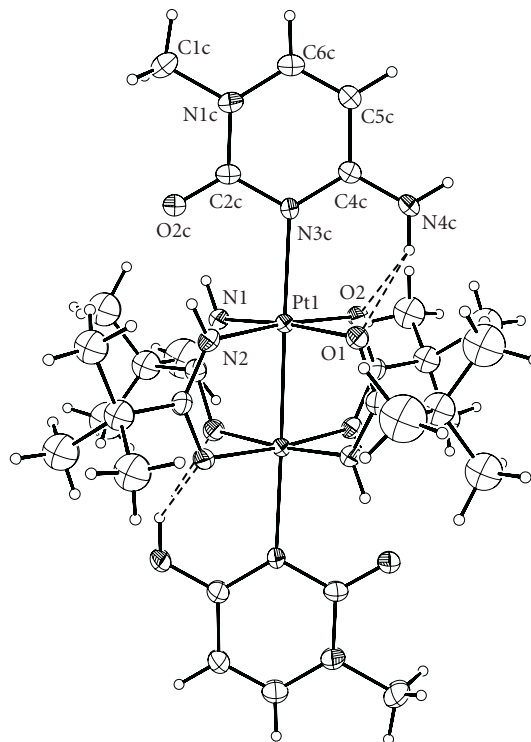


FIGURE 3: View of the $[\text{Pt}_2\{\text{HN}=\text{C}(\text{Bu}^t)\text{O}\}_4(1\text{-MeC})_2]^{2+}$ complex showing the atomic numbering scheme of most important atoms. The *tert*-butyl groups are disordered and can occupy two different positions; only one position is shown for clarity. Displacement ellipsoids are drawn at 20% probability level.

[59]. Each nitrate anion (nitrate oxygens O6, O7, and O8) is anchored to one 1-MeC through a hydrogen bond ($\text{N}4\text{c} \cdots \text{O}8 = 2.85(1) \text{ \AA}$, $(\text{N}4\text{c})\text{H}42\text{c} \cdots \text{O}8 = 2.00(1) \text{ \AA}$, $\text{N}4\text{c}\text{-H}42\text{c} \cdots \text{O}8 = 167(1)^\circ$, Figure 4).

In the crystal packing, complex molecules are located (with the inversion center) at the four corners and at the center of face A. The crystal packing is mainly governed by hydrogen bonds between complexes and 1,4-dioxane molecules. Each molecule of 1,4-dioxane (1,4-dioxane oxygens O4 and O5) bridges two adjacent molecules of complex ($\text{N}2 \cdots \text{O}4 = 2.98(1) \text{ \AA}$, $(\text{N}2)\text{H}2 \cdots \text{O}4 = 2.19(1) \text{ \AA}$, $\text{N}2\text{-H}2 \cdots \text{O}4 = 152(1)^\circ$; $\text{N}1^i \cdots \text{O}5 = 3.02(1) \text{ \AA}$ ($\text{N}1^i)\text{H}1^i \cdots \text{O}5 = 2.25(1) \text{ \AA}$, $\text{N}1^i\text{-H}1^i \cdots \text{O}5 = 149(1)^\circ$; $i = -x, -y + 1/2, z - 1/2$). In this way each molecule of complex is surrounded by four molecules of dioxane connecting the former complex to the four adjacent complex molecules on face A (Figure 4).

The *tert*-butyl groups are disordered and each set of three methyl groups can occupy two different positions, each position with occupancy factor 0.5. Also the 1,4-dioxane solvent molecules are disordered. The position is fixed for the two oxygen atoms while the four carbon atoms can occupy two different positions each one with occupancy factor 0.5. In each case the 1,4-dioxane molecule adopts a chair conformation.

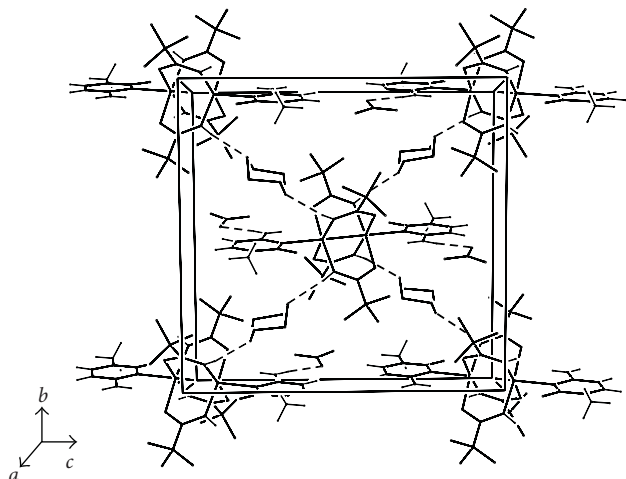


FIGURE 4: View of the crystal packing along the *a* direction for $[\text{Pt}_2\{\text{HN}=\text{C}(\text{Bu}^t)\text{O}\}_4(1\text{-MeC})_2](\text{NO}_3)_2 \cdot 2(1,4\text{-dioxane})$. Since the *tert*-butyl groups and the dioxane molecules are disordered, only one occupation site is shown for clarity.

4. Conclusions

The coordination of 9-EtG and 1-MeC to the axial sites of quadruply bridged dinuclear species of platinum(III) has been established. The complexes are stable in solution as well as in the solid state. Complex **1** is one of the few examples of dinuclear platinum(III) species with axially bound guanines, while complex **2** is, to the best of our knowledge, the first compound of this type (axially bound 1-MeC). The axial Pt–N3 bond in **2** is 0.010 Å longer than the axial Pt–N7 bond in **1**. Since the Pt–Pt core is very similar in the two cases, we argue that the longer distance found in **2** is indicative of a weaker binding of 1-MeC as compared to 9-EtG. Previous attempts to bind 1-MeC in the axial positions of a dinuclear platinum(III) complex, (e.g., *cis*- $[\text{Pt}_2(\text{NH}_3)_4(1\text{-Mec-N}3,\text{N}4)_2\text{XY}]Z_n$, X and Y stand for axial ligands of different types and Z stands for counteranion(s)) have been unsuccessful [52]. In contrast our dinuclear Pt(III) core, with four pivaloamidate bridging ligands, readily binds nucleobases, comprising 1-MeC, forming stable compounds. It is possible that the presence in the equatorial platinum coordination plane of groups with good H-bond donor/acceptor properties, and therefore able to establish additional bonds with the apical ligands, gives a decisive contribution to the formation of such complexes. H-bond interaction causes, in the case of **1**, a downfield shift of the pivaloamidate amidic proton by 1.12 ppm and, in the case **2**, a downfield shift of one aminic proton of 1-MeC by 1.64 ppm. In the latter case the H-bond is bifurcated and the 1-MeC aminic proton, (N4c)H41c, interacts, simultaneously, with the oxygen atoms of two *cis* pivaloamidate ligands. In principle, the 1-MeC could form, in addition to the H-bond described above, also an H-bond between the 1-MeC oxygen, O2c, and the pivaloamidate amidic protons; such an H-bond, however, does not form or is extremely weak (downfield shift of the

amidic proton of only 0.51 ppm as compared to 1.12 ppm observed in compound **1**). A possible cause of weakness of the latter H-bond is the dihedral angle of 45° between 1-MeC and pivaloamidate planes; such an angle is optimal for the bifurcated H-bond involving the aminic group but is detrimental for a potential H-bond involving the 1-MeC oxygen. In fact it appears that, while a proton can interact with two oxygens (bifurcated H-bond), one oxygen can only interact with one proton (regular H-bond as observed in compound **1**).

“Lantern shaped” platinum(III) complexes have been shown, by Cervantes and coworkers, to be endowed with antitumor activity (e.g., $[\text{Pt}_2(2\text{-mercaptopyrimidine})_4\text{Cl}_2]$ and $[\text{Pt}_2(2\text{-mercaptopyridine})_4\text{Cl}_2]$) [30–32]. It will be worth investigating the antitumor activity of our amidate complexes for which we have shown a greater propensity to form adducts with nucleobases in apical positions.

Acknowledgments

The authors thank the University of Bari, the EC (COST action D39), and the Consorzio Interuniversitario di Ricerca in Chimica dei Metalli nei Sistemi Biologici (CIRCMSB) for support. The authors gratefully acknowledge Professor Ferdinando Scordari and Dr. Ernesto Mesto (University of Bari) for the X-ray diffraction data collection.

References

- [1] G. Natile, F. P. Intini, and C. Pacifico, “Diplatinum(III) complexes: chemical species more widely spread than suspected,” in *Cisplatin: Chemistry and Biochemistry of a Leading Anticancer Drug*, B. Lippert, Ed., pp. 429–453, Wiley-WCH, Weinheim, Germany, 1999.
- [2] K. Matsumoto and K. Sakai, “Structures and reactivities of platinum-blues and the related amidate-bridged platinum(III) compounds,” *Advanced Inorganic Chemistry*, vol. 49, pp. 375–427, 1999.
- [3] K. Umakoshi and Y. Sasaki, “Quadruply bridged dinuclear complexes of platinum, palladium, and nickel,” *Advanced Inorganic Chemistry*, vol. 40, pp. 187–239, 1993.
- [4] R. Z. Pellicani, F. P. Intini, L. Maresca, E. Mesto, C. Pacifico, and G. Natile, “The first example of a dinuclear platinum(III) complex with three bridging ligands,” *European Journal of Inorganic Chemistry*, no. 8, pp. 1635–1642, 2006.
- [5] R. Cini, F. P. Fanizzi, F. P. Intini, and G. Natile, “Synthesis and X-ray structural characterization of the first unbridged diplatinum(III) compound: bis[bis(1-imino-1-hydroxy-2,2-dimethylpropane)trichloroplatinum(III)],” *Journal of the American Chemical Society*, vol. 113, no. 20, pp. 7805–7806, 1991.
- [6] G. Bandoli, P. A. Caputo, F. P. Intini, M. F. Sivo, and G. Natile, “Synthesis and X-ray structural characterization of two unbridged diplatinum(III) compounds: *cis*- and *trans*-Bis[bis(1-imino-1-methoxyethane)trichloroplatinum(III)]. Transient species in the oxidation of platinum(II) to platinum(IV),” *Journal of the American Chemical Society*, vol. 119, no. 43, pp. 10370–10376, 1997.
- [7] L. S. Hollis and S. J. Lippard, “New reaction chemistry of *cis*-diammineplatinum(II) with α -pyridone. Crystalline relatives

- of the α -pyridone blue," *Journal of the American Chemical Society*, vol. 103, no. 5, pp. 1230–1232, 1981.
- [8] L. S. Hollis and S. J. Lippard, "Redox properties of *cis*-diammineplatinum α -pyridone blue and related complexes. Synthesis, structure, and electrochemical behavior of *cis*-diammineplatinum(III) dimers with bridging α -pyridonate ligands," *Inorganic Chemistry*, vol. 22, no. 18, pp. 2605–2614, 1983.
- [9] T. V. O'Halloran, M. M. Roberts, and S. J. Lippard, "Synthesis, structure, and ^{195}Pt NMR solution studies of a reactive binuclear platinum(III) complex: $[\text{Pt}_2(\text{en})_2 \cdot (\text{C}_5\text{H}_4\text{NO})_2(\text{NO}_2)(\text{NO}_3)](\text{NO}_3)_2 \cdot 0.5\text{H}_2\text{O}$," *Inorganic Chemistry*, vol. 25, no. 7, pp. 957–964, 1986.
- [10] D. P. Bancroft and F. A. Cotton, "Tetramethyldiplatinum(III) (Pt-Pt) complexes with 2-hydroxypyridinato bridging ligands. 3. Compounds with diethyl sulfide as the axial ligand," *Inorganic Chemistry*, vol. 27, no. 22, pp. 4022–4025, 1988.
- [11] E. S. Peterson, D. P. Bancroft, D. Min, F. A. Cotton, and E. H. Abbott, "Proton, carbon-13, and platinum-195 nuclear magnetic resonance spectroscopy of hydroxypyridinate-bridged dinuclear platinum(III) complexes. Equilibria and mechanism of bridging ligand rearrangement," *Inorganic Chemistry*, vol. 29, no. 2, pp. 229–232, 1990.
- [12] K. Matsumoto and K. Harashima, "A tetranuclear tervalent platinum complex with α -pyrrolidonate and deprotonated ammine bridging ligands, $[(\text{NO}_3)(\text{NH}_3)_2\text{Pt}^{\text{III}} \cdot (\text{C}_4\text{H}_6\text{NO})_2\text{Pt}^{\text{III}}(\text{NH}_3)(\mu\text{-NH}_2)]_2(\text{NO}_3)_4$," *Inorganic Chemistry*, vol. 30, no. 15, pp. 3032–3034, 1991.
- [13] T. Abe, H. Moriyama, and K. Matsumoto, "Synthesis, crystal structure, and ^{13}C NMR spectra of α -pyrrolidonate-bridged head-to-head $[\text{Pt}^{\text{III}}_2(\text{NH}_3)_4(\text{C}_4\text{H}_6\text{NO})_2(\text{NO}_2)(\text{NO}_3)](\text{NO}_3)_2 \cdot \text{H}_2\text{O}$ and electrochemical study on conversion of the binuclear platinum(III)," *Inorganic Chemistry*, vol. 30, no. 22, pp. 4198–4204, 1991.
- [14] K. Matsumoto, J. Matsunami, K. Mizuno, and H. Uemura, "Organometallic chemistry of an amidate-bridged dinuclear Pt(III) complex: axial Pt(III)-alkyl σ -bond formation in the reaction with acetone," *Journal of the American Chemical Society*, vol. 118, no. 37, pp. 8959–8960, 1996.
- [15] B. Lippert, H. Schöllhorn, and U. Thewalt, "Platinum in its unusual oxidation state +III: diplatinum(III) complexes with the model nucleobase 1-methyluracil," *Zeitschrift für Naturforschung*, vol. 38, no. 11, pp. 1441–1445, 1983.
- [16] B. Lippert, H. Schöllhorn, and U. Thewalt, "Facile substitution of NH_3 ligands in a diplatinum(III) complex of 1-methyluracil," *Inorganic Chemistry*, vol. 25, no. 4, pp. 407–408, 1986.
- [17] B. Lippert, H. Schöllhorn, and U. Thewalt, "Additive *trans* influences of the axial ligand and metal-metal bond in a diplatinum(III) complex leading to an asymmetric structure with penta- and hexacoordination of the two metals," *Journal of the American Chemical Society*, vol. 108, no. 3, pp. 525–526, 1986.
- [18] H. Schöllhorn, P. Eisenmann, U. Thewalt, and B. Lippert, "Diplatinum(III) complexes with bridging 1-methyluracil ligands in head-tail arrangement: synthesis, structures, and solution behavior," *Inorganic Chemistry*, vol. 25, no. 19, pp. 3384–3391, 1986.
- [19] B. Lippert, "Diplatinum(III) complexes of 1-methyluracil: solution behavior and interactions with mono and dinuclear platinum(II) species," in *Recent Advances in Di and Polynuclear Chemistry*, P. Braunstein, Ed., vol. 12, pp. 715–720, New Journal of Chemistry, 1988.
- [20] H. Schöllhorn, U. Thewalt, and B. Lippert, " Pt^{III} co-ordination through C(5) of 1-methyluracil: the first example of a Pt-nucleobase complex containing a Pt-C bond," *Journal of the Chemical Society, Chemical Communications*, no. 3, pp. 258–260, 1986.
- [21] T. Wienkötter, M. Sabat, G. Fusch, and B. Lippert, "Dimerization of *trans*- $[\text{Pt}(\text{NH}_3)(1\text{-MeC-N3})(\text{H}_2\text{O})_2]^{2+}$ and oxidation to a diplatinum(III) species in the presence of glycine. Relevance for platinum cytosine blue," *Inorganic Chemistry*, vol. 34, no. 5, pp. 1022–1029, 1995.
- [22] A. Dolmella, F. P. Intini, C. Pacifico, G. Padovano, and G. Natile, "Structural characterization of the 'lantern-shaped' platinum(III) complex $[\text{Pt}_2\text{Cl}_2\{\text{N}(\text{H})\text{C}(\text{Bu}^t)\text{O}\}_4]$," *Polyhedron*, vol. 21, no. 3, pp. 275–280, 2002.
- [23] G. Bandoli, A. Dolmella, F. P. Intini, C. Pacifico, and G. Natile, "Synthesis and structural characterization of isomeric 'lantern-shaped' platinum(III) complexes of formula $[\text{Pt}_2(\text{PPh}_3)\text{X}\{\text{N}(\text{H})\text{C}(\text{R})\text{O}\}_4](\text{NO}_3)_2$ ($\text{X}=\text{PPh}_3, \text{H}_2\text{O}$)," *Inorganica Chimica Acta*, vol. 346, pp. 143–150, 2003.
- [24] D. M. L. Goodgame, R. W. Rollins, A. M. Z. Slawin, D. J. Williams, and P. W. Zard, "Synthesis and X-ray structural studies of some dinuclear platinum(III) complexes of pyrimidine-2-thione and 2-thiouracil," *Inorganica Chimica Acta*, vol. 120, no. 1, pp. 91–101, 1986.
- [25] K. Umakoshi, I. Kinoshita, A. Ichimura, and S. Ooi, "Binuclear platinum(II) and -(III) complexes of pyridine-2-thiol and its 4-methyl analogue. Synthesis, structure, and electrochemistry," *Inorganic Chemistry*, vol. 26, no. 21, pp. 3551–3556, 1987.
- [26] F. A. Cotton, J. H. Matonic, and C. A. Murillo, "Completion of the series of $\text{Pt}_2(\text{ArNC}(\text{H})\text{NAr})_4^n$, $n = 0, +1, +2$, compounds, with Pt-Pt sigma bond orders of 0, 1/2, 1, respectively," *Inorganica Chimica Acta*, vol. 264, no. 1-2, pp. 61–65, 1997.
- [27] D. Cornacchia, R. Z. Pellicani, F. P. Intini, C. Pacifico, and G. Natile, "Solution behavior of amidine complexes: an unexpected *cis/trans* isomerization and formation of di- and trinuclear platinum(III) and platinum(II) species," *Inorganic Chemistry*, vol. 48, no. 22, pp. 10800–10810, 2009.
- [28] C. Bellitto, A. Flamini, L. Gastaldi, and L. Scaramuzza, "Halogen oxidation of tetrakis(dithioacetato)diplatinum(II) complexes, $\text{Pt}_2(\text{CH}_3\text{CS}_2)_4$. Synthesis and characterization of $\text{Pt}_2(\text{CH}_3\text{CS}_2)_4\text{X}_2$ ($\text{X} = \text{Cl}, \text{Br}, \text{I}$) and structural, electrical, and optical properties of linear-chain (μ -iodo)tetrakis(dithioacetato)diplatinum, $\text{Pt}_2(\text{CH}_3\text{CS}_2)_4\text{I}$," *Inorganic Chemistry*, vol. 22, no. 3, pp. 444–449, 1983.
- [29] R. Usón, J. Fornies, L. R. Falvello, et al., "Synthesis and structure of two dinuclear anionic complexes, with Pt(III)-Pt(III) bonds and unprecedented $(\text{C}_6\text{F}_4\text{O})^{2-}$ or $\{\text{C}_6\text{F}_4(\text{OR})_2\}^{2-}$ ($\text{R} = \text{Me}, \text{Et}$) quinone-like bridging ligands," *Journal of the American Chemical Society*, vol. 116, no. 16, pp. 7160–7165, 1994.
- [30] G. Cervantes, S. Marchal, M. J. Prieto, et al., "DNA interaction and antitumor activity of a Pt(III) derivative of 2-mercaptopyridine," *Journal of Inorganic Biochemistry*, vol. 77, no. 3-4, pp. 197–203, 1999.
- [31] G. Cervantes, M. J. Prieto, and V. Moreno, "Antitumour activity of a Pt(III) derivative of 2-mercaptopyrimidine," *Metal-Based Drugs*, vol. 4, no. 1, pp. 9–18, 1997.
- [32] V. M. González, M. A. Fuertes, M. J. Pérez-Alvarez, et al., "Induction of apoptosis by the bis-Pt(III) complex $[\text{Pt}_2(2\text{-mercaptopyrimidine})_4\text{Cl}_2]$," *Biochemical Pharmacology*, vol. 60, no. 3, pp. 371–379, 2000.
- [33] N. Saeki, N. Nakamura, T. Ishibashi, et al., "Mechanism of ketone and alcohol formations from alkenes and alkynes on the head-to-head 2-pyridonate-bridged

- cis*-diammineplatinum(III) dinuclear complex," *Journal of the American Chemical Society*, vol. 125, no. 12, pp. 3605–3616, 2003.
- [34] M. Ochiai, Y.-S. Lin, J. Yamada, H. Misawa, S. Arai, and K. Matsumoto, "Reactions of a platinum(III) dimeric complex with alkynes in water: novel approach to α -aminoketone, α -iminoketone, and α , β -diimine via ketonyl-Pt(III) dinuclear complexes," *Journal of the American Chemical Society*, vol. 126, no. 8, pp. 2536–2545, 2004.
- [35] K. Matsumoto, "Inorganic and organometallic chemistry of Pt^{III} complexes having a delocalized Pt^{III}-Pt^{III} bond," *Russian Chemical Bulletin*, vol. 52, no. 12, pp. 2577–2587, 2003.
- [36] Bruker, SAINT-IRIX, Bruker AXS Inc., Madison, Wis, USA, 2003.
- [37] G. M. Sheldrick, *SADABS: Program for Empirical Absorption Correction of Area Detector Data*, University of Göttingen, Göttingen, Germany, 1996.
- [38] M. C. Burla, M. Camalli, B. Carrozzini, et al., "SIR2002: the program," *Journal of Applied Crystallography*, vol. 36, no. 5, p. 1103, 2003.
- [39] G. M. Sheldrick, *Programs for Crystal Structure Analysis (Release 97-2)*, Institut für Anorganische Chemie der Universität, Göttingen, Germany, 1998.
- [40] M. Nardelli, "Parst: a system of Fortran routines for calculating molecular structure parameters from results of crystal structure analyses," *Computers and Chemistry*, vol. 7, no. 3, pp. 95–98, 1983.
- [41] M. Nardelli, "PARST95—an update to PARST: a system of Fortran routines for calculating molecular structure parameters from the results of crystal structure analyses," *Journal of Applied Crystallography*, vol. 28, no. 5, p. 659, 1995.
- [42] L. J. Farrugia, "WinGX suite for small-molecule single-crystal crystallography," *Journal of Applied Crystallography*, vol. 32, no. 4, pp. 837–838, 1999.
- [43] L. J. Farrugia, "ORTEP-3 for windows—a version of ORTEP-III with a graphical user interface (GUI)," *Journal of Applied Crystallography*, vol. 30, no. 5, p. 565, 1997.
- [44] A. Hegmans, E. Freisinger, E. Zangrando, et al., "Tris- and tetrakis(1-methylcytosine) complexes of Pt(II): syntheses and X-ray structures of [Pt(1-MeC-N3)₃Cl]⁺ and [Pt(1-MeC-N3)₄]²⁺ compounds," *Inorganica Chimica Acta*, vol. 279, no. 2, pp. 152–158, 1998.
- [45] J. D. Orbell, L. G. Marzilli, and T. J. Kistenmacher, "Preparation, 1H NMR spectrum and structure of *cis*-diamminebis(1-methylcytosine)platinum(II) nitrate-1-methylcytosine. *Cis* steric effects in pyrimidine ring-bound *cis*-bis(nucleic acid base)platinum(II) compounds," *Journal of the American Chemical Society*, vol. 103, no. 17, pp. 5126–5133, 1981.
- [46] L. S. Hollis, M. M. Roberts, and S. J. Lippard, "Synthesis and structures of platinum(III) complexes of α -pyridone, [X(NH₃)₂Pt(C₅H₄NO)₂Pt(NH₃)₂X](NO₃)₂ · nH₂O, (X⁻ = Cl⁻, NO₂⁻, Br⁻)," *Inorganic Chemistry*, vol. 22, no. 24, pp. 3637–3644, 1983.
- [47] A. Erxleben, S. Metzger, J. F. Britten, C. J. L. Lock, A. Albinati, and B. Lippert, "Model of the most abundant DNA interstrand cross-link of transplatin: X-ray structures of two modifications and H bonding behavior in the solid state and in solution of *trans*-[Pt(NH₃)₂(1-MeC-N3)(9-EtGH-N7)](ClO₄)₂ · nH₂O (1-MeC=1-methylcytosine; 9-EtGH=9-ethylguanine)," *Inorganica Chimica Acta*, vol. 339, pp. 461–469, 2002.
- [48] B. Lippert, G. Raudaschl, C. J. L. Lock, and P. Pilon, "Real' model compounds for intrastrand cross-linking of two guanine bases by cisplatin: crystal structures of *cis*-diamminebis(9-ethylguanine-N7)platinum(II) dichloride trihydrate, [Pt(NH₃)₂(C₇H₉N₅O)₂]Cl₂ · 3H₂O, and *cis*-diamminebis(9-ethylguanine-N7)platinum(II) sesquichloride hemibicarbonate sesquihydrate, [Pt(NH₃)₂(C₇H₉N₅O)₂]Cl_{1.5}(HCO₃)_{0.5} · 1.5H₂O," *Inorganica Chimica Acta*, vol. 93, no. 1, pp. 43–50, 1984.
- [49] M. S. Ali, S. R. A. Khan, H. Ojima, et al., "Model platinum nucleobase and nucleoside complexes and antitumor activity: X-ray crystal structure of [Pt^{IV}(*trans*-1*R*,2*R*-diaminocyclohexane)*trans*-(acetate)₂(9-ethylguanine)Cl]NO₃ · H₂O," *Journal of Inorganic Biochemistry*, vol. 99, no. 3, pp. 795–804, 2005.
- [50] R. K. O. Sigel, M. Sabat, E. Freisinger, A. Mower, and B. Lippert, "Metal-modified base pairs involving different donor sites of purine nucleobases: *trans*-[a₂Pt(7,9-DimeG-N1)(9-EtGH-N7)]²⁺ and *trans*-[a₂Pt(7,9-DimeG-N1)(9-EtGH-N7)]⁺ (a = NH₃ or CH₃NH₂; 9-EtGH = 9-ethylguanine; 7,9-dimeg = 7,9-dimethylguanine). Possible relevance to metalated DNA triplex structures," *Inorganic Chemistry*, vol. 38, no. 7, pp. 1481–1490, 1999.
- [51] S. Shamsuddin, M. S. Ali, K. H. Whitmire, and A. R. Khokhar, "Synthesis characterization and X-ray crystal structures of *cis*-1,4-diaminocyclohexane-platinum(II) nucleobase adducts," *Polyhedron*, vol. 26, no. 3, pp. 637–644, 2007.
- [52] G. Kampf, M. Willermann, E. Zangrando, L. Randaccio, and B. Lippert, "Axial guanine binding to a diplatinum(III) core," *Chemical Communications*, no. 8, pp. 747–748, 2001.
- [53] G. Kampf, M. Willermann, E. Freisinger, and B. Lippert, "Diplatinum(III) complexes with bridging 1-methylcytosinate ligands and variable axial ligands, including guanine nucleobases," *Inorganica Chimica Acta*, vol. 330, no. 1, pp. 179–188, 2002.
- [54] M. C. Etter, "Encoding and decoding hydrogen-bond patterns of organic compounds," *Accounts of Chemical Research*, vol. 23, no. 4, pp. 120–126, 1990.
- [55] K. Aoki and Md. Abdu. Salam, "Interligand interactions affecting specific metal bonding to nucleic acid bases. A case of [Rh₂(OAc)₄], [Rh₂(HNOCCF₃)₄], and [Rh₂(OAc)₂ · (HNOCCF₃)₂] toward purine nucleobases and nucleosides," *Inorganica Chimica Acta*, vol. 339, pp. 427–437, 2002.
- [56] J. F. Britten, B. Lippert, C. J. L. Lock, and P. Pilon, "Platinum(II) complexes with terminal hydroxo and aquo groups: crystal structures of hydroxo-*cis*-diammine(1-methylcytosine-N3)platinum(II) nitrate dihydrate, [Pt(OH)(NH₃)₂(C₅H₇N₃O)]NO₃ · 2H₂O, and *cis*-diammineaquo(1-methylcytosine-N3)platinum(II) dinitrate hydrate, [Pt(NH₃)₂ · (H₂O)(C₅H₇N₃O)](NO₃)₂ · H₂O," *Inorganic Chemistry*, vol. 21, no. 5, pp. 1936–1941, 1982.
- [57] R. Faggiani, B. Lippert, C. J. L. Lock, and R. Pfab, "Crystal structure of *cis*-diammine(1-methylcytosine-N3)(thyminato-N1)platinum(II) perchlorate, *cis*-[Pt(NH₃)₂ · (C₅H₅N₂O₂)(C₅H₇N₃O)]ClO₄, and its 1H NMR and vibrational spectra and those of the corresponding mono- and trihydrates," *Inorganic Chemistry*, vol. 20, no. 8, pp. 2381–2386, 1981.
- [58] H. Schöllhorn, R. Beyerle-Pfner, U. Thewalt, and B. Lippert, "Unusual four-membered chelate rings of platinum(IV) with a cytosine nucleobase," *Journal of the American Chemical Society*, vol. 108, no. 13, pp. 3680–3688, 1986.
- [59] R. Taylor, O. Kennard, and W. Versichel, "Geometry of the N-H · · · O=C hydrogen bond. 2. Three-center (bifurcated) and four-center (trifurcated) bonds," *Journal of the American Chemical Society*, vol. 106, no. 1, pp. 244–248, 1984.

Research Article

Antioxidative Activity of Ferrocenes Bearing 2,6-Di-*Tert*-Butylphenol Moieties

E. R. Milaeva,¹ S. I. Filimonova,¹ N. N. Meleshonkova,¹ L. G. Dubova,² E. F. Shevtsova,² S. O. Bachurin,² and N. S. Zefirov¹

¹Organic Chemistry Department, M.V. Lomonosov Moscow State University, 119991, Moscow, Russia

²Institute of Physiologically Active Compounds, Russian Academy of Sciences, 142432, Chernogolovka, Russia

Correspondence should be addressed to E. R. Milaeva, milaeva@org.chem.msu.ru

Received 28 December 2009; Accepted 30 March 2010

Academic Editor: Spyros Perlepes

Copyright © 2010 E. R. Milaeva et al. This is an open access article distributed under the Creative Commons Attribution License, which permits unrestricted use, distribution, and reproduction in any medium, provided the original work is properly cited.

The antioxidative activity of ferrocenes bearing either 2,6-di-*tert*-butylphenol or phenyl groups has been compared using DPPH (1,1-diphenyl-2-picrylhydrazyl) test and in the study of the in vitro impact on lipid peroxidation in rat brain homogenate and on some characteristics of rat liver mitochondria. The results of DPPH test at 20°C show that the activity depends strongly upon the presence of phenolic group but is improved by the influence of ferrocenyl fragment. The activity of N-(3,5-di-*tert*-butyl-4-hydroxyphenyl)iminomethylferrocene (**1**), for instance, was 88.4%, which was higher than the activity of a known antioxidant 2,6-di-*tert*-butyl-4-methylphenol (BHT) (48.5%), whereas the activity of N-phenyl-iminomethylferrocene **2** was almost negligible –2.9%. The data obtained demonstrate that the compounds with 2,6-di-*tert*-butylphenol moiety are significantly more active than the corresponding phenyl analogues in the in vitro study of lipid peroxidation in rat brain homogenate. Ferrocene **1** performs a promising behavior as an antioxidant and inhibits the calcium-dependent swelling of mitochondria. These results allow us to propose the potential cytoprotective (neuroprotective) effect of ditopic compounds containing antioxidant 2,6-di-*tert*-butylphenol group and redox active ferrocene fragment.

1. Introduction

Oxidative stress has been found to play a critical role in numerous disease conditions including neurodegeneration [1–3].

The antioxidative defense system in living organism regulates a disturbance in the prooxidant-antioxidant balance and protects the cell damage induced by high level of oxidative stress. Among the classes of well-known natural antioxidants-vitamins E group, ascorbic acid, glutathione, and so forth, α -tocopherol and its synthetic analogues, sterically hindered phenols, are of particular importance [4]. The substituted 2,6-dialkylphenols are widely used as inhibitors of free radicals formation in the oxidative destruction of natural and synthetic substrates. The mechanism of their physiological action is associated with the stable phenoxyl radicals' formation in the process of hydrogen atom abstraction by highly reactive peroxy radicals of lipids [5].

The goal of this study was to optimize the effect of 2,6-di-*tert*-butylphenol and to increase the stability of

the corresponding phenoxyl radicals responsible for their antioxidative activity. The approach based on modification of phenolic antioxidants *via* incorporation of ferrocenyl moiety in their molecules seems to be a promising one. Previously we have reported the synthesis, electrochemical characteristics, and ESR study of novel ferrocenes with redox active 2,6-di-*tert*-butylphenol fragments (compounds **1,3**) [6]. These compounds exhibit the properties of multistep redox systems, and the intramolecular electron transfer between two redox active sites of the molecule (the phenol and ferrocene groups) was observed. The high stability of phenoxyl radical species formed in the oxidation is in agreement with a certain degree of electronic delocalization over the molecule.

On the other hand, the ferrocene derivatives show a wide spectrum of physiological activity [7–9].

The incorporation of ferrocene into an anticancer drug tamoxifen, a selective estrogen receptor modulator, containing phenol was reported. The activity of these novel ferrocene derivatives (ferrocifens) was found to be associated with the

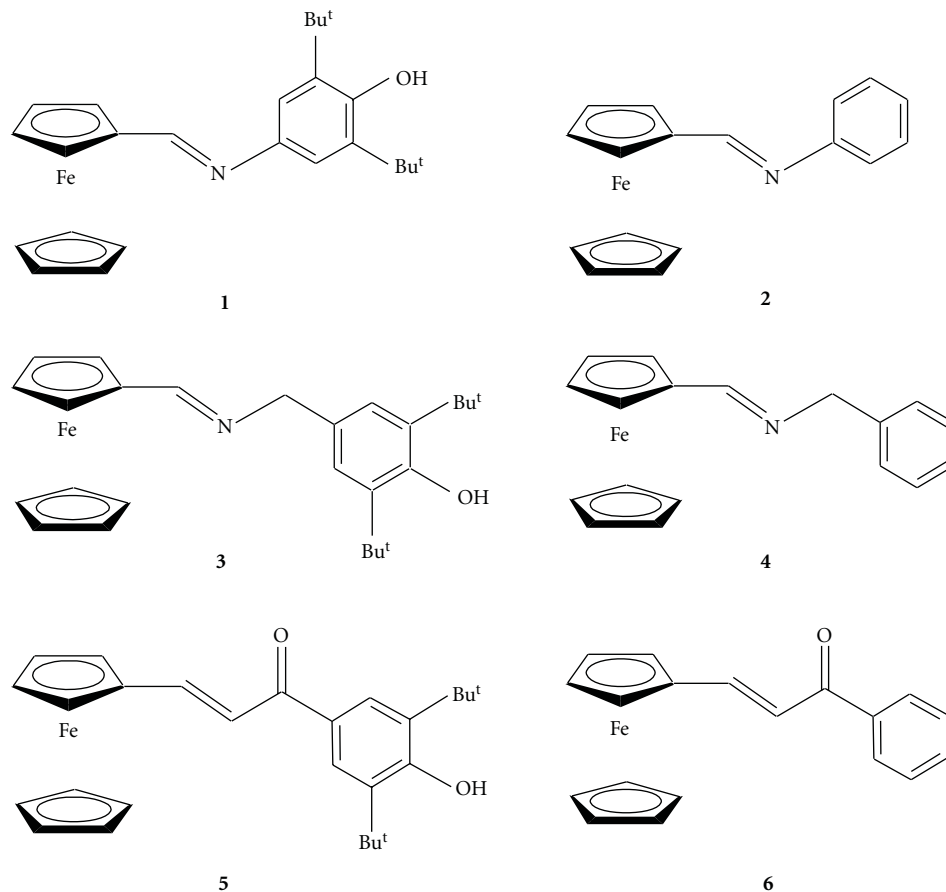


FIGURE 1: Structures of compounds 1–6.

proton-coupled electron transfer between ferrocenium ion and phenol group that occurs in their oxidized species [10–12].

The antioxidative activity in scavenging of superoxide radical-anion $O_2^{\cdot-}$ and HO^{\cdot} radical was observed for recently synthesized ferrocenes containing nitroxides radicals as substituents [13].

As it has been reported earlier, diselenides having redox-active ferrocenyl units show peroxidase-like antioxidant activity mimicking selenoenzyme glutathione peroxidase that protects the cell membranes from oxidative damage [14].

In our previous study, we have observed the modulation of the antioxidative effect of metalloporphyrins bearing 2,6-di-*tert*-butylphenol pendants by the metal nature [15].

In this study we compared the antioxidative activity of 1–6 presenting the pairs of compounds bearing either 3,5-di-*tert*-butyl-4-hydroxyphenyl or phenyl substituents linked to the ferrocene by various spacers (Figure 1).

2. Materials and Methods

2.1. Ferrocenes. N-(3,5-di-*tert*-butyl-4-hydroxyphenyl)-iminomethylferrocene (1), N-phenyl-iminomethylferrocene (2), N-(3,5-di-*tert*-butyl-4-hydroxybenzyl)-iminomethylferrocene (3), N-benzyliminomethylferrocene (4), (3,5-di-*tert*-

butyl-4-hydroxyphenyl)-3-ferrocenylpropen-2-on (5), and phenyl-3-ferrocenylpropen-2-on (6) were synthesized as described previously [6, 16].

2.2. DPPH Radical Scavenging Activity. The free radical-scavenging activity was evaluated using the stable radical DPPH, according to the method described by Brand-Williams et al. [17] with a slight modification.

Each compound was tested for antioxidant activity against DPPH radical at a molar 1:1 ratio. One mL of antioxidant solution in methanol was added to 1 mL of DPPH solution in methanol so that the final DPPH and antioxidant concentration can be 0.1 mM. The samples were incubated for 30 minutes at 20°C in methanol and the decrease in the absorbance of DPPH solution was measured at 517 nm, using a Thermo Evolution 300 BB spectrophotometer. The results were expressed as scavenging activity, calculated as follows:

$$\text{Scavenging activity, \%} = \left[\frac{(A_0 - A_1)}{A_0} \right] \times 100. \quad (1)$$

The concentration of antioxidant needed to decrease 50% of the initial substrate concentration (EC_{50}) is a parameter widely used to measure the antioxidant effect [18]. For determination of EC_{50} , the values of DPPH solution

absorbance which decrease after 30 minutes were used. The EC_{50} values were calculated graphically by plotting scavenging activity against compound concentration. Different sample concentrations (0.01, 0.02, 0.05, and 0.1 mM) were used in order to obtain kinetic curves and to calculate the EC_{50} values. The lower EC_{50} means the higher antioxidant activity.

2.3. Rat Brain Homogenates (RBH) and Rat Liver Mitochondria (RLM) Preparation. On the day of the experiment, adult Wistar male rats fasted overnight were euthanized in a CO_2 -chamber followed by decapitation. The procedure was in compliance with the Guidelines for Animal Experiments at Institute of Physiologically Active Compounds of Russian Academy of Sciences.

The brains were rapidly removed and homogenized in 0.12 M HEPES/0.15 M NaCl, pH 7.4 buffer (HBS) (10 mg/gr wet weight) and used immediately for assay.

Mitochondria were isolated from homogenates of livers of adult Wistar strain rats, fasted overnight, in a 5 mM HEPES buffer, pH 7.4, containing 210 mM mannitol, 70 mM sucrose, and 1 mM EDTA, by conventional differential centrifugation [19].

Protein concentrations in RBH and RLM were determined by the biuret assay using bovine serum albumin as a standard [20].

2.4. Fe^{3+} -Induced Lipid Peroxidation Assay. The extent of lipid peroxidation (LP) was estimated by the levels of malondialdehyde measured using the thiobarbituric acid reactive substances (TBARS) assay. Isolated mitochondria are metabolically active and tightly coupled as shown by respiratory control ratio values, which were about 4 with glutamate-malate as substrate as measured by mitochondrial oxygen consumption at Oroboros oxygraph (Anton Paar, Austria) in a medium containing 10 mM KH_2PO_4 (or NaH_2PO_4), 60 mM KCl, 60 mM Tris, 5 mM $MgCl_2$, 110 mM mannitol, and 0.5 mM EDTA- Na_2 , pH 7.4.

Study of compounds influence on LP of the RBH was carried out at 30 °C for 40 minutes in 0.25 mL of the RBH in HBS (2 mg of protein · mL⁻¹) in the presence or absence of compounds or vehicle (DMSO). LP was induced by using Fe^{3+} (0.5 mM $Fe(NH_4)(SO_4)_2$) as an oxidizing agent [21]. Then 0.25 mL aliquots were mixed with 0.5 mL thiobarbituric acid (TBA) medium containing 250 mM HCl, 15% trichloroacetic acid, and 3 mM TBA, heated at 95 °C for 15 minutes, cooling at 4 °C then probes centrifuged (10 minutes at 10 000 g) and the supernatants transferred into 96-plate and absorbance was measured at 530–620 nm at the Wallac Victor 1420 Multilabel Counter (PerkinElmer Wallac).

All the experiments were performed using four independent experiments with different brain homogenate preparations. Data are normalized to control probe with oxidant as 100% and blank probe with diluent but without oxidizing agent. Preliminary experiments were done in the absence of compounds interaction with thiobarbituric acid. The values are expressed as mean% ± SD. The concentrations of ferrocenes giving half-maximal inhibition (IC_{50}) of LP were determined by dose-effect analysis.

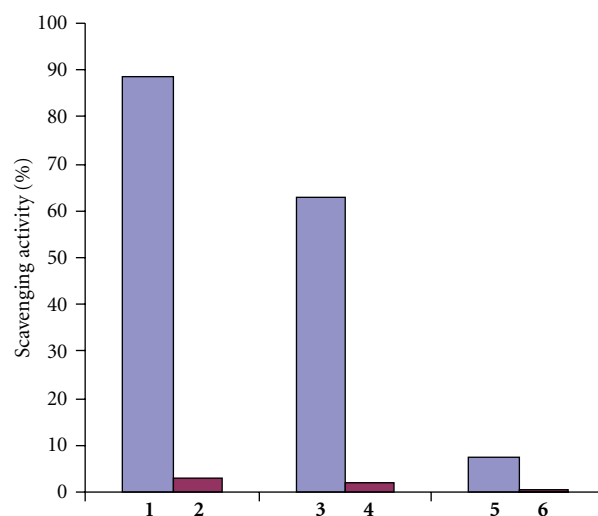


FIGURE 2: Scavenging activity for compounds 1–6 in DPPH test (MeOH, 20 °C, 100 μ M).

2.5. Mitochondrial Swelling Assay. Mitochondrial swelling caused by influx of solutes through open mitochondrial permeability transition (MPT) pores results in an increase in light transmission (i.e., a reduced turbidity). This turbidity change offers a convenient and frequently used assay of the MPT by measurement of absorbance in mitochondrial suspensions. The MPT induced by Ca^{2+} was monitored by absorbance changes at 540 nm in a Beckman DU 640 spectrophotometer in 1 mL of buffer A plus 0.8 μ M rotenone, 5 mM succinate, 1 mM KH_2PO_4 , and 0.5 mg protein of isolated liver mitochondria at 30 °C and continuous stirring [19]. Swelling rate is quantified as $\Delta A_{540}/\text{min}/\text{mg}$, calculated, in all cases, from a tangent to the steepest portion of the plot of A_{540} versus time.

2.6. Measurement of Mitochondrial Membrane Potential. The same experimental conditions were used for the assessment of alterations of the mitochondrial membrane potential, except that safranin was included in incubation medium at a final concentration of 10 μ M and succinate was added after the compound. This concentration of safranin was determined before hand as the optimal compromise between signal/baseline ratio and interference of safranin itself with swelling induced by Ca/Pi (safranin tended to enhance Ca/Pi-induced swelling at concentrations above 20 μ M) [19]. Changes in the status of the MPT pore are assessed spectrophotometrically at 524 versus 554 nm in a Beckman DU 640 spectrophotometer at 30 °C and continuous stirring.

3. Results and Discussion

We have compared the antioxidative activity of 1–6 presenting the pairs of compounds bearing either 3,5-di-*tert*-butyl-4-hydroxyphenyl or phenyl substituents linked to the ferrocene by various spacers (Figure 1).

The scavenging activity has been studied in the process of hydrogen atom transfer to the stable free radical DPPH

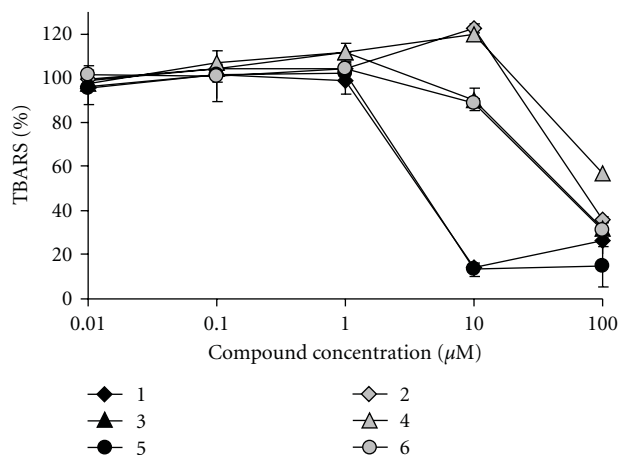


FIGURE 3: The relative content of TBARS in the lipid peroxidation of rat brain homogenates as nonenzymatic process in the presence of 10 μM 1–6 (0.5 mM $\text{Fe}(\text{NH}_4)(\text{SO}_4)_2$).

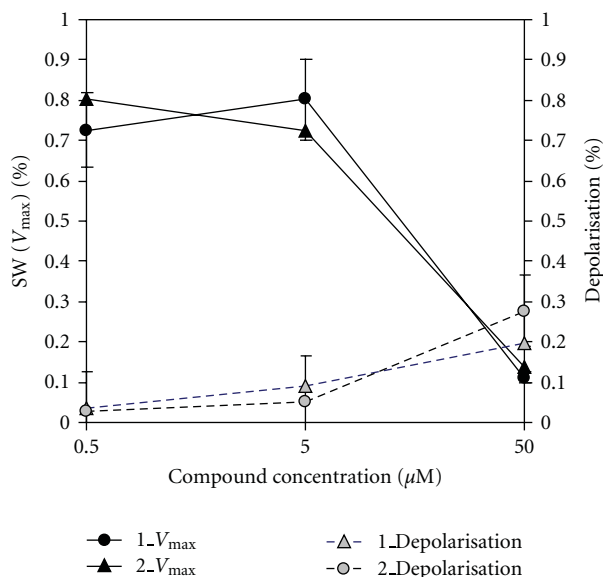


FIGURE 4: Influence of 0.1 mM ferrocenes 1 and 2 on mitochondrial swelling and transmembrane potential (the values were determined and expressed as % of control).

[22]. The results of DPPH test at 20°C show that the activity depends strongly upon the presence of phenolic group in the presented pairs of compounds. The activity of 1, for instance, was 88.4% that is higher than that of a known antioxidant 2,6-di-*tert*-butyl-4-methylphenol (BHT) (48.5%) whereas the activity of 2 bearing phenyl substituent was almost negligible –2.9% (Figure 2). The values of scavenging activity of compounds 3, 5 were lower, and in the case of 3 the decrease in activity was more pronounced. Evidently the activity extent of the compounds tested depends on their molecular structures. The HO-group of 2,6-di-*tert*-butylphenol is the key site in the molecule that is involved in hydrogen transfer to DPPH. However, despite the presence of ferrocene moiety in all the compounds

TABLE 1: The values of IC_{50} in the antioxidative activity assay in rat brain homogenates for compounds 1–6.

Compound	IC_{50} μM (0.5 mM $\text{Fe}(\text{NH}_4)(\text{SO}_4)_2$)
1	3.7 ± 1.0
2	70.4 ± 11.1
3	47.3 ± 2.4
4	100 ± 15.0
5	3.9 ± 1.8
6	47.8 ± 1.6

they differ significantly containing linkers of various length and conjugation ability ($-\text{CH}=\text{N}-$, 1; $-\text{CH}=\text{N}-\text{CH}_2-$, 2; $-\text{CH}=\text{CH}-\text{C}(\text{O})-$, 3). The decrease of conjugation in their molecules containing either CH_2 or CO groups in linkers leads to the decrease of metal influence on the stability of radicals formed as it has been observed previously [6]. However, it should be mentioned that the activity of 3 is much higher than that of 5 with N atom possessing a lone electron pair in linker that improves the influence of ferrocene moiety.

To compare the activity of compounds under investigation with that of widely known antioxidant parameter, EC_{50} was determined for the more efficient ferrocene 1 and 2,6-di-*tert*-butyl-4-methylphenol (BHT). EC_{50} values after 30 minutes of experiment at 20°C for 1 and BHT are 34.6 and 105.4 μM , respectively. Therefore, the result obtained shows a more pronounced effect of ferrocenyl derivative of 2,6-di-*tert*-butylphenol.

In order to study the antioxidant effect of ferrocenes 1–6 in biologically significant *in vitro* test system, we have investigated the compounds influence on Fe^{3+} -induced peroxidation of brain homogenate lipids (LP) as a nonenzymatic process by addition of $(\text{NH}_4)\text{Fe}(\text{SO}_4)_2$. The level of LP was followed by the accumulation of products that reacted with thiobarbituric acid—TBARS. The samples of Wistar strain rats homogenates were divided as following: one control homogenate and samples of homogenate with addition of compounds under investigation. TBARS concentrations were determined in homogenates by measuring the intensity of the solution color at 530 nm using UV-VIS spectroscopy [23].

The data of antioxidative activity assay of 1–6 presenting the pairs of compounds bearing either 3,5-di-*tert*-butyl-4-hydroxyphenyl or phenyl substituents linked to the ferrocene by various spacers are shown in Figure 3. The IC_{50} values are summarized in Table 1.

The data of antioxidative activity assay of ferrocenes 1–6 indicate the influence of 2,6-di-*tert*-butylphenol group as it was observed in DPPH test. Ferrocene 1 performs an effective inhibitory action in concentrations range at 10–100 μM (Figure 3, curve 1). The decrease in peroxidation level is more than 10%.

In contrast to DPPH test, the data of this assay reveal the antioxidant activity of all studied compounds. These results allow us to suggest that the ferrocene moiety participates in antioxidative potential of these compounds. However,

the compounds **1**, **3**, **5** bearing 2,6-di-*tert*-butylphenol are significantly more active than the corresponding phenyl analogues. This effect is most obvious at concentration 10 μM of compounds (Figure 3). Moreover, at this concentration some pro-oxidant effect of compounds **2** and **4** could be observed. This fact might be associated with the influence of iron center in the molecules of ferrocenes that participates in redox processes and therefore promotes the peroxidation.

The involvement of ferrocene group in the peroxidation process might be associated with the oxidation of Fe^{2+} to Fe^{3+} in the oxidative medium that leads to the formation of ferrocenium cation. As it was proved earlier [24] ferrocenium cations react easily with molecular oxygen and produce reactive peroxy radical cations. On the other hand, in the presence of antioxidant, namely BHT, ferrocenium cation can be stabilized due to the reduction that takes place between the cation and antioxidant. The principal consequence of this electron/proton coupled reaction is the reversibility of ferrocene/ferrocenium redox system. This fact might support the proposition of the intramolecular redox process in ferrocene species containing 2,6-di-*tert*-butylphenol fragment (compounds **1**, **3**, **5**).

To study proapoptotic/antiapoptotic effect of ferrocene **1** with 2,6-d-*tert*-butylphenol group which shows the more promising activity in both tests and to compare it with the effect of its analog **2** bearing phenyl substituent, we have investigated the influence of these compounds on two main characteristics of mitochondria: calcium-induced mitochondrial swelling (SW) that represents the mitochondrial permeability pores opening (which causes cell death), and mitochondrial membrane potential.

It was shown that at concentration 0.1 mM ferrocenes **1** and **2** slightly depolarize the mitochondria (up to 25%) (Figure 4). On the other hand, these compounds inhibit the calcium-dependent swelling of mitochondria and this effect could not be the consequence of the depolarisation only. In both cases the effects on mitochondrial swelling and mitochondrial membrane potential obtained for ferrocene **1** are less pronounced than for **2**. These data allow us to propose the potential cytoprotective (neuroprotective) effect of compounds studied.

4. Conclusion

The antioxidative activity of ferrocenes bearing either 2,6-di-*tert*-butylphenol or phenyl groups, studied using DPPH test, depends strongly upon the presence of phenol group and the conjugation between peroxy radical formed and ferrocene unit. The compounds **1**, **3**, **5** bearing 2,6-di-*tert*-butylphenol are significantly more active than the corresponding phenyl analogues in the in vitro lipid peroxidation in rat brain homogenate. N-(3,5-di-*tert*-butyl-4-hydroxyphenyl)-iminomethylferrocene (**1**) performs a promising behavior as an antioxidant and inhibits the calcium-dependent swelling of mitochondria. The results allow us to propose the potential cytoprotective (neuroprotective) effect of ditopic compounds containing antioxidant 2,6-di-*tert*-butylphenol group and redox active ferrocene fragment.

Abbreviations

BHT:	butylated hydroxytoluene (2,6-di- <i>tert</i> -butyl-4-methylphenol)
DPPH:	1,1-diphenyl-2-picrylhydrazyl (α,α -diphenyl- β -picrylhydrazyl)
HBS:	HEPES buffered saline
LP:	lipid peroxidation
MPT:	mitochondrial permeability transition
RBH:	rat brain homogenate
RLM:	rat liver mitochondria
TBA:	thiobarbituric acid
TBARS:	thiobarbituric acid reactive substances.

Acknowledgments

The financial support of RFBR (Grants 08-03-00844, 09-03-00090, 09-03-12261, and 10-03-01137) and the program N9 "Biomolecular and Medicinal Chemistry" of Russian Academy of Sciences are gratefully acknowledged.

References

- [1] L. Migliore and F. Coppedè, "Environmental-induced oxidative stress in neurodegenerative disorders and aging," *Mutation Research*, vol. 674, no. 1-2, pp. 73–84, 2009.
- [2] H. Kozłowski, A. Janicka-Kłos, J. Brasun, E. Gaggelli, D. Valensin, and G. Valensin, "Copper, iron, and zinc ions homeostasis and their role in neurodegenerative disorders (metal uptake, transport, distribution and regulation)," *Coordination Chemistry Reviews*, vol. 253, no. 21-22, pp. 2665–2685, 2009.
- [3] R. R. Crichton and R. J. Ward, *Metal-Based Neurodegeneration. From Molecular Mechanisms to Therapeutic Strategies*, John Wiley & Sons, Chichester, UK, 2006.
- [4] E. Denisov, *Handbook of Antioxidants*, CRC Press, Boca Raton, Fla, USA, 1995.
- [5] E. Niki, Y. Yoshida, Y. Saito, and N. Noguchi, "Lipid peroxidation: mechanisms, inhibition, and biological effects," *Biochemical and Biophysical Research Communications*, vol. 338, no. 1, pp. 668–676, 2005.
- [6] N. N. Meleshonkova, D. B. Shpakovsky, A. V. Fionov, A. V. Dolganov, T. V. Magdesieva, and E. R. Milaeva, "Synthesis and redox properties of novel ferrocenes with redox active 2,6-di-*tert*-butylphenol fragments: the first example of 2,6-di-*tert*-butylphenoxyl radicals in ferrocene system," *Journal of Organometallic Chemistry*, vol. 692, no. 24, pp. 5339–5344, 2007.
- [7] G. Jaouen, Ed., *Bioorganometallics. Biomolecules, Labeling, Medicine*, Wiley-VCH, New York, NY, USA, 2006.
- [8] D. R. van Staveren and N. Metzler-Nolte, "Bioorganometallic chemistry of ferrocene," *Chemical Reviews*, vol. 104, no. 12, pp. 5931–5985, 2004.
- [9] "The bioorganometallic chemistry of ferrocene," in *Ferrocenes: Ligands, Materials and Biomolecules*, P. Stepnicka, Ed., pp. 499–639, John Wiley & Sons, New York, NY, USA, 2008.
- [10] E. Hillard, A. Vessières, L. Thouin, G. Jaouen, and C. Amatore, "Ferrocene-mediated proton-coupled electron transfer in a series of ferrocifen-type breast-cancer drug candidates," *Angewandte Chemie International Edition*, vol. 45, no. 2, pp. 285–290, 2005.
- [11] A. Vessières, S. Top, W. Beck, E. Hillard, and G. Jaouen, "Metal complex SERMs (selective oestrogen receptor modulators).

- The influence of different metal units on breast cancer cell antiproliferative effects," *Dalton Transactions*, no. 4, pp. 529–541, 2006.
- [12] A. Vessières, S. Top, P. Pigeon, et al., "Modification of the estrogenic properties of diphenols by the incorporation of ferrocene. Generation of antiproliferative effects in vitro," *Journal of Medicinal Chemistry*, vol. 48, no. 12, pp. 3937–3940, 2005.
- [13] X. Qiu, H. Zhao, and M. Lan, "Novel ferrocenyl nitroxides: synthesis, structures, electrochemistry and antioxidative activity," *Journal of Organometallic Chemistry*, vol. 694, no. 24, pp. 3958–3964, 2009.
- [14] G. Mugesh, A. Panda, H. B. Singh, N. S. Punekar, and R. J. Butcher, "Diferrocenyl diselenides: excellent thiol peroxidase-like antioxidants," *Chemical Communications*, no. 20, pp. 2227–2228, 1998.
- [15] E. R. Milaeva, O. A. Gerasimova, Z. Jingwei, et al., "Synthesis and antioxidative activity of metalloporphyrins bearing 2,6-di-*tert*-butylphenol pendants," *Journal of Inorganic Biochemistry*, vol. 102, no. 5–6, pp. 1348–1358, 2008.
- [16] V. Yu. Tyurin, A. P. Gluchova, N. N. Meleshonkova, and E. R. Milaeva, "Electrochemical method of antioxidative activity assay based on DPPH test," submitted to *Russian Chemical Bulletin*.
- [17] W. Brand-Williams, M. E. Cuvelier, and C. Berset, "Use of a free radical method to evaluate antioxidant activity," *Food Science and Technology*, vol. 28, no. 1, pp. 25–30, 1995.
- [18] P. Molyneux, "The use of the stable free radical diphenylpicrylhydrazyl (DPPH) for estimating antioxidant activity," *Songklanakarin Journal of Science and Technology*, vol. 26, no. 2, pp. 211–219, 2004.
- [19] I. V. Serkov, E. F. Shevtsova, L. G. Dubova, et al., "Interaction of docosahexaenoic acid derivatives with mitochondria," *Doklady Biological Sciences*, vol. 414, no. 1, pp. 187–189, 2007.
- [20] A. G. Gornall, C. J. Bardawill, and M. M. David, "Determination of serum proteins by means of the biuret reaction," *Journal of Biological Chemistry*, vol. 177, pp. 751–766, 1949.
- [21] J. K. Callaway, P. M. Beart, and B. Jarrott, "A reliable procedure for comparison of antioxidants in rat brain homogenates," *Journal of Pharmacological and Toxicological Methods*, vol. 39, no. 3, pp. 155–162, 1998.
- [22] M. C. Foti, C. Daquino, I. D. Mackie, G. A. DiLabio, and K. U. Ingold, "Reaction of phenols with the 2,2-diphenyl-1-picrylhydrazyl radical. Kinetics and DFT calculations applied to determine ArO-H bond dissociation enthalpies and reaction mechanism," *Journal of Organic Chemistry*, vol. 73, no. 23, pp. 9270–9282, 2008.
- [23] C. Paquot and A. Hantfenne, *Standard Methods for the Analysis of Oils, Fats and Derivatives*, Blackwell Scientific, Oxford, UK, 7th edition, 1987.
- [24] J. P. Hurvois and C. Moinet, "Reactivity of ferrocenium cations with molecular oxygen in polar organic solvents: decomposition, redox reactions and stabilization," *Journal of Organometallic Chemistry*, vol. 690, no. 7, pp. 1829–1839, 2005.

Research Article

Studies of the Antiproliferative Activity of Ruthenium (II) Cyclopentadienyl-Derived Complexes with Nitrogen Coordinated Ligands

Virtudes Moreno,¹ Julia Lorenzo,² Francesc X. Aviles,² M. Helena Garcia,³ João P. Ribeiro,^{3,4} Tânia S. Morais,³ Pedro Florindo,³ and M. Paula Robalo^{5,6}

¹ Department de Química Inorgànica, Universitat de Barcelona, Martí y Franquès 1-11, 08028 Barcelona, Spain

² Institut de Biotecnologia i de Biomedecina, Universitat Autònoma de Barcelona, Bellaterra, 08193 Barcelona, Spain

³ Centro de Ciências Moleculares e Materiais, Faculdade de Ciências da Universidade de Lisboa, Campo Grande, 1749-016 Lisboa, Portugal

⁴ Centro de Investigaciones Biológicas, CSIC, Ramiro de Maeztu 9, 28040 Madrid, Spain

⁵ Centro de Química Estrutural, Complexo I, Instituto Superior Técnico, Avenue Rovisco Pais, 1049-001 Lisboa, Portugal

⁶ Departamento de Engenharia Química, Instituto Superior de Engenharia de Lisboa, Avenue Conselheiro Emídio Navarro, 1, 1959-007 Lisboa, Portugal

Correspondence should be addressed to Virtudes Moreno, virtudes.moreno@qi.ub.es

Received 9 February 2010; Accepted 20 April 2010

Academic Editor: Spyros P. Perlepes

Copyright © 2010 Virtudes Moreno et al. This is an open access article distributed under the Creative Commons Attribution License, which permits unrestricted use, distribution, and reproduction in any medium, provided the original work is properly cited.

Four cationic ruthenium(II) complexes with the formula $[\text{Ru}(\eta^5\text{-C}_5\text{H}_5)(\text{PPh}_3)_2]^+$, with L = 5-phenyl-1H-tetrazole (TzH) **1**, imidazole (ImH) **2**, benzo[1,2-b;4,3-b'] dithio-phen-2-carbonitrile (Bzt) **3**, and [5-(2-thiophen-2-yl)-vinyl]-thiophene-2-carbonitrile] (Tvt) **4** were prepared and characterized in view to evaluate their potentialities as antitumor agents. Studies by Circular Dichroism indicated changes in the secondary structure of ct-DNA. Changes in the tertiary structure of pBR322 plasmid DNA were also observed in gel electrophoresis experiment and the images obtained by atomic force microscopy (AFM) suggest strong interaction with pBR322 plasmid DNA; the observed decreasing of the viscosity with time indicates that the complexes do not intercalate between DNA base pairs. Compounds **1**, **2**, and **3** showed much higher cytotoxicity than the cisplatin against human leukaemia cancer cells (HL-60 cells).

1. Introduction

The driving force for the studies of metal-based drugs in the treatment of cancer has been certainly the enormous impact of cisplatin. This platinum complex continues to be applied in 50%–70% of all cancer patients, usually in combination with other drugs [1]. Nevertheless, the undesirable side-effects of cisplatin, its inactivity against many cancer cell lines and tumors metastasis [2] has stimulated the search for new effective drugs, in the field of nonplatinum-based anticancer drugs [3–5]. Although the promising results for compounds derived of several metals such as titanium [6], iron [7], gold [8], gallium [9], and tin [10], it appears that the ruthenium derivatives occupy already a prominent position

due to success of $[\text{ImH}][\text{trans-RuCl}_4(\text{DMSO})\text{Im}]$, NAMI-A, $[\text{ImH}][\text{trans-RuCl}_4\text{Im}_2]$ (Im = imidazole) and (Hind) $[\text{trans-RuCl}_4(\text{ind})_2]$, and KP1019, (ind = indazole) in progressing through clinical trials [11–13]. The main drawback of the coordination compounds concerning clinical trials has been related to their instability and complicated ligand exchange chemistry. Thus, organometallic field appeared as an attractive field to provide organoruthenium complexes as suitable drug candidates. Under this perspective, the studies already reported are quite promising, in some families of ruthenium η^6 -arene derivatives which were found active against hypotoxic tumor cells [14, 15], in vitro breast and colon carcinoma cells [16, 17], inhibition of the growth of the human ovarian cancer cells line A2780 [18], and mammary

cancer cell line [19]. Studies on π -arene compounds have been recently reviewed [20, 21]. Although the literature is scarce in studies concerning ruthenium η^5 -cyclopentadienyl (RuCp) derivatives, it appears of interest the results already found for compounds containing the “CpRu(CO)” fragment and pyridocarbazole derived ligands which revealed to be potent and selective inhibitors for protein kinases GSK-3 and Pim-1 [22].

Our approach in this field has been the study of compounds derived of “RuCp” containing N-heteroaromatic sigma coordinated ligands [23] and CpRu(η^6 -arene) where the structures of the η^6 -arene ligands were based on two or three fused rings [24]. Our studies by AFM revealed a strong interaction with the plasmid pBR322 DNA. The obtained images showed compaction, supercoiling and kinks in the DNA forms. Circular Dichroism and viscosity measurements on ct-DNA also indicated that the complexes interact with the double helix. Compounds **1**, **2**, and **3** showed much higher cytotoxicity than the cisplatin against human leukaemia cancer cells (HL-60 cells). The compound **4** gave a lower IC₅₀ value than cisplatin at 24 hours and a similar value at 72 hours. Moreover, some other CpRu compounds previously studied showed also significant effect of toxicity in Lovo and MiaPaCa cells in the nanomolar range [23].

2. Results and Discussion

Our continuing studies on the family of [Ru(η^5 -C₅H₅)(PP)]⁺ fragment containing complexes in view of studies of cytotoxicity led us to the synthesis of two new cationic complexes of the type [Ru(η^5 -C₅H₅)(PPh₃)₂L]⁺ where the metal atom is σ bound to the donor nitrogen atom of the heteroaromatic ligands L = 5-phenyl-1H-tetrazole (TzH) and imidazole (ImH).

Having in mind that different structures of the coordinated molecule L, can lead to different interactions with DNA, two other known compounds were also prepared and studied. One of these compounds presents the ligand L as a wide planar system based on a thiophene-benzene-thiophene ortho-fused rings structure, namely, benzo[1, 2-b; 4, 3-b']dithio-phen-2-carbonitrile [25] (**Bzt**), while the ligand of the other compound is based on a long planar structure, namely, [5-(2-thiophen-2-yl)-vinyl]-thiophene-2-carbonitrile (**Tvt**) [26].

The complexes [Ru(η^5 -C₅H₅)(PPh₃)₂L][PF₆] with L = 5-phenyl-1H-tetrazole (**1**) and imidazole (**2**) were prepared by the general method of halide abstraction of [Ru(η^5 -C₅H₅)(PPh₃)₂Cl] with thallium hexafluorophosphate in the presence of the adequate ligand (Scheme 1). The starting material [Ru(η^5 -C₅H₅)(PPh₃)₂Cl] was prepared according to the literature [27] and the mentioned ligands were used as purchased. Compounds [RuCp(PPh₃)₂(Bzt)][PF₆] **3** and [RuCp(PPh₃)₂(Tvt)][PF₆] **4** and the corresponding ligands were prepared and characterised following our previous publications [25, 26].

Compounds were obtained in good yields and recrystallized by slow diffusion of diethyl ether in dichloromethane solutions. The new compounds were fully characterized by

FT-IR, ¹H, ¹³C, and ³¹P NMR spectroscopies; elemental analyses were in accordance with the proposed formulations.

2.1. Spectroscopic Studies. The main feature on the ¹H NMR chemical shifts of the coordinated ligands is a general trend of shielding of the protons of the heteroaromatic rings with special relevance for the proton adjacent to the N coordinated atom. This effect, also observed on other related compounds [28], might be due to the influence of the organometallic moiety on the ring current of the heteroaromatic ligands.

Interestingly, compound **2** shows one signal at 11.53 ppm, integrating perfectly for one proton and attributed to the NH proton of imidazole which, in the same solvent, could not be found in the free imidazole. This observation is in good agreement with the observed shielding on the other protons of the heteroaromatic ring upon coordination. Accordingly, ¹³C NMR spectra showed a general deshielding up to 13.6 ppm on the carbons of the coordinated ligand, this effect being more pronounced on compound **2**.

The ³¹P NMR spectra revealed equivalency of both P atoms of the phosphines, with a singlet at ~42 ppm, with the expected deshielding upon coordination to the metal centre, and the septet relative to the counter ion PF₆⁻ at -144 ppm.

The FT-IR spectra typically showed the characteristic bands of the Cp and Ph aromatic rings in the region 3040–3080 cm⁻¹, and the characteristic bands of the PF₆ anion at 840 and 560 cm⁻¹.

2.2. Electrochemical Studies. The electrochemical properties of the ligands and the new Ru(II) complexes **1** and **2** were examined by cyclic voltammetry in acetonitrile and dichloromethane solutions (1 × 10⁻³ M) using 0.2 M tetrabutylammonium hexafluorophosphate (TBAPF₆) as supporting electrolyte. The redox potentials measured at the scan rate of 0.2 V/s are reported in Table 1. The electrochemical behaviour of complexes **3** and **4** was already reported [25, 26].

The cyclic voltammogram of TzH ligand is characterized by one irreversible redox process at E_{pa} = -0.69 V with the corresponding reductive wave at E_{pc} = -0.99 V in acetonitrile, being these values of -0.50 V and -0.80 V, respectively, in dichloromethane. Due to the insolubility of ImH in dichloromethane, its electrochemistry was only studied in acetonitrile and revealed two irreversible processes, one oxidation at E_{pa} = +1.42 V without the cathodic counterpart and one reduction at E_{pc} = -0.88 V without the corresponding anodic complement.

Both complexes were electroactive in the sweep range ±1.8 V and displayed one-electron quasi-reversible coupled redox wave in dichloromethane solution, as showed in Figure 1. The oxidative couple exhibited by the complexes **1** and **2** with E_{1/2} at 1.24 and 1.06 V, respectively, is attributed to the Ru(II)/Ru(III) redox process in accordance with our earlier results in some analogous ruthenium compounds [25, 26, 29], these values being lower than those found for complexes **3** and **4**. At negative potentials, it was not found any redox process that could be related with the

TABLE 1: Electrochemical data for the $[\text{RuCp}(\text{PPh}_3)_2\text{L}][\text{PF}_6]$ ($\text{L} = \text{TzH}, \text{ImH}$) complexes and the free ligands in dichloromethane and acetonitrile.

Dichloromethane					
Compound	E_{pa} (V)	E_{pc} (V)	$E_{1/2}$ (V)	ΔE^a (mV)	I_c/I_a
TzH	-0.50	-0.80	—	—	—
ImH^b	—	—	—	—	—
<u>1</u>	1.27	1.21	1.24	60	1.0
<u>2</u>	1.10	1.02	1.06	80	1.0
Acetonitrile					
Compound	E_{pa} (V)	E_{pc} (V)	$E_{1/2}$ (V)	ΔE^a (mV)	I_c/I_a
TzH	-0.69	-0.99	—	—	—
ImH	1.42	—	—	—	—
	—	-0.88	—	—	—
	1.22	—	—	—	—
<u>1</u>	0.86	—	—	—	—
	—	-0.70	—	—	—
	1.25	—	—	—	—
<u>2</u>	0.92	—	—	—	—
	—	-0.47	—	—	—

^a $\Delta E = E_{\text{pa}} - E_{\text{pc}}$; ^bInsoluble in dichloromethane.

TABLE 2: IC_{50} values of ruthenium compounds, and cisplatin against HL-60 cells.

Complex	IC_{50} (μM) 72 hours	IC_{50} (μM) 24 hours
$[\text{Ru}(\eta^5\text{-C}_5\text{H}_5)(\text{PPh}_3)_2\text{TzH}]^+ \mathbf{1}$	0.69 ± 0.16	0.95 ± 0.15
$[\text{Ru}(\eta^5\text{-C}_5\text{H}_5)(\text{PPh}_3)_2\text{ImH}]^+ \mathbf{2}$	0.53 ± 0.05	0.57 ± 0.09
$[\text{Ru}(\eta^5\text{-C}_5\text{H}_5)(\text{PPh}_3)_2\text{Bdt}]^+ \mathbf{3}$	0.94 ± 0.085	1.46 ± 0.25
$[\text{Ru}(\eta^5\text{-C}_5\text{H}_5)(\text{PPh}_3)_2\text{Tvt}]^+ \mathbf{4}$	2.26 ± 0.53	5.89 ± 0.67
CDDP	2.15 ± 0.1	15.61 ± 1.15

ligands. During the electrochemical study of complex **1** some passivation occurred at the platinum electrode, probably due to any potential-induced polymerisation processes in this solvent, originated by the ligand.

The electrochemical behaviour of the studied complexes in acetonitrile was quite different. The cyclic voltammograms were characterised by one first irreversible oxidation process at $E_{\text{pa}} = 0.86$ V and $E_{\text{pa}} = 0.92$ V for complexes **1** and **2** appearing a second irreversible oxidation process at $E_{\text{pa}} = 1.22$ V for complex **1** and $E_{\text{pa}} = 1.25$ V for complex **2**.

By analogy with the electrochemistry run in dichloromethane, this second anodic wave was attributed to the oxidation $\text{Ru}^{\text{II}}/\text{Ru}^{\text{III}}$ for the present studied complexes. In order to identify the species responsible for the first oxidation process, some additional experiments were carried out. It was postulated that the most likely candidate would be the cationic complex $[\text{RuCp}(\text{PPh}_3)_2(\text{NCMe})]^+$, originated in the electrochemical cell, by substitution of the 5-phenyl-1H-tetrazole and imidazole ligands by the acetonitrile coordinative solvent.

Experiments in the nmr tube, with a sample solution of compound **2** in CD_3CN revealed a slow substitution of the imidazole ligand by the solvent. In effect, only few

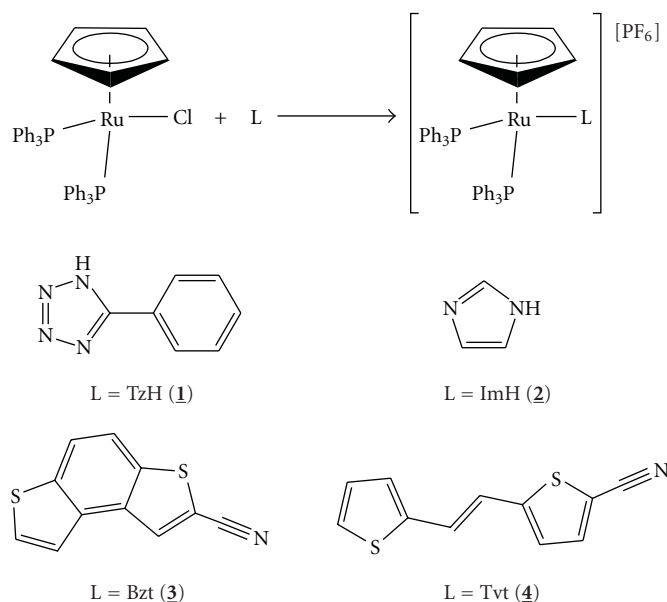
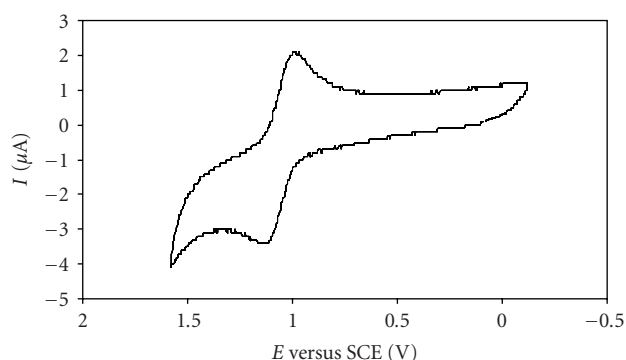
hours later a significant amount of the new compound was found in the ^1H and ^{31}P NMR spectra, being a conversion of about 90% found only 72 hours later. Although this slow substitution process is not likely to occur at the electrochemistry time scale, the electrochemistry of compound $[\text{RuCp}(\text{PPh}_3)_2(\text{NCMe})][\text{PF}_6]$, prepared in the bench for this purpose, was studied in the same experimental conditions of compounds **1** and **2** to discard this hypothesis. The voltammogram only revealed one oxidative process occurring at $\sim E_{\text{pa}} = 1.48$ V, attributed to the oxidation $\text{Ru}^{\text{II}}/\text{Ru}^{\text{III}}$.

Although no further experiments were carried out, it seems that one possible explanation for the waves occurring at $E_{\text{pa}} = 0.86$ V and $E_{\text{pa}} = 0.92$ V for complexes **1** and **2**, can be an irreversible oxidation occurring at the coordinated ligands.

The ligand-based reduction waves were found at $E_{\text{pc}} = -0.70$ V and -0.47 V for complexes **1** and **2**, respectively, while for the corresponding free ligands the values were $E_{\text{pc}} = -0.99$ V and -0.88 V. Thus, the corresponding potentials were in the order $\text{TzH} < \text{ImH} < \mathbf{1} < \mathbf{2}$, with the ruthenium complexes showing the most facile reductions. The stability of the pair $\text{Ru}^{\text{II}}/\text{Ru}^{\text{III}}$ showed by the electrochemical

TABLE 3: Percentage of HL-60 cells in each state after treatment with metal complexes at IC₅₀ concentration for 24 hours of incubation.

Treatment (IC ₅₀ 24 hours μM)	% vital cells (R1)	% apoptotic cells (R2)	% dead cells (R3)	% damaged cells (R4)
Control	91.1	4.8	3.9	0.2
CDDP	55.0	40.7	3.6	0.7
[Ru(η ⁵ -C ₅ H ₅)(PPh ₃) ₂ TzH] ⁺ 1	74.7	19.9	5.0	0.4
[Ru(η ⁵ -C ₅ H ₅)(PPh ₃) ₂ ImH] ⁺ 2	62.6	29.8	7.3	0.3
[Ru(η ⁵ -C ₅ H ₅)(PPh ₃) ₂ Bzt] ⁺ 3	60.0	20.8	13.3	5.9
[Ru(η ⁵ -C ₅ H ₅)(PPh ₃) ₂ Tvt] ⁺ 4	51.4	18.1	21.0	9.5

SCHEME 1: Reaction scheme for the synthesis of the [Ru(η⁵-C₅H₅)(PPh₃)₂(L)][PF₆] complexes **1–4** and the structures of the ligands L.FIGURE 1: Cyclic voltammogram of compound **2** in dichloromethane at sweep rate of 200 mV/s.

studies carried out in dichloromethane suggests the possible existence of Ru(III) analogues of compounds **1** and **2** which interest might be their potentiality as bio reductive prodrugs.

3. Biological Activity

3.1. Circular Dichroism. In Figures 2(a)–2(d), the circular dichroism spectra of the compounds at several molar ratio

ruthenium complex DNA are shown. After 24 hours of incubation at 37°C, changes in molar ellipticity can be observed for the complexes **1**, **2**, **3**, and **4**. These changes in the wavelength and the ellipticity of free DNA indicate modifications on the secondary structure of DNA as consequence of the interaction of the complexes with DNA. In spite of the substitution of ligands by N atoms of DNA bases could be possible, the most probable hypothesis is to consider weak interactions of the ligands with DNA through hydrogen bonds.

3.2. Atomic Force Microscopy (AFM). AFM pictures of DNA pBR322, and DNA incubated with the complexes **1–4** are shown in Figures 3–6.

The AFM image (Figure 3) corresponding to DNA incubated with compound **1** in comparison with free DNA shows typical modifications in the DNA forms, supercoiling, kinks and compaction. Compound **2** (Figure 4) also modifies DNA forms, although the appearance of kinks is more evident. In the case of compounds with the ligands Bzt and Tvt, compounds **3** and **4** (Figures 5 and 6, resp.) the interaction with DNA is stronger. In the case of compound **3**, the first image shows some DNA forms affected by supercoiling and kinks. In the two other images only a few

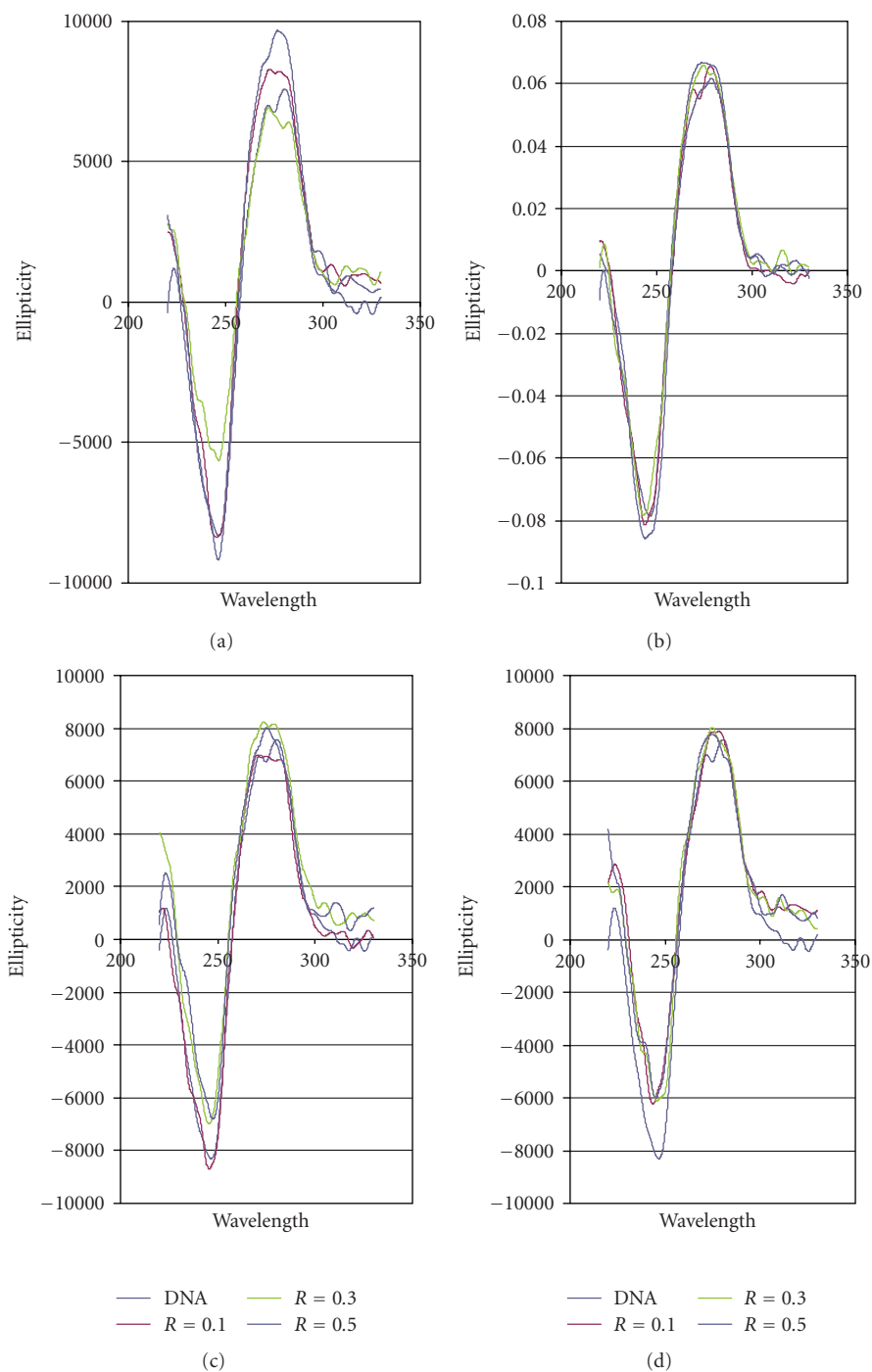


FIGURE 2: Circular Dichroism spectra of ct-DNA incubated with the complexes at molar ratios 0.1, 0.3, and 0.5, at 37°C for 24 hours (a) complex 1, (b) complex 2, (c) complex 3, and (d) complex 4.

forms can be observed but in them strong modification can be appreciated. Finally, in the case of compound **4**, the image shows several DNA forms with kinks and microfolds. These modifications in comparison to the free pBR322 indicate that the four compounds interact with DNA. Additional measurements of the variation of viscosity with time at constant temperature show a decreasing of the viscosity, what allow us to conclude that there is not intercalation of

the ligands between base pairs of DNA. (See supplementary material available online at doi: 10.1155/2010/963834.)

3.3. Electrophoretic Mobility. The influence of the compounds on the tertiary structure of DNA was determined by its ability to modify the electrophoretic mobility of the covalently closed circular (*ccc*) and open (*oc*) forms of pBR322 plasmid DNA. Figure 4 shows, from right to left, the

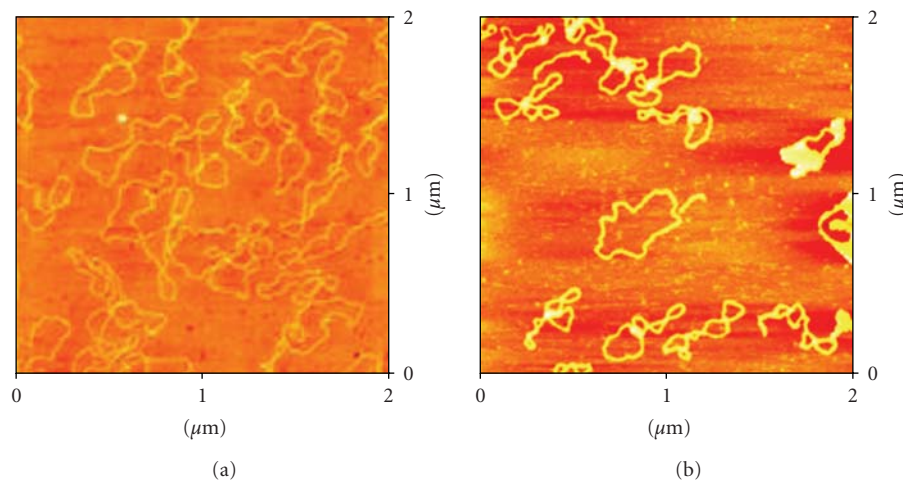


FIGURE 3: AFM image of the (a) free plasmid pBR322 DNA, and (b) plasmid pBR322 DNA incubated with the complex $[\text{RuCp}(\text{PPh}_3)_2(\text{TzH})][\text{PF}_6]$ **1** $r_f = 0.5$.

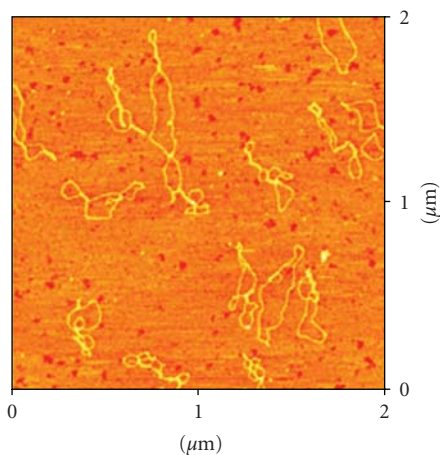


FIGURE 4: AFM image of the plasmid pBR322 DNA incubated with the complex $[\text{RuCp}(\text{PPh}_3)_2(\text{ImH})][\text{PF}_6]$ **2** $r_f = 0.5$.

mobility of the native pBR322 plasmid DNA and the plasmid DNA incubated with cisplatin as a reference, and with the compounds **1–4**. The behavior of the gel electrophoretic mobility of pBR322 plasmid and DNA ruthenium compounds adducts show changes compatible with the AFM images. In the pattern corresponding to the pBR322 plasmid DNA (lane 6) a clean difference between the OC and CCC bands can be observed. In lane 5, the typical coalescence of the two bands for cisplatin is evident. In the zone between OC and CCC bands in lanes 1–4 corresponding to the DNA incubated with ruthenium complexes, new bands (lane 4, compound **4**) or one continuous band (lanes 1–3, compounds **1–3**) appear indicating the presence of DNA forms with different mobility in agarose gel.

3.4. Cytotoxicity of the Ruthenium Complexes against HL-60 Cells. The effect of the ruthenium complexes was examined on human leukaemia cancer cells (HL-60) using the MTT

assay, a colorimetric determination of cell viability during *in vitro* treatment with a drug. The assay, developed as an initial stage of drug screening, measures the amount of MTT reduction by mitochondrial dehydrogenase and assumes that cell viability (corresponding to the reductive activity) is proportional to the production of purple formazan that is measured spectrophotometrically. A low IC_{50} is desired and implies cytotoxicity or antiproliferation at low drug concentrations.

The drugs tested in this experiment were cisplatin, $[\text{Ru}(\eta^5\text{-C}_5\text{H}_5)(\text{PPh}_3)_2\text{TzH}]^+$ **1**, $[\text{Ru}(\eta^5\text{-C}_5\text{H}_5)(\text{PPh}_3)_2\text{ImH}]^+$ **2**, $[\text{Ru}(\eta^5\text{-C}_5\text{H}_5)(\text{PPh}_3)_2\text{Bdt}]^+$ **3**, and $[\text{Ru}(\eta^5\text{-C}_5\text{H}_5)(\text{PPh}_3)_2\text{Tvt}]^+$ **4**.

Cells were exposed to each compound continuously for a 24 hours or a 72 hours period of time and then assayed for growth using the MTT endpoint assay. Figure 8 shows the dose-response curves of these drugs in terms of the drug effect on the growth of the HL-60 cells. The IC_{50} values of complex **1**, complex **2**, complex **3**, complex **4** and cisplatin for the growth inhibition of HL-60 cells were summarized in Table 2.

All of these ruthenium complexes exhibited antitumor effect against HL-60 cells. It was notable that complex **4** exerted the least potent effect among all the complexes, but this effect is better than that of cisplatin at 24 hours and the IC_{50} are very similar at 72 hours. The cytotoxicities displayed by **1**, **2**, and **3** were comparable with **3** slightly over **1** and **2**.

3.5. Quantification of Apoptosis by Annexin V Binding and Flow Cytometry. We have also analysed by Annexin V-PI flow cytometry whether complexes **1**, **2**, **3**, and **4** are able to induce apoptosis in HL-60 cells after 24 hours of incubation at equitoxic concentrations (IC_{50} values). Annexin V binds phosphatidyl serine residues, which are asymmetrically distributed towards the inner plasma membrane but migrate to the outer plasma membrane during apoptosis [30].

As it can be seen in Table 3, all metal complexes induce cell death mainly by apoptosis. Complexes **1** and **2** are

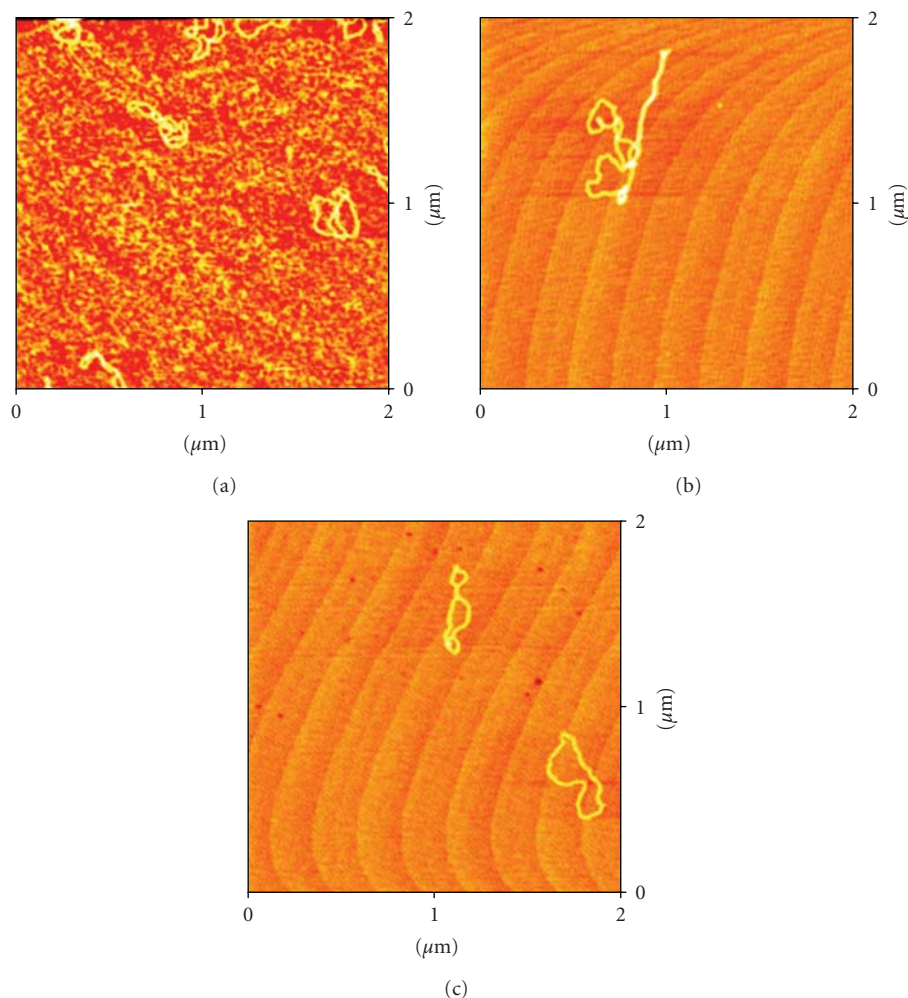


FIGURE 5: Three AFM images (different $2 \times 2 \mu\text{m}$ areas on mica surface) of the plasmid pBR322 DNA incubated with the complex $[\text{RuCp}(\text{PPh}_3)_2(\text{Bzt})][\text{PF}_6]$ **3** $r_i = 0.5$.

less toxic than complexes **3** and **4**, the first two complexes induced less necrotic or damage cells at IC_{50} treatment.

4. Conclusion

The complexes were tested for potential antitumor activity against the human promyelocytic leukemia cell line HL-60 using a MTT assay. The four complexes tested possess excellent antitumor activities, with IC_{50} values lower than that of cisplatin. It cannot be discarded that one of the targets of the antitumor process would be the DNA, because interaction of the four compounds with DNA (ct-DNA or pBR322 plasmid DNA) has been demonstrated by CD, Electrophoretic mobility, and AFM studies.

5. Experimental Protocols

All the syntheses were carried out under dinitrogen atmosphere using current Schlenk techniques and the solvents

used were dried using standard methods [31]. The starting material $[\text{Ru}(\eta^5\text{-C}_5\text{H}_5)(\text{PPh}_3)_2\text{Cl}]$ was prepared following the method described in the literature [27]. Compounds $[\text{RuCp}(\text{PPh}_3)_2(\text{Bzt})][\text{PF}_6]$ **3** and $[\text{RuCp}(\text{PPh}_3)_2(\text{Tvt})][\text{PF}_6]$ **4** were previously characterised [25, 26]. FT-IR spectra were recorded in a Mattson Satellite FT-IR spectrophotometer with KBr pellets; only significant bands are cited in text. ^1H -, ^{13}C -, and ^{31}P -NMR spectra were recorded on a Bruker Advance 400 spectrometer at probe temperature. The ^1H and ^{13}C chemical shifts are reported in parts per million (ppm) downfield from internal Me_4Si and the ^{31}P NMR spectra are reported in ppm downfield from external standard, 85% H_3PO_4 . Elemental analyses were obtained at Laboratório de Análises, Instituto Superior Técnico, using a Fisons Instruments EA1108 system. Data acquisition, integration and handling were performed using a PC with the software package EAGER-200 (Carlo Erba Instruments). Electronic spectra were recorded at room temperature on a Jasco V-560 spectrometer in the range of 200–900 nm.

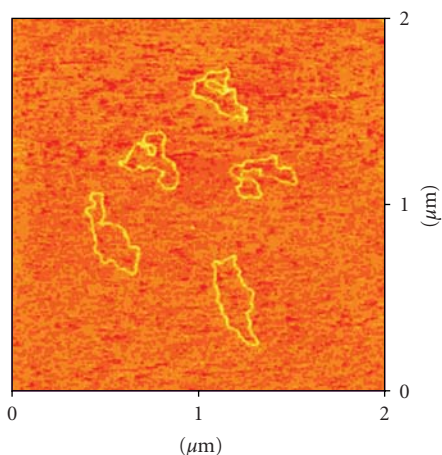


FIGURE 6: AFM image of the plasmid pBR322 DNA incubated with the complex $[\text{RuCp}(\text{PPh}_3)_2(\text{Tvt})][\text{PF}_6]$ **4** $r_i = 0.5$.

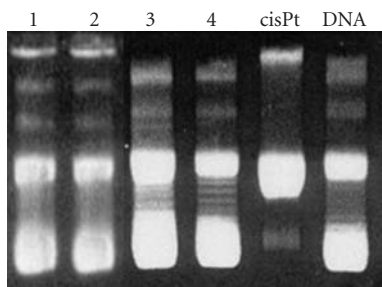


FIGURE 7: Agarose gel electrophoretic mobility of DNA pBR322 treated with compounds **1** (lane 1); compound **2** (lane 2); compound **3** (lane 3); compound **4** (lane 4); **cisplatin** (lane 5) and DNA pBR322 (lane 6).

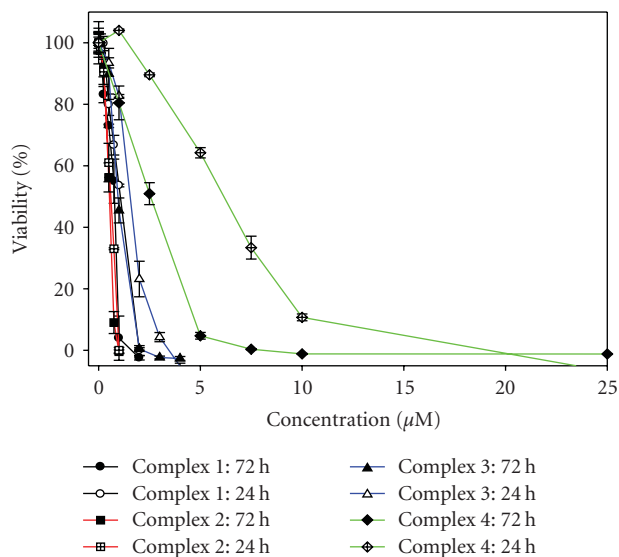
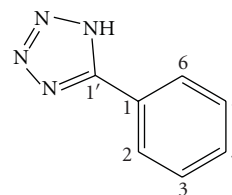


FIGURE 8: Inhibitory effects of complexes **1**, **2**, **3** and **4** on tumor cell proliferation in vitro.

5.1. Synthesis of $[\text{CpRu}(\text{PPh}_3)_2(\text{TzH})][\text{PF}_6]$ (**1**).



To a suspension of $[\text{CpRu}(\text{PPh}_3)_2\text{Cl}]$ (0.73 g; 1 mmol) in THF : CH_2Cl_2 (3 : 1) was added 5-phenyl-1H-tetrazole (0.15 g; 1.1 mmol) followed by the addition of TlPF_6 (0.35 g; 1 mmol). The orange mixture was slightly warmed at 35°C during 30 minutes and turned yellow. The precipitate of TlCl was removed by cannula-filtration and the solvent evaporated. The yellow oil residue was treated with *n*-hexane and the obtained solid was recrystallized from dichloromethane/ethyl ether. Yield: 80 %.

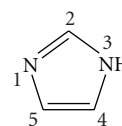
^1H NMR [CDCl_3 , Me_4Si , δ/ppm]: 7.70 [*d*, 2, $\text{H}_2 + \text{H}_6(\text{TzH})$; $J_{2,6} = 7.7$ Hz]; 7.50–7.44 [*m*, 3, $\text{H}_3 + \text{H}_4 + \text{H}_5(\text{TzH})$]; 7.35 [*t*, 6, $\text{H}_{\text{para}}(\text{PPh}_3)$]; 7.24 [*t*, 12, $\text{H}_{\text{meta}}(\text{PPh}_3)$]; 7.17 [*d*, 12, $\text{H}_{\text{ortho}}(\text{PPh}_3)$]; 4.46 [*s*, 5, $\eta^{5\text{-C}_5\text{H}_5}$].

^{13}C NMR [CDCl_3 , δ/ppm]: 156.95 (C_1 , TzH); 136.82 (C_q , PPh_3); 134.07 (C_4 , TzH); 132.16 (CH , PPh_3); 130.26 ($\text{C}_3 + \text{C}_5$, TzH); 129.70 (CH , PPh_3); 125.45 (CH , PPh_3); 128.07 ($\text{C}_2 + \text{C}_6$, TzH); 127.72 (C_1 , TzH); 83.47 (C_5H_5).

^{31}P NMR [CDCl_3 , δ/ppm]: 41.9 [*s*, PPh_3]; -144.1 [*sept*, PF_6^-].

FT-IR [KBr , cm^{-1}]: 3057 (w); 2984 (w); 2913 (w); 2836 (w); 2760 (w); 2699 (w); 2609 (wm); 2550 (w); 2481 (w); 1608 (w); 1563 (wm); 1481 (m); 1434 (ms); 1410 (m); 1312 (w); 1185 (w); 1163 (w); 1089 (ms); 997 (m); 840 (s); 745 (ms); 697 (s); 557 (ms); 521 (S); 496 (ms); UV-Vis. in CH_2Cl_2 , $\lambda_{\text{max}}/\text{nm}$ ($\epsilon/\text{M}^{-1}\text{cm}^{-1}$): 250 (21176), 348 (7603); Elem. Anal. Found: C 58.93; H 4.21; N 5.70; Calc. for $\text{C}_{48}\text{H}_{41}\text{N}_4\text{P}_3\text{F}_6\text{Ru}$; C, 58.72; H, 4.21; N, 5.71.

5.2. Synthesis of $[\text{CpRu}(\text{PPh}_3)_2(\text{ImH})][\text{PF}_6]$ (**2**).



To a solution of $[\text{CpRu}(\text{PPh}_3)_2\text{Cl}]$ (0.20 g; 0.275 mmol) in dichloromethane (25 mL), imidazole was added (0.02 g; 0.3 mmol) followed by the addition of TlPF_6 (0.11 g; 0.3 mmol). The reaction was carried out at room temperature with vigorous stirring during 14 hours with the change of colour from orange to yellow. The precipitate of TlCl was removed by cannula-filtration and the solvent evaporated. The product was washed with *n*-hexane and recrystallized from dichloromethane/ethyl ether. Yield: 70%.

^1H NMR [$(\text{CD}_3)_2\text{CO}$, Me_4Si , δ/ppm]: 11.53 [*s*, 1, $\text{NH}(\text{Im})$]; 7.46 [*t*, 6, $\text{H}_{\text{para}}(\text{PPh}_3)$]; 7.37 [*t*, 12, $\text{H}_{\text{meta}}(\text{PPh}_3)$]; 7.23 [*d*, 12, $\text{H}_{\text{ortho}}(\text{PPh}_3)$]; 4.57 [*s*, 5, $\eta^{5\text{-C}_5\text{H}_5}$], $\text{H}_2 + \text{H}_4 + \text{H}_5$ (Im) obscured by PPh_3 . ^{13}C NMR [$(\text{CD}_3)_2\text{CO}$, δ/ppm]: 144.2 (C_2 , Im); 135.5 ($\text{C}_4 + \text{C}_5$, Im); 133.61 (PPh_3); 133.55 (PPh_3); 133.50 (PPh_3); 130.0 (PPh_3); 128.42 (PPh_3); 128.38

(PPh₃); 128.33; 117.8 (Im); 82.6 (Cp); ³¹P NMR [(CD₃)₂CO, δ/ppm]: 42.04 (s, PPh₃); -144.04 (sept, PF₆⁻).

FT-IR [KBr, cm⁻¹]: 3056 (w); 2955 (w); 1480 (m); 1434 (s); 1089 (m); 999 (w); 840 (s); 745 (s); 696 (S); 557 (s); 522 (s).

UV-Vis. in CH₂Cl₂, λ_{max}/nm (ε/M⁻¹cm⁻¹): 248 (21200), 273 (8162), 348 (3285); Elem. Anal. Found: C, 58.19; H, 4.68; N, 3.16. Found for C₄₄H₃₉N₂P₃F₆Ru: C, 58.47; H, 4.35; N, 3.10.

5.3. Electrochemical Experiments. Cyclic voltammograms of ligands and complexes were obtained using a EG and G Princeton Applied Research Model 273A potentiostat/galvanostat monitored with a personal computer loaded with Electrochemistry PowerSuite v2.51 software from Princeton Applied Research at room temperature. A three-electrode configuration small capacity cell was equipped with a platinum-disk working electrode (1.0 mm diameter), a silver-wire pseudo-reference electrode connected by a Lugging capillary and a platinum wire auxiliary electrode. The electrochemical experiments were performed in 0.2 M solutions of TBAPF₆ in dichloromethane or acetonitrile, under a nitrogen atmosphere and the redox potentials were measured using ferrocene as the internal standard. The redox potential values were quoted relative to the SCE by using the ferrocenium/ferrocene redox couple ($E_{p/2} = 0.46$ or 0.40 V versus SCE for dichloromethane or acetonitrile, resp.) [32].

The supporting electrolyte was purchased from Aldrich Chemical Co., recrystallized from ethanol, washed with diethyl ether and dried under vacuum at 110°C for 24 hours. Reagent grade acetonitrile and dichloromethane were dried over P₄O₁₀ and CaH₂, respectively, and distilled under nitrogen atmosphere before use.

5.4. Biological Assays

5.4.1. DNA Interaction Studies

Circular Dichroism. All compounds were dissolved in an aqueous solution (prepared with milli-Q water) of 4% DMSO (2 mg compound/5 mL). The stock solutions were freshly prepared before use. The samples were prepared by addition of aliquots of these stock solutions to the appropriate volume of Calf Thymus DNA in a TE buffer solution (50 mM NaCl, 10 mM tris-(hydroxymethyl)aminomethane hydrochloride (Tris-HCl), 0.1 mM H₄edta, pH 7.4) (5 mL). The amount of complex added to the DNA solution was designated as r_i (the input molar ratio of Ru to nucleotide and it is calculated with formula

$$r_i = \frac{m \times M_{\text{nuc}} \times Am}{C \times Mr \times V}, \quad (1)$$

where m = mass of the compound (μg); M_{nuc} = medium nuclear mass per nucleotide (330 g/mol); C = concentration of the DNA solution (μg/ml); Mr = molecular mass of each compound (g/mol); V = total volume of each sample (5 mL). As a blank, a solution in TE of free native DNA was used. The CD spectra of DNA in the presence or absence of complexes

(DNA concentration 20 μg/mL, molar ratios $r_i = 0.10, 0.30, 0.50$) were recorded at room temperature, after 24 hours incubation at 37°C, on a JASCO J-720 spectropolarimeter with a 450 W xenon lamp using a computer for spectral subtraction and noise reduction. Each sample was scanned twice in a range of wavelengths between 220 and 330 nm. The CD spectra drawn are the average of three independent scans. The data are expressed as average residue molecular ellipticity (θ) in degrees·cm²·dmol⁻¹.

Viscosity Measurements. Viscosity experiments were carried out with an AND-SV-1 viscometer in a water bath using a water jacket accessory and maintained the constant temperature at 25°C. A range of 200–370 μL of 5 mM solutions of the different compounds were added in 2 mL of 100 mM ct-DNA solution. The flow time was measured by a digital stop watch.

Atomic Force Microscopy (TMAFM). DNA pBR322 was heated at 60° for 10 minutes to obtain OC form. Stock solution was 1 mg/mL in a buffer solution of HEPES (4 mM Hepes, pH 7.4/2 mM MgCl₂). Each sample contained 1 μL of DNA pBR322 of concentration 0.25 μg/μL for a final volume of 40 μL. The amount of drug added is also expressed as r_i . AFM samples were prepared by casting a 3-μL drop of test solution onto freshly cleaved Muscovite green mica disks as the support. The drop was allowed to stand undisturbed for 3 minutes to favour the adsorbate-substrate interaction. Each DNA-laden disk was rinsed with Milli-Q water and was blown dry with clean compressed argon gas directed normal to the disk surface. Samples were stored over silica prior to AFM imaging. All Atomic Force Microscopy (AFM) observations were made with a Nanoscope III Multimode AFM (Digital Instrumentals, Santa Barbara, CA). Nano-crystalline Si cantilevers of 125-nm length with a spring constant of 50 N/m average ended with conical-shaped Si probe tips of 10-nm apical radius and cone angle of 35° were utilized. High-resolution topographic AFM images were performed in air at room temperature (relative humidity < 40%) on different specimen areas of 2 × 2 μm operating in intermittent contact mode at a rate of 1–3 Hz.

Gel Electrophoresis of Ruthenium Complexes-pBR322. pBR 322 DNA aliquots (0.25 μg/mL) were incubated in TE buffer (10 mM Tris.HCl, 1 mM EDTA, pH = 7,5) at molar ratio $r_i = 0.50$ for electrophoresis study. Incubation was carried out in the dark at 37°C for 24 hours. 4 μL of charge marker were added to aliquots parts of 20 μL of the compound-DNA complex. The mixture was electrophoresed in agarose gel (1% in TBE buffer, Tris-Borate-EDTA) for 5 hours at 1.5 V/cm. Afterwards, the DNA was dyed with ethidium bromide solution (0.75 μg/mL in TBE) for 6 hours. A sample of free DNA was used as control. The experiment was carried out in an ECOGEN horizontal tank connected to a PHARMACIA GPS 200/400 variable potential power supply and the gel was photographed with an image Master VDS, Pharmacia Biotech.

5.5. Tumor Cell Lines and Culture Conditions. The cell line used in this experiment was the human acute promyelocytic leukaemia cell line HL-60 (American Type Culture Collection (ATCC)). Cells were routinely maintained in RPMI-1640 medium supplemented with 10% (v/v) heat inactivated foetal bovine serum, 2 mmol/L glutamine, 100 U/mL penicillin, and 100 μ g/mL streptomycin (Gibco BRL, Invitrogen Corporation, Netherlands) in a highly humidified atmosphere of 95% air with 5% CO₂ at 37°C.

Cytotoxicity Assays. Growth inhibitory effect of ruthenium complexes on the leukaemia HL-60 cell line was measured by the microculture tetrazolium, [3-(4,5-dimethylthiazol-2-yl)-2,5-diphenyltetrazolium bromide, MTT] assay [33]. Briefly, cells growing in the logarithmic phase were seeded in 96-well plates (10⁴ cells per well), and then were treated with varying doses of ruthenium complexes and the reference drug cisplatin at 37°C for 24 or 72 hours. For each of the variants tested, four wells were used. Aliquots of 20 μ L of MTT solution were then added to each well. After 3 hours, the colour formed was quantified by a spectrophotometric plate reader at 490 nm wavelength. The percentage cell viability was calculated by dividing the average absorbance of the cells treated with a platinum complex by that of the control; IC₅₀ values (drug concentration at which 50% of the cells are viable relative to the control) were obtained by GraphPad Prism software, version 4.0.

In Vitro Apoptosis Assay. Induction of apoptosis in vitro by ruthenium compounds was determined by a flow cytometric assay with Annexin V-FITC by using an Annexin V-FITC Apoptosis Detection Kit (Roche) [30]. Exponentially growing HL-60 cells in 6-well plates (5 × 10⁵ cells/well) were exposed to concentrations equal to the IC₅₀ of the ruthenium drugs for 24 hours. Afterwards, the cells were subjected to staining with the Annexin V-FITC and propidium iodide. The amount of apoptotic cells was analyzed by flow cytometry (BD FACSCalibur).

Acknowledgments

The authors thank Fundação para a Ciência e Tecnologia for financial support (PTDC/ QUI/ 66148/ 2006) and Ministerio de Ciencia e Innovación de España for financial support (CTQ2008-02064) and BIO2007-6846-C02-01. P. Florindo thanks FCT for his PhD Grant (SFRH/BD/12432/2003). The authors also thank Dr. Francisca Garcia (Cell Culture Facility), Manuela Costa (Cytometry Facility), and Maria J. Prieto (AFM) for technical assistance.

References

- [1] H. Köpf and P. Köpf-Maier, "Titanocen-dichlorid—das erste metallocen mit cancerostatischer wirksamkeit," *Angewandte Chemie*, vol. 91, no. 6, pp. 509–512, 2006.
- [2] T. M. Klapötke, H. Köpf, I. C. Tornieporth-Oetting, and P. S. White, "Synthesis, characterization, and structural investigation of the first bioinorganic titanocene(IV) α -amino acid complexes prepared from the antitumor agent titanocene dichloride," *Organometallics*, vol. 13, no. 9, pp. 3628–3633, 1994.
- [3] Y. K. Yan, M. Melchart, A. Habtemariam, and P. J. Sadler, "Organometallic chemistry, biology and medicine: ruthenium arene anticancer complexes," *Chemical Communications*, no. 38, pp. 4764–4776, 2005.
- [4] K. Strohfeldt and M. Tacke, "Bioorganometallic fulvene-derived titanocene anti-cancer drugs," *Chemical Society Reviews*, vol. 37, no. 6, pp. 1174–1187, 2008.
- [5] C. G. Hartinger and P. J. Dyson, "Bioorganometallic chemistry—from teaching paradigms to medicinal applications," *Chemical Society Reviews*, vol. 38, no. 2, pp. 391–401, 2009.
- [6] E. Meléndez, "Titanium complexes in cancer treatment," *Critical Reviews in Oncology/Hematology*, vol. 42, no. 3, pp. 309–315, 2002.
- [7] J. L. Buss, B. T. Greene, J. Turner, F. M. Torti, and S. V. Torti, "Iron chelators in cancer chemotherapy," *Current Topics in Medicinal Chemistry*, vol. 4, no. 15, pp. 1623–1635, 2004.
- [8] L. Messori and G. Marcon, "Gold complexes as antitumor agents," *Metal Ions in Biological Systems*, vol. 42, pp. 385–424, 2004.
- [9] M. A. Jakupec, M. Galanski, and B. K. Keppler, "The effect of cytoprotective agents in platinum anticancer therapy," *Metal Ions in Biological Systems*, vol. 42, pp. 179–208, 2004.
- [10] Q. Li, M. F. C. Guedes da Silva, and A. J. L. Pombeiro, "Diorganotin(IV) derivatives of substituted benzohydroxamic acids with high antitumor activity," *Chemistry: A European Journal*, vol. 10, no. 6, pp. 1456–1462, 2004.
- [11] C. G. Hartinger, S. Zorbas-Seifried, M. A. Jakupec, B. Kynast, H. Zorbas, and B. K. Keppler, "From bench to bedside—preclinical and early clinical development of the anticancer agent indazolium *trans*[tetrachlorobis(1*H*-indazole)ruthenate(III)] (KP1019 or FFC14A)," *Journal of Inorganic Biochemistry*, vol. 100, no. 5–6, pp. 891–904, 2006.
- [12] S. Kapitzka, M. Pongratz, M. A. Jakupec et al., "Heterocyclic complexes of ruthenium(III) induce apoptosis in colorectal carcinoma cells," *Journal of Cancer Research and Clinical Oncology*, vol. 131, no. 2, pp. 101–110, 2005.
- [13] M. A. Jakupec, V. B. Arion, S. Kapitzka et al., "KP1019 (FFC14A) from bench to bedside: preclinical and early clinical development—an overview," *International Journal of Clinical Pharmacology and Therapeutics*, vol. 43, no. 12, pp. 595–596, 2005.
- [14] C. S. Allardyce, P. J. Dyson, D. J. Ellis, and S. L. Heath, "[Ru(η^6 -*p*-cymene)Cl₂(pta)] (pta = 1,3,5-triaza-7-phosphatricyclo-[3.3.1.1]decane): a water soluble compound that exhibits pH dependent DNA binding providing selectivity for diseased cells," *Chemical Communications*, no. 15, pp. 1396–1397, 2001.
- [15] C. S. Allardyce, P. J. Dyson, D. J. Ellis, P. A. Salter, and R. Scopelliti, "Synthesis and characterisation of some water soluble ruthenium(II)-arene complexes and an investigation of their antibiotic and antiviral properties," *Journal of Organometallic Chemistry*, vol. 668, no. 1–2, pp. 35–42, 2003.
- [16] Y. N. V. Gopal, D. Jayaraju, and A. K. Kondapi, "Inhibition of topoisomerase II catalytic activity by two ruthenium compounds: a ligand-dependent mode of action," *Biochemistry*, vol. 38, no. 14, pp. 4382–4388, 1999.
- [17] Y. N. V. Gopal, N. Konuru, and A. K. Kondapi, "Topoisomerase II antagonism and anticancer activity of coordinated derivatives of [RuCl₂(C₆H₆)(dmso)]," *Archives of Biochemistry and Biophysics*, vol. 401, no. 1, pp. 53–62, 2002.

- [18] R. E. Morris, R. E. Aird, P. S. Murdoch et al., "Inhibition of cancer cell growth by ruthenium(II) arene complexes," *Journal of Medicinal Chemistry*, vol. 44, no. 22, pp. 3616–3621, 2001.
- [19] L. A. Huxham, E. L. S. Cheu, B. O. Patrick, and B. R. James, "The synthesis, structural characterization, and in vitro anti-cancer activity of chloro(p-cymene) complexes of ruthenium(II) containing a disulfoxide ligand," *Inorganica Chimica Acta*, vol. 352, pp. 238–246, 2003.
- [20] H. A. Wee and P. J. Dyson, "Classical and non-classical ruthenium-based anticancer drugs: towards targeted chemotherapy," *European Journal of Inorganic Chemistry*, no. 20, pp. 4003–4018, 2006.
- [21] A. F. A. Peacock and P. J. Sadler, "Medicinal organometallic chemistry: designing metal arene complexes as anticancer agents," *Chemistry: An Asian Journal*, vol. 3, no. 11, pp. 1890–1899, 2008.
- [22] J. Maksimoska, L. Feng, K. Harms et al., "Targeting large kinase active site with rigid, bulky octahedral ruthenium complexes," *Journal of the American Chemical Society*, vol. 130, no. 47, pp. 15764–15765, 2008.
- [23] M. H. Garcia, T. S. Morais, P. Florindo et al., "Inhibition of cancer cell growth by ruthenium(II) cyclopentadienyl derivative complexes with heteroaromatic ligands," *Journal of Inorganic Biochemistry*, vol. 103, no. 3, pp. 354–361, 2009.
- [24] A. Valente, "Síntese de metalocenos de ruténio e avaliação das suas potencialidades antitumorais," M.S. thesis, Faculty of Sciences of University of Lisbon, 2007.
- [25] M. H. Garcia, P. Florindo, M. F. M. Piedade et al., "Synthesis of organometallic Ru(II) and Fe(II) complexes containing fused rings hemi-helical ligands as chromophores. Evaluation of non-linear optical properties by HRS," *Journal of Organometallic Chemistry*, vol. 693, no. 18, pp. 2987–2999, 2008.
- [26] M. H. Garcia, P. Florindo, M. F. M. Piedade et al., "Synthesis and structural characterization of ruthenium(II) and iron(II) complexes containing 1,2-di-(2-thienyl)-ethene derived ligands as chromophores," *Journal of Organometallic Chemistry*, vol. 694, no. 3, pp. 433–445, 2009.
- [27] M. I. Bruce and N. J. Windsor, "Cyclopentadienyl-ruthenium and -osmium chemistry. IV. Convenient high-yield synthesis of some cyclopentadienyl ruthenium or osmium tertiary phosphine halide complexes," *Australian Journal of Chemistry*, vol. 30, pp. 1601–1604, 1977.
- [28] H. Mishra and R. Mukherjee, "Half-sandwich η^6 -benzene Ru(II) complexes of pyridylpyrazole and pyridylimidazole ligands: synthesis, spectra, and structure," *Journal of Organometallic Chemistry*, vol. 691, no. 16, pp. 3545–3555, 2006.
- [29] J. M. C. Rodrigues, "Síntese de Novos Materiais Organometálicos com Propriedades de Não-linearidade Óptica," Ph.D. thesis, Faculty of Sciences of University of Lisbon, 1999.
- [30] I. Vermes, C. Haanen, H. Steffens-Nakken, and C. Reutelingsperger, "A novel assay for apoptosis. Flow cytometric detection of phosphatidylserine expression on early apoptotic cells using fluorescein labelled Annexin V," *Journal of Immunological Methods*, vol. 184, no. 1, pp. 39–51, 1995.
- [31] D. D. Perrin, W. L. F. Amarego, and D. R. Perrin, *Purification of Laboratory Chemicals*, Pergamon, New York, NY, USA, 2nd edition, 1980.
- [32] N. G. Connelly and W. E. Geiger, "Chemical redox agents for organometallic chemistry," *Chemical Reviews*, vol. 96, no. 2, pp. 877–910, 1996.
- [33] T. Mosmann, "Rapid colorimetric assay for cellular growth and survival: application to proliferation and cytotoxicity assays," *Journal of Immunological Methods*, vol. 65, no. 1-2, pp. 55–63, 1983.

Research Article

Measuring the Cytochrome *c* Nitrite Reductase Activity—Practical Considerations on the Enzyme Assays

Célia M. Silveira,¹ Stéphane Besson,^{1,2} Isabel Moura,¹ José J. G. Moura,¹
and M. Gabriela Almeida^{1,3}

¹REQUIMTE, Departamento de Química, CQFB, Faculdade de Ciências e Tecnologia, Universidade Nova de Lisboa, 2829-516 Caparica, Portugal

²Faculdade de Ciências Médicas, Universidade Lusófona de Humanidades e Tecnologias, Campo Grande 376, 1749-024 Lisboa, Portugal

³Escola Superior de Saúde Egas Moniz, Monte de Caparica, 2829-511 Caparica, Portugal

Correspondence should be addressed to M. Gabriela Almeida, mga@dq.fct.unl.pt

Received 16 January 2010; Accepted 3 May 2010

Academic Editor: Evy Manessi-Zoupa

Copyright © 2010 Célia M. Silveira et al. This is an open access article distributed under the Creative Commons Attribution License, which permits unrestricted use, distribution, and reproduction in any medium, provided the original work is properly cited.

The cytochrome *c* nitrite reductase (ccNiR) from *Desulfovibrio desulfuricans* ATCC 27774 is able to reduce nitrite to ammonia in a six-electron transfer reaction. Although extensively characterized from the spectroscopic and structural points-of-view, some of its kinetic aspects are still under explored. In this work the kinetic behaviour of ccNiR has been evaluated in a systematic manner using two different spectrophotometric assays carried out in the presence of different redox mediators and a direct electrochemical approach. Solution assays have proved that the specific activity of ccNiR decreases with the reduction potential of the electronic carriers and ammonium is always the main product of nitrite reduction. The catalytic parameters were discussed on the basis of the mediator reducing power and also taking into account the location of their putative docking sites with ccNiR. Due to the fast kinetics of ccNiR, electron delivering from reduced electron donors is rate-limiting in all spectrophotometric assays, so the estimated kinetic constants are apparent only. Nevertheless, this limitation could be overcome by using a direct electrochemical approach which shows that the binding affinity for nitrite decreases whilst turnover increases with the reductive driving force.

1. Introduction

Cytochrome *c* nitrite reductase (ccNiR) is involved in the pathway called dissimilatory nitrate reduction to ammonia, thereby playing an important part in the biogeochemical nitrogen cycle. This enzyme catalyzes the six-electron reduction of nitrite (NO₂⁻) to ammonia (NH₄⁺) (1) and its existence has been demonstrated in bacterial strains from almost every taxonomic branch. However, the best studied ccNiRs were isolated from proteobacteria that belong to subdivisions γ (ex: *Escherichia coli*) [1], δ (ex: *Desulfovibrio desulfuricans* ATCC 27774) [2], or ϵ (ex: *W. succinogenes* or *Sulfospirillum deleyianum*) [3, 4]. The reaction mechanism has been particularly well studied in *Wolinella succinogenes*. The proposed model was based on the crystallographic observation of reaction intermediates and suggests that

nitrite is reduced to ammonia without the release of nitric oxide, hydroxylamine, or any other intermediate [5]:



In addition to nitrite, some ccNiRs were shown to reduce other substrates like nitric oxide, hydroxylamine, *o*-methylhydroxylamine [6], or sulphite [7, 8].

The physiological form of the enzyme is believed to be a double trimer of 2 NrfA and 1 NrfH subunits [9]. The catalytic subunit NrfA is a periplasmic membrane-associated pentaheme cytochrome *c* where the short distances between hemes allow a fast and efficient electron transfer. The active site has been reported as an unusual lysine-coordinated high-spin heme [4, 10]. NrfH is a small membrane-bound cytochrome comprising four *c*-type heme groups and it serves a double purpose. On one hand, it anchors the

catalytic subunits to the membrane: in *D. desulfuricans*, NrfH and NrfA form a strong complex that is only completely dissociated in the presence of SDS [11]. On the other hand, it serves as a quinol oxidase, transferring electrons from the quinone pool to the catalytic subunits [11, 12].

Kinetic studies of ccNiR have been largely based on classical spectrophotometric methods using methyl viologen (MV) as an electron source [1, 2, 6–8, 13, 14]. Although these protocols provide a satisfactory turnover, the investigation of the enzyme behaviour requires a more systematic study. The use of a variety of artificial electron donors, with different redox potentials or ionic charges, might shed light on electron entry points and donor-protein interactions and provide rigorous criteria to establish new reliable protocols. However, practical details on the experimental conditions (mediator concentration should not be limiting, subtraction of noncatalytic reactions, etc.) are rarely taken into account. Moreover, the list of available redox mediators is not long: besides being suitable electron carriers to the enzyme, they must also have chromophore groups that enable the reaction monitoring by UV-Vis spectrophotometry.

Searching in another direction, Protein Film Voltammetry is a promising alternative to the conventional methods used in kinetic studies. In this technique, an extremely small amount of a redox protein is adsorbed onto a solid electrode as an electroactive film. By applying a driving force (potential difference) the protein molecules exchange electrons directly with the electrode surface and the resultant current flow is recorded as a function of the electrode potential. In the case of an enzyme, and in the presence of its substrate, the catalytic process results in a steady-state electron flow whose detection allows instantaneous measurement of turnover rates. The electrode itself works as the redox partner of the enzyme; as so, no electron shuttle species or cosubstrates are mediating the process and no inhibition or interference reactions are expected [14]. Pyrolytic graphite (PG) electrodes have shown to be very suitable for the direct electrochemical study of redox proteins. Nonetheless, following immobilization on the electrode surface, enzymes may retain or not their catalytic properties [15–18].

The aim of our work was to compare and discuss different experimental approaches to assess nitrite reductase activity, thereby contributing to the development of an efficient method, applicable in a broad range of experimental conditions. The kinetic behaviour of ccNiR was studied by two spectroscopic techniques and also by electrochemical assays, according to the experimental designs depicted in Figure 1.

For the spectroscopic techniques several redox mediators were used, namely, MV, Diquat (DQ), Phenosafranine (PS), Anthraquinone-2-sulphonate (AQS), and Indigo Carmine (IC).

This preliminary work could be quite relevant for the mechanistic study of nitrite reduction by ccNiR [19] as well as for paving the way towards the construction of new nitrite biosensors. In fact, several proposals of *D. desulfuricans* ccNiR-based nitrite biosensors were recently made, using different electronic mediators (MV and AQS) for enzyme

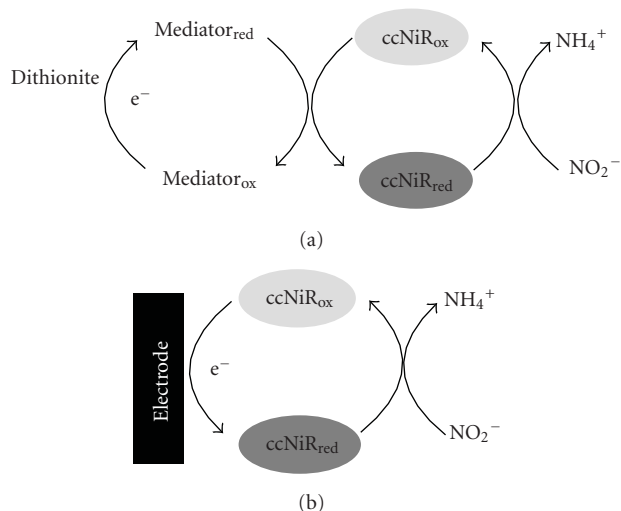


FIGURE 1: Reaction schemes for solution (a) and electrochemical (b) assays of ccNiR activity.

activation [20–24]. In order to find the optimal conditions for biosensor operation and to make a consistent comparison between the analytical properties of the proposed systems, one should fully control the correspondent homogeneous enzymatic kinetics.

2. Experimental

2.1. Reagents. The multihemic nitrite reductase (ccNiR) ($1.0 \text{ mg} \cdot \text{mL}^{-1}$) was purified from *D. desulfuricans* ATCC 27774 cells as previously described [11] and stored in $0.1 \text{ mol} \cdot \text{L}^{-1}$ phosphate buffer, pH 7.6, at -20°C . The protein concentration was determined with the Bicinchoninic Acid Protein Assay Kit (Sigma) using horse heart cytochrome *c* (Sigma) as standard.

1,1'-dimethyl-4,4'-bipyridinium dichloride (methyl viologen, MV), hydroxylamine, *n*-(1-naphthyl)ethylenediamine, and phenol were purchased from Sigma. Sodium nitroprusside, 3,7-diamino-5-phenylphenazinium chloride (phenosafranine, PS), 5,5'-indigo sulfonic acid disodium (indigo carmine, IC), diquat monohydrate (diquat, DQ), anthraquinone-2-sulphonate (AQS), sodium dithionite, potassium chloride, sodium nitrite, ammonium chloride, disodium hydrogen phosphate, sodium dihydrogen phosphate, and sulphanilamide were all from Merck. Hydrochloric acid was from Riedel-de-Haen. All chemicals were of analytical grade.

2.2. Enzymatic Measurements

2.2.1. Discontinuous Assay. This assay involved two steps: the enzymatic conversion of nitrite to ammonia followed by the quantitative determination of both nitrite and ammonia present in the reaction mixture. For the enzymatic step, a 1 mL assay was prepared containing 0.2 M phosphate buffer pH 7.6, 0.5 mM sodium nitrite, 0.5 mM of mediator (0.25 mM in the case of PS, AQS, and IC), and appropriately

diluted enzyme. In order to obtain comparable results, the mediator concentrations were levelled to provide the same reducing equivalents, since PS, AQS, and IC supply 2 electrons per molecule and the other mediators are one electron donors (when dithionite reduced). The reaction was initiated by the addition of 0.5 mM of sodium dithionite (in buffer solution), and after a particular incubation period (from 2 to 10 minutes) at 37°C, the reaction was stopped by oxidation of dithionite through vigorous stirring. The quantification of nitrite and ammonia was performed by the Griess [25] and indophenol blue [2, 26] methods, respectively. In control experiments performed without enzyme, using inactivated enzyme and without substrate, no ammonia formation (or nitrite consumption) was detected. One unit of enzyme activity is defined as the amount of enzyme that catalyzed the reduction of 1 μmol of nitrite per minute.

2.2.2. Continuous Assay. Kinetic data was obtained by monitoring the reoxidation of the mediators used as electron sources for enzyme turnover. The assay mixtures were prepared in a septum-stoppered quartz cell containing 0.16 mM of the mediators (except for PS-0.08 mM) and properly diluted ccNiR. Total cell volume was 2.5 mL completed with 0.2 M phosphate buffer, pH 7.6. The cell was purged with argon for 10 minutes before starting the reaction, while it was incubated at 37°C. Then, an appropriate volume of sodium dithionite was added into the cell with a syringe (typically *ca.* 20 μL to achieve a final concentration in the cell of 0.16 mM, or 10 μL when using PS) to reduce the mediators. The total volume could slightly vary from assay to assay due to some dithionite degradation following the solution deoxygenation step (the complete reduction of the mediators was assured by controlling the absorbance of their reduced forms).

The absorbance was measured for 30 seconds to establish a baseline (the rate of mediator non-enzymatic reoxidation, to be subtracted from nitrite reduction rates) and the reaction was subsequently started by the addition of nitrite stock solutions (1 and 10 mM). Kinetic measurements were made by following the rate of the change in light absorption of the mediators (604 nm for MV ($\epsilon_{604\text{nm}} = 13.6\text{ mM} \cdot \text{cm}^{-1}$), 460 nm for DQ ($\epsilon_{460\text{nm}} = 2.7\text{ mM} \cdot \text{cm}^{-1}$) and 540 nm for PS ($\epsilon_{540\text{nm}} = 18.4\text{ mM} \cdot \text{cm}^{-1}$)) in the presence of nitrite. Control assays performed in the absence of nitrite or enzyme showed little or no bleaching of the reduced mediators. Absorbance was measured with a Diode array spectrophotometer (Agilent Technologies 8453A UV-Vis). Kinetic parameters K_M and k_{cat} were determined using the software Graph Pad Prism 4.

2.2.3. Electrochemical Assays. Chronoamperometry experiments (electrode potential was stepped and the current was measured) were performed with an Autolab electrochemical analyzer (PGSTAT12, Eco Chemie) under the control of GPES software (Eco Chemie). Electrode rotation was driven with an electrode rotator also controlled by GPES. The experiments were performed with a speed rotation of 600 rpm. A three-electrode cell configuration, composed of a silver/silver chloride reference electrode (Ag/AgCl),

a platinum wire counter electrode, and a PG working electrode, was used. All potentials were quoted against NHE (+197 mV Ag/AgCl). The experiments were carried at 37°C in a single compartment cell containing 20 mL of supporting electrolyte (0.1 mol \cdot L⁻¹ phosphate buffer, pH 7.6). Solutions in the electrochemical cell were purged with argon before measurements and the argon atmosphere was maintained during the experiments by continuously flushing the cell. Protein films were prepared by depositing a 10 μL drop of enzyme solution on the electrode surface. After 10 minutes, the electrode was washed with buffer and placed in the electrochemical cell. The protein surface coverage as estimated by the integration of the cyclic voltammogram of ccNiR obtained in the absence of nitrite was *ca.* 4 pmol \cdot cm⁻². The electrode response to nitrite was evaluated by successively adding small volumes of nitrite stock solutions (1, 10 and 100 mM), while continuously recording the activity. Control experiments showed no detectable faradaic current in the absence of ccNiR.

2.3. Molecular Docking Simulations. The atomic coordinates of *D. desulfuricans* ccNiR were obtained from the Brookhaven Protein Data Bank (entry 1OAH.pdb) [10]. Mediator structures were obtained from PubChem database (entries 15939 (MV), 6795 (DQ), 65733 (PS), 8551 (AQS), and 5284351 (IC)). The atomic coordinates of the mediators and ccNiR were used as input files for the docking algorithm PatchDock [27, 28], which creates potential complexes sorted according to shape complementarity criteria. The obtained complexes are sorted by a scoring function that considers both geometric fit and atomic desolvation energy. A root mean square deviation clustering of 4 Å is then applied to the complexes to discard redundant solutions. With this algorithm, the native result is typically found in the top 100 solutions and often among the top 10. The top 20 solutions obtained in this study were very similar to each other. Thus, to avoid presenting confusing pictures we decided to show only the first 5. Structure manipulation was done with the UCSF Chimera package [29].

3. Results and Discussion

3.1. Mediated Spectrophotometry. In the early stage of this study we investigated the influence of the electron donor in product formation. In particular, we intended to check if nitrite is directly converted to ammonia and no intermediates are accumulated during the course of the enzymatic reaction. We thus used a simple fixed-time method (single point), in which direct measurements of the reaction substrate and product were made [2]. In Figure 2(a) nitrite consumption and ammonia formation curves, traced in the presence of methyl viologen, diquat, phenosafranine, anthraquinone-2-sulphonate, and indigo carmine, are represented. Comparing the ammonia and nitrite contents we could confirm 100% conversion with all the mediators, except for indigo carmine (75%) as shown in Figure 2(b). The latter has the highest reduction potential tested (-145 mV); thus, we can speculate that the reaction

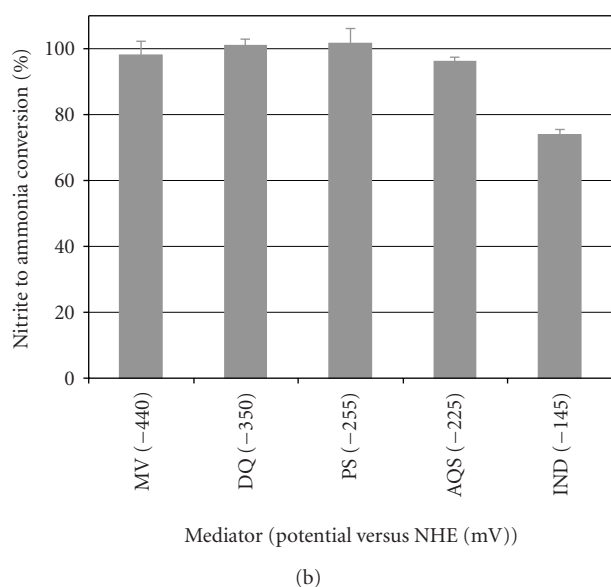
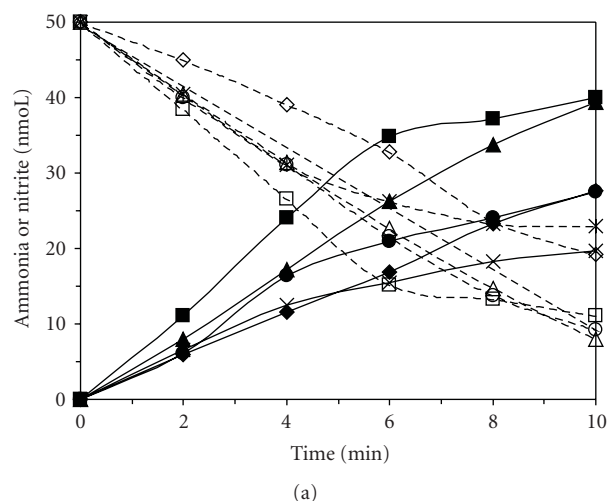


FIGURE 2: (a) Progression curves for ammonia (filled symbols) and nitrite (open symbols) for ccNiR reaction, in the presence of equivalent electron concentrations of dithionite reduced mediators at 37°C. MV (■□); DQ (◆◇); PS (●○); AQS (▲△) and IC (XX). Enzyme concentration was 0.7 nM for MV, DQ, and PS assays, 7 nM for AQS, and 14 nM for IC. (b) Nitrite to ammonia conversion percentages in the presence of each mediator.

is not complete and less reduced intermediates or products other than ammonium may be formed. No further studies were performed to corroborate this result, since efficient quantitation methods for reaction intermediates have yet to be established [7].

The specific activity of ccNiR for nitrite and hydroxylamine was determined with all mediators, also using this discontinuous method. ccNiR hydroxylamine reducing activity was obtained by determining the amount of ammonia produced in the assay (hydroxylamine conversion percentages were not calculated, given that this substrate was not quantified). As shown in Figure 3, the activities for nitrite were at least 10 times greater than the activities

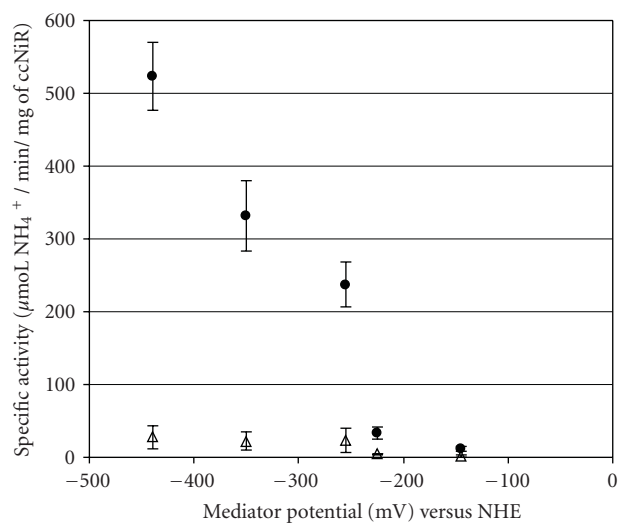


FIGURE 3: ccNiR specific activities determined with an equivalent electron concentration of the mediators and with a saturating nitrite (●) and hydroxylamine (△) concentration. Incubation time was 4 minutes, that is, within the period of ammonia production at a linear rate. Dithionite was used as reducing agent. All assays were performed at 37°C. Enzyme concentration was 0.7 nM for MV, DQ and PS assays, 7 nM for AQS, and 14 nM for IC.

for hydroxylamine, thus confirming nitrite as the specific substrate for ccNiR. Specific activity values were found to decrease with the potential of the electron carrier, indicating methyl viologen (the lowest potential mediator) as the most suitable electron donor for ccNiR. Activities are in the range found for ccNiRs from other organisms [1, 2, 6, 8, 31].

Molecular docking studies were performed to evaluate the interaction between ccNiR and the redox mediators (Figure 4). From the best five solutions obtained with the molecular docking algorithm PatchDock [27, 28] we could validate MV as a convenient mediator for ccNiR reduction, since it interacts with a region closer to the electron transfer heme groups of the protein. In contrast, the highest potential mediators IC and AQS, which provided the lowest specific activities for nitrite reduction, interact with the enzyme in the interface between the two catalytic subunits, distant from any electron transfer hemes. Most of the top five solutions found for PS and DQ were also located in regions distant from the heme clusters, with the exception of DQ that has one putative docking site close to the catalytic heme.

The kinetic parameters for nitrite reductases are usually determined using the spectroscopic continuous method assay, in which the rate of reoxidation of a viologen cosubstrate gives an indirect measurement of enzyme activity [1, 6, 8, 13]. Although time-consuming, this type of method offers advantages relatively to the discontinuous assay applied above, since it allows direct tracking of the progress curve of the reaction, therefore making it relatively easy to estimate initial rates, spot any deviations from the initial linear phase of the reaction, and detect anomalous behaviours [32]. For this study, only the three lowest potential mediators (MV, DQ, and PS) were selected. The initial rates of ccNiR reaction

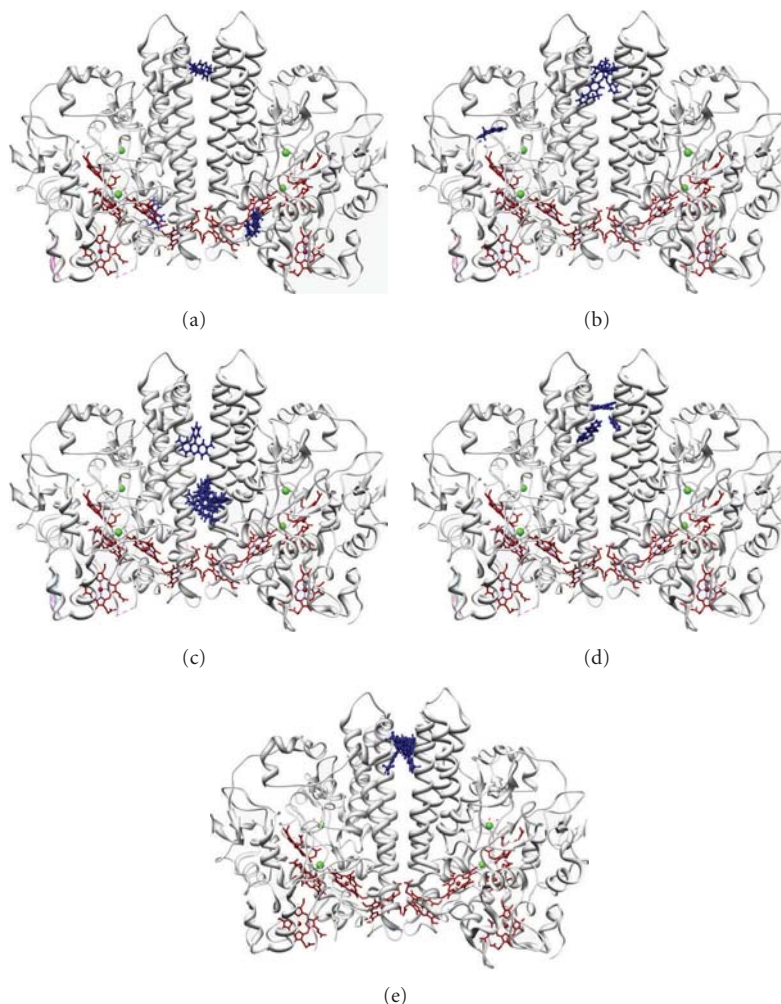


FIGURE 4: Interaction complexes of ccNiR with the mediators (a) MV, (b) DQ (c) PS, (d) AQS, and (e) IC. First five solutions are obtained with the molecular docking algorithm PatchDock. Heme groups are depicted in black and mediators are represented in ball and stick form.

were calculated from the changes in absorbance over time. In other words, the initial rate of mediator reoxidation, upon nitrite injection, was calculated by taking the first-derivative of the first part of the progression curve, thus considering a *pseudo*-1st-order reaction. In some cases the initial linear portion of the assay was sufficiently prolonged to allow the calculation of the initial rate reaction just by plotting a tangent to the first part of the assay curve, therefore considering a zero-order reaction rate.

An important consideration that must be drawn from the obtained results is that the reactions are not taking place at saturating mediator levels. The initial reaction velocities measured over a range of concentrations of MV, DQ, and PS, within the normal parameters used in spectroscopic assays (absorbance values between 0.5 and 2) were influenced by the mediator concentration (results not shown). Electron delivering from reduced electron donors is probably rate-limiting in this type of assay. This is not surprising since the need of six electrons per substrate molecule associated to the high catalytic rates of ccNiR demands a great supply of reducing equivalents. Therefore, the amount of electron

donor in the reaction vessel should be increased, but this involves experimental challenges. The concentration of coloured mediators, such as MV and DQ (reduced forms), is always limited by the validity range of the Lambert-Beer's law; the absorbance eventually reaches such high levels that the apparatus no longer responds linearly to the increasing concentrations. Problem solving could have been provided by the nonabsorbing reduced form of phenosafranine, but its low solubility constituted another obstacle. Without a perfect option, and with the aim of obtaining a set of comparable kinetic data, we decided to level the concentration of the reducing equivalents that each mediator supplies (*cf.* experimental section). The obtained results are shown in Figure 5. In the presence of varying substrate concentrations the nitrite reducing activity follows a Michaelis-Menten profile for all mediators.

The apparent K_M and turnover numbers were calculated from data fitting to the Michaelis-Menten equation (Table 1). Although kinetic parameters are in the same order of magnitude, there is no coherent variation of the catalytic constant with the potential. In particular, the electronic

TABLE 1: Kinetic parameters for nitrite reduction catalysed by *D. desulfuricans* ccNiR obtained by the continuous spectrophotometric and the amperometric assays.

Mediator/ Potential (vs NHE)	K_M^{app} (μM)	Homogeneous		Electrochemical		
		$k_{\text{cat}}^{\text{app}}$ (s^{-1})	k_{cat}/K_M ($\text{s}^{-1} \cdot \mu\text{M}^{-1}$)	K_M (μM)	$k_{\text{cat}}(\text{s}^{-1})^*$	k_{cat}/K_M ($\text{s}^{-1} \cdot \mu\text{M}^{-1}$)
Phenosafranine/−255 mV	2.7 ± 0.4	79 ± 3	29	9.2 ± 0.1	120 ± 1	13
Diquat/−350 mV	6.4 ± 0.6	1064 ± 23	166	28.1 ± 0.4	382 ± 2	14
Methyl viologen/−440 mV	15.0 ± 3.6	738 ± 45	49	33.3 ± 0.7	762 ± 4	23

* Turnover number was determined according to [30].

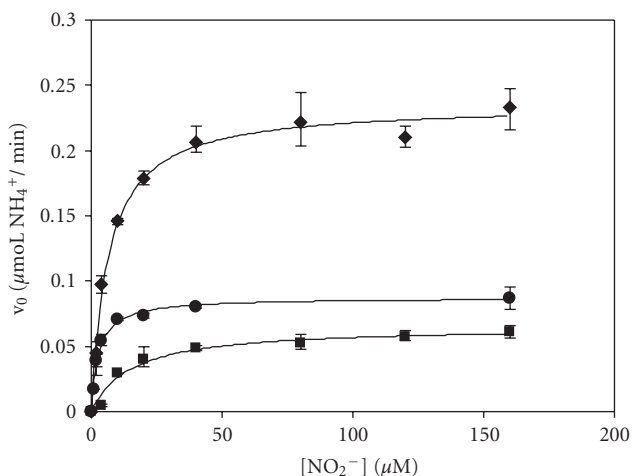


FIGURE 5: Enzyme activities determined using equivalent electron concentrations (0.16 mM) of MV (■), DQ (◆), PS (●), at 37°C, over increasing nitrite concentrations. The solid lines represent the simulations to the Michaelis-Menten equation. Enzyme concentration was 0.6 nM for MV, 1.5 nM for DQ, and 7.4 nM for PS assays.

carrier that gave the highest k_{cat} value is diquat, which has an intermediate reduction potential. This indicates a clear influence of the mediator nature on the measured activities, determined by other aspects than the reduction potential. Perhaps the electron transfer rate from DQ to the protein is much faster, enabling higher turnovers. In fact, according to the docking studies, DQ may interact differently with ccNiR, having some chances to deliver electrons directly to the catalytic site (Figure 4).

The high k_{cat} value for DQ was also unexpected since in the discontinuous assay, the highest specific activity was observed for MV. A possible explanation can come from the fact that anaerobic conditions were maintained in the continuous method, but not in the discontinuous. As a result, in the latter assay the concentration of the reduced species is not properly controlled, as it is in the continuous mode (e.g., incomplete diquat reduction). This brings our attention to the artefacts that can be generated by indirect enzymatic assays based on measurements of electronic carriers.

The binding affinity for nitrite decreased consistently with the reduction potential (K_M rise). Possibly, in a fully reduced state the protein may adopt a structural conformation that somewhat diminishes the affinity for nitrite.

3.2. Direct Electrochemistry. The alternative method for determining nitrite reductase activity relied on a heterogeneous electron transfer reaction using an electrochemical technique. Herein ccNiR was adsorbed on the surface of a PG electrode that delivered electrons directly to the enzyme, thus converting it to its active state (Figure 1(b)). Due to the high activity of multihemic nitrite reductases it is difficult to eliminate mass-transport limitations in these experiments [15, 33]. An electrode rotation speed of 600 rpm was used in this work, which corresponds to 95% of the limiting current (not affected by mass transport). This was considered as a sufficient reflection of the steady-state activity of ccNiR. In this way, we were also able to avoid turbulence and flow irreproducibility generated at high electrode rotation speeds, by eddy currents and vortices forming around the edges of the revolving electrode [34].

The ccNiR activity for nitrite was determined by amperometric titration (Figure 6) using potentials equivalent to the ones provided by the redox mediators used in the spectroscopic assays (−440 mV for MV, −350 mV for DQ, and −255 mV for PS). In this way, in spite of varying the protein reduction level, the experimental conditions are fully comparable.

ccNiR films on the PG electrode exhibited turnovers equivalent to those measured in the solution assays (Table 1). Hence, the catalytic activity of the biofilm was greatly maintained. More importantly, the expected trend of increasing k_{cat} with the electrode reductive driving force was here observed. This should be related to the use of the same electron delivering system (PG electrode) at the three operating potentials, thus eliminating any variability coming from the use of different electronic mediators.

The Michaelis-Menten constants were slightly higher than those obtained in the solution assays. This may reflect a small effect of enzyme adsorption or mass transport. Yet, the binding affinity for nitrite also decreases with the reduction potential. Nonetheless, if one considers the k_{cat}/K_M factor, the catalytic efficiency increases slightly with the reducing power regardless of the experimental approach.

4. Conclusions

The kinetic properties of ccNiR were studied using different methods. One of our goals was to study the influence of the electron donor of the reaction on the homogeneous kinetic parameters of ccNiR. As shown, below a sufficient reducing power ($E < -250$ mV), nitrite was always converted

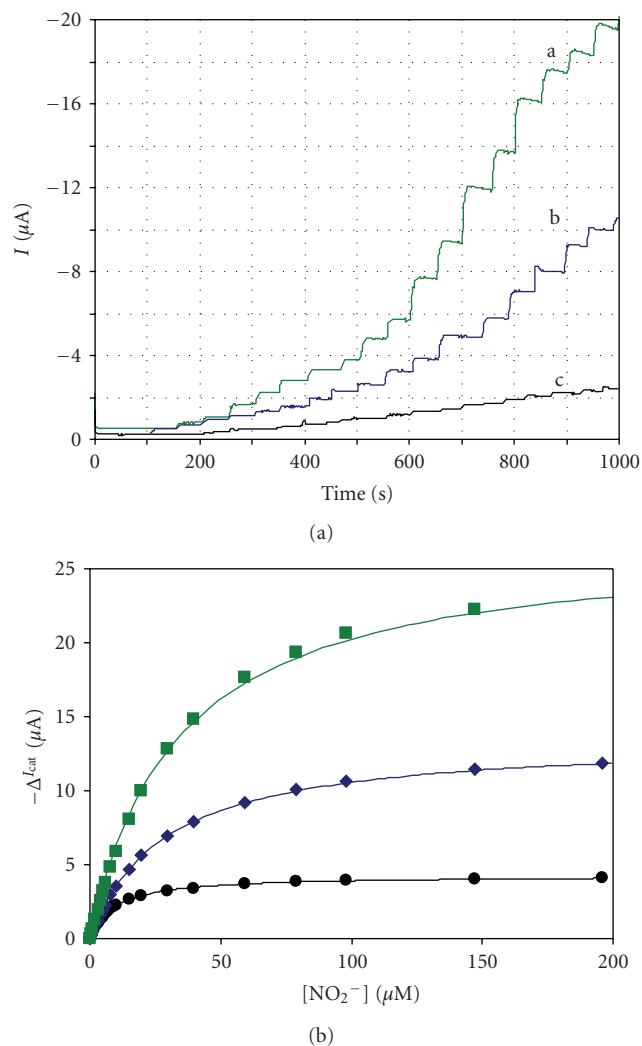


FIGURE 6: (a) Amperograms of PG electrodes with immobilized ccNiR, in the presence of increasing amounts of nitrite, recorded at (a) -440 mV, (b) -350 mV, and (c) -255 mV. (b) Michaelis-Menten fittings to the calibration curves performed at -440 mV (■), -350 mV (◆), and -255 mV (●). The assays were carried out at 37°C with an electrode rotation speed of 600 rpm. The solid lines represent the Michaelis-Menten simulations of enzyme kinetics.

stoichiometrically to ammonia. However, the chemical structure of the electronic carrier may have a certain impact on ccNiR activity, most likely at the level of the mediator-protein interaction and the subsequent intermolecular electron transfer. Apparently, the enzyme has a greater affinity for diquat than for the others mediators.

Methyl viologen was confirmed as the most suitable electron donor, since it provided the highest specific activity for nitrite. Moreover, it was the mediator that interacted more closely with the electron transfer hemes of ccNiR, as observed in the molecular docking studies.

We also conclude that we could not avoid the nonsaturating mediator conditions when using spectrophotometric techniques. As so, rate-limiting by electron donors is a pending issue and only apparent kinetic constants could

be assessed. It should be stressed that this topic has not been considered in previous works. Thus, data presented in the literature should be evaluated carefully, taking into consideration the experimental conditions. Although the present study does not provide a way to determine real parameters describing the homogeneous kinetics, it indicates electrochemistry as a good alternative to techniques depending on chromophore mediators.

Our future plans should cover the study of ccNiR's interaction with substrates other than nitrite and hydroxylamine. A systematic study of enzyme inhibition, the influence of pH, ionic strength, and temperature should be very useful to understand the kinetic mechanism of ccNiRs and for developing a robust electrochemical biosensor.

Acknowledgment

The authors thank the financial support funded by Fundação para a Ciência e Tecnologia (POCI/QUI/58026/2004 and SFRH/BD/28921/2006).

References

- [1] V. A. Bamford, H. C. Angove, H. E. Seward et al., "Structure and spectroscopy of the periplasmic cytochrome c nitrite reductase from *Escherichia coli*," *Biochemistry*, vol. 41, no. 9, pp. 2921–2931, 2002.
- [2] M. C. Liu and H. D. Peck Jr., "The isolation of a hexaheme cytochrome from *Desulfovibrio desulfuricans* and its identification as a new type of nitrite reductase," *Journal of Biological Chemistry*, vol. 256, no. 24, pp. 13159–13164, 1981.
- [3] J. Simon, R. Gross, O. Einsle, P. M. H. Kroneck, A. Kröger, and O. Klimmek, "A NapC/NirT-type cytochrome c (NrfH) is the mediator between the quinone pool and the cytochrome c nitrite reductase of *Wolinella succinogenes*," *Molecular Microbiology*, vol. 35, no. 3, pp. 686–696, 2000.
- [4] O. Einsle, A. Messerschmidt, P. Stach et al., "Structure of cytochrome c nitrite reductase," *Nature*, vol. 400, no. 6743, pp. 476–480, 1999.
- [5] O. Einsle, A. Messerschmidt, R. Huber, P. M. H. Kroneck, and F. Neese, "Mechanism of the six-electron reduction of nitrite to ammonia by cytochrome c nitrite reductase," *Journal of the American Chemical Society*, vol. 124, no. 39, pp. 11737–11745, 2002.
- [6] P. Stach, O. Einsle, W. Schumacher, E. Kurun, and P. M. H. Kroneck, "Bacterial cytochrome c nitrite reductase: new structural and functional aspects," *Journal of Inorganic Biochemistry*, vol. 79, no. 1–4, pp. 381–385, 2000.
- [7] P. Lukat, M. Rudolf, P. Stach et al., "Binding and reduction of sulfite by cytochrome c nitrite reductase," *Biochemistry*, vol. 47, no. 7, pp. 2080–2086, 2008.
- [8] I. C. Pereira, I. A. Abreu, A. V. Xavier, J. LeGall, and M. Teixeira, "Nitrite reductase from *Desulfovibrio desulfuricans* (ATCC 27774)—a heterooligomer heme protein with sulfite reductase activity," *Biochemical and Biophysical Research Communications*, vol. 224, no. 3, pp. 611–618, 1996.
- [9] M. L. Rodrigues, T. Oliveira, P. M. Matias et al., "Crystallization and preliminary structure determination of the membrane-bound complex cytochrome c nitrite reductase from *Desulfovibrio vulgaris* Hildenborough," *Acta Crystallographica F*, vol. 62, no. 6, pp. 565–568, 2006.

- [10] C. A. Cunha, S. Macieira, J. M. Dias et al., "Cytochrome c nitrite reductase from *Desulfovibrio desulfuricans* ATCC 27774. The relevance of the two calcium sites in the structure of the catalytic subunit (NrfA)," *Journal of Biological Chemistry*, vol. 278, no. 19, pp. 17455–17465, 2003.
- [11] M. G. Almeida, S. Macieira, L. L. Gonçalves et al., "The isolation and characterization of cytochrome c nitrite reductase subunits (NrfA and NrfH) from *Desulfovibrio desulfuricans* ATCC 27774. Re-evaluation of the spectroscopic data and redox properties," *European Journal of Biochemistry*, vol. 270, no. 19, pp. 3904–3915, 2003.
- [12] M. L. Rodrigues, T. F. Oliveira, I. A. C. Pereira, and M. Archer, "X-ray structure of the membrane-bound cytochrome c quinol dehydrogenase NrfH reveals novel haem coordination," *EMBO Journal*, vol. 25, no. 24, pp. 5951–5960, 2006.
- [13] T. V. Tikhonova, A. Slutsky, A. N. Antipov et al., "Molecular and catalytic properties of a novel cytochrome c nitrite reductase from nitrate-reducing haloalkaliphilic sulfur-oxidizing bacterium *Thioalkalivibrio nitratireducens*," *Biochimica et Biophysica Acta*, vol. 1764, no. 4, pp. 715–723, 2006.
- [14] T. A. Clarke, P. C. Mills, S. R. Pooock et al., "*Escherichia coli* cytochrome c nitrite reductase NrfA," *Methods in Enzymology*, vol. 437, pp. 63–77, 2008.
- [15] H. C. Angove, J. A. Cole, D. J. Richardson, and J. N. Butt, "Protein film voltammetry reveals distinctive fingerprints of nitrite and hydroxylamine reduction by a cytochrome c nitrite reductase," *Journal of Biological Chemistry*, vol. 277, no. 26, pp. 23374–23381, 2002.
- [16] J. D. Gwyer, H. C. Angove, D. J. Richardson, and J. N. Butt, "Redox-triggered events in cytochrome c nitrite reductase," *Bioelectrochemistry*, vol. 63, no. 1-2, pp. 43–47, 2004.
- [17] J. D. Gwyer, D. J. Richardson, and J. N. Butt, "Inhibiting *Escherichia coli* cytochrome c nitrite reductase: voltammetry reveals an enzyme equipped for action despite the chemical challenges it may face in vivo," *Biochemical Society Transactions*, vol. 34, no. 1, pp. 133–135, 2006.
- [18] C. Léger and P. Bertrand, "Direct electrochemistry of redox enzymes as a tool for mechanistic studies," *Chemical Reviews*, vol. 108, no. 7, pp. 2379–2438, 2008.
- [19] J. Heinecke and P. C. Ford, "Mechanistic studies of nitrite reactions with metalloproteins and models relevant to mammalian physiology," *Coordination Chemistry Reviews*, vol. 254, no. 3-4, pp. 235–247, 2010.
- [20] M. G. Almeida, C. M. Silveira, and J. J. G. Moura, "Biosensing nitrite using the system nitrite reductase/Nafion/methyl viologen—a voltammetric study," *Biosensors and Bioelectronics*, vol. 22, no. 11, pp. 2485–2492, 2007.
- [21] H. Chen, C. Mousty, S. Cosnier, C. Silveira, J. J. G. Moura, and M. G. Almeida, "Highly sensitive nitrite biosensor based on the electrical wiring of nitrite reductase by [ZnCr-AQS] LDH," *Electrochemistry Communications*, vol. 9, no. 9, pp. 2240–2245, 2007.
- [22] M. Scharf, C. Moreno, C. Costa et al., "Electrochemical studies on nitrite reductase towards a biosensor," *Biochemical and Biophysical Research Communications*, vol. 209, no. 3, pp. 1018–1025, 1995.
- [23] S. Da Silva, S. Cosnier, M. G. Almeida, and J. J. G. Moura, "An efficient poly(pyrrole-viologen)-nitrite reductase biosensor for the mediated detection of nitrite," *Electrochemistry Communications*, vol. 6, no. 4, pp. 404–408, 2004.
- [24] Z. Zhang, S. Xia, D. Leonard et al., "A novel nitrite biosensor based on conductometric electrode modified with cytochrome c nitrite reductase composite membrane," *Biosensors and Bioelectronics*, vol. 24, no. 6, pp. 1574–1579, 2009.
- [25] J. D. Nicholas and A. Nason, "Determination of nitrate and nitrite," *Methods in Enzymology*, vol. 3, pp. 981–984, 1957.
- [26] R. L. Searcy, N. M. Simms, J. A. Foreman, and L. M. Rergouist, "A study of the specificity of the Berthelot colour reaction," *Clinica Chimica Acta*, vol. 12, no. 2, pp. 170–175, 1965.
- [27] D. Duhovny, R. Nussinov, and H. Wolfson, "Efficient unbound docking of rigid molecules," in *Proceedings of the 2nd Workshop on Algorithms in Bioinformatics (WABI '02)*, R. Guigo and D. Gusfield, Eds., vol. 2452 of *Lecture Notes in Computer Science*, Springer, Rome, Italy, 2002.
- [28] D. Schneidman-Duhovny, Y. Inbar, R. Nussinov, and H. J. Wolfson, "PatchDock and SymmDock: servers for rigid and symmetric docking," *Nucleic Acids Research*, vol. 33, no. 2, pp. W363–W367, 2005.
- [29] E. F. Pettersen, T. D. Goddard, C. C. Huang et al., "UCSF Chimera—a visualization system for exploratory research and analysis," *Journal of Computational Chemistry*, vol. 25, no. 13, pp. 1605–1612, 2004.
- [30] M. G. Almeida, C. M. Silveira, B. Guigliarelli et al., "A needle in a haystack: the active site of the membrane-bound complex cytochrome c nitrite reductase," *FEBS Letters*, vol. 581, no. 2, pp. 284–288, 2007.
- [31] I. A. C. Pereira, J. LeGall, A. V. Xavier, and M. Teixeira, "Characterization of a heme c nitrite reductase from a non-ammonifying microorganism, *Desulfovibrio vulgaris* Hildenborough," *Biochimica et Biophysica Acta*, vol. 1481, no. 1, pp. 119–130, 2000.
- [32] K. F. Tipton, "Principles of enzyme assay and kinetic studies," in *Enzyme Assays: A Practical Approach*, Oxford University Press, Oxford, UK, 1993.
- [33] J. D. Gwyer, D. J. Richardson, and J. N. Butt, "Diode or tunnel-diode characteristics? Resolving the catalytic consequences of proton coupled electron transfer in a multi-centered oxidoreductase," *Journal of the American Chemical Society*, vol. 127, no. 43, pp. 14964–14965, 2005.
- [34] P. M. S. Monk, *Fundamentals of Electroanalytical Chemistry*, John Wiley & Sons, New York, NY, USA, 2002.

Research Article

Antineoplastic Activity of New Transition Metal Complexes of 6-Methylpyridine-2-carbaldehyde-N(4)-ethylthiosemicarbazone: X-Ray Crystal Structures of $[\text{VO}_2(\text{mpETSC})]$ and $[\text{Pt}(\text{mpETSC})\text{Cl}]$

Shadia A. Elsayed,¹ Ahmed M. El-Hendawy,² Sahar I. Mostafa,³ Bertrand J. Jean-Claude,⁴ Margarita Todorova,⁴ and Ian S. Butler¹

¹ Department of Chemistry, McGill University, Montreal, QC, Canada H3A 2K6

² Chemistry Department, Faculty of Science, Mansoura University, Damietta 34517, Egypt

³ Chemistry Department, Faculty of Science, Mansoura University, Mansoura, Egypt

⁴ Department of Medicine, Royal Victoria Hospital, Montreal, QC, Canada H3A 1A1

Correspondence should be addressed to Ian S. Butler, ian.butler@mcgill.ca

Received 14 March 2010; Accepted 14 April 2010

Academic Editor: Spyros Perlepes

Copyright © 2010 Shadia A. Elsayed et al. This is an open access article distributed under the Creative Commons Attribution License, which permits unrestricted use, distribution, and reproduction in any medium, provided the original work is properly cited.

New complexes of dioxovanadium(V), zinc(II), ruthenium(II), palladium(II), and platinum(II) with 6-methylpyridine-2-carbaldehyde-N(4)-ethylthiosemicarbazone (HmpETSC) have been synthesized. The composition of these complexes is discussed on the basis of elemental analyses, IR, Raman, NMR (¹H, ¹³C, and ³¹P), and electronic spectral data. The X-ray crystal structures of $[\text{VO}_2(\text{mpETSC})]$ and $[\text{Pt}(\text{mpETSC})\text{Cl}]$ are also reported. The HmpETSC and its $[\text{Zn}(\text{HmpETSC})\text{Cl}_2]$ and $[\text{Pd}(\text{mpETSC})\text{Cl}]$ complexes exhibit antineoplastic activity against colon cancer human cell lines (HCT 116).

1. Introduction

Interest in thiosemicarbazone chemistry has flourished for many years, largely as a result of its wide range of uses, for example, as antibacterial, antifungal, chemotherapeutic, and bioanalytical agents [1–6]. One particular area of thiosemicarbazone chemistry that has been increasing in importance recently involves biologically active metal complexes of thiosemicarbazone-based chelating (NNS) agents. As the coordination of the metal ions to thiosemicarbazones improves their efficacy and improve their bioactivity [6]. In this concept, zinc(II), palladium(II), and platinum(II) complexes of pyridine-2-carboxaldehyde thiosemicarbazone and substituted pyridine thiosemicarbazone were tested against human cancer breast and bladder cell lines and found to be selectively cytotoxic to these malignant cell carcinoma [7, 8]. We have previously studied the chemotherapeutic potential of a series of Mo(VI), Pd(II), Pt(II), and Ag(I) complexes with N,O; N,S and O,O-donors. These complexes were found to display significant anticancer activity against *Ehrlich ascites tumor cell* (EAC) in albino

mice [9–12]. Copper(II) complexes of 6-methylpyridine-2-carbaldehyde and its N(4)-methyl, ethyl, and phenyl thiosemicarbazones have been reported as well as their activity against pathogenic fungi [13]. In this paper, we report the synthesis and spectroscopic characterizations of new complexes of 6-methylpyridine-2-carbaldehyde-N(4)-ethylthiosemicarbazone (HmpETSC, Figure 1) with V(V), Zn(II), Ru(II), Pd(II), and Pt(II). The X-ray crystal structures of $[\text{VO}_2(\text{mpETSC})]$ and $[\text{Pt}(\text{mpETSC})\text{Cl}]$ have been reported. Also, the anticancer activity of HmpETSC and its Zn(II) and Pd(II) complexes toward colon cancer human cell lines has been tested.

2. Experimental

All reagents were purchased from Alfa/Aesar and Aldrich. $[\text{RuCl}_2(\text{PPh}_3)_3]$ was prepared as previously reported in [14]. Infrared spectra were recorded using a Nicolet 6700 Diamond ATR spectrometer in the 200–4000 cm^{-1} range. Raman spectra were recorded on in Via Renishaw

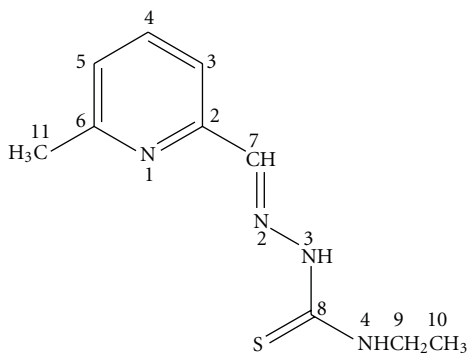


FIGURE 1: Structure of 6-methylpyridine-2-carbaldehyde-N(4)-ethylthiosemicarbazone (HmpETSC).

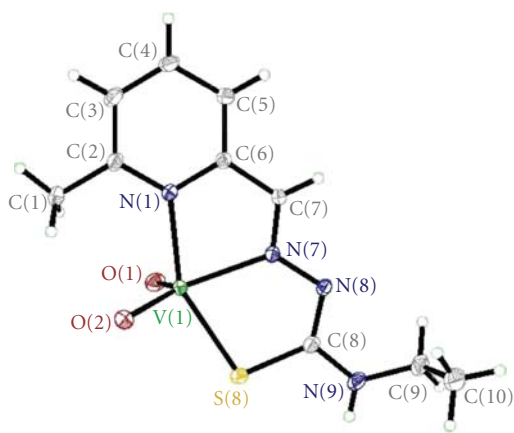


FIGURE 2: Structure of $[VO_2(mpETSC)]$ with numbering scheme.

spectrometer using 785 nm laser excitation. NMR spectra were recorded on Varian Mercury 500 MHz spectrometer in DMSO- d_6 with TMS as reference. Electronic spectra were recorded in DMF using Hewlett-Packard 8453 Spectrophotometer. Elemental analyses and X-ray crystallography were performed in Université De Montréal. The human cancer cell lines were obtained from the American Type Culture Collection (ATCC catalog number): HCT116 human colorectal carcinoma (CCL-247). Cells were maintained in Roswell Park Memorial Institute (RPMI-1640) medium (Wisent Inc., St-Bruno, Canada) supplemented with 10% FBS, 10 mM HEPES, 2 mM L-gutamine, and 100 μ g/mL penicillin/streptomycin (GibcoBRL, Gaithersburg, MD). All assay cells were plated 24 hours before drug treatment.

2.1. Preparation of the Ligand: 6-Methylpyridine-2-carboxaldehyde-N(4)-ethylthiosemicarbazone (HmpETSC). 6-Methylpyridine-2-carboxaldehyde (1.21 g, 10 mmol) in ethanol (10 cm^3) was added to N(4)-ethylthiosemicarbazide (1.19 g, 10 mmol) in ethanol-water solution (V/V 1:1, 80 cm^3) followed by the addition of drops of glacial acetic acid. The reaction mixture was refluxed for 3 hours. The precipitate obtained was filtered off, washed with water and ethanol,

and recrystallized from ethanol then dried in vacuo. m. p. = 201°C. Elemental analytical calculation for $C_{10}H_{13}N_4S$: C, 54.0, H, 6.4; N, 25.2; S, 14.4% found C, 54.0, H, 6.3; N, 25.1; S, 14.2%.

2.2. Preparation of the Complexes

2.2.1. $[VO_2(mpETSC)]$. To a solution of HmpETSC (0.044 g, 0.2 mmol) in acetonitrile (10 cm^3), $[VO(acac)_2]$ (0.053 g, 0.2 mmol) was added. The reaction mixture was refluxed for 1 hour. Upon cooling the yellowish green solution, orange precipitate was obtained. It was filtered off, washed with ethanol, and dried in vacuo. The brown crystals suitable for X-Ray crystallography were obtained by a slow evaporation of a solution of the complex in acetonitrile. The yield was 50% (based on the metal). Elemental analytical calculation for $C_{10}H_{13}N_4O_2SV$: C, 39.5; H, 4.3; N, 18.4; S, 10.5% found C, 39.4; H, 4.0; N, 18.2; S, 10.3%.

2.2.2. $[Zn(HmpETSC)Cl_2]$. A methanolic solution (10 cm^3) of HmpETSC (0.044 g, 0.2 mmol) was added to $ZnCl_2$ (0.027 g, 0.2 mmol) in methanol (10 cm^3). The reaction mixture was refluxed for 2 hours, and the off-white product obtained was filtered off, washed with methanol, then dried in air. The yield was 35% (based on the metal). Elemental analytical calculation for $C_{10}H_{14}Cl_2N_4SZn$: C, 33.5; H, 3.9; N, 15.6; S, 8.9% found C, 33.7; H, 3.7; N, 15.5; S, 8.8%.

2.2.3. $[Ru(PPh_3)_2(mpETSC)_2]$. A hot ethanolic solution of HmpETSC (0.044 g, 0.2 mmol) was added to $[RuCl_2(PPh_3)_3]$ (0.1 g, 0.1 mmol). Et_3N (0.02 cm^3 , 0.2 mmol) was then added and the reaction mixture was refluxed for 2 hours. The red brown solution was filtered and upon reducing the volume by evaporation a brown solid was isolated. It was filtered off, washed with ethanol and ether. The yield was 33% (based on the metal). Elemental analytical calculation for $C_{56}H_{56}N_8P_2RuS_2$: C, 63.0; H, 5.3; N, 10.5; S, 6.0% found that C, 62.8; H, 5.1; N, 10.4; S, 5.8%.

2.2.4. $[Pd(mpETSC)Cl]$. A solution of $K_2[PdCl_2]$ (0.1 g, 0.3 mmol) in water (2 cm^3) was added to HmpETSC (0.066 g, 0.3 mmol) in methanolic solution of KOH (0.018 g, 0.3 mmol; 15 cm^3). The reaction mixture was stirred at room temperature for 24 hours. The orange precipitate was filtered off, washed with water methanol, and finally air-dried. Yield was 60% (based on metal). Elemental analytical calculation for $C_{10}H_{13}ClN_4PdS$: C, 33.1; H, 3.6; N, 15.4; S, 8.8% found C, 33.4; H, 3.2; N, 15.2; S, 8.5%.

2.2.5. $[Pt(mpETSC)Cl]$. An aqueous solution (3 cm^3) of K_2PtCl_4 (0.042 g, 0.1 mmol) was added dropwise to a methanolic solution of HmpETSC (0.022 g, 0.1 mmol; 15 cm^3). The reaction mixture was stirred overnight at room temperature. Upon evaporation of the solvent, fine red crystals were observed. These were suitable for single crystal X-ray crystallography. Yield was 25% (based on metal). Elemental analytical calculation for $C_{10}H_{13}ClN_4PtS$: C, 26.6;

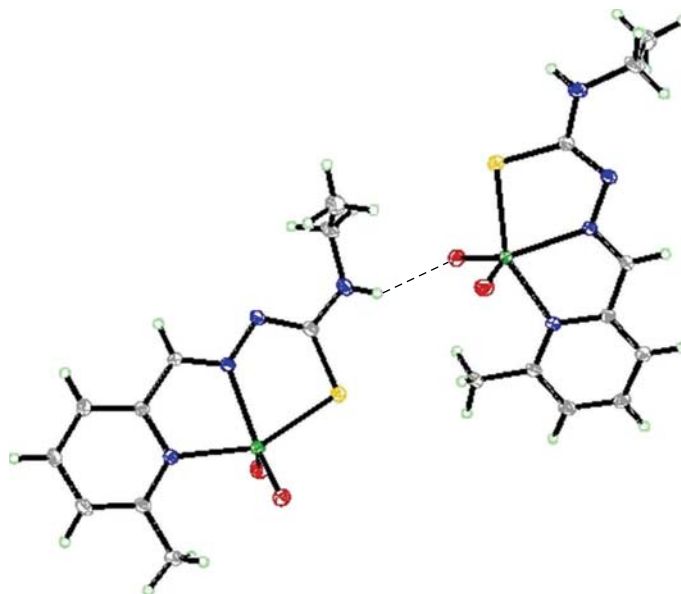


FIGURE 3: Hydrogen bonding interaction in the lattice of $[\text{VO}_2(\text{mpETSC})]$.

H, 2.9; N, 12.4; S, 7.1% found C, 26.8; H, 2.8; N, 12.1; S, 6.9%.

2.3. X-Ray Crystallography. The crystal structure were measured on The X-Ray Crystal Structure Unit, using a Bruker Platform diffractometer, equipped with a Bruker MART 4 K Charger-Coupled Device (CCD) Area Detector using the program APEX II and a Nonius Fr591 rotating anode (Copper radiation) equipped with Montel 200 optics. The crystal-to-detector distance was 5 cm, and the data collection was carried out in 512×512 pixel mode. The initial unit cell parameters were determined by the least-squares fit of the angular setting of strong reflections, collected by a 10.0 degree scan in 33 frames over three different parts of the reciprocal space (99 frames total). One complete sphere of data was collected.

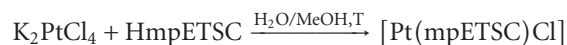
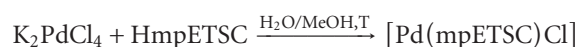
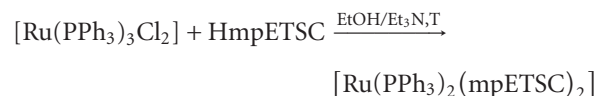
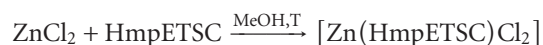
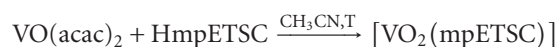
The crystals of $[\text{VO}_2(\text{mpETSC})]$ and $[\text{Pt}(\text{mpETSC})\text{Cl}]$ were mounted on the diffractometer, and the unit cell dimensions and intensity data were measured at 200 K. The structures were solved by the least-squares fit of the angular setting of strong reflections based on F^2 . The relevant crystal data and experimental conditions along with the final parameters are reported in Table 1.

2.4. Antineoplastic Testing. In the growth inhibition assay, HCT116 cells were plated at 5,000 cells/well in 96-well flat-bottomed microtiter plates (Costar, Corning, NY). After 24-hour incubation, cells were exposed to different concentrations of each compound continuously for four days. Briefly, following HmpETSC and its Zn(II) and Pd(II) complexes treatment, cells were fixed using $50 \mu\text{l}$ of cold trichloroacetic acid (50%) for 60 minutes at 4°C , washed with water, stained with 0.4% sulforhodamine B (SRB) for 4 hours at room

temperature, rinsed with 1% acetic acid, and allowed to dry overnight [15]. The resulting colored residue was dissolved in $200 \mu\text{l}$ Tris base (10 mM, pH 10.0), and optical density was recorded at 490 nm using a microplate reader ELx808 (BioTek Instruments). The results were analyzed by Graph Pad Prism (Graph Pad Software, Inc., San Diego, CA), and the sigmoidal dose response curve was used to determine 50% cell growth inhibitory concentration (IC_{50}). Each point represents the average of two independent experiments performed in triplicate.

3. Results and Discussion

3.1. Synthesis and Physical Properties of the Complexes. The preparative reactions for the complexes can be represented by the following equations:



All the complexes are microcrystalline or amorphous powder, stable in the normal laboratory atmosphere, and slightly soluble in common organic solvent but completely soluble in DMF and DMSO.

TABLE 1: Crystal data and structure refinement for VO₂(mpETSC) and Pt(mpETSC)Cl.

	[VO ₂ (mpETSC)]	[Pt(mpETSC)Cl]
Empirical formula	C ₁₀ H ₁₃ N ₄ O ₂ SV	C ₁₀ H ₁₃ ClN ₄ PtS
Formula weight	304.24	451.84
Temperature	200 K	150 K
Wavelength	1.54178 Å	1.54178 Å
Crystal system	Monoclinic	Monoclinic
Space group	P21/c	P21/n
Unit cell dimensions		
a(Å), α (°)	8.5583(2), 90°	12.9824(2), 90
b(Å), β (°)	13.4934(3), 03.679(1) ^o	b = 7.0655(1). 94.454(1) ^o
c(Å), γ (°)	11.2697(3), 90°	c = 13.6601(2), 90
Volume (Å ³)	1264.52(5) (Å ³)	1249.22(3) (Å ³)
Z, Density (calculated) g/cm ³	4; 1.598 g/cm ³	4; 2.402 g/cm ³
Absorption coefficient	8.122 mm ⁻¹	24.402 mm ⁻¹
F(000)	624	848
Crystal size	0.26 × 0.10 × 0.06 mm	0.12 × 0.08 × 0.02 mm
Theta range for data collection (°)	5.20 to 72.30°	4.53 to 72.13
Index ranges	-10 ≤ h ≤ 10, -16 ≤ k ≤ 16, -13 ≤ l ≤ 13	-15 ≤ h ≤ 15, -8 ≤ k ≤ 8, -16 ≤ l ≤ 16
Reflections collected	16371	15858
Independent reflections	2468 [R _{int} = 0.033]	2442 [R _{int} = 0.045]
Absorption correction	Semi-empirical from equivalents	Semi-empirical from equivalents
Max. and min. transmission	0.6143 and 0.3013	0.6138 and 0.3359
Refinement method	Full-matrix least-squares on F ²	Full-matrix least-squares on F ²
Data/restraints/parameters	2468/0/169	2442/0/157
Goodness-of-fit on F ²	1.150	1.065
Final R indices [I>2σ(I)]	R ₁ = 0.0318, wR ₂ = 0.0881	R ₁ = 0.0277, wR ₂ = 0.0951
R indices (all data)	R ₁ = 0.0326, wR ₂ = 0.0887	R ₁ = 0.0307, wR ₂ = 0.0993
Extinction coefficient		0.00036(6)
Largest diff. peak and hole	0.414 and -0.711 e/Å ³	1.579 and -1.242 e/Å ³

TABLE 2: Infrared and Raman spectral data of HmpETSC and its complexes^a.

Compound	ν(NH)	ν(HC=N)	ν(C=C)	ν(N=CS)	ν(N-N)	ν(CS)	ν(M-N)	ν(M-S)	ν(M-Cl)
HmpETSC	3267	1589	1530	—	992	812	—	—	—
		1607	1579		1006	824			
[VO ₂ (mpETSC)]	3214	1652	1613	1576	1017	787	427		926 ^b
		1651	1570	1586	1019	754	427	343	937 ^b
[Zn(HmpETSC)Cl ₂]	3290	1625	1596		1009	805	466		
		1626	1598		1009	793	427	317	300
[Ru(PPh ₃) ₂ (mpETSC) ₂]	3383	1572	1528	1479	999	788	465		
[Pd(mpETSC)Cl]	3286	1608	1582	1572	1008	784	454		
		1617	1580	1570	1022	787	462	345	297
[Pt(mpETSC)Cl]	3322	1607	1580	1570sh	1020	779	424		
		1609	1584	1564	1009	779	421	330	306

^aRaman data are in *bolds*, ^bν(O=V=O) sym and asym.

3.2. *Infrared and Raman Spectra.* The infrared and Raman spectral assignments of the ligand, HmpETSC, and its reported complexes are listed in Table 2. HmpETSC has the characteristic thioamide moiety (-HN-C(S)NH₂Et), which can be present in either thione or thiol form (Figure 1) [16, 17]. The IR and Raman spectra of HmpETSC show

the absence of absorption band in 2500–2600 cm⁻¹ region indicating the presence of the free HmpETSC in thione form [18]. HmpETSC shows a strong IR band at 1589 cm⁻¹, observed at 1607 cm⁻¹ in the Raman, which is corresponding to the azomethine, ν(HC=N), group [13, 19]. In the spectra of the complexes, the shift of this band to higher frequency

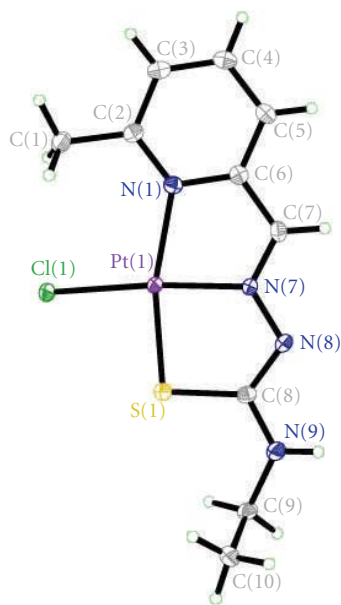


FIGURE 4: Structure of [Pt(mpETSC)Cl] with numbering scheme.

is observed, suggesting the participation of azomethine nitrogen in the coordination to metal ions [20, 21]. This feature is further supported by the shift of $\nu(\text{N-N})$ band in the free ligand (at 992 and 1006 cm^{-1} in IR and Raman, respectively) to higher frequencies upon complexation [18, 22]. On the other hand, the participation of the deprotonated thiol sulfur in coordination was indicated by the shift of the IR band at 812 cm^{-1} (at 824 cm^{-1} in the Raman) in the free ligand to lower frequencies in the complexes [19, 23]. This view is supported by the absence of $\nu(\text{N(3)H})$ vibration with the observation of new band near 1570 cm^{-1} in the complexes which may assign to $\nu(\text{N(3)=C})$ [24]. Furthermore, the coordination of pyridine nitrogen atom is indicated through the positive shift of the ring deformation band in HmpETSC near 582 and 586 cm^{-1} in the IR and Raman spectra, respectively [25]. Both IR and Raman spectral data suggest mononegative tridentate (N, N, S⁻) behavior of mpETSC⁻. In case of [Zn(HmpETSC)Cl₂], the $\nu(\text{N(3)H})$ band is observed at lower wave number as the thione sulfur participates in coordination [26]. Also, there is no shift observed in the pyridine ring deformation mode, that is, HmpETSC acts as a neutral bidentate ligand through both thione sulfur and azomethine nitrogen atoms [25].

The spectra of the complexes show that new bands in the IR and Raman near 450 cm^{-1} may assign to $\nu(\text{M-N})$ [27]. Also, the far IR and Raman spectra show new bands near 325 and 300 cm^{-1} can be assigned to $\nu(\text{M-S})$ and $\nu(\text{M-Cl})$, respectively [9, 10].

In the $940\text{--}920\text{ cm}^{-1}$ region the IR spectrum of the complex [VO₂(mpETSC)] shows two strong bands characteristic of the *cis*-VO₂ moiety [28, 29].

The presence of the coordinated PPh₃ in the complex [Ru(PPh₃)₂(mpETSC)₂] is confirmed by the appearance of the characteristic $\nu(\text{P-C}_{\text{ph}})$ and $\delta(\text{C-CH})$ band at 1085 and 720 cm^{-1} , respectively [30].

3.3. NMR Spectra. Table 3 shows the ¹H-NMR spectral data of HmpETSC and its reported complexes in DMSO-d₆ (see Figure 1 for numbering scheme) which are in a great agreement with those reported in the literature [13, 31, 32]. In the spectrum of free HmpETSC, the singlet observed at δ 11.62 ppm assigned to N(3)H is disappeared in the spectra of the complexes indicating that the coordination takes place through the deprotonated thiol sulfur atom [33]. In [Zn(HmpETSC)Cl₂], this band is observed at δ 11.63 ppm, confirming the data observed in the IR and Raman spectra that the coordination of HmpETSC to Zn(II) occurs through the thione sulfur atom [34]. As expected, the singlet observed at δ 8.02 ppm in the free ligand assigned to the azomethine H(7)C=N proton shows downfield shift in the complexes (δ 8.22–8.71 ppm), due to the involvement of azomethine nitrogen in coordination [16, 33]. The spectrum of HmpETSC shows singlet at δ 8.66 ppm assigned to the thioamide N(4)H proton, this signal is shifted upfield upon complexation [32, 34]. This feature may be due to the sequence of establishment of hydrogen bonds formation [35, 36]. The spectrum of HmpETSC exhibits triplet and quartet signals at δ 1.14 and 3.58 ppm assigned to H(10) and H(9), respectively. Also, the pyridine protons appear in δ 7.22–8.059 ppm region [33]. As expected, these protons are shifted downfield complexes (except in case of [Zn(HmpETSC)Cl₂]) due to the decrease in the electron density caused by electron withdrawal by the metal ions from the sulfur, azomethine nitrogen, and pyridine nitrogen atoms.

¹³C-NMR assignments of the HmpETSC and its complexes are listed in Table 4 and are in agreement with the reported data [13]. The spectrum of the free ligand shows number of resonances at δ 14.98, 24.49, 38.81, 117.69, 123.78, 137.14, 142.74, 153.18, 158.28, and 177.28 ppm, assigned to C(10), C(11), C(9), C(5), C(3), C(4), C(7), C(6), C(2), and C(8), respectively. In the complexes, the resonances of the carbon atoms adjacent to the coordination sites (C(7), C(8), C(2), and C(6)) are shifted downfield relatively to their positions in the free ligand [37, 38]. This feature may be due to an increase in current brought about by coordination to azomethine nitrogen, pyridine nitrogen, and deprotonated thiol sulfur atoms [25, 39]. In the spectrum of [Zn(HmpETSC)Cl₂] complex, the resonances arising from C(6), C(2) are more or less in the same positions as in the free ligand indicating that HmpETSC acts as a neutral bidentate ligand through thione sulfur and azomethine nitrogen atoms [25].

The ³¹P-NMR spectrum of [Ru(PPh₃)₂(mpETSC)₂] shows a sharp singlet at δ 52.48 ppm, suggesting the presence of the two PPh₃ groups in *trans*-configuration [30].

3.4. Electronic Spectra. The electronic spectrum of HmpETSC shows bands at 340 and 300 nm assigned to $\pi \rightarrow \pi^*$ and $n \rightarrow \pi^*$ of the azomethine and pyridine ring transitions, respectively [40, 41]. In the complexes, both transitions undergo blue shifts indicating the coordination *via* the azomethine and pyridine nitrogen atoms [42].

The electronic spectra of [M(mpETSC)Cl] (M(II) = Pd, Pt) show that two bands near 475 and 330 nm can be assigned

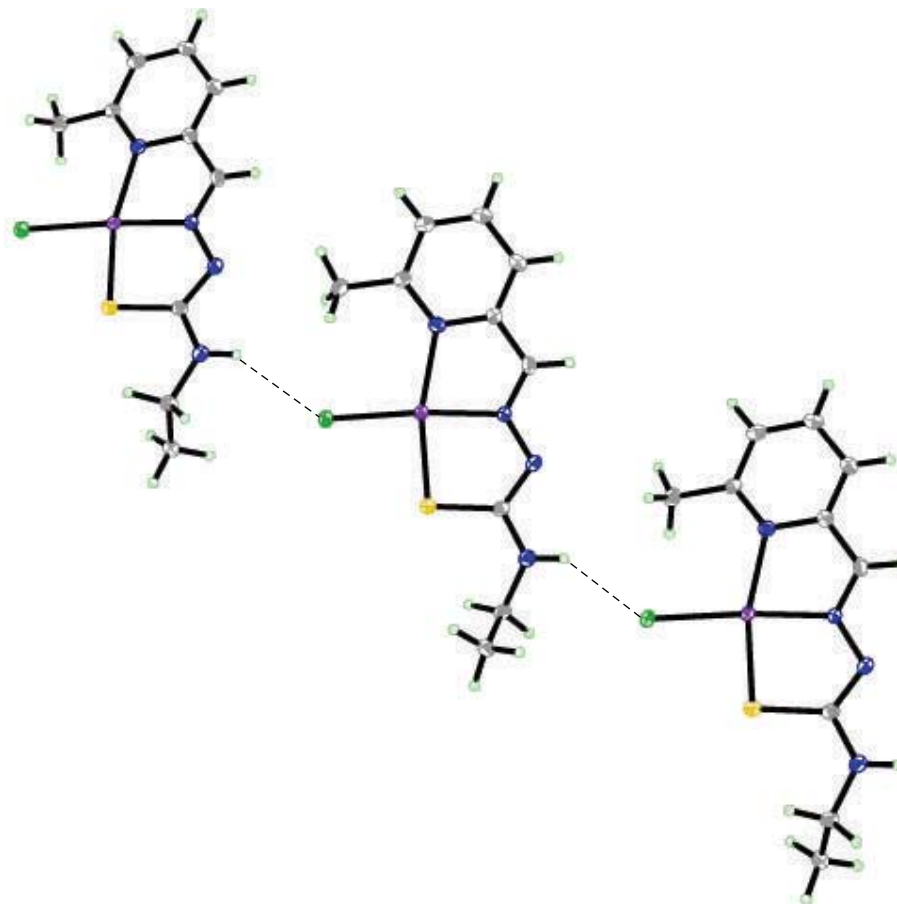


FIGURE 5: Hydrogen bonding interaction in the lattice of [Pt(mpETSC)Cl].

TABLE 3: $^1\text{H-NMR}$ spectral data of HmpETSC and its complexes.

Compound	H(3) (d)	H(4) (t)	H(5) (d)	H(7)CH=N (s)	H(9) (q)	H(10) (t)	Me(py) (s)	N(3)H (s)	N(4)H (s)
HmpETSC	8.06	7.71	7.22	8.02	3.58	1.14	2.45	11.62	8.67
[VO ₂ (mpETSC)]	7.56	8.11	7.67	8.58	3.32	1.12	2.48	—	8.19
[Zn(HmpETSC)Cl ₂]	8.02	7.73	7.23	8.71	3.58	1.13	2.46	11.63	8.67
[Ru(PPh ₃) ₂ (mpETSC) ₂]	7.55	7.45	7.38	8.63	3.34	0.88	2.38	—	— ^a
[Pd(mpETSC)Cl]	7.55	7.95	7.38	8.22	3.23	1.07	2.49	—	7.95
[Pt(mpETSC)Cl]	7.55	8.55	7.46	8.22	3.31	1.08	2.48	—	7.98

^a Overlapped with Ph protons.TABLE 4: $^{13}\text{C-NMR}$ spectral data of HmpETSC and its complexes.

Compound	C(2)	C(3)	C(4)	C(5)	C(6)	C(HC=N)	(C(C=S))	C(9)	C(10)	C(11)
HmpETSC	158.28	123.78	137.14	117.69	153.18	142.74	177.28	38.81	14.98	24.49
[VO ₂ (mpETSC)]	163.16	127.39	142.76	123.26	153.75	149.43	175.46	39.82	14.85	26.34
[Zn(HmpETSC)Cl ₂]	158.01	124.01	137.59	118.06	152.82	142.22	177.25	38.83	14.94	24.07
[Ru(PPh ₃) ₂ (mpETSC) ₂]	157.32	127.08	137.82	117.45	155.44	143.41	183.48	36.37	15.94	24.94
[Pd(mpETSC)Cl]	163.54	127.87	140.56	123.52	157.64	149.90	178.56	41.85	14.74	25.70
[Pt(mpETSC)Cl]	164.02	129.06	140.61	123.56	157.88	146.54	180.45	40.55	14.92	25.93

TABLE 5: Selected bond lengths and bond angles for [VO₂(mpETSC)].

bond lengths (Å)		Bond angles (°)	
V(1)–O(1)	1.6145(12)	O(2)–V(1)–S(8)	96.73(5)
V(1)–O(2)	1.6356(12)	N(1)–V(1)–S(8)	151.43(4)
V(1)–N(1)	2.1333(14)	N(7)–V(1)–S(8)	76.48(4)
V(1)–N(7)	2.1651(13)	C(8)–S(8)–V(1)	100.39(6)
V(1)–S(8)	2.3800(5)	C(2)–N(1)–C(6)	118.72(14)
S(8)–C(8)	1.7472(17)	C(2)–N(1)–V(1)	125.52(11)
N(1)–C(2)	1.351(2)	C(6)–N(1)–V(1)	115.75(11)
N(1)–C(6)	1.361(2)	C(7)–N(7)–N(8)	116.94(13)
N(7)–C(7)	1.287(2)	C(7)–N(7)–V(1)	116.04(10)
N(7)–N(8)	1.3708(17)	N(8)–N(7)–V(1)	127.01(10)
N(8)–C(8)	1.322(2)	C(8)–N(8)–N(7)	111.43(13)
N(9)–C(8)	1.339(2)	C(8)–N(9)–C(9)	124.07(16)
N(9)–C(9)	1.454(2)	N(1)–C(2)–C(3)	120.41(16)
C(1)–C(2)	1.494(2)	N(1)–C(2)–C(1)	119.13(15)
C(2)–C(3)	1.398(2)	C(3)–C(2)–C(1)	120.45(15)
C(3)–C(4)	1.379(3)	C(4)–C(3)–C(2)	120.71(15)
C(4)–C(5)	1.390(2)	C(3)–C(4)–C(5)	118.81(16)
C(5)–C(6)	1.385(2)	C(6)–C(5)–C(4)	118.35(16)
C(6)–C(7)	1.451(2)	N(1)–C(6)–C(5)	122.94(16)
C(9)–C(10)	1.509(3)	N(1)–C(6)–C(7)	115.08(14)
		C(5)–C(6)–C(7)	121.98(15)
		N(7)–C(7)–C(6)	117.71(14)
		N(8)–C(8)–N(9)	118.62(15)
		N(8)–C(8)–S(8)	124.50(12)
		N(9)–C(8)–S(8)	116.87(13)
		N(9)–C(9)–C(10)	112.49(17)
		O(1)–V(1)–O(2)	107.64(7)
		O(1)–V(1)–N(1)	96.08(6)
		O(2)–V(1)–N(1)	101.30(6)
		O(1)–V(1)–N(7)	113.29(6)
		O(2)–V(1)–N(7)	139.07(6)
		N(1)–V(1)–N(7)	75.37(5)
		O(1)–V(1)–S(8)	99.35(5)

TABLE 6: Bond lengths [Å] and angles [°] related to the hydrogen bonding for [VO₂(mpETSC)].

D-H	..A	d(D-H)	d(H..A)	d(D..A)	<DHA
N(9)–H(9)	O(2) no. 1	0.82(2)	2.30(2)	2.994(2)	144(2)

Symmetry transformations used to generate equivalent atoms: no. 1 $-x + 1$, and $y - 1/2, -z + 3/2$.

to $^1A_{1g} \rightarrow ^1B_{1g}$ and $^1A_{1g} \rightarrow ^1E_g$ transitions, respectively, in square planar configurations [9–12].

The electronic spectrum of the diamagnetic [Ru^{II}(PPh₃)₂(mpETSC)₂] shows bands at 532, 354, and 393 nm ($^1A_{1g} \rightarrow ^1T_{1g}$, $^1A_{1g} \rightarrow ^1T_{2g}$, and ligand (p-dp) transitions, respectively). These are attributed to a low-spin octahedral geometry around Ru(II) [10–12].

The electronic spectrum of the diamagnetic [VO₂(mpETSC)] shows that two bands at 440 and 360 nm

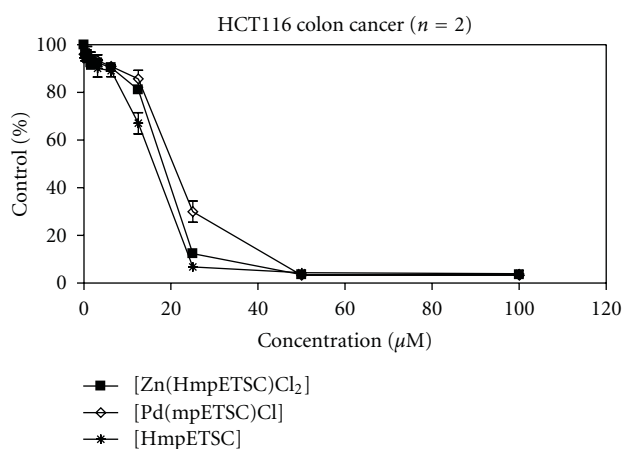
may be assigned to MLCT and $n-\pi^*$ transitions, respectively [43].

3.5. X-Ray Crystallography. The structure of the complexes [VO₂(mpETSC)] and [Pt(mpETSC)Cl], together with the atoms numbering scheme adopted is shown in Figures 2, 3, 4, and 5, respectively. The selected bond distances and bond angles of the complexes are listed in Tables 5, 6, 7, and 8, respectively. The complexes [VO₂(mpETSC)] and [Pt(mpETSC)Cl] are crystallized in monoclinic lattice with space group symmetry P21/c and P21/n, respectively.

The X-ray crystal structure of [VO₂(mpETSC)] shows that the vanadium(V) atom has a distorted square pyramidal environment in which mpETSC⁻ is coordinated to the metal ion as a tridentate chelating agent binding *via* the deprotonated thiolat sulfur S(8), the azomethine nitrogen N(7), and pyridine nitrogen N(1) atoms, yielding two five-membered chelate rings (Figure 2) with bond distances

TABLE 7: Selected bond lengths and bond angles for the [Pt(mpETSC)Cl] complex.

bond lengths (Å)		Bond angles (°)	
Pt(1)–N(7)	1.979(5)	C(8)–S(1)–Pt1	95.02(11)
Pt(1)–N(1)	2.116(3)	C(2)–N(1)–C(6)	118.6(3)
Pt(1)–S(1)	2.2533(8)	C(2)–N(1)–Pt1	132.4(2)
Pt(1)–Cl(1)	2.3178(15)	C(6)–N(1)–Pt1	109.0(2)
S(1)–C(8)	1.757(3)	C(7)–N(7)–N(8)	121.8(5)
N(1)–C(2)	1.350(4)	C(7)–N(7)–Pt1	116.1(4)
N(1)–C(6)	1.370(5)	N(8)–N(7)–Pt1	121.9(3)
N(7)–C(7)	1.287(8)	C(8)–N(8)–N(7)	113.4(4)
N(7)–N(8)	1.365(6)	C(8)–N(9)–C(9)	127.1(3)
N(8)–C(8)	1.333(5)	N(1)–C(2)–C(3)	120.3(3)
N(9)–C(8)	1.331(4)	N(1)–C(2)–C(1)	119.7(3)
N(9)–C(9)	1.449(4)	C(3)–C(2)–C(1)	120.0(3)
C(1)–C(2)	1.494(4)	C(4)–C(3)–C(2)	121.1(3)
C(2)–C(3)	1.400(5)	C(3)–C(4)–C(5)	118.4(3)
C(3)–C(4)	1.370(5)	C(6)–C(5)–C(4)	119.1(3)
C(4)–C(5)	1.389(5)	N(1)–C(6)–C(5)	122.3(3)
C(5)–C(6)	1.381(5)	N(1)–C(6)–C(7)	116.5(4)
C(6)–C(7)	1.426(8)	C(5)–C(6)–C(7)	121.2(4)
C(9)–C(10)	1.491(5)	N(7)–C(7)–C(6)	117.7(6)
		N(9)–C(8)–N(8)	116.8(3)
		N(9)–C(8)–S(1)	118.8(3)
		N(8)–C(8)–S(1)	124.4(3)
		N(9)–C(9)–C(10)	113.1(3)
		N(7)–Pt1–N(1)	80.15(16)
		N(7)–Pt1–S(1)	85.25(14)
		N(1)–Pt1–S(1)	165.40(8)
		N(7)–Pt1–Cl1	174.13(12)
		N(1)–Pt1–Cl1	105.02(8)
		S(1)–Pt1–Cl1	89.57(4)

FIGURE 6: Antineoplastic activity in human colon carcinoma HCT116 cells by a growth inhibition SRB assay after 96-hour treatment of HmpETSC, [Zn(HmpETSC)Cl₂], and [Pd(mpETSC)Cl].

(V–N(1), 2.1333(14) Å, V–N(7), 2.1651(13) Å, and V–S(8), 2.3800(5) Å). The other two sites are occupied by oxo ligands

TABLE 8: Bond lengths (Å) and angles (°) related to the hydrogen bonding for [Pt(mpETSC)Cl].

D–H	..A	d(D–H)	d(H..A)	d(D..A)	<DHA
N(9)–H(9)	Cl1 no. 1	0.88	2.62	3.372(3)	143.6

Symmetry transformations used to generate equivalent atoms: no. 1 $x + 1/2$, $-y + 3/2$, and $z + 1/2$.

TABLE 9: Antineoplastic activity in human colon tumor cell lines (HCT116) by growth inhibition SRB assay after 96-hour treatment.

Compound	HmpETSC	[Zn(HmpETSC)Cl ₂]	[Pd(mpETSC)Cl]
IC ₅₀ , µM	14.59	16.96	20.65
SD	0.81	0.46	1.60

O(1) and O(2) in *cis*-configuration. The O(1) occupies the basal position with mpETSC[−] donor while the O(2) occupies the apical position (V–O(1), 1.6145(12) Å and V–O(2), 1.6356(12) Å) [42]. In the present complex [VO₂(mpETSC)], the bond distances C(8)–N(8), 1.322(2) Å and C(7)–N(7), 1.287(2) Å are not intermediate between single and double

bonds, but they are closer to double bonds. Also, the N(7)-N(8), 1.322(2) Å bond length is very close to a single bond (Table 5). Moreover, the C(8)-S(8) bond length in the complex (1.7472(7) Å) is intermediate between a C-S double bond (1.62 Å) and a C-S single bond (1.82 Å), indicating that this bond maintains a partial double-bond character [42]. The bond angles data, N(1)-V-N(7), 75.37(5)°; N(7)-V-S(8), 76.48(4)°, O(2)-V-S(8), 96.73(5)°, O(1)-V-O(2), 107.64(7)°, O(1)-V-N(1), 96.08(6)°, indicate that the complex has a distorted square pyramidal geometry, which may be attributed to the restricted bite angles of mpETSC⁻ [44, 45]. The network structure is stabilized by the intermolecular hydrogen bonding interaction, N(9)H.....O(2) bond (Table 6, Figure 3).

In case of [Pt(mpETSC)Cl], mpETSC⁻ is also coordinated platinum(II) in the same tridentate manner, and chloride atom has taken up the fourth coordination site on Pt(II) in planar configuration (Figure 4). The bond lengths, Pt-N(1), 2.116(8) Å, Pt-N(7), 1.979(5) Å, Pt-S(1), 2.2533(8) Å, Pt-Cl(1), 2.3178(3) Å, in the complex are longer than those found in other reported square-planar platinum(II) complexes with N,S-donors [34–36, 42]. The data show that [Pt(mpETSC)Cl] has short N-N and long C-S bond lengths (Table 7) compared with other reported complexes. The bond angles of N(1)-Pt-S(1), 165.40(8)° and N(7)-Pt-Cl(1), 174.13(12)° are deviated substantially from that expected for a regular square-planar geometry. The monomer units of this complex are linked together into polymeric net chain through N(9)H.....Cl intermolecular hydrogen bonds as shown in Table 8 and Figure 5 [46].

3.6. Antineoplastic Activity. HmpETSC, [Zn(HmpETSC)Cl₂], and [Pd(mpETSC)Cl] were tested for their antineoplastic activity against the human colon tumor cell lines (HCT 116). The three compounds exhibited remarkable growth inhibitory activities with mean IC₅₀ values of 14.59, 16.96, and 20.65 μM, respectively (Table 9 and Figure 6). 2-Formyl and 2-acetylpyridine-N(4)-ethylthiosemicarbazones and their complexes [M(f4Et)₂] and [M(Ac4Et)₂] (M(II) = Pd, Pt, f4Et, Ac4Et = 2-formyl and 2-acetylpyridine-N(4)-ethylthiosemicarbazone) have been tested in a panel of human colon, breast, and ovary tumor cell lines and were found to exhibit very remarkable growth inhibitory activities with mean IC₅₀ values of 0.9–0.5 nM [47]. It is clear that the complexation of f4Et and Ac4Et in [Pd(f4Et)₂], [Pd(Ac4Et)₂], [Pt(f4Et)₂], and [Pt(Ac4Et)₂] modified their activities towards the tumor cells [47]. The complex [Zn(HmpETSC)Cl₂] exhibits much better antineoplastic activity against HCT 116 compared to [Pd(mpETSC)Cl] which is more active than [Pt(mpETSC)Cl]. The substitution and modes of chelations of HmpETSC in the complexes [Zn(HmpETSC)Cl₂] and [Pd(mpETSC)Cl] are different than both f4Et and Ac4Et in the reported Pd(II) and Pt(II) complexes [48]. As reported, *cis*-N₂ and *cis*-S₂ configuration in the complexes [M(f4Et)₂] and [M(Ac4Et)₂] (M(II) = Pd, Pt) display their significant antitumor activity [46, 49]. Also, in the [Zn(HmpETSC)Cl₂], HmpETSC acts as a neutral bidentate chelating agent which is different than

its behavior (mononegative tridentate) in [Pd(mpETSC)Cl]. Furthermore, the presence of the intermolecular hydrogen bonds in the later complex may reduce its antineoplastic activity [48].

4. Conclusion

The aim of this report is to study the structure and antineoplastic activity of 6-methylpyridine-2-carbaldehyde-N(4)-ethylthiosemicarbazone (HmpETSC) and its complexes with dioxovanadium(V), zinc(II), ruthenium(II), palladium(II), and platinum(II). The X-ray crystal structure of the complexes [VO₂(mpETSC)] and [Pt(mpETSC)Cl] was reported. HmpETSC behaves as mononegative tridentate through the pyridine nitrogen, azomethine nitrogen and the deprotonated thiol sulfur atoms except in case of Zn(II) complex, it behaves as a neutral bidentate through azomethine nitrogen and thione sulfur atoms. HmpETSC and its Zn(II) and Pd(II) complexes show antineoplastic activity against the human colon tumor cell lines (HCT 116).

Acknowledgments

This research was supported by an NSERC (Canada) Discovery grant (ISB) and a scholarship from the Ministry of Higher Education, Egypt (S.E.).

References

- [1] V. B. Arion, M. A. Jakupc, M. Galanski, P. Unfried, and B. K. Keppler, "Synthesis, structure, spectroscopic and in vitro antitumor studies of a novel gallium(III) complex with 2-acetylpyridine 4N-dimethylthiosemicarbazone," *Journal of Inorganic Biochemistry*, vol. 91, no. 1, pp. 298–305, 2002.
- [2] C. C. García, B. N. Brousse, and M. J. Carlucci et al., "Inhibitory effect of thiosemicarbazone derivatives on Junin virus replication in vitro," *Antiviral Chemistry & Chemotherapy*, vol. 14, no. 2, pp. 99–105, 2003.
- [3] W.-X. Hu, W. Zhou, C.-N. Xia, and X. Wen, "Synthesis and anticancer activity of thiosemicarbazones," *Bioorganic and Medicinal Chemistry Letters*, vol. 16, no. 8, pp. 2213–2218, 2006.
- [4] E. M. Jouad, G. Larcher, and M. Allain et al., "Synthesis, structure and biological activity of nickel(II) complexes of 5-methyl 2-furfural thiosemicarbazone," *Journal of Inorganic Biochemistry*, vol. 86, no. 2-3, pp. 565–571, 2001.
- [5] A. Gölcü, M. Dolaz, H. Demirelli, M. Diorak, and S. Serin, "Spectroscopic and analytic properties of new copper(II) complex of antiviral drug valacyclovir," *Transition Metal Chemistry*, vol. 31, no. 5, pp. 658–665, 2006.
- [6] E. J. Blanz Jr. and F. A. French, "The carcinostatic activity of 5-hydroxy-2-formylpyridine thiosemicarbazone," *Cancer Research*, vol. 28, no. 12, pp. 2419–2422, 1968.
- [7] D. Kovala-Demertzi, P. N. Yadav, J. Wiecek, S. Skoulika, T. Varadinova, and M. A. Demertzis, "Zinc(II) complexes derived from pyridine-2-carbaldehyde thiosemicarbazone and (1E)-1-pyridin-2-ylethan-1-one thiosemicarbazone. Synthesis, crystal structures and antiproliferative activity of zinc(II) complexes," *Journal of Inorganic Biochemistry*, vol. 100, no. 9, pp. 1558–1567, 2006.

- [8] D. Kovala-Demertzi, M. A. Demertzi, and V. Varagi et al., "Antineoplastic and cytogenetic effects of platinum(II) and palladium(II) complexes with pyridine-2-carboxaldehyde-thiosemicarbazone," *Chemotherapy*, vol. 44, no. 6, pp. 421–426, 1998.
- [9] S. I. Mostafa, "Mixed ligand complexes with 2-piperidine-carboxylic acid as primary ligand and ethylene diamine, 2,2'-bipyridyl, 1,10-phenanthroline and 2(2'-pyridyl)quinoxaline as secondary ligands: preparation, characterization and biological activity," *Transition Metal Chemistry*, vol. 32, no. 6, pp. 769–775, 2007.
- [10] S. I. Mostafa, "Synthesis, characterization and antineoplastic activity of 5-chloro-2,3-dihydropyridine transition metal complexes," *Journal of Coordination Chemistry*, vol. 61, no. 10, pp. 1553–1567, 2008.
- [11] S. I. Mostafa and F. A. Badria, "Synthesis, spectroscopic, and anticancerous properties of mixed ligand palladium(II) and silver(I) complexes with 4,6-diamino-5-hydroxy-2-mercaptopyrimidine and 2,2'-bipyridyl," *Metal-Based Drugs*, vol. 2008, Article ID 723634, 7 pages, 2008.
- [12] I. M. Gabr, H. A. El-Asmy, M. S. Emmam, and S. I. Mostafa, "Synthesis, characterization and anticancer activity of 3-aminopyrazine-2-carboxylic acid transition metal complexes," *Transition Metal Chemistry*, vol. 34, no. 4, pp. 409–418, 2009.
- [13] D. X. West, S. L. Dietrich, I. Thientanavanich, C. A. Brown, and A. E. Liberta, "Copper(II) complexes of 6-methyl-2-formylpyridine ⁴N-substituted thiosemicarbazones," *Transition Metal Chemistry*, vol. 19, no. 2, pp. 195–200, 1994.
- [14] T. A. Stephenson and G. Wilkinson, "New complexes of ruthenium (II) and (III) with triphenylphosphine, triphenylarsine, trichlorostannate, pyridine and other ligands," *Journal of Inorganic and Nuclear Chemistry*, vol. 28, no. 4, pp. 945–956, 1966.
- [15] P. Skehan, R. Storeng, and D. Scudiero et al., "New colorimetric cytotoxicity assay for anticancer-drug screening," *Journal of the National Cancer Institute*, vol. 82, no. 13, pp. 1107–1112, 1990.
- [16] V. K. Sharma, S. Srivastava, and A. Srivastava, "Spectroscopic, thermal and biological studies on some trivalent ruthenium and rhodium NS chelating thiosemicarbazone complexes," *Bioinorganic Chemistry and Applications*, vol. 2007, Article ID 68374, 2007.
- [17] M. A. Ali, N. E. H. Ibrahim, R. J. Butcher, J. P. Jasinski, J. M. Jasinski, and J. C. Bryan, "Synthesis and Characterization of some four-and five-coordinate copper(II) complexes of 6-methyl-2-formylpyridinethiosemicarbazone," *Polyhedron*, vol. 17, no. 11-12, pp. 1803–1809, 1998.
- [18] O. E. Offiong and S. Martelli, "Stereochemistry and antitumour activity of platinum metal complexes of 2-acetylpyridine thiosemicarbazones," *Transition Metal Chemistry*, vol. 22, no. 3, pp. 263–269, 1997.
- [19] S. I. Mostafa and M. M. Bekheit, "Synthesis and structure studies of complexes of some second row transition metals with 1-(phenylacetyl and phenoxyacetyl)-4-phenyl-3-thiosemicarbazide," *Chemical and Pharmaceutical Bulletin*, vol. 48, no. 2, pp. 266–271, 2000.
- [20] Y. K. Bhoon, "Magnetic and EPR properties of Mn(II), Fe(III), Ni(II) and Cu(II) complexes of thiosemicarbazone of α -hydroxy- β -naphthaldehyde," *Polyhedron*, vol. 2, no. 5, pp. 365–368, 1983.
- [21] D. X. West and D. S. Galloway, "Transition metal ion complexes of thiosemicarbazones derived from 2-acetylpyridine. Part 3. The 3-hexamethyleneimine derivative," *Transition Metal Chemistry*, vol. 13, no. 6, pp. 410–414, 1988.
- [22] S. Singh, N. Bharti, F. Naqvi, and A. Azam, "Synthesis, characterization and in vitro antimetastatic activity of 5-nitrothiophene-2-carboxaldehyde thiosemicarbazones and their Palladium (II) and Ruthenium (II) complexes," *European Journal of Medicinal Chemistry*, vol. 39, no. 5, pp. 459–465, 2004.
- [23] S. Chandra and L. K. Gupta, "EPR, mass, IR, electronic, and magnetic studies on copper(II) complexes of semicarbazones and thiosemicarbazones," *Spectrochimica Acta—Part A*, vol. 61, no. 1-2, pp. 269–275, 2005.
- [24] D. X. West, J. K. Swearingen, J. Valdés-Martínez, et al., "Spectral and structural studies of iron(III), cobalt(II,III) and nickel(II) complexes of 2-pyridineformamide N(4)-methylthiosemicarbazone," *Polyhedron*, vol. 18, no. 22, pp. 2919–2929, 1999.
- [25] S. A. Elsayed, A. M. El-Hendawy, S. I. Mostafa, and I. S. Butler, "Transition metal complexes of 2-formylpyridinethiosemicarbazone (HFpyTSC) and X-Ray crystal structures of [Pd(FpyTSC)(PPh₃)₂][PF₆]⁻ and [Pd(FpyTSC)(SCN)]⁺," *Inorganica Chimica Acta*. In press.
- [26] T. S. Lobana, R. Sharma, G. Bawa, and S. Khanna, "Bonding and structure trends of thiosemicarbazone derivatives of metals—an overview," *Coordination Chemistry Reviews*, vol. 253, no. 7-8, pp. 977–1055, 2009.
- [27] D. X. West, A. E. Liberta, and S. B. Padhye et al., "Thiosemicarbazone complexes of copper(II): structural and biological studies," *Coordination Chemistry Reviews*, vol. 123, no. 1-2, pp. 49–71, 1993.
- [28] S. Samanta, D. Ghosh, S. Mukhopadhyay, A. Endo, T. J. R. Weakley, and M. Chaudhury, "Oxovanadium(IV) and - (V) complexes of dithiocarbamate-based tridentate Schiff base ligands: syntheses, structure, and photochemical reactivity of compounds involving imidazole derivatives as coligands," *Inorganic Chemistry*, vol. 42, no. 5, pp. 1508–1517, 2003.
- [29] E. Kwiatkowski, G. Romanowski, W. Nowicki, M. Kwiatkowski, and K. Suwińska, "Dioxovanadium(V) Schiff base complexes of N-methyl-1,2-diaminoethane and 2-methyl-1,2-diaminopropane with aromatic O-hydroxyaldehydes and o-hydroxyketones: synthesis, characterisation, catalytic properties and structure," *Polyhedron*, vol. 22, no. 7, pp. 1009–1018, 2003.
- [30] T. S. Lobana, G. Bawa, R. J. Butcher, B.-J. Liaw, and C. W. Liu, "Thiosemicarbazones of ruthenium(II): crystal structures of [bis(diphenylphosphino)butane][bis(pyridine-2-carbaldehydethiosemicarbazonato)] ruthenium(II) and [bis(triphenylphosphine)] [bis(benzaldehydethiosemicarbazonato)] ruthenium(II)," *Polyhedron*, vol. 25, no. 15, pp. 2897–2903, 2006.
- [31] K. R. Koch, "A multinuclear NMR study of platinum(II) complexes of N-Phenyl and N-(3-Allyl) Substituted 2-(2-Pyridinemethylene) hydrazine carbothioamides," *Journal of Coordination Chemistry*, vol. 22, no. 4, pp. 289–298, 1990.
- [32] R. Pedrido, M. J. Romero, M. R. Bermejo, M. Martínez-Calvo, A. M. González-Noya, and G. Zaragoza, "Coordinative trends of a tridentate thiosemicarbazone ligand: synthesis, characterization, luminescence studies and desulfurization processes," *Dalton Transactions*, no. 39, pp. 8329–8340, 2009.
- [33] W. Hernández, J. Paz, A. Vaisberg, E. Spodine, R. Richter, and L. Beyer, "Synthesis, characterization, and in vitro cytotoxic activities of benzaldehyde thiosemicarbazone derivatives and their palladium (II) and platinum (II) complexes against

- various human tumor cell lines,” *Bioinorganic Chemistry and Applications*, vol. 2008, Article ID 690952, 2008.
- [34] D. Kovala-Demertzi, P. N. Yadav, J. Wiecek, S. Skoulika, T. Varadinova, and M. A. Demertzis, “Zinc(II) complexes derived from pyridine-2-carbaldehyde thiosemicarbazone and (1E)-1-pyridin-2-ylethan-1-one thiosemicarbazone. Synthesis, crystal structures and antiproliferative activity of zinc(II) complexes,” *Journal of Inorganic Biochemistry*, vol. 100, no. 9, pp. 1558–1567, 2006.
- [35] M. R. Bermejo, A. M. González-Noya, M. Martínez-Calvo, et al., “New neutral metal complexes from the 4-*N*-phenylthiosemicarbazone-2- pyridinecarboxaldehyde ligand - ¹¹³Cd and ²⁰⁷Pb NMR studies,” *Zeitschrift für Anorganische und Allgemeine Chemie*, vol. 633, no. 11-12, pp. 1911–1918, 2007.
- [36] R. Pedrido, A.M. González-Noya, M. J. Romero, et al., “Pentadentate thiosemicarbazones as versatile chelating systems. A comparative structural study of their metallic complexes,” *Dalton Transactions*, no. 47, pp. 6776–6787, 2008.
- [37] K. R. Koch, “Cationic and neutral bis(4-*p*-tolylthiosemicarbazido)platinum(II) complexes: a preparative as well as ¹H and ¹⁹⁵Pt NMR study of the question of *cis/trans* isomerism,” *Inorganica Chimica Acta*, vol. 147, no. 2, pp. 227–232, 1988.
- [38] A. Castineiras, D. X. West, H. Gebremedhin, and T. J. Romack, “Cobalt(III) complexes with 2-acetyl- and 2-formylpyridine 4*N*-methylthiosemicarbazones,” *Inorganica Chimica Acta*, vol. 216, no. 1-2, pp. 229–236, 1994.
- [39] W. P. Griffith and S. I. Mostafa, “Complexes of 3-hydroxypyridin-2-one and 1,2-dimethyl-3-hydroxypyridin-4-one with second and third row elements of groups 6, 7 and 8,” *Polyhedron*, vol. 11, no. 23, pp. 2997–3005, 1992.
- [40] I. C. Mendes, J. P. Moreira, N. L. Speziali, A. S. Mangrich, J. A. Takahashi, and H. Beraldo, “N(4)-tolyl-2-benzoylpyridine thiosemicarbazones and their copper(II) complexes with significant antifungal activity. Crystal structure of N(4)-paratolyl-2-benzoylpyridine thiosemicarbazone,” *Journal of the Brazilian Chemical Society*, vol. 17, no. 8, pp. 1571–1577, 2006.
- [41] I. C. Mendes, J. P. Moreira, A. S. Mangrich, S. P. Balena, B. L. Rodrigues, and H. Beraldo, “Coordination to copper(II) strongly enhances the in vitro antimicrobial activity of pyridine-derived N(4)-tolyl thiosemicarbazones,” *Polyhedron*, vol. 26, no. 13, pp. 3263–3270, 2007.
- [42] M. A. Ali, A. H. Mirza, R. J. Butcher, M. T. H. Tarafder, T. B. Keat, and A. M. Ali, “Biological activity of palladium(II) and platinum(II) complexes of the acetone Schiff bases of *S*-methyl- and *S*-benzylthiosemicarbazate and the X-ray crystal structure of the [Pd(asme)₂] (asme=anionic form of the acetone Schiff base of *S*-methylthiosemicarbazate) complex,” *Journal of Inorganic Biochemistry*, vol. 92, no. 3-4, pp. 141–148, 2002.
- [43] I. C. Mendes, L. M. Botion, A. V. M. Ferreira, E. E. Castellano, and H. Beraldo, “Vanadium complexes with 2-pyridineformamide thiosemicarbazones: in vitro studies of insulin-like activity,” *Inorganica Chimica Acta*, vol. 362, no. 2, pp. 414–420, 2009.
- [44] P. I. S. Maia, F. R. Pavan, and C. Q. F. Leite et al., “Vanadium complexes with thiosemicarbazones: synthesis, characterization, crystal structures and anti-*Mycobacterium tuberculosis* activity,” *Polyhedron*, vol. 28, no. 2, pp. 398–406, 2009.
- [45] A. Sreekanth, S. Sivakumar, and M. R. P. Kurup, “Structural studies of six and four coordinate zinc(II), nickel(II) and dioxovanadium(V) complexes with thiosemicarbazones,” *Journal of Molecular Structure*, vol. 655, no. 1, pp. 47–58, 2003.
- [46] D. Kovala-Demertzi, M. A. Demertzis, J. R. Miller, C. Papadopoulou, C. Dodorou, and G. Filousis, “Platinum(II) complexes with 2-acetyl pyridine thiosemicarbazone: synthesis, crystal structure, spectral properties, antimicrobial and antitumour activity,” *Journal of Inorganic Biochemistry*, vol. 86, no. 2-3, pp. 555–563, 2001.
- [47] D. Kovala-Demertzi, A. Boccarelli, M. A. Demertzis, and M. Coluccia, “In vitro antitumor activity of 2-acetyl pyridine 4*N*-ethyl thiosemicarbazone and its platinum(II) and palladium(II) complexes,” *Chemotherapy*, vol. 53, no. 2, pp. 148–152, 2007.
- [48] A. I. Matesanz and P. Souza, “Palladium and platinum 3,5-diacetyl-1,2,4-triazol bis(thiosemicarbazones): chemistry, cytotoxic activity and structure-activity relationships,” *Journal of Inorganic Biochemistry*, vol. 101, no. 2, pp. 245–253, 2007.
- [49] K. I. Goldberg, J. Valdes-Martínez, G. Espinosa-Pérez, L. J. Ackerman, and D. X. West, “Palladium(II) and platinum(II) complexes of 6-methyl-2-acetylpyridine 3-hexamethyleneiminylthiosemicarbazones: a structural and spectral study,” *Polyhedron*, vol. 18, no. 8-9, pp. 1177–1182, 1999.

Research Article

Computational Modeling of the Mechanism of Urease

Håkan Carlsson and Ebbe Nordlander

Chemical Physics, Center for Chemistry and Chemical Engineering, Lund University, Box 124, 221 00 Lund, Sweden

Correspondence should be addressed to Ebbe Nordlander, ebbe.nordlander@chemphys.lu.se

Received 9 April 2010; Accepted 31 May 2010

Academic Editor: Spyros P. Perlepes

Copyright © 2010 H. Carlsson and E. Nordlander. This is an open access article distributed under the Creative Commons Attribution License, which permits unrestricted use, distribution, and reproduction in any medium, provided the original work is properly cited.

In order to elucidate aspects of the mechanism of the hydrolytic enzyme urease, theoretical calculations were undertaken on a model of the active site, using density functional theory. The bridging oxygen donor that has been found in the crystal structures was determined to be a hydroxide ion. The initial coordination of urea at the active site occurs most likely through the urea oxygen to the nickel ion with the lowest coordination number. This coordination can be made without much gain in energy. The calculations also showed that weak coordination of one of the urea amine nitrogen atoms to the second nickel atom is energetically feasible. Furthermore, a proposed mechanism including a tetrahedral intermediate generated by hydrolytic attack on the urea carbon by the bridging hydroxide was modeled, and the tetrahedral intermediate was found to be energetically unfavorable relative to terminal coordination of the substrate (urea).

1. Introduction

The hydrolytic enzyme urease is responsible for the catalytic decomposition of urea to volatile ammonia and carbon dioxide [1]. The enzyme releases ammonia and carbamate, which in turn spontaneously generate the products. The enzyme was studied early [2] and has generated interest for several reasons. It has been suggested to play a role in bacteria-induced ulcers [3, 4], and its activity has also been found to have implications in agriculture through the volatilization of urea—a commonly used fertilizer—that is generated by the enzyme [5]. Urease was also the first enzyme to be found to be dependent on nickel for its function [6], which has made it an interesting target site for bioinorganic model chemists [7].

The protein structure of urease from *Klebsiella aerogenes* was first solved in 1995 in [8], and since then several other structures of the enzyme, with or without bound inhibitors have been determined [9–12], including structures from *Bacillus pasteurii* [10–12] and *Helicobacter pylori* [13]. The active site contains two nickel ions with an interatomic distance of about 3.5 Å (Figure 1). The ions are bridged by a carbamylated lysine and an oxygen donor. In addition to the bridges, one of the nickel ions (Ni1) is coordinated by two histidines and a water molecule. The coordination of Ni2 is

similar to the one of Ni1 and includes two histidine residues, a water molecule and a terminally bound aspartate.

A number of proposals have been made regarding possible reaction mechanisms. Consensus has been reached regarding the initial coordination of urea to the active site, which has been suggested to occur through the urea oxygen attacking the vacant coordination site on Ni1 (Figure 2), but there are divergent proposals regarding the subsequent steps. The initially suggested mechanism involves the attack on the urea carbon by a hydroxide that is terminally bound to Ni2. This leads to an intermediate that bridges the two metals and can release ammonia to form products [14, 15]. Based on the structure of an inhibitor complex, Benini et al. [12, 16] suggested a mechanism involving a secondary coordination of one of the urea nitrogen atoms to Ni2, which positions the substrate for an attack from the bridging hydroxide (water). The bridging coordination of the urea substrate was supported by Pearson et al. [17], but these investigators have suggested that the nucleophile is not the bridging hydroxide, but rather a water/hydroxide coordinated to Ni2.

A few computational studies on the mechanism of urease have been published during the past decade. These include molecular mechanics studies by Zimmer [18, 19] and Smyj [20] and DFT studies by Merz et al. [21, 22]. The latter density functional study was carried out at the B3LYP

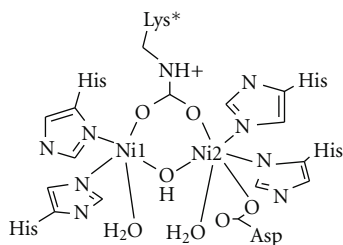


FIGURE 1: Schematic depiction of the structure of the active site of *Bacillus pasteurii* urease [11].

level and modeled the entire direct coordination sphere of the dinickel site with the coordinated amino acid residues truncated so that the full functional group (imidazole (His), carbamate (carbamylated Lys) and carboxylate (Asp)) were represented. This study aimed to discern between the two proposed mechanisms that involve a bridging substrate [16, 17], but it also evaluated the original suggestion that urea is terminally coordinated. For the mechanism involving a bridging intermediate, the density functional study indicated that the bridging hydroxide is the actual nucleophile, but it was found that the rate determining transition states of these mechanisms and that involving a terminally coordinated urea molecule were very similar and that it was not possible to discriminate between these mechanisms on the basis of the calculations. In more recent molecular dynamics and quantum mechanical simulations, Estiu and Merz [23, 24] have detected initial coordination modes of urea that involve either terminal coordination to Ni1 or a bridging coordination with coordination of the urea carbonyl moiety to Ni1 and simultaneous hydrogen-bonding interaction with one of the amine nitrogens with the bridging hydroxide, depending on the protonation state of surrounding amino acid residues.

In this paper, we wish to present DFT-based calculations that have been carried out in order to study the urease mechanism. The structure of the active site after initial urea coordination has been modeled. The theory involving an attack by the bridging oxygen donor has been tested. Activation data from the literature, which list energies of activation to circa 50 kJ/mol [25, 26] were compared with the energy differences between the starting structure and identified intermediates.

2. Results and Discussion

Because of the computational expense of the DFT method, a survey was done to find the smallest dependable model on which to base the rest of the study. Three model systems were investigated. The smallest system contained only the atoms within three to four bonds from the metal ions. The second contained all atoms of the coordinating amino acid residues up to and including the α -carbons. The third model system also included some nonbonded residues in close vicinity. As starting structure, the native urease crystal structure from *Bacillus pasteurii* (PDB code 2UBP) was

used [11]. In the model survey, the structure from the protein was extracted and then geometrically minimized. A possible intermediate structure with urea bond to Ni1 was also studied. The result showed that all the structures gave very similar results, both geometrically and in the difference of energy between the two studied models. This result indicated that the smallest of the models was suitable for the study. In the chosen model, only metal-bound ligands were included. The histidine residues were modeled as imidazoles, the aspartate residue was capped as a methyl group at the β -carbon while the carbamylated lysine was terminated similarly at the ϵ -carbon (Figure 1). The remaining ligands were left unchanged.

2.1. Determining the Resting Structure. Since the information provided by X-ray crystallography, especially protein crystallography, may be insufficient to accurately determine the presence and location of hydrogen atoms, different depictions of the nature of the bridging oxygen donor have been published [28–30]. As a part of preparing a suitable starting structure for the study, three different bridging ligands were considered, namely, O^{2-} (**1a**), OH^- (**1**), and H_2O (**1b**). In order to avoid hydrogen bonding to the bridging ligand, which could by itself drastically change the energy of the structure, the aspartate ligand was turned away from the nickel center by rotating it 135° counterclockwise around the Ni–O bond. To allow comparison between the different structures throughout the study, the energy of the substrates (urea and water) and further on the intermediate compounds were added to the resulting energy of each calculated structure. In calculating the contributing energies, the energy of a “free” proton was needed. Due to the many histidines conveniently located around the active site, the energy of a proton was determined by the energy difference of a protonated histidine and a neutral histidine, which were both calculated independent of the urease model. The result from the calculations can be seen in Table 1. In the comparison of the different possible oxygen donors, the structure with the lowest energy (by a comfortable margin) was the hydroxide-bridged complex (structure **1**). The energies of structure **1a** and **1b** were 101 and 33 kJ/mol higher than for structure **1**, respectively. The identity of the bridging hydroxide ligand is in agreement with the computational results obtained by Suárez et al. [21]. If the bridging ligand was water and the aspartate side chain was allowed to point towards the bridging ligand, a proton transfer from the water to the aspartate occurred during the geometry optimization. This observed proton transfer is an indirect confirmation of the instability of the model complex **1b**. The overall structure of the energetically favoured model complex **1** is very similar to the published X-ray structure. The interatomic distance is slightly shorter (3.48 versus 3.6 Å in 2UBP), and the site also differs in the orientation of the rotated aspartate.

2.2. Coordination of Urea. In order to determine the mode of interaction as urea coordinates to the active site of urease, a docking experiment between the optimized model complex

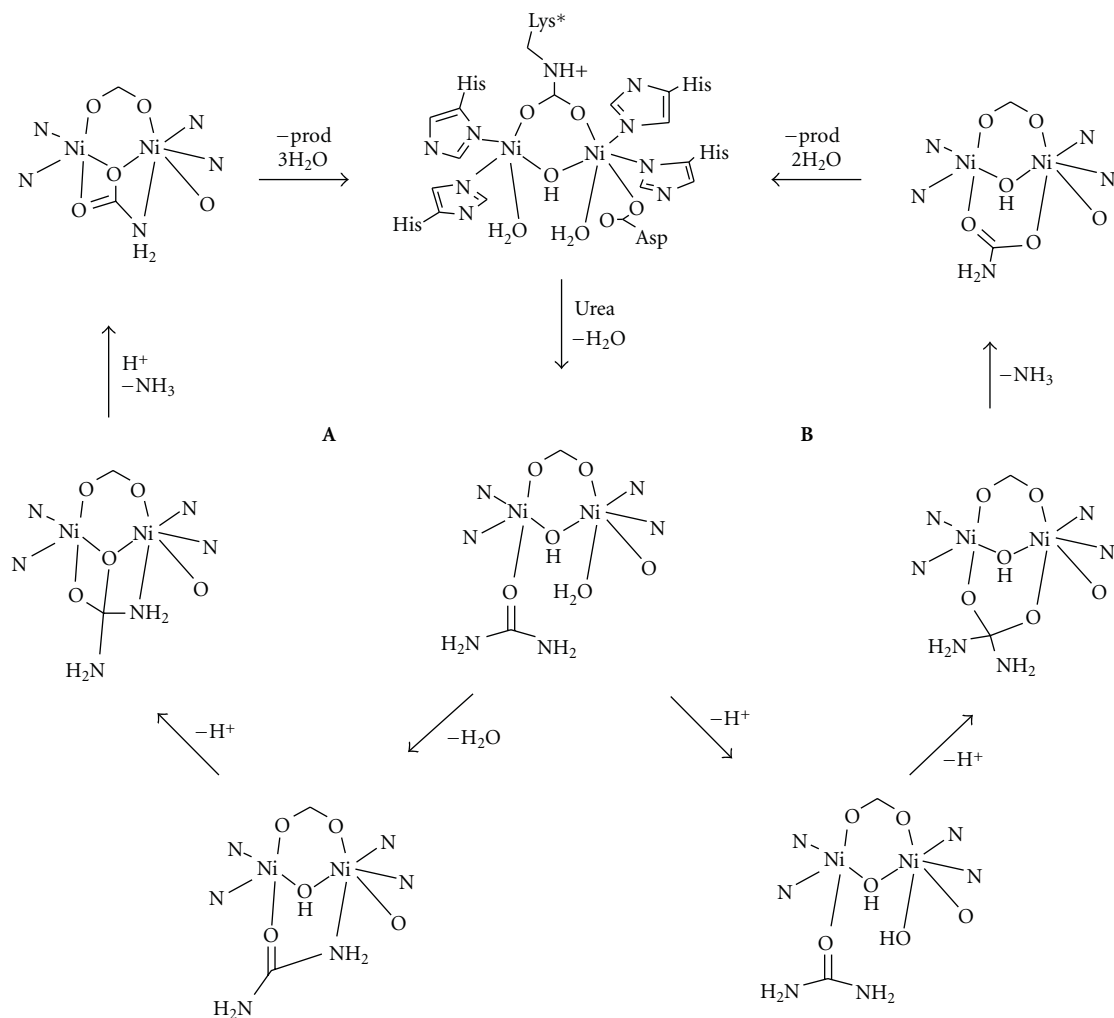
FIGURE 2: Schematic depiction of two proposed mechanisms for urease, **A** [11] and **B** [15].

TABLE 1: Energy results from the calculation of the resting structure.

Structure	Calculated energy (Hartree)	Added small molecules	Adjusted energy (Hartree)	Relative energy (kJ/mol)
1 (OH)	-13.6629	Urea and water	-15.9521	0
1a (O)	-13.6446	Urea, water and H ⁺	-15.9134	101.
1b (H ₂ O)	-13.6300	Urea, water and -H ⁺	-15.9395	32.9

1 and urea was carried out. A series of optimizations were performed moving urea from a distant position outside the active site and stepwise closer until a binding interaction was attained. Initially, urea was placed in the plane of the nickel ions and the carbamate oxygen atoms, approximately 5.5 Å from the site. In order not to favor coordination to a specific nickel, the distance between the carbamate carbon atom and the urea oxygen was chosen as the progressive distance. In the first optimization, this distance was 8 Å. After a number of iterations, which did not always result in the most favorable structure, the optimization was stopped, and the distance was shortened. This process was carried out

repeatedly until urea was bound. The qualitative result was that urea stayed in a relatively centered position during the approach but as it came closer to the active site, it migrated towards Ni1, where it finally settled in a binding interaction with nickel. The urea coordinated through its oxygen atom in *trans* position to the carbamylated lysine on Ni1. Another effect of the stepwise optimization was that the water-Ni1 bond distance increased until finally water was released. The water molecule was omitted from the structure, which was reoptimized to structure **2** (Figure 3). The final urea to nickel distance is 2.12 Å. Compared to structure **1**, the internuclear distance is approximately the same (3.47 versus 3.48 Å).

TABLE 2: Energy results from the calculation of the first coordination of urea.

Structure	Calculated energy (Hartree)	Added small molecules	Adjusted energy (Hartree)	Relative energy (kJ/mol)
2 (Ni1 <i>trans</i>)	-14.8816	2 water	-15.9376	0
2a (Ni1 <i>cis</i>)	-14.3368	3 water	-15.9209	82.0
2b (Ni2)	-14.8821	2 water	-15.9381	36.7

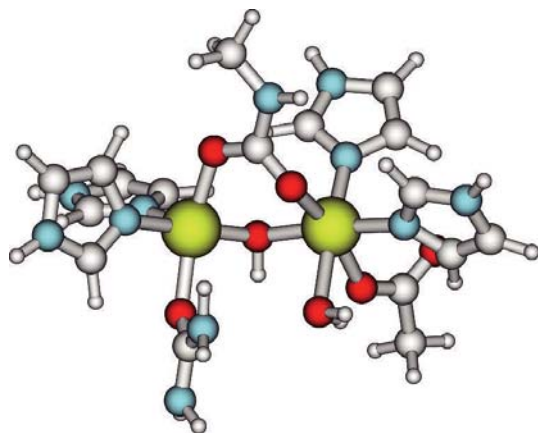


FIGURE 3: Structure of complex 2—depicting the initial coordination of urea. The program Molden(see [27]) was used to generate the graphics.

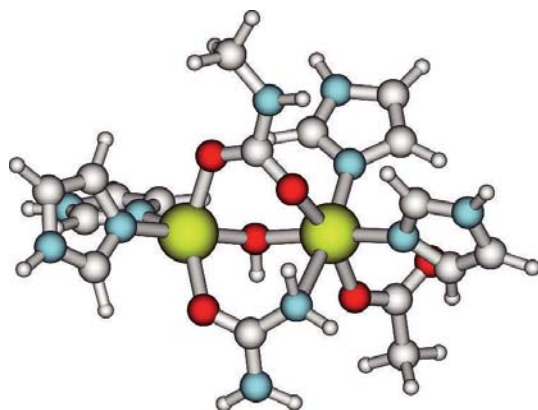


FIGURE 4: Structure of complex 3. One of the urea nitrogen atoms is coordinated to Ni2, thus replacing the water molecule on Ni2.

No major rearrangements are in other words needed in the binding of urea.

To test the viability of complex 2 as the first bound interaction between the urease active site and the substrate, some other possible structures were tested. The first one was coordination by urea *trans* to one of the histidines on Ni1, replacing the bound water (structure 2a). A second alternative model was achieved by replacing the water molecule on Ni2 by coordinated urea (structure 2b). The resulting energies are shown in Table 2. The two alternative structures are both disfavored by more than 30 kJ/mol relative to 2; this

is a significant energy difference comparable to ΔH^\ddagger for the whole reaction.

2.3. Tetrahedral Intermediate. In order to assess the possibility of a tetrahedral intermediate in the catalytic reaction of urease [16], a number of probable intermediates along the proposed pathway were studied. The choice of intermediates was based on what could be gathered from the suggested pathway and chemical intuition. Starting from 2, the search for the most favorable configuration for complex 3, in which one of the urea nitrogen atoms coordinates to Ni2, was done using a similar approach as in the two earlier cases. The distance between the closest urea nitrogen atom and Ni2 was fixed and shortened stepwise. During the approach, the Ni2-water distance grew longer until the water molecule was finally omitted and the structure with Ni2 and one of the urea nitrogen atoms within binding distance was optimized. The optimized structure for complex 3 is shown in Figure 4. One of the nitrogen atoms has approached Ni2 to a bonding interaction. This replaces the water molecule on Ni2.

Starting from 3, a nucleophilic attack on the bridging substrate was modeled by shortening the distance between the urea carbon atom and the bridging oxygen (Figure 5). The direct approach was again determined by stepwise optimizations. During the approach, the O-H bond in the bridging hydroxyl group was lengthened, and the proton was removed in the final optimized structure (4). Complex 5 was obtained by protonating the uncoordinated urea nitrogen atom in order to facilitate the release of ammonia. This lengthened the carbon nitrogen distance, but the intermediate was kept without completely removing the ammonia molecule. In complex 6, involving the dissociation of ammonia to yield carbamate, the ammonia was completely removed (deleted) from the structure, and the structure of the resultant complex was optimized. The remaining structures were based on the resting state, 1. The differences between complexes 1, 7, and 8 are the molecules that are added to get the comparable energy. In complex 7, which involves the dissociation of carbamate, which gets protonated, and recoordination of water, the released carbamic acid and the previously released ammonia are added in order to obtain a comparable energy. The released carbamic acid is then assumed to spontaneously break down to carbon dioxide and ammonia, which are added in the optimization of complex 8.

The energies of the proposed intermediates and inter-nuclear distances are summarized in Table 3. A graphical representation of the modelled reaction pathway is shown in Figure 5. There was a moderate increase in energy of about

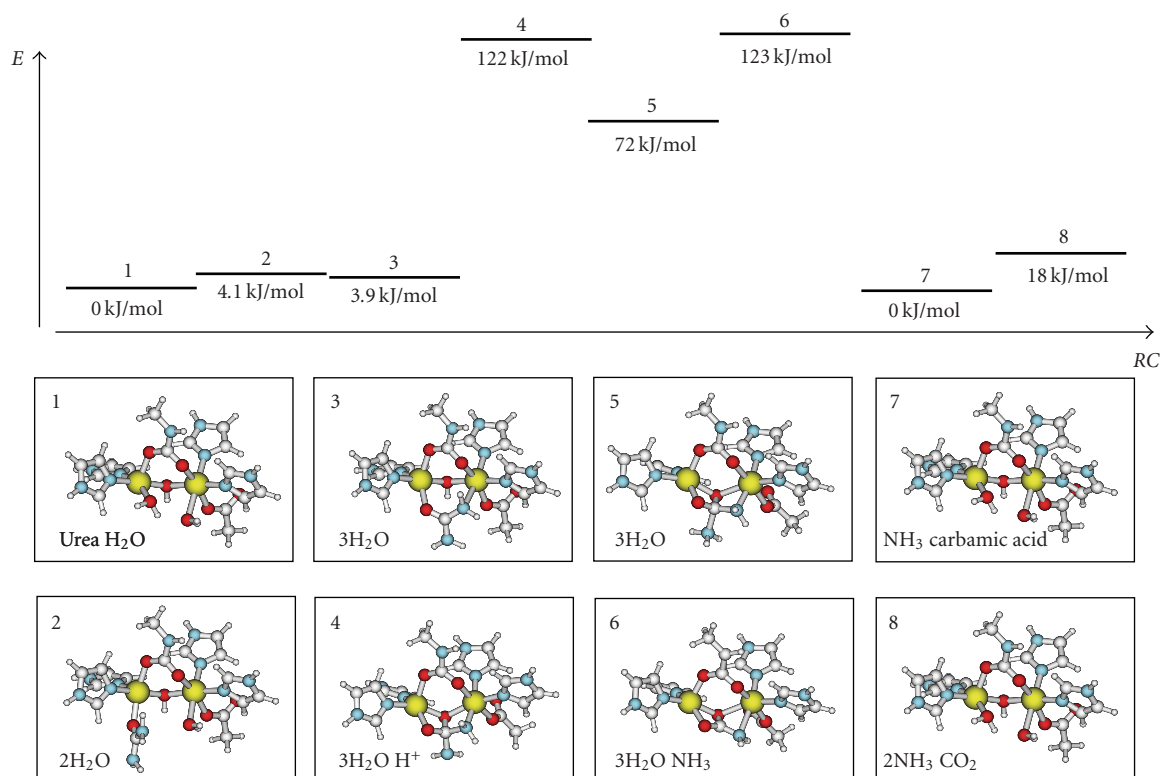


FIGURE 5: A reaction diagram showing the calculated energies of the intermediates found in the computational simulation of the urease reaction with the structures and added small molecules in boxes below (see text for detailed description of the intermediates).

TABLE 3: Energy results from the calculation of the mechanism involving a tetrahedral intermediate (mechanism A, Figure 2).

Structure	Calculated energy (Hartree)	Added small molecules	Adjusted energy (Hartree)	Relative energy (kJ/mol)
1	-13.6629	urea and water	-15.9521	0
2	-14.8816	2 water	-15.9376	38.0
3	-14.3532	3 water	-15.9373	38.9
4	-14.3315	3 water and one H ⁺	-15.8951	150
5	-14.3150	3 water	-15.8991	139
6	-13.6828	ammonia and 3 water	-15.8981	142
7	-13.6629	ammonia and carbamic acid	-15.9505	-33.9
8	-13.6629	2 ammonia and carbon dioxide	-15.9451	18.3

40 kJ/mol before and after binding urea. Rather surprisingly, the formation of the ensuing coordination of one of the nitrogen atoms to Ni₂ (structure 3) did not lead to any larger energy change. The bridging coordination of urea was only disfavored over the terminally bound state by approximately 0.9 kJ/mol. However, it should be noted that the transition state is not studied and may be significantly higher. The Ni-Ni distance is again very similar, 3.47 Å. The effect on the urea molecule was also rather small. The C-N distance was 1.37 Å for the nitrogen coordinated to nickel, while the free nitrogen carbon bond was found to be approximately 1.35 Å. The distances in 2 were both about 1.36 Å. The geometry

around the coordinated nitrogen had also shifted from a nearly planar structure, which is typical for urea, to a clear sp³ hybridized configuration. The optimized Ni-N(urea) distance is rather long (2.51 Å), suggesting a weak interaction. The Ni1-O(urea) bond distance was more or less unchanged.

The formation of 4 was found to require a fair amount of energy, as a large movement within the dinuclear site was needed to form the tetrahedral intermediate. The bridging oxygen donor between the two metals moved away from the nickel atoms and was positioned within bonding distance to the urea carbon. The Ni-O(phenolate) distance in structure

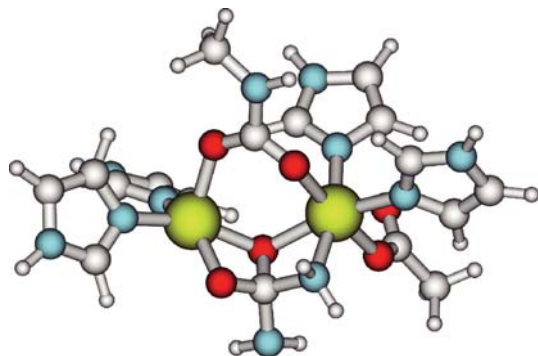


FIGURE 6: Structure of complex 4—the tetrahedral intermediate. The bridging hydroxide and the urea have moved closer together so that a bond is formed. This was found to release the proton associated with the hydroxide bridge.

3 was 2.01 (Ni1) and 2.04 (Ni2) Å and in structure 4, 2.07 (Ni1) and 2.16 Å (Ni2), respectively. In 4, the partial double bond character of the C–N bonds in urea has disappeared and the hybridization of the carbon is clearly sp^3 . The C–N bonds are longer, 1.46 and 1.51 (see Figure 6) versus 1.37 and 1.35 Å in structure 3. The nickel atoms have moved away from each other, and the internuclear distance is now 3.66 Å. The coordination of the bridging hydroxide has pulled urea closer to the dinuclear site, and the bonded Ni–N(urea) distance is shortened from 2.51 Å in 3 to 2.09 Å in 4. The energy difference to go from structure 3 to 4 has been calculated to 111 kJ/mol. Considering that a transition state will lie higher in energy, it may be argued that the modeled reaction pathway is not likely to be a part of the mechanism of urease, which was earlier found to have an activation energy of 50 kJ/mol.

The protonation of the uncoordinated urea nitrogen atom, to start the dissociation of ammonia, relieved some of the energy in structure 4. The energy for the resultant structure 5 is about 11 kJ/mol lower than in the previous structure. The protonated nitrogen moves away from the product carbon and was in the optimized state 1.70 Å from the carbon, which is about 0.20 Å further than in structure 4. The geometry around the carbon has again started to become more planar. This has led to a strain that is relayed to the nickel ions, which have moved even further apart. The Ni–Ni distance was determined to 3.80 Å, which is a fairly long distance for this site. The move towards a completely planar product continued in structure 6, in which ammonia was formally removed. This again pushes the nickel ions apart to 3.92 Å and adds energy to the structure. The energy for structure 6 is 142 kJ/mol higher than in the resting state. This energy is relieved in complex 7 and 8 when the product is released and water is recoordinates.

As seen in Figure 5, the energy needed for the suggested pathway exceeds the empirically determined activation energy of 50 kJ/mol. Even if one assumes a large uncertainty in the calculated energies, they indicate that the tetrahedral intermediate is not a part of the urease mechanism. The activation energy for the calculated mechanism is expected to exceed 150 kJ/mol.

3. Conclusions

The binding and hydrolysis of urea at the active site of urease has been modeled. The resting state of the enzyme (active site) has been calculated. The calculations indicate that the bridging oxygen donor is a hydroxide ion; this structure is 101 and 32.9 kJ/mol more stable than the corresponding oxo- or water complexes. In agreement with previous inorganic model studies [31, 32] and proposed mechanisms [15–17, 21], the calculation further suggested that urea initially binds through its oxygen atom to Ni1 in the active site. The coordination was directed to the *trans* position relative to the carbamylated lysine, and the water ligand of the resting state was released.

A study of the proposed mechanism involving a tetrahedral intermediate based on the bridging hydroxy group (mechanism A, Figure 2) was carried out. In the study, four additional possible intermediates were studied. It was found that it is energetically possible to coordinate one of the urea nitrogen atoms to Ni2, but further transformation including the formation of a tetrahedral intermediate based on the bridging hydroxyl group is energetically unfavourable. Published empirical data gives activation energies of about 50 kJ/mol while the calculations indicate that 150 kJ/mol would be needed to reach the tetrahedral intermediate. Further studies involving computational modelling of the alternative mechanism involving nucleophilic attack by a terminally bound hydroxide on terminally bound urea (mechanism B, Figure 2) will be undertaken, and detection of transition states for the different mechanisms will be investigated.

Computational Details

The density functional calculations were performed with the Amsterdam Density Functional (ADF) program, version 2003.01 [33–37], using an uncontracted triple- ξ STO basis set with frozen cores and an added polarization function. The implementation of the local density approximation (LDA) uses the standard Slater exchange term [38] and the correlation term due to Vosko, Wilk, and Nusair [39]. Geometries were optimized at the LDA level using analytical energy gradients within a spin-restricted formalism [36]. Total binding energies were calculated at the LDA geometries using Becke's 1988 [40] and Perdew's 1986 [41] gradient-corrected functionals for exchange and correlation, respectively. In all calculations a COSMO type solvent correction was applied by assuming a solvent dielectric constant of 4, mimicking internal protein conditions. Default convergence criteria were employed throughout. The calculations were carried out on the Lund University supercomputer facility LUNARC.

Acknowledgments

This paper is dedicated to Professor Nick. Hadjiladis in recognition of his contributions to bioinorganic and inorganic chemistry. This work has been supported by a grant from the Swedish Research Council (VR). The authors thank

Professor Ulf Ryde for helpful discussions, and are also indebted to the directors of LUNARC for the use of this supercomputing facility.

References

- [1] P. A. Karplus, M. A. Pearson, and R. P. Hausinger, "70 years of crystalline urease: what have we learned?" *Accounts of Chemical Research*, vol. 30, no. 8, pp. 330–337, 1997.
- [2] J. B. Sumner, "The isolation and crystallization of the enzyme urease," *The Journal of Biological Chemistry*, vol. 69, pp. 435–441, 1926.
- [3] H. L. T. Mobley, M. D. Island, and R. P. Hausinger, "Molecular biology of microbial ureases," *Microbiological Reviews*, vol. 59, no. 3, pp. 451–480, 1995.
- [4] K. Stingl and H. De Reuse, "Staying alive overdosed: how does *Helicobacter pylori* control urease activity," *International Journal of Medical Microbiology*, vol. 295, no. 5, pp. 307–315, 2005.
- [5] J. M. Bremner, "Recent research on problems in the use of urea as a nitrogen fertilizer," *Fertilizer Research*, vol. 42, no. 1–3, pp. 321–329, 1995.
- [6] N. E. Dixon, C. Gazzola, R. L. Blakeley, and B. Zerner, "Jack Bean urease (EC 3.5.1.5). A metalloenzyme. A simple biological role for nickel?" *Journal of the American Chemical Society*, vol. 97, no. 14, pp. 4131–4133, 1975.
- [7] D. E. Fenton, "Urease—a muse for the coordination chemist," *Proceedings of the Indian National Science Academy Part A*, vol. 70, no. 2, pp. 311–328, 2004.
- [8] E. Jabri, M. B. Carr, R. P. Hausinger, and P. A. Karplus, "The crystal structure of urease from *Klebsiella aerogenes*," *Science*, vol. 268, no. 5213, pp. 998–1004, 1995.
- [9] M. A. Pearson, L. O. Michel, R. P. Hausinger, and P. A. Karplus, "Structures of Cys319 variants and acetohydroxamate-inhibited *Klebsiella aerogenes* urease," *Biochemistry*, vol. 36, no. 26, pp. 8164–8172, 1997.
- [10] S. Benini, W. R. Rypniewski, K. S. Wilson, S. Ciurli, and S. Mangani, "The complex of *Bacillus pasteurii* urease with β -mercaptoethanol from X-Ray data at 1.65-Å resolution," *The Journal of Biological Inorganic Chemistry*, vol. 3, no. 3, pp. 268–273, 1998.
- [11] S. Benini, W. R. Rypniewski, K. S. Wilson, S. Miletti, S. Ciurli, and S. Mangani, "A new proposal for urease mechanism based on the crystal structures of the native and inhibited enzyme from *Bacillus pasteurii*: why urea hydrolysis costs two nickels," *Structure*, vol. 7, no. 2, pp. 205–216, 1999.
- [12] S. Benini, W. R. Rypniewski, K. S. Wilson, S. Ciurli, and S. Mangani, "Structure-based rationalization of urease inhibition by phosphate: novel insights into the enzyme mechanism," *The Journal of Biological Inorganic Chemistry*, vol. 6, no. 8, pp. 778–790, 2001.
- [13] N.-C. Ha, S.-T. Oh, J. Y. Sung, K. A. Cha, M. H. Lee, and B.-H. Oh, "Supramolecular assembly and acid resistance of *Helicobacter pylori* urease," *Nature Structural Biology*, vol. 8, no. 6, pp. 505–509, 2001.
- [14] N. E. Dixon, P. W. Riddles, C. Gazzola, R. L. Blakeley, and B. Zerner, "Jack bean urease (EC 3.5.1.5). V. On the mechanism of action of urease on urea, formamide, acetamide, N-methylurea, and related compounds," *Canadian Journal of Biochemistry*, vol. 58, no. 12, pp. 1335–1344, 1980.
- [15] S. J. Lippard, "At last—the crystal structure of urease," *Science*, vol. 268, no. 5213, pp. 996–997, 1995.
- [16] F. Musiani, E. Arnofi, R. Casadio, and S. Ciurli, "Structure-based computational study of the catalytic and inhibition mechanisms of urease," *The Journal of Biological Inorganic Chemistry*, vol. 3, no. 8, pp. 300–314, 2001.
- [17] M. A. Pearson, I.-S. Park, R. A. Schaller, L. O. Michel, P. A. Karplus, and R. P. Hausinger, "Kinetic and structural characterization of urease active site variants," *Biochemistry*, vol. 39, no. 29, pp. 8575–8584, 2000.
- [18] M. Zimmer, "Molecular mechanics evaluation of the proposed mechanisms for the degradation of urea by urease," *Journal of Biomolecular Structure and Dynamics*, vol. 17, no. 5, pp. 787–797, 2000.
- [19] M. Zimmer, "Are classical molecular mechanics calculations still useful in bioinorganic simulations?" *Coordination Chemistry Reviews*, vol. 253, no. 5–6, pp. 817–826, 2009.
- [20] R. P. Smyj, "A conformational analysis study of a nickel(II) enzyme: urease," *Journal of Molecular Structure: THEOCHEM*, vol. 391, no. 3, pp. 207–223, 1997.
- [21] D. Suárez, N. Díaz, and K. M. Merz Jr., "Ureases: quantum chemical calculations on cluster models," *Journal of the American Chemical Society*, vol. 125, no. 50, pp. 15324–15337, 2003.
- [22] G. Estiu and K. M. Merz Jr., "Enzymatic catalysis of urea decomposition: elimination or hydrolysis?" *Journal of the American Chemical Society*, vol. 126, no. 38, pp. 11832–11842, 2004.
- [23] G. Estiu and K. M. Merz Jr., "Catalyzed decomposition of urea. Molecular dynamics simulations of the binding of urea to urease," *Biochemistry*, vol. 45, no. 14, pp. 4429–4443, 2006.
- [24] G. Estiu and K. M. Merz Jr., "Competitive hydrolytic and elimination mechanisms in the urease catalyzed decomposition of urea," *Journal of Physical Chemistry B*, vol. 111, no. 34, pp. 10263–10274, 2007.
- [25] R. E. Muck, "Urease activity in bovine feces," *Journal of Dairy Science*, vol. 65, no. 11, pp. 2157–2163, 1982.
- [26] C. C. Moyo, D. E. Kissel, and M. L. Cabrera, "Temperature effects on soil urease activity," *Soil Biology and Biochemistry*, vol. 21, no. 7, pp. 935–938, 1989.
- [27] G. Schaftenaar and J. H. Noordik, "Molden: a pre- and post-processing program for molecular and electronic structures," *Journal of Computer-Aided Molecular Design*, vol. 14, no. 2, pp. 123–134, 2000.
- [28] A. M. Barrios and S. J. Lippard, "Amide hydrolysis effected by a hydroxo-bridged dinickel(II) complex: insights into the mechanism of urease," *Journal of the American Chemical Society*, vol. 121, no. 50, pp. 11751–11757, 1999.
- [29] D. E. Fenton, "Structural diversity in oligonuclear nickel(II) complexes of unsymmetrical compartmental ligands," *Inorganic Chemistry Communications*, vol. 5, no. 7, pp. 537–547, 2002.
- [30] B. Hommerich, H. Schwöppe, D. Volkmer, and B. Krebs, "Model complexes for ureases: a dinickel(II) complex with a novel asymmetric ligand and comparative kinetic studies on catalytically active zinc, cobalt, and nickel complexes," *Zeitschrift für anorganische und allgemeine Chemie*, vol. 625, no. 1, pp. 75–82, 1999.
- [31] H. Carlsson, M. Haukka, and E. Nordlander, "Hydrolytically active tetranuclear nickel complexes with structural resemblance to the active site of urease," *Inorganic Chemistry*, vol. 41, no. 20, pp. 4981–4983, 2002.
- [32] H. Carlsson, J.-M. Haukka, A. Bousseksou, J.-M. Latour, and E. Nordlander, "Nickel complexes of carboxylate-containing polydentate ligands as models for the active site of urease," *Inorganic Chemistry*, vol. 43, no. 26, pp. 8252–8262, 2004.

- [33] E. J. Baerends, D. E. Ellis, and P. Ros, "Self-consistent molecular Hartree-Fock-Slater calculations I. The computational procedure," *Chemical Physics*, vol. 2, no. 1, pp. 41–51, 1973.
- [34] G. te Velde and E. J. Baerends, "Numerical integration for polyatomic systems," *Journal of Computational Physics*, vol. 99, no. 1, pp. 84–98, 1992.
- [35] C. F. Guerra, J. G. Snijders, G. te Velde, and E. J. Baerends, "Towards an order-N DFT method," *Theoretical Chemistry Accounts*, vol. 99, no. 6, pp. 391–403, 1998.
- [36] L. Versluis and T. Ziegler, "The determination of molecular structures by density functional theory. The evaluation of analytical energy gradients by numerical integration," *The Journal of Chemical Physics*, vol. 88, no. 1, pp. 322–328, 1988.
- [37] G. te Velde, F. M. Bickelhaupt, S. J. A. van Ginsbergen, et al., "Chemistry with ADF," *Journal of Computational Chemistry*, vol. 22, no. 9, pp. 931–967, 2001.
- [38] J. C. Slater, "Statistical exchange-correlation in the self-consistent field," *Advances in Quantum Chemistry*, vol. 6, no. 1, pp. 1–92, 1972.
- [39] S. H. Vosko, L. Wilk, and M. Nusair, "Accurate spin-dependent electron liquid correlation energies for local spin density calculations: a critical analysis," *Canadian Journal of Physics*, vol. 58, no. 8, pp. 1200–1211, 1980.
- [40] A. D. Becke, "Density-functional exchange-energy approximation with correct asymptotic behavior," *Physical Review A*, vol. 38, no. 6, pp. 3098–3100, 1988.
- [41] J. P. Perdew, "Density-functional approximation for the correlation energy of the inhomogeneous electron gas," *Physical Review B*, vol. 33, no. 12, pp. 8822–8824, 1986.

Research Article

Structural Properties, Cytotoxicity, and Anti-Inflammatory Activity of Silver(I) Complexes with tris(*p*-tolyl)Phosphine and 5-Chloro-2-Mercaptobenzothiazole

L. Kyros,¹ N. Kourkoumelis,² M. Kubicki,³ L. Male,⁴ M. B. Hursthouse,⁴ I. I. Verginadis,⁵ E. Gouma,⁵ S. Karkabounas,⁵ K. Charalabopoulos,⁵ and S. K. Hadjikakou¹

¹ Section of Inorganic and Analytical Chemistry, Department of Chemistry, University of Ioannina, 45110 Ioannina, Greece

² Medical Physics Laboratory, Medical School, University of Ioannina, 45110 Ioannina, Greece

³ Department of Chemistry, A. Mickiewicz University, ul. Grunwaldzka 6, 60-780 Poznań, Poland

⁴ Department of Chemistry, University of Southampton, Highfield, Southampton SO17 1BJ, UK

⁵ Department of Experimental Physiology, Medical School, University of Ioannina, 45110 Ioannina, Greece

Correspondence should be addressed to S. K. Hadjikakou, shadjika@uoi.gr

Received 2 October 2009; Accepted 18 December 2009

Academic Editor: Spyros Perlepes

Copyright © 2010 L. Kyros et al. This is an open access article distributed under the Creative Commons Attribution License, which permits unrestricted use, distribution, and reproduction in any medium, provided the original work is properly cited.

The synthesis and characterization of the silver(I) chloride complex of formula $\{[\text{AgCl}(\text{CMBZT})(\text{TPTP})_2] \cdot (\text{MeOH})\}$ (**1**) (CMBZT = 5-chloro-2-mercaptobenzothiazole, TPTP = tris(*p*-tolyl)phosphine) is described. Also the structure of the hydrate derivative $\{[\text{AgCl}(\text{TPTP})_3] \cdot (0.5 \cdot \text{H}_2\text{O})\}$ (**2**) of the corresponding known anhydrous silver complex (Zartilas et al., 2009), and the polymorph **3** of the known $[\text{AgI}(\text{TPTP})_3]$ complex (Zartilas et al., 2009) were determined and compared with the known ones. In addition, the structure of the known one silver(I) cluster $\{[\text{AgI}(\text{TPTP})_4]\}$ (**4**) (Meijboom et al., 2009) was re-determined at 120(2) K and possible Ag-Ag interactions were analyzed. The compounds **1–4** were characterized by X-ray crystallography at r.t (**1**) and 120 K (**2–4**). All these complexes and $\{[(\text{Et}_3\text{NH})^+]_2 \cdot [\text{Ag}_6(\mu_3\text{-Hmna})_4(\mu_3\text{-mna})_2]^{2-} \cdot (\text{DMSO})_2 \cdot (\text{H}_2\text{O})\}$ (**5**) (Hmna = 2-mercaptopyridine-4-thione) were evaluated for cytotoxic and anti-inflammatory activity. The *in vitro* testing of cytotoxic activity of **1–5** against leiomyosarcoma cancer cells (LMS), were evaluated with Trypan Blue and Thiazolyl Blue Tetrazolium Bromide or 3-(4,5-dimethylthiazol-2-yl)-2,5-diphenyltetrazolium bromide (MTT) assays. The flow cytometry assay for complex **1** and showed that at 15 μM of **1**, 62.38% of LMS cells undergo apoptosis, while 7% of LMS cells undergo cell necrosis. The antitumor activity of **3** is comparable with that of its reported polymorph (Zartilas et al., 2009). The anti-inflammatory, activity of complexes **1–3** and **5** was also studied. The activity towards cell viability was $2 > 3 > 5 > 1 > 4$, while the order of the inhibitory activity in cell growth proliferation follows the order, $2 > 3 > 1 > 4 > 5$. The anti-inflammatory activity on the other hand is $1 > 2 > 5 > \dots > 3$.

1. Introduction

Silver(I) complexes with sulfur containing ligands exhibit a wide range of applications in medicine, in analytical chemistry and in the polymer industry [1–5]. The biomedical applications and uses of silver(I) complexes are related to their antibacterial action [6, 7] which appears to involve interaction with DNA [8]. Silver sulphadiazine is a topical anti-infective, used worldwide for dermal injuries, approved by the US Food and Drug Administration [9]. It has a broad antibacterial spectrum including virtually all microbial species likely to infect the burn wound [9]. Recently, Ag(I)

complexes have also been studied for their antitumor activity [10–12]. The results showed that $[\text{AgBr}(\text{TPTP})_3]$ complex possessed the strongest activity against leukemia (L1210), human T-lymphocyte (Molt4/C8 and CEM) and LMS cells [12]. The exact mechanism of the anti-tumor action of Ag(I) compounds is still unknown. It is well known, however, that many drugs which inhibit the growth of tumor cells act either by interfering with DNA bases and/or nucleotides or with the metalloenzymes that are necessary for the rapid growth of malignant cells [13, 14]. Thus, the molecular design and structural characterization of silver(I) complexes is an intriguing aspect of bioinorganic chemistry and metal-based

drugs research [15, 16]. The ability of silver(I) complexes to adopt geometries with variable nuclearities and structural diversity also makes the study of silver(I) chemistry very attractive [3–5, 17]. This self-assembly process between metal ions and ligands is known to depend on steric and interactive information stored in the ligand and is governed by the metal ions through the demands of their coordination geometry [18, 19]. Recently, a new type of aromaticity, due to a cyclical delocalization of d as well as $(d-p)$ π -type orbital electron density instead of the usual p orbitals on metal-ligand rings, has been reported [20–29], which may introduce greater stability to the higher-order structures.

This paper, reports the synthesis of the new mixed ligand silver(I) chloride complex with the heterocyclic thioamide 5-chloro-2-mercaptobenzothiazole (CMBZT, $C_7H_4ClNS_2$) and tri(*p*-tolyl)phosphine (TPTP, $C_{21}H_{21}P$) (Scheme 1) of formula $\{[AgCl(CMBZT)(TPTP)_2] \cdot (MeOH)\}$ (**1**). The hydrate $\{[AgCl(TPTP)_3] \cdot (0.5 \cdot H_2O)\}$ (**2**) of the known anhydrous silver complex [10] and a polymorph, **3**, of the known $[AgI(TPTP)_3]$ complex [10, 30] were also isolated. The crystal structure of **4** $\{[AgI(TPTP)_4]\}$ has been previously reported at 100(2) K [31] but we have extended our studies here in the determination of its quasiaromaticity, which results in strong Ag–Ag interactions and thus greater stability, using data collected at 120 K. Complexes **1–4** and the known silver(I) cluster $\{[(Et_3NH)^+]_2 \cdot [Ag_6(\mu_3-Hmna)_4(\mu_3-mna)_2]^{2-} \cdot (DMSO)_2 \cdot (H_2O)\}$ (**5**) ($H_2MNA = 2$ -mercaptonicotinic acid, $C_6H_5NO_2S$) [32] were tested for their *in vitro* cytostatic activity against leiomyosarcoma cancer cells from Wistar rats. Finally, the anti-inflammatory activity of complexes **1–3** and **5** were also evaluated and the results correlated with those of their anti-tumor activity.

2. Results and Discussion

2.1. General Aspects. Complex **1** was synthesized by heating at 50°C an acetonitrile/methanol solution of silver(I) chloride, TPTP and CMBZT in 1 : 2 : 1 molar ratio (reaction 1):



Complexes **2–4** [10, 30, 31] were synthesized by heating, under reflux, a toluene solution of silver(I) halides with TPTP in the appropriate molar ratio. Finally, the water soluble cluster **5** was prepared according to methods reported previously [32]. Complex **1** was characterized first by elemental analyses and spectroscopic methods. Crystals of complexes **1–3** are stable in air but were kept in darkness. Complexes **1–3** were soluble in MeCN, $CHCl_3$, CH_2Cl_2 , DMSO, DMF and CH_3OH , while complex **4** is slightly soluble in DMSO. Complex **5** is highly soluble in water, in DMSO and in DMF.

2.2. Vibrational Spectroscopy. The vibrational thioamide bands I and II, appear at 1496 and 1305 cm^{-1} in the IR

spectra of complex **1** and lie at lower wavenumbers compared to the corresponding vibrational bands of the free ligands CMBZT, observed at 1504 and 1313 cm^{-1} [33]. Thioamide bands III–IV were observed at 1040–918 cm^{-1} in the spectra of the free ligand C–P and appear at 1026 and 905 cm^{-1} , respectively, in the spectra of **1**. The bands at 1093 cm^{-1} in the IR spectra of **1** and **2–4** are assigned to the symmetric vibrations of the $\nu(C-P)$ bond [10]. Those at 515, 509 cm^{-1} **1**, 515, 509 cm^{-1} **2**, 516, 505 cm^{-1} **3** and 516, 505 cm^{-1} **4** are assigned to the antisymmetric vibrations of the $\nu(C-P)$ bond [10]. The corresponding $\nu(C-P)$ bands of the free tri-*p*-tolylphosphine ligand are found at 1089 cm^{-1} for the symmetric vibration and at 516 cm^{-1} , 505 cm^{-1} for the anti-symmetric vibration. The bands at 169, 179, 125 and at 127 cm^{-1} in the Far-IR spectra of complexes **1–4** were assigned to the vibrations of the Ag–X bonds (X = Cl, I), respectively, [10]. The vibration at 248 cm^{-1} in the spectra of **1** is attributed to the Ag–S bonds [34].

2.3. Crystal and Molecular Structure of $\{[AgCl(CMBZT)(TPTP)_2] \cdot (MeOH)\}$ (1**) and Structural Properties of $\{[AgCl(TPTP)_3] \cdot (0.5 \cdot H_2O)\}$ (**2**) and $[AgI(TPTP)_3]$ (**3**).** We have recently reported the crystal structure of the dehydrated complex $[AgCl(TPTP)_3]$ at 293 K [10]. The structure of $\{[AgCl(TPTP)_3] \cdot (0.5 \cdot H_2O)\}$ (**2**), described here, has been determined at 120 K. The structure of $[AgI(TPTP)_3]$ (**3**), determined at 120 K, is a new polymorph of the complex reported previously at 293 K and 140 K [10, 30]. Strong Ag–Ag interactions, due to quasiaromaticity calculated, were found in the structure of complex **4** re-determined at 120 K (With Ag–Ag bond distance of 3.1182(3) Å) (Figure 3).

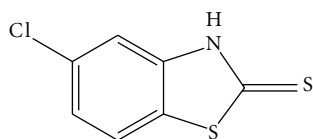
The crystal structures of complexes **1–2** are shown in Figures 1 and 2, while selected bond lengths and angles for **1–3** are given in Table 1 in comparison with those found in [10].

Two P atoms from the TPTP ligands, one S from CMBZT and one Cl atom form the tetrahedral arrangement around the Ag ion in complex **1**. The two Ag–P bond lengths are $Ag1-P1 = 2.4357(18)$ Å and $Ag1-P2 = 2.5013(16)$ Å which correspond closely with those found in $[Ag(PPh_3)(L)Br]_2$ ($PPh_3 =$ triphenylphosphine and $L = 2$ pyrimidine-2-thione) where $Ag(1)-P(1) = 2.4390(7)$ Å [34] and in $[Ag_2X_2(l-SpySH)_2(PPh_3)_2]$ (X = Cl, Br and $l-SpySH =$ pyridine-2-thione) where the Ag–P bond distances are 2.435(1) Å and 2.441(1) Å, respectively, [35].

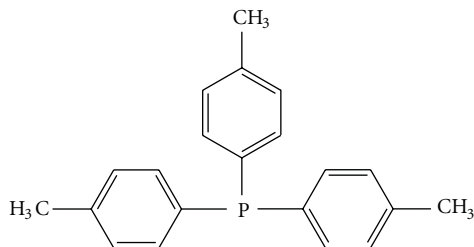
The Ag–S bond distance in **1** ($Ag1-S32 = 2.6486(16)$ Å) is longer than the corresponding bond distances reported for the terminal Ag–S bonds found in $[Ag(PPh_3)(L)Br]_2$ ($PPh_3 =$ triphenylphosphine and $L = 2$ pyrimidine-2-thione) ($Ag(1)-S(1) = 2.5548(9)$ Å [34]) and in $[Ag_2X_2(\mu-SpySH)_2(PPh_3)_2]$ (X = Cl, Br and $\mu-SpySH =$ pyridine-2-thione) ($Ag-S_{terminal}$ are 2.583(1) Å and 2.608(1) Å, resp., [35]). The Ag–S bond distance in **1** is closer to the bond length of bridging Ag–S bonds measured in $[Ag_2X_2(\mu-SpySH)_2(PPh_3)_2]$ (X = Cl, Br and $\mu-SpySH =$ pyridine-2-thione) ($Ag-S_{bridging}$ are 2.721(1) Å and 2.631(1) Å, resp., [35]). This might be

TABLE 1: Selected bond lengths (Å) and angles (deg) for compounds 1–3 with e.s.d.'s in parentheses in comparison with those found in [10, 30].

1 at 293(2) K	2 at 120 K		3 at 120 K		[AgCl(TPTP) ₃] at 293 K [10]		[AgI(TPTP) ₃] (polymorph of 3) at 140 K [10]		[AgI(TPTP) ₃] (polymorph of 3) at 293 K [10]		
	Bond Distances (Å)	Bond Distances (Å)	Bond Distances (Å)	Bond Distances (Å)	Bond Distances (Å)	Bond Distances (Å)					
Ag1–P1	2.4357(18)	Ag1–P1	2.5159(13)	Ag1–P1	2.5566(12)	Ag1–P1	2.511(2)	Ag1–P1	2.5208(15)	Ag1–P1	2.5294(17)
Ag1–P2	2.5013(16)	Ag1–P2	2.5438(13)	Ag1–P2	2.5347(11)	Ag1–P2	2.518(2)	Ag1–P2	2.5453(15)	Ag1–P2	2.558(2)
Ag1–S32	2.6486(16)	Ag1–P3	2.5342(14)	Ag1–P3	2.5609(11)	Ag1–P3	2.504(2)	Ag1–P3	2.5444(13)	Ag1–P3	2.5529(17)
Ag1–Cl4	2.6736(13)	Ag1–Cl1	2.6109(13)	Ag1–Cl1	2.6186(17)	Ag1–Cl1	2.8359(8)	Ag1–I1	2.8736(6)	Ag1–I1	2.8655(9)
C32–S32	1.666(4)										
C32–N33	1.345(5)										
N33–H33	1.0323										
Bond Angles (°)	Bond Angles (°)	Bond Angles (°)	Bond Angles (°)	Bond Angles (°)	Bond Angles (°)	Bond Angles (°)	Bond Angles (°)	Bond Angles (°)	Bond Angles (°)	Bond Angles (°)	Bond Angles (°)
P1–Ag1–P2	129.05(5)	P1–Ag1–P3	115.56(5)	P1–Ag1–P3	108.40(4)	P3–Ag1–P1	111.40(7)	I1–Ag1–P1	101.55(4)	I1–Ag1–P1	102.37(5)
P1–Ag1–S32	109.04(5)	P1–Ag1–P2	118.85(4)	P2–Ag1–P1	115.89(4)	P3–Ag1–P2	114.32(8)	I1–Ag1–P2	112.12(4)	I1–Ag1–P2	111.54(5)
P2–Ag1–S32	103.91(6)	P3–Ag1–P2	108.03(4)	P2–Ag1–P3	118.22(4)	P1–Ag1–P2	112.77(7)	I1–Ag1–P3	98.57(3)	I1–Ag1–P3	99.44(5)
P1–Ag1–Cl4	113.91(5)	P1–Ag1–Cl1	104.56(5)	P1–Ag1–Cl1	108.88(5)	P3–Ag1–I1	103.79(5)	P1–Ag1–P2	118.13(5)	P1–Ag1–P2	117.81(6)
P2–Ag1–Cl4	95.13(5)	P3–Ag1–Cl1	109.07(5)	P3–Ag1–Cl1	99.54(5)	P1–Ag1–I1	101.52(6)	P1–Ag1–P3	111.87(5)	P1–Ag1–P3	111.94(6)
S32–Ag1–Cl4	102.30(5)	P2–Ag1–Cl1	99.04(5)	P2–Ag1–Cl1	104.17(5)	P2–Ag1–I1	111.95(6)	P2–Ag1–P3	112.31(5)	P2–Ag1–P3	111.77(6)

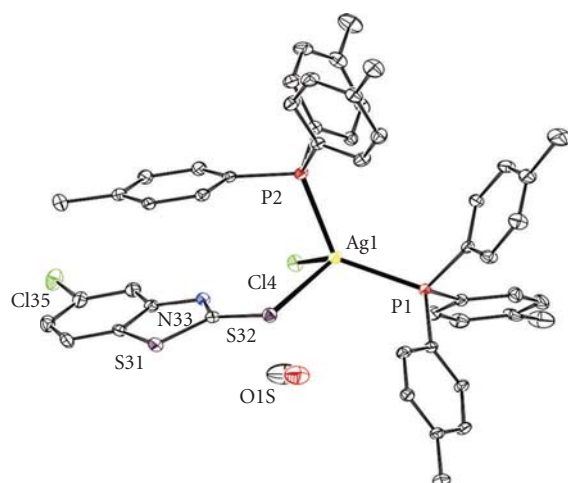


CMBZT

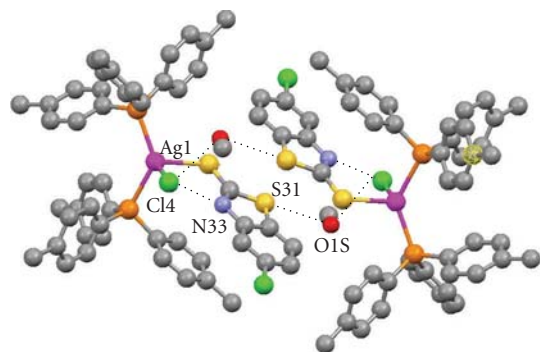


TPTP

SCHEME 1



(a)



(b)

FIGURE 1: (a) ORTEP diagram of the crystal structure of complex 1. (b) Intramolecular interactions ($N33 \cdots Cl4$, $S31 \cdots O1S$ and $O1S \cdots Cl4$) in 1.

due to intramolecular contact $S31 \cdots O1S_{(i)} = 3.240(6) \text{ \AA}$ (Figure 1(b)) (the symmetry transformation used to generate the equivalent atoms for (i) = $-x, -y, 1 - z$).

The $Ag1-Cl4$ bond distance in 1 is $2.6736(13) \text{ \AA}$ and is longer than the corresponding $Ag-Cl$ bond distance found in $[Ag_2Cl_2(\mu-S-pySH)_2(PPH_3)_2]$ ($pySH = \text{pyridine-2-thione}$) ($Ag-Cl = 2.530(1) \text{ \AA}$ [35]). This is due to the participation of the Cl atom in two strong hydrogen bonding interactions,

one inter-molecular ($N33 \cdots Cl4 = 3.083(4) \text{ \AA}$) and one intramolecular ($O1S \cdots Cl4 = 3.147(5) \text{ \AA}$) (Figure 1(b)). The hydrogen bonding interactions which involve the O atom of the methanol lead to the formation of a dimer (Figure 1(b)).

The bond angles around the Ag atom show variations from those in an ideal tetrahedron and range from $P1-Ag1-P2 = 129.05(5)^\circ$ to $P2-Ag1-Cl4 = 95.13(5)^\circ$ (see Table 1).

The refinement of the absolute structure of 2 showed that it consists of a mixture of enantiomers with ratio 0.81 : 0.19. Significant differences between the bond distances and angles of complex 2 at 120 K and the anhydrous form at 293 were observed and the values are also given in Table 1 for comparison. Although, the $Ag-P$ bond lengths are shortened by decreasing the temperature (Table 1), the $Ag-Cl$ bond distance remains unchanged (Table 1). This is attributed to the formation of a strong hydrogen bonding interaction involving the Cl atom in 2 ($H1B[O1] \cdots Cl1 = 2.42(10) \text{ \AA}$, $O1-H1B \cdots Cl1 = 150(18)^\circ$) (Figure 2(b)), in contrast to the case of the dehydrated complex $[AgCl(TPTP)_3]$, where no such bonds are formed.

The crystal structure of complex 3 determined at 120 K (this work) is a new polymorphic form of the corresponding structures determined at 140 K and 293 K [10] (120 K: monoclinic in space group $C2/c$ with $a = 22.7429(10) \text{ \AA}$, $b = 11.0093(3) \text{ \AA}$, $c = 44.8281(18) \text{ \AA}$, $\beta = 102.9780(10)^\circ$, and at 140 K. At 293 K: triclinic in space group $P-1$ with (140 K) $a = 11.0058(5) \text{ \AA}$, $b = 11.4509(5) \text{ \AA}$, $c = 22.9459(8) \text{ \AA}$, $\alpha = 99.461(3)^\circ$, $\beta = 91.648(3)^\circ$, $\gamma = 106.350(4)^\circ$ [10]. The general trend in complex 3 is the increasing of bond lengths; by increasing of temperature, for example the average $Ag-P$ bond lengths in the various polymorphs are: at 120 K (new polymorph) 2.511 \AA , at 140 K (old polymorph) 2.537 \AA and at 293 K (old polymorph) 2.547 \AA . More important changes were observed in the bond angles between the three polymorphs (see Table 1).

Strong $Ag-Ag$ interactions exist in the structure of complex 4, consisted of four silver(I) ions bridged by μ_3 -iodide ions, forming a prismatic core (Figure 3) and are described here for the first time (both $Ag-Ag = 3.1182(3) \text{ \AA}$), with the $Ag-Ag$ bond distances being shorter than the sum of their van der Waals radii ($4.20-4.74 \text{ \AA}$ [36]) indicating a $d^{10}-d^{10}$ interaction.

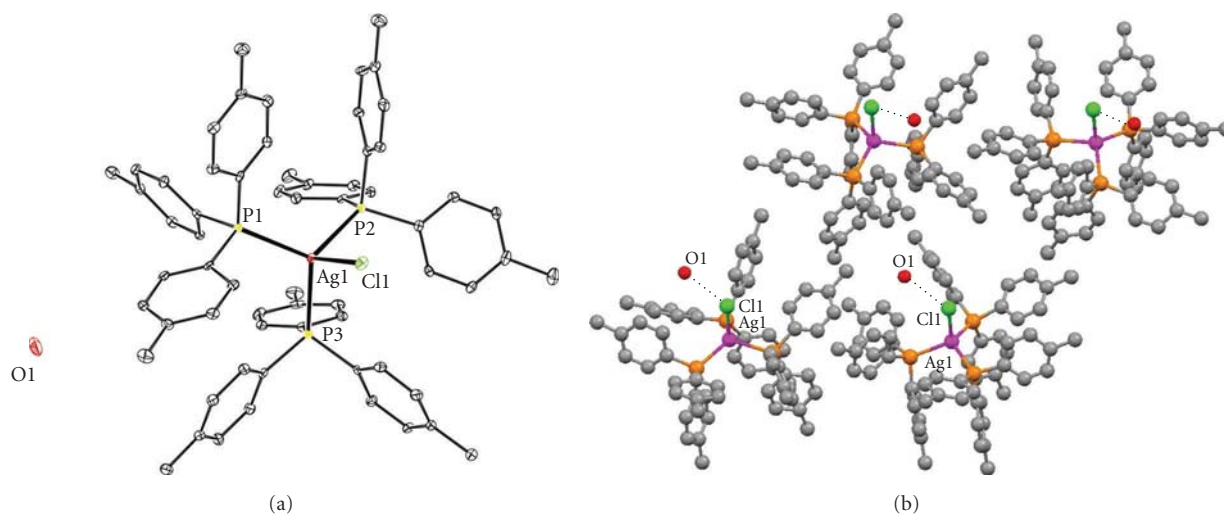


FIGURE 2: (a) ORTEP diagram of the crystal structure of complex 2. (b) Packing diagram and hydrogen bonding interactions (Cl1···O1) in 2.

2.4. Computational Studies. A computational study utilizing the method of nucleus-independent chemical shifts (NICS) was employed for 4 in order to verify the Ag–Ag bonding interactions. Theoretical as well as experimental evidence of aromaticity in all-metal systems [20–29, 37–39] has attracted immense attention. This type of molecule contains either an aromatic cycle completely composed of metal atoms [40] or ligand-stabilized aromatic clusters with the ligands being either terminal or bridging adjacent metal atoms [41, 42]. In addition, aromatic clusters involving d-orbitals in pseudo-octahedral and in tetrahedral three-dimensional metal cages were comprehensively studied by the use of DFT methods [43]. In this work, we extend our study of aromaticity applied to laboratory data [10, 29] by means of magnetic criteria, using the method of nucleus-independent chemical shifts (NICS) proposed by Corminboeuf et al. in 1996 [21] to assess the aromatic character of cyclic structures. The calculated NICS indexes were obtained by calculating the negative isotropic value of the absolute NMR shieldings at the Ag₄I₄ cluster centre (P1) and at distances ranging from –3.0 to +3.0 Å in all three dimensions with a step of 1.0 Å resulting in 19 ghost atoms plus one ghost atom located at the centre (P2) of the plane delimited by the three nearest Ag atoms (NICS-3Ag) (Figure 3(a)). Significantly negative (i.e., magnetically shielded) NICS values (in ppm) indicate aromaticity while small (close to zero) NICS values represent non-aromaticity.

The variation of NMR shieldings along the three C_2 axes with the distance from the cluster barycentre is illustrated in Figure 3(b). The inner region is shielded up to –11.4 ppm at a distance of ± 1 Å whereas NICS(0) is –7.1 ppm. The corresponding value for benzene, at the same level of theory, is –9.0 ppm. The results are indicative of diatropic regions attributed to the electron delocalization of d or (d-p) π -type orbital electron density between the four Ag and I atoms [10, 25, 26, 29, 44] which also justifies the equalization of the Ag–I bonds in the homometallic cluster. The symmetrical fluctuations of the NICS values as well as the similar ones

obtained along X and Y axes are explained by the S_4 symmetry motif adopted by the Ag₄I₄ fragment. Lower NICS values are found along the Z axis due to the weak bonding interaction between the two Ag atoms sited at 3.539 Å apart; this distance is closer to the twice the van der Waals radius for silver (4.20–4.74 Å [36]). NICS-3Ag value is –7.3 ppm, consistent with the above results. This quasi aromaticity results in strong Ag–Ag interactions and in higher stability of the Ag₄I₄ core.

2.5. Biological Tests

2.5.1. Cytotoxicity. Complexes 1–4 and the water soluble silver(I) cluster of formula $\{[(Et_3NH)^+]_2 \cdot [Ag_6(\mu_3-Hmna)_4(\mu_3-mna)_2]^{2-} \cdot (DMSO)_2 \cdot (H_2O)\}$ (5) (H₂MNA = 2-mercaptopyridine, C₆H₅NO₂S) [32], were tested for their in vitro cytotoxic activity against leiomyosarcoma cancer cells (LMS) (mesenchymal tissue) from the Wistar rat, polycyclic aromatic hydrocarbons (PAH, benzo[a]pyrene) carcinogenesis. The cell viability and the cell growth proliferation activities were evaluated with Trypan Blue and Thiazolyl Blue Tetrazolium Bromide (MTT) assays, respectively. The IC₅₀ values for cell viability are: $8 \pm 0.39 \mu M$ (1), $0.8 \pm 0.08 \mu M$ (2), $1.5 \pm 0.06 \mu M$ (3), $13.2 \pm 0.42 \mu M$ (4) and $4.5 \pm 0.23 \mu M$ (5). Thus, the order of the complexes activity towards cell viability is $2 > 3 > 5 > 1 > 4$, indicating that complex 2 is the strongest one. The IC₅₀ values for cell growth proliferation are: $13.7 \pm 3.06 \mu M$ (1), $1.3 \pm 0.2 \mu M$ (2), $2.9 \pm 0.31 \mu M$ (3), $21.2 \pm 1.93 \mu M$ (4) and $40.3 \pm 2.62 \mu M$ (5). The order of the inhibitory activity of the complexes in cell growth proliferation is $2 > 3 > 1 > 4 > 5$. Thus, the chloride containing complex 2 showed the strongest activity against LMS cells. The IC₅₀ value for cell viability determined for 2 is similar to the corresponding value found for the de-hydrated complex ($0.7 \mu M$) [10]. However, the IC₅₀ value for cell viability determined for

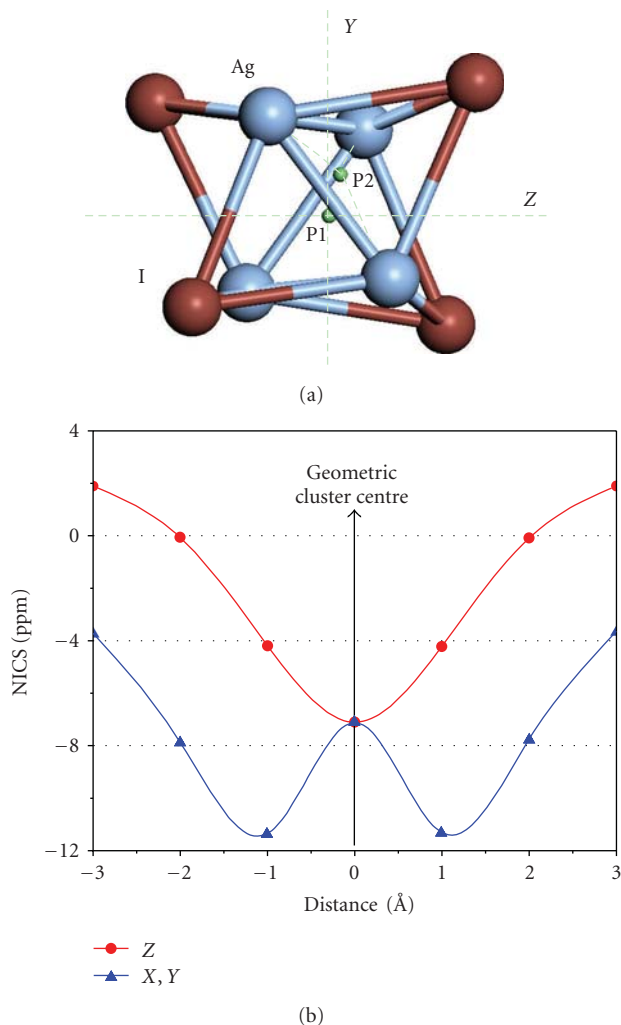


FIGURE 3: (a) The C_2 axes in the Ag_4I_4 core of the cluster **4**, along which NICS values have been calculated. (b) Plot of the NICS values calculated along the three C_2 axes.

3 varies significantly (twofold) from the corresponding value found for its polymorphic form ($0.8 \mu\text{M}$) [10]. The higher IC_{50} value in cell viability found for **4** ($13.2 \mu\text{M}$) compared with the corresponding ones for **1–3** ($0.8–8 \mu\text{M}$) might be attributed to the high stability of **4** due to the quasaromaticity detected (see above).

The activities of complexes **2**, **3**, and **5**, against cells viability are comparable to that of cisplatin, with the corresponding (IC_{50}) value for cisplatin against LMS cells being $4–5 \mu\text{M}$ [12]. However, the inhibitory activities of complexes **1–4**, on the cells growth proliferation are higher than that of cisplatin, with IC_{50} value against LMS cells being $25 \mu\text{M}$.

It is noteworthy to mention that none of the complexes **1–5** showed any activity on cell growth proliferation of MRC-5 cells (normal human fetal lung fibroblast).

2.5.2. Flow Cytometry. A flow cytometry assay was used to quantify apoptotic or necrotic cells treated with compound **1**.

Treated and untreated LMS cells were stained with Annexin V-FITC and Propidium Iodide (PI). Figure 4, shows the dose-dependent cytotoxic response in LMS cells through apoptosis when treated with **1**. Compared to untreated LMS cells which showed a total of 9.22% of background cell death, the cells treated with complex **1** at $8 \mu\text{M}$ showed 10.37% apoptosis (early apoptotic cells (Ann+/PI-) and late apoptotic cells (Ann+/PI+)) and 1.20% necrosis. When LMS cells were treated with $12 \mu\text{M}$ of **1**, the cell death was increased to 29.37% apoptosis (early and late apoptotic cells) and 3.84% necrosis. At higher than the IC_{50} concentration of **1** ($15 \mu\text{M}$), 62.38% of LMS cells were early and late apoptotic cells and 7.05% were necrotic. Thus, **1** causes a dose-dependent cytotoxic response in LMS cells through apoptosis. Although, no direct comparison can be made due to the different cell lines used, the apoptosis of HeLa cells induced by $33.75 \mu\text{M}$ solution of organogold(III) complexes containing the “pincer” iminophosphorane ligand ($2-C_6H_4-PPh_2=NPh$) of formula $[Au\{\kappa^2-C,N-C_6H_4(PPh_2=N(C_6H_5)-2)\}Cl_2]$ is 23.3% [45], in contrast to the 62.38% of **1** against LMS cells, which might indicate stronger interaction of **1** with DNA.

2.5.3. Anti-Inflammatory Activity. Apoptotic cell death requires interaction of the complexes with DNA, which results into antimicrobial activity and to the burn wound recovery of the complexes [9]. Complexes **1–3** and **5** were tested for their anti-inflammatory activity. Figure 5 shows the changes of the burnt surface of animals after 21 days treatment with solvent (glyceryl trioctanoate) and complexes **1–3** and **5** in contrast to the burnt surface at 0 days, in comparison with the corresponding value for the untreated animals (control). The animals of the control group showed 7.38% decrease of the burnt surface, while the animals of the solvent group showed 15.67% decrease of the burnt surface. Furthermore, animals of the group treated with **1**, **2** and **5**, showed 51.33%, 39.32% and 26.76% decrease of the burnt surface, respectively. Therefore, the order of the anti-inflammatory activity caused by silver(I) complexes is $1 > 2 > 5 > \dots > 3$. Thus, the chloride containing complexes **1** and **2** were found to decrease the burnt surface most effectively. The mixed ligand Ag(I) with phosphine and the thione CMBZT, complex **1**, showed the strongest anti-burn activity which might be due to the synergistic effect of the chlorine and thioamide ligands.

3. Conclusions

Silver(I) halide complex **1** was synthesized and characterized by single crystal X-ray diffraction analysis. Complex **2** X-ray crystal structure on the other hand, showed that it deferred from the structure of complex $[AgCl(TPTP)_3]$ [10] containing a water molecule. The re-determination of the structure of $[AgI(TPTP)_3]$ (**3**) determined at 120 K is a new polymorphic form of the complex reported previously at 293 K and 140 K [10]. A computational study using the method of nucleus-independent chemical shifts (NICS) showed that the Ag_4I_4 core of complex **4** exhibits strong

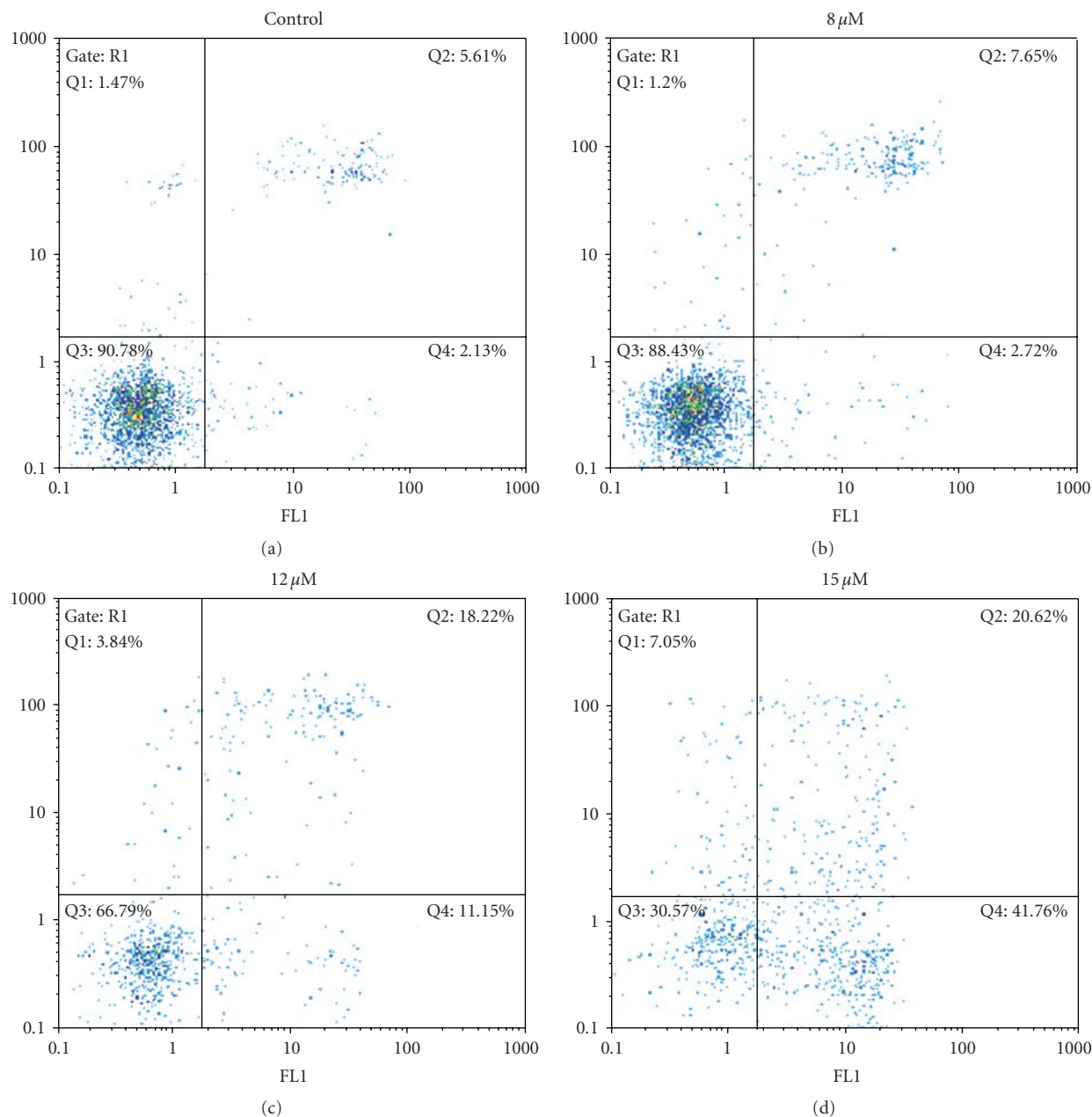


FIGURE 4: Flow cytometry assay summary results for LMS cells, treated with various concentrations of **1** (8, 12, and 15 μM) for 48 hours of incubation, in comparison with the untreated cells (control).

quasiaromaticity, which at the inner region is shielded up to -11.4 ppm, resulting in the formation of strong Ag–Ag bonds.

The results of testing complexes **1–5**, for their in vitro cytotoxic activity against leiomyosarcoma cancer cells (LMS) (mesenchymal tissue) from the Wistar rat, polycyclic aromatic hydrocarbons (PAH, benzo[a]pyrene) carcinogenesis, showed that the chloride containing complex **2** had the strongest activity against LMS cells. The order of the complexes activity towards cell viability is $2 > 3 > 5 > 1 > 4$, while the order of the inhibitory activity of the complexes in cell growth proliferation is $2 > 3 > 1 > 4 > 5$. The IC_{50}

value for cell viability determined for **2** is similar to the corresponding value found for the de-hydrated complex [10]. However, the IC_{50} value for cell viability determined for **3** (crystallized in monoclinic, C2/c space group), varies significantly (twofold) from the corresponding value found for its polymorphic form (crystallized in triclinic, P-1 space group) [10]. The low biological activity of **4** might be attributed to its high stability due to the quasiaromaticity detected. The type of cell death in the case of complex **1** was also evaluated by use of a flow cytometric assay.

The results showed that **1** causes a dose-dependent cytotoxic response in LMS cells through apoptosis. Apoptotic

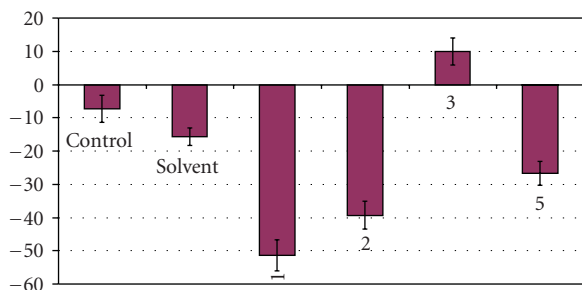


FIGURE 5: Change of the burnt surfaces after 21 days treatment with the solvent and complexes 1–3 and 5 in contrast to the burnt surface at 0 days.

cell death requires interaction of the complexes with DNA, which results into their antimicrobial activity and to the burn wound recovery [9].

The chloride containing complexes **1** and **2** were also found to decrease the burnt surface most effectively. The order of the anti-inflammatory activity caused by silver(I) complexes is $1 > 2 > 5 > \dots > 3$. The mixed ligand Ag(I) with phosphine and the thione CMBZT, complex **1**, showed the strongest anti-inflammatory activity which might be due to the synergistic effect of the chloride and thioamide ligands. Among complexes **1–3** and **5**, complex **2**, which showed the strongest activity against cells viability and the highest inhibitory activity against cells proliferation, also found to exhibit strong burn wood recovery activity.

4. Experimental

4.1. Materials and Instruments. All solvents used were of reagent grade. Silver(I) chloride and Silver(I) iodide were prepared by mixing aqueous solutions of AgNO_3 with the appropriate amount of NaCl and NaI (Merck or Aldrich), respectively. The precipitates were filtered off and dried in darkness. Tri-*p*-tolyl-phosphine and 5-chloro-2-mercaptobenzothiazole (Fluka, Aldrich) were used with no further purification. Melting points were measured in open tubes with a Stuart Scientific apparatus and are uncorrected. IR spectra in the region of $4000\text{--}370\text{ cm}^{-1}$ were obtained from KBr discs, while far-IR spectra in the region of $400\text{--}30\text{ cm}^{-1}$ were obtained from polyethylene discs, with a Perkin-Elmer Spectrum GX FT-IR spectrophotometer.

4.2. Synthesis and Crystallization of $\{[\text{AgCl}(\text{CMBZT})(\text{TPTP})_2] \cdot (\text{MeOH})\}$ (1**), $\{[\text{AgCl}(\text{TPTP})_3] \cdot (0.5 \cdot \text{H}_2\text{O})\}$ (**2**), $[\text{AgI}(\text{TPTP})_3]$ (**3**) and $\{[\text{AgI}(\text{TPTP})_4]\}$ (**4**).** Complex **1** was synthesized as follows: A solution of 0.202 g CMBZT (0.5 mmol) in 10 ml methanol was added to a suspension of 0.072 g AgCl (0.5 mmol) and 0.304 g TPTP (1 mmol) in 10 ml acetonitrile and the mixture was stirred for 1 hour at 50°C . The clear solution was filtered off and the filtrate was kept in darkness. After a few days a pale yellow powder was precipitated. Crystals of complex **1** suitable for X-ray crystallographic analysis were obtained from a toluene/chloroform solution. Complexes **2–4** were prepared

by heading toluene solutions of the appropriate amounts of silver(I) halides with TPTP under reflux for 3 hours. The clear solutions were filtered off and the filtrates were kept in darkness. Colorless crystals of complexes **2–4** suitable for X-ray crystallographic analysis were grown from the filtrates.

- 1:** Yield: 44%; m.p: $178\text{--}181^\circ\text{C}$; $\{[\text{C}_{49}\text{H}_{46}\text{P}_2\text{AgCl}_2\text{NS}_2] \cdot (\text{CH}_3\text{OH})\}$ (MW = 985.7); elemental analysis: found C = 60.75%, H = 5.21%, N = 1.39%, S = 6.87%; calcd: C = 60.92%, H = 5.11%, N = 1.42%, S = 6.50%. MID-IR (cm^{-1}) (KBr): 3013, 2915, 1496, 1305, 1093, 1026, 802, 658, 515, 509, Far-IR (cm^{-1}) (polyethylene): 248, 169.
- 2:** Yield: 80%; m.p: $199\text{--}205^\circ\text{C}$; $\{[\text{C}_{63}\text{H}_{63}\text{P}_3\text{AgCl}] \cdot (0.5 \text{H}_2\text{O})\}$ (MW = 1065.4); elemental analysis: found C = 70.55%, H = 6.24%; calcd: C = 70.43%, H = 6.09%. MID-IR (cm^{-1}) (KBr): 3013, 2911, 1093, 800, 516, 509, Far-IR (cm^{-1}) (polyethylene): 179.
- 3:** Yield: 83%; m.p: $145\text{--}152^\circ\text{C}$; $\{[\text{C}_{63}\text{H}_{63}\text{P}_3\text{AgI}]\}$ (MW = 1147.8); elemental analysis: found C = 65.30%, H = 5.87%; calcd: C = 65.92%, H = 5.53%. MID-IR (cm^{-1}) (KBr): 3008, 2915, 1093, 802, 516, 505, Far-IR (cm^{-1}) (polyethylene): 125.
- 4:** Yield: 56%; m.p: $278\text{--}283^\circ\text{C}$; $\{[\text{C}_{84}\text{H}_{84}\text{P}_4\text{Ag}_4\text{I}_4]\}$ (MW = 2156.5); elemental analysis: found C = 46.28%, H = 3.88%; calcd: C = 46.79%, H = 3.92%. MID-IR (cm^{-1}) (KBr): 3013, 2911, 1095, 802, 516, 505, Far-IR (cm^{-1}) (polyethylene): 127.

4.3. X-Ray Structure Determination. X-ray diffraction data from the crystals of **1** were collected on a KUMA KM4CCD four-circle diffractometer [46] with a CCD detector, using graphite-monochromated MoK_α radiation ($\lambda = 0.71073\text{ \AA}$) at $293(2)\text{ K}$. Unit cell parameters were determined by a least-squares fit [47]. All data were corrected for Lorentz-polarization effects and absorption [47, 48]. The structure was solved by direct methods using SHELXS-97 [49] and refined by a full-matrix least-squares procedure on F^2 with SHELXL-97 [49]. All non-hydrogen atoms were refined anisotropically while hydrogen atoms were located at calculated positions and refined using a “riding model” with isotropic displacement parameters based on the equivalent isotropic displacement parameter (U_{eq}) of the parent atom.

X-ray diffraction data from the crystals of **2** and **3** were collected on a Bruker APEXII CCD diffractometer and data from crystals of **4** were collected on a Bruker CCD diffractometer, both at the window of a Bruker FR591 rotating anode ($\lambda = 0.71073\text{ \AA}$) at $120(2)\text{ K}$. The data collections were driven by COLLECT [50] and processed by DENZO [51]. Absorption corrections were applied using SADABS [52]. The structures of **2** and **3** were solved using SHELXS-97 [49] while that of **4** was solved in SIR2004 [53] and all three structures were refined in SHELXL-97 [49]. All non-hydrogen atoms were refined anisotropically. In **2** there is a water molecule present in the structure at 50% occupancy for which the hydrogen atom positions were located in the electron density. The remaining hydrogen atoms of **2** and all

TABLE 2: Crystal data and structure refinement details for complexes 1–4.

	1; 293 K	2; 120 K	3; 120 K	4; 120 K
Empirical formula	C ₅₀ H ₅₀ AgCl ₂ NOP ₂ S ₂	C ₆₃ H ₆₄ AgClO _{0.5} P ₃	C ₆₃ H ₆₃ AgIP ₃	C ₈₄ H ₈₄ Ag ₄ I ₄ P ₄
Fw	985.7	1065.4	1147.8	2156.5
Temperature (K)	293(2)	120(2)	120(2)	120(2)
Cryst. System	Triclinic	Orthorhombic	Monoclinic	Tetragonal
Space group	P1	Pna2 ₁	C2/c	I4 ₁ /a
a, Å	11.226(4)	20.2646(4)	22.7429(10)	24.0727(2)
b, Å	13.659(5)	26.0074(5)	11.0093(3)	24.0727(2)
c, Å	18.227(7)	10.5020(2)	44.8281(18)	13.8592(2)
α, deg	98.97(3)	90	90	90
β, deg	98.08(3)	90	102.9780(10)	90
γ, deg	113.97(4)	90	90	90
V, Å ³	2457.4(16)	5534.86(19)	10937.5(7)	8031.34(15)
Z	4	4	8	4
ρ _{calcd} , g cm ⁻³	1.332	1.279	1.394	1.783
μ, mm ⁻¹	0.7	0.5	1.1	2.6
R, wR2 [I > 2σ(I)],	0.0458, 0.1279	0.0598, 0.1073	0.0723, 0.2064	0.0299, 0.0773

those in **3** and **4** were refined using a “riding model” in a similar manner to those in structure **1**. For structure **2** the refined absolute structure parameter was 0.19 (3), indicating that the structure consists of a mixture of enantiomers with ratio 0.81 : 0.19. Significant crystal data are given in Table 2.

Supplementary data are available from CCDC, 12 Union Road, Cambridge CB2 1EZ, UK, (e-mail: deposit@ccdc.cam.ac.uk), on request, quoting the deposition numbers CCDC 715884 (**1**), 717733 (**2**), 717734 (**3**) and 717735 (**4**), respectively.

4.4. Computational Details. Calculations based on the molecular geometry acquired via X-ray diffraction methods were carried out with the Gaussian03W program package [54]. Magnetic shielding tensors for a ghost atom placed at different interior and near exterior positions of the Ag₄I₄ cluster were computed using the gauge-independent atomic orbital (GIAO) DFT method [55–57] within the B3LYP level of theory. Nucleus independent chemical shift (NICS) values were estimated with the B3LYP function using the Los Alamos ECP plus double zeta (LANL2DZ) basis set for the Ag atoms and the 6-311G(d,p) for all the others.

4.5. Biological Tests

4.5.1. Trypan Blue Assay. A trypan blue dye exclusion assay was used to determine cell viability. A cell suspension was prepared using brief trypsinization (250 μL of trypsin-incubation at 37°C, 95% O₂, 5% CO₂). An equal volume of PBS was added and the suspension was mixed with 500 μL of 0.4% Trypan blue solution and left for 5 minutes at room temperature. The stained (dead) cells and the total cells per square of the cell chamber were counted using Neubauer cytometer after 24 hours of incubation with different concentrations of complexes **1–4** and **5**.

4.5.2. MTT Assay. Cell growth inhibition was analyzed using the 3-(4,5-dimethylthiazol-2-yl)-2,5-diphenyltetrazolium bromid (MTT) assay. LMS cells cultured on 96-well plates were washed with PBS. A solution containing different concentrations of complexes **1–4** and **5** was then added. After incubation for 24 hours, 50 μL of MTT was added in each well from a stock solution (5 mg/ml), and incubated for an additional 4 hours. Blue formazans were eluted from cells by adding 50 μL of DMSO under gentle shaking and absorbance was determined at 570 nm (subtract background absorbance measured at 690 nm) using a microplate spectrophotometer (Multiskan Spectrum, Thermo Fisher Scientific, Waltham, USA).

4.5.3. Flow Cytometry. LMS cells were seeded onto six-well plates at a density of 6 × 10⁴ cells per well and incubated for 24 hours before the experiment. Cells were washed with PBS, treated with media containing various concentrations of **1** in DMSO (8, 12 and 15 μM) and incubated for 48 hours. Supernatants and cells collected were centrifuged and cell pellets were suspended in calcium buffer 1× at a rate 10⁵ cells/100 μL. Cells were stained with Annexin (BD 556420) and Propidium Iodide (Sigma P4864) in a dark room for 15 minutes. DNA content was determined on a FACScan flow cytometer (Partec ML, Partec GmbH, Germany). Percentage of apoptotic, necrotic and decompensate cells were calculated over all viable cells (100%).

4.6. Anti-Inflammatory Activity

4.6.1. Substances Preparation. The complexes **1–3** and **5** were dissolved in Glyceryl trioctanoate minimum 99% (from Sigma-T9126), to a concentration of 2 × 10⁻⁴ M and the solutions were kept at 4°C during the experiment.

4.6.2. Animal Preparation. All animals were anaesthetized with 1 ml of anaesthetic cocktail (50 mgr/10 ml Midazolam, 50 mgr/10 ml Ketamine, Sodium Chloride 0.9% at a ratio 1.5/0.5/3) given into the peritoneal. After anaesthetization and 5 cm² of skin removal, all animals were burnt for 5 seconds at a specific area by candescent steely stamp. This stamp had been put over a Bunsen lamp for at least 10 minutes. The average of the total burnt surface area represented 1.6% of the total body surface. The burnt area was cleaned by a sterilized dry paper and impressed on a clear paper by a permanent marker, in order to estimate the burnt surface area. A planimeter was also used to determine the burnt surface.

After burning, the animals were separated into 6 groups (6 animals in each group). The first group was the control group (CG) in which the 6 animals had no treatment. The second group was the solvent group (SG), in which all the animals were treated only with the glyceryl trioctanoate as solvent. The other 4 groups were the experiment groups (EG1-EG4), in which animals were treated with the solutions of the complexes in glyceryl trioctanoate. The treatment was performed by inducted 1.75 ml/day solutions over the burnt area. The treatment was continued for 20 days for all groups. At the 21st day the final burnt surface areas were estimated.

4.6.3. Animals and Its Treatment. Female Wistar rats (36), aged 5 months and weighting almost 190 gr were reared in the laboratory in community cages at controlled room temperature (20 ± 2°C), with controlled lighting (12 h light/12 h dark). Standard Wistar rat diet and water *ad libitum* were used in all the experiments.

Experiments on animals were handled with human care in accordance with the National Institutes of Health guidelines and the European Union directive for the care and the use of laboratory animals (Greek presidential decree No. 160 1991).

Acknowledgment

This work was carried out in partial fulfilment of the requirements for the graduate studies of L. K. under the supervision of S. K. H.

References

- [1] B. Krebs and G. Hengel, "Transition-metal thiolates: from molecular fragments of sulfidic solids to models for active centers in biomolecules," *Angewandte Chemie International Edition*, vol. 30, no. 7, pp. 769–788, 1991.
- [2] P. G. Blower and J. R. Dilworth, "Thiolato-complexes of the transition metals," *Coordination Chemical Reviews*, vol. 76, pp. 121–185, 1987.
- [3] E. S. Raper, "Complexes of heterocyclic thione donors," *Journal of Coordination Chemistry*, vol. 61, pp. 115–184, 1985.
- [4] E. S. Raper, "Copper complexes of heterocyclic thioamides and related ligands," *Coordination Chemical Reviews*, vol. 129, no. 1-2, pp. 91–156, 1994.
- [5] E. S. Raper, "Complexes of heterocyclic thionates—part 1: complexes of monodentate and chelating ligands," *Coordination Chemical Reviews*, vol. 153, pp. 199–255, 1996.
- [6] J. E. F. Reynolds, Ed., *Martindale the Extra Pharmacopoeia*, The Pharmaceutical Press, London, UK, 28th edition, 1982.
- [7] M. Wruble, "Colloidal silver sulfonamides," *Journal of the American Pharmacists Association*, vol. 32, no. 11, pp. 80–82, 1943.
- [8] H. S. Rosenkranz and S. Rosenkranz, "Silver sulfadiazine: interaction with isolated deoxyribonucleic acid," *Antimicrobial Agents and Chemotherapy*, vol. 2, no. 5, pp. 373–379, 1972.
- [9] C. L. Fox Jr. and S. M. Modak, "Mechanism of silver sulfadiazine action on burn wound infections," *Antimicrobial Agents and Chemotherapy*, vol. 5, no. 6, pp. 582–588, 1974.
- [10] S. Zartilas, S. K. Hadjikakou, N. Hadjiliadis, et al., "Tetrameric 1:1 and monomeric 1:3 complexes of silver(I) halides with tri(p-tolyl)-phosphine: a structural and biological study," *Inorganica Chimica Acta*, vol. 362, no. 3, pp. 1003–1010, 2009.
- [11] P. C. Zachariadis, S. K. Hadjikakou, N. Hadjiliadis, et al., "Synthesis, characterization and in vitro study of the cytostatic and antiviral activity of new polymeric silver(I) complexes with Ribbon structures derived from the conjugated heterocyclic thioamide 2-mercapto-3,4,5,6-tetra-hydropyrimidine," *European Journal of Inorganic Chemistry*, vol. 2004, no. 7, pp. 1420–1426, 2004.
- [12] S. K. Hadjikakou, I. I. Ozturk, M. N. Xanthopoulou, et al., "Synthesis, structural characterization and biological study of new organotin(IV), silver(I) and antimony(III) complexes with thioamides," *Journal of Inorganic Biochemistry*, vol. 102, no. 5-6, pp. 1007–1015, 2008.
- [13] J. J. Roberts and J. M. Pascoe, "Cross-linking of complementary strands of DNA in mammalian cells by antitumour platinum compounds," *Nature*, vol. 235, pp. 282–284, 1972.
- [14] M. N. Xanthopoulou, S. K. Hadjikakou, N. Hadjiliadis, et al., "Biological studies of new organotin(IV) complexes of thioamide ligands," *European Journal of Medicinal Chemistry*, vol. 43, pp. 327–327, 2008.
- [15] K. Nomiya, Y. Kondoh, H. Nagano, and M. Oda, "Characterization by electrospray ionization (ESI) mass spectrometry of an oligomeric, anionic thiomalato-silver(I) complex showing biological activity," *Journal of The Chemical Society, Chemical Communications*, pp. 1679–1680, 1995.
- [16] K. Nomiya, S. Takahashi, and R. Noguchi, "Synthesis and crystal structure of a hexanuclear silver(I) cluster [Ag(Hmna)]₆ · 4H₂O (H₂mna = 2-mercaptocotinic acid) and a supramolecular gold(I) complex H[Au(Hmna)₂] in the solid state, and their antimicrobial activities," *Journal of the Chemical Society: Dalton Transactions*, pp. 2091–2097, 2000.
- [17] P. G. Blower and J. R. Dilworth, "Thiolato-complexes of the transition metals," *Coordination Chemical Reviews*, vol. 76, pp. 121–185, 1987.
- [18] J.-M. Lehn, *Supramolecular Chemistry Concepts and Perspectives*, Wiley-VCH, Weinheim, Germany, 1995.
- [19] M. Hong, W. Su, R. Cao, M. Fujita, and J. Lu, "Assembly of silver(I) polymers with helical and lamellar structures," *European Journal of Chemistry*, vol. 6, no. 3, pp. 427–431, 2000.
- [20] P. V. R. Schleyer, C. Maerker, A. Dransfeld, H. Jiao, and N. J. Hommes, "Nucleus-independent chemical shifts: a simple and efficient aromaticity probe," *Journal of the American Chemical Society*, vol. 118, no. 26, pp. 6317–6318, 1996.
- [21] C. Corminboeuf, C. S. Wannere, D. Roy, R. B. King, and P. V. R. Schleyer, "Octahedral and tetrahedral coinage metal clusters: is three-dimensional d-orbital aromaticity viable?" *Inorganic Chemistry*, vol. 45, no. 1, pp. 214–219, 2006.

- [22] C. S. Wannere, C. Corminboeuf, Z.-X. Wang, M. D. Wodrich, R. Bruce King, and P. V. R. Schleyer, "Evidence for d orbital aromaticity in square planar coinage metal clusters," *Journal of the American Chemical Society*, vol. 127, no. 15, pp. 5701–5705, 2005.
- [23] A. C. Tsipis and C. A. Tsipis, "Ligand-stabilized aromatic three-membered gold rings and their sandwichlike complexes," *Journal of the American Chemical Society*, vol. 127, no. 30, pp. 10623–10638, 2005.
- [24] C. A. Tsipis, E. E. Karagiannis, P. F. Kladou, and A. C. Tsipis, "Aromatic gold and silver 'rings': hydrosilver(I) and hydrogold(I) analogues of aromatic hydrocarbons," *Journal of the American Chemical Society*, vol. 126, no. 40, pp. 12916–12929, 2004.
- [25] A. C. Tsipis and C. A. Tsipis, "Hydrometal analogues of aromatic hydrocarbons: a new class of cyclic hydrocoppers(I)," *Journal of the American Chemical Society*, vol. 125, no. 5, pp. 1136–1137, 2003.
- [26] C. A. Tsipis, "DFT study of "all-metal" aromatic compounds," *Coordination Chemical Reviews*, vol. 249, no. 24, pp. 2740–2762, 2005.
- [27] J. Li, C.-W. Liu, and J.-X. Lu, "Theoretical studies of (d-p) bonding, electronic spectra, and reactivities in homo- and heterometallic clusters: $[\text{Mo}_{3-n}\text{W}_n\text{X}_4(\text{H}_2\text{O})_6]^{4+}$ (X = O, S, Se, Te; $n = 0 - 3$)," *Journal of Cluster Science*, vol. 7, no. 3, pp. 469–500, 1996.
- [28] Z. Chen, "Multicentered bonding and quasi-aromaticity in metal-chalcogenide cluster chemistry," *Journal of Cluster Science*, vol. 6, no. 3, pp. 357–377, 1995.
- [29] S. Zartilas, N. Kourkoumelis, S. K. Hadjikakou, et al., "A new silver(I) aggregate having an octagonal Ag_4S_4 Core Where μ_3 -S bonding interactions lead to a nanotube assembly that exhibits quasaromaticity," *Butler European Journal Inorganic Chemistry*, vol. 2007, no. 9, pp. 1219–1224, 2007.
- [30] R. Meijboom, "Iodotris(tri-*p*-tolylphosphine)silver(I)," *Acta Crystallographica*, vol. E63, pp. m78–m79, 2007.
- [31] R. Meijboom, A. Muller, and A. Roodt, "Tetra- μ_3 -iodotetrakis[(tri-*p*-tolylphosphine- κ P)-silver(I)]," *Acta Crystallographica*, vol. E62, pp. m2162–m2164, 2006.
- [32] P. C. Zachariadis, S. K. Hadjikakou, N. Hadjiliadis, et al., "Synthesis, study and structural characterization of a new water soluble hexanuclear silver(I) cluster with the 2-mercaptotriacetic acid with possible antiviral activity," *Inorganica Chimica Acta*, vol. 343, pp. 361–365, 2003.
- [33] M. N. Xanthopoulou, S. K. Hadjikakou, N. Hadjiliadis, et al., "Synthesis, structural characterization and in vitro cytotoxicity of organotin(IV) derivatives of heterocyclic thioamides, 2-mercaptobenzothiazole, 5-chloro-2-mercaptobenzothiazole, 3-methyl-2-mercaptobenzothiazole and 2-mercaptotriacetic acid," *Journal of Inorganic Biochemistry*, vol. 96, no. 2-3, pp. 425–434, 2003.
- [34] P. J. Cox, P. Aslanidis, P. Karagiannidis, and S. K. Hadjikakou, "Silver(I) complexes with heterocyclic thiones and tertiary phosphines as ligands—part 4: dinuclear complexes of silver(I) bromide: The crystal structure of bis[bromo-(pyrimidine-2-thione)(triphenylphosphine)silver(I)]," *Inorganica Chimica Acta*, vol. 310, no. 2, pp. 268–272, 2000.
- [35] T. S. Lobana, R. Sharma, and R. J. Butcher, "Pyridine-2-thione (pySH) derivatives of silver(I): synthesis and crystal structures of dinuclear $[\text{Ag}_2\text{Cl}_2(\mu\text{-S-pySH})_2(\text{PPh}_3)_2]$ and $[\text{Ag}_2\text{Br}_2(\mu\text{-S-pySH})_2(\text{PPh}_3)_2]$ complexes," *Polyhedron*, vol. 27, no. 5, pp. 1375–1380, 2008.
- [36] S. S. Batsanov, "Van der waals radii of elements," *Inorganic Materials*, vol. 37, no. 9, pp. 871–885, 2001, translated from *Neorganicheskie Materialy*, vol. 37, pp. 1031–1046, 2001.
- [37] X. Li, A. E. Kuznetsov, H. Zhang, A. I. Boldyrev, and L. Wang, "Observation of all-metal aromatic molecules," *Science*, vol. 291, no. 5505, pp. 859–861, 2001.
- [38] X. Huang, H. J. Zhai, B. Kiran, and L. S. Wang, "Observation of d-orbital aromaticity," *Angewandte Chemie International Edition*, vol. 44, no. 44, pp. 7251–7254, 2005.
- [39] S. Erhardt, G. Frenking, Z. Chen, and P. V. R. Schleyer, "Aromatic boron wheels with more than one carbon atom in the center: $\text{C}_2\text{B}_{8,3}\text{B}_9^{3+}$, and $\text{C}_5\text{B}_{11}^+$," *Angewandte Chemie International Edition*, vol. 44, no. 7, pp. 1078–1082, 2005.
- [40] S. Wannere, C. Corminboeuf, Z. X. Wang, M. D. Wodrich, R. B. King, and P. V. R. Schleyer, "Evidence for d orbital aromaticity in square planar coinage metal clusters," *Journal of the American Chemical Society*, vol. 127, no. 15, pp. 5701–5705, 2005.
- [41] E. Janssens, S. Neukemans, F. Vanhoutte, et al., "Ionization potentials and structures of small indium monoxide clusters," *Journal of Chemical Physics*, vol. 118, pp. 5862–5871, 2003.
- [42] R. B. King, "Chemical bonding topology of ternary transition metal-centered bismuth cluster halides: from molecules to metals," *Inorganic Chemistry*, vol. 42, no. 26, pp. 8755–8761, 2003.
- [43] C. Corminboeuf, C. S. Wannere, D. Roy, R. B. King, and P. V. R. Schleyer, "Octahedral and tetrahedral coinage metal clusters: is three-dimensional d-orbital aromaticity viable?" *Inorganic Chemistry*, vol. 45, no. 1, pp. 214–219, 2006.
- [44] Z. Chen and R. B. King, "Spherical aromaticity: recent work on fullerenes, polyhedral boranes, and related structures," *Chemical Reviews*, vol. 105, no. 10, pp. 3613–3642, 2005.
- [45] N. Shaik, A. Martínez, I. Augustin, et al., "Synthesis of apoptosis-inducing iminophosphorane organogold(III) complexes and study of their interactions with biomolecular targets," *Inorganic Chemistry*, vol. 48, no. 4, pp. 1577–1587, 2009.
- [46] KUMA KM-4CCD User Manual, KUMA Diffraction, Wroclaw, Poland, 1999.
- [47] CRYCALIS, "Program for Reduction of the Data from KUMA CCD Diffractometer," KUMA Diffraction, Wroclaw, Poland, 1999.
- [48] R. H. Blessing, "DREADD—data reduction and error analysis for single-crystal diffractometer data," *Journal of Applied Crystallography*, vol. 22, pp. 396–397, 1989.
- [49] G. M. Sheldrick, "A short history of SHELX," *Acta Crystallography A*, vol. 64, pp. 112–122, 2008.
- [50] R. W. W. Hooft, *COLLECT Data Collection Software*, Nonius B. V., Delft, The Netherlands, 1998.
- [51] Z. Otwinowski and W. Minor, "Processing of X-ray diffraction data collected in oscillation mode," in *Methods in Enzymology*, C. W. Carter Jr. and R. M. Sweet, Eds., vol. 276 of *Macromolecular Crystallography A*, pp. 307–326, Academic Press, New York, NY, USA, 1997.
- [52] G. M. Sheldrick, *SADABS*, Bruker AXS, Madison, Wis, USA, 2007.
- [53] M. C. Burla, R. Caliendo, M. Camalli, et al., "SIR2004: an improved tool for crystal structure determination and refinement," *Journal of Applied Crystallography*, vol. 38, pp. 381–388, 2005.
- [54] M. J. Frisch, G. W. Trucks, H. B. Schlegel, et al., "Gaussian 03, Revision C.02," Gaussian, Wallingford, Conn, USA, 2004.

- [55] R. M. Weeny, "Perturbation theory for the fock-dirac density matrix," *Physical Review*, vol. 126, no. 3, pp. 1028–1034, 1962.
- [56] J. L. Dodds, R. McWeeny, and A. Sadlej, "Open-shell states in perturbation-dependent non-orthogonal basis sets," *Journal Molecular Physics*, vol. 41, no. 6, pp. 1419–1430, 1980.
- [57] R. Ditchfield, "Self-consistent perturbation theory of diamagnetism—I: a gauge-invariant LCAO method for N.M.R. chemical shifts," *Molecular Physics*, vol. 27, no. 4, pp. 789–807, 1974.

Research Article

Synthesis, Solution, and Structural Characterization of Tetrahydrofuranyl-2,2-Bisphosphonic Acid Disodium Salt

Elena Maltezo¹, Marios Stylianou¹, Sudeshna Roy¹, Chryssoula Drouza², and Anastasios D. Keramidas¹

¹Department of Chemistry, University of Cyprus, 1678 Nicosia, Cyprus

²Agricultural Production and Biotechnology and Food Science, Cyprus University of Technology, 3036 Lemesos, Cyprus

Correspondence should be addressed to Anastasios D. Keramidas, akeramid@ucy.ac.cy

Received 2 January 2010; Accepted 26 February 2010

Academic Editor: Spyros Perlepes

Copyright © 2010 Elena Maltezo et al. This is an open access article distributed under the Creative Commons Attribution License, which permits unrestricted use, distribution, and reproduction in any medium, provided the original work is properly cited.

Bisphosphonates are biologically relevant therapeutics for bone disorders and cancer. Reaction of γ -chlorobutyric acid, phosphorus acid, and phosphorus trichloride without the use of solvent gave the tetrahydrofuranyl-2,2-bisphosphonate sodium salt ($\text{Na}_2\text{H}_2\text{L}$). The $\text{Na}_2\text{H}_2\text{L}$ was isolated, characterized in solution by ^1H , ^{13}C , and ^{31}P NMR spectroscopy and in solid state by single X-Ray crystallography. The crystal structure showed that the $\text{Na}_2\text{H}_2\text{L}$ forms in the crystal infinite two-dimensional sheets stacked one parallel to the other. A comparison of the chelating properties of H_2L^{2-} with similar hydroxyl bisphosphonate ligands shows that the strength of the Na–O(furanyl/hydroxyl) bond is directly related to the total charge of the ligand anion.

1. Introduction

Bisphosphonates (BPs) represent a very important class of compounds known for their medicinal and other properties [1, 2]. In contrast to the naturally occurring pyrophosphate P–O–P group, these compounds contain a characteristic P–C–P bridge, which is chemically and enzymatically nonhydrolyzable. BPs exhibit specific affinity towards bone, which makes them an excellent therapeutic for bone resorption diseases (especially osteoporosis, Paget's disease, tumour induced osteolysis, hypercalcemia originated from malignancy) by inhibition of farnesyl diphosphate synthase (FPPS) and for bone tumour caused by metastatic breast tumours [3–5]. The biological activity of bisphosphonates has been found to be dependent on the structure [6], lipophilicity [7], and bone binding affinity [8] of the compounds. For example, the structure of the side chain of bisphosphonates is important in determining the potency of individual bisphosphonates in biological models, and this includes a potential role for the side chain in modulating bone binding. The presence and position of an oxygen or nitrogen atom within the side chain of bisphosphonates are directly related to their relative potency and bone binding affinity. In general, the

oxygen/nitrogen containing bisphosphonates exhibits high bone binding affinities, which might be expected to reduce efficacy. However, some of these molecules are very potent and the difference in potency has been attributed to the inhibition of FPPS. Therefore, the structural characterization of bisphosphonates is very important tool for the elucidation of the mechanisms of the bone binding and biological activity and for the design of new, more potent compounds.

Herein, we report the synthesis, solution characterization, and crystal structure of the sodium salt of tetrahydrofuranyl-2,2-bisphosphonate ($\text{Na}_2\text{H}_2\text{L}$). In the crystal the compound forms, the unusual for bisphosphonates, two-dimensional parallel sheets arrangement. A comparison of the chelating properties of H_2L^{2-} with similar hydroxyl bisphosphonate ligands shows that the Na–O(furanyl/hydroxyl) bond length increases as the charge of the ligand decreases. Thus, the weak Na–O(furanyl) interaction is attributed to the -2 charge of the ligand.

2. Materials and Methods

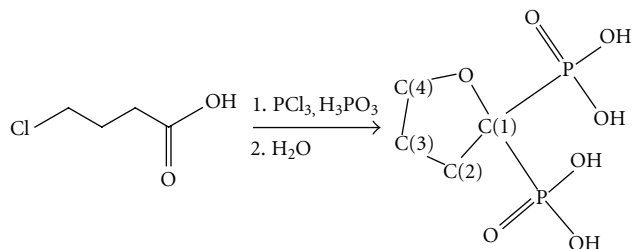
2.1. Materials. The chemicals obtained from commercial sources were reagents grade and used as received. Solvents

were freshly distilled and water was doubly distilled. γ -Chlorobutyric acid, phosphorus acid, and D_2O were purchased from Sigma-Aldrich. Sodium hydroxide and phosphorus trichloride were purchased from Merck. Ethyl alcohol and methyl alcohol were bought from BDH. The synthesis was performed in inert Argon atmosphere.

2.2. Synthesis and Crystallization of Tetrahydrofuran-2,2-Bisphosphonic Acid Disodium Salt (Na_2H_2L). A mixture of γ -chlorobutyric acid (7.12 g, 58.1 mmol), phosphorus acid (3.38 g, 41.2 mmol), and phosphorus trichloride (10.9 g, 79.4 mmol) was heated slowly to reach the temperature $80^\circ C$ over an hour under constant flow of argon. The two-phase mixture was refluxed for 4 hours at $80^\circ C$ and the viscous yellow mass was stirred vigorously for 10 hours at $60^\circ C$. Precooled water (125 mL) was added slowly to the mixture under stirring as evolution of gaseous HCl was observed. The water (110 mL) was constantly removed by distillation from the orange reaction mass. Another 150 mL of water was added to the mixture and allowed to cool down slowly to room temperature ($25^\circ C$). The pH of the reaction mixture was adjusted to 3 by careful addition of 4 M NaOH solution. Absolute ethyl alcohol (150 mL) was poured slowly to the resulting yellow solution in order to induce crystallisation. White solid was formed after 12 hours stirring at $25^\circ C$ and collected by filtration. The yellow filtrate was again treated with ethyl alcohol (100 mL) to obtain another batch of white solid. Total three batches were collected and for the crude product the yield was calculated to be 9.75 g, (65% based on γ -chlorobutyric acid). Crystallisation was performed by layering concentrated aqueous solution (pH = 4.2) of Na_2H_2L with methyl alcohol. Samples for NMR measurements were prepared by dissolution of the crystals in D_2O . The atoms have been numbered according to the numbering in Scheme 1. 1H NMR $\delta(D_2O, ppm)$: 3.90 (t, $^2J_{H,H} = 6.7$ Hz, two protons H(4)); 2.30 (m, $^2J_{H,H} = 6.7$ Hz, $^3J_{H,P} = 16.0$ Hz, two protons, H(2)); 1.99 (p, $^2J_{H,H} = 6.7$ Hz, two protons H(3)). ^{13}C NMR $\delta(D_2O, ppm)$: 81.3 (t, $^1J_{C,P} = 144$ Hz), C(1); 70.3, C(4); 30.2, C(3); 26.8 (t, $^2J_{C,P} = 2.26$ Hz), C(2). ^{31}P NMR $\delta(D_2O, ppm)$: 21.9 (t, $^3J_{H,P} = 16.0$ Hz). Anal. Calcd. for $C_4H_8Na_2O_7P_2$ (f.w.: 276.02): C, 17.41; H, 2.92. Found: C, 17.38; H, 2.89.

2.3. NMR Studies. The one-dimensional 1H , ^{13}C , and ^{31}P spectra were recorded in a 300 MHz Avance Bruker spectrophotometer at 300.13 MHz for 1H , 121.46 MHz for ^{31}P , and 75.47 MHz for ^{13}C with a 5 mm multinucleus probe at ambient temperature ($25^\circ C$) in D_2O solution. A 30° -pulse width and 1-second relaxation delay were applied for 1H , ^{31}P , and ^{13}C NMR spectra.

2.4. X-Ray Crystallography. Crystal data, details of data collection, and refinement of crystal structure of Na_2H_2L are provided in Table 1. The intensity data for the compound were collected at 100 K on an *XCalibur III 4-cycle diffractometer*, equipped with a CCD camera detector. The experimental data were collected using Mo $K\alpha$ radiation ($\lambda = 0.7107 \text{ \AA}$) at a crystal-to-detector distance 60 mm. The structure was solved



SCHEME 1: Synthetic methodology for synthesis of Na_2H_2L along with the numbering scheme of C-atoms for NMR peak assignments.

TABLE 1: Crystallographic and experimental data for compound Na_2H_2L .^{a, b}

Empirical formula	$C_4H_8Na_2O_7P_2$
Formula mass	274.01
Crystal system	Triclinic
Space group	$P-1$
$a/\text{\AA}$	6.327 (5)
$b/\text{\AA}$	6.967 (5)
$c/\text{\AA}$	11.805 (5)
$\alpha/^\circ$	93.067 (5)
$\beta/^\circ$	96.222 (5)
$\gamma/^\circ$	113.594 (5)
$V/\text{\AA}^3$	471.4 (5)
Z	2
$D_c/g\text{ cm}^{-3}$	1.930
Absorption coefficient/ cm^{-1}	0.564
$F(000)$	276
θ range for data collection/ $^\circ$	3.7788–62.3061
	$-7 \leq h \leq 7$
Ranges for h, k, l	$-8 \leq h \leq 7$
	$-11 \leq h \leq 13$
Reflections collected/unique	2384/1451
R_{int}	0.0218
Data/restraints/parameters	3667/0/171
GOF on F^2	1.158
a, b in weighting scheme	0.1390/0.0668
Final R/R_w indices ($I > 2\sigma(I)$)	0.0572/0.2162
Final R/R_w indices (all data)	0.0827/0.2288

^aAll structures determined at $T = 100$ K using Mo $K\alpha$ radiation ($\lambda = 0.71073 \text{ \AA}$).

^b $R = \sum ||F_o| - |F_c|| / \sum |F_o|$, $wR = [\sum w(|F_o|^2 - |F_c|^2) / \sum w|F_o|^2]^{1/2}$, $GOF = [\sum |w(F_o^2 - F_c^2)| / (n - p)]^{1/2}$, $w = 1 / [\sigma^2(F_o^2) + (aP)^2 + bP]$, where $P = (F_o^2 + 2F_c^2) / 3$.

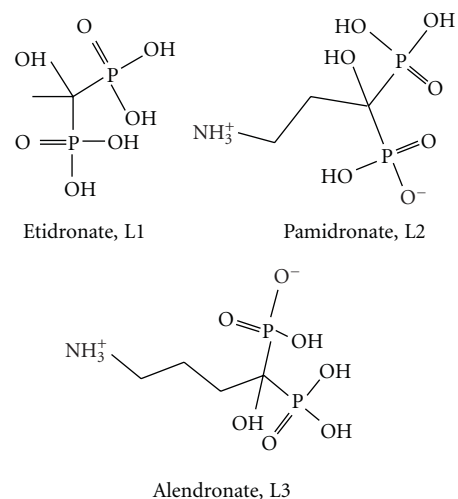
by direct methods using the programs SHELXS-86 and refined anisotropically (nonhydrogen atoms) by full-matrix least squares on F^2 [9, 10]. The H atoms were calculated geometrically and refined with riding model with isotropic displacement parameters. The programs ORTEP-3 [11] and Diamond-3 were used for diagrams and WINGX [12] was used to prepare material for publication.

3. Results and Discussion

3.1. Synthesis. Compound $\text{Na}_2\text{H}_2\text{L}$ has been synthesized by heating at 80°C the mixture of γ -chlorobutyric acid, phosphorus acid, and phosphorus trichloride (Scheme 1). This molecule has been previously synthesized by Kieczkowski et al. [13] following a similar procedure by heating the mixture at 65°C in methanesulfonic acid. However, the product isolated from that reaction had always been contaminated with the methanesulfonate salt and the yield of the reaction was less than 30%. In contrast, the reaction without the use of solvent gave pure product and yield more than 60%. Upon completion of the reaction, it is quenched with water. The product was crystallized by addition of ethanol in an aqueous solution of $\text{Na}_2\text{H}_2\text{L}$ at pH 3.0. It is worth to notice that the isolated compound is the disodium salt of the bisphosphonate anion although it has been isolated at pH lower than that of the monosodium salt (pH 4.3) by Kieczkowski et al. This difference is attributed to the different methodology used for the crystallization of the product.

3.2. Solution Characterization. The molecule was characterized in aqueous solution by ^1H , ^{13}C , and ^{31}P NMR spectroscopy. The J coupling constants were used to confirm the assignments made by the NMR spectra. The ^{31}P NMR spectrum gave one triplet due to the coupling ($^3J_{\text{HP}} = 16.0$ Hz) of phosphorus nuclei with the two H(2) protons at 21.9 ppm. This chemical shift is close to the chemical shifts of other hydroxyl bisphosphonates such as etidronate (L1, Scheme 2) (22.9 ppm) [14]. The ^{13}C spectrum of $\text{Na}_2\text{H}_2\text{L}$ showed a triplet assigned to C(1). The splitting of this peak is assigned to the strong coupling of C(1) with the two phosphorus atoms ($^1J_{\text{CP}} = 144.0$ Hz). The weak coupling of C(2) with the two phosphorus nuclei ($^2J_{\text{C,P}} = 2.26$ Hz) gives a triplet feature for this peak that can be easily distinguished from the peak assigned to C(3). The ^1H NMR spectrum exhibits a triplet for H(4) protons (due to the coupling with the two H(3) protons), a quintuplet for H(3) (due to the coupling with the two H(2) and two H(4) protons), and a multiplet for H(2) (due to the coupling with the two H(3) protons and the two P atoms).

3.3. X-Ray Crystallographic Structure. The molecular structure of $\text{Na}_2\text{H}_2\text{L}$ is shown in Figures 1 and 2(a). Crystallographic data are provided in Table 1. Tables 3 and 4 contain the interatomic bond lengths and angles of $\text{Na}_2\text{H}_2\text{L}$. The bisphosphonate anion in the structure of $\text{Na}_2\text{H}_2\text{L}$ possesses an overall -2 charge, thus two of the phosphonate oxygen atoms are deprotonated ($\text{P}-\text{O}^-$), two have protons attached ($\text{P}-\text{OH}$), and two form double bond with phosphorus ($\text{P}=\text{O}$). Both phosphorous atoms exhibit distorted tetrahedral geometries. The P–O bond lengths are close to 1.50 \AA for the P–O(deprotonated) and 1.57 \AA for the P–OH(protonated). Although the P–OH bonds can be located very easily by inspection of the bond distances, the P–O $^-$ and P=O cannot be distinguished because of the charge delocalization over the $^-\text{O}-\text{P}=\text{O}$ groups. The bond angles around P(1), P(2) range from $104.0(4)$ to $116.4(3)^\circ$. The O–P–O angles involving the two unprotonated oxygen atoms



SCHEME 2: Molecular structures of etidronate, pamidronate, and alendronate and abbreviations used in the document.

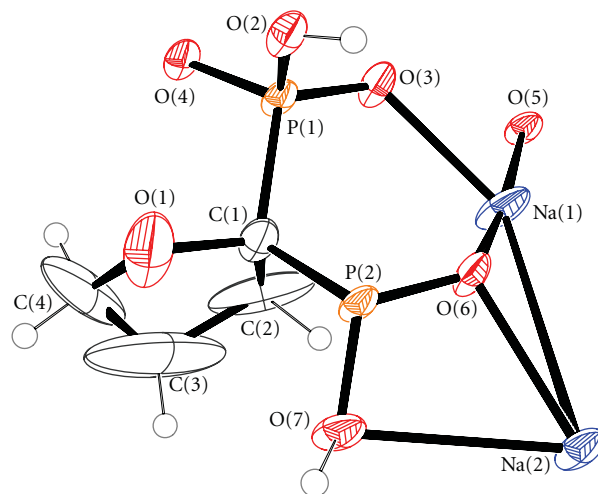


FIGURE 1: ORTEP representation of the main structural motif observed in $\text{Na}_2\text{H}_2\text{L}$. Ellipsoids are drawn at the 50% probability level.

are the largest ones in both phosphonate groups. The two phosphorus centers are fairly close ($3.087(3) \text{ \AA}$), due to their bisectonal positions relative to C(1) on the furanyl ring ($\text{P}(1)-\text{C}(1)-\text{P}(2) = 114.7(5)^\circ$). The P...P distance is a little larger than the distance ($3.035(3) \text{ \AA}$) observed in the crystal structure of nitrogen containing respective molecule, the pyrrolidine-2,2-diylbisphosphonic acid [15].

The coordination sphere is different for each of the two sodium atoms (Figures 3(a) and 3(b)). The Na(1) exhibits a distorted octahedral environment defined by O(5), O(4), O(2), O(6), O(3), and O(3'). The Na(2) exhibits a capped octahedral geometry with the O(1), O(2), O(3), O(5), O(6), and O(6') to define an octahedron and the O(7) added to the triangular face defined by O(1), O(3), and O(6). The Na–O bond distances range between $2.327(7)$ and $2.872(7) \text{ \AA}$ with the Na(2)–O(7) to exhibit the longest bond distance. The sodium-centered octahedrons and capped octahedrons form

TABLE 2: Selected bond lengths (Å) for Na₂H₂L.

C(1)–O(1)	1.48 (2)	P(1)–O(2)	1.571 (8)
C(1)–C(2)	1.50 (2)	P(1)–O(3)	1.499 (7)
C(2)–C(3)	1.59 (3)	P(1)–O(4)	1.499 (5)
C(3)–C(4)	1.50 (4)		
C(4)–O(1)	1.42 (2)	P(2)–O(5)	1.507 (7)
C(1)–P(1)	1.834 (9)	P(2)–O(6)	1.493 (7)
C(1)–P(2)	1.833 (7)	P(2)–O(7)	1.567 (7)
Na(1)–O(2)	2.625 (7)	Na(2)–O(1)	2.79 (2)
Na(1)–O(3)	2.335 (7)	Na(2)–O(2)	2.494 (8)
Na(1)–O(3')	2.671 (8)	Na(2)–O(3)	2.371 (7)
Na(1)–O(4)	2.449 (8)	Na(2)–O(5)	2.405 (7)
Na(1)–O(5)	2.480 (7)	Na(2)–O(6)	2.423 (8)
Na(1)–O(6)	2.327 (7)	Na(2)–O(6')	2.458 (6)

^aStandard deviations are given in parentheses.

^bSymmetry operations: $x, y, z; -x, -y, -z$.

TABLE 3: Selected bond angles (°) for Na₂H₂L.

O(2)–P(1)–O(3)	110.7 (3)	O(5)–P(2)–O(6)	115.1 (3)
O(2)–P(1)–O(4)	105.5 (3)	O(5)–P(2)–O(7)	110.1 (4)
O(3)–P(1)–O(4)	116.4 (4)	O(6)–P(2)–O(7)	109.3 (4)
C(1)–P(1)–O(2)	105.2 (4)	C(1)–P(2)–O(5)	108.6 (4)
C(1)–P(1)–O(3)	110.9 (4)	C(1)–P(2)–O(6)	109.2 (4)
C(1)–P(1)–O(4)	107.4 (4)	C(1)–P(2)–O(7)	104.0 (4)
O(1)–C(1)–P(1)	106.5 (6)	O(1)–C(1)–P(2)	105.2 (6)
C(2)–C(1)–P(1)	107.9 (8)	C(2)–C(1)–P(2)	110.7 (8)
O(1)–C(1)–C(2)	112.0 (9)	P(1)–C(1)–P(2)	114.6 (5)
C(1)–O(1)–C(4)	105 (1)	C(1)–C(2)–C(3)	100 (1)
O(1)–C(4)–C(3)	107 (2)	C(2)–C(3)–C(4)	103 (2)

^aStandard deviations are given in parentheses.

^bSymmetry operations: $x, y, z; -x, -y, -z$.

TABLE 4: Selected bond lengths for Na⁺ and Ca²⁺ bisphosphonate complexes. The L, L1, L2, L3 bisphosphonates are according to Scheme 2.

Compound	Charge of bisphosphonate anion	M–O _{hydroxy/furanyl} /Å	Shortest M–O _{phosphoryl} /Å	Longest M–O _{phosphoryl} /Å	References
Na ₂ H ₂ L	(–2)	2.79 (1)	2.327 (7)	2.873 (8)	This work
CaH ₂ L1	(–2)	2.608 (2)	2.352 (1)	2.608 (2)	[16]
NaH ₃ L1	(–1)	2.470 (4)	2.230 (4)	2.447 (4)	[17]
NaH ₃ L1	(–1)	2.463 (2)	2.293 (3)	2.444 (2)	[18]
CaH ₂ L2	(–2)	^a	2.288 (1)	2.387 (1)	[19]
Na ₂ H ₂ L2	(–2)	2.828 (3)	2.274 (3)	2.691 (3)	[20]
NaH ₃ L2	(–1)	2.537 (2)	2.261 (2)	2.438 (2)	[21]
CaH ₂ L3	(–2)	^a	2.304 (1)	2.345 (1)	[22]

^a Non bonding distance above 3Å.

an edge-sharing linear array directed along the axis (1,1,0) of the crystal (Figure 3(a)). These arrays are connected to each other with the diphosphonate anions (Figure 3(b)) forming infinite 2D sheets. The two-dimensional networks are stacked one over the other along axis c (Figure 3(c)).

The distance between the mean planes defined from the atoms of two successive sheets is 11.668(5) Å. This distance is actually the length of the c axis. The furanyl rings are located above and below the 2D structures insulating the sodium ions in each layer. It is possible that this unusual for

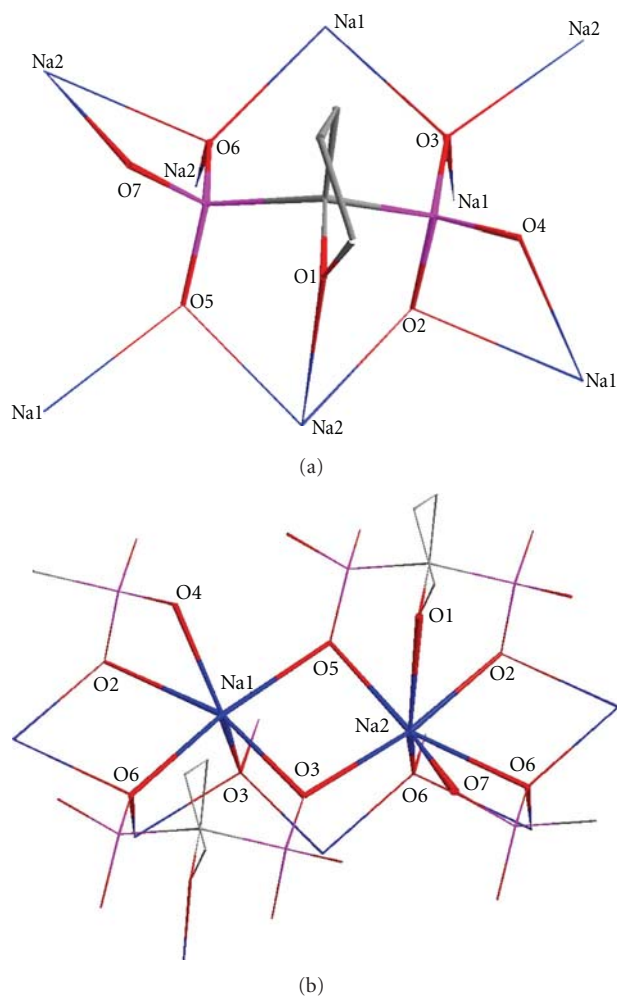


FIGURE 2: (a) Stick representation of H_2L^{2-} showing the connectivity with sodium ions. (b) Stick representation of Na_2H_2L showing the coordination environment of sodium ions.

diphosphonates two-dimensional structure is induced by the hydrophobic furanyl rings which prevent any electrostatic interlayer interactions.

A recent study [23] has shown that bisphosphonates binding strength can be calculated by summarizing the interactions of the phosphonate groups, the side chain groups, the hydroxyl group, and the hydrophobic group of the ligand with the bone surface. Most importantly, it has been found that although the $-OH$ group is necessary for the strong binding of phosphonates on the bone, the interaction of the $-OH$ with the bone surface is weak. Selected bond lengths of $Na^+-O/Ca^{2+}-O$ of similar tetrahydrofuranyl-2,2-bisphosphonate compounds extracted from their crystal structure are shown in Table 4. The comparison shows that the chelating properties of the ligands are in good agreement with their binding properties on bone surface. Thus, the bond distances between the donor oxygen atoms of bisphosphonate ligand and the cations might give an estimation of the bisphosphonates bone binding strength. The $(Na^+/Ca^{2+})-O(\text{phosphoryl})$ bond distances are similar,

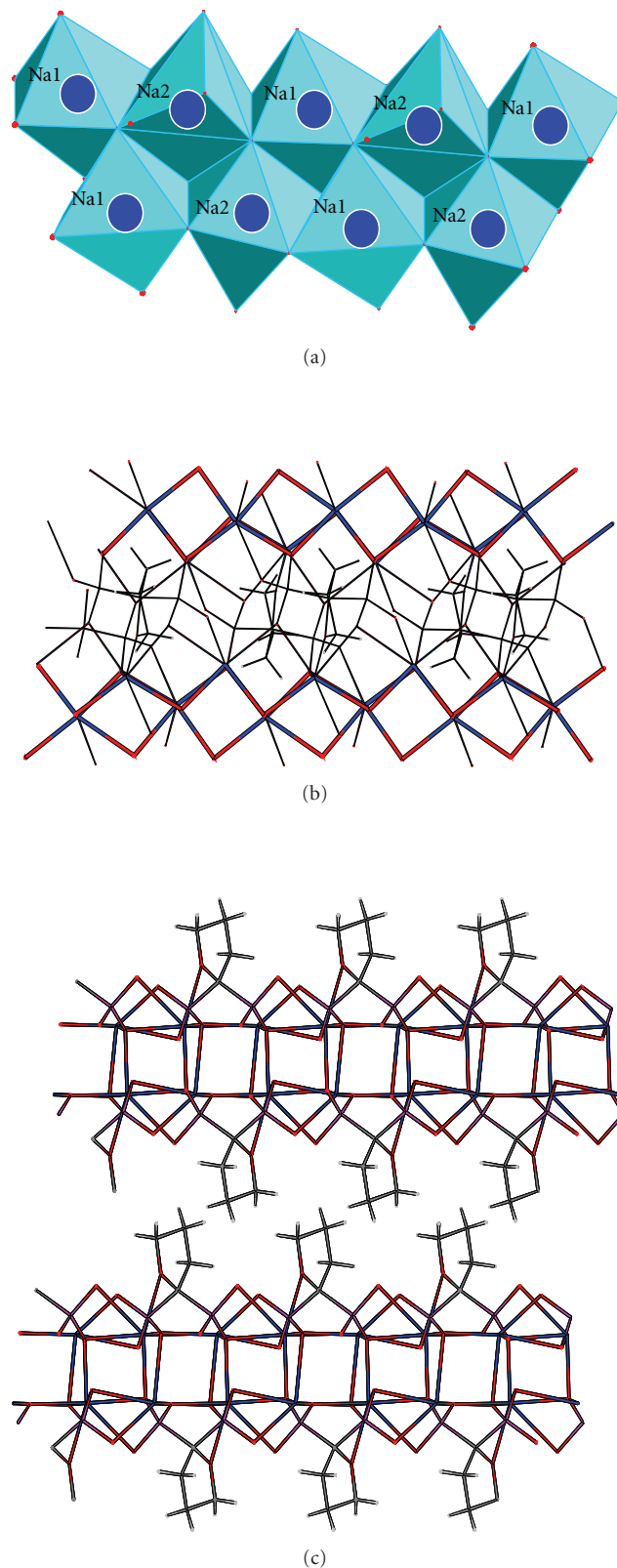


FIGURE 3: (a) Sodium-centered polyhedral connected to each other to form linear arrays along axis $(1,1,0)$. (b) Connection of the linear sodium arrays with bisphosphonate anions to form two dimensional sheets. (c) Two layers stacked one parallel to the other along axis c .

within the range 2.261 to 2.873 Å, suggesting that the interaction of all phosphonate groups with the bone is of similar strength for all ligands. In all crystal structures of the calcium salts of the bisphosphonates, except the structure of etidronate, the metal ion is ligated only to the phosphonate oxygen atoms. The charge of the ligand in all calcium structures is -2 . In contrast, the Na^+ ions have been found to be ligated both to the phosphonate and the hydroxyl oxygen in the structures of the sodium salts of the respective ligands. However, the Na^+-O bond length is much shorter in the structures of monoanion bisphosphonate structures (~ 2.5 Å) than in the respective dianions (~ 2.8 Å) including $\text{Na}_2\text{H}_2\text{L}$. Apparently, this bond length comparison indicates that the $\text{Na}^+-\text{O}(\text{hydroxyl}/\text{furanlyl})$ bond strength is directly dependent on the total charge of the bisphosphonate ligand; the bond length increases by decreasing the charge of the ligand. In addition, the weak interaction of hydroxyl group with the bone [23] also suggests that the total charge of the ligand that binds the bone surface is -2 .

The Na^+-O bond distances found in the crystal structure of $\text{Na}_2\text{H}_2\text{L}$ are close to the respective bond distance of $\text{Na}_2\text{H}_2\text{L}_2$ ($\text{L}_2 = \text{pamidronate}$, Scheme 2) showing that the contribution of these bonds for bone binding is similar [20]. However, the tetrahydrofuranlyl side chain does not contain any group that will contribute to the bone binding, thus it is expected that H_2L^{2-} will be a weaker bone binder than $\text{H}_2\text{L}_1^{2-}$, $\text{H}_2\text{L}_2^{2-}$, and $\text{H}_2\text{L}_3^{2-}$ (Scheme 2).

4. Conclusions

The tetrahydrofuranlyl-2,2-bisphosphonic acid has been prepared with an efficient method without the use of solvent, producing pure product in high yield over 60%. The crystal structure of the complex showed that the disodium salt of bisphosphonate crystallizes forming two-dimensional sheets stacked parallel one over the other.

The results of this study show that the crystallographic characterization of a widely used class of drug molecules, the bisphosphonate salts, provide important information on their biological activity (bone binding, FPPS inhibition), and can be used for the design of new more active molecules. The bisphosphonates binding strength with bone can be calculated by summarizing the interactions of the phosphonate groups, the side chain groups, the hydroxyl group, and the hydrophobic group of the ligand with the bone surface. The crystallographic data of the $\text{Na}^+/\text{Ca}^{2+}$ salts of bisphosphonate show that the interaction of the $-\text{OH}$ group with the metal ions is weak which is in agreement with the results from a recent study [23] on the interaction of the bisphosphonates with bone surface. Furthermore a comparison of $\text{Na}^+/\text{Ca}^{2+}$ bisphosphonate structures shows that the strength of the $\text{Na}-\text{O}(\text{hydroxyl}/\text{furanlyl})$ bond reduces with the decrease of the total bisphosphonate anion charge.

Acknowledgment

The authors thank the Research Promotion Foundation of Cyprus for the financial support of this work with the proposal YTEIA/BIOΣ/0308(BIE)/03.

References

- [1] W. M. Abdou and A. A. Shaddy, "The development of bisphosphonates for therapeutic uses, and bisphosphonate structure-activity consideration," *Arkivoc*, vol. 2009, no. 9, pp. 143–182, 2009.
- [2] H. Fleisch, "Bisphosphonates: mechanisms of action," *Endocrine Reviews*, vol. 19, no. 1, pp. 80–100, 1998.
- [3] J. J. Body, R. Bartl, P. Burckhardt, et al., "Current use of bisphosphonates in oncology," *Journal of Clinical Oncology*, vol. 16, no. 12, pp. 3890–3899, 1998.
- [4] R. G. G. Russell and M. J. Rogers, "Bisphosphonates: from the laboratory to the clinic and back again," *Bone*, vol. 25, no. 1, pp. 97–106, 1999.
- [5] H. Fleisch, "Bisphosphonates in osteoporosis," *European Spine Journal*, vol. 12, supplement 2, pp. S142–S146, 2003.
- [6] R. G. G. Russell, "Determinants of structure-function relationships among bisphosphonates," *Bone*, vol. 40, no. 5, supplement 2, pp. S21–S25, 2007.
- [7] Y. Zhang, R. Cao, F. Yin, et al., "Lipophilic bisphosphonates as dual farnesyl/geranylgeranyl diphosphate synthase inhibitors: an X-ray and NMR investigation," *Journal of the American Chemical Society*, vol. 131, no. 14, pp. 5153–5162, 2009.
- [8] G. H. Nancollas, R. Tang, R. J. Phipps, et al., "Novel insights into actions of bisphosphonates on bone: differences in interactions with hydroxyapatite," *Bone*, vol. 38, no. 5, pp. 617–627, 2006.
- [9] G. M. Sheldrick, "SHELX-86: program for the solution of crystal structures," 1990.
- [10] G. M. Sheldrick, "SHELXL-97, program for crystal structure refinement," 1997.
- [11] L. J. Farrugia, "ORTEP-3 for windows—a version of ORTEP-III with a graphical user interface (GUI)," *Journal of Applied Crystallography*, vol. 30, no. 5, p. 565, 1997.
- [12] L. J. Farrugia, "WinGX suite for small-molecule single-crystal crystallography," *Journal of Applied Crystallography*, vol. 32, no. 4, pp. 837–838, 1999.
- [13] G. R. Kieczkowski, R. B. Jobson, D. G. Melillo, D. F. Reinhold, V. J. Grenda, and I. Shinkai, "Preparation of (4-amino-1-hydroxybutylidene)bisphosphonic acid sodium salt, MK-217 (alendronate sodium). An improved procedure for the preparation of 1-hydroxy-1,1-bisphosphonic acids," *Journal of Organic Chemistry*, vol. 60, no. 25, pp. 8310–8312, 1995.
- [14] I. Cukrowski, L. Popović, W. Barnard, S. O. Paul, P. H. van Rooyen, and D. C. Liles, "Modeling and spectroscopic studies of bisphosphonate-bone interactions. The Raman, NMR and crystallographic investigations of Ca-HEDP complexes," *Bone*, vol. 41, no. 4, pp. 668–678, 2007.
- [15] G. Olive, D. D. Ellis, D. Siri, et al., "Zwitterionic pyrrolidine-2,2-diylbis(phosphonic acid) at 100, 150 and 293 K," *Acta Crystallographica, Section C*, vol. 56, no. 6, pp. 720–722, 2000.
- [16] V. A. Uchtman, "Structural investigations of calcium binding molecules. II. The crystal and molecular structures of calcium dihydrogen ethane-1-hydroxy-1,1-diphosphonate dihydrate, $\text{CaC}(\text{CH}_3)(\text{OH})(\text{PO}_3\text{H})_2 \cdot 2\text{H}_2\text{O}$; implications for polynuclear complex formation," *The Journal of Physical Chemistry*, vol. 76, no. 9, pp. 1304–1310, 1972.
- [17] Z. Wu, Z. Liu, P. Tian, et al., "Two Cr^{III} containing metal-1-hydroxyethylidenediphosphonate compounds: synthesis, structure, and morphology," *Crystal Research and Technology*, vol. 41, no. 10, pp. 1049–1054, 2006.

- [18] L. M. Shkol'nikova, A. A. Masyuk, and E. G. Afonin, "Structural chemistry of 1-hydroxyethylidenediphosphonic acid complexes," *Koordinatsionnaya Khimiya*, vol. 16, p. 902, 1990 (Russian).
- [19] D. Fernández, D. Vega, and A. Goeta, "The calcium-binding properties of pamidronate, a bone-resorption inhibitor," *Acta Crystallographica Section C*, vol. 58, no. 10, pp. m494–m497, 2002.
- [20] D. Vega, D. Fernández, and J. A. Ellena, "Disodium pamidronate," *Acta Crystallographica Section C*, vol. 58, no. 2, pp. m77–m80, 2002.
- [21] K. Stahl, S. P. Treppendahl, H. Preikschat, and E. Fischer, "Sodium 3-ammonio-1-hydroxypropylidene-1,1-bisphosphonate- monohydrate," *Acta Crystallographica Section E*, vol. 61, no. 1, pp. m132–m134, 2005.
- [22] D. Fernández, D. Vega, and A. Goeta, "Alendronate zwitterions bind to calcium cations arranged in columns," *Acta Crystallographica Section C*, vol. 59, no. 12, pp. m543–m545, 2003.
- [23] S. Mukherjee, C. Huang, F. Guerra, K. Wang, and E. Oldfield, "Thermodynamics of bisphosphonates binding to human bone: a two-site model," *Journal of the American Chemical Society*, vol. 131, no. 24, pp. 8374–8375, 2009.

Research Article

Organotin Compound Derived from 3-Hydroxy-2-formylpyridine Semicarbazone: Synthesis, Crystal Structure, and Antiproliferative Activity

Joanna Wiecek,¹ Dimitra Kovala-Demertzi,¹ Zbigniew Ciunik,² Joanna Wietrzyk,³ Maria Zervou,⁴ and Mavroudis A. Demertzis¹

¹Inorganic and Analytical Chemistry, Department of Chemistry, University of Ioannina, 45110 Ioannina, Greece

²Faculty of Chemistry, University of Wrocław, 14 F. Joliot-Curie St., 50-383 Wrocław, Poland

³Institute of Immunology and Experimental Therapy, Polish Academy of Sciences, 12 R Weigl St, 53-114 Wrocław, Poland

⁴Laboratory of Molecular Analysis, Institute of Organic and Pharmaceutical Chemistry, National Hellenic Research Foundation, 48, Vas. Constantinou Ave, 11635 Athens, Greece

Correspondence should be addressed to Dimitra Kovala-Demertzi, dkovala@cc.uoi.gr

Received 13 January 2010; Accepted 18 February 2010

Academic Editor: Evy Manessi-Zoupa

Copyright © 2010 Joanna Wiecek et al. This is an open access article distributed under the Creative Commons Attribution License, which permits unrestricted use, distribution, and reproduction in any medium, provided the original work is properly cited.

The novel diphenyltin(IV) compound [Ph₂(HyFoSc)Sn] (**2**), where H₂HyFoSc (**1**) is 3-hydroxy-2-formylpyridine semicarbazone, was prepared and characterized by vibrational and NMR (¹H, ¹³C) spectroscopy. The structure of [Ph₂(HyFoSc)Sn] was confirmed by single-crystal X-ray crystallography. The doubly deprotonated ligand is coordinated to the tin atom through the enolic-oxygen, the azomethine-nitrogen, and phenolic-oxygen, and so acts as an anionic tridentate ligand with the ONO donors. Two carbon atoms complete the fivefold coordination at the tin(IV) center. Intermolecular hydrogen bonding, C–H → π, and π → π interactions combine to stabilize the crystal structure. Compounds **1** and **2** have been evaluated for antiproliferative activity *in vitro* against the cells of three human tumor cell lines: MCF-7 (human breast cancer cell line), T24 (bladder cancer cell line), A549 (nonsmall cell lung carcinoma), and a mouse fibroblast L-929 cancer cell line.

1. Introduction

Organotin compounds are of interest in view of their considerable structural diversity [1]. Increasing interest in organotin(IV) chemistry has arisen in the last few decades and is attributed to their significantly important biological properties. Several di- and tri-organotin species have shown potential as antineoplastic and antituberculosis agents [2–5]. The binding ability of organotin compounds towards DNA depends on the coordination number and nature of groups bonded to the central tin atom. The phosphate group of DNA-sugar backbones usually acts as an anchoring site and DNA base-nitrogen binding is extremely effective and this often results in the stabilization of the octahedrally coordinated tin center. Recent studies have showed that low doses of organotins can exhibit antitumoral activity and have suggested a mode of action via a gene-mediated pathway in

the cancer cells, opening a new research subarea on organotin compounds [6].

Thio- and semicarbazones (TSC) possess a wide range of bioactivities, and their chemistry and pharmacological applications have been extensively investigated. The more significant bioactivities of a variety of semicarbazones (antiprotozoa, anticonvulsant) and thiosemicarbazones (antibacterial, antifungal, antitumoral, antiviral) and their metal complexes have been reviewed together with proposed mechanisms of action and structure-activity relationships [7, 8]. Casas et al. [9] have surveyed structural aspects of main group metal complexes of semicarbazones and thiosemicarbazones. The survey shows that heterocyclic and nonheterocyclic TSC's are very versatile coordination agents with these elements [9].

Following our interest in the chemistry and pharmacological properties of thiosemicarbazones [10–17] and towards organotins [18–21], herein, the preparation and

spectroscopic characterization of a novel semicarbazone and a novel diphenyl organotin compound derived from the reaction of SnPh_2O with 3-hydroxy-2-formylpyridine semicarbazone H_2HyFoSc (**1**) are described with the final goal of developing new biologically active pharmaceuticals. The results of the cytotoxic activity of **1**, SnPh_2O , and of the organotin compound (**2**) against the cells of three human cancer cell lines: MCF-7 (human breast cancer cell line), T24 (bladder cancer cell line), A549 (non-small cell lung carcinoma), and a mouse fibroblast L-929 cancer cell line are also reported. To our knowledge, this is the first report of synthesis of **1** and **2**.

2. Experimental

2.1. General and Instrumental. The reagents (Aldrich, Merck, Sigma) were used as supplied while the solvents were purified according to standard procedures. Melting points were determined in open capillaries and are uncorrected. Infrared and far-infrared spectra were recorded on a Perkin-Elmer Spectrum GX FT IR System spectrophotometer using KBr pellets ($4000\text{--}400\text{ cm}^{-1}$) and nujol mulls dispersed between polyethylene disks ($400\text{--}40\text{ cm}^{-1}$). The ^1H , ^{13}C NMR spectra were recorded on a Bruker AC-300 MHz and on a Varian 600 MHz spectrometer. The spectra were acquired at room temperature (298 K). The chemical shifts are reported in ppm with respect to the references (external tetramethylsilane (TMS) for ^1H and ^{13}C NMR). Elemental analyses were carried out by the microanalytical service of the University of Ioannina, Greece.

2.2. Synthesis

2.2.1. 3-Hydroxypyridine-2-carbaldehyde Semicarbazone (1). Commercially available 3-hydroxy-(2-hydroxymethyl) pyridine hydrochloride was oxidized with MnO_2 , prepared by heating MnCO_3 for 12 h at 300°C , according to [22, 23] to afford 3-hydroxypyridine-2-carbaldehyde as a yellow powder, yield 62%, and m.p. 77°C . The aldehyde (2 mmol) in EtOH (6 mL) was then reacted with a solution of semicarbazide hydrochloride (2 mmol) in H_2O (3 mL) at 80°C for 2 h. Then, the mixture was kept in a refrigerator overnight. The resulting yellow powder was filtered off and recrystallized from EtOH. The powder was washed with cold EtOH and dried in vacuo over silica gel at $40\text{--}50^\circ\text{C}$ for 4 h to afford **1** as a yellow powder, yield 75%, and m.p. 230°C . UV-Vis for **1** (DMF) λ/nm ($\log\epsilon$): 383 (2.78); 330 sh (3.48); 320 (3.50). IR cm^{-1} : 3275 m, 3208 m ($\nu(\text{OH})$); 3147 s, 3080 m, 2920 ($\nu(\text{NH}_2, \text{NH})$); 1664 ($\nu(\text{C}=\text{O})$), 1583 s ($\nu(\text{C}=\text{N})$); 1322 ($\nu(\text{C}-\text{O})$); 916 s ($\nu(\text{NN})$). ^1H -NMR (DMSO- d_6): δ 12.36 (br, NH), 11.23 (s, C3-OH), 8.05 (d, H4), 7.80 (t, H5), 8.35 (d, H6), 8.14 (s, H7), 6.75 (br, NH_2); ^{13}C -NMR: δ 131.4 (C2), 154.0 (C3), 126.4 (C4), 126.4 (C5), 133.70 (C6), 134.7 (C7), 155.9 (C8=O). Anal. calc. for $\text{C}_7\text{H}_8\text{N}_4\text{O}_2$ (180.0 g mol^{-1}): C 46.7, H 4.5, N 31.10; found: C 46.6, H 4.3, N 31.3%.

2.2.2. $[\text{Ph}_2(\text{HyFoSc})\text{Sn}]$ (2**).** Diphenyltin(IV) oxide (0.578 g, 2.0 mmol) and 3-hydroxypyridine-2-carbaldehyde semicarbazone (0.360 g, 2.0 mmol) in benzene (100 mL) were

refluxed for 24 h under azeotropic removal of H_2O (Dean-Stark trap). The resulting clear solution was concentrated *in vacuo* to a small volume. The oily product was chilled and triturated with distilled diethyl ether (Et_2O) to give a yellow solid. The yellow powder was recrystallized from distilled ether and was dried *in vacuo* over silica gel. Yield 24%; m.p. 209°C . UV-Vis for **2** (DMF) λ/nm ($\log\epsilon$): 388br (3.87); 331 sh (4.15); 320 (4.18). IR cm^{-1} : 3144 s, 3065 m, ($\nu(\text{NH}_2)$); 1664 ($\nu(\text{C}=\text{O})$), 1542 s ($\nu(\text{C}=\text{N})$); 1283 ($\nu(\text{C}-\text{O})$); 997 s ($\nu(\text{NN})$) 339 sh, 321 ms ($\nu(\text{SnC})$); 446 sh ($\nu(\text{SnN}_{\text{C}=\text{N}}$); 284 mw ($\nu(\text{SnO}_{\text{C}=\text{O}}$); 248 mw ($\nu(\text{SnO})$). ^1H -NMR (DMSO- d_6): δ 7.30 (d, H4), 7.36 (t, H5), 8.15 (d, H6), 8.20 (s, H7), 6.74 (br, NH_2), 7.95 (s, Ho), 7.45, 7.57 (m, Hm,p). ^{13}C -NMR: δ 137.5 (C2), 153.2 (C3), 128.0 (C4), 128.2 (C5), 138.0 (C6), 139.5 (C7), 155.8 (C8=O), 134.7 (Co), 127.7 (Cm), 127.2 (Cp). Anal. calc. for $\text{C}_{19}\text{H}_{16}\text{N}_4\text{O}_2\text{Sn}$ (451.0 g mol^{-1}) C, 50.6; H, 3.6; N, 12.4; Found: C, 50.4; H, 3.7; N, 12.3%. Crystals suitable for X-ray analysis were obtained by slow evaporation of a freshly distilled diethyl ether solution of **2**.

2.3. X-Ray Crystallography. Crystal data are given in Table 1, together with refinement details. All measurements were performed on a Kuma KM4CCD kappa-axis diffractometer with graphite-monochromated $\text{MoK}\alpha$ radiation ($\lambda = 0.71073\text{ \AA}$). The data were corrected for Lorentz and polarization effects. An analytical absorption correction was applied to the data using a multifaceted crystal model [24]. Data reduction and analysis were carried out with the Kuma Diffraction (Wroclaw) programs. The structure was solved by direct-methods and refined by a full-matrix least-squares method on all F^2 data using the SHELXL97 [25]. Nonhydrogen atoms were refined with anisotropic displacement parameters; all hydrogen atoms were located from different Fourier maps. The C-bound H atoms were refined with the riding model approximation, while the N-bound H-atoms were freely refined isotropically. Molecular graphics were performed with PLATON 2004 [26].

Crystallographic data for **2** have been deposited with the Cambridge Crystallographic Data Centre, CCDC, 634269 for compound **3**. Copies of this information may be obtained free of charge from The Director, CCDC, 12, Union Road, Cambridge CB2 1EZ [FAX +44(1223)336-033] or e-mail deposit@ccdc.cam.ac.uk or <http://www.ccdc.cam.ac.uk>.

2.4. Antiproliferative Assay In Vitro

Compounds. Test solutions of the tested compounds (1 mg/mL) were prepared by dissolving the substance in $100\text{ }\mu\text{L}$ of DMSO completed with $900\text{ }\mu\text{L}$ of tissue culture medium. Afterwards, the tested compounds were diluted in culture medium to reach the final concentrations of 100, 50, 10, 1, and $0.1\text{ ng}/\mu\text{L}$. The solvent (DMSO) in the highest concentration used in the test did not reveal any cytotoxic activity.

Cells. The cell lines are maintained in the Cell Culture Collection of the University of Ioannina. Twenty-four hours before addition of the tested agents, the cells were plated in 96-well plates at a density of 10^4 cells per well. The

TABLE 1: X-ray crystal data and structure refinement for **2**.

Empirical formula	C ₁₉ H ₁₆ N ₄ O ₂ Sn
Formula weight	451.05
Temperature (K)	100(2)
Crystal system	Monoclinic
Space group	P2 ₁ /n
Crystal size (mm)	0.17 × 0.20 × 0.23
<i>a</i> (Å)	10.5498(6)
<i>b</i> (Å)	12.5794(7)
<i>c</i> (Å)	13.9477(8)
β (°)	103.594(5)
Volume (Å ³)	1799.2(2)
<i>Z</i>	4
<i>D</i> _{calcd} (g cm ⁻³)	1.665
Absorption coefficient (mm ⁻¹)	1.441
θ range for data collection (°)	3.0–36.6
Reflections collected	29597
Independent reflections (<i>R</i> _{int})	8324 (0.056)
Data/parameters	8324/243
Goodness-of-Fit (<i>F</i> ²)	0.857
Final <i>R</i> indices (<i>I</i> > 2 σ (<i>I</i>))	0.037
<i>wR</i>	0.062
Maximum and minimum residuals (e ⁻ Å ⁻³)	1.03/–0.74

MCF-7 cells were cultured in the D-MEM (Modified Eagle's Medium) medium supplemented with 1% antibiotic and 10% fetal calf serum. L-929 cells were grown in Hepes-buffered RPMI 1640 medium supplemented with 10% fetal calf serum, penicillin (50 U/mL), and streptomycin (50 mg/mL). A-549 cells were grown in F-12K Ham's medium supplemented with 1% glutamine, 1% antibiotic/antimycotic, 2% NaHCO₃, and 10% fetal calf serum. The cell cultures were maintained at 37°C in a humid atmosphere saturated with 5% CO₂. Cell numbers were counted by the Trypan blue dye exclusion method. MCF-7, L-929, and A-549 cells were determined by the sulforhodamine B assay [27], while T24 cells by the MTT assay [28]. The *in vitro* tests were performed as described previously [29].

3. Results and Discussion

3.1. Synthesis. Compound **1** was synthesized by means of the Heinert–Martell reaction (Scheme 1) [22]. The corresponding diorganotin compound **2** was prepared by reacting diorganotin(IV) oxide with the semicarbazone in benzene solution in a 1 : 1 molar ratio.

3.2. Crystal Structure of 2. A perspective view of **2**, together with the atom-labelling scheme, is given in Figure 1 and selected bond lengths and angles are given in Table 2.

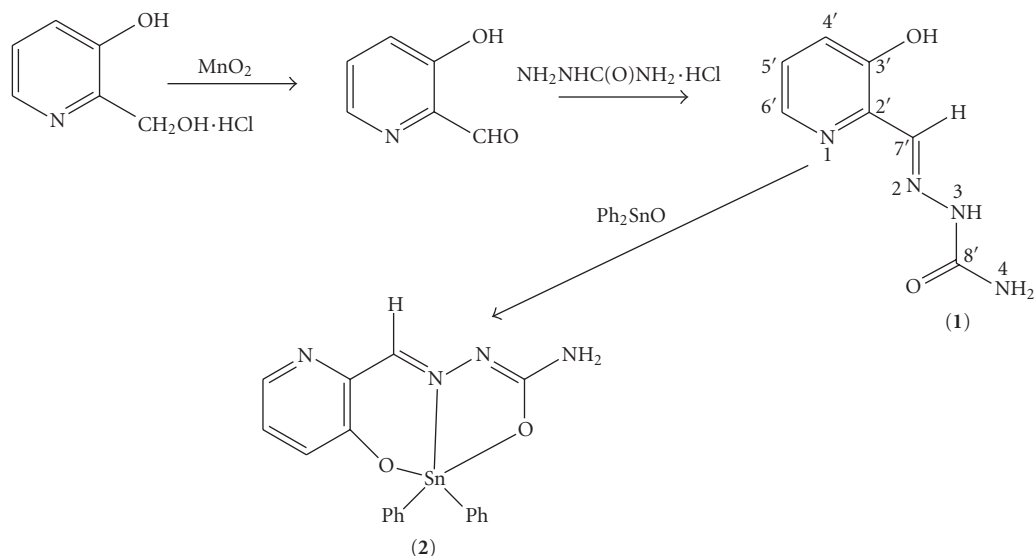
The doubly deprotonated ligand is coordinated to the tin atom through the enolic-oxygen, azomethine-nitrogen, and phenolic-oxygen atoms. Two carbon atoms complete the fivefold coordination at the diorganotin(IV)

fragment. Analysis of the shape determining angles using the approach of Addison et al. [30] yields $\tau = 0.54$ ($\tau = 0.0$ and 1.0 for *SPY* and *TBPY* geometries, resp.). The metal coordination geometry is therefore described as distorted trigonal bipyramidal with the O(2) and O(1) atoms occupying the apical positions around the tin atom.

The dianionic, tridentate ONO ligand has a ZEZ configuration, Figure 1. The coordinated part of the ligand is made of three rings, two chelates Sn(1)O(2)N(1)N(2)C(4) (I) and Sn(1)O(1)N(1)C(1)C(2)C(3) (II) and one heterocyclic ring (III). The dihedral angles between the planes of the rings I and II, I and III are 7.17(7) and 10.32(9), respectively, indicating that the ligand as a whole deviates from planarity. The C(3)–N(1) bond length is 1.298(3) Å and is close to the distance of a double bond (1.28 Å). The deprotonation of the N(2)H group produces a negative charge, which is delocalized in the C(3)–N(1)–N(2)–C(4) moiety. The distortion from the ideal trigonal-bipyramidal configuration is shown by the O(1)–Sn(1)–O(2) angle of 156.78(6)°, which deviates from the ideal value of 180°, due in part to the ligand constraint. All the metal-donor bond distances, Table 2, are similar to other organotin complexes presented in the literature [18–21].

The polar hydrogen atoms on N(3) participate in two intermolecular hydrogen bonds. The monomers of **2** are connected into dimers by a pair of cooperative hydrogen bonds [see Table 3 for geometric parameters describing these interactions]. Further, adjacent dimers are connected by C–H···N contacts, as illustrated in Figure 2. The presence of additional C–H → π and π → π contacts further stabilizes the crystal structure.

3.3. Spectroscopic Studies. In the IR spectrum of H₂HyFoSc (**1**), the strong bands at 3147 and 3088 cm⁻¹ are assigned to the asymmetric and symmetric modes of terminal NH₂, respectively. The ν (NH) band appears at 2920 cm⁻¹. The strong broad band at ca. 2650 cm⁻¹ is assigned to the ν (NH···O) and ν (OH···O) mode due to strong intra- or intermolecular hydrogen bonding. The absence of the ν (NH) stretching motion at **2** is indicative of deprotonation of the amide proton. The strong broad band at ca. 2650 cm⁻¹ at **2** is probably due to the ν (NH···N) intermolecular hydrogen bonds as confirmed by X-ray crystallography. The coordination of the azomethine-N atom to the tin center was suggested in the IR spectrum by a shift of the ν (C=N) band to a lower frequency, along with the occurrence of a ν (N–N) band to higher frequency [12, 13, 16]. An IR band at 1322 cm⁻¹ for **1** was assigned to ν (C–O). This band was found to be shifted to 1283–1289 cm⁻¹, in the spectrum of **2**, which indicates the coordination of this O atom. The low energy of the ν (C=O) vibration in the spectra of **1**, that is, 1664 cm⁻¹, is indicative that the carbonyl O-atom is involved in hydrogen bonding. The replacement of the hydrogen by the metal atom does not shift this band to lower frequency. Coordination of the imine nitrogen is also consistent with the presence of a band at 446 cm⁻¹, assignable to ν (Sn–N). Bands at 284 and 248 cm⁻¹ are assigned to ν (Sn–O_{c=o}) and ν (Sn–O_{c-o}), respectively [18–21].



SCHEME 1: The reaction scheme for synthesis of 1 and 2.

TABLE 2: Selected bond lengths (Å) and angles (°) for complex 2.

Sn(1)–O(1)	2.073 (2)	O(1)–Sn(1)–O(2)	156.78(6)
Sn(1)–O(2)	2.152(2)	O(1)–Sn(1)–N(1)	84.71(6)
Sn(1)–N(1)	2.166(2)	O(1)–Sn(1)–C(8)	98.51(7)
Sn(1)–C(8)	2.115(2)	O(1)–Sn(1)–C(14)	95.64(7)
Sn(1)–C(14)	2.121(2)	O(2)–Sn(1)–N(1)	73.14(6)
O(1)–C(1)	1.326(2)	O(2)–Sn(1)–C(8)	95.84(7)
O(2)–C(4)	1.297(2)	O(2)–Sn(1)–C(14)	91.13(7)
N(1)–N(2)	1.388(2)	N(1)–Sn(1)–C(8)	110.80(7)
N(1)–C(3)	1.298(3)	N(1)–Sn(1)–C(14)	123.88(7)
N(2)–C(4)	1.329(3)	C(8)–Sn(1)–C(14)	124.44(8)
N(3)–C(4)	1.338(3)	Sn(1)–O(1)–C(1)	132.5(2)
N(4)–C(2)	1.361(3)	Sn(1)–O(2)–C4	113.6(2)
N(4)–C(7)	1.330(3)	Sn(1)–N(1)–N(2)	116.2(2)

TABLE 3: Geometric parameters for hydrogen bonds and for C–H \cdots π and $\pi\cdots\pi$ interactions in 2.

D	H	A	H \cdots A	D \cdots A
N(3)–H(3A) \cdots N(4) ⁽ⁱ⁾		2.29(2)	3.070(3)	175(3)
N(3)–H(3B) \cdots O(2) ⁽ⁱⁱ⁾		2.07(3)	2.925(2)	183(4)
C(3)–H(3) \cdots N(2) ⁽ⁱ⁾		2.34(2)	3.280(3)	170(3)
C(19)–H(19) \cdots O(2)		2.51(2)	3.087(3)	119
C–H(I) \rightarrow Cg(J) ^(a)		H–Cg	C–Cg	\angle C–H–Cg
C(7)–H(7) \rightarrow Cg(5) ⁽ⁱⁱⁱ⁾	2.76	3.619(2)	151	
C(12)–H(12) \rightarrow Cg(5) ^(iv)	2.86	3.722(3)	152	
Cg(I) \rightarrow Cg(J) ^(a)	Cg–Cg ^(b)	β ^(c)	CgI–Perp ^(d)	CgJ–Perp ^(e)
Cg(3) \rightarrow Cg(4) ^(v)	3.824(2)	10.55	3.7122(8)	3.759(2)
Cg(4) \rightarrow Cg(3) ^(iv)	3.823(2)	10.55	3.759(2)	3.7121(8)

^(a) Where Cg(3), Cg(4), and Cg(5) are referred to the centroids N(4)C(1)C(2)C(5)C(6)C(7), C(8)–C(14), and C(14)–C(19); ^(b) Cg–Cg is the distance between ring centroids; symmetry transformations, (i) $2 - x, 1 - y, -z$; (ii) $1 - x, 1 - y, -z$; (iii) $1 + x, y, z$; (iv) $-1/2 + x, 1/2 - y, -1/2 + z$; (v) $1/2 + x, 1/2 - y, 1/2 + z$; ^(c) Where β is the angle Cg(I) \rightarrow Cg(J) or Cg(i) \rightarrow Me vector and normal to plane I ($^\circ$); ^(d) CgI–Perp is the perpendicular distance of Cg(I) on ring J; ^(e) CgJ–Perp is the perpendicular distance of Cg(J) on ring I.

TABLE 4: The antiproliferative activity in vitro of $H_2HyFoSc$ and its organotin complex **2** (expressed as ID_{50} (μM)) against MCF-7, T-24, A-549, and L-929 cancer cell lines.

Compounds	L-929	A-549	T-24	MCF-7
[$H_2HyFoSc$] (1)	n.a	175.0	n.a.	164.0
[$Ph_2(HyFoSc)Sn$] (2)	1.19	0.086	n.a.	8.65
[Ph_2SnO]	10.73	47.10	n.a	3.46
Cisplatin	0.69	1.53	41.7	8.00

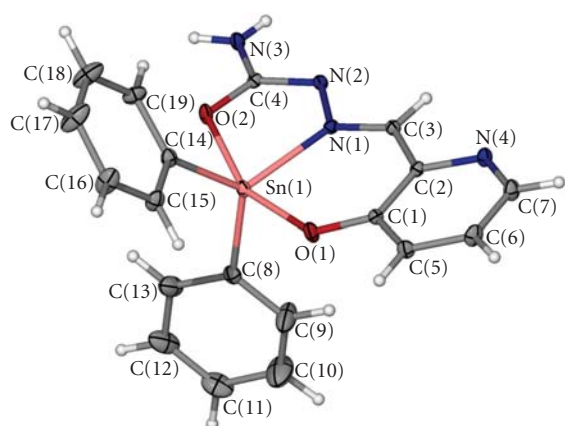


FIGURE 1: Molecular structure of the diorganotin complex **2**. Thermal ellipsoids are drawn at the 40% probability level.

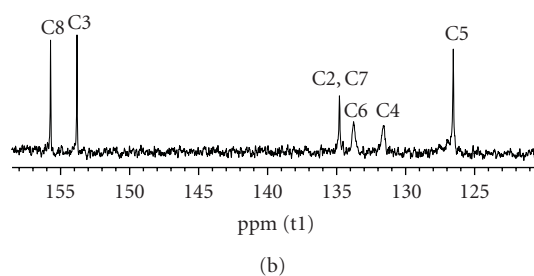
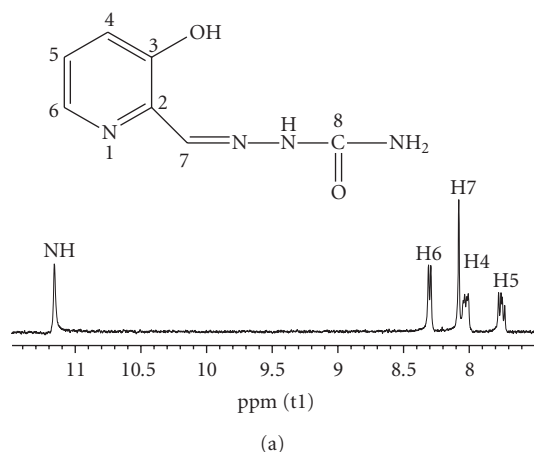


FIGURE 3: 1H NMR (a) and ^{13}C NMR (b) spectrum of the ligand (**1**).

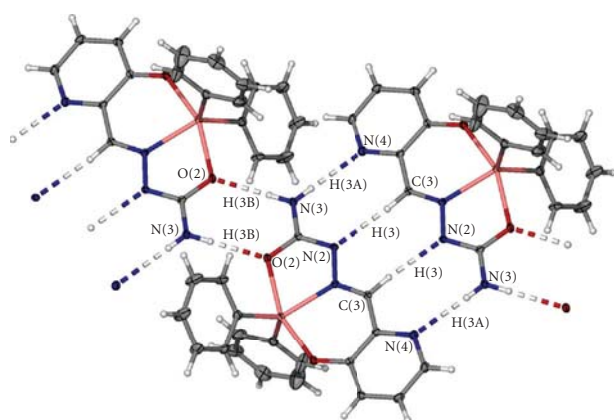


FIGURE 2: Arrangement of the intermolecular hydrogen bonds in **2**. Thermal ellipsoids are drawn at the 40% probability level.

1H - and ^{13}C -NMR Spectra. In the 1H -NMR spectrum of **1**, the N(3)-H resonance at δ 12.30 and C-OH at δ 11.23 ppm indicates that these H atoms are involved in hydrogen bonding, Figure 3. In the 1H -NMR spectrum of **2**, the formyl H-atom H-C(7) was shifted downfield upon coordination, which indicates variations in the electron density at position 7. Deshielding of carbons C4, C5, and C7 is observed in complexes, which is related to the electrophilicity of the tin atom. A σ -charge donation from the C-O and N donors to the tin center removes electron density from the ligand and produces this deshielding which will attenuate at positions remote from the tin center, Figure 4.

3.4. Pharmacology. Antiproliferative Activity In Vitro. Pd(II) and Pt(II) complexes of 2-carbaldehyde thiosemicarbazone, $HFoTsc$, were found to be active in vivo against leukemia P388 cells and Pt(II) complexes of N4-ethyl 2-formyl and 2-acetylpyridine thiosemicarbazones showed cytotoxicity and were found to be able to overcome the cisplatin-resistance of A2780/Cp8 cells [10–16]. Also, Zn(II) complexes of 2-carbaldehyde thiosemicarbazone, $HFoTsc$, and 2-acetylpyridine thiosemicarbazone, $HAcTsc$, were found active against the MCF-7 (human breast cancer cell line), T24 (bladder cancer cell line), and a mouse L-929 (a fibroblast-like cell line cloned from strain L) [29]. Compounds **1** and **2** and the organotin oxide precursor of **2** were tested for their anti-proliferative activity in vitro against the cells of three human cancer cell lines: MCF-7 (human breast cancer cell line), T24 (bladder cancer cell line), A549 (non-small cell lung carcinoma), and a mouse fibroblast L-929 cell line [see Table 4 for a summary of the cytotoxicity data].

The IC_{50} values for $H_2HyFoSc$ (**1**) against the MCF-7 and A-549 cell lines are 164 and 175 μM , respectively, while

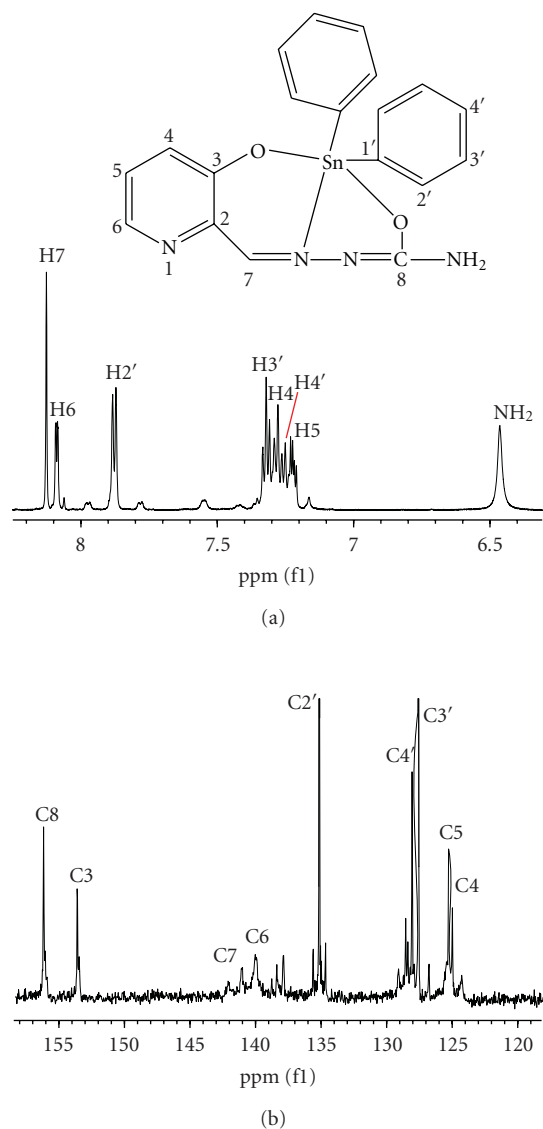


FIGURE 4: ^1H NMR (a) and ^{13}C NMR (b) spectrum of the complex (2).

against the L-929 and T-24 cell lines IC_{50} are $>555\ \mu\text{M}$. Thus, **1** is considered as nonactive against these tested cell lines. Compound **2** is also considered nonactive against T24 cell line. The IC_{50} values for **2** against the L-929 and MCF-7 cell lines are 1.19 and $8.65\ \mu\text{M}$, respectively. These values are in the same range as observed for cisplatin and Ph_2SnO , indicating that the observed cytotoxicity is probably due to the cytotoxicity of Ph_2SnO . Compound **2** may then be considered as a vehicle for activation of the Ph_2SnO as the cytotoxic agent. The IC_{50} value for **2** against A-549 is $0.086\ \mu\text{M}$ and therefore **2** is significantly more active compared to Ph_2SnO ($47.1\ \mu\text{M}$) and cisplatin ($1.53\ \mu\text{M}$), respectively. Compound **2** is thus 547.7 and 17.8 times more cytotoxic than the Ph_2SnO and cisplatin, respectively, against this cell line. Thus, **2** exhibits selectivity and is considered as an agent with potential antitumor activity against A-549 tumor cell line and can therefore be a candidate for further stages of screening in vitro and/or in vivo.

Acknowledgments

J. W. thanks I. K. Y. for a scholarship for her Ph.D. and the authors also thank the NMR Centrum of University of Ioannina. This paper is dedicated to Professor N. Hadjiliadis for his contribution to the advancement of Inorganic Chemistry.

References

- [1] V. Chandrasekhar, S. Nagendran, and V. Baskar, "Organotin assemblies containing Sn-O bonds," *Coordination Chemistry Reviews*, vol. 235, no. 1-2, pp. 1-52, 2002.
- [2] M. Gielen, "Organotin compounds and their therapeutic potential: a report from the Organometallic Chemistry Department of the Free University of Brussels," *Applied Organometallic Chemistry*, vol. 16, no. 9, pp. 481-494, 2002.
- [3] D. Kovala-Demertzi, "Recent advances on non-steroidal anti-inflammatory drugs, NSAIDs: organotin complexes of NSAIDs," *Journal of Organometallic Chemistry*, vol. 691, no. 8, pp. 1767-1774, 2006.
- [4] V. Dokorou, D. Kovala-Demertzi, J. P. Jasinski, A. Galani, and M. A. Demertzi, "Synthesis, spectroscopic studies, and crystal structures of phenylorganotin derivatives with [bis(2,6-dimethylphenyl)amino]benzoic acid: novel antituberculosis agents," *Helvetica Chimica Acta*, vol. 87, no. 8, pp. 1940-1950, 2004.
- [5] D. Kovala-Demertzi, V. N. Dokorou, J. P. Jasinski, et al., "Organotin flufenamates: synthesis, characterization and antiproliferative activity of organotin flufenamates," *Journal of Organometallic Chemistry*, vol. 690, no. 7, pp. 1800-1806, 2005.
- [6] S. Tabassum and C. Pettinari, "Chemical and biotechnological developments in organotin cancer chemotherapy," *Journal of Organometallic Chemistry*, vol. 691, no. 8, pp. 1761-1766, 2006.
- [7] H. Beraldo and D. Gambino, "The wide pharmacological versatility of semicarbazones, thiosemicarbazones and their metal complexes," *Mini-Reviews in Medicinal Chemistry*, vol. 4, no. 1, pp. 31-39, 2004.
- [8] A. G. Quiroga and C. N. Ranninger, "Contribution to the SAR field of metallated and coordination complexes: studies of the palladium and platinum derivatives with selected thiosemicarbazones as antitumoral drugs," *Coordination Chemistry Reviews*, vol. 248, no. 1-2, pp. 119-133, 2004.
- [9] J. S. Casas, M. S. García-Tasende, and J. Sordo, "Main group metal complexes of semicarbazones and thiosemicarbazones. A structural review," *Coordination Chemistry Reviews*, vol. 209, no. 1, pp. 197-261, 2000.
- [10] D. Kovala-Demertzi, A. Domopoulou, M. A. Demertzi, G. Valle, and A. Papageorgiou, "Palladium(II) complexes of 2-acetylpyridine N(4)-methyl, N(4)-ethyl and N(4)-phenyl-thiosemicarbazones. Crystal structure of chloro(2-acetylpyridine N(4)-methylthiosemicarbazonato) palladium(II). Synthesis, spectral studies, in vitro and in vivo antitumour activity," *Journal of Inorganic Biochemistry*, vol. 68, no. 2, pp. 147-155, 1997.
- [11] D. Kovala-Demertzi, P. N. Yadav, M. A. Demertzi, and M. Coluccia, "Synthesis, crystal structure, spectral properties and cytotoxic activity of platinum(II) complexes of 2-acetyl pyridine and pyridine-2-carbaldehyde N(4)-ethyl-thiosemicarbazones," *Journal of Inorganic Biochemistry*, vol. 78, no. 4, pp. 347-354, 2000.

- [12] Z. Iakovidou, A. Papageorgiou, M. A. Demertzis, et al., "Platinum(II) and palladium(II) complexes with 2-acetylpyridine thiosemicarbazone: cytogenetic and antineoplastic effects," *Anti-Cancer Drugs*, vol. 12, no. 1, pp. 65–70, 2001.
- [13] D. Kovala-Demertzi, M. A. Demertzis, J. R. Miller, C. Papadopoulou, C. Dodorou, and G. Filousis, "Platinum(II) complexes with 2-acetyl pyridine thiosemicarbazone: synthesis, crystal structure, spectral properties, antimicrobial and antitumour activity," *Journal of Inorganic Biochemistry*, vol. 86, no. 2-3, pp. 555–563, 2001.
- [14] D. Kovala-Demertzi, M. A. Demertzis, V. Varagi, et al., "Antineoplastic and cytogenetic effects of platinum(II) and palladium(II) complexes with pyridine-2-carboxyaldehyde-thiosemicarbazone," *Chemotherapy*, vol. 44, no. 6, pp. 421–426, 1998.
- [15] D. Kovala-Demertzi, M. A. Demertzis, J. R. Miller, C. S. Frampton, J. P. Jasinski, and D. X. West, "Structure of bis(2-acetylpyridine 3-hexamethyleiminythiosemicarbazonato) palladium(II), a potential antitumor complex," *Journal of Inorganic Biochemistry*, vol. 92, no. 2, pp. 137–140, 2002.
- [16] D. Kovala-Demertzi, M. A. Demertzis, E. Filiou, et al., "Platinum(II) and palladium(II) complexes with 2-acetyl pyridine 4N-ethyl thiosemicarbazone able to overcome the cis-platin resistance. Structure, antibacterial activity and DNA strand breakage," *BioMetals*, vol. 16, no. 3, pp. 411–418, 2003.
- [17] D. Kovala-Demertzi, T. Varadinova, P. Genova, P. Souza, and M. A. Demertzis, "Platinum(II) and palladium(II) complexes of pyridine-2-carbaldehyde thiosemicarbazone as alternative antihpes simplex virus agents," *Bioinorganic Chemistry and Applications*, vol. 2007, Article ID 56165, 6 pages, 2007.
- [18] M. A. Demertzis, S. K. Hadjikakou, D. Kovala-Demertzi, A. Koutsodimou, and M. Kubicki, "Organotin-drug interactions. Organotin adducts of tenoxicam: synthesis and characterization of the first organotin complex of tenoxicam," *Helvetica Chimica Acta*, vol. 83, no. 10, pp. 2787–2801, 2000.
- [19] A. Galani, M. A. Demertzis, M. Kubicki, and D. Kovala-Demertzi, "Organotin-drug interactions. Organotin adducts of lornoxicam, synthesis and characterisation of the first complexes of lornoxicam," *European Journal of Inorganic Chemistry*, no. 9, pp. 1761–1767, 2003.
- [20] V. Dokorou, Z. Ciunik, U. Russo, and D. Kovala-Demertzi, "Synthesis, crystal structures and spectroscopic studies of diorganotin derivatives with mefenamic acid," *Journal of Organometallic Chemistry*, vol. 630, no. 2, pp. 205–214, 2001.
- [21] V. Dokorou, M. A. Demertzis, J. P. Jasinski, and D. Kovala-Demertzi, "Synthesis and spectroscopic studies of diorganotin derivatives with 2-[(2,6-dimethylphenyl)amino]benzoic acid," *Journal of Organometallic Chemistry*, vol. 689, no. 2, pp. 317–325, 2004.
- [22] D. Heinert and A. E. Martell, "Pyridoxine and pyridoxal analogs. II. Infrared spectra and hydrogen bonding," *Journal of the American Chemical Society*, vol. 81, no. 15, pp. 3933–3943, 1959.
- [23] M. A. Demertzis, P. N. Yadav, and D. Kovala-Demertzi, "Palladium(II) complexes of the thiosemicarbazone and N-ethylthiosemicarbazone of 3-hydroxypyridine-2-carbaldehyde: synthesis, properties, and X-ray crystal structure," *Helvetica Chimica Acta*, vol. 89, no. 9, pp. 1959–1970, 2006.
- [24] CrysAlis RED, "Version 1.171.13 beta (release 14.11.2003 CrysAlis171 VC++)," Oxford Diffraction Ltd.
- [25] G. M. Sheldrick, *SHELXL 97 and SHELXS 97, Program for Crystal-Structure Refinement*, University of Göttingen, Göttingen, Germany, 1997.
- [26] A. L. Spek, *PLATON. A Program for the Automated Generation of a Variety of Geometrical Entities*, University of Utrecht, Utrecht, The Netherlands, 2004.
- [27] P. Skehan, R. Storeng, D. Scudiero, et al., "New colorimetric cytotoxicity assay for anticancer-drug screening," *Journal of the National Cancer Institute*, vol. 82, no. 13, pp. 1107–1112, 1990.
- [28] M. Ohno and T. Abe, "Rapid colorimetric assay for the quantification of leukemia inhibitory factor (LIF) and interleukin-6 (IL-6)," *Journal of Immunological Methods*, vol. 145, no. 1-2, pp. 199–203, 1991.
- [29] D. Kovala-Demertzi, P. N. Yadav, J. Wiecek, S. Skoulika, T. Varadinova, and M. A. Demertzis, "Zinc(II) complexes derived from pyridine-2-carbaldehyde thiosemicarbazone and (1E)-1-pyridin-2-ylethan-1-one thiosemicarbazone. Synthesis, crystal structures and antiproliferative activity of zinc(II) complexes," *Journal of Inorganic Biochemistry*, vol. 100, no. 9, pp. 1558–1567, 2006.
- [30] A. W. Addison, T. N. Rao, J. Reedijk, J. Van Rijn, and G. C. Verschoor, "Synthesis, structure, and spectroscopic properties of copper(II) compounds containing nitrogen-sulphur donor ligands; the crystal and molecular structure of aqua[1,7-bis(N-methylbenzimidazol-2'-yl)-2,6-dithiaheptane]copper(II) perchlorate," *Journal of the Chemical Society, Dalton Transactions*, no. 7, pp. 1349–1356, 1984.

Research Article

Synthesis and Characterization of a Linear $[\text{Mn}_3(\text{O}_2\text{CMe})_4(\text{py})_8]^{2+}$ Complex

Eleni E. Moushi,¹ Christos Kizas,¹ Vassilios Nastopoulos,² and Anastasios J. Tasiopoulos¹

¹ Department of Chemistry, University of Cyprus, 1678 Nicosia, Cyprus

² Department of Chemistry, University of Patras, 26500 Patras, Greece

Correspondence should be addressed to Anastasios J. Tasiopoulos, atasio@ucy.ac.cy

Received 16 March 2010; Accepted 25 March 2010

Academic Editor: Spyros Perlepes

Copyright © 2010 Eleni E. Moushi et al. This is an open access article distributed under the Creative Commons Attribution License, which permits unrestricted use, distribution, and reproduction in any medium, provided the original work is properly cited.

Two new compounds that consist of the linear trinuclear manganese(II) cation $[\text{Mn}_3(\text{O}_2\text{CMe})_4(\text{py})_8]^{2+}$ cocrystallizing with different counteranions (I_3^- , [1]; ClO_4^- , [2]) are reported. Complex 1 was prepared from the reaction of $[\text{Mn}(\text{O}_2\text{CMe})_2] \cdot 4\text{H}_2\text{O}$ with I_2 in $\text{MeCO}_2\text{H}/\text{py}$, whereas complex 2 was isolated from the reaction of $[\text{Mn}_3\text{O}(\text{O}_2\text{CMe})_6(\text{py})_3] \cdot \text{py}$ with $[\text{Mn}(\text{ClO}_4)_2] \cdot 6\text{H}_2\text{O}$ in MeCN/py . The crystal structures of both compounds were determined by single crystal X-ray crystallography. Magnetic susceptibility studies that were performed in microcrystalline powder of 1 in the 2–300 K range revealed the presence of antiferromagnetic exchange interactions that resulted in an $S = 5/2$ ground spin state.

1. Introduction

Oligonuclear Mn carboxylate clusters have attracted significant interest since they have been located in the active site of metalloenzymes [1] and also often have interesting and sometimes novel magnetic properties [2]. Undoubtedly, the most well-known oligonuclear cluster that appears in biological systems is the tetranuclear Mn complex that is present in the active site of photosystem II and is responsible for the light driven oxidation of water to molecular dioxygen [3–7]. Other Mn compounds observed in the active sites of metalloenzymes involve mononuclear (e.g., in Mn-superoxide dismutases) [8] and dinuclear (e.g., in Mn-catalases) complexes [8, 9]. In all those compounds, the ligation of the Mn ions is provided mainly by O- and N-donor atoms from the various aminoacid residues present in the metalloproteins. In order to prepare functional and structural models of the Mn compounds that are present in metalloenzymes, efforts have been centered on the synthesis and study of manganese carboxylate complexes with various chelating N-donor ligands, such as 2,2'-bipyridine (bpy) [10–13], 1,10-phenanthroline (phen) [10, 14–16], and 2-(2-pyridyl)benzimidazole [17]. As a result a

plethora of dinuclear, trinuclear and tetranuclear manganese compounds containing carboxylate groups or/and nitrogen-donor ligands have been prepared and characterized [4, 7, 10–30]. Such complexes are of significant interest not only as potential functional and structural models of the metal clusters present in Mn-containing metalloenzymes but also as precursors for the isolation of new model compounds. In particular, trinuclear Mn compounds have attracted significant attention since they appear as discrete metal clusters with various topologies including linear [10–26], triangular [27], V-shaped [28], and so forth, clusters and also as building blocks in multidimensional coordination polymers [29]. Linear trinuclear manganese (II) clusters with various molecular formulas such as $[\text{Mn}_3(\text{O}_2\text{CR})_6(\text{L})_2]$ [10–20] and $[\text{Mn}_3(\text{O}_2\text{CR})_4(\text{L}')_2]$ [21–23] have been prepared with several types of carboxylates, bidentate (L), and tridentate or tetradentate (L') chelates and also terminal ligands.

Herein, we report the synthesis, structural characterization, and magnetic properties of a new linear manganese(II) cation, $[\text{Mn}_3(\text{O}_2\text{CMe})_4(\text{py})_8]^{2+}$ which cocrystallizes with two different counteranions (I_3^- , [1] and ClO_4^- , [2]). The cation of 1 and 2 represents the first linear trinuclear Mn^{II} unit that contains only carboxylate and pyridine ligands and

TABLE 1: Crystallographic data for complexes **1** and **2**.

	1	2
Formula ^(a)	C ₄₈ H ₅₂ Mn ₃ N ₈ O ₈ I ₆	C ₄₈ H ₅₂ Mn ₃ N ₈ O ₁₆ Cl ₂
<i>M_w</i>	1795.20	1232.70
Crystal System	Monoclinic	Monoclinic
Space group	P2 ₁ /n	P2 ₁ /n
<i>a</i> /Å	15.2694(7)	21.7552(5)
<i>b</i> /Å	13.8883(4)	11.0081(2)
<i>c</i> /Å	15.2919(6)	23.4535(4)
β /°	109.041(5)	107.917(2)
<i>V</i> /Å ³	3065.5(2)	5344.3(2)
<i>Z</i>	2	4
T/K	100(2)	100(2)
λ ^(b) , Å	0.71073	0.71073
<i>D_c</i> , g/cm ⁻³	1.945	1.532
μ (Mo K α)/mm ⁻¹	3.682	0.874
Refl. collected/unique (<i>R</i> _{int})	23443/7336 (0.0455)	34188/9376 (0.0733)
Obs. refl. [<i>I</i> > 2 σ (<i>I</i>)]	5655	4469
<i>R</i> 1% ^(c)	0.0285	0.0382
<i>wR</i> 2 ^(d)	0.0640	0.0636
Goodness of fit on <i>F</i> ²	0.952	0.736
Largest diff. peak/hole/e ⁻ /Å ⁻³	1.172/-1.043	0.366/-0.298

^(a)Including counteranions. ^(b)Graphite monochromator. ^(c) $R1 = \sum |F_o| - |F_c| / \sum |F_o|$. ^(d) $wR2 = [\sum [w(F_o^2 - F_c^2)^2] / \sum [wF_o^2]^2]^{1/2}$, $w = 1/[\sigma^2(F_o^2) + (m \cdot p)^2 + n \cdot p]$, $p = [\max(F_o^2, 0) + 2F_c^2]/3$, and *m* and *n* are constants.

a rare example of a linear Mn^{II}₃ cluster that is stabilized with carboxylate and terminal ligands without containing any polydentate chelates [30].

2. Experimental

2.1. Materials. All manipulations were performed under aerobic conditions using materials (reagent grade) and solvents as received; water was distilled in-house. [Mn₃O(O₂CMe)₆(py)₃] \cdot py was prepared as described elsewhere [27]. *Warning: Although we encountered no problems, appropriate care should be taken in the use of the potentially explosives perchlorate anion.*

2.2. Syntheses of Compounds

2.2.1. [Mn₃(O₂CMe)₄(py)₈](I₃)₂ [1]. Solid I₂ (2.07 g, 8.16 mmol) was added to the yellowish solution of [Mn(O₂CMe)₂] \cdot 4H₂O (2.00 g, 8.16 mmol) in MeCOOH/py (10/20 mL). The resulting red-brown solution was left under magnetic stirring for ~45 minutes, filtered off and the filtrate was left undisturbed at room temperature. After a few weeks, dark brown crystals of **1** suitable for X-ray crystallography were formed. The crystals were collected by filtration, washed with MeCOOH/py (5/10 mL) and dried in vacuum. The yield was ~60% based on total Mn content. A sample for crystallography was maintained in contact with the mother liquor to prevent the loss of interstitial solvent. *Anal. Calc.* for C₄₈H₅₂Mn₃N₈O₈I₆ [1]: C, 32.11; H, 2.92; N, 6.24. Found: C 31.89; H 2.79; N 6.10%. IR data (KBr pellet,

cm⁻¹): $\tilde{\nu} = 3435$ (m), 3059 (m), 1599 (s), 1580 (s), 1564 (s, br), 1483 (m), 1441 (s, br), 1350 (m), 1215 (m), 1151 (m), 1067 (m), 1038 (m), 1005 (m), 752 (m), 700 (s), 683 (m), 650 (m), 629 (m).

2.2.2. [Mn₃(O₂CMe)₄(py)₈](ClO₄)₂ [2]

Method A. To a solution of [Mn₃O(O₂CMe)₆(py)₃] \cdot py (0.294 g, 0.345 mmol) in MeCN/py (10/2 mL) was added Mn(ClO₄)₂ \cdot 6H₂O (0.125 g, 0.345 mmol) and pdH₂ (0.10 mL, 0.105 g, 1.38 mmol) and the mixture was left under magnetic stirring for ~30 minutes. The resulting dark red-brown slurry was filtered off and the dark red-brown filtrate was left undisturbed at room temperature. After few weeks yellow crystals appeared, suitable for X-ray structural determination. The crystals were isolated by filtration, washed with a copious amount of MeCN/py, and dried in vacuum; yield, ~20% based on total ClO₄⁻ content. A sample for crystallography was maintained in contact with the mother liquor to prevent the loss of interstitial solvent. *Anal. Calc.* for C₄₈H₅₂Mn₃N₈O₁₆Cl₂ [2]: C, 46.77; H, 4.25; N, 9.09. Found: C 46.63; H 4.09; N 8.95%.

Method B. Method A was repeated in a mixture of MeCN/py (10/4 mL) without using H₂pd. The yield was ~9% based on on total ClO₄⁻ content.

2.3. X-Ray Crystallography. Data were collected on an Oxford-Diffraction Xcalibur diffractometer, equipped with a CCD area detector and a graphite monochromator utilizing

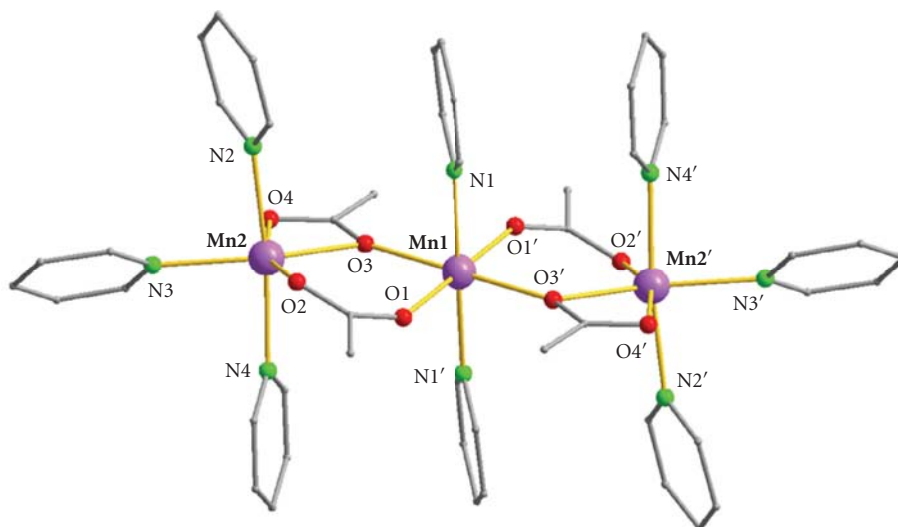


FIGURE 1: A partially labeled plot of the cation of **1**. Color code: Mn, purple; O, red; N, green; C, grey. H atoms are omitted for clarity.

Mo-K α radiation ($\lambda = 0.71073 \text{ \AA}$). Suitable crystals were attached to glass fibers using paratone-N oil and transferred to a goniostat where they were cooled for data collection. Unit cell dimensions were determined and refined by using 12271 ($3.07 \leq \theta \leq 30.27^\circ$) and 5746 ($3.06 \leq \theta \leq 30.29^\circ$) reflections for **1** and **2**, respectively. Empirical absorption corrections (multiscan based on symmetry-related measurements) were applied using CrysAlis RED software [31]. The structures were solved by direct methods using SIR92 [32], and refined on F^2 using full-matrix least squares with SHELXL97 [33]. Software packages used: CrysAlis CCD [31] for data collection, CrysAlis RED [31] for cell refinement and data reduction, WINGX for geometric calculations [34], and DIAMOND [35] and MERCURY [36] for molecular graphics. The non-H atoms were treated anisotropically, whereas the hydrogen atoms were placed in calculated, ideal positions and refined as riding on their respective carbon atoms. Unit cell data and structure refinement details are listed in Table 1.

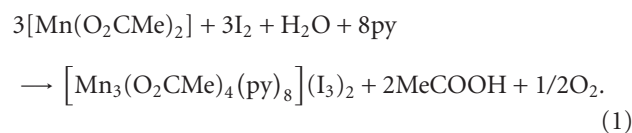
2.4. Physical Measurements. Elemental analyses were performed by the in-house facilities of the Chemistry Department, University of Cyprus. IR spectra were recorded on KBr pellets in the $4000\text{--}400 \text{ cm}^{-1}$ range using a Shimadzu Prestige-21 spectrometer. Variable-temperature DC magnetic susceptibility data down to 1.80 K were collected on a Quantum Design MPMS-XL SQUID magnetometer equipped with a 70 kG (7 T) DC magnet. Diamagnetic corrections were applied to the observed paramagnetic susceptibilities using Pascal's constants. Samples were embedded in solid eicosane, unless otherwise stated, to prevent torquing.

3. Results and Discussions

3.1. Syntheses. Both complexes were prepared serendipitously during our investigations on two different synthetic methods. The first one involved the use of iodine as an oxidizing

agent in various reactions of $[\text{Mn}(\text{O}_2\text{CMe})_2] \cdot 4\text{H}_2\text{O}$, while the second one included the employment of 1,3-propanediol (pdH_2) in reactions with $[\text{Mn}_3\text{O}(\text{O}_2\text{CMe})_6(\text{py})_3] \cdot \text{py}$.

One of the most successful strategies to polynuclear Mn clusters has been the oxidation of a Mn^{2+} starting material with the use of various oxidizing agents, often in the presence of a chelating ligand. Several oxidants have been employed for this purpose such as MnO_4^- , Ce^{IV} , peroxides, bromate, and iodine to form high-oxidation state Mn species [4, 7, 28]. Although the use of iodine as oxidant in Mn cluster chemistry has been reported in the past [4, 7], the oxidation of Mn^{2+} salts from iodine under various conditions is a rather unexplored synthetic method. Compound **1** was prepared during our investigations on reactions of $[\text{Mn}(\text{O}_2\text{CMe})_2] \cdot 4\text{H}_2\text{O}$ with iodine in $\text{MeCOOH}/\text{pyridine}$. A large amount of MeCOOH was used in order to avoid the formation of various Mn oxides/hydroxides that precipitate at basic conditions. Thus, the reaction of $[\text{Mn}(\text{O}_2\text{CMe})_2] \cdot 4\text{H}_2\text{O}$ with solid I_2 in a 1 : 1 ratio in MeCOOH/py (10/20 mL) resulted in the formation of dark brown crystals of **1** in $\sim 60\%$ yield. The formation of **1** is summarized in (1):



Despite the presence of an oxidant (I_2) in the reaction mixture, the final product (compound **1**) contains only Mn^{2+} ions. We believe that species that contain Mn ions in higher oxidation states are also formed but are quite soluble and thus do not precipitate from the reaction solution.

Another synthetic method to new polynuclear Mn clusters employed recently by our group involves the use of aliphatic diols such as pdH_2 in Mn cluster chemistry. These studies have resulted in a number of new polynuclear clusters and coordination polymers with coordinated

TABLE 2: Selected interatomic distances (Å) and angles for complex 1.

Bond Distances (Å)			
Mn1···Mn2			3.799(2)
Mn1–O1			2.154(2)
Mn1–O3			2.196(2)
Mn1–N1			2.247(2)
Mn2–O2			2.093(2)
Mn2–O3			2.234(2)
Mn2–N3			2.235(2)
Mn2–O4			2.276(2)
Mn2–N2			2.288(2)
Mn2–N4			2.295(2)
Bond Angles (°)			
O1–Mn1–O1	180.0	O2–Mn2–O3	103.82(7)
O1–Mn1–O3	90.90(7)	O2–Mn2–N3	108.98(7)
O1'–Mn1–O3	89.10(7)	O3–Mn2–N3	146.90(7)
O3–Mn1–O3'	180.0	N3–Mn2–O4	89.50(7)
O1–Mn1–N1	90.57(7)	O2–Mn2–N2	90.28(8)
O1'–Mn1–N1	89.43(7)	O3–Mn2–N2	96.50(7)
O3–Mn1–N1	87.20(7)	N3–Mn2–N2	87.73(8)
O3'–Mn1–N1	92.80(7)	O4–Mn2–N2	86.28(7)
O1–Mn1–N1	90.57(7)	O3–Mn2–N4	89.30(7)
N1–Mn1–N1'	180.0(2)	N2–Mn2–N4	173.85(8)
		Mn1–O3–Mn2	118.07(7)

TABLE 3: Bond valence sum (BVS)^(a,b) calculations for complexes 1 and 2.

	Complex 1			Complex 2		
	Mn ^{II}	Mn ^{III}	Mn ^{IV}	Mn ^{II}	Mn ^{III}	Mn ^{IV}
Mn1	<u>2.00</u>	1.87	1.90	<u>1.92</u>	1.81	1.81
Mn2	<u>1.90</u>	1.79	1.80	<u>2.05</u>	1.91	1.95
				<u>1.91</u>	1.80	1.81

^(a)The underlined value is the one closest to the charge for which it was calculated. ^(b)The oxidation state is the nearest whole number to the underlined value.

pdH₂ ligands [37–40]. Many of these compounds were isolated from reactions that were involving the use of [Mn₃O(O₂CMe)₆(py)₃]·py as a starting material [37, 38]. These studies, apart from compounds that contain coordinated pdH₂ ligands, have also resulted in complexes that do not include the diol in their asymmetric unit, with 2 being one of the members of this family. Thus, compound 2 was initially prepared from the reaction of [Mn₃O(O₂CMe)₆(py)₃]·py with Mn(ClO₄)₂·6H₂O in the presence of pdH₂ in a 1:1:4 ratio in MeCN/py (10/2 mL) in 20% yield. When the identity of 2 was established and known that it contained neither coordinated nor lattice pdH₂/pd²⁻ ligands, the reaction resulted in the formation of 2 was repeated without including pdH₂ in the reaction mixture. This reaction gave a few crystals of 2. Various modifications were applied in this reaction in order to optimize its yield. Finally, the larger yield (achieved when no pdH₂ was included in the reaction mixture) was ~9% and obtained when an extra amount of pyridine (4 more mL) was

added to the reaction solution. The exact role of pdH₂ in the assembly of 2 and how its use results in larger reaction yield still remain unidentified.

3.2. Description of the Structures. The molecular structure of complex 1 is presented in Figure 1 and selected interatomic distances and angles for 1 are listed in Table 2. Bond valence sum (BVS) calculations for the metal ions of 1 and 2 are given in Table 3. The crystal structures of 1 and 2 present a striking similarity with the main difference between them being their counter-ions and thus only that of 1 will be described here.

Compound 1 crystallizes in the monoclinic P2₁/n space group and comprises the [Mn₃(O₂CMe)₄(py)₈]²⁺ cation and two I₃⁻ counteranions. The cation of 1 (Figure 1) consists of a linear array of three Mn^{II} ions coordinated by four acetate groups and eight terminal pyridine molecules. The oxidation states of the Mn ions were determined by BVS calculations (Table 3), charge considerations, and inspection

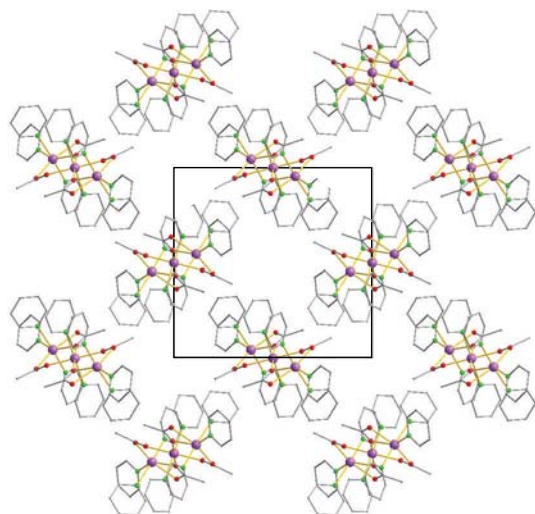


FIGURE 2: A representation of the packing of complex **1**. Mn, purple; O, red; C, grey. H atoms are omitted for clarity.

of metric parameters. The central metal ion of the trinuclear unit (Mn1), which is located on a crystallographic inversion center, is ligated by four oxygen atoms from four different acetate ligands and two molecules of pyridine adopting a distorted octahedral coordination geometry. All four acetate ligands bridge two Mn ions with two of them operating in the common *syn-syn- η^1 : η^1 : μ_2* fashion, whereas the other two function in the less common monoatomically bridging *η^2 : η^1 : μ_2* mode. The above mentioned carboxylate bridging modes have also been observed in several other linear trinuclear manganese (II) complexes [10–23]. However, in most linear Mn^{II}_3 complexes each pair of Mn^{II} ions is held together by at least three bridging ligands, whereas in **1** the neighboring Mn ions are connected through two bridging ligands only. One exception in this situation is the compound $[\text{Mn}_3(\text{O}_2\text{CMe})_6(\text{H}_2\text{O})(\text{phen})_2]$ where one pair of Mn ions is linked through two acetate ligands, whereas the second one is held together by three bridging MeCOO^- ligands [16]. The consequence of the presence of less bridging ligands in **1** is the larger $\text{Mn}\cdots\text{Mn}$ separation (3.799 (2) Å) compared to the values observed in other linear trinuclear Mn^{II} complexes which are within the range of 3.2–3.7 Å [10–23]. The observed separation of 3.799 Å is slightly smaller than that (3.868 (4) Å) between the Mn ions bridged by two acetate ligands in $[\text{Mn}_3(\text{O}_2\text{CMe})_6(\text{H}_2\text{O})(\text{phen})_2]$. However, the $\text{Mn}\cdots\text{Mn}$ distance in the other pair of Mn ions of the latter is significantly shorter (3.489 Å) and thus the average $\text{Mn}\cdots\text{Mn}$ separation falls within the range observed for the other linear trinuclear Mn^{II} complexes.

The distorted octahedral coordination environment around each terminal metal ion (Mn2) is completed by three pyridine molecules. The $\text{Mn}_2\text{N}_3\text{O}_3$ octahedron is significantly distorted, with the main distortion arising from the acute O3–Mn2–O4 angle (58.24 (7)°). The $\text{Mn}_1\text{N}_2\text{O}_4$ octahedron is almost perfect. All Mn–N and Mn–O bond lengths of the two crystallographically independent manganese ions are within the expected range for octahedral high-spin Mn^{II} complexes.

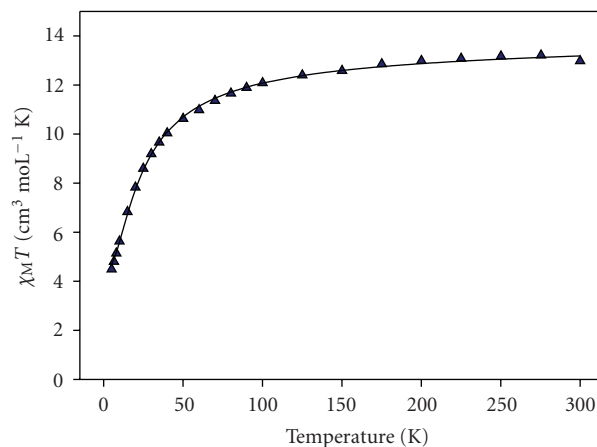


FIGURE 3: Plot of $\chi_M T$ versus T for **1**. The solid line is the fit of the experimental data; see the text for the fit parameters.

A close examination of the packing of **1** revealed that the trinuclear molecules are nearly perpendicular to each other (Figure 2) and there are no significant hydrogen bonding interactions between neighboring units of **1**.

3.3. Magnetic Properties. Solid-state dc magnetic susceptibility studies were performed on a powdered crystalline sample of **1** in a 0.1 T field and in the 5.0–300 K temperature range. The obtained data are plotted as $\chi_M T$ versus T in Figure 3.

The $\chi_M T$ product at 300 K for **1** is $12.98 \text{ cm}^3 \text{ mol}^{-1} \text{ K}$, slightly smaller than the value expected for three Mn^{II} ($S = 5/2$) noninteracting ions ($13.125 \text{ cm}^3 \text{ mol}^{-1} \text{ K}$, $g = 2$) indicating the existence of antiferromagnetic exchange interactions. This is corroborated by the continuous decrease of $\chi_M T$ upon cooling down to $10.63 \text{ cm}^3 \text{ mol}^{-1} \text{ K}$ at ~ 50 K. Below that temperature, the decrease is more abrupt, with $\chi_M T$ reaching a value of $4.49 \text{ cm}^3 \text{ mol}^{-1} \text{ K}$ at 5 K. The 5 K $\chi_M T$ value is very close to the spin-only ($g = 2$) value of $4.375 \text{ cm}^3 \text{ mol}^{-1} \text{ K}$ for a spin ground state $S = 5/2$. These results are indicative of antiferromagnetic exchange interactions between the Mn ions of **1** that lead to a spin ground state of $S = 5/2$.

The magnetic susceptibility was simulated taking into account only one isotropic intracluster magnetic interaction, J , between Mn1 and Mn2 centers since the exchange interaction between the terminal Mn ions of **1** and also of most of the known linear Mn^{II}_3 complexes is negligible ($J' = 0$) [10, 11, 15, 16] because of the large $\text{Mn}\cdots\text{Mn}$ separation (for **1** $\text{Mn}2\cdots\text{Mn}2' = 7.598(1) \text{ Å}$). Application of the van Vleck equation [41] to the Kambe's vector coupling scheme [42] allows the determination of a theoretical χ_M versus T expression for **1** from the following Hamiltonian:

$$H = -2J(\hat{S}_1\hat{S}_2 + \hat{S}_1\hat{S}_{2'}), \quad (2)$$

using the numbering scheme of Figure 1, where $S_1 = S_2 = S_{2'} = 5/2$. This expression was used to fit the experimental data giving $J = -1.50 \text{ K}$ and $g = 2.00$ (solid line, Figure 3).

A temperature-independent paramagnetism (TIP) term was held constant at $600 \times 10^{-6} \text{ cm}^3 \text{ mol}^{-1} \text{ K}$.

The obtained J value is smaller than values reported in the literature for other linear Mn^{II}_3 clusters with three bridging ligands per manganese pair which in most cases range from ~ -2.5 to $\sim -7 \text{ K}$ [18]. This behaviour could be rationalized on the basis of the existence of only two bridging ligands per manganese pair and larger $\text{Mn} \cdots \text{Mn}$ separations in **1** as was discussed in detail above (description of the structures). There are, however, examples of linear Mn^{II}_3 clusters with J values comparable to that of **1**, such as $[\text{Mn}_3(\text{L}^1)_2(\mu\text{-O}_2\text{CMe})_4] \cdot 2\text{Et}_2\text{O}$ ($\text{HL}^1 = (1\text{-hydroxy-4-nitrobenzyl})((2\text{-pyridyl)methyl})((1\text{-methylimidazol-2-yl)methyl)amine$) ($J = -1.7 \text{ K}$) [21].

4. Conclusions

A new linear trinuclear manganese(II) complex $[\text{Mn}_3(\text{O}_2\text{CMe})_4(\text{py})_8]^{2+}$ cocrystallizing with I_3^- [1] and ClO_4^- [2] has been synthesized serendipitously. Compound **1** was prepared in an attempt to oxidize $[\text{Mn}(\text{O}_2\text{CMe})_2] \cdot 4\text{H}_2\text{O}$ with I_2 in MeCOOH/py , whereas compound **2** was initially isolated during our investigations on reactions of $[\text{Mn}_3\text{O}(\text{O}_2\text{CMe})_6(\text{py})_3] \cdot \text{py}$ with $\text{Mn}(\text{ClO}_4)_2 \cdot 6\text{H}_2\text{O}$ in the presence of pdH_2 in MeCN/py and was resynthesized in lower yield without adding pdH_2 in the reaction mixture. Although several linear trinuclear Mn^{II} complexes have been prepared and studied, the cation of **1** and **2** has several novel structural features including: (i) different type of ligation since **1** and **2** are the first examples of linear trinuclear Mn clusters with only acetate and pyridine ligands and (ii) different number of bridging ligands between each pair of Mn^{II} ions, since **1** and **2** are rare examples of linear Mn^{II}_3 clusters with only two bridging ligands linking each pair of Mn^{II} ions. Variable temperature dc magnetic susceptibility studies revealed the existence of antiferromagnetic interactions between the Mn ions of **1** resulting in an $S_T = 5/2$ spin ground state.

Acknowledgments

The authors thank the Cyprus Research Promotion Foundation (Grant: TEXNO/0506/06), for financial support of this research. This paper is dedicated to Professor Nick Hadjiliadis for his retirement.

References

- [1] V. L. Pecoraro, *Manganese Redox Enzymes*, VCH Publishers, New York, NY, USA, 1992.
- [2] R. Bagai and G. Christou, "The Drosophila of single-molecule magnetism: $[\text{Mn}_{12}\text{O}_{12}(\text{O}_2\text{CR})_{16}(\text{H}_2\text{O})_4]$," *Chemical Society Reviews*, vol. 38, no. 4, pp. 1011–1026, 2009.
- [3] J. Barber, "Photosynthetic energy conversion: natural and artificial," *Chemical Society Reviews*, vol. 38, no. 1, pp. 185–196, 2009.
- [4] S. Mukhopadhyay, S. K. Mandal, S. Bhaduri, and W. H. Armstrong, "Manganese clusters with relevance to photosystem II," *Chemical Reviews*, vol. 104, no. 9, pp. 3981–4026, 2004.
- [5] A. Mishra, W. Wernsdorfer, K. A. Abboud, and G. Christou, "The first high oxidation state manganese-calcium cluster: relevance to the water oxidizing complex of photosynthesis," *Chemical Communications*, no. 1, pp. 54–56, 2005.
- [6] W. Ruttinger and G. C. Dismukes, "Synthetic water-oxidation catalysts for artificial photosynthetic water oxidation," *Chemical Reviews*, vol. 97, no. 1, pp. 1–24, 1997.
- [7] R. Manchanda, G. W. Brudvig, and R. H. Crabtree, "High-valent oxomanganese clusters: structural and mechanistic work relevant to the oxygen-evolving center in photosystem II," *Coordination Chemistry Reviews*, vol. 144, pp. 1–38, 1995.
- [8] V. L. Pecoraro, M. J. Baldwin, and A. Gelasco, "Interaction of manganese with dioxygen and its reduced derivatives," *Chemical Reviews*, vol. 94, no. 3, pp. 807–826, 1994.
- [9] A. J. Wu, J. E. Penner-Hahn, and V. L. Pecoraro, "Structural, spectroscopic, and reactivity models for the manganese catalases," *Chemical Reviews*, vol. 104, no. 2, pp. 903–938, 2004.
- [10] S. G. Baca, Y. Sevryugina, R. Clérac, I. Malaestean, N. Gerbeleu, and M. A. Petrukhina, "Linear trinuclear manganese(II) complexes: crystal structures and magnetic properties," *Inorganic Chemistry Communications*, vol. 8, no. 5, pp. 474–478, 2005.
- [11] S. Menage, S. E. Vitols, P. Bergerat, et al., "Structure of the linear trinuclear complex $\text{Mn}_3^{\text{II}}(\text{CH}_3\text{CO}_2)_6(\text{bpy})_2$. Determination of the J electron-exchange parameter through magnetic susceptibility and high-field magnetization measurements," *Inorganic Chemistry*, vol. 30, no. 12, pp. 2666–2671, 1991.
- [12] G. Christou, "Manganese carboxylate chemistry and Its biological relevance," *Accounts of Chemical Research*, vol. 22, no. 9, pp. 328–335, 1989.
- [13] G. Fernandez, M. Corbella, J. Mahia, and M. A. Maestro, "Polynuclear Mn^{II} complexes with chloroacetate bridge—syntheses, structure, and magnetic properties," *European Journal of Inorganic Chemistry*, no. 9, pp. 2502–2510, 2002.
- [14] K. Tsuneyoshi, H. Kobayashi, and H. Miyamae, "Structure of hexa- μ -acetato- $1\text{K}^3\text{O} : 2\text{K}^3\text{O}' ; 2\text{K}^3\text{O} : 3\text{K}^3\text{O}'$ -bis(1,10-phenanthroline)-1- $\text{K}^2\text{N}^1, \text{N}^{10} ; 2\text{K}^2\text{N}^1, \text{N}^{10}$ -trimanganese(II)," *Acta Crystallographica Section C-Crystal Structure Communication*, vol. 49, pp. 233–236, 1993.
- [15] R. L. Rardin, P. Poganiuch, A. Bino, et al., "Synthesis and characterization of trinuclear iron(II) and manganese(II) carboxylate complexes: structural trends in low valent iron and manganese carboxylates," *Journal of the American Chemical Society*, vol. 114, no. 13, pp. 5240–5249, 1992.
- [16] M. Wang, C.-B. Ma, H.-S. Wang, C.-N. Chen, and Q.-T. Liu, "Synthesis and characterization of two linear trinuclear complexes $[\text{M}_3(\text{MeCOO})_6(\text{H}_2\text{O})(\text{phen})_2] \cdot \text{H}_2\text{O}$ ($\text{M} = \text{Co}, \text{Mn}$)," *Journal of Molecular Structure*, vol. 873, no. 1–3, pp. 94–100, 2008.
- [17] V. Tangoulis, D. A. Malamatar, K. Soulti, et al., "Manganese(II/II/II) and manganese(III/II/III) trinuclear compounds. Structure and solid and solution behavior," *Inorganic Chemistry*, vol. 35, no. 17, pp. 4974–4983, 1996.
- [18] V. Gómez, D. A. Malamatar, K. Soulti, et al., "Versatility in the coordination modes of n -chlorobenzoato ligands: synthesis, structure and magnetic properties of three types of polynuclear Mn^{II} Compounds," *European Journal of Inorganic Chemistry*, no. 29–30, pp. 4471–4482, 2009.
- [19] C. C. Stoumpos, I. A. Gass, C. J. Milios, et al., "The use of di-2-pyridyl ketone in manganese(II) benzoate chemistry: two novel Mn_3^{II} linkage isomers containing the ketone form of the ligand and a neutral Mn_4^{II} cubane containing the ligand in its gem-diolate(-1) form," *Inorganic Chemistry Communications*, vol. 11, no. 2, pp. 196–202, 2008.

- [20] C. J. Milios, T. C. Stamatatos, P. Kyritsis, et al., "Phenyl 2-pyridyl ketone and its oxime in manganese carboxylate chemistry: synthesis, characterisation, X-ray studies and magnetic properties of mononuclear, trinuclear and octanuclear complexes," *European Journal of Inorganic Chemistry*, no. 14, pp. 2885–2901, 2004.
- [21] M. Kloskowski, D. Pursche, R.-D. Hoffmann, et al., "Novel trinuclear $Mn^{II}/Mn^{II}/Mn^{II}$ complexes—crystal structures and catalytic properties," *Zeitschrift für Anorganische und Allgemeine Chemie*, vol. 633, no. 1, pp. 106–112, 2007.
- [22] H. Asada, K. Hayashi, S. Negoro, M. Fujiwara, and T. Matsushita, "Preparation and structures of trinuclear manganese(II) complexes with *N*-2-pyridylmethylidene-2-hydroxy-5-substituted-phenylamine," *Inorganic Chemistry Communications*, vol. 6, no. 2, pp. 193–196, 2003.
- [23] D. Pursche, M. U. Triller, N. Reddig, A. Rompel, and B. Krebs, "Synthesis and characterization of $[Mn_3(ppi)_2(\mu-OAc)_4(H_2O)_2] \cdot 2MeOH$ —unusual structural properties of a trinuclear oxygen-rich manganese complex," *Zeitschrift für Anorganische und Allgemeine Chemie*, vol. 629, no. 1, pp. 24–28, 2003.
- [24] M. Hirotsu, M. Kojima, W. Mori, and Y. Yoshikawa, "Steric control of polynuclear manganese complexes by the use of tripodal tetradentate ligands," *Bulletin of the Chemical Society of Japan*, vol. 71, no. 12, pp. 2873–2884, 1998.
- [25] D. P. Kessissoglou, M. L. Kirk, M. S. Lah, et al., "Structural and magnetic characterization of trinuclear, mixed-valence manganese acetates," *Inorganic Chemistry*, vol. 31, no. 26, pp. 5424–5432, 1992.
- [26] Y.-G. Li, L. Lecren, W. Wernsdorfer, and R. Clérac, "Antiferromagnetic order in a supramolecular assembly of manganese trimers based on imidazole and Schiff-base ligands," *Inorganic Chemistry Communications*, vol. 7, no. 12, pp. 1281–1284, 2004.
- [27] J. B. Vincent, H.-R. Chang, K. Folting, J. C. Huffman, G. Christou, and D. N. Hendrickson, "Preparation and physical properties of trinuclear oxo-centered manganese complexes of the general formulation $[Mn_3O(O_2CR)_6L_3]^{0,+}$ ($R = Me$ or Ph ; $L =$ a neutral donor group) and the crystal structures of $[Mn_3O(O_2CMe)_6(pyr)_3](pyr)$ and $[Mn_3O(O_2CPh)_6(pyr)_2(H_2O)] \cdot 0.5MeCN$," *Journal of the American Chemical Society*, vol. 109, no. 19, pp. 5703–5711, 1987.
- [28] S. Bhaduri, M. Pink, and G. Christou, "Towards a synthetic model of the photosynthetic water oxidizing complex: $[Mn_3O_4(O_2CMe)_4(bpy)_2]$ containing the $[Mn_3^{IV}(\mu-O_4)]^{4+}$ core," *Chemical Communications*, no. 20, pp. 2352–2353, 2002.
- [29] S. Zartilas, E. E. Moushi, V. Nastopoulos, A. K. Boudalis, and A. J. Tasiopoulos, "Two new coordination polymers containing the triangular $[Mn_3O(O_2CR)_6]^{0/+}$ units," *Inorganica Chimica Acta*, vol. 361, no. 14–15, pp. 4100–4106, 2008.
- [30] R. A. Reynolds III, W. R. Dunham, and D. Coucouvanis, "Kinetic lability, structural diversity, and oxidation reactions of new oligomeric, anionic carboxylate-pyridine complexes," *Inorganic Chemistry*, vol. 37, no. 6, pp. 1232–1241, 1998.
- [31] Oxford diffraction, *CrysAlis CCD and CrysAlis RED, Version 1.171.32.15*, Oxford Diffraction Ltd, Oxford, UK, 2008.
- [32] A. Altomare, G. Cascarano, C. Giacovazzo, et al., "SIR92—a program for automatic solution of crystal structures by direct methods," *Journal of Applied Crystallography*, vol. 27, no. 6, p. 435, 1994.
- [33] G. M. Sheldrick, *SHELXL97—A Program for The Refinement of Crystal Structure*, University of Göttingen, Göttingen, Germany, 1997.
- [34] L. J. Farrugia, "WinGX suite for single crystal small molecule crystallography," *Journal of Applied Crystallography*, vol. 32, no. 4, pp. 837–838, 1999.
- [35] K. Brandenburg, *DIAMOND. Version 3.1d.*, Crystal Impact GbR, Bonn, Germany, 2006.
- [36] C. F. Macrae, P. R. Edgington, P. McCabe, et al., "Mercury: visualization and analysis of crystal structures," *Journal of Applied Crystallography*, vol. 39, no. 3, pp. 453–457, 2006.
- [37] E. E. Moushi, T. C. Stamatatos, W. Wernsdorfer, V. Nastopoulos, G. Christou, and A. J. Tasiopoulos, "A family of 3D coordination polymers composed of Mn_{19} magnetic units," *Angewandte Chemie International Edition*, vol. 45, no. 46, pp. 7722–7725, 2006.
- [38] E. E. Moushi, C. Lampropoulos, W. Wernsdorfer, V. Nastopoulos, G. Christou, and A. J. Tasiopoulos, "A large $[Mn_{10}Na]_4$ loops," *Inorganic Chemistry*, vol. 46, no. 10, pp. 3795–3797, 2007.
- [39] E. E. Moushi, T. C. Stamatatos, W. Wernsdorfer, V. Nastopoulos, G. Christou, and A. J. Tasiopoulos, "A Mn_{17} octahedron with a giant ground-state spin: occurrence in discrete form and as multidimensional coordination polymers," *Inorganic Chemistry*, vol. 48, no. 12, pp. 5049–5051, 2009.
- [40] E. E. Moushi, T. C. Stamatatos, V. Nastopoulos, G. Christou, and A. J. Tasiopoulos, "A new family of octanuclear Mn complexes with a rod-like topology," *Polyhedron*, vol. 28, no. 15, pp. 3203–3208, 2009.
- [41] J. H. Van Vleck, *The Theory of Electric and Magnetic Susceptibility*, Oxford University Press, Oxford, UK, 1932.
- [42] K. Kambe, "On the paramagnetic susceptibilities of some polynuclear complex salts," *Journal of the Physical Society of Japan*, vol. 5, pp. 48–51, 1950.

Research Article

Synthesis and Supramolecular Structure of a (5-(3-(1*H*-tetrazol-5-yl)phenyl)-1*H*-tetrazole) Cobalt Complex

George E. Kostakis,¹ Christopher E. Anson,² and Annie K. Powell^{1,2}

¹Institute of Nanotechnology, Karlsruhe Institute of Technology, Postfach 3640, 76021 Karlsruhe, Germany

²Institute of Inorganic Chemistry, Karlsruhe Institute of Technology, Engessertsrasse 15, 76131 Karlsruhe, Germany

Correspondence should be addressed to George E. Kostakis, george.kostakis@kit.edu

Received 3 March 2010; Accepted 30 March 2010

Academic Editor: Spyros Perlepes

Copyright © 2010 George E. Kostakis et al. This is an open access article distributed under the Creative Commons Attribution License, which permits unrestricted use, distribution, and reproduction in any medium, provided the original work is properly cited.

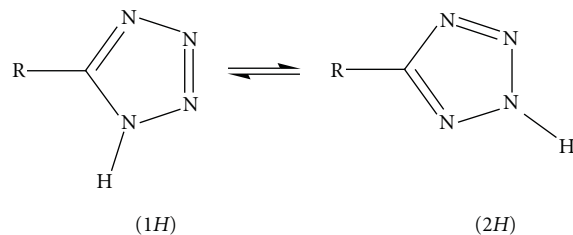
The reaction of $\text{CoCl}_2 \cdot 6\text{H}_2\text{O}$ with *m*-BDTH₂ (1,3-benzeneditetrazol-5-yl) leads to $[\text{Co}(\text{C}_8\text{H}_6\text{N}_8)_2(\text{H}_2\text{O})_2(\text{CH}_3\text{CN})_2]\text{Cl}_2$ (**1**). Both tetrazolic groups remain protonated existing in a 1*H* tautomeric form. A trifurcated chlorine atom and stacking interactions assemble compound **1** into a three-dimensional network.

1. Introduction

Tetrazoles are a class of organic heterocyclic compounds which consist of a five-membered ring of four nitrogen atoms and one carbon atom (Scheme 1). In the design of drug molecules, tetrazoles and tetrazole derivatives have generally been avoided because their explosive and flammable nature makes them a safety concern for process-scale synthesis. Nevertheless, tetrazoles such as Losartan [1] and Candesartan [2] are angiotensin II receptor antagonist drugs used mainly to treat high blood pressure (hypertension). Moreover, a well-known tetrazole is dimethyl thiazolyl diphenyl tetrazolium salt (MTT), which is used in the MTT assay of the respiratory activity of live cells in cell culture [3]. 5-substituted-1*H*-tetrazoles (RCN₄H) usually can be utilised as metabolism-resistant isosteric replacements for carboxylic acids (RCO₂H) in SAR-driven medicinal chemistry analogue syntheses, while it has been found that they have comparable pK_a values to the corresponding carboxylic acids (RCO₂H) [4]. Therefore, the study of the structures of tetrazoles is relevant to several aspects of medicinal chemistry, as, indeed, is their coordination chemistry given the increasing importance of metal-based drugs incorporating known therapeutic organic agents [5].

5-substituted-1*H*-tetrazoles, often termed tetrazolic acids, can be found in neutral, anionic, or cationic form, and they can act as ligands in metal complexes, form salts, and can be both acceptors and donors for hydrogen bonding. Such tetrazolic acids exist in an approximately 1:1 ratio of the 1*H*- and 2*H*-tautomeric forms (Scheme 1). It has been reported that the two positional isomers **1** and **2** may be differentiated on the NMR timescale [6, 7], while theoretical calculations show that the 2*H*-tautomers are the more stable isomers, although they were found to have a larger degree of electron delocalization than 1*H*-tautomers [8]. Over the last decade, the synthetic procedures of such compounds have been improved [9, 10]; consequently more attention has been focused on the coordinating behaviour of such compounds. Thus, the 5-substituted-1*H*-tetrazoles have been used as versatile building blocks for molecular coordination networks, also called coordination polymers or metal organic frameworks [11, 12] as well as hydrogen bonded frameworks [13–16].

Recently, we embarked on a study of the coordination behaviour of various 5-substituted-1*H*-tetrazoles [13–16], and this article describes part of this systematic study where we report the synthesis and crystal structure of $[\text{Co}(m\text{-BDTH}_2)_2(\text{H}_2\text{O})_2(\text{CH}_3\text{CN})_2]\text{Cl}_2$ (**1**) where *m*-BDTH₂ = 1,3-benzeneditetrazol-5-yl.



SCHEME 1: The two possible tautomers of 5-substituted tetrazoles.

2. Experimental

2.1. General. All chemicals and solvents used for the synthesis were obtained from commercial sources and were used as received. The reaction was carried out under aerobic conditions. Elemental analysis (C, H, N) was performed at the Institute of Inorganic Chemistry, Karlsruhe Institute of Technology, using an Elementar Vario EL analyzer. Fourier transform IR spectra were measured on a Perkin-Elmer Spectrum One spectrometer with samples prepared as KBr discs.

2.2. Preparation of the Ligand and Compound (1). *m*-BDTH₂ was prepared as described previously [7]. A solution of *m*-BDTH₂ (0.021 g, 0.1 mmol) in CH₃CN/EtOH (ratio 1:1, total volume 20 ml) was added dropwise to a stirred solution of CoCl₂ 6H₂O (24 mg, 0.1 mmol). The resulting dark blue solution was refluxed for 2 hours, filtered and left to evaporate slowly. Orange crystals of [Co(C₈H₆N₈)₂(H₂O)₂(CH₃CN)₂]Cl₂ (**1**) were formed after slow evaporation of the solution (Yield: 27 mg, 80%). Calc. for C₂₀H₂₂Cl₂CoN₁₈O₂, (**1**): C, 35.55; H, 3.28; N, 37.34. Found C, 35.69; H, 3.31; N, 37.32%. IR (KBr, cm⁻¹) = 3338 (s), 3053 (w), 2896 (m), 2846 (m), 2822 (m), 2737 (w), 2317 (m), 2290 (m), 1711 (w), 1621 (w), 1553 (s), 1481 (s), 1459 (s), 1374 (m), 1256 (m), 1169 (m), 1144 (w), 1127 (w), 1084 (s), 1029 (s), 999 (m), 906 (w), 872 (m), 802 (s), 762 (s), 733 (s), 705 (s), 684 (s).

2.3. X-Ray Crystallography. Single-crystal X-ray crystallographic data of **1** were collected at 100 K on a Bruker SMART Apex CCD diffractometer using graphite-monochromated Mo-K α radiation. Crystallographic data and details of the measurement and refinement are summarized in Table 1. Semiempirical absorption corrections were made using SADABS [17]. The structures were solved using direct methods followed by full-matrix least-squares refinement against F^2 (all data) using SHELXTL [18]. Anisotropic refinement was used for all non-H atoms; all H atoms were refined (both coordinates and isotropic temperature factors) without restraints, except for the methyl H-atoms on the acetonitrile solvent molecules, which were refined as a rigid tetrahedral group, but with the torsional angle allowed to refine (AFIX 137 in SHELXTL). The crystallographic data and refinement parameters are listed in Table 1.

TABLE 1: Crystal data and structure refinement for **1**.

Empirical formula	C ₂₀ H ₂₂ Cl ₂ CoN ₁₈ O ₂	
Formula weight	676.39	
Temperature	100(2) K	
Wavelength	0.71073 Å	
Crystal system	Triclinic	
Space group	<i>P</i> -1	
Unit cell dimensions	<i>a</i> = 8.3341 (4) Å	α = 84.682 (1)°
	<i>b</i> = 8.4696 (5) Å	β = 73.522 (1)°
	<i>c</i> = 11.4730 (6) Å	γ = 65.938 (1)°
Volume	708.85 (7) Å ³	
Z	1	
Density (calculated)	1.584 Mg/m ³	
Absorption coefficient	0.85 mm ⁻¹	
F(000)	345	
Crystal size	0.36 × 0.31 × 0.25 mm	
	−10 ≤ <i>h</i> ≤ 10,	
Index ranges	−10 ≤ <i>k</i> ≤ 11,	
	−14 ≤ <i>l</i> ≤ 14	
Reflections collected	5965	
Independent reflections	3132 [R (int) = 0.0148]	
Data/parameters	3132/229	
Goodness-of-fit <i>S</i> on F^2	1.071	
R indices [<i>I</i> > 2σ(<i>I</i>)]	R1 = 0.0337, wR2 = 0.0854	
R indices (all data)	R1 = 0.0364, wR2 = 0.0871	
Largest diff. peak and hole	0.750 and −0.314 e.Å ⁻³	

3. Results and Discussion

3.1. Crystal Structure of 1. Compound **1** was characterized crystallographically and found to belong to the triclinic *P*-1 space group. Selected distances (Å) and angles (°) are presented in Table 2. The Co(II) atom is six-coordinate with an octahedral geometry. The coordination sphere is occupied by two nitrogen N(3) atoms provided by two *m*-BDTH₂ ligands, two acetonitrile, and two water molecules. Both tetrazolic groups remain protonated existing in a 1H tautomeric form. To our knowledge this is the first example showing the neutral form. Only one of the two aryl moieties is coordinated to the Co(II) atom through the

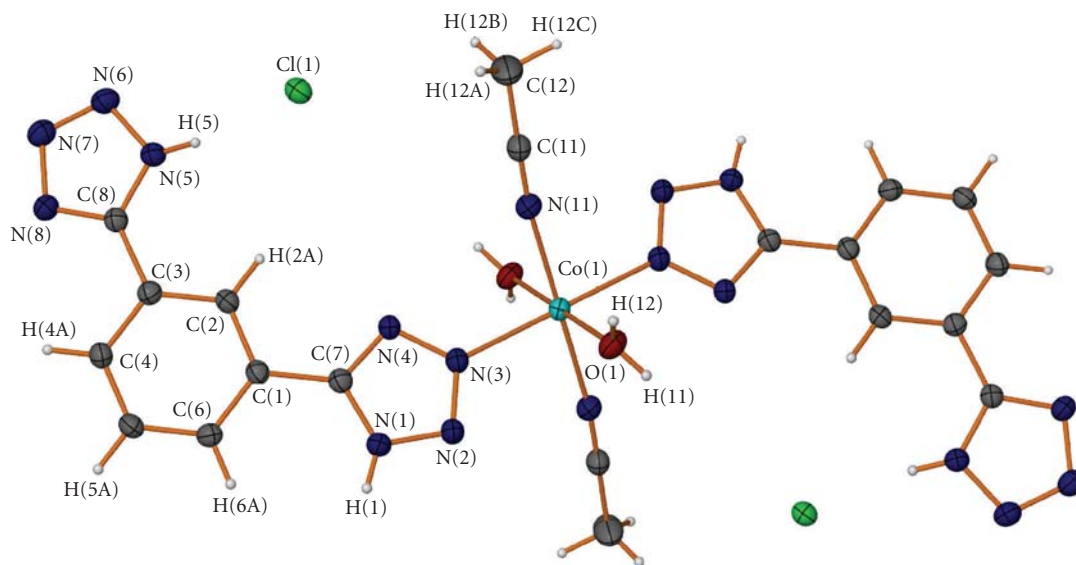


FIGURE 1: View of the cobalt complex in **1**, shown in approximately the same orientation, with the atom-labelling scheme. Ellipsoids represent displacement parameters at the 40% probability level.

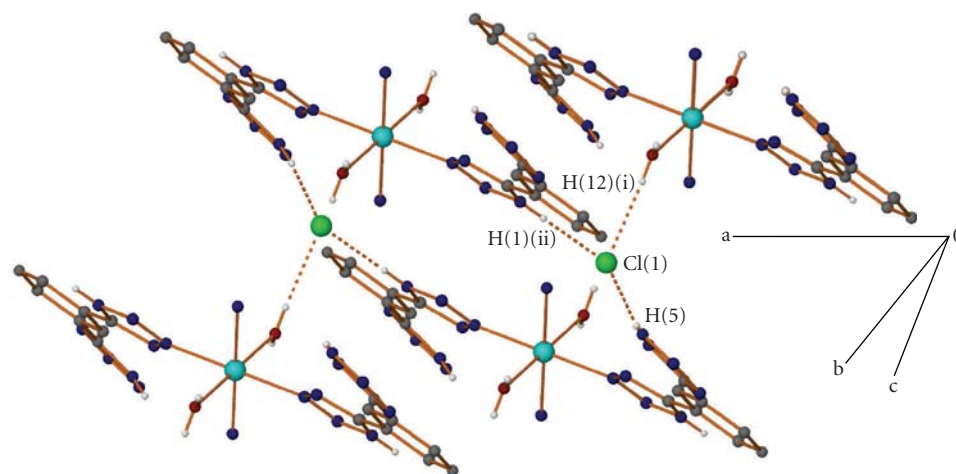


FIGURE 2: A projection of the hydrogen bonded layer formed in **1**, parallel to *a* axis. The organic hydrogen atoms and acetonitrile carbon atoms have been omitted for clarity.

nitrogen atom N3 (Figure 1). The dihedral angles between the planes through the coordinated tetrazole, the central aryl moiety, and the noncoordinated tetrazole are 5.87° and 9.8° , respectively.

In compound **1** there are two different kinds of interactions that lead to the formation of a 3D supramolecular architecture, namely, hydrogen bonding and stacking interactions. The chlorine atom is part of a trifurcated hydrogen bonding arrangement (Table 3) between three different cations. In this way a layer parallel to the *a* axis is formed (Figure 2). The first H-bond involves hydrogen atom H(5) of the noncoordinated tetrazolic group, the second involves hydrogen atom H(12) of the coordinated water molecule and the third involves hydrogen atom H(1) of the coordinated tetrazole group. In addition, a fourth hydrogen

bond is located between hydrogen atom H(11) of water molecule and nitrogen atom N(7) of the noncoordinated tetrazolic group, forming an infinite 1D-chain perpendicular to the *a* axis. These 1D chains interact with each other through weak $\pi-\pi$ stacking interactions involving all the aryl moieties (Table 3). A stronger interaction occurs between the central ring and the noncoordinated tetrazole group, while there is also an interaction with an adjacent coordinated tetrazolic group belonging to a third 1D chain (Figure 3).

3.2. FT-IR Spectroscopy. The IR spectrum of **1** displays broad bands centred at 3338 cm^{-1} , in agreement with the presence of H-bonded water molecules. The bands at 2317 (m) , 2290 (m) , can be attributed to the $\nu(\text{CN})$ of the acetonitrile

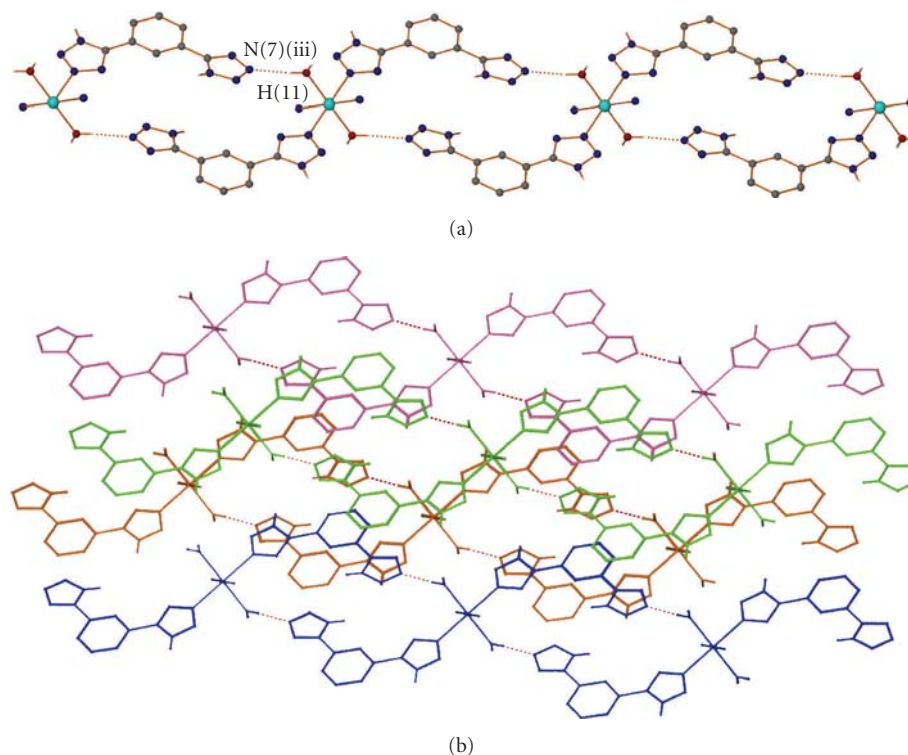


FIGURE 3: (a) A projection of the hydrogen bonded layer formed in **1** perpendicular to *a* axis; a view of **1** showing the $\pi - \pi$ interaction. (b) The hydrogen-bonded layers are drawn in different colours to emphasize the stacking interactions between the aryl rings that lead to a 3D supramolecular architecture. Chlorine atoms, the organic hydrogen atoms, and acetonitrile carbon atoms have been omitted for clarity.

TABLE 2: Bond lengths [Å] and angles [°] for **1**.

Co(1)–O(1)	2.0362 (14)	O(1)–Co(1)–N(2)#1	90.95 (6)
Co(1)–N(9)	2.1089 (16)	O(1)–Co(1)–N(2)	89.05 (6)
Co(1)–N(2)	2.1536 (15)	N(9)–Co(1)–N(2)	89.51 (6)
O(1)–Co(1)–O(1)#1	180.0	N(2)#1–Co(1)–N(2)	179.999 (1)
O(1)–Co(1)–N(9)	89.10 (6)	N(9)#1–Co(1)–N(2)	90.49 (6)
O(1)–Co(1)–N(9)#1	90.90 (6)	N(9)–Co(1)–N(9)#1	180.0

Symmetry transformations used to generate equivalent atoms: #1 – $x + 1, -y + 1, -z + 1$.

TABLE 3: Hydrogen bonding and stacking interactions in **1**.

D–H...A	d(D–H)	d(H...A)	d(D...A)	<(DHA)
N(1)–H(1)...Cl(1)#1	0.81	2.270	3.083	176
N(5)–H(5)...Cl(1)#2	0.84	2.240	3.0708	169
O(1)–H(11)...N(7)#3	0.80	1.990	2.7840	173
O(1)–H(12)...Cl(1)	0.77	2.380	3.4137	176
Centroids	Centroids dist (Å)	L sq planes dist (Å)	Offset (Å)	
a...b#4	3.7908 (10)	3.221	1.999	
c...b#5	3.5059 (11)	3.310	1.156	
b...b#4	4.0389 (10)	3.385	2.203	

Symmetry codes: #1 – $x, 1 - y, 1 - z$, #2 $1 - x, -y, 1 - z$, #3 $x, 1 + y, -1 + z$, #4 $2 - x, 1 - y, -z$, #5 $2 - x, 2 - y, z$

a N(1)–N(2)–N(3)–N(4)–C(7), b C(1)–C(2)–C(3)–C(4)–C(5)–C(6), c N(5)–N(6)–N(7)–N(8)–C(8)

while the bands at 1553, 1481, 1459, 802, 762, 733, 705, and 684 cm^{-1} are characteristic of the nondeprotonated ligand [13].

4. Conclusions

In this article, we have examined the interaction of m -BDTH₂ = 1, 3-benzeneditetrazol-5-yl with $\text{CoCl}_2 \cdot 6\text{H}_2\text{O}$. The absence of any base in the reaction mixture prevents deprotonation of the ligand, and in addition to the fact that the ligand coordinates via the nitrogen atom at position 2 on the ring, the hydrogen atom on the nitrogen at position 1 could be located and refined giving clear evidence that the tetrazole is in the 1H tautomeric form (Scheme 1, left). Both the tetrazolic groups of the ligand remain protonated and in the 1H tautomeric form and, to our knowledge, this is the first example of a coordination compound with this neutral form. The trifurcated hydrogen bonding arrangement at the chloride counterion and stacking interactions assemble compound **1** into a three-dimensional supramolecular network. The present finding provides new structural data, which could enhance the understanding of the structural aspects of 5-substituted-1H-tetrazoles. This work represents a part of our systematic efforts to determine new synthetic pathways in the binary system metal/5-substituted-1H-tetrazoles, and further studies on the influence of other parameters on the hydrogen-bonded structural motifs are in progress.

Supplementary Data

CCDC 768261 contains the supplementary crystallographic data for **1**. These data can be obtained free of charge via <http://www.ccdc.cam.ac.uk/conts/retrieving.html>, or from the Cambridge Crystallographic Data Centre, 12 Union Road, Cambridge CB2 1EZ, UK; fax: (+44) 1223-336-033; or e-mail: deposit@ccdc.cam.ac.uk.

Acknowledgment

The authors are grateful to the DFG Center for Functional Nanostructures for financial support. This work is dedicated to Professor Nick Hadjiladis for his retirement.

References

- [1] V. Segarra, M. I. Crespo, F. Pujol, et al., "Phosphodiesterase inhibitory properties of losartan. Design and synthesis of new lead compounds," *Bioorganic and Medicinal Chemistry Letters*, vol. 8, no. 5, pp. 505–510, 1998.
- [2] M. A. Pfeffer, K. Swedberg, C. B. Granger, et al., "Effects of candesartan on mortality and morbidity in patients with chronic heart failure: the CHARM-overall programme," *Lancet*, vol. 362, no. 9386, pp. 759–766, 2003.
- [3] T. Mosmann, "Rapid colorimetric assay for cellular growth and survival: application to proliferation and cytotoxicity assays," *Journal of Immunological Methods*, vol. 65, no. 1-2, pp. 55–63, 1983.
- [4] R. J. Herr, "5-substituted-1H-tetrazoles as carboxylic acid isosteres: medicinal chemistry and synthetic methods," *Bioorganic and Medicinal Chemistry*, vol. 10, no. 11, pp. 3379–3393, 2002.
- [5] S. J. Wittenberger, "Recent developments in tetrazole chemistry. A review," *Organic Preparations and Procedures International*, vol. 26, pp. 499–531, 1994.
- [6] H. B. Jonassen, J. H. Nelson, D. L. Schmitt, R. A. Henry, and D. W. Moore, "Platinum- and palladium-tetrazole complexes," *Inorganic Chemistry*, vol. 9, no. 12, pp. 2678–2681, 1970.
- [7] S. Achamlale, A. Elachqar, A. El Hallaoui, et al., "Synthesis of biheterocyclic- α -amino acids," *Amino Acids*, vol. 17, no. 2, pp. 149–163, 1999.
- [8] N. Sadlej-Sosnowska, "Application of natural bond orbital analysis to delocalization and aromaticity in C-substituted tetrazoles," *Journal of Organic Chemistry*, vol. 66, no. 26, pp. 8737–8743, 2001.
- [9] Z. P. Demko and K. B. Sharpless, "Preparation of 5-substituted 1H-tetrazoles from nitriles in water," *Journal of Organic Chemistry*, vol. 66, no. 24, pp. 7945–7950, 2001.
- [10] Z. P. Demko and K. B. Sharpless, "An intramolecular [2 + 3] cycloaddition route to fused 5-heterosubstituted tetrazoles," *Organic Letters*, vol. 3, no. 25, pp. 4091–4094, 2001.
- [11] J. Tao, Z.-J. Ma, R.-B. Huang, and L.-S. Zheng, "Synthesis and characterization of a tetrazolate-bridged coordination framework encapsulating D_{2h}-symmetric cyclic (H₂O)₄ cluster arrays," *Inorganic Chemistry*, vol. 43, no. 20, pp. 6133–6135, 2004.
- [12] W. Ouellette, A. V. Prosvirin, K. Whitenack, K. R. Dunbar, and J. Zubietta, "A thermally and hydrolytically stable microporous framework exhibiting single-chain magnetism: structure and properties of [Co₂(H_{0.67}bdt)₃] · 20 H₂O," *Angewandte Chemie International Edition*, vol. 48, no. 12, pp. 2140–2143, 2009.
- [13] G. E. Kostakis, G. Abbas, C. E. Anson, and A. K. Powell, "3-D porous framework: [Ln(H₂O)_n]³⁺ ions act as pillars between π -stacked and H-bonded sheets of (m -BDTH)[−] organic anions in [Ln(H₂O)_n] (m -BDTH)₃ · 9(H₂O) (Ln = Pr, n = 9; Ln = Gd, n = 8)," *CrystEngComm*, vol. 10, no. 9, pp. 1117–1119, 2008.
- [14] G. E. Kostakis, G. Abbas, C. E. Anson, and A. K. Powell, "Inclusion of a well resolved T4(2)6(2) water tape in a H-bonded, (4,7)-binodal 3D network," *CrystEngComm*, vol. 11, no. 1, pp. 82–86, 2009.
- [15] G. E. Kostakis, A. Mavrandonakis, G. Abbas, et al., "An in-depth essay on a hydrogen bonded 3-D framework possessing hydrophobic layers and hydrophilic pillars," *CrystEngComm*, vol. 11, no. 11, pp. 2480–2487, 2009.
- [16] G. E. Kostakis, K. C. Mondal, C. E. Anson, and A. K. Powell, "Influence of the metal radius in the dimensionality of H-bonded metal supra molecular frameworks," *Polyhedron*, vol. 29, pp. 24–29, 2010.
- [17] G. M. Sheldrick, *SADABS (the Siemens Area Detector Absorption Correction)*, University of Göttingen, Göttingen, Germany, 1996.
- [18] G. M. Sheldrick, "A short history of SHELX," *Acta Crystallographica Section A*, vol. 64, no. 1, pp. 112–122, 2007.

Research Article

Diorganotin Complexes of a Thiosemicarbazone, Synthesis: Properties, X-Ray Crystal Structure, and Antiproliferative Activity of Diorganotin Complexes

Joanna Wiecek,¹ Dimitra Kovala-Demertzi,¹ Zbigniew Ciunik,² Maria Zervou,³ and Mavroudis A. Demertzis¹

¹ Sector of Inorganic and Analytical Chemistry, Department of Chemistry, University of Ioannina, 45110 Ioannina, Greece

² Faculty of Chemistry, University of Wrocław, 14 F. Joliot-Curie Street, 50-383 Wrocław, Poland

³ Institute of Organic and Pharmaceutical Chemistry, National Hellenic Research Foundation, Vas. Constantinou 48, 11635 Athens, Greece

Correspondence should be addressed to Dimitra Kovala-Demertzi, dkovala@cc.uoi.gr

Received 8 February 2010; Accepted 31 March 2010

Academic Editor: Spyros Perlepes

Copyright © 2010 Joanna Wiecek et al. This is an open access article distributed under the Creative Commons Attribution License, which permits unrestricted use, distribution, and reproduction in any medium, provided the original work is properly cited.

The synthesis and spectral characterization of novel diorganotin complexes with 3-hydroxypyridine-2-carbaldehyde thiosemicarbazone, **H₂L** (**1**), [SnMe₂(L)] (**2**), [SnBu₂(L)] (**3**), and [SnPh₂(L)] (**4**) are reported. The single-crystal X-ray structure of complex [SnPh₂(L)(DMSO)] (**5**) shows that the ligand is doubly deprotonated and is coordinated as tridentate ligand. The six coordination number is completed by two carbon atoms of phenyl groups. There are two similar monomers **5a** (Sn1) and **5b** (Sn51) in the asymmetric unit. The monomers **5a** and **5b** are linked through intermolecular hydrogen bonds of N–H–O and C–H–S type. C–H → π, intermolecular interactions, intra- and intermolecular hydrogen bonds stabilize this structure and leads to aggregation and a supramolecular assembly. The IR and NMR (¹H, ¹³C and ¹¹⁹Sn) spectroscopic data of the complexes are reported. The in vitro cytotoxic activity has been evaluated against the cells of three human cancer cell lines: MCF-7 (human breast cancer cell line), T-24 (bladder cancer cell line), A-549 (nonsmall cell lung carcinoma) and a mouse L-929 (a fibroblast-like cell line cloned from strain L). Compounds **1**, **3**, and **4** were found active against all four cell lines. Selectivity was observed for complexes **3** and **4** which were found especially active against MCF-7 and T-24 cancer cell lines.

1. Introduction

Organotin(IV) compounds find wide applications as catalysts and stabilizers, and certain derivatives are used as biocides, as antifouling agents and for wood preservation. It has been observed that several diorganotin adducts show potential as antineoplastic and antituberculosis agents [1–4].

Thiosemicarbazone derivatives are of considerable interest due to their antibacterial, antimalarial, antiviral, and antitumor activity [5, 6]. In our laboratory, the chemistry of thiosemicarbazones has been an extremely active area of research, primarily because of the beneficial biological (namely, antiviral and antitumor) activities of their transition-metal complexes [7–9]. 3-Hydroxypyridine-2-carbaldehyde thiosemicarbazone (**1**) is a member of the so-called α-(N)-heterocyclic carbaldehyde thiosemicarbazones

(HCTs), which are the most potent known inhibitors of ribonucleoside diphosphate reductase. Compounds (**1**) and 5-hydroxypyridine-2-carbaldehyde thiosemicarbazone have shown high anticancer activity in animal models but were found to be readily glucuronidated and rapidly excreted [10]. The multiple dissociation constants of the ligand **H₂L** (**1**) and the crystal structure of the complex of Pd(II) with **1**, [Pd(HL)Cl] have been studied by us [11]. This work is an extension of previously studied complexes of thiosemicarbazones with palladium(II), platinum(II), zinc(II), and organotin(IV) with potentially interesting biological activities [12–14].

The present paper includes the interaction of SnPh₂O (where R is methyl, butyl, and phenyl groups) with 3-Hydroxypyridine-2-carbaldehyde thiosemicarbazone (**H₂L**) and the crystal structure of the complex [SnPh₂(L)(DMSO)]

(5). IR and NMR spectroscopic data are reported. The results of the cytotoxic activity of diorganotin complexes have been evaluated for antiproliferative activity *in vitro* against human cancer cell lines: MCF-7, T-24, A-549, and a mouse L-929.

2. Experimental

2.1. General and Instrumental. All reagents were commercially available (Aldrich or Merck) and used as supplied. Solvents were purified and dried according to standard procedures. Melting points (m.p.) were determined in open capillaries and are uncorrected. IR and far-IR spectra were recorded on a Perkin Elmer Spectrum GX Fourier transform spectrophotometer using KBr pellets (4000–400 cm^{-1}) and nujol mulls dispersed between polyethylene disks (400–40 cm^{-1}). The free ligand was dissolved in $(\text{CD}_3)_2\text{SO}$ and ^1H , $^1\text{H}-^1\text{H}$ COSY and ^{13}C spectra were acquired on a BRUKER 300 MHz spectrometer. Compounds 2–4 were dissolved in CDCl_3 and were spectroscopically characterized by the use of ^1D and ^2D NMR spectroscopy on a Varian 600 MHz spectrometer. Experimental data were processed using VNMR and WinNMR routines. Chemical shifts (δ) are reported in ppm while spectra were referenced by the standard experimental setup. ^{119}Sn NMR spectra were acquired on the Varian 600 MHz and tin spectra were referenced by the use of external solution of Me_4Sn in C_6D_6 . The splitting of proton resonances in the reported ^1H -NMR spectra is defined as s = singlet, d = doublet, t = triplet, and m = multiplet. The chemical shifts are reported in ppm for ^1H and ^{13}C NMR. Elemental analyses were carried out by the microanalytical service of the University of Ioannina, Greece.

2.2. Synthesis of the Ligand and the Complexes

3-Hydroxypyridine-2-Carbaldehyde Thiosemicarbazone (1). The ligand was synthesized according to a published procedure [11]. The white powder was recrystallized from cold ethanol and was dried *in vacuo* over silica gel. Yield: 75%. Bright-yellow powder. M.p. 209°C. IR (cm^{-1}): 3555 s, 3451 m $\nu(\text{OH})$; 3291 m, 3194 m, $\nu(\text{NH}_2, \text{NH})$; 1639 s, $\nu(\text{C}=\text{N})$; 1229 s, $\nu(\text{C}-\text{O})$; 1098 s, $\nu(\text{NN})$; 827 s, $\nu(\text{C}=\text{S})$. ^1H -NMR: 11.50 (s, OH); 9.62 (s, H-N(3)); 8.12 (d, H-C(1), $^3\text{J} = 4.2$ Hz); 7.26 (dd, H-C(2), $^3\text{J} = 8.5$, $^4\text{J} = 4.2$ Hz); 7.30 (dd, H-C(3), $^3\text{J} = 8.4$, $^4\text{J} = 1.4$ Hz); 8.34 (s, H-C(6)); 8.00, 8.24 (br. s, NH_2). ^{13}C -NMR: 178.0 C(7); 153.1 C(4); 144.4 C(6); 141.1 C(1); 137.6 C(5); 125.3 C(2); 124.2 C(3). Anal. calc. for $\text{C}_7\text{H}_8\text{N}_4\text{OS}$ (196.04): C, 42.8; H, 4.1; N, 28.6; S, 16.3; found: C, 42.6; H, 3.9; N, 28.2; S, 16.0%.

$\text{SnMe}_2(\text{L})$ (2). Dimethyltin(IV) oxide (0.033 g, 0.2 mmole) and 3-hydroxypyridine-2-carbaldehyde thiosemicarbazone (0.0392 g, 0.2 mmole) in benzene (20 mL) were stirred and were refluxed for 12 hours under azeotropic removal of water (Dean-Stark trap). The resulting clear solution was rotary evaporated under vacuum to a small volume (2 mL), chilled and triturated with diethyl ether to give a white solid. The powder was recrystallized from distilled diethyl ether and dried *in vacuo* over silica gel to give yellow solid; mp.

228–230°C, Yield 35%. IR (cm^{-1}): 3296 m, $\nu(\text{NH}_2)$; 1580 s, $\nu(\text{C}=\text{N})$; 1176 s, $\nu(\text{C}-\text{O})$; 1111 s, $\nu(\text{NN})$; 804 w, $\nu(\text{C}=\text{S})$; 583 m, 564 $\nu(\text{Sn}-\text{C})$; 431 m, $\nu(\text{Sn}-\text{N})$; 231 m, $\nu(\text{Sn}-\text{O})$; 376s, $\nu(\text{Sn}-\text{S})$. ^1H -NMR: 8.09 (dd, H-C(1), $^3\text{J} = 4.2$, $^4\text{J} = 1.4$ Hz); 7.18 (dd, H-C(2), $^3\text{J} = 8.5$, $^4\text{J} = 4.2$ Hz); 7.08 (d, H-C(3), $^3\text{J} = 8.5$, $^4\text{J} = 1.4$ Hz); 8.76 (s, H-C(6)); 5.09 (br. s, NH_2); 0.89 (s, CH_3 , $^2\text{J} (^{117/119}\text{Sn}-^1\text{H}) = 35.7$ Hz). ^{13}C -NMR: 168.8 C(7); 163.4 C(4); 161.5 C(6); 140.2 C(1); 135.4 C(5); 127.6 C(2); 128.9 C(3); 6.22 (CH_3 , $\text{J} (^{117/119}\text{Sn}-^{13}\text{C}) = 309$ Hz). ^{119}Sn NMR: $\delta = -94.5$. Anal. calc. for $\text{C}_9\text{H}_{12}\text{N}_4\text{OSSn}$ (343.0): C, 31.5; H, 3.5; N, 16.3; S, 9.3; found: C, 31.5; H, 3.7; N, 16.0; S, 9.1 %.

$\text{SnBu}_2(\text{L})$ (3). Dibutyltin(IV) oxide (0.0498 g, 0.2 mmole) and 3-hydroxypyridine-2-carbaldehyde thiosemicarbazone (0.0392 g, 0.2 mmole) in benzene (20 mL) were stirred and were refluxed for 12 hours under azeotropic removal of water (Dean-Stark trap). The resulting clear solution was rotary evaporated under vacuum to a small volume (2 mL), chilled and triturated with diethyl ether to give a white solid. The powder was recrystallized from distilled diethyl ether and dried *in vacuo* over silica gel to give yellow solid; mp. 126–128°C, Yield 41%. IR (cm^{-1}): 3292 m, $\nu(\text{NH}_2)$; 1577 s, $\nu(\text{C}=\text{N})$; 1173 s, $\nu(\text{C}-\text{O})$; 1114 s, $\nu(\text{NN})$; 805 w, $\nu(\text{C}=\text{S})$; 578 ms, 560 sh $\nu(\text{Sn}-\text{C})$; 418 m, $\nu(\text{Sn}-\text{N})$; 247 m, $\nu(\text{Sn}-\text{O})$; 394 ms, $\nu(\text{Sn}-\text{S})$. ^1H -NMR: 8.05 (dd, H-C(1), $^3\text{J} = 4.2$, $^4\text{J} = 1.3$ Hz); 7.16 (dd, H-C(2), $^3\text{J} = 8.5$, $^4\text{J} = 4.2$ Hz); 7.07 (dd, H-C(3), $^3\text{J} = 8.5$, $^4\text{J} = 1.3$ Hz); 8.82 (s, H-C(6)); 5.22 (br. s, NH_2); 0.87 (t, 7.3 Hz, H δ); 1.32 (m, H γ); 1.54, 1.64 (H α , β). ^{13}C -NMR: 167.7 C(7); 162.5 C(4); 160.0 C(6); 138.7 C(1); 134.5 C(5); 126.8 C(2); 128.0 C(3); 26.9 (C α , $\text{J} (^{117/119}\text{Sn}-^{13}\text{C}) = 265$ Hz); 28.2 (C β); 27.3 (C γ); 14.6 (C δ). ^{119}Sn NMR: $\delta = -194.4$. Anal. calc. for $\text{C}_{16}\text{H}_{18}\text{N}_4\text{OSSn}$ (537.2): C, 42.2; H, 5.7; N, 13.1; S, 7.5; found: C, 42.0; H, 5.9; N, 13.2; S, 7.4 %.

$\text{SnPh}_2(\text{L})$ (4). Diphenyltin(IV) oxide (0.0578 g, 0.2 mmole) and 3-hydroxypyridine-2-carbaldehyde thiosemicarbazone (0.0392 g, 0.2 mmole) in benzene (20 mL) were stirred and were refluxed for 12 hours under azeotropic removal of water (Dean-Stark trap). The resulting clear solution was rotary evaporated under vacuum to a small volume (2 mL), chilled and triturated with diethyl ether to give a white solid. The powder was recrystallized from distilled diethyl ether and dried *in vacuo* over silica gel to give yellow solid; mp. 186–188°C, Yield 34%. IR (cm^{-1}): 3269 m, $\nu(\text{NH}_2)$; 1589 s, $\nu(\text{C}=\text{N})$; 1185 s, $\nu(\text{C}-\text{O})$; 1118 s, $\nu(\text{NN})$; 808 m, $\nu(\text{C}=\text{S})$; 322 ms, 303 sh $\nu(\text{Sn}-\text{C})$; 419 m, $\nu(\text{Sn}-\text{N})$; 248 m, $\nu(\text{Sn}-\text{O})$; 370 ms, $\nu(\text{Sn}-\text{S})$. ^1H -NMR: 8.02(d, H-C(1), $^3\text{J} = 4.2$ Hz); 7.18(dd, H-C(2), $^3\text{J} = 8.5$, $^4\text{J} = 4.2$ Hz); 7.29 (d, H-C(3), $^3\text{J} = 8.5$ Hz); 8.88 (s, H-C(6)); 5.37 (br. s, NH_2); 7.82 (d, 7.7 Hz, Ho-Ph); 7.34–7.30 (m, Hm, p-Ph). ^{13}C -NMR: 167.4 C(7); 164.0 C(4); 161.5 C(6); 140.2 C(1); 135.4 C(5); 127.8 C(2); 129.3 C(3); 142.1 (Sn-Cph, $\text{J} (^{117/119}\text{Sn}-^{13}\text{C}) = 424$ Hz); 135.8 (Co-Ph, $^2\text{J} (^{117/119}\text{Sn}-^{13}\text{C}) = 28$ Hz); 128.8 (Cm-Ph, $^3\text{J} (^{117/119}\text{Sn}-^{13}\text{C}) = 37$ Hz); 130.2 (Cp-Ph, $^4\text{J} (^{117/119}\text{Sn}-^{13}\text{C}) = 8.7$ Hz); ^{119}Sn NMR: $\delta = -227.2$. Anal. calc. for $\text{C}_{19}\text{H}_{16}\text{N}_4\text{OSSn}$ (663.1): C, 48.9; H, 3.5; N, 12.0; S, 6.9; found: C, 48.6; H, 3.5; N, 10.7; S, 6.8%.

TABLE 1: X-ray crystal data and structure refinement.

	5
Empirical formula	C ₂₁ H ₂₂ N ₄ O ₂ S ₂ Sn
Formula weight	545.24
Temperature/ (K)	100 (2)
Wavelength/ (Å)	0.71073
Crystal system	Triclinic
Space group	P-1
<i>a</i> (Å)	9.4663 (4)
<i>b</i> (Å)	14.7350 (7)
<i>c</i> (Å)	16.6374 (7)
α (°)	94.871 (4)
β (°)	96.434 (4)
γ (°)	90.793 (4)
Volume (Å ³)	2297.1 (2)
<i>Z</i>	4
Dc (Mg/m ³)	1.577
Absorption coefficient (mm ⁻¹)	1.319
F(000)	1096
Crystal size (mm)	0.32 × 0.28 × 0.16
Diffraction	Kuma KM4CCD
Theta range for data collection (°)	3.14–36.65
Ranges of <i>h</i> , <i>k</i> , <i>l</i>	–15 → 15, –24 → 20, –27 → 27
Reflections collected	35235
Independent reflections (Rint)	18670 (0.0381)
Completeness to 2 θ = 36.65	81.9%
Data/parameters	18670/541
Goodness-of-fit (<i>F</i> ²)	0.920
Final R1/wR2 indices [<i>I</i> > 2 σ (<i>I</i>)]	0.0336/0.0768
Largest diff. peak/hole (e/Å ³)	2.090/–1.098

2.3. *X-Ray Crystallography.* Crystals of complex **5**, suitable for X-ray analysis, were obtained by slow crystallization of **4** from a mixture of solvents C₆H₆/toluene/DMSO/CH₃CN. Crystal data **5** are given in Table 1, together with refinement details. All measurements of crystals were performed in low temperature using an Oxford Cryosystem device on a Kuma KM4CCD κ -axis diffractometer with graphite-monochromated Mo K α radiation. The data were corrected for Lorentz and polarization effects. No absorption correction was applied. Data reduction and analysis were carried out with the Oxford Diffraction (Poland) Sp. z o.o (formerly Kuma Diffraction Wroclaw, Poland) programs. Crystal structure was solved by direct methods (program SHELXS97) and refined by the full-matrix least-squares method on all *F*² data using the SHELXL97 [15] programs. Nonhydrogen atoms were refined with anisotropic displacement parameters; hydrogen atoms were included from geometry of molecules and $\Delta\rho$ maps. During the refinement process they treated as riding atoms. Molecular graphics were performed from PLATON2003 [16, 17].

Crystallographic data, that is, atomic coordinates, thermal parameters, bond lengths, and bond angles (CCDC number 634270 for **5**), have been deposited with the

Cambridge Crystallographic Data Centre. Copies of available material can be obtained, free of charge, on application to CCDC, 12 Union Road, Cambridge CB2 1EZ, UK, (fax: +44-1223-336033 or e-mail: deposit@ccdc.cam.ac.uk or http://www.ccdc.cam.ac.uk).

2.4. *Antiproliferative Assay In Vitro.* The results of cytotoxic activity in vitro are expressed as IC₅₀-the concentration of compound (in μ M) that inhibits a proliferation rate of the tumor cells by 50% as compared to control untreated cells. The compounds **1–4** were tested for their antiproliferative activity in vitro against the cells of four human cancer cell lines: against the cells of three human cancer cell lines: MCF-7 (human breast cancer cell line), T-24 (bladder cancer cell line), A-549 (nonsmall cell lung carcinoma), and a mouse fibroblast L-929 cell line.

Compounds. Test solutions of the compounds tested (1 mg/mL) were prepared by dissolving the substance in 100 μ L of DMSO completed with 900 μ L of tissue culture medium. Afterwards, the tested compounds were diluted in culture medium to reach the final concentrations of 100, 50, 10, 1 and 0.1 ng/ μ L. The solvent (DMSO) in the highest concentration used in test did not reveal any cytotoxic activity. *Cells.* The cell lines are maintained in the Cell Culture Collection of the University of Ioannina. Twenty-four hours before addition of the tested agents, the cells were plated in 96-well plates at a density of 10⁴ cells per well. The MCF-7 cells were cultured in the D-MEM (Modified Eagle's Medium) medium supplemented with 1% antibiotic and 10% fetal calf serum. L-929 cells were grown in Hepes-buffered RPMI 1640 medium supplemented with 10% fetal calf serum, penicillin (50 U/mL), and streptomycin (50 mg/mL). A-549 cells were grown in F-12K Ham's medium supplemented with 1% glutamine, 1% antibiotic/antimycotic, 2% NaHCO₃, and 10% fetal calf serum. The cell cultures were maintained at 37°C in a humid atmosphere saturated with 5% CO₂. Cell number was counted by the Trypan blue dye exclusion method. MCF-7, L-929, and A-549 cells were determined by the sulforhodamine B assay [18], while T-24 cells by the MTT assay [19]. The in vitro tests were performed as described previously [20].

3. Results and Discussion

3.1. Spectroscopy

3.1.1. *Infrared Spectroscopy.* The bands at 3555 and 3451 cm⁻¹ are assigned to ν (OH) mode while the medium-strong intensity bands at around 3291 and 3194 cm⁻¹ in the spectra of H₂L are assigned to ν (NH₂) and ν (NH), respectively. The significant changes in the ligand bands upon complexing are the decrease in ν (C=N) and increase in ν (N–N) and the absence of the large systematic shifts of $\nu_{as}(\text{NH}_2)$ to lower frequencies. These data indicate coordination through the nitrogen of the azomethine group and no interaction between the terminal amino nitrogen and the metal ion. The ν (CS) band at 827 cm⁻¹ is less intense

in the complexes **2–4** and is shifted to a lower frequency, suggesting coordination of the metal through sulfur. Coordination of the thiolato S-atom was further indicated by a decrease in the energy of the thioamide band as well as by the presence of a band at ca. 370 cm^{-1} assignable to $\nu(\text{Sn-S})$. An IR band at 1229 cm^{-1} for **1** was assigned to $\nu(\text{C-O})$. This band was found to be shifted to $1185\text{--}1173\text{ cm}^{-1}$, in the spectra of the complexes **2–4**. Coordination of the phenolic-O atom was further indicated by the presence of a band at ca. $250\text{--}230\text{ cm}^{-1}$ assignable to $\nu(\text{Sn-O})$. From the metal-ligand stretching vibrations, which are below 600 cm^{-1} , it is possible to assign the bands characteristic for $\nu(\text{SnC})$. Also, the bands at $394\text{--}370\text{ cm}^{-1}$ and $431\text{--}418\text{ cm}^{-1}$ are assigned to $\nu(\text{SnS})$ and $\nu(\text{SnN})$, respectively, and the bands at $250\text{--}230\text{ cm}^{-1}$ are assigned at $\nu(\text{SnO})$ stretching vibrations [20, 21].

3.1.2. NMR Spectra. ^1H and ^{13}C resonances of the ligand H_2L as well as of the complexes **2–4** bearing di-methyl, n-butyl, and phenyl groups attached to the central tin atom were unambiguously assigned by the use of 2D $^1\text{H}\text{--}^1\text{H}$ gCOSY, ^1H , $^{13}\text{C}\text{--HSQC}$, and ^1H , $^{13}\text{C}\text{--HMBC}$ experiments.

In the ^1H NMR spectra of (H_2L) (**1**) the broad singlet at δ 11.60 was attributed to OH group in accordance with [22] and the broad signal at δ 9.75 ppm was assigned to NH group. These two groups apparently participate in H-bonding with the nucleophilic solvent molecules (DMSO) or with other ligand molecules. These two signals are abolished upon interaction with the metal, indicating deprotonation of these groups and possible coordination to the tin(IV) atom at **2–4**. The absence of peaks corresponding to the imino proton NH and OH proton in the spectrum of **2–4** indicates that the nitrogen and oxygen are present in the deprotonated form and the ligand is dideprotonated. A sharp resonance peak appearing at ca. 5 ppm in all complexes is attributed to the NH_2 group. This is also confirmed by integration of the ^1H spectral profile while additionally the use of CDCl_3 eliminates the formation of H-bonding or complexation with the participation of solvent molecules as was the case with the ligand alone. In the ^1H -NMR spectra of the complexes **2–4**, the formyl H-atom H-C(6) was shifted upon coordination, which indicated variations in the electron density at position 6. This signal was shifted downfield, in accordance with a decreased electron density at site C6 in the complexes.

The C=S resonance of the thiosemicarbazone moiety in the free ligand resonated at 178.0 ppm. All complexes showed an upfield shift of C7 peak in the order of ~ 10 ppm compared with the free ligand, indicating the complexation of tin(IV) to the sulphur atom which apparently is related with an increased electron density at this site on complexation, due probably to π -back bonding for thiolato sulphur [21]. All the complexes exhibit downfield shifts of the C3, C4, and C6. This deshielding, in accordance with decreased electron density upon complexation, is indicative of Sn-O and Sn-N (azomethine nitrogen) bonds. These data indicate that the complexes are formed by ligand deprotonation followed by metallation, a structural motive that seems to be stable both

in the solid state and in CDCl_3 solution. ^{119}Sn chemical shifts of compounds **2–4** were found between -94.4 and -227.2 in accordance with five-coordinate tin center [23].

3.2. Molecular Structure. Crystals of complex **5**, suitable for X-ray analysis, were obtained by slow crystallization of **4** from a mixture of solvents C_6H_6 /toluene/DMSO/ CH_3CN . The crystal structure is shown in Figure 1. Crystal data are given in Table 1, together with refinement details. Bond lengths and angles are given in Table 2. There are two similar monomers **5a** (Sn1) and **5b** (Sn51) in the asymmetric unit. The double deprotonated ligand is coordinated as tridentate ligand *via* the phenolic oxygen O(1), the azomethine nitrogen N(3), and thiolato sulfur S(1) atoms. The molecule of DMSO is coordinated to the tin through oxygen O(2) atom. The six coordination number is completed by two carbon atoms of phenyl groups. The organic molecule acts as anionic tridentate with the ONS donors placed in the same side. The dianionic, tridentate ligand has a ZEZ configuration for the oxygen, nitrogen, and sulfur donor centers. The coordinated ligand consists of three rings, one heterocyclic and two chelates, SnSNNC and SnONCC, I and II, respectively. For monomers **5a** and **5b** the dihedral angles between the planes of the rings I and II are $14.47(6)$ and $12.59(6)^\circ$, respectively and between the ring II and the pyridyl ring are $7.4(5)$ and $8.1(2)^\circ$, respectively, indicating that the ligand as a whole in the two monomers deviates from planarity.

The C-S bond lengths $1.747(2)$, $1.749(2)$ Å for **5a** and **5b**, respectively, are shorter than a single bond (1.81 Å), but longer than a double bond (1.62 Å), suggesting partial single bond character. The C(14)-N(3) bond length, $1.301(2)$ Å, is close to a double bond (1.28 Å). The S-C bond distances are consistent with increased single-bond character while both thioamide C-N distances indicate increased double bond character. The negative charge of the deprotonated ligand is delocalized over the thiosemicarbazone moiety. This is indicative of the coordinated thiosemicarbazone's greater conjugation and more delocalized electron density. The Sn-N(3) bond distance is longer than the sum of the covalent radii (2.15 Å), which indicates strong bond, while the bond distance Sn-S, $2.5141(5)$, $2.519(5)$ Å, though much shorter than the sum of the van der Waals radii (4.0 Å), indicates a weak bond [21]. The C-Sn C bond angle is equal to $105.87(7)$, $104.58(7)^\circ$, and the bond angles C(7)-Sn-N(3) and C(1)-Sn-O(2) are $160.47(6)$, $165.59(6)$ and $162.80(6)$, $166.89(6)^\circ$ for **5a** and **5b**, respectively.

The two monomers **5a** and **5b** are linked through two intermolecular hydrogen bonds of N(51)-H(51B)-O(1) and of C(8)-H(8)-S(51) type (The N-O distance is $3.013(2)$ Å and the C-S distance is $3.673(2)$ Å). The monomers of **5a** form hydrogen-bonded dimers linked by two N(1)-H(1A)-N(4) hydrogen bonds involving the amino N(1)-H(1A) hydrogen atom and the pyridyl N(4) nitrogen. The monomers of **5a** are also linked by another C(14)-H(14)-N(2) hydrogen bond involving the formyl C(14)-H(14) hydrogen and the adjacent imino nitrogen N(2) and vice versa of centro-symmetrically related pairs of molecules. The observed hydrogen bonding patterns are of the DA=AD

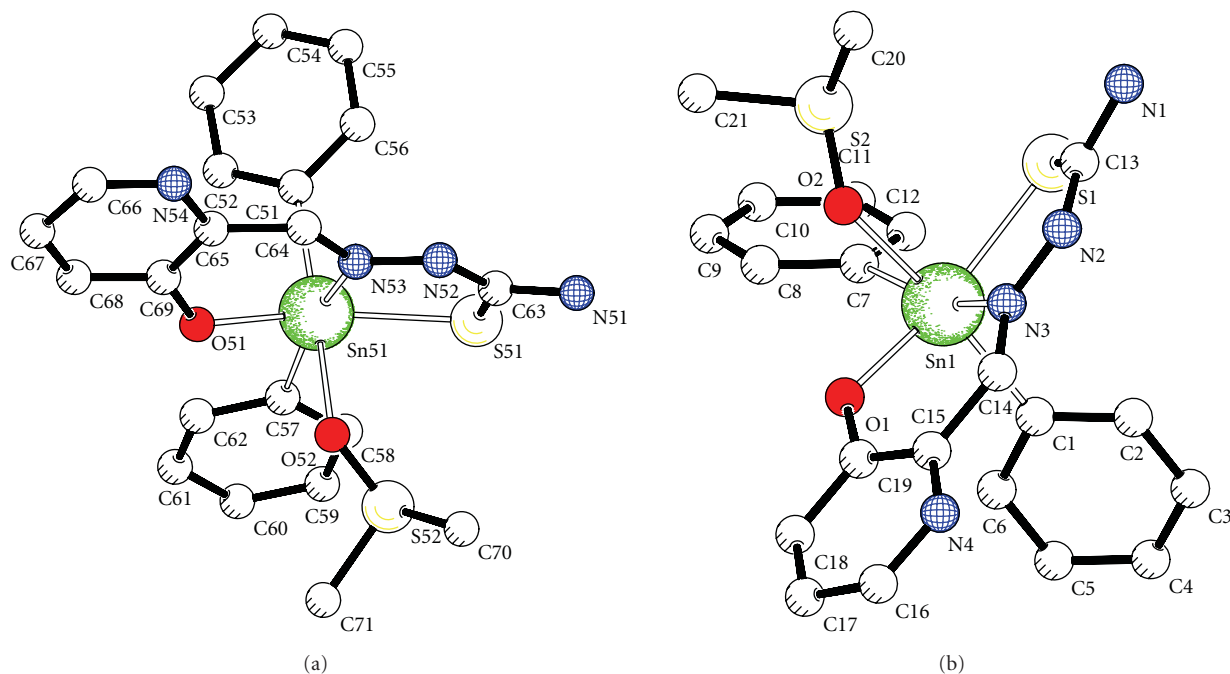


FIGURE 1: Molecular structure of the diorganotin complex 5.

TABLE 2: Bond lengths (Å) and angles (°) for complex 5.

5a		5b	
Sn(1)–S(1)	2.5141(5)	Sn(51)–S(51)	2.5190(5)
Sn(1)–O(1)	2.087(2)	Sn(51)–O(51)	2.088(2)
Sn(1)–O(2)	2.337(2)	Sn(51)–O(52)	2.345(2)
Sn(1)–N(3)	2.251(2)	Sn(51)–N(53)	2.262(2)
Sn(1)–C(1)	2.164(2)	Sn(51)–C(51)	2.157(2)
Sn(1)–C(7)	2.149(2)	Sn(51)–C(57)	2.151(2)
S(1)–C(13)	1.747(2)	S(51)–C(63)	1.749(2)
S(2)–O(2)	1.528(2)	S(52)–O(52)	1.528(2)
S(2)–C(20)	1.791(3)	S(52)–C(70)	1.777(3)
S(2)–C(21)	1.789(2)	S(52)–C(71)	1.787(3)
O(1)–C(19)	1.326(2)	O(51)–C(69)	1.320(2)
N(2)–N(3)	1.380(2)	N(52)–N(53)	1.375(2)
S(1)–Sn(1)–O(1)	156.25(4)	S(51)–Sn(51)–O(51)	155.68(4)
S(1)–Sn(1)–O(2)	84.87(3)	S(51)–Sn(51)–O(52)	83.23(3)
S(1)–Sn(1)–N(3)	77.37(4)	S(51)–Sn(51)–N(53)	77.71(4)
S(1)–Sn(1)–C(1)	101.71(5)	S(51)–Sn(51)–C(51)	100.07(5)
S(1)–Sn(1)–C(7)	95.51(5)	S(51)–Sn(51)–C(57)	100.30(5)
O(1)–Sn(1)–O(2)	76.08(5)	O(51)–Sn(51)–O(52)	77.25(5)
O(1)–Sn(1)–N(3)	84.11(5)	O(51)–Sn(51)–N(53)	83.46(5)
O(1)–Sn(1)–C(1)	94.05(6)	O(51)–Sn(51)–C(51)	95.98(6)
O(1)–Sn(1)–C(7)	97.14(6)	O(51)–Sn(51)–C(57)	93.14(6)
O(2)–Sn(1)–N(3)	75.34(5)	O(52)–Sn(51)–N(53)	75.65(5)
O(2)–Sn(1)–C(1)	165.59(6)	O(52)–Sn(51)–C(51)	166.89(6)
O(2)–Sn(1)–C(7)	86.01(6)	O(52)–Sn(51)–C(57)	87.15(6)
N(3)–Sn(1)–C(1)	93.44(6)	N(53)–Sn(51)–C(51)	92.55(7)
N(3)–Sn(1)–C(7)	160.47(6)	N(53)–Sn(51)–C(57)	162.80(6)
C(1)–Sn(1)–C(7)	105.87(7)	C(51)–Sn(51)–C(57)	104.58(7)

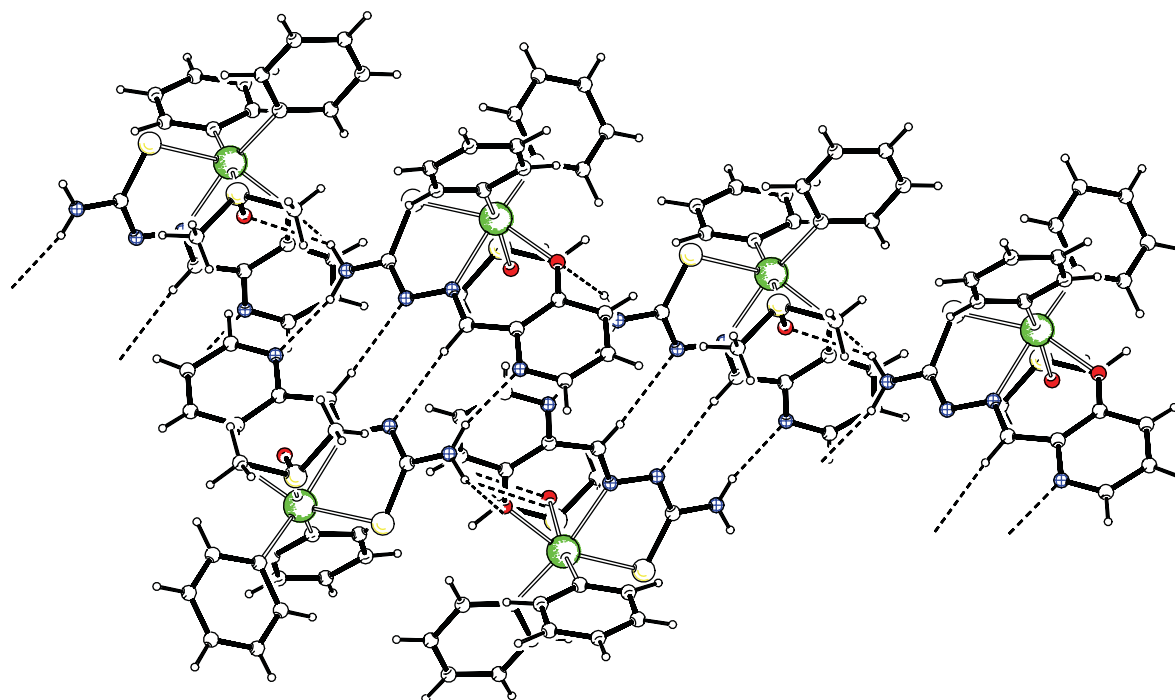


FIGURE 2: Arrangement of the intermolecular hydrogen bonds in 5.

TABLE 3: C–H \rightarrow π interactions and intermolecular hydrogen bonds for 5.

C–H(I) \rightarrow Cg(J) ^a		H–Cg	C–Cg	\angle C–H–Cg	
C(11)–H(11) [1] \rightarrow Cg(4) ⁽ⁱ⁾		2.71	3.5394	159	
C(60)–H(60) [2] \rightarrow Cg(5) ⁽ⁱⁱ⁾		2.66	3.4118	135	
D	H	A ^b	H \cdots A	D \cdots A	\angle D–H \cdots A
	N(1)–H(1A) \cdots N(4) ⁽ⁱⁱⁱ⁾		2.13	3.005(2)	165
	N(1)–H(1B) \cdots O(51) ^(iv)		2.28	3.065(2)	150
	N(1)–H(1B) \cdots O(52) ^(iv)		2.55	3.124(2)	124
	N(51)–H(51A) \cdots N(54) ^(v)		2.16	2.993(3)	168
	N(51)–H(51B) \cdots O(1)		2.24	3.013(2)	152
	C(8)–H(8) \cdots S(51)		2.84	3.673(2)	143
	C(14)–H(14) \cdots N(2) ⁽ⁱⁱⁱ⁾		2.50	3.442(2)	175
	C(58)–H(58) \cdots S(51)		2.85	3.564(2)	127
	C(62)–H(62) \cdots O(51)		2.55	3.132(2)	118
	C(64)–H(64) \cdots N(52) ^(v)		2.58	3.483(2)	174

^aWhere Cg(4) and Cg(5) are referred to the rings C(1)–C(6) and C(7)–C(12); ^bCg–Cg is the distance between ring centroids; symmetry transformations, (i) $1-x, -y, -z$; (ii) $1-x, 1-y, -z$; (iii) $1-x, -y, 1-z$; (iv) $x, -1+y, z$; (v) $2-x, 1-y, 1-z$.

type. Also, the monomers of **5b** form hydrogen-bonded dimers and are linked by two hydrogen bonds, the N(51)–H(51A)–N(54) and C(64)–H(64)–N(52) (Figure 2). C–H \rightarrow π intermolecular interactions intra- and intermolecular hydrogen bonds [24] stabilize this structure and lead to a supramolecular assembly, and Table 3 and Figure 3.

3.3. Pharmacology. Antiproliferative Activity In Vitro. Complexes of *N*4-ethyl 2-acetylpyridine thiosemicarbazone with platinum(II) or palladium(II) were tested in a panel of human tumor cell lines of different origins (breast, colon,

and ovary cancers) and *cis-platin*-refractory/resistant cell lines and were found to exhibit very remarkable growth inhibitory activities with mean IC₅₀ values of 0.9–0.5 nM and support the hypothesis that both [Pt(Ac4Et)₂] and [Pd(Ac4Et)₂] complexes can be characterized by cellular pharmacological properties distinctly different from those of *cis-platin* [8]. The complexes [ZnCl₂(Fo4Npypipe)] and [ZnCl₂(Ac4Npypipe)] where Fo4Npypipe and Ac4Npypipe are the monoion of 2-formyl pyridine N(4)-1-(2-pyridyl)-piperazinyl thiosemicarbazone and 2-acetyl pyridine N(4)-1-(2-pyridyl)-piperazinyl thiosemicarbazone have been evaluated in vitro against MCF-7, T-24, A-549, and L-929 cell

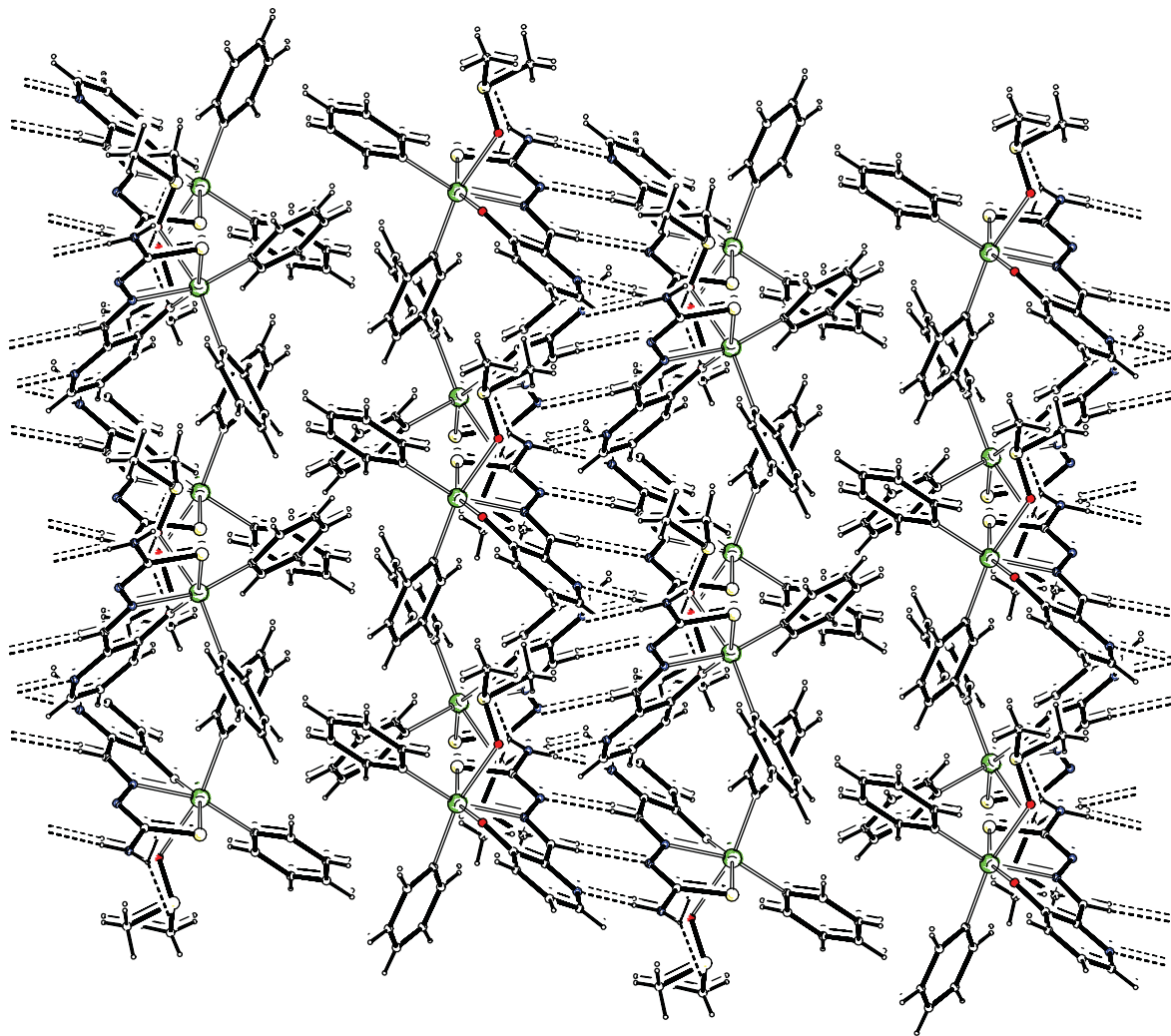
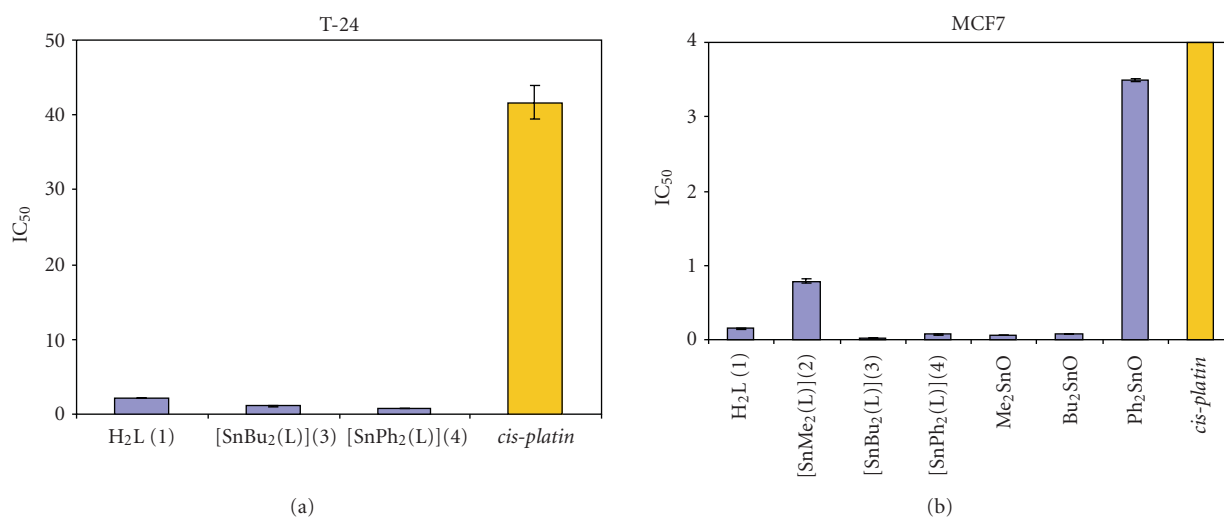

 FIGURE 3: A view of the extended network of 5 along the b axis.

 FIGURE 4: The antiproliferative activity in vitro expressed as $IC_{50} \pm SD$ (μM) against (a) T-24 and (b) MCF-7 cancer cell lines.

TABLE 4: The antiproliferative activity in vitro of 1–4, expressed as $IC_{50} \pm SD$ (μM) against MCF-7, T-24, A-549, and L-929 cancer cell lines.

	L929	A549	T24	MCF7
H₂L (1)	2.5 ± 0.03	0.81 ± 0.02	2.09 ± 0.03	0.153 ± 0.01
[SnMe ₂ (L)] (2)	7.29 ± 0.04	9.04 ± 0.05	<292	0.79 ± 0.03
[SnBu ₂ (L)] (3)	1.05 ± 0.02	0.77 ± 0.03	1.1 ± 0.05	1.97 × 10⁻² ± 0.2 × 10⁻²
[SnPh ₂ (L)] (4)	1.37 ± 0.03	0.83 ± 0.02	0.73 ± 0.02	7.28 × 10⁻² ± 0.5 × 10⁻²
Me ₂ SnO	<607	17.9 ± 0.86	<607	6.0 × 10⁻² ± 0.2 × 10⁻²
Bu ₂ SnO	<402	10.4 ± 0.41	<402	8.1 × 10⁻² ± 0.4 × 10⁻²
Ph ₂ SnO	10.7 ± 0.5	47.1 ± 0.49	<346	3.5 ± 0.02
cisplatin	0.69 ± 0.03	1.53 ± 0.10	41.66 ± 2.2	7.99 ± 0.31

lines and it was found to exhibit remarkable antiproliferative activity with mean IC_{50} values of 0.2–20 μM [12]. The diphenylorganotin(IV) complex with pyruvic acid thiosemicarbazone has been tested against MCF-7, T-24, A-549, and L-929 cell lines and was found especially active against MCF-7 and T-24 cancer cells [21].

The antiproliferative activity of compounds is presented in Table 4 along with the activity of *cis-platin* and diorganotin(IV) oxides. Results showed that the ligand as well as the complexes **3** and **4** demonstrated excellent antiproliferative activity, IC_{50} values range from 0.02–2.5 μM , against all cell lines tested, while for *cis-platin* the IC_{50} values range from 0.7–41 μM . The diorganotin(IV) oxides are nontoxic against L-929 and T-24 cancer cell lines and exhibit poor cytotoxic activity in A-549 and excellent antiproliferative activity against MCF-7 cancer cell line.

The ligand **1** is more cytotoxic compared to *cis-platin* against the A-549, T-24 and MCF-7 cell lines and less cytotoxic against L-929 cell lines. The diorganotin complex **2** is nontoxic against T-24 cell line, less cytotoxic against A-549 and L-929, and more cytotoxic against MCF-7 cell line compared to *cis-platin*. The diorganotin complexes **3** and **4** are in the same μM range compared to *cis-platin* against L-929 and A-549 cancer cell lines and more cytotoxic against T-24 and MCF-7 cancer cell lines. The IC_{50} values for the ligand, **1**, against MCF-7 and T-24 cell lines are 0.15 μM and 2.09 μM , respectively, and against A-549 and L-929 cell lines are 0.81 μM and 2.5 μM , respectively. Ligand is 19.8 ± 1.3 and 52.4 ± 4.6 times more active than *cis-platin* against T-24 and MCF-7 cell lines, respectively. The IC_{50} values for **3** against MCF-7 and T-24 cell lines are 1.97 × 10⁻² μM and 1.1 μM , respectively, and against A-549 and L-929 cell lines are 0.77 μM and 1.05 μM , respectively. Complex **3** is 403.6 ± 20.2 times more active than *cis-platin* against MCF-7 cell line and 37.9 ± 3.1 times more active than *cis-platin* against T-24 cell line. The IC_{50} values for **4** against MCF-7 and T-24 cell lines are 7.28 × 10⁻² μM and 0.73 μM , respectively, and against A-549 and L-929 cell lines are 0.83 μM and 1.37 μM , respectively. Complex **4** is 110.3 ± 9.9 times more active than *cis-platin* against MCF-7 cell line and 57.1 ± 3.9 times more active than *cis-platin* against T-24 cell line. Compounds **1**, **3**, and **4** were found active against all four cell lines. Selectivity was observed for complexes **3** and **4** which were found

especially active against MCF-7 and T-24 cancer cell lines. The mentioned evident differences in the antiproliferative action of the ligand and its diorganotin(VI) complexes indicate that these complexes really exist under the condition of the biological tests. Interestingly enough, **3** and **4** were found to be more potent cytotoxic agent than the prevalent benchmark metallodrug, *cis-platin*, under the same experimental conditions measured by us. The superior activity of **3** and **4** assumes significance in light of the fact that *cis-platin* is undisputedly the most studied and widely used metallopharmaceutical for cancer therapy known to date. It is noteworthy the high selectivity against MCF-7 and T-24 cancer cell lines.

Acknowledgment

The first author thanks I.K.Y. for a scholarship for her Ph.D. The authors also thank the NMR centre of ten University of Ioannina. This paper is dedicated to Professor Dr. N. Hadjiliadis for his contribution to the advancement of inorganic chemistry in Greece.

References

- [1] S. J. Blunden, P. A. Cusack, and R. Hill, *Industrial Uses of Tin Chemicals*, Royal Society of Chemistry, London, UK, 1985.
- [2] V. Chandrasekhar, S. Nagendran, and V. Baskar, "Organotin assemblies containing Sn-O bonds," *Coordination Chemistry Reviews*, vol. 235, no. 1-2, pp. 1–52, 2002.
- [3] S. Tabassum and C. Pettinari, "Chemical and biotechnological developments in organotin cancer chemotherapy," *Journal of Organometallic Chemistry*, vol. 691, no. 8, pp. 1761–1766, 2006.
- [4] D. Kovala-Demertzi, "Recent advances on non-steroidal anti-inflammatory drugs, NSAIDs: organotin complexes of NSAIDs," *Journal of Organometallic Chemistry*, vol. 691, no. 8, pp. 1767–1774, 2006.
- [5] H. Beraldo and D. Gambino, "The wide pharmacological versatility of semicarbazones, thiosemicarbazones and their metal complexes," *Mini-Reviews in Medicinal Chemistry*, vol. 4, no. 1, pp. 31–39, 2004.
- [6] A. Gomez Quiroga and C. Navarro Ranninger, "Contribution to the SAR field of metallated and coordination complexes: studies of the palladium and platinum derivatives with

- selected thiosemicarbazones as antitumoral drugs,” *Coordination Chemistry Reviews*, vol. 248, no. 1-2, pp. 119–133, 2004.
- [7] D. Kovala-Demertzi, M. A. Demertzis, E. Filiou, et al., “Platinum(II) and palladium(II) complexes with 2-acetyl pyridine 4N-ethyl thiosemicarbazone able to overcome the *cis*-platin resistance. Structure, antibacterial activity and DNA strand breakage,” *BioMetals*, vol. 16, no. 3, pp. 411–418, 2003.
- [8] D. Kovala-Demertzi, A. Boccarelli, M. A. Demertzis, and M. Coluccia, “In vitro antitumor activity of 2-acetyl pyridine 4N-ethyl thiosemicarbazone and its platinum(II) and palladium(II) complexes,” *Chemotherapy*, vol. 53, no. 2, pp. 148–152, 2007.
- [9] D. Kovala-Demertzi, P. Nath Yadav, J. Wiecek, S. Skoulika, T. Varadinova, and M. A. Demertzis, “Zinc(II) complexes derived from pyridine-2-carbaldehyde thiosemicarbazone and (1E)-1-pyridin-2-ylethan-1-one thiosemicarbazone. Synthesis, crystal structures and antiproliferative activity of zinc(II) complexes,” *Journal of Inorganic Biochemistry*, vol. 100, no. 9, pp. 1558–1567, 2006.
- [10] R. A. Finch, M.-C. Liu, S. P. Grill, et al., “Triapine (3-aminopyridine-2-carboxaldehyde-thiosemicarbazone): a potent inhibitor of ribonucleotide reductase activity with broad spectrum antitumor activity,” *Biochemical Pharmacology*, vol. 59, no. 8, pp. 983–991, 2000.
- [11] M. A. Demertzis, P. Nath Yadav, and D. Kovala-Demertzi, “Palladium(II) complexes of the thiosemicarbazone and N-ethylthiosemicarbazone of 3-hydroxypyridine-2-carbaldehyde: synthesis, properties, and X-ray crystal structure,” *Helvetica Chimica Acta*, vol. 89, no. 9, pp. 1959–1970, 2006.
- [12] D. Kovala-Demertzi, A. Papageorgiou, L. Papathanasis, et al., “In vitro and in vivo antitumor activity of platinum(II) complexes with thiosemicarbazones derived from 2-formyl and 2-acetyl pyridine and containing ring incorporated at N(4)-position: synthesis, spectroscopic study and crystal structure of platinum(II) complexes with thiosemicarbazones, potential anticancer agents,” *European Journal of Medicinal Chemistry*, vol. 44, no. 3, pp. 1296–1302, 2009.
- [13] D. Kovala-Demertzi, V. Dokorou, A. Primikiri, et al., “Organotin meclofenamic complexes: synthesis, crystal structures and antiproliferative activity of the first complexes of meclofenamic acid—novel anti-tuberculosis agents,” *Journal of Inorganic Biochemistry*, vol. 103, no. 5, pp. 738–744, 2009.
- [14] D. Kovala-Demertzi, A. Alexandratos, A. Papageorgiou, P. Nath Yadav, P. Dalezis, and M. A. Demertzis, “Synthesis, characterization, crystal structures, in vitro and in vivo antitumor activity of palladium(II) and zinc(II) complexes with 2-formyl and 2-acetyl pyridine N(4)-1-(2-pyridyl)-piperazinyl thiosemicarbazone,” *Polyhedron*, vol. 27, no. 13, pp. 2731–2738, 2008.
- [15] G. M. Sheldrick, “Phase annealing in shelx-90- direct methods for larger structures,” *Acta Crystallographica Section A*, vol. 46, pp. 467–473, 1990.
- [16] G. M. Sheldrick, “SHELXL-97,” Program for the Refinement of Crystal Structures, University of Goettingen, Goettingen, Germany, 1997.
- [17] A. L. Spek, *PLATON, A Multipurpose Crystallographic Tool*, Utrecht University, Utrecht, The Netherlands, 2003.
- [18] P. Skehan, R. Storeng, D. Scudiero, et al., “New colorimetric cytotoxicity assay for anticancer-drug screening,” *Journal of the National Cancer Institute*, vol. 82, no. 13, pp. 1107–1112, 1990.
- [19] M. Ohno and T. Abe, “Rapid colorimetric assay for the quantification of leukemia inhibitory factor (LIF) and interleukin-6 (IL-6),” *Journal of Immunological Methods*, vol. 145, no. 1-2, pp. 199–203, 1991.
- [20] K. Nakamoto, *Infrared and Raman Spectra of Inorganic and Coordination Compounds*, John Wiley & Sons, New York, NY, USA, 4th edition, 1986.
- [21] J. Wiecek, V. Dokorou, Z. Ciunik, and D. Kovala-Demertzi, “Organotin complexes of pyruvic acid thiosemicarbazone: synthesis, crystal structures and antiproliferative activity of neutral and cationic diorganotin complexes,” *Polyhedron*, vol. 28, no. 15, pp. 3298–3304, 2009.
- [22] A. Lycka, J. Jirman, and J. Holecek, “Magnitudes and relative signs of J(Sn-119, C-13) and J(Sn-119, H) coupling-constants in some organotin(IV) compounds using 2D Nmr methods,” *Magnetic Resonance in Chemistry*, vol. 29, no. 12, pp. 1212–1215, 1991.
- [23] B. Wrackmeyer, “¹¹⁹Sn-NMR parameters,” *Annual Reports on NMR Spectroscopy*, vol. 16, pp. 73–186, 1985.
- [24] M. C. Etter, “Encoding and decoding hydrogen-bond patterns of organic compounds,” *Accounts of Chemical Research*, vol. 23, no. 4, pp. 120–126, 1990.

Research Article

Synthesis and Biological Evaluation of New CRH Analogues

Spyridon Papazacharias,¹ Vassiliki Magafa,¹ Nicole Bernad,² George Pairas,¹
Georgios A. Spyroulias,¹ Jean Martinez,² and Paul Cordopatis¹

¹Laboratory of Pharmacognosy and Chemistry of Natural Products, Department of Pharmacy, University of Patras, 26500 Patras, Greece

²Institut des Biomolécules Max Mousseron (IBMM), UMR-CNRS, Faculté de Pharmacie, Universités Montpellier 1 et 2, 15 Av. C. Flahault, 34093 Montpellier, France

Correspondence should be addressed to Vassiliki Magafa, magafa@upatras.gr

Received 24 February 2010; Accepted 20 April 2010

Academic Editor: Spyros Perlepes

Copyright © 2010 Spyridon Papazacharias et al. This is an open access article distributed under the Creative Commons Attribution License, which permits unrestricted use, distribution, and reproduction in any medium, provided the original work is properly cited.

A series of 7 new human/rat Corticotropin Releasing Hormone (h/r-CRH) analogues were synthesized. The induced alterations include substitution of Phe at position 12 with D-Phe, Leu at positions 14 and 15 with Aib and Met at positions 21 and 38 with Cys(Et) and Cys(Pr). The analogues were tested regarding their binding affinity to the CRH-1 receptor and their activity which is represented by means of percentage of maximum response in comparison to the native molecule. The results indicated that the introduction of Aib, or Cys derivatives although altering the secondary structure of the molecule, did not hinder receptor recognition and binding.

1. Introduction

Ever since its identification by Vale et al. [1], Corticotropin Releasing Hormone (CRH) has proven to be a major neuromodulator responsible not only for the secretion of ACTH by the anterior pituitary gland but also for the regulation of the endocrine, autonomic, immunological and behavioral responses to stress [2–4]. Furthermore, this 41-amino acid neuropeptide displays a plethora of additional roles in either physiological homeostasis or pathogenic manifestations varying from the well-established implication on neuropsychiatric disorders [5, 6] to the yet to be clarified actions on various forms of cardiovascular diseases [7] obesity [8] or gut motility [9], among others. A series of studies demonstrating the extent and perplexity of the roles and implications of CRH led to the identification of other peptides appearing to possess a similar role [10–13].

Both the isolation and characterization of the CRH family receptors has been achieved revealing two receptor subtypes, one of them appearing as three splice variants (CRH-R1, CRH-R2 α , CRH-R2 β , and CRH-R2 γ). A binding

protein (CRH-BP) was also described [14–18]. The most-studied receptor types are CRH-R1, CRH-R2 α , and CRH-R2 β not only due to their vast distribution but also for their implication in physiological functions or disorders of great importance. CRH-R1 is broadly distributed in the brain and the pituitary gland but also appears in a number of peripheral tissues [19]. It possesses a critical role in mediating the hypophysiotropic action of CRH [20] but furthermore is involved in anxiogenic behaviours, depression and anxiety [21], anorexia and bulimia, drug seeking and withdrawal, and seizure [22, 23]. CRH-R2 α is mainly a brain receptor whereas CRH-R2 β is largely expressed in the periphery. The role of CRH-R2 is more diverse since it extends from “stress-coping” responses (anxiolysis, hypotension) to gastric emptying, regulation of energy expenditure, anti-inflammatory, and other actions of CRH [24]. However, further and complete understanding of the hormone-receptor interaction on its chemical basis is essential mainly since it can provide a solid basis for the development of CRH analogues with potent therapeutical implications.

Two distinct categories of CRH receptor ligands (of either agonistic or antagonistic character) have been developed, namely, peptide and nonpeptide ligands. The latter are unambiguously a large and diverse family but only few of these small molecules entered clinical development and still none of them found its way to the market [25]. The former category is more likely to yield clear information regarding the interaction between the peptide and its receptor.

Towards this goal, extensive SAR studies have been carried out. Single amino acid modification studies identified the key regions of the peptide for agonist/antagonist properties as well as for the receptor binding affinity. Based on these studies, the assignment of the molecule's secondary structure was feasible leading to the establishment of an α -helical structure (showing high amphiphilicity) for CRH-related peptides as the preferred conformation [9]. Notably, the helical nature of the molecule varies from 20% in solution to 80% upon binding [26].

A hypothesis was that stabilization of the α -helix could affect positively the activity of either agonists or antagonists. Subsequent studies affirmed this conjecture establishing that conformationally restrained analogues present increased potency. In addition, modifications on hydrophilicity/hydrophobicity or acidity/basicity of some residues were crucial in altering the potency of an analogue [26].

Introduction of D-amino acids leading to stabilization of β -turns, can provide analogues with increased potency but not all residues are susceptible to such an alteration, leading even to the opposite effect. However, the D-Phe¹² substitution has proven to be a favorable one especially combined with other advantageous modifications such as the replacement of Met at positions 21 and 38 with Nle. Thus, it has been shown that [D-Phe¹²]CRH is twice as potent and [D-Phe¹², Nle^{21,38}]CRH₂₁₋₄₁ is 15 times more potent than α -helical CRH [26].

The present study presents the synthesis of 7 new h/r-CRH analogues bearing minor modifications on the key amino acids side chain, regarding their electrochemical nature (Table 1). Specifically, we discuss the replacement of Leu at positions 14 and 15 with α -Aminoisobutyric acid (Aib), which apart from introducing a bend in the peptide backbone can stabilize the α -helix structure [27, 28], and also the replacement of Met at positions 21 and 38. The amino acids used for the latter modification are Cysteine(Ethyl) [Cys(Et)], an isoster of Met and Cysteine(Propyl) [Cys(Pr)] that possesses a slightly more hydrophobic side chain than Cys(Et). The analogues were tested regarding their ability to induce the formation of intracellular cAMP in comparison to natural CRH measured by means of luciferase activity.

2. Experimental

2.1. Materials. 2-chlorotrityl-chloride resin bearing a Rink-Bernatowitz linker and 9-Fluorenylmethoxycarbonyl (Fmoc)-protected amino acids were supplied by CBL Patras. All solvents and reagents used for solid-phase peptide synthesis were purchased from Bachem AG and

Novabiochem and were used without further purification being of analytical quality. Nonnatural amino acid derivatives Cysteine (Ethyl) [Cys(Et)] and Cysteine (Propyl) [Cys(Pr)] were prepared according to literature [29].

2.2. Peptide Synthesis and Purification. Synthesis of the analogues was performed via Fmoc solid phase methodology [30] utilizing either Rink Amide MBHA resin [31] or 2-chlorotrityl-chloride resin [32] bearing a Rink-Bernatowitz linker [33] to provide the peptide amide. The side-chain protection used for the Fmoc-protected amino acids was the trityl group (Trt) for His, Asn, and Gln, the *tert*-butyl group (Bu^t) for Asp, Tyr, Glu, Ser and Thr, the *tert*-butyloxy-carbonyl group (Boc) for Lys and the 2,2,4,6,7-pentamethyl-dihydrobenzofuran-5-sulphonyl group (Pbf) for Arg. Stepwise synthesis of the peptide analogues was preferred to convergent synthesis due to the lack of Gly or Pro moieties at convenient positions in the amino acid sequence. The amino acids were coupled at three-fold excess using diisopropylcarbodiimide/1-hydroxybenzotriazole (DIC/HOBt) [34, 35] in Dimethylformamide (DMF) and, if necessary, 2-(1H-benzotriazole-1-yl)-1,1,3,3-tetramethyluroniumhexafluorophosphate (TBTU)/HOBt/diisopropyl ethylamine (DIEA) in DMF [36]. After 2 hours coupling time at room temperature, the ninhydrin test [37] was performed to estimate the completeness of the reaction with the exception of coupling on a Pro residue where the Chloranil test was employed to confirm reaction's completion point [38]. Fmoc groups were removed by treatment with 20% piperidine in DMF for 5 minutes followed by a prolonged treatment with the same solution for 20 minutes to ensure complete removal. The final cleavage of the peptide from the solid support together with the removal of the side-chain protecting groups was accomplished by treatment with a solution (15 mL/g peptide resin) of trifluoroacetic acid (TFA)/1,2-ethanedithiol/anisole/triethylsilane/water (94:2.5:0.5:1.5:1.5, v/v) for 4 hours at room temperature. The obtained mixture underwent solvent evaporation followed by anhydrous ethyl ether precipitation to yield the final crude peptide.

All the products were purified by gel filtration chromatography on Sephadex G-25 (fine) using 25% acetic acid as eluent. Final purification was achieved by preparative high performance liquid chromatography (HPLC, Pharmacia LKB-2250) on reversed-phase support C-18 with a linear gradient from 30 to 85% acetonitrile (0.1% TFA) for 35 minutes at a flow rate 1.5 mL/min and UV detection at 230 and 254 nm. The appropriate fractions were pooled and lyophilized. Analytical HPLC (Pharmacia LKB-2210) equipped with a Nucleosil 100 C₁₈ column (5 μ m particle size; 250 \times 4.6 mm) produced single peaks with at least 98% of the total peptide peak integrals. The solvent system used was the same as that for the semipreparative HPLC. All products gave single spots on thin layer chromatography (TLC, Merck precoated silica gel plates, type G₆₀-F₂₅₄) in the solvent systems: (A) 1-butanol: acetic acid: water (4:1:5, upper phase) and (B) 1-butanol: acetic acid: water: pyridine (15:3:10:6). The final characterization of the peptide sequence was

TABLE 1: Structure of synthesized CRH analogues.

	Human/Rat CRH	Analogue 1	Analogue 2	Analogue 3	Analogue 4	Analogue 5	Analogue 6	Analogue 7
1	S							
2	E							
3	E							
4	P							
5	P							
6	I							
7	S							
8	L							
9	D							
10	L							
11	T							
12	<u>E</u>	D-phe						
13	H							
14	<u>L</u>	Aib						
15	<u>L</u>		Aib					
16	R							
17	E							
18	V							
19	L							
20	E							
21	<u>M</u>			Cys(Et)		Cys(Et)	Cys(Pr)	Cys(Pr)
22	A							
23	R							
24	A							
25	E							
26	Q							
27	L							
28	A							
29	Q							
30	Q							
31	A							
32	H							
33	S							
34	N							
35	R							
36	K							
37	L							
38	<u>M</u>				Cys(Pr)	Cys(Pr)	Cys(Et)	Cys(Pr)
39	E							
40	I							
41	I							

achieved by Electrospray Ionisation-Mass Spectrometry (ESI-MS, Micromass-Platform LC instrument). An example of analytical HPLC-chromatograms and ESI-MS spectrum are shown in Figure 1 for analogue 7. The physiochemical properties of the new analogues are summarized in Table 2.

2.3. *Biological Assays.* The capacity of CRH and related peptide analogues to stimulate cyclic AMP generation was monitored in LLC-PK1 cells cotransfected with cDNA of

CRH-R1 and CRE. For transfection the method of electroporation was applied and 40 millions of LLC-PK1 cells were prepared and washed in cytomix 1X transfection medium. The electroporation medium consisted of 1000 μ L of cytomix 2X, 864 μ L of sterilized water, 80 μ L of ATP 50 mM, 3.2 mg of glutathion, 20 μ g of CRH-R1 cDNA and 20 μ g of CRE cDNA. 500 μ L of the above solution were transferred in the electroporation device and after remaining for 10 minutes a standard growth medium was added (DMEM without

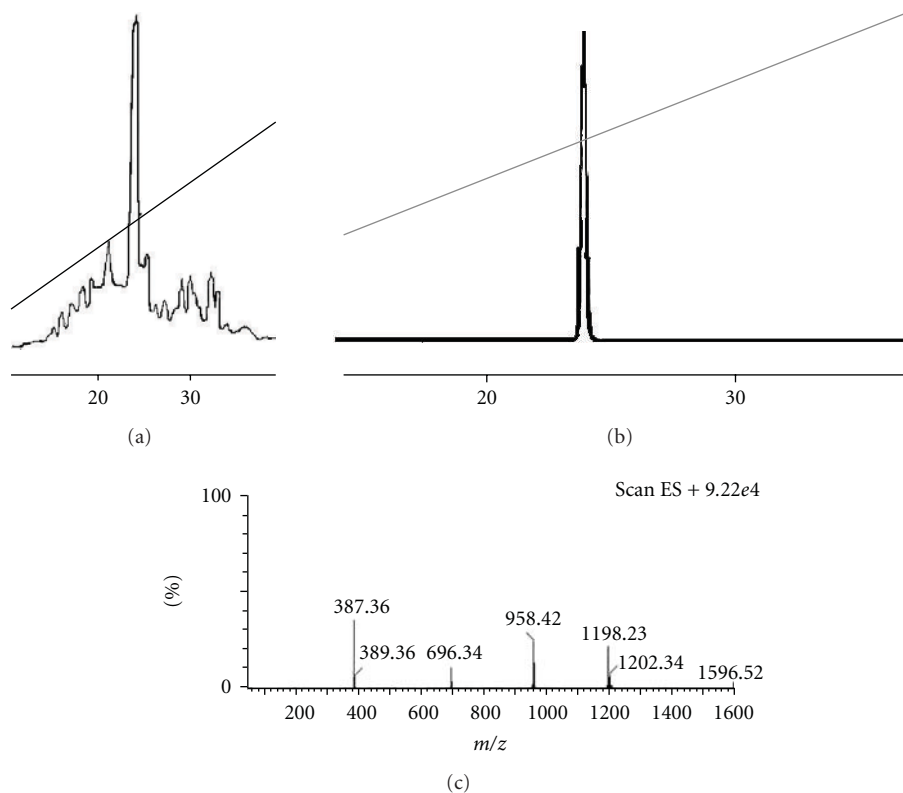


FIGURE 1: (a) Analytical HPLC chromatogram of crude analogue [D-Phe¹², Cys(Pr)²¹, Cys(Pr)³⁸]CRH previously chromatographed on a semipreparative C18 column. (b) Analytical HPLC chromatogram of analogue [D-Phe¹², Cys(Pr)²¹, Cys(Pr)³⁸]CRH upon rechromatography on the same column. (c) Mass spectra of analogue [D-Phe¹², Cys(Pr)²¹, Cys(Pr)³⁸]CRH resulting from ESI-MS analysis [$MW_{\text{calc}} = 4785.58$; $(M + 4)_{\text{obs}}^{4+}/4 = 1198.2$; $(M + 3)_{\text{obs}}^{3+}/3 = 1596.5$].

TABLE 2: Physicochemical properties of h/r-CRH analogues used in the present study.

	Analogues	Yield ^a (%)	HPLC ^b		TLC, R_f^c	
			t_R (min)	A	B	
1	[D-Phe ¹² , Aib ¹⁴]CRH	41	22.79	0.22	0.39	
2	[D-Phe ¹² , Aib ¹⁵]CRH	38	22.85	0.21	0.38	
3	[D-Phe ¹² , Cys(Et) ²¹]CRH	39	23.05	0.19	0.37	
4	[D-Phe ¹² , Cys(Pr) ³⁸]CRH	37	23.28	0.20	0.36	
5	[D-Phe ¹² , Cys(Et) ²¹ , Cys(Pr) ³⁸]CRH	33	24.07	0.18	0.35	
6	[D-Phe ¹² , Cys(Pr) ²¹ , Cys(Et) ³⁸]CRH	35	23.99	0.17	0.33	
7	[D-Phe ¹² , Cys(Pr) ²¹ , Cys(Pr) ³⁸]CRH	36	24.32	0.17	0.34	

^aYields were calculated on the basis of the amino acid content of the resin. All peptides were at least 98% pure.

^bFor elution conditions, see the Experimental Section.

^cSolvent systems and conditions are reported in the Experimental Section.

phenol red with glutamine, antibiotics, and 10% FCS) to a total volume of 50 mL. The suspension was distributed in 8 plates of 24 wells each, by adding 1 mL per well, and was allowed to pre-incubate for 24 hours. The growth medium was aspirated and replaced with fresh one followed by another preincubation for 24 hours. The cells were then challenged with graded concentrations (10^{-6} to 10^{-11} M) of the test peptides and incubated for 7 hours at 37°C. After that, the medium with the added peptides was removed, the cells were washed twice with PBS 1X, 100 μ L of lysis buffer 1X per well were added, the plates were left at

room temperature for 30 minutes and then stored at -80°C overnight. The luciferase activity was measured with the use of a luminometer after the addition of 50 μ L of lysed cell preparation and 50 μ L of bioluminescence medium per well in a 96 well plate luminometer.

3. Results

3.1. Peptide Synthesis and Purification. All analogues shown in Table 2 were synthesized either manually or automatically

TABLE 3: Binding affinities of h/r-CRH analogues.

	Analogues	Binding affinity ^a IC ₅₀ (nM)
	h/r-CRH	17.3
1	[D-Phe ¹² , Aib ¹⁴]CRH	226
2	[D-Phe ¹² , Aib ¹⁵]CRH	8.4
3	[D-Phe ¹² , Cys(Et) ²¹]CRH	28.5
4	[D-Phe ¹² , Cys(Pr) ³⁸]CRH	35
5	[D-Phe ¹² , Cys(Et) ²¹ , Cys(Pr) ³⁸]CRH	7.0
6	[D-Phe ¹² , Cys(Pr) ²¹ , Cys(Et) ³⁸]CRH	3.4
7	[D-Phe ¹² , Cys(Pr) ²¹ , Cys(Pr) ³⁸]CRH	17.3

^aThe values given are averages from 3 experiments performed in duplicates.

TABLE 4: Biological activity of h/r-CRH analogues.

	Analogues	Biological activity
	h/r-CRH	100% activity (Full agonist)
1	[D-Phe ¹² , Aib ¹⁴]CRH	(Partial Agonist, 60% Response max/CRH)
2	[D-Phe ¹² , Aib ¹⁵]CRH	(Partial Agonist, 60% Response max/CRH)
3	[D-Phe ¹² , Cys(Et) ²¹]CRH	(Full Agonist, 110% Response max/CRH)
4	[D-Phe ¹² , Cys(Pr) ³⁸]CRH	(Partial Agonist, 60% Response max/CRH)
5	[D-Phe ¹² , Cys(Et) ²¹ , Cys(Pr) ³⁸]CRH	(Partial Agonist, 70% Response max/CRH)
6	[D-Phe ¹² , Cys(Pr) ²¹ , Cys(Et) ³⁸]CRH	(Partial Agonist, 60% Response max/CRH)
7	[D-Phe ¹² , Cys(Pr) ²¹ , Cys(Pr) ³⁸]CRH	(Partial Agonist, 80% Response max/CRH)

on the Rink Amide MBHA resin or the 2-chlorotrityl-chloride resin bearing a Rink-Bernatowitz linker as solid support by using standard coupling procedures and Fmoc/Bu^t strategy. The overall yield of the syntheses of the CRH analogues was in the range 33–41% (calculated on the amount of linker initially coupled to the resin). Higher yields were obtained using the Rink Amide MBHA as solid support.

The synthetic procedure did not present significant complications due to the highly helical nature of the analogues despite the considerable size of the CRH analogues. ESI mass spectrometry confirmed that the purified products were indeed the desired peptides and analytical HPLC revealed a purity of over than 98% for the synthetic analogues.

3.2. Biological Activity. The results of the biological evaluation regarding the synthesized analogues are set out in Tables 3 and 4. The IC₅₀ values (Table 3) indicate a not very wide but nonetheless notable variety in the affinity to the receptor for the studied analogues. Specifically, three of the analogues, namely, [D-Phe¹², Aib¹⁵]CRH, [D-Phe¹², Cys(Et)²¹, Cys(Pr)³⁸]CRH, and [D-Phe¹², Cys(Pr)²¹, Cys(Et)³⁸]CRH, present a higher affinity to the receptor (IC₅₀=8.4 nM, IC₅₀=7.0 nM and IC₅₀=3.4 nM, resp.) which is approximately 2, 2.5, and 5 times that of the natural h/r-CRH (IC₅₀=17.3 nM). [D-Phe¹², Aib¹⁴]CRH is the analogue that presents the higher IC₅₀ value (226 nM) indicating a smaller affinity to the receptor, roughly 13 times lower than that of the hormone. The other three analogues appear to have the same ([D-Phe¹², Cys(Pr)²¹, Cys(Pr)³⁸]CRH, IC₅₀=17.3 nM) or slightly

reduced ([D-Phe¹², Cys(Et)²¹]CRH, IC₅₀=28.5 nM and [D-Phe¹², Cys(Pr)³⁸]CRH, IC₅₀=35.0 nM) affinity compared to CRH.

Regarding the activity of the analogues which is represented by means of percentage of maximum response compared to that of h/r-CRH (Table 4), the only analogue that presents a higher percentage is [D-Phe¹², Cys(Et)²¹]CRH (full agonist, 110% response max/CRH). All other analogues are partial agonists and induce a maximum response that varies between 60 and 80 per cent of the maximum response induced by CRH.

4. Discussion

The design and synthesis of the seven analogues was based on observations and results already mentioned above and likely to yield products with desirable properties. D-Phe¹² substitution was a modification present in all analogues since it brings only a positive contribution to the potency and the activity of the analogue. Substitution of Leu at positions 14 and 15 with Aib was based on studies demonstrating that α -aminoisobutyric acid is a helix-promoter/stabilizer, which increases the helix propensity of a peptide fragment towards, either α - or 3_{10} -helix, by restriction of the backbone conformational freedom. Aib, on the other hand, apart from its tendency to form constrained helices, is also known for its ability to bend helical peptides. The conformational features of the analogue [D-Phe¹², Aib¹⁵]CRH have already been studied through 1D and 2D *J*-correlated ¹H NMR spectroscopy [39].

Biological evaluation of the two Aib containing analogues revealed that they both present the same activity which is 60 percent that of the natural hormone and thus, they appear to be partial agonists of CRH. However, when the IC_{50} values are taken under consideration, the two analogues significantly vary regarding their affinity to the receptor. Although the only difference in their secondary structure is the position of the Aib moiety (14 or 15) and furthermore, the two positions are adjacent, [D-Phe¹², Aib¹⁵]CRH presents a roughly 27 times higher affinity than [D-Phe¹², Aib¹⁴]CRH. An NMR study of [D-Phe¹², Aib¹⁴]CRH and consequent comparison with the results already extrapolated for [D-Phe¹², Aib¹⁵]CRH is the best means to clarify the effect of the Aib substitution on the molecule conformation and consequently on its binding to the receptor. All the same, a primary estimation could be that the positions 14 and 15 although important for binding to the receptor might not belong to the region that is responsible for the hormone's action since no alteration is observed on the biological activity for the two analogues.

Cys(Et) and Cys(Pr) are two nonnatural amino acid residues that have already been used in the synthesis of peptides (e.g., Angiotensin II) [40] yielding interesting results. The fact that Cys (S-Et) is an isoster of Met along with the enhanced potency of the analogues with substituted Met²¹ or Met³⁸ were basically taken into account for the design of the analogues. Cys (S-Pr) was used since it bears a side-chain that on one hand possesses the S atom present in Met and on the other hand has a longer aliphatic unit than Met or Cys(Et). Two of the analogues were monosubstituted regarding the Met residues, [D-Phe¹², Cys(Et)²¹]CRH, and [D-Phe¹², Cys(Pr)³⁸]CRH, and three had a double substitution of Met, [D-Phe¹², Cys(Et)²¹, Cys(Pr)³⁸]CRH, [D-Phe¹², Cys(Pr)²¹, Cys(Et)³⁸]CRH and [D-Phe¹², Cys(Pr)²¹, Cys(Pr)³⁸]CRH.

Both [D-Phe¹², Cys(Et)²¹]CRH and [D-Phe¹², Cys(Pr)³⁸]CRH present reduced affinity to the receptor compared to CRH, which is approximately half that of the hormone. Notably, when these modifications are combined in the [D-Phe¹², Cys(Et)²¹, Cys(Pr)³⁸]CRH analogue, the affinity appears to enhance significantly. However, this combination does not have the same impact on the activity of the molecule. [D-Phe¹², Cys(Et)²¹]CRH is the only of the studied analogues that presents a higher than CRH activity (110% that of the hormone) whereas [D-Phe¹², Cys(Pr)³⁸]CRH shows reduced activity (60% that of CRH). The activity of [D-Phe¹², Cys(Et)²¹, Cys(Pr)³⁸]CRH, although slightly higher than that of the latter monosubstituted analogue is considerably lower than that of the former one. This could mean that the negative effect of Cys(Pr)³⁸ is more prominent than the positive one of Cys(Et)²¹. As for the affinity, no safe assumptions can be made until further NMR studies are performed on these molecules.

The results regarding [D-Phe¹², Cys(Pr)²¹, Cys(Pr)³⁸]CRH indicate that double substitution with Cys(Pr) does not affect the affinity of the molecule to the receptor and decreases only slightly its activity. When the Cys(Pr) residue is applied at position 38 the IC_{50} value is negatively affected and the molecule shows a 40% decrease in activity compared

to CRH. The reversal of this image with the application of Cys(Pr)²¹ could be attributed to a positive effect of this moiety on the molecule but this assumption can be confirmed only by the study of the [D-Phe¹², Cys(Pr)²¹]CRH analogue that remains to be performed.

The analogue presenting the lowest IC_{50} value is [D-Phe¹², Cys(Pr)²¹, Cys(Et)³⁸]CRH, indicating a 5-fold increased affinity to the receptor compared to the native hormone and also to the [D-Phe¹², Cys(Pr)²¹, Cys(Pr)³⁸]CRH. Regarding the two CRH analogues it could be assumed that the difference in affinity is connected with the residue at position 38, where the Cys(Et) substitution appears to be more favorable compared to Cys(Pr) substitution.

Considering all the aforementioned remarks, the conclusions are (i) regarding the introduction of Aib, position 15 is preferable to position 14 since it yielded analogues with higher affinity to the receptor; (ii) although the introduction of Aib modifies the secondary structure and can alter significantly the affinity to the receptor, the Aib containing analogues can still be characterised as partial agonists; (iii) affinity to the receptor and activity do not necessarily coincide and analogues that excel in the one may fall short to the other; (iv) simple or combined modifications with Cys(Et) or Cys(Pr) in position 21 or/and position 38 did not hinder receptor recognition leading, in the most of the cases, to partial agonists with the exception of the analogue [D-Phe¹², Cys(Et)²¹]CRH which presents full agonistic activity.

Acknowledgment

State Scholarships Foundation (S.P.) is acknowledged for financial support.

References

- [1] W. Vale, J. Spiess, C. Rivier, and J. Rivier, "Characterization of a 41-residue ovine hypothalamic peptide that stimulates secretion of corticotropin and β -endorphin," *Science*, vol. 213, no. 4514, pp. 1394–1397, 1981.
- [2] W. Vale, C. Rivier, M. R. Brown et al., "Chemical and biological characterization of corticotropin releasing factor," *Recent Progress in Hormone Research*, vol. 39, pp. 245–270, 1983.
- [3] F. A. Antoni, "Hypothalamic control of adrenocorticotropin secretion: advances since the discovery of 41-residue corticotropin-releasing factor," *Endocrine Reviews*, vol. 7, no. 4, pp. 351–378, 1986.
- [4] D. N. Orth, "Corticotropin-releasing hormone in humans," *Endocrine Reviews*, vol. 13, no. 2, pp. 164–191, 1992.
- [5] F. Holsboer, "The rationale for corticotropin-releasing hormone receptor (CRH-R) antagonists to treat depression and anxiety," *Journal of Psychiatric Research*, vol. 33, no. 3, pp. 181–214, 1999.
- [6] A. Erhardt, M. Ising, P. G. Unschuld et al., "Regulation of the hypothalamic-pituitary-adrenocortical system in patients with panic disorder," *Neuropsychopharmacology*, vol. 31, no. 11, pp. 2515–2522, 2006.

- [7] D. G. Parkes, R. S. Weisinger, and C. N. May, "Cardiovascular actions of CRH and urocortin: an update," *Peptides*, vol. 22, no. 5, pp. 821–827, 2001.
- [8] J. Raber, S. Chen, L. Mucke, and L. Feng, "Corticotropin-releasing factor and adrenocorticotrophic hormone as potential central mediators of OB effects," *The Journal of Biological Chemistry*, vol. 272, no. 24, pp. 15057–15060, 1997.
- [9] P. J. Gilligan, D. W. Robertson, and R. Zaczek, "Corticotropin releasing factor (CRF) receptor modulators: progress and opportunities for new therapeutic agents," *Journal of Medicinal Chemistry*, vol. 43, no. 9, pp. 1641–1660, 2000.
- [10] J. Vauhan, C. Donaldson, J. Bittencourt et al., "Urocortin, a mammalian neuropeptide related to fish urotensin I and to corticotropin-releasing factor," *Nature*, vol. 378, no. 6554, pp. 287–292, 1995.
- [11] S. Y. Hsu and A. J. W. Hsueh, "Human stresscopin and stresscopin-related peptide are selective ligands for the type 2 corticotropin-releasing hormone receptor," *Nature Medicine*, vol. 7, no. 5, pp. 605–611, 2001.
- [12] T. M. Reyes, K. Lewis, M. H. Perrin et al., "Urocortin II: a member of the corticotropin-releasing factor (CRF) neuropeptide family that is selectively bound by type 2 CRF receptors," *Proceedings of the National Academy of Sciences of the United States of America*, vol. 98, no. 5, pp. 2843–2848, 2001.
- [13] K. Lewis, C. Li, M. H. Perrin et al., "Identification of urocortin III, an additional member of the corticotropin-releasing factor (CRF) family with high affinity for the CRF₂ receptor," *Proceedings of the National Academy of Sciences of the United States of America*, vol. 98, no. 13, pp. 7570–7575, 2001.
- [14] D. T. Chalmers, T. W. Lovenberg, D. E. Grigoriadis, D. P. Behan, and E. B. De Souza, "Corticotrophin-releasing factor receptors: from molecular biology to drug design," *Trends in Pharmacological Sciences*, vol. 17, no. 4, pp. 166–172, 1996.
- [15] W. A. Kostich, A. Chen, K. Sperle, and B. L. Largent, "Molecular identification and analysis of a novel human corticotropin-releasing factor (CRF) receptor: the CRF(2 γ) receptor," *Molecular Endocrinology*, vol. 12, no. 8, pp. 1077–1085, 1998.
- [16] O. Valdenaire, T. Giller, V. Breu, J. Gottowik, and G. Kilpatrick, "A new functional isoform of the human CRF₂ receptor for corticotropin-releasing factor," *Biochimica et Biophysica Acta*, vol. 1352, no. 2, pp. 129–132, 1997.
- [17] B. E. DeSouza, W. T. Lovenberg, T. D. Chalmers, et al., "Heterogeneity of corticotropin releasing factor receptors: multiple targets for the treatment of CNS and inflammatory disorders," *Annual Reports in Medicinal Chemistry*, vol. 30, pp. 21–30, 1995.
- [18] P. J. Lowry, R. J. Woods, and S. Baigent, "Corticotropin releasing factor and its binding protein," *Pharmacology Biochemistry and Behavior*, vol. 54, no. 1, pp. 305–308, 1996.
- [19] R. Chen, K. A. Lewis, M. H. Perrin, and W. W. Vale, "Expression cloning of a human corticotropin-releasing-factor receptor," *Proceedings of the National Academy of Sciences of the United States of America*, vol. 90, no. 19, pp. 8967–8971, 1993.
- [20] G. W. Smith, J.-M. Aubry, F. Dellu et al., "Corticotropin releasing factor receptor 1-deficient mice display decreased anxiety, impaired stress response, and aberrant neuroendocrine development," *Neuron*, vol. 20, no. 6, pp. 1093–1102, 1998.
- [21] L. Facci, D. A. Stevens, M. Pangallo, D. Franceschini, S. D. Skaper, and P. J. L. M. Strijbos, "Corticotropin-releasing factor (CRF) and related peptides confer neuroprotection via type 1 CRF receptors," *Neuropharmacology*, vol. 45, no. 5, pp. 623–636, 2003.
- [22] S. C. Heinrichs and Y. Taché, "Therapeutic potential of CRF receptor antagonists: a gut-brain perspective," *Expert Opinion on Investigational Drugs*, vol. 10, no. 4, pp. 647–659, 2001.
- [23] Z. Sarnyai, Y. Shaham, and S. C. Heinrichs, "The role of corticotropin-releasing factor in drug addiction," *Pharmacological Reviews*, vol. 53, no. 2, pp. 209–243, 2001.
- [24] D. Richard, Q. Lin, and E. Timofeeva, "The corticotropin-releasing factor family of peptides and CRF receptors: their roles in the regulation of energy balance," *European Journal of Pharmacology*, vol. 440, no. 2–3, pp. 189–197, 2002.
- [25] G. R. Valdez, "Development of CRF₁ receptor antagonists as antidepressants and anxiolytics: progress to date," *CNS Drugs*, vol. 20, no. 11, pp. 887–896, 2006.
- [26] P. A. Keller, L. Elfick, J. Garner, J. Morgan, and A. McCluskey, "Corticotropin releasing hormone: therapeutic implications and medicinal chemistry developments," *Bioorganic and Medicinal Chemistry*, vol. 8, no. 6, pp. 1213–1223, 2000.
- [27] N. Gibbs, R. B. Sessions, P. B. Williams, and C. E. Dempsey, "Helix bending in alamethicin: molecular dynamics simulations and amide hydrogen exchange in methanol," *Biophysical Journal*, vol. 72, no. 6, pp. 2490–2495, 1997.
- [28] C. Toniolo, G. M. Bonora, V. Barone et al., "Conformation of pleiomers of α -aminoisobutyric acid," *Macromolecules*, vol. 18, no. 5, pp. 895–902, 1985.
- [29] D. Theodoropoulos, "Synthesis of certain S-substituted L-cysteines," *Acta Chemica Scandinavica*, vol. 13, no. 383, p. 384, 1959.
- [30] G. B. Fields and R. L. Noble, "Solid phase peptide synthesis utilizing 9-fluorenylmethoxycarbonyl amino acids," *International Journal of Peptide and Protein Research*, vol. 35, no. 3, pp. 161–214, 1990.
- [31] H. Rink, "Solid-phase synthesis of protected peptide fragments using a trialkoxy-diphenyl-methylester resin," *Tetrahedron Letters*, vol. 28, no. 33, pp. 3787–3790, 1987.
- [32] K. Barlos, O. Chatzi, D. Gatos, and G. Stavropoulos, "2-Chlorotriptyl chloride resin: studies on anchoring of Fmoc-amino acids and peptide cleavage," *International Journal of Peptide and Protein Research*, vol. 37, no. 6, pp. 513–520, 1991.
- [33] M. S. Bernatowicz, S. B. Daniels, and H. Köster, "A comparison of acid labile linkage agents for the synthesis of peptide C-terminal amides," *Tetrahedron Letters*, vol. 30, no. 35, pp. 4645–4648, 1989.
- [34] W. König and R. Geiger, "A new method for synthesis of peptides: activation of the carboxyl group with dicyclohexylcarbodiimide using 1-hydroxybenzotriazoles as additives," *Chemische Berichte*, vol. 103, no. 3, pp. 788–798, 1970.
- [35] D. Sarantakis, J. Teichman, E. L. Lien, and R. L. Fenichel, "A novel cyclic undecapeptide, WY-40,770, with prolonged growth hormone release inhibiting activity," *Biochemical and Biophysical Research Communications*, vol. 73, no. 2, pp. 336–342, 1976.
- [36] R. Knorr, A. Trzeciak, W. Bannwarth, and D. Gillissen, "New coupling reagents in peptide chemistry," *Tetrahedron Letters*, vol. 30, no. 15, pp. 1927–1930, 1989.
- [37] E. Kaiser, R. L. Colestock, C. D. Bossinger, and P. I. Cook, "Color test for detection of free terminal amino groups in the solid-phase synthesis of peptides," *Analytical Biochemistry*, vol. 34, no. 2, pp. 595–598, 1970.

- [38] T. Vojkovsky, "Detection of secondary amines on solid phase," *Peptide Research*, vol. 8, no. 4, pp. 236–237, 1995.
- [39] G. A. Spyroulias, S. Papazacharias, G. Pairas, and P. Cordopatis, "Monitoring the structural consequences of Phe12 → D-Phe and Leu15 → Aib substitution in human/rat corticotropin releasing hormone: implications for design of CRH antagonists," *European Journal of Biochemistry*, vol. 269, no. 24, pp. 6009–6019, 2002.
- [40] J. Pérodin, R. Bouley, E. Escher et al., "Angiotensin II analogues with sulphur-containing side-chains in position 5. A structure-activity relationship study," *Arzneimittel-Forschung/Drug Research*, vol. 50, no. 6, pp. 526–529, 2000.

Research Article

Mononuclear and Dinuclear Manganese(II) Complexes from the Use of Methyl(2-pyridyl)ketone Oxime

Constantinos G. Efthymiou,^{1,2} Vassilios Nastopoulos,¹ Catherine Raptopoulou,³
Anastasios Tasiopoulos,⁴ Spyros P. Perlepes,¹ and Constantina Papatriantafyllopoulou²

¹ Department of Chemistry, University of Patras, 265 04 Patras, Greece

² Department of Chemistry, University of Florida, Gainesville, FL 32611-7200, USA

³ Institute of Materials Science, National Centre of Scientific Research "Demokritos", 153 10 Aghia Paraskevi Attikis, Greece

⁴ Department of Chemistry, University of Cyprus, 1678 Nicosia, Cyprus

Correspondence should be addressed to Constantina Papatriantafyllopoulou, cpapat@chem.ufl.edu

Received 23 March 2010; Accepted 3 May 2010

Academic Editor: Evy Manessi-Zoupa

Copyright © 2010 Constantinos G. Efthymiou et al. This is an open access article distributed under the Creative Commons Attribution License, which permits unrestricted use, distribution, and reproduction in any medium, provided the original work is properly cited.

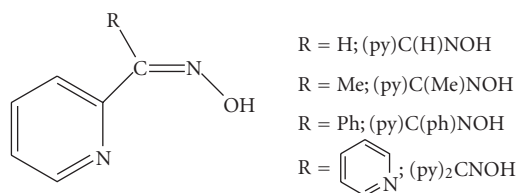
The reactions of methyl(2-pyridyl)ketone oxime, (py)C(Me)NOH, with manganese(II) sulfate monohydrate have been investigated. The reaction between equimolar quantities of $\text{MnSO}_4 \cdot \text{H}_2\text{O}$ and (py)C(Me)NOH in H_2O lead to the dinuclear complex $[\text{Mn}_2(\text{SO}_4)_2\{(\text{py})\text{C}(\text{Me})\text{NOH}\}_4] \cdot (\text{py})\text{C}(\text{Me})\text{NOH}$, **1** \cdot (py)C(Me)NOH, while employment of NaOMe as base affords the compound $[\text{Mn}(\text{HCO}_2)_2\{(\text{py})\text{C}(\text{Me})\text{NOH}\}_2]$ (**2**). The structures of both compounds have been determined by single crystal X-ray diffraction. In both complexes, the organic ligand chelates through its nitrogen atoms. The IR data are discussed in terms of the nature of bonding and the structures of the two complexes.

1. Introduction

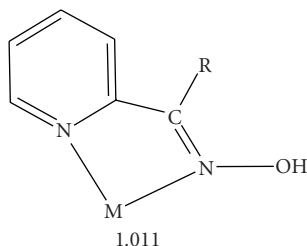
There is currently a renewed interest in the coordination chemistry of oximes [1]. The research efforts are driven by a number of considerations. One of these is that they are considered to be reasonable models for the biologically significant imidazole donor group of the amino acid histidine [2]. Thus, they potentially can be used for the synthesis of various nuclearity metal clusters to model M_x sites in biomolecules, including elucidating the structure and mechanism of action of the CaMn_4 core of the water oxidizing complex within the photosynthetic apparatus of green plants and cyanobacteria [3, 4]. In addition, metal complexes of oximes can be used in several other applications, that is, the solution of pure chemical problems [5, 6], the development of new oxygen activation catalysts based on nickel(II) polyoximate complexes [7] and the application of metal ion/oxime systems as efficient catalysts for the hydrolysis of organonitriles [8]. In the latter, metal ions can behave as extremely strong activators of RCN molecules towards nucleophilic attack by $\text{OH}^-/\text{H}_2\text{O}$. Other applications of

metal complexes of oximes include the design of Ca^{2+} - and Ba^{2+} -selective receptors based on site-selective transmetallation of polynuclear zinc (II)/polyoxime complexes [9], the study of metal-ion assisted organic transformations [10], and the mechanistic investigation of corrosion inhibition by Acorga P5000 (a modern corrosion inhibitor comprising 5-nonylsalicylaldoxime as a mixture of carbon-chain isomers) on iron surfaces [11]. Note also that oximate ligands are employed in the synthesis of homo- and heterometallic [1, 12] clusters and coordination polymers [13] with interesting magnetic properties, including single-molecule magnetism [14–16], and single-chain magnetism [17] behavior.

Ligands containing one oxime group and one pyridyl group, without other donor sites, are popular in coordination chemistry. Metal-free pyridine oximes exhibit a plethora of biological properties including action on the cardiovascular system, sedative, antidepressant, antispasmodic, cytotoxic, antiviral, and bactericidal activities, while they are good antidotes for poisoning by organophosphorus compounds [18]. Most of these ligands contain a 2-pyridyl group, and thus are named 2-pyridyl oximes,



SCHEME 1: General structural formula and abbreviations of simple 2-pyridyl oximes, including methyl(2-pyridyl)ketone oxime [(py)C(Me)NOH].



SCHEME 2: The common coordination mode of the neutral 2-pyridyl oximes and the Harris notation [26] which describes this mode.

(py)C(R)NOH (Scheme 1). The anionic forms of these molecules, (py)C(R)NO⁻, are versatile ligands for a variety of research objectives, including μ_2 and μ_3 behaviour; the activation of 2-pyridyl oximes by 3d-metal centers towards further reactions is also becoming a fruitful area of research. The majority of the metal complexes of these ligands have been prepared in the last 15 years and much of their chemistry remains to be explored in more detail [1].

With only few exceptions [19, 20], the hitherto structurally characterized metal complexes containing neutral 2-pyridyl oximes as ligands are *mononuclear*. The donor atoms of the neutral 2-pyridyl oximes in metal complexes are the nitrogen atom of the oxime group and the nitrogen atom of the pyridyl group. Thus, (py)C(R)NOH behave as *N,N'*-chelating ligands (see Scheme 2) making necessary the employment of additional inorganic or organic anions to complete the coordination sphere of the metal centre or to balance the charge of the complex cation. A variety of *monoanions* have been used for this reason, for example, PhCO₂⁻ [21], Cl⁻ [22, 23], Br⁻ [24], and NO₃⁻ [25]. Recently, we have started a research program to explore the use of the sulfate ion, SO₄²⁻, in 3d-metal/2-pyridyl oxime chemistry, instead of the abovementioned *monoanionic* ligands. The possible advantages of using SO₄²⁻ include (i) the possibility of triggering aggregation of preformed smaller species into new products, and (ii) the possible diversion of known reaction systems developed using inorganic *monoanions* to new species as a result of the higher charge and higher denticity of the sulfate ligand.

The sulfate ion [27] is currently a ligand of intense interest. The μ_2 , μ_3 , μ_4 , μ_5 , μ_8 , or μ_{10} potential of SO₄²⁻ (Scheme 3) prompted as to combine 2-pyridyl oximes with the sulfate ligand to aim at new types of compounds.

In this paper, we report the synthesis and the X-ray structural characterization of the two new Mn(II) complexes [Mn₂(SO₄)₂{(py)C(Me)NOH}₄]·(py)C(Me)NOH (**1**·(py)C(Me)NOH) and [Mn(HCO₂)₂{(py)C(Me)NOH}₂] (**2**) which contain the neutral methyl(2-pyridyl)ketone oxime as organic ligand. The IR data are discussed in terms of the nature of bonding and the structures of the two complexes.

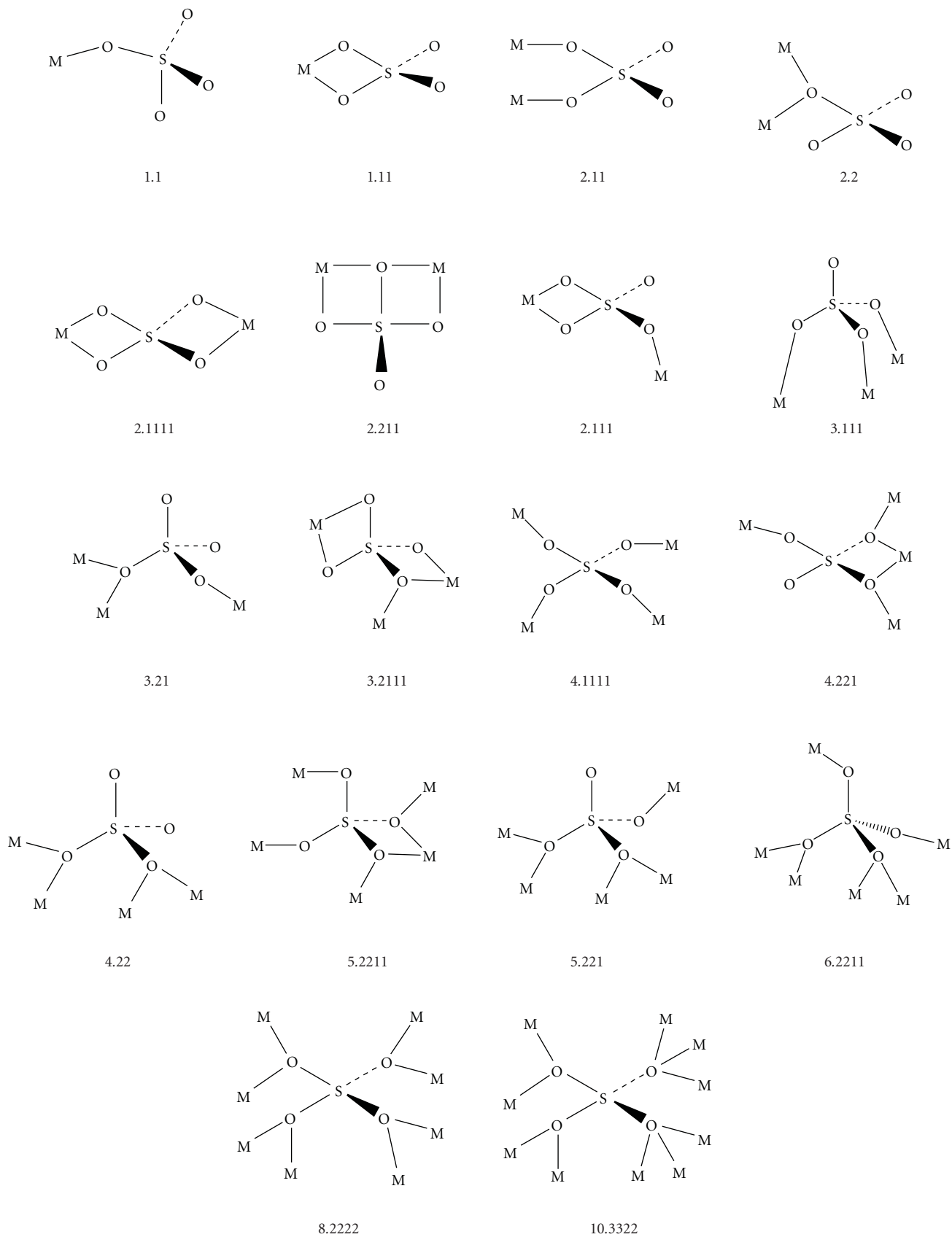
2. Experiments

All manipulations were performed under aerobic conditions using materials and solvents as received. IR spectra were recorded on a Perkin-Elmer PC16 FT-IR spectrometer with samples prepared as KBr pellets.

[Mn₂(SO₄)₂{(py)C(Me)NOH}₄]·(py)C(Me)NOH (**1**·(py)C(Me)NOH). Solid MnSO₄·H₂O (0.067 g, 0.40 mmol) was added to a slurry of (py)C(Me)NOH (0.054 g, 0.40 mmol) in H₂O (15 cm³); the solid soon dissolved and the solution was stirred for 1 hour at room temperature. The resultant solution was left for slow evaporation. After one week, yellow crystals appeared which were collected by filtration, washed with cold H₂O (1 cm³), cold MeOH (1 cm³) and ice-cold Et₂O (2 cm³), and dried in air. The yield was 79% (based on the metal). Found %: C, 42.94; H, 3.89; N, 14.51. Calc % for C₃₅H₄₀O₁₃N₁₀S₂Mn₂: C, 42.78; H, 4.10; and N, 14.25. Selected IR data (KBr, cm⁻¹): 3420 (wb), 3150 (m), 3069 (m), 2843 (m), 2363 (w), 2343 (w), 1654 (w), 1593 (s), 1561 (m), 1476 (s), 1437 (m), 1327 (m), 1285 (w), 1215 (m), 1124 (s), 1080 (s), 1030 (s), 1010 (s), 989 (s), 781 (s), 748 (m), 683 (m), 631 (m), 592 (m), 561 (w), 494 (w), 452 (w), and 447 (w).

[Mn(HCO₂)₂{(py)C(Me)NOH}₂](**2**). Solid NaOMe (0.090 g, 1.50 mmol) was added to a colourless solution of (py)C(Me)NOH (0.204 g, 1.50 mmol) in CH₂Cl₂ (20 cm³); the solid soon dissolved. Solid MnSO₄·H₂O (0.250 g, 1.50 mmol) was then added and the resulting solution was stirred for 24 hours at room temperature. A small quantity of undissolved material was removed by filtration and the dark brown filtrate layered with Et₂O (40 cm³). Slow mixing gave X-ray quality yellow crystals of the product. The crystals were collected by filtration, washed with cold H₂O (1 cm³), cold MeOH (2 cm³), and ice-cold Et₂O (2 × 3 cm³), and dried in air. The yield was 45% (based on the metal). Found %: C, 46.95; H, 4.26; N, 13.43. Calc % for C₁₆H₁₈O₆N₄Mn: C, 46.82; H, 4.13; N, 13.98. Selected IR data (KBr, cm⁻¹): 3412 (mb), 3073 (w), 2362 (m), 1846 (m), 1597 (s), 1562 (s), 1475 (s), 1436 (m), 1365 (s), 1348 (s), 1326 (m), 1250 (w), 1165 (w), 1137 (m), 1042 (s), 961 (m), 782 (s), 751 (s), 683 (m), 562 (w), and 458 (w).

2.1. X-Ray Crystallography. For **1**·(py)C(Me)NOH, X-Ray data were collected at 298 K using a Crystal Logic Dual Goniometer diffractometer with graphite-monochromated Mo-K_α radiation ($\lambda = 0.71073 \text{ \AA}$). Lorentz, polarization, and Ψ -scan absorption corrections were applied using Crystal Logic software. Symmetry equivalent data were averaged



SCHEME 3: The up to now crystallographically established coordination modes of the sulfato ligand and the Harris notation [26] which describes these modes.

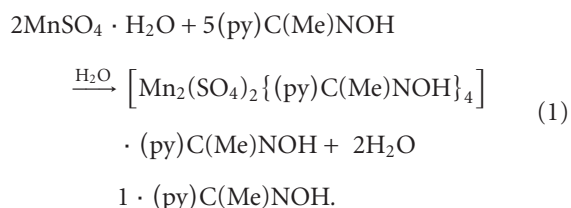
with $R_{\text{int}} = 0.0084$, to give 3727 independent reflections from a total 3964 collected. The structure was solved by direct methods and refined by full-matrix least-squares on F^2 , using 3727 reflections and refining 325 parameters. All non-hydrogen atoms were refined anisotropically. Hydrogen atoms were either located by difference maps and were refined isotropically or were introduced at calculated positions as riding on bonded atoms.

For **2**, X-ray data were collected at 100 K using a Oxford Diffraction diffractometer with graphite-monochromated Mo- K_{α} radiation ($\lambda = 0.71073 \text{ \AA}$). Symmetry equivalent data were averaged with $R_{\text{int}} = 0.0160$, to give 9343 independent reflections from a total of 13039 collected. The structure was solved by direct methods and refined by full-matrix least-squares on F^2 , using 9343 reflections and refining 258 parameters. All non-hydrogen atoms were refined anisotropically. Hydrogen atoms were either located by difference maps and were refined isotropically or were introduced at calculated positions as riding on bonded atoms.

Details of the data collection and refinement for **1**·(py)C(Me)NOH and **2** are given in Table 1.

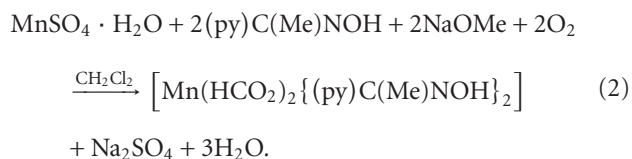
3. Results and Discussion

3.1. Synthetic Comments. Treatment of $\text{MnSO}_4 \cdot \text{H}_2\text{O}$ with one equivalent of (py)C(Me)NOH in H_2O gave a colorless solution from which the new dinuclear compound $[\text{Mn}_2(\text{SO}_4)_2\{(\text{py})\text{C}(\text{Me})\text{NOH}\}_4] \cdot (\text{py})\text{C}(\text{Me})\text{NOH}$ (**1**·(py)C(Me)NOH) was obtained in ~80% yield. Its formation can be summarized in (1).



The nonstoichiometric $\text{MnSO}_4 \cdot \text{H}_2\text{O}$ to (py)C(Me)NOH reaction ratio (1:1) employed for the preparation of **1**·(py)C(Me)NOH (Section 2) did not prove detrimental to the formation of the complex. With the identity of **1**·(py)C(Me)NOH established by single-crystal X-ray crystallography, the “correct” stoichiometry (1:2.5) was employed and led to the pure compound in high yield.

As a next step, we decided to add base in the reaction mixture targeting the deprotonation of the organic ligand. Thus, treatment of $\text{MnSO}_4 \cdot \text{H}_2\text{O}$ with one equivalent of (py)C(Me)NOH and one equivalent of NaOMe in CH_2Cl_2 gave a dark brown solution from which the mononuclear compound $[\text{Mn}(\text{HCO}_2)_2\{(\text{py})\text{C}(\text{Me})\text{NOH}\}_2]$ (**2**) was obtained. Its formation can be summarized in (2)



To our surprise, an amount of the methoxide ions did not act as proton acceptors but they got oxidized to formates (HCO_2^-) during the aerial aggregation process [28]. Thus, the organic ligand in **2** is neutral. As expected, the nature of the base is crucial for the identity of the product; employment of NEt_3 , NMe_4OH , NEt_4OH , $\text{LiOH} \cdot \text{H}_2\text{O}$ etc. leads to dark brown oily materials that have not been characterized. Also, note that: (i) The color of **2** (yellow) is different than the color of the reaction mixture (dark brown, this colour is characteristic of Mn^{III} or $\text{Mn}^{\text{II/III}}$ species), and (ii) a similar reaction, but with (py)C(ph)NOH instead of (py)C(Me)NOH, yields the octanuclear mixed-valent cluster $[\text{Mn}^{\text{II}}_4 \text{Mn}^{\text{III}}_4 \text{O}_4(\text{NO}_3)_2\{(\text{py})\text{C}(\text{ph})\text{NO}\}_8(\text{HCOO})_2(\text{MeOH})_2]$ [29] whose core consists of two butterfly subunits. These observations indicate that compound **2** is not the only product of the reaction and that, presumably, a higher nuclearity cluster, with the metals at higher oxidation states, is present in solution. Work is in progress to isolate the second product from the reaction mixture.

3.2. Description of Structures. Selected interatomic distances and angles for complexes **1**·(py)C(Me)NOH and **2** are listed in Tables 2 and 4, respectively. The molecular structures of the two compounds are shown in Figures 1 and 2.

Complex **1**·(py)C(Me)NOH crystallizes in the triclinic space group $P-1$. Its structure consists of dinuclear $[\text{Mn}_2(\text{SO}_4)_2\{(\text{py})\text{C}(\text{Me})\text{NOH}\}_4]$ molecules and (py)C(Me)NOH molecules in the crystal lattice. The dinuclear molecules lie on a crystallographic inversion center. The two Mn^{II} atoms are bridged by two $\eta^1:\eta^1:\mu_2$ or 2.1100 (Harris notation [26]) sulfato ligands; two N,N' -chelating (py)C(Me)NOH ligands complete six coordination at each metal center. The ligating atoms of (py)C(Me)NOH are the nitrogen atoms of the neutral oxime and 2-pyridyl groups. Thus, adopting the Harris notation, (py)C(Me)NOH behaves as an 1.011 ligand.

The coordination sphere of the Mn^{II} ion in **1**·(py)C(Me)NOH exhibits a slightly distorted octahedral geometry as a consequence of the relatively small bite angles of the chelating ligands [$\text{N}1-\text{Mn}-\text{N}2=70.11(10)$, $\text{N}11-\text{Mn}-\text{N}12=70.19(10)^\circ$]. Both sulfato oxygen atoms O(31) and O(32') are *trans* to the pyridyl nitrogen atoms N(1) and N(11), respectively. Each metal center adopts the *cis-cis-trans* configuration considering the position of the coordinated SO_4^{2-} oxygen, pyridyl nitrogen and oxime nitrogen atoms, respectively. The *cis* arrangement of the oxime groups seems unfavourable, probably due to the steric hindrance arising from the methyl group upon oxime coordination. The long $\text{Mn} \cdots \text{Mn}'$ distance [$5.040(2) \text{ \AA}$] is a consequence of the presence of the two *syn, anti* sulfato bridges.

The molecular structure of **1**·(py)C(Me)NOH is stabilized by intramolecular hydrogen bonds (Table 3). Each coordinated (py)C(Me)NOH oxime group is strongly hydrogen bonded to an uncoordinated O atom of the sulfato ligand (O33 or O33'). Thus, O33 (and its symmetry equivalent) participates in two hydrogen bonds.

TABLE 1: Crystal data and structure refinement for **1**·(py)C(Me)NOH and **2**.

Empirical formula	C ₃₅ H ₄₀ Mn ₂ N ₁₀ O ₁₃ S ₂	C ₁₆ H ₁₈ MnN ₄ O ₆
Formula weight	982.77	417.28
Crystal size	0.75 × 0.50 × 0.40	0.25 × 0.20 × 0.20
Crystal system	triclinic	monoclinic
Space group	P-1	P2 ₁ /n
θ range for data collection. ^o	5.5 ≤ θ ≤ 11.0	3.4 ≤ θ ≤ 30.1
<i>a</i> , Å	9.627(4)	10.6538(5)
<i>b</i> , Å	9.962(4)	14.3935(7)
<i>c</i> , Å	11.750(4)	11.8231(8)
α , °	92.610(10)	90.00
β , °	96.560(10)	90.264(7)
γ , °	107.450(10)	90.00
<i>V</i> , Å ³	1064.2(7)	1813.00(17)
<i>Z</i>	1	4
ρ_{calcd} , gcm ⁻³	1.534	1.529
μ , mm ⁻¹	0.766	0.770
<i>GOF</i>	1.116	1.009
<i>R1</i> ^a	0.0443	0.0344
<i>wR2</i> ^b	0.1125	0.0948

$$^a I > 2\sigma(I), R_1 = \sum(|F_o| - |F_c|) / \sum(|F_o|)$$

$$^b wR_2 = \{\sum[w(F_o^2 - F_c^2)^2] / \sum[w(F_o^2)^2]\}^{1/2}$$

TABLE 2: Selected bond lengths (Å) and angles (°) for **1**·(py)C(Me)NOH.^a

Mn–O31	2.089(2)	Mn – N2	2.287(3)
Mn–O32'	2.102(3)	Mn – N11	2.300(3)
Mn–N1	2.287(3)	Mn – N12	2.283(3)
O31–Mn–O32'	101.06(11)	O32' – Mn–N12	94.84(11)
O31–Mn–N1	164.21(11)	N1–Mn–N2	70.11(10)
O31–Mn–N2	95.50(11)	N1–Mn–N11	88.37(10)
O31–Mn–N11	87.21(10)	N1–Mn–N12	94.52(10)
O31–Mn–N12	98.23(10)	N2–Mn–N11	97.89(10)
O32'–Mn–N1	87.06(11)	N2–Mn–N12	161.24(10)
O32'–Mn–N2	95.00(11)	N11–Mn–N12	70.19(10)
O32'–Mn–N11	163.96(11)		

^aPrimes denote symmetry-related atoms.

Complex **2** crystallizes in the monoclinic space group P2₁/n and its structure consists of mononuclear [Mn(HCO₂)₂{(py)C(Me)NOH}₂] molecules. Two bidentate chelating (py)C(Me)NOH molecules (1.011 [26], see Scheme 2) and two monodentate HCO₂⁻ ions create six-coordination at the Mn^{II} ion. The coordination geometry of the metal ion is distorted octahedral. As **1**·(py)C(Me)NOH, complex **2** is the *cis-cis-trans* isomer considering the positions of the coordinated HCO₂⁻ oxygen, pyridyl nitrogen and oxime nitrogen atoms, respectively.

Intramolecular hydrogen bonds are present in the structure of **2** (Table 5). The oximic oxygen atom of each (py)C(Me)NOH ligand is very strongly intramolecularly hydrogen bonded to one uncoordinated formate oxygen atom.

Complexes **1**·(py)C(Me)NOH and **2** join a small but growing family of structurally characterized metal complexes containing the neutral or anionic forms of methyl(2-pyridyl)ketone oxime as ligands. The 1.011 ligation mode is the exclusive one for the metal complexes containing the neutral ligand [22, 24, 30].

The structurally characterized Mn complexes of (py)C(Me)NOH and/or (py)C(Me)NO⁻ [14, 31–33] are collected in Table 6, together with the cores of the polynuclear complexes and the ligands' coordination modes for convenient comparison. Closer inspection of Table 6 reveals that compound **1** is the first member of this subfamily in which the Mn^{II} ions are linked by the SO₄²⁻ ion. Complex **2** can be compared with the compound [Mn^{II}(O₂CPh)₂{(py)C(Me)NOH}₂] [33] which

TABLE 3: Dimensions of the hydrogen bonds in complex **1**·(py)C(Me)NOH.^a

D–H···A	D···A [Å]	H···A [Å]	D–H···A [°]	Symmetry Operator of A
O(1)–H(O1)···O(33)	2.644	1.967	154.5	<i>x, y, z</i>
O(11')–H(O11')···O(33)	2.598	1.720	174.8	<i>x, y, z</i>

^aA = acceptor, D = donor.TABLE 4: Selected bond lengths (Å) and angles (°) for **2**.

Mn–O3	2.125(1)	Mn–N2	2.248(1)
Mn–O5	2.091(1)	Mn–N3	2.305(1)
Mn–N1	2.272(1)	Mn–N4	2.264(1)
O3–Mn–O5	95.48(5)	O5–Mn–N4	95.61(4)
O3–Mn–N1	87.76(5)	N1–Mn–N2	70.98(4)
O3–Mn–N2	94.27(5)	N1–Mn–N3	89.65(5)
O3–Mn–N3	172.60(5)	N1–Mn–N4	90.78(5)
O3–Mn–N4	102.46(5)	N2–Mn–N3	91.43(5)
O5–Mn–N1	172.03(5)	N2–Mn–N4	154.80(5)
O5–Mn–N2	101.47(5)	N3–Mn–N4	70.64(5)
O5–Mn–N3	87.99(4)		

TABLE 5: Dimensions of the hydrogen bonds in complex **2**.^a

D–H···A	D···A [Å]	H···A [Å]	D–H···A [°]	Symmetry Operator of A
O(1)–H(O1)···O(6)	2.542	1.710	167.2	<i>x, y, z</i>
O(2)–H(O2)···O(4)	2.585	1.777	165.4	<i>x, y, z</i>

^aA = acceptor, D = donor.TABLE 6: Formulae, coordination modes of the ligands, and cores of the structurally characterized Mn complexes of (py)C(Me)NOH and/or (py)C(Me)NO[−].

Complex ^a	Coordination modes ^b	Core ^c	Ref.
[Mn ^{III} ₃ O(O ₂ CMe) ₃ {(py)C(Me)NO} ₃] ⁺	2.111	[Mn ₃ (μ ₃ -O)] ⁷⁺	[14]
[Mn ^{III} ₃ O(O ₂ CEt) ₃ {(py)C(Me)NO} ₃] ⁺	2.111	[Mn ₃ (μ ₃ -O)] ⁷⁺	[14]
[Mn ^{III} Cl ₂ {(py)C(Me)NO}{(py)C(Me)NOH} ₂]	1.011		[32]
[Mn ^{II} (O ₂ CPh) ₂ {(py)C(Me)NOH} ₂]	1.011		[33]
[Mn ^{II} ₄ Mn ^{III} ₄ O ₂ (OH) ₂ (O ₂ CPh) ₁₀ {(py)C(Me)NO} ₄]	2.111	[Mn ₈ (μ ₄ -O) ₂ (μ ₃ -OH) ₂] ¹⁴⁺	[33]
[Mn ^{II} ₂ Mn ^{IV} (OMe) ₂ {(py)C(Me)NO} ₄ Br ₂]	2.111	[Mn ₃ (μ ₃ -OMe) ₂] ⁶⁺	[31]
[Mn ^{II} ₂ Mn ^{III} ₆ O ₄ (OMe){(py)C(Me)NO} ₉ {(py)C(Me)NOH} ₄] ⁴⁺	2.111, 3.211	[Mn ₈ (μ ₃ -O) ₄ (μ-OMe)(μ-OR'')] ^{11+d}	[31]
[Mn ^{II} ₂ (SO ₄) ₂ {(py)C(Me)NOH} ₄]	1.011		This work
[Mn ^{II} (HCO ₂) ₂ {(py)C(Me)NOH} ₂]	1.011		This work

^aCounterions and lattice solvent molecules have been omitted; ^b using the Harris notation [26]; ^conly for the polynuclear complexes; ^d R'' = (py)C(Me)N.

contains terminal PhCO₂[−] ions, instead of HCO₂[−] in **2**; the HCO₂[−] versus PhCO₂[−] change has little structural effect.

3.3. IR Spectra. Complexes **1** and **2** exhibit medium to strong intensity IR bands at ~3400 cm^{−1}, assignable to ν(H) vibrations of the (py)C(Me)NOH molecules. The

broadness and relatively low frequency of these bands are both indicative of hydrogen bonding.

The ν(C=N)_{oxime} and ν(N–O)_{oxime} vibrations for the free ligand appear as medium intensity bands at 1566 and 1116 cm^{−1}, respectively [34, 35]. The 1116 cm^{−1} band is shifted to a lower wavenumber in **1** and **2** (**1**, 1080; **2**, 1042 cm^{−1}). This shift is attributed to the coordination

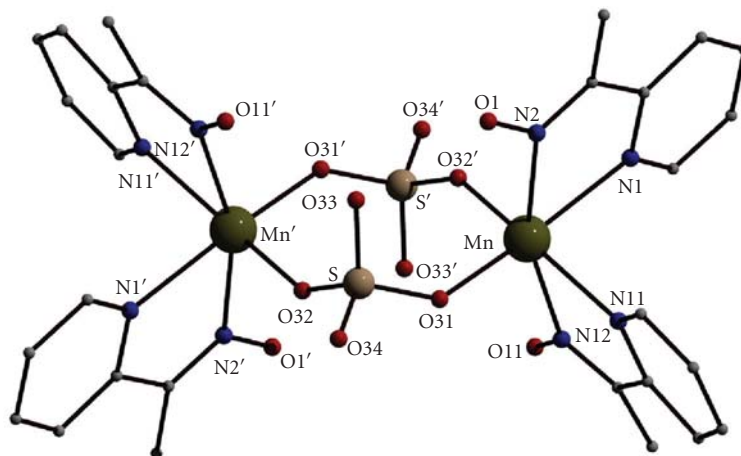


FIGURE 1: The dinuclear molecule present in $1 \cdot (\text{py})\text{C}(\text{Me})\text{NOH}$. Primes are used for the symmetry-related atoms.

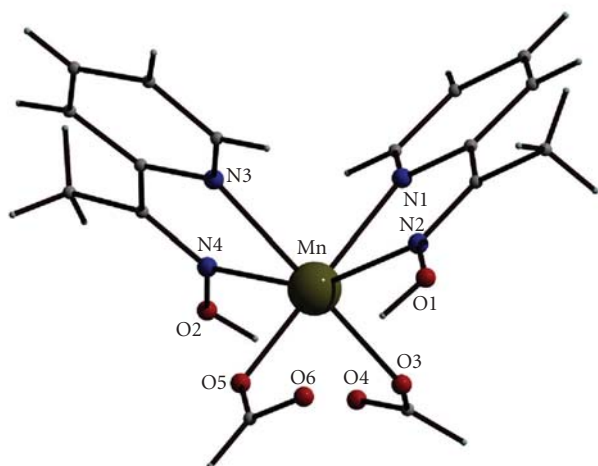


FIGURE 2: The molecular structure of compound 2.

of the neutral oxime nitrogen [22]. The strong band at 1124 cm^{-1} in the spectrum of $1 \cdot (\text{py})\text{C}(\text{Me})\text{NOH}$ should also have a $\nu(\text{N}-\text{O})_{\text{oxime}}$ character resulting from the presence of lattice $(\text{py})\text{C}(\text{Me})\text{NOH}$ molecules in the structure. Several bands appear in the $1655\text{--}1400 \text{ cm}^{-1}$ region for both complexes; contribution from the $\nu(\text{C}=\text{N})_{\text{oxime}}$ and $\delta(\text{OH})$ modes ($>1580 \text{ cm}^{-1}$) are expected in this region, but overlap with the stretching vibrations of the aromatic rings and the carboxylate groups (for **2**) renders assignments and discussion of the coordination shifts difficult.

The in-plane deformation band of the 2-pyridyl ring of free $(\text{py})\text{C}(\text{Me})\text{NOH}$ at 637 cm^{-1} shifts upwards in **1** (683 cm^{-1}) and **2** (683 cm^{-1}), confirming the involvement of the ring-N atom in coordination [36]. The appearance of a medium intensity band at 631 cm^{-1} in the spectrum of $1 \cdot (\text{py})\text{C}(\text{Me})\text{NOH}$ is indicative of the presence of lattice $(\text{py})\text{C}(\text{Me})\text{NOH}$ molecules in this complex.

The IR spectrum of the free, that is, ionic, sulfate (the SO_4^{2-} ion belongs to the T_d point group) consists of two bands at ~ 1105 and $\sim 615 \text{ cm}^{-1}$, assigned to the $\nu_3(F_2)$ stretching [$\nu_d(\text{SO})$] and $\nu_4(F_2)$ bending [$\delta_d(\text{OSO})$] modes, respectively [27, 37, 38]. The $\nu_1(A_1)$ stretching [$\nu_s(\text{SO})$] and $\nu_2(E)$ bending [$\delta_d(\text{OSO})$] modes are not IR-active (these are Raman-active). The coordination of SO_4^{2-} to metal ions decreases the symmetry of the group and the ν_3 and ν_4 modes are split [27, 37, 38]. In the case, the SO_4^{2-} -site symmetry is lowered from T_d to C_{3v} (monodentate coordination), both ν_1 and ν_2 appear in the IR spectrum with weak to medium intensity, while ν_3 and ν_4 each splits into two bands in both IR and Raman spectra [37]. When the SO_4^{2-} -site symmetry is lowered from T_d to C_{2v} (bidentate chelating or bridging coordination), again ν_1 and ν_2 appear in the IR spectrum (ν_2 splits into two Raman modes), while ν_3 and ν_4 each splits into three IR-active and Raman-active vibrations [37]. The crystallographically established symmetry of the sulfato groups in $1 \cdot (\text{py})\text{C}(\text{Me})\text{NOH}$ is C_{2v} . The bands at 1215 , 1124 and 1080 (overlapping with the $\text{N}-\text{O}_{\text{oxime}}$ stretch) cm^{-1} are attributed to the ν_3 modes [37, 39], while the bands at 592 , 631 and 683 cm^{-1} (the latter two overlapping with the in-plane 2-pyridyl deformations) are assigned to the ν_4 modes [37, 38]. The band at 1010 cm^{-1} and the two weak features at 494 and 452 cm^{-1} can be assigned to the ν_1 and ν_2 modes, respectively. The appearance of two ν_2 bands is consistent with a symmetry at the sulfato groups lower than C_{2v} [37, 39]. Thus, from the vibrational spectroscopy viewpoint, the sulfato ligands of $1 \cdot (\text{py})\text{C}(\text{Me})\text{NOH}$ appear to have C_i symmetry (and not C_{2v} as deduced from their bidentate character). When the SO_4^{2-} -site symmetry is lowered from T_d to C_i , ν_3 and ν_4 each splits into three IR-active vibrations, ν_2 splits into two ones, while ν_1 appears as a single band [37, 39]. This spectroscopic feature in $1 \cdot (\text{py})\text{C}(\text{Me})\text{NOH}$ is attributed to the fact that one uncoordinated oxygen atom of each bidentate bridging sulfate is hydrogen bonded to the oxygen atoms of the neutral oxime groups (see Table 3) resulting in a further lowering of the sulphate symmetry [39].

The $\nu(\text{CO}_2)$ bands are difficult to assign in the spectrum of **2** due to the appearance of various stretching vibrations in the 1600–1400 cm^{-1} region and thus the application of the spectroscopic criterion of Deacon and Phillips [40] is very difficult.

4. Conclusions

The use of the sulfate ligand in combination with neutral (py)C(Me)NOH in Mn(II) chemistry has provided access to the two new neutral complexes $[\text{Mn}_2(\text{SO}_4)_2\{(\text{py})\text{C}(\text{Me})\text{NOH}\}_4] \cdot (\text{py})\text{C}(\text{Me})\text{NOH}$ (**1** · (py)C(Me)NOH) and $[\text{Mn}(\text{HCO}_2)_2\{(\text{py})\text{C}(\text{Me})\text{NOH}\}_2]$ (**2**), the latter being sulphate-free. In both complexes, the organic ligand chelates through its nitrogen atoms. The sulfate anion bridges the two Mn^{II} atoms in **1**. Compounds **1** · (py)C(Me)NOH and **2** join a small family of structurally characterized manganese complexes containing the neutral or anionic forms of methyl(2-pyridyl)ketone oxime as ligands, while they are new examples of structurally characterized compounds in which (py)C(Me)NOH exists exclusively in its neutral form.

Analogues of **1** · (py)C(Me)NOH and **2** with phenyl(2-pyridyl)ketone oxime, (py)C(ph)NOH, are not known to date, and it is currently not evident whether the stability of these species is dependent on the particular nature of the 2-pyridyl oxime ligand. We are studying this matter. Synthetic efforts are also in progress to “activate” the μ_3 to μ_6 bridging potential of the sulfate ligand in Mn complexes containing 2-pyridyl oximes and/or their anions as a means to get access to clusters and polymers with interesting structural and magnetic properties. Studies on the biological activity of **1** · (py)C(Me)NOH and **2** are also planned.

5. Supplementary Information

CCDC 757892 and 757893 contain the supplementary crystallographic data for **1** · (py)C(Me)NOH and **2**. These data can be obtained free of charge via <http://www.ccdc.cam.ac.uk/conts/retrieving.html>, or from the Cambridge Crystallographic Data Centre, 12 Union Road, Cambridge CB2 1EZ, UK; fax: (+44)1223-336033; or e-mail: deposit@ccdc.deposit@ccdc.cam.ac.uk.

Acknowledgments

This work was supported by the Cyprus Research Promotion Foundation (Grant DIETHNIS/STOXOS/0308/14). In dedication to Professor Nick Hadjiliadis for his retirement and for his important contributions to Bioinorganic Chemistry.

References

[1] C. J. Milios, T. C. Stamatatos, and S. P. Perlepes, “The coordination chemistry of pyridyl oximes,” *Polyhedron*, vol. 25, no. 1, pp. 134–194, 2006.

[2] D. T. Rosa, J. A. Krause Baue, and M. J. Baldwin, “Structural and spectroscopic studies of the versatile coordination chemistry of the chiral ligand *N,N*-bis(1-propan-2-onyl oxime)-L-methionine *N'*-methylamide with Ni^{II} and Zn^{II},” *Inorganic Chemistry*, vol. 40, no. 7, pp. 1606–1613, 2001.

[3] K. Sauer, J. Yano, and V. K. Yachandra, “X-ray spectroscopy of the photosynthetic oxygen-evolving complex,” *Coordination Chemistry Reviews*, vol. 252, no. 3–4, pp. 318–335, 2008.

[4] A. Mishra, J. Yano, Y. Pushkar, V. K. Yachandra, K. A. Abboud, and G. Christou, “Heteronuclear Mn-Ca/Sr complexes, and Ca/Sr EXAFS spectral comparisons with the Oxygen-Evolving Complex of Photosystem II,” *Chemical Communications*, no. 15, pp. 1538–1540, 2007.

[5] D. Burdinski, F. Birkelbach, T. Weyhermüller et al., “Encapsulation by a chromium(III)-containing bicyclic ligand cage. synthesis, structures, and physical properties of heterometal complexes $\text{Cr}^{\text{III}}\text{M}^{\text{I}}\text{Cr}^{\text{III}}$ [$\text{M} = (\text{H}^+)_2, \text{Li}(\text{I}), \text{Mg}(\text{II}), \text{Cu}(\text{II}), \text{Ni}(\text{II}), \text{Ni}(\text{IV}), \text{Co}(\text{III}), \text{Fe}(\text{II}), \text{Fe}(\text{III}), \text{Mn}(\text{II})$],” *Inorganic Chemistry*, vol. 37, no. 5, pp. 1009–1020, 1998.

[6] V. Yu. Kukushkin and A. J. L. Pombeiro, “Oxime and oximate metal complexes: unconventional synthesis and reactivity,” *Coordination Chemistry Reviews*, vol. 181, no. 1, pp. 147–175, 1999.

[7] M. J. Goldcamp, S. E. Robison, J. A. Krause Bauer, and M. J. Baldwin, “Oxygen reactivity of a nickel(II)-polyoximate complex,” *Inorganic Chemistry*, vol. 41, no. 9, pp. 2307–2309, 2002.

[8] M. N. Kopylovich, V. Yu. Kukushkin, M. Haukka, J. J. R. Fraústo da Silva, and A. J. L. Pombeiro, “Zinc(II)/ketoxime system as a simple and efficient catalyst for hydrolysis of organonitriles,” *Inorganic Chemistry*, vol. 41, no. 18, pp. 4798–4804, 2002.

[9] S. Akine, T. Taniguchi, T. Saiki, and T. Nabeshima, “Ca²⁺- and Ba²⁺-selective receptors based on site-selective transmetalation of multinuclear polyoxime-zinc(II) complexes,” *Journal of the American Chemical Society*, vol. 127, no. 2, pp. 540–541, 2005.

[10] A. J. L. Pombeiro and V. Yu. Kukushkin, “Reactivity of coordinated oximes,” in *Comprehensive Coordination Chemistry II*, J. A. McCleverty and T. J. Meyer, Eds., vol. 1, pp. 631–637, Elsevier, Amsterdam, The Netherlands, 2004.

[11] J. M. Thorpe, R. L. Beddoes, D. Collison et al., “Surface coordination chemistry: corrosion inhibition by tetranuclear cluster formation of iron with salicylaldehyde,” *Angewandte Chemie: International Edition*, vol. 38, no. 8, pp. 1119–1121, 1999.

[12] S. Khanra, T. Weyhermüller, E. Bill, and P. Chaudhuri, “Deliberate synthesis for magnetostructural study of linear tetranuclear complexes $\text{B}^{\text{III}}\text{Mn}^{\text{II}}\text{Mn}^{\text{II}}\text{B}^{\text{III}}$, $\text{Mn}^{\text{III}}\text{Mn}^{\text{II}}\text{Mn}^{\text{II}}\text{Mn}^{\text{III}}$, $\text{Mn}^{\text{IV}}\text{Mn}^{\text{II}}\text{Mn}^{\text{II}}\text{Mn}^{\text{IV}}$, $\text{Fe}^{\text{III}}\text{Mn}^{\text{II}}\text{Mn}^{\text{II}}\text{Fe}^{\text{III}}$, $\text{Cr}^{\text{III}}\text{Mn}^{\text{II}}\text{Mn}^{\text{II}}\text{Cr}^{\text{III}}$. Influence of terminal ions on the exchange coupling,” *Inorganic Chemistry*, vol. 45, no. 15, pp. 5911–5923, 2006.

[13] D. Robertson, J. F. Cannon, and N. Gerasimchuk, “Double-stranded metal-organic networks for one-dimensional mixed valence coordination polymers,” *Inorganic Chemistry*, vol. 44, no. 23, pp. 8326–8342, 2005.

[14] T. C. Stamatatos, D. Foguet-Albiol, C. C. Stoumpos et al., “Initial example of a triangular single-molecule magnet from ligand-induced structural distortion of a $[\text{Mn}_3^{\text{III}}\text{O}]^{7+}$ complex,” *Journal of the American Chemical Society*, vol. 127, no. 44, pp. 15380–15381, 2005.

- [15] C. J. Milios, C. P. Raptopoulou, A. Terzis et al., "Hexanuclear manganese(III) single-molecule magnets," *Angewandte Chemie: International Edition*, vol. 43, no. 2, pp. 210–212, 2003.
- [16] C. J. Milios, A. Vinslava, A. G. Whittaker et al., "Microwave-assisted synthesis of a hexanuclear Mn^{III} single-molecule magnet," *Inorganic Chemistry*, vol. 45, no. 14, pp. 5272–5274, 2006.
- [17] H. Miyasaka, R. Clérac, K. Mizushima et al., "[Mn₂(saltmen)₂Ni(pao)₂(L)₂(A)₂ with L = pyridine, 4-picoline, 4-*tert*-butylpyridine, *N*-methylimidazole and A = ClO₄⁻, BF₄⁻, PF₆⁻, ReO₄⁻: a family of single-chain magnets," *Inorganic Chemistry*, vol. 42, no. 25, pp. 8203–8213, 2003.
- [18] E. Abele, R. Abele, and E. Lukevics, "Pyridine oximes: synthesis, reactions, and biological activity," *Chemistry of Heterocyclic Compounds*, vol. 39, no. 7, pp. 825–865, 2003.
- [19] M. Alexiou, I. Tsivikas, C. Dendrinou-Samara et al., "High nuclearity nickel compounds with three, four or five metal atoms showing antibacterial activity," *Journal of Inorganic Biochemistry*, vol. 93, no. 3–4, pp. 256–264, 2003.
- [20] C. Papatriantafyllopoulou, G. E. Kostakis, C. P. Raptopoulou, A. Terzis, S. P. Perlepes, and J. C. Plakatouras, "Investigation of the MSO₄ · xH₂O (M = Zn, x = 7; M = Cd, x = 8/3)/methyl 2-pyridyl ketone oxime reaction system: a novel Cd(II) coordination polymer versus mononuclear and dinuclear Zn(II) complexes," *Inorganica Chimica Acta*, vol. 362, no. 7, pp. 2361–2370, 2009.
- [21] C. J. Milios, P. Kyritsis, C. P. Raptopoulou et al., "Di-2-pyridyl ketone oxime [(py)₂CNOH] in manganese carboxylate chemistry: mononuclear, dinuclear and tetranuclear complexes, and partial transformation of (py)₂CNOH to the *gem*-diolate(2-) derivative of di-2-pyridyl ketone leading to the formation of NO₃⁻," *Dalton Transactions*, no. 3, pp. 501–511, 2005.
- [22] C. Papatriantafyllopoulou, C. P. Raptopoulou, A. Terzis, E. Manessi-Zoupa, and S. P. Perlepes, "Investigation of the zinc chloride/methyl(2-pyridyl)ketone oxime reaction system: a mononuclear complex and an inverse 12-metallacrown-4 cluster," *Zeitschrift für Naturforschung*, vol. 61, no. 1, pp. 37–46, 2006.
- [23] M. Alexiou, C. Dendrinou-Samara, C. P. Raptopoulou, A. Terzis, and D. P. Kessissoglou, "From monomer zinc-oxamate complexes to tetranuclear inverse 12-membered and octanuclear 12-membered metallacrowns," *Inorganic Chemistry*, vol. 41, no. 18, pp. 4732–4738, 2002.
- [24] K. Riggle, T. Lynde-Kernell, and E. O. Schlemper, "Synthesis and X-ray structures of Ni(II) complexes of 1-(2-pyridinyl)ethanone oxime," *Journal of Coordination Chemistry*, vol. 25, pp. 117–125, 1992.
- [25] R. Cibulka, I. Čisárová, J. Ondráček, F. Liška, and J. Ludvík, "Electrochemical reductions of Ni²⁺, Cu²⁺ and Zn²⁺ complexes of azinyl methyl ketoximes on mercury," *Collection of Czechoslovak Chemical Communications*, vol. 66, no. 1, pp. 170–184, 2001.
- [26] R. A. Coxall, S. G. Harris, D. K. Henderson, S. Parsons, P. A. Tasker, and R. E. P. Winpenny, "Inter-ligand reactions: in situ formation of new polydentate ligands," *Journal of the Chemical Society, Dalton Transactions*, no. 14, pp. 2349–2356, 2000.
- [27] C. Papatriantafyllopoulou, E. Manessi-Zoupa, A. Escuer, and S. P. Perlepes, "The sulfate ligand as a promising 'player' in 3d-metal cluster chemistry," *Inorganica Chimica Acta*, vol. 362, no. 3, pp. 634–650, 2009.
- [28] S. Y. Nurova, E. P. Turevskaya, V. G. Kessler, and M. I. Yanovskaya, *The Chemistry of Metal Alkoxides*, Kluwer Academic Publishers, Dordrecht, The Netherlands, 2002.
- [29] C. Papatriantafyllopoulou, A. Tasiopoulos, and S. P. Perlepes, unpublished results.
- [30] C. Papatriantafyllopoulou, C. P. Raptopoulou, A. Terzis, J. F. Janssens, S. P. Perlepes, and E. Manessi-Zoupa, "Reactions of nickel(II) sulfate hexahydrate with methyl(2-pyridyl)ketone oxime: two mononuclear sulfato complexes containing the neutral ligand," *Zeitschrift für Naturforschung*, vol. 62, no. 9, pp. 1123–1132, 2007.
- [31] C. C. Stoumpos, T. C. Stamatatos, H. Sartzi et al., "Employment of methyl 2-pyridyl ketone oxime in manganese non-carboxylate chemistry: Mn^{II}Mn^{IV} and Mn^{II}Mn^{III} complexes," *Dalton Transactions*, no. 6, pp. 1004–1015, 2009.
- [32] J. Zuo, J. Dou, D. Li, D. Wang, and Y. Sun, "Dichlorido[1-(2-pyridyl)ethanone oximate][1-(2-pyridyl)ethanone oxime]manganese(III)," *Acta Crystallographica E*, vol. 63, no. 12, pp. m3183–m3184, 2007.
- [33] C. C. Stoumpos, T. C. Stamatatos, V. Psycharis, C. P. Raptopoulou, G. Christou, and S. P. Perlepes, "A new Mn^{II}Mn^{III} cluster from the use of methyl 2-pyridyl ketone oxime in manganese carboxylate chemistry: synthetic, structural and magnetic studies," *Polyhedron*, vol. 27, no. 18, pp. 3703–3709, 2008.
- [34] C. Papatriantafyllopoulou, G. Aromi, A. J. Tasiopoulos et al., "Use of the sulfato ligand in 3d-metal cluster chemistry: a family of hexanuclear nickel(II) complexes with 2-pyridyl-substituted oxime ligands," *European Journal of Inorganic Chemistry*, no. 18, pp. 2761–2774, 2007.
- [35] P. Chaudhuri, M. Winter, U. Flörke, and H.-J. Haupt, "An effectively diamagnetic oximate-bridged asymmetric dinuclear copper(II) complex with a Cu(II)I bond," *Inorganica Chimica Acta*, vol. 232, no. 1–2, pp. 125–130, 1995.
- [36] A. B. P. Lever and E. Mantovani, "The far-infrared and electronic spectra of some bis-ethylenediamine and related complexes of copper(II) and the relevance of these data to tetragonal distortion and bond strengths," *Inorganic Chemistry*, vol. 10, no. 4, pp. 817–826, 1971.
- [37] K. Nakamoto, *Infrared and Raman Spectra of Inorganic and Coordination Compounds*, Wiley, New York, NY, USA, 4th edition, 1986.
- [38] C. Papatriantafyllopoulou, C. G. Efthymiou, C. P. Raptopoulou et al., "Initial use of the di-2-pyridyl ketone/sulfate 'blend' in 3d-metal cluster chemistry: preparation, X-ray structures and physical studies of zinc(II) and nickel(II) cubanes," *Journal of Molecular Structure*, vol. 829, no. 1–3, pp. 176–188, 2007.
- [39] C. Papatriantafyllopoulou, C. G. Efthymiou, C. P. Raptopoulou, A. Terzis, E. Manessi-Zoupa, and S. P. Perlepes, "Mononuclear versus dinuclear complex formation in nickel(II) sulfate/phenyl(2-pyridyl)ketone oxime chemistry depending on the ligand to metal reaction ratio: synthetic, spectral and structural studies," *Spectrochimica Acta A*, vol. 70, no. 4, pp. 718–728, 2008.
- [40] G. B. Deacon and R. J. Phillips, "Relationships between the carbon-oxygen stretching frequencies of carboxylate complexes and the type of carboxylate coordination," *Coordination Chemistry Reviews*, vol. 33, pp. 227–250, 1980.

Research Article

Kinetic Studies and Mechanism of Hydrogen Peroxide Catalytic Decomposition by Cu(II) Complexes with Polyelectrolytes Derived from L-Alanine and Glycylglycine

Spyridon Skounas,¹ Constantinos Methenitis,¹ George Pneumatikakis,¹
and Michel Morcellet²

¹*Inorganic Chemistry Laboratory, Department of Chemistry, University of Athens, Panepistimiopolis, 15771 Athens, Greece*

²*Laboratoire de Chimie Macromoléculaire, UMR 8009 CNRS, Université des Sciences et Technologies de Lille, 59655 Villeneuve d'Ascq, France*

Correspondence should be addressed to Constantinos Methenitis, methenitis@chem.uoa.gr

Received 23 March 2010; Accepted 30 May 2010

Academic Editor: Spyros Perlepes

Copyright © 2010 Spyridon Skounas et al. This is an open access article distributed under the Creative Commons Attribution License, which permits unrestricted use, distribution, and reproduction in any medium, provided the original work is properly cited.

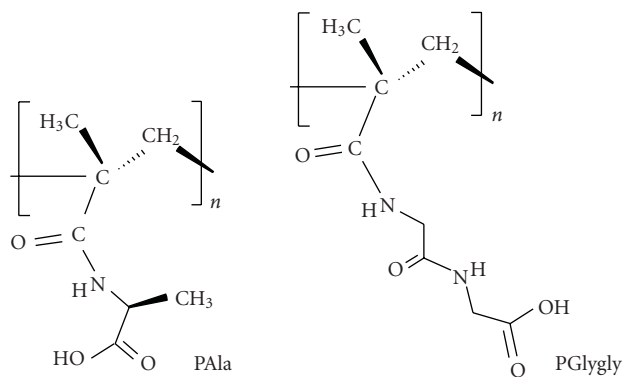
The catalytic decomposition of hydrogen peroxide by Cu(II) complexes with polymers bearing L-alanine (PAla) and glycylglycine (PGlygly) in their side chain was studied in alkaline aqueous media. The reactions were of pseudo-first order with respect to $[H_2O_2]$ and $[L-Cu(II)]$ (L stands for PAla or PGlygly) and the reaction rate was increased with pH increase. The energies of activation for the reactions were determined at pH 8.8, in a temperature range of 293–308 K. A suitable mechanism is proposed to account for the kinetic data, which involves the Cu(II)/Cu(I) redox pair, as has been demonstrated by ESR spectroscopy. The trend in catalytic efficiency is in the order PGlygly > PAla, due to differences in modes of complexation and in the conformation of the macromolecular ligands.

1. Introduction

The formation of complexes between macromolecular ligands and transition metal ions has been widely investigated [1–6]. Synthetic macromolecular systems, offer the possibility of modelling the complexation and reactivity of metal ions with biological ligands [7]. The systems especially that are made up of synthetic polyelectrolytes could be considered as simple but representative models for studying biological ligand-metal interactions [7–9]. The thermodynamic and structural characterization of these metal ions complexes would help in understanding the mechanism and the binding mode of the metals both to proteins and to substrate molecules.

The decomposition of hydrogen peroxide has been used as a model reaction for the investigation of the catalytic activity of various metal complexes and has also been studied as a catalase model, although the catalytic mechanism has not been thoroughly elucidated [1, 2, 10–21]. It has been

known for about a century that the decomposition of H_2O_2 to H_2O and O_2 is drastically accelerated by many metal ions [14–19]. Complexes of copper (II) especially with various ligands acting as catalysts have been investigated in depth and disagreements over mechanistic details, involving intermediate radicals or complexes, have lasted for decades. The formation of copper peroxide complexes both in acidic and alkaline solutions has been confirmed and a mechanism not involving any radicals has been suggested [17, 18]. On the other hand, the existence of OH^\cdot radicals in the decomposition of H_2O_2 , catalyzed by Cu(II), in alkaline media in the presence of biological reductants has been, convincingly, demonstrated [20–22]. The difference in reactivity of Cu(II) complexes towards H_2O_2 is due to the change in the redox potential of Cu(II) ions as a result of ligation with different ligands [23]. It was supposed that a superoxide-copper (I) complex is formed $[HO_2-Cu(I)(Ligand)]$ from the complex $[HO_2-Cu(II)(Ligand)]$ in which an instantaneous electron transfer occurs [21]. Other investigators



SCHEME 1: The polyelectrolytes poly-N-methacryloyl-L-alanine (PALa) and poly-N-methacryloyl-glycylglycine (PGlygly).

suggested the formation of a Cu(III)-peroxo complex, as a consequence of the interaction of Cu(II) ions with H_2O_2 , this species producing highly reactive $\text{OH}\cdot$ radicals [24–30]. Recently, a mechanism involving both Cu(I)/Cu(II) and Cu(II)/Cu(III) redox pairs has been reported [31]. It has also been proposed that in slight alkaline and neutral pH region, the decomposition of H_2O_2 by copper complexes may proceed by a combination of a molecular mechanism, in which a presumed intermediate species $[\text{CuL}(\text{HO}_2^-)]^+$, reacts with $[\text{HO}_2^-]$, a free-radical mechanism involving reversible oxidation reduction of a cupric-cuprous couple, and the formation of free radicals, for example, $\text{HO}_2\cdot$ and $\text{HO}\cdot$, leading to a chain reaction [32]. Other researchers have mentioned the formation of a peroxo-copper complex (brown compound) in the homogeneous and heterogeneous H_2O_2 decomposition with different Cu(II) complex ions that are by themselves active catalysts for H_2O_2 decomposition [33].

A series of polymers that are referred to as “nonpeptide amino acid-based polymers” or as “amino acid-derived polymers with modified backbones” [34] was previously synthesized and shown to exhibit polyelectrolyte and metal complexation behavior [35–40]. In previous works it has been shown that the complexes of Cu(II) with polyelectrolytes derived from glutamic and aspartic acids exhibit substantial catalytic activity in the decomposition of H_2O_2 in alkaline media [41, 42]. Key feature in these systems is the coordination of the ligands to Cu(II) through two amidic N^- from adjacent amino acids [41, 42]. In the present work, we investigate the catalytic activity of Cu(II) complexes with polyelectrolytes derived from alanine, PALa, and diglycine, PGlygly, (Scheme 1) towards the H_2O_2 decomposition in alkaline solutions. A suitable mechanism is proposed to account for the kinetic and ESR spectroscopic studies.

2. Experimental Section

2.1. Materials and Methods. All chemicals were of analytical reagent grade and were employed without further purification. The poly(N-methacryloyl-L-alanine) (PALa) and poly(N-methacryloyl-diglycine) (PGlygly) were prepared by

polymerization of the corresponding monomers, carried out in dioxane (p.a Merck) at 60°C with AIBN (azobisisobutyronitrile) as initiator. The monomers N-methacryloyl-L-alanine and N-methacryloyl-diglycine were prepared from methacryloyl chloride (tech. 90%, with 150 ppm phenothiazine, Aldrich Chem.Co) and L-alanine (optical purity >99, 5% NT, Fluca) and glycinoglycine (>99, 5% NT, Fluka), respectively, according to the method of Kulkarni and Morawetz [43]. Full experimental details of the synthesis of these compounds have been published earlier [35, 37]. $\text{Cu}(\text{ClO}_4)_2 \cdot 6\text{H}_2\text{O}$ (Fluca) was used as the metal ion source. Water was obtained from a Milli-Q purification system (Millipore), which was feeded with doubly distilled water. The concentration of Cu(II) solutions was determined by complexometric titrations with EDTA. Working solutions of hydrogen peroxide were prepared weekly by volumetric dilution of 30% (v/v) H_2O_2 (AR. grade, Merck) and were standardized daily by titration with potassium permanganate. It was found that the natural decomposition rate of aqueous H_2O_2 solution was less than 1% in 24 h.

The decomposition of H_2O_2 catalyzed by Cu(II) complexes can be kinetically monitored by removing aliquots of the reaction mixture at predetermined intervals and titrating the undecomposed H_2O_2 with standard KMnO_4 solutions (0.04–0.05 N), standardized with $(\text{COONa})_2$ (primary standard). The decomposition of hydrogen peroxide was carried out in a thermostated cell at four different temperatures between 293 and 308 K (± 0.1 K). The pH of the solutions was adjusted between 7 and 11 with buffer solution of H_3BO_3 - NaClO_4 and the appropriate quantities of NaOH 0.1 M and between 6–7 with buffer solution of phosphate. The pH measurements were performed using a digital Xenon pHmeter and a RUSSEL CMAWL/3.7/180 combined electrode. Standardization was done at 25°C with Russel buffers (potassium hydrogen phthalate at pH 4, potassium dihydrogen orthophosphate-disodium hydrogen orthophosphate at pH 7 and sodium hydrogen carbonate/sodium carbonate at pH 10). The chosen concentration range of H_2O_2 was 3.3×10^{-3} to 1.3×10^{-2} M. The analytical concentration of Cu(II) ranged from 1.3×10^{-4} to 7.8×10^{-4} M and the $[\text{ligand}]/[\text{metal}]$ ratio (R) was chosen to be 4 and 8. The decomposition of H_2O_2 was halted with the addition of H_2SO_4 . Acidification effectively halted the alkaline decomposition at the desired time and titrations with potassium permanganate in acidic media could be carried out even 1 h later without significant discrepancy.

2.2. EPR Measurements. The measurements were made in frozen (77 K) aliquots of the solutions of the reactions between the systems L-Cu(II) (L stands for PALa and PGlygly) ($R = 4$, $[\text{Cu(II)}] = 1.0 \times 10^{-3}$) and H_2O_2 at pH between 8.0 and 9.0 at 298 K, taken out at different times and carried out on a Bruker ESP-300 spectrometer (X-band) with 100 kHz field modulation, 9.3 GHz microwave frequency and equipped with a standard low-temperature apparatus. The hyperfine coupling constants and g-factors were calibrated by comparison with DPPH (2,2-diphenyl-1-picrylhydrazyl) ($g = 2.0028$)

3. Results and Discussion

3.1. Solution Structure of the Complexes. The presence of both the carboxyl and the amidic groups in the ligands (Scheme 1) gives the possibility of different complex type formation. Although the exact geometry of the formed complexes cannot be reached because of the complexity of the macromolecular structures, the atoms of the ligands which interact with the Cu(II) ions and the stoichiometry of the formed complexes can be determined. Based on the potentiometric and spectroscopic results, molecular structures for the dominant copper(II)-PAla species existing in aqueous solutions were previously proposed in [35, 36]. At $\text{pH} < 4$ the complex formation involves two carboxylates and water molecules (type (I) complex); at $\text{pH} > 4$ another complex, a chelate with the participation of a deprotonated N atom of the amide function, starts to form (type (II) complex), that gradually becomes the main species. At $\text{pH} > 9$ complexes which involve two deprotonated amide N are also detected (type (III) complexes). For PGlygly-Cu(II) systems, at $\text{pH} < 9.5$ different complexes involving carboxylates, water molecules and/or hydroxyls are detected (type (I) complexes) [39]. At $\text{pH} > 9.5$ complexes with the participation of deprotonated N atoms of the amide functions are, as previously, also formed (type (III) complexes, unpublished results). It must be mentioned that at $\text{pH} > 9$ hydrolysis, in some extent, of the above copper complexes occurs and the formed copper hydroxides do not precipitate but could be firmly bounded to the soluble polyelectrolytes [44, 45].

3.2. Catalytic Properties. A number of experiments were performed to study the effect of pH, H_2O_2 , and Cu(II) concentrations and temperature on the initial rate of the catalytic decomposition of H_2O_2 from the PAla-Cu(II) and PGlygly-Cu(II) systems. The reaction velocities at $t \rightarrow 0$ (v_0) were determined graphically from the tangential slopes of the curves, at zero time, which represent the concentration of hydrogen peroxide in respect to the elapsed reaction time. Thus the initial rate, v_0 , was expressed as $v_0 = (dc/dt)_{t \rightarrow 0}$.

Characteristic changes in the colour of the reaction solutions take place during the course of the reactions. The clear sky blue solutions of Cu(II) complexes turn into blurred blue-green after the addition of H_2O_2 . Gradually, they become yellow-green and when concentrations of hydrogen peroxide higher than 1.3×10^{-2} M are used, a yellow-brown solid precipitates from the solutions with $\text{pH} > 9.5$. No attempt was made to investigate the nature of this precipitate. Small bubbles of oxygen are formed during the reaction. Within a week the reaction solutions did not get the initial colour. Blank experiments were performed and no catalytic activity was observed when solutions containing only the polymers in the absence of Cu(II) were used, in the whole pH range. At the pH range under investigation copper hydroxide is precipitated in the absence of the polyelectrolytes.

The reactions are found to be of pseudo-first order with respect to H_2O_2 (Figure 1) for all the studied pH and $[\text{H}_2\text{O}_2]/\text{catalyst}$ ratios. The order of the reactions was not found to decrease with the increase of the initial H_2O_2

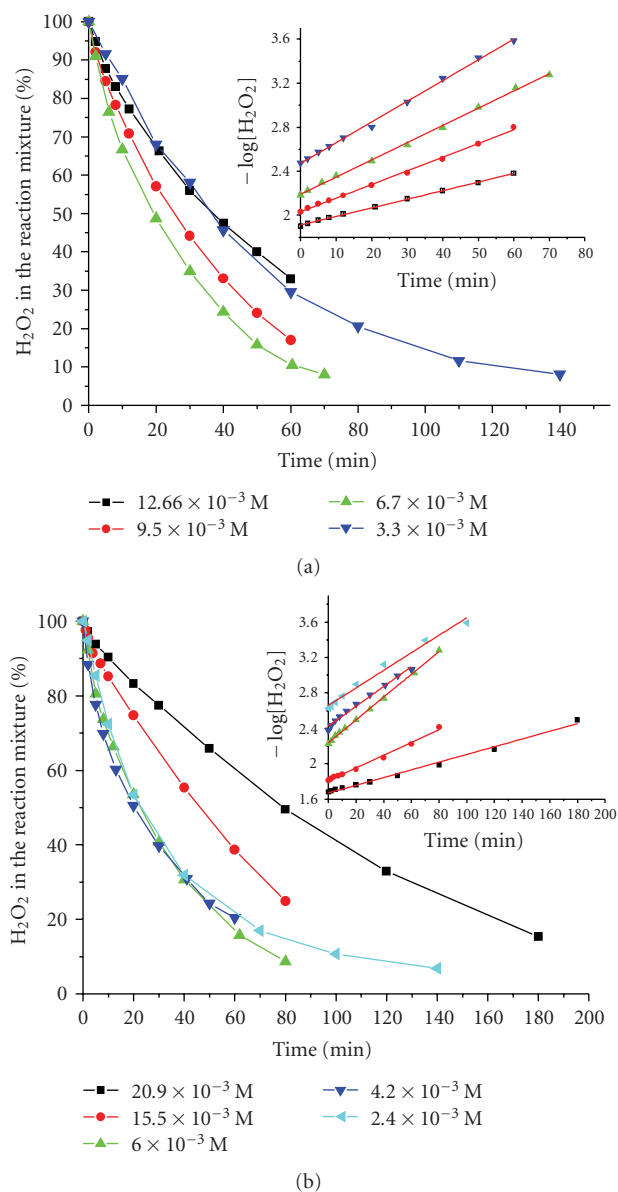


FIGURE 1: The variation of $[\text{H}_2\text{O}_2]$ in the reaction mixture (% of the initial concentration) and (insert) negative logarithm of titrated H_2O_2 concentration versus time, from solutions of different initial $[\text{H}_2\text{O}_2]$ at $\text{pH} = 8.7$ for the system (a) PAla-Cu(II), $[\text{PAla}] = 2.0 \times 10^{-3}$ M, $[\text{Cu}^{2+}] = 5.0 \times 10^{-4}$ M. $T = 298$ K. (b) PGlygly-Cu(II), $[\text{PGlygly}] = 2.0 \times 10^{-3}$ M, $[\text{Cu}^{2+}] = 5.0 \times 10^{-4}$ M. $T = 298$ K.

concentration. The reactions were, also, found to be of pseudo-first order with respect to the total concentration of Cu(II) (Figure 2) for all the studied pH and $[\text{H}_2\text{O}_2]/\text{catalyst}$ ratios.

The dependence of the reaction rates on pH is given in Figure 3. The rates of H_2O_2 decomposition are pH-dependent. The observed rates $\{d[\text{H}_2\text{O}_2]/dt\}_{t \rightarrow 0, \text{obs}}$ are very low below $\text{pH}:8$ and strongly increase in the alkaline region. The order was found to be between -0.4 and -0.8 with respect to $[\text{H}^+]$, depending on the $[\text{H}_2\text{O}_2]$. A possible explanation is discussed forward in the text.

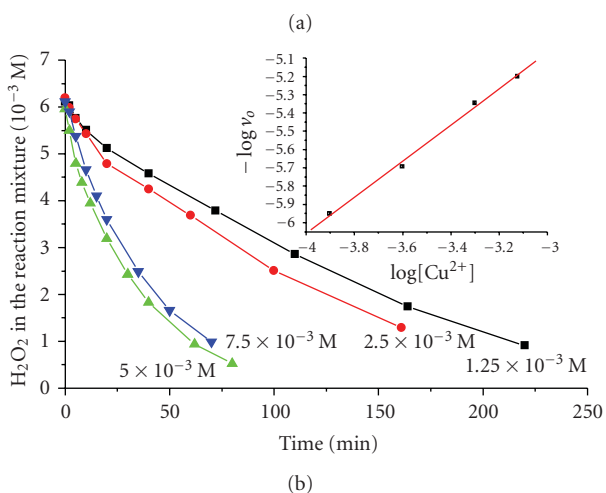
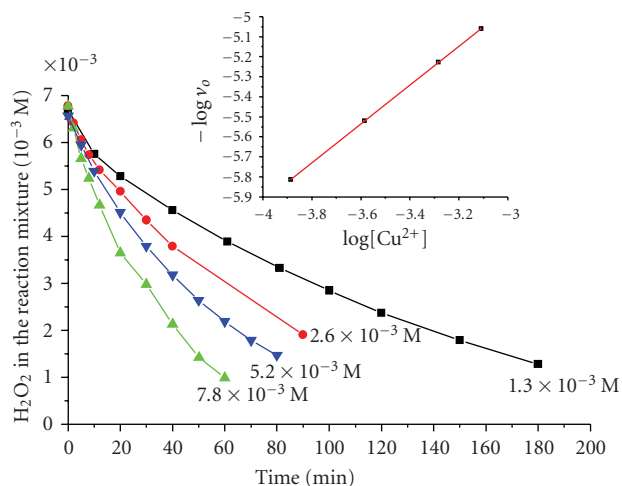


FIGURE 2: The variation of $[H_2O_2]$ in the reaction mixture (% of the initial concentration) versus time for different Cu(II) concentrations, and (insert) logarithm of the initial rate (v_0) versus logarithm of the $[Cu(II)]$ for the system (a) Pala-Cu(II), $R = [PAla]/[Cu(II)] = 4$, initial concentration $[H_2O_2] = 6.8 \times 10^{-3}$ M, $pH = 8.5$, $T = 298$ K. (b) PGlygly-Cu(II), $R = [PGlygly]/[Cu(II)] = 4$, initial concentration $[H_2O_2] = 6.2 \times 10^{-3}$ M, $pH = 8.9$, $T = 298$ K.

3.2.1. Effect of Temperature Activation Parameters. Using Arrhenius plots (Figure 4) and the Arrhenius equation the activation energies, E_a , were calculated at $pH 8.8$ (Table 1).

The difference in the activation energy values between the PGlygly-Cu(II) system and the Pala-Cu(II) system should reflect not only the different microenvironment of the Cu(II) ions, but also the differences of the macromolecular ligands. In these two systems, key feature is the coordination of the ligand derived from alanine to each Cu(II) through deprotonated amide nitrogens and carboxylates [35, 36] and of the ligand derived from diglycine to each Cu(II) through carboxylates [39, 46]. (Indeed, in the first coordination sphere of Cu(II) ions amidic nitrogen(s) and oxygens are involved in the Pala system, while only oxygens are involved in the case of the PGlygly.) Furthermore, the distance of the copper centers from the polymeric backbone is smaller in the

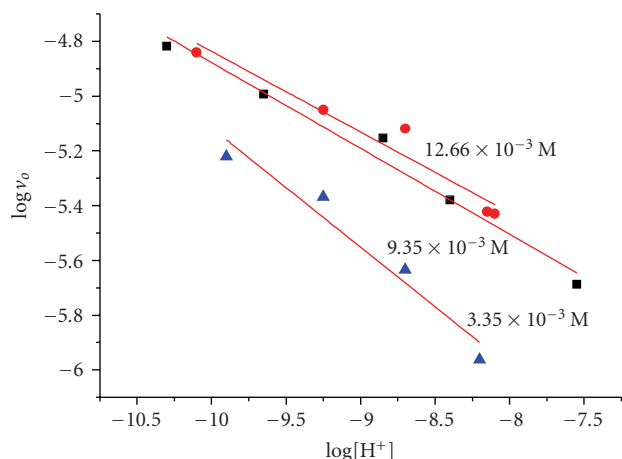


FIGURE 3: The variation of the logarithm of the initial rate (v_0) versus logarithm of $[H^+]$ at different hydrogen peroxide concentrations for the system Pala-Cu(II), $[PAla] = 2.0 \times 10^{-3}$ M, $[Cu^{2+}] = 5.0 \times 10^{-4}$ M. $T = 298$ K.

Pala than in the PGlygly system. As this distance increases, not only the approach of small molecules to the metal centers is more favorable, but also any structural changes around the metals are made more easily. The different mode of complexation of the two systems is, also, reflected on the differences in the variations of the enthalpies of activation, ΔH^\ddagger , for the two systems, as ΔH^\ddagger is a measure of the height of the energy barrier that should be overcome to reach the transition state and is related to the strengths of the intra- and intermolecular bonds which participate in the reaction leading to the transition state.

3.2.2. ESR Measurements. To verify the above assumptions, the catalytic reactions that take place in solutions with pH in the range 8-9 were, also, followed with ESR spectroscopy, in order to gain some insight of the mechanism and to deduce evidence for the participating intermediates. The change of the intensity of the axial ESR signal of paramagnetic Cu(II) during the course of the reactions was monitored and the existence of any new signal, due to any newly formed paramagnetic Cu(II) species, was investigated.

The two systems exhibited a completely different behavior. For the Pala-Cu(II) system we can detect three stages of the reaction (Figure 5). In the first, very short stage, a slight increase in the intensity of the signal is observed. In the second stage a rapid decrease in the intensity occurs until it reaches about 20% of the starting intensity without entire disappearance. In the final stage the signal starts building up again in a slow rate without ever reaching the original intensity. From our results it was not easy to assign any new EPR absorbing Cu(II) species, formed during the reaction. Furthermore, as any additional spectral lines in the area of $g = 4$ were not detected, any Cu(II)-Cu(II) strong antiferromagnetic coupling was precluded to be the reason for the decrease in the intensity of the signal [47, 48]. Finally, as the formation of a diamagnetic Cu(III) complex (d^8 low-spin complex) can also be ruled out, since it requires ligands

TABLE 1: Calculated energy parameters for the decomposition of H_2O_2 from the systems PAla-Cu(II) and PGlygly-Cu(II), respectively. $T = 298 \text{ K}$, $[\text{Cu}^{2+}] = 5.2 \times 10^{-4} \text{ M}$, $[\text{PAla}] = 2.0 \times 10^{-3} \text{ M}$, $[\text{PGlygly}] = 2.0 \times 10^{-3} \text{ M}$, $R = 4$, $[\text{H}_2\text{O}_2] = 6.7 \times 10^{-3} \text{ M}$, $\text{pH} = 8.8$.

	$E_a^\#$ (Kcal·mol ⁻¹)	$\Delta G^\#$ (Kcal·mol ⁻¹)	$\Delta H^\#$ (Kcal·mol ⁻¹)	$\Delta S^\#$ (cal·K ⁻¹ ·mol ⁻¹)
PAla-Cu(II)	19.2 (± 1.1)	13.6	18.6 (± 1.1)	16.8
PGlygly-Cu(II)	14.6 (± 3.6)	13.3	14.0 (± 3.6)	2.1

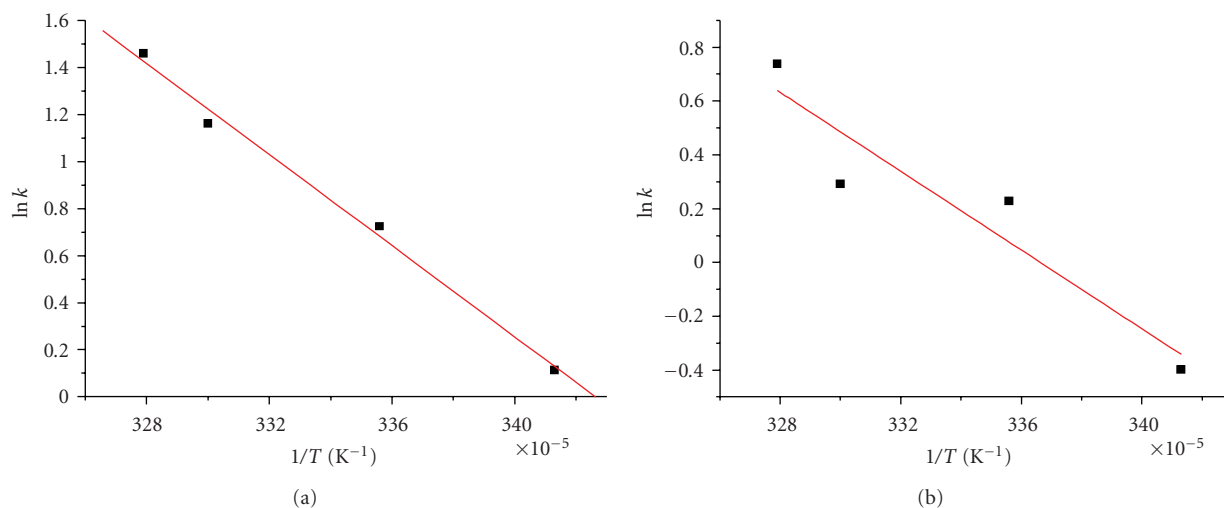


FIGURE 4: Arrhenius plots for the system (a) PAla-Cu(II), $[\text{PAla}] = 2.0 \times 10^{-3} \text{ M}$, $[\text{Cu}^{2+}] = 5.0 \times 10^{-4} \text{ M}$, $[\text{H}_2\text{O}_2] = 6.7 \times 10^{-3} \text{ M}$, $\text{pH} = 8.8$ (b) PGlygly-Cu(II), $[\text{PGlygly}] = 2.0 \times 10^{-3} \text{ M}$, $[\text{Cu}^{2+}] = 5.0 \times 10^{-4} \text{ M}$, $[\text{H}_2\text{O}_2] = 6.7 \times 10^{-3} \text{ M}$, $\text{pH} = 8.8$.

able to give strong fields as tetrapeptides or ligands able to give a four-nitrogen in plane coordination [49], and no evidence of ESR lines due to paramagnetic Cu(III) complexes could be found, the reduction of EPR-silent Cu(I) complex is strongly suggested. The small initial increase in the intensity of the signal could be explained as the result of the adoption from the negatively charged macromolecular catalyst of a more extended structure that enables the approach of the, also, negatively charged peroxy anion that comes from the dissociation of H_2O_2 that occurs at this pH. In this structure, the metallic centers are further apart from each other and any small spin exchange between them is diminished.

The system PGlygly-Cu(II) shows a signal with an initial intensity of 20% of the initial intensity of the signal of the system PAla-Cu(II), for the same total Cu(II) concentration. The signal does not decrease in intensity as the reaction proceeds, but instead constantly increases. It finally reaches a plateau when the intensity equals the initial intensity of the signal of the PAla-Cu(II) system. This striking difference could not be explained only by the different nature of the catalytic sites (Cu(II) complexes), without taking into account that these sites are a part of a three-dimensional macromolecule. As the experimental conditions (pH, ionic strength, Cu(II) and polymer concentrations, temperature) of the formation of the complexes as well as the anchoring groups (amides and carboxylates) are exactly the same, the difference in the modes of complexation must be related to conformational effects. Indeed the complex formation between a polyelectrolyte and a metal ion causes many

effects, mainly arising from changes in the net charge of the polymer and changes in the electrostatic interactions [2, 50, 51]. In previous works we have reported the effect of the complexation of Cu(II) ions on the hydrodynamic behavior of the PAla and PGlygly [39, 52]. In these works viscosimetric studies clearly demonstrated the formation of intramolecular Cu(II)-carboxylates complexes, which lead to the folding of the macromolecules. At higher pH values, when amide nitrogens replace carboxylates on the coordination sphere of Cu(II), only neighboring side chains are involved in complex formation, resulting in the unfolding of the macromolecules.

As a result of the differences in the complexation modes and the macromolecular ligand conformations of the two systems at the pH range under investigation, the mutual approach of the copper centers is feasible for PGlygly-Cu(II) complex but not for PAla-Cu(II). Consequently extensive Cu(II)-Cu(II) spin interactions may arise only in the PGlygly-Cu(II) system. These spin interactions explain the much smaller intensity of the initial signal in the PGlygly-Cu(II) system, as has been observed in other systems where copper-copper dipole interactions are promoted by the ligands [53, 54]. No signals were observed near $g = 4$ and $G = (g_{\parallel} - 2)/(g_{\perp} - 2)$ is greater than 4, indicating negligible exchange interactions [48, 55]. The approach of H_2O_2 and complexation to Cu(II) cause the unfolding of the macromolecule, as has been observed elsewhere [56], breaking the existing intra- and inter-crossings between the chains of the polymer. This results in the reduction of the spin interactions between copper centers and consequently

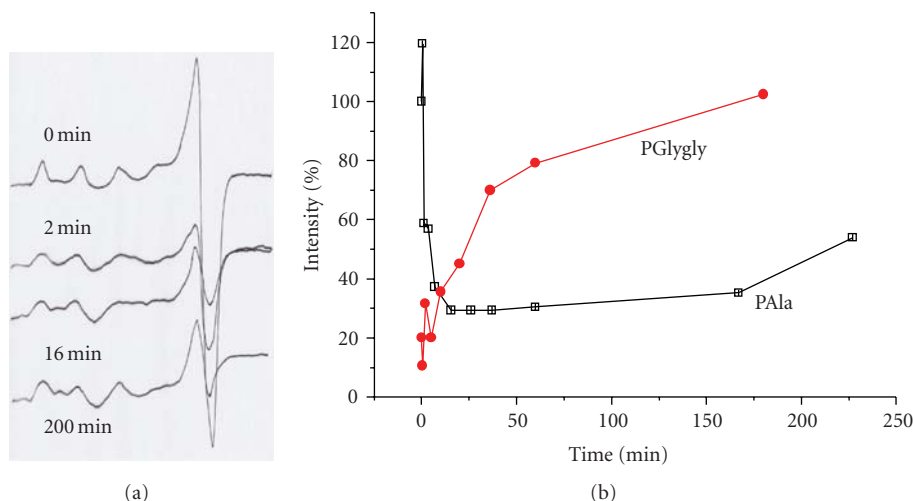


FIGURE 5: (a) EPR spectra of a frozen solution (77 K) of Pala-Cu(II) at different reaction times. $[\text{Cu(II)}] = 1.0 \times 10^{-3} \text{ M}$, $R = [\text{PAla}]/[\text{Cu(II)}] = 4$, $\text{pH} = 8.7$. (b) The variation of the intensity of Cu(II) signal, as (%) of the initial signal ($t = 0 \text{ min}$), during the reaction time for the systems Pala-Cu(II) and PGlygly-Cu.

the increase of the intensity of the paramagnetic signal. Obviously, the magnitude of the increase is bigger than the magnitude of the simultaneous decrease due to the reduction of Cu(II) to Cu(I). Furthermore, it seems that the reoxidation step $\{\text{Cu(I)} \text{ to } \text{Cu(II)}\}$ is much quicker for the PGlygly polymer, as after 3 hrs from the beginning of the reaction all the copper is in the Cu(II) state, while for the Pala polymer only 20% of the copper is in the Cu(II) state at the same time.

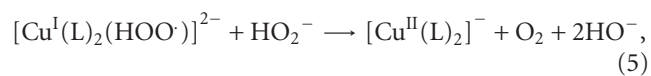
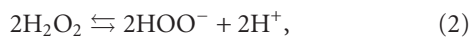
We did not detect any new signals due to different from the initial Cu(II) species, for the period of a week. Thus, our experimental data cannot support the degradation process that has been reported for other systems [57].

3.2.3. Kinetics and Mechanism. Kinetic studies in the conditions mentioned above showed that the initial rate of the decomposition of H_2O_2 is proportional to $[\text{H}_2\text{O}_2]$, $[\text{CuL}_2]$. For a given pH stands

$$v_o = -d \frac{[\text{H}_2\text{O}_2]}{dt} = k_{\text{obs}}[\text{CuL}_2][\text{H}_2\text{O}_2], \quad (1)$$

(k_{obs} depends on the pH of the solution).

The following reactions are consistent with the above-mentioned observed rate law and the thermodynamic and spectroscopic measurements



It is assumed that step (4) is the rate determining step of the reaction, as the reduction of Cu(II) requires geometrical changes around the metal center. According to the Franck-Condon principle, before the electron-transfer the coordinate bonds between the cupric ion and the ligands must be stretched and the cupric complex must be rearranged to a structure which can accept one electron. This mechanism is in agreement with the suggestion for other macromolecular systems [21] and can explain the change in rate in going to more alkaline conditions, as the dependence of the redox potential of the couple HO_2^\cdot ($\text{O}_2^{\cdot-}$)/ H_2O_2 (HO_2^-) on pH is very well known. The redox potential drops from 1.4 to 0.18 V over the pH range 0–14 [21]. It is obvious that the oxidation of H_2O_2 to HO_2^\cdot or $\text{O}_2^{\cdot-}$ by Cu(II) is more favorable in more alkaline conditions. This kind of mechanism does not involve any diffusible radical species in accordance to previous proposed mechanism [10, 18], but several very rapid intermediate steps between (4) and (5) may exist which include the participation of radicals. This should explain the nonlinear dependence of the initial rate of the reaction from $[\text{H}^+]$ as well as the formation of the brown peroxo-copper precipitate at high H_2O_2 concentrations, but from our data no conclusion can be drawn about the possible structures of these intermediate species

4. Conclusions

The complexes of copper (II) with the functional polymers Pala and PGlygly act as catalysts in the decomposition of H_2O_2 at alkaline conditions. The trend in catalytic efficiency is in the order PGlygly > Pala, due to differences in the modes of complexation and the adopted conformations of the macromolecules upon complexation. The catalytic decomposition depends upon the concentration of H_2O_2 , the concentration of the catalyst, temperature, and pH of

the reacting solutions. The rate of the reaction is of pseudo-first order with respect to the concentration of H_2O_2 and the concentration of the catalyst at the pH range 7–10. The proposed mechanism involves reduction of Cu(II) to Cu(I), during the slow rate determining step.

Acknowledgments

The authors thank the General Secretariat of Research and Technology (GSRT), Project 91EΔ831 and the University of Athens for financial support.

References

- [1] M. Kaneko and E. Tsuchida, "Formation, characterization, and catalytic activities of polymer-metal complexes," *Journal of Polymer Science, Macromolecular Reviews*, vol. 16, pp. 397–522, 1981.
- [2] E. Tsuchida and H. Nishide, "Polymer-metal complexes and their catalytic activity," *Advances in Polymer Science*, no. 24, pp. 1–87, 1977.
- [3] Y. Kurimura, "Macromolecule metal complexes—reactios and molecular recognition," *Advances in Polymer Science*, vol. 90, pp. 105–138, 1989.
- [4] J. François, C. Heitz, and M. M. Mestdagh, "Spectroscopic study (u.v.-visible and electron paramagnetic resonance) of the interactions between synthetic polycarboxylates and copper ions," *Polymer*, vol. 38, no. 21, pp. 5321–5332, 1997.
- [5] M. Palumbo, A. Cosani, M. Terbojevich, and E. Peggion, "Metal complexes of poly(α -amino acids). Interaction of Cu (II) ions with poly(L-lysine) in the 0-Structure," *Biopolymers*, vol. 17, pp. 243–246, 1978.
- [6] W. Bal, M. Dyba, F. Kasprzykowski et al., "How non-bonding amino acid side-chains may enormously increase the stability of a Cu(II)—peptide complex," *Inorganica Chimica Acta*, vol. 283, no. 1, pp. 1–11, 1998.
- [7] H. J. van den Berg and G. Challa, "Polymeric models of reactive biological systems," in *Syntheses and Separations Using Functional Polymers*, D. C. Sherrington and P. Hodge, Eds., pp. 227–264, Wiley, New York, NY, USA, 1988.
- [8] J. J. Grodzinski, "Biomedical application of functional polymers," *Reactive and Functional Polymers*, vol. 39, no. 2, pp. 99–138, 1999.
- [9] E. A. Bekturov, S. E. Kudaibergenov, and V. B. Sigitov, "Complexation of amphoteric copolymer of 2-methyl-5-vinylpyridine-acrylic acid with copper(II) ions and catalase-like activity of polyampholyte-metal complexes," *Polymer*, vol. 27, no. 8, pp. 1269–1272, 1986.
- [10] H. Sigel, K. Wyss, B. E. Fischer, and B. Priejs, "Metal ions and hydrogen peroxide. Catalase-like activity of Cu^{2+} in aqueous solution and its promotion by the coordination of 2,2'-bipyridyl," *Inorganic Chemistry*, vol. 18, no. 5, pp. 1354–1358, 1979.
- [11] G. S. Vinodkumar and B. Mathew, "Polymer-metal complexes of glycine functions supported on N,N'-methylene-bis-acrylamide (NNMBA)-crosslinked polyacrylamides: synthesis, characterisation and catalytic activity," *European Polymer Journal*, vol. 34, no. 8, pp. 1185–1190, 1998.
- [12] L. Jose and V. N. R. Pillai, "Catalase-like activity of divinylbenzene (DVB)-crosslinked polyacrylamide supported amino metal complexes," *European Polymer Journal*, vol. 32, no. 12, pp. 1431–1435, 1996.
- [13] L. Jose and V. N. R. Pillai, "Catalase-like activity of triethyleneglycol dimethacrylate-crosslinked polyacrylamide supported metal complexes," *Polymer*, vol. 39, no. 1, pp. 229–233, 1998.
- [14] F. Haber and J. Weiss, "The catalytic decomposition of hydrogen peroxide by iron salts," *Proceedings of the Royal Society A*, vol. 147, pp. 332–351, 1934.
- [15] W. G. Barb, J. H. Baxendale, P. George, and K. R. Hargrave, "Reactions of ferrous and ferric ions with hydrogen peroxide. Part II. The ferric ion reaction," *Transactions of the Faraday Society*, vol. 47, pp. 591–616, 1951.
- [16] M. L. Kremer and G. Stein, "The catalytic decomposition of hydrogen peroxide by ferric perchlorate," *Transactions of the Faraday Society*, vol. 55, pp. 959–973, 1959.
- [17] A. Glasner, "203. The constitution of copper peroxide and the catalytic decomposition of hydrogen peroxide," *Journal of the Chemical Society*, pp. 2464–2467, 1959.
- [18] H. Sigel, C. Flierl, and R. Griesser, "On the kinetics and mechanism of the decomposition of hydrogen peroxide, catalyzed by the Cu^{2+} -2,2'-bipyridyl complex," *Journal of the American Chemical Society*, vol. 91, no. 5, pp. 1061–1064, 1969.
- [19] M. L. Kremer, "Complex versus free radical mechanism for the catalytic decomposition of H_2O_2 by ferric ions," *International Journal of Chemical Kinetics*, vol. 17, pp. 1299–1314, 1985.
- [20] G. Vierke, "Electron spin resonance spectra of the reaction products of copper(II) hydroxide suspensions in methanol with hydrogen peroxide and of polycrystalline copper(II) hydroxide and copper(II) peroxide," *Journal of the Chemical Society, Faraday Transactions 1*, vol. 69, pp. 1523–1531, 1973.
- [21] Y. Luo, K. Kustin, and I. R. Epstein, "Systematic design of chemical oscillators. 44. Kinetics and mechanism of hydrogen peroxide decomposition catalyzed by copper(2+) in alkaline solution," *Inorganic Chemistry*, vol. 27, pp. 2489–2496, 1988.
- [22] T. Ozawa and A. Hanaki, "The first ESR spin-trapping evidence for the formation of hydroxyl radical from the reaction of copper(II) complex with hydrogen peroxide in aqueous solution," *Journal of the Chemical Society, Chemical Communications*, no. 5, pp. 330–332, 1991.
- [23] T. Ozawa, A. Hanaki, K. Onodera, M. Kasai, and Y. Matsushima, "Can copper(II) complexes activate hydrogen peroxide? : ESR-spin trapping studies," *Journal of Pharmacobio-Dynamics*, vol. 13, supplement 2, 1991.
- [24] K. Hayakawa and S. Nakamura, "The decomposition of hydrogen peroxide with metal complexes. I. The catalytic decomposition of hydrogen peroxide by the ammine-copper(II) complex ions in an aqueous solution," *Bulletin of the Chemical Society of Japan*, vol. 47, pp. 1162–1167, 1974.
- [25] P. Tachon, "Ferric and cupric ions requirement for DNA single-strand breakage by H_2O_2 ," *Free Radical Research Communications*, vol. 7, no. 1, pp. 1–10, 1989.
- [26] G. R. A. Johnson, N. B. Nazhat, and R. A. Saadalla-Nazhat, "Reaction of the aquocopper(I) ion with hydrogen peroxide: evidence against hydroxyl free radical formation," *Journal of the Chemical Society, Chemical Communications*, no. 7, pp. 407–408, 1985.
- [27] H. C. Sutton and C. C. Winterbourn, "On the participation of higher oxidation states of iron and copper in Fenton reactions," *Free Radical Biology and Medicine*, vol. 6, no. 1, pp. 53–60, 1989.
- [28] M. Masarwa, H. Cohen, D. Meyerstein, D. L. Hickman, A. Bakac, and J. H. Espenson, "Reactions of low-valent transition-metal complexes with hydrogen peroxide. Are they

- "fenton-like" or not? 1. The case of Cu^+ aq and Cr^{2+} aq," *Journal of the Chemical Society*, vol. 110, no. 13, pp. 4293–4297, 1988.
- [29] G. Czapski, S. Goldstein, and D. Meyerstein, "What is unique about superoxide toxicity as compared to other biological reductants? A hypothesis," *Free Radical Research Communications*, vol. 4, no. 4, pp. 231–236, 1988.
- [30] G. R. A. Johnson and N. B. Nazhat, "Kinetics and mechanism of the reaction of the bis(1,10-phenanthroline)copper(I) ion with hydrogen peroxide in aqueous solution," *Journal of the American Chemical Society*, vol. 109, no. 7, pp. 1990–1994, 1987.
- [31] M. Jezowska-Bojczuk, W. Leśniak, W. Bal et al., "Molecular mechanism of hydrogen peroxide conversion and activation by Cu(II)-amikacin complexes," *Chemical Research in Toxicology*, vol. 14, no. 10, pp. 1353–1362, 2001.
- [32] J. Schubert, V. S. Sharma, E. R. White, and L. S. Bergelson, "Catalytic decomposition of hydrogen peroxide by copper chelates and mixed ligand complexes of histamine in the presence of phosphate buffer in the neutral pH region," *Journal of the American Chemical Society*, vol. 90, no. 16, pp. 4476–4478, 1968.
- [33] M. Y. El-Sheikh, F. M. Ashmawy, I. A. Salem, and A. B. Zaki, "Heterogeneous decomposition of hydrogen peroxide with transition metal-ammine complexes I. Kinetics of catalytic decomposition of hydrogen peroxide in presence of resins in the form of ammine- Cu (II) complex ions in aqueous medium," *Zeitschrift für Physikalische Chemie*, vol. 268, pp. 595–606, 1987.
- [34] S. L. Bourke and J. Kohn, "Polymers derived from the amino acid L-tyrosine: polycarbonates, polyarylates and copolymers with poly(ethylene glycol)," *Advanced Drug Delivery Reviews*, vol. 55, no. 4, pp. 447–466, 2003.
- [35] C. Methenitis, J. Morcellet-Sauvage, and M. Morcellet, "The interaction of poly(N-methacryloyl-L-alanine) with copper (II) 1. Potentiometric study," *Polymer Bulletin*, vol. 12, no. 2, pp. 133–139, 1984.
- [36] C. Methenitis, J. Morcellet-Sauvage, and M. Morcellet, "The interaction of poly(N-methacryloyl-L-alanine) with copper (II) 2. Spectroscopic study," *Polymer Bulletin*, vol. 12, no. 2, pp. 141–147, 1984.
- [37] C. Methenitis, J. Morcellet, G. Pneumatikakis, and M. Morcellet, "Polymers with amino acids in their side chain: conformation of polymers derived from glycylglycine and phenylalanine," *Macromolecules*, vol. 27, no. 6, pp. 1455–1460, 1994.
- [38] C. Methenitis, G. Pneumatikakis, M. Pitsikalis, J. Morcellet, and M. Morcellet, "Polymers with amino-acids in their side-chain. Conformation of poly(N-methacryloyl-L-methionine)," *Journal of Polymer Science Part A*, vol. 33, pp. 2233–2239, 1995.
- [39] C. Methenitis, J. Morcellet, G. Pneumatikakis, and M. Morcellet, "Copper coordination by polymers with glycylglycine, phenylalanine or methionine in the side chain: potentiometric and viscosimetric study," *European Polymer Journal*, vol. 39, no. 4, pp. 687–696, 2003.
- [40] A. Lekchiri, J. Morcellet, and M. Morcellet, "Complex formation between copper (II) and poly(N-methacryloyl-L-asparagine)," *Macromolecules*, vol. 20, no. 1, pp. 49–53, 1987.
- [41] A. Lekchiri, M. Brighli, C. Methenitis, J. Morcellet, and M. Morcellet, "Complexation of a polyelectrolyte derived from glutamic acid with copper(II). Catalase-like activity of the complexes," *Journal of Inorganic Biochemistry*, vol. 44, no. 4, pp. 229–238, 1991.
- [42] A. Lekchiri, A. Castellano, J. Morcellet, and M. Morcellet, "Copper complexes and catalase-like activity of a polyelectrolyte derived from aspartic acid," *European Polymer Journal*, vol. 27, no. 11, pp. 1271–1278, 1991.
- [43] R. K. Kulkarni and H. Morawetz, "Effect of asymmetric centers on free radical polymerization and the properties of polymers: methacrylyl alanine, methacrylyl glutamic acid, acrylyl glutamic acid, and their polymers," *Journal of Polymer Science*, vol. 54, no. 160, pp. 491–503, 1961.
- [44] H. Yokoi, S. Kawata, and M. Iwaizumi, "Interaction modes between heavy metal ions and water-soluble polymers. 1. Spectroscopic and magnetic reexamination of the aqueous solutions of cupric ions and poly(vinyl alcohol)," *Journal of the American Chemical Society*, vol. 108, no. 12, pp. 3358–3361, 1986.
- [45] H. Yokoi, Y. Mori, and Y. Fujise, "Studies on the complex formation between iron(III) or copper(II) and poly(vinyl alcohol) in terms of inclusion of the Metal Hydroxide-Like Clusters," *Bulletin of the Chemical Society of Japan*, vol. 68, pp. 2061–2065, 1995.
- [46] S. Skounas, C. Methenitis, and M. Morcellet, "Copper coordination by polymers with glycylglycine, phenylalanine or methionine in the side chain: Spectroscopic studies," Unpublished results.
- [47] M. González-Álvarez, G. Alzuet, J. Borrás, S. García-Granda, and J. M. Montejo-Bernardo, "Structural and functional models for the dinuclear copper active site in catechol oxidases: synthesis, X-ray crystal structures, magnetic and spectroscopic properties of μ -methoxo-bridged dinuclear copper(II) complexes with N-substituted sulfonamide ligands," *Journal of Inorganic Biochemistry*, vol. 96, no. 4, pp. 443–451, 2003.
- [48] A. Pezeshk, F. T. Greenaway, and J. R. J. Sorenson, "Barbiturate copper complexes: preparation and spectral studies," *Inorganica Chimica Acta*, vol. 80, pp. 191–195, 1983.
- [49] S. T. Kirksey Jr., T. A. Neubecker, and D. W. Margerum, "Thermally stable copper(III)- and nickel(III)-tripeptide complexes and their photochemical decomposition in acid solution," *Journal of the American Chemical Society*, vol. 101, no. 6, pp. 1631–1633, 1979.
- [50] Y. Ikeda, M. Beer, M. Schmidt, and K. Huber, " Ca^{2+} and Cu^{2+} induced conformational changes of sodium polymethacrylate in dilute aqueous solution," *Macromolecules*, vol. 31, no. 3, pp. 728–733, 1998.
- [51] E. Tsuchida, H. Nishide, and T. Nishiyama, "Kinetic discussion on the catalysis of copper-partially-quaternized poly(vinylpyridine) complexes," *Journal of Polymer Science Part A*, no. 47, pp. 35–46, 1974.
- [52] A. Lekchiri, C. Methenitis, J. Morcellet, and M. Morcellet, "Effect of the complexation with copper(II) on the hydrodynamic behaviour of some polyelectrolytes," *Polymer Bulletin*, vol. 17, no. 2, pp. 119–125, 1987.
- [53] V. Malatesta, A. Gervasini, and F. Morazzoni, "Chelation of copper(II) ions by doxorubicin and 4'-epidoxorubicin: ESR evidence for a new complex at high anthracycline/copper molar ratios," *Inorganica Chimica Acta*, vol. 136, no. 2, pp. 81–85, 1987.
- [54] T. Breyer, F. W. Breitbarth, and W. Vogelsberger, "EPR spectroscopic investigation of the sol-gel transition in modified tetraethylorthosilicate gels," *Journal of Colloid and Interface Science*, vol. 266, no. 1, pp. 153–159, 2003.
- [55] B. J. Hathaway, "Copper," *Coordination Chemistry Reviews*, vol. 52, pp. 87–169, 1983.

- [56] G. Multhaupt, T. Ruppert, A. Schlicksupp et al., "Copper-binding amyloid precursor protein undergoes a site-specific fragmentation in the reduction of hydrogen peroxide," *Biochemistry*, vol. 37, no. 20, pp. 7224–7230, 1998.
- [57] R. P. Bonomo, R. Marchelli, and G. Tabbi, "Study of H_2O_2 interaction with copper(II) complexes with diamino- diamide type ligands, diastereoisomeric dipeptides, and tripeptides," *Journal of Inorganic Biochemistry*, vol. 60, no. 3, pp. 205–218, 1995.

Research Article

Zinc(II) and Nickel(II) Benzoate Complexes from the Use of 1-methyl-4,5-diphenylimidazole

Konstantina A. Kounavi,¹ Manolis J. Manos,² Anastasios J. Tasiopoulos,²
Spyros P. Perlepes,¹ and Vassilios Nastopoulos¹

¹Department of Chemistry, University of Patras, 265 04 Patras, Greece

²Department of Chemistry, University of Cyprus, 1678 Nicosia, Cyprus

Correspondence should be addressed to Vassilios Nastopoulos, nastopoulos@chemistry.upatras.gr

Received 3 April 2010; Accepted 14 May 2010

Academic Editor: Evy Manessi-Zoupa

Copyright © 2010 Konstantina A. Kounavi et al. This is an open access article distributed under the Creative Commons Attribution License, which permits unrestricted use, distribution, and reproduction in any medium, provided the original work is properly cited.

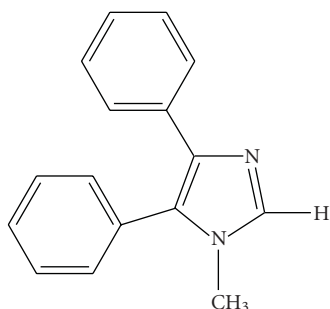
Two new complexes, $[\text{Zn}(\text{O}_2\text{CPh})_2(\text{L})_2] \cdot 2\text{MeOH}$ ($\mathbf{1} \cdot 2\text{MeOH}$) and $[\text{Ni}_2(\text{O}_2\text{CPh})_4(\text{L})_2] \cdot 2\text{MeCN}$ ($\mathbf{2} \cdot 2\text{MeCN}$), have been synthesized and characterized by X-ray analysis in the course of an ongoing investigation of the $\text{M}^{\text{II}}/\text{X}^-/\text{L}$ [$\text{M}^{\text{II}} = \text{Co}, \text{Ni}, \text{Cu}, \text{Zn}$; $\text{X}^- = \text{Cl}^-, \text{Br}^-, \text{I}^-, \text{NCS}^-, \text{NO}_3^-, \text{N}_3^-, \text{PhCO}_2^-$; $\text{L} = 1\text{-methyl-4,5-diphenylimidazole}$] reaction system, aiming at understanding and assessing the relative strength and the way in which the intermolecular interactions control the supramolecular organization of these compounds. In the mononuclear complex $\mathbf{1} \cdot 2\text{MeOH}$, the benzoate ion acts as a monodentate ligand resulting in a distorted tetrahedral N_2O_2 coordination environment. Complex $\mathbf{2} \cdot 2\text{MeCN}$ exhibits a dinuclear paddle-wheel structure; each Ni^{II} has a square pyramidal NiNO_4 chromophore with four benzoate oxygens in the basal plane and the pyridine-type nitrogen atom of one ligand L at the apex. The structure of $\mathbf{1} \cdot 2\text{MeOH}$ is stabilized by intramolecular π - π interactions between aromatic rings of adjacent 4,5-diphenylimidazole moieties; it is a feature also evidenced in similar compounds of the type $[\text{MX}_2\text{L}_2]$.

1. Introduction

Imidazole and its derivatives have played a formative role in the development of coordination chemistry [1, 2]. Many hundreds of neutral complexes and complex ions containing imidazoles have been prepared and characterized. The variety of spectroscopic properties and stoichiometries observed led to an improved understanding of the geometry and bonding in complexes and provided a touchstone for bonding theories. Imidazoles are particularly interesting ligands in bioinorganic [3, 4] and metallosupramolecular [5] chemistry. In the former field, imidazoles mimic the side chain of histidine and are valuable in biological modeling. Metalloenzyme synthetic models target the enzyme active site structure, spectroscopy, and mechanism of action. Further, bioinorganic models may also lead to compounds which mimic enzyme function and provide new reagents or catalysts for practical application. In the latter field, the presence of both donor atoms to metal ions and hydrogen bond donors within imidazoles, combined with the π -excessive

character of the 5-membered heterocyclic ring, can lead to intermolecular assembly of metal complexes through ligand-ligand or ligand-inorganic anion interactions. In spite of the enormous scientific literature on metal complexes with simple imidazoles as ligands, there is in fact relatively little known about the coordination and metallosupramolecular chemistry of heavily substituted imidazoles [1].

It is well established nowadays that the most prominent intermolecular interactions responsible for the supramolecular organization of metal complexes are hydrogen bonds and π - π stacking interactions [6–11]. With this in mind, an investigation has recently been initiated to determine the crystal structures of a designed series of transition metal complexes using heavily substituted imidazole ligands aiming at understanding the relative strength and the way in which these interactions control the noncovalent assembly of molecular building blocks in supramolecular systems [12]. In particular, 1-methyl-4,5-diphenylimidazole (L) (Scheme 1), a monodentate ligand capable of forming π - π interactions, has been selected to initiate our studies. So far, there have



SCHEME 1: Drawing of the ligand 1-methyl-4,5-diphenylimidazole.

been only few studies on the coordination chemistry of L [13, 14]. The general reaction system currently in use involves $M^{II}/X^-/L$ [$M^{II} = \text{Co, Ni, Cu, Zn}$; $X^- = \text{Cl}^-, \text{Br}^-, \text{I}^-, \text{RCO}_2^-, \text{NO}_3^-, \text{NCS}^-, \text{N}_3^-$] in various solvents and the first Co(II) and Zn(II) complexes have already been reported [12].

In this study we present our results on the $M^{II}/\text{PhCO}_2^-/L$ [$M^{II} = \text{Co, Ni, Cu, Zn}$] system. So far, two new complexes, namely, $[\text{Zn}(\text{O}_2\text{CPh})_2(\text{L})_2] \cdot 2\text{MeOH}$ (**1·2MeOH**) and $[\text{Ni}_2(\text{O}_2\text{CPh})_4(\text{L})_2] \cdot 2\text{MeCN}$ (**2·2MeCN**) have been synthesized and characterized by elemental analyses, IR spectra, and single-crystal X-ray analysis.

2. Experimental

2.1. Materials and Instruments. Chemicals (reagent grade) were purchased from Merck and Alfa Aesar. All manipulations were performed under aerobic conditions using materials and solvents as received; water was distilled in-house. The ligand 1-methyl-4,5-diphenylimidazole (L) was synthesized as already described in a previous work [15]. Microanalyses (C, H, N) were performed by the University of Ioannina (Greece) Microanalytical Laboratory using an EA 1108 Carlo Erba analyzer. IR spectra were recorded on a Perkin-Elmer PC 16 FT-IR spectrometer with samples prepared as KBr pellets.

2.2. Compound Preparation

2.2.1. Preparation of $[\text{Zn}(\text{O}_2\text{CPh})_2(\text{L})_2] \cdot 2\text{MeOH}$ (1·2MeOH**).** This compound was synthesized by a solvothermal reaction of L (0.18 g, 0.75 mmol) and $\text{Zn}(\text{O}_2\text{CPh})_2 \cdot 2\text{H}_2\text{O}$ (0.10 g, 0.30 mmol) in MeOH (8 mL). The reaction mixture was loaded into a Teflon-lined stainless steel autoclave with inner volume of 20 mL, and then the sealed autoclave was heated under autogenous pressure at 150°C for 3 days. Upon slow (5°C/h) cooling to ambient temperature, colourless prismatic crystals of **1·2MeOH** (suitable for X-ray crystallography) appeared, which were collected by filtration, washed with cold EtOH (2 × 2 mL) and Et₂O (2 × 5 mL), and dried in air; yield ca. 40% (based on the metal). A sample for crystallography was maintained in contact with the mother liquor to prevent the loss of lattice solvent. *Anal. Calc.* for **1·2MeOH**: C, 68.61; H, 5.53; N, 6.67%. *Found*: C, 68.30; H, 5.41;

N, 6.88%. IR data (KBr, cm^{-1}): 3446 (mb), 3130 (m), 3054 (m), 2924 (w), 1624 (s), 1570 (s), 1520 (s), 1484 (m), 1446 (m), 1366 (s), 1256 (m), 1196 (m), 1174 (w), 1126 (m), 1072 (m), 1024 (m), 1000 (w), 978 (m), 920 (m), 838 (m), 788 (s), 774 (s), 744 (sh), 720 (s), 700 (s), 680 (m), 650 (m), 580 (m), 512 (w).

2.2.2. Preparation of $[\text{Ni}_2(\text{O}_2\text{CPh})_4(\text{L})_2] \cdot 2\text{MeCN}$ (2·2MeCN**).** A pale yellow solution of L (0.29 g, 1.25 mmol) in MeCN/ CH_2Cl_2 (30 mL, 1:1 v/v) was treated with solid $\text{Ni}(\text{O}_2\text{CPh})_2 \cdot 2\text{H}_2\text{O}$ (0.17 g, 0.50 mmol). The resulting green slurry was stirred at ambient temperature for 20 min. The solution was filtered and the green filtrate was left undisturbed in a closed vial at room temperature. After 15 days, light-green crystals of **1·2MeCN** suitable for X-ray analysis formed were collected by filtration, washed with cold EtOH (2 × 2 mL) and Et₂O (2 × 5 mL), and dried in air. Yield ca. 60% (based on the metal). A sample for crystallography was maintained in contact with the mother liquor to prevent the loss of lattice solvent. *Anal. Calc.* for **2·2MeCN**: C, 66.69; H, 4.73; N, 7.29%. *Found*: C, 66.81; H, 4.40; N, 7.38%. IR data (KBr, cm^{-1}): 3134 (m), 3060 (m), 1626 (s), 1570 (s), 1522 (s), 1492 (w), 1444 (sh), 1418 (s), 1402 (s), 1254 (w), 1202 (m), 1174 (w), 1072 (m), 1024 (m), 978 (m), 922 (w), 842 (w), 786 (m), 776 (sh), 720 (s), 700 (s), 682 (m), 648 (m), 538 (w), 476 (m).

2.3. X-Ray Crystallography. Selected single crystals of **1·2MeOH** and **2·2MeCN** were covered with Paraton N oil and mounted on the tip of a glass capillary. X-ray data for both compounds were collected (ω -scans) on an Oxford Diffraction Xcalibur diffractometer under a flow of nitrogen gas at 100(2) K (MoK α radiation). For data collection and reduction the CrysAlis CCD and RED packages were employed [16], respectively. The reflection intensities were corrected for absorption (multiscan method), the structures were solved by direct methods with SIR92 [17] and refined by full-matrix least-squares on F^2 with SHELXL-97 [18]. All nonhydrogen atoms were refined anisotropically. All hydrogen atoms bound to carbon atoms were introduced at calculated positions applying the riding model [$\text{C}(sp^2)\text{-H}$ and $\text{C}(sp^3)\text{-H}$ 0.93 and 0.96 Å, respectively; $U_{\text{iso}}(\text{H}) = 1.2U_{\text{eq}}(\text{C})$ (1.5 for $\text{C}sp^3$ methyl groups) of their parent C atom]. The hydroxyl hydrogen atoms of the solvent molecules in **1·2MeOH** were located by difference maps and their positions were refined isotropically [$U_{\text{iso}}(\text{H}) = 1.5U_{\text{eq}}(\text{O})$] applying a soft distance restraint. All geometric calculations were carried out using WINGX [19], PLATON [20], and MERCURY [21] packages; molecular graphics were prepared with DIAMOND [22]. Details of the data collection and refinement are summarized in Table 1.

CCDC-771769 and CCDC-771770 contain the crystallographic data for **1·2MeOH** and **2·2MeCN**, respectively. These data can be obtained free of charge via <http://www.ccdc.cam.ac.uk/conts/retrieving.html>, or from the Cambridge Crystallographic Data Centre, 12 Union Road, Cambridge CB2 1EZ, UK; fax: (+44) 1223-336-033; or e-mail: deposit@ccdc.cam.ac.uk.

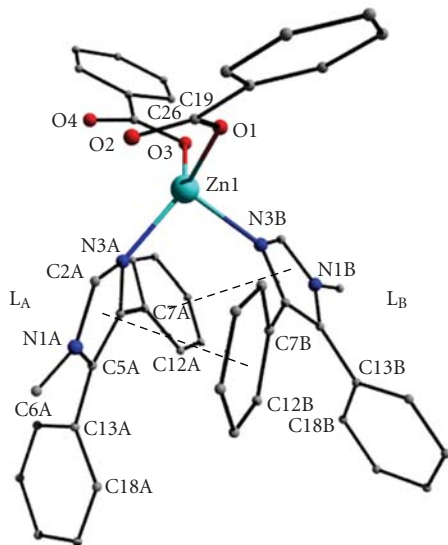


FIGURE 1: A partially labeled plot of complex $1 \cdot 2\text{MeOH}$. The methanol molecules and the hydrogen atoms have been omitted for clarity. The intramolecular π - π interactions between the two ligands L_A and L_B are shown with dashed lines. Ring numeration: A1: N1A–C2A–N3A–C4A–C5A; A2: C7A to C12A; A3: C13A to C18A; B1: N1B–C2B–N3B–C4B–C5B; B2: C7B to C12B, B3: C13B to C18B.

3.2. Description of the Structures. The molecular structures of complexes $1 \cdot 2\text{MeOH}$ and $2 \cdot 2\text{MeCN}$ are shown in Figures 1 and 2, respectively, selected bond lengths, angles, and torsion angles are listed in Table 2. To facilitate comparison, both compounds have the same (where applicable) atom, ring, and ligand numbering (ligand L_A : rings A1, A2 and A3; ligand L_B : rings B1, B2 and B3; see Figure 1).

Complex $1 \cdot 2\text{MeOH}$ consists of neutral mononuclear $[\text{Zn}(\text{O}_2\text{CPh})_2(\text{L})_2]$ molecules and methanol molecules in the lattice in a 1:2 ratio; it crystallizes in the monoclinic space group $P2_1/n$. The two benzoate ions coordinate to Zn(II) in a monodentate fashion; this results in a distorted tetrahedral environment about the Zn(II) centre comprising two benzoate oxygen atoms and two pyridine-type, imidazole nitrogen donor atoms from the two 1-methyl-4,5-diphenylimidazole (L) molecules. Both benzoate species are planar. The L_A and L_B ligands of the complex are “antiparallel” with their methyl groups pointing at opposite directions. The overall conformation of L_A and L_B is similar. The angle between the mean planes of the phenyl rings A2/A3 and B2/B3 is $70.5(1)^\circ$ and $67.0(1)^\circ$, respectively. Moreover, the imidazole ring A1 is facing the phenyl ring B2 [$10.5(1)^\circ$] and, similarly, the imidazole ring B1 is facing the phenyl ring A2 [$4.9(1)^\circ$] forming weak intramolecular interligand π - π interactions among those pairs of rings (Table 3). It seems that steric effects and the distorted tetrahedral geometry of the Zn(II) centre [$\text{N3A–Zn1–N3B} = 96.6(1)^\circ$] facilitate those π - π interactions. Similar intramolecular π - π interactions between L_A and L_B have also been reported for Pd^{II} [14], and Co^{II} and Ni^{II} [12] complexes with L , in a series of analogous complexes of

TABLE 2: Selected interatomic distances (\AA), angles and torsion angles ($^\circ$) for $1 \cdot 2\text{MeOH}$ and $2 \cdot 2\text{MeCN}$.

Compound	$1 \cdot 2\text{MeOH}$	$2 \cdot 2\text{MeCN}$
M	Zn	Ni
$\text{M} \cdots \text{M}^i$		2.734(1)
M–N3A	2.007(1)	2.017(2)
M–N3B	2.065(1)	
M–O1	1.947(1)	2.015(2)
M–O3	1.950(1)	2.039(2)
M–O2		2.008(2)
M–O4		2.026(2)
N3A–M–N3B	96.6(1)	
N3A–M–O1	123.4(1)	91.9(1)
N3A–M–O2		103.3(1)
N3A–M–O3	123.9(1)	98.2(1)
N3A–M–O4		96.7(1)
N3B–M–O1	103.0(1)	
N3B–M–O3	97.2(1)	
O1–M–O3	105.7(4)	88.0(1)
O1–M–O4		89.9(1)
O2–M–O3		90.7(1)
O2–M–O4		87.4(1)
C19–M–C26	112.46(4)	
A2–A3*	70.5(1)	61.9(1)
B2–B3*	67.0(1)	
C4A–C5A–C13A–C14A	–57.8(2)	–53.0(4)
C4B–C5B–C13B–C14B	–56.8(2)	
C5A–C4A–C7A–C12A	–46.6(2)	–40.5(4)
C5B–C4B–C7B–C12B	–37.3(2)	

* Angle between the mean-planes of the named phenyl rings (see Figure 1). Symmetry codes: (i) $1/2 - x, 1/2 - y, 1 - z$.

other divalent metals with L [26] as well as in Cu^{II} and Zn^{II} complexes of 2-[2'-(4',6'-di-*tert*-butylhydroxyphenyl)]-4,5-diphenylimidazole [27, 28]. This structural feature records a preferable mode of packing between adjacent ligands bearing the 4,5-diphenylimidazole moiety and provides stabilization within the complex; it also supports the suitability of the ligand L as a crystal engineering tool, namely, its effect, through the π - π interactions, in the assembly and packing of complexes in inorganic supramolecular chemistry [29, 30]. The length of the C–C and C–N bonds of the imidazole groups, for both $1 \cdot 2\text{MeOH}$ and $2 \cdot 2\text{MeCN}$, are as expected in [31]; the Zn–N and Zn–O bond lengths are normal for this kind of compound.

One of the methanol molecules (O5) in the lattice is involved in two strong intramolecular O–H \cdots O hydrogen bonds to the noncoordinated oxygen atom (O2) of one benzoate and to the second methanol (O6) molecule. There is also a weak C–H \cdots O (benzoate) interaction involving the noncoordinated oxygen atom (O4) of the other benzoate ligand. The packing of the molecules in the crystal lattice proceeds through normal van der Waals contacts and some weak intermolecular C–H \cdots O interactions contributing to the supramolecular assembly of the structure (Table 4).

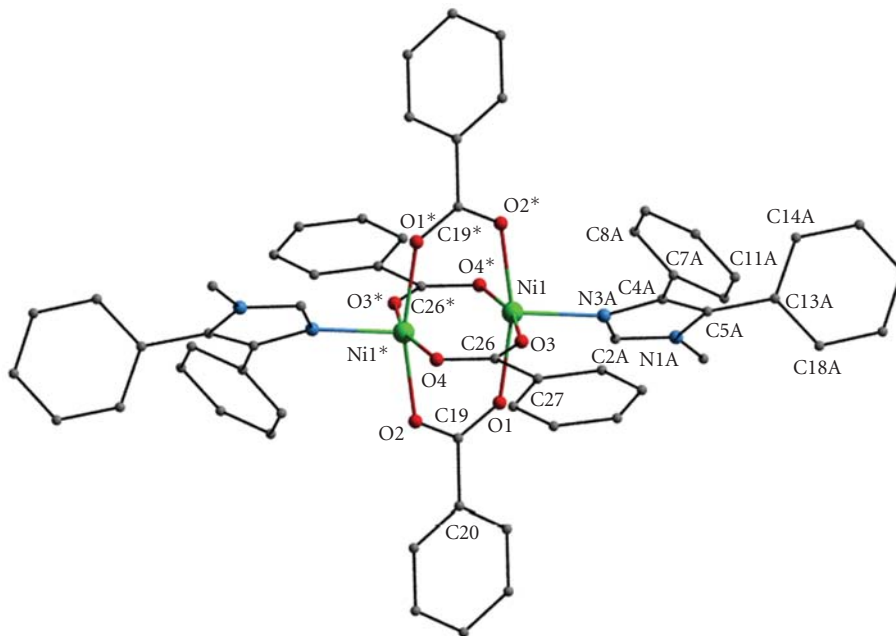


FIGURE 2: A partially labeled plot of the dinuclear complex $2 \cdot 2\text{MeCN}$. The acetonitrile molecules and the hydrogen atoms have been omitted for clarity. Asterisks are used for symmetry related ($1/2 - x, 1/2 - y, 1 - z$) atoms.

TABLE 3: Geometrical details (\AA , $^\circ$) of the intramolecular π - π interactions between L_A and L_B ligands for complex $1 \cdot 2\text{MeOH}$.

	Rings	Distance/Angle
Distance between ring centroids	A1-B2	3.547(1)
	B1-A2	3.622(1)
Perpendicular distance between ring planes	A1-B2	3.437(1)
	B1-A2	3.363(1)
Centroid offset	A1-B2	0.876(1)
	B1-A2	1.346(1)
Dihedral angle between ring mean-planes	A1-B2	10.5(1)
	B1-A2	4.9(1)

It is known that $\text{C-H} \cdots \text{O}$ bonds could play a role in the organization of crystal packing, especially when classic hydrogen bonding is absent [32–35]. A view of the crystal packing of complex $1 \cdot 2\text{MeOH}$ is shown in Figure 3.

The dinuclear paddle-wheel type complex $2 \cdot 2\text{MeCN}$, $[\text{Ni}_2(\text{O}_2\text{CPh})_4(\text{L})_2] \cdot 2\text{MeCN}$, crystallizes in the monoclinic space group $C2/c$ with two solvate acetonitrile molecules. The asymmetric unit comprises half molecule of the complex and one acetonitrile molecule, and the structure is generated by inversion at the midpoint of the $\text{Ni} \cdots \text{Ni}$ distance. The four bidentate benzoate groups bridge the two Ni ions in a paddle-wheel arrangement about the $\text{Ni} \cdots \text{Ni}$ axis. Thus, each Ni^{II} atom is penta-coordinated exhibiting a square pyramidal geometry with the apex occupied by the pyridine-type, imidazole nitrogen donor atom (N3A) of one monodentate 1-methyl-4,5-diphenylimidazole ligand.

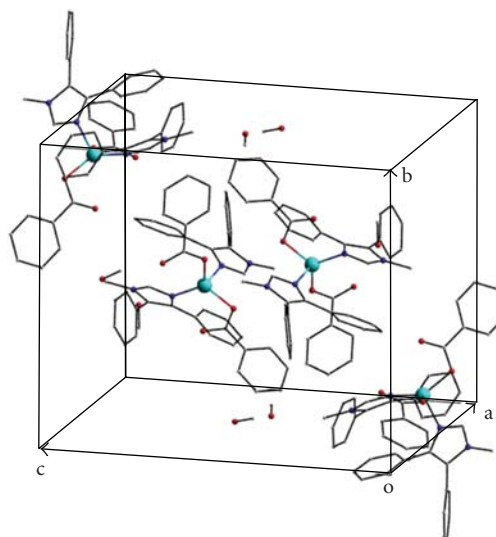


FIGURE 3: View of the crystal packing of complex $1 \cdot 2\text{MeOH}$. The hydrogen atoms have been omitted for clarity. Zn: turquoise; O: red; N: blue; C: grey.

The Ni to apical N3A atom distance is 2.017(2), the four Ni–O(benzoate) bond lengths range from 2.008(2) to 2.039(2) \AA , and the $\text{Ni} \cdots \text{Ni-N3A}$ angle is $160.8(1)^\circ$. The Ni atom lies 0.266(1) \AA out of the least-squares basal plane towards N3A atom. The $\text{Ni} \cdots \text{Ni}$ distance is 2.734(1) \AA , shorter than the maximum distance of $\sim 3.5 \text{\AA}$ that the tetracarboxylate paddle-wheel motif can accommodate for metal-metal separations. The acetonitrile molecule is linked

TABLE 4: Hydrogen-bond geometries for 1·2MeOH and 2·2MeCN (Å, °).

D-H···A	D-H	H···A	D···A	D-H···A
<i>Complex 1·2MeOH</i>				
O6-H6···O5	0.855(19)	1.916(19)	2.764(2)	172(2)
O5-H5···O2 ⁱ	0.847(17)	1.913(17)	2.738(2)	165(2)
C8B-H8B···O1	0.93	2.50	3.282(2)	142
C6B-H6B3···O1 ⁱⁱ	0.96	2.432	3.370(2)	166
C33-H33B···O4 ⁱ	0.96	2.52	3.423(2)	157
<i>Complex 2·2MeCN</i>				
C8A-H8A···O2	0.93	2.30	3.151(3)	152
C34-H34C···O1 ⁱⁱⁱ	0.96	2.50	3.371(4)	151

Symmetry codes: (i) $-1+x, -1+y, z$; (ii) $2-x, 2-y, -z$; (iii) $x, 1+y, z$.

to the complex via a weak C-H···O1(benzoate) interaction (Table 4). The bridged dinuclear structure $M_2(\eta^1:\eta^1:\mu-O_2CR)_4(\text{ligand})_2$, first documented in 1953 for copper(II) acetate monohydrate, is ubiquitous in modern coordination chemistry [36]. It is found not only for carboxylates of many transition elements, but also for dimers containing a wide variety of other triatomic bridging ligands. This structural type is associated with a spectrum of metal-metal interactions ranging from no interactions, weak or moderate spin-pairing in the copper(II) carboxylates, various orders of metal-metal bonding, to the “super-short” metal-metal bonds ($M-M < 2 \text{ \AA}$). The axial groups are normally monodentate ligands but they may represent interdimer association into a polymeric structure or may be absent.

It should be mentioned that attempts were made to prepare metal(II)-benzoate complexes with the 1-methyl-4,5-diphenylimidazole ligand for the divalent metals Co, Ni, Cu, and Zn, varying the factors that could affect the self-assembly of supramolecular architectures (such as the solvents used, temperature, counter-ion, the ligand-to-metal ratio, method of preparation, etc.). However, our trials yielded only the present two crystalline materials. It seems that the capability of the benzoate group to adopt different ligation modes plays, at least in the present case, a role in the formation of different coordination structural types.

4. Conclusions

The use of 1-methyl-4,5-diphenylimidazole ligand (L) in reactions with $Zn(O_2CPh)_2 \cdot 2H_2O$ and $Ni(O_2CPh)_2 \cdot 2H_2O$ has yielded the mononuclear $[Zn(O_2CPh)_2(L)_2] \cdot 2MeOH$ complex (1·2MeOH) and the dinuclear $[Ni_2(O_2CPh)_4(L)_2] \cdot 2MeCN$ (2·2MeCN) compound. The different benzoate binding mode to the metals used, monodentate in the former and bidentate in the latter complex, has led to two different coordination geometries for the two divalent metals. The characteristic structural pattern [12] of the intramolecular $\pi-\pi$ interactions between aromatic rings of adjacent 4,5-diphenylimidazole moieties of the two L ligands is also present in the structure of 1·2MeOH and contributes to the stability and rigidity of the structure.

Acknowledgment

This paper was supported by the Research Committee of the University of Patras, Greece (K. Caratheodory program, Grant no C.585 to Vassilios Nastopoulos).

References

- [1] P. J. Steel, “Aromatic nitrogen heterocycles as bridging ligands: a survey,” *Coordination Chemistry Reviews*, vol. 106, pp. 227–265, 1990.
- [2] E. C. Constable, *Metals and Ligand Reactivity: An Introduction to the Organic Chemistry of Metal Complexes*, Verlag Chemie, Weinheim, Germany, 1996.
- [3] H.-B. Kraatz and N. Metzler-Nolte, *Concepts and Models in Bioinorganic Chemistry*, Wiley-VCH, Weinheim, Germany, 2006.
- [4] S. J. Lippard and J. M. Berg, *Principles of Bioinorganic Chemistry*, University Science Books, Mill Valley, Calif, USA, 1994.
- [5] J. W. Steed and J. L. Atwood, *Supramolecular Chemistry*, Wiley, Chichester, UK, 2000.
- [6] J.-M. Lehn, “Supramolecular chemistry,” *Science*, vol. 260, no. 5115, pp. 1762–1763, 1993.
- [7] J.-M. Lehn, *Supramolecular Chemistry. Concepts and Perspectives*, Wiley-VCH, Weinheim, Germany, 1995.
- [8] A. I. Kitaigorodsky, *Kitaigorodsky, Molecular Crystals and Molecules*, Academic Press, New York, NY, USA, 1973.
- [9] J.-M. Lehn, “Perspectives in supramolecular chemistry—from molecular recognition towards molecular information processing and self-organization,” *Angewandte Chemie. International Edition*, vol. 29, no. 11, pp. 1304–1319, 1990.
- [10] P. S. Corbin, S. C. Zimmerman, P. A. Thiessen, N. A. Hawryluk, and T. J. Murray, “Complexation-induced unfolding of heterocyclic ureas. Simple foldamers equilibrate with multiply hydrogen-bonded sheetlike structures,” *Journal of the American Chemical Society*, vol. 123, no. 43, pp. 10475–10488, 2001.
- [11] C. B. Aakeröy and K. R. Seddon, “The hydrogen bond and crystal engineering,” *Chemical Society Reviews*, vol. 22, no. 6, pp. 397–407, 1993.
- [12] K. A. Kounavi, C. Papatrifaftyllopoulou, A. J. Tasiopoulos, S. P. Perlepes, and V. Nastopoulos, “The supramolecular chemistry of metal complexes with heavily substituted imidazoles as ligands: cobalt(II) and zinc(II) complexes of 1-methyl-4,5-diphenylimidazole,” *Polyhedron*, vol. 28, no. 15, pp. 3349–3355, 2009.
- [13] C. P. Raptopoulou, S. Paschalidou, A. A. Pantazaki et al., “Bis(acetato)bis(1-methyl-4,5-diphenylimidazole)copper(II): preparation, characterization, crystal structure, DNA strand breakage and cytogenetic effect,” *Journal of Inorganic Biochemistry*, vol. 71, no. 1–2, pp. 15–27, 1998.
- [14] A. Hadzovic and D. Song, “Synthesis, characterization, and reactivity of a versatile dinuclear palladium β -diiminate complex,” *Organometallics*, vol. 27, no. 6, pp. 1290–1298, 2008.
- [15] J. McMaster, R. L. Beddoes, D. Collison, D. R. Eardley, M. Helliwell, and C. D. Garner, “A bis(diimidazole)copper complex possessing a reversible Cu^{II}/Cu^I couple with a high redox potential,” *Chemistry—A European Journal*, vol. 2, no. 6, pp. 685–693, 1996.
- [16] *CrysAlis CCD and CrysAlis RED, Programs for Data Collection, Cell Refinement and Data Reduction*, Version 1.171.32.15, Oxford Diffraction Ltd, Oxford, UK, 2008.

- [17] A. Altomare, G. Cascarano, C. Giacovazzo, et al., "SIR92—a program for automatic solution of crystal structures by direct methods," *Journal of Applied Crystallography*, vol. 27, p. 435, 1994.
- [18] G. M. Sheldrick, *SHELXL-97, A program for the refinement of crystal structures from diffraction data*, University of Göttingen, Germany, 1997.
- [19] L. J. Farrugia, "WinGX suite for small-molecule single-crystal crystallography," *Journal of Applied Crystallography*, vol. 32, no. 4, pp. 837–838, 1999.
- [20] A. L. Spek, *PLATON. A multipurpose crystallographic tool*, Utrecht University, The Netherlands, 2003.
- [21] C. F. Macrae, P. R. Edgington, P. McCabe et al., "Mercury: visualization and analysis of crystal structures," *Journal of Applied Crystallography*, vol. 39, no. 3, pp. 453–457, 2006.
- [22] K. Brandenburg, *DIAMOND, Program for crystal and molecular structure visualization*, Release 3.1f, Crystal Impact GbR, Bonn, Germany, 2008.
- [23] E. K. Brechin, "Using tripodal alcohols to build high-spin molecules and single-molecule magnets," *Chemical Communications*, no. 41, pp. 5141–5153, 2005.
- [24] G. B. Deacon and R. J. Phillips, "Relationships between the carbon-oxygen stretching frequencies of carboxylato complexes and the type of carboxylate coordination," *Coordination Chemistry Reviews*, vol. 33, pp. 227–250, 1980.
- [25] D. Martínez, M. Motevalli, and M. Watkinson, "Is there really a diagnostically useful relationship between the carbon-oxygen stretching frequencies in metal carboxylate complexes and their coordination mode?" *Dalton Transactions*, vol. 39, no. 2, pp. 446–455, 2010.
- [26] K. A. Kounavi, et al., unpublished results.
- [27] L. Benisvy, A. J. Blake, D. Collison et al., "A phenoxyl radical complex of copper(II)," *Chemical Communications*, no. 18, pp. 1824–1825, 2001.
- [28] L. Benisvy, A. J. Blake, D. Collison et al., "A phenol-imidazole pro-ligand that can exist as a phenoxyl radical, alone and when complexed to copper(II) and zinc(II)," *Dalton Transactions*, no. 10, pp. 1975–1985, 2003.
- [29] I. Dance, *Perspectives in Supramolecular Chemistry: The Crystal as a Supramolecular Entity*, vol. 2, Wiley, Chichester, UK, 1995.
- [30] C. B. Aakeröy, "Crystal engineering: strategies and architectures," *Acta Crystallographica Section B*, vol. 53, no. 4, pp. 569–586, 1997.
- [31] F. H. Allen, O. Kennard, D. G. Watson, L. Brammer, A. G. Orpen, and R. Taylor, "Tables of bond lengths determined by x-ray and neutron diffraction. Part 1. Bond lengths in organic compounds," *Journal of the Chemical Society, Perkin Transactions 2*, no. 12, pp. S1–S19, 1987.
- [32] G. R. Desiraju, *Crystal Engineering. The Design of Organic Solids*, Elsevier, Amsterdam, The Netherlands, 1989.
- [33] G. R. Desiraju, "The C–H···O hydrogen bond: structural implications and supramolecular design," *Accounts of Chemical Research*, vol. 29, no. 9, pp. 441–449, 1996.
- [34] G. A. Jeffrey, *An Introduction to Hydrogen Bonding*, Oxford University Press, Oxford, UK, 1997.
- [35] T. Steiner, "The hydrogen bond in the solid state," *Angewandte Chemie. International Edition*, vol. 41, no. 1, pp. 48–76, 2002.
- [36] S. P. Perlepes, J. C. Huffman, and G. Christou, "Preparation and characterization of triply-bridged dinuclear copper(II) complexes containing the $[\text{Cu}_2(\mu - \text{OH})(\mu - \text{X})(\mu - \text{OAc})]^+$ core (X = Cl, Br), and the crystal structure of $[\text{Cu}_2(\text{OH})\text{Cl}(\text{OAc})(\text{bpy})_2](\text{ClO}_4) \cdot \text{H}_2\text{O}$," *Polyhedron*, vol. 10, no. 19, pp. 2301–2308, 1991.

Review Article

Tetramic and Tetrionic Acids as Scaffolds in Bioinorganic and Bioorganic Chemistry

G. Athanasellis,^{1,2,3} O. Igglessi-Markopoulou,¹ and J. Markopoulos²

¹Laboratory of Organic Chemistry, School of Chemical Engineering, National Technical University of Athens, 15773 Athens, Greece

²Laboratory of Inorganic Chemistry, Department of Chemistry, University of Athens, Panepistimiopolis, 15771 Athens, Greece

³ALAPIS Pharmaceuticals, R & D Centre, Pallini, 15302 Attiki, Greece

Correspondence should be addressed to J. Markopoulos, jmmarko@chem.uoa.gr

Received 28 December 2009; Accepted 23 February 2010

Academic Editor: Spyros Perlepes

Copyright © 2010 G. Athanasellis et al. This is an open access article distributed under the Creative Commons Attribution License, which permits unrestricted use, distribution, and reproduction in any medium, provided the original work is properly cited.

Tetramic and tetrionic acids are naturally occurring molecules with a variety of biological activities. In this review article, we present the general strategies for the synthesis of these compounds and we reveal the functionalized groups that are responsible for their properties. We also set out their coordinating modes with up-to-date bibliographical references.

1. Introduction

Tetramic acids, pyrrolidine-2,4-dione derivatives, are naturally occurring molecules synthesized by numerous organisms and found in a variety of natural products [1, 2]. This class of five membered heterocycles has attracted significant attention due to the broad range of biological activities they exhibit. This activity comprises of antibiotic and antiviral, cytotoxicity, mycotoxicity, as well as inhibition of the cell cycle. Various examples of tetramic acid derivatives isolated from the nature are streptolydigin which inhibits RNA polymerase [3], the melophlin family of compounds which have shown antimicrobial activity [4], equisetin and its homologue trichosetin with inhibitory activity against Gram positive bacteria [5, 6], and reutericyclin which exhibits a wide range of pharmacological activities [7, 8]. In addition, a series of derivatives have been patented by Bayer CropScience as ingredients for fungicidal and herbicidal use [9].

On the other hand, tetrionic acids, 4-hydroxy-[5H] furan-2-ones, are compounds with antibiotic, antiviral, antineoplastic, and anticoagulant activity [10, 11]. Compounds which have been isolated from natural products and exhibit such activity are tetronasin [12], RK-682 [2, 13], the well-known family of compounds named vulpinic acids [14, 15] and many others.

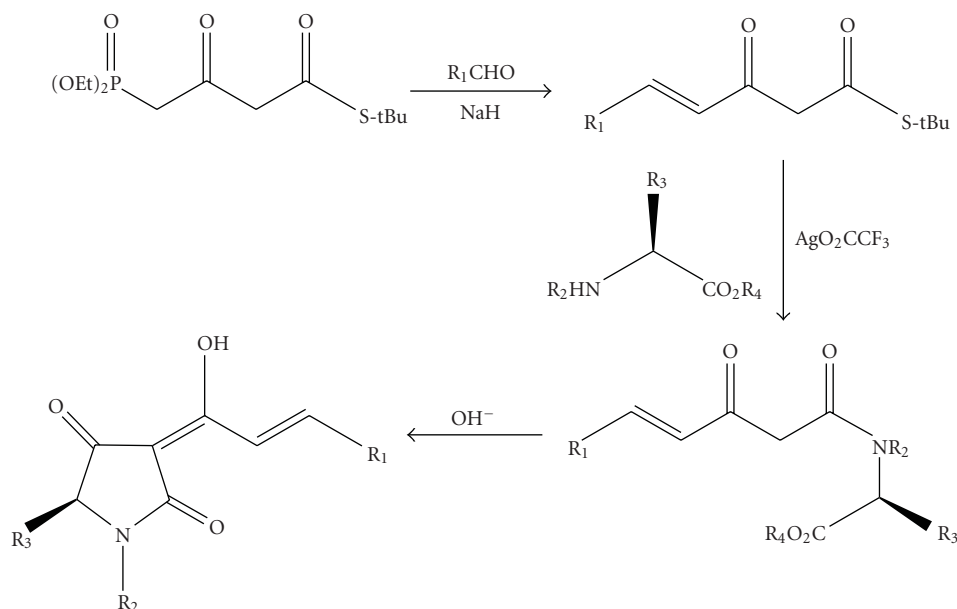
For a long time, we have been involved in the chemistry of tetramic and tetrionic acids and the design of new strategies

for the preparation of small heterocyclic molecules. Their synthesis has been accomplished based on a similar strategy starting from the appropriate precursors, suitably protected α -amino acids for tetramic and α -hydroxy acids for tetrionic acids, using the N-hydroxybenzotriazole methodology for the synthesis of their active esters.

2. Synthesis of Tetramic Acids

Owing to the importance of tetramic acid derivatives, numerous approaches to their synthesis have been developed. They mainly make use of amino acid-derived precursors whose stereochemical integrity remains more or less conserved in the structure of the products. Significant studies on the synthesis of such optically active compounds have been made by Ley et al. [16] who used a series of β -ketoamides as intermediates for the preparation of enantiomerically pure 3-acyl tetramic acids, based on the Lacey methodology for the synthesis of tetramic acids by N-acylation of α -amino acids (Scheme 1).

On the other hand, Andrews et al. [17] provided an N-acyloxazolidine derivative of L-serine as a suitable precursor for the construction of chiral substituted tetramic acids with high enantiomeric excess. Other methodologies based on the enantioselective Lacey-Dieckmann cyclization, requiring strongly basic conditions, have also been reported [18, 19]



SCHEME 1: Synthesis of optically active tetramic acids by Leyet et al. [16].

whereas Jouin and coworkers have proposed the use of Meldrum acid in the presence of isoprenyl chloroformate and DMAP reagents [20]. Recently, Schobert and Jagusch proposed an expedient synthesis of tetramic acids from α -amino esters, in which the cyclization route involved a domino addition-Wittig alkenation reaction with immobilized triphenylphosphoranylidene ketene under neutral nonracemizing conditions [21]. Acylation to 3-acyltetramic acids was then performed with the appropriate acyl chloride and boron trifluoride-diethyl etherate under microwave irradiation. This route was followed in the synthesis of natural products like reutericyclin (Scheme 2).

Our first attempt to use N-hydroxybenzotriazole in the synthesis of heterocyclic compounds was made in the field of tetramic acids [22]. We applied the "one-pot" synthetic strategy which comprises of a C-acylation reaction between the N-hydroxybenzotriazole ester of the appropriate optically active amino acid **1** and diethyl malonate **3**. When the product was not the corresponding tetramic acid **4–6** but the C-acylation compound **A**, a cyclization reaction under basic conditions was performed to afford the corresponding tetramic acid **7–9** (Scheme 3).

The crucial parameter on the synthesis of the N-acylated-3-ethoxycarbonyl tetramic acids **4–6** or N-H-3-ethoxycarbonyl tetramic acids **7–9** is the molar ratio between the N-acylated amino acid **1** and diethyl malonate **3**. We observed that when diethyl malonate **3** was used in molar excess (2 equiv.), the oily product containing the C-acylation compound **A** and diethyl malonate **3** was obtained. On the other hand, when diethyl malonate **3** was used in stoichiometric ratio (1 equiv.), the N-acetyl-3-ethoxycarbonyl tetramic acids **4–6** were obtained as white solids. The enantiomeric purity of the final products was tested by HPLC and the results were in the range 82%–96%*ee*.

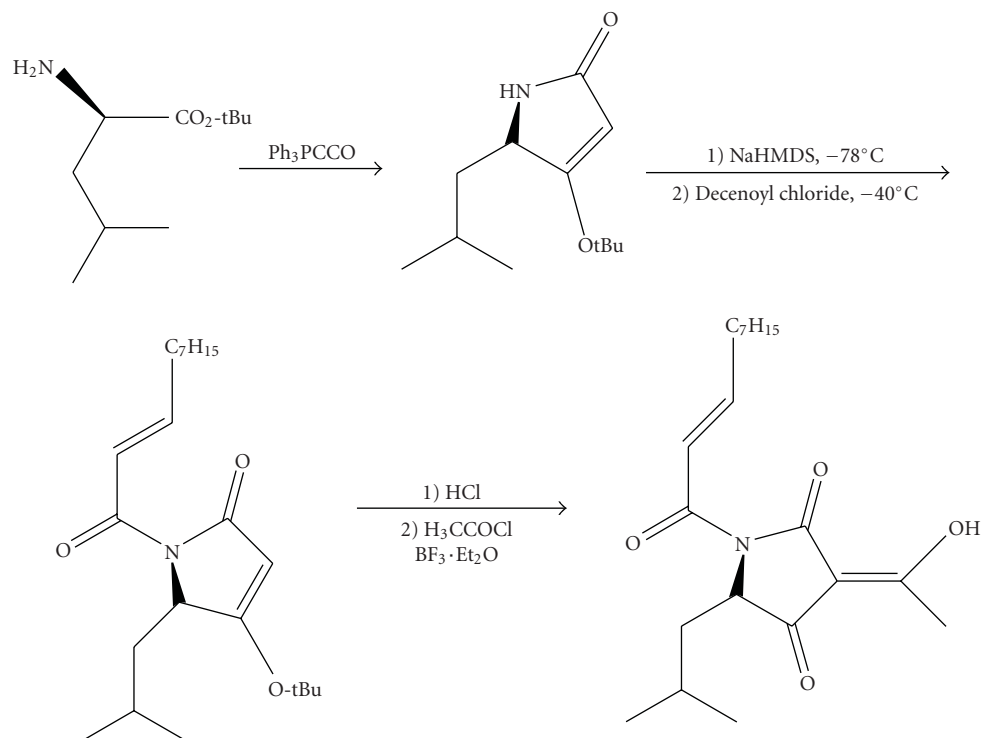
These results indicate the success of the proposed methodology to maintain the stereochemical integrity of the corresponding α -amino acids. Another advantage of the proposed methodology is that there is no need for isolating the intermediate N-hydroxybenzotriazole esters of the chiral α -amino acids, in contrast to previously described methodologies. This fact reduces the time for the synthesis of the desired products and is beneficial for the overall yield of the reaction (45%–75%). Therefore, the reaction is simple, inexpensive, easily scaled up and proceeds with low racemization.

3. Synthesis of Tetronic Acids

Given our interest on the synthesis of tetramic acids and their coordination compounds, we have oriented our interest on the chemistry of tetronic acids.

In the literature, there are a number of reliable methods for the synthesis of such derivatives. Several methodologies include Dieckmann cyclization [23], cycloaddition [24], oxidation [25], Wittig-Claisen [26], lactonization [27], and enzymatic reactions [28]. A few years ago, the synthesis of 3-acyl-5-methoxycarbonyl tetronic acids has been reported from our research group [29]. A new strategy for the synthesis of functionalized tetronic acids was developed by Schobert and coworkers [30], applying the "domino" process, which comprises of the reaction between the esters of α -hydroxy acids and the cumulated phosphorus ylide ketylenidetriphenylphosphorane (Scheme 4).

In addition, the one pot synthesis of 3-aryl- unsubstituted, mono- and disubstituted at 5 position of the heterocyclic nucleus tetronic acids, as well as three natural vulpinic acids have been recently studied by Malligner and



SCHEME 2: Synthesis of reutericyclin by Schobertand Jagush [21].

coworkers based on a tandem transesterification/Dieckmann condensation reaction (Scheme 5) [31].

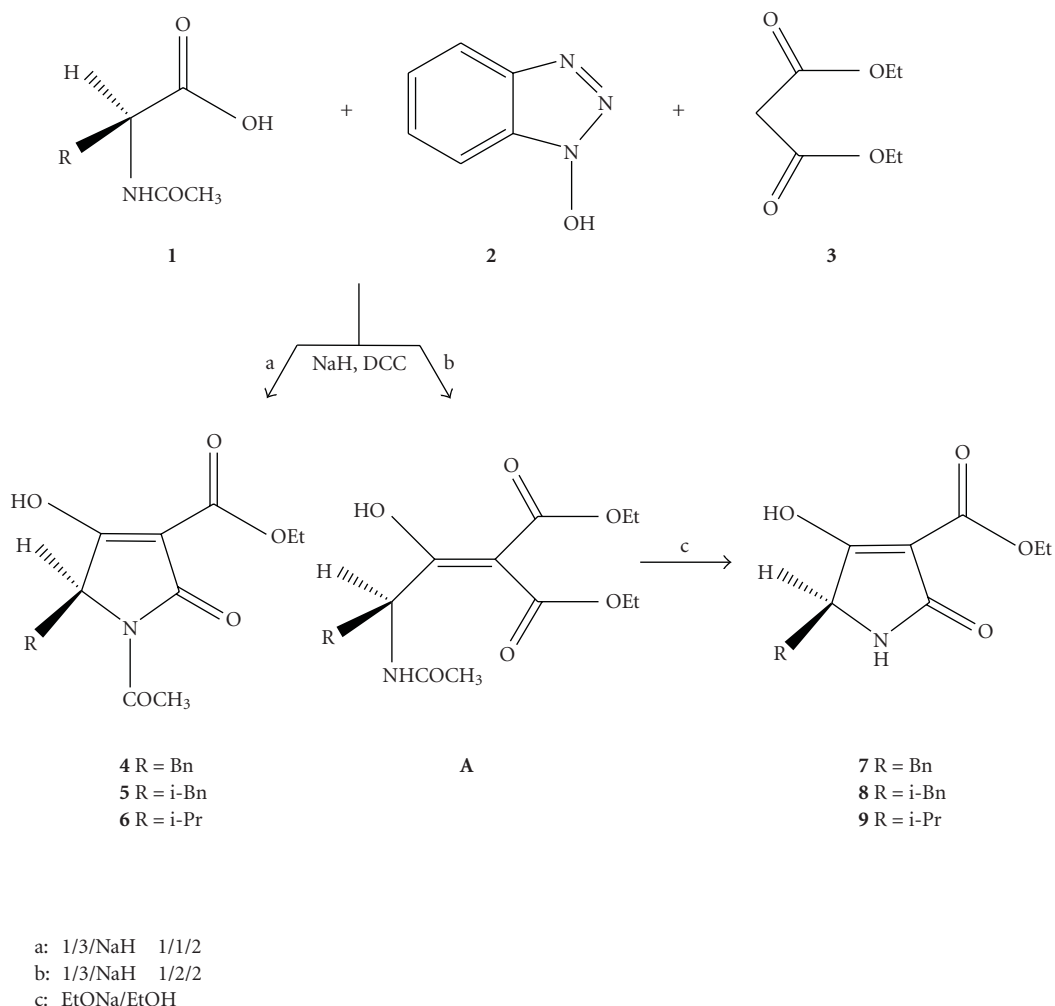
As a logical extension of our previous efforts on the synthesis of small heterocyclic compounds, we decided to investigate the condensation reaction of N-hydroxybenzotriazole esters of O-protected α -hydroxy acids and active methylene compounds bearing appropriate substituents suitable for preparing highly functionalized tetronic acid derivatives with pharmacological interest [32]. Generally, a definite short-step methodology for producing chiral 3-substituted tetronic acids or their γ -hydroxy ester precursors via a C-acylation reaction between the N-hydroxybenzotriazole ester of an appropriate O-protected- α -hydroxy acid and the desired active methylene compound was accomplished (Scheme 6).

The proposed strategy comprises of a C-acylation reaction between an active methylene compound **3** and the N-hydroxybenzotriazole ester of the appropriate O-protected- α -hydroxy acid **1**. In cases where the main product of the C-acylation reactions were the functionalized 4-acetoxy-3-hydroxybutenoates **7–14**, we used these γ -hydroxy esters for the preparation of the corresponding tetronic acid derivatives **15–21** under acidic conditions (MeOH, 10% HCl). At this point, it is important to notice that the lactonization of the β -hydroxybutenoates proceeded without racemization of stereogenic centers at C-5. One first remark in our proposed synthetic route is that only the O-acetylglycolic acid **1a** gave the corresponding tetronic acids **4–6** via one-step reaction. In contrast, S-mandelic acid **1b**, α -hydroxyisobutyric acid **1c**, L- α -hydroxyisovaleric acid **1d**, and L- α -hydroxyisocaproic acid **1e** gave the corresponding

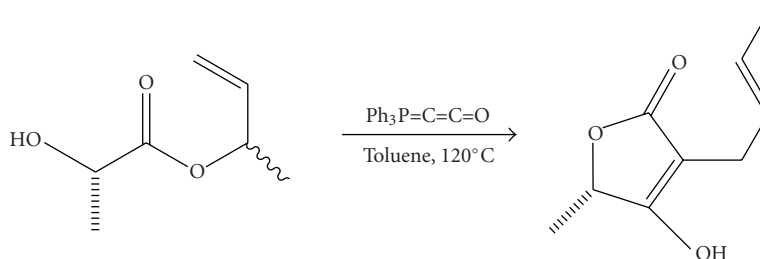
γ -acetoxy- β -hydroxybutenoates **7–14** as oily products. These intermediates were treated with 10% HCl in MeOH at room temperature for 24 or 48 hours to afford the corresponding tetronic acids **15, 16**, and **18–21** have been found to be optically active as shown by their optical rotations. This observation is in full accordance with the results obtained in the synthesis of tetramic acids [22].

4. Tetramic Acids as Quorum Sensing Molecules

The survival of microorganisms may contain the mechanism of eliminating the presence of other such organisms through the destruction of their transmembrane permeability. In such a context, the scientific team of D. K. Janda has extensively studied the role of 3-oxo-dodecanoyl homoserine lactone (3-oxo- C_{12} -HSL) in *P. aeruginosa* sp [33–35]. Based on the fact that 3-oxo- C_{12} -HSL can be easily converted to the corresponding tetramic acid (C_{12} -TA) through a non-enzymatic Claisen “internal rearrangement”, the antimicrobial activity of these two compounds was examined. Therefore, 3-oxo- C_{12} -HSL has an action mainly on host cells acting as “quorum sensing” molecule (QS), whereas its conversion to the C_{12} -TA is important in order to inhibit the life of bacterial competitors. In addition, C_{12} -TA has no inhibitory activity on mammalian cells in contrast to other tetramic acids which were developed as potent antibiotics [36, 37] and the precursor 3-oxo- C_{12} -HSL. Although the mode of action of tetramic acid remains to be established, this molecule is a potent “iron chelator” (see [35] and references



SCHEME 3: Synthesis of tetramic acids.



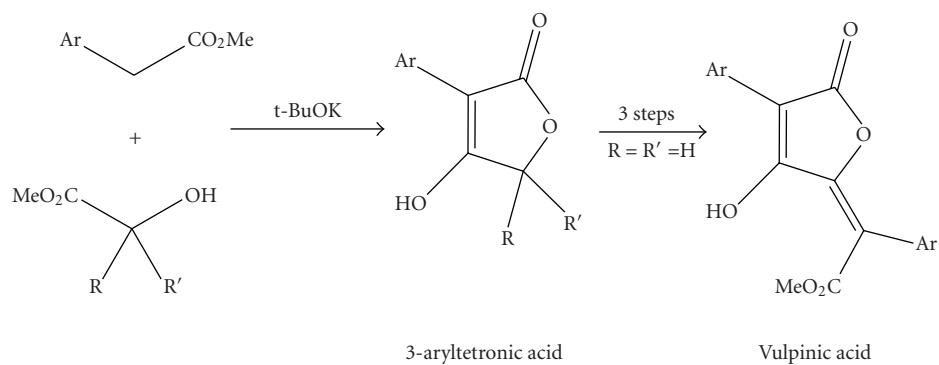
SCHEME 4: Synthesis of tetronic acids by Schobert et al. [30].

therein). Consequently, it is clear that the discovery and synthesis of tetramic acids which are derived from naturally existing “homoserine lactones” is a new challenging avenue in medicinal chemistry.

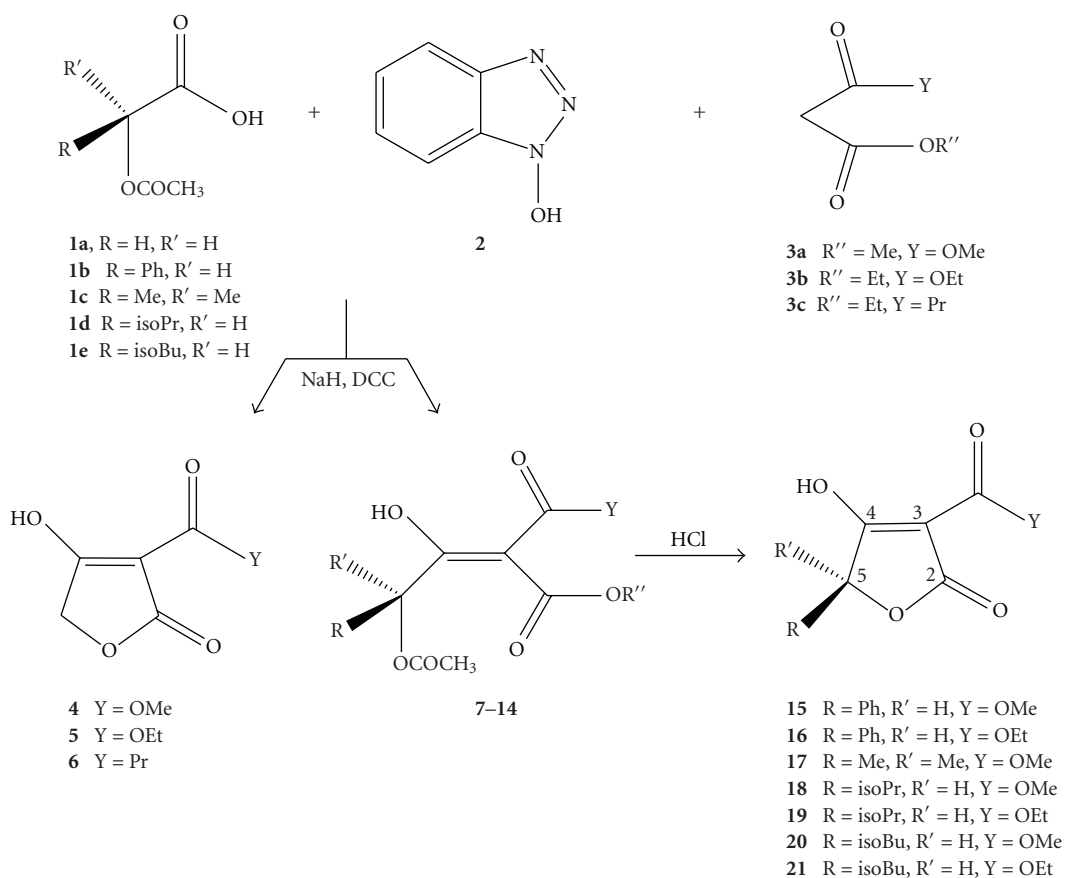
5. Tetramic Acid Coordination Compounds

Early studies on fungal toxins have demonstrated that tetramic acids tend to occur naturally as metal-chelate complexes [38]. Metal chelation by tetramic acid nucleus

seems to be important for transport across membranes in biological tissues [2]. Tetramic acids possessing a 3-acyl group have the ability to chelate divalent metal ions. For instance, tenuazonic acid from the fungus *Phoma sorghina* has shown to form complexes with Ca(II) and Mg(II) [39] as well as heavier metals such as Cu(II), Ni(II), and Fe(III) [40, 41]. Furthermore, the research group of Biersack et al. has extensively studied melophlins, a group of 3-acyl-N-methyl tetramic acids, as far as their synthesis and biological activity is concerned, and it has presented the synthesis of complexes



SCHEME 5: Synthesis of 3-aryltetronic acids as precursors for vulpinic acids by Mallinger et al. [31].



SCHEME 6: Synthesis of tetronic acids.

of melophlins with Mg, Zn, Ga, La, and Ru [42]. The chelation mode is the well-known complexation through the oxygen atom of the exocyclic carbonyl group (attached at position 3 of the heterocyclic nucleus) and the ketonic moiety of position 4 (E-isomer) or position 2 (Z isomer), respectively (Scheme 9). The biological evaluation of the new complexes showed antiproliferative activity against various cancer cells. Likewise, cyclopiazonic acid (CPA) [43] is a toxic indole tetramic acid produced by various fungi and found to inhibit SERCA (a well-studied member of the P-type ATPase family in the rabbit skeletal muscle). The way CPA works was

studied through its chelation mode with Mg(II), Mn(II), and Ca(II), and it was revealed that the bivalent way of chelation is desirable in order to enhance the cytoplasmic cation access pathway.

Our research group interest deals with the coordination capabilities of various heterocyclic compounds containing the β,β' -dicarbonyl system. Among others, we have prepared new metal complexes with pyrrolidine-2,4-dione derivatives, in order to improve their pharmacological profile by binding them to metal ions. As it was already reported in the literature [1, 2], the biological activity of some tetramic acid derivatives

significantly has been enhanced by binding to metal ions. It was found that in some cases the metal complexes obtained revealed higher biological activity than their ligands.

Over the past years, we synthesized two novel ligands based on tetramic acid core, the N-acetyl-3-benzoyl and 3-butanoyltetramic acids, with binding sites suitable for chelation of Co(II), Ni(II), Cu(II), Cd(II), and Hg(II) species [44] (Scheme 7). Starting from these ligands, complexes with 1:1 and 1:2 metal to ligand stoichiometries were prepared. The magnetic and spectroscopic properties of the Co(II), Ni(II), and Cu(II) halide and thiocyanate complexes of formula MX_2L (L = tetramic acid ligand) indicate that these contain six-coordinated metals with both bridging anions and tetramic acids. The acids appear to be bonded to the metals possibly through the nitrogen atom and a carbonyl oxygen atom and the IR spectra indicate the Cd(II) and Hg(II) complexes to be possibly tetrahedral.

The rhodium (I) complexes $[\text{Rh}(\text{acac})\{\text{P}(\text{OPh})_3\}_2]$ and $[\text{Rh}(\text{acac})(\text{CO})\text{PPh}_3]$ (acac = acetylacetonate) in the presence of triphenyl-phosphite or phosphine, respectively, are catalyst precursors for the hydroformulation of olefins under mild conditions [45]. The substitution of acac by other chelating molecules, including the β -diketonate, moiety has been less well studied for rhodium complexes.

The preparation of rhodium(I) complexes containing the N-acetyl-3-butanoyltetramic acid (Habta) together with their structural characterization via X-ray analysis of $[\text{Rh}(\text{abta})\{\text{P}(\text{OPh})_3\}_2]$, their ^1H , ^{13}C , ^{31}P NMR spectra, and IR measurements have been investigated [46].

The addition of 1 equiv of Habta to a solution of $[\text{Rh}(\text{acac})(\text{CO})_2]$ in CH_2Cl_2 results in complete substitution of acac by abta with formation of $[\text{Rh}(\text{abta})(\text{CO})_2]$ which underwent displacement of CO by either $\text{P}(\text{OPh})_3$ or PPh_3 to give $[\text{Rh}(\text{abta})(\text{CO})\text{L}]$ L = $\text{P}(\text{OPh})_3$ or PPh_3 and $[\text{Rh}(\text{abta})\{\text{P}(\text{OPh})_3\}_2]$.

The ^{13}C NMR spectrum of $[\text{Rh}(\text{abta})(\text{CO})_2]$ consists of two equally intense resonances due to rhodium carbonyls which are equivalents as a result of the asymmetry of coordinated abta. Spectroscopic data for all the abta complexes are consistent with its coordination O,O'-mode through the functionalities associated with C(4) and the acyl group at C(3) in the pyrrolidinone ring, as by X-ray crystallography. The IR spectrum of $[\text{Rh}(\text{abta})(\text{CO})_2]$ showed two equally intense $\nu(\text{CO})$ bands at 2095 and 2027 cm^{-1} owing to the fast substitution of acac (νCO 2085, 2014 cm^{-1} in $[\text{Rh}(\text{acac})(\text{CO})_2]$), whereas a strong absorption in the range 1605–1612 cm^{-1} can be attributed to a combination of the $\nu(\text{CO})$ and $\nu(\text{C}=\text{C})$ vibrations of coordinated data.

The 5-arylidene-3-alkanoyl tetramic acids contain important structural adjuncts, namely, an enolic β,β' -tricarboxyl moiety, a lipophilic 3-alkanoyl substituent, and a hydrophobic group at the 5-position which allow them to anticipate versatile activity. Moreover, the β,β' -tricarboxyl moiety provides them with sites available for metal complexation. These properties prompted us to study the synthesis and the complexation reaction of 5-benzylidene-3-hexanoyl tetramic acid (BHTA) with the halides of Mg(II), Ba(II), and Zn(II) [47]. Interest in complexes of Mg(II) arises from the antibiotic "Magnesidin", containing

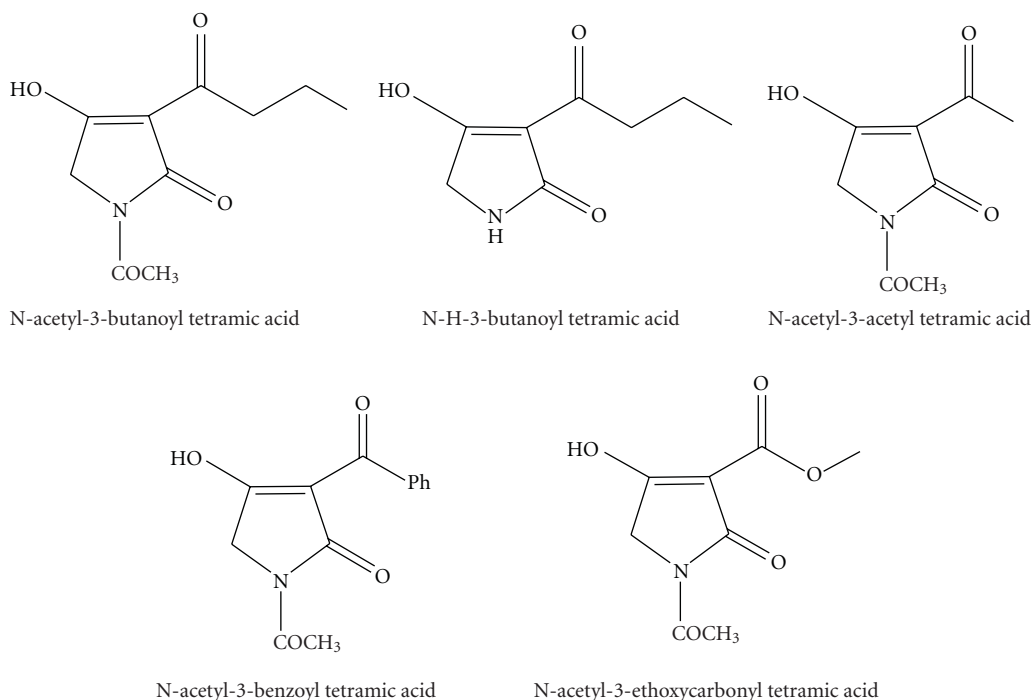
the 5-ethylidene-3-alkanoyl acids with Mg(II) [48]. The structure of the novel complexes of Mg(II) and Ba(II) followed the pattern of two metal ions and three ligands in the complex structure whereas the complexation reaction with Zn(II) halide afforded a complex comprising of the metal ion and two ligands (Scheme 8). Elemental analyses and FAB MS spectra revealed structures of the formulae $\text{Mg}_2\text{L}_3(\text{OH})\cdot 4\text{H}_2\text{O}$, $\text{Ba}_2\text{L}_3(\text{OH})\cdot 6\text{H}_2\text{O}$, and $\text{ZnL}_2\cdot 4.5\text{H}_2\text{O}$. In the ^{13}C NMR spectra of the complex with Zn, the appearance of two signals at different values for each carbonyl carbon is the proof of the existence of two five-membered inequivalent chelate rings, whereas in the complexes of Mg and Ba the NMR spectra exhibit three resonances for the carbonyl carbons. These signals are not equally intense, an indication for the presence of three tautomers which are interconverted by a relatively slow metal-oxygen dissociation-association process on the NMR time scale.

The structural investigation of the metal 5-benzylidene-3-alkanoyl tetramic acid is important to analyze both the ligating abilities of tetramic acids and the effects of coordination on the conformation of the HL/L⁻ molecules.

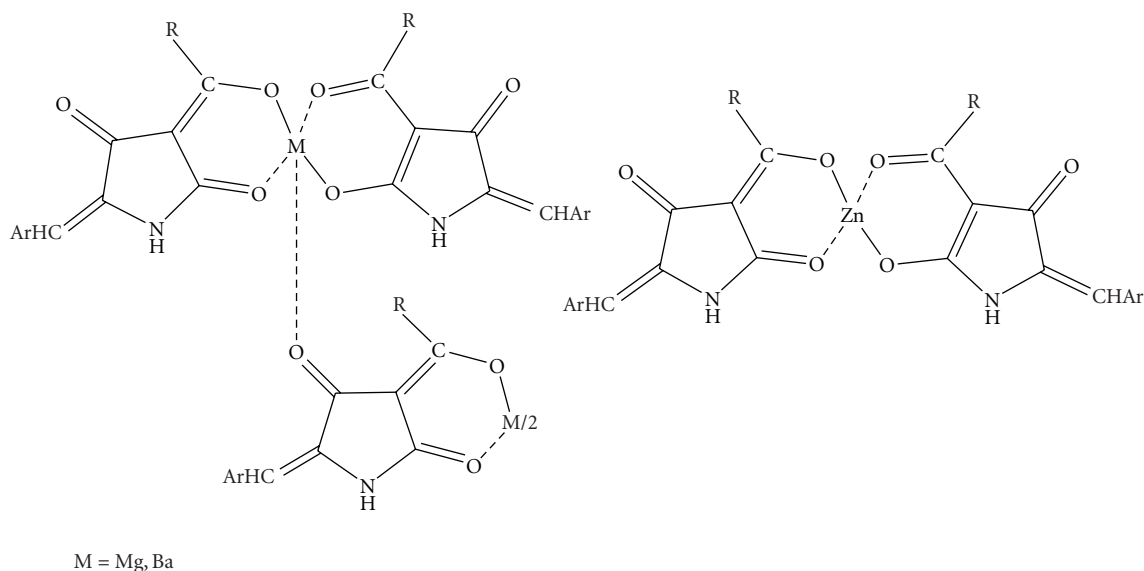
It is well-known that N and O play a key role in the coordination of metals at the active sites of numerous metallo-biomolecules. Therefore, a number of Cu(II), Co(II), Ni(II) and Zn(II) acetate complexes containing the enolate N-acetyl-3-butanoyltetramic acid and its phenylhydrazone derivative analogues were studied [49]. The reaction in 1:1 ratio afforded complexes of the general formula $\text{M}(\text{OAc})(\text{L-H})\cdot \text{H}_2\text{O}$ whereas the reaction in 1:2 ligand to metal ratio gave complexes of the formula $\text{M}(\text{L-H})_2\cdot \gamma\text{H}_2\text{O}$. The way the ligand is complexed to the metal ion was proved by X-ray analysis of the crystals obtained from the reaction of the ligand with $\text{Cu}(\text{OAc})_2\cdot \text{H}_2\text{O}$. The enolate of the ligand is complexed through the oxygen atoms of the hydroxyl group of position 4 and the carbonyl oxygen of the acyl moiety attached at position 3 of the heterocyclic ring. In this complex, copper possibly adopts a slightly distorted octahedral coordination geometry. The reaction of the ligand with Zn(II) acetate in 1:1 and 1:2 ratio, respectively, gave complexes where the deprotonated ligand was further deacylated at the nitrogen atom in the first situation but not in the second one. In addition, a new ligand was then synthesized, the phenylhydrazone of the previously used tetramic acid (Scheme 9), and its complexes with Cu(II) and Co(II) in 1:1 and 1:2 ratio were formed. The structures exhibited the general formulae $\text{M}(\text{OAc})(\text{L-H})$ and $\text{M}(\text{L-H})_2$, respectively, as described for the tetramic acid. In contrast to the situation with Zn(II) acetate, the reaction of the phenylhydrazone of tetramic acid with $\text{Zn}(\text{OAc})_2\cdot 2\text{H}_2\text{O}$ irrespective of the metal to ligand ratio afforded $\text{Zn}(\text{OAc})(\text{L-H})$ containing the deacylated ligand.

Finally, the solid state structure of $[\text{Cu}(\text{abta})_2(\text{py})_2]\cdot 2\text{H}_2\text{O}$ has been determined by single crystal X-ray diffraction. It shows that copper adapts a slightly distorted octahedral coordination geometry with ligand adopting an O,O'-mode of coordination via the functionalities associated with C4 and the acetyl group at C3 in the pyrrolidine ring.

New platinum (II) complexes containing 3-alkanoyl tetramic acids have shown to exhibit a broad spectrum



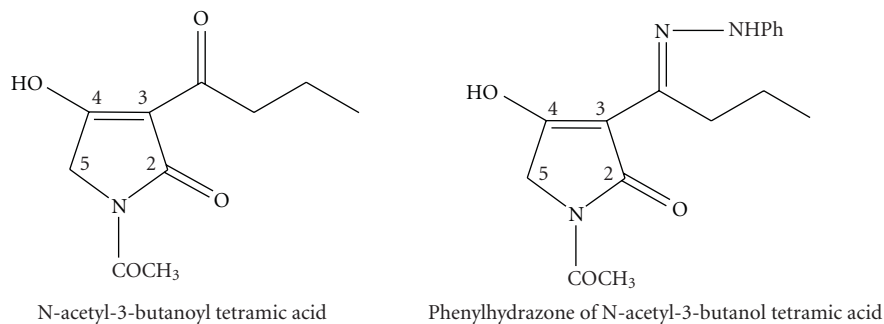
SCHEME 7: 3-substituted tetramic acids.



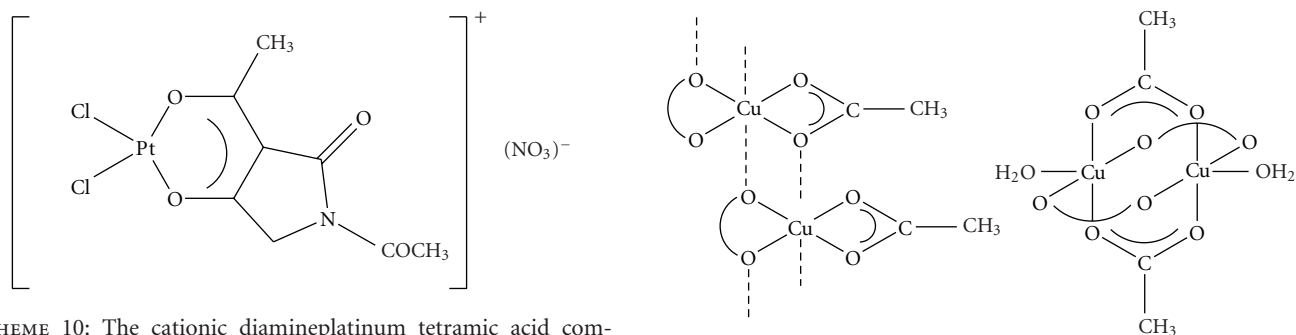
SCHEME 8: Metal complexes of 5-benzylidene-3-acyl tetramic acids.

of biological properties. Although the synthesis and the antitumor activity of these complexes is mentioned in two patents [50, 51], no details are given concerning the structure of the complexes. There is a large body of experimental evidence suggesting that the success of platinum complexes in killing tumor cells results from the ability to damage DNA by forming various types of covalent adducts [52, 53]. Encouraged by promising chemotherapeutic properties of “cisplatin” complexes, we investigated the coordination ability of N,3-diacetyl tetramic acid (Hata) with

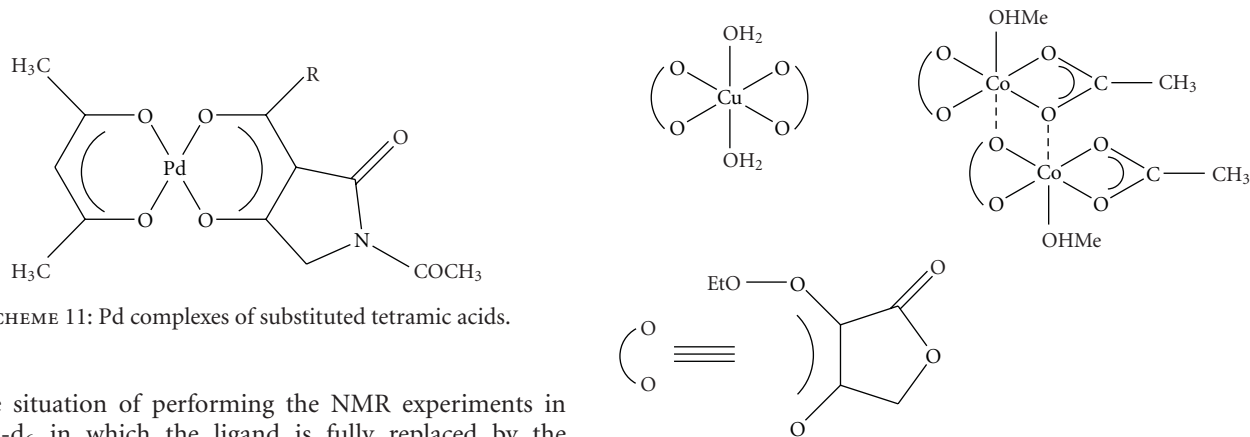
cis-(NH₃)₂PtCl₂, (dach)PtCl₂, (en)PtCl₂ and K₂PtCl₄. The structure of the isolated complexes was investigated by means of IR, NMR, ESI-MS Spectroscopy, and molar conductivity measurements [54]. The pattern of complexation of the deprotonated ligand follows possibly the known bidentate mode through the oxygen atoms of the 3-acyl moiety and the hydroxyl group of position 4 of the heterocyclic nucleus (Scheme 10). The coordination sphere around Pt(II) can be described as distorted square-planar and the stability of the ligand in its complexation ability remains except



SCHEME 9: N-acetyl-3-butanoyl tetramic acid and its phenylhydrazone derivative.



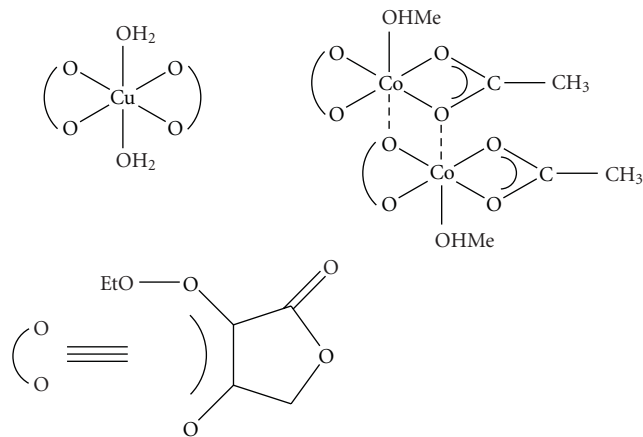
SCHEME 10: The cationic diamineplatinum tetramic acid complexes.



SCHEME 11: Pd complexes of substituted tetramic acids.

for the situation of performing the NMR experiments in DMSO- d_6 in which the ligand is fully replaced by the solvent molecules in the metal complex. These complexes have similarities with complexes between alkanoyl tetramic acids and Pt(II) which were patented since they exhibited interesting biological activities. In this context the structure evaluation of our complexes is very useful in order to perform structure-activity relationship experiments with the previous complexes.

The ability of N-acetyl-3-butanoyltetramic acid (Habta) enolate ligand to substitute acetylacetonate from $[\text{Rh}(\text{acac})(\text{CO})_2]$ prompted us to study the progressive displacement of acac from $[\text{Pd}(\text{acac})_2]$ complexes which occurs on reaction with different tetramic acids $[\text{L} = \text{N},3\text{-diacetyl (Hata), N-acetyl-3-butanoyl (Habta), and N-acetyl-3-ethoxycarbonyl (Haceta)}]$ [55]. In the first two situations (3-acyl and 3-butanoyl tetramic acids), the displacement afforded complexes of the general formulae $[\text{Pd}(\text{acac})(\text{L-H})]$ in 1:1 and 1:2 ratio of reaction, but in the situation of 3-ethoxycarbonyl tetramic acid the only isolated complex was



SCHEME 12: Metal complexes of substituted tetronic acids.

$[\text{Pd}(\text{acac})(\text{L-H})]$ even in 1:4 ratio of reaction. On the other hand, the reaction of all the above tetramic acids in aqueous solution of $\text{K}_2[\text{PdCl}_4]$ gave complexes of the general formula $[\text{Pd}(\text{L-H})_2]$. The study of the structure of complexes with NMR Spectroscopy showed that there is only one isomer in complexes $[\text{Pd}(\text{acac})(\text{L-H})]$ whereas in complexes $[\text{Pd}(\text{L-H})_2]$ two isomers are apparent, which are evaluated as the "cis" and "trans" isomers based on the possible bidentate complexation of the ligand through the oxygen atoms of the pyrrolidine nucleus (Scheme 11). Addition of a Lewis base, such as pyridine, to a chloroform solution of $[\text{Pd}(\text{abta})_2]$, forms a Lewis base adduct, $[\text{Pd}(\text{py})_4(\text{abta})_2]$ which has been characterized by X-ray analysis and shown to contain a square planar $\text{Pd}(\text{py})_4$ group with *trans*-monodentate weakly bonded abta groups.

6. Tetronic Acid Coordination Compounds

The coordination mode of tetronic acids is a research field with great interest and many examples in the recent literature can be found. Complexes of tetronic acids with Cu(II) have been synthesized and their biological activity was elucidated [56], whereas a number of complexes of 3-acyl tetronic acids with Pd(II) and Pt(II) have also been reported [57, 58]. Finally, complexes with several metal ions have proved the existence of 1:2 or 1:3 ratios (metal:ligand) either by conductometric or pH-metric titrations [59] or by X-Ray crystallographic analysis [60].

The complexation mode of 3-ethoxycarbonyl tetronic acid (L = HETA) with acetates and chlorides of Cu(II) and Co(II) was studied based on measurements of magnetic susceptibility and EPR Spectroscopy [61]. The complexes isolated were Cu(OAc)(L-H), Cu₂(OAc)₂(L-H)₂(H₂O)₂, Cu(L-H)₂(H₂O)₂ and Co₂(OAc)₂(L-H)₂(MeOH)₂ (Scheme 12). The isolated complexes of Cu(II) and Co(II) acetates with HETA in 1:1 ratio have a possible octahedral stereochemistry with bidentate coordination mode through O(4) and O(6) of the tetronate ring as indicated by the shift to lower wavenumbers of the lactone and diketone characteristic bands. In addition, magnetic susceptibility measurements showed that no reduction to Cu(I) occurred whereas the result for Co(II) complex gives evidence of octahedral stereochemistry. The chloride Cu(II) complex with HETA in 1:2 ratio has a possible octahedral stereochemistry, whereas the exclusion of dinuclear species was achieved through EPR measurements. However both Cu(II) complexes showed the presence of two sets of EPR signals indicating an inhomogeneity of centers; some of them point to a mononuclear structure, while the others adopt a dinuclear structure. Moreover, EPR studies for these compounds showed the possible mononuclear and dinuclear structures, respectively. In summary, we have prepared a plausible model for the copper, cobalt β,β'-tricarboxyl coordination compounds. Our proposed model may help define some of the unusual features associated with copper and cobalt metallobiochemistry.

References

- [1] B. J. L. Royles, "Naturally occurring tetramic acids: structure, isolation, and synthesis," *Chemical Reviews*, vol. 95, no. 6, pp. 1981–2001, 1995.
- [2] R. Schober and A. Schlenk, "Tetramic and tetronic acids: an update on new derivatives and biological aspects," *Bioorganic and Medicinal Chemistry*, vol. 16, no. 8, pp. 4203–4221, 2008.
- [3] S. Tuske, S. G. Sarafianos, X. Wang, et al., "Inhibition of bacterial RNA polymerase by streptolydigin: stabilization of a straight-bridge-helix active-center conformation," *Cell*, vol. 122, no. 4, pp. 541–552, 2005.
- [4] S. Aoki, K. Higuchi, Y. Ye, R. Satari, and M. Kobayashi, "Melophlins A and B, novel tetramic acids reversing the phenotype of ras- transformed cells, from the marine sponge *Melophlus sarassinorum*," *Tetrahedron*, vol. 56, no. 13, pp. 1833–1836, 2000.
- [5] N. J. Phillips, J. T. Goodwin, A. Fraiman, R. J. Cole, and D. G. Lynn, "Characterization of the *Fusarium* toxin equisetin: the use of phenylboronates in structure assignment," *Journal of the American Chemical Society*, vol. 111, no. 21, pp. 8223–8231, 1989.
- [6] E. C. Marfori, S. Kajiyama, E.-I. Fukusaki, and A. Kobayashi, "Trichosetin, a novel tetramic acid antibiotic produced in dual culture of *Trichoderma harzianum* and *Catharanthus roseus* callus," *Zeitschrift für Naturforschung*, vol. 57, no. 5-6, pp. 465–470, 2002.
- [7] A. Holtzel, M. G. Ganzle, G. J. Nicholson, W. P. Hammes, and G. Jung, "The first low molecular weight antibiotic from lactic acid bacteria: reutericyclin, a new tetramic acid," *Angewandte Chemie*, vol. 39, no. 15, pp. 2766–2768, 2000.
- [8] U. Marquardt, D. Schmid, and G. Jung, "Racemic synthesis of the new antibiotic tetramic acid reutericyclin," *Synlett*, no. 8, pp. 1131–1132, 2000.
- [9] R. Fischer, S. Lehr, and D. Feucht, "2-ethyl-4,6-dimethyl-phenyl-substituted tetramic acid derivative as pest control agents and/or herbicides," WO 2005/048710, 2005.
- [10] D. Tejedor and F. García-Tellado, "Synthesis and chemistry of tetronic acids," *Organic Preparations and Procedures International*, vol. 36, no. 1, pp. 33–59, 2004.
- [11] A. L. Zografos and D. Georgiadis, "Synthetic strategies towards naturally occurring tetronic acids," *Synthesis*, no. 19, pp. 3157–3188, 2006.
- [12] D. H. Davies, E. W. Snape, P. J. Suter, T. J. King, and C. P. Falshaw, "Structure of antibiotic M139603; x-ray crystal structure of the 4-bromo-3,5-dinitrobenzoyl derivative," *Journal of the Chemical Society, Chemical Communications*, no. 20, pp. 1073–1074, 1981.
- [13] B. E. Roggo, F. Petersen, R. Delmendo, H. B. Jenny, H. H. Peter, and J. Roesel, "3-alkanoyl-5-hydroxymethyl tetronic acid homologues and resistomycin: new inhibitors of HIV-1 protease I. Fermentation, isolation and biological activity," *Journal of Antibiotics*, vol. 47, no. 2, pp. 136–142, 1994.
- [14] G. Pattenden, M. W. Turvill, and A. P. Chorlton, "Maleic anhydrides in synthesis. Preparation of furan-2(5H)-one phosphonate derivatives and a new synthesis of pulvinic acids and pulvone analogues," *Journal of the Chemical Society, Perkin Transactions 1*, no. 10, pp. 2357–2361, 1991.
- [15] Y. Bourdreux, E. Bodio, C. Willis, C. Billaud, T. Le Gall, and C. Mioskowski, "Synthesis of vulpinic and pulvinic acids from tetronic acid," *Tetrahedron*, vol. 64, no. 37, pp. 8930–8937, 2008.
- [16] S. V. Ley, S. C. Smith, and P. R. Woodward, "Further reactions of t-butyl 3-oxobutanthioate and t-butyl 4-diethylphosphono-3-oxobutanthioate: carbonyl coupling reactions, amination, use in the preparation of 3-acyltetramic acids and application to the total synthesis of fuligorubin A," *Tetrahedron*, vol. 48, no. 6, pp. 1145–1174, 1992.
- [17] M. D. Andrews, A. G. Brewster, K. M. Crapnell, et al., "Regioselective Dieckmann cyclisations leading to enantiopure highly functionalised tetramic acid derivatives," *Journal of the Chemical Society—Perkin Transactions 1*, no. 2, pp. 223–235, 1998.
- [18] L. A. Paquette, D. Macdonald, L. G. Anderson, and J. Wright, "A triply convergent enantioselective total synthesis of (+)-ikarugamycin," *Journal of the American Chemical Society*, vol. 111, no. 20, pp. 8037–8039, 1989.
- [19] R. C. F. Jones and M. Tankard, "A new sequence for the synthesis of 3-(poly)enoilyltetramic acids," *Journal of the Chemical Society, Perkin Transactions 1*, no. 1, pp. 240–241, 1991.

- [20] P. Jouin, B. Castro, and D. Nisato, "Stereospecific synthesis of N-protected statine and its analogues via chiral tetramic acid," *Journal of the Chemical Society, Perkin Transactions 1*, pp. 1177–1182, 1987.
- [21] R. Schobert and C. Jagusch, "An expedient synthesis of 3-acyltetramic acids of the melophlin family from α -aminoesters and immobilized Ph_3PCCO ," *Tetrahedron*, vol. 61, no. 9, pp. 2301–2307, 2005.
- [22] G. Athanasellis, E. Gavrielatos, and O. Igglessi-Markopoulou, "One-pot synthesis of optically active tetramic acids from amino acids mediated by 1-hydroxybenzotriazole," *Synlett*, no. 10, pp. 1653–1655, 2001.
- [23] P. M. Booth, C. M. J. Fox, and S. V. Ley, "Preparation of acyltetronic acids using t-butyl acetoethoacetate: total synthesis of the fungal metabolites carolic, carlosic, and carlic acids," *Journal of the Chemical Society, Perkin Transactions 1*, pp. 121–129, 1987.
- [24] R. C. F. Jones, K. A. M. Duller, and S. I. E. Vulto, "1,3-Dipolar cycloaddition route to oxygen heterocyclic triones," *Journal of the Chemical Society, Perkin Transactions 1*, no. 3, pp. 411–416, 1998.
- [25] A. Mittra, M. Yamashita, I. Kawasaki, H. Murai, T. Yoshioka, and S. Ohta, "A useful oxidation procedure for the preparation of 3-alkanoyltetronic acids," *Synlett*, vol. 1997, no. 8, pp. 909–910, 1997.
- [26] R. Schobert, S. Muller, and H.-J. Bestmann, "One-pot synthesis of α, γ -disubstituted tetronic acids from α -hydroxyallyl esters: a novel "tandem-wittig-claisen"-reaction," *Synlett*, vol. 5, pp. 425–426, 1995.
- [27] F. Effenberger and J. Syed, "Stereoselective synthesis of biologically active tetronic acids," *Tetrahedron Asymmetry*, vol. 9, no. 5, pp. 817–825, 1998.
- [28] H. Buhler, A. Bayer, and F. Effenberger, "A convenient synthesis of optically active 5,5-disubstituted 4-amino- and 4-hydroxy-2(5H)-furanones from (S)-ketone cyanohydrins," *Chemistry*, vol. 6, no. 14, pp. 2564–2571, 2000.
- [29] C. A. Mitsos, A. L. Zografos, and O. Igglessi-Markopoulou, "Regioselective ring opening of malic acid anhydrides by carbon nucleophiles. Application in the synthesis of chiral tetronic acids," *Journal of Organic Chemistry*, vol. 65, no. 18, pp. 5852–5853, 2000.
- [30] R. Schobert, G. J. Gordon, A. Bieser, and W. Milius, "3-Functionalized tetronic acids from domino rearrangement/cyclization/ring-opening reactions of allyl tetronates," *European Journal of Organic Chemistry*, no. 18, pp. 3637–3647, 2003.
- [31] A. Mallinger, T. L. Gall, and C. Mioskowski, "3-Aryltetronic acids: efficient preparation and use as precursors for vulpinic acids," *Journal of Organic Chemistry*, vol. 74, no. 3, pp. 1124–1129, 2009.
- [32] G. Athanasellis, O. Igglessi-Markopoulou, and J. Markopoulos, "Novel short-step synthesis of optically active tetronic acids from chiral α -hydroxy acids mediated by 1-hydroxybenzotriazole," *Synlett*, no. 10, pp. 1736–1738, 2002.
- [33] G. F. Kaufmann, R. Sartorio, S. H. Lee, et al., "Antibody interference with N-Acyl homoserine lactone-mediated bacterial quorum sensing," *Journal of the American Chemical Society*, vol. 128, no. 9, pp. 2802–2803, 2006.
- [34] G. F. Kaufmann, R. Sartorio, S.-H. Lee, et al., "Revisiting quorum sensing: discovery of additional chemical and biological functions for 3-oxo-N-acylhomoserine lactones," *Proceedings of the National Academy of Sciences of the United States of America*, vol. 102, no. 2, pp. 309–314, 2005.
- [35] C. A. Lowery, J. Park, C. Gloeckner, et al., "Defining the mode of action of tetramic acid antibacterials derived from *Pseudomonas aeruginosa* quorum sensing signals," *Journal of the American Chemical Society*, vol. 131, no. 40, pp. 14473–14479, 2009.
- [36] R. Yendapally, J. G. Hurdle, E. I. Carson, R. B. Lee, and R. E. Lee, "N-substituted 3-acetyltetramic acid derivatives as antibacterial agents," *Journal of Medicinal Chemistry*, vol. 51, no. 5, pp. 1487–1491, 2008.
- [37] J. G. Hurdle, R. Yendapally, D. Sun, and R. E. Lee, "Evaluation of analogs of reutericyclin as prospective candidates for treatment of staphylococcal skin infections," *Antimicrobial Agents and Chemotherapy*, vol. 53, no. 9, pp. 4028–4031, 2009.
- [38] R. T. Gallagher, J. L. Richard, H. M. Stahr, and R. J. Cole, "Cyclopiazonic acid production by aflatoxigenic and non-aflatoxigenic strains of *Aspergillus flavus*," *Mycopathologia*, vol. 66, no. 1–2, pp. 31–36, 1978.
- [39] P. S. Steyn and C. J. Rabie, "Characterization of magnesium and calcium tenuazonate from *Phoma sorghina*," *Phytochemistry*, vol. 15, no. 12, pp. 1977–1979, 1976.
- [40] M.-H. Lebrun, P. Duvert, and F. Gaudemer, "Complexation of the fungal metabolite tenuazonic acid with copper (II), iron (III), nickel (II), and magnesium (II) ions," *Journal of Inorganic Biochemistry*, vol. 24, no. 3, pp. 167–181, 1985.
- [41] M. Fujita, Y. Nakao, S. Matsunaga, et al., "Ancorinosides B-D, inhibitors of membrane type 1 matrix metalloproteinase (MT1-MMP), from the marine sponge *Penares sollasi* Thiele," *Tetrahedron*, vol. 57, no. 7, pp. 1229–1234, 2001.
- [42] B. Biersack, R. Diestel, C. Jagusch, F. Sasse, and R. Schobert, "Metal complexes of natural melophlins and their cytotoxic and antibiotic activities," *Journal of Inorganic Biochemistry*, vol. 103, no. 1, pp. 72–76, 2009.
- [43] M. Laursen, M. Bublitz, K. Moncoq, et al., "Cyclopiazonic acid is complexed to a divalent metal ion when bound to the sarcoplasmic reticulum Ca^{2+} -ATPase," *Journal of Biological Chemistry*, vol. 284, no. 20, pp. 13513–13518, 2009.
- [44] O. Markopoulou, J. Markopoulos, and D. Nicholls, "Synthesis of 3-butanoyl- and 3-benzoyl-4-hydroxy-3-pyrrolin-2-ones and their complexes with metal ions," *Journal of Inorganic Biochemistry*, vol. 39, no. 4, pp. 307–316, 1990.
- [45] A. M. Trzeciak and J. J. Ziolkowski, "1,5-Hexadiene selective hydroformylation reaction catalyzed with $\text{Rh}(\text{acac})\text{P}((\text{OPh})_2)_2/\text{P}(\text{OPh})_3$ and $\text{Rh}(\text{acac})(\text{CO})(\text{PPh}_3)_2/\text{PPh}_3$ complexes," *Journal of Organometallic Chemistry*, vol. 464, no. 1, pp. 107–111, 1994.
- [46] B. T. Heaton, C. Jacob, J. Markopoulos, et al., "Rhodium(I) complexes containing the enolate of N-acetyl-3-butanoyltetramic acid (Habta) and the crystal structure of $[\text{Rh}(\text{abta})\text{P}((\text{OPh})_2)_2]$," *Journal of the Chemical Society, Dalton Transactions*, no. 8, pp. 1701–1706, 1996.
- [47] M. Petroliagi, O. Igglessi-Markopoulou, and J. Markopoulos, "Complexation and spectroscopic studies of 5-Benzylidene-3-hexanoyl tetramic acid (BHTA) with magnesium (II), zinc (II) and barium (II) ions," *Heterocyclic Communications*, vol. 6, no. 2, pp. 157–164, 2000.
- [48] N. Imamura, K. Adachi, and H. Sano, "Magnesidin A, a component of marine antibiotic magnesidin, produced by *Vibrio gazogenes* ATCC29988," *Journal of Antibiotics*, vol. 47, no. 2, pp. 257–261, 1994.
- [49] E. Gavrielatos, C. Mitsos, G. Athanasellis, et al., "Copper(II), cobalt(II), nickel(II) and zinc(II) complexes containing the enolate of N-acetyl-3-butanoyltetramic acid (Habta) and its phenylhydrazone derivative analogues. Crystal structure of

- [Cu(abta)₂(py)₂] · 2H₂O,” *Journal of the Chemical Society, Dalton Transactions*, no. 5, pp. 639–644, 2001.
- [50] M. Keiichi, H. Sakie, M. Masato, and H. Satoru, Japan Kokai Tokkyo Koho, JP, 01,313,488 [89,313,488] (Cl. C07F15/00), 1989.
- [51] H. Sakie, M. Keiichi, M. Masato, and H. Satoru, Japan Kokai Tokkyo Koho, JP, 02 48,591 [90 48,591] (Cl. C07F15/00), 1990.
- [52] S. J. Lippard and J. M. Berg, *Principles of Bioinorganic Chemistry*, University Science Books, Mill Valley, Calif, USA, 1994.
- [53] N. Hadjiliadis and E. Sletten, *Metal Complex-DNA Interactions*, John Wiley & Sons, New York, NY, USA, 2009.
- [54] E. Gavrielatos, G. Athanasellis, O. Igglessi-Markopoulou, and J. Markopoulos, “Cationic diamineplatinum(II) complexes containing the enolate of N,3-acetyl-4-hydroxypyrrrolin-2-one,” *Inorganica Chimica Acta*, vol. 344, pp. 128–132, 2003.
- [55] E. Gavrielatos, G. Athanasellis, B. T. Heaton, et al., “Palladium(II)/β-diketonate complexes containing the enolates of N-acetyl-3-acyltetramic acids: crystal structure of the Lewis base adduct, [Pd(py)₄](abta)₂,” *Inorganica Chimica Acta*, vol. 351, no. 1, pp. 21–26, 2003.
- [56] K. Tanaka, K. Matsuo, and Y. Nakaizumi, “Structure-activity relationships in tetronic acids and their copper(II) complexes,” *Chemical and Pharmaceutical Bulletin*, vol. 27, no. 8, pp. 1901–1906, 1979.
- [57] H. Kawai, T. Imaoka, and G. Hata, “Process for the production of antitumor platinum complexes,” PCT International Patent Application, WO 9634000, 1996.
- [58] J. R. Lusty and P. Pollet, “Palladium complexes involving tetronic acid derivatives,” *Inorganica Chimica Acta*, vol. 78, no. C, pp. L7–L8, 1983.
- [59] G. S. Manku, R. D. Gupta, A. N. Bhat, and B. D. Jain, “Physicochemical investigations of some bivalent ion complexes with oximidobenzotetronic acid and their comparison with the corresponding 2-nitroso-1-naphthol complexes,” *Journal of the Indian Chemical Society*, vol. 47, no. 8, pp. 776–782, 1970.
- [60] G. Reck, B. Schultz, A. Zschunke, O. Tietze, and J. Haferkorn, “Crystal structures of nickel(II) and copper(II)-Schiff-bases complexes with tetramic and tetronic acid subunits,” *Zeitschrift für Kristallographie*, vol. 209, no. 12, pp. 969–974, 1994.
- [61] J. Markopoulos, G. Athanasellis, G. Zahariou, S. Kikionis, and O. Igglessi-Markopoulou, “Coordination behavior of 3-Ethoxycarbonyltetronic acid towards Cu(II) and Co(II) metal ions,” *Bioinorganic Chemistry and Applications*, vol. 2008, Article ID 547915, 6 pages, 2008.

Research Article

Biofunctional Characteristics of Lignite Fly Ash Modified by Humates: A New Soil Conditioner

Konstantinos Chassapis,¹ Maria Roulia,¹ Evangelia Vrettou,¹ Despina Fili,² and Monica Zervaki²

¹*Inorganic Chemistry Laboratory, Department of Chemistry, University of Athens, Panepistimiopolis, 157 71 Athens, Greece*

²*School of Chemical Engineering, National Technical University of Athens, 9 Heroon Polytechniou, Zografou Campus, 157 73 Athens, Greece*

Correspondence should be addressed to Konstantinos Chassapis, chassapis@chem.uoa.gr

Received 29 December 2009; Accepted 2 March 2010

Academic Editor: Spyros Perlepes

Copyright © 2010 Konstantinos Chassapis et al. This is an open access article distributed under the Creative Commons Attribution License, which permits unrestricted use, distribution, and reproduction in any medium, provided the original work is properly cited.

Fly ash superficially modified with humic substances from the Megalopolis lignitic power plant was prepared and evaluated for agricultural uses. UV-vis spectrophotometry and IR spectroscopy revealed that fly ash shows high sorption efficiency towards humic substances. Adsorption proceeds stepwise via strong Coulombic and hydrophobic forces of attraction between guest and host materials. Langmuir, Freundlich, BET, Harkins-Jura, and Dubinin-Radushkevich isotherm models were employed to evaluate the ongoing adsorption and shed light to the physicochemical properties of the sorbent-adsorbate system. Humic substances desorption and microbial cultivation experiments were also carried out to examine the regeneration of the humates under washing and explore the possibility of this material acclimatizing in real soil conditions, both useful for biofunctional agricultural applications.

1. Introduction

Fly ash is an amorphous mixture of ferroaluminosilicate minerals generated from the combustion of ground or powdered coal at 400–1500°C and belongs to the coal combustion by-products in power plants produced from bituminous, subbituminous, and lignite combustion. Fly ash is the mineral residue consisting of small particles that are carried up and out of the boiler in the flow of exhaust gases and are collected from the stack gases using electrostatic precipitators, flue gas desulphurization systems, and bag houses [1]. Approximately 70% of the by-product is fly ash collected in electrostatic precipitators, which is the most difficult to handle [2]. This fact pinpoints the necessity for environment-friendly uses of fly ash. Fly ash is mostly used as a substitute for Portland cement in manufacturing roofing tiles and as structural fill, sheetrock, agricultural fertilizer, and soil amendment [3, 4]. Chemically, 90%–99% of fly ash is comprised of Si, Al, Fe, Ca, Mg, Na, and K with Si and Al forming the major matrix. The mineralogical, physical, and

chemical properties of fly ash depend on the nature of parent coal [5, 6]. All these applications are based on the presence of basic mineral elements resembling earth's crust, which makes them excellent substituent for natural materials.

The Greek peaty lignite of the Megalopolis Basin, formed during the Quaternary period and comprising significant quantities of humic substances and inorganic content [7, 8], may be an effective raw material for obtaining both humic substances and fly ash. During the last fifty years, Megalopolis lignite has been almost solely utilized for power generation producing solid wastes such as fly ash, bottom ash, boiler slag, and flue gas desulphurization materials, which have been commonly treated as wastes.

Agricultural utilization of fly ash has been originally proposed mostly thanks to its considerable K, Ca, Mg, S, and P contents [5, 9–11]. It was also realized that fly ash addition could also decrease the bulk density of soils, which, in turn, improved soil porosity and workability and enhanced water retention capacity [9]. Additionally, acidic or alkaline fly ash, may be of agronomic benefit buffering

the soil pH [5, 12, 13] and improving the soil nutrient status, thus increasing plant growth and nutrient uptake [14, 15]. The electrical conductivity of soil also increases with fly ash application and so does the metal content. Mixtures of swine manure with fly ash proved to increase the availability of Ca and Mg balancing the ratio between monovalent and bivalent cations, which otherwise proves detrimental to the soil [16]. This is of major importance as the presence of Ca can enhance flocculation or aggregation of soil particles, particularly clay, keeping soil friable, thus allowing both water and roots to penetrate hard and compact soil layers.

Compared to traditional soil-conditioning materials as asbestos, fly ash seems more advantageous as it is an environmentally safe material, contains plant nutrients, and can be used in biological cultivations (EU dir 889/08). Additionally, it is a low-cost material and, thanks to its granular composition, is readily applicable.

Humic substances are natural organic matter ubiquitous in water, soil, and sediments produced from the decay of animal and plant tissues and/or microbial activity. They are multifunctional amorphous biopolymers composed of hundreds of organic constituents including carbohydrates and condensed aromatic rings substituted by carboxylic, phenolic, and methoxyl groups [17], which may serve as an ideal ligand for bioinorganic applications. Their role in soil environment and their contribution in sustaining plant growth are of significant importance. Soil structure (water retention, texture, and workability), biological activity, and sequestration (chemical bioavailability, bioaccumulation, and transport of nutrients) are properties and processes of the global ecosystem directly affected by humic substances. The major challenge in research arises from the extended diversity of humic substances due to their large chemical heterogeneity and geographical variability [18].

Until now, fly ash has been used only as humic acid adsorbent for waste treatment [19, 20]. Therefore, the possibility of producing a material combining both the humic substances and fly ash advantages would appear particularly attractive.

In this work, fly ash superficially modified with humic substances (both derived from the Greek peaty lignite of the Megalopolis Basin) was prepared. UV-vis spectrophotometry and IR spectroscopy were employed to characterize the adsorption process. Five adsorption models were selected to envisage the physicochemical properties of the sorbent-adsorbate system based on the fundamental considerations and theoretical hypotheses of the specific isotherms. Humic substances desorption experiments were also carried out to determine the release rate of the humates adsorbed under washing. Additionally, cultivation experiments of microorganisms were processed to evaluate the possibility of acclimatizing this material in real soil conditions, useful for biofunctional agricultural applications.

2. Materials and Methods

Both humic substances and fly ash were extracted from the Greek peaty lignite of the Megalopolis Basin, Greece. The

selection of lignite was based on the rich content of humic substances in the particular lignite field [7, 8, 17]. Fly ash is a by-product during lignite combustion in Megalopolis power plants. Samples of fly ash were also received from the Ptolemais Basin (Kardia) for comparison purpose.

The extraction of humic substances from Megalopolis lignite using KOH solutions has been described previously as humates originating from low-rank coals are almost completely soluble in aqueous alkali [17]. A Varian Cary 3E UV-vis spectrophotometer was used to estimate the concentrations of humic substances at $\lambda_{\max} = 550$ nm. Prior to calculations a linear calibration curve was established by plotting absorbance against humic substances content.

In order to investigate the adsorption of humic substances on fly ash the following procedure was applied: 50 mL of humic substances solution were mixed with 1 g fly ash. The mixture was left under stirring for 1 hour at ambient temperature (291 K) and constant pH and then filtered to separate the humates. The concentration of humic substances in the solution was determined spectrophotometrically as described above and the retention of the adsorbate onto adsorbent (mg g^{-1}) was calculated by the following equation:

$$Q_e = \frac{(C_0 - C_e)}{m} V, \quad (1)$$

where Q_e is the equilibrium concentration of humic substances on the adsorbent (mg g^{-1}), C_0 their initial concentration in solution (mg L^{-1}), C_e the equilibrium concentration of humic substances in solution (mg L^{-1}), m the mass of adsorbent (g), and V the volume of the humic substances solution (L).

Adsorption experiments were also repeated at 308, 323, 338, and 353 K and at several pH values to study the effect of temperature and acidity, respectively. In all cases, a humic substances concentration range 1.90 to 39.1 g L^{-1} was applied. The effect of time on humate retention was also investigated in a 2- to 180-minute range.

Desorption experiments were carried out in humic-loaded fly ash (0.5 g) by washing with distilled water (10 mL). The aqueous extract was centrifuged from fly ash and the concentration of the humic substances released in water was calculated spectrophotometrically.

For the determination of microorganisms the method of progressive dilution in liquid media by direct plating was used. In the case of bacteria specimens, 1g of the material tested was mixed with 10 mL Ringer solution (2.25 g L^{-1} NaCl, 0.10 g L^{-1} KCl, 0.12 g L^{-1} $\text{CaCl}_2 \cdot 2\text{H}_2\text{O}$ and 0.05 g L^{-1} NaHCO_3). Nutrient agar was added as growing medium. The samples were incubated at 310 K for 48 hours prior to counting colonies. For the cultivation of fungi 1 g of the sample was mixed with 2 mL Ringer solution. Sabouraud was used as growing medium and X900 vials were also added to increase the selectivity. The samples were incubated at 303 K for 7 days prior to counting colonies and fungi identification. Two replicates per dilution were plated and counted. All materials and equipment used were sterile. Control cultures were also ran in the absence of the studied compounds.

The microbial population was counted in cfu g^{-1} of the compound tested.

A Perkin-Elmer 883 IR spectrophotometer was employed to record infrared spectra; pellets of the specimens were prepared after mixing with dry KBr. The chemical analyses of fly ash samples were obtained from EDXRF measurements on a MDX1000 OXFORD spectrophotometer. Solids were separated from solutions with the use of an MLW T 54 centrifuge (15 minutes at $3600 \text{ minutes}^{-1}$). Acidity measurements were carried out by a SANXIN PHS-3D pH meter.

3. Results and Discussion

3.1. Parameters of Adsorption. The time of sorbent-adsorbate interaction and the acidity of the solution, both useful in setting up the adsorption process, are of great importance in adsorption phenomena. The retention of humic substances on fly ash increased only during the first 30 minutes and then remained practically constant; that is, equilibrium was attained. The solution acidity affects both the surface charge of the adsorbent and the protonation/deprotonation equilibria of the adsorbate. Figure 1 indicates that neutral humic solutions mostly favor the adsorption of humic substances onto fly ash. An increase in pH facilitates deprotonation of both fly ash and humic substances while at low pH values both sorbent and adsorbate become positively charged. Carboxylic groups, the principal source of charge development in natural organic matter, are ionized in $\text{pH} = 4\text{-}5$ [21]. Neutrality of humic substances solution seems to compensate the repulsive forces developed in homonymous charges in both host and guest materials, thus, favoring adsorption.

The effect of pH clearly shows that Coulombic interactions are involved in adsorption. However, the low cation exchange capacity of the Megalopolis fly ash ($2.5 \text{ meq}/100 \text{ g}$) cannot account for the whole amount of the adsorbate and, thus, insinuates additional dispersive host-guest interactions of hydrophobic nature (van der Waals, $\pi\text{-}\pi$, $\text{CH}\text{-}\pi$) and hydrogen bonds induced by the hydrophobic domains present in the humic superstructures [18].

3.2. Adsorbent Effect. Four different ashes (two fly ashes and two bottom ashes) from the Megalopolis and Ptolemais (Kardia) Basins were tested for the adsorption of humic substances. The chemical composition and properties of these ashes are presented in Table 1. Table 2 points out significant differences in adsorption of humic substances on these ashes. Specifically, both Megalopolis ashes retain more humic substances compared with the corresponding Kardia ones, a fact initially ascribed to the differences in the silicate content (Table 1).

In order to explain this observation, IR spectra were received (Figure 2) to determine changes in structure additional to the changes in the chemical composition of the adsorbents. The main infrared bands are located at approximately 3450 cm^{-1} and 1640 cm^{-1} for O–H stretching and O–H bending, respectively [22]. The band at 1460 cm^{-1} represents the sodium carbonate resulting from carbonation [23].

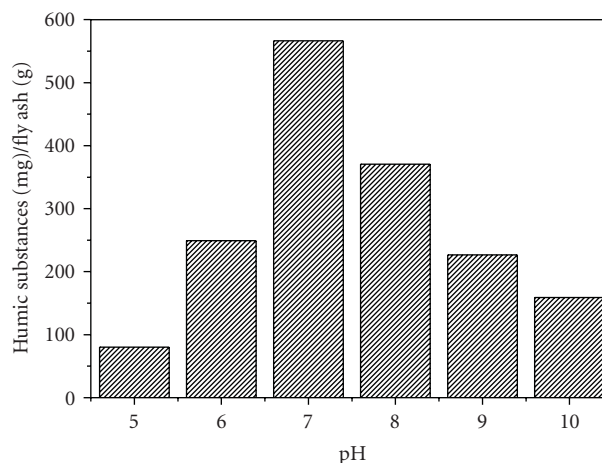


FIGURE 1: Retention of humic substances with pH.

However, major differences are observed in the $850\text{-}1200\text{-cm}^{-1}$ envelope providing information on the silicate backbone. Particularly, the intense band at about 1090 cm^{-1} (accompanied by a shoulder at about 1175 cm^{-1}) has been attributed to the asymmetric stretching vibrations of Si–O–Si bridges [22]. Such Si–O–Si bridges can be broken either by creation of nonbridging oxygen atoms in Si–O⁻ bonds (which are charge-compensated by metal ions) or by hydrolysis effects leading to the formation of Si–OH bonds in Q_n structures (Figure 3). The presence of nonbridging oxygen atoms leads to a weakening of the aluminosilicate network manifested as a pronounced shift towards lower frequencies in IR spectra. On this basis, the $850\text{-}1200\text{-cm}^{-1}$ envelope in both Megalopolis ashes is wider and more intense, particularly at lower wavenumbers, indicating a less “polymerized” silicate structure that readily adsorbs higher amounts of humic substances compared with the Kardia’s corresponding ones, most probably via a cation exchange mechanism.

This explanation is fully compatible with the significant increase in adsorption of Kardia’s bottom ash compared with the fly ash. The presence of intense absorption bands peaking at wavelengths lower than 1000 cm^{-1} , in the case of the bottom ash, demonstrates changes in the matrix, that is, the existence of many nonbridging oxygen atoms responsible for humic adsorption.

3.3. Equilibrium Adsorption. The values of equilibrium humic content, Q_e , on fly ash as a function of the equilibrium humic concentration in solution, C_e , at several temperatures (291, 308, 323, 338, and 353 K) are plotted in Figure 4. All isotherms appear sigmoidal, corresponding to a type II adsorption isotherm according to the Brunauer-Deming-Deming-Teller (BDDT) classification, this feature becoming more distinct with increasing temperature. Adsorption of humic substances onto fly ash ranges from 40 to $1300 \text{ mg humics/g fly ash}$ at 291 and 353 K, respectively. Adsorption capacity increases with temperature from 760 to $1300 \text{ mg humics/g fly ash}$ at 291 and 353 K, respectively (Figure 4).

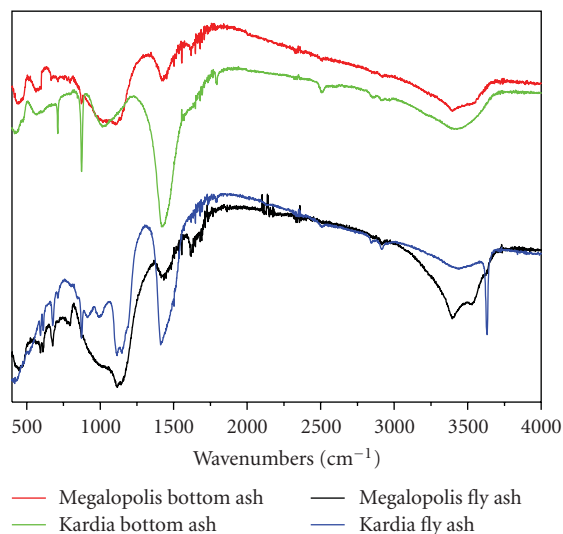


FIGURE 2: IR spectra of Megalopolis and Kardia ashes.

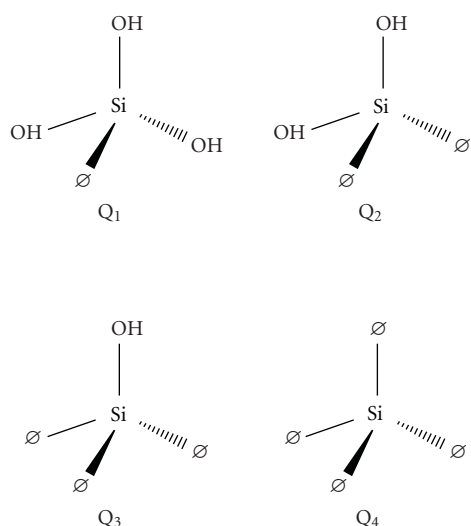


FIGURE 3: Schematic structures of silicate tetrahedral units, Q_n , with n denoting the number of oxygen atoms bridging two silicon centers (\emptyset = bridging oxygen atom).

Endothermic adsorption processes usually indicate processes activated in a reaction-kinetic sense representing the combined effects of temperature on both the rate of approach to equilibrium and the position of the equilibrium itself. This encounters the surpassing of the energy barriers by the adsorbate to diffuse through narrow constrictions of the fly ash surface to cavities beyond. In addition, adsorption is accompanied by other subprocesses, for example, conformational changes, multiple equilibria, and retention mechanisms, which, when lumped together, contribute to the endothermic character of the adsorption. Thus, the “knee” in the adsorption isotherm represents an adsorption restart, possibly due to multilayer formation and/or the beginning of another adsorption subprocess.

TABLE 1: Chemical analyses of fly ashes.

	Megalopolis		Kardia	
	Fly ash	Bottom Ash	Fly ash	Bottom Ash
SiO_2^a	39.6	41.7	23.0	17.8
Al_2O_3^a	15.9	14.1	12.6	8.4
Fe_2O_3^a	8.53	8.47	7.5	3.58
CaO^a	18.3	24.6	44.7	29.9
MgO^a	2.75	4.10	3.58	2.39
Na_2O^a	0.484	0.58	0.33	0.19
K_2O^a	1.72	1.79	2.20	0.40
SO_3^a	4.52	4.31	5.5	3.44
pH ^b	11.8	9.8	12.5	8.8

^a% w/w,

^b10% w/w in fly ash.

TABLE 2: Adsorption of humic substances on several bottom and fly ashes.

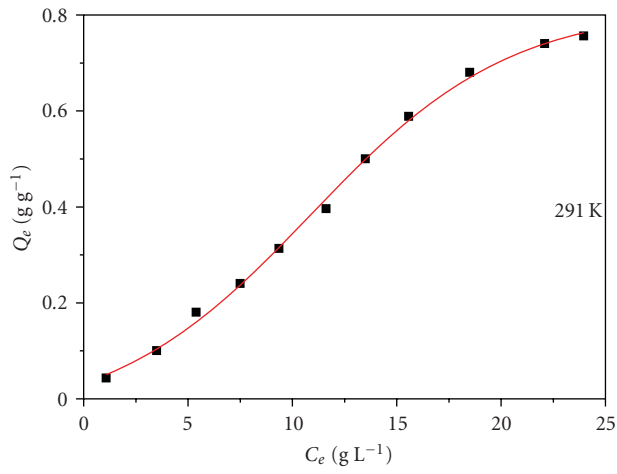
Adsorbent	Retention (g humic substances/g ash)
Fly ash	
Megalopolis	1.72
Kardia	0.62
Bottom ash	
Megalopolis	2.21
Kardia	1.31

3.4. Adsorption Isotherms. Five of the most valid adsorption models, that is, the Langmuir, Freundlich, BET, Harkins-Jura, and Dubinin-Radushkevich (DR) isotherm equations, were fit to the experimental data of humate adsorption onto fly ash particles. The aim was to reveal distinct physicochemical properties that characterize both the adsorbents and the sorption process. The Langmuir equation [24], although widely applied, cannot describe the adsorption adequately ($R^2 < 0.67$) in our case. This is not unexpected, since this theoretical model does not apply to Type II adsorption isotherms.

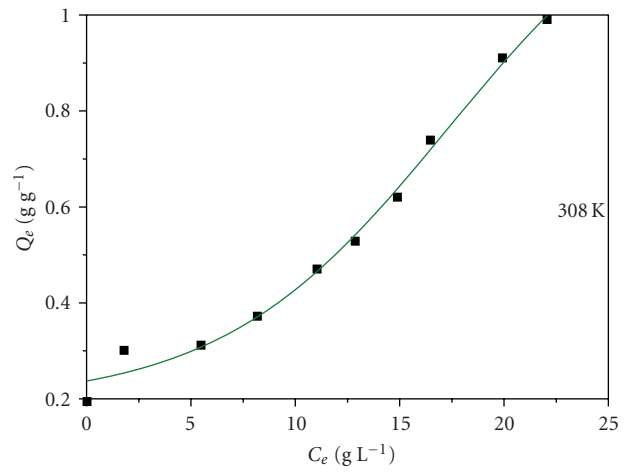
On the other hand, the Freundlich isotherm [25] provides a good mathematical model to describe the adsorption (Table 3) pinpointing heterogeneously distributed adsorption sites. Such an uneven arrangement of the heterogeneously adsorbed humates has been proved to promote the development of local multilayers and aggregates of the adsorbate [26].

The BET equation [27] describes adequately the adsorption behavior of humates onto fly ash particles, although this model tacitly assumes a homogeneous adsorption surface and gives a linear region only at the lower concentrations of adsorbate where a condensed film exists. On this basis, the applicability of the BET equation results from the existence of different homogeneous surface patches where adsorption occurs consecutively, so that the isotherm actually consists of an assortment of numerous steps each one corresponding to the adsorption occurring at these patches [26, 28].

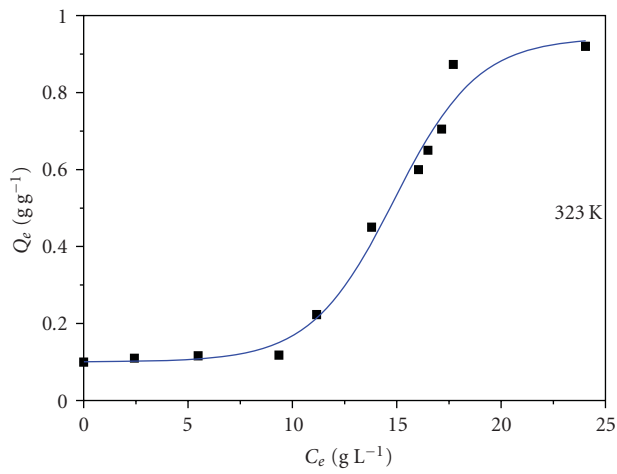
The Harkins-Jura model [29] is mostly based on the assumption of a nonuniform distribution of the adsorption



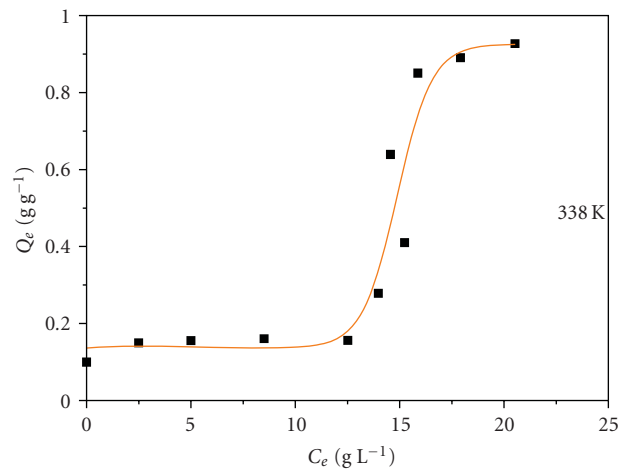
(a)



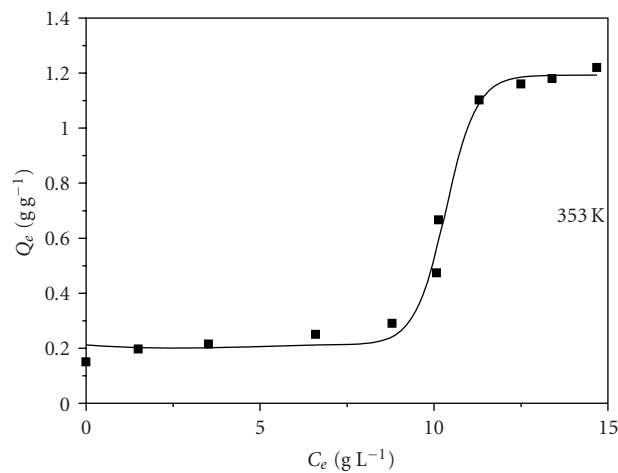
(b)



(c)



(d)



(e)

FIGURE 4: Adsorption of humic substances onto fly ash with temperature.

TABLE 3: Correlation coefficients of the linear adsorption equations.

Isotherm equation	Temperature (K)	R^2
Langmuir $C_e/Q_e = 1/KQ_m + (1/Q_m)C_e$	291	0.625
	308	0.608
	323	0.565
	338	0.445
	353	0.664
Freundlich $\log Q_e = \log K_F + (1/n) \log C_e$	291	0.989
	308	0.962
	323	0.871
	338	0.722
	353	0.759
BET $C_e/Q_e(1-C_e) = 1/X_m K_B + ((K_B-1)/X_m K_B) C_e$	291	0.996
	308	0.929
	323	0.844
	338	0.880
	353	0.910
Harkins-Jura $1/Q_e^2 = B/A - (1/A) \log C_e$	291	0.840
	308	0.969
	323	0.792
	338	0.520
	353	0.834
Dubinin-Radushkevich $\ln Q_e = \ln X_m - \beta[RT \ln(1 + (1/C_e))]^2$	291	0.957
	308	0.856
	323	0.985
	338	0.806
	353	0.893

sites and is not applicable unless a condensed film is shaped. Compared with the BET theory the existence of a linear region is much more extensive involving higher adsorbate concentrations. However, the assembling of multilayers in the case of humate adsorption seems to meet better the BET theory requirements as the correlation coefficients of the Harkins-Jura equation summarized in Table 3 are lower.

The DR model [30] presupposes a Gaussian distribution of the adsorption space with respect to the adsorption potential. The adsorption is considered to be the result of the adsorbate molecule entering into a pore; the process is described according to the Polanyi comprehension of the energetics inside the empty space of solids and applies rather to structurally homogeneous systems. Although it is widely applied in Type I isotherms, this model fits quite satisfactorily the experimental data of humate adsorption onto fly ash (Table 3). This may be due to the facts that the DR equation does not reduce to Henry's law at low adsorbate concentrations, the linear region is also extensive, involving higher adsorbate concentrations, and that it applies at low adsorbent loadings. Van der Waals forces to account for host-guest interactions are also encountered.

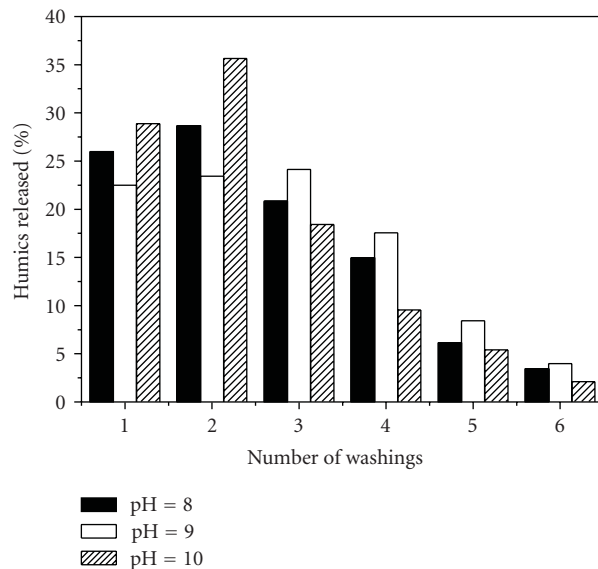


FIGURE 5: Desorption of humic substances by washing.

From the DR plots, the mean energy of the adsorption, E , can be calculated using the following relationship:

$$E = \frac{1}{\sqrt{2\beta}}. \quad (2)$$

The values of E do not exceed 0.2 kJ g^{-1} of adsorbate, accounting for strong forces of attraction, more intense than the Van der Waals forces.

3.5. Desorption Studies. Desorption experiments were carried out to evaluate the ability of fly ash to render back the humic substances adsorbed, useful in potential applications of superficially modified fly ash as a slow-release fertilizer. Humic substances could not be released neither in acid nor in neutral environments; thus, experiments were processed in the alkaline area ($\text{pH} = 8\text{--}10$). Higher pH values were not tested because of their lack of importance for soil applications. The results presented in Figure 5 demonstrate that most of the humates (80%) were released during the first three washings; yet humics could be still identified after the sixth washing of fly ash. These observations clearly indicate that humic substances associate strongly with fly ash allowing for their slow release during repeated washing under alkaline conditions.

3.6. Microbial Populations. Microbial tests were carried out to determine the bacteria and fungi populations as the native microbial population in soil plays a vital role in the recycling of C, N, and P of the biosphere and, therefore, is critical for fertility and plant growth. Megalopolis fly ash proved sterile but humic-loaded samples produced 5×10^4 bacteria. It is important to note that a fertile agricultural soil contains about 10^7 and 5×10^5 bacteria and fungi, respectively [31]. *Penicillium* spp, *Aureobasidium* spp, *Alternaria* spp, *Aspergillus* spp, *Mucor* spp, *Rhizopus* spp, *Rhizomucor* spp,

TABLE 4: Trace elements concentrations in Megalopolis fly ash.

Substance	Concentration (ppm)
TiO ₂	0.823 ^a
P ₂ O ₅	0.233 ^a
SrO	0.107 ^a
BaO	680
MnO	620
Cr ₂ O ₃	410
NiO	390
V ₂ O ₅	340
ZnO	160
CuO	130
ZrO ₂	110
Rb ₂ O	88
MoO ₃	73
PbO	58
Cl	43
Br	39
Y ₂ O ₃	7

^a% w/w.

and *Cladosporium* spp were identified, typical in soil and tissue degradation products. The population of fungi leveled the one found in a fertile agricultural soil. These observations annotate that fly ash partly favors the development of microbial life. This may be due to the fact that, as chemical analysis of trace elements shows, the Megalopolis fly ash (Table 4) contains metals that, in high concentrations, may be proved toxic to microbes restraining their growth. The presence of these trace elements causes no environmental risk as the increased pH of the Megalopolis fly ash (about 12) impairs the leaching of the metals [32]. However, it may set limitations regarding the mixing ratio of humic-loaded fly ash with soil in agricultural applications.

4. Conclusions

Humic-loaded fly ash was prepared at various humic to fly ash ratios. The Greek peaty lignite of the Megalopolis Basin was used as raw material for obtaining both fly ash and humates. Retention was studied at 291, 308, 323, 338, and 353 K and at several pH values. The adsorption capacity was found to increase at neutral pH and, also, with raise of temperature, that is, from 760 to 1300 mg humics/g fly ash at 291 K and 353 K, respectively. Fly ash demonstrated a high affinity towards humic substances and adsorption proceeded stepwise via strong Coulombic and hydrophobic forces of attraction between guest and host materials. Langmuir, Freundlich, BET, Harkins-Jura, and Dubinin-Radushkevich isotherm models were employed to evaluate the ongoing adsorption and shed light to the physicochemical properties of the sorbent-adsorbate system. Both the slow release of adsorbed humic substances during washing and the

existence of microbial populations are considered advantageous for employing humic-loaded fly ash in biofunctional agricultural applications, that is, in biological cultivations substituting traditional soil-conditioning materials.

The importance of this study from an economic standpoint is emphasized by the advantageous preparation of humic-modified fly ash from power plant wastes. Its production could also prove profitable, thanks to the extended coal reserves worldwide, strongly supporting the viability of the research on this field.

Acknowledgment

The authors are pleased to acknowledge the assistance of Associate Professor P. Markaki and Mrs. M. Tavoulari in microbial cultivation experiments.

References

- [1] S. V. Mattigod, D. Rai, L. E. Eary, and C. C. Ainsworth, "Geochemical factors controlling the mobilization of inorganic constituents from fossil fuel combustion residues. I. Review of the major elements," *Journal of Environmental Quality*, vol. 19, no. 2, pp. 188–201, 1990.
- [2] S. Jala and D. Goyal, "Fly ash as a soil ameliorant for improving crop production—a review," *Bioresource Technology*, vol. 97, no. 9, pp. 1136–1146, 2006.
- [3] S. K. Antiohos and S. Tsimas, "A novel way to upgrade the coarse part of a high calcium fly ash for reuse into cement systems," *Waste Management*, vol. 27, no. 5, pp. 675–683, 2007.
- [4] S. K. Antiohos, V. G. Papadakis, E. Chaniotakis, and S. Tsimas, "Improving the performance of ternary blended cements by mixing different types of fly ashes," *Cement and Concrete Research*, vol. 37, no. 6, pp. 877–885, 2007.
- [5] D. C. Adriano, A. L. Page, A. A. Elseewi, A. C. Chang, and I. Straughan, "Utilization and disposal of fly ash and other coal residues in terrestrial ecosystems: a review," *Journal of Environmental Quality*, vol. 9, no. 3, pp. 333–344, 1980.
- [6] C. L. Carlson and D. C. Adriano, "Environmental impacts of coal combustion residues," *Journal of Environmental Quality*, vol. 22, no. 2, pp. 227–247, 1993.
- [7] K. Chassapis, M. Roulia, and D. Tsigirigi, "Chemistry of metal-humic complexes contained in Megalopolis lignite and potential application in modern organomineral fertilization," *International Journal of Coal Geology*, vol. 78, no. 4, pp. 288–295, 2009.
- [8] K. Chassapis and M. Roulia, "Evaluation of low-rank coals as raw material for Fe and Ca organomineral fertilizer using a new EDXRF method," *International Journal of Coal Geology*, vol. 75, no. 3, pp. 185–188, 2008.
- [9] A. L. Page, A. A. Elseewi, and I. R. Straughan, "Physical and chemical properties of fly ash from coal-fired power plants with reference to environmental impacts," *Residue Reviews*, vol. 71, pp. 83–120, 1979.
- [10] R. Sikka and B. D. Kansal, "Effect of fly-ash application on yield and nutrient composition of rice, wheat and on pH and available nutrient status of soils," *Bioresource Technology*, vol. 51, no. 2–3, pp. 199–203, 1995.
- [11] N. Kalra, H. C. Joshi, A. Chaudhary, R. Choudhary, and S. K. Sharma, "Impact of flyash incorporation in soil on germination of crops," *Bioresource Technology*, vol. 61, no. 1, pp. 39–41, 1997.

- [12] D. El-Mogazi, D. J. Lisk, and L. H. Weinstein, "A review of physical, chemical, and biological properties of fly ash and effects on agricultural ecosystems," *Science of the Total Environment*, vol. 74, no. 1, pp. 1–37, 1988.
- [13] A. A. Elsewi, S. R. Grimm, A. L. Page, and I. R. Straughan, "Boron enrichment of plants and soils treated with coal ash," *Journal of Plant Nutrition*, vol. 3, pp. 409–427, 1981.
- [14] R. L. Aitken, D. J. Campbell, and L. C. Bell, "Properties of Australian fly ash relevant to their agronomic utilization," *Australian Journal of Soil Research*, vol. 22, pp. 443–453, 1984.
- [15] D. C. Elfving, C. A. Bache, W. H. Gutenmann, and D. J. Lisk, "Analyzing crops grown on waste-amended soils," *BioCycle*, vol. 22, no. 6, pp. 44–47, 1981.
- [16] L. Giardini, "Aspetti agronomici della gestione dei reflui zootecnici," *Rivista di Ingegneria Agraria*, vol. 12, pp. 679–689, 1991.
- [17] K. Chassapis, M. Roulia, and G. Nika, "Fe(III)-humate complexes from megalopolis peaty lignite: a novel eco-friendly fertilizer," *Fuel*, vol. 89, no. 7, pp. 1480–1484, 2010.
- [18] A. Piccolo, "The supramolecular structure of humic substances: a novel understanding of humus chemistry and implications in soil science," *Advances in Agronomy*, vol. 75, pp. 57–134, 2002.
- [19] S. Wang, T. Terdkiatburana, and M. O. Tadó, "Single and co-adsorption of heavy metals and humic acid on fly ash," *Separation and Purification Technology*, vol. 58, no. 3, pp. 353–358, 2008.
- [20] S. Wang and Z. H. Zhu, "Humic acid adsorption on fly ash and its derived unburned carbon," *Journal of Colloid and Interface Science*, vol. 315, no. 1, pp. 41–46, 2007.
- [21] A. G. Kalinichev and R. J. Kirkpatrick, "Molecular dynamics simulation of cationic complexation with natural organic matter," *European Journal of Soil Science*, vol. 58, no. 4, pp. 909–917, 2007.
- [22] M. Roulia, K. Chassapis, J. A. Kapoutsis, E. I. Kamitsos, and T. Savvidis, "Influence of thermal treatment on the water release and the glassy structure of perlite," *Journal of Materials Science*, vol. 41, no. 18, pp. 5870–5881, 2006.
- [23] V. F. F. Barbosa, K. J. D. MacKenzie, and C. Thaumaturgo, "Synthesis and characterisation of materials based on inorganic polymers of alumina and silica: sodium polysialate polymers," *International Journal of Inorganic Materials*, vol. 2, no. 4, pp. 309–317, 2000.
- [24] I. Langmuir, "The adsorption of gases on plane surfaces of glass, mica and platinum," *Journal of the American Chemical Society*, vol. 40, no. 9, pp. 1361–1403, 1918.
- [25] H. Freundlich, "Über die Adsorption in Lösungen," *Zeitschrift für physikalische Chemie*, vol. 57, pp. 385–470, 1906.
- [26] M. Roulia and A. A. Vassiliadis, "Sorption characterization of a cationic dye retained by clays and perlite," *Microporous and Mesoporous Materials*, vol. 116, no. 1–3, pp. 732–740, 2008.
- [27] S. Brunauer, P. H. Emmett, and E. Teller, "Adsorption of gases in multimolecular layers," *Journal of the American Chemical Society*, vol. 60, no. 2, pp. 309–319, 1938.
- [28] S. J. Gregg and K. S. W. Sing, *Adsorption, Surface Area and Porosity*, Academic Press, London, UK, 2nd edition, 1982.
- [29] W. D. Harkins and G. Jura, "Surfaces of solids. XIII. A vapor adsorption method for the determination of the area of a solid without the assumption of a molecular area, and the areas occupied by nitrogen and other molecules on the surface of a solid," *Journal of the American Chemical Society*, vol. 66, no. 8, pp. 1366–1373, 1944.
- [30] L. V. Radushkevich and M. M. Dubinin, "The equation of the characteristic curve of activated charcoal," *Doklady Akademii Nauk SSSR*, vol. 55, pp. 327–329, 1947.
- [31] T. Hattori, *Microbial Life in the Soil. An Introduction*, Marcel Dekker, New York, NY, USA, 1973.
- [32] W. Wang, Y. Qin, D. Song, and K. Wang, "Column leaching of coal and its combustion residues, Shizuishan, China," *International Journal of Coal Geology*, vol. 75, no. 2, pp. 81–87, 2008.

Research Article

Kinetics and Mechanism of the Reaction between Chromium(III) and 2,3-Dihydroxybenzoic Acid in Weak Acidic Aqueous Solutions

Athinoula L. Petrou, Vladimiro Thoma, and Konstantinos Tampouris

Laboratory of Inorganic Chemistry, University of Athens, Panepistimioupolis, 15771 Athens, Greece

Correspondence should be addressed to Athinoula L. Petrou, athpetrou@chem.uoa.gr

Received 17 November 2009; Accepted 10 March 2010

Academic Editor: Spyros P. Perlepes

Copyright © 2010 Athinoula L. Petrou et al. This is an open access article distributed under the Creative Commons Attribution License, which permits unrestricted use, distribution, and reproduction in any medium, provided the original work is properly cited.

The reaction between chromium(III) and 2,3-dihydroxybenzoic acid (2,3-DHBA) takes place in at least three stages, involving various intermediates. The ligand (2,3-DHBA)-to-chromium(III) ratio in the final product of the reaction is 1 : 1. The first stage is suggested to be the reaction of $[\text{Cr}(\text{H}_2\text{O})_5(\text{OH})]^{2+}$ with the ligand in weak acidic aqueous solutions that follows an I_d mechanism. The second and third stages do not depend on the concentrations of chromium(III), and their activation parameters are $\Delta H_{2(\text{obs})}^\ddagger = 61.2 \pm 3.1 \text{ kJmol}^{-1}$, $\Delta S_{2(\text{obs})}^\ddagger = -91.1 \pm 11.0 \text{ JK}^{-1}\text{mol}^{-1}$, $\Delta H_{3(\text{obs})}^\ddagger = 124.5 \pm 8.7 \text{ kJmol}^{-1}$, and $\Delta S_{3(\text{obs})}^\ddagger = 95.1 \pm 29.0 \text{ JK}^{-1}\text{mol}^{-1}$. These two stages are proposed to proceed via associative mechanisms. The positive value of $\Delta S_{3(\text{obs})}^\ddagger$ can be explained by the opening of a four-membered ring (positive entropy change) and the breaking of a hydrogen bond (positive entropy change) at the associative step of the replacement of the carboxyl group by the hydroxyl group at the chromium(III) center (negative entropy change in associative mechanisms). The reactions are accompanied by proton release, as shown by the pH decrease.

1. Introduction

Pathogens have developed many strategies to cope with iron limitation caused by plants and mammals in order to restrict their unwanted growth in them. One of the best-known methods (strategies) is through the synthesis of small molecules that can act as iron chelators known as siderophores [1]. 2,3-Dihydroxybenzoic acid (2,3-DHBA) is a monocatechol siderophore. This ligand is a triprotic acid H_3L , and the values of K_1 and K_2 refer to the protonation constants of the two hydroxylate groups and K_3 refers to that of the carboxyl group. At 25°C and Ionic Strength 0.2 M the average values of the accepted constants for 2,3-DHPA are $\log(K_2/\text{M}^{-1}) = 9.86 \pm 0.04$ and $\log(K_3/\text{M}^{-1}) = 3.00 \pm 0.27$. $\log(K_1/\text{M}^{-1})$ ranges between 10 and >14 at 25°C and Ionic Strength 0.02–1.0 M [2]. In the molecule, intramolecular hydrogen bonds are formed between the hydroxyl groups and the carboxyl group [3]. Complexes of 2,3-DHBA with various metal ions, for example, Al^{3+} , VO^{2+} , Mn^{2+} , Fe^{3+} , Cu^{2+} , Cd^{2+} , and so forth, have been prepared and their equilibrium constants

have been determined [2]. Catecholic type of coordination was also suggested for the Fe(III)-2,3-DHBA complex [4, 5].

Chromium(III) is an essential for life trace element and its role has been extensively studied. At low concentrations it is beneficial to many plant species, whereas, in the same plants, at higher concentrations it is toxic. In the roots, concentrations of 175 ppm have been shown to be harmless. At concentrations between 375 and 400 ppm toxicities were evident. The above suggests the existence of a tolerating mechanism in the roots [6].

The aim of this work is to study and determine the kinetics and suggest a mechanism of the substitution reactions between chromium(III) and 2,3-DHBA. Knowledge of the mechanism will further contribute in the understanding of the role of organic ligands in the uptake of metals by plants because metal ions are transferred by organic ligands from the roots to certain parts of the plants. Such ligands are humic substances and products of their decomposition, that is, organic acids. One of such organic ligands is 2,3-DHBA (Figure 1).

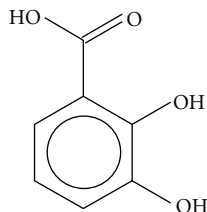
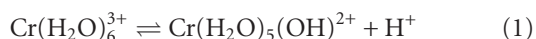


FIGURE 1: 2,3-Dihydroxybenzoic acid (2,3-DHBA).

2. Experimental Section

2.1. Reagents and Materials. The reactants used were of analytical grade. 2,3-DHBA (Ferak Berlin) was used as received and was dissolved in dilute (0.1 M) solution of KOH (Merck) for pH adjustment for the ligand to be dissolved, in concentrations ranging from 3.9×10^{-3} to 7.8×10^{-3} M. Stock solutions of Cr(III) were prepared from $\text{Cr}(\text{NO}_3)_3 \cdot 9\text{H}_2\text{O}$ (Fluka). The chromium(III) concentrations ranged between $(5-14) \times 10^{-2}$ M. The ionic strength was adjusted using KNO_3 . The solutions of 2,3-DHBA were used soon after their preparation in order to avoid transformation and decomposition reactions. The addition of the Cr(III) solution kept the pH below 4 due to its acidic hydrolysis:



The UV-Vis spectrum of the chromium(III) solution and of the ligand along with spectra of its oxidation products at various times after dissolution are given in Figure 2.

2.2. Kinetic Experiments. All kinetic experiments were conducted at pH values below 4 in the presence of air. The kinetics was followed spectrophotometrically by recording the absorbances at various reaction times after mixing (Figure 3). The absorbances were recorded on a Hitachi Model 100-60 spectrophotometer. They refer to the substitution of water molecules in the $[\text{Cr}(\text{H}_2\text{O})_6]^{3+}$ coordination sphere by 2,3-DHBA and were followed at 573 nm where the biggest absorbance difference between the final product and the initial mixture of $[\text{Cr}(\text{H}_2\text{O})_6]^{3+}/2,3\text{-DHBA}$ exists.

First-order rate constants were estimated with a nonlinear least-squares fit.

Pseudo-first-order conditions, that is, excess of Cr(III) which results in acidic solution due to its hydrolysis, were applied for all the kinetic experiments. Experiments in excess of ligand (2,3-DHBA) were not possible to be performed due to low solubility and oxidation problems of the ligand in alkaline solutions in air. The alkaline solution results in the reaction mixture under the experimental conditions. The KOH solution is added in order to enhance solubility. The oxidation of the ligand is shown in Figure 2, lower spectra.

The temperatures of the kinetic experiments ranged between 16°C and 37°C to avoid acceleration of the ligand's decomposition/autoxidation.

The plots of $\ln(A_t - A_\infty)$ where A_t and A_∞ are absorbances at time t and after the completion of the corresponding reaction step against time were found to be

non-linear (Figure 4); they have curvature at short reaction times and have a constant slope at larger reaction times.

Contribution of the uncomplexed Cr(III) species in the absorbance values, mainly due to the excess of Cr(III), does not interfere in the graphs (Figures 4 and 5) because it is included in both A_t and A_∞ and is thus eliminated due to the subtraction of A_∞ from A_t . The recorded values of A_∞ were very close to the true values which were obtained by plotting $A = f(t)$; in this way confirmation of the completion of the certain step of the reaction was possible.

The rate constants were calculated according to methods found in the literature [7, 8], assuming two consecutive first-order (or pseudo-first-order) steps:



The above reaction sequence admits of two mathematical solutions, and the sets of the rate constants are such that the fast and slow kinetic steps are interchanged [7, 9, 10].

The $k_{3(\text{obs})}$ values were obtained from the slope ($-k_3$) of the linear second part (long-time part) of the $\ln(A_t - A_\infty) = f(t)$ plot.

The $k_{2(\text{obs})}$ values for $A \rightarrow B$ step were evaluated by the method of Weyh and Hamm [8] using the rate equation

$$A_t - A_\infty = a_2 \cdot e^{-k_{2(\text{obs})}t} + a_3 \cdot e^{-k_{3(\text{obs})}t}. \quad (3)$$

Values of a_2 and a_3 are dependent upon the rate constants and the extinction coefficients. At various times t , $\Delta = A_t - A_\infty - a_3 \cdot e^{-k_{3(\text{obs})}t} = a_2 \cdot e^{-k_{2(\text{obs})}t}$ (Figure 4). Hence, $\ln \Delta = \text{constant} - k_{2(\text{obs})}t$ and the $k_{2(\text{obs})}$ values were found from the slope of the plots of $\ln \Delta$ versus t for small values of reaction time. A typical plot appears in Figure 5.

At times longer than three to four half-lives of the $B \rightarrow C$ step, a reaction involving oxidation of the ligand takes place, resulting in anomalous further absorbance changes. This reaction was not studied.

The above assumptions for the existence of two consecutive steps for the reaction under study and the calculation of $k_{2(\text{obs})}$ and $k_{3(\text{obs})}$ values fit with all the experimental data, at all temperatures. Table 1 gives the $k_{2(\text{obs})}$ and $k_{3(\text{obs})}$ values for this reaction of 2,3-DHBA with Cr(III) at various temperatures (289 K, 293 K, 297 K, 304 K, and 310 K).

The activation parameters $\Delta H_{2(\text{obs})}^\ddagger$, $\Delta S_{2(\text{obs})}^\ddagger$, and $\Delta H_{3(\text{obs})}^\ddagger$, $\Delta S_{3(\text{obs})}^\ddagger$ corresponding to $k_{2(\text{obs})}$ and $k_{3(\text{obs})}$, respectively, were calculated from the linear Eyring plots (Figures 6(a) and 6(b)) and are presented in Table 2.

2.3. pH Measurements. Measurements of the pH values of various reaction mixtures versus time at constant temperatures were recorded using a SANXIN PHS-3D pH model pH meter. These values were plotted against time giving $\text{pH} = f(t)$, that is, $-\log[H^+] = f(t)$. A typical graph is shown in Figure 7(a). A $\text{pH} = f(t)$ graph of a blank sample, containing only Cr(III) solution is presented in Figure 7(b), for comparison.

2.4. Isolation in the Solid Form. The isolation of the final product of the reaction (complex C) in the solid form

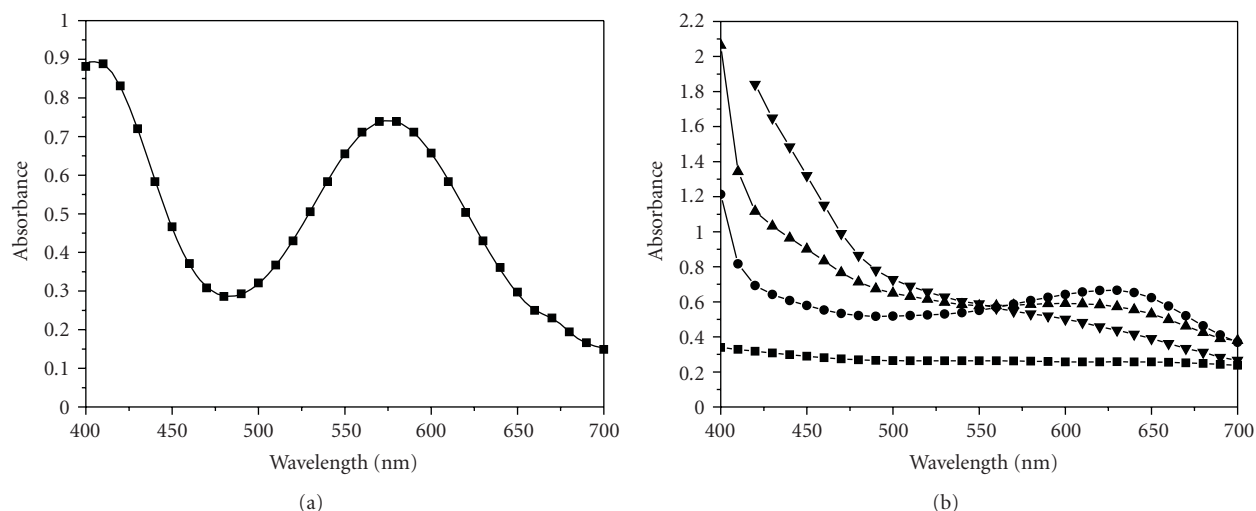


FIGURE 2: UV-Vis spectra of Cr(III) (a) and 2,3-DHBA (b). Conditions: (a) Chromium(III) Spectrum: $[\text{Cr(III)}] = 0.050 \text{ M}$, $T = 298 \text{ K}$. Spectrophotometric cell path $d = 1 \text{ cm}$. (b) 2,3-DHBA Spectra: $[2,3\text{-DHBA}] = 0.040 \text{ M}$, $T = 298 \text{ K}$. \blacksquare — 2,3-DHBA reduced, \bullet — 2,3-DHBA oxidized (minutes), \blacktriangle — 2,3-DHBA oxidized (hours), \blacktriangledown — 2,3-DHBA oxidized (a few days). Spectrophotometric cell path $d = 1 \text{ cm}$.

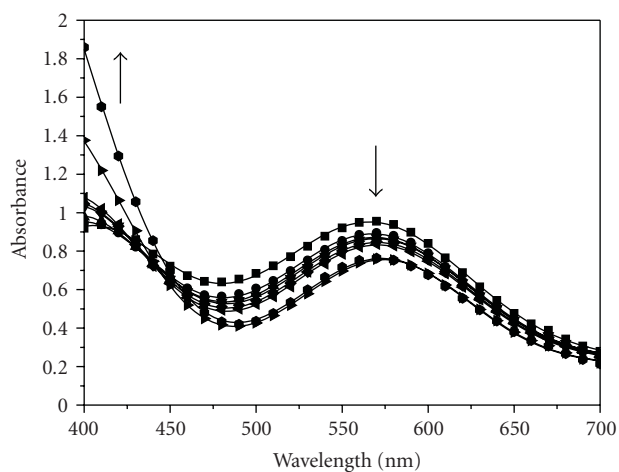


FIGURE 3: UV-Vis spectra of Cr(III)/2,3-DHBA mixture at various times after mixing. Conditions: $[\text{Cr(III)}]_0 = 0.036 \text{ M}$, $[2,3\text{-DHBA}]_0 = 0.011 \text{ M}$, and $T = 296 \text{ K}$. Spectrophotometric cell path $d = 1 \text{ cm}$. \blacksquare — 0:00 hours, \bullet — 1:00 hour, \blacktriangle — 2:00 hours, \blacktriangledown — 3:00 hours, \blacklozenge — 4:00 hours, \blacktriangleleft — 5:00 hours, \blacktriangleright — 29:00 hours, \bullet — a few days.

from Cr(III)/2,3-DHBA mixtures was achieved by addition of quantities of KOH in reaction mixtures of various stoichiometries. The elemental analyses show that only one ligand molecule enters the coordination sphere of the metal and they were conducted for C, H, and N and gave C = 10.62%, H = 3.66%, and N = 1.38%.

3. Results and Discussion

The form of the metal ion that reacts with the ligand 2,3-DHBA is $[\text{Cr}(\text{H}_2\text{O})_5\text{OH}]^{2+}$ since it is well known that the hydroxy complex $[\text{Cr}(\text{H}_2\text{O})_5(\text{OH})]^{2+}$ is highly more reactive

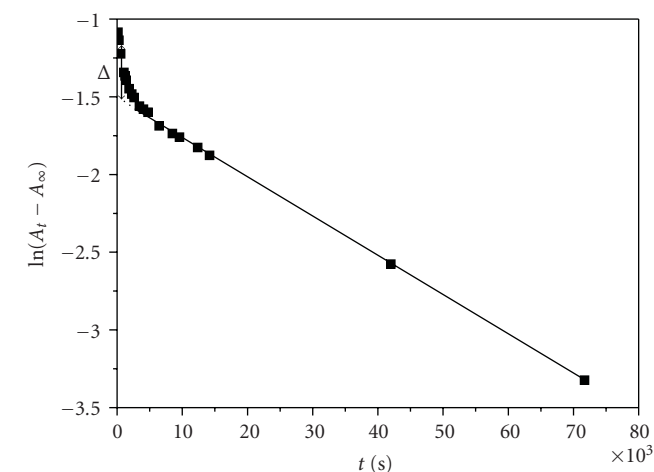
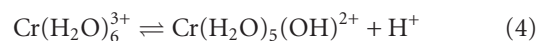


FIGURE 4: A typical non-linear plot of $\ln(A_t - A_\infty)$ versus time. The value of Δ that corresponds at time $t = 1 \times 10^3 \text{ s}$ is shown. Conditions: $[2,3\text{-DHBA}]_0 = 0.039 \text{ M}$, $[\text{Cr(III)}]_0 = 0.05$, $d = 1 \text{ cm}$ cell, and $T = 289 \text{ K}$.

than $[\text{Cr}(\text{H}_2\text{O})_6]^{3+}$. The K_a for the reaction



is about 10^{-4} [11, 12]. At pH lower than 4 the chromium(III) complex exists mainly in the hexa-aqua monomeric form. Its spectrum shows maxima at 575 nm and 410 nm (at the visible region). An amount of $[\text{Cr}(\text{H}_2\text{O})_5(\text{OH})]^{2+}$ is though always present under the above conditions. In the experiments reported here that are conducted over the pH range 3-4 the reaction should be considered as taking place first with $[\text{Cr}(\text{H}_2\text{O})_5(\text{OH})]^{2+}$ rather than with $[\text{Cr}(\text{H}_2\text{O})_6]^{3+}$, since a fast first step is taking place and it is very well known that

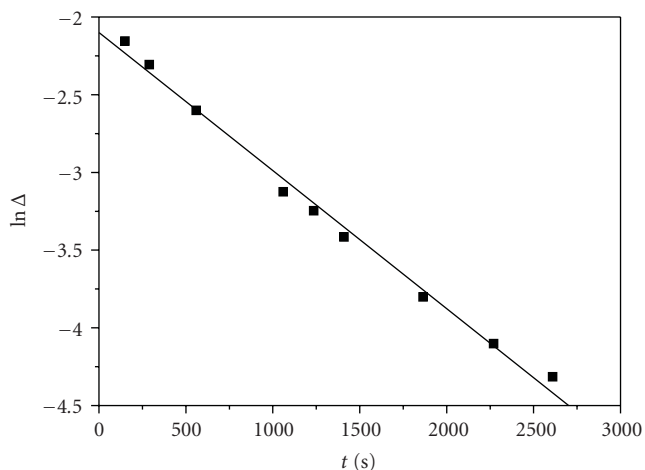


FIGURE 5: A typical plot of $\ln \Delta$ versus time. Conditions: $[2, 3\text{-DHBA}]_0 = 0.039 \text{ M}$, $[\text{Cr(III)}]_0 = 0.05$, $d = 1 \text{ cm}$ cell, and $T = 289 \text{ K}$.

TABLE 1: Values of $k_{2(\text{obs})}$ and $k_{3(\text{obs})}$ at various temperatures.

$k_{2(\text{obs})} \times 10^3 \text{ (s}^{-1}\text{)}$	$k_{3(\text{obs})} \times 10^5 \text{ (s}^{-1}\text{)}$	$T \text{ (K)}$
0.94	2.29	289
1.29	3.14	293
1.68	7.46	297
3.58	23.02	304
6.05	76.47	310

$\text{Cr}(\text{H}_2\text{O})_6^{3+}$ is very substitution inert. In the ligand molecule there are two intramolecular hydrogen bonds, one between adjacent hydroxyl groups and the other between the hydroxyl group and the carbonyl oxygen atom [13] (Scheme 1).

The violet $[\text{Cr}(\text{H}_2\text{O})_6]^{3+}$ (Figure 2(a)) and the light brown solution of the ligand (Figure 2(b)) on mixing give a violet-colored solution due to the excess of $[\text{Cr}(\text{H}_2\text{O})_6]^{3+}$ since the final UV-Vis spectrum resembles that of $[\text{Cr}(\text{H}_2\text{O})_6]^{3+}$.

The formation and subsequent transformation (substitution) kinetics suggest that a first complex A is formed (Scheme 1). In the kinetic experiments we assume that we start with complex A. This implies that the subsequent two slow steps, k_2 and k_3 (which were studied), did not contribute to the formation of complex A (first step) at the region of temperatures studied (16–37°C).

The $\ln(A_t - A_\infty)$ versus time plots are indicative of a complex reaction, actually a consecutive two first-order steps series of reaction (according to the analysis described in the experimental part). The two slow consecutive steps were found to be nondependent on chromium(III) concentration (Figures 8(a) and 8(b)), implying that a first fast complexation step took already place. Thus, at least three steps k_1 , k_2 , and k_3 are taking place (Scheme 1).

The first step (k_1) that is taking place with the $[\text{Cr}(\text{H}_2\text{O})_5\text{OH}]^{2+}$ reacting species proves the suggested reaction through the hydroxy form of chromium(III) and not through the hexa-aqua form, $[\text{Cr}(\text{H}_2\text{O})_6]^{3+}$, since the

substitution rate constants of the latter species would be very small.

The carboxylic and hydroxyl groups of the ligand (2,3-DHBA) are blocked (protonated, or hydrogen-bonded) and so the attacks by chromium(III) can take place only by removing protons, a fact that is measured by the pH decrease of the solution (Figure 7(a)).

A possible mechanism consistent with all experimental data is shown in Scheme 1. The attack of $[\text{Cr}(\text{H}_2\text{O})_5(\text{OH})]^{2+}$ at the hydrogen-bonded carboxylic group of 2,3-DHBA leads to complex A; complexation results in destruction of the hydrogen bonding; the consequence of the $[\text{Cr}(\text{H}_2\text{O})_5(\text{OH})]^{2+}$ usage in complexation is shift of the equilibrium of (4) to the right.

In conjugate base mechanisms the conjugate base, being present as a small fraction of the total, reacts and then takes a proton as it would naturally do. So, rapid protonation equilibrium follows the first formed species (A') favoring the formation of the aqua species (complex A).

The reaction of $[\text{Cr}(\text{H}_2\text{O})_5(\text{OH})]^{2+}$ with the hydrogen-bonded ligand results in substitution of a water molecule in the Cr(III) coordination sphere, by the carboxylic group, with the water molecule being the one that is located trans to the OH group of the species $[\text{Cr}(\text{H}_2\text{O})_5(\text{OH})]^{2+}$ and is labile. For step 1 (k_1) an I_d mechanism is suggested since the conjugate base $[\text{Cr}(\text{H}_2\text{O})_5(\text{OH})]^{2+}$ reacts according to such a mechanism [14]. This is because of the strong labilizing effect, which is induced by the coordinated OH^- , presumably, on the trans H_2O molecule. This leads to a 10^2 – 10^3 -fold enhanced reaction rate for the hydroxy-aqua over the hexaaqua ion [14].

Complex A reacts in two consecutive steps (k_2, k_3) to give B and C. The activation parameters deduced from the temperature-dependence experiments are used for proposing structures of the activated complexes (Scheme 2) and for proposing the mechanisms that are taking place (Scheme 1).

The spectra of Figure 3 correspond to the reaction mixture at various times after mixing at 296 K, and the mixture contains the species A, B, and C (Scheme 1).

The $k_{2(\text{obs})}$ and $k_{3(\text{obs})}$ dependence on chromium(III) concentration (Figures 8(a) and 8(b)) was studied at the temperature range 16–37°C in order (a) to find if a second or third chromium(III) ion is reacting with the already formed complex A and (b) to be able to calculate the activation parameters ΔH^\ddagger and ΔS^\ddagger , for the two steps. The studies show that (a) the two steps are independent on Cr(III) concentration meaning that the transformations taking place in the two steps are taking place within the already formed first complex A, that is, chelation to form complex B and then breaking of one Cr–O bond and formation of another Cr–O bond in order to form a new chelate, that bears less tension, that is, it is more stable. The four-membered ring is transformed at step 3 to a six-membered ring. (b) The calculations revealed that, going from complex A to complex B, $\Delta S^\ddagger < 0$, that is, the transition state is more organized than the reactants, i.e. complex A^\ddagger is having chelate rings, that is, less freedom than complex A. From complex B to complex C, $\Delta S^\ddagger > 0$, that is, there is increase in freedom and so the complex B^\ddagger is less organized than complex B having a

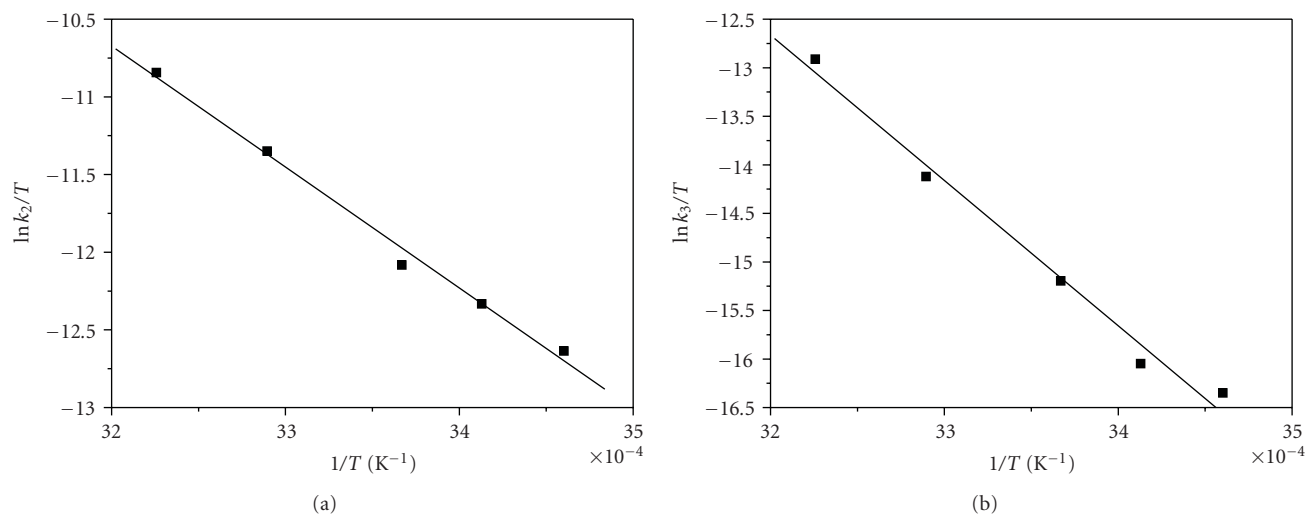
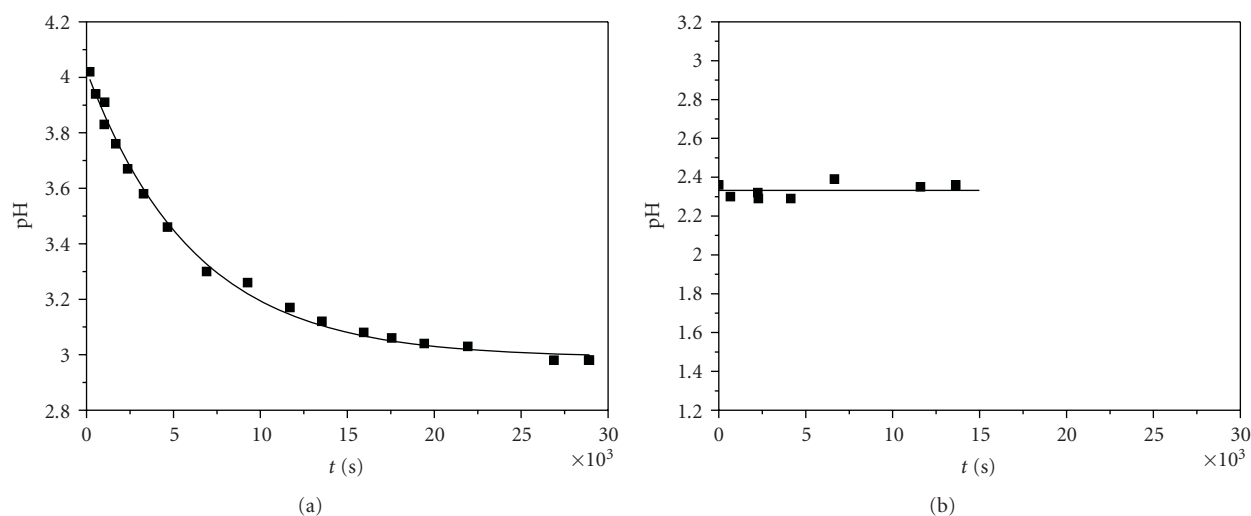


FIGURE 6: (a) Eyring plot for step 2. (b) Eyring plot for step 3.

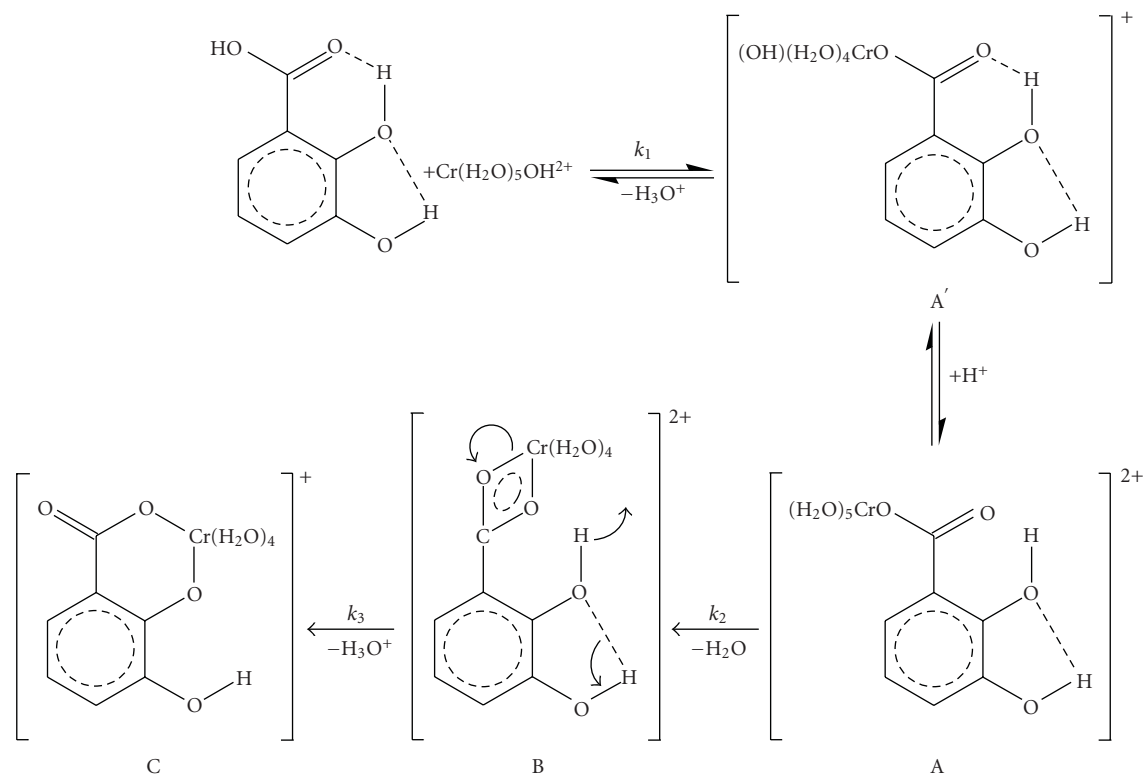
FIGURE 7: (a) $\text{pH} = f(t)$ for the reaction between 2,3-DHBA and Cr(III) in aqueous solutions. Conditions: $[\text{2,3-DHBA}]_0 = 0.01 \text{ M}$, $[\text{Cr(III)}]_0 = 0.10 \text{ M}$, $[\text{KOH}]_0 = 0.1 \text{ M}$ (stock solution added in the mixture), and $T = 298 \text{ K}$. (b) $\text{pH} = f(t)$ of a blank sample. Conditions $[\text{Cr(III)}]_0 = 0.1 \text{ M}$, and $T = 298 \text{ K}$.TABLE 2: Activation parameters for steps $A \xrightarrow{k_2} B$ and $B \xrightarrow{k_3} C$.

$\Delta H_{2(\text{obs})}^\ddagger$ (kJ mol^{-1})	$\Delta S_{2(\text{obs})}^\ddagger$ ($\text{JK}^{-1} \text{ mol}^{-1}$)	$\Delta H_{3(\text{obs})}^\ddagger$ (kJ mol^{-1})	$\Delta S_{3(\text{obs})}^\ddagger$ ($\text{JK}^{-1} \text{ mol}^{-1}$)
61.2 ± 3.1	-91.1 ± 11.0	124.5 ± 8.7	95.1 ± 29.0

six-membered ring instead of a four-membered ring and not having a hydrogen bond that exists in complex B.

For step 2 (k_2) the negative value of ΔS^\ddagger , the independence of k_2 on Cr(III) concentrations and the increase in absorbance, that is, of the extinction coefficients, led to the assignment of the observed transformations as *associatively activated substitution* of water molecules from the Cr(III) coordination sphere. Associative mechanism has

been supported to operate in reactions of Cr(III) [15–17]. For step 3 (k_3) a positive ΔS^\ddagger is observed indicating a less organized transition state than the reactants (complex B). This suggests more degrees of freedom in the corresponding transition state. Actually the suggestion of a six-membered ring (complex C) instead of a four-membered ring (step 2, complex B) is having less tension. Also the destruction of the hydrogen bond gives more freedom and thus less organization in the molecule explaining the positive entropy of activation of step 3. Since associative mechanism has been supported to operate in reactions of Cr(III), the transformations that take place at the Cr(III) center are associatively activated but the overall rearrangements that take place at the activated stage lead to overall positive value of the entropy of activation.



SCHEME 1: A possible mechanism of the reaction between chromium(III) and 2,3-dihydroxybenzoic acid in weak acidic aqueous solutions.

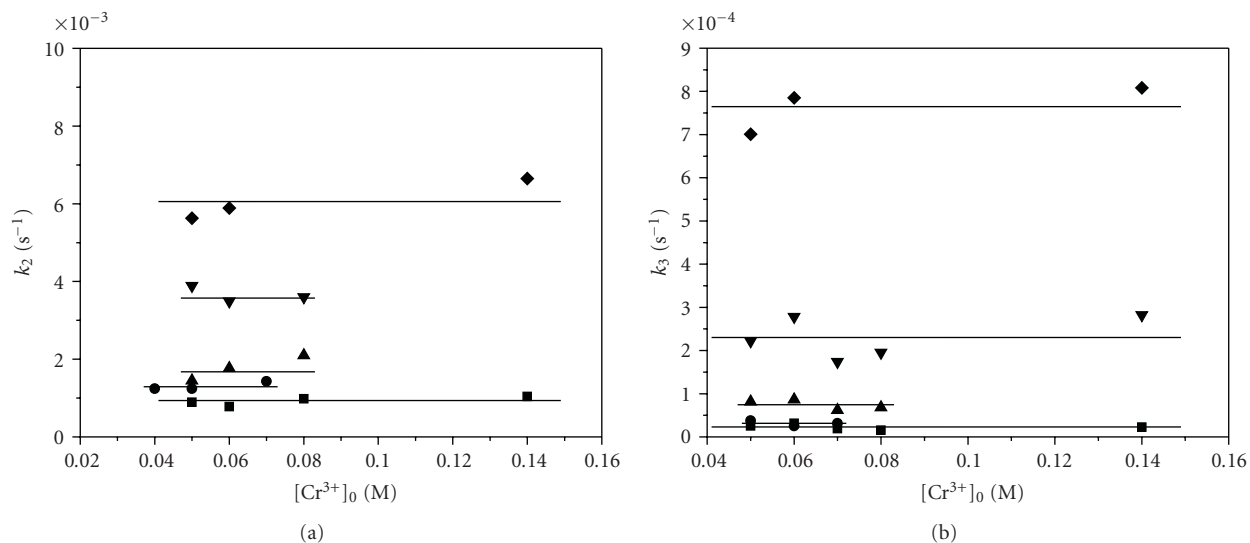
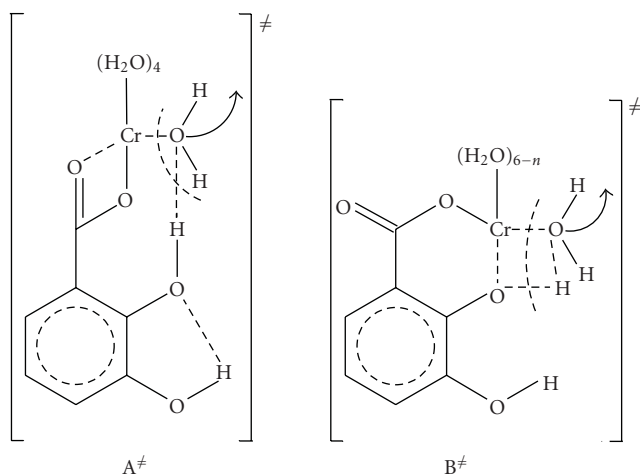


FIGURE 8: (a): Dependence of $k_{2(\text{obs})}$ on Cr(III) concentrations at various temperatures for the reactions $\text{A} \xrightarrow{k_2} \text{B} \xrightarrow{k_3} \text{C}$. ■— 289 K, ●— 293 K, ▲— 297 K, ▼— 304 K, ◆— 310 K. (b): Dependence of $k_{3(\text{obs})}$ on Cr(III) concentrations at various temperatures for the reactions $\text{A} \xrightarrow{k_2} \text{B} \xrightarrow{k_3} \text{C}$. ■— 289 K, ●— 293 K, ▲— 297 K, ▼— 304 K, ◆— 310 K.

By isolating the Cr(III)/2,3-DHBA final complex (complex C) in the solid form, elemental analyses were conducted and are in agreement with a 1:1 Cr(III)/2,3-DHBA ratio of complex C. An empirical formula for complex C is suggested according to the elemental analysis data:

[2,3-DHBA-_{3H} · Cr(H₂O)₄K · KNO₃ · 6H₂O · 4KOH] for which the calculated percentages are C = 11.2%, H = 3.61%, and N = 1.87%. The experimental values are C = 10.62%, H = 3.66%, and N = 1.38%. The catecholic mode of binding was found to operate in the coordination complexes



SCHEME 2: Activated complexes A[‡] and B[‡].

of 3,4-dihydroxyphenylpropionic acid (dihydrocaffeic acid), 3,4-dihydroxyphenylpropenoic acid (caffeic acid), and 3,4-dihydroxybenzoic acid (3,4-DHBA) with Cr(III) [18–20]. This type of binding was also reported for complexes of dihydrocaffeic, caffeic, and ferulic acids with Co(II), Ni(II), Cu(II), Fe(III), Mn(II), Mn(III), V(V), V(IV,V), and Zn(II) [21–25]. In the case of the reaction of 2,3-dihydroxybenzoic acid with chromium(III) the strong hydrogen bonds that exist intra- and intermolecularly cause the deviation from the above mode of binding. Though the substitution mechanisms at the chromium(III) center are associative ($\Delta S^\ddagger < 0$, step 2, step 3), the total change in the entropy of activation in the final step (step 3) is finally positive due to the destruction of the remaining hydrogen bond at the transition state of step 3, along with the destruction of a four-membered ring and the formation of a six-membered ring. This positive value of ΔS_3^\ddagger led us to suggest the mechanism that is shown in Scheme 1, not proposing a final(catecholic)chelation step as in the previous cases [18–20] that were studied by us.

4. Conclusions

The reaction between Cr(III) and 2,3-Dihydroxy-benzoic acid in weak acidic aqueous solutions was investigated, and the experimental results are consistent with a three-step mechanism in which the initial attack (step 1, substitution of water molecules from the coordination sphere of Cr(III) by the ligand through complexation) takes place between the acid molecule and the $[\text{Cr}(\text{H}_2\text{O})_5\text{OH}]^{2+}$ complex following an I_d mechanism. The carboxylate bound Cr(III), complex A, is followed by two consecutive nonchromium(III)-dependent steps (step 2 and step 3). These two steps are assigned as chelation and isomerisation steps, supported to be associatively activated at the Cr(III) center. The reactions are followed by a pH decrease because proton release is taking place during the overall mechanism. The negative value of the entropy of activation of step 2, the positive value of the entropy of activation of step 3, the independence on Cr(III) concentrations, the increase of the extinction coefficients,

the pH decrease due to the release of protons upon the various transformations and the 1:1 stoichiometry of the final complex C led to the proposed mechanism in Scheme 1.

Acknowledgment

The authors acknowledge financial support from the Research Account of Athens University (Grant no. 70/4/7564).

References

- [1] B. H. Bellaire, P. H. Elzer, C. L. Baldwin, and R. M. Roop II, "Production of the siderophore 2,3-dihydroxybenzoic acid is required for wild-type growth of *Brucella abortus* in the presence of erythritol under low-iron conditions in vitro," *Infection and Immunity*, vol. 71, no. 5, pp. 2927–2932, 2003.
- [2] L. H. J. Lajunen, R. Portanova, J. Piispanen, and M. Tolazzi, "Analytical chemistry division commission on equilibrium data," *Pure and Applied Chemistry*, vol. 69, no. 2, pp. 329–381, 1997.
- [3] N. Okabe and H. Kyoyama, "2,3-dihydroxybenzoic acid," *Acta Crystallographica Section E*, vol. 57, pp. o715–o716, 2001.
- [4] J. Xu and R. B. Jordan, "Equilibrium and kinetic studies of the complexing of iron(III) by 1,2-dihydroxybenzene derivatives," *Inorganic Chemistry*, vol. 27, no. 8, pp. 1502–1507, 1988.
- [5] J. Xu and R. B. Jordan, "Kinetics and mechanism of the oxidation of 2,3-dihydroxybenzoic acid by iron(III)," *Inorganic Chemistry*, vol. 27, no. 25, pp. 4563–4566, 1988.
- [6] E. I. Ochiai, "General principles of biochemistry of the elements," in *Biochemistry of the Elements*, E. Frieden, Ed., Plenum Press, New York, NY, USA, 1987.
- [7] J. H. Espenson, *Chemical Kinetics and Reaction Mechanisms*, McGraw–Hill, New York, NY, USA, 1981.
- [8] J. A. Weyh and R. E. Hamm, "Aqueation of the cis-bis(iminodiacetato)chromate(III) and trans(fac)-bis(methyliminodiacetato)chromate(III) ions in acidic aqueous medium," *Inorganic Chemistry*, vol. 8, no. 11, pp. 2298–2302, 1969.
- [9] N. W. Alcock, D. J. Benton, and P. Moore, "Kinetics of series first-order reactions. Analysis of spectrophotometric data by the method of least squares and an ambiguity," *Transactions of the Faraday Society*, vol. 66, pp. 2210–2213, 1970.
- [10] D. A. Buckingham, D. J. Francis, and A. M. Sargeson, "Hydrolysis and nitrosation of the $(\text{NH}_3)_5\text{CoNCO}^{2+}$ ion. Evidence for $(\text{NH}_3)_5\text{CoNHCOOH}^{2+}$ and $(\text{NH}_3)_5\text{Co}^{3+}$ intermediates," *Inorganic Chemistry*, vol. 13, no. 11, pp. 2630–2639, 1974.
- [11] C. F. Baes and R. E. Mesner, *The Hydrolysis of Cations*, John Wiley & Sons, New York, NY, USA, 1976.
- [12] F. A. Cotton, G. Wilkinson, C. A. Murillo, and M. Bochmann, *Advanced Inorganic Chemistry*, John Wiley & Sons, New York, NY, USA, 6th edition, 1999.
- [13] N. Okabe and H. Kyoyama, "2,3-dihydroxybenzoic acid," *Acta Crystallographica Section E*, vol. 57, no. 12, pp. o1224–o1226, 2001.
- [14] R. F. Wilkins, *Kinetics and Mechanisms of Reactions of Transition Metal Complexes*, VCH, New York, NY, USA, 2nd edition, 1991.
- [15] T. Ramasami and A. G. Sykes, "Mechanistic implications of kinetic data for the formation and aqueation of acidopen-taamminechromium(III) complexes, $\text{Cr}(\text{NH}_3)_5\text{X}^{2+}$, $\text{X}^- = \text{NCS}^-$, $\text{CCl}_3\text{CO}_2^-$, CF_3CO_2^- , Cl^- , Br^- , and I^- . Evidence for a dissociative mechanism," *Inorganic Chemistry*, vol. 15, no. 11, pp. 2885–2891, 1976.

- [16] T. W. Swaddle and D. R. Stranks, "Mechanistic information from pressure and temperature effects on the rate of transfer of oxygen-18 from aquopentaamminechromium(III) and aquopentaamminerhodium(III) ions to solvent water," *Journal of the American Chemical Society*, vol. 94, no. 24, pp. 8357–8360, 1972.
- [17] A. L. Petrou, "Kinetics and mechanism of the reaction between chromium(II) and 1,2-bis(2-pyridyl)ethylene in acidic aqueous solutions," *Journal of the Chemical Society, Dalton Transactions*, no. 24, pp. 3771–3775, 1993.
- [18] A. L. Petrou, P. Paraskevopoulou, and M. Chrysikopoulou, "Kinetics and mechanism of the reaction between chromium(III) and 3,4-dihydroxyphenylpropionic (dihydrocaffeic) acid in weak acidic aqueous solutions," *Journal of Inorganic Biochemistry*, vol. 98, no. 1, pp. 123–132, 2004.
- [19] V. Thoma, K. Tampouris, and A. L. Petrou, "Kinetics and mechanism of the reaction between chromium(III) and 3,4-dihydroxy-phenyl-propenoic acid (caffeic acid) in weak acidic aqueous solutions," *Bioinorganic Chemistry and Applications*, vol. 2008, Article ID 624583, 7 pages, 2008.
- [20] K. Zavitsanos, K. Tampouris, and A. L. Petrou, "Reaction of chromium(III) with 3,4-dihydroxybenzoic acid : kinetics and mechanism in weak acidic aqueous solutions," *Bioinorganic Chemistry and Applications*, vol. 2008, Article ID 212461, 8 pages, 2008.
- [21] A. L. Petrou, M. V. Koromantzou, and J. M. Tsangaris, "Coordination complexes of 3,4-dihydroxyphenylpropionic acid (dihydrocaffeic acid) with copper(II), nickel(II), cobalt(II) and iron(III)," *Transition Metal Chemistry*, vol. 16, no. 1, pp. 48–52, 1991.
- [22] A. L. Petrou, "Binuclear vanadium(V) and vanadium(IV, V) complexes of dihydrocaffeic, caffeic and ferulic acids," *Transition Metal Chemistry*, vol. 18, no. 5, pp. 462–466, 1993.
- [23] A. L. Petrou and S. P. Perlepes, "Preparation and properties of manganese(II) and manganese(III) complexes possessing ligands with carboxylate and phenolic/phenoxide groups," *Chimika Chronika*, vol. 23, pp. 155–168, 1994.
- [24] A. L. Petrou and S. P. Perlepes, "Oligonuclear zinc(II) complexes of dianion of hydrocaffeic, caffeic and ferulic acids," *Chimika Chronika*, vol. 24, pp. 133–146, 1995.
- [25] A. L. Petrou, M. V. Koromantzou, and J. M. Tsangaris, "Coordination complexes of caffeic and ferulic acids with Cu(II), Ni(II), Co(II) and Fe(III)," *Chimika Chronika*, vol. 22, pp. 189–204, 1993.

Research Article

Synthesis, Characterization, DNA Binding, and Photocleavage Activity of Oxorhenium (V) Complexes with α -Diimine and Quinoxaline Ligands

Christiana A. Mitsopoulou and Constantinos Dagas

Laboratory of Inorganic Chemistry, Department of Chemistry, University of Athens, Panepistimiopolis, Zografou, Athens 157 71, Greece

Correspondence should be addressed to Christiana A. Mitsopoulou, cmitsop@chem.uoa.gr

Received 11 March 2010; Accepted 1 April 2010

Academic Editor: Spyros Perlepes

Copyright © 2010 C. A. Mitsopoulou and C. Dagas. This is an open access article distributed under the Creative Commons Attribution License, which permits unrestricted use, distribution, and reproduction in any medium, provided the original work is properly cited.

The complex $[\text{ReOCl}_3\text{pq}]$ (**1**) (where pq = 2-(2'-pyridyl)quinoxaline) has been synthesized and fully characterized by UV-Vis, FTIR, 1 and 2D NMR, and cyclic voltammetry (CV). The DNA-binding properties of the complex **1** as well as of the compounds $[\text{ReOCl}_3\text{bpy}]$ (**2**), $[\text{ReOCl}_3\text{phen}]$ (**3**), and pq (**4**) were investigated by UV-spectrophotometric (melting curves), CV (cyclic voltammetry), and viscosity measurements. Experimental data suggest that complex **1** intercalates into the DNA base pairs. Upon irradiation, complex **1** was found to promote the cleavage of plasmid pBR 322 DNA from supercoiled form I to nicked form II. The mechanism of the DNA cleavage by complex **1** was also investigated.

1. Introduction

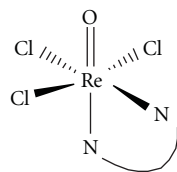
For many years transition metal complexes have piqued curiosity owing to their efficient DNA binding and cleavage properties under physiological conditions [1–14]. It has been demonstrated that inorganic complexes can be used in footprinting studies, as sequence specific DNA binding agents, as diagnostic agents in medicinal applications, and for genomic research. Among different modes of DNA cleavage, oxidative cleavage of DNA upon irradiation with visible light is of main interest due to the potential applications of such compounds in photodynamic therapy of cancer [3, 15] and references therein.

On the other hand, coordination chemistry of rhenium has been extensively developed in recent years due, to a large extent, to the fact that its complexes with diimine ligands display long lifetimes and also short-lived rhenium isotopes hold promise as β -emitters in radiotherapy [14, 16, 17]. The chemistry of oxorhenium complexes arouses particular interest among these compounds not only for their implication in various reactions of industrial and biological importance, including olefin epoxidation and catalysis by cytochrome P-450 [18, 19], but also for their lipophilic

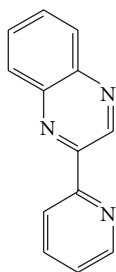
character and the oxidation states of rhenium that is Re(I) to Re (VI) [17].

In this context, the design, synthesis, and reactivity of novel rhenium oxocomplexes have become the aim of several laboratories, including ours. To the best of our knowledge, studies on oxorhenium (V) complexes incorporating planar aromatic ligands that could bind to DNA have not been studied before. Nevertheless, quinoxaline (pq) has recently received considerable attention [20, 21]. The structure of the quinoxaline ligand is recognized from a great number of natural compounds such as riboflavin and molybdopterines, and can be used as antibacterial, antiviral, anticancer, antihelmintic, and insecticidal agent [22]. In addition, it adopts a planar conformation when chelates to a metal ion [20, 23, 24]. This planar appendage provides a handle for intercalative binding to DNA, positioning the complex for enhanced reactivity toward DNA.

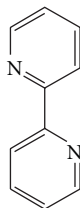
In this paper, we present the synthesis and characterization of the oxorhenium (V) complex, $[\text{ReOCl}_3\text{pq}]$ (**1**). In order to elucidate the reactivity of this compound, we have also synthesized the complexes $[\text{ReOCl}_3\text{bpy}]$ (**2**) and $[\text{ReOCl}_3\text{phen}]$ (**3**) and studied their intercalating abilities. The ligands 2'-pyridylquinoxaline (**4**), 2,2'-bipyridine (**5**),



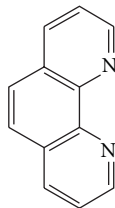
Where N–N:
 pq = 1
 bpy = 2
 phen = 3



pq (4)



bpy (5)



phen (6)

FIGURE 1: Structures of the complexes 1–3 and the corresponding α -diimine ligands.

and 1-10-phenanthroline (6) belong to quinoxaline or diimine class of organic compounds (Figure 1).

The interaction of these compounds with double stranded calf thymus DNA has been investigated using circular dichroism spectroscopy (CD), DNA thermal denaturation analysis (melting point), CV, and viscosity measurements. The photocleavage reaction on DNA has been monitored by agarose gel electrophoresis. Understanding the interactions between the compounds under study and DNA, and their ability to damage DNA with photoactivation by visible light would be the first step toward the development of rhenium-based drugs which might be useful in photobiological applications such as photodynamic therapy.

2. Experimental

2.1. Materials. 2-(2'-pyridyl)quinoxaline [25, 26] and $[\text{ReOCl}_3(\text{PPh}_3)_2]$ [27] were prepared by reported procedures. All reactions and manipulations were conducted under a pure argon atmosphere using standard Schlenk techniques. Ultra-pure Milli-Q water (18.2 m Ω) was used in all experiments. Reagent grade solvents were dried and distilled by usual methods and the solvents were stored over molecular sieves (4Å). The chemicals were purchased by Aldrich and used as received. Calf thymus DNA (CT DNA) and pBR322 supercoiled plasmid DNA (stored at: -20°C) were purchased from Sigma (St. Louis, MO).

2.2. Methods and Instrumentation. Microanalysis (C, H, N) was carried out with a Euro Vector EA 3000 analyser. FT-IR spectra in solution and in KBr pellets were recorded on a Nicolet Magna IR 560 spectrophotometer with a

1.0 cm^{-1} resolution. UV-Vis spectroscopy was recorded on a Varian Cary 300E spectrophotometer at $25 \pm 0.2^\circ\text{C}$ using cuvettes of 1 cm path length. The ^1H NMR spectra were obtained at room temperature using a Varian Unity Plus 300 MHz spectrometer. Samples were run in a 5 mm probe with deuterated solvents as internal lock and reference. The assignment of the ^1H NMR spectra of the free ligands and of the complexes is based on 2D NMR experiments (^1H - ^1H COSY). A Fisons VG Quattro instrument with a VG Biotech Electrospray source, having a hexapole lens was employed for ESI-MS analysis [28].

Photolysis experiments were carried out with a 1000 W Xenon lamp in an Oriel, model 68820, Universal Arc. Lamp source was selected with appropriate interference filter (Corning).

Cyclic voltammetric (CV) measurements were performed in a single compartment cell with a three electrode configuration on a Pine AFCBP1 (pine Instrument Company, Groove City, PA, USA). Glassy carbon was the working electrode, and the reference electrode was a saturated calomel electrode (SCE). A platinum wire was used as the counter electrode.

All the experiments involving interaction of the complexes with DNA were conducted in twice distilled phosphate buffer (Titrisol, 5 mM) and NaCl (4 mM) and adjusted to pH = 7.00 or 5.00 with hydrochloric acid. A solution of calf thymus DNA (CT-DNA) in the buffer gave a ratio of UV absorbance at 260 and 280 nm of ca. 1.8-1.9:1, indicating that the DNA was sufficiently free of protein [29]. The concentration of DNA in nucleotide phosphate was determined by UV absorbance at 260 nm after dilution. The extinction coefficient, ϵ_{260} was taken as $6600 \text{ M}^{-1} \text{ cm}^{-1}$ [29]. Stock solutions were stored at 4°C and used after no more than 4 d. Supercoiled plasmid pBR322 DNA was stored at -20°C and its concentration in base pairs was determined by UV absorbance at 260 nm after appropriate dilutions taking ϵ_{260} as $13 \text{ } 100 \text{ M}^{-1} \text{ cm}^{-1}$.

2.3. DNA Binding Studies. Thermal denaturation experiments were performed with a Varian Cary 300 spectrophotometer. Samples for T_m measurements were obtained by adding 100 μL of a freshly prepared stock solution of rhenium compound, dissolved in the buffer (4 mM NaCl, 0.096 M KH_2PO_4 , 0.2 M Na_2HPO_4 , pH 5.0 or 4 mM NaCl, 0.026 M KH_2PO_4 , 0.041 M Na_2HPO_4 , pH 7.0), to 1.00 mL of a calf thymus DNA solution (60 $\mu\text{g}/\text{mL}$) and incubating at 25°C for 24 hours. As the solubility of compound 1 is poor in net water, it was firstly dissolved in MeOH (in any case the ratio of MeOH: water is no higher than 5:95). Under these circumstances, complex 1 is stable for at least a period of five days. Absorbance versus temperature profiles of DNA were measured at 258 nm in the temperature range from 25°C to 95°C . Temperature was raised in 0.5°C increments, and DNA complex samples were allowed to equilibrate for 1 minute at each temperature. The melting temperature (T_m) of DNA was determined as the middle point of the hyperchromic transition. To correct the absorbance spectrum of DNA from the contribution of each of the studied compounds, the

buffer solution of the corresponding complex at the same concentration in the sample was used as a blank.

Viscosity measurements were carried out using a Schott Geräte AVS 310 viscometer maintained at a constant temperature at $25.0(\pm 0.1)^\circ\text{C}$ in a thermostatic bath. DNA samples with approximately 200 base pairs in average length were prepared by sonication in order to minimize complexities arising from DNA flexibility. Flow time was measured with a digital stopwatch, while each sample was measured three times, and an average flow time was calculated. Data are presented as $(\eta/\eta_0)^{1/3}$ versus $1/r$, where $r = [\text{DNA}]/[\text{complex } 1]$, η is the viscosity of DNA in the presence of complex, and η_0 is the relative viscosity of DNA alone. The relative viscosity of DNA in the presence and absence of the metal complex was calculated using the expression $\eta = (t - t_0)/t_0$, where t is the observed flow time of the DNA solution and t_0 the flow rate of buffer alone. According to Cohen and Eisenberg [30] the relationship between the relative solution viscosity (η/η_0) and contour length (L/L_0) is given by the equation $L/L_0 = (\eta/\eta_0)^{1/3}$, where L_0 denotes the apparent molecular length in the absence of the metal complex.

2.4. DNA Photocleavage. For the gel electrophoresis experiment, pBR322 supercoiled plasmid DNA (0.1 lg) was treated with the Re (V) complexes in 50 mM Tris-acetate, 18 mM NaCl buffer (pH 7.2), and the solution was then irradiated at room temperature with a light $>400\text{ nm}$ (100 W) inside a photoreactor. The samples were analyzed by electrophoresis for 1 hour at 100 V in Tris-acetate buffer containing 1% agarose gel. The gels were imaged with a BioSure UV-Transilluminator and photographed using a Picture Works Photo Enhancer v3.2 digital camera equipped with a $10\ \mu\text{g/mL}$ ethidium bromide filter.

2.5. Synthesis of Complexes. In this context, rhenium (V) metal complexes with bidentate (N,N) type ligands as 2-(2'-pyridyl)quinoxaline (pq) **4**, 2,2'-bipyridine (bpy) **5**, and 1,10-phenanthroline (phen) **6**, have been amply studied.

Ligands **5** and **6** were purchased by Aldrich and used as received, whereas ligand **4** was synthesized according to published procedures [26, 31].

2.5.1. Synthesis of $[\text{ReOCl}_3\text{pq}]$ (1). Potassium perhenate (KReO_4) was used as a starting material. A solution of triphenylphosphine (PPh_3) (5.15 g, 18 mmol) in hot ethanol (29 mL) was added in a boiling mixture of potassium perhenate (1 g, 3.4 mmol), hydrochloric acid 37% (5.72 mL), and ethanol (5.72 mL). A yellow solid precipitates. The mixture was refluxed for 30 minutes and after cooling to room temperature, the yellow precipitate was filtered off, washed with ethanol, and dried *in vacuo*. By this procedure the precursor $[\text{ReOCl}_3(\text{PPh}_3)_2]$ was obtained. The ligand pq was added in a solution of $[\text{ReOCl}_3(\text{PPh}_3)_2]$ in dry methanol (20 mL) under stirring, and the mixture was heated to continuous reflux for 24 hours at 50°C . After cooling to room temperature, the resultant dark purple precipitate was filtered off, washed with diethylether, and dried *in vacuo*.

Yield: 57%. (0.732 g) $^1\text{H NMR}$ (300 MHz; CD_3OD ; s, singlet; d, doublet; t, triplet; m, multiplet): δ 9.73(s, 1H, $\text{H}_{3\text{pq}}$), 8.15, 8.25(mt, 2H, $\text{H}_{7-10\text{pq}}$), 7.92(mt, 2H, $\text{H}_{8-9\text{pq}}$), 7.48(d, 1H, $\text{H}_{16\text{pq}}$, $J = 8.0$), 8.08(mt, 1H, $\text{H}_{15\text{pq}}$), 8.91(mt, 1H, $\text{H}_{14\text{pq}}$), 8.65(d, 1H, $\text{H}_{13\text{pq}}$, $J = 5.5$). Absorption spectrum: $\lambda_{\text{max}}(\text{MeOH}) = 571.0\text{ nm}$ ($\epsilon = 3330\text{ M}^{-1}\text{ cm}^{-1}$), $\lambda_{\text{max}}(\text{MeOH}) = 732.1\text{ nm}$ ($\epsilon = 1227\text{ M}^{-1}\text{ cm}^{-1}$). FT-IR spectrum: 939(vs) cm^{-1} ($\nu\text{Re=O}$), 1630(m,br), 1580(w) and 1420(m) cm^{-1} ($\nu\text{C-N}$) and ($\nu\text{C=C}$). Anal. Calcd for ReOCl_3pq : C 30.27; H 1.76; N 8.15; Cl 20.62; O 3.10. Found: C 30.97; H 1.74; N 8.19%. ES-MS (CH_3CN : m/z (M-H^+)) 516.8.

2.5.2. Synthesis of $[\text{ReOCl}_3\text{bpy}]$ (2). This compound was prepared by refluxing $[\text{ReOCl}_3(\text{PPh}_3)_2]$ (0.83 g, 1 mmol) and bpy (1.3 mmol) in methanol (50 mL) for 6 hours using the procedure employed for **1**. A red microcrystalline material was isolated.

Yield: 88%. (0.554 g) $^1\text{H NMR}$ (300 MHz; CD_3COCD_3 ; s, singlet; d, doublet; t, triplet; m, multiplet): δ 9.09(d, 2H, $\text{H}_{6-9\text{bpy}}$, $J = 7.9$), 8.03(d, 2H, $\text{H}_{12-13\text{bpy}}$, $J = 5.9$), 7.84(t, 2H, $\text{H}_{4-11\text{bpy}}$), 7.37(t, 2H, $\text{H}_{5-10\text{bpy}}$). Absorption spectrum: $\lambda_{\text{max}}(\text{MeOH}) = 480.8\text{ nm}$ ($\epsilon = 3430\text{ M}^{-1}\text{ cm}^{-1}$), $\lambda_{\text{max}}(\text{MeOH}) = 750.2\text{ nm}$ ($\epsilon = 1450\text{ M}^{-1}\text{ cm}^{-1}$). FT-IR spectrum: 988 cm^{-1} ($\nu\text{Re=O}$), 1640–1570 cm^{-1} ($\nu\text{C=C}$, (bpy)). Anal. Calcd for ReOCl_3bpy : C 25.84; H 1.74; N 6.03; Cl 22.89; O 3.44. Found: C 26.03; H 1.79; N 6.19%. ES-MS (CH_3CN : m/z (M-Cl^+)) 465.9.

2.5.3. Synthesis of $[\text{ReOCl}_3\text{phen}]$ (3). This compound was prepared by refluxing $\text{ReOCl}_3(\text{PPh}_3)_2$ (0.83 g, 1 mmol) and phen (0.26 g 1.3 mmol) in methanol (50 mL) for 48 hours using the procedure employed for **1**. A dark red microcrystalline material was isolated.

Yield: 84%. (0.843 g) $^1\text{H NMR}$ (300 MHz; CD_3COCD_3 ; s, singlet; d, doublet; t, triplet; m, multiplet): δ 8.90(d, 2H, $\text{H}_{2-9\text{phen}}$, $J = 6.9$), 8.37(d, 2H, $\text{H}_{4-11\text{phen}}$), 7.40(s, H_{phen}), 7.69(mt, H_{phen}). Absorption spectrum: $\lambda_{\text{max}}(\text{MeOH}) = 459.6\text{ nm}$ ($\epsilon = 3200\text{ M}^{-1}\text{ cm}^{-1}$), $\lambda_{\text{max}}(\text{MeOH}) = 739.6\text{ nm}$ ($\epsilon = 1100\text{ M}^{-1}\text{ cm}^{-1}$). FT-IR spectrum: 985 cm^{-1} ($\nu\text{Re=O}$), 1628(w), 1605(m), 1575(w), 1520(m) cm^{-1} (νCN and $\nu\text{C=C}$, (phen)). Anal. Calcd for $\text{ReOCl}_3\text{phen}$: C 29.37; H 2.05; N 5.71; Cl 21.67; O 3.26. Found: C 30.03; H 2.17; N 5.99%. ES-MS (CH_3CN : m/z (M-Cl^+)) 489.8.

3. Results and Discussion

3.1. Synthesis. 2-(2'-pyridyl)quinoxaline (pq) is produced via an unusual condensation reaction from 2-acetylpyridine and 1,2-diaminobenzene and has been extensively studied because of its rich coordination chemistry. 2-(2'-pyridyl)quinoxaline belongs to the general class of quinoxalines which are natural products, used as antibiotics and form polymers with peculiar magnetic and electric properties. Their significant redox chemistry and photochemistry are responsible for many considerable intra and intermolecular electron transfer organic and biochemical processes. The aforementioned ligand as well as bpy and phen has been coordinated to the oxorhenium moiety.

The most significant m/z peaks in ESI-mass spectra of complexes **1–3** are given in the Synthesis Section. They correspond to the molecular weight of the complex increased by one unit for complex **1**, so that $[M-H]^+$ form is attributed, implying that a proton has been attached on the N(3) atom of the quinoxaline ring. On the other hand, complexes **2** and **3** eliminate a -Cl atom providing the form $[M-Cl]^+$. Surprisingly, we were not able to isolate crystalline complex from the oxorhenium-quinoxaline system in which only the typical chelate bonding of an α -diimine ring is present. In fact, up to now only few oxorhenium- α -diimine crystal structures have appeared in the literature though it is well-known that radioactive ^{186}Re and ^{188}Re are important diagnostic nuclear agents. Actually, the crystal structure of the $\text{ReOCl}_3\text{phen}$ was recently reported [32]. According to the data presented therein, the rhenium atom is in a distorted octahedral environment with the three chloride ligands arranged in a meridional fashion and the oxo ligand *trans* to the nitrogen atom of the phenanthroline. As the complexes under study **1** and **2** are isomorphous to **3**, we expect to adopt similar geometries.

3.2. Characterization of $[\text{ReOCl}_3(\alpha\text{-diimine})]$ Complexes

3.2.1. Infrared Data. The IR spectra of **1**, **2**, and **3** exhibit very strong bands at 939, 988, and 985 cm^{-1} , respectively, assignable to the $\nu(\text{Re}=\text{O})$ mode. These values compare well with those reported for rhenium (V) complexes containing a chelating ligand in their coordination sphere [32]. The characteristic bands corresponding to the $\nu(\text{CN})$ and $\nu(\text{C}=\text{C})$ modes of the quinoxaline and diimine ligand appear in the range 1680–1420 cm^{-1} in the IR spectra of the complexes **1–3** [20, 25, 32].

3.2.2. NMR Spectroscopy. The oxorhenium complexes **1–3** give well-defined ^1H -NMR spectra, which permit unambiguous identification and assessment of purity. The proton chemical shifts are assigned with the aid of ^1H -COSY experiments (provided in Section 2).

It is worth to discuss the complexation of 2-(2'-pyridyl)quinoxaline to the $[\text{ReOCl}_3(\text{PPh}_3)_2]$ moiety since it entails two major changes: the first involves the configuration of 2-2'pq switching from the *syn/cis*- to the *anti/trans*-conformation, while the second is related to the withdrawal of its electron density by the metal. These changes are reflected on the NMR spectra of the complex. Figure 2 displays the ^1H - ^1H COSY spectra of the free ligand L and of the complex, which are important for assigning of the 1D-NMR peaks.

The NMR spectrum of the coordinated ligand L differs from that of the free ligand (Figure 2) mainly due to the separation of H_5 and H_8 signals and to an overall downfield shift. The latter is due to the reducing electron charge of the protons after coordination of the ligand. The most downfield shifted peak remains the $\text{H}_3(\text{s})$ [31]. The same switching from *syn/cis*- to the *anti/trans*-conformation is also observed in the spectrum due to the complexation of 2-2'-bipyridine ligand.

TABLE 1: Electrochemical and absorption data of the oxorhenium (V) complexes.

Complex	$E_{1/2}/\text{V}$ versus SCE ^a		$\lambda_{\text{max}}/\text{nm}$	$\lambda_{\text{max}}/\text{nm}$
	E_{pa} (V)	E_{pc} (V)	$(\epsilon/\text{M}^{-1}\text{cm}^{-1})^{\text{b}}$	$(\epsilon/\text{M}^{-1}\text{cm}^{-1})^{\text{c}}$
[ReOCl ₃ pq] (1)	-0.52	-0.70	268.5 (4835)	272.4 (4820)
			571.0 (3330)	581.2 (3520)
			732.1 (1227)	738.3 (1337)
[ReOCl ₃ bpy] (2)	-0.54	-0.72	295.3 (4315)	294.1 (4330)
			480.8 (3430)	493.0 (3520)
			750.2 (1450)	753.0 (1480)
[ReOCl ₃ phen] (3)	-0.44	-0.61	270.6 (4580)	268.3 (4350)
			459.6 (3200)	463.7 (3300)
			739.6 (1100)	745.0 (1150)

^aAll complexes were measured in 0.1 M TBABF₄-DMF; error in potential was ± 0.01 V; $T = 25 \pm 0.2^\circ\text{C}$; scan rate = 100 mV \cdot s⁻¹

^bIn CH₃OH, [C] = 10⁻² M

^cIn CH₃COCH₃, [C] = 10⁻² M.

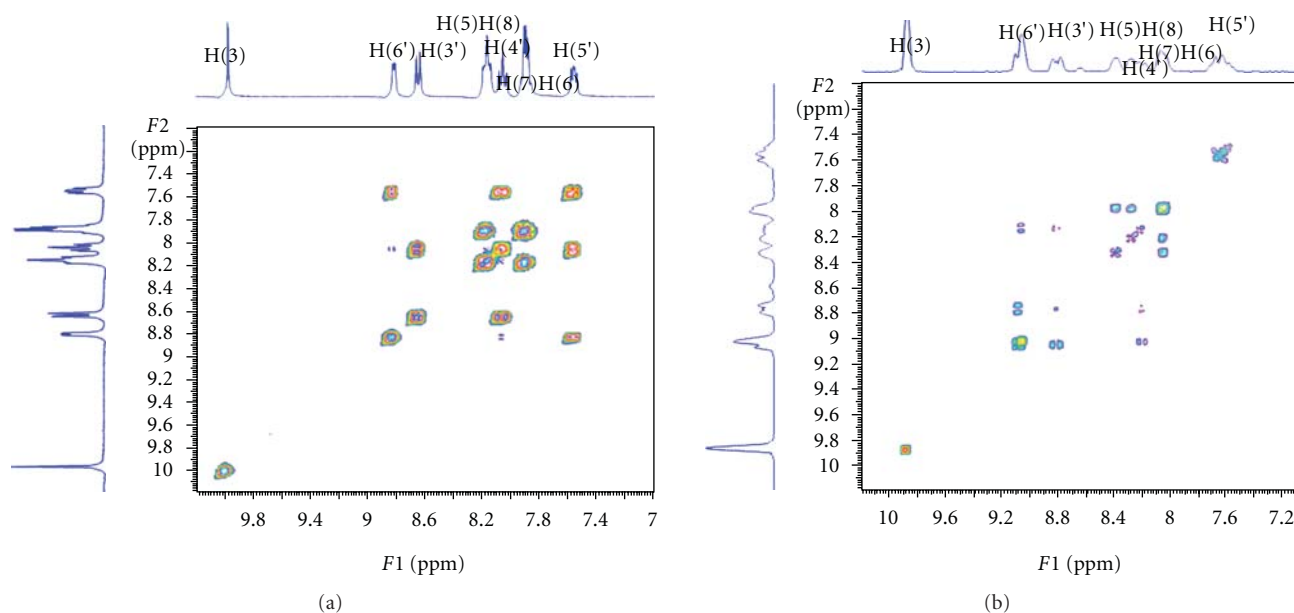
3.2.3. UV-Vis Spectroscopy. The electronic absorption spectra of $[\text{ReOCl}_3(\alpha\text{-diimine})]$ in the area between 300 and 800 nm are shown in Table 1. The UV-Vis spectra of **1–3** exhibit few intense bands in the range of 570–200 nm and a weak absorption in the low range 730–750 nm. According to TD-DFT calculations [32], the longest wavelength experimental band of **1**, **2**, and **3** at 732, 750, and 739 nm, respectively, is attributed to the transition of $d \rightarrow d$ character. The broad MLCT absorption band appears at 571, 480, and 459 nm for complexes **1**, **2**, and **3**, respectively. It originates from the d_{Re} orbitals to the $\pi_{\alpha\text{-diimine}}^*$ orbitals [32] and it is blue shifted in less polar solvents (Table 1), indicating its charge transfer character. The higher energy absorption bands at UV region are attributed to ligand-ligand charge transfer transitions, namely, $(\pi)\text{Cl}/(\pi)\text{O}/(\pi)\text{diimine} \rightarrow \pi^*(\text{diimine})$, interligand transitions.

3.2.4. Electrochemical Behaviour of Complexes. The redox properties of the compounds **1–3** have been investigated by cyclic voltammetry, at a Pt electrode, usually in a 0.1 M TBABF₄-DMF solution at $25 \pm 0.2^\circ\text{C}$, and the measured redox potentials (in V versus SCE) are given in Table 1. Solutions were deoxygenated by purging with argon gas for 15 minutes prior to the measurements; during the measurements a stream of argon was passed over the solution. All the studied complexes exhibit (Table 1) a reduction wave which is usually followed, at the lowest potential, by a second one. These waves often correspond to single-electron reversible processes, being assigned to the $d^n \rightarrow d^{n+1}$ and $d^{n+1} \rightarrow d^{n+2}$ metal reductions. Previous studies have shown that the diimine ligand influences the reduction potential of the compounds. The oxidation for all three complexes occurs at very similar potentials. Both reduction potentials occur at negative potentials.

TABLE 2: Melting temperatures of CT-DNA in 10 mM buffer (pH 7.0 and pH 5.0) in the presence of complexes 1–3, before and after irradiation ($\lambda = 420\text{--}1000\text{ nm}$).

C.T.-DNA + ^a	pH	R = 0.025			R = 0.050			R = 0.025*			R = 0.050*		
		T_m °C	ΔT_m	%hyp	T_m °C	ΔT_m	%hyp	T_m °C	ΔT_m	%hyp	T_m °C	ΔT_m	%hyp
[ReOCl ₃ pq]	7.0	80.1	+9.2	18.0	81.8	+10.9	13.0	77.9	+7.0	12.0	79.1	+9.0	12.0
(1)	5.0	81.1	+8.0	27.0	80.2	+7.1	19.0	78.1	+5.0	28.0	79.1	+6.0	19.0
[ReOCl ₃ bpy]	7.0	76.9	+6.0	44.0	76.9	+6.0	39.0	75.4	+4.5	45.0	75.1	+5.0	36.0
(2)	5.0	76.1	+3.0	20.0	77.1	+4.0	20.0	73.1	+0.0	20.0	76.1	+3.0	20.0
[ReOCl ₃ phen]	7.0	71.1	+0.2		71.4	+0.5		70.9	+0.0		74.2	+0.3	
(4)	5.0	73.1	+0.0		73.3	+0.2		73.1	-0.0		73.1	+0.0	

*Illuminated samples. ^aThe melting point of the free CT-DNA is 70.9°C (pH 7.0) and 73.1°C (pH 5.0).

FIGURE 2: COSY-NMR spectra of pq (a) and [ReOCl₃pq] (b) in methanol.

3.3. Biological Assays

3.3.1. T_m Measurements. The study of the melting curves of C.T.-DNA indicates that the interaction of DNA with the oxorhenium (V) complexes **1** and **2**, leads to the stabilization of the double helix in proportion to the ratio $r = [\text{ReOCl}_3(\alpha\text{-diimine})]/[\text{CT-DNA}]$ (Table 2). The stabilization can be assumed by the raising of the T_m which is finally observed in analogy with r , reaching at +10.85°C for **1** at $r = 0.05$ and $\text{pH} = 7.0$ (Figure 3). In the presence of all three complexes (**1**–**3**) the thermal stabilization of CT-DNA is observed in the series $\mathbf{1} > \mathbf{2} > \mathbf{3}$. Moreover, the reduction of the final hyperchromicity and the decrease of the slope of melting curves (increase of the transition) provide a strong evidence of the interaction which leads to DNA helix stabilization [33]. “Premelting effects” of the double helix which could be caused by the binding of oxorhenium (V) complexes, probably via allosteric effects, are rather not taking place since they would result in DNA helix destabilization [34]. The reversibility measurements of the **1** and **3** binding to CT-DNA (cooling the samples and reheating them) showed completely super-imposable results onto the first heating

scans. This suggests that the species present in the solution of **1** or **3**, do not alone inhibit reannealing, associating irreversibly with the single strand which is similar to the results obtained for the free ligands. Although the complex [ReOCl₃phen] is isostructural to the complexes [ReOCl₃pq] and [ReOCl₃bpy], it presents different behaviour when interacts with CT-DNA. In both buffered pH 7.0 and pH 5.0 solutions, at all ratios, the melting points of CT-DNA are almost the same with free CT-DNA. Identical results have been obtained when CT-DNA was treated with all free ligands under investigation. So we can conclude that there is almost no interaction between the complex [ReOCl₃phen] and CT DNA. No observable changes are measured after irradiation.

3.3.2. CV Studies. Electrochemical investigation of complex-DNA interactions can provide a useful complement to other methods and yield information about the mechanism of the interaction [23, 24, 35]. Figure 4 shows the cyclic voltammograms of the complex at the absence and the presence of DNA. A new irreversible redox peak appeared

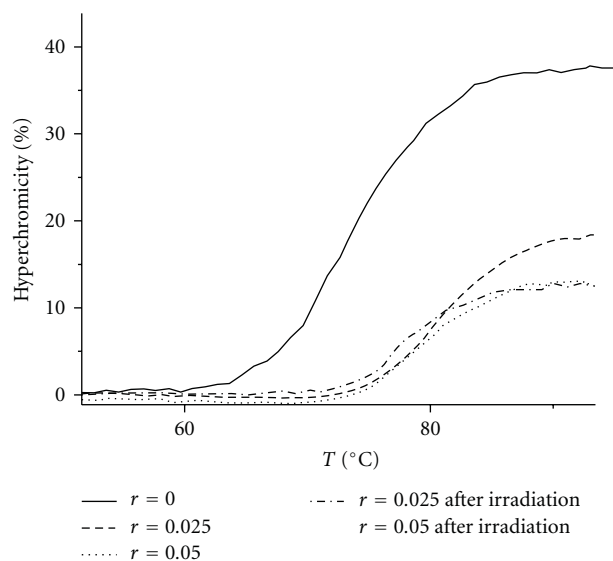


FIGURE 3: Thermal denaturation curves of C.T.-DNA in the presence of the complex ReOCl_3pq before and after irradiation at increasing molar ratios r , $\text{pH} = 7.0$.

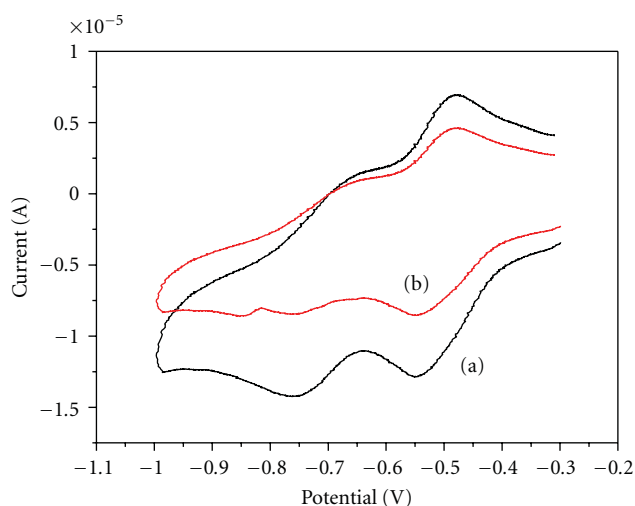


FIGURE 4: Cyclic voltammogram of **1** (0.1 mM). (a) in the absence and (b) in the presence of DNA. Supporting electrolyte 0.1 mM TBABF_4 in DMF.

after the addition of CT DNA to complex **1**, whereas the intensity of all peaks decreased significantly, suggesting the existence of an interaction between **1** and CT DNA. The observed decrease in current can be attributed both to the intercalation of complex **1** into the base pairs of DNA by the planar pq ligand [23, 24] and to an equilibrium mixture of free and DNA-bound complex to the electrode surface [35]. The experimental results are different for **2**, where the current intensity of all the peaks decreased significantly after addition of CT DNA, and for **3** where no changes are observed in its cyclic voltammogram implying that complex **3** does not interact with DNA.

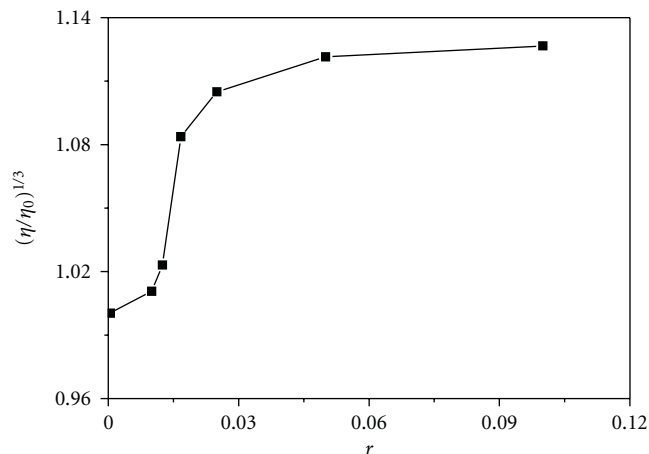


FIGURE 5: Effect of increasing amounts of complex **1** (0–100 μM) on the relative viscosity of CT-DNA (100 μM).

3.3.3. Viscosity Measurements. Optical photophysical probe provides necessary but not sufficient clues to support binding modes [24, 36], whereas hydrodynamic measurements that are sensitive to the length change are regarded as the most critical tests of a binding model in solution. Thus, to further clarify the interaction between **1** and DNA, we carried out viscosity measurements. Because the latter are ionic-strength-and-concentration dependent, we used a buffer of the same ionic strength for all measurements. Figure 5 shows the relative viscosity of DNA (100 μM) in the presence of varying amounts of complex **1**. As we observe, the relative viscosity increases from 0.98 to 1.14 in relative low ratios, $[\text{complex}]/[\text{DNA}]$, while it remains almost constant there after. The observed increase is at the same extent with the one observed when an intercalator is used, for example ethidium bromide—a well known intercalator, at the same ratios as complex **1** [24, 37]. This behaviour suggests that complex **1** intercalates to CT-DNA in accordance with the previous results.

3.3.4. DNA Photocleavage. The ability of complex **1** to cleave DNA upon irradiation was determined by agarose gel electrophoresis [38]. When circular plasmid DNA in the presence of an inorganic molecule is subject to electrophoresis, relatively fast migration will be observed for the intact supercoil form (Form I). If scission occurs on one strand (nicking), the supercoil will relax to generate a slower-moving open circular form (Form II). If both strands are cleaved, a linear form (Form III) that migrates between Forms I and II will be generated [38]. Figure 6 shows gel electrophoresis separation of pBR 322 DNA after incubation with complex **1** and irradiation by visible light ($\lambda > 400 \text{ nm}$) for 1 hour. Complex **1** exhibited concentration-dependent single-strand cleavage of supercoiled Form I into nicked Form II. Control experiment (lane 0) suggests that untreated DNA does not show any cleavage upon irradiation, with increasing concentration of **1** (lanes 1–3); the amount of Form I of pBR322 DNA diminishes gradually, whereas

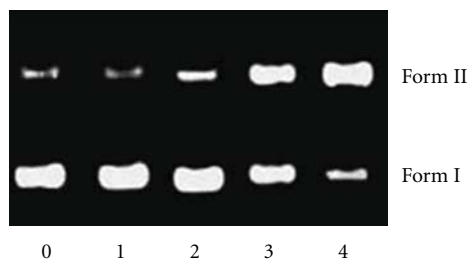


FIGURE 6: Photoactivated cleavage of pBR 322 DNA in the presence of Re(V) complex, light after 60 minutes irradiation at $\lambda > 400$ nm. Lane 0, DNA alone; lanes 1–4, in the different concentrations of complex 1: (1) 0; (2) 20; (3) 40; (4) 60 μ M.

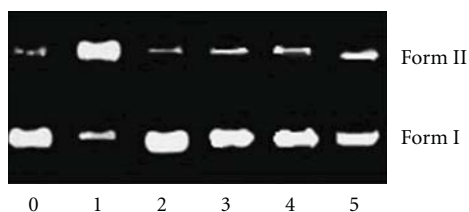


FIGURE 7: Photoactivated cleavage of pBR 322 DNA in the presence of 20 μ M of complex 1 and different inhibitors after irradiation at $\lambda > 400$ nm for 60 minutes. Lane 0, DNA control; lane 1, no inhibitor; lanes 2–6: (2) histidine (5 mM), (3) DMSO (0.2 M), (4) ethanol (0.2 M), (5) sodium formate (5 mM).

that of Form II increases. Under comparable experimental conditions, complex 2 exhibits more effective DNA cleavage activity than complex 1. In order to identify the nature of the reactive species that are responsible for the photo-activated cleavage of the plasmid DNA, we further investigated the influence of different potentially inhibiting agents. In the case of complex 1 (Figure 7), studies with the single oxygen quencher histidine were carried out and the plasmid cleavage was inhibited (lane 2), which confirmed that the singlet oxygen was involved in the cleavage. At the same time, in the presence of different hydroxyl radical scavengers such as DMSO (lane 3), ethanol (lane 4) and sodium formate (lane 5), different degrees of inhibition in the photo-induced cleavage of the plasmid by complex 1 were also observed. This indicates that hydroxyl radical also plays a significant role in the photocleavage mechanism for 1, and the photoreduction of ReO complexes with concomitant hydroxide oxidation is an important step in the DNA cleavage reaction [38].

4. Conclusions

In summary, a new oxorhenium (V) complex namely, $[\text{ReOCl}_3\text{pq}]$ (1) together with its isostructural $[\text{ReOCl}_3\text{bpy}]$ (2) and $[\text{ReOCl}_3\text{phen}]$ (3) has been synthesized and characterized by elemental analyses, FT-IR, UV-Vis spectra, 1D, and 2D NMR, ESI-MS, and CV. The interactions between complexes 1–3 (as well as all *a*-diimine ligands) and calf thymus DNA have been investigated using UV-spectra, thermal denaturation measurements, CV, and viscosity measurements. Furthermore, the photocleavage of the

plasmid pBR 322 DNA has been investigated by agarose gel electrophoresis. Remarkably, our results reveal that both complexes 1 and 2 bind to DNA by intercalation, with the planar diimine (pq or bpy) ligands stacked between the base pairs of the DNA. Complex 1 can efficiently cleave the plasmid pBR 322 DNA, upon irradiation whereas the reactive species responsible for its cleavage are the singlet oxygen and the hydroxyl radical. The thermal stabilization of DNA is reversed to the promoted photocleavage at physiological pH and temperature, indicating the differences in interactions between the base pairs of DNA and the ground or the excited state of the complexes. Similar observations have also been reported for rhenium (I) complexes [39, 40]. These complexes may be useful to probe nucleic acid structures and in the development of DNA agents. More detailed photophysical and biophysical studies designed to address the nature of the interactions of oxorhenium (V) are underway.

Acknowledgment

This work is financially supported by Special Research Account of NKUA. This paper is dedicated to Professor Dr. Nick Hadjiliadis with our best wishes in his retirement.

References

- [1] G. M. Blackburn and M. J. Gait, Eds., *Nucleic Acids in Chemistry and Biology*, Oxford University Press, New York, NY, USA, 1996.
- [2] H. T. Chifotides, K. M. Koshlap, L. M. Perez, and K. R. Dunbar, "Novel binding interactions of the DNA fragment d(pGpG) cross-linked by the antitumor active compound tetrakis(μ -carboxylato)dirhodium(II,II)," *Journal of the American Chemical Society*, vol. 125, no. 35, pp. 10714–10724, 2003.
- [3] A. K. Patra, S. Roy, and A. R. Chakravarty, "Synthesis, crystal structures, DNA binding and cleavage activity of l-glutamine copper(II) complexes of heterocyclic bases," *Inorganica Chimica Acta*, vol. 362, no. 5, pp. 1591–1599, 2009.
- [4] M. L. Kopka, C. Yoon, D. Goodsell, P. Pjura, and R. E. Dickerson, "The molecular origin of DNA-drug specificity in netropsin and distamycin," *Proceedings of the National Academy of Sciences of the United States of America*, vol. 82, no. 5, pp. 1376–1380, 1985.
- [5] M. Coll, C. A. Frederick, A. H. Wang, and A. Rich, "A bifurcated hydrogen-bonded conformation in the d(A.T) base pairs of the DNA dodecamer d(CGCAAATTTGCG) and its complex with distamycin," *Proceedings of the National Academy of Sciences of the United States of America*, vol. 84, no. 23, pp. 8385–8389, 1987.
- [6] M. S. Searle and K. J. Embrey, "Sequence-specific interaction of Hoechst 33258 with the minor groove of an adenine-tract DNA duplex studied in solution by ^1H NMR spectroscopy," *Nucleic Acids Research*, vol. 18, no. 13, pp. 3753–3762, 1990.
- [7] W. Leupin, W. J. Chazin, S. Hyberts, W. A. Denny, and K. Wuthrich, "NMR studies of the complex between the decadeoxynucleotide d-(GCATTAATGC) $_2$ and a minor-groove-binding drug," *Biochemistry*, vol. 25, no. 20, pp. 5902–5910, 1986.

- [8] W. D. Wilson, C. R. Krishnamoorthy, Y.-H. Wang, and J. C. Smith, "Mechanism of intercalation: ion effects on the equilibrium and kinetic constants for the interaction of propidium and ethidium with DNA," *Biopolymers*, vol. 24, no. 10, pp. 1941–1961, 1985.
- [9] C. A. Frederick, L. D. Williams, G. Ughetto, et al., "Structural comparison of anticancer drug-DNA complexes: adriamycin and daunomycin," *Biochemistry*, vol. 29, no. 10, pp. 2538–2549, 1990.
- [10] A. H.-J. Wang, G. Ughetto, G. J. Quigley, and A. Rich, "Interactions between an anthracycline antibiotic and DNA: molecular structure of daunomycin complexed to d(CpGpTpApCpG) at 1.2-Å resolution," *Biochemistry*, vol. 26, no. 4, pp. 1152–1163, 1987.
- [11] G. Sava, R. Gagliardi, A. Bergamo, E. Alessio, and G. Mestroni, "Treatment of metastases of solid mouse tumours by NAMI-A: comparison with cisplatin, cyclophosphamide and dacarbazine," *Anticancer Research*, vol. 19, no. 2, pp. 969–972, 1999.
- [12] J. L. Bear, C.-L. Yao, L.-M. Liu, et al., "Synthesis, molecular structure, and electrochemical properties of two geometric isomers of tetrakis(μ -2-anilinopyridinato)dirhodium complexes," *Inorganic Chemistry*, vol. 28, no. 7, pp. 1254–1262, 1989.
- [13] C. A. Crawford, E. F. Day, V. P. Saharan, et al., " N^7, O^6 bridging 9-ethylguanine (9-EtGH) groups in dinuclear metal-metal bonded complexes with bond orders of one, two or four," *Chemical Communications*, no. 10, pp. 1113–1114, 1996.
- [14] H. T. Chifotides, K. M. Koshlap, L. M. Perez, and K. R. Dunbar, "Unprecedented head-to-head conformers of d(GpG) bound to the antitumor active compound tetrakis(μ -carboxylato)dirhodium(II,II)," *Journal of the American Chemical Society*, vol. 125, no. 35, pp. 10703–10713, 2003.
- [15] S. Monro, J. Scott, A. Chouai, et al., "Photobiological activity of Ru(II) dyads based on (Pyren-1-yl)ethynyl derivatives of 1, 10-Phenanthroline," *Inorganic Chemistry*, vol. 49, no. 6, pp. 2889–2900, 2010.
- [16] C. Metcalfe, M. Webb, and J. A. Thomas, "A facile synthetic route to bimetallic ReI complexes containing two dppz DNA intercalating ligands," *Chemical Communications*, no. 18, pp. 2026–2027, 2002.
- [17] T. W. Jackson, M. Kojima, and R. M. Lambrecht, "Rhenium diamino dithiol complexes. III lipophilic ligands for endotherapeutic radiopharmaceuticals," *Australian Journal of Chemistry*, vol. 53, no. 11–12, pp. 983–987, 2000.
- [18] R. H. Holm, "Metal-centered oxygen atom transfer reactions," *Chemical Reviews*, vol. 87, no. 6, pp. 1401–1449, 1987.
- [19] S. B. Seymore and S. N. Brown, "Charge effects on oxygen atom transfer," *Inorganic Chemistry*, vol. 39, no. 2, pp. 325–332, 2000.
- [20] I. Veroni, C. Makedonas, A. Rontoyianni, and C. A. Mitsopoulou, "An experimental and DFT computational study of a novel zerovalent tetracarbonyl tungsten complex of 2-(2'-pyridyl)quinoxaline," *Journal of Organometallic Chemistry*, vol. 691, no. 3, pp. 267–281, 2006.
- [21] A. Garoufis, A. Koutsodimou, N. Katsaros, C.-A. Mitsopoulou, and N. Hadjiliadis, "Mixed ligand Ru(II) complexes with 2,2'-bipyridine and 2-(2'-pyridyl)quinoxaline," *Polyhedron*, vol. 18, no. 3–4, pp. 361–369, 1998.
- [22] B. Zarranz, A. Jaso, I. Aldana, and A. Monge, "Synthesis and anticancer activity evaluation of new 2-alkylcarbonyl and 2-benzoyl-3-trifluoromethyl-quinoxaline 1,4-di-N-oxide derivatives," *Bioorganic and Medicinal Chemistry*, vol. 12, no. 13, pp. 3711–3721, 2004.
- [23] C. A. Mitsopoulou, C. E. Dagas, and C. Makedonas, "Synthesis, characterization, DFT studies and DNA binding of mixed platinum (II) complexes containing quinoxaline and 1,2-dithiolate ligands," *Journal of Inorganic Biochemistry*, vol. 102, no. 1, pp. 77–86, 2008.
- [24] C. A. Mitsopoulou, C. E. Dagas, and C. Makedonas, "Characterization and DNA interaction of the Pt(II)(pq)(bdt) complex: a theoretical and experimental research," *Inorganica Chimica Acta*, vol. 361, no. 7, pp. 1973–1982, 2008.
- [25] I. Veroni, C. A. Mitsopoulou, and F. J. Lahoz, "Isolation, X-ray structure and properties of an unusual pentacarbonyl(2,2'-pyridyl-quinoxaline) tungsten complex," *Journal of Organometallic Chemistry*, vol. 691, no. 26, pp. 5955–5963, 2006.
- [26] S. Kasselouri, A. Garoufis, A. Katehanakis, G. Kalkanis, S. P. Perlepes, and N. Hadjiliadis, "1:1 metal complexes of 2-(2'-pyridyl)quinoxaline, a ligand unexpectedly formed by the reaction between 2-acetylpyridine and 1,2-phenylenediamine," *Inorganica Chimica Acta*, vol. 207, no. 2, pp. 255–258, 1993.
- [27] J. Chatt and G. A. Rowe, "Complex compounds of tertiary phosphines and a tertiary arsine with rhenium (V), rhenium (III) and rhenium (II)," *Dalton Transactions*, pp. 4019–4024, 1962.
- [28] P. Falaras, C.-A. Mitsopoulou, D. Argyropoulos, et al., "Synthesis, cyclic voltammetric and electrospray mass spectrometric studies of a series of tris-substituted 1,2-dithiolene complexes of tungsten and molybdenum," *Inorganic Chemistry*, vol. 34, no. 18, pp. 4536–4542, 1995.
- [29] M. E. Reichmann, S. A. Rice, C. A. Thomas, and P. Doty, "A further examination of the molecular weight and size of desoxypentose nucleic acid," *Journal of the American Chemical Society*, vol. 76, no. 11, pp. 3047–3053, 1954.
- [30] G. Cohen and H. Eisenberg, "Viscosity and sedimentation study of sonicated DNA-proflavine complexes," *Biopolymers*, vol. 8, pp. 45–49, 1969.
- [31] I. Veroni, A. Rontoyianni, and C. A. Mitsopoulou, "Synthesis and characterization of a novel complex: Mo(CO) 4-[2-(2'-pyridyl)quinoxaline]. An insight based on experimental and theoretical data," *Dalton Transactions*, no. 2, pp. 255–260, 2003.
- [32] B. Machura, R. Kruszynski, M. Jaworska, J. Kłak, and J. Mroziński, "Synthesis, crystal, molecular and electronic structure of [ReOCl₃(phen)] and [ReCl₂(phen)(PPh₃)₂](ReO₄) complexes," *Polyhedron*, vol. 25, no. 13, pp. 2537–2549, 2006.
- [33] H. Mao, Z. Deng, F. Wang, T. M. Harris, and M. P. Stone, "An intercalated and thermally stable FAPY adduct of aflatoxin B1 in a DNA duplex: structural refinement from ¹H NMR," *Biochemistry*, vol. 37, no. 13, pp. 4374–4387, 1998.
- [34] P. K. Ganguli and T. Theophanides, "Premelting phenomenon in DNA caused by the antitumor drug cis-dichlorodiammineplatinum," *Inorganica Chimica Acta*, vol. 55, pp. L43–L45, 1981.
- [35] P. J. Cox, G. Psomas, and C. A. Bolos, "Characterization and DNA-interaction studies of 1,1-dicyano-2,2-ethylene dithiolate Ni(II) mixed-ligand complexes with 2-amino-5-methyl thiazole, 2-amino-2-thiazoline and imidazole. Crystal structure of [Ni(i-MNT)(2a-5mt)₂]," *Bioorganic and Medicinal Chemistry*, vol. 17, no. 16, pp. 6054–6062, 2009.
- [36] D. Lawrence, V. G. Vaidyanathan, and B. U. Nair, "Synthesis, characterization and DNA binding studies of two mixed ligand complexes of ruthenium(II)," *Journal of Inorganic Biochemistry*, vol. 100, no. 7, pp. 1244–1251, 2006.

- [37] D.-L. Ma, C.-M. Che, F.-M. Siu, M. Yang, and K.-Y. Wong, "DNA binding and cytotoxicity of ruthenium(II) and rhenium(I) complexes of 2-amino-4-phenylamino-6-(2-pyridyl)-1,3,5-triazine," *Inorganic Chemistry*, vol. 46, no. 3, pp. 740–749, 2007.
- [38] V. Rajendiran, M. Murali, E. Suresh, S. Sinha, K. Somsundaram, and M. Palaniandavar, "Mixed ligand ruthenium(ii) complexes of bis(pyrid-2-yl)-/bis(benzimidazol-2-yl)-dithioether and diimines: study of non-covalent DNA binding and cytotoxicity," *Dalton Transactions*, no. 1, pp. 148–163, 2008.
- [39] V. W.-W. Yam, K. K.-W. Lo, K.-K. Cheung, and R. Y.-C. Kong, "Deoxyribonucleic acid binding and photocleavage studies of rhenium(I) dipyridophenazine complexes," *Dalton Transactions*, no. 12, pp. 2067–2072, 1997.
- [40] H. D. Stoeffler, N. B. Thornton, S. L. Temkin, and K. S. Schanze, "Unusual photophysics of a rhenium(I) dipyridophenazine complex in homogenous solution and bound to DNA," *Journal of the American Chemical Society*, vol. 117, no. 27, pp. 7119–7128, 1995.

Research Article

Synthetic Peptides as Structural Maquettes of Angiotensin-I Converting Enzyme Catalytic Sites

Zinovia Spyranti,¹ Athanassios S. Galanis,¹ George Pairas,¹ Georgios A. Spyroulias,¹ Evy Manessi-Zoupa,² and Paul Cordopatis¹

¹ Department of Pharmacy, University of Patras, GR-26504, Patras, Greece

² Department of Chemistry, University of Patras, GR-26504, Patras, Greece

Correspondence should be addressed to Georgios A. Spyroulias, g.a.spyroulias@upatras.gr and Paul Cordopatis, pacord@upatras.gr

Received 15 January 2010; Accepted 16 March 2010

Academic Editor: Spyros Perlepes

Copyright © 2010 Zinovia Spyranti et al. This is an open access article distributed under the Creative Commons Attribution License, which permits unrestricted use, distribution, and reproduction in any medium, provided the original work is properly cited.

The rational design of synthetic peptides is proposed as an efficient strategy for the structural investigation of crucial protein domains difficult to be produced. Only after half a century since the function of ACE was first reported, was its crystal structure solved. The main obstacle to be overcome for the determination of the high resolution structure was the crystallization of the highly hydrophobic transmembrane domain. Following our previous work, synthetic peptides and Zinc(II) metal ions are used to build structural maquettes of the two Zn-catalytic active sites of the ACE somatic isoform. Structural investigations of the synthetic peptides, representing the two different somatic isoform active sites, through circular dichroism and NMR experiments are reported.

1. Introduction

Angiotensin Converting Enzyme (ACE) catalyses the conversion of angiotensin-I (AI) to the vasoconstrictor angiotensin-II (AII) [1] and inactivates the vasodilatory peptide bradykinin by removing C-terminal dipeptides [2]. The inhibition of ACE enzymatic activity against AI was considered as one of the major challenges against hypertensive disease and congestive heart failure [3]. Over the past 20 years, ACE inhibitors have presented significant cardioprotective and vasculoprotective activity, by reducing oxidative stress and inflammation in the endothelium. Moreover, ACE inhibitors have been effective in improving blood flow and flow-mediated vasodilation. Inhibition of the angiotensin converting enzyme significantly reduces cardiovascular risk in a broad range of high-risk patients [4, 5].

ACE is a Zinc Metallopeptidase and one of the major components of the Renin-Angiotensin System (RAS) that regulates blood pressure [6–8]. In human, ACE is expressed as a somatic isoform in endothelial, epithelial, and neuroepithelial cells and as a smaller isoform only in male

germinal cells. Somatic ACE (1306 AA, 150 kDa) consists of two homologous domains, one at each terminal, containing zinc catalytic sites (N- and C-zinc catalytic sites) [9]. The testis isoform is composed of 732 residues (83 kDa) with the 665-residue C-terminal domain being identical to the C-terminal domain of the somatic form [10–13]. Both isoforms possess a zinc-binding domain, with the somatic isoform containing one additional high homology active site (N-catalytic site). ACE active sites possess the characteristic HEXXH Zn-binding motif (the two His comprise the first two Zn-ligands) and falls into the gluzincin family [14]. The third Zn ligand, glutamic acid, is sited 23 residues towards the enzyme C-terminal at the second characteristic sequence EAXGD [15]. The fourth zinc ligand is a water molecule.

In subsequent to our previous work [16, 17], novel synthetic peptides have been investigated as structural maquettes, in order to shed further light on the conformational characteristics of both somatic isoform catalytic site domains.

Design, peptide synthesis, and a thorough investigation of the optimal conditions in order to mimic as closely



FIGURE 1: Synthetic peptide maquettes of the N- and C- active site domains of human somatic ACE (sACE). Sequence numbering of peptides, sACE, testis isoform (tACE) and crystal structures domains. The different residues among the two sequences are highlighted.

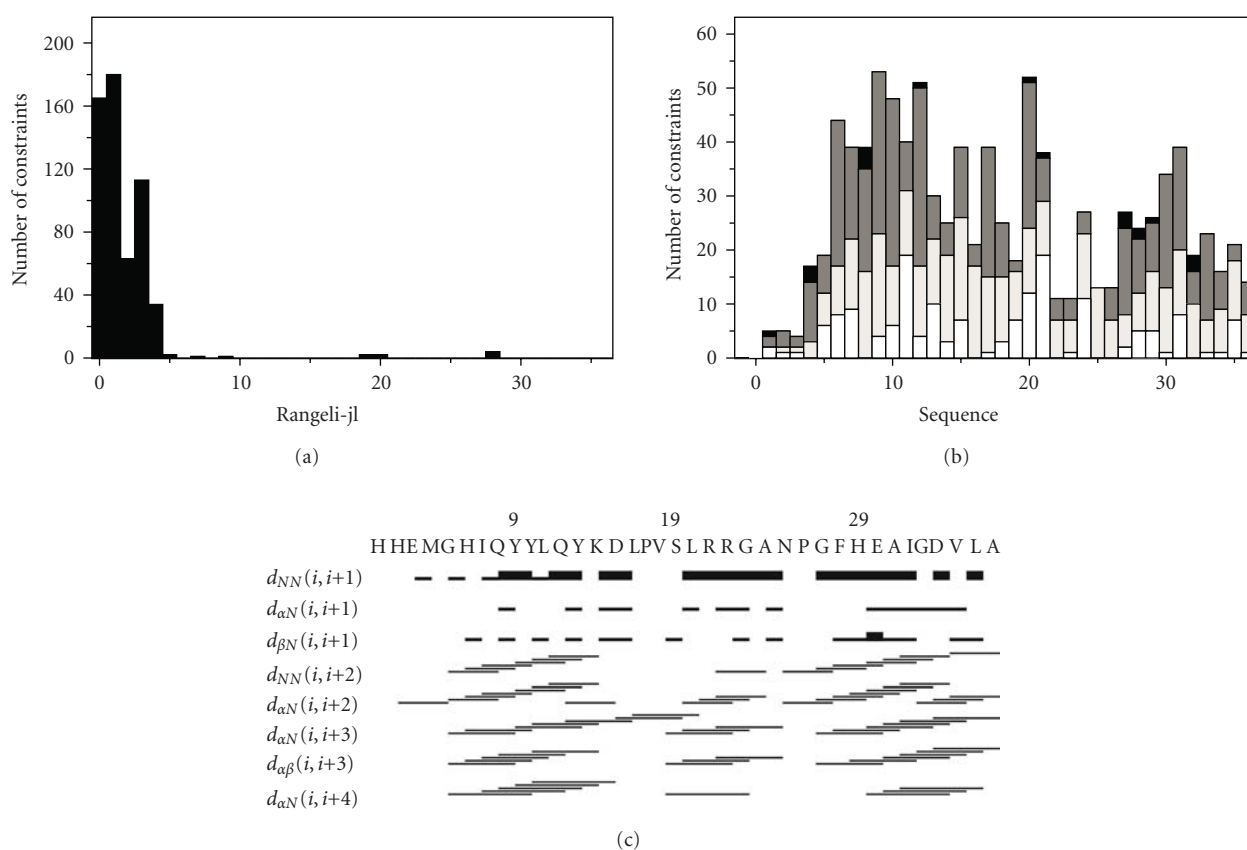


FIGURE 2: (a) Short-, medium-, and long-range connectivities. (b) Number of NOE constraints per residue (white, gray, dark gray, and black vertical bars represent, resp., intraresidue, sequential, medium-range and long-range connectivities). (c) Schematic representation of the sequential and medium range NOEs involving HN, H α , and H β protons for Zn²⁺-ACE_N(37) (corresponds to His³⁶⁰-Ala³⁹⁶ of the human somatic form).

as possible the structure of the enzyme native active sites are reported. The peptide structures have been determined through circular dichroism and NMR experiments.

The conformational differences of the peptide maquettes representing the two sACE active sites have been also investigated. Moreover, the NMR solution structures of the peptides are being compared to the crystal structure of somatic ACE_N active site [18] and the testis ACE isoform (tACE) [19] that corresponds to the somatic ACE_C domain.

In general, we report herein a work, which exploits the potential of peptide chemistry to synthesize polypeptides that represent protein domains or functional fragments and applies a step-by-step investigation strategy able to extract crucial structural data, especially for the metal active sites of enzymes/proteins or others biopolymers, whose biological expression and crystallization are difficult to be acquired, such as GPCRs and highly hydrophobic transmembrane proteins.

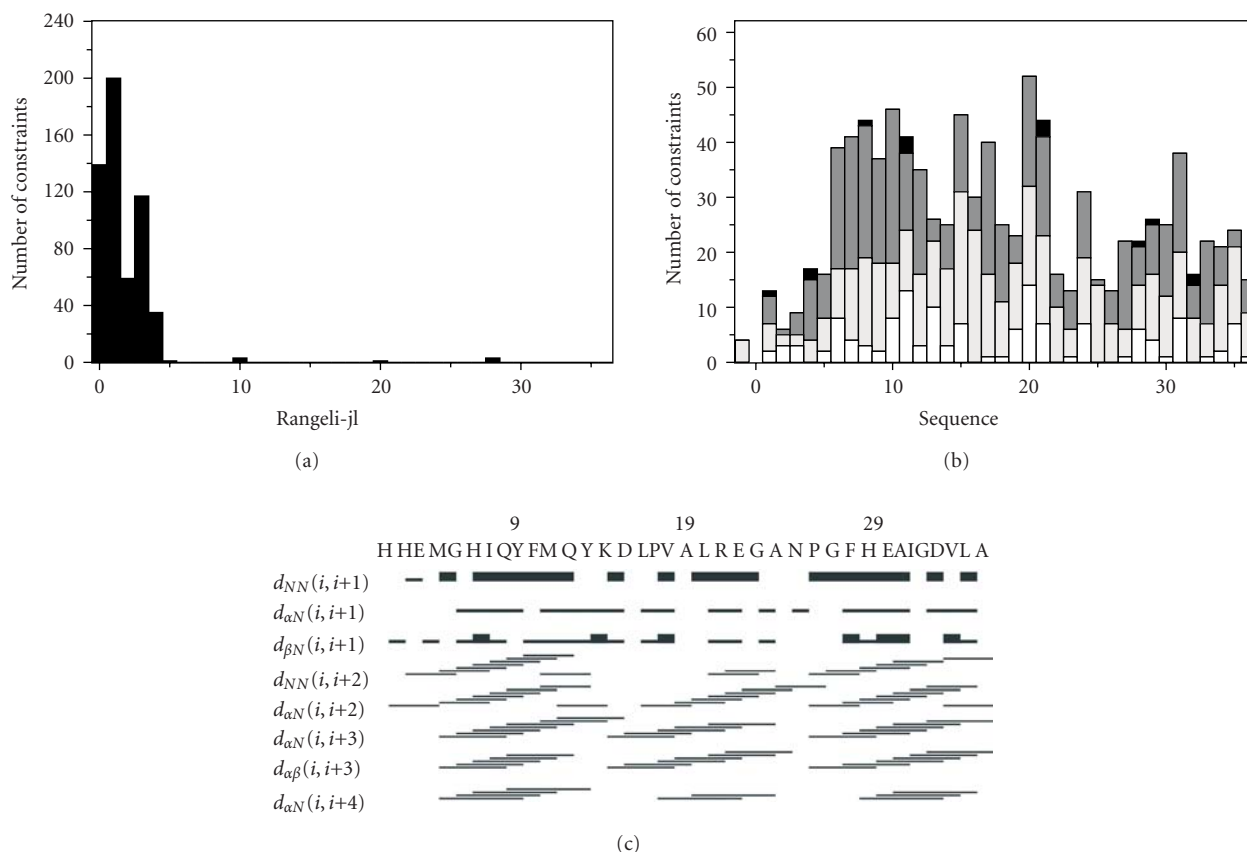


FIGURE 3: (a) Short-, medium-, and long-range connectivities. (b) Number of NOE constraints per residue (white, gray, dark gray, and black vertical bars represent, resp., intraresidue, sequential, medium-range, and long-range connectivities). (c) Schematic representation of the sequential and medium range NOEs involving HN, H α , and H β protons for Zn²⁺-ACE_C(37) (corresponds to His⁹⁵⁸-Ala⁹⁹⁴ of the human somatic form).

2. Materials and Methods

2.1. Peptide Synthesis. Both peptides representing the domains of the two somatic ACE (sACE) active sites ACE_N(37): sACE(360–396); ACE_C(37): sACE(958–994) were synthesized on solid support by Fmoc/tBu chemistry, as previously described [15]. Sequence enumeration of the synthetic peptides and the corresponding domains of the human somatic isoform as well as the numbering of the C- (tACE) and N-domain (ACE_N) crystal structures are shown in Figure 1.

2.2. Circular Dichroism Experiments. CD experiments were acquired for both ACE_N(37) and ACE_C(37) peptides, monitoring the effect of different trifluoroethanol (TFE) concentration, pH values, and Zn²⁺ addition on their conformations. Spectra were recorded on a Jasco 710 spectropolarimeter using quartz cells of 1.0 cm and 0.5 cm path length, in the far-UV (200 nm–260 nm) at a scanning rate of 100 nm/min, a time constant of 1 s, and a bandwidth of 1 nm. Spectral resolution was 0.2 nm, and 4 scans were averaged per spectrum.

The concentration used for each sample was 0.3–0.35 mg/ml of pure peptide in a buffer of 50 mM Tris-HCl

and 200 mM NaCl. The effect of TFE on the peptide conformation was monitored for 0%–100% TFE (v/v), 25 °C, and pH = 7.0. Spectra of different pH values ranging from 2.6 to 7.0 were recorded for the Zn-containing ACE_N(37) peptide, at 65% TFE and 25 °C. Quantitative evaluation of secondary structure according to the CD data was calculated using the CDNN CD Spectra Deconvolution Program obtained from <http://bioinformatik.biochemtech.unihalle.de/cdnn/> [20]. The CD spectra are reported in molar ellipticity as mdeg × cm²/dmol according to molecular masses and peptide length.

2.3. Nuclear Magnetic Resonance Experiments. 5 mg of peptide samples were dissolved in a mixture of 65% TFE in H₂O, containing 50 mM Tris buffer and 200 mM NaCl. ZnCl₂ was added in a slight excess of the peptide equivalents (1:1.1) until 0.5 ml final sample volume, with the peptide concentration being approximately 2 mM at pH value 4.9–5.1.

Data were acquired at 298 K on a Bruker Avance 600 MHz spectrometer. ¹H 1D NMR spectra were recorded using spectral width of 12–17 ppm with or without presaturation of the H₂O signal. ¹H-¹H 2D TOCSY [21, 22] were recorded using the MLEV-17 spin lock sequence using $\tau_m = 80$ ms.

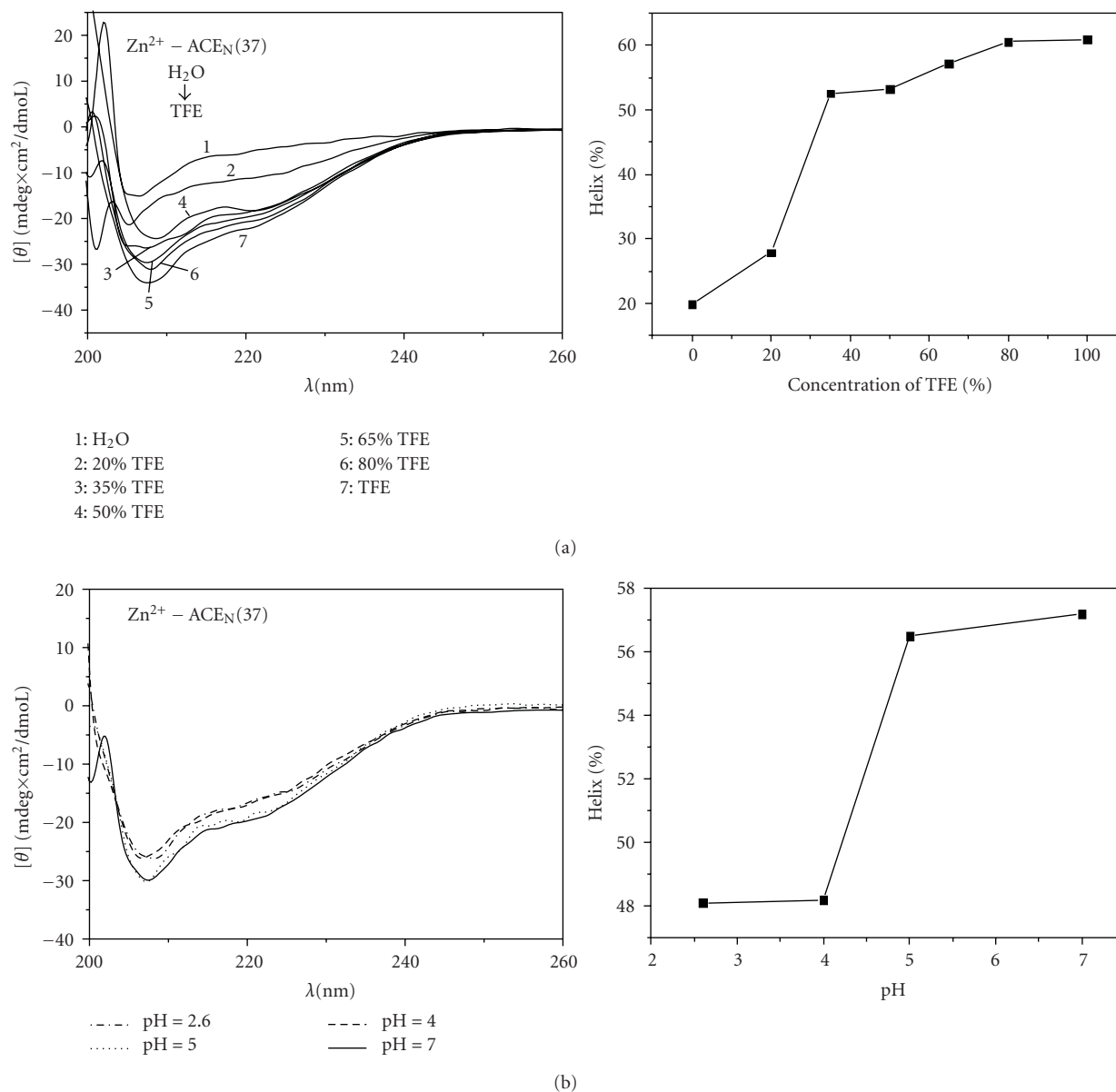


FIGURE 4: Circular dichroism spectra (left) and corresponding diagrams (right) of helical content through data analysis by CDNN software of (a) 2,2,2-trifluoroethanol (TFE) range from 0% to 100% of Zn^{2+} -ACE_N(37) samples, at pH = 5.0, $T = 25^\circ\text{C}$, 50 mM Tris-HCl, and 200 mM NaCl and (b) of pH range from 2.6 to 7 of Zn^{2+} -ACE_N(37) samples, at 65% TFE, $T = 25^\circ\text{C}$, 50 mM Tris-HCl, and 200 mM NaCl.

¹⁵N HSQC and ¹³C HSQC spectra [23, 24] have been recorded at 500 MHz equipped with cryoprobe for ¹⁵N/¹³C nuclei in natural abundance. ¹H-¹H TPPI NOESY [25, 26] spectra were acquired using mixing time $\tau_m = 200$ ms applying water suppression during the relaxation delay and mixing time. For data processing and spectral analysis, the standard Bruker software (XWIN-NMR 3.5) and XEASY program [27] (ETH, Zurich) were used.

1318 and 1578 NOESY cross-peaks were assigned in both dimensions for ACE_C(37), and ACE_N(37), respectively, in TFE aqueous solution (TFE/H₂O 2:1). The number of unique cross-peaks was 753 and 773 for ACE_C(37) and ACE_N(37), respectively. Their intensities were converted into upper limit distances through CALIBA [28]. The NOE-

derived structural information extracted from the analysis of NOESY spectra acquired in aqueous TFE solutions under identical experimental conditions for both peptides were introduced to DYANA [29, 30] software for structure calculation (Figures 2 and 3). Structural calculations have been performed on IBM RISC6000 and xw4100/xw4200 HP Linux workstations. The family ensemble of Zn^{2+} -ACE_N(37) peptide presents root mean square deviation (RMSD) values of $0.65 \pm 0.21 \text{ \AA}$ and $1.25 \pm 0.24 \text{ \AA}$ for backbone and heavy atoms, respectively, and the average target function was found to be $0.39 \pm 0.0164 \text{ \AA}^2$. The RMSD values of the Zn^{2+} -ACE_C(37) peptide were $0.55 \pm 0.23 \text{ \AA}$ and $1.04 \pm 0.27 \text{ \AA}$ for backbone and heavy atoms, respectively, and target function lies in the range $0.60 \pm 4.78 \times 10^{-2} \text{ \AA}^2$.

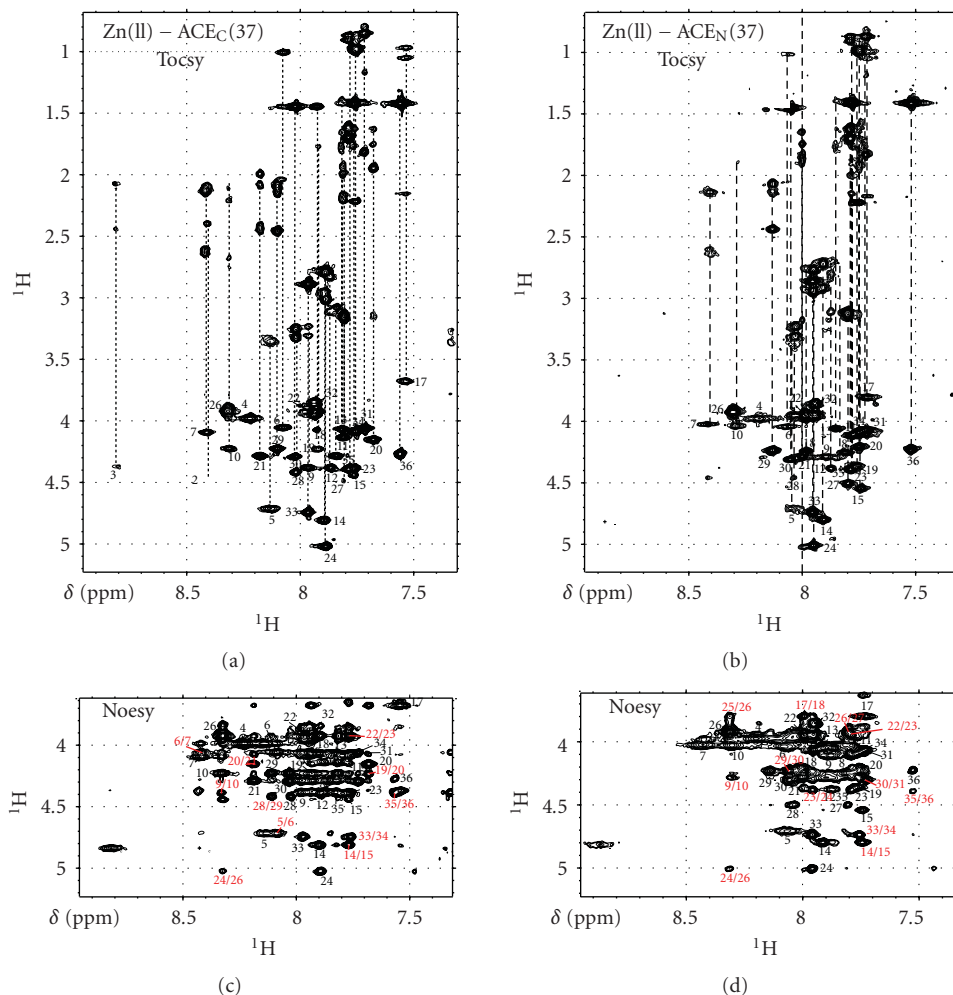


FIGURE 5: Fingerprint regions of 600 MHz TOCSY ((a) ACE_C(37) and (b) ACE_N(37)) and NOESY ((c) ACE_C(37) and (d) ACE_N(37)) spectra recorded at $T = 298$ K. The sequential connectivity pattern shown indicates the peptide sequence-specific resonance assignment.

3. Results and Discussion

3.1. α -Helix Content Measurements through Circular Dichroism Data. The Circular Dichroism (CD) experiments provided a qualitative determination of the peptide secondary structure elements in different TFE concentrations, pH values, and metal addition, leading to the determination of high resolution experimental conditions (Figure 4).

Specifically, the Zn²⁺-ACE_N(37) peptide presents an unfolded structure with low α -helical content in aqueous solution. Low TFE concentrations (up to 20%) do not seem to have major effect on the peptide conformation (Figure 4(a)). However, the CD spectrum of the sample containing 35% TFE shows two intense minima at 208 and 220 nm, characteristics of α -helical structure. Thus, for TFE concentration ranging from 20% to 35%, an abrupt structural change takes place, leading to a dramatical increase of α -helix content from 26% to 52%. At higher TFE concentrations (50%–100%), no remarkable alteration of the helical content is noticed. In more detail, the α -helical content is increased from 54% to 60%, for TFE

concentration increasing from 50% to 100%, indicating secondary structure stability of the Zn²⁺-ACE_N(37) peptide at alcohol concentration greater than 50%. Similar results were obtained for the Zn²⁺-ACE_C(37) peptide (data not shown). As a conclusion, the synthetic peptides exhibit a remarkable tendency to adopt helical conformation.

In order to investigate the pH effect on the α -helical content of the Zn²⁺-ACE_N(37) peptide, CD measurements were performed in 65% of TFE at 25°C, at acidic, low acidic, and neutral pH values. Spectra representing two sets of pH values nearly overlap, thus suggesting that the secondary structure of ACE peptides exhibit minor differences at these pH values (Figure 4(b)). In particular, at acidic (pH 2.6) and mild acidic (pH 4.0) conditions, the Zn-containing ACE_N(37) solutions possess approximately 48% α -helical content while at pH values of 5.0 and 7.0, the helicity of the ACE_N(37) in the presence of Zn²⁺ ions is found to be approximately 57.0%.

3.2. NMR Spectra Assignment of Zn²⁺-ACE_N(37) and Zn²⁺-ACE_C(37) Peptides. Thirty-six out of 37 residues of the

TABLE 1: ^1H , ^{15}N , and ^{13}C chemical shifts (ppm) of the residues in the Zn^{2+} -ACE_N(37) peptide at 298K (H₂O/TFE-*d*2 34%/66% v/v, pH = 4.9).

Residue	HN/N	Ha/Cα	Hβ/Cβ	Other	
1	His		4.45	Hδ2 7.30; Hε18.44	
		55.39		Cδ 120.02 Cε1 139.44	
2	His	7.99	4.84	3.38/3.29	Hδ2 7.32; Hε1 8.45
	N 117.01	55.84	28.45	Cδ2 120.05 Cε1 137.64	
3	Glu	8.45	4.47	2.15/2.14	γCH ₃ 2.65/2.62
	N 121.15	56.81	31.91	Cγ 31.90	
4	Met		4.35	2.13/2.09	Hγ 2.49/2.44
		57.51	33.70	Cγ 34.78	
5	Gly	8.22	3.98		
	N 109.59	45.79			
6	His	8.22	4.72	3.41/3.39	Hδ2 7.26; Hε1 8.50
	N 119.31	57.08	28.57	Cδ 119.93 Cε1 136.27	
7	Ile	8.11	4.05	2.07	Hγ 1.70/1.32; γCH ₃ 1.03 δCH ₃ 0.98
	N 122.73	64.30	38.04	Cγ1 28.30 Cγ2 16.79 Cδ 12.22	
8	Gln	8.47	4.03	2.14/2.11	Hγ 2.44; δNH ₂ 6.55/7.14
	N 120.70	59.13	28.91	Cγ 33.65 Nε2 110.97	
9	Tyr	7.84	4.26	3.12	Hδ 6.96; Hε 6.75;
	N 120.77	60.88	38.03	Cδ1 133.66 Cε1 117.77	
10	Tyr	7.87	4.29	3.26/3.22	Hδ 7.19; Hε 6.89;
	N 120.23.	60.82	38.11	Cδ1 132.73 Cε1 117.87	
11	Leu	8.34	4.04	1.99/1.91	Hγ 1.53; δCH ₃ 0.94
	N 119.99	57.26	41.69	Cγ 28.36 Cδ 21.77/24.48	
12	Gln	7.81	4.11	2.01/1.91	Hγ 2.24/2.16; δNH ₂ 6.42/6.99
	N 118.28	57.58	28.81	Cγ 33.54 Nε2 110.97	
13	Tyr	7.91	4.38	3.10/2.82	Hδ 7.00; Hε 6.76
	N 120.43	59.51	35.59	Cδ1 132.82 Cε1 117.83	
14	Lys	7.90	4.06	1.82/1.79	Hγ 1.39; δCH ₃ 1.63; εCH ₃ 3.03
	N 120.21	57.55	31.61	Cγ 23.71 Cδ 28.57 Cε 42.06	
15	Asp	7.93	4.80	2.92/2.76	
	N 118.92	53.56	39.48		
16	Leu	7.76	4.54	1.79	Hγ1.58; δCH ₃ 0.94/0.94
	123.89	54.95	41.64	Cγ 28.43 Cδ 23.05/24.36	
17	Pro		4.45	2.39/1.95	Hγ 2.02/1.97; Hδ 3.88/3.64
		63.27	31.32	Cγ 26.69 Cδ 50.27	
18	Val	7.74	3.79	2.17	γCH ₃ 1.06/1.01
	N 120.40	65.07	31.81	Cγ 20.89/20.12	
19	Ser	8.02	4.23	3.99/3.95	
	N 116.85	60.48			
20	Leu	7.82	4.36	1.77	Hγ 1.68; δCH ₃ 0.94/0.89
	N 122.93	56.20	41.96	Cγ 28.50 Cδ 22.29/24.73	
21	Arg	7.77	4.20	1.93	Hγ 1.76/1.65; Hδ 3.20; Hε 7.05
	N 120.34	57.49	30.15	Cγ 26.99 Cδ 43.13 Nε 135.56	
22	Arg	8.05	4.28	1.89/1.85	Hγ 1.75/1.64; Hδ 3.17; Hε 7.15
	N 121.00	57.05	30.14	Cγ 26.92 Cδ 43.07 Nε 135.62	
23	Gly	8.00	3.95		
	N 109.07	45.43			
24	Ala	7.81	4.39	1.43	
	N 124.37	52.21	19.05		
25	Asn	7.98	5.02	2.96/2.79	δNH ₂ 6.63/7.47
	N 119.26	51.13	39.17	Nδ2 113.31	
26	Pro		4.44	2.32/1.98	Hγ 2.07/2.00; Hδ 3.92/3.83
		61.79	29.10	Cγ 26.76 Cδ 50.28	

TABLE 1: Continued.

Residue	HN/N	Ha/C α	H β /C β	Other
27	Gly	8.34 N 108.58	3.94 43.10	
28	Phe	7.83 N 122.56	4.50 56.50	3.15/3.13 H δ 7.25; H ϵ 7.29; H ζ 7.18 Cδ 130.90/129.60 Cϵ 130.95/129.53 Cζ 131.21
29	His	8.05 N 119.37	4.44 54.41	3.32/3.25 H δ 7.31; H ϵ 8.51 Cδ 119.91 Cϵ 139.03
30	Glu	8.15 N 121.57	4.23 54.73	2.15/2.10 γ CH ₃ 2.45 Cγ 33.54
31	Ala	8.07 N 125.19	4.31 51.07	1.46 15.87
32	Ile	7.76 N 118.79	4.06 61.44	1.83 35.60 H γ 1.44/1.18; γ CH ₃ 0.88; δ CH ₃ 0.82 Cγ 27.34 Cγ 2 16.84 Cδ 12.08
33	Gly	7.96 N 110.69	3.95/3.87 43.26	
34	Asp	7.97 N 120.70	4.74 51.72	2.89 36.82
35	Val	7.78 N 120.34	4.08 60.78	2.23 29.97 γ CH ₃ 1.00 Cγ 20.31/24.50
36	Leu	7.82 N 122.65	4.40 52.58	1.72 39.65 H γ 1.38; δ CH ₃ 0.92/0.88 Cγ 27.26 Cδ 24.16/22.01
37	Ala	7.56 N 128.06	4.25 50.34	1.43 16.51

backbone of both Zn²⁺-ACE peptides have been identified through the analysis of the TOCSY spectra (Figure 5). ¹H spin systems of the His, Phe and Tyr aromatic rings were identified with the combined use of [¹H-¹H]-TOCSY and NOESY spectra (Tables 1 and 2). The two proline residues existing in each construct were found to be at *trans* conformation for both peptides manifested by strong H δ (i)Pro- H α (i-1) NOE connectivities.

3.3. NMR Solution Models of Zn²⁺-ACE_N(37) & Zn²⁺-ACE_C(37) Peptides. As far as the N-terminal Zn-binding motif of ACE_N(37) peptide, which contains the two histidyl ligands, is concerned, no definite conformation could be determined due to conformational averaging. A 7-residue fragment close to the N-terminal (Gln⁸-Asp¹⁵) adopts helical structure, which consists partly of an α -helix for the 8-11 fragment and of a short ₃₁₀-helix for the rest of the four-residue segment. A second fragment comprised of 7 residues close to peptide C-terminal (His²⁹-Leu³⁶) adopts a well formed α -helical structure. As far as the intermediate fragment of the 23-residue spacer between the two binding motifs is concerned, no helical conformation has been identified. The proximity of the two “active sites helices” is manifested by long-range NOEs concerning backbone and side-chain protons of His²-Glu³⁰, Gly⁵-Gly³⁴, Tyr⁹-Phe²⁸ see (Figure S1) in Supplementary Material available online at doi: 10.1155/2010/820476, as well as Tyr⁹-His³⁰ (Figure 6).

The Zn²⁺-ACE_C(37) backbone is characterized by the high content of helical structure. Two helical conformations were observed at both N- and C-termini, spanning residues

His⁶-Lys¹⁴ and Phe²⁸-Val³⁵, respectively. Moreover, a ₃₁₀-helix comprised of a 5-residue segment (Ala¹⁹-Gly²³) has been identified for the intermediate fragment. In accordance with the Zn²⁺-ACE_N(37) peptide, the two zinc-binding motifs of Zn²⁺-ACE_C(37) are in spatial proximity as manifested by long-range NOEs, such as those between His⁶/Ile⁷ and His²⁹ as well as Gln⁸/Gln¹² with Ala¹⁹ (Figure 7).

3.4. Solution Structure of Zn²⁺-ACE_N(37) versus Zn²⁺-ACE_C(37). Although the overall fold of the two Zn²⁺-ACE peptides exhibits significant similarities, some striking differences, mainly related to the helical extent are detected (Figure 8). The double substitution of Tyr¹⁰ and Leu¹¹ in ACE_N(37) with Phe¹⁰ and Met¹¹ in ACE_C(37) does not impose any structural change, and the α -helix conformation of this segment remains. The nonhelical character of the N-terminal pentapeptide, which comprises the first Zn²⁺-binding motif, followed by a helical domain of eight to nine residues is conserved in both ACE peptides. However, small differences in NOEs are observed, regarding residues Ile⁷, Phe¹⁰/Tyr¹⁰, and Leu¹¹/Met¹¹ in ACE_N(37) and ACE_C(37) peptide, respectively. Because of the differentiation in position 10, the long range NOEs of the vicinal Tyr⁹ with Phe²⁸ and His²⁹ that are presented in ACE_N(37) peptide, are not detected in ACE_C(37). Furthermore, a long-range NOE between H ϵ of Arg²¹ and H ϵ of Phe²⁸ detected only in Zn²⁺-ACE_N(37) peptide suggests the existence of a loop with the two residues coming close to each other, confirming a tertiary slight structural difference among the two peptides in terms of the orientation of the two zinc-binding motif

TABLE 2: ^1H , ^{15}N , and ^{13}C chemical shifts (ppm) of the residues in the Zn^{2+} -ACE_C(37) peptide at 298K ($\text{H}_2\text{O}/\text{TFE-d}_2$ 34%/66% v/v. pH = 4.9).

Residue	HN/N	H α /C α	H β /C β	Other
1	His		4.44 55.45	H δ 2 7.34; H ϵ 1 8.48 Cδ2 120.14 Cϵ1 141.76
2	His	7.92 N 117.71	4.83 55.86	3.41/3.37 28.53 H δ 27.31; H ϵ 18.42 Cδ2 119.85 Cϵ1 136.29
3	Glu	8.44 N 121.00	4.47 56.93	2.15 31.82 γCH_3 2.64 C γ 31.95
4	Met		4.30 58.52	2.12/2.06 33.59 H γ 2.44; C γ 34.85
5	Gly	8.22 N 109.22	3.98 45.83	
6	His	8.22 N 119.42	4.69 57.33	3.39 28.64 H δ 27.25; H ϵ 1 8.50 Cδ2 119.79 Cϵ1 138.23
7	Ile	8.06 N 122.46	4.04 64.13	2.07 38.09 H γ 1.71/1.31; γCH_3 1.03 δCH_3 0.97 Cγ1 28.41 Cγ2 16.81 Cδ 12.18
8	Gln	8.44 N 121.01	4.08 59.04	2.15/2.11 28.57 H γ 2.42; δNH_2 6.54/7.13 C γ 33.52 Nϵ2 110.83
9	Tyr	7.90 N 120.96	4.27 61.02	3.12 38.21 H δ 6.95; H ϵ 6.76 Cδ1 132.67 Cϵ1 117.74
10	Phe	8.07 N 120.42	4.37 60.74	3.33/3.26 38.84 H δ 7.31; H ϵ 7.37 H ζ 7.34 Cδ 131.03/129.50 Cϵ 131.00/129.43 Cζ 131.36
11	Met	8.43 N 118.65	4.21 57.43	2.23/2.15 33.58 H γ 2.79/2.72 C γ 32.35
12	Gln	7.81 N 118.68	4.14 57.74	2.00/1.90 28.75 H γ 2.22/2.17; δNH_2 6.40/6.70 C γ 33.50 Nϵ2 110.86
13	Tyr	7.92 N 120.02	4.38 59.46	3.13/2.82 39.33 H δ 7.00; H ϵ 6.74 Cδ 132.81 Cϵ 117.84
14	Lys	7.85 N 120.09	4.05 57.76	1.78/1.81 31.58 H γ 1.39; δCH_3 1.64; ϵCH_3 3.05 C γ 23.68 Cδ 28.76 Cϵ 42.19
15	Asp	7.90 N 118.79	4.83 53.53	2.93/2.77 39.51
16	Leu	7.78 123.98	4.46 56.77	1.79 41.25 H γ 1.77; δCH_3 0.943/0.97 C γ 26.83 Cδ 23.25/24.05
17	Pro		4.39 64.61	2.41/1.89 31.21 H γ 2.11/2.07; H δ 3.66/3.87 C γ 26.79 Cδ 50.16
18	Val	7.60 N 120.40	3.68 65.47	2.17 31.77 γCH_3 1.07/0.98 C γ 20.23/21.25
19	Ala	7.94 N 123.38	4.08 54.68	1.46 18.08
20	Leu	7.95 N 123.48	4.25 56.69	1.78 41.91 H γ 1.63; δCH_3 0.92/0.89 C γ 27.43 Cδ 22.06/24.33
21	Arg	7.70 N 120.14	4.15 57.82	1.96 30.09 H γ 1.75/1.63; H δ 3.15; H ϵ 7.06 C γ 26.80 Cδ 42.96 Nϵ 135.38
22	Glu	8.23 N 119.39	4.30 57.01	2.10/2.00 28.25 γCH_3 2.46/2.42 C γ 33.01
23	Gly	7.95 N 108.22	3.93 45.70	
24	Ala	7.78 N 123.97	4.40 52.25	1.45 18.47
25	Asn	7.90 N 118.78	5.03 51.01	3.03/2.81 39.09 δNH_2 6.61/7.50 Nδ2 113.04

TABLE 2: Continued.

Residue	HN/N	Ha/C α	H β /C β	Other	
26	Pro	8.34 N 108.27	4.45 64.33	2.35/2.01 31.50	H γ 2.07/2.02; H δ 3.91/3.85 C γ 26.84 C δ 50.43
27	Gly	7.83 N 122.54	3.94 45.73	3.16 39.20	H δ 7.24; H ϵ 7.28; H ζ 7.15 C δ 130.90/129.43 C ϵ 130.94/129.55 C ζ 131.15
28	Phe	8.03 N 118.86	4.40 57.20	3.32/3.28 28.38	H $\delta 2$ 7.33; H $\epsilon 1$ 8.51 C $\delta 2$ 119.94 C $\epsilon 1$ 135.99
29	His	8.15 N 121.32	4.22 57.33	2.16/2.12 27.91	γ CH $_3$ 2.46 C γ 33.66
30	Glu	8.05 N 124.86	4.28 53.62	1.47 18.02	
31	Ala	7.75 N 118.32	4.05 64.06	1.89 38.03	H γ 1.41/1.18; γ CH $_3$ 0.85; δ CH $_3$ 0.80 C $\gamma 1$ 27.29 C $\gamma 2$ 16.80 C δ 12.02
32	Ile	7.94 N 110.35	3.90/3.86 45.81		
33	Gly	7.97 N 120.63	4.74 54.30	2.88 39.45	
34	Asp	7.77 N 120.04	4.08 63.48	2.24 32.45	γ CH $_3$ 0.99 C γ 20.23/23.01
35	Val	7.83 N 125.55	4.39 55.14	1.71 42.14	H γ 1.63; δ CH $_3$ 0.92/0.88 C γ 28.74 C δ 24.36/21.98
36	Leu	7.55 N 128.05	4.24 52.89	1.43 19.23	
37	Ala				

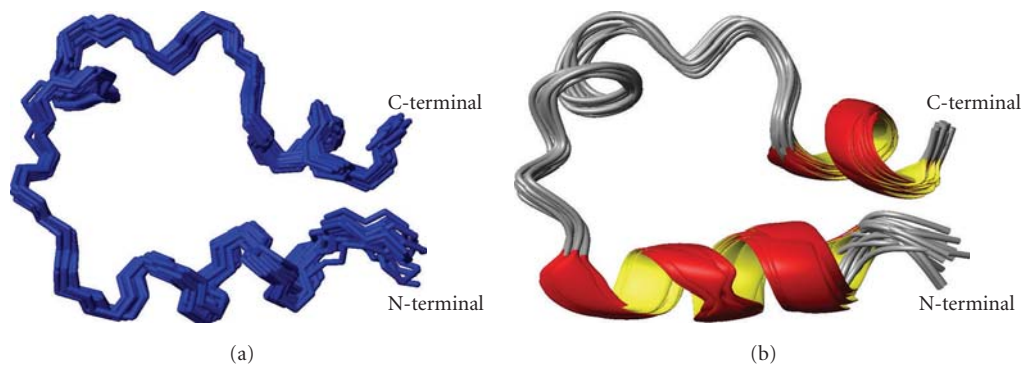


FIGURE 6: (a) Ensemble of DYANA 30 best models of the Zn²⁺-ACE_N(37) (corresponds to His³⁶⁰-Ala³⁹⁶ of the human somatic form) calculated with NMR data. (b) Ribbon diagram of Zn²⁺-ACE_N(37) peptide.

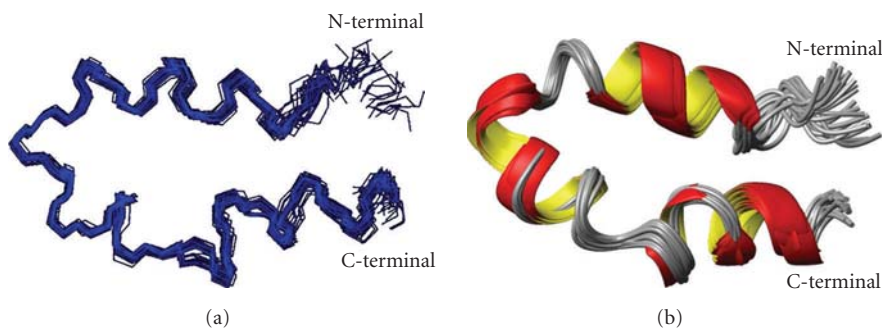


FIGURE 7: (a) Ensemble of DYANA 30 best models of the Zn²⁺-ACE_C(37) (corresponds to His⁹⁵⁸-Ala⁹⁹⁴ of the human somatic form), calculated with NMR data. (b) Ribbon diagram of Zn²⁺-ACE_C(37) peptide.

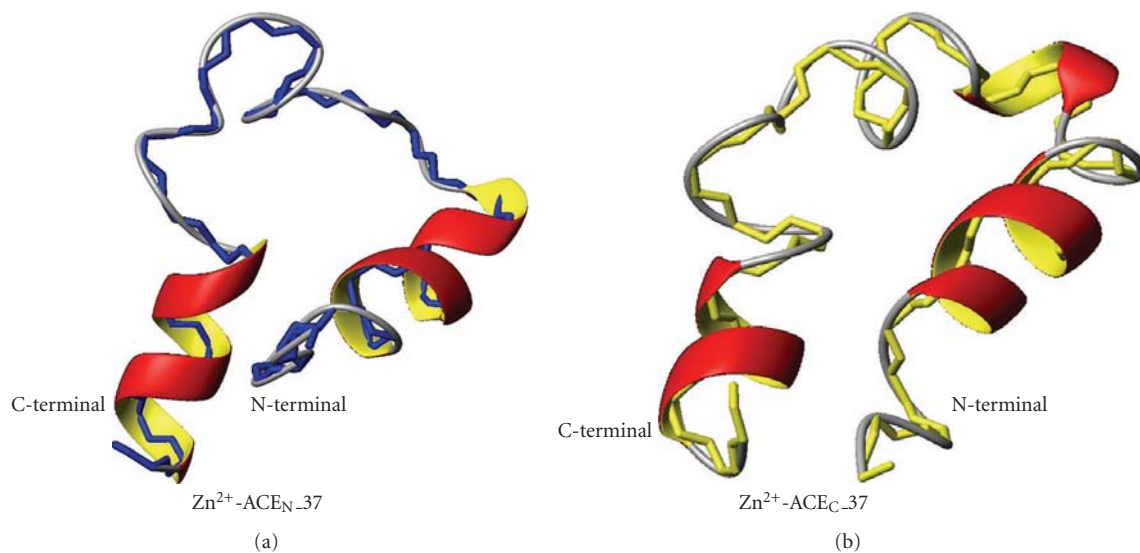


FIGURE 8: Backbone and ribbon representation of the solution structures of both Zn²⁺-ACE_N(37) (a) (corresponds to His³⁶⁰-Ala³⁹⁶ of the human somatic form) and Zn²⁺-ACE_C(37) (b) (corresponds to His⁹⁵⁸-Ala⁹⁹⁴ of the human somatic form).

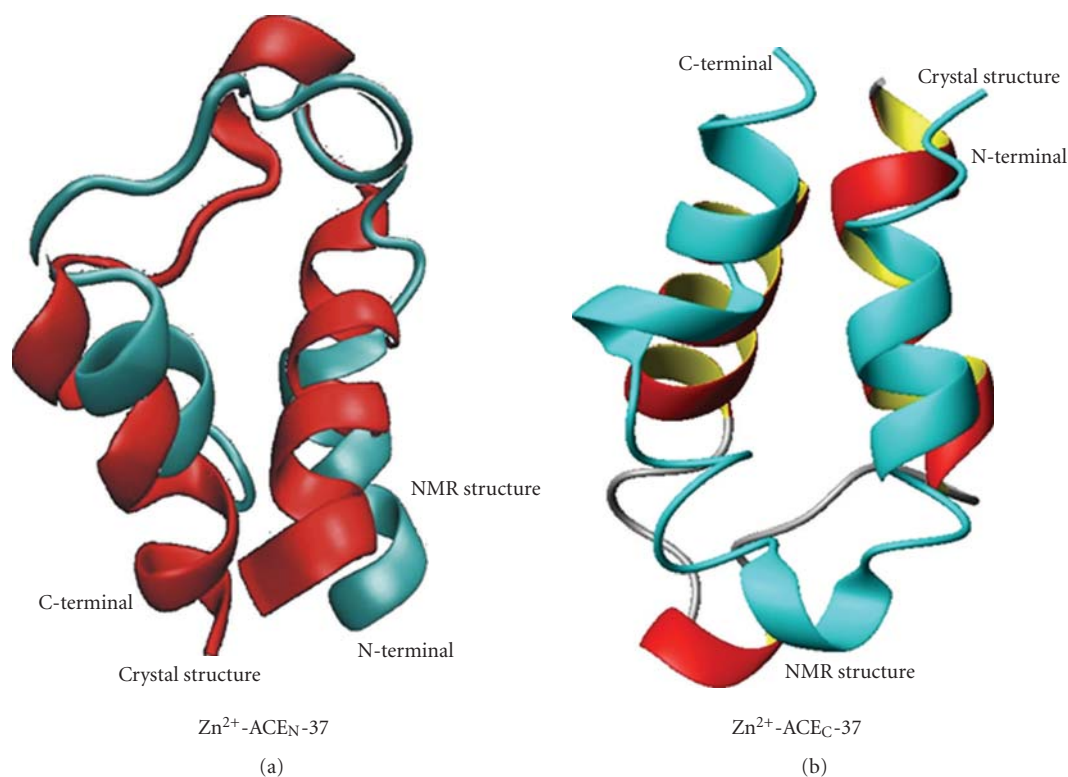


FIGURE 9: Superimposition of the crystal structure (in red) and the solution structure derived from NMR data (in cyan) of Zn²⁺-ACE_N(37) peptide (a) and Zn²⁺-ACE_C(37) peptide (b).

helices. In ACE_C(37) peptide, the two side chains of these residues are oriented almost parallel to each other pointing though to opposite orientation providing a more “extended” conformation for this segment. Additionally, a helix of the C-termini is observed in both peptides.

The substitutions of the amino acids at positions 19 (Ser¹⁹/Ala¹⁹) and 22 (Arg²²/Glu²²) of the peptide sequence

seem to differentiate the structure of the two peptides. The most important diversity among the structures of the ACE_{N/C} peptides regards the 5-residue spanning α -helix (Ala¹⁹-Gly²³) of the intermediate spacer between the two zinc-binding motifs, detected only in the ACE_C(37) peptide. The absence of the intermediate helix in the ACE_N(37) peptide probably provides a less constrained domain to the

N-active site of the somatic form in a crucial socket region for the substrate binding. As a conclusion, the presence or absence of the helical structure of the intermediate spacer determines the relative position of the two terminal helices and differentiates the active-site cavity structure and volume, where the substrate is accommodated. Both active sites of the somatic form act as carboxy dipeptidase, hydrolyzing the amide bond and releasing the C-terminal dipeptide from a native substrate [1]. Additionally, only the ACE_N domain presents endopeptidase activity, by releasing the C-terminal tripeptide of the GnRH hormone and the tetrapeptide of the native octapeptide Enkephalin [12]. Accommodation of these peptides in active or not mode for proteolytic cleavage, might be influenced by the conformation of the interhelical spacer.

3.5. NMR Solution Structure versus X-Ray. The overall fold of both synthetic peptides solution structures presents high similarity to the corresponding domain of the crystal structure of the testis ACE isoform [19] (tACE has identical sequence with the C-domain of the ACE somatic isoform) and the somatic ACE_N domain [18]. Minor differences exist regarding the length of the helices at the termini of the peptides (Figure 9). The backbone RMSD value for the family of 20 NMR structures of the ACE_N peptide and the crystal structure (2C6F) was found to be 1.42 Å and the corresponding RMSD value calculated for the mean NMR structure and the X-ray structure was found to be 3.802 Å. The backbone RMSD value for the family of 20 NMR structures of the ACE_C peptide and the crystal structure (1O8A) was found to be 0.775 Å and the corresponding RMSD value calculated for the mean NMR structure and the X-ray structure was found to be 3.595 Å.

In the tACE X-ray structure, two helical fragments are present at the N- and C- terminal, both comprising a 12-residue segment (Figure 9). For ACE_N crystal structure the N-terminal 13-residue fragment exhibits a helical conformation, as well as the entire C-terminal 12-residue fragment (Figure 9(a)). Regarding the intermediate spacer among the two zinc-binding motifs, an additional helix region consisting of 3 amino acids is present at both tACE and ACE_N X-ray structures. In the case of the NMR derived structure, a shorter helical fragment has been observed for both termini. The obtained data for the Zn²⁺-ACE_N(37) suggest that as far as the N-terminal is concerned a 10-residue fragment (His⁶-Asp¹⁵) and as far as the C-terminal is concerned a 8-residue fragment (His²⁹-Leu³⁶) exhibit helical conformation. Similar results have been obtained for the synthetic peptide representing the C-catalytic domain of the human somatic form and the corresponding domain of the testis form. Differences among the ACE catalytic site maquettes and X-ray structures might be due to the fact that the native N- and C-domains exhibit compact structures, and packing of the structure elements in the interior of the enzyme where the catalytic center is cited diminishes the conformational flexibility of the two active-site helices.

Concerning the intermediate spacer between the two zinc-binding motifs, the X-ray models present an additive

3-residue helical segment residue, concerning residues 18-20 (numbering of crystal structure: tACE: Val³⁹⁹-Leu⁴⁰¹; ACE_N: Val³⁷⁷-Leu³⁷⁹). NMR solution structure of the Zn²⁺-ACE_C(37) peptide resulted in significantly similar conformation. At ACE_C(37) peptide, a 3₁₀ helix is formed for the 5-residue segment Ala¹⁹-Gly²³. Instead, no helical conformation has been detected for the Zn²⁺-ACE_N(37) peptide, according to the NMR data and the DYANA calculations. However, both structures of tACE and sACE_N have been further solved in complex with the typical ACE inhibitor, lisinopril [19] (Figures S2 and S3). Among them, a helical structure is identified for the intermediate spacer only in the tACE-lisinopril structure, while in the sACE_N-lisinopril model the helical segment is absent. The modifications of positions 19 and 22 in the sACE_N peptide are probably playing an important role in the structural diversity of the spacer and are consequently crucial for the different activity and substrate specificity of these two active sites.

As a conclusion, the conformation of the synthetic peptides and the orientation of the two helical motifs upon zinc coordination are remarkably similar to the native structure, indicating the ACE catalytic site maquettes as reliable models of the enzyme active centre. The detected differences are clearly depended on the physicochemical properties of the peptides in solution compared to the crystal structures.

4. Conclusions

NMR studies of the synthetic peptides generated structures that successfully simulate the crystal structures of ACE C- and N-domains. Circular dichroism experiments provided important data, compensate not only for experimental conditions of the NMR analysis, but also for the elucidation of the structural characteristics of the two peptides, corresponding to the two somatic isoform ACE catalytic sites domains. The TFE use in aqueous mixtures, the proper pH value, as well as the presence of the Zn-ion create a solution environment, in which peptides adopt a similar fold to the native structure. The NMR data and the computational analysis led to structural models of the peptides, which are in great agreement with the X-ray structures. The secondary structure features of the peptides that correspond to the sequence of the ACE catalytic sites X-ray structures Zn²⁺-ACE_N(37) to ACE_N; Zn²⁺-ACE_C(37) to tACE present minor differences compared to the crystal structures. Furthermore, the ACE maquettes and the X-ray structures present significant similarities in the orientation of the active site helices, in respect of the position of the zinc ligands for metal coordination. On the other hand, the peptide representing the N-catalytic site lacks the helix of the intermediate region. Thus, the two terminal helices of the C-catalytic site maquette are found closer than those in ACE_N, illustrating potential differences into the catalytic site pocket for substrate selectivity, binding, and accommodation. This crucial difference might possibly explain the functional diversity of the two somatic isoforms of the human ACE. This approach might be helpful in the reconstitution of

other enzymes' active sites with unknown structures. In *gluzincins*, the spacer among the two zinc-binding motifs is regarded as of great importance for the specificity of the native substrates and external ligands, such as inhibitors. As far as somatic ACE is concerned, both active sites exhibit carboxy dipeptidase function while only the N-catalytic site exhibits also endopeptidase activity.

In the work reported here, crucial structural data for solution conformations have been extracted even though the crystal structure of testis ACE has been solved. Due to the functional diversity of the two ACE active sites, the "structure-based drug design" of the next generation of pharmaceutical agents, which specifically inhibit one of the two zinc catalytic domains of somatic ACE, is of major importance for the preferential modulation of ACE proteolytic activity towards a more effective treatment of hypertensive patients.

Abbreviations

ACE:	Angiotensin-I Converting Enzyme
sACE:	ACE somatic isoform
tACE:	ACE testis isoform
ACE _N :	N-domain of sACE
ACE _C :	C-domain of sACE
TFE:	2,2,2-trifluoroethanol
DQF-COSY:	Double-quantum-filtered phase-sensitive correlated spectroscopy
Tris:	Tris(hydroxymethyl)aminomethane
TOCSY:	Total Correlated Spectroscopy
NOE:	Nuclear Overhauser effect
NOESY:	Nuclear Overhauser effect spectroscopy
TPPI:	Time-proportional phase incrementation
WATERGATE:	Water suppression by gradient-tailored excitation
RMSD:	Root Mean Square Deviation
REM:	Restrained Energy Minimization
GPCRs:	G-protein coupled receptors.

Acknowledgments

G. A. Spyroulias and Z. Spyranti wish to thank EU-NMR program Grant RII3-026145 (Center of Magnetic Resonance no. (CERM), University of Florence) for access to NMR instrumentation. G. A. Spyroulias also acknowledges a short-term EMBO grant (ASTF 53.00-03). Z. Spyranti and A. S. Galanis contributed equally to this work. Dr. Maria Pelekanou is also acknowledged for assistance in CD measurements.

References

- [1] R. L. Soffer, "Angiotensin converting enzyme and the regulation of vasoactive peptides," *Annual Review of Biochemistry*, vol. 45, pp. 73–94, 1976.
- [2] E. G. Erdos, "Angiotensin I converting enzyme and the changes in our concepts through the years," *Hypertension*, vol. 16, no. 4, pp. 363–370, 1990.
- [3] H. Gavras, "Angiotensin converting enzyme inhibition and its impact on cardiovascular disease," *Circulation*, vol. 81, no. 1, pp. 381–388, 1990.
- [4] The Heart Outcomes Prevention Evaluation Study Investigators, "Effects of an angiotensin-converting-enzyme inhibitor, ramipril, on cardiovascular events in high-risk patients," *New England Journal of Medicine*, vol. 342, pp. 145–153, 2000.
- [5] PEACE Trial Investigators, "Angiotensin-converting-enzyme inhibition in stable coronary artery disease," *New England Journal of Medicine*, vol. 351, no. 20, pp. 2058–2068, 2004.
- [6] T. Inagami, "The renin-angiotensin system," *Essays in Biochemistry*, vol. 28, pp. 147–164, 1994.
- [7] M. A. Ondetti and D. W. Cushman, "Enzymes of the renin-angiotensin system and their inhibitors," *Annual Review of Biochemistry*, vol. 51, pp. 283–308, 1982.
- [8] A. Roks, H. Buikema, Y. M. Pinto, and W. H. van Gilst, "The renin-angiotensin system and vascular function. The role of angiotensin II, angiotensin-converting enzyme, and alternative conversion of angiotensin I," *Heart and Vessels*, vol. 12, pp. 119–124, 1997.
- [9] P. Bunning, B. Holmquist, and J. F. Riordan, "Substrate specificity and kinetic characteristics of angiotensin converting enzyme," *Biochemistry*, vol. 22, no. 1, pp. 103–110, 1983.
- [10] M. R. W. Ehlers, E. A. Fox, D. J. Strydom, and J. F. Riordan, "Molecular cloning of human testicular angiotensin-converting enzyme: the testis isozyme is identical to the C-terminal half of endothelial angiotensin-converting enzyme," *Proceedings of the National Academy of Sciences of the United States of America*, vol. 86, no. 20, pp. 7741–7745, 1989.
- [11] A.-L. Lattion, F. Soubrier, J. Allegrini, C. Hubert, P. Corvol, and F. Alhenc-Gelas, "The testicular transcripts of the angiotensin I-converting enzyme encodes for the ancestral, non-duplicated form of the enzyme," *FEBS Letters*, vol. 252, no. 1–2, pp. 99–104, 1989.
- [12] M. R. W. Ehlers and J. F. Riordan, "Angiotensin-converting enzyme: zinc- and inhibitor-binding stoichiometries of the somatic and testis isozymes," *Biochemistry*, vol. 30, no. 29, pp. 7118–7126, 1991.
- [13] M. J. Rieder, S. L. Taylor, A. G. Clark, and D. A. Nickerson, "Sequence variation in the human angiotensin converting enzyme," *Nature Genetics*, vol. 22, no. 1, pp. 59–62, 1999.
- [14] N. M. Hooper, "Families of zinc metalloproteases," *FEBS Letters*, vol. 354, no. 1, pp. 1–6, 1994.
- [15] G. A. Spyroulias, A. S. Galanis, G. Pairas, E. Manessi-Zoupa, and P. Cordopatis, "Structural features of angiotensin-I converting enzyme catalytic sites: conformation studies in solution, homology models and comparison with other zinc metallopeptidases," *Current Topics in Medicinal Chemistry*, vol. 4, no. 4, pp. 403–429, 2004.
- [16] A. S. Galanis, G. A. Spyroulias, R. Pierattelli, et al., "Zinc binding in peptide models of angiotensin-I converting enzyme active sites studied through ¹H-NMR and chemical shift perturbation mapping," *Biopolymers*, vol. 69, no. 2, pp. 244–252, 2003.
- [17] A. S. Galanis, G. A. Spyroulias, G. Pairas, E. Manessi-Zoupa, and P. Cordopatis, "Solid-phase synthesis and conformational properties of angiotensin converting enzyme catalytic-site peptides: the basis for a structural study on the enzyme-substrate interaction," *Biopolymers*, vol. 76, no. 6, pp. 512–526, 2004.
- [18] H. R. Corradi, S. L. U. Schwager, A. T. Nchinda, E. D. Sturrock, and K. R. Acharya, "Crystal structure of the N domain of

- human somatic angiotensin I-converting enzyme provides a structural basis for domain-specific inhibitor design," *Journal of Molecular Biology*, vol. 357, no. 3, pp. 964–974, 2006.
- [19] R. Natesh, S. L. U. Schwager, E. D. Sturrock, and K. R. Acharya, "Crystal structure of the human angiotensin-converting enzyme-lisinopril complex," *Nature*, vol. 421, no. 6922, pp. 551–554, 2003.
- [20] G. Bohm, R. Muhr, and R. Jaenicke, "Quantitative analysis of protein far UV circular dichroism spectra by neural networks," *Protein Engineering*, vol. 5, no. 3, pp. 191–195, 1992.
- [21] L. Braunschweiler and R. R. Ernst, "Coherence transfer by isotropic mixing: application to proton correlation spectroscopy," *Journal of Magnetic Resonance*, vol. 53, no. 3, pp. 521–528, 1983.
- [22] A. Bax and D. G. Davis, "MLEV-17-based two-dimensional homonuclear magnetization transfer spectroscopy," *Journal of Magnetic Resonance*, vol. 65, no. 2, pp. 355–360, 1985.
- [23] A. D. Bax and S. Grzesiek, "Methodological advances in protein NMR," *Accounts of Chemical Research*, vol. 26, no. 4, pp. 131–138, 1993.
- [24] A. G. Palmer III, J. Cavanagh, P. E. Wright, and M. Rance, "Sensitivity improvement in proton-detected two-dimensional heteronuclear correlation NMR spectroscopy," *Journal of Magnetic Resonance*, vol. 93, no. 1, pp. 151–170, 1991.
- [25] D. Marion and K. Wüthrich, "Application of phase sensitive two-dimensional correlated spectroscopy (COSY) for measurements of ^1H - ^1H spin-spin coupling constants in proteins," *Biochemical and Biophysical Research Communications*, vol. 113, no. 3, pp. 967–974, 1983.
- [26] J. Jeener, B. H. Meier, P. Bachmann, and R. R. Ernst, "Investigation of exchange processes by two-dimensional NMR spectroscopy," *Journal of Chemical Physics*, vol. 71, no. 11, pp. 4546–4553, 1979.
- [27] C. Eccles, P. Güntert, M. Billeter, and K. Wüthrich, "Efficient analysis of protein 2D NMR spectra using the software package EASY," *Journal of Biomolecular NMR*, vol. 1, no. 2, pp. 111–130, 1991.
- [28] P. Güntert, W. Braun, and K. Wüthrich, "Efficient computation of three-dimensional protein structures in solution from nuclear magnetic resonance data using the program DIANA and the supporting programs CALIBA, HABAS and GLOMSA," *Journal of Molecular Biology*, vol. 217, no. 3, pp. 517–530, 1991.
- [29] P. Güntert, C. Mumenthaler, and K. Wüthrich, "Torsion angle dynamics for NMR structure calculation with the new program DYANA," *Journal of Molecular Biology*, vol. 273, no. 1, pp. 283–298, 1997.
- [30] K. Wüthrich, M. Billeter, and W. Braun, "Pseudo-structures for the 20 common amino acids for use in studies of protein conformations by measurements of intramolecular proton-proton distance constraints with nuclear magnetic resonance," *Journal of Molecular Biology*, vol. 169, no. 4, pp. 949–961, 1983.

Research Article

A Synthetic Approach of New *Trans*-Substituted Hydroxylporphyrins

Dimitra Daphnomili,¹ Maria Grammatikopoulou,¹ Catherine Raptopoulou,²
George Charalambidis,¹ Theodore Lazarides,¹ and Athanasios G. Coutsolelos¹

¹Laboratory of Bioinorganic Coordination Chemistry, Department of Chemistry, School of Sciences, University of Crete, P.O. Box 2208, Heraklion 71003, Crete, Greece

²Institute of Materials Science, NCSR "Demokritos", Aghia Paraskevi Attikis, 15310, Greece

Correspondence should be addressed to Athanasios G. Coutsolelos, coutsole@chemistry.uoc.gr

Received 6 February 2010; Accepted 4 March 2010

Academic Editor: Spyros P. Perlepes

Copyright © 2010 Dimitra Daphnomili et al. This is an open access article distributed under the Creative Commons Attribution License, which permits unrestricted use, distribution, and reproduction in any medium, provided the original work is properly cited.

The synthesis of new *trans* A₂B₂-substituted porphyrins bearing oxygenic substituent (methoxy, acetoxy, hydroxy) at the periphery of the ring are described. All of the synthesized products were characterized by ¹H-N.M.R., ¹³C-N.M.R., and H.R.M.S. Electrochemical studies revealed two one-electron oxidations and two reductions. In addition, the X-ray structure of one methoxy-derivative was determined.

1. Introduction

In the last years porphyrin derivatives have been developed or are under development for use as photosensitizers for photoelectronic materials such as sensors [1] and photosensitized solar cells [2]. Because of their interesting optical properties, porphyrin molecules have been investigated as artificial light harvesting antennae. Carbon-based donor-acceptor hybrid materials have been reported where, in many cases, the porphyrin molecule is covalently attached [3, 4]. Among the great diversity of porphyrins with a specific pattern of substituents, *trans*-substituted porphyrins with functional groups at the periphery of the ring act as precursors for supermolecular structures.

During the past decades a great effort has been directed towards the synthesis of porphyrins [5, 6]. Porphyrins with nearly all sorts of substituents at the periphery of the 18 π -electron system are now accessible. The synthetic procedures followed were mainly based on the Adler-Longo reaction of the condensation of pyrrole with various aldehydes.

In the field of *trans*-substituted porphyrins an attractive route for the synthesis of these key structural components found in a wide range of model systems [7] was developed by Lindsey's group [8–10]. The synthetic approach

of Lindsey's group was based on the convenient preparation of 5-substituted dipyrromethanes [8]. Condensation of a dipyrromethane with an aldehyde in a MacDonald-type synthesis has been used for the preparation of a wide range of *trans* A₂B₂ type *meso*-substituted porphyrins [8, 11, 12].

Based on this method we tried to explore the possibility of the synthesis of *meso*-substituted *trans* hydroxyporphyrins due to the ability of the hydroxy group to link substructures over the porphyrin plane. Hydroxyporphyrins can act as precursors for the synthesis of porphyrin dimers serving as host molecules [13]. Furthermore a series of hydroxyporphyrins has been tested as photosensitizers in photodynamic therapy (PDT) [14, 15]. For their synthesis the methoxy- or acetoxy-derivatives were prepared first.

2. Experimental

2.1. Measurements. ¹H-N.M.R. and ¹³C-N.M.R. spectra were recorded on a Bruker AMX-500 MHz N.M.R. spectrometer using chloroform-D₃ as a solvent. Resonances in the ¹H-N.M.R. were referenced versus the residual proton signal of the solvent.

Absorption spectra were collected on a Perkin-Elmer Lambda 6 grating spectrophotometer. Cyclic voltammetry experiments were performed in an AUTOLAB PGSTAT20. MS spectra were recorded on Bruker MALDI TOF/TOF ultraflextreme.

X-ray diffraction measurements were conducted on a STOE IPDS II diffractometer using graphite-monochromated Mo K α radiation. A dark blue crystal with approximate dimensions 0.50 \times 0.40 \times 0.14 mm was mounted on a capillary. Intensity data were recorded using 2 θ scan (2 θ_{\max} = 46.5, 1°/min). The structure was solved by direct methods and refined on F_o^2 values using SHELX [16]. All nonhydrogen atoms were refined anisotropically; all of the hydrogen atoms were introduced at calculated positions as riding on bonded atoms and were refined isotropically.

2.2. Synthesis of Porphyrinic Compounds. The preparation of 5-mesityl dipyrromethane was based on previously published procedures [8].

2.2.1. 5,15 Dimesityl-10,20 Bis(3-Methoxyphenyl)Porphyrin 1. 3.8 mmol (1 gr) of 5-mesityl dipyrromethane and 3.8 mmol of 3-methoxybenzaldehyde were dissolved in 400 mL of CH₂Cl₂ (A.C.S. grade) under argon atmosphere. 7.12 mmol TFA were added and the reaction mixture was stirred for 30 min at room temperature. 3.8 mmol (0.86 gr) of DDQ were added and the mixture was further stirred for 1 hour. The reaction mixture was filtered through a column of Al₂O₃ (6 cm \times 8 cm) using CH₂Cl₂ as eluent until the color of the solution was pale brown. The solvent was removed under reduced pressure and the solid was dissolved in 50 mL of toluene, heating at reflux for 1 hour, after the addition of 0.38 mmol of DDQ. After cooling at room temperature the solvent was removed and the solid was purified by a column chromatography. A column of Al₂O₃ was performed with CH₂Cl₂ as eluent (yield 22%):

MS: [M]⁺ 758.3631,

UV-Visible: λ_{\max} (toluene, 5.3 \times 10⁻⁵ M)/(log ϵ /M⁻¹ cm⁻¹): 401 (sh, 4.79), 419 (Soret, 5.54), 482 (sh, 3.84), 513 (Q, 4.28), 550 (Q, 3.90), 591 (Q, 3.92), 647 (Q, 3.72),

¹H-N.M.R. (500 MHz, CDCl₃, 300 K) δ = 8.86 (d, 4H, J = 4.6 Hz, pyrrole); 8.71 (d, 4H, J = 4.6 Hz, pyrrole). *Phenyl Group*: δ = 7.84 (m, 4H, 2,6-ph); 7.66 (tr, 2H, J = 8 Hz, 3-ph); 7.35 (dd, 2H, J = 8 Hz, 4-ph); 4.02 (s, 6H, -OCH₃). *Mesityl Group*: δ = 7.31 (s, 4H, 3,5-mes); 1.88 (s, 12H, 2,6-mes); 2.66 (s, 6H, 4-mes); -2.60 (s, 2H, N-pyrrole).

2.2.2. 5,15 Dimesityl-10,20 Bis(2-Methoxyphenyl)Porphyrin 2. The standard procedure described above was followed obtaining 0.38 gr of **2** as a mixture of the two atropisomers (yield 26%):

MS: [M]⁺ 758.3630,

UV-Visible: λ_{\max} (toluene, 6.2 \times 10⁻⁵ M)/(log ϵ /M⁻¹ cm⁻¹): 401 (sh, 4.78), 419 (Soret, 5.55), 482 (sh,

3.87), 515 (Q, 4.30), 550 (Q, 3.91), 591 (Q, 3.91), and 647 (Q, 3.76),

¹H-N.M.R. (500 MHz, CDCl₃, 300 K) δ = 8.73 (d, 4H, J = 4.6 Hz, pyrrole); 8.65 (d, 4H, J = 4.6 Hz, pyrrole). *Phenyl Group*: δ = 8.03 (d, 2H, J = 7.2 Hz, 6-ph); 7.82 (tr, 2H, J = 7.6 Hz, 4-ph); 7.36 (dd, 4H, J = 8.5 Hz, 3,5-ph); 3.63 (s, 6H, -OCH₃). *Mesityl Group*: δ = 7.29 (s, 4H, 3,5-mes); 1.87 (s, 12H, 2,6-mes); ^(a)1.89 (s, 6H); ^(b)1.86 (s, 6H); ^(b)2.65 (s, 6H, 4-mes); -2.51 (s, 2H, N-pyrrole).

(a) α , β atropisomer,

(b) α , α atropisomer.

2.2.3. 5,15 Dimesityl-10,20 Bis(4-Acetoxyphenyl)Porphyrin 3. The procedure described for **1** was followed. The product was obtained after repeat washings with cold ethanol and recrystallization from CH₂Cl₂/Hexane/EtOH (10/1/5 v/v/v) at -5°C overnight (yield 27%):

UV-Visible: λ_{\max} (toluene, 1.6 \times 10⁻⁴ M)/(log ϵ /M⁻¹ cm⁻¹): 399 (sh, 4.85), 418 (Soret, 5.48), 480 (sh, 3.98), 513 (Q, 4.36), 549 (Q, 4.04), 591 (Q, 4.02), and 647 (Q, 3.92),

¹H-N.M.R. (500 MHz, CDCl₃, 300 K) δ = 8.85 (d, 4H, J = 4.5 Hz, pyrrole); 8.73 (d, 4H, J = 4.5 Hz, pyrrole). *Phenyl Group*: δ = 8.25 (d, 4H, J = 8 Hz, 2,6-ph); 7.52 (d, 4H, J = 8.5 Hz, 3,5-ph); 2.52 (s, 6H, -OOCCH₃). *Mesityl Group*: δ = 7.32 (s, 4H, 3,5-mes); 2.67 (s, 6H, 4-mes); 1.89 (s, 12H, 2,6-mes); -2.51 (s, 2H, N-pyrrole).

2.2.4. 5,15 Dimesityl-10,20 Bis(4-Methoxyphenyl)Porphyrin 4. The standard procedure described above was followed (yield 26%):

UV-Visible (CH₂Cl₂): λ_{\max} (toluene, 2 \times 10⁻⁴ M)/(log ϵ /M⁻¹ cm⁻¹): 420 (5.67), 516 (4.27), 552 (3.95), 592 (3.75), and 649 (3.71),

¹H-N.M.R. (500 MHz, CDCl₃, 300 K) δ = 8.85 (d, 4H J = 5 Hz, pyrrole); 8.71 (d, 4H, J = 4.5 Hz, pyrrole). *Phenyl Group* δ = 8.16 (d, 4H, J = 7.5 Hz, 2,6-ph); δ = 7.30 (m, 4H, 3-ph); δ = 4.10 (s, 6H, -OCH₃). *Mesityl Group*: δ = 7.30 (s, 4H, 3,5-mes); 2.65 (s, 6H, 4-mes); 1.87 (s, 12H, 2,6-mes); -2.56 (s, 2H, N-pyrrole).

2.2.5. 5,15 Dimesityl-10,20 Bis(3-Hydroxyphenyl)Porphyrin 5. 0.079 mmol (0.06 gr) of porphyrin **1** was dissolved in 8 mL of dry CH₂Cl₂ under Ar atmosphere. The solution was cooled at -78°C and BBr₃ (1.85 mmol) was added dropwise under vigorous stirring. The reaction mixture was allowed to stand at r.t. for 5 hours. Aqueous saturate NaHCO₃ was added carefully and the organic layer was washed with saturate NaCl solution and dried over MgSO₄. After the removal of the solvent the product was chromatographed on SiO₂ column (2 cm \times 4 cm). With CH₂Cl₂/EtOH (100/0.2 v/v), traces of unreacted porphyrin were eluted while the product was

obtained with CH₂Cl₂/EtOH (100/5 v/v) as eluents (yield 85%):

MS: [M+H]⁺ 731.3399,

UV-Visible: λ_{\max} (toluene, 4.2×10^{-5} M)/(log ϵ /M⁻¹ cm⁻¹): 402 (sh, 4.80), 420 (Soret, 5.54), 480 (sh, 3.98), 515 (Q, 4.29), 552 (Q, 4.06), 593 (Q, 3.95), and 650 (Q, 3.89),

¹H-N.M.R. (500 MHz, CDCl₃, 300 K) δ = 8.86 (d, 4H, J = 4.5 Hz, pyrrole); 8.71 (d, 4H, J = 4.5 Hz, pyrrole). *Phenyl Group*: δ = 7.82 (d, 2H, J = 7.8 Hz, 6-ph); 7.70 (s, 2H, 2-ph); 7.60 (tr, 2H, J = 8 Hz, 5-ph); 7.25 (d, 2H, J = 7 Hz, 4-ph); 5.45 (s br, 2H, OH). *Mesityl Group*: δ = 7.26 (s, 4H, 3,5-mes); 2.66 (s, 6H, 4-mes); 1.79 (s, 12H, 2,6-mes); -2.60 (s, 2H, N-pyrrole).

2.2.6. *5,15 Dimesityl-10,20 Bis(2-Hydroxyphenyl)Porphyrin 6*. The procedure was the same as for compound 5. Compound 6 is a mixture of two atropisomers that were separated by column chromatography on SiO₂ (5 cm × 2 cm). The α , β (R_f: 0.95 in CH₂Cl₂) is eluted with CH₂Cl₂/Hexane (6/4 v/v) and α , α (R_f: 0.25 in CH₂Cl₂) is eluted with 0.5% EtOH /CH₂Cl₂.

MS: [M+H]⁺ 731.3398,

UV-Visible: λ_{\max} (toluene, 3.4×10^{-4} M)/(log ϵ /M⁻¹ cm⁻¹): 402 (sh, 4.78), 420 (Soret, 5.55), 480 (sh, 3.83), 515 (Q, 4.32), 552 (Q, 3.99), 593 (Q, 3.92), and 650 (Q, 3.86),

6 $\alpha\beta$: ¹H-N.M.R. (500 MHz, CDCl₃, 300 K) δ = 8.84 (d, 4H, J = 4.5 Hz, pyrrole); 8.74 (d, 4H, J = 4.5 Hz, pyrrole). *Phenyl Group*: δ = 8.0 (dd, 2H, J = 7 Hz, 6-ph); 7.73 (tr, 2H, J = 8 Hz, 4-ph); 7.37 (d, 2H, J = 8.5 Hz, 5-ph); 7.34 (d, 2H, J = 8 Hz, 3-ph); 5.37 (s br, 2H, -OH). *Mesityl Group*: δ = 7.31 (s, 4H, 3,5-mes); 2.65 (s, 6H, 4-mes); 1.85 (s, 12H, 2,6-mes); -2.59 (s, 2H, N-pyrrole),

6 $\alpha\alpha$: ¹H-N.M.R. (500 MHz, CDCl₃, 300 K) δ = 8.85 (d, 4H, J = 4.5 Hz, pyrrole); 8.74 (d, 4H, J = 4.5 Hz, pyrrole). *Phenyl Group*: δ = 8.03 (dd, 2H, J = 7.5 Hz, 6-ph); 7.71 (tr, 2H, J = 7.5 Hz, 4-ph); 7.37 (d, 2H, J = 8 Hz, 5-ph); 7.34 (d, 2H, J = 8 Hz, 3-ph); 5.32 (s br, 2H, -OH). *Mesityl Group*: δ = 7.30 (s, 4H, 3,5-mes); 2.65 (s, 6H, 4-mes); 1.88 (s, 6H); 1.83 (s, 6H); -2.58 (s, 2H, N-pyrrole).

2.2.7. *5,15 Dimesityl-10,20 Bis(4-Hydroxyphenyl)Porphyrin 7*

Method 1. The procedure was the same as for compound 5 and compound 4.

Method 2. 0.25 mmol (0.2 gr) of porphyrin 3 were added in 10 mL of THF. 7.38 mmol KOH were dissolved in 5 mL of EtOH and the resulting alcoholic solution was added dropwise. The solution was stirred for 30 min at room temperature and then refluxed for a further 2 hours. After cooling at room temperature the solution was acidified by carefully adding glacial acetic acid. 15 mL of CH₂Cl₂ were

TABLE 1: Redox data of dimethoxy derivatives^(a).

Compound	E _{1/2ox} (V versus SCE)	E _{1/2red} (V versus SCE)
Compound 1	0.96; 1.40	-1.34; -1.68
Compound 2	0.94; 1.36	-1.34; -1.71
Compound 4	0.92; 1.37	-1.33; -1.66

^(a) Redox potentials were determined by cyclic voltammetry at room temperature in dry and deoxygenated CH₂Cl₂ containing 0.1 M of tetrabutylammonium hexafluorophosphate as supporting electrolyte and a solute concentration in the range of 1.5×10^{-3} M. A Saturated Calomel Electrode (SCE) was used as reference. Under these conditions, the reversible oxidation of ferrocene was E_{1/2Fc} = +0.47 V. The error on the reported potentials is ± 0.01 V.

added and the organic layer was washed with sat. NaCl solution. After being dried over MgSO₄, the solvent was removed giving 0.165 gr of 7 (yield 90%):

MS: [M+H]⁺ 731.3399,

UV-Visible: λ_{\max} (toluene, 6.2×10^{-5} M)/(log ϵ /M⁻¹ cm⁻¹): 402 (sh, 4.60), 420 (Soret, 5.30), 478 (sh, 3.79), 515 (Q, 4.04), 550 (Q, 3.84), 592 (Q, 3.76), and 650 (Q, 3.71),

¹H-N.M.R. (500 MHz, CDCl₃, 300 K) δ = 8.85 (d, 4H, J = 4.5 Hz, pyrrole); 8.67 (d, 4H, J = 4.5 Hz, pyrrole). *Phenyl Group*: δ = 8.03 (d, 4H, J = 6.5 Hz, 2,6-ph); 7.19 (d, 4H, J = 6 Hz, 3,5-ph). *Mesityl Group*: δ = 7.38 (s, 4H, 3,5-mes); 2.61 (s, 6H, 4-mes); 1.82 (s, 12H, 2,6-mes); -2.60 (s, 2H, N-pyrrole).

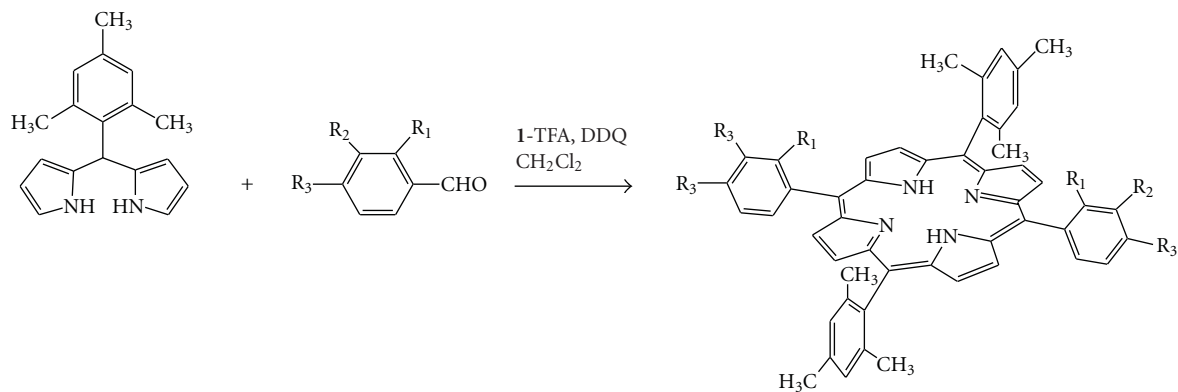
3. Results and Discussion

Following Lindsey's methodology, *trans*-methoxyporphyrins 1, 2 and 4 were synthesized as precursors for 5 and 6 while for compound 7 the precursors were 3 and 4 (Scheme 1).

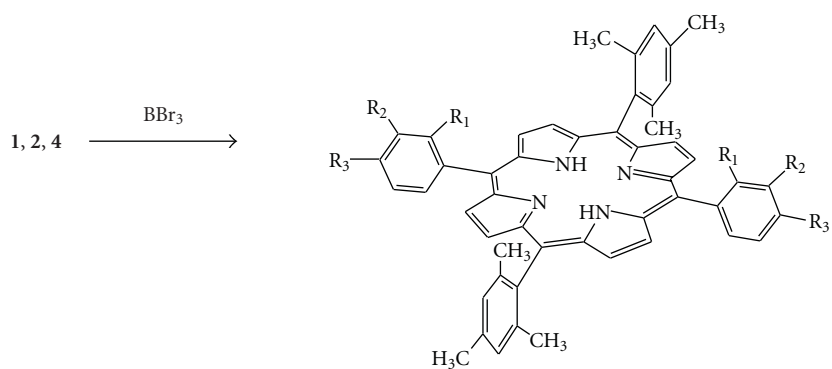
The choice of acetoxy- or methoxy- as protecting groups was based on published results for the formation of a dipyrrole product from an attempted synthesis of arylporphyrins with *o*-acetoxybenzaldehyde [17].

Compound 2 is a mixture of atropisomers that proved to be inseparable despite our repeated efforts for chromatographic separation. Compounds 5 and 6 were obtained by cleavage of the methyl ether by BBr₃ (Scheme 1), while 7 is obtained by alkaline hydrolysis of the ester group or alternatively by cleavage of the methoxy group. The two isomers of compound 6 (Scheme 2) in contrast to these of 2 are easily separated by silica gel chromatography. **6 $\alpha\beta$** is eluted with CH₂Cl₂/Hexane (6/4 v/v) while the more polar **6 $\alpha\alpha$** is eluted with 0.5% EtOH /CH₂Cl₂.

The two isomers (Scheme 2) were characterized by ¹H-N.M.R. spectroscopy. A characteristic feature is that in **6 $\alpha\beta$** the *o*-Me of the mesityl group appears as a singlet while in **6 $\alpha\alpha$** the *o*-Me group gives two separate singlets, while no other remarkable spectroscopic difference was observed for the two isomers. In 2 since it is a mixture of the two isomers its N.M.R. spectrum shows these three groups of peaks. For derivatives 3 and 1 the *o*-H and *m*-H are equivalent giving one

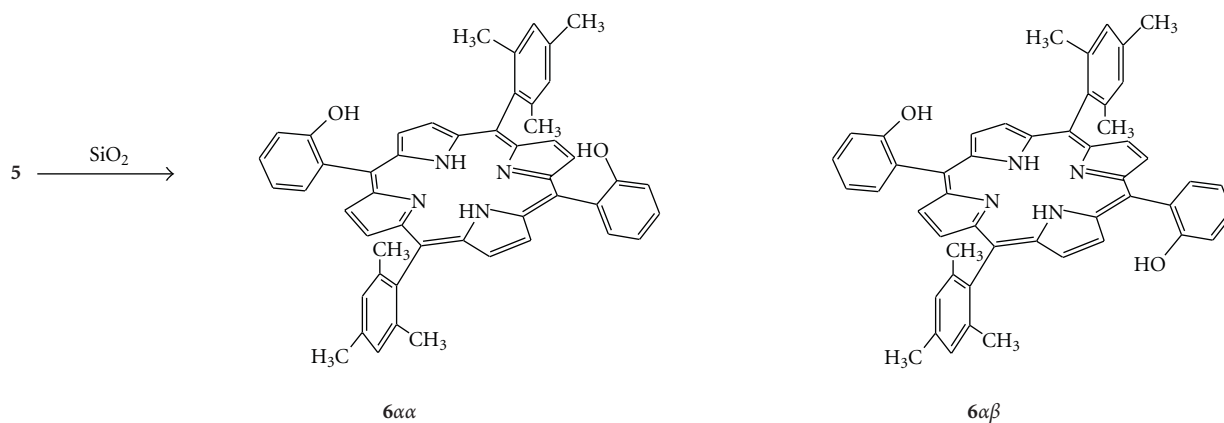


- 1 $R_1 = H, R_2 = OCH_3, R_3 = H$,
 2 $R_1 = OCH_3, R_2 = H, R_3 = H$ (two atropisomers),
 3 $R_1 = H, R_2 = H, R_3 = OOCCH_3$,
 4 $R_1 = H, R_2 = H, R_3 = OCH_3$.



- 5 $R_1 = H, R_2 = OH, R_3 = H$,
 6 $R_1 = OH, R_2 = H, R_3 = H$ (two atropisomers),
 7 $R_1 = H, R_2 = H, R_3 = OH$.

SCHEME 1: Reaction scheme.

SCHEME 2: $6\alpha\alpha$ and $6\alpha\beta$ atropisomers.

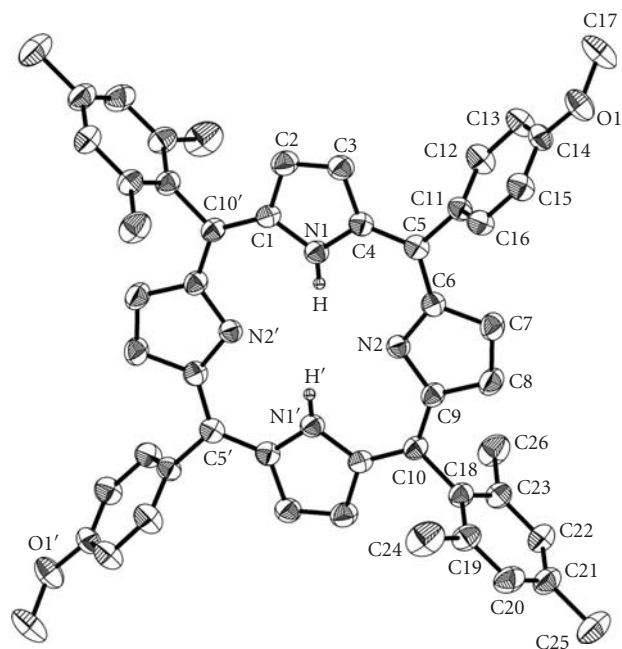


FIGURE 1: Partially labeled plot of **4** with ellipsoids drawn at 30% thermal probability. Hydrogen atoms have been omitted for clarity. Primed atoms are generated by symmetry operation: (')- x , $-y$, $-z$.

signal for each group. The hydrolysis product **5** the o -H are no longer equivalent resonating at 7.82 ppm and 7.70 ppm.

Characteristic in the ^{13}C -N.M.R. is the signal at 170 ppm for the carbonyl carbon of **3** and at 56 ppm of $-\text{OCH}_3$ group for **1** and **2** that disappears in the ^{13}C -N.M.R. spectra of the hydrolysis products. Similar characteristic I.R. peaks for **3** at 1763 cm^{-1} for $\nu(\text{C}=\text{O})$ str. no longer exist in **7** while they are also observed two new peaks, one at 1162 cm^{-1} and another one at 1200 cm^{-1} for $(\text{C}-\text{O})$ stretching vibrations. In methoxy derivatives two bands, one at 1050 cm^{-1} [$\nu(\text{C}-\text{O}-\text{C})$ sym. str.] and one at 1282 cm^{-1} [$\nu(\text{C}-\text{O}-\text{C})$ asym. str.], are observed.

For all of the methoxy derivatives electrochemical studies were performed by cyclic voltammetry. The redox potentials measured are the typical ones for meso-substituted porphyrins [18] that exhibited two one-electron reversible oxidations and two one-electron reversible reductions (Table 1).

The structure of derivative **4** is centrosymmetric (Table 2) and the asymmetric unit contains half of the porphyrin molecule and one water solvate molecule, which was found disordered and refined over three positions with occupation factors summing one (Figure 1).

The rather large values of dihedral angles formed between the porphyrin C_{20}N_4 mean plane, the mesityl phenyl ring (84.72°), and the methoxyphenyl ring (65.12°) indicate that there is no twist distortion of the porphyrin skeleton, together with the small average absolute displacement of the C_m atom (0.032 \AA) from the porphyrin core. The displacement of the two $-\text{OCH}_3$ groups is 0.643 \AA alternative from the porphyrin plane.

In conclusion in this work we have reported the preparation of new porphyrinic complexes bearing the

TABLE 2: Crystallographic data for $4 \cdot 2\text{H}_2\text{O}$.

$4 \cdot 2\text{H}_2\text{O}$	
Formula	$\text{C}_{52}\text{H}_{50}\text{N}_4\text{O}_4$
F_w	794.96
Space group	$P2_1/n$
a (\AA)	17.288(4)
b (\AA)	8.2587(17)
c (\AA)	17.829(4)
α ($^\circ$)	90
β ($^\circ$)	106.15(3)
γ ($^\circ$)	90
V (\AA^3)	2445.1(9)
Z	2
T ($^\circ\text{C}$)	25
Radiation	Mo $K\alpha$
ρ_{calcd} (g cm^{-3})	1.080
μ (mm^{-1})	0.069
Reflections with $I > 2\sigma(I)$	2338
R_1^a	0.0723
wR_2^a	0.1890

$$^a w = 1/[\sigma^2(F_o^2) + (\alpha P)^2 + bP] \text{ and } P = [\max(F_o^2, 0) + 2F_c^2]/3.$$

appropriate groups in order to functionalize specific sides of the aromatic macrocycle. The formed complexes are fully characterized. The formation and the properties of macromolecule structures with the formed complexes as precursors will be published elsewhere.

Acknowledgment

This research was supported by the Seventh Framework Programme REGPOT-2008-1 no. 229927 with the acronym BIOSOLENUTI through the Special Research Account of the University of Crete.

References

- [1] Y. Xu, Z. Liu, X. Zhang, et al., "A graphene hybrid material covalently functionalized with porphyrin: synthesis and optical limiting property," *Advanced Materials*, vol. 21, no. 12, pp. 1275–1279, 2009.
- [2] C. M. Drain, A. Varotto, and I. Radivojevic, "Self-organized porphyrinic materials," *Chemical Reviews*, vol. 109, no. 5, pp. 1630–1658, 2009.
- [3] G. Pagona, A. S. D. Sandanayaka, Y. Araki, et al., "Covalent functionalization of carbon nanohorns with porphyrins: nanohybrid formation and photoinduced electron and energy transfer," *Advanced Functional Materials*, vol. 17, no. 10, pp. 1705–1711, 2007.
- [4] G. Pagona, A. S. D. Sandanayaka, T. Hasobe, et al., "Characterization and photoelectrochemical properties of nanostructured thin film composed of carbon nanohorns covalently functionalized with porphyrins," *Journal of Physical Chemistry C*, vol. 112, no. 40, pp. 15735–15741, 2008.
- [5] J. S. Lindsey, in *The Porphyrin Handbook*, K. M. Kadish, K. M. Smith, and R. Guilard, Eds., vol. 1, pp. 45–118, Academic Press, Boston, Mass, USA, 2000.

- [6] J. W. Buchler, in *The Porphyrins*, D. Dolphin, Ed., vol. 1, pp. 389–483, Academic Press, London, UK, 1978.
- [7] J. S. Lindsey, *Metalloporphyrin—Catalyzed Oxidations*, Kluwer Academic Publishers, Dordrecht, The Netherlands, 1994.
- [8] B. J. Littler, Y. Ciringh, and J. S. Lindsey, “Investigation of conditions giving minimal scrambling in the synthesis of trans-porphyrins from dipyrromethanes and aldehydes,” *The Journal of Organic Chemistry*, vol. 64, no. 8, pp. 2864–2872, 1999.
- [9] B. J. Littler, M. A. Miller, C.-H. Hung, et al., “Refined synthesis of 5-substituted dipyrromethanes,” *The Journal of Organic Chemistry*, vol. 64, no. 4, pp. 1391–1396, 1999.
- [10] P. D. Rao, B. J. Littler, G. R. Geier, and J. S. Lindsey, “Efficient synthesis of monoacyl dipyrromethanes and their use in the preparation of sterically unhindered trans-porphyrins,” *The Journal of Organic Chemistry*, vol. 65, no. 4, pp. 1084–1092, 2000.
- [11] D. T. Gryko and M. Tasior, “Simple route to meso-substituted trans-A2B2-porphyrins bearing pyridyl units,” *Tetrahedron Letters*, vol. 44, no. 16, pp. 3317–3321, 2003.
- [12] K. Ladomenou, G. Charalambidis, and A. G. Coutsolelos, “A strategic approach for the synthesis of new porphyrin rings, attractive for heme model purpose,” *Tetrahedron*, vol. 63, no. 13, pp. 2882–2887, 2007.
- [13] K. Tashiro, T. Aida, J.-Y. Zheng, et al., “A cyclic dimer of metalloporphyrin forms a highly stable inclusion complex with C60,” *Journal of the American Chemical Society*, vol. 121, no. 40, pp. 9477–9478, 1999.
- [14] J. A. Lacey, D. Phillips, L. R. Milgrom, G. Yahioglu, and R. D. Rees, “Photophysical studies of some 5,10,15,20-tetraarylethynylporphyrinatozinc(II) complexes as potential lead compounds for photodynamic therapy,” *Photochemistry and Photobiology*, vol. 67, no. 1, pp. 97–100, 1998.
- [15] D. A. James, D. P. Arnold, and P. G. Parsons, “Potency and selective toxicity of tetra(hydroxyphenyl)porphyrins in human melanoma cells, with and without exposure to red light,” *Photochemistry and Photobiology*, vol. 59, no. 4, pp. 441–447, 1994.
- [16] G. M. Sheldrick, “A short history of SHELX,” *Acta Crystallographica Section A*, vol. 64, no. 1, pp. 112–122, 2007.
- [17] J. A. S. Cavaleiro, M. D. F. P. N. Condesso, M. M. Olmstead, D. E. Oram, K. M. Snow, and K. M. Smith, “An anomalous dipyrrole product from attempted synthesis of a tetraarylporphyrin,” *The Journal of Organic Chemistry*, vol. 53, no. 25, pp. 5847–5849, 1988.
- [18] K. M. Kadish, E. Van Caemelbecke, and R. Royal, in *The Porphyrin Handbook*, K. M. Kadish, K. M. Smith, and R. Guilard, Eds., vol. 8, chapter 55, pp. 1–97, Academic Press, San Diego, Calif, USA, 2000.

Research Article

Interactions of Trivalent Lanthanide Cations with a New Hexadentate Di-Schiff Base: New Lanthanide(III) Complexes from (NE,N'E)-2,2'-(ethane-1,2-diylbis(oxy))bis(N-(pyridin-2-ylmethylene)ethanamine)

Mantha Tsiouri,¹ Konstantina Skorda,² Christos Papadimitriou,¹ Yang Li,³
J. Derek Woollins,³ and John C. Plakatouras¹

¹ Department of Chemistry, University of Ioannina, 451 10 Ioannina, Greece

² Faculty of Physics and Chemistry, Hellenic Army Academy, 166 73 Vari, Greece

³ School of Chemistry, University of St. Andrews, North Haugh, St. Andrews, Fife, Scotland, KY16 9ST, UK

Correspondence should be addressed to John C. Plakatouras, iplakatu@cc.uoi.gr

Received 22 April 2010; Accepted 2 May 2010

Academic Editor: Spyros Perlepes

Copyright © 2010 Mantha Tsiouri et al. This is an open access article distributed under the Creative Commons Attribution License, which permits unrestricted use, distribution, and reproduction in any medium, provided the original work is properly cited.

The novel lanthanide(III) complexes $[\text{Ln}(\text{NO}_3)_2\text{L}](\text{NO}_3) \cdot 3\text{MeOH}$ ($\text{Ln} = \text{La}$ **1**, Pr **2**) and $[\text{Ln}(\text{NO}_3)_3\text{L}](\text{NO}_3) \cdot 2\text{MeOH}$ ($\text{Ln} = \text{Gd}$ **3**, Yb **4**), where $\text{L} = (\text{NE}, \text{N}'\text{E})\text{-}2,2'\text{-}(\text{ethane-}1,2\text{-diylbis(oxy))bis(N-(pyridin-}2\text{-ylmethylene)ethanamine)}$, have been obtained by direct reaction of the Schiff base ligand and the corresponding hydrated lanthanide(III) nitrates in methanol. All complexes were characterized spectroscopically and thermogravimetrically. Complex **4** was also characterized with crystallographic studies: orthorhombic $\text{P}2_12_12_1$, $a = 10.6683(14)$, $b = 13.4752(15)$, $c = 19.3320(26)$ Å. In the molecular structure of **4**, Yb(III) is surrounded by all donor atoms of the Schiff base (four nitrogen and two oxygen atoms) and four oxygen atoms belonging to two bidentate chelating nitrate ligands.

1. Introduction

Schiff base metal complexes have a key role in the development of coordination chemistry, resulting in an enormous number of publications, ranging from pure synthetic work to modern physicochemical and biochemically relevant studies of metal complexes [1].

The lanthanide cations can promote Schiff base condensation and can give access to complexes of otherwise inaccessible ligands. This fact, in combination with the applications of lanthanide macrocyclic complexes emerging from biology and medicine, has boosted research on these areas [2].

One of the major applications of lanthanide complexes in medicine is their use as water proton relaxation agents for NMR imaging [3, 4]. The research in this field is directed towards the synthesis of stable, nontoxic, highly

paramagnetic molecules with the ability to improve efficiently the contrast of the magnetic resonance image. The number of coordinated water molecules on the paramagnetic center (usually gadolinium(III)) greatly contributes to the relaxivity (the efficiency with which the complex enhances the proton relaxation rates of water) of the contrast agent. Initially polyaminocarboxylates were utilized as ligands for the preparation of such complexes, with $[\text{Gd}(\text{DTPA})(\text{H}_2\text{O})]^{2-}$ ($\text{DTPAH}_5 = \text{diethylenetriaminepentaacetic acid}$) being the most commonly used contrast agent. Though the aforementioned agent has a high stability constant, reducing the toxic effect of the free metal ion, its disadvantage is the availability of only one water coordination site.

A large number of articles have been published on lanthanide complexes with the hexadentate Schiff base derived by the condensation of 2,6-diacetylpyridine and

ethylenediamine [5–16]. These complexes are stable enough under physiological conditions. However, only recently, research work dealing with the various aspects involving different physicochemical properties and complexation behaviour of tetradentate Schiff bases has appeared in the literature, primarily focusing on the separation of actinides from lanthanides in nuclear reprocessing [17] and catalytic properties [18].

Previously, we have reported the synthesis and the structural and spectroscopic characterization of lanthanide complexes with N,N'-bis[1-(pyridin-2-yl)ethylidene]ethane-1,2-diamine [19] and N,N'-bis(pyridin-2-yl-methylene)benzene-1,2-diamine [20]. It was found that the ethylenediamine "hinge" of the di-Schiff base ligand eliminates the possibility of coplanar coordination of the four nitrogen donors [19] while when we changed the ethylene diamine moiety with 1,2-phenylenediamine to force planar coordination of the tetradentate di-Schiff base, we ended up with the lanthanide cations outside of the four nitrogens plane [20]. In a different work, [21], we found that N,N'-bis(pyridin-2-ylmethylene)cyclohexane-1,2-diamine has an intermediate coordinating behaviour to the lanthanides.

In a previous work, the utilization of 8-hydroxyquinoline-2-carboxaldehyde for the preparation of Schiff bases leads to products with poor solubility [22]. The next step in our research is to elongate the diamine part of the above-mentioned ligands, incorporating donor atoms, and study the structure and the stability of the prepared complexes. Since the denticity of the ligands is increased, we expected more stable complexes. Herein we report the synthesis and characterization of four new lanthanide complexes with (NE,N'E)-2,2'-(ethane-1,2-diylbis(oxy))bis(N-(pyridin-2-yl-methylene)ethanamine), a ligand derived by the condensation of 2,2'-(ethane-1,2-diylbis(oxy))diethanamine and pyridine-2-carboxaldehyde.

2. Experimental

2.1. Materials and Instrumentation. All manipulations were carried out under aerobic conditions. Metal salts and organic molecules were purchased from Aldrich and used as received. Solvents were of analytical grade (Lab-Scan Chemical Co) and used without further purification. C, H, and N analyses, IR (4000–370 cm⁻¹) and far-IR (600–30 cm⁻¹) [20], and UV/Vis spectra in the solid state [23] and in solution, [24] thermal studies, and room temperature magnetochemical measurements [20] were carried out as previously described.

2.2. Preparation of the Compounds. The ligand (NE,N'E)-2,2'-(ethane-1,2-diylbis(oxy))bis(N-(pyridin-2-ylmethylene)-ethanamine) was synthesized from the condensation of 2,2'-(ethane-1,2-diylbis(oxy))diethanamine and pyridine-2-carboxaldehyde *in situ*.

To a stirred solution of pyridine-2-carboxaldehyde (0.40 g, 3.73 mmol) in methanol (15 mL), a solution of 2,2'-(ethane-1,2-diylbis(oxy))diethanamine (0.27 g, 1.86 mmol) in methanol (5 mL) was added. The resulting yellowish

TABLE 1: Crystal data and structure refinement for 4.

[Yb(NO ₃) ₂ L](NO ₃)·2MeOH	
Empirical formula	C ₂₀ H ₃₀ N ₇ O ₁₃ Yb
Formula weight	749.55
Temperature	93(2) K
Wavelength	0.71069 Å
Crystal system, Space group	Orthorhombic, P2 ₁ 2 ₁ 2 ₁
Unit cell dimensions	<i>a</i> = 10.668(5) Å <i>b</i> = 13.475(5) Å <i>c</i> = 19.332(5) Å
Volume	2779.0(18) Å ³
Z, Density (calc.)	4, 1.792 g/cm ³
Absorption coefficient	3.441 mm ⁻¹
<i>F</i> (000)	1492
Crystal size	0.21 × 0.1 × 0.08 mm ³
Completeness to theta = 25.00°	99.6%
Reflections (collected/independent)	18754/6025 [<i>R</i> (int) = 0.0217]
Data/restraints/parameters	6025/0/403
Goodness-of-fit on <i>F</i> ²	1.079
Final <i>R</i> indices [<i>I</i> > 2σ(<i>I</i>)]	<i>R</i> ₁ = 0.0193, <i>wR</i> ₂ = 0.0434
<i>R</i> indices (all data)	<i>R</i> ₁ = 0.0198, <i>wR</i> ₂ = 0.0437
Absolute structure parameter	0.599(6)
Largest diff. peak and hole	1.778 and -0.743 eÅ ⁻³

solution was refluxed for 1 hr, and to this the corresponding hydrated lanthanide nitrate (1.86 mmol) in 10 ml of methanol was added. The resulting solutions were heated for a further 30 min and then was left undisturbed to evaporate at room temperature, and yielded microcrystalline solids after three days. The solids were isolated by filtration, washed with a small amount of cold methanol (*ca.* 2 mL) and diethyl ether (2 × 10 mL), and dried under vacuum, over silica gel. The yields were within the range of 55%–65%. A small portion of the mother liquid of complex 4 was layered with diethyl ether to yield a few small colourless blocks, suitable for X-ray structural studies.

[La(NO₃)₂L](NO₃)·3MeOH (1) Anal. Calc. for C₂₃H₃₄N₇O₁₄La: C, 35.80; H, 4.45; N, 12.71. Found: C, 35.96; H, 4.09; N, 12.57%. Selected IR data (cm⁻¹): 3377 mw [m(O–H)], 3070 w [m(C–H)_{ar}], 2980 w [m(C–H)_{al}], 1759 m, 1733 m [*ν*₁ + *ν*₄ of the nitrate], 1641 s [m(C=N)], 1590 ms, 1572 m [ring stretching vibrations], 1492 versus [*ν*₁(A₁) of the nitrate], 1309 versus [*ν*₅(B₂) of the nitrate], 1018 m [*ν*₂(A₁) of the nitrate], 636 m [*δ*(py)], 410 w [*γ*(py)]. TGA/DTA (N₂, 1 atm): 50°C–91°C (–MeOH, found: 12.81, cald.: 12.46%, endotherm), 245°C–380°C (decomposition, sharp exotherm), 591°C (final plateau, La₂O₃, found: 20.91, cald.: 21.11%).

[Pr(NO₃)₂L](NO₃)·3MeOH (2) Anal. Calc. for C₂₃H₃₄N₇O₁₄Pr: C, 35.71; H, 4.44; N, 12.68. Found: C, 35.63%; H, 4.00%; N, 12.39%. Selected IR data (cm⁻¹): 3389 mw [m(O–H)], 3069 w [m(C–H)_{ar}], 2981 w [m(C–H)_{al}], 1762 m, 1731 m [*ν*₁ + *ν*₄ of the nitrate], 1645 s [m(C=N)], 1592 ms, 1571 m [ring stretching vibrations], 1490 versus [*ν*₁(A₁) of the nitrate], 1311 versus [*ν*₅(B₂)

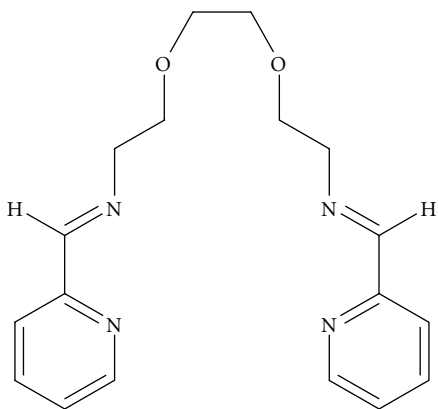
TABLE 2: Selected bond distances (Å) and angles (°) for [Yb(NO₃)₂L](NO₃)·2MeOH (4).

Bond distances				
Yb(1)–N(2)	2.410(3)	Yb(1)–O(6)	2.424(2)	
Yb(1)–O(4)	2.425(2)	Yb(1)–O(1)	2.428(2)	
Yb(1)–N(3)	2.433(3)	Yb(1)–O(2)	2.439(2)	
Yb(1)–O(7)	2.477(2)	Yb(1)–N(1)	2.531(3)	
Yb(1)–N(4)	2.538(2)	Yb(1)–O(3)	2.543(2)	
Yb(1)–N(6)	2.878(2)	Yb(1)–N(5)	2.909(3)	
Bond angles				
N(2)–Yb(1)–O(6)	72.51(8)	N(2)–Yb(1)–O(4)	116.04(8)	
O(6)–Yb(1)–O(4)	140.00(7)	N(2)–Yb(1)–O(1)	131.78(8)	
O(6)–Yb(1)–O(1)	76.60(8)	O(4)–Yb(1)–O(1)	69.55(7)	
N(2)–Yb(1)–N(3)	160.59(8)	O(6)–Yb(1)–N(3)	115.07(8)	
O(4)–Yb(1)–N(3)	70.63(8)	O(1)–Yb(1)–N(3)	67.34(8)	
N(2)–Yb(1)–O(2)	67.19(8)	O(6)–Yb(1)–O(2)	69.61(7)	
O(4)–Yb(1)–O(2)	78.14(8)	O(1)–Yb(1)–O(2)	67.75(8)	
N(3)–Yb(1)–O(2)	131.79(8)	N(2)–Yb(1)–O(7)	113.47(7)	
O(6)–Yb(1)–O(7)	52.03(7)	O(4)–Yb(1)–O(7)	129.66(8)	
O(1)–Yb(1)–O(7)	71.37(7)	N(3)–Yb(1)–O(7)	65.75(7)	
O(2)–Yb(1)–O(7)	114.18(7)	N(2)–Yb(1)–N(1)	65.39(8)	
O(6)–Yb(1)–N(1)	76.95(8)	O(4)–Yb(1)–N(1)	143.01(8)	
O(1)–Yb(1)–N(1)	139.88(8)	N(3)–Yb(1)–N(1)	98.00(9)	
O(2)–Yb(1)–N(1)	128.01(8)	O(7)–Yb(1)–N(1)	68.60(8)	
N(2)–Yb(1)–N(4)	98.28(8)	O(6)–Yb(1)–N(4)	145.03(7)	
O(4)–Yb(1)–N(4)	74.70(7)	O(1)–Yb(1)–N(4)	127.32(8)	
N(3)–Yb(1)–N(4)	64.96(9)	O(2)–Yb(1)–N(4)	138.96(7)	
O(7)–Yb(1)–N(4)	106.83(7)	N(1)–Yb(1)–N(4)	68.74(8)	
N(2)–Yb(1)–O(3)	67.07(8)	O(6)–Yb(1)–O(3)	131.84(7)	
O(4)–Yb(1)–O(3)	51.21(8)	O(1)–Yb(1)–O(3)	112.70(7)	
N(3)–Yb(1)–O(3)	111.73(8)	O(2)–Yb(1)–O(3)	71.32(7)	
O(7)–Yb(1)–O(3)	174.40(7)	N(1)–Yb(1)–O(3)	107.42(8)	
N(4)–Yb(1)–O(3)	67.71(7)	N(2)–Yb(1)–N(6)	93.83(7)	
O(4)–Yb(1)–N(6)	140.30(7)	O(1)–Yb(1)–N(6)	71.05(7)	
N(3)–Yb(1)–N(6)	90.01(8)	O(2)–Yb(1)–N(6)	91.46(7)	
N(1)–Yb(1)–N(6)	71.87(8)	N(4)–Yb(1)–N(6)	128.73(7)	
O(3)–Yb(1)–N(6)	57.89(7)	N(2)–Yb(1)–N(5)	91.86(8)	
O(6)–Yb(1)–N(5)	143.58(7)	O(1)–Yb(1)–N(5)	91.67(7)	
N(3)–Yb(1)–N(5)	90.64(8)	O(2)–Yb(1)–N(5)	74.03(7)	
O(7)–Yb(1)–N(5)	154.67(7)	N(1)–Yb(1)–N(5)	126.83(8)	
N(4)–Yb(1)–N(5)	68.13(7)	N(6)–Yb(1)–N(5)	160.92(7)	
Structural characteristics of H-bonds				
D–H···A	d(D–H)	d(H···A)	d(D···A)	<(DHA)
O(12)–H(4S)···O(11)	1.00(8)	1.89(8)	2.828(4)	156(7)
O(13)–H(8S)···O(12)#1	0.98(5)	1.79(5)	2.758(4)	170(5)

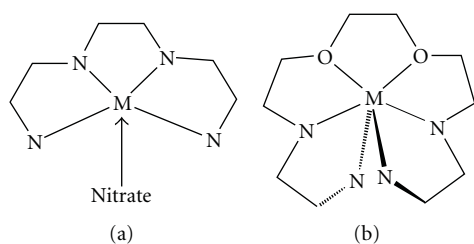
Symmetry transformations used to generate equivalent atoms: #1 $-x + 2, y - (1/2), -z + (3/2)$.

of the nitrate], 1020 m [$\nu_2(A_1)$ of the nitrate], 637 m [$\delta(\text{py})$], 406 w [$\gamma(\text{py})$]. $\mu_{\text{eff}} = 3.47$ BM at 21°C. TGA/DTA (N₂, 1 atm): 61°C–92°C (–MeOH, found: 12.01, calcd.: 12.43%, endotherm), 257°C–337°C (decomposition, sharp exotherm), 547°C (final plateau, Pr₆O₁₁, found: 21.99, calcd.: 22.01%).

[Gd(NO₃)₂L](NO₃)·2MeOH (3) Anal. Calc. for C₂₂H₃₀N₇O₁₃Gd: C, 34.86; H, 4.00; N, 12.94. Found: C, 34.87; H, 3.72; N, 13.00%. Selected IR data (cm⁻¹): 3386 m w [m(O–H)], 3070 w [m(C–H)_{ar}], 2982 w [m(C–H)_{al}], 1767 m, 1734 m [$\nu_1 + \nu_4$ of the nitrate], 1642 s [m(C=N)], 1590 ms, 1573 m [ring stretching vibrations], 1488 versus



SCHEME 1: The ligand (NE,N'E)-2,2'-(ethane-1,2-diylbis(oxy)) bis(N-(pyridin-2-yl-methylene)ethanamine) (L).



SCHEME 2: A schematic representation of the coordination of the Schiff base ligands used, to lanthanides. (a) References 18–21, (b) This work.

$[\nu_1(A_1)$ of the nitrate], 1310 versus $[\nu_5(B_2)$ of the nitrate], 1030 m $[\nu_2(A_1)$ of the nitrate], 630 m $[\delta(py)]$, 417 w $[\gamma(py)]$. $\mu_{\text{eff}} = 7.96$ BM at 21°C. TGA/DTA (N_2 , 1 atm): 51°C–70°C (–MeOH, found: 8.98, calcd.: 9.12%, endotherm), 283°C–345°C (decomposition, sharp exotherm), 508°C (final plateau, Gd_2O_3 , found: 23.57, calcd.: 23.92%).

$[Yb(NO_3)_2L](NO_3) \cdot 2MeOH$ (4) Anal. Calc. for $C_{22}H_{30}N_7O_{13}Yb$: C, 34.15; H, 3.92; N, 12.68. Found: C, 34.17; H, 3.77; N, 13.59%. Selected IR data (cm^{-1}): 3401 mw $[m(O-H)]$, 3078 w $[m(C-H)_{ar}]$, 2967 w $[m(C-H)_{al}]$, 1762 m, 1738 m $[\nu_1 + \nu_4$ of the nitrate], 1633 s $[m(C=N)]$, 1581 ms, 1562 m [ring stretching vibrations], 1497 versus $[\nu_1(A_1)$ of the nitrate], 1308 versus $[\nu_5(B_2)$ of the nitrate], 1039 m $[\nu_2(A_1)$ of the nitrate], 618 m $[\delta(py)]$, 422 w $[\gamma(py)]$. $\mu_{\text{eff}} = 7.96$ BM at 21°C. TGA/DTA (N_2 , 1 atm): 48°C–71°C (–MeOH, found: 8.45, calcd.: 8.80%, endotherm), 288°C–361°C (decomposition, sharp exotherm), 545°C (final plateau, Yb_2O_3 , found: 25.01, calcd.: 25.47%).

2.3. X-Ray Crystallography. X-ray crystal data (Table 1) were collected at 93 K by using a Rigaku MM007 High brilliance RA generator/confocal optics and Mercury CCD system. Intensities were corrected for Lorentz polarization and for absorption. The structure was solved by direct methods [SIR-97]. [25] Hydrogen atoms bound to carbon were idealised. Structural refinement was obtained with full-matrix least-squares based on F^2 by using the program SHELXL. [26] The crystal was a racemic twin and refined smoothly

using TWIN and BASF commands incorporated in SHELX. CCDC 776362 contains the supplementary crystallographic data for this paper. These data can be obtained free of charge via <http://www.ccdc.cam.ac.uk/conts/retrieving.html> or from the Cambridge Crystallographic Data centre, 12 Union Road, Cambridge CB2 1EZ, UK; fax (+44) 1223-336-033; E-mail: deposit@ccdc.cam.ac.uk.

3. Results and Discussion

Complexes 1–4 were prepared by direct reaction of the hydrated lanthanide nitrate salts and the Schiff base ligand starting materials in methanol in 1 : 1 : 2 metal to diamine to aldehyde molar ratio. Though it seems that the ligand (Scheme 1) can be prepared by the direct reaction of its constituents (2, 2'-(ethane-1,2-diylbis(oxy))diethanamine and pyridine-2-carboxaldehyde in 1:2 molar ratio), it was impossible to isolate it in a solid form. This is probably due to the relatively long dietheric chain between the Schiff base moieties. Attempts to prepare the 1 : 2 complexes using larger excess of the ligand parts and different solvents lead to impure products with unidentified formulae.

The crystal structure of complex 4 (Figure 1(a)) consists of cationic complexes $[Yb(NO_3)_2L]^+$, nitrate anions, and two methanol molecules per metal ion held together with hydrogen bonds and C–H $\cdots \pi$ interactions. The Yb^{III} atom, being ten coordinated, is surrounded by six oxygen atoms belonging to two bidentate chelating nitrate ligands and to the etherate part of the ligand and four (two imino and two pyridine) nitrogen atoms belonging to the Schiff base ligand. The coordination polyhedron is much distorted and can be better described, according to Robertson [27], being between a Hoard dodecahedron and a decatetrahedron. (Figure 1(b)).

The Yb–O bond distances span the range 2.424–2.543 Å and they are in good agreement with previously reported values [7, 8, 17–21, 28], taking into account the lanthanide contraction. Though neutral, the etheric oxygen atoms appear to be coordinated to Yb^{III} stronger than the nitrates (mean Yb–O_{nitrate} = 2.47, Yb–O_{ether} = 2.43 Å). There are two probable reasons for this behavior: (a) the macrochelate effect, since the ligand contains six sequential donor atoms and (b) the coordination behavior of the nitrate ligands which are both asymmetrically chelated. There are no important differences in the coordination characteristics of the nitrate ligands. Additionally, both of the coordinated nitrates are coplanar to Yb(1), as indicated by the Yb(1)–O_{coordinated}–N–O_{free} torsion angles which are all larger than 175°C. The mean Yb–N distance is 2.478 Å, with the Yb–N_{imino} being shorter than the corresponding Yb–N_{pyridine} and is in agreement with our previous data [19–21].

The major differences from our previous work on lanthanoid coordination chemistry with Schiff bases rise from the size and the denticity of the ligand. When tetradentate N_4 ligands were used, (Scheme 2(a)) the four nitrogen donor atoms are coplanar and the metal ion lies approximately on the plane formed. There is also space for a nitrate ligand to approach and bind the lanthanide cation. In the present case, the two chelating pyridine Schiff base coordination sites

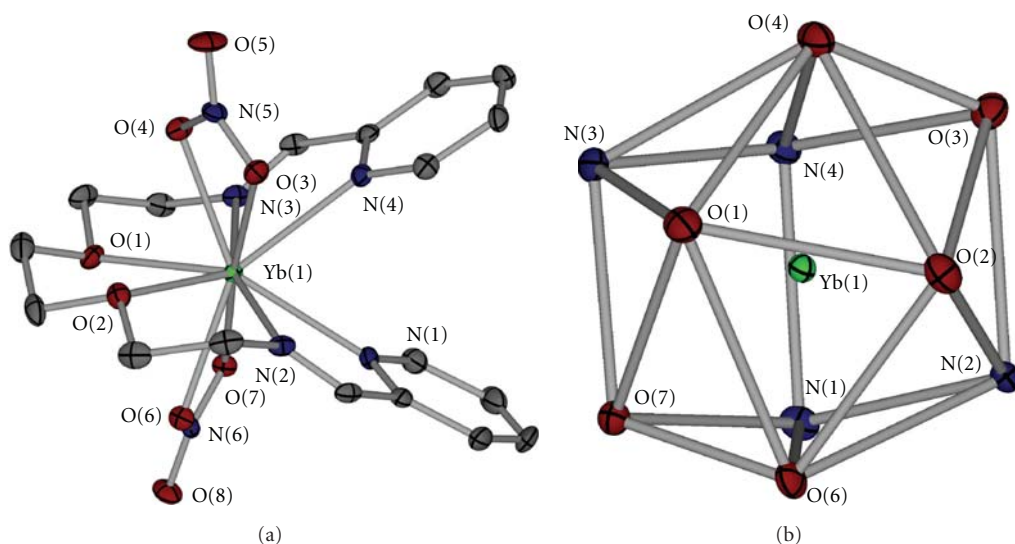


FIGURE 1: (a) A thermal ellipsoid plot of the cation in **4**, including a partial labelling scheme. The hydrogen atoms have been omitted for clarity. (b) The coordination polyhedron about Yb(1) in **4**.

exist, but their distances have been significantly increased. In addition, between the nitrogen chelating sites are present two more oxygen donor atoms which eventually bind the lanthanide. (Scheme 2(b)) Furthermore, there is no space to accommodate six donor atoms on the same plane about Yb^{III} and this results in the exclusion of the pyridine nitrogen away of the plane formed (max deviation from the mean plane: 0.051 Å) by the two oxygen and the two imino nitrogen atoms. This way the two pyridine rings are pointing up and down of the plane with a dihedral angle of $53.846(5)^\circ$. With the tetradentate Schiff bases being coordinated to lanthanides, there is enough room for three nitrato ligands to coordinate to the metal. Increasing the denticity of the ligand to six, only two nitrato ligands appear in the coordination sphere of the metal.

The ionic nitrate interacts with H-bonds with the solvated methanol molecules. Surprisingly, the coordinated nitrates are not involved in hydrogen bonding interactions. This is probably due to their location in cavities with organic surfaces in the crystal.

Comparison of the infrared spectra of the prepared complexes can lead us rather safely to the conclusion that the four complexes are isostructural or at least that both the nitrato and the Schiff base ligands are coordinated in the same manner. Assignment of the nitrate bands has been made as reported previously [29].

The room temperature effective magnetic moments of complexes **2**, **3**, and **4** show little deviation from the Van Vleck theoretical values.

The values of the bonding parameters β (nephelauxetic ratio) and δ (Sinha's parameter) of the Pr^{III} complex **2** are calculated from the solid state f - f spectra by standard equations. Those are 1.003 and -0.30 , respectively, and they suggest that the interaction between the trivalent lanthanide and the ligands is essentially electrostatic and that there is very small participation of the $4f$ orbitals in bonding [30].

All complexes behave similarly when heated under nitrogen. Complexes **1** and **2** lose their solvated methanol molecules above its boiling point, while **3** and **4** lose the solvated molecules about methanol's boiling point. This is an indication of stronger H-bonding in their structures. The intermediates are reasonably stable (up to ca. 280°C) and decompose violently due to the nitrates. The final residues, which are obtained above 490°C , correspond to the sesquioxides except for **2**, which corresponds to Pr_6O_{11} .

Preliminary relaxometric data have shown that **3** is pretty stable in aqueous medium in addition to its increased solubility due to the ionic character. Tailoring, with major goal to increase the stability of lanthanide complexes, of new ligands based on the Schiff base described here and previously [18–22] is in progress.

Acknowledgments

This research was cofunded by the European Union in the framework of the program “Heraklitos” of the “Operational Program for Education and Initial Vocational Training” of the 3rd Community Support Framework of the Hellenic Ministry of Education, funded by 25% from national sources and by 75% from the European Social Fund (ESF).

References

- [1] M. A. V. Ribeiro da Silva, M. D. M. C. Ribeiro da Silva, M. J. S. Monte, J. M. Gonçalves, and É. M. R. Fernandes, “Energetics of metal-ligand binding in copper(II) and nickel(II) complexes of two Schiff bases,” *Journal of the Chemical Society, Dalton Transactions*, no. 7, pp. 1257–1262, 1997.
- [2] V. Alexander, “Design and synthesis of macrocyclic ligands and their complexes of lanthanides and actinides,” *Chemical Reviews*, vol. 95, no. 2, pp. 273–342, 1995.

- [3] R. B. Lauffer, "Paramagnetic metal complexes as water proton relaxation agents for NMR imaging: theory and design," *Chemical Reviews*, vol. 87, no. 5, pp. 901–927, 1987.
- [4] J. Hall, R. Häner, S. Aime et al., "Relaxometric and luminescence behaviour of triaqua-hexaazamacrocyclic complexes, the gadolinium complex displaying a high relaxivity with a pronounced pH dependence," *New Journal of Chemistry*, vol. 22, no. 6, pp. 627–631, 1998.
- [5] P. H. Smith, J. R. Brainard, D. E. Morris, G. D. Jarvinen, and R. R. Ryan, "Solution and solid-state characterization of europium and gadolinium schiff base complexes and assessment of their potential as contrast agents in magnetic resonance imaging," *Journal of the American Chemical Society*, vol. 111, no. 19, pp. 7437–7443, 1989.
- [6] J. de O. Cabral, M. F. Cabral, W. J. Cummins, M. G. B. Drew, A. Rodgers, and S. M. Nelson, "Hexagonal bipyramidal alkaline earth and lead(II) complexes of a hexa-imine macrocyclic ligand," *Inorganica Chimica Acta*, vol. 30, pp. L313–L316, 1978.
- [7] J. D. J. Backer-Dirks, C. J. Gray, F. A. Hart, M. B. Hursthouse, and B. C. Schoop, "Preparation and properties of complexes of lanthanides with a hexadentate nitrogen-donor macrocycle: X-ray crystal structure of the complex $[\text{La}(\text{NO}_3)_3\text{L}]$," *Journal of the Chemical Society, Chemical Communications*, no. 17, pp. 774–775, 1979.
- [8] A. M. Arif, J. D. J. Backer-Dirks, C. J. Gray, F. A. Hart, and M. B. Hursthouse, "Syntheses, X-ray structures, and properties of complexes of macrocyclic hexaimines with lanthanide nitrates," *Journal of the Chemical Society, Dalton Transactions*, no. 7, pp. 1665–1673, 1987.
- [9] G. Bombieri, F. Benetollo, A. Polo, L. De Cola, D. L. Smailes, and L. M. Vallarino, "Synthesis, characterization, and crystal structure of a hexaaza macrocyclic complex of lutetium(III)," *Inorganic Chemistry*, vol. 25, no. 8, pp. 1127–1132, 1986.
- [10] F. Benetollo, A. Polo, G. Bombieri, K. K. Fonda, and L. M. Vallarino, "X-ray crystal structures and nuclear magnetic resonance spectra of macrocyclic complexes of neodymium(III) and europium(III)," *Polyhedron*, vol. 9, no. 11, pp. 1411–1422, 1990.
- [11] G. Bombieri, F. Benetollo, A. Polo, K. K. Fonda, and L. M. Vallarino, "NMR, luminescence, and X-ray crystallographic studies of the interaction of uncharged N-donor ligands with europium(III) in the macrocyclic complex $[\text{Eu}(\text{CH}_3\text{COO})_2(\text{C}_{22}\text{H}_{26}\text{N}_6)]\text{Cl} \cdot 4(\text{H}_2\text{O})$," *Polyhedron*, vol. 10, no. 12, pp. 1385–1394, 1991.
- [12] S. W. A. Bligh, N. Choi, W. J. Cummins, E. G. Evagorou, J. D. Kelly, and M. McPartlin, "Yttrium(III) and lanthanide(III) metal complexes of an 18-membered hexaaza tetraimine macrocycle—crystal structure of the gadolinium(III) complex," *Journal of the Chemical Society, Dalton Transactions*, no. 23, pp. 3369–3376, 1994.
- [13] F. Benetollo, G. Bombieri, K. K. Fonda, and L. M. Vallarino, "Interaction of β -diketones with La^{III} , Eu^{III} and Y^{III} complexes of the six-nitrogen-donor macrocyclic ligand $\text{C}_{22}\text{H}_{26}\text{N}_6$ and crystal structure of $[\text{Eu}(\text{CH}_3\text{COO}) * (\text{C}_6\text{H}_5\text{CO})_2\text{CH} * (\text{C}_{22}\text{H}_{26}\text{N}_6)](\text{CH}_3\text{COO}) \cdot 6(\text{H}_2\text{O})$," *Polyhedron*, vol. 16, no. 11, pp. 1907–1919, 1997.
- [14] G. Bombieri, F. Benetollo, A. Polo, L. De Cola, W. T. Hawkins, and L. M. Vallarino, "Synthesis, characterization, and x-ray crystal structure of tris-isothiocyanato complexes of the yttrium(III) and europium(III) ions with a six-nitrogen-donor macrocyclic ligand," *Polyhedron*, vol. 8, no. 17, pp. 2157–2167, 1989.
- [15] K. K. Fonda, D. L. Smailes, L. M. Vallarino et al., "Interaction of neutral and anionic o-donor organic ligands with europium(III) in the macrocyclic complex $[\text{Eu}(\text{CH}_3\text{COO})_2(\text{C}_{22}\text{H}_{26}\text{N}_6)]\text{Cl} \cdot 4\text{H}_2\text{O}$ and crystal structure of $[\text{Eu}(\text{CH}_3\text{COO})_2(\text{C}_{22}\text{H}_{26}\text{N}_6)](\text{CH}_3\text{COO}) \cdot 9\text{H}_2\text{O}$," *Polyhedron*, vol. 12, no. 5, pp. 549–562, 1993.
- [16] S. W. A. Bligh, N. Choi, E. G. Evagorou, M. McPartlin, and K. N. White, "Dimeric yttrium(III) and neodymium(III) macrocyclic complexes: potential catalysts for hydrolysis of double-stranded DNA," *Journal of the Chemical Society, Dalton Transactions*, no. 21, pp. 3169–3172, 2001.
- [17] M. G. B. Drew, M. R. St. J. Foreman, M. J. Hudson, and K. F. Kennedy, "Structural studies of lanthanide complexes with tetradentate nitrogen ligands," *Inorganica Chimica Acta*, vol. 357, no. 14, pp. 4102–4112, 2004.
- [18] S. Kano, H. Nakano, M. Kojima, N. Baba, and K. Nakajima, "An effect of the ionic radii of lanthanide(III) ions on the structure and catalytic properties of chiral Schiff base-lanthanide(III) complexes," *Inorganica Chimica Acta*, vol. 349, pp. 6–16, 2003.
- [19] S. Gourbatsis, J. C. Plakatouras, V. Nastopoulos, C. J. Cardin, and N. Hadjiliadis, " $[\text{Pr}(\text{NO}_3)_3\text{L}]$: a mononuclear ten-coordinate lanthanide(III) complex with a tetradentate di-Schiff base," *Inorganic Chemistry Communications*, vol. 2, no. 10, pp. 468–471, 1999.
- [20] M. Tsiouri, J. C. Plakatouras, A. Garoufis, V. Nastopoulos, and N. Hadjiliadis, "Interactions of trivalent lanthanide cations with tetradentate schiff bases. Synthesis and characterization of lanthanide(III) complexes with $\text{N,N}'$ -bis(pyridin-2-ylmethylene)benzene-1,2-diamine," *Inorganic Chemistry Communications*, vol. 5, no. 10, pp. 844–847, 2002.
- [21] M. Tsiouri, N. Hadjiliadis, T. Arslan, B. M. Kariuki, and J. C. Plakatouras, "Interactions of trivalent lanthanide cations with tetradentate Schiff bases: new lanthanide(III) complexes from $(1\text{S}, 2\text{S}, \text{N}^1\text{E}, \text{N}^2\text{E})\text{-N,N}'$ -bis(pyridin-2-ylmethylene)cyclohexane-1,2-diamine," *Inorganic Chemistry Communications*, vol. 9, no. 4, pp. 429–432, 2006.
- [22] T. Arslan, C. Öğretir, M. Tsiouri, J. C. Plakatouras, and N. Hadjiliadis, "Interactions of trivalent lanthanide cations with a hexadentate Schiff base derived from the condensation of ethylenediamine with 8-hydroxyquinoline-2-carboxaldehyde," *Journal of Coordination Chemistry*, vol. 60, no. 6, pp. 699–710, 2007.
- [23] F. J. Quaezhaegens, H. O. Desseyn, S. P. Perlepes, J. C. Plakatouras, B. Bracke, and A. T. H. Lenstra, "Synthesis, spectroscopy and thermal properties of the nickel(II), palladium(II) and copper(II) complexes of bis(aminoalkyl)-oxamides (= LH_2) including the crystal structure of $\text{Cu}_2\text{L}(\text{NO}_3)_2$," *Transition Metal Chemistry*, vol. 16, no. 1, pp. 92–101, 1991.
- [24] M. Mylonas, A. Kretzel, J. C. Plakatouras, N. Hadjiliadis, and W. Bal, "The binding of Ni(II) ions to terminally blocked hexapeptides derived from the metal binding -ESHH- motif of histone H2A," *Journal of the Chemical Society, Dalton Transactions*, no. 22, pp. 4296–4306, 2002.
- [25] A. Altomare, M. C. Burla, M. Camalli et al., "SIR97: a new tool for crystal structure determination and refinement," *Journal of Applied Crystallography*, vol. 32, no. 1, pp. 115–119, 1999.
- [26] G. M. Sheldrick, *SHELX97—Programs for Crystal Structure Analysis (Release 97-2)*, Institut für Anorganische Chemie der Universität, Göttingen, Germany, 1998.

- [27] B. E. Robertson, "Coordination polyhedra with nine and ten atoms," *Inorganic Chemistry*, vol. 16, no. 11, pp. 2735–2742, 1977.
- [28] I. Baxter, S. R. Drake, M. B. Hursthouse et al., "Effect of polyether ligands on stabilities and mass transport properties of a series of gadolinium(III) β -diketonate complexes," *Inorganic Chemistry*, vol. 34, no. 6, pp. 1384–1394, 1995.
- [29] A. B. P. Lever, E. Mantovani, and B. S. Ramaswamy, "Infrared combination frequencies in coordination complexes containing nitrate groups in various coordination environments—probe for metal—nitrate interaction," *Canadian Journal of Chemistry*, vol. 49, no. 11, pp. 1956–1965, 1971.
- [30] R. K. Agarwal, K. Arora, and R. K. Sarin, "Magneto and spectral studies of lanthanide(III) nitrate complexes of 4-vinylpyridine," *Synthesis and Reactivity in Inorganic and Metal-Organic Chemistry*, vol. 24, no. 5, pp. 735–747, 1994.

Research Article

In Search for Titanocene Complexes with Improved Cytotoxic Activity: Synthesis, X-Ray Structure, and Spectroscopic Study of Bis(η^5 -cyclopentadienyl)difluorotitanium(IV)

Elias Koleros,¹ Theocharis C. Stamatatos,¹ Vassilis Psycharis,² Catherine P. Raptopoulou,² Spyros P. Perlepes,¹ and Nikolaos Klouras¹

¹Department of Chemistry, University of Patras, 26504 Patras, Greece

²National Center of Scientific Research, "Demokritos" (NCSR), Institute of Materials Science, Aghia Paraskevi, 15310 Attikis, Greece

Correspondence should be addressed to Nikolaos Klouras, n.klouras@chemistry.upatras.gr

Received 27 March 2010; Accepted 3 May 2010

Academic Editor: Evy Manessi-Zoupa

Copyright © 2010 Elias Koleros et al. This is an open access article distributed under the Creative Commons Attribution License, which permits unrestricted use, distribution, and reproduction in any medium, provided the original work is properly cited.

The 1 : 2 reaction of $[\text{Ti}(\eta^5\text{-C}_5\text{H}_5)_2\text{Cl}_2]$ and AgF in $\text{CHCl}_3/\text{H}_2\text{O}$ yielded the fluoro analog $[\text{Ti}(\eta^5\text{-C}_5\text{H}_5)_2\text{F}_2]$ (**1**) in almost quantitative yield (C_5H_5 is the cyclopentadienyl group). The coordination about the Ti^{IV} atom formed by two fluoro ligands and the centroids of the cyclopentadienyl rings is distorted tetrahedral. The compound crystallizes in the orthorhombic space group $C2cm$. The lattice constants are $a = 5.9055(4)$, $b = 10.3021(5)$, $c = 14.2619(9)$ Å, and $\alpha = \beta = \gamma = 90^\circ$. The complex has been characterized by elemental analyses and spectroscopic (IR, ^1H NMR) data. A structural comparison of the four members of the $[\text{Ti}(\eta^5\text{-C}_5\text{H}_5)_2\text{X}_2]$ family of complexes ($\text{X} = \text{F}, \text{Cl}, \text{Br}, \text{I}$) is attempted.

1. Introduction

One of the first metal complexes discovered to exhibit biological activity has been cisplatin, $[\text{Pt}(\text{NH}_3)_2\text{Cl}_2]$ [1]. It is considered as one of the most efficient drugs for the treatment of certain types of cancer; however, drug toxicity and resistance limit its utilization for a broader range of diseases. In recent years, there has been a growing interest in the development of nonplatinum-based anticancer therapeutics. The main goal is to increase the variety of potential drugs, which may lead to higher activities enabling the administration of lower doses, attack of different types of tumour cells, solution of drug resistance problems, better selectivity and to lower toxicity. Non-platinum complexes may introduce numerous options for coordination numbers and geometries, oxidation states, affinity for certain types of biological ligands, and so forth, and may thus operate by different mechanisms. One class of such complexes are metallocene dihalides.

Metallocene dihalides, $[\text{M}(\eta^5\text{-C}_5\text{H}_5)_2\text{X}_2]$ ($\text{M} = \text{Ti}, \text{V}, \text{Nb}, \text{Mo}, \text{Re}$; $\text{X} = \text{halide ligand}$; $\text{C}_5\text{H}_5 = \text{Cp}$, the cyclopentadienyl group), are a relatively new class of small hydrophobic

organometallic anticancer agents that exhibit antitumour activities against cancer cell lines, such as leukaemias P388 and L1210, colon 38 and Lewis lung carcinomas, B16 melanoma, solid and fluid Ehrlich ascites tumours and also against human colon, renal and lung carcinomas transplanted into athymic mice [2–5]. Titanocene dichloride, $[\text{Ti}(\eta^5\text{-C}_5\text{H}_5)_2\text{Cl}_2]$, is the most widely studied metallocene compound as a cytotoxic anticancer agent, which means that it can selectively kill cancer cells, and was used in phase I and II clinical trials [6–13]. However, the efficacy of $[\text{Ti}(\eta^5\text{-C}_5\text{H}_5)_2\text{Cl}_2]$ in phase II clinical trials in patients with metastatic renal cell carcinoma [12] or metastatic breast cancer [13] was too low to be pursued. As titanium is present in many biomaterials, such as in food in the form of a whitening pigment, it is not unreasonable to conceive that it may be incorporated into drugs and into living systems, with particularly low toxicity [14].

In 2008, a novel class of substituted titanocene dichlorides, the so-called "benzyl-substituted titanocenes", with improved cytotoxic activity were developed and tested for their potential application as anticancer drugs [15]. The cytotoxic activity can also be influenced by substitution

of the two chloride ligands. More recently, Huhn and co-workers reported the synthesis and cytotoxicity of selected benzyl-substituted fluorotitanocene derivatives that showed a cytotoxic activity 3–5 fold higher than that of the respective dichlorides [16]. In the same paper, the X-ray structure analysis of two of the titanocene difluoride derivatives was also described. The prototype of the latter compounds is titanocene difluoride, $[\text{Ti}(\eta^5\text{-C}_5\text{H}_5)_2\text{F}_2]$, which itself (i) exhibits strong antitumor, anti-inflammatory and anti-arthritis activity as well as immunosuppressant effects [17, 18], (ii) reduces significantly the rates of crystal growth of hydroxyapatite (the model compound for the inorganic component of bones and teeth, observed in pathological calcifications of the articular cartilage) [19], and (iii) is an effective catalyst for the reduction of lactones and imines, reductive-deoxygenative coupling of amides, hydrogenation of olefins, and defluorination of saturated perfluorocarbons [20].

Surprisingly, the crystal structure of bis(η^5 -cyclopentadienyl)difluorotitanium(IV) is not known. In the present work, we describe the first X-ray diffraction study of $[\text{Ti}(\eta^5\text{-C}_5\text{H}_5)_2\text{F}_2]$, providing structural data which will probably be important in structure-activity investigations of new titanocene difluorides, a promising class in terms of medical applications.

2. Experiments

Reagents and solvents were purchased from commercial sources, and were purified (where necessary) and dried before use by standard procedures. The starting titanocene dichloride, $[\text{Ti}(\eta^5\text{-C}_5\text{H}_5)_2\text{Cl}_2]$, was synthesized under an argon atmosphere using dried THF by the method of Wilkinson and Birmingham [21] and recrystallized from boiling toluene. All manipulations were performed under aerobic conditions. Microanalyses (C, H) were performed by the University of Patras (Greece) Microanalytical Laboratory using an EA 1108 Carlo Erba analyzer. IR spectra ($4000\text{--}450\text{ cm}^{-1}$) were recorded on a Perkin-Elmer 16 PC FT-spectrometer with samples prepared as KBr pellets. The ^1H NMR spectrum of the complex in CDCl_3 was recorded with a Bruker Avance 400 MHz spectrometer; chemical shifts are reported relative to tetramethylsilane. Conductivity measurements were carried out at 25°C using an Ehrhardt-Metzger, type L21, conductivity bridge.

$[\text{Ti}(\eta^5\text{-C}_5\text{H}_5)_2\text{F}_2]$ (**1**) was synthesized in a plastic bottle from a solution of the dichloride, $[\text{Ti}(\eta^5\text{-C}_5\text{H}_5)_2\text{Cl}_2]$ (5 mmol), in CHCl_3 by adding a freshly prepared aqueous solution of AgF (10 mmol) according to the procedure described in [22]. The reaction mixture was shaken vigorously for 20 minutes at room temperature. During this time, the colour of the organic phase changed from red to orange and finally to yellow. The yellow CHCl_3 phase was separated from the aqueous phase, containing the white precipitate of AgCl , through a separatory funnel and filtered. Condensation of the yellow filtrate under reduced pressure gave a fluffy lemon-yellow solid that was dried *in vacuo* over silica gel and recrystallized from toluene. Yield 90% and m.p. 235°C (dec.) Lemon-yellow, needle-like crystals of **1** suitable

TABLE 1: Crystallographic data and structure refinement for complex **1**.

Empirical formula	$\text{C}_{40}\text{H}_{40}\text{Ti}_4\text{F}_8$
Formula weight (g mol^{-1})	864.32
Colour and habit	Yellow prisms
Crystal size (mm)	$0.75 \times 0.10 \times 0.10$
Crystal system	Orthorhombic
Space group	$C2cm$
<i>Unit cell dimensions</i>	
$a, \text{\AA}$	5.9055(4)
$b, \text{\AA}$	10.3021(5)
$c, \text{\AA}$	14.2616(9)
$\alpha, ^\circ$	90
$\beta, ^\circ$	90
$\gamma, ^\circ$	90
$V, \text{\AA}^3$	867.66(9)
Z	1
$\rho, \text{Mg m}^{-3}$	1.654
T, K	160(2)
Radiation (\AA)	$\text{Cu K}\alpha$ ($\lambda = 1.54178$)
μ, mm^{-1}	8.207
$F(000)$	440
θ range ($^\circ$)	8.61–59.99
<i>Index ranges, $^\circ$</i>	
	$-6 \leq h \leq 6$
	$-11 \leq k \leq 11$
	$-14 \leq l \leq 12$
Measured reflections	2894
Unique reflections	613 ($R_{\text{int}} = 0.0947$)
Reflections used [$I > 2\sigma(I)$]	535
Parameters refined	60
GoF (on F^2)	1.100
$R1^a$ [$I > 2\sigma(I)$]	0.0668
$wR2^b$ [$I > 2\sigma(I)$]	0.1469
$(\Delta\rho)_{\text{max}}/(\Delta\rho)_{\text{min}}, \text{e \AA}^{-3}$	1.183/–0.680

$$^a R1 = \Sigma(|F_o| - |F_c|)/\Sigma(|F_o|). \quad ^b wR2 = \{\Sigma[w[(F_o^2 - F_c^2)^2]/\Sigma(w(F_o^2)^2)]\}^{1/2}.$$

for X-ray analysis were obtained by vapour diffusion of petroleum ether into a CHCl_3 solution of the product placed in an H-shaped tube. Anal. Calc. for $\text{C}_{40}\text{H}_{40}\text{F}_2\text{Ti}$ (216.08): C, 55.59; H, 4.66. Found: C, 55.28; H, 4.62. Selected IR data ($\text{KBr}, \text{cm}^{-1}$): 3108 (s), 1442 (s), 1362 (w), 1016 (s), 874 (m), 822 (vs), 610 (w), 564 (s), 539 (m). ^1H NMR (400 MHz, CDCl_3): δ 6.53 (t).

2.1. X-Ray Crystallographic Studies. A yellow prismatic crystal of **1** was taken directly from the mother liquid and immediately cooled to -113°C . Diffraction measurements were made on a Rigaku R-AXIS SPIDER Image Plate diffractometer using graphite monochromated $\text{Cu K}\alpha$ radiation. Data collection (ω -scans) and processing (cell refinement, data reduction and empirical absorption correction) were performed using the CRYSTALCLEAR program package [23]. Important crystal data and parameters for data collection and refinement are listed in Table 1. The structure was

TABLE 2: Selected bond lengths (Å) and angles (°) for complex **1**.^a

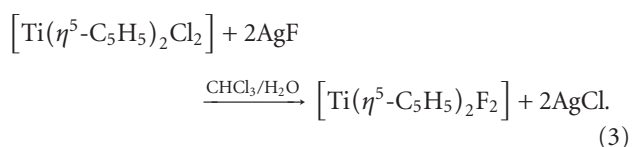
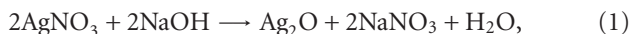
Ti-F(1)	1.853(4)	Ti-C(3)	2.363(9)
Ti-F(2)	1.859(4)	Ti-C(4)	2.365(10)
Ti-C(1)	2.375(11)	Ti-C(5)	2.396(11)
Ti-C(2)	2.400(11)	Ti-Cp	2.066
C(1)-C(2)	1.358(15)	C(4)-C(5)	1.386(14)
C(2)-C(3)	1.396(14)	C(5)-C(1)	1.390(15)
C(3)-C(4)	1.411(16)	mean C-C	1.388
F(1)-Ti-F(2)	96.0(2)	F(1)-Ti-Cp	107.30
Cp-Ti-Cp'	128.53	F(2)-Ti-Cp	106.46
C(1)-C(2)-C(3)	108.6(10)	C(4)-C(5)-C(1)	107.5(10)
C(2)-C(3)-C(4)	106.8(7)	C(5)-C(1)-C(2)	109.2(13)
C(3)-C(4)-C(5)	107.8(8)	Aver. C-C-C	108.0

^aPrimed atoms are related to the unprimed ones by the symmetry operation $x, y, 1/2-z$.

solved by direct methods using SHELXS-97 [24] and refined by full-matrix least-squares techniques on F^2 with SHELXL-97 [25]. Hydrogen atoms of the cyclopentadienyl (Cp) group were introduced at calculated positions as riding on bonded atoms. All non-H atoms were refined anisotropically. In the structure of **1**, the carbon atoms of one of the two Cp rings are disordered over symmetry-related positions. CCDC 771089 contains the supplementary crystallographic data for this paper. These data can be obtained free of charge at <http://www.ccdc.cam.ac.uk/conts/retrieving.html> (or from the Cambridge Crystallographic Data Centre, 12 Union Road, Cambridge CB2 1EZ, UK; Fax: (internat.) ++44-1223/336-033; E-mail: deposit@ccdc.cam.ac.uk).

3. Results and Discussion

3.1. Synthetic Comments. The title compound was first prepared by Wilkinson and Birmingham in 1954 by dissolving the bromo analog, $[\text{Ti}(\eta^5\text{-C}_5\text{H}_5)_2\text{Br}_2]$, in hot 12 *N* hydrofluoric acid and heating on a steam-bath until the solution was pale yellow in colour. On cooling, yellow crystals were received which were recrystallized from 3 *N* hydrofluoric acid solution [21]. Among the other published in the literature methods, we selected that described by Pink in his Thesis. The method uses AgF prepared *in situ*, which gives the best yields in the shortest time [29]. The preparation of **1** involves the reactions represented by the stoichiometric equations (1)–(3):



The two first steps ((1) and (2)) are necessary because AgF decomposes upon staying. Experiments with commercial AgF always lead to poor yields. Another method for a high-yield synthesis of **1** was developed by Ruzicka and coworkers

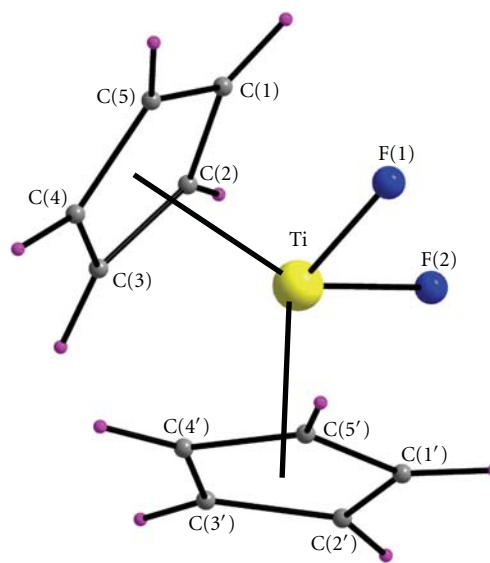


FIGURE 1: Labeled PovRay representation of complex **1** with the atom numbering scheme. Primes are used for symmetry-related atoms. Colour scheme: Ti^{IV} , yellow; F, blue; C, gray; H, purple.

[30] and involves the 1 : 2 reaction of $[\text{Ti}(\eta^5\text{-C}_5\text{H}_5)_2\text{Cl}_2]$ and the good fluorinating agent $\{2\text{-}[(\text{CH}_3)_2\text{NCH}_2]\text{C}_6\text{H}_4\}(\text{n-Bu})_2\text{SnF}$ in CH_2Cl_2 .

Complex **1** is, like $[\text{Ti}(\eta^5\text{-C}_5\text{H}_5)_2\text{Cl}_2]$, a very stable compound. It dissolves easily in common organic solvents such as chloroform, methanol, benzene, toluene and is much more soluble in water than are the other congener halides, even at room temperature, without decomposition. A decent water solubility is essential for a satisfactory cytotoxic activity of titanium(IV) complexes. Its molar conductivity (H_2O , 10^{-3} M, 25°C) is less than $5 \text{ S cm}^2 \text{ mol}^{-1}$. This means that, in contrast to the other corresponding titanocene dihalides, the fluoride ligands in **1** are hydrolytically stable. In this case, the water solubility and negligible molar conductivity could be attributed to the formation of hydrogen bonds between the electronegative F^- ligands of **1** and the H_2O molecules rather than to a dissociation of the complex to species

TABLE 3: Comparison of some important molecular parameters (average values) for the four prototype titanocene dihalogenides, $[\text{Ti}(\eta^5\text{-C}_5\text{H}_5)_2\text{X}_2]$.

Compound	Ti-Cp ^a (Å)	Ti-X (Å)	Cp-Ti-Cp (°)	X-Ti-X (°)	Ref.
$[\text{Ti}(\eta^5\text{-C}_5\text{H}_5)_2\text{F}_2]$	2.066	1.856	128.5	96.0	present work
$[\text{Ti}(\eta^5\text{-C}_5\text{H}_5)_2\text{Cl}_2]$	2.059	2.364	131.0	94.5	[26]
$[\text{Ti}(\eta^5\text{-C}_5\text{H}_5)_2\text{Br}_2]$	2.058	2.493	131.6	94.9	[27]
$[\text{Ti}(\eta^5\text{-C}_5\text{H}_5)_2\text{I}_2]$	2.045	2.769	132.3	92.8	[28]

^aCp = η^5 -cyclopentadienyl ring.

TABLE 4: Comparison of unit cell parameters for the four prototype titanocene dihalogenides, $[\text{Ti}(\eta^5\text{-C}_5\text{H}_5)_2\text{X}_2]$.

Compound	<i>a</i> (Å)	<i>b</i> (Å)	<i>c</i> (Å)	α (°)	β (°)	γ (°)	Crystal system	Ref.
$[\text{Ti}(\eta^5\text{-C}_5\text{H}_5)_2\text{F}_2]$	5.9055(4)	10.3021(5)	14.2616(9)	90	90	90	Orthorhombic	present work
$[\text{Ti}(\eta^5\text{-C}_5\text{H}_5)_2\text{Cl}_2]$	7.882(5)	19.478(10)	12.156(9)	90.46(2)	102.58(2)	143.49(2)	Triclinic	[26]
$[\text{Ti}(\eta^5\text{-C}_5\text{H}_5)_2\text{Br}_2]$	7.872(5)	11.807(5)	12.310(3)	107.62(3)	100.83(4)	90.69(4)	Triclinic	[27]
$[\text{Ti}(\eta^5\text{-C}_5\text{H}_5)_2\text{I}_2]$	13.426(4)	7.173(2)	13.096(4)	90	116.686(5)	90	Monoclinic	[28]

^aCp = η^5 -cyclopentadienyl ring.

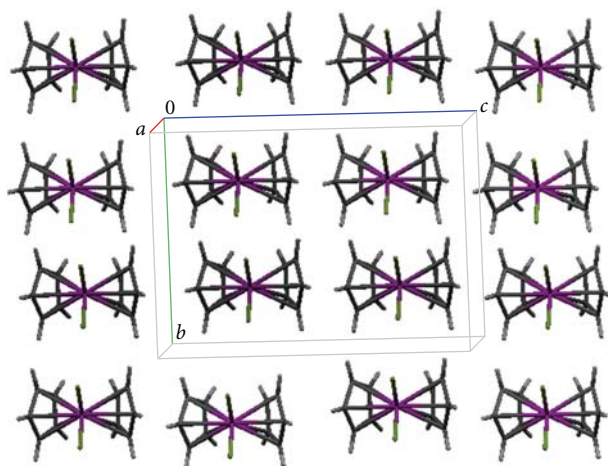


FIGURE 2: Drawing of the crystalline packing of complex 1.

like $[\text{Ti}(\eta^5\text{-C}_5\text{H}_5)_2(\text{H}_2\text{O})_2]^{2+}$ and F^- . The oxophilicity of Ti^{IV} makes complexes of this metal ion with organic and inorganic ligands highly susceptible to hydrolysis. Complexes of hydrolytic instability are not biologically active, probably due to rapid formation of inactive aggregates [14].

3.2. Spectroscopic Characterization. The IR spectra of π -bonded cyclopentadienyl metal complexes have been studied [31–33]. In the IR spectrum of **1** the bands at 3108, 1442, 1016, 874/822 and 610 cm^{-1} can be assigned [31–33] to the $\nu(\text{CH})$, $\nu(\text{CC})$, $\delta(\text{CH})$, $\pi(\text{CH})$ and $\delta(\text{CCC})$ vibrational modes, respectively. The bands at 564 and 539 cm^{-1} are assigned [32] to the $\nu_1(A_1)$ and $\nu_6(B_1)$ (under C_{2v} point group symmetry) stretching modes of the terminal $\text{Ti}^{\text{IV}}\text{-F}$ bonds.

The ^1H NMR spectrum (CDCl_3) of **1** shows a triplet peak at $\delta = 6.53\text{ ppm}$ corresponding to the equivalent protons of the $\eta^5\text{-C}_5\text{H}_5$ protons [31, 34]. The triplet character of

the signal is due to the small 3J coupling (1.7 Hz) between the cyclopentadienyl protons and the fluoro nuclei in the molecule [34].

3.3. Description of Structure. The molecular structure and a crystal packing diagram of **1** are shown in Figures 1 and 2, respectively. Bond lengths and angles are listed in Table 2.

The structure of **1** consists of isolated $[\text{Ti}^{\text{IV}}(\eta^5\text{-C}_5\text{H}_5)_2\text{F}_2]$ molecules. The molecule has the familiar, distorted tetrahedral shape found in the chloro [26], bromo [27] and iodo [28] members of the $[\text{Ti}^{\text{IV}}(\eta^5\text{-C}_5\text{H}_5)_2\text{X}_2]$ family of complexes. The distorted tetrahedral structure arises if we consider the Cp ring centroids as each occupying one coordination site around the metal ion. The cyclopentadienyl centroid-titanium-cyclopentadienyl centroid angle is 128.53° , and the fluorine-titanium-fluorine angle is 96.0° . The TiF_2 group defines a symmetry plane and there is thus one crystallographically independent Cp ligand. The plane defined by the Ti^{IV} atom and the centroids of the Cp rings bisects the F-Ti-F bond angle. Thus, the molecule has a 2-fold symmetry about the line of intersection of this plane and the plane of the F-Ti-F bond angle; its point group symmetry is C_{2v} . The Cp ring is planar to $\pm 0.019\text{ \AA}$. The least-squares planes of the two symmetry related Cp rings in the bent $(\text{Cp})_2\text{Ti}$ fragment of **1** form a dihedral angle of 53.49° . The two Cp rings exhibit a staggered conformation. The angle between the normals to ring planes is 53.83° .

The five Ti-C bond lengths range from 2.363(9) to 2.400(11) Å. This narrow range establishes a distinct *pentahapto* coordination mode for each Cp ligand in **1**. The mean Ti-C bond distance (2.380 Å) is in agreement with the corresponding values of other bis(cyclopentadienyl)titanium(IV) complexes, for example, the value of 2.370 Å in $[\text{Ti}(\eta^5\text{-C}_5\text{H}_5)_2\text{Cl}_2]$ [26]. The $\text{Ti}^{\text{IV}}\text{-F}$ bond distances [1.853(4), 1.859(4) Å] are similar to those found in other 4-coordinate titanium(IV) complexes containing terminal Ti-F bonds [16, 35, 36]. The C-C bond lengths in the Cp ring of **1** with an average value of 1.388 Å are within the usual range

reported for organometallic complexes containing Cp⁻ rings [27].

Since the single-crystal, X-ray structures of all the four members of the [Ti(η^5 -C₅H₅)₂X₂] (X = F, Cl, Br, I) family are now known, we feel it is interesting to compare some of their important structural and crystallographic parameters. The comparisons are presented in Tables 3 and 4, respectively. The average distance from the Ti^{IV} atom to the ring centroid and the angle between the vectors from the metal center to each of the ring centroids vary by less than 0.025 Å and 4°, respectively, across the four complexes. The F-Ti-F angle (96.0°) is slightly wider than the corresponding X-Ti-X (X = Cl, Br, I) angles (92.8–94.5°) suggesting that electronic, rather than steric, effects influence this angle. The fluoro complex **1** has the largest X-Ti-X and the smallest Cp-Ti-Cp angle. As expected, the average titanium-halogen distances follow the sequence Ti-F < Ti-Cl < Ti-Br < Ti-I.

4. Conclusions

The important message of this work is that we have structurally characterized the last member, namely the fluoro complex, of the [Ti(η^5 -C₅H₅)₂X₂] (X = halogenide) family of complexes. Although the preparation of **1** was reported ~55 years ago, its exact molecular and crystal structure remained unknown until our report in this work. Studies are now underway in our laboratories to investigate the reactivity pattern of **1** with bidentate and tridentate N- or/and O-based ligands, and to study the hydrolytic behavior and cytotoxic activities of the resulting products. It should be mentioned that the fluoride ions themselves, if present in the products, are not cytotoxic at concentrations below 10⁻³ M [16].

Acknowledgment

This paper is dedicated to Professor Dr. Nick Hadjiliadis for his contribution to the advancement of Bioinorganic Chemistry.

References

- [1] S. J. Lippard and J. M. Berg, *Principles of Bioinorganic Chemistry*, University Science Books, Mill Valley, Calif, USA, 1994.
- [2] P. Köpf-Maier, "Tumor inhibition by metallocenes: ultrastructural localization of titanium and vanadium in treated tumor cells by electron energy loss spectroscopy," *Naturwissenschaften*, vol. 67, pp. 415–426, 1980.
- [3] P. Köpf-Maier, "Antitumor activity of titanocene dichloride in xenografted human renal-cell carcinoma," *Anticancer Research*, vol. 19, no. 1 A, pp. 493–504, 1999.
- [4] M. M. Harding and G. Modski, "Antitumor metallocenes: structure-activity studies and interactions with biomolecules," *Current Medical Chemistry*, vol. 7, pp. 1289–1303, 2000.
- [5] G. Mokdsi and M. M. Harding, "Inhibition of human topoisomerase II by the antitumor metallocenes," *Journal of Inorganic Biochemistry*, vol. 83, no. 2-3, pp. 205–209, 2001.
- [6] C. V. Christodoulou, D. R. Ferry, D. W. Fyfe et al., "Phase I trial of weekly scheduling and pharmacokinetics of titanocene dichloride in patients with advanced cancer," *Journal of Clinical Oncology*, vol. 16, no. 8, pp. 2761–2769, 1998.
- [7] K. Mross, P. Robben-Bathe, L. Edler et al., "Phase I clinical trial of a day-1, -3, -5 every 3 weeks schedule with titanocene dichloride (MKT 5) in patients with advanced cancer: a study of the phase I study group of the association for medical oncology (AIO) of the German Cancer Society," *Onkologie*, vol. 23, no. 6, pp. 576–579, 2000.
- [8] A. Korfel, M. E. Scheulen, H.-J. Schmoll et al., "Phase I clinical and pharmacokinetic study of titanocene dichloride in adults with advanced solid tumors," *Clinical Cancer Research*, vol. 4, no. 11, pp. 2701–2708, 1998.
- [9] B. Desoize, "Metals and metal compounds in cancer treatment," *Anticancer Research*, vol. 24, no. 3 A, pp. 1529–1544, 2004.
- [10] F. Caruso and M. Rossi, "Antitumor titanium compounds," *Mini-Reviews in Medicinal Chemistry*, vol. 4, no. 1, pp. 49–60, 2004.
- [11] E. Meléndez, "Titanium complexes in cancer treatment," *Critical Reviews in Oncology/Hematology*, vol. 42, no. 3, pp. 309–315, 2002.
- [12] G. Lümmer, H. Sperling, H. Luboldt, T. Otto, and H. Rübber, "Phase II trial of titanocene dichloride in advanced renal-cell carcinoma," *Cancer Chemotherapy and Pharmacology*, vol. 42, no. 5, pp. 415–417, 1998.
- [13] N. Kröger, U. R. Kleeberg, K. Mross, L. Edler, G. Saß, and D. K. Hossfeld, "Phase II clinical trial of titanocene dichloride in patients with metastatic breast cancer," *Onkologie*, vol. 23, no. 1, pp. 60–62, 2000.
- [14] E. Y. Tshuva and D. Peri, "Modern cytotoxic titanium(IV) complexes; insights on the enigmatic involvement of hydrolysis," *Coordination Chemistry Reviews*, vol. 253, no. 15-16, pp. 2098–2115, 2009.
- [15] K. Strohsfeldt and M. Tacke, "Bioorganometallic fulvene-derived titanocene anti-cancer drugs," *Chemical Society Reviews*, vol. 37, no. 6, pp. 1174–1187, 2008.
- [16] S. Eger, T. A. Immel, J. Claffey et al., "Titanocene difluorides with improved cytotoxic activity," *Inorganic Chemistry*, vol. 49, no. 4, pp. 1292–1294, 2010.
- [17] P. Köpf-Maier, B. Hesse, R. Voiglaender, and H. Köpf, "Tumor inhibition by metallocenes: antitumor activity of titanocene dihalides (C₅H₅)₂TiX₂ (X = F, Cl, Br, I, NCS) and their application in buffered solutions as a method for suppressing drug-induced side effects," *Journal of Cancer Research and Clinical Oncology*, vol. 97, no. 1, pp. 31–39, 1980.
- [18] D. P. Fairlie, M. W. Whitehouse, and J. A. Broomhead, "Irritancy and anti-inflammatory activity of bis(η^5 -cyclopentadienyl)titanium(IV) complexes in rats," *Chemico-Biological Interactions*, vol. 61, no. 3, pp. 277–291, 1987.
- [19] E. Dalas, N. Klouras, and C. Maniatis, "Inhibition of hydroxyapatite formation by titanocenes," *Langmuir*, vol. 8, no. 3, pp. 1003–1006, 1992.
- [20] M. W. Carson and E. Lilly, "Difluorobis(cyclopentadienyl)titanium," in *Encyclopedia of Reagents for Organic Synthesis*, John Wiley & Sons, 2003.
- [21] G. Wilkinson and J. M. Birmingham, "Bis-cyclopentadienyl compounds of Ti, Zr, V, Nb and Ta," *Journal of the American Chemical Society*, vol. 76, no. 17, pp. 4281–4284, 1954.
- [22] G. Brauer, *Handbuch der Präparativen Anorganischen Chemie*, vol. 1, F. Enke, Stuttgart, Germany, 6th edition, 1962.
- [23] Rigaku/MS, *Crystal Clear*, Rigaku/MS, The Woodlands, Tex, USA, 2005.
- [24] G. M. Sheldrick, *SHELXS-97: Structure Solving Program*, University of Göttingen, Göttingen, Germany, 1997.
- [25] G. M. Sheldrick, *SHELXL-97: Crystal Structure Refinement Program*, University of Göttingen, Göttingen, Germany, 1997.

- [26] A. Clearfield, D. K. Warner, C. H. Saltarriaga-Molina, R. Ropal, and I. Bernal, "Structural studies of $(\pi\text{-C}_5\text{H}_5)_2\text{MX}_2$ complexes and their derivatives. The structure of bis(π -cyclopentadienyl)titanium dichloride," *Canadian Journal of Chemistry*, vol. 53, pp. 1622–1629, 1975.
- [27] N. Klouras, V. Nastopoulos, I. Demakopoulos, and I. Leban, "Molecular and crystal structure of bis(cyclopentadienyl)titanium(IV) dibromide, $\text{Ti}(\eta^5\text{-C}_5\text{H}_5)_2\text{Br}_2$," *Zeitschrift für Anorganische und Allgemeine Chemie*, vol. 619, pp. 1927–1930, 1993.
- [28] L. I. Strunkina, M. Kh. Minacheva, K. A. Lyssenko et al., "Interaction of titanium(III) zwitterionic complex $\text{Cp}[\eta^5\text{-C}_5\text{H}_4\text{B}(\text{C}_6\text{F}_5)_3]\text{Ti}$ with organic halides: synthesis and X-ray crystal structure determination of zwitterionic titanocene monohalides," *Journal of Organometallic Chemistry*, vol. 691, no. 4, pp. 557–565, 2006.
- [29] H. Pink, *Über reaktionen von biscyclopentadienyl-titan(IV)-verbindungen $(\text{C}_5\text{H}_5)_2\text{TiX}_2$ mit hydriden und doppelhydriden*, Doctorate thesis, München, Germany, 1959.
- [30] J. Bareš, P. Novák, M. Nádvořník et al., "Monomeric triorganotin(IV) fluorides containing a C,N-chelating ligand," *Organometallics*, vol. 23, no. 12, pp. 2967–2971, 2004.
- [31] P. M. Druce, B. M. Kingston, M. F. Lappert, T. R. Spalding, and R. C. Srivastava, "Metallocene halides. Part I. Synthesis, spectra, and redistribution equilibria of di- π -cyclopentadienyldihalogeno-titanium(IV), -zirconium-(IV), and -hafnium(IV)," *Journal of the Chemical Society A*, pp. 2106–2110, 1969.
- [32] K. Nakamoto, *Infrared and Raman Spectra of Inorganic and Coordination Compounds*, John Wiley & Sons, New York, NY, USA, 4th edition, 1986.
- [33] D. Hartley and M. J. Ware, "The vibrational spectra and assignment of bis-(π -cyclopentadienyl)-iron(II) and the bis-(π -cyclopentadienyl)cobalt(III) cation," *Journal of the Chemical Society A*, pp. 138–142, 1969.
- [34] K. K. Banger and A. K. Brisdon, "The first early transition metal perfluorovinyl complexes: the synthesis of $\text{Cp}_2\text{M}(\text{CF}=\text{CF}_2)_n\text{X}_{2-n}$ ($\text{Cp} = \eta^5\text{-C}_5\text{H}_5^-$; $\text{M} = \text{Ti, Zr}$; $\text{X} = \text{Cl}$ or F) and structures of $\text{Cp}_2\text{Ti}(\text{CF}=\text{CF}_2)_n\text{X}_{2-n}$ ($\text{X} = \text{Cl, F}$) via Ti K-edge EXAFS studies," *Journal of Organometallic Chemistry*, vol. 582, no. 2, pp. 301–309, 1999.
- [35] C. H. Winter, X.-X. Zhou, and M. J. Heeg, "Approaches to hexane-soluble cationic organometallic Lewis acids. Synthesis, structure, and reactivity of titanocene derivatives containing polysilylated cyclopentadienyl ligands," *Inorganic Chemistry*, vol. 31, no. 10, pp. 1808–1815, 1992.
- [36] A. J. Edwards, N. J. Burke, C. M. Dobson, K. Prout, and S. J. Heyes, "Solid state NMR and X-ray diffraction studies of structure and molecular motion in ansa-titanocenes," *Journal of the American Chemical Society*, vol. 117, no. 16, pp. 4637–4653, 1995.

Research Article

The Catalytic Function of Nonheme Iron (III) Complex for Hydrocarbon Oxidation

Giorgos Bilis and Maria Louloudi

Department of Chemistry, University of Ioannina, 45110 Ioannina, Greece

Correspondence should be addressed to Maria Louloudi, mlouloud@uoi.gr

Received 13 March 2010; Accepted 10 May 2010

Academic Editor: Spyros Perlepes

Copyright © 2010 G. Bilis and M. Louloudi. This is an open access article distributed under the Creative Commons Attribution License, which permits unrestricted use, distribution, and reproduction in any medium, provided the original work is properly cited.

A detailed catalytic study of $LFe^{III}Cl$ (where $L = 3\text{-}\{2\text{-}[2\text{-}(3\text{-hydroxy-1,3-diphenyl-allylideneamino)-ethylamino]-ethylimino}\text{-1,3-diphenyl-propen-1-ol}\}$) for hydrocarbon oxidation was carried out, focusing on the role of solvent, atmospheric dioxygen, and oxidant on catalytic efficiency. The data showed that $LFe^{III}Cl$ catalyst was efficient in homogeneous hydrocarbon oxidations providing significant yields. Moreover, *tert*-BuOOH provided comparable oxidation yields with H_2O_2 , slightly favoring the formation of alcohols and ketones *versus* epoxides. Dioxygen intervened in the catalytic reaction, influencing the nature of oxidation products. The polarity of solvent strongly influenced the reaction rates and the nature of oxidation products. A mechanistic model is postulated assuming that $LFe^{III}Cl$ functions *via* the formation of iron-hydroperoxo-species, followed by a radical-based mechanistic path.

1. Introduction

Hydrocarbon oxidation, under mild and environmental friendly conditions, is an important research field, since industrial processes, especially in pharmaceutical industry, are based on the efficiency of direct and selective transformation of hydrocarbons in oxygen-containing products such as aldehydes, ketones alcohols, diols, and epoxides [1, 2]. However, selective oxidation of alkanes, under mild conditions, is a difficult task due to their chemical inertness. Nevertheless, in nature many iron enzymes activate dioxygen and catalyze the stereospecific oxidation of C=C or C-H bonds [3, 4]. Heme iron-proteins such as hemoglobin, myoglobin and cytochromes oxygenase [5] and nonheme enzymes such as methane monooxygenase [6, 7] and Rieske dioxygenases [8, 9] are able to oxidize hydrocarbons [10] *via* biochemical oxygen transport and electron-transfer reactions.

The objective to construct convenient artificial systems for efficient hydrocarbon oxidation using biomimetic iron complexes [11, 12] as catalysts [13–15] by activating green oxidants is particularly interesting. Bioinspired catalytic systems commonly use mild oxidants such as dioxygen, hydrogen peroxide, or *tert*-butyl hydrogen peroxide (TBHP) [16–

20]. In this context, stereoselective hydroxylation, epoxidation, and *cis*-dihydroxylation by synthetic iron-biomimetic catalysts have been reported [21–29]. Iron-peroxo species are invoked to be part of the mechanism of several bioinspired oxidation catalysts [30, 31]. More particularly, iron-complexes react with H_2O_2 or alkyl hydroperoxides forming low-spin $Fe^{III}OOH$ [32, 33] or $Fe^{III}OOR$ [34, 35] which are the key-species in oxidation reactions [16].

Recently, we have reported the synthesis and characterization of the ligand $3\text{-}\{2\text{-}[2\text{-}(3\text{-hydroxy-1,3-diphenyl-allylideneamino)-ethylamino]-ethylimino}\text{-1,3-diphenyl-propen-1-ol}\}$ and its immobilization on silica surface *via* formation of covalent bridging between the ligand secondary amine and the silica OH-groups [36, 37]. Herein for brevity this ligand will be named **L**. The corresponding Mn(II) [36, 37] and Fe(III) [38] catalysts were shown to have remarkable catalytic activity in hydrocarbons oxidation using H_2O_2 as oxidant.

In the present contribution, we report a detailed catalytic study of $LFe^{III}Cl$ focusing mainly on the influence of (a) atmospheric dioxygen, (b) solvent system, and (c) oxidant on its catalytic efficiency. The obtained information is compared with previous data of the $LFe^{III}Cl$ catalyst, and mechanistic aspects are also discussed.

2. Experimental

2.1. General. All substrates were purchased from Aldrich, in their highest commercial purity, stored at 5°C and purified by passage through a column of basic alumina prior to use. Hydrogen peroxide was 30% aqueous solution and tert-BuOOH was 5 M solution in decane.

Infrared spectra were recorded on a Spectrum GX Perkin-Elmer FT-IR System. UV-Vis spectra were recorded using a UV/VIS/NIR JASCO Spectrophotometer. The iron amount was determined by Flame Atomic Absorption spectroscopy on a Perkin-Elmer AAS-700 spectrometer. Mössbauer spectra were recorded with a constant acceleration spectrometer using a ^{57}Co (Rh) source at room temperature and a variable-temperature. X-band Electron Paramagnetic Resonance (EPR) spectra were recorded using a Bruker ER200D spectrometer at liquid N_2 temperatures, equipped with an Agilent 5310A frequency counter. The spectrometer was running under a home-made software based on LabView described earlier [39]. Mass spectra were measured on a Agilent 1100 Series LC-MSD-Trap-SL spectrometer and solution. Thermogravimetric analyses were carried out using Shimadzu DTG-60 analyser. GC analysis was performed using an 8000 Fisons chromatograph with a flame ionization detector and a Shimadzu GC-17A gas chromatograph coupled with a GCMS-QP5000 mass spectrometer.

2.2. Catalysts Preparation and Characterization

2.2.1. Preparation of $\text{LFe}^{\text{III}}\text{Cl}$. To a stirred solution of ethanol and acetonitrile (15 ml) containing the ligand $\text{L} = 3\text{-}\{2\text{-}[2\text{-}(3\text{-hydroxy-1,3-diphenyl-allylideneamino})\text{-ethylamino}]\text{-ethylimino}\}\text{-1,3-diphenyl-propen-1-ol}$ [36, 37] a solution of FeCl_3 in a mixture of EtOH and CH_3CN was added slowly. The resulting mixture was stirred for 24 h at room temperature. Partially solvent evaporation resulted in separation of an orange solid product. The obtained $\text{LFe}^{\text{III}}\text{Cl}$ complex was washed with EtOH and CH_3CN and dried under reduced pressure.

2.2.2. Characterization of $\text{LFe}^{\text{III}}\text{Cl}$. Iron analysis by Flame Atomic Absorbance Spectroscopy and ESI-MS analysis indicated a molecular peak at m/z 605.2 that is attributed in $[\text{LFeCl} + \text{H}]^+$ formation. The IR bands at 3297, 1591, and 1523 cm^{-1} were attributed to the $\nu(\text{NH})$, $\nu(\text{C}=\text{N})$, and $\delta(\text{NH})$ vibrations. In the spectrum of the metal-free ligand L , the corresponding vibrations were detected at 3350, 1600, and 1535 cm^{-1} ; this shift indicates metal coordination to imine- and amine-nitrogen. In the IR spectra of L and the $\text{LFe}^{\text{III}}\text{Cl}$ the $\nu(\text{C}-\text{O})$ vibration was appeared at 1398 and 1389 cm^{-1} , respectively, suggesting strong coordination of Fe to the enolic oxygen atoms of the ligand L . Information about the iron center was obtained by Electron Paramagnetic Resonance (EPR) and Mössbauer spectroscopy. At 78 K, the Mössbauer parameters are $\delta = 0.50\text{ mm/s}$ and $\Delta_{\text{EQ}} = 0.54\text{ mm/s}$ indicating an octahedral high-spin $\text{Fe}^{\text{III}}(S = 5/2)$ center, with the iron bound to nitrogen and oxygen atom donors [40]. The EPR spectrum of solid $\text{LFe}^{\text{III}}\text{Cl}$ is characterised by two peaks at $g = 4.3$ and 9.2, characteristic

of a high-spin $\text{Fe}^{\text{III}}(S = 5/2)$ center in a rhombic ligand-field characterized by $E/D \sim 0.33$ [41]. The UV-Vis spectrum of $\text{LFe}^{\text{III}}\text{Cl}$ in CH_3CN contains absorption bands at 282 ($\epsilon = 20800\text{ M}^{-1}\text{ cm}^{-1}$) and 314 nm ($\epsilon = 25580\text{ M}^{-1}\text{ cm}^{-1}$) due to intraligand transitions in the imine- and phenyl-groups [42]. The absorptions at 413 nm ($\epsilon = 7100\text{ M}^{-1}\text{ cm}^{-1}$) and 512 nm ($\epsilon = 2000\text{ M}^{-1}\text{ cm}^{-1}$) are attributed to LMCT [43]. The low-intensity 512 nm absorption can be attributed to charge transfer from ligand oxygen atoms to metal centre ($p_\pi \rightarrow \text{Fe}^{\text{III}} d_\pi$). Usually, a ($p_\pi \rightarrow \text{Fe}^{\text{III}} d_{\sigma^*}$) transition is also observed at higher energy than the $p_\pi \rightarrow \text{Fe}^{\text{III}} d_\pi$ transition and could be related to the transition at 413 nm [35, 36]. The presence of $\text{Fe}^{\text{III}}\text{-Cl}$ bond also allows the presence of LMCT involving chloride $p_\pi \rightarrow \text{Fe}^{\text{III}} d_\pi$ orbitals [43, 44].

2.3. Catalytic Evaluation

2.3.1. GC-MS. H_2O_2 or tert-BuOOH diluted in solvent (CH_3CN or tert-amylalcohol) was slowly added (within a period of 5 min) to a solvent solution containing the catalyst and the substrate, at room temperature (25°C). For brevity in the text [H_2O_2 in tert-amylalcohol] will be referred as system A, [H_2O_2 in CH_3CN] as system B, and [tert-BuOOH in CH_3CN] as system C, respectively. As an internal standard, acetophenone or bromobenzene were used. Catalytic reactions were initiated by adding the oxidant into reaction mixture.

The progress of the reaction was monitored by GC-MS, by removing small samples of the reaction mixture. The yields reported herein are based on the amount of oxidant H_2O_2 converted to oxygenated products. To establish the identity of the products unequivocally, the retention times and spectral data were compared to those of commercially available compounds. Blank experiments showed that, without catalyst, no oxidative reactions take place.

2.3.2. Reaction Conditions

(1) Optimization of [Oxidant:Substrate] Ratio. To explore the optimum [oxidant-substrate] molar ratio, a first set of catalytic experiments was performed where the amount of substrate was kept constant and the amount of H_2O_2 was varied. Subsequently, a second set of catalytic experiments was run for varied amounts of substrate, using the optimum amount of H_2O_2 found in the first screening. For this screening, cyclooctene (Figure 1(a)), cyclohexene (Figure 1(b)), styrene (Figure 1(c)), and cyclohexane (Figure 1(d)) were tested. It is noted that H_2O_2 was diluted in acetonitrile (1/10 v/v) prior use, and it was introduced into the reaction mixture slowly.

Based on the data of Figures 1(a)–1(d), the higher oxidation yield was obtained by small amounts of H_2O_2 and large excess of substrate. This is consistent with the current view that (a) high oxidant concentration causes oxidative destruction of catalyst, (b) large excess of substrate protects the catalyst from oxidative degradation, and, moreover, (c) this substrate large excess minimizes the overoxidation of initial oxidation products [45].

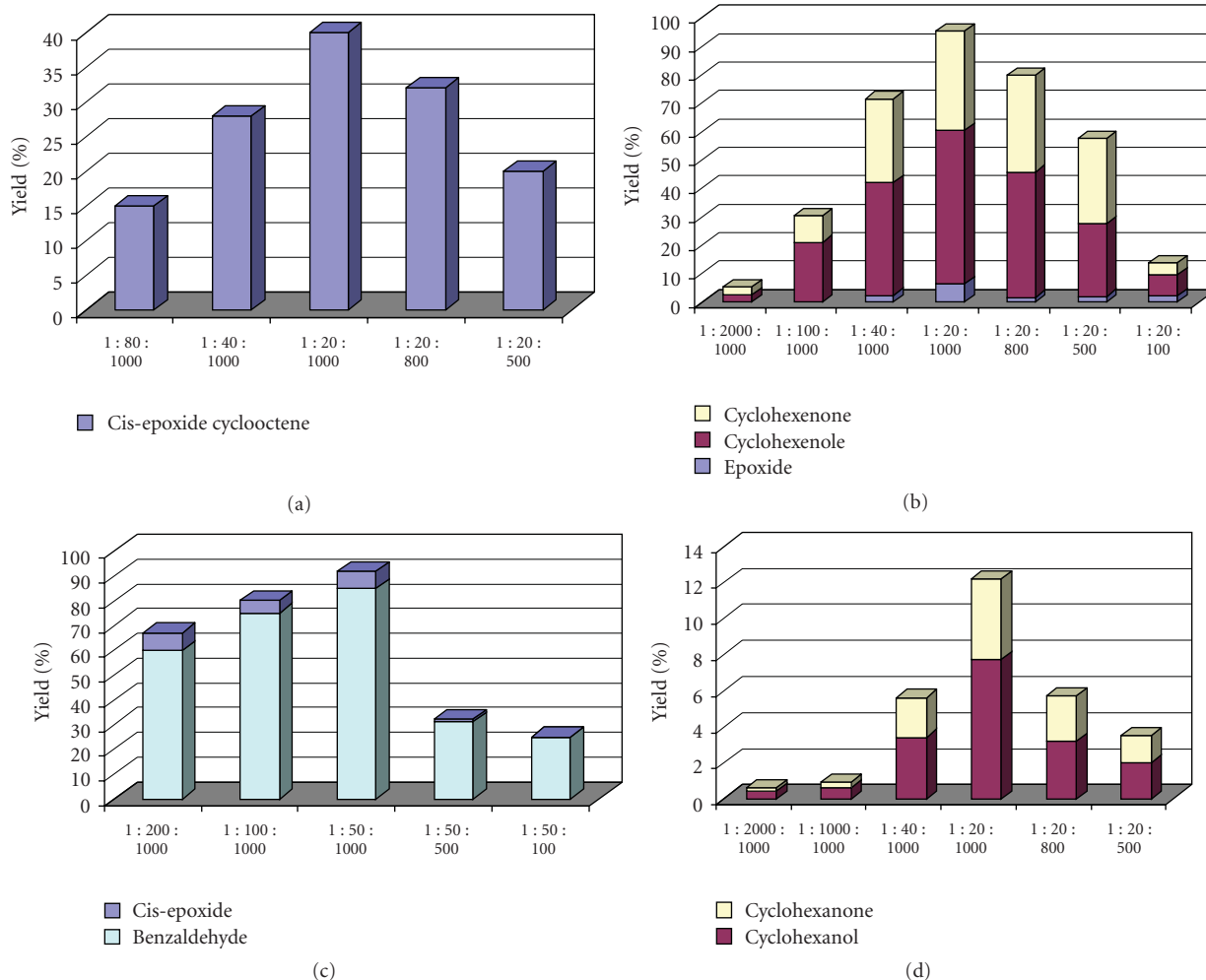


FIGURE 1: (a) Cis-cyclooctene oxidation is catalysed by $\text{LFe}^{\text{III}}\text{Cl}$ at varied Substrate-Oxidant molar ratio in CH_3CN with H_2O_2 . (b) Cyclohexene oxidation is catalysed by $\text{LFe}^{\text{III}}\text{Cl}$ at varied Substrate-Oxidant molar ratio in CH_3CN with H_2O_2 . (c) Styrene oxidation is catalysed by $\text{LFe}^{\text{III}}\text{Cl}$ at varied Substrate-Oxidant molar ratio in CH_3CN with H_2O_2 . (d) Cyclohexane oxidation is catalysed by $\text{LFe}^{\text{III}}\text{Cl}$ at varied Substrate-Oxidant molar ratio in CH_3CN with H_2O_2 . For all figures The given ratio is catalyst : oxidant : substrate.

Based on analogous experiments for all the substrates used in the present study, we found that for cyclohexene, methyl-cyclohexene, cyclooctene, limonene, and cyclohexane oxidation, the optimum molar ratio of [catalyst:oxidant:substrate] was equal to [1:20:1000] and for styrene, trans- β -methyl styrene and cis-stilbene oxidation, this molar ratio was equal to [1:50:1000].

(2) *Excess of Dioxygen.* Iron-based catalysts, in the presence of dioxygen, often adopt radical mechanistic paths. Thus, the $\text{LFe}^{\text{III}}\text{Cl}$ catalyst was evaluated in oxidation reactions with H_2O_2 , (a) under atmospheric air *versus* (b) under inert Ar atmosphere (Table 1, Figure 2).

Based on the data of Table 1, it is observed that (a) the total yield of some oxidation reactions under air was over 100%; moreover, (b) the total oxidation yield under Ar was decreased. Especially, alcohol and ketone yields were strongly decreased under Ar. This suggests O_2 -involvement in the oxidation process which possibly propagates a

radical autooxidation [46, 47] of the more reactive oxygen-containing products such as alcohols and ketones. Thus, to record reliable data, all catalytic experiments herein were performed under a vigorous Ar purge to avoid any trace of O_2 .

(3) *Solvent Effect on the Reaction Time.* The time course profiles of the $\text{LFe}^{\text{III}}\text{Cl}$ -catalysed oxidation of cyclohexene with H_2O_2 in CH_3CN and in *tert*-amylalcohol are given in Figure 3. According to these data the catalytic reaction was practically accomplished within 4 h in CH_3CN and within 12 h in *tert*-amylalcohol. Thus, the reaction rate is strongly influenced by solvent. This effect could be related to the solvent polarity. However, in both solvents, the total yield of cyclohexene oxidation is quite high providing 88.5% in CH_3CN and 79.0% in *tert*-amylalcohol. It is noted that cyclohexene oxidation, in CH_3CN with *tert*-BuOOH as oxidant, was complete within 2 h, resulting in a 76.3% total yield.

TABLE 1: Hydrocarbon oxidations catalyzed by LFeCl with H₂O₂ in CH₃CN under atmospheric air and under Ar.

substrate	products	LFeCl under Ar ^c Yield (%)	LFeCl under Ar ^c Total yield (%)	LFeCl under air ^c Yield (%)	LFeCl under air ^c Total yield (%)
Cyclohexene ^a	cis-epoxide	6.5		3.5	
	2-cyclohexenol	52.0		61.5	
	2-cyclohexenone	30.0	88.5	43.2	108.2
1-Methyl-cyclohexene ^a	cis-epoxide	20.0		21.0	
	1-methyl-2-cyclohexen-1-ol	25.6		22.6	
	3-methyl-2-cyclohexen-1-ol	42.0		45.3	
	3-methyl-2-cyclohexen-1-one	8.8	96.4	52.0	140.9
Cyclooctene ^a	cis- epoxide	37.0	37.0	41.0	41.0
Styrene ^b	epoxide	7.5		7.0	
	phenyl-acetaldehyde	7.0		3.5	
	benzaldehyde	35.0	49.5	94.5	105.0
Methyl-Styrene ^b	trans-epoxide	41.9		29.0	
	methyl-benzyl-ketone	11.3		2.0	
	benzaldehyde	40.0	93.2	90.0	121.0
Cis- stylbene ^b	cis-epoxide	15.8		6.0	
	benzaldehyde	36.0	51.8	36.0	42.0

^aConditions: ratio of catalyst : H₂O₂ : substrate = 1 : 20 : 1000. ^bConditions: ratio of catalyst : H₂O₂ : substrate = 1 : 50 : 1000. ^c Reactions were completed within 4 h.

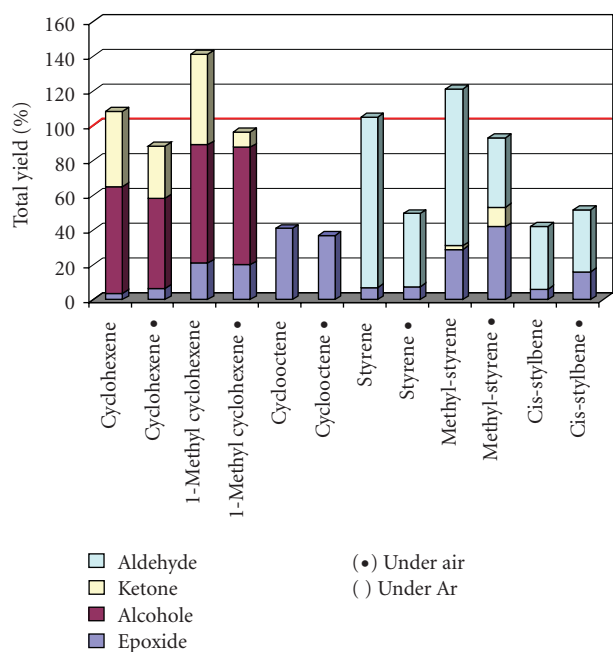


FIGURE 2: Bar chart representation of oxidations catalyzed by LFe^{III}Cl with H₂O₂ in CH₃CN under atmospheric air and under Ar.

3. Results and Discussion

3.1. Hydrocarbon Oxidation by the Fe^{III}-Catalysts. The catalytic activity of LFe^{III}Cl for hydrocarbon oxidation was evaluated using *tert*-BuOOH and H₂O₂ as oxidants in

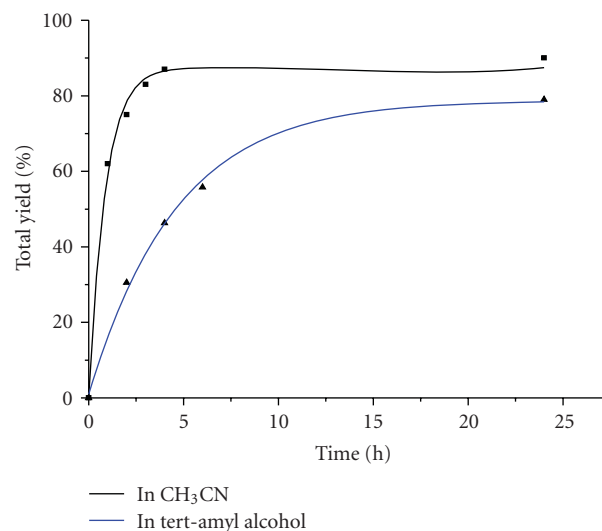


FIGURE 3: Time-dependent reaction profiles for cyclohexene oxidation catalysed by LFe^{III}Cl with H₂O₂ in CH₃CN and tert-amylalcohol.

either CH₃CN or *tert*-amylalcohol. Cyclohexene, methyl-cyclohexene, cyclooctene, limonene, and cyclohexane were used as substrates with a ratio of catalyst : oxidant : substrate equal to 1:20:1000 and styrene, trans- β -methyl styrene and cis-stilbene with a ratio of catalyst:oxidant:substrate equal to 1:50:1000. All oxidation reactions were carried out at room temperature under Ar atmosphere as described in details in Experimental Section. The obtained catalytic

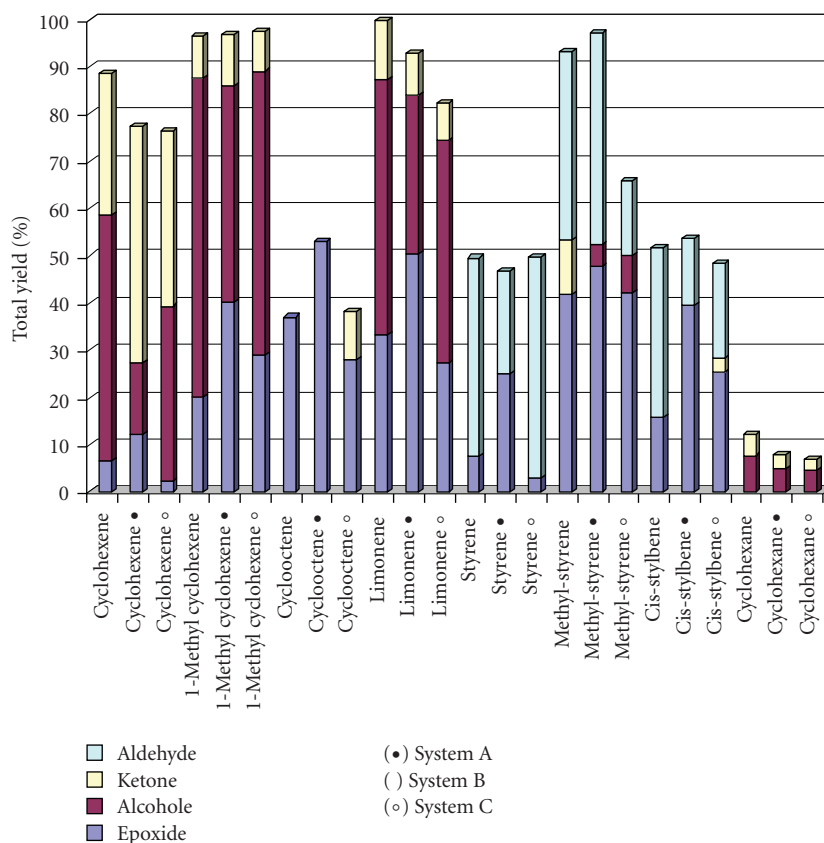


FIGURE 4: Distribution of oxidation products catalyzed by $\text{LFe}^{\text{III}}\text{Cl}$, (a) in *tert*-amylalcohol with H_2O_2 , (b) in CH_3CN with H_2O_2 , and (c) in CH_3CN with *tert*-BuOOH. See Table 2 for further details.

results are summarized in Table 2. Figure 4 provides a histogram-plot of the data of Table 2. The catalytic data of $\text{LFe}^{\text{III}}\text{Cl}$ with H_2O_2 in CH_3CN were taken from [38] and are included here for comparison.

Based on Table 2 we observe that cyclohexene and limonene oxidation catalyzed by the $\text{LFe}^{\text{III}}\text{Cl}$ provided oxidation products with a combined yield of 79.0% and 93.7%, respectively, in *tert*-amylalcohol with H_2O_2 (system A), 88.5% and 99.8% in CH_3CN with H_2O_2 (system B), and 76.3% and 82.34% in CH_3CN with *tert*-BuOOH (system C). Cyclohexene undergoes mainly allylic oxidation forming 2-cyclohexene-1-ol and 2-cyclohexene-1-one (with yields 16.0% and 50.7%, resp., by system A, 52.0% and 30.0% by system B, and 37.0% and 37.0% by system C). However cyclohexene epoxidation is also observed, providing low epoxide yields 12.3%, 6.5%, and 2.3% by systems A, B, and C, respectively. It is note that in *tert*-amylalcohol, the yield of epoxide and ketone increases, while the alcohol yield is reduced.

The major products detected from limonene oxidation were (i) two epoxides (*cis*- and *trans*-) derived from epoxidation of the electron-rich double bond at 1,2- position and (ii) alcohols derived from hydroxylation of the double bond at 1- and 2-position and from hydroxylation at 6-position closed to 1,2-double bond. Oxidation products from the more accessible, though less electron-rich, double bond at

8,9-position were not observed. Additionally, considerable amounts of the corresponding ketone at 6-position were also formed. In summary, the yield (a) of limonene-epoxides (*cis*-1,2 and *trans*-1,2) was found to be 51.2% in system A, 33.3% in system B, and 27.4% in system C, (b) of limonene-alcohols (1-ol, 2-ol, and 6-ol) 33.5%, 54.0%, and 46.9%, respectively and (c) of 6-ketone 9.0%, 12.5%, and 8% in systems A, B, and C respectively. These data provide a total catalytic oxidation of limonene 93.7%, 99.8%, and 82.3% achieved by $\text{LFe}^{\text{III}}\text{Cl}$, respectively, in *tert*-amylalcohol with H_2O_2 (system A), in CH_3CN with H_2O_2 (system B), and in CH_3CN with *tert*-BuOOH (system C).

When methyl-cyclohexene was used as substrate, the detected oxidation products were *cis*-epoxide, 1-methyl-2-cyclohexen-1-ol, 3-methyl-2-cyclohexen-1-ol, and 3-methyl-2-cyclohexen-1-one. The corresponding yields found to be [40.0%, 20.0%, and 29.0%], [21.3%, 25.6%, and 23.7%], [24.5% 42.0%, and 36.3%], and [10.9%, 8.8%, and 8.5%] in catalytic systems A, B, and C, respectively. Generally, methyl-substituted alkenes are more reactive towards both epoxidation and allylic oxidation. Our findings confirm this aspect providing total yield of methyl-cyclohexene oxidation 93.7%, 98.8%, and 83.3% by the present catalytic systems.

Cis-cyclooctene as substrate afforded a single-product reaction with H_2O_2 catalysed by $\text{LFe}^{\text{III}}\text{Cl}$ resulting only in

TABLE 2: Hydrocarbon oxidation by $LFe^{III}Cl$ catalyst.

substrate	products	LFeCl ^c		LFeCl ^d		LFeCl ^e	
		Yield (%)	Total yield (%)	Yield (%)	Total yield (%)	Yield (%)	Total yield (%)
Cyclohexene ^a	cis-epoxide	12.3		6.5		2.3	
	2-cyclohexenol	16.0		52.0		37.0	
	2-cyclohexenone	50.7	79.0	30.0	88.5	37.0	76.3
1-Methyl-cyclohexene ^a	cis-epoxide	40.0		20.0		29.0	
	1-methyl-2-cyclohexen-1-ol	21.3		25.6		23.7	
	3-methyl-2-cyclohexen-1-ol	24.5		42.0		36.3	
	3-methyl-2-cyclohexen-1-one	10.9	96.7	8.8	96.4	8.5	97.5
Cyclooctene ^a	cis-epoxide	53.0		37.0		28.0	
	2-cyclooctenone	—	53.0		37.0	10.0	38.0
Limonene ^a	cis-1,2 epoxide	34.4		21.0		18.0	
	trans-1,2 epoxide	16.8		12.3		9.4	
	limonene alcohol ^f	33.5 ^h		54.0 ^g		46.9 ⁱ	
	limonene ketone ^j	9.0	93.7	12.5	99.8	8.0	82.3
Styrene ^b	epoxide	25.0		7.5		3.0	
	phenyl-acetaldehyde	1.6		7.0		1.6	
	benzaldehyde	20.0	46.6	35.0	49.5	45.0	49.6
Methyl-styrene ^b	trans-epoxide	47.7		41.9		42.0	
	methyl-benzyl-alcohol	4.5		—		8.0	
	methyl-benzyl-ketone	—	11.3		—		
	benzaldehyde	45.0	97.2	40.0	93.2	15.8	65.8
Cis-stilbene ^b	cis-epoxide	9.5		15.8		2.4	
	trans-epoxide	30.0		—		23.0	
	stylben-cetone	—		—		3.0	
	benzaldehyde	14.0	53.5	36.0	51.8	20.0	48.4
Cyclohexane ^a	cyclohexanol	5.0		7.7		4.6	
	cyclohexanone	3.0	8.0	4.4	12.1	2.4	7.0

^aConditions: ratio of catalyst : oxidant : substrate = 1 : 20 : 1000. ^bConditions: ratio of catalyst : oxidant : substrate = 1 : 50 : 1000. ^cReactions were completed within 12 h in *tert*-amylalcohol with H₂O₂ as oxidant. ^dReactions were completed within 4 h in CH₃CN with H₂O₂ as oxidant. ^eReactions were completed within 1 h in CH₃CN with *tert*-BuOOH as oxidant. ^fLimonene alcohols were found to be a mixture of 1-ol, 2-ol, and 6-ol. ^g54% yield corresponds to 23% for 1-ol, 13.5% for 2-ol, and 17.5% for 6-ol. ^h33.5% yield corresponds to 9.0% for 1-ol, 6.5% for 2-ol, and 18.0% for 6-ol. ⁱ46.9 yield corresponds to 26.0% for 1-ol, 8.97% for 2-ol, and 11.93% for 6-ol. ^jThe only observed ketone is the 6-one.

cis-cyclooctene epoxide with 53.0% and 37.0% yields in systems A and B, respectively. However, the use of *tert*-BuOOH as oxidant provided 28% epoxide and 10% 2-cyclooctenone. Generally, cyclooctene occurs more readily epoxydation than allylic oxidation; however, here with *tert*-BuOOH, overoxidized 2-cyclooctenone derived from allylic oxidation was also detected.

Cis-stilbene oxidation in catalytic systems A and C provided *cis*- and *trans*-epoxides as major products [9.5% and 30% in system A] and [2.4% and 23.0% in C]. Benzaldehyde as oxidative cleavage product was also formed with yields 14% and 20%, respectively. In Catalytic system B, the detected products were benzaldehyde with yield 36.0% and *cis*-stilbene epoxide with yields 15.8%.

Styrene oxidation provided benzaldehyde as major product derived by oxidative cleavage of the exo-cyclic double bond with yields 20.0%, 35.0%, and 45.0% in systems A, B, and C, respectively. However, epoxide and phenyl acetaldehyde have been also formed by direct oxidation of the same double bond with [25.0% and 1.6%] in system A, [7.5% and 7.0%] in system B, and [3.0% and 1.6%] in system C. Overall, styrene was oxidised by LFe^{III}Cl in different oxidation conditions providing total yields from 46.6% to 49.6%.

The methyl-substituted styrene, *trans*- β -methyl styrene, is more reactive than styrene showing total oxidation yields 97.2%, 93.2%, and 65.8% in catalytic systems A, B, and C, respectively. The identified products were *trans*-epoxide

(47.7%, 41.9%, and 42.0%) and benzaldehyde as oxidation cleavage adduct (45.0%, 40.0%, and 15.8%). In some cases, methyl-benzyl-ketone and methyl-benzyl-alcohol were also detected.

Finally, cyclohexane oxidation by the present Fe^{III} -catalyst, in the three A, B, and C catalytic conditions, gave cyclohexanol and cyclohexanone with combined yields 8.0%, 12.2%, and 7.0% while the corresponding alcohol/ketone (A/K) ratio was found to be 1.66, 1.75, and 1.71, respectively.

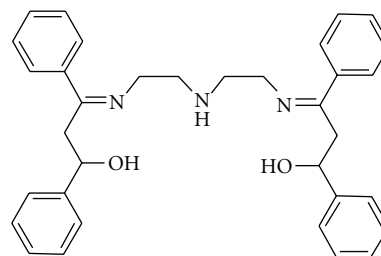
3.2. Mechanistic Considerations. The A/K ratio in cyclohexane can be used as a criterion of the presence and lifetime of free alkyl radical intermediates [31] as follows: (i) when $A/K = 1$, then we assume that the alkyl radicals are long-lived with a strong tendency to interact with O_2 to form alkyl-peroxy-radicals [45]. At the end, following a Russell-type terminal stage [48], recombination of these radicals results in the formation of equimolar amounts of alcohol and ketone [21, 31]. (ii) When $A/K > 1$, the radical $\cdot\text{OH}$ is formed by a metal-based system and the metal center reacts directly to form the corresponding alcohol. This is consistent with the formation of $\text{Fe}^{\text{III}}\text{-OOH}$ intermediate and the homolytic cleavage of O–O bond to $\cdot\text{HO}$ radical and oxoiron(IV) followed by electrophilic addition of metal-based species to the substrate.

Hydrocarbon oxidations catalyzed by $\text{LFe}^{\text{III}}\text{Cl}$ presented comparable selectivity and distribution of oxidation products, in the three experimental conditions studied herein. This implies similar mechanistic path in the catalysis. Generally, $\text{LFe}^{\text{III}}\text{Cl}$ is able to generate iron-hydroperoxo-species under the mild oxidation conditions used. It is known from other nonheme iron systems that $\text{Fe}^{\text{III}}\text{-OOH}$ could be either (a) a precursor or (b) itself an oxidant [22, 28, 46]. In the first case, possible homolytic cleavage of O–O bond leads to an $\text{Fe}^{\text{IV}}=\text{O}$ species and reactive $\cdot\text{HO}$ radical while a heterolytic cleavage generates an $\text{Fe}^{\text{V}}=\text{O}$ and an OH^- species [22, 28, 46]. Herein, the major oxidation products of alkenes are alcohols and ketones, mainly derived by an allylic oxidation reaction. However, considerable amounts of epoxides have been also formed. Taking into account that the detected allylic oxidation products are the main component of the observed oxidation yield, a dominant radical mechanistic path is suggested. This suggestion is further supported by detection of traces of the compounds illustrated in Scheme 2. Their formation could be a result of (a) interaction between two allyl-radicals formed on substrates and (b) interaction of an allyl-radical on substrate and a hydro-peroxo radical.

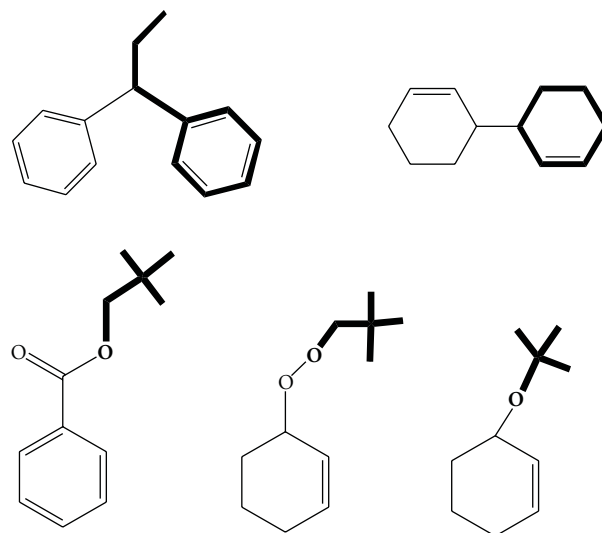
In this context, when *tert*-amylalcohol—a less polar solvent—was used with H_2O_2 , the reaction time is considerably longer, the yield of the corresponding epoxides increased, and the yield of radical mechanism products, that is, alcohols and ketones decreases. On the other hand, the use of *tert*-BuOOH as oxidant enhanced the yield of the corresponding alcohols and ketones.

4. Conclusion

The $\text{LFe}^{\text{III}}\text{Cl}$ catalyst was efficient in homogeneous hydrocarbon oxidations providing significant yields. The catalytic



SCHEME 1: Schematic representation of ligand [3-{2-[2-(3-hydroxy-1,3-diphenyl-allylideneamino)-ethylamino]-ethylimino}-1,3-diphenyl-propen-1-ol] (L).



SCHEME 2: Schematic representation of detected byproducts.

experiments (a) were performed under inert argon atmosphere excluding any trace of O_2 which favors radical oxidation paths and (b) included large excess of substrate, protecting the catalyst from oxidative degradation and minimizing the overoxidation of initial oxidation products. *tert*-BuOOH provided comparable oxidation yields with H_2O_2 ; nevertheless it slightly favors the formation of alcohols and ketones *versus* epoxides. The polarity of solvent strongly influences the reaction rate and the nature of oxidation products. We suggest that $\text{LFe}^{\text{III}}\text{Cl}$ functions *via* the formation of iron-hydroperoxo-species and the dominant mechanistic path is a radical one.

References

- [1] K. Furuhashi, "Biological routes to optically active epoxides," in *Chirality in Industry*, A. N. Collins, G. N. Sheldrake, and J. Crosby, Eds., pp. 167–186, John Wiley & Sons, London, UK, 1992.
- [2] U. Sundermeier, C. Döbler, and M. Beller, "Recent developments in the osmium-catalyzed dihydroxylation of olefins," in *Modern Oxidation Methods*, J. E. Backvall, Ed., p. 1, Wiley-VCH, Weinheim, Germany, 2004.

- [3] M. Costas, M. P. Mehn, M. P. Jensen, and L. Que Jr., "Dioxygen activation at mononuclear nonheme iron active sites: enzymes, models, and intermediates," *Chemical Reviews*, vol. 104, no. 2, pp. 939–986, 2004.
- [4] R. Mas-Ballesté, M. Costas, T. Van Den Berg, and L. Que Jr., "Ligand topology effects on olefin oxidations by bio-inspired $[\text{Fe}^{\text{II}}(\text{N}_2\text{Py}_2)]$ catalysts," *Chemistry—A European Journal*, vol. 12, no. 28, pp. 7489–7500, 2006.
- [5] K. Shikama, "The molecular mechanism of autoxidation for myoglobin and hemoglobin: a venerable puzzle," *Chemical Reviews*, vol. 98, no. 4, pp. 1357–1373, 1998.
- [6] M. Merckx, D. A. Kopp, M. H. Sazinsky, J. L. Blazyk, J. Müller, and S. J. Lippard, "Dioxygen activation and methane hydroxylation by soluble methane monooxygenase: a tale of two irons and three proteins," *Angewandte Chemie International Edition*, vol. 40, no. 15, pp. 2782–2807, 2001.
- [7] S. C. Pulver, W. A. Froland, J. D. Lipscomb, and E. I. Solomon, "Ligand field circular dichroism and magnetic circular dichroism studies of component B and substrate binding to the hydroxylase component of methane monooxygenase," *Journal of the American Chemical Society*, vol. 119, no. 2, pp. 387–395, 1997.
- [8] M. D. Wolfe, J. V. Parales, D. T. Gibson, and J. D. Lipscomb, "Single turnover chemistry and regulation of O_2 activation by the oxygenase component of naphthalene 1,2-dioxygenase," *Journal of Biological Chemistry*, vol. 276, no. 3, pp. 1945–1953, 2001.
- [9] A. Karlsson, J. V. Parales, R. E. Parales, D. T. Gibson, H. Eklund, and S. Ramaswamy, "Crystal structure of naphthalene dioxygenase: side-on binding of dioxygen to iron," *Science*, vol. 299, no. 5609, pp. 1039–1042, 2003.
- [10] R. H. Holm, P. Kennepohl, and E. I. Solomon, "Structural and functional aspects of metal sites in biology," *Chemical Reviews*, vol. 96, no. 7, pp. 2239–2314, 1996.
- [11] V. K. Sivasubramanian, M. Ganesan, S. Rajagopal, and R. Ramaraj, "Iron(III)-salen complexes as enzyme models: mechanistic study of oxo(salen)iron complexes oxygenation of organic sulfides," *Journal of Organic Chemistry*, vol. 67, no. 5, pp. 1506–1514, 2002.
- [12] X. Shan and L. Que Jr., "High-valent nonheme iron-oxo species in biomimetic oxidations," *Journal of Inorganic Biochemistry*, vol. 100, no. 4, pp. 421–433, 2006.
- [13] K. C. Gupta, A. Kumar Sutar, and C.-C. Lin, "Polymer-supported Schiff base complexes in oxidation reactions," *Coordination Chemistry Reviews*, vol. 253, no. 13–14, pp. 1926–1946, 2009.
- [14] R. B. Bedford, D. W. Bruce, R. M. Frost, J. W. Goodby, and M. Hird, "Iron(III) salen-type catalysts for the cross-coupling of aryl Grignards with alkyl halides bearing β -hydrogens," *Chemical Communications*, no. 24, pp. 2822–2823, 2004.
- [15] K. P. Bryliakov and E. P. Talsi, "Evidence for the formation of an iodosylbenzene(salen)iron active intermediate in a (salen)iron(III)-catalyzed asymmetric sulfide oxidation," *Angewandte Chemie International Edition*, vol. 43, no. 39, pp. 5228–5230, 2004.
- [16] L. Que Jr. and W. B. Tolman, "Recurring structural motifs in bioinorganic chemistry," in *Bio-Coordination Chemistry*, J. A. McCleverty and T. J. Meyer, Eds., vol. 8 of *Comprehensive Coordination Chemistry II*, Elsevier, Oxford, UK, 2004.
- [17] E. Y. Tshuva and S. J. Lippard, "Synthetic models for non-heme carboxylate-bridged diiron metalloproteins: strategies and tactics," *Chemical Reviews*, vol. 104, no. 2, pp. 987–1012, 2004.
- [18] A. L. Feig and S. J. Lippard, "Reactions of non-heme iron(II) centers with dioxygen in biology and chemistry," *Chemical Reviews*, vol. 94, no. 3, pp. 759–805, 1994.
- [19] C. He and Y. Mishina, "Modeling non-heme iron proteins," *Current Opinion in Chemical Biology*, vol. 8, no. 2, pp. 201–208, 2004.
- [20] J.-U. Rohde, M. R. Bukowski, and L. Que Jr., "Functional models for mononuclear nonheme iron enzymes," *Current Opinion in Chemical Biology*, vol. 7, no. 6, pp. 674–682, 2003.
- [21] K. Chen and L. Que Jr., "Evidence for the participation of a high-valent iron-oxo species in stereospecific alkane hydroxylation by a non-heme iron catalyst," *Chemical Communications*, no. 15, pp. 1375–1376, 1999.
- [22] M. Costas, A. K. Tipton, K. Chen, D.-H. Jo, and L. Que Jr., "Modeling rieske dioxygenases: the first example of iron-catalyzed asymmetric cis-dihydroxylation of olefins," *Journal of the American Chemical Society*, vol. 123, no. 27, pp. 6722–6723, 2001.
- [23] K. Chen, M. Costas, J. Kim, A. K. Tipton, and L. Que Jr., "Olefin cis-dihydroxylation versus epoxidation by non-heme iron catalysts: two faces of an FeIII-OOH coin," *Journal of the American Chemical Society*, vol. 124, no. 12, pp. 3026–3035, 2002.
- [24] P. D. Oldenburg, A. A. Shteinman, and L. Que Jr., "Iron-catalyzed olefin cis-dihydroxylation using a bio-inspired N,N,O-ligand," *Journal of the American Chemical Society*, vol. 127, no. 45, pp. 15672–15673, 2005.
- [25] C. P. Horwitz, D. R. Fooksman, L. D. Vuocolo, S. W. Gordon-Wylie, N. J. Cox, and J. T. Collins, "Ligand design approach for securing robust oxidation catalysts," *Journal of the American Chemical Society*, vol. 120, pp. 4867–4868, 1998.
- [26] T. J. Collins, "TAML oxidant activators: a new approach to the activation of hydrogen peroxide for environmentally significant problems," *Accounts of Chemical Research*, vol. 35, no. 9, pp. 782–790, 2002.
- [27] J. M. Rowland, M. Olmstead, and P. K. Mascharak, "Syntheses, structures, and reactivity of low spin iron(III) complexes containing a single carboxamido nitrogen in a $[\text{FeN5L}]$ chromophore," *Inorganic Chemistry*, vol. 40, no. 12, pp. 2810–2817, 2001.
- [28] M. Klopstra, G. Roelfes, R. Hage, R. M. Kellogg, and B. L. Feringa, "Non-heme iron complexes for stereoselective oxidation: tuning of the selectivity in dihydroxylation using different solvents," *European Journal of Inorganic Chemistry*, vol. 4, pp. 846–856, 2004.
- [29] F. G. Gelalcha, G. Anilkumar, M. K. Tse, A. Brückner, and M. Beller, "Biomimetic iron-catalyzed asymmetric epoxidation of aromatic alkenes by using hydrogen peroxide," *Chemistry—A European Journal*, vol. 14, no. 25, pp. 7687–7698, 2008.
- [30] L. Que Jr. and R. Y. N. Ho, "Dioxygen activation by enzymes with mononuclear non-heme iron active sites," *Chemical Reviews*, vol. 96, no. 7, pp. 2607–2624, 1996.
- [31] M. Costas, K. Chen, and L. Que Jr., "Biomimetic nonheme iron catalysts for alkane hydroxylation," *Coordination Chemistry Reviews*, vol. 200–202, pp. 517–544, 2000.
- [32] M. Lubben, A. Meetsma, E. C. Wilkinson, B. Feringa, and L. Que Jr., "Nonheme iron centers in oxygen activation: characterization of an iron(III) hydroperoxide intermediate," *Angewandte Chemie International Edition in English*, vol. 34, no. 13–14, pp. 1512–1514, 1995.

- [33] I. Bernal, I. M. Jensen, K. B. Jensen, C. J. McKenzie, H. Toftlund, and J. Tuchagues, "Iron(II) complexes of polydentate aminopyridyl ligands and an exchangeable sixth ligand; Reactions with peroxides," *Journal of the Chemical Society, Dalton Transactions*, no. 22, pp. 3667–3675, 1995.
- [34] J. Kim, E. Larka, E. C. Wilkinson, and L. Que Jr., "An alkylperoxoiron(III) intermediate and its role in the oxidation of aliphatic C-H Bonds," *Angewandte Chemie (International Edition in English)*, vol. 34, no. 18, pp. 2048–2051, 1995.
- [35] B. J. Wallar and J. D. Lipscomb, "Dioxygen activation by enzymes containing binuclear non-heme iron clusters," *Chemical Reviews*, vol. 96, no. 7, pp. 2625–2657, 1996.
- [36] M. Louloudi, K. Mitopoulou, E. Evaggelou, Y. Deligiannakis, and N. Hadjiliadis, "Homogeneous and heterogenized copper(II) complexes as catechol oxidation catalysts," *Journal of Molecular Catalysis A*, vol. 198, no. 1-2, pp. 231–240, 2003.
- [37] C. Vartzouma, E. Evaggellou, Y. Sanakis, N. Hadjiliadis, and M. Louloudi, "Alkene epoxidation by homogeneous and heterogenised manganese(II) catalysts with hydrogen peroxide," *Journal of Molecular Catalysis A*, vol. 263, no. 1-2, pp. 77–85, 2007.
- [38] G. Bilis, K. C. Christoforidis, Y. Deligiannakis, and M. Louloudi, "Hydrocarbon oxidation by homogeneous and heterogeneous non-heme iron (III) catalysts with H₂O₂," *Catalysis Today*. In press.
- [39] G. Grigoropoulou, K. C. Christoforidis, M. Louloudi, and Y. Deligiannakis, "Structure-catalytic function relationship of SiO₂-immobilized mononuclear Cu complexes: an EPR study," *Langmuir*, vol. 23, no. 20, pp. 10407–10418, 2007.
- [40] D. P. E. Dickson and F. J. Berry, *Mossbauer Spectroscopy*, Cambridge University Press, Cambridge, UK, 1996.
- [41] J. Peisach, W. E. Blumberg, S. Ogawa, E. A. Rachmilewitz, and R. Oltzik, "The effects of protein conformation on the heme symmetry in high spin ferric heme proteins as studied by electron paramagnetic resonance," *Journal of Biological Chemistry*, vol. 246, no. 10, pp. 3342–3355, 1971.
- [42] A. Dhakshinamoorthy and K. Pitchumani, "Clay-anchored non-heme iron-salen complex catalyzed cleavage of C=C bond in aqueous medium," *Tetrahedron*, vol. 62, no. 42, pp. 9911–9918, 2006.
- [43] G. C. Silva, G. L. Parrilha, N. M. F. Carvalho et al., "A bio-inspired Fe(III) complex and its use in the cyclohexane oxidation," *Catalysis Today*, vol. 133–135, no. 1–4, pp. 684–688, 2008.
- [44] F. Farzaneh, M. Poorkhosravani, and M. Ghandi, "Utilization of immobilized biomimetic iron complexes within nanoreactors of Al-MCM-41 as cyclohexane oxidation catalyst," *Journal of Molecular Catalysis A*, vol. 308, no. 1-2, pp. 108–113, 2009.
- [45] S. Tanase and E. Bouwman, "Selective conversion of hydrocarbons with H₂O₂ using biomimetic non-heme iron and manganese oxidation catalysts," *Advances in Inorganic Chemistry*, vol. 58, pp. 29–75, 2006.
- [46] G. Roelfes, M. Lubben, R. Hage, L. Que Jr., and B. L. Feringa, "Catalytic oxidation with a non-heme iron complex that generates a low-spin Fe(III)OOH intermediate," *Chemistry—A European Journal*, vol. 6, no. 12, pp. 2152–2159, 2000.
- [47] P. A. MacFaul, K. U. Ingold, D. D. M. Wayner, and L. Que Jr., "A putative monooxygenase mimic which functions via well-disguised free radical chemistry," *Journal of the American Chemical Society*, vol. 119, no. 44, pp. 10594–10598, 1997.
- [48] F. Gozzo, "Radical and non-radical chemistry of the Fenton-like systems in the presence of organic substrates," *Journal of Molecular Catalysis A*, vol. 171, no. 1-2, pp. 1–22, 2001.

Research Article

Zinc Binding Properties of Engineered RING Finger Domain of Arkadia E3 Ubiquitin Ligase

Christos T. Chasapis, Ariadni K. Loutsidou, Malvina G. Orkoula, and Georgios A. Spyroulias

Department of Pharmacy, University of Patras, Panepistimioupoli, Rion, 26504 Patras, Greece

Correspondence should be addressed to Christos T. Chasapis, cchasapis@upatras.gr and Georgios A. Spyroulias, g.a.spyroulias@upatras.gr

Received 15 March 2010; Accepted 12 May 2010

Academic Editor: Spyros P. Perlepes

Copyright © 2010 Christos T. Chasapis et al. This is an open access article distributed under the Creative Commons Attribution License, which permits unrestricted use, distribution, and reproduction in any medium, provided the original work is properly cited.

Human Arkadia is a nuclear protein consisted of 989 amino acid residues, with a characteristic RING domain in its C-terminus. The RING domain harbours the E3 ubiquitin ligase activity needed by Arkadia to ubiquitinate its substrates such as negative regulators of TGF- β signaling. The RING finger domain of Arkadia is a RING-H2 type and its structure and stability is strongly dependent on the presence of two bound Zn(II) ions attached to the protein frame through a defined Cys3-His2-Cys3 motif. In the present paper we transform the RING-H2 type of Arkadia finger domain to nonnative RING sequence, substituting the zinc-binding residues Cys⁹⁵⁵ or His⁹⁶⁰ to Arginine, through site-directed mutagenesis. The recombinant expression, in *Escherichia coli*, of the mutants C955R and H960R reveal significant lower yield in respect with the native polypeptide of Arkadia RING-H2 finger domain. In particular, only the C955R mutant exhibits expression yield sufficient for recombinant protein isolation and preliminary studies. Atomic absorption measurements and preliminary NMR data analysis reveal that the C955R point mutation in the RING Finger domain of Arkadia diminishes dramatically the zinc binding affinity, leading to the breakdown of the global structural integrity of the RING construct.

1. Introduction

RING finger is a characteristic protein sequence motif that was first identified in the protein product of the human gene *RING1—Really Interesting New Gene 1*—which is located proximal to the major histocompatibility region on chromosome 6 [1]. The RING finger domain is a cysteine/histidine-rich, zinc-chelating domain that promotes both protein-protein and protein-DNA interactions [2]. It is defined as Cys¹-Xaa₂-Cys²-Xaa₉₋₃₉-Cys³-Xaa₁₋₃-His⁴-Xaa₂₋₃-Cys/His⁵-Xaa₂-Cys⁶-Xaa₄₋₄₈-Cys⁷-Xaa₂-Cys⁸ (where Xaa can be any amino acid residue). Two zinc atoms are complexed by the cysteine/histidine residues in a “cross-brace” manner, to provide correct folding and biological activity to the RING domain Figure 1(a) [3, 4]. The distinctive cross-brace arrangement of the two tetrahedral zinc binding sites endows the RING domain with a globular conformation, characterized by a central α -helix and variable-length loops separated by several small β -strands. RING finger motifs

are further subdivided, depending on whether a cysteine or histidine residue is found at Cys/His⁵ within the motif. Thus they are classified as being either a RING-HC (Cys⁵) or a RING-H2 (His⁵) type. The metal binding properties of some RING finger domains have been investigated in a preliminary manner, using synthetic peptides that bear the amino acid sequence of BRCA1 and HDM2 [5, 6]. It is well-established that RING fingers can also bind other than zinc metal ions, such as cobalt (II) and cadmium (II) [7–9].

Human Arkadia is a nuclear protein of 994 amino acid open reading frame (ORF) that exhibits no sequence similarity with any other known protein apart from the RING-H2 finger topology in its C-terminal region [10]. Mouse Arkadia ORF differs in length by 5 residues (989 aa) but their C-terminal 124 residue segments bear identical amino acid sequence. Arkadia has been shown to function as an E3 ubiquitin ligase [11]. E3 ligases participate actively at the last step of the protein degradation through the ubiquitination pathway [12, 13]. Additionally, RING E3 ubiquitin ligases

ubiquitination pathway, is misformed. Herein we present the production of two nonnative RING finger domains of mouse Arkadia: C955R and H960R Figure 1(b), through site-directed mutagenesis. The recombinant expression in *Escherichia coli* of the mutants C955R and H960R reveals significant lower yield in respect with the native polypeptide of Arkadia RING-H2 finger domain. Only the C955R mutant exhibits expression yield sufficient for recombinant protein isolation and the protocol applied was based on that used for the wt of Arkadia RING-H2 finger domain [21]. Since zinc binding is considered to be critical to proper folding and activity of the RING-H2 domain of Arkadia, the nonnative polypeptides were expressed in zinc-loaded growth media. Zinc contents of the wt and mutant C955R RING construct were determined by Atomic Absorption measurements. Finally, the folding state and the structural integrity of the holo-RING constructs were monitored through ^1H and 2D ^1H - ^{15}N -HSQC spectroscopy.

2. Materials and Methods

2.1. Plasmids, Bacterial Strains, and Growth Media. *E. coli* DH5 α (Invitrogen) was used as the host strain for cloning and plasmid propagation and *E. coli* BL21(DE3) (Stratagene) as the host strain for the expression vector pGEX-4T-1 (Amersham Biosciences). Both strains were routinely grown in Luria-Bertani (LB hereafter) broth or on plates of LB agar, supplemented with ampicillin (100 $\mu\text{g}/\text{ml}$) for both transformed DH5 α and BL21(DE3) strains. Induction was carried out in M9 medium supplemented with 2 ml/l of solution Q (40 mM HCl, 50 mg/l $\text{FeCl}_2 \cdot 4\text{H}_2\text{O}$, 184 mg/l $\text{CaCl}_2 \cdot 2\text{H}_2\text{O}$, 64 mg/l H_3BO_3 , 18 mg/l $\text{CoCl}_2 \cdot 6\text{H}_2\text{O}$, 340 mg/l ZnCl_2 , 605 mg/l $\text{Na}_2\text{Mo}_4 \cdot 2\text{H}_2\text{O}$, 40 mg/l $\text{MnCl}_2 \cdot 4\text{H}_2\text{O}$) and 10 ml/l of vitamin mix (500 mg/l thiamine, 100 mg/l biotin, 100 mg/l choline chloride, 100 mg/l folic acid, 100 mg/l niacinamide, 100 mg/l pantothenic acid, 100 mg/l pyridoxal, 10 mg/l riboflavin).

2.2. Cloning, Expression, Purification, and Isotopic Labeling of Arkadia RING Constructs. The protocol adopted to express and purify the nonnative RING constructs of Arkadia was essentially the same as that previously reported to produce the wt of the RING-H2 construct [10]. The expression plasmids for the presented mutants were obtained from that of wt RING-H2 through the Quickchange (Stratagene) mutagenesis kit. ^{15}N isotopic labeling of the mutant C955R was obtained using M9 medium supplemented with 2 g/l $^{15}\text{NH}_4\text{Cl}$ as nitrogen source.

2.3. Preliminary Protein Characterization. The purity of all polypeptides was checked by SDS-PAGE in 17% polyacrylamide gels after staining of protein bands with Coomassie Blue R-250. The concentration of RING domains of Arkadia was determined by using two methods: the first is based on the extinction coefficients at 280 nm of each construct, as estimated by PROTPARAM software

(<http://www.expasy.org/tools/protparam.html/>) and the second, which is more accurate, on the Quick start Bradford protein assay (BIORAD) [22].

2.4. Atomic Absorption Spectrometry. Elemental analysis for zinc was performed employing Atomic Absorption Spectrometry (Perkin Elmer AAnalyst 300). The zinc content was measured in wt RING-H2 and the mutant C955R RING constructs. In order to exclude any matrix effect in zinc measurements, the standard addition method was applied [23]. Four samples were prepared for the first construct, the unspiked and three aliquots (spiked) to which known amounts of the analyte zinc from a stock standard solution (AA Panreac 1.000 ± 0.002 g/l Zn) were added (Table 1). For the nonnative construct, three samples were prepared, respectively: the unspiked and two spiked. The spiked concentration ranged from 0 (unspiked sample) to 0.6 ppm. The volume was kept equal for all samples by means of addition of PBS buffer. Preliminary tests assured that the overall concentration of zinc was lying within the linear range of the technique (1 ppm). Absorbance of all samples at the appropriate wavelength (213.9 nm) was measured twice. An appropriate calibration curve for each protein was constructed (Table 3, Figure 3). The concentration of zinc in the unspiked samples was determined, dividing the intercept by the slope of calibration curve [23].

2.5. NMR Spectroscopy. 1D ^1H -NMR and ^1H - ^{15}N HSQC spectra were recorded at 298 K on a Bruker Avance 600 MHz spectrometer, equipped with a cryogenically cooled pulsed-field gradient triple-resonance probe (TXI) and on a Bruker Avance DRX 400 MHz, equipped with two multinuclear broadband probes (inverse BBI and direct BBO). ^1H 1D spectra were acquired in the 16 ppm spectral width using a variety of pulse sequence for water suppression and spectra were calibrated relatively to the water proton resonances. The 2D ^{15}N HSQC spectra were acquired using a spectral width of 40 ppm for ω_1 and 8 ppm for ω_2 . The NMR samples contained 1 mM and 0.2 mM protein of wt Arkadia and mutant construct C955R, respectively, in 50 mM phosphate buffer, pH = 7, in the presence of 90% $\text{H}_2\text{O}/10\%$ D_2O .

3. Results and Discussion

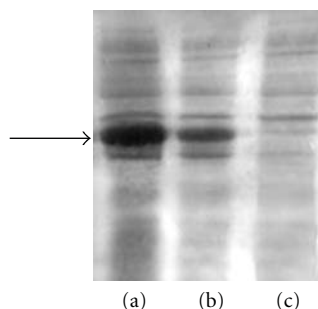
The C-terminal RING finger domains of wt and Arkadia mutants were expressed in M9 minimal growth media supplemented with ZnCl_2 . Both of the mutants: C955R and H960R, reveal remarkably lower expression yield in respect with the native polypeptide of Arkadia RING-H2 finger domain. Small-scale test expression of RING constructs in the absence of ZnCl_2 suggests that additional zinc enrichment of growth media does not affect the expression yield of soluble RING constructs. In Figure 2, it is presented the total cell lysate of wt (a), the mutant C955R (b) and H960R (c), at 37°C with ZnCl_2 at a final concentration 100 μM . Finally, from the above mutants, the expression yield of the C955R mutant was sufficient for recombinant protein isolation and preliminary studies.

TABLE 1: Samples of each construct spiked with Zn prepared and analyzed.

Sample	Volume of the unknown protein sample used (μl)	Final volume of the sample (ml)	Spiked Concentration of Zn (ppm)
<i>RING-H2 construct</i>			
A	15.0	5.0	0
B	15.0	5.0	0.2
C	15.0	5.0	0.4
D	15.0	5.0	0.6
<i>Mutant RING construct (C955R)</i>			
A	9.0	2.0	0
B	9.0	2.0	0.1
C	9.0	2.0	0.2

TABLE 2: Cumulative results of zinc: protein ratio for the samples analyzed.

Protein sample	Zn concentration (mM)	Protein concentration (mM)	Zn : protein ratio
RING-H2	1.04300 (± 0.00460)	0.498 (± 0.001)	2.094
Mutant RING (C955R)	0	0.201 (± 0.001)	0

FIGURE 2: The total cell lysate of wt (a), the mutant C955R (b), and H960R (c) at 37°C with ZnCl_2 at a final concentration 100 μM .

Elemental analysis for zinc was performed employing Atomic Absorption Spectrometry. A calibration curve for each protein sample (Figure 3) was constructed as described in Section 2. The concentration of zinc in the unspiked sample of both constructs was determined, dividing the intercept by the slope of the calibration curves [23] (Table 3). The concentration of zinc in the initial samples of 0.5 mM RING-H2 and 0.2 mM C955R mutant of Arkadia was calculated to be 1 mM and 0 mM, respectively, (Table 2). It should, also, be stressed that the zinc content of the constructs remained stable in excess of ZnCl_2 in the growth media ($>100 \mu\text{M}$). The atomic absorption measurements of the native RING construct suggest a stoichiometry of two zinc ions per molecule, a value that is in agreement with the classic binding properties of RING fingers. However, the elemental analysis of the C955R mutant suggests that the mutated construct does not bind zinc at all, indicating that the substitution of one of the three cysteines in the second tetrahedral zinc binding motif abolishes the global metal binding capacity of the hole polypeptide.

It is known that the protein structure of the Arkadia zinc loaded wt RING-H2 domain is well folded and the zinc incorporation is a major determinant for its structure and stability [17–21]. Indeed, when EDTA was added to a sample of the Arkadia RING finger domain at a 1:1 molar ratio with respect to Zn(II) substantial changes were observed for a number of residues in a ^1H - ^{15}N HSQC spectrum. Further addition of EDTA up to a final Zn:EDTA molar ratio of 1:2 led to dramatic changes in the ^1H - ^{15}N HSQC typical for structureless polypeptide [21]. The 1D ^1H -NMR spectrum of C955R mutant (Figure 4(a)) and its comparison with the 1D NMR spectrum of the wt (Figure 4(b)) suggests that the C955R RING construct is not a folded protein.

Heteronuclear NMR spectroscopy, and especially 2D ^1H - ^{15}N -HSQC experiments provides the fingerprint spectrum of each polypeptide and are diagnostic tools for the folding properties and aggregation state of recombinant proteins. Additionally, this technique can probe fine structural rearrangements upon amino acids substitutions and for this reason it is applied to probe the effect of C955R mutation. Indeed, the ^1H - ^{15}N -HSQC exhibits dramatic changes in respect with the spectrum of the native RING construct, with no signal dispersion of the backbone amide groups (Figure 4). This remarkable lack of the chemical shift dispersion is almost identical to that observed in the HSQC spectrum of the unstructured wt RING construct, due to the presence of EDTA excess [21]. EDTA is a powerful metal chelating agent and competes the RING polypeptide for zinc binding. Excess of EDTA in RING Finger solution uptakes the zinc ion and RING polypeptide structure collapses as evidenced by the HSQC. Mutation of the Cys⁹⁵⁵ by Arg seems to result to an unstructured polypeptide that has abolished the zinc binding ability.

The substitution of the His⁹⁶⁰ and Cys⁹⁵⁵ residues by an Arg was driven by the fact that Arg, according to Blosom matrix, is among the residues with the higher probability to

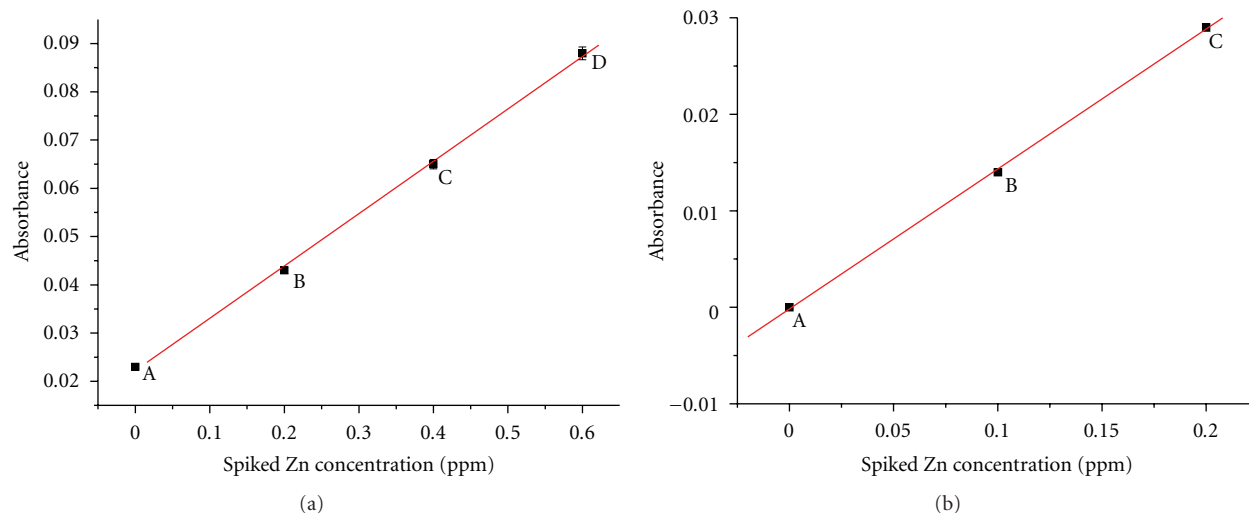


FIGURE 3: Calibration curves for the additions of zinc in (a) RING-H2 and (b) mutant RING (C955R) of Arkadia.

TABLE 3: Linear regression data for the calibration curves.

Protein sample	Intercept (A)	Slope (B)	Correlation Coefficient (R)
RING-H2	0.02220 (± 0.00009)	0.10850 (± 0.00240)	0.99951 (± 0.00107)
Mutant-RING (C955R)	-0.00002 (± 0.00004)	0.14500 (± 0.00289)	0.99980 (± 0.00004)

substitute His in polypeptide sequence, due to the similar length and nature of its side chain and its basic character. Additionally, its linear side-chain is not expected to impose significant steric interaction that may alter dramatically the spatial geometry of the other potential Zn(II) binding residues (three Cysteines). Since the expression yield of the H960R mutant was very low for protein isolation, preliminary studies were performed only for the C955R mutant. It is proposed that the new mutated motif does not bind zinc at all, in contrast to the stoichiometry of two zinc ions per molecule for the native RING construct. Although the alteration occurred in the second binding motif, both binding sites are losing their metal binding capacity. Additionally, NMR spectroscopy indicates that C955R mutant of RING Arkadia undergoes significant structural rearrangements losing its proper folding, in respect with the native polypeptide. This result may provide new insights into the sequential metal loading by the two tetrahedral binding sites of the RING-H2 domain of Arkadia. Since the net effect of the C955R substitution is the collapse of the structure it is suggested that the second site may be an important regulator that affects the formation of the first site and the overall metal-dependent folding of the polypeptide. In the past, the sequential binding was considered to be a general characteristic of RING finger domains, but its biological significance has not yet been established [5, 24, 25]. One characteristic example is the metal binding properties of peptide corresponding to the RING finger domain from the tumor suppressor gene product BRCA1. It is found that the

above metal binding is thermodynamically *sequential* with cobalt(II) almost saturating one of the two sites in each polypeptide prior to binding to the other site. Analysis of the absorption spectra due to cobalt(II) bound to the two sites revealed that the higher affinity site is comprised of four cysteinate ligands whereas the lower affinity site has three cysteinate and one histidine ligands. Upon binding a metal ion to site 1 (Cys4), the peptide becomes somewhat more structured and, perhaps, more rigid in a manner that affects the regions involved in forming site 2 (Cys3His). This, in turn, increases the difficulty in binding a metal ion to site 2, leading to the observed anticooperativity [5]. The same metal binding properties were found in the RING finger domain of HDM2 C-terminal domain. In this case the metal binds to the higher-affinity binding site were monitored through fluorescence energy transfer, revealing two binding events separately: the stronger binding site C4 and the weaker one C3H. Furthermore, synthetic knockout mutants not only enabled to assign the coordinating residues in the HDM2 RING finger domain but also revealed that metal binding to HDM2 was also anticooperative [6].

In summary, we reinforce the theory that substitution of zinc-binding amino acids in RING finger domains may possess an immense role in the biochemical and biological activity of RING Finger E3 ligases. Herein, we demonstrate that even one point mutation (C955R) in the RING finger domain of Arkadia can have a dramatic effect in the domain structure, leading to the breakdown of the global structural integrity of the RING construct. This phenomenon is

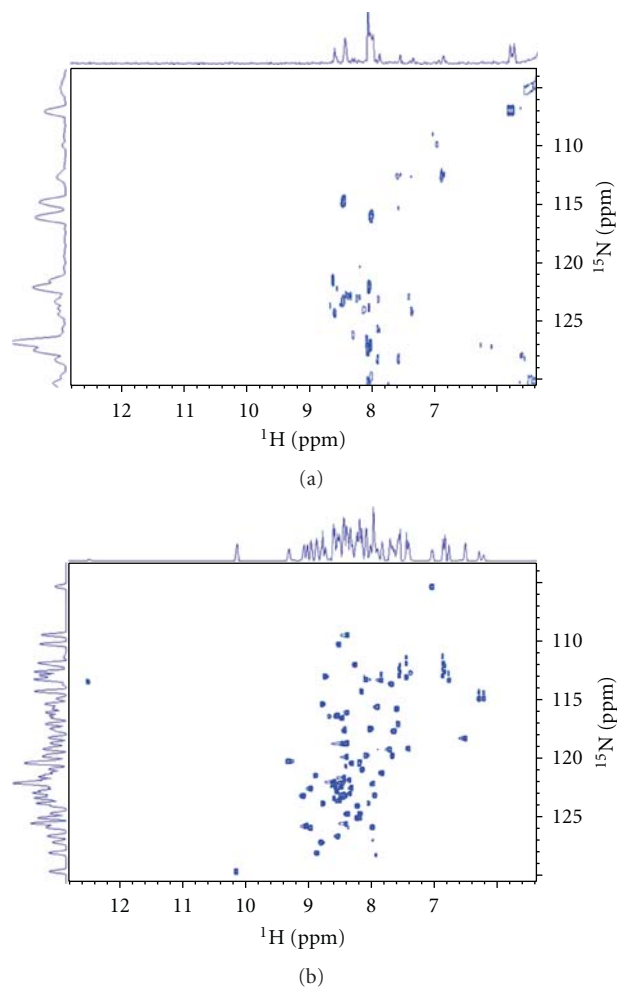


FIGURE 4: The 1D ^1H -NMR of amide proton resonances (7,5–10 ppm) and ^1H - ^{15}N HSQC of the mutant (a) and the native RING (b).

expected to prevent the formation of a E3-E2 productive complex and finally to reduce its ubiquitin ligase activity. In the past, similar results have been reported regarding mutants in the zinc binding motif of HDM2 (429–491). RING finger domain (such as His452Ala and His457Ala) was studied through NMR spectroscopy revealing a lack of dispersion and broad resonances in ^{15}N -HSQC spectra, characteristic of unfolded protein [26]. The correlation between mutations in the RING finger domain of E3 ligases and their ubiquitination activity was well established in the past through the detection of mutations within the BRCA1 RING domain that predispose to cancer due to the abolishment of BRCA1 ligase activity [27]. Furthermore, site mutations in the RING finger of E3 ligases are associated with various consequences in biological processes such as their unusual distribution in the cell, like the large cytoplasmic and nuclear inclusion of the two mutant isoforms of Parkin RING finger protein [28]. In this light, the verification of this probable occurrence of a sequential metal binding by the wt/mutant of RING finger domains of Arkadia and the study of their mechanism remain to be done.

Abbreviations

RING: Really interesting new gene
 TGF- β : Transforming growth factor β
 NMR: Nuclear Magnetic Resonance.

Acknowledgments

G. Spyroulias and C. Chasapis wish to thank Dr. Vasso Episkopou for kindly providing the plasmid containing full length of Arkadia, EU-NMR program Grant no. RII3-026145 (CERM; Center of Magnetic Resonance, University of Florence) and Center of Instrumental Analysis of University of Patras for access to NMR instrumentation. G. Spyroulias also acknowledges a Research Committee, “K. Karatheodori” Research Grant (No. C.181).

References

- [1] P. S. Freemont, “The RING finger. A novel protein sequence motif related to the zinc finger,” *Annals of the New York Academy of Sciences*, vol. 684, pp. 174–192, 1993.
- [2] P. S. Freemont, “RING for destruction?” *Current Biology*, vol. 10, no. 2, pp. R84–R87, 2000.
- [3] K. L. B. Borden and P. S. Freemont, “The RING finger domain: a recent example of a sequence-structure family,” *Current Opinion in Structural Biology*, vol. 6, no. 3, pp. 395–401, 1996.
- [4] A. J. Saurin, K. L. B. Borden, M. N. Boddy, and P. S. Freemont, “Does this have a familiar RING?” *Trends in Biochemical Sciences*, vol. 21, no. 6, pp. 208–214, 1996.
- [5] P. C. Roehm and J. M. Berg, “Sequential metal binding by the RING finger domain of BRCA1,” *Biochemistry*, vol. 36, no. 33, pp. 10240–10245, 1997.
- [6] Z. Lai, D. A. Freedman, A. J. Levine, and G. L. McLendon, “Metal and RNA binding properties of the hdm2 RING finger domain,” *Biochemistry*, vol. 37, no. 48, pp. 17005–17015, 1998.
- [7] R. Lovering, I. M. Hanson, K. L. B. Borden, et al., “Identification and preliminary characterization of a protein motif related to the zinc finger,” *Proceedings of the National Academy of Sciences of the United States of America*, vol. 90, no. 6, pp. 2112–2116, 1993.
- [8] A. G. Von Arnim and X.-W. Deng, “Ring finger motif of *Arabidopsis thaliana* COP1 defines a new class of zinc-binding domain,” *The Journal of Biological Chemistry*, vol. 268, no. 26, pp. 19626–19631, 1993.
- [9] C. Upton, L. Schiff, S. A. Rice, T. Dowdeswell, X. Yang, and G. McFadden, “A poxvirus protein with a RING finger motif binds zinc and localizes in virus factories,” *Journal of Virology*, vol. 68, no. 7, pp. 4186–4195, 1994.
- [10] V. Episkopou, R. Arkell, P. M. Timmons, J. J. Walsh, R. L. Andrew, and D. Swan, “Induction of the mammalian node requires Arkadia function in the extraembryonic lineages,” *Nature*, vol. 410, no. 6830, pp. 825–830, 2001.
- [11] K. J. Mavrakis, R. L. Andrew, K. L. Lee, et al., “Arkadia enhances Nodal/TGF-beta signaling by coupling phospho-Smad2/3 activity and turnover,” *PLoS Biology*, vol. 5, no. 3, article e67, 2007.
- [12] A. Hershko and A. Ciechanover, “The ubiquitin system,” *Annual Review of Biochemistry*, vol. 67, pp. 425–479, 1998.
- [13] J. Adams, “The proteasome: structure, function, and role in the cell,” *Cancer Treatment Reviews*, vol. 29, no. 1, pp. 3–9, 2003.

- [14] M. Lakshmanan, U. Bughani, S. Duraisamy, M. Diwan, S. Dastidar, and A. Ray, "Molecular targeting of E3 ligases—a therapeutic approach for cancer," *Expert Opinion on Therapeutic Targets*, vol. 12, no. 7, pp. 855–870, 2008.
- [15] T. R. Pray, F. Parlati, J. Huang, et al., "Cell cycle regulatory E3 ubiquitin ligases as anticancer targets," *Drug Resistance Updates*, vol. 5, no. 6, pp. 249–258, 2002.
- [16] Y. Sun, "Targeting E3 ubiquitin ligases for cancer therapy," *Cancer Biology & Therapy*, vol. 2, no. 6, pp. 623–629, 2003.
- [17] C. T. Chasapis and G. A. Spyroulias, "RING finger E3 ubiquitin ligases: structure and drug discovery," *Current Pharmaceutical Design*, vol. 15, no. 31, pp. 3716–3731, 2009.
- [18] D. Koinuma, M. Shinozaki, A. Komuro, et al., "Arkadia amplifies TGF- β superfamily signalling through degradation of Smad7," *The EMBO Journal*, vol. 22, no. 24, pp. 6458–6470, 2003.
- [19] L. Levy, M. Howell, D. Das, S. Harkin, V. Episkopou, and C. S. Hill, "Arkadia activates Smad3/Smad4-dependent transcription by triggering signal-induced SnoN degradation," *Molecular and Cellular Biology*, vol. 27, no. 17, pp. 6068–6083, 2007.
- [20] Y. Nagano, K. J. Mavrakis, K. L. Lee, et al., "Arkadia induces degradation of SnoN and c-Ski to enhance transforming growth factor- β signaling," *The Journal of Biological Chemistry*, vol. 282, no. 28, pp. 20492–20501, 2007.
- [21] N. G. Kandias, C. T. Chasapis, V. Episkopou, D. Bentrop, and G. A. Spyroulias, "High yield expression and NMR characterization of Arkadia E3 ubiquitin ligase RING-H2 finger domain," *Biochemical and Biophysical Research Communications*, vol. 378, no. 3, pp. 498–502, 2009.
- [22] M. M. Bradford, "A rapid and sensitive method for the quantitation of microgram quantities of protein utilizing the principle of protein dye binding," *Analytical Biochemistry*, vol. 72, no. 1–2, pp. 248–254, 1976.
- [23] D. A. Skoog, F. J. Holler, and T. A. Nieman, *Principles of Instrumental Analysis*, Brooks Cole, Florence, Ky, USA, 5th edition, 1997.
- [24] K. L. B. Borden, M. N. Boddy, J. Lally, et al., "The solution structure of the RING finger domain from the acute promyelocytic leukaemia proto-oncoprotein PML," *The EMBO Journal*, vol. 14, no. 7, pp. 1532–1541, 1995.
- [25] A. G. von Arnim and X.-W. Deng, "Ring finger motif of *Arabidopsis thaliana* COP1 defines a new class of zinc-binding domain," *The Journal of Biological Chemistry*, vol. 268, no. 26, pp. 19626–19631, 1993.
- [26] M. Kostic, T. Matt, M. A. Martinez-Yamout, H. J. Dyson, and P. E. Wright, "Solution structure of the Hdm2 C2H2C4 RING, a domain critical for ubiquitination of p53," *Journal of Molecular Biology*, vol. 363, no. 2, pp. 433–450, 2006.
- [27] H. Ruffner, C. A. P. Joazeiro, D. Hemmati, T. Hunter, and I. M. Verma, "Cancer-predisposing mutations within the RING domain of BRCA1: loss of ubiquitin protein ligase activity and protection from radiation hypersensitivity," *Proceedings of the National Academy of Sciences of the United States of America*, vol. 98, no. 9, pp. 5134–5139, 2001.
- [28] M. R. Cookson, P. J. Lockhart, C. McLendon, C. O'Farrell, M. Schlossmacher, and M. J. Farrer, "RING finger 1 mutations in Parkin produce altered localization of the protein," *Human Molecular Genetics*, vol. 12, no. 22, pp. 2957–2965, 2003.

Research Article

Hydrogen-Bonded Networks Based on Cobalt(II), Nickel(II), and Zinc(II) Complexes of N,N'-Diethylurea

Labrini Drakopoulou,¹ Catherine P. Raptopoulou,²
Aris Terzis,² and Giannis S. Papaefstathiou³

¹Department of Chemistry, University of Patras, 265 04 Patras, Greece

²Institute of Materials Science, National Centre of Scientific Research "Demokritos", 153 10 Aghia Paraskevi Attikis, Greece

³Laboratory of Inorganic Chemistry, Department of Chemistry, National and Kapodistrian University of Athens, Panepistimiopolis, 157 71 Zografou, Greece

Correspondence should be addressed to Giannis S. Papaefstathiou, gspapaef@chem.uoa.gr

Received 8 April 2010; Accepted 1 May 2010

Academic Editor: Spyros Perlepes

Copyright © 2010 Labrini Drakopoulou et al. This is an open access article distributed under the Creative Commons Attribution License, which permits unrestricted use, distribution, and reproduction in any medium, provided the original work is properly cited.

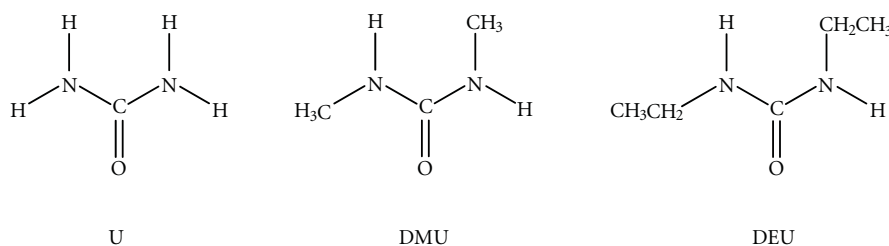
N,N'-diethylurea (DEU) was employed as a ligand to form the octahedral complexes $[M(\text{DEU})_6]^{2+}$ (M=Co, Ni and Zn). Compounds $[\text{Co}(\text{DEU})_6](\text{BF}_4)_2$ (**1**), $[\text{Co}(\text{DEU})_6](\text{ClO}_4)_2$ (**2**), $[\text{Ni}(\text{DEU})_6](\text{ClO}_4)_2$ (**3**), and $[\text{Zn}(\text{DMU})_6](\text{ClO}_4)_2$ (**4**) have been prepared from the reactions of DEU and the appropriate hydrated metal(II) salts in EtOH in the presence of 2,2-dimethoxypropane. Crystal structure determinations demonstrate the existence of $[M(\text{DEU})_6]^{2+}$ cations and ClO_4^- (in **2–4**) or BF_4^- (in **1**) counterions. The $[M(\text{DEU})_6]^{2+}$ cations in the solid state are stabilized by a *pseudochelate* effect due to the existence of six strong intracationic N-H...O_(DEU) hydrogen bonds. The $[M(\text{DEU})_6]^{2+}$ cations and counterions self-assemble to form hydrogen-bonded 2D architectures in **2–4** that conform to the **kgd** (kagome dual) network, and a 3D hydrogen-bonded **rtl** (rutile) network in **1**. The nature of the resulting supramolecular structures is influenced by the nature of the counter-ion. The complexes were also characterized by vibrational spectroscopy (IR).

1. Introduction

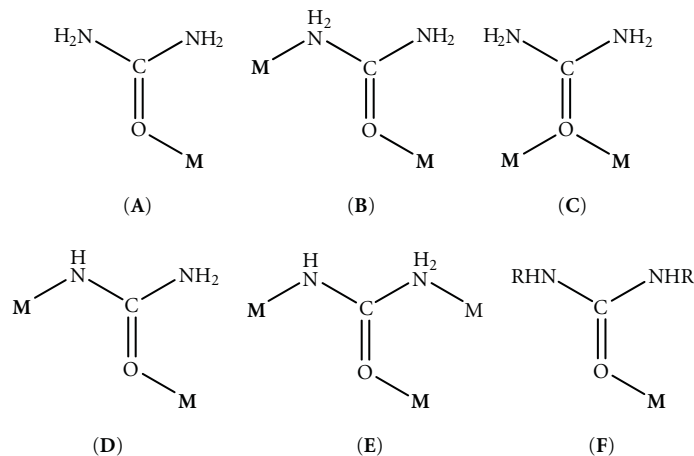
In 1828, Wöhler attempted to synthesize ammonium cyanate by reacting silver isocyanate (AgNCO) with ammonium chloride (NH₄Cl). The outcome of this failed attempt was urea H₂NCONH₂ (**U**, Scheme 1) which represents the first organic molecule synthesized in the laboratory from purely inorganic materials [1]. Urea has also been recognized as the first organic molecule that was synthesized without the involvement of any living system [1]. Nowadays, urea represents not only an important molecule in biology [2] but also an important raw material in chemical industry [3].

Restricting further discussion to the coordination chemistry of urea and its substituted derivatives, metal-urea complexes have attracted considerable interest since the discovery of the active site of urease, a metalloenzyme that catalyzes the hydrolysis of urea into carbon dioxide and

ammonia [4, 5]. Considerable efforts have been devoted to devise useful bioinorganic models for the active site of urease and provide information for the intermediates and its catalytic mechanism. That in turn drove to the structural and spectroscopic characterization of many metal-urea complexes [6]. Urea usually coordinates as a monodentate ligand through the oxygen atom, forming a C=O...M angle considerably smaller than 180°, in accordance with the *sp*² hybridization of the O atom (**A** in Scheme 2). The rare N,O-bidentate coordination mode (**B** in Scheme 2) has been found in a very limited number of cases [7, 8], while in $[\text{Hg}_2\text{Cl}_4\text{U}_2]$ each U molecule bridges the two Hg^{II} atoms through the oxygen atom [9] (**C** in Scheme 2). Of particular chemical/biological interest is the ability of U to undergo metal-promoted deprotonation [4, 10]; the monoanionic ligand H₂NCONH⁻ adopts the μ_2 (**D** in Scheme 2) and μ_3 (**E** in Scheme 2) coordination modes.



SCHEME 1: Ligands discussed in the text (U = urea, DMU = N,N'-dimethylurea and DEU = N,N'-diethylurea).



SCHEME 2: The crystallographically established coordination modes of urea (U) and its symmetrically substituted alkyl derivatives (RHNCONHR).

The N,N'-alkyl symmetrically substituted derivatives of urea (RHNCONHR), such as the N,N'-dimethylurea (DMU) and N,N'-diethylurea (DEU) (Scheme 1) have only been found to coordinate as monodentate ligands through the oxygen atom (F in Scheme 2).

Urea and its substituted derivatives have been extensively studied within the frame of organic crystal engineering due to their ability to form extended hydrogen bonded frameworks. In particular, symmetrically substituted ureas (i.e., RHNCONHR) form α -networks with each urea molecule donating two hydrogen bonds and "chelating" the carbonyl oxygen of the next molecule in the network. In contrast to the great number of studies concerning free ureas [11–15], little is known about the supramolecular structures based on hydrogen bonding interactions between simple metal-ureas complexes. Over the last decade, we have been studying the coordination chemistry of urea and its symmetrically substituted derivative DMU [16–21]. In all cases, ureas form stable complexes which are further connected to create extended frameworks by intermolecular/interionic hydrogen bond interactions. Despite the large number of metal-urea complexes which have been structurally characterized, the metal-DMU complexes are considerably less studied while there only three reports with crystal structures of metal-DEU complexes [22–24]. In this report we present our first results from the study of metal-DEU complexes, extending the known crystal structures of metal-DEU complexes to seven.

2. Experiments

All manipulations were performed under aerobic conditions using materials and solvents as received. IR spectra were recorded on a Perkin-Elmer PC16 FT-IR spectrometer with samples prepared as KBr pellets. C, H and N elemental analyses were performed with a Carlo Erba EA 108 analyzer.

Caution. Perchlorate salts are potentially explosive. Although no detonation tendencies have been observed in our experiments, caution is advised and handling of only small quantities is recommended.

[Co(DEU)₆](BF₄)₂ (1). A pink solution of Co(BF₄)₂·6H₂O (0.68 g, 2.0 mmol) in EtOH (30 mL) and dimethoxypropane (DMP) (2.5 mL) was refluxed for 20 minutes, cooled to room temperature and then treated with solid DEU (1.40 g, 12 mmol). No noticeable colour change occurred. The reaction mixture was refluxed for a further 15 minutes, cooled to room temperature, and layered with Et₂O (30 mL). Slow mixing gave pink crystals suitable for X-ray crystallography, which were collected by filtration, washed with cold EtOH (2 mL) and Et₂O, and dried *in vacuo* over CaCl₂. Typical yields were in the 70–80% range. Found %: C, 38.96; H, 7.59; N, 17.90. Calc % for C₃₀H₇₂N₁₂O₆CoB₂F₈: C, 38.77; H, 7.81; N, 18.08. IR data (KBr, cm⁻¹): 3332 sb, 2976 s, 2934 m, 2878 m, 1626 vs, 1576 vs, 1482 w, 1454 m, 1380 m,

1338 m, 1294 m, 1160 m, 1142 m, 1110 sb, 1032 s, 922 w, 890 w, 768 m, 578 mb.

$[Co(DEU)_6](ClO_4)_2$ (**2**). A pink-red solution of $Co(ClO_4)_2 \cdot 6H_2O$ (0.73 g, 2.0 mmol) in EtOH (20 mL) and dimethoxypropane (DMP) (2.5 mL) was refluxed for 20 minutes, cooled to room temperature and then treated with solid DEU (1.40 g, 12 mmol). No noticeable colour change occurred. The reaction mixture was refluxed for a further 20 minutes, cooled to room temperature, and layered with Et_2O (50 mL). Slow mixing gave pink crystals suitable for X-ray crystallography, which were collected by filtration, washed with cold EtOH (2 mL) and Et_2O , and dried *in vacuo* over $CaCl_2$. Typical yields were in the 75–85% range. Found %: C, 37.92; H, 7.49; N, 17.80. Calc % for $C_{30}H_{72}N_{12}O_{14}CoCl_2$: C, 37.74; H, 7.60; N, 17.60. IR data (KBr, cm^{-1}): 3332 sb, 2972 s, 2934 m, 2876 w, 1628 vs, 1570 vs, 1482 w, 1452 w, 1378 w, 1338 w, 1296 w, 1264 w, 1142 s, 1114 s, 1086 s, 922 w, 890 w, 768 w, 626 m.

$[Ni(DEU)_6](ClO_4)_2$ (**3**). A pale green solution of $Ni(ClO_4)_2 \cdot 6H_2O$ (0.73 g, 2.0 mmol) in EtOH (15 mL) and dimethoxypropane (DMP) (2.5 mL) was refluxed for 15 minutes, cooled to room temperature and then treated with solid DEU (1.40 g, 12 mmol). No noticeable colour change occurred. The reaction mixture was refluxed for a further 20 minutes, cooled to room temperature, and layered with Et_2O (30 mL). Slow mixing gave green crystals suitable for X-ray crystallography, which were collected by filtration, washed with cold EtOH (2 mL) and Et_2O , and dried *in vacuo* over $CaCl_2$. Typical yields were in the 75–85% range. Found %: C, 37.90; H, 7.45; N, 17.82. Calc % for $C_{30}H_{72}N_{12}O_{14}NiCl_2$: C, 37.75; H, 7.60; N, 17.61. IR data (KBr, cm^{-1}): 3328 sb, 2976 m, 2934 w, 2876 w, 1636 vs, 1570 vs, 1508 w, 1450 m, 1380 w, 1334 w, 1268 m, 1146 s, 1118 s, 1086 s, 922 w, 772 w, 626 m.

$[Zn(DEU)_6](ClO_4)_2$ (**4**). A colourless solution of $Zn(ClO_4)_2 \cdot 6H_2O$ (0.74 g, 2.0 mmol) in EtOH (10 mL) and dimethoxypropane (DMP) (2.5 mL) was refluxed for 20 minutes, cooled to room temperature, and then treated with solid DEU (1.40 g, 12 mmol). The colourless reaction mixture was refluxed for a further 20 minutes, cooled to room temperature, and layered with Et_2O (25 mL). Slow mixing gave colourless crystals suitable for X-ray crystallography, which were collected by filtration, washed with cold EtOH (2 mL) and Et_2O , and dried *in vacuo* over $CaCl_2$. Typical yields were in the 75–85% range. Found %: C, 37.62; H, 7.39; N, 17.60. Calc % for $C_{30}H_{72}N_{12}O_{14}ZnCl_2$: C, 37.49; H, 7.55; N, 17.49. IR data (KBr, cm^{-1}): 3340 sb, 2972 s, 2932 m, 2876 w, 1624 vs, 1582 vs, 1484 w, 1456 w, 1380 w, 1334 w, 1262 m, 1144 s, 1114 s, 1088 s, 924 w, 772 w, 636 m.

2.1. X-ray Crystallography. X-ray data were collected at 298 K using a Crystal Logic Dual Goniometer diffractometer with graphite-monochromated Mo- K_α radiation ($\lambda = 0.71073 \text{ \AA}$). Lorentz, polarization, and Ψ -scan absorption corrections were applied using Crystal Logic software. The structures

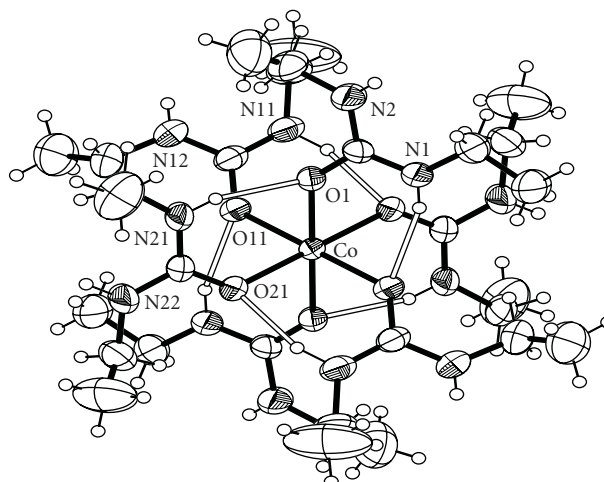
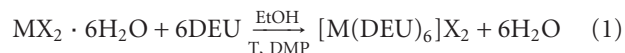


FIGURE 1: An ORTEP representation of the cation $[Co(DEU)_6]^{2+}$ present in complex **1**. Open bonds indicate intramolecular hydrogen bonds. The symmetry-equivalent atoms are not labeled.

were solved by direct methods using SHELXS-86 [25] and refined by full-matrix least-squares techniques on F^2 with SHELXL-97 [26]. Details of the data collection and refinement are given in Table 1. Topological analysis of the nets was performed using TOPOS program package [27, 28].

3. Results and Discussion

3.1. Synthetic Comments. The preparation of the three complexes reported here is summarized in (1):



$M = Co, X = BF_4$ (**1**); $M = Co, X = ClO_4$ (**2**); $M = Ni, X = ClO_4$ (**3**); $M = Zn, X = ClO_4$ (**4**).

2,2-dimethoxypropane (DMP), is a known dehydrating agent which under heating eliminates the possibility of $[M(H_2O)_6]^{2+}$ formation in solution.

Complexes **1–4** seem to be the only products from the $MX_2 \cdot 6H_2O/DEU$ reaction systems ($M=Co, Ni, Zn, X=ClO_4$ and $M=Co, X=BF_4$). Changing the solvent from EtOH to MeCN to THF and Me_2CO as well as the $DEU : M^{II}$ reaction ratio from 6 : 1 to 12 : 1, 8 : 1, 4 : 1 and 3 : 1 does not seem to influence the identity of the products.

3.2. Description of Structures. Bond distances and angles for complexes **1, 2, 3** and **4** are listed in Tables 2, 3, 4, and 5, respectively. ORTEP plots of the cations $[Co(DEU)_6]^{2+}$, $[Ni(DEU)_6]^{2+}$, and $[Zn(DEU)_6]^{2+}$ present in complexes **1, 2, 3**, and **4** are shown in Figures 1, 2, 3, and 4, respectively. Details of the hydrogen bonds of **1, 2, 3**, and **4** are provided in Tables 6, 7, 8, and 9, respectively. Complexes **2, 3**, and **4** crystallise in the triclinic space group $P\bar{1}$ and are isostructural. Complex **1** crystallizes in the monoclinic space group $P2_1/c$. The structures of **2–4** consist of almost perfect octahedral $[M(DEU)_6]^{2+}$ cations and ClO_4^- counterions, while the same $[M(DEU)_6]^{2+}$ cation and BF_4^- anions are

TABLE 1: Crystal data and structure refinement for 1–4.

Compound	1	2	3	4
Empirical formula	C ₃₀ H ₇₂ B ₂ CoF ₈ N ₁₂ O ₆	C ₃₀ H ₇₂ CoCl ₂ N ₁₂ O ₁₄	C ₃₀ H ₇₂ NiCl ₂ N ₁₂ O ₁₄	C ₃₀ H ₇₂ ZnCl ₂ N ₁₂ O ₁₄
Formula weight	929.52	954.81	954.59	961.26
Crystal size	0.10 × 0.20 × 0.20	0.10 × 0.15 × 0.20	0.10 × 0.15 × 0.20	0.10 × 0.20 × 0.20
Crystal system	monoclinic	triclinic	triclinic	triclinic
Space group	<i>P</i> 2 ₁ / <i>c</i>	<i>P</i> $\bar{1}$	<i>P</i> $\bar{1}$	<i>P</i> $\bar{1}$
θ range for data collection. °	1.85 ≤ θ ≤ 25.00	1.93 ≤ θ ≤ 25.00	1.76 ≤ θ ≤ 25.00	1.76 ≤ θ ≤ 25.00
<i>a</i> , Å	9.495(3)	13.341(5)	9.063(3)	9.092(6)
<i>b</i> , Å	22.063(7)	11.935(4)	11.951(6)	11.978(9)
<i>c</i> , Å	12.615(4)	9.052(3)	13.357(6)	13.370(10)
α , °	90	101.925(12)	114.54(2)	114.34(2)
β , °	109.932(11)	100.871(11)	100.74(2)	100.91(2)
γ , °	90	114.455(10)	102.03(2)	102.07(2)
<i>V</i> , Å ³	2484.6(14)	1221.3(7)	1225.1(9)	1233.7(15)
<i>Z</i>	2	1	1	1
ρ_{calcd} , g cm ⁻³	1.242	1.298	1.294	1.294
μ , mm ⁻¹	0.423	0.528	0.572	0.672
<i>GOF</i>	1.024	1.054	1.054	1.055
<i>R</i> 1 ^a	0.0615	0.0571	0.0570	0.0817
<i>wR</i> 2	0.1978	0.1723	0.1799	0.2533

^a*I* > 2 σ (*I*).

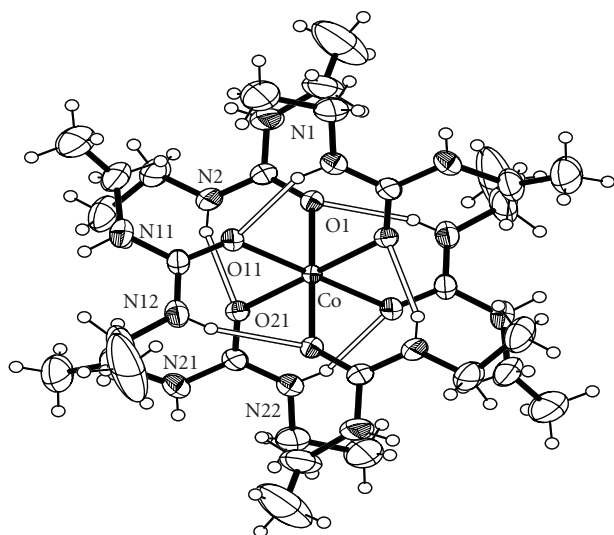


FIGURE 2: An ORTEP representation of the cation [Co(DEU)₆]²⁺ present in complex 2. Open bonds indicate intramolecular hydrogen bonds. The symmetry-equivalent atoms are not labeled.

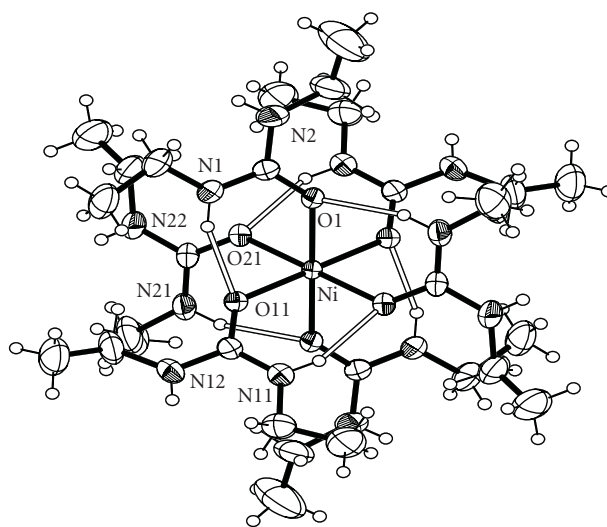


FIGURE 3: An ORTEP representation of the cation [Ni(DEU)₆]²⁺ present in complex 3. Open bonds indicate intramolecular hydrogen bonds. The symmetry-equivalent atoms are not labeled.

present in the structure of 1. In all four structures, the metal ion sits on an inversion centre and is surrounded by six O-bonded DEU ligands. The M–O_(DEU) bond distances in 1–4 are comparable to those in [M(DMU)₆]²⁺ [17, 18]. The average M–O_(DEU) bond lengths change according to the sequence 1 [2.098 Å] \cong 2 [2.096 Å] > 3 [2.072 Å] < 4 [2.108 Å] following the Irving-Williams series [29]. The DEU molecules in 1–4 are coordinated in a bent fashion forming

C=O...M angles ranging from 127.6° to 132.5°. This is the usual way of coordination of urea and its derivatives and has been observed in the similar [M(DMU)₆]X₂ complexes [16–21]. Linearly or approximately linearly coordinated ureas are rare and have been observed only in a few cases [21]. There are six strong intramolecular (intracationic) hydrogen bonds inside each cation with atoms N(1), N(11), and N(21) (and their symmetry equivalents) as donors, and atoms

TABLE 2: Selected bond lengths (Å) and angles (°) for **1**.

Co–O(1)	2.094(2)	N(11)–C(13)	1.327(5)
Co–O(11)	2.088(2)	C(13)–N(12)	1.323(5)
Co–O(21)	2.112(2)	N(12)–C(14)	1.456(7)
O(1)–C(3)	1.262(4)	C(14)–C(15)	1.417(8)
O(11)–C(13)	1.267(4)	C(21)–C(22)	1.451(8)
O(21)–C(23)	1.256(4)	C(22)–N(21)	1.456(5)
C(1)–C(2)	1.486(6)	N(21)–C(23)	1.325(5)
C(2)–N(1)	1.450(5)	C(23)–N(22)	1.335(5)
N(1)–C(3)	1.331(5)	N(22)–C(24)	1.450(6)
C(3)–N(2)	1.325(5)	C(24)–C(25)	1.390(9)
N(2)–C(4)	1.462(7)	B–F(1)	1.279(6)
C(4)–C(5)	1.372(9)	B–F(2)	1.311(9)
C(11)–C(12)	1.289(9)	B–F(3)	1.331(8)
C(12)–N(11)	1.459(6)	B–F(4)	1.265(10)
O(11)#1–Co–O(11)	180.00(19)	C(3)–N(2)–C(4)	124.0(4)
O(11)#1–Co–O(1)	92.93(10)	C(5)–C(4)–N(2)	111.7(6)
O(11)–Co–O(1)	87.07(10)	C(11)–C(12)–N(11)	119.0(7)
O(11)#1–Co–O(1)#1	87.07(10)	C(13)–N(11)–C(12)	126.9(4)
O(11)–Co–O(1)#1	92.93(10)	O(11)–C(13)–N(12)	119.6(4)
O(1)–Co–O(1)#1	180.00(8)	O(11)–C(13)–N(11)	120.4(3)
O(11)#1–Co–O(21)#1	86.69(10)	N(12)–C(13)–N(11)	120.0(4)
O(11)–Co–O(21)#1	93.31(10)	C(13)–N(12)–C(14)	125.1(4)
O(1)–Co–O(21)#1	87.20(10)	C(15)–C(14)–N(12)	112.8(6)
O(1)#1–Co–O(21)#1	92.80(10)	C(21)–C(22)–N(21)	113.9(5)
O(11)#1–Co–O(21)	93.31(10)	C(23)–N(21)–C(22)	127.9(4)
O(11)–Co–O(21)	86.69(10)	O(21)–C(23)–N(21)	121.0(3)
O(1)–Co–O(21)	92.80(10)	O(21)–C(23)–N(22)	120.1(3)
O(1)#1–Co–O(21)	87.20(10)	N(21)–C(23)–N(22)	119.0(3)
O(21)#1–Co–O(21)	180.00(12)	C(23)–N(22)–C(24)	124.3(4)
C(3)–O(1)–Co	132.5(2)	C(25)–C(24)–N(22)	114.1(6)
C(13)–O(11)–Co	127.6(2)	F(4)–B–F(1)	111.2(9)
C(23)–O(21)–Co	129.7(2)	F(4)–B–F(2)	103.0(7)
N(1)–C(2)–C(1)	111.0(4)	F(1)–B–F(2)	115.0(6)
C(3)–N(1)–C(2)	125.8(3)	F(4)–B–F(3)	105.1(8)
O(1)–C(3)–N(2)	119.9(4)	F(1)–B–F(3)	115.1(5)
O(1)–C(3)–N(1)	121.2(3)	F(2)–B–F(3)	106.3(7)
N(2)–C(3)–N(1)	118.9(4)		

Symmetry transformation used to generate equivalent atoms: #1 $-x, -y, -z$.

O(1), O(11) and O(21) (and their symmetry equivalents) as acceptors for **1**, **3** and **4** and N(2), N(12) and N(22) (and their symmetry equivalents) as donors, and atoms O(1), O(11) and O(21) (and their symmetry equivalents) as acceptors for **2**. These intracationic hydrogen bonds create six-membered *pseudochelate* rings providing extra stabilization to the $[M(\text{DEU})_6]^{2+}$ cation. Overall the structural characteristics, that is, bond distances, angles and intracationic hydrogen bonding interactions in the $[M(\text{DEU})_6]^{2+}$ resemble those found in the $[M(\text{DMU})_6]^{2+}$ cations [17, 18] with an exception regarding two additional C–H \cdots O H-bonds (and their symmetry equivalent) found in $[\text{Co}(\text{DMU})_6](\text{ClO}_4)_2$ and $[\text{Co}(\text{DMU})_6](\text{BF}_4)_2$ [18]. Complexes **1–4** extend to

seven the number of structurally characterised DEU compounds. The three, previously structurally characterised, compounds are $[\text{SnBr}_4(\text{DEU})_2]$ [22], $[\text{Fe}(\text{DEU})_6](\text{ClO}_4)_2$ [23] and $[\text{Mn}(\text{DEU})_6][\text{MnBr}_4]$ [24]. Complexes **2–4** are isostructural to $[\text{Fe}(\text{DEU})_6](\text{ClO}_4)_2$. The average Fe–O_{DEU} bond distance is 2.105 following the Irving–Williams series as stated above.

Although the intracationic H-bonding interactions are the same along the $[M(\text{DEU})_6]^{2+}$ series as well as very similar with those found in the $[M(\text{DMU})_6]^{2+}$ cations, the intermolecular/interionic interactions are quite different. That the complexes **2–4** are isostructural implies that the interionic hydrogen bonding interactions are the same.

TABLE 3: Selected bond lengths (Å) and angles (°) for **2**.

Co–O(1)	2.090(2)	N(11)–C(13)	1.329(4)
Co–O(11)	2.100(2)	C(13)–N(12)	1.323(5)
Co–O(21)	2.097(2)	N(12)–C(14)	1.446(5)
O(1)–C(3)	1.259(4)	C(14)–C(15)	1.213(9)
O(11)–C(13)	1.260(4)	C(21)–C(22)	1.424(7)
O(21)–C(23)	1.265(4)	C(22)–N(21)	1.456(6)
C(1)–C(2)	1.329(8)	N(21)–C(23)	1.330(4)
C(2)–N(1)	1.455(6)	C(23)–N(22)	1.324(4)
N(1)–C(3)	1.329(4)	N(22)–C(24)	1.457(5)
C(3)–N(2)	1.328(4)	C(24)–C(25)	1.489(7)
N(2)–C(4)	1.455(4)	Cl–O(34)	1.257(8)
C(4)–C(5)	1.488(6)	Cl–O(32)	1.295(5)
C(11)–C(12)	1.456(7)	Cl–O(31)	1.307(5)
C(12)–N(11)	1.455(6)	Cl–O(33)	1.386(8)
O(1)#1–Co–O(1)	180.00(9)	C(3)–N(2)–C(4)	125.7(3)
O(1)#1–Co–O(21)	86.56(9)	N(2)–C(4)–C(5)	110.8(4)
O(1)–Co–O(21)	93.44(9)	N(11)–C(12)–C(11)	112.4(4)
O(1)#1–Co–O(21)#1	93.44(9)	C(13)–N(11)–C(12)	123.5(3)
O(1)–Co–O(21)#1	86.56(9)	O(11)–C(13)–N(12)	121.2(3)
O(21)–Co–O(21)#1	180.00(16)	O(11)–C(13)–N(11)	120.4(3)
O(1)#1–Co–O(11)	93.24(9)	N(12)–C(13)–N(11)	118.4(3)
O(1)–Co–O(11)	86.76(9)	C(13)–N(12)–C(14)	127.8(4)
O(21)–Co–O(11)	86.22(8)	C(15)–C(14)–N(12)	120.2(5)
O(21)#1–Co–O(11)	93.78(8)	C(21)–C(22)–N(21)	113.4(5)
O(1)#1–Co–O(11)#1	86.76(9)	C(23)–N(21)–C(22)	123.9(3)
O(1)–Co–O(11)#1	93.24(9)	O(21)–C(23)–N(22)	121.1(3)
O(21)–Co–O(11)#1	93.78(8)	O(21)–C(23)–N(21)	120.3(3)
O(21)#1–Co–O(11)#1	86.22(8)	N(22)–C(23)–N(21)	118.6(3)
O(11)–Co–O(11)#1	180.00(11)	C(23)–N(22)–C(24)	126.2(3)
C(3)–O(1)–Co	129.82(19)	N(22)–C(24)–C(25)	110.0(4)
C(13)–O(11)–Co	129.3(2)	O(34)–Cl–O(32)	114.5(8)
C(23)–O(21)–Co	129.46(18)	O(34)–Cl–O(31)	119.6(7)
C(1)–C(2)–N(1)	115.3(6)	O(32)–Cl–O(31)	112.1(5)
C(3)–N(1)–C(2)	123.4(3)	O(34)–Cl–O(33)	98.7(9)
O(1)–C(3)–N(2)	121.6(3)	O(32)–Cl–O(33)	105.0(7)
O(1)–C(3)–N(1)	119.8(3)	O(31)–Cl–O(33)	104.2(6)
N(2)–C(3)–N(1)	118.5(3)		

Symmetry transformation used to generate equivalent atoms: #1 $-x, -y, -z$.

Therefore, only the hydrogen bonding of the representative complex **4** will be discussed. The $[\text{Zn}(\text{DEU})_6]^{2+}$ and ClO_4^- ions in **4** have assembled to create an infinite 2D network through three crystallographically independent intermolecular (interionic) $\text{N-H} \cdots \text{O}_{(\text{perchlorate})}$ hydrogen bonds (and their symmetry related) (Figure 5). Each perchlorate accepts three hydrogen bonds with the O(31), O(32), and O(33) atoms acting as hydrogen bond acceptors while each $[\text{Zn}(\text{DEU})_6]^{2+}$ connects to six ClO_4^- anions through the remaining N-H groups (Figure 5). As a consequence of the participation of O(31), O(32), and O(33) in hydrogen bonding, the Cl–O(31), Cl–O(32), and Cl–O(33) bond lengths [1.402(1), 1.318(1) and 1.440(1) Å, resp.] are slightly longer

than the Cl–O(34) [1.290(1) Å]. In this arrangement, a binodal (3,6)-connected network forms with Schläfli symbol $(4^3)_2(4^6 \cdot 6^6 \cdot 8^3)$ (Figure 6). This two-dimensional (2D) hydrogen-bonded **kgd** net is the dual of the kagome **kgm**-(3.6.3.6) net. It is worth noting that the 2D network adopted by **2–4** was not adopted by any of the $[\text{M}(\text{DMU})_6](\text{ClO}_4)_2$ complexes [17, 18] suggesting that the substitution of DMU by DEU substantially changes the intermolecular (interionic) interactions probably due to the larger ethyl groups (in DEU) instead of the smaller methyl groups (in DMU). Similar 2D networks have been adopted by $[\text{Zn}(\text{DMU})_6](\text{ClO}_4)_2$ [17] and $[\text{Co}(\text{DMU})_6](\text{BF}_4)_2$ [18] with the ClO_4^- and the BF_4^- anions acting as 3-connected nodes and the $[\text{M}(\text{DMU})_6]^{2+}$

TABLE 4: Selected bond lengths (Å) and angles (°) for **3**.

Ni–O(1)	2.068(2)	N(11)–C(13)	1.323(5)
Ni–O(11)	2.073(2)	C(13)–N(12)	1.334(5)
Ni–O(21)	2.076(2)	N(12)–C(14)	1.461(6)
O(1)–C(3)	1.257(4)	C(14)–C(15)	1.415(8)
O(11)–C(13)	1.266(4)	C(21)–C(22)	1.337(16)
O(21)–C(23)	1.263(4)	C(22)–N(21)	1.460(5)
C(1)–C(2)	1.498(7)	N(21)–C(23)	1.322(5)
C(2)–N(1)	1.462(5)	C(23)–N(22)	1.335(5)
N(1)–C(3)	1.329(5)	N(22)–C(24)	1.454(6)
C(3)–N(2)	1.336(5)	C(24)–C(25)	1.462(8)
N(2)–C(4)	1.458(7)	Cl–O(34)	1.274(8)
C(4)–C(5)	1.368(9)	Cl–O(32)	1.298(5)
C(11)–C(12)	1.488(7)	Cl–O(31)	1.310(6)
C(12)–N(11)	1.459(5)	Cl–O(33)	1.378(9)
O(1)#1–Ni–O(1)	180.00(11)	C(3)–N(2)–C(4)	123.0(4)
O(1)#1–Ni–O(11)	86.68(10)	C(5)–C(4)–N(2)	114.0(6)
O(1)–Ni–O(11)	93.32(10)	N(11)–C(12)–C(11)	110.5(4)
O(1)#1–Ni–O(11)#1	93.32(10)	C(13)–N(11)–C(12)	126.5(3)
O(1)–Ni–O(11)#1	86.68(10)	O(11)–C(13)–N(11)	121.6(3)
O(11)–Ni–O(11)#1	180.00(17)	O(11)–C(13)–N(12)	120.0(3)
O(1)#1–Ni–O(21)#1	86.72(10)	N(11)–C(13)–N(12)	118.4(3)
O(1)–Ni–O(21)#1	93.28(10)	C(13)–N(12)–C(14)	123.8(4)
O(11)–Ni–O(21)#1	93.76(10)	C(15)–C(14)–N(12)	113.9(5)
O(11)#1–Ni–O(21)#1	86.24(10)	C(21)–C(22)–N(21)	117.1(9)
O(1)#1–Ni–O(21)	93.28(10)	C(23)–N(21)–C(22)	128.0(4)
O(1)–Ni–O(21)	86.72(10)	O(21)–C(23)–N(21)	121.5(3)
O(11)–Ni–O(21)	86.24(10)	O(21)–C(23)–N(22)	119.7(4)
O(11)#1–Ni–O(21)	93.76(10)	N(21)–C(23)–N(22)	118.8(3)
O(21)#1–Ni–O(21)	180.00(13)	C(23)–N(22)–C(24)	123.8(4)
C(3)–O(1)–Ni	130.2(2)	N(22)–C(24)–C(25)	112.7(5)
C(13)–O(11)–Ni	129.4(2)	O(34)–Cl–O(32)	113.6(8)
C(23)–O(21)–Ni	129.5(2)	O(34)–Cl–O(31)	118.5(8)
N(1)–C(2)–C(1)	110.3(4)	O(32)–Cl–O(31)	113.0(5)
C(3)–N(1)–C(2)	125.5(3)	O(34)–Cl–O(33)	98.6(10)
O(1)–C(3)–N(1)	121.9(3)	O(32)–Cl–O(33)	105.1(7)
O(1)–C(3)–N(2)	119.8(3)	O(31)–Cl–O(33)	105.7(7)
N(1)–C(3)–N(2)	118.3(3)		

Symmetry transformation used to generate equivalent atoms: #1 $-x, -y, -z$.

acting as 6-connected nodes but the connections are achieved through two N-H \cdots X and one C-H \cdots X hydrogen bonds (and their symmetry equivalents), (X = O_(perchlorate) or F_(tetrafluoroborate), resp.).

The intermolecular hydrogen bonding interactions in **1** are far more interesting than those in **2–4**. The [Co(DEU)₆]²⁺ and the BF₄[−] anions have assembled to create a three-dimensional (3D) hydrogen-bonded framework through three crystallographically independent intermolecular (interionic) N-H \cdots F_(tetrafluoroborate) hydrogen bonds (and their

symmetry equivalents). Each BF₄[−] accepts three hydrogen bonds with the F(1), F(2) and F(3) atoms acting as hydrogen bond acceptors while each [Co(DEU)₆]²⁺ connects to six BF₄[−] anions through the remaining N-H groups (Figure 7). In this arrangement, a (3,6)-connected network forms with the [Co(DEU)₆]²⁺ cations acting as the 6-connected nodes and the BF₄[−] anions as the 3-connected nodes. Although the connectivity of each ion seems identical to that found in **2–4**, the arrangement of the [Co(DEU)₆]²⁺ and BF₄[−] ions is quite different resulting in a binodal 3D hydrogen-bonded

TABLE 5: Selected bond lengths (Å) and angles (°) for **4**.

Zn–O(1)	2.108(3)	N(11)–C(13)	1.330(6)
Zn–O(11)	2.107(3)	C(13)–N(12)	1.328(6)
Zn–O(21)	2.111(3)	N(12)–C(14)	1.470(9)
O(1)–C(3)	1.265(5)	C(14)–C(15)	1.313(12)
O(11)–C(13)	1.263(5)	C(21)–C(22)	1.208(14)
O(21)–C(23)	1.279(5)	C(22)–N(21)	1.469(7)
C(1)–C(2)	1.485(10)	N(21)–C(23)	1.315(7)
C(2)–N(1)	1.457(6)	C(23)–N(22)	1.328(6)
N(1)–C(3)	1.331(6)	N(22)–C(24)	1.437(9)
C(3)–N(2)	1.337(6)	C(24)–C(25)	1.496(10)
N(2)–C(4)	1.452(8)	Cl–O(34)	1.29(2)
C(4)–C(5)	1.431(10)	Cl–O(32)	1.318(12)
C(11)–C(12)	1.510(9)	Cl–O(31)	1.402(13)
C(12)–N(11)	1.461(6)	Cl–O(33)	1.440(16)
O(11)#1–Zn–O(11)	180.0(2)	C(3)–N(2)–C(4)	124.0(5)
O(11)#1–Zn–O(1)#1	92.91(13)	C(5)–C(4)–N(2)	113.5(7)
O(11)–Zn–O(1)#1	87.09(13)	N(11)–C(12)–C(11)	109.7(5)
O(11)#1–Zn–O(1)	87.09(13)	C(13)–N(11)–C(12)	124.8(4)
O(11)–Zn–O(1)	92.91(13)	O(11)–C(13)–N(12)	119.8(4)
O(1)#1–Zn–O(1)	180.00	O(11)–C(13)–N(11)	121.5(4)
O(11)#1–Zn–O(21)	92.83(12)	N(12)–C(13)–N(11)	118.7(4)
O(11)–Zn–O(21)	87.17(12)	C(13)–N(12)–C(14)	123.6(5)
O(1)#1–Zn–O(21)	93.04(12)	C(15)–C(14)–N(12)	116.1(8)
O(1)–Zn–O(21)	86.96(12)	C(21)–C(22)–N(21)	121.2(8)
O(11)#1–Zn–O(21)#1	87.17(12)	C(23)–N(21)–C(22)	128.4(5)
O(11)–Zn–O(21)#1	92.83(12)	O(21)–C(23)–N(21)	121.3(4)
O(1)#1–Zn–O(21)#1	86.96(12)	O(21)–C(23)–N(22)	119.2(5)
O(1)–Zn–O(21)#1	93.04(12)	N(21)–C(23)–N(22)	119.4(4)
O(21)–Zn–O(21)#1	180.00(18)	C(23)–N(22)–C(24)	124.9(5)
C(3)–O(1)–Zn	129.5(3)	N(22)–C(24)–C(25)	112.6(7)
C(13)–O(11)–Zn	129.6(3)	O(34)–Cl–O(32)	122.9(10)
C(23)–O(21)–Zn	128.7(3)	O(34)–Cl–O(31)	124.7(11)
N(1)–C(2)–C(1)	109.9(5)	O(32)–Cl–O(31)	109.2(7)
C(3)–N(1)–C(2)	126.0(4)	O(34)–Cl–O(33)	85.0(9)
O(1)–C(3)–N(1)	120.6(4)	O(32)–Cl–O(33)	106.6(8)
O(1)–C(3)–N(2)	120.5(4)	O(31)–Cl–O(33)	97.5(8)
N(1)–C(3)–N(2)	118.9(4)		

Symmetry transformation used to generate equivalent atoms: #1 $-x, -y, -z$.TABLE 6: Dimensions of the unique hydrogen bonds (distances in Å and angles in °) for complex **1**.[†]

D [‡] –H···A [§]	D [‡] ···A [§]	H···A [§]	<D [‡] HA [§]
N(1)–H(1)···O(11)a	2.952(1)	2.177(1)	158.68(3)
N(11)–H(11)···O(21)a	2.878(1)	1.983(1)	156.88(2)
N(21)–H(21)···O(1)	2.861(1)	2.060(1)	160.05(3)
N(2)–H(2)···F(1)b	2.930(1)	2.272(1)	159.06(3)
N(12)–H(12)···F(2)c	2.947(1)	2.247(1)	163.27(3)
N(22)–H(22)···F(3)	2.964(1)	2.135(1)	151.44(2)

[†] Symmetry transformation used to generate equivalent atoms: a $-x, -y, -z$; b $1-x, 0.5+y, 0.5-z$; c $1-x, -y, 1-z$.[‡]D = donor atom.[§]A = acceptor atom.

TABLE 7: Dimensions of the unique hydrogen bonds (distances in Å and angles in °) for complex 2.[†]

D [‡] -H...A [§]	D [‡] ...A [§]	H...A [§]	<D [‡] HA [§]
N(2)-H(2)...O(21)	2.905(1)	2.154(1)	155.07(4)
N(12)-H(12)...O(1)a	2.914(1)	2.177(1)	159.29(3)
N(22)-H(22)...O(11)a	2.908(1)	2.153(1)	153.49(2)
N(1)-H(1)...O(31)b	3.081(1)	2.381(1)	151.68(3)
N(11)-H(11)...O(32)	3.013(1)	2.234(1)	150.97(2)
N(21)-H(21)...O(33)c	3.072(1)	2.386(1)	160.41(5)

[†] Symmetry transformation used to generate equivalent atoms: a -x, -y, -z; b -x, 1-y, 1-z; c 1-x, 1-y, 1-z.

[‡]D = donor atom.

[§]A = acceptor atom.

TABLE 8: Dimensions of the unique hydrogen bonds (distances in Å and angles in °) for complex 3.[†]

D [‡] -H...A [§]	D [‡] ...A [§]	H...A [§]	<D [‡] HA [§]
N(1)-H(1)...O(11)	2.886(1)	2.055(1)	156.94(5)
N(11)-H(11)...O(21)a	2.892(1)	2.082(1)	155.01(5)
N(21)-H(21)...O(1)a	2.890(2)	2.091(1)	154.16(6)
N(2)-H(2)...O(31)	3.097(1)	2.343(1)	159.73(6)
N(12)-H(12)...O(33)b	3.077(2)	2.390(1)	156.88(5)
N(22)-H(22)...O(32)c	3.038(1)	2.369(1)	144.26(5)

[†] Symmetry transformation used to generate equivalent atoms: a -x, -y, -z; b x, y, 1+z; c 1-x, 1-y, -z.

[‡]D = donor atom.

[§]A = acceptor atom.

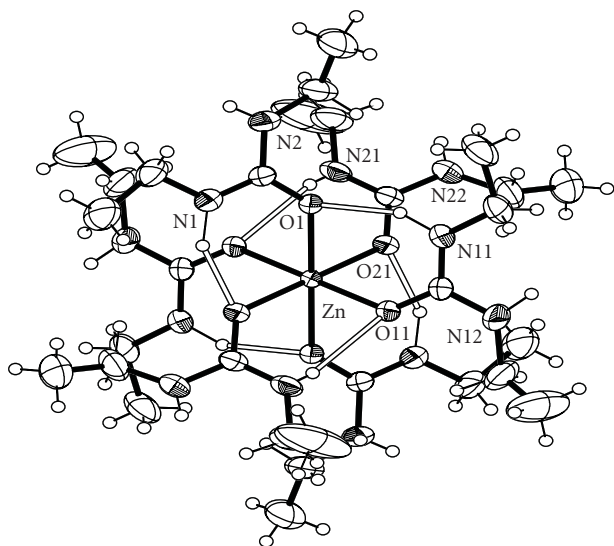


FIGURE 4: An ORTEP representation of the cation $[\text{Co}(\text{DEU})_6]^{2+}$ present in complex 4. Open bonds indicate intramolecular hydrogen bonds. The symmetry-equivalent atoms are not labeled.

network with a rutile (**rtl**) topology [30, 31] and Schläfli symbol $(4.6^2)_2(4^2.6^{10}.8^3)$ (Figure 8). It is worth noting that none of the $[\text{M}(\text{DMU})_6]\text{X}_2$ complexes [17, 18] adopts a 3D net.

3.3. *Vibrational Spectra of the Complexes.* Table 10 gives diagnostic IR bands of the free ligand and complexes 1–4. Assignments have been given in comparison with the

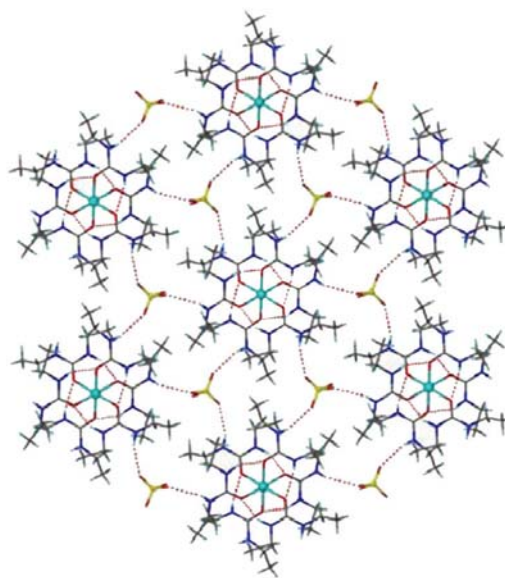


FIGURE 5: A view of the 2D framework formed by hydrogen bonding between the $[\text{Zn}(\text{DEU})_6]^{2+}$ cations and the ClO_4^- anions in 4. The same framework is adopted by complexes 2 and 3.

data obtained for the free DMU [32], the free DEU [33] and its Co(II) and Ni(II) complexes [34]. The bands with $\nu(\text{CN})$ character are situated at higher wavenumbers in the spectra of 1–4 than for free DEU, whereas the $\nu(\text{CO})$ band shows a frequency decrease. These shifts are consistent with oxygen coordination, suggesting the presence of $^+\text{N}=\text{C}-\text{O}^-$

TABLE 9: Dimensions of the unique hydrogen bonds (distances in Å and angles in °) for complex 4.[†]

D [‡] -H...A [§]	D [‡] ...A [§]	H...A [§]	<D [‡] HA [§]
N(1)-H(1)...O(21)a	2.905(2)	1.876(1)	150.35(6)
N(11)-H(11)...O(1)	2.904(2)	1.932(1)	152.80(6)
N(21)-H(21)...O(11)a	2.921(2)	2.314(2)	162.75(10)
N(2)-H(2)...O(33)	3.153(2)	2.392(2)	160.19(8)
N(12)-H(12)...O(31)b	3.086(2)	2.234(1)	155.95(7)
N(22)-H(22)...O(32)c	3.035(2)	2.365(1)	150.81(8)

[†] Symmetry transformation used to generate equivalent atoms: a $-x, -y, -z$; b $x, y, 1-z$; c $1-x, 1-y, 1-z$.

[‡]D = donor atom.

[§]A = acceptor atom.

TABLE 10: Most characteristic and diagnostic IR fundamentals (cm⁻¹) for DEU and complexes 1–4.^a

Assignments	DEU	1	2	3	4
$\nu(\text{NH})$	3342 sb	3332 sb	3332 sb	3328 sb	3340 sb
$\nu(\text{CH})$	2973 s, 2932 m, 2874 m	2976 s, 2934 m, 2878 m	2972 s, 2934 m, 2876 w	2976 m, 2934 w, 2876 w	2972 s, 2932 m, 2876 w
$\nu_{\text{as}}(\text{CN})_{\text{amide}} + \delta_{\text{as}}\nu(\text{NH})$	1625 vs	1576 vs	1570 vs	1570 vs	1582 vs
$\nu(\text{CO})$	1586 vs	1626 vs	1628 vs	1636 vs	1624 vs
$\delta_{\text{s}}(\text{NH})$	1540 m sh	1454 m	1452 w	1450 m	1456 w
$\delta_{\text{as}}(\text{NH}) + \nu_{\text{as}}(\text{CN})_{\text{amide}}$	1259 m	1338 m	1338 w	1334 w	1334 w

^aKBr pellets.

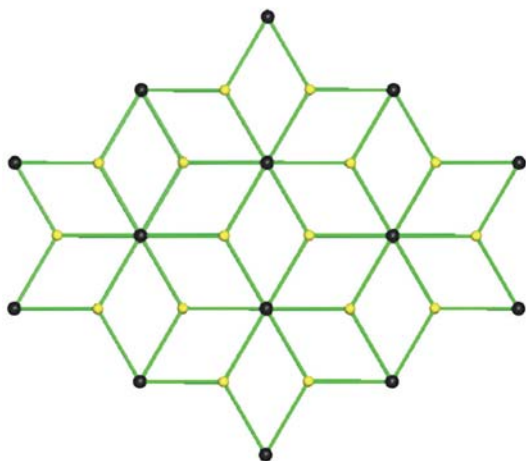


FIGURE 6: A view of the 2D hydrogen-bonded **kgd**-(4³)₂(4⁶.6⁶.8³) net adopted by complexes 2–4. Black spheres represent the 6-connected [M(DEU)₆]²⁺ cations [M = Co (2), Ni (3) and Zn (4)] and yellow spheres the 3-connected ClO₄⁻ anions.

resonant forms [17, 18]. Upon coordination *via* oxygen, the positively charged metal ion stabilizes the negative charge on the oxygen atom; the NCO group now occurs in its polar resonance form and the double bond character of the CN bond increases, while the double bond character of the CO bond decreases, resulting in an increase of the CN stretching frequency with a simultaneous decrease in the CO stretching frequency [17, 18]. The $\nu_3(\text{F}_2)$ [$\nu_d(\text{BF})$] and $\nu_4(\text{F}_2)$ [$\delta_d(\text{BF})$] vibrations of the tetrahedral (point

group T_d) BF₄⁻ anion appear at 1100-1000 and at 522–580 cm⁻¹ (broad bands), respectively, in the IR spectrum of 1 [35]. The IR spectra of 2–4 exhibit strong bands at ~1100 and 626 cm⁻¹ due to the $\nu_3(\text{F}_2)$ and $\nu_4(\text{F}_2)$ vibrations, respectively, of the uncoordinated ClO₄⁻ [35]. The broad character and splitting of the band at ~1100 cm⁻¹ indicate the involvement of the ClO₄⁻ ion in hydrogen bonding as it was established crystallographically (see above).

4. Conclusions

Following our studies on the coordination chemistry of urea (U) and N,N'-dimethylurea (DMU), N,N'-diethylurea (DEU) was employed as a ligand to form the stable octahedral complexes [M(DEU)₆]²⁺ with cobalt(II), nickel(II) and zinc(II). The structural characteristics of the [M(DEU)₆]²⁺ cation are very similar to the DMU analogs, that is, [M(DMU)₆]²⁺. All six DEU molecules are coordinated to metal centre in a bent fashion forming a C=O...M angle of ~130°, while six strong intracationic N-H...O_(DEU) hydrogen bonds stabilize the [M(DEU)₆]²⁺ cations by creating six six-membered *pseudochelate* rings. The [M(DEU)₆]²⁺ cations and counterions (ClO₄⁻ or BF₄⁻) self-assemble to form extended hydrogen-bonded architectures *via* 3 unique N-H...X hydrogen bonds, (X = O_(perchlorate) or F_(tetrafluoroborate)). The nature of the resulting supramolecular architectures is influenced by the nature of the counter-ion since the presence of ClO₄⁻ counter-ions gives rise to the formation of 2D hydrogen-bonded networks that conform to the **kgd** net while the presence of BF₄⁻ counter-ions results in a 3D hydrogen-bonded net with an **rtl** topology. By comparing the supramolecular architectures of the [M(DEU)₆]₂

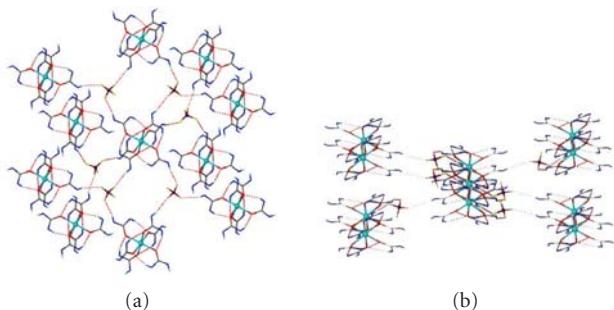


FIGURE 7: Views of the 3D framework formed by hydrogen bonds between the $[\text{Co}(\text{DEU})_6]^{2+}$ cations and the BF_4^- anions in **1**.

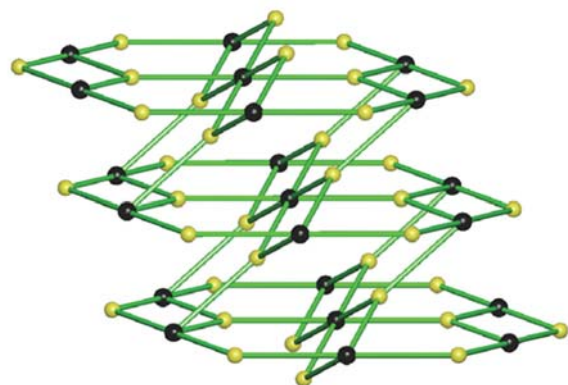


FIGURE 8: A view of the binodal 3D hydrogen-bonded $\text{rtl}-(4.6^2)_2(4^2.6^{10}.8^3)$ net that **1** adopts. Black spheres represent the 6-connected $[\text{Co}(\text{DEU})_6]^{2+}$ cations and yellow spheres the 3-connected BF_4^- anions.

($X=\text{ClO}_4$ or BF_4) and the $[\text{M}(\text{DMU})_6]\text{X}_2$ ($X=\text{ClO}_4$ or BF_4) we can conclude that the substitution of DMU by DEU considerably affected the nature of the hydrogen-bonded networks. We are presently pursuing our studies on the coordination chemistry of urea and its symmetrically or unsymmetrically substituted alkyl derivatives to generate a rich variety of hydrogen-bonded networks.

Acknowledgment

G. S. Papaefstathiou thanks the Special Account for Research Grants (SARG) of the National and Kapodistrian University of Athens for funding this paper.

References

- [1] K. C. Nicolaou and T. Montagnon, *Molecules that Changed the World*, Wiley-VCH, Weinheim, Germany, 2008.
- [2] W. F. Boron and E. L. Boulpaep, *Medical Physiology*, Updated Edition, Saunders, Philadelphia, Pa, USA, 2004.
- [3] J. H. Meessen and H. Petersen, "Urea," in *Ullmann's Encyclopedia of Industrial Chemistry*, Electronic Release, Wiley-VCH, Weinheim, Germany, 6th edition, 2002.
- [4] F. Meyer, M. Konrad, and E. Kaifer, "Novel μ_3 -coordination of urea at a nickel(II) site: structure, reactivity and ferromagnetic superexchange," *European Journal of Inorganic Chemistry*, no. 11, pp. 1851–1854, 1999.
- [5] H. E. Wages, K. L. Taft, and S. J. Lippard, " $[\text{Ni}_2(\text{OAc})_3(\text{urea})(\text{tmen})_2](\text{OTf})$ and $[\text{Ni}(\text{OAc})(\text{urea})_2(\text{tmen})](\text{OTf})$, model complexes for the enzyme urease," *Inorganic Chemistry*, vol. 32, no. 23, pp. 4985–4987, 1993.
- [6] T. Theophanides and P. D. Harvey, "Structural and spectroscopic properties of metal-urea complexes," *Coordination Chemistry Reviews*, vol. 76, pp. 237–264, 1987.
- [7] P. S. Gentile, P. Carfagno, S. Haddad, and L. Campisi, "The preparation of the bidentate urea complex $[\text{Co}(\text{urea})_4](\text{NO}_3)_2$," *Inorganica Chimica Acta*, vol. 6, no. C, pp. 296–298, 1972.
- [8] D. S. Sagatys, R. C. Bott, G. Smith, K. A. Byriel, and C. H. L. Kennard, "The preparation and crystal structure of a polymeric (1 : 1)—silver nitrate-urea complex, $[(\text{AgNO}_3)_2(\text{CH}_4\text{N}_2\text{O})_2]_n$," *Polyhedron*, vol. 11, no. 1, pp. 49–52, 1992.
- [9] K. Lewinski, J. Sliwinski, and L. Lebioda, "Structure of (urea)mercury(II) chloride and the effects of strain on ligand properties of urea," *Inorganic Chemistry*, vol. 22, no. 16, pp. 2339–2342, 1983.
- [10] S. V. Kryatov, A. Y. Nazarenko, P. D. Robinson, and E. V. Rybak-Akimova, "A dinuclear iron (III) complex with a bridging urea anion: implications for the urease mechanism," *Chemical Communications*, no. 11, pp. 921–922, 2000.
- [11] S. Subramanian and M. J. Zaworotko, "Exploitation of the hydrogen bond: recent developments in the context of crystal engineering," *Coordination Chemistry Reviews*, vol. 137, pp. 357–401, 1994.
- [12] X. Zhao, Y.-L. Chang, F. W. Fowler, and J. W. Lauher, "An approach to the design of molecular solids. The ureylenedicarboxylic acids," *Journal of the American Chemical Society*, vol. 112, no. 18, pp. 6627–6634, 1990.
- [13] T. L. Nguyen, F. W. Fowler, and J. W. Lauher, "Commensurate and incommensurate hydrogen bonds. An exercise in crystal engineering," *Journal of the American Chemical Society*, vol. 123, no. 44, pp. 11057–11064, 2001.
- [14] P. S. Corbin, S. C. Zimmerman, P. A. Thiessen, N. A. Hawryluk, and T. J. Murray, "Complexation-induced unfolding of heterocyclic ureas. Simple foldamers equilibrate with multiply hydrogen-bonded sheetlike structures," *Journal of the American Chemical Society*, vol. 123, no. 43, pp. 10475–10488, 2001.
- [15] S. Swaminathan and B. M. Craven, "The crystal structure and molecular thermal motion of urea at 12, 60 and 123 K from neutron diffraction," *Acta Crystallographica*, vol. B40, pp. 300–306, 1984.
- [16] E. Manessi-Zoupa and G. S. Papaefstathiou, "Synthesis, x-ray structure and characterization of a complex containing the hexakis(urea)cobalt(II) cation and lattice urea molecules," *Bioinorganic Chemistry and Applications*, vol. 2007, Article ID 51567, 7 pages, 2007.
- [17] R. Keuleers, H. O. Desseyn, G. S. Papaefstathiou et al., "Hydrogen-bonded networks based on manganese(II), nickel(II), copper(II) and zinc(II) complexes of N,N'-dimethylurea," *Transition Metal Chemistry*, vol. 28, no. 5, pp. 548–557, 2003.
- [18] G. S. Papaefstathiou, R. Keuleers, C. J. Milios et al., "The hexakis(N,N'-dimethylurea)cobalt(II) cation: a flexible building block for the construction of hydrogen bonded networks," *Zeitschrift für Naturforschung*, vol. 58b, no. 1, pp. 74–84, 2003.

- [19] E. Diamantopoulou, G. S. Papaefstathiou, A. Terzis, C. P. Raptopoulou, H. O. Desseyn, and S. P. Perlepes, "Hydrogen bonded networks based on lanthanide(III) complexes of N,N'-dimethylurea (DMU): preparation, characterisation, and crystal structures of $[\text{Nd}(\text{DMU})_6][\text{NdCl}_6]$ and $[\text{Nd}(\text{NO}_3)_3(\text{DMU})_3]$," *Polyhedron*, vol. 22, no. 6, pp. 825–835, 2003.
- [20] R. Keuleers, G. S. Papaefstathiou, C. P. Raptopoulou, S. P. Perlepes, and H. O. Desseyn, "Comparative study of the metal-ligand bond strength in $\text{Mn}^{\text{II}}/\text{X}/\text{U}$ complexes (X = Cl, Br, I; U = urea)," *Journal of Molecular Structure*, vol. 525, no. 1–3, pp. 173–183, 2000.
- [21] R. Keuleers, G. S. Papaefstathiou, C. P. Raptopoulou, V. Tangoulis, H. O. Desseyn, and S. P. Perlepes, "Tris(N,N'-dimethylurea)bis(nitrato-O,O')manganese(II), the first example of a seven-coordinate manganese (II) complex with a monodentate organic ligand," *Inorganic Chemistry Communications*, vol. 2, no. 10, pp. 472–475, 1999.
- [22] S. Calogero, U. Russo, G. Valle, P. W. C. Barnard, and J. D. Donaldson, "A study of cis-octahedral compounds of tin(IV) halides with thiourea or urea type ligands," *Inorganica Chimica Acta*, vol. 59, pp. 111–116, 1982.
- [23] U. Russo, G. Valle, and S. Calogero, "Hexakis(diethylurea)iron(II) perchlorate, $\text{C}_{30}\text{H}_{72}\text{Cl}_2\text{FeN}_{12}\text{O}_{14}$," *Crystal Structure Communications*, vol. 9, pp. 443–448, 1980.
- [24] J. Delaunay and R. P. Hugel, "Molecular structure of hexakis(N,N'-diethylurea)manganese(II) tetrabromomanganate(II)," *Inorganic Chemistry*, vol. 28, no. 12, pp. 2482–2485, 1989.
- [25] G. M. Sheldrick, *SHELXS-86, Structure Solving Program*, University of Göttingen, Göttingen, Germany, 1986.
- [26] G. M. Sheldrick, *SHELXL-97, Program for the Refinement of Crystal Structures from Diffraction Data*, University of Göttingen, Göttingen, Germany, 1997.
- [27] <http://www.topos.ssu.samara.ru>.
- [28] V. A. Blatov, "Multipurpose crystallochemical analysis with the program package TOPOS," *IUCr CompComm Newsletter*, pp. 4–38, 2006.
- [29] H. Irving and R. J. P. Williams, "The stability of transition-metal complexes," *Journal of the Chemical Society*, pp. 3192–3210, 1953.
- [30] M. O'Keeffe, M. Eddaoudi, H. Li, T. Reineke, and O. M. Yaghi, "Frameworks for extended solids: geometrical design principles," *Journal of Solid State Chemistry*, vol. 152, no. 1, pp. 3–20, 2000.
- [31] O. D. Friedrichs, M. O'Keeffe, and O. M. Yaghi, "The CdSO_4 , rutile, cooperite and quartz dual nets: interpenetration and catenation," *Solid State Sciences*, vol. 5, no. 1, pp. 73–78, 2003.
- [32] R. Keuleers, H. O. Desseyn, B. Rousseau, and C. Van Alsenoy, "Solids modeled by ab initio crystal field methods. 21. Study of the structure and vibrational spectrum of N,N'-dimethylurea in the gas phase and in its Cc crystal phase," *Journal of Physical Chemistry A*, vol. 104, no. 25, pp. 5946–5954, 2000.
- [33] Y. Mido, "Infrared spectra and configurations of dialkylureas," *Spectrochimica Acta Part A*, vol. 28, no. 8, pp. 1503–1518, 1972.
- [34] J. P. Barbier and R. Hugel, "New complexes of cobalt(II) and nickel(II) salts with N,N'-diethylurea," *Inorganica Chimica Acta*, vol. 18, no. C, pp. 253–256, 1976.
- [35] K. Nakamoto, *Infrared and Raman Spectra of Inorganic and Coordination Compounds*, John Wiley and Sons, New York, NY, USA, 4th edition, 1986.

Research Article

Structurally Diverse Metal Coordination Compounds, Bearing Imidodiphosphinate and Diphosphinoamine Ligands, as Potential Inhibitors of the Platelet Activating Factor

Alexandros B. Tsoupras,¹ Maria Roulia,² Eleftherios Ferentinos,² Ioannis Stamatopoulos,² Constantinos A. Demopoulos,¹ and Panayotis Kyritsis²

¹Biochemistry Laboratory, Faculty of Chemistry, National and Kapodistrian University of Athens, Panepistimiopolis, Zografou, 15771 Athens, Greece

²Inorganic Chemistry Laboratory, Faculty of Chemistry, National and Kapodistrian University of Athens, Panepistimiopolis, Zografou, 15771 Athens, Greece

Correspondence should be addressed to Panayotis Kyritsis, kyritsis@chem.uoa.gr

Received 15 March 2010; Accepted 3 May 2010

Academic Editor: Spyros Perlepes

Copyright © 2010 Alexandros B. Tsoupras et al. This is an open access article distributed under the Creative Commons Attribution License, which permits unrestricted use, distribution, and reproduction in any medium, provided the original work is properly cited.

Metal complexes bearing dichalcogenated imidodiphosphinate $[R_2P(E)NP(E)R'_2]^-$ ligands (E = O, S, Se, Te), which act as (E,E) chelates, exhibit a remarkable variety of three-dimensional structures. A series of such complexes, namely, square-planar $[Cu\{(OPPh_2)(OPPh_2)N-O, O\}_2]$, tetrahedral $[Zn\{(EPPH_2)(EPPH_2)N-E, E\}_2]$, E = O, S, and octahedral $[Ga\{(OPPh_2)(OPPh_2)N-O, O\}_3]$, were tested as potential inhibitors of either the platelet activating factor (PAF)- or thrombin-induced aggregation in both washed rabbit platelets and rabbit platelet rich plasma. For comparison, square-planar $[Ni\{(Ph_2P)_2N-S-CHMePh-P, P\}X_2]$, X = Cl, Br, the corresponding metal salts of all complexes and the $(OPPh_2)(OPPh_2)NH$ ligand were also investigated. $Ga(O, O)_3$ showed the highest anti-PAF activity but did not inhibit the thrombin-related pathway, whereas $Zn(S, S)_2$, with also a significant PAF inhibitory effect, exhibited the highest thrombin-related inhibition. $Zn(O, O)_2$ and $Cu(O, O)_2$ inhibited moderately both PAF and thrombin, being more effective towards PAF. This work shows that the PAF-inhibitory action depends on the structure of the complexes studied, with the bulkier $Ga(O, O)_3$ being the most efficient and selective inhibitor.

1. Introduction

Extensive research work over the last few years has revealed a remarkable structural variability of transition metal compounds bearing dichalcogenated imidodiphosphinate type of ligands, that is, $[R_2P(E)NP(E)R'_2]^-$, E = O, S, Se, Te; R, R' = various aryl or alkyl groups. These ligands have been shown to display great coordinating versatility, producing both single and multinuclear metal complexes, with a variety of bonding modes [1–3]. The coordinating flexibility of these (E,E) chelating ligands is attributed, mainly, to their large (ca. 4 Å) E ··· E bite, which would accommodate a range of coordination sphere geometries. For instance, it was recently shown that the $[^1Pr_2P(Se)NP(Se)^1Pr_2]^-$ ligand affords both tetrahedral and square-planar complexes of

Ni(II) [4], in agreement with an earlier observation on the analogous $[Ph_2P(S)NP(S)Ph_2]^-$ ligand [5]. Moreover, the nature of the R and R' peripheral groups of the $[R_2P(S)NP(S)R'_2]^-$ ligand has been shown to affect the geometry of the complexes formed upon its coordination to Ni(II) [6, 7]. In a more general sense, depending on the nature of the metal ion, the chalcogen E atom and the R peripheral group, complexes bearing the above type of ligands were shown to contain rather diverse coordination spheres [8]. Such structural differences are of significant importance, as they are expected to lead not only to different stereochemical characteristics, but also to varied electronic properties of the metal site, which, in turn, could potentially result in significant biological reactivity [9].

The aim of this work was to investigate a series of structurally diverse metal coordination compounds bearing dichalcogenated imidodiphosphate ligands, as potential inhibitors of PAF (1-*O*-alkyl-2-acetyl-*sn*-glycero-3-phosphocholine). PAF is a phospholipid signalling molecule of the immune system and a significant mediator of inflammation. PAF transmits outside-in signals to intracellular transduction systems in a variety of cell types, including key cells of the innate immune and haemostatic systems, such as neutrophils, monocytes, and platelets [10, 11]. In addition, it exhibits biological activity through specific membrane PAF-receptors, coupled with G-proteins. The binding of PAF on its receptor induces intracellular signaling pathways that lead to several cellular activation mechanisms, depending on the cell or tissue type [12]. It is well established that increased PAF-levels in blood or tissues lead to various inflammatory manifestations [10–12] such as cardiovascular, renal and periodontal diseases [13–16], allergy [17], diabetes [18], cancer [19] and AIDS [20].

A great variety of chemical compounds, both natural and synthetic, have demonstrated an inhibitory effect towards the PAF-induced biological activities, acting either through direct antagonistic/competitive effects by binding to the PAF-receptor, or through indirect mechanisms. In the latter case, the biofunctionality seems to correlate with changes in the membrane microenvironment of the PAF-receptor. Natural and synthetic PAF antagonists exhibit variable chemical structures that might lead to different pharmacological profiles. Since PAF is assumed to play a central role in many diseases, the effects of its antagonists have been widely studied in experimentally induced pathologies and in clinical studies [21–24].

The use of metal complexes as potential pharmaceuticals is increasingly gaining ground [25, 26]. Particularly, complexes of Ga(III) bearing (O,O) chelating ligands have been studied thoroughly as promising nonplatinum compounds with superior anticancer activity and lower side effects [27, 28]. These complexes have also shown anti-inflammatory activity towards rheumatoid arthritis or Alzheimer's disease [25]. Cu(II) complexes have been investigated as anticancer agents, based on the assumption that endogenous metals may be less toxic [29]. In addition, Ni(II) and Cu(II) complexes have been screened for their *in vitro* antibacterial and antifungal activity [30], whereas Zn(II) complexes have been investigated as agents against diabetes mellitus and ulcer [31]. A mechanistic understanding of how metal complexes exhibit their biological activity is crucial to their clinical success, as well as to the rational design of new compounds with improved pharmacological properties. In that respect, the *in vitro* investigation of novel metal complexes with targeted biomolecules may prove extremely valuable, before the *in vivo* tests in animal models.

In this study, we examined the *in vitro* effects of representative bis- or tris-chelated complexes of dichalcogenated imidodiphosphate ligands, involving Cu(II), Zn(II) and Ga(III) centers, against PAF-induced biological activities. For this purpose, the potent inhibitory effect of these metal complexes was studied on PAF-induced platelet aggregation towards both washed rabbit platelets (WRPs) and rabbit

platelet rich plasma (PRP). The complexes investigated contain diverse metal coordination spheres, exhibiting square-planar, tetrahedral and octahedral geometries. In addition, two square-planar complexes of Ni(II), bearing one bidentate diphosphinoamine ligand [32] and two halide ions were also investigated, with a view of revealing the necessary structural features, among this set of coordination compounds, that would ensure efficient and selective inhibition of PAF. Moreover, the inhibitory action of some of these complexes towards thrombin was also investigated, in order to probe their selectivity with respect to either the PAF- or the thrombin-dependent platelet aggregation.

2. Experimental Part

2.1. Materials and Methods. The following complexes were prepared according to published procedures: [Cu{(OPPh₂)(OPPh₂)N-O, O₂}] [33], [Zn{(OPPh₂)(OPPh₂)N-O, O₂}] [34], [Zn{(SPPPh₂)(SPPPh₂)N-S, S₂}] [35], [Ga{(OPPh₂)(OPPh₂)N-O, O₃}] [36], [Ni{(Ph₂P)₂N-S-CHMePh-P, P}Cl₂] [37]. These complexes are abbreviated as Cu(O,O)₂, Zn(O,O)₂, Zn(S,S)₂, Ga(O,O)₃ and Ni(P,P)Cl₂, respectively. The synthesis of the analogous to Ni(P,P)Cl₂, bromide-containing Ni(P,P)Br₂ complex, was carried out according to the published procedure [37], with the exception of using Ni(DME)Br₂ (DME = 1,2-dimethoxyethane) as a starting material. The detailed synthesis and characterization of Ni(P,P)Br₂ will be described elsewhere. The (OPPh₂)(OPPh₂)NH ligand was prepared as described in the literature [38]. The following metal salts, CuCl₂, ZnCl₂, Ga(NO₃)₃·9H₂O and NiCl₂·6H₂O, were also tested for comparison purposes. All chemical reagents used were purchased from Sigma-Aldrich (St. Louis, Mo, USA).

UV-vis spectra were recorded in a Varian Cary 3E spectrophotometer.

Bovine serum albumin (BSA), PAF (1-*O*-hexadecyl-2-acetyl-*sn*-glycero-3-phosphocholine), thrombin and analytical solvents for the biological assays were purchased from Sigma.

Centrifugations were performed in a Heraeus Labofug 400R and a Sorvall RC-5B refrigerated super-speed centrifuge (Sigma-Aldrich). Aggregation studies were performed in a Chrono-Log aggregometer (model 400, Haver-town, Pa, USA) coupled to a Chrono-Log recorder (Haver-town) at 37°C with constant stirring at 1200 rpm.

2.2. Biological Assay on WRPs and Rabbit PRP. The potential inhibitory effect of a range of metal complexes towards PAF-related biological activities was estimated by biological assays based on WRPs aggregation [10]. The examined metal complexes were first dissolved in dimethylsulfoxide (DMSO), at an initial concentration of (4–8) × 10⁻³ M. Subsequently, different aliquots of the complexes' solutions were added in a BSA solution (2.5 mg BSA/mL of saline). PAF was also dissolved in the same BSA solution. The metal salts were dissolved in saline. The platelet aggregation induced by PAF (4.4 × 10⁻¹¹ M final concentration in the

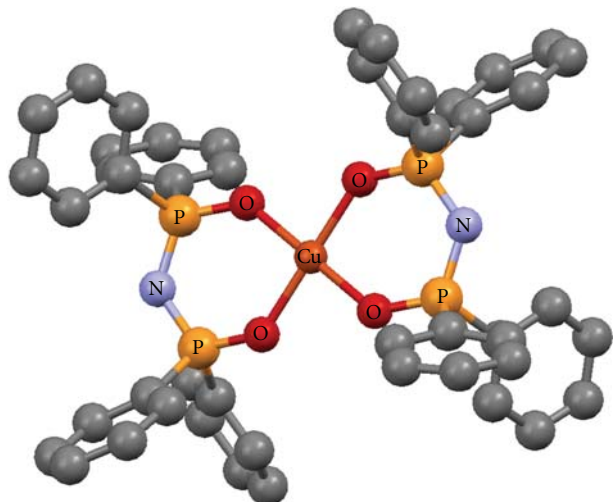


FIGURE 1: Crystal structure of $[\text{Cu}\{(\text{OPPh}_2)(\text{OPPh}_2)\text{N-O}, \text{O}\}_2]$ [33]. Color code: Cu (brown), O (red), P (orange), N (light blue), C (grey).

aggregometer cuvette) or by thrombin (0.1 IU) on WRPs, was measured before (considered as 0% inhibition) and after the addition of the sample examined. A linear plot of inhibition percentage (ranging from 20% to 80%) versus the concentration of the sample was established for each metal complex. From this curve, the concentration of the sample that inhibited 50% of the PAF-induced aggregation (IC_{50}) was calculated. Biological assays were performed several times ($n > 3$), according to methods of Demopoulos et al. [10] and Lazanas et al. [39], so as to ensure reproducibility. The same procedure was also followed in the case of rabbit PRP, as previously described [40].

2.3. Statistical Methods. All results were expressed as mean \pm standard deviation (SD). The t-test was employed to assess differences among the IC_{50} values of each metal complex against either the PAF- or thrombin-induced aggregation. Differences were considered to be statistically significant when the statistical p value was smaller than 0.05. Data were analyzed using a statistical software package (SPSS for Windows, 16.0, 2007, SPSS Inc. Chicago, IL) and Microsoft Excel 2007.

3. Results

3.1. Molecular Structures and Stability of the Complexes. The crystallographic structures of $\text{Cu}(\text{O},\text{O})_2$ [33], $\text{Zn}(\text{O},\text{O})_2$ [34], $\text{Ga}(\text{O},\text{O})_3$ [36] and $\text{Ni}(\text{P},\text{P})\text{Cl}_2$ [37], as well as the $(\text{OPPh}_2)(\text{OPPh}_2)\text{NH}$ ligand [41] have been already described (Figures 1–5). A variety of metal core geometries is demonstrated: $\text{Cu}(\text{O},\text{O})_2$ and $\text{Ni}(\text{P},\text{P})\text{Cl}_2$ are square-planar, whereas $\text{Zn}(\text{O},\text{O})_2$ is tetrahedral and $\text{Ga}(\text{O},\text{O})_3$ is octahedral. The $\text{Zn}(\text{S},\text{S})_2$ and $\text{Ni}(\text{P},\text{P})\text{Br}_2$ complexes are expected to be structurally similar to $\text{Zn}(\text{O},\text{O})_2$ and $\text{Ni}(\text{P},\text{P})\text{Cl}_2$, respectively. UV-vis absorption spectra of the light blue DMSO solutions of $\text{Cu}(\text{O},\text{O})_2$ confirmed that the complex was stable for the

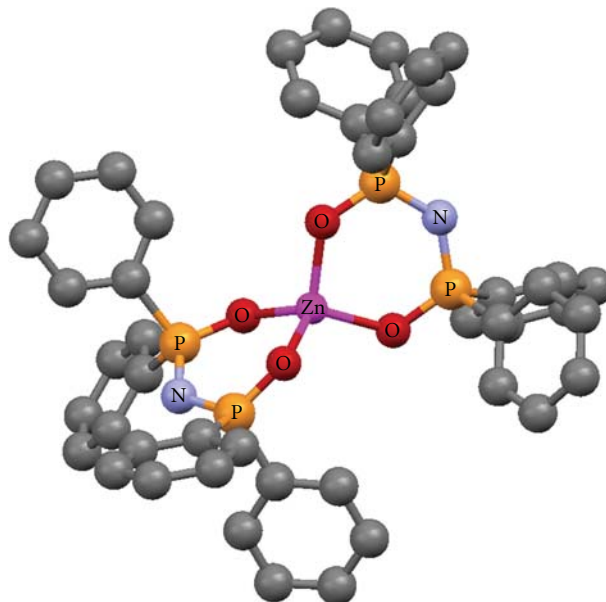


FIGURE 2: Crystal structure of $[\text{Zn}\{(\text{OPPh}_2)(\text{OPPh}_2)\text{N-O}, \text{O}\}_2]$ [34]. Color code: Zn (pink), O (red), P (orange), N (light blue), C (grey).

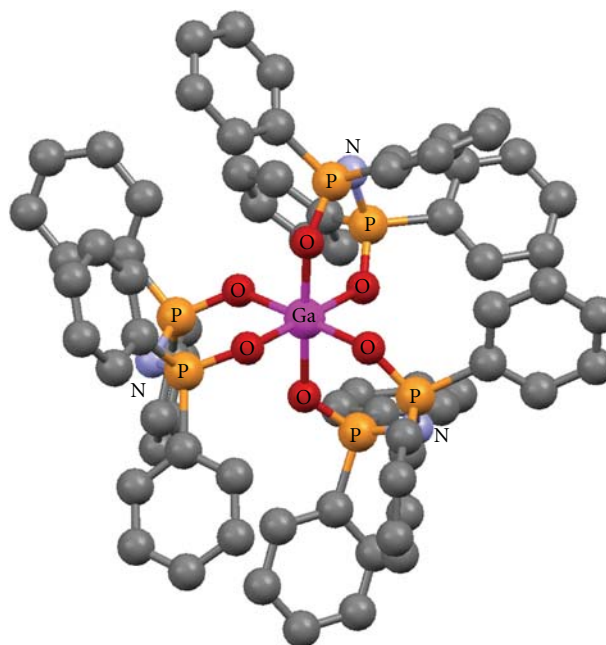


FIGURE 3: Crystal structure of $[\text{Ga}\{(\text{OPPh}_2)(\text{OPPh}_2)\text{N-O}, \text{O}\}_3]$ [36]. Color code: Ga (pink), O (red), P (orange), N (light blue), C (grey).

time-span of the study. This is expected since $\text{Cu}(\text{O},\text{O})_2$ and the rest of the dichalcogenated imidodiphosphate complexes, contain highly stable six-membered M-E-P-N-P-E chelating rings [1, 2]. On the other hand, for $\text{Ni}(\text{P},\text{P})_2\text{X}_2$, $\text{X} = \text{Cl}, \text{Br}$, the intensity of the absorption maximum was gradually decreasing. Therefore, degradation of the

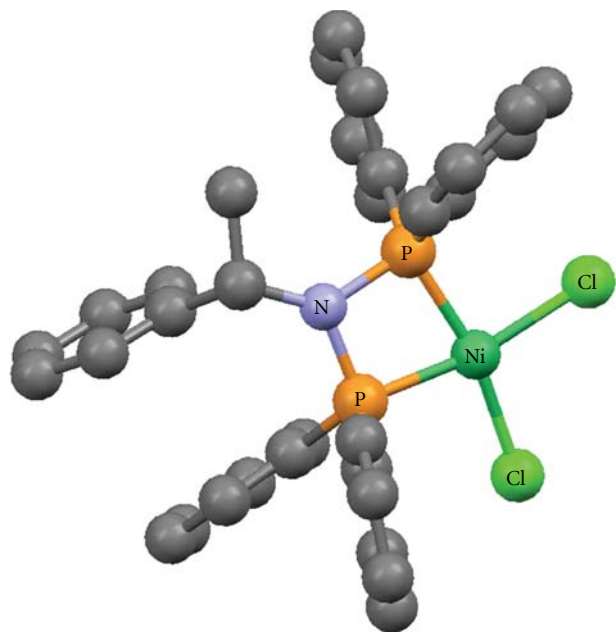


FIGURE 4: Crystal structure of $[\text{Ni}\{(\text{Ph}_2\text{P})_2\text{N-S-CHMePh-P,P}\}\text{Cl}_2]$ [37]. Color code: Ni (green), Cl (light green), P (orange), N (light blue), C (grey).

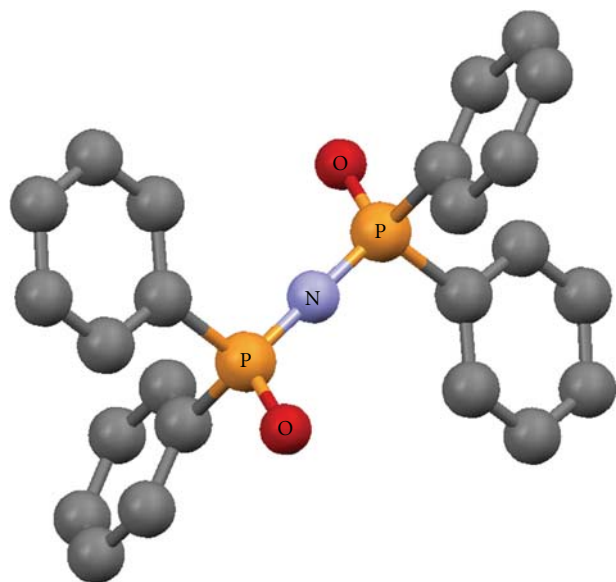


FIGURE 5: Crystal structure of the $(\text{OPPh}_2)(\text{OPPh}_2)\text{NH}$ ligand [41]. Color code: O (red), P (orange), N (light blue), C (grey).

complexes at some extent is likely, which is expected to affect their inhibitory action.

3.2. Inhibitory Effect of Metal Complexes and Metal Salts towards the PAF-Induced WRP's Aggregation. All metal complexes under investigation inhibited the PAF-induced aggregation of WRPs. This inhibitory effect was expressed by their IC_{50} value (Figure 6). Among the metal complexes tested, $\text{Ga}(\text{O},\text{O})_3$ exhibited the strongest inhibitory effect

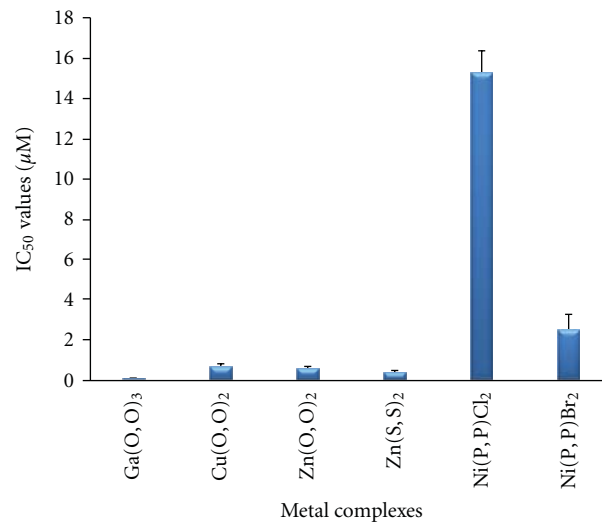


FIGURE 6: The inhibitory effect of metal complexes towards the PAF-induced WRP's aggregation.

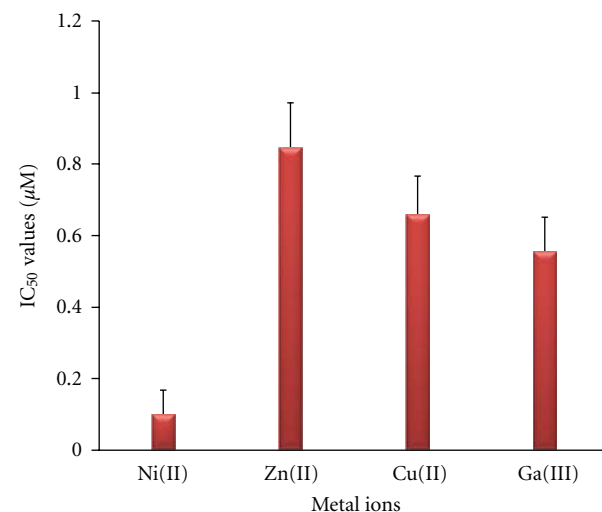


FIGURE 7: The inhibitory effect of metal salts towards the PAF-induced WRP's aggregation.

towards the PAF-induced WRP's aggregation, with an IC_{50} value of 62.4 ± 45.0 nM, which is more than one order of magnitude lower compared to the IC_{50} value of the other complexes tested. The $\text{Cu}(\text{O},\text{O})_2$, $\text{Zn}(\text{O},\text{O})_2$ and $\text{Zn}(\text{S},\text{S})_2$ complexes also exhibited a significant inhibitory effect, with IC_{50} values (300–600 μM) being more than one order of magnitude smaller compared to the value of the $\text{Ni}(\text{P},\text{P})\text{Cl}_2$ and $\text{Ni}(\text{P},\text{P})\text{Br}_2$ complexes.

In order to assess whether the observed inhibitory effect of the metal complexes was due to their properties—mainly their three-dimensional structure—we also tested the corresponding metal salts. All metal salts examined exhibited a weak inhibitory effect, with their IC_{50} values ranging between 0.1 and 1 mM (Figure 7), significantly lower than those of the corresponding metal complexes ($p < 0.001$) (Figure 6). Moreover, since $\text{Ga}(\text{O},\text{O})_3$ showed

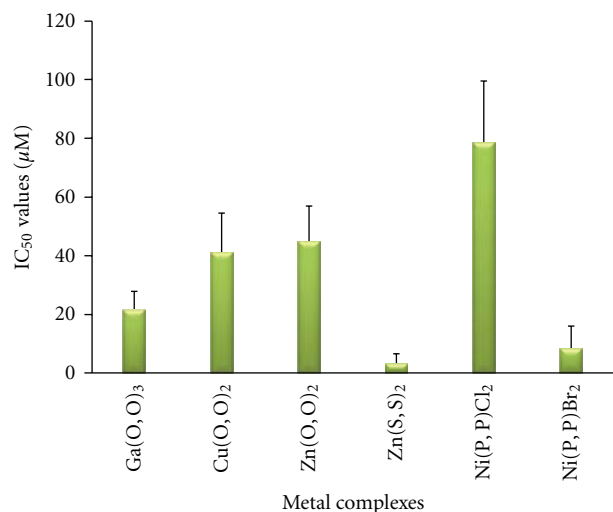


FIGURE 8: The inhibitory effect of metal complexes towards the PAF-induced rabbit PRP aggregation.

TABLE 1: The inhibitory effect of metal complexes towards the thrombin-induced WRP's aggregation.

Metal complex	IC ₅₀ value (μM)
Ga(O, O) ₃	—
Cu(O, O) ₂	7.86 ± 4.77
Zn(O, O) ₂	12.80 ± 5.62
Zn(S, S) ₂	0.594 ± 0.41

the most prominent inhibitory effect, we also examined the corresponding (OPPh₂)₂(OPPh₂)NH ligand, which has already been structurally characterized [41]. This compound exhibited a significantly smaller inhibitory effect (two orders of magnitude) against PAF (IC₅₀ = 1.57 ± 0.37 μM) compared with the Ga(O, O)₃ complex (p < 0.001). This ligand's IC₅₀ value is clearly smaller than those of the metal salts, but significantly greater than those of the Cu(O, O)₂ and Zn(O, O)₂ complexes (p < 0.05).

3.3. Inhibitory Effect of Metal Complexes and Metal Ions against the Thrombin-Induced WRP's Aggregation. The metal complexes exhibiting the stronger inhibitory effect against the PAF-induced WRP's aggregation were further tested for their potential inhibitory effect towards the thrombin-induced WRP's aggregation [10]. The data of Table 1 show that, among all complexes tested, Ga(O, O)₃ did not inhibit thrombin, even at concentrations up to 10⁻⁴ M, while Zn(S, S)₂ showed the strongest inhibitory effect, displaying an IC₅₀ value at least one order of magnitude smaller than that of Cu(O, O)₂ and Zn(O, O)₂.

3.4. Inhibitory Effect of Metal Complexes and Metal Ions against the PAF-Induced Rabbit PRP Aggregation. The metal complexes that inhibited the PAF-induced WRP's aggregation were further tested for their potential inhibitory effect against the PAF-induced rabbit PRP aggregation. All metal

complexes indeed showed such inhibitory behavior, with IC₅₀ values presented in Figure 8. The Ga(O, O)₃, Zn(S, S)₂ and Ni(P, P)Br₂ complexes exhibited the highest inhibitory effect, since their IC₅₀ values were significantly lower than that of all the other complexes tested (p < 0.05).

Moreover, we also tested the potential inhibitory effect of the corresponding metal salts. From all metal salts tested, only CuCl₂ exhibited a weak inhibitory effect (IC₅₀ = 12.3 ± 1.13 mM), three orders of magnitude larger than that of its corresponding Cu(O, O)₂ complex (p < 0.001). On the contrary, the Ga(III), Ni(II) and Zn(II) salts did not inhibit the PAF-induced aggregation of rabbit PRP. Similarly, the (OPPh₂)₂(OPPh₂)NH ligand did not show such an inhibitory action.

4. Discussion

The successful application of several anti-PAF agents [11–24], and metal complexes [25–31] towards various inflammatory pathological situations, led us to study the effect of the metal complexes described above towards PAF-related biological activities. In that respect, we have primarily studied the *in vitro* effects of these compounds on the PAF-induced platelet aggregation. We have previously showed that *cis*-[RhL₂Cl₂]Cl, L = 2-(2'-pyridyl)quinoxaline, is a potent inhibitor of this type, having an IC₅₀ value of 210 nM (at 0.02 nM PAF), with the inhibitory effect taking place, partly, through the PAF-receptor dependent way [42].

In this study, the biological assays were focused on the PAF-induced WRP's and rabbit PRP aggregation. In particular, our study on WRPs probes the anti-PAF activity of metal complexes under the experimental conditions applied, while, in the case of rabbit PRP, the conclusions drawn pinpoint the effect of these compounds towards the PAF activation at more similar to the *in vivo* conditions. Our work leads to the unprecedented conclusion that several metal complexes inhibited the PAF-induced aggregation towards both WRPs and rabbit PRP, in a dose-dependent manner. Significantly higher concentrations (at least one order of magnitude) of each compound were needed in order to inhibit the PAF-induced aggregation of rabbit PRP, compared to those needed in order to inhibit the corresponding aggregation of WRPs. The metal complexes with the most prominent anti-PAF activity were additionally tested towards the thrombin-induced aggregation of WRPs.

The IC₅₀ values reflect the inhibition strength of each metal complex, since a low IC₅₀ value reveals stronger inhibition of the PAF-induced aggregation for a given metal complex concentration. It is of significant importance that the IC₅₀ values of these compounds (expressed as μM) against the PAF-induced aggregation are comparable with the IC₅₀ values of some of the most potent PAF receptor antagonists, namely WEB2170, BN52021, and Rupatadine (0.02, 0.03 and 0.26 μM, resp.) [43–45]. This observation demonstrates that the metal complexes in question exhibit a strong inhibitory effect against the PAF activity. The octahedral Ga(O, O)₃ complex, which contains the larger number (12) of phenyl rings in the second coordination

sphere (Figure 3), is clearly the bulkier compared to the rest of the complexes studied (Figures 1, 2, and 4). This tris-chelated complex exhibited the strongest inhibitory effect against the PAF-induced aggregation of WRP, with an IC_{50} value of $0.062 \pm 0.045 \mu M$. The fact that this complex did not inhibit the thrombin-induced aggregation of WRP, even at high doses, suggests that it antagonizes the platelet aggregation through the selective inhibition of the PAF-receptor pathway. Moreover, since the complexes of Cu(II) (square planar) and Zn(II) (tetrahedral), bearing the same $(OPPh_2)(OPPh_2)NH$ ligand, exhibited an appreciable but lower inhibitory effect against the PAF-induced aggregation of both WRP and rabbit PRP compared to $Ga(O,O)_3$, it is concluded that this action depends primarily on the complexes' three-dimensional structure. This proposal is also supported by the fact that the corresponding metal salts either inhibited weakly the PAF-induced WRP's aggregation, or showed no inhibitory action at all when tested in rabbit PRP. As far as the inhibitory effect of $ZnCl_2$ is concerned, our results are consistent with those reported earlier [46].

It should be stressed that, even though the $(OPPh_2)(OPPh_2)NH$ ligand (Figure 5) inhibited the PAF-induced aggregation of WRP, this effect was significantly less prominent compared with the effects observed in the case of the metal complexes studied. In addition, this ligand did not influence the PAF-induced aggregation of rabbit PRP, a fact that confirms the importance of specific structural characteristics of the inhibitors. Moreover, it emphasizes that the coordination of metal ions to ligands, each separately showing some PAF-inhibitory action, enhances these inhibitory properties. Similar phenomena of pharmacological profile enhancement are also reported in the case of classic anti-inflammatory drugs like indomethacin, as well as antioxidants such as bioflavonoid rutin and naringin, coordinated to transition metals [47–50]. Similar behavior was also established in the case of Cu(II) and Pt(II) complexes with various ligands [25, 50–52].

Besides their anti-PAF activity, $Cu(O,O)_2$ and $Zn(O,O)_2$ inhibited also the thrombin-induced aggregation of WRP, but at higher concentrations than those tested against PAF, suggesting that these metal complexes exhibit a more general anti-inflammatory action, which, however, is more specific towards the PAF-related pathway. As far the tetrahedral $Zn(S,S)_2$ complex is concerned, it exhibited the highest inhibitory effect against the PAF-induced aggregation of rabbit PRP, even when compared with that of $Ga(O,O)_3$. At the same time, this complex showed also a strong inhibitory effect against the PAF-induced aggregation of WRP, which although lower than that of $Ga(O,O)_3$, it is almost twice as strong (statistically borderline significant with $p = 0.065$) than that of $Zn(O,O)_2$ and $Cu(O,O)_2$. Also, this complex inhibited strongly the thrombin-induced aggregation of WRP, at similar concentrations with those tested against PAF in WRP, having an IC_{50} value at least one order of magnitude lower than those of $Zn(O,O)_2$ and $Cu(O,O)_2$. This result suggests that $Zn(S,S)_2$ exhibits a more general anti-inflammatory activity, since it can equally inhibit both the PAF and thrombin-related activities. Taking

also into account that in severe inflammatory procedures implicated in cancer situations like melanoma, the PAF- and thrombin-activated pathways are interrelated, thus regulating, for instance, both the melanoma cell adhesion and its metastasis [53, 54], compounds such as $Zn(S,S)_2$, $Zn(O,O)_2$ and $Cu(O,O)_2$, with inhibitory effects towards both PAF and thrombin-related activities, are promising candidates as potential anticancer or antithrombotic agents.

Regarding the square-planar complexes of Ni(II) studied in this work, both $Ni(P,P)Cl_2$ and $Ni(P,P)Br_2$ only weakly inhibited the PAF-induced aggregation of WRP compared with the imidodiphosphinate-containing complexes. The gradual degradation of these complexes in DMSO, documented by their UV-vis spectra, is the most likely explanation for this observation. However, the fact that, in the case of rabbit PRP, the $Ni(P,P)Br_2$ complex exhibited a noticeable inhibitory effect against the PAF-induced aggregation, at levels comparable to those of $Ga(O,O)_3$ and $Zn(S,S)_2$ (Figure 8), shows that the integrity of its structure is sufficiently retained. The observed instability of $Ni(P,P)X_2$, $X = Cl, Br$, in DMSO renders them unsuitable for inhibitory action, at least under the conditions employed in this work. Therefore, the thrombin-induced WRP's aggregation by these complexes was not investigated.

5. Conclusions

A series of metal complexes, bearing dichalcogenated imidodiphosphinate ligands, inhibited the PAF-induced aggregation of both WRP and rabbit PRP, at concentrations comparable with those of classical PAF-inhibitors. The compounds with the stronger anti-PAF activities exhibited different specificity against the thrombin-induced platelet aggregation: $Ga(O,O)_3$, with the highest anti-PAF activity, did not inhibit the thrombin-related pathway, whereas $Zn(S,S)_2$, with also a strong inhibitory effect against PAF, exhibited the highest inhibition against thrombin. On the other hand, $Zn(O,O)_2$ and $Cu(O,O)_2$ inhibited moderately both PAF and thrombin, being more effective towards PAF. The metal salts and the $(OPPh_2)(OPPh_2)NH$ ligand showed no appreciable anti-PAF or antithrombin activity. By comparing the relative inhibitory activities of all compounds studied, it is concluded that the biological activities of the metal complexes depend, at least in part, on their stereochemical properties. In this respect, the more spherical and bulky structure of $Ga(O,O)_3$ seems to be the most suitable for a PAF-related inhibitory action. On the contrary, this complex is totally inactive towards the thrombin-related pathway. Whether this remarkable selectivity is indeed due to a more efficient interaction of $Ga(O,O)_3$ with the PAF-receptor, remains to be investigated in future studies. It is of interest that similar tris-chelated Ga(III) complexes have shown significant pharmaceutical action towards various pathological cases [27, 28]. The exploration of additional complexes of variable metal ions and three-dimensional structures is clearly needed, in an effort to further elucidate the necessary electronic or structural features for a significant and selective PAF- or thrombin-related inhibitory function.

Acknowledgments

P. Kyritsis thanks the Special Account of the University of Athens (Grant 7575) and the Empirikion Foundation for funding, as well as Dr G. S. Papaefstathiou for a gift of $\text{Ga}(\text{NO}_3)_3 \cdot 9\text{H}_2\text{O}$. The referees of the manuscript are thanked for their constructive comments. This article is dedicated to Professor Nick Hadjiliadis, on the occasion of his retirement.

References

- [1] C. Silvestru and J. E. Drake, "Tetraorganodichalcogenoimidodiphosphorus acids and their main group metal derivatives," *Coordination Chemistry Reviews*, vol. 223, no. 1, pp. 117–216, 2001.
- [2] I. Haiduc, "Dichalcogenoimidodiphosphinato ligands," in *Comprehensive Coordination Chemistry II: From Biology to Nanotechnology*, vol. 1, pp. 323–347, Elsevier, Amsterdam, The Netherlands, 2003.
- [3] T. Chivers, J. Konu, J. S. Ritch, M. C. Copsey, D. J. Eisler, and H. M. Tuononen, "New tellurium-containing ring systems," *Journal of Organometallic Chemistry*, vol. 692, no. 13, pp. 2658–2668, 2007.
- [4] N. Levesanos, S. D. Robertson, D. Maganas et al., " $\text{Ni}[(\text{EP}^i\text{Pr}_2)_2\text{N}]_2$ complexes: stereoisomers ($E = \text{Se}$) and square-planar coordination ($E = \text{Te}$)," *Inorganic Chemistry*, vol. 47, no. 8, pp. 2949–2951, 2008.
- [5] E. Simón-Manso, M. Valderrama, and D. Boys, "Synthesis and single-crystal characterization of the square planar complex $[\text{Ni}\{(\text{SPPPh}_2)_2\text{N-S, S'}\}_2] \cdot 2\text{THF}$," *Inorganic Chemistry*, vol. 40, no. 14, pp. 3647–3649, 2001.
- [6] R. Rösler, C. Silvestru, G. Espinosa-Pérez, I. Haiduc, and R. Cea-Olivares, "Tetrahedral versus square-planar NiS_4 core in solid-state bis(dithioimidodiphosphinato)nickel(II) chelates. Crystal and molecular structures of $\text{Ni}[(\text{SPR}_2)(\text{SPPPh}_2)\text{N}]_2(\text{R} = \text{Ph, Me})$," *Inorganica Chimica Acta*, vol. 241, no. 2, pp. 47–54, 1996.
- [7] D. Maganas, A. Grigoropoulos, and S. S. Staniland, "Tetrahedral and square-planar $\text{Ni}[(\text{SPR}_2)_2\text{N}]_2$ complexes, $\text{R} = \text{Ph} \& \text{Pr}$ revisited: experimental and theoretical analysis of interconversion pathways, structural preferences and spin delocalization," *Inorganic Chemistry*, vol. 49, no. 11, pp. 5079–5093, 2010.
- [8] T. Q. Ly and J. D. Woollins, "Bidentate organophosphorus ligands formed via P-N bond formation: synthesis and coordination chemistry," *Coordination Chemistry Reviews*, vol. 176, no. 1, pp. 451–481, 1998.
- [9] E. I. Solomon, R. K. Szilagyi, S. DeBeer George, and L. Basumallick, "Electronic structures of metal sites in proteins and models: contributions to function in blue copper proteins," *Chemical Reviews*, vol. 104, no. 2, pp. 419–458, 2004.
- [10] C. A. Demopoulos, R. N. Pinckard, and D. J. Hanahan, "Platelet-activating factor. Evidence for 1-O-alkyl-2-acetyl-sn-glycerol-3-phosphorylcholine as the active component (a new class of lipid chemical mediators)," *Journal of Biological Chemistry*, vol. 254, no. 19, pp. 9355–9358, 1979.
- [11] G. A. Zimmerman, T. M. McIntyre, S. M. Prescott, and D. M. Stafforini, "The platelet-activating factor signaling system and its regulators in syndromes of inflammation and thrombosis," *Critical Care Medicine*, vol. 30, no. 5, pp. S294–S301, 2002.
- [12] D. M. Stafforini, T. M. McIntyre, G. A. Zimmerman, and S. M. Prescott, "Platelet-activating factor, a pleiotropic mediator of physiological and pathological processes," *Critical Reviews in Clinical Laboratory Sciences*, vol. 40, no. 6, pp. 643–672, 2003.
- [13] G. Montrucchio, G. Alloati, and G. Camussi, "Role of platelet-activating factor in cardiovascular pathophysiology," *Physiological Reviews*, vol. 80, no. 4, pp. 1669–1699, 2000.
- [14] C. A. Demopoulos, H. C. Karantonis, and S. Antonopoulou, "Platelet activating factor—a molecular link between atherosclerosis theories," *European Journal of Lipid Science and Technology*, vol. 105, no. 11, pp. 705–716, 2003.
- [15] J. M. López-Novoa, "Potential role of platelet activating factor in acute renal failure," *Kidney International*, vol. 55, no. 5, pp. 1672–1682, 1999.
- [16] L. M. McManus and R. N. Pinckard, "PAF, a putative mediator of oral inflammation," *Critical Reviews in Oral Biology and Medicine*, vol. 11, no. 2, pp. 240–258, 2000.
- [17] A. Kasperska-Zajac, Z. Brzoza, and B. Rogala, "Platelet-activating factor (PAF): a review of its role in asthma and clinical efficacy of PAF antagonists in the disease therapy," *Recent Patents on Inflammation and Allergy Drug Discovery*, vol. 2, no. 1, pp. 72–76, 2008.
- [18] N. Nathan, Y. Denizot, M. C. Huc et al., "Elevated levels of paf-acether in blood of patients with type 1 diabetes mellitus," *Diabete & Metabolisme*, vol. 18, no. 1, pp. 59–62, 1992.
- [19] A. B. Tsoupras, C. Iatrou, C. Frangia, and C. A. Demopoulos, "The implication of platelet activating factor in cancer growth and metastasis: potent beneficial role of PAF-inhibitors and antioxidants," *Infectious Disorders—Drug Targets*, vol. 9, no. 4, pp. 390–399, 2009.
- [20] A. B. Tsoupras, M. Chini, N. Tsogas et al., "Anti-platelet-activating factor effects of highly active antiretroviral therapy (HAART): a new insight in the drug therapy of HIV infection?" *AIDS Research and Human Retroviruses*, vol. 24, no. 8, pp. 1079–1086, 2008.
- [21] J. M. Negro Álvarez, J. C. Miralles López, J. L. Ortiz Martínez, A. Abellán Alemán A, and R. Rubio Del Barrio, "Platelet-activating factor antagonists," *Allergologia et Immunopathologia*, vol. 25, no. 5, pp. 249–258, 1997.
- [22] S. Desquand, "Effects of PAF antagonists in experimental models—possible therapeutic implications," *Thérapie*, vol. 48, no. 6, pp. 585–597, 1993.
- [23] M. Koltai, D. Hosford, P. Guinot, A. Esanu, and P. Braquet, "Platelet activating factor (PAF). A review of its effects, antagonists and possible future clinical implications. I," *Drugs*, vol. 42, no. 1, pp. 9–29, 1991.
- [24] M. Koltai, D. Hosford, P. Guinot, A. Esanu, and P. Braquet, "PAF: a review of its effects, antagonists and possible future clinical implications. II," *Drugs*, vol. 42, no. 2, pp. 174–204, 1991.
- [25] C. X. Zhang and S. J. Lippard, "New metal complexes as potential therapeutics," *Current Opinion in Chemical Biology*, vol. 7, no. 4, pp. 481–489, 2003.
- [26] S. H. van Rijt and P. J. Sadler, "Current applications and future potential for bioinorganic chemistry in the development of anticancer drugs," *Drug Discovery Today*, vol. 14, pp. 1089–1197, 2009.
- [27] R. Timerbaev, "Advances in developing tris(8-quinolinolato)gallium(III) as an anticancer drug: critical appraisal and prospects," *Metallomics*, vol. 1, pp. 193–198, 2009.
- [28] M. A. Jakupec and B. K. Keppler, "Gallium in cancer treatment," *Current Topics in Medicinal Chemistry*, vol. 4, no. 15, pp. 1575–1583, 2004.

- [29] C. Marzano, M. Pellei, F. Tisato, and C. Santini, "Copper complexes as anticancer agents," *Anti-Cancer Agents in Medicinal Chemistry*, vol. 9, no. 2, pp. 185–211, 2009.
- [30] Z. H. Chohan, "Metal-based antibacterial and antifungal sulfonamides: synthesis, characterization, and biological properties," *Transition Metal Chemistry*, vol. 34, no. 2, pp. 153–161, 2009.
- [31] H. Sakurai, A. Katoh, and Y. Yoshikawa, "Chemistry and biochemistry of insulin-mimetic vanadium and zinc complexes. Trial for treatment of diabetes mellitus," *Bulletin of the Chemical Society of Japan*, vol. 79, no. 11, pp. 1645–1664, 2006.
- [32] R. P. Kamalesh Babu, S. S. Krishnamurthy, and M. Nethaji, "Short-bite chiral diphosphazanes derived from (S)- α -methyl benzyl amine and their Pd, Pt and Rh metal complexes," *Tetrahedron Asymmetry*, vol. 6, no. 2, pp. 427–438, 1995.
- [33] A. Silvestru, A. Rotar, J. E. Drake, et al., "Synthesis, spectroscopic characterization, and structural studies of new Cu(I) and Cu(II) complexes containing organophosphorus ligands, and crystal structures of $(\text{Ph}_3\text{P})_2\text{Cu}[\text{S}_2\text{PMe}_2]$, $(\text{Ph}_3\text{P})_2\text{Cu}[(\text{OPPh}_2)_2\text{N}]$, $\text{Cu}[(\text{OPPh}_2)_2\text{N}]_2$, and $\text{Cu}[(\text{OPPh}_2)(\text{SPPPh}_2)\text{N}]_2$," *Canadian Journal of Chemistry*, vol. 79, pp. 983–991, 2001.
- [34] A. Silvestru, D. Ban, and J. E. Drake, "Zinc(II) tetraorganodichalcogenoimidodiphosphinates. Crystal and molecular structure of $\text{Zn}[(\text{OPPh}_2)_2\text{N}]_2$," *Revue Roumaine de Chimie*, vol. 47, no. 10–11, pp. 1077–1084, 2002.
- [35] A. Davison and E. S. Switkes, "The stereochemistry of four-coordinate bis(imidodiphosphinato)metal(II) chelate complexes," *Inorganic Chemistry*, vol. 10, no. 4, pp. 837–842, 1971.
- [36] V. García-Montalvo, R. Cea-Olivares, D. J. Williams, and G. Espinosa-Pérez, "Stereochemical consequences of the bismuth atom electron lone pair, a comparison between MX_6E and MX_6 systems. Crystal and molecular structures of $\text{tris}[N-(P,P\text{-diphenylphosphinoyl})-P,P\text{-diphenylphosphinimidato}]$ bismuth(III), $[\text{Bi}\{(\text{OPPh}_2)_2\text{N}\}_3]$, -indium(III), $[\text{In}\{(\text{OPPh}_2)_2\text{N}\}_3] \cdot \text{C}_6\text{H}_6$, and -gallium(III), $[\text{Ga}\{(\text{OPPh}_2)_2\text{N}\}_3] \cdot \text{CH}_2\text{Cl}_2$," *Inorganic Chemistry*, vol. 35, no. 13, pp. 3948–3953, 1996.
- [37] G. C. Vougioukalakis, I. Stamatopoulos, N. Petzetakis et al., "Controlled vinyl-type polymerization of norbornene with a nickel(II) diphosphinoamine/methylaluminumoxane catalytic system," *Journal of Polymer Science A*, vol. 47, no. 20, pp. 5241–5250, 2009.
- [38] F. T. Wang, J. Najdzionek, K. L. Leneker, H. Wasserman, and D. M. Braitsch, "Facile synthesis of imidotetraphenyldiphosphinic acids," *Synthesis and Reactivity in Inorganic and Metal-Organic Chemistry*, vol. 8, pp. 119–125, 1978.
- [39] M. Lazanas, C. A. Demopoulos, S. Tournis, S. Koussissis, K. Labrakis-Lazanas, and X. Tsarouhas, "PAF of biological fluids in disease: I.V. Levels in blood in allergic reactions induced by drugs," *Archives of Dermatological Research*, vol. 280, no. 2, pp. 124–126, 1988.
- [40] D. Tsoukatos, C. A. Demopoulos, A. D. Tselepis et al., "Inhibition of cardiolipins of platelet-activating factor-induced rabbit platelet activation," *Lipids*, vol. 28, no. 12, pp. 1119–1124, 1993.
- [41] H. Noth, "Crystal and molecular-structure of imido-tetraphenyl-dithio-phosphinic acid and imido-tetraphenyl-diphosphinic acid," *Zeitschrift für Naturforschung B*, vol. 37, pp. 1491–1498, 1982.
- [42] A. I. Philippopoulos, N. Tsantila, C. A. Demopoulos, C. P. Raptopoulou, V. Likodimos, and P. Falaras, "Synthesis, characterization and crystal structure of the *cis*- $[\text{RhL}_2\text{Cl}_2]\text{Cl}$ complex with the bifunctional ligand (L) 2-(2'-pyridyl)quinoxaline. Biological activity towards PAF (Platelet Activating Factor) induced platelet aggregation," *Polyhedron*, vol. 28, no. 15, pp. 3310–3316, 2009.
- [43] H. O. Heuer, "Involvement of platelet-activating factor (PAF) in septic shock and priming as indicated by the effect of hexazepinoic PAF antagonists," *Lipids*, vol. 26, no. 12, pp. 1369–1373, 1991.
- [44] J. R. Fletcher, A. G. DiSimone, and M. A. Earnest, "Platelet activating factor receptor antagonist improves survival and attenuates eicosanoid release in severe endotoxemia," *Annals of Surgery*, vol. 211, no. 3, pp. 312–316, 1990.
- [45] I. Izquierdo, M. Merlos, and J. García-Rafanell, "Rupatadine: a new selective histamine H1 receptor and platelet-activating factor (PAF) antagonist. A review of pharmacological profile and clinical management of allergic rhinitis," *Drugs of Today*, vol. 39, no. 6, pp. 451–468, 2003.
- [46] Y. Huo, J. Ekholm, and D. J. Hanahan, "A preferential inhibition by Zn^{2+} on platelet activating factor- and thrombin-induced serotonin secretion from washed rabbit platelets," *Archives of Biochemistry and Biophysics*, vol. 260, no. 2, pp. 841–846, 1988.
- [47] I. B. Afanas'ev, E. A. Ostrakhovitch, E. V. Mikhali'chik, G. A. Ibragimova, and L. G. Korkina, "Enhancement of antioxidant and anti-inflammatory activities of bioflavonoid rutin by complexation with transition metals," *Biochemical Pharmacology*, vol. 61, no. 6, pp. 677–684, 2001.
- [48] C. T. Dillon, T. W. Hambley, B. J. Kennedy et al., "Gastrointestinal toxicity, antiinflammatory activity, and superoxide dismutase activity of copper and zinc complexes of the antiinflammatory drug indomethacin," *Chemical Research in Toxicology*, vol. 16, no. 1, pp. 28–37, 2003.
- [49] D. Kovala-Demertzi, D. Hadjipavlou-Litina, M. Staninska, A. Primikiri, C. Kotoglou, and M. A. Demertzis, "Anti-oxidant, in vitro, in vivo anti-inflammatory activity and antiproliferative activity of mefenamic acid and its metal complexes with manganese(II), cobalt(II), nickel(II), copper(II) and zinc(II)," *Journal of Enzyme Inhibition and Medicinal Chemistry*, vol. 24, no. 3, pp. 742–752, 2009.
- [50] G. Mohan, R. Nagar, S. C. Agarwal, K. M. A. Mehta, and C. S. Rao, "Syntheses and anti-inflammatory activity of diphenylamine-2,2'-dicarboxylic acid and its metal complexes," *Journal of Enzyme Inhibition and Medicinal Chemistry*, vol. 20, no. 1, pp. 55–60, 2005.
- [51] R. M. S. Pereira, N. E. D. Andrades, N. Paulino et al., "Synthesis and characterization of a metal complex containing naringin and Cu, and its antioxidant, antimicrobial, anti-inflammatory and tumor cell cytotoxicity," *Molecules*, vol. 12, no. 7, pp. 1352–1366, 2007.
- [52] E. Pontiki, D. Hadjipavlou-Litina, and A. T. Chaviara, "Evaluation of anti-inflammatory and antioxidant activities of copper (II) Schiff mono-base and copper(II) Schiff base coordination compounds of dien with heterocyclic aldehydes and 2-amino-5-methyl-thiazole," *Journal of Enzyme Inhibition and Medicinal Chemistry*, vol. 23, no. 6, pp. 1011–1017, 2008.
- [53] V. O. Melnikova, K. Balasubramanian, G. J. Villares et al., "Crosstalk between protease-activated receptor 1 and platelet-activating factor receptor regulates melanoma cell adhesion molecule (MCAM/MUC18) expression and melanoma metastasis," *Journal of Biological Chemistry*, vol. 284, no. 42, pp. 28845–28855, 2009.
- [54] V. O. Melnikova and M. Bar-Eli, "Inflammation and melanoma metastasis," *Pigment Cell and Melanoma Research*, vol. 22, no. 3, pp. 257–267, 2009.

Research Article

Kinetics and Mechanisms of the Chromium(III) Reactions with 2,4- and 2,5-Dihydroxybenzoic Acids in Weak Acidic Aqueous Solutions

Kimón Zavitsanos and Athinoula L. Petrou

Laboratory of Inorganic Chemistry, Department of Chemistry, University of Athens, Panepistimioupolis, 15771 Athens, Greece

Correspondence should be addressed to Athinoula L. Petrou, athpetrou@chem.uoa.gr

Received 10 April 2010; Accepted 26 May 2010

Academic Editor: Spyros Perlepes

Copyright © 2010 K. Zavitsanos and A. L. Petrou. This is an open access article distributed under the Creative Commons Attribution License, which permits unrestricted use, distribution, and reproduction in any medium, provided the original work is properly cited.

The reactions of 2,4- and 2,5-dihydroxybenzoic acids (dihydroxybenzoic acid, DHBA) with chromium(III) in weak acidic aqueous solutions have been shown to take place in at least two stages. The first stage of the reactions has an observed rate constant $k_{1(\text{obs})} = k_1[\text{DHBA}] + C$ and the corresponding activation parameters are $\Delta H_{1(2,4)}^\ddagger = 49,5 \text{ kJ/mol}^{-1}$, $\Delta S_{1(2,4)}^\ddagger = -103,7 \text{ J mol}^{-1} \text{ K}^{-1}$, $\Delta H_{1(2,5)}^\ddagger = 60,3 \text{ kJ/mol}^{-1}$, and $\Delta S_{1(2,5)}^\ddagger = -68,0 \text{ J mol}^{-1} \text{ K}^{-1}$. These are composite activation parameters and the breaking of the strong intramolecular hydrogen bonding in the two ligands is suggested to be the first step of the (composite) first stage of the reactions. The second stage is ligand concentration independent and is thus attributed to a chelation process. The corresponding activation parameters are $\Delta H_{2(2,4)}^\ddagger = 45,13 \text{ kJ/mol}^{-1}$, $\Delta S_{2(2,4)}^\ddagger = -185,9 \text{ J mol}^{-1} \text{ K}^{-1}$, $\Delta H_{2(2,5)}^\ddagger = 54,55 \text{ kJ/mol}^{-1}$, and $\Delta S_{2(2,5)}^\ddagger = -154,8 \text{ J mol}^{-1} \text{ K}^{-1}$. The activation parameters support an associative mechanism for the second stage of the reactions. The various substitution processes are accompanied by proton release, resulting in pH decrease.

1. Introduction

Chromium at low concentrations has been proved to be beneficial to many plant species, being toxic in the same plants at higher concentrations [1]. The bioinorganic chemistry of chromium(III) and its biological role is not very well studied because (a) chromium(III) complexes are substitution inert and this implies that a catalytic role is forbidden, (b) chromium(III) complexes are generally redox inactive especially with most of the biological ligands, (c) the electronic spectra of the chromium(III) complexes usually lack of intense characteristics such as charge-transfer bands (an exception being organochromium complexes, i.e., complexes bearing Cr-C σ -bonds [2–4]), and (d) the paramagnetic nature of chromium(III) (spin 3/2) does not allow studies with NMR techniques [5]. A chromium(III) compound however has been identified as a reactive component of the Glucose Tolerance Factor, GTF [6], where the chromium(III) coordination sphere is occupied by various amino-acids. A biomolecule, termed as low-molecular-weight chromium-

binding substance (LMWCr) or chromoduline, is known. It has been isolated from the liver and kidneys of several species. It is an oligopeptide which contains glycine, cysteine, aspartic, and glutamic acid residues [6, 7]. A biomimetic to chromoduline molecule, the trinuclear cation $[\text{Cr}_3\text{O}(\text{O}_2\text{CCH}_2\text{CH}_3)_6(\text{H}_2\text{O})_3]^+$ has been reported [8].

Phenolic acids are examples of phenolic compounds that are present in fruits and plants and constitute a big fraction of the chemical structure of humic substances. The phenolic acids play an important role, probably, in the ability of humic substances to coordinate with the metals, increasing thus their bioavailability [9–11].

The phenolic acids that were studied for their reactions with chromium(III) and are presented here are 2,4-dihydroxybenzoic acid (2,4-DHBA) and 2,5-dihydroxybenzoic acid (2,5-DHBA) (Figure 1).

We wish to report, in this work, the kinetics and mechanisms of the reactions between Cr(III) and 2,4- and 2,5-dihydroxybenzoic acids. The two ligands bear both phenolic and carboxylic sites and the study of the mechanisms of

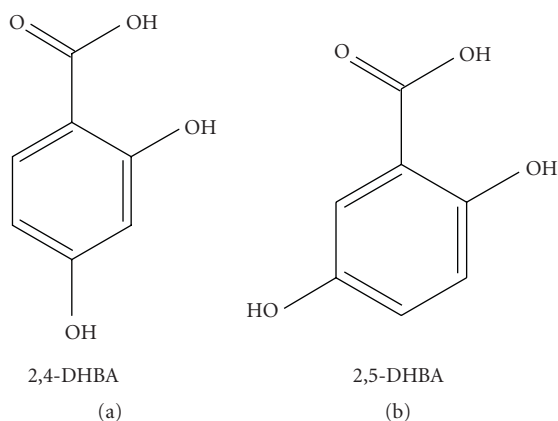


FIGURE 1

their complex formation with chromium(III) as well as the stability of the complexes formed will help in the understanding of the role of complexation in the uptake of chromium(III) by plants.

2. Experimental Results

2.1. Reagents and Materials. All reagents used were of analytical grade. Dihydroxybenzoic acids (Alfa Aesar) were used as received. They were dissolved in water in concentrations ranging $6.64 \cdot 10^{-3}$ – $4.87 \cdot 10^{-2}$ M (2,4-DHBA) and $4.42 \cdot 10^{-3}$ – $4.87 \cdot 10^{-2}$ M (2,5-DHBA). In order to avoid transformation and decomposition reactions, the ligand solutions were used shortly after their preparation. Stock solutions of Cr(III) were prepared using $\text{Cr}(\text{NO}_3)_3 \cdot 9\text{H}_2\text{O}$. Adjustment of the ionic strength was done with KNO_3 . Due to Cr(III) acidic hydrolysis the pH was constantly kept below 4.

2.2. Kinetic Experiments. The kinetic experiments were carried out at pH values below 4.0 in the presence of air. The kinetics was followed at various wavelengths yielding identical results. The absorbances and the electronic spectra were recorded on a Varian Cary 3E, UV-vis spectrophotometer. Pseudo-first-order conditions were employed for all the experiments. The plots of $\ln(A_t - A_\infty)$ (first stage) and $\ln(A_\infty - A_t)$ (second stage) against time, where A_t and A_∞ are absorbances at time t and, after the completion of the reaction, were found to be linear for both ligands (Figure 2). The rate constants were calculated from the slope of the lines. At different temperatures for various ligand and chromium(III) concentrations, the experimental results show similar behavior. The uncomplexed Cr(III) species absorbance is not causing a problem in the graphs (Figure 2) since it is included in both A_t and A_∞ and is thus eliminated.

The k_1 (first stage) and k_2 (second stage) values at various temperatures are given in Table 1.

Analysis according to activated complex theory gives the activation parameters $\Delta H_{1(2,4)}^\ddagger$, $\Delta S_{1(2,4)}^\ddagger$ for 2,4-DHBA/Cr(III), $\Delta H_{1(2,5)}^\ddagger$, $\Delta S_{1(2,5)}^\ddagger$ for (2,5-DHBA)/Cr(III), corresponding to k_1 (the first stage of the reaction),

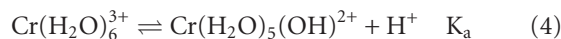
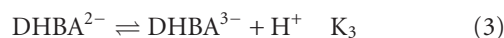
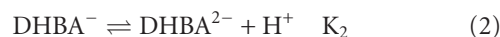
calculated from the linear Eyring plots. Activation parameters corresponding to k_2 (the second stage of the reaction for both 2,4- and 2,5-DHBA/Cr(III)) were also calculated from the corresponding linear Eyring plots. All the values of the activation parameters thus obtained are given in Table 2.

The values of A_∞ used in Figure 2 and the other graphs were very close to the true values since they were also obtained by plotting $A = f(t)$ at the certain wavelengths. In this way it was possible to check if the reaction was completed. For the reactions studied, A_∞ was obtained after more than 3 half-lives.

3. Discussion

3.1. Kinetics and Mechanisms. Strong hydrogen bonding (intramolecular) occurs in the ligand molecules (2,4- and 2,5-DHBA). Complexation with chromium(III) can occur only after the breaking of these strong bonds. The two ligands exist as neutral molecules (abbreviated as DHBA) and monoanions (abbreviated as DHBA^-). At pH < 4 chromium(III) exists mainly as hexa-aqua monomeric ion, $[\text{Cr}(\text{H}_2\text{O})_6]^{3+}$ or Cr^{3+} , the species $[\text{Cr}(\text{H}_2\text{O})_5(\text{OH})]^{2+}$ or $[\text{Cr}(\text{OH})]^{2+}$ being present in small amounts. However, reaction with $[\text{Cr}(\text{H}_2\text{O})_5(\text{OH})]^{2+}$ should be considered over the pH range 3–4 since pK_a ($\text{Cr}^{3+}/[\text{Cr}(\text{OH})]^{2+}$) is about 4 [12, 13].

The dissociation equilibria of the two ligands (acids) and the $[\text{Cr}(\text{H}_2\text{O})_6]^{3+}$ complex are



The reaction is suggested to be a multistep process since there is a decrease in absorbance at short reaction times and increase at longer reaction times. Because of protonation of the ligands, the groups (hydroxyls and carboxyl) are efficiently blocked and thus the attacks by chromium(III) can take place on them only upon the release of protons, provided that the strong hydrogen bonds have been first broken. This causes a pH decrease in the solution (Figure 3).

The fact that the second first-order step was found to be independent on ligand and chromium(III) concentrations suggests transformations that take place within the first complex that is formed upon the first attack by Cr(III) on the ligand.

In the first step, reaction between the reactive forms of the reactants and chromium(III) takes place, which results in the formation of complex A. The first step that is characterized by an absorbance decrease is revealed through experiments conducted at low temperatures. This step is

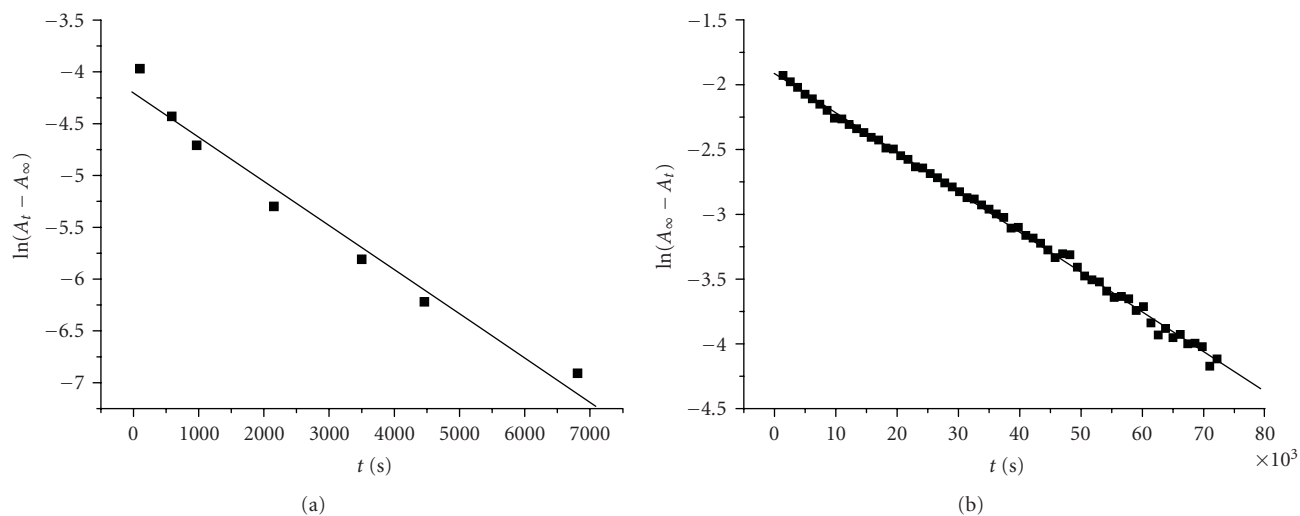


FIGURE 2: Plots of $\ln(A_t - A_\infty)$ (first stage) and $\ln(A_\infty - A_t)$ (second stage) versus time (a) $[2,4\text{-DHBA}] = 2,92 \cdot 10^{-2}$ M, $[\text{Cr(III)}] = 2,50 \cdot 10^{-3}$ M, $T = 281$ K, (b) $[2,5\text{-DHBA}] = 8,85 \cdot 10^{-3}$ M, $[\text{Cr(III)}] = 8,10 \cdot 10^{-2}$ M, $T = 308$ K.

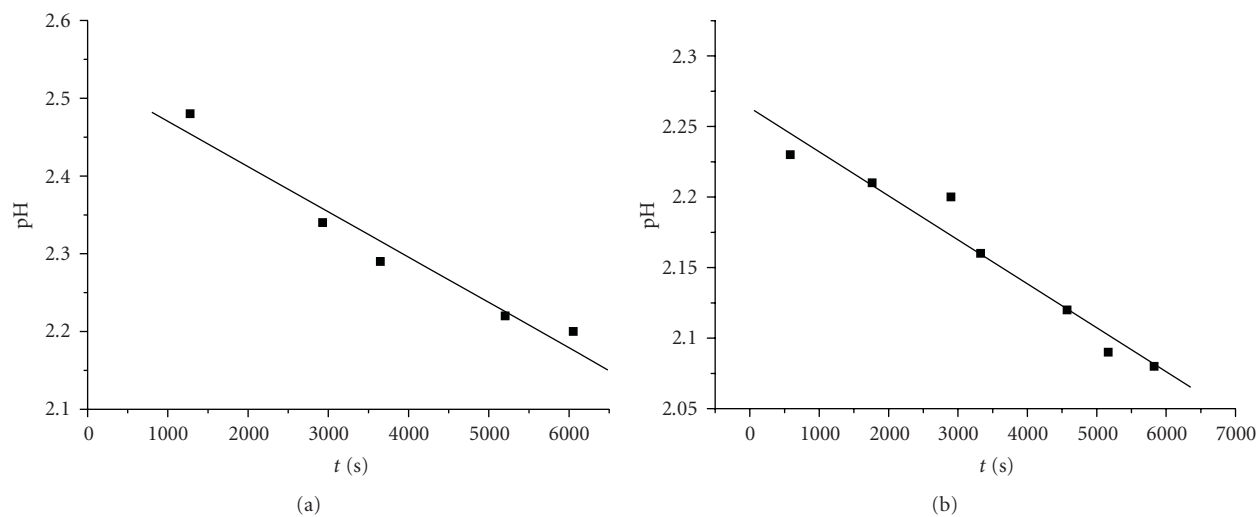


FIGURE 3: The pH versus time plots of typical mixtures of DHBA/Cr(III). Conditions: (a) $[2,4\text{-DHBA}]_0 = 4,87 \cdot 10^{-2}$ M, $[\text{Cr(III)}]_0 = 2,50 \cdot 10^{-3}$ M, $T = 298$ K; (b) $[2,5\text{-DHBA}]_0 = 4,87 \cdot 10^{-2}$ M, $[\text{Cr(III)}]_0 = 2,50 \cdot 10^{-3}$ M, $T = 298$ K.

TABLE 1: Values of k_1 and k_2 at various temperatures.

2,4-DHBA			2,5-DHBA		
T(K)	$k_1(\text{M}^{-1}\text{s}^{-1}) (\cdot 10^{+2})$	$k_2(\text{s}^{-1}) (\cdot 10^{+5})$	T(K)	$k_1(\text{M}^{-1}\text{s}^{-1}) (\cdot 10^{+2})$	$k_2(\text{s}^{-1}) (\cdot 10^{+5})$
281	1.57		279	0.87	
287	2.10		283	1.24	
290	2.14		291	2.12	
296	5.06		298	4.17	
298		1.45	298		1.40
303		1.86	303		1.89
308		2.88	308		2.78
313		3.95	313		4.44
313		3.48	313		4.31

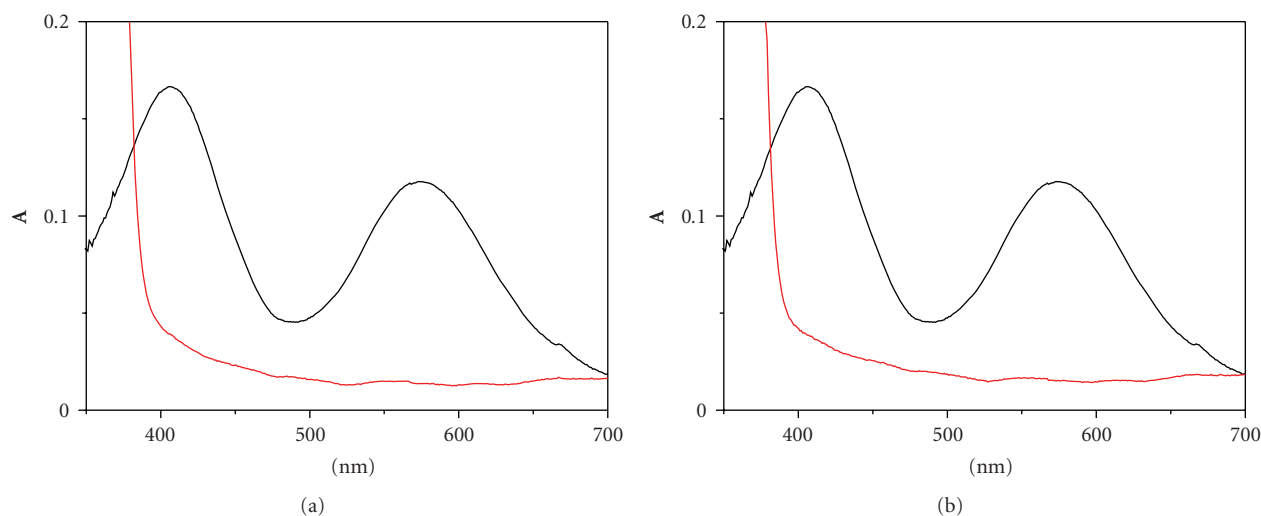


FIGURE 4: UV-vis spectra of Cr(III)/DHBA solutions: (a) $[\text{Cr(III)}] = 9.0 \cdot 10^{-3} \text{ M}$ and $[2,4\text{-DHBA}] = 9.0 \cdot 10^{-3} \text{ M}$; (b) $[\text{Cr(III)}] = 9.0 \cdot 10^{-3} \text{ M}$ and $[2,5\text{-DHBA}] = 9.0 \cdot 10^{-3} \text{ M}$.

TABLE 2: Activation parameters for steps 1 (k_1) and 2 (k_2) for the reactions of the two ligands 2,4- and 2,5-DHBA with chromium(III).

	2,4-DHBA	2,5-DHBA
ΔH_1^\ddagger (kJ/mol $^{-1}$)	49,5	60,3
ΔS_1^\ddagger (J mol $^{-1}$ K $^{-1}$)	-103,7	-68,0
ΔH_2^\ddagger (kJ/mol $^{-1}$)	45,13	54,55
ΔS_2^\ddagger (J mol $^{-1}$ K $^{-1}$)	-185,9	-154,8

followed by the slower second step, which is independent on both ligand and chromium(III) concentrations.

The formation of a light green complex, C_1 , from an initially violet ($\text{Cr}_{(\text{aq})}^{3+}$) and a colourless ligand solution (Figure 4) is observed upon mixing of the reactants. The characterisation of C_1 , the light green complex, as an oxygen-bound chromium(III) compound is supported by the UV/vis spectra ($\lambda_{\text{max}} = 579, 415 \text{ nm}$) and the formation kinetics and subsequent transformation (substitution) kinetics. All of the kinetic data and the associated spectra obtained during the decrease in absorbance are presumed to begin with the already associated complex C_1 .

In Figure 5 spectra of the reaction mixture are recorded at various times after mixing, starting from complex C_1 . The final spectrum corresponds to complex C_2 . Spectra recorded at intermediate times correspond to mixtures of C_1 and C_2 .

3.1.1. First Stage of the Reaction: First Attack of Chromium(III) on the Ligands. The first stage ($k_{1(\text{obs})}$) is characterized by an absorbance decrease at 575nm (a d-d transition of $\text{Cr}_{(\text{aq})}^{3+}$). The attacks of $[\text{Cr}(\text{H}_2\text{O})_5\text{OH}]^{2+}$ at the carboxylic ligand groups leading to the complexes C_1 , and C_2 result in shifting equilibrium (4) to the right. The k_1 pathways occur by

attacks of $[\text{Cr}(\text{H}_2\text{O})_5\text{OH}]^{2+}$ at the carboxylic ligand groups leading to complexes which in the presence of H^+ are fast protonated.

In order to obtain information on how many ligands react at the first step, the dependence of $k_{1(\text{obs})}$ on the ligand concentration was studied. The kinetics of the first stage of the reaction ($k_{1(\text{obs})}$) followed a first-order rate law. The first-order rate constant was found to have a linear dependence on ligand concentration (Figure 6), that is, to obey to the relation $k_{1(\text{obs})} = k_1[\text{DHBA}] + C$.

Measurements were conducted for the reactions of 2, 4-DHBA with chromium(III) at 281, 287, 290, 296 K and for 2, 5-DHBA with chromium(III) at 279, 283, 291, 298 K.

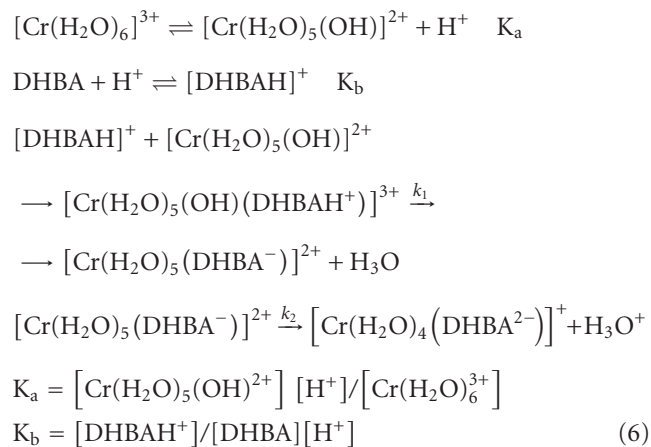
Below temperature 298 K the plots in Figure 6 are linear within experimental error, and above temperature 298 K the second reaction (k_2) involving the chelation becomes significant.

In our study of 3,4-dihydroxyphenylpropionic acid with chromium(III) [14] we observed an inverse dependence on $[\text{H}^+]$ which was discussed for the possibility of ligand- H^+ that is, DHBA^- reacting with $\text{Cr}_{\text{aq}}^{3+}$ or DHBA reacting with $[\text{Cr}(\text{OH})]^{2+}$.

An I_d mechanism is expected for step 1 since the reactive species can only be the conjugate base $[\text{Cr}(\text{H}_2\text{O})_5\text{OH}]^{2+}$ for the reactions of which dissociative mechanism I_d is supported [15], because of the strong labilizing effect of the coordinated OH^- presumably on the trans H_2O which results to a 10^2 - 10^3 -fold enhanced rate for the hydroxy- over the hexa-aqua ion.

Thus, for the first attack, a reaction between $[\text{Cr}(\text{OH})]^{2+}$ and the protonated molecule of the ligand can be proposed (Scheme 1), the reaction resulting in proton release (pH decrease). Upon the chelation reaction that follows, proton release takes also place resulting in further pH decrease. Hence for the reactions of 2,4-DHBA and 2,5-DHBA with

chromium(III), the mechanism which can be proposed, according to the experimental results (rate laws), is



Hence, $R = k_1 [\text{DHBAH}^+] [\text{Cr}(\text{H}_2\text{O})_5(\text{OH})^{2+}]$ and by substituting $[\text{Cr}(\text{H}_2\text{O})_5(\text{OH})^{2+}]$ and $[\text{DHBAH}^+]$, results the following:

$$R = k_1 K_b [\text{DHBA}][\text{H}^+] K_a [\text{Cr}(\text{H}_2\text{O})_6^{3+}] / [\text{H}^+] = k_1 K_b K_a [\text{DHBA}][\text{Cr}(\text{H}_2\text{O})_6^{3+}] \text{ and } k_{1(\text{obs})} = k_1 K_b K_a [\text{DHBA}] \text{ (in excess DHBA).}$$

The $k_{2(\text{obs})}$ dependence on chromium(III) and ligand concentration were studied in order to find if another Cr(III) ion and / or ligand molecule is entering the compound C_1 which is produced in step 1.

The concentrations of DHBA and of Cr(III) have no effect on the observed rate constants $k_{2(\text{obs})}$ in the range of concentrations applied as is shown in Figure 7. Higher concentrations were not possible to be achieved due to solubility reasons of 2,4- and 2,5-DHBA in weak acidic aqueous solutions. The $k_{2(\text{obs})}$ values, for the DHBA and chromium(III) concentration range studied, at various temperatures are given in Table 1 and the corresponding $\Delta H_{2(\text{obs})}^\ddagger$, $\Delta S_{2(\text{obs})}^\ddagger$ values in Table 2.

The activation parameters are deduced from the temperature dependence experiments and lead to structures of the activated complexes and of the type of mechanism taking place. The negative values of ΔS_1^\ddagger ($\Delta S_{1(\text{obs})}^\ddagger$) suggest an associative mechanism for the first stage of the reaction. $[\text{Cr}(\text{H}_2\text{O})_5\text{OH}]^{2+}$, however, as stated above, reacts/follows an I_d mechanism. This suggests that composite activation parameters $\Delta H_{1(\text{obs})}^\ddagger = \Delta H_0 + \Delta H_1^\ddagger$ and $\Delta S_{1(\text{obs})}^\ddagger = \Delta S_0 + \Delta S_1^\ddagger$ are applied where ΔH_0 and ΔS_0 correspond to a pre-equilibrium K_0 and ΔH_1^\ddagger and ΔS_1^\ddagger correspond to the first step (complexation, k_1).

Thus the resulting negative values of ΔS^\ddagger as well as the resulting values of ΔH^\ddagger do not correspond to step 1, which is taking place by an I_d mechanism due to the reactive species $[\text{Cr}(\text{H}_2\text{O})_5\text{OH}]^{2+}$.

The negative values of $\Delta S_{2(\text{obs})}^\ddagger$, the independence on ligand(s) and chromium(III) concentrations of $k_{2(\text{obs})}$, the increase of the extinction coefficients (increase in absorbance), and the pH decrease (Figure 3) led to the assignment of the studied transformations as associatively activated substitution reactions of water molecules from

the Cr(III) coordination sphere by the ligand(s) through chelation, with concomitant proton release (Scheme 1).

The absorbance increase of the second stage is due to the chelation and the pH decrease is due to the release of protons upon the course of these reactions (Figure 3, Scheme 1). These changes are attributed to the formation of an oxygen-bound chromium(III)-DHBA acid complex (k_1) followed by chelation (k_2).

Stoichiometry of 1:1 for the reaction of Cr(III) with 2,4- and 2,5-DHBA is proposed, according to the observed k_1 dependence on ligand concentration and the chelation reactions in the Cr(III) center. In accordance with the stoichiometry resulting from the kinetics are the elemental analysis results for the isolated in the solid form final product. The isolation was achieved by addition of KOH solution in the final reaction mixture. Thus the experimental percentages C = 11.82% and H = 3.49% correspond to the formula $[\text{Cr}(\text{2,5-DHBA}_{-3\text{H}})(\text{H}_2\text{O})_4] \cdot 3\text{KNO}_3 \cdot 8\text{H}_2\text{O}$ (MW = 722) for which the calculated percentages (theoretical values) for C and H are C = 11.63% and H = 3.74%.

Hence, the formation of C_2 , the final chelated complex, occurs actually in at least two stages.

3.1.2. Structures of the Activated Complexes C_1^\ddagger and C_2^\ddagger .

These are given in Scheme 2. Associative mechanisms have been found to be operative in reactions of Cr(III) [4, 16, 17]. The negative values of the entropies of activation ΔS^\ddagger that have been calculated for our systems suggest an associative mode of activation. The original complex C_1 could also be a chelate itself. This could easily explain the formation of compounds containing Cr-O bonds. The negative entropies of activation ΔS^\ddagger , however, suggest the formation of more structured transition states from the less organized reactants. Therefore, complex C_1 is not in chelated form and the mechanisms shown in Scheme 1 are thus supported. If the k_2 path proceed via attack by an external ligand on the complex C_1 , the k_2 path could be ligand concentration dependent. In the suggested mechanism the phenolic groups act as internal attacking groups to the chromium-bound H_2O molecules and supply a proton to the H_2O in the same complex (Scheme 2), which is released as H_3O^+ .

The final product C_2 could be chelated at the carboxylic group through its oxygens. This alternative is not supported because a five-membered ring, which is formed according to the suggested mechanism, is more stable than the four-membered ring which would result if chelation at the carboxylic group took place.

The UV/vis spectrum which exhibits a maximum at 575 nm and a shoulder at 412 nm (d-d transitions of Cr(III)) upon complexation changes, as expected, due to continuous changes in the ligand field. This is caused by the new ligand(s) which enters in the coordination sphere of Cr(III). Water molecules are being replaced by the ligand groups leading to C_1 and finally to C_2 . The conditions are kept acidic suggesting that oxidation does not take place and the only changes that are expected in the spectrum are only those being caused by the change of the ligand field. This means that only a shift of the maximum and disappearance

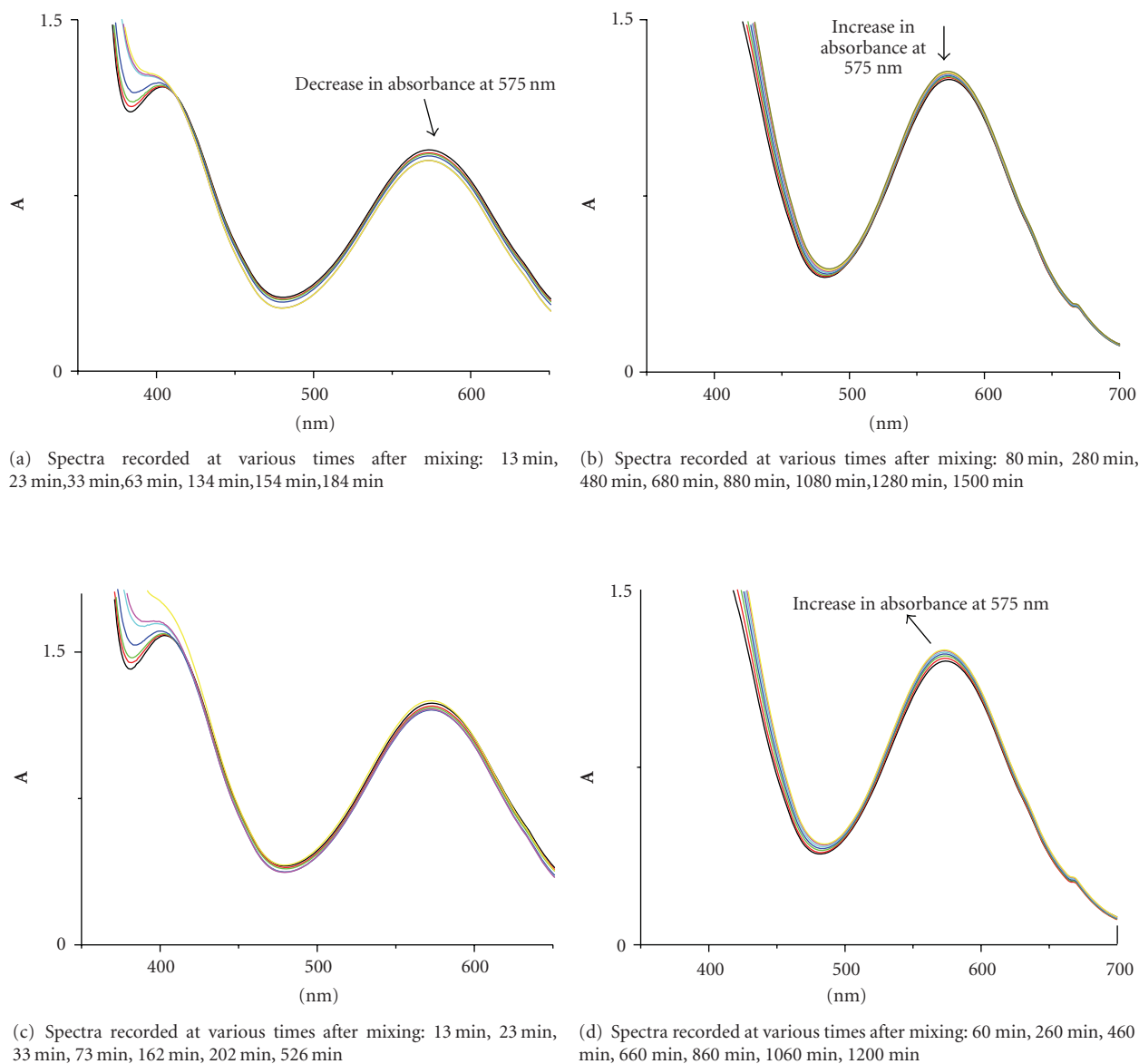


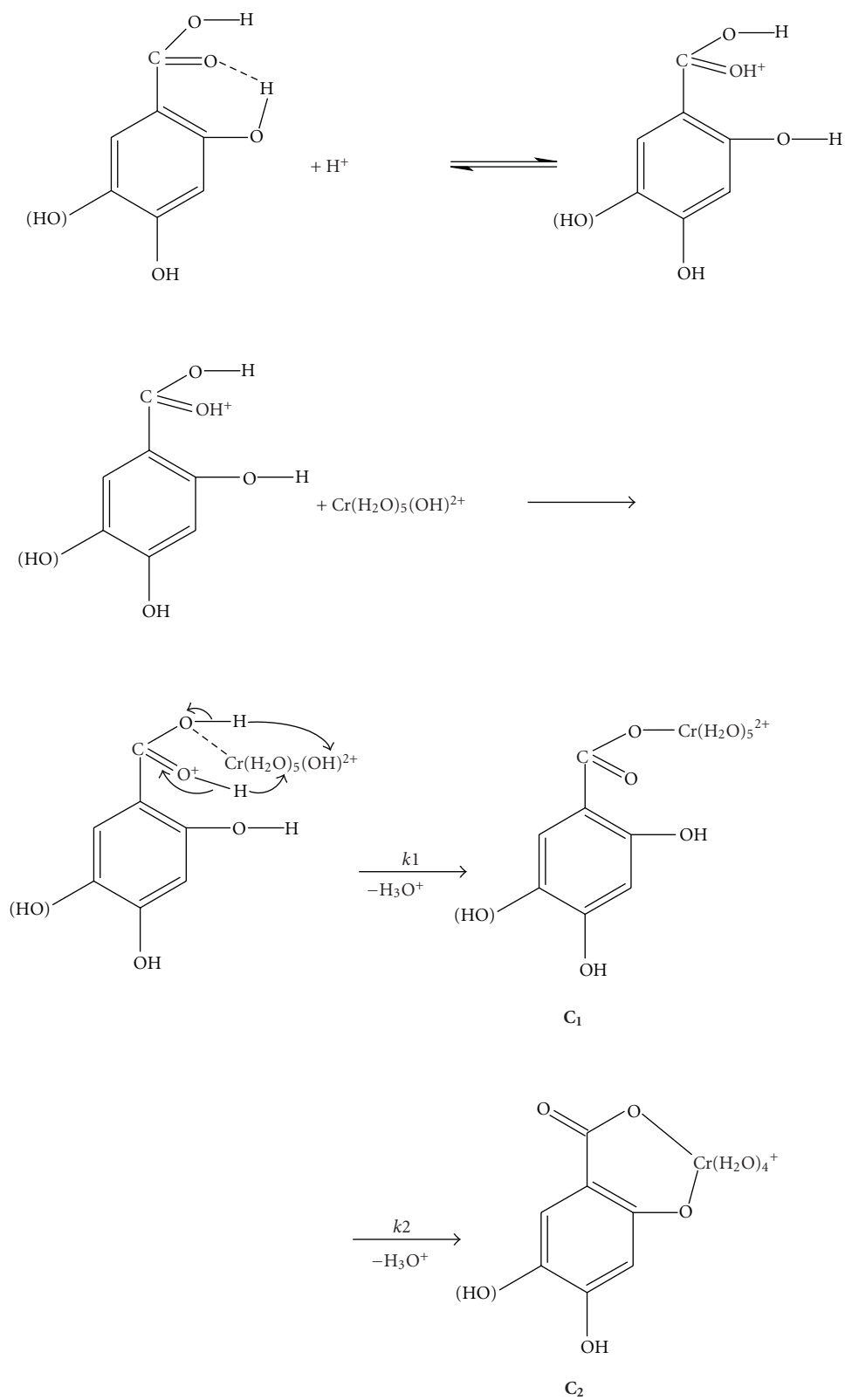
FIGURE 5: (a) UV-Vis spectra of the reaction mixture Cr(III)/2,4-DHBA. Spectra on the left: $[2,4\text{-DHBA}] = 8,85 \cdot 10^{-3} \text{ M}$, $[\text{Cr(III)}] = 0,067 \text{ M}$, $T = 288 \text{ K}$. Spectra on the right: $[2,4\text{-DHBA}] = 8,85 \cdot 10^{-3} \text{ M}$, $[\text{Cr(III)}] = 0,09 \text{ M}$, $T = 298 \text{ K}$. (b) UV-Vis spectra of the reaction mixture Cr(III)/2,5-DHBA. Spectra on the left: $[2,5\text{-DHBA}] = 8,85 \cdot 10^{-3} \text{ M}$, $[\text{Cr(III)}] = 0,09 \text{ M}$, $T = 288 \text{ K}$. Spectra on the right: $[2,5\text{-DHBA}] = 8,85 \cdot 10^{-3} \text{ M}$, $[\text{Cr(III)}] = 0,09 \text{ M}$, $T = 298 \text{ K}$.

of the shoulder in the UV region take place; this last change is due to the high absorptivities of the resulting complexes that hide the shoulder.

The chelation of the first formed complex produces PhO-bound chromium(III) species, characterized by the UV/vis spectra and the kinetic behavior which are typical of other known complexes containing Cr-O bond(s) [16, 17].

3.2. Structure of the Complexes-Mode of Binding. The isolation of a pure product C_2 is already mentioned (page 18) that corresponds to the formula $[\text{Cr}(2,5\text{-DHBA}_{-3\text{H}})(\text{H}_2\text{O})_4] \cdot 3\text{KNO}_3 \cdot 8\text{H}_2\text{O}$ according to the elemental

analysis and all other experimental data that suggest, as previously discussed, that binding is taking place through the carboxylic and the nearby phenolic group (Scheme 1, for ligands 2,4- and 2,5-DHBA). Catecholic type of binding is established in the coordination complexes of dihydrocaffeic, caffeic and ferulic acids with Co(II), Ni(II), Cu(II), Fe(III), Mn(II), Mn(III), V(V), V(IV,V), Zn(II) [18–22], and dihydroxyphenylpropionic acid (dihydrocaffeic acid) with Cr(III) [14]. The same type of coordination, that is, catecholic, has been also suggested for the reaction of caffeic acid with Cr(III) [23] and 3,4-dihydroxybenzoic acid with Cr(III) [24]. In some of the above presented structures both catecholic



SCHEME 1: A possible mechanism of the reactions of Chromium(III) with 2,4- and 2,5-dihydroxybenzoic acids in weak acidic aqueous solutions.

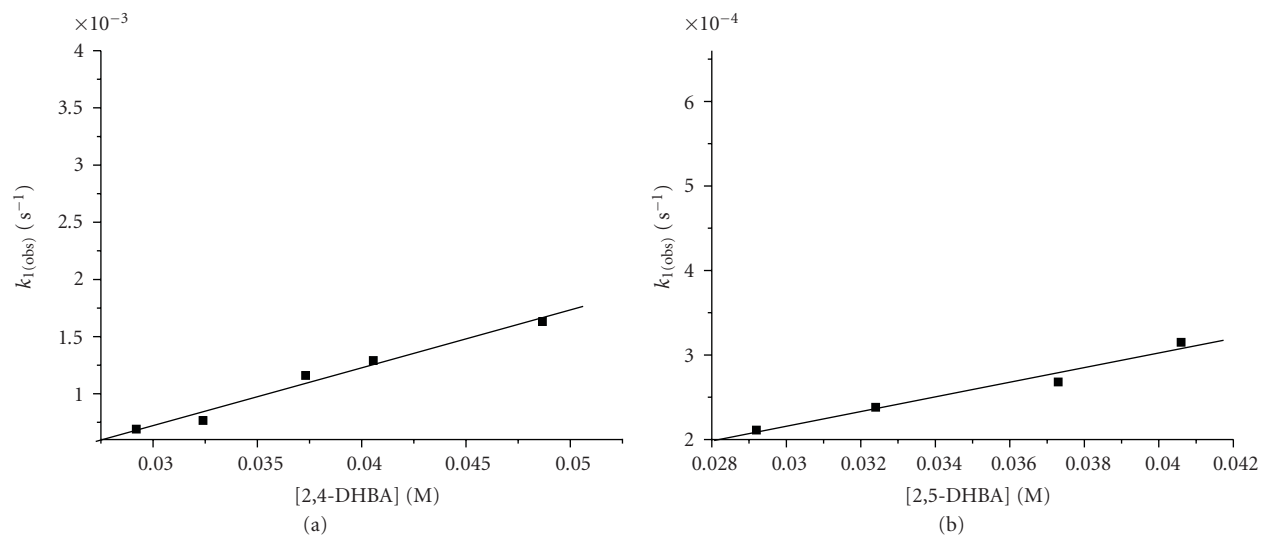


FIGURE 6: Ligand concentration dependence of $k_{1(\text{obs})}$. Conditions: (a) $[2,4\text{-DHBA}] = 2,92\text{--}4,87 \cdot 10^{-2} \text{ M}$, $[\text{Cr(III)}] = 2,50 \cdot 10^{-3} \text{ M}$, $T = 296 \text{ K}$, (b) $[2,5\text{-DHBA}] = 2,92\text{--}4,06 \cdot 10^{-2} \text{ M}$, $[\text{Cr(III)}] = 2,50 \cdot 10^{-3} \text{ M}$, $T = 279 \text{ K}$.

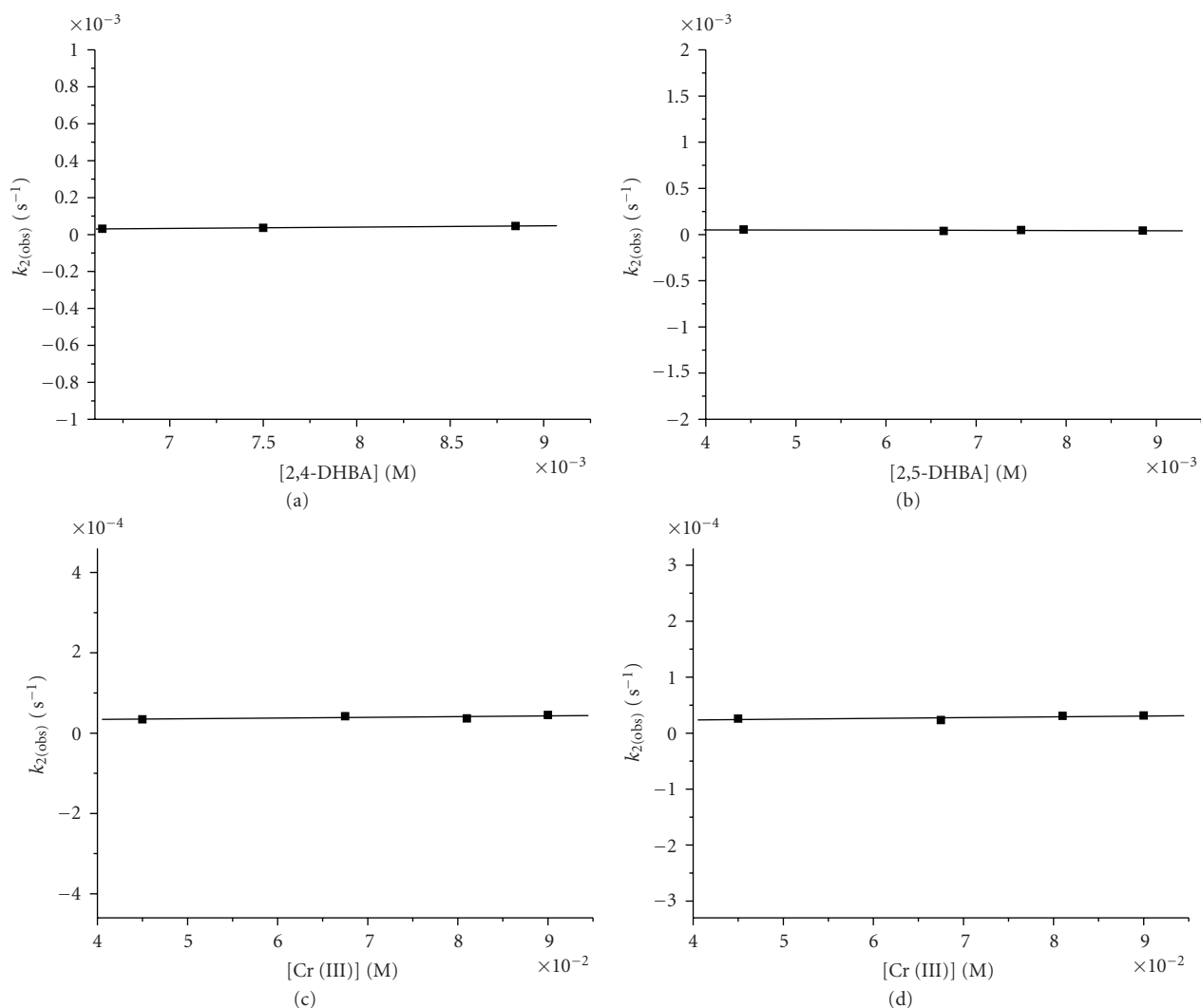
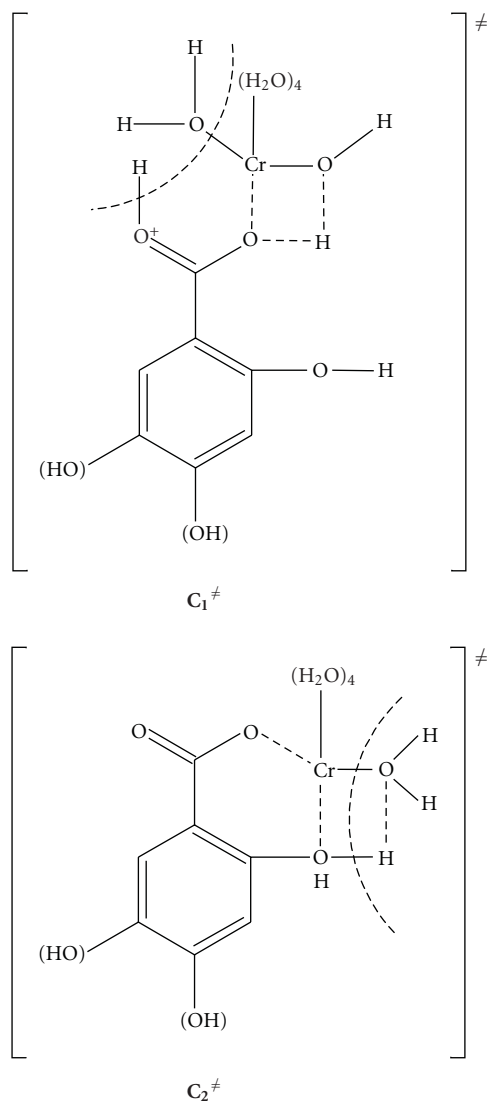


FIGURE 7: Ligand and Cr(III) concentration dependence of $k_{2(\text{obs})}$. Conditions: (a) $[2,4\text{-DHBA}] = (6.64\text{--}8.85) \cdot 10^{-3} \text{ M}$, $[\text{Cr(III)}] = 1.25 \cdot 10^{-3} \text{ M}$, $T = 313 \text{ K}$, (b) $[2,5\text{-DHBA}] = (4.42\text{--}8.85) \cdot 10^{-3} \text{ M}$, $[\text{Cr(III)}] = 1.25 \cdot 10^{-3} \text{ M}$, $T = 313 \text{ K}$, (c) $[2,4\text{-DHBA}] = 8.85 \cdot 10^{-3} \text{ M}$, $[\text{Cr(III)}] = (4.5\text{--}9.00) \cdot 10^{-2} \text{ M}$, $T = 313 \text{ K}$, (d) $[2,5\text{-DHBA}] = 8.85 \cdot 10^{-3} \text{ M}$, $[\text{Cr(III)}] = (4.5\text{--}9.0) \cdot 10^{-2} \text{ M}$, $T = 308 \text{ K}$.

SCHEME 2: Activated complexes C_1^\ddagger and C_2^\ddagger .

and carboxylic binding is observed. Catecholic type of coordination was found in Fe(III)-2,3-dihydroxybenzoic acid complex for which the kinetics of the coordination and oxidation process have been reported [25, 26]. In the systems studied in this work (2,4- and 2,5-dihydroxybenzoic acids and chromium(III)), binding is supported to take place between chromium(III) and the carboxylic and the 2-phenolic group of the ligands. Analogous binding between the carboxylic and the 2-phenolic group of the ligand was reported for the reaction between chromium(III) and 2,3-dihydroxybenzoic acid [27].

4. Conclusions

Our results indicate that the reactions between chromium(III) and 2,4- and 2,5-DHBA in weak acidic aqueous solutions follow a two-step mechanism according to which an initial step 1 consisting of an attack between the acid molecule (ligand) and the $[\text{Cr}(\text{H}_2\text{O})_5\text{OH}]^{2+}$ complex to give

a carboxylate bound Cr(III) is followed by a nonligand and nonchromium(III)-dependent step assigned to be a chelation step due to the negative entropies of activation. Both steps are followed by pH decrease suggesting that proton release is taking place. The protons are released in an associatively activated mode.

The first step depends on 2,4- or 2,5-DHBA concentration and $[\text{Cr}(\text{H}_2\text{O})_5\text{OH}]^{2+}$ is the reactive metal complex. This is followed by a slower step, the rate of which depends only on the concentrations of their respective intermediate complexes C_1 , with negative entropies of activation, suggesting that the transition states are associatively activated.

The negative values of the entropies of activation of the second step, the independence on ligand and chromium(III) concentrations of their rate, the displacement of the wavelengths maxima, the increase of the extinction coefficients, the pH decrease due to release of protons upon complexation, and the various transformations lead to the mechanism presented in Scheme 1. The observed transformations are assigned as substitution of water molecules from the coordination sphere of Cr(III) by the ligand through complexation followed by chelation. A dissociative I_d mechanism is supported for step 1 and an associative mechanism for step 2.

Acknowledgment

The authors acknowledge financial support from the Research Account of Athens University (Grant no. 70/4/7564).

References

- [1] E.-I. Ochiai, *General Principles of Biochemistry of the Elements in Biochemistry of the Elements*, edited by E. Frieden, Plenum Press, New York, NY, USA, 1987.
- [2] A. Petrou, E. Vrachnou-Astra, and D. Katakis, "A new series of organochromium complexes formed in aqueous solutions," *Inorganica Chimica Acta*, vol. 39, pp. 161–171, 1980.
- [3] A. Petrou, E. Vrachnou-Astra, J. Konstantatos, N. Katsaros, and D. Katakis, "Kinetics and mechanisms of aquation of some σ -bonded organochromium complexes," *Inorganic Chemistry*, vol. 20, no. 4, pp. 1091–1096, 1981.
- [4] A. L. Petrou, "Kinetics and mechanism of the reaction between chromium(II) and 1,2-bis(2-pyridyl)ethylene in acidic aqueous solutions," *Journal of the Chemical Society, Dalton Transactions*, no. 24, pp. 3771–3775, 1993.
- [5] J. B. Vincent, "Recent advances in the biochemistry of chromium(III)," *Journal of Trace Elements in Experimental Medicine*, vol. 16, no. 4, pp. 227–236, 2003.
- [6] A. Yamamoto, O. Wada, and T. Ono, "Isolation of a biologically active low-molecular-mass chromium compound from rabbit liver," *European Journal of Biochemistry*, vol. 165, no. 3, pp. 627–631, 1987.
- [7] C. M. Davis and J. B. Vincent, "Isolation and characterization of a biologically active chromium oligopeptide from bovine liver," *Archives of Biochemistry and Biophysics*, vol. 339, no. 2, pp. 335–343, 1997.
- [8] C. Michele Davis, A. C. Royer, and J. B. Vincent, "Synthetic multinuclear chromium assembly activates insulin receptor kinase activity: functional model for low-molecular-weight chromium-binding substance," *Inorganic Chemistry*, vol. 36, no. 23, pp. 5316–5320, 1997.

- [9] G. Cockerham and B. S. Shane, *Basic Environmental Toxicology*, CRC Press, London, UK, 1994.
- [10] V. M. Dudarchik, T. P. Smychnik, and A. A. Terentyev, *XIXth International Conference on Polyphenols*, Lille, France, 1998.
- [11] T. Lehtonen, J. Peuravuori, and K. Pihlaja, "Degradative analysis of aquatic fulvic acid: CuO oxidation versus pyrolysis after tetramethylammonium hydroxide treatments in air and helium atmospheres," *Analytica Chimica Acta*, vol. 511, no. 2, pp. 349–356, 2004.
- [12] C. F. Baes and R. E. Mesner, *The Hydrolysis of Cations*, John Wiley & Sons, New York, NY, USA, 1976.
- [13] F. A. Cotton, G. Wilkinson, C. A. Murillo, and M. Bochmann, *Advanced Inorganic Chemistry*, John Wiley & Sons, New York, NY, USA, 6th edition, 1999.
- [14] A. L. Petrou, P. Paraskevopoulou, and M. Chrysikopoulou, "Kinetics and mechanism of the reaction between chromium(III) and 3,4-dihydroxyphenylpropionic (dihydrocaffeic) acid in weak acidic aqueous solutions," *Journal of Inorganic Biochemistry*, vol. 98, no. 1, pp. 123–132, 2004.
- [15] R. F. Wilkins, *Kinetics and Mechanisms of Reactions of Transition Metal Complexes*, VCH, New York, NY, USA, 2nd edition, 1991.
- [16] T. W. Swaddle and D. R. Stranks, "Mechanistic information from pressure and temperature effects on the rate of transfer of oxygen-18 from aquopentaamminechromium(III) and aquopentaamminerhodium(III) ions to solvent water," *Journal of the American Chemical Society*, vol. 94, no. 24, pp. 8357–8360, 1972.
- [17] T. Ramasami and A. G. Sykes, "Mechanistic implications of kinetic data for the formation and aquation of acidopentaamminechromium(III) complexes, $\text{Cr}(\text{NH}_3)_5\text{X}^{2+}$, $\text{X}^- = \text{NCS}^-$, $\text{CCl}_3\text{CO}_2^-$, CF_3CO_2^- , Cl^- , Br^- , and I^- . Evidence for a dissociative mechanism," *Inorganic Chemistry*, vol. 15, no. 11, pp. 2885–2891, 1976.
- [18] A. L. Petrou, M. V. Koromantzou, and J. M. Tsangaris, "Coordination complexes of 3,4-dihydroxyphenylpropionic acid (dihydrocaffeic acid) with copper(II), nickel(II), cobalt(II) and iron(III)," *Transition Metal Chemistry*, vol. 16, no. 1, pp. 48–52, 1991.
- [19] A. L. Petrou, "Binuclear vanadium(V) and vanadium(IV, V) complexes of dihydrocaffeic, caffeic and ferulic acids," *Transition Metal Chemistry*, vol. 18, no. 5, pp. 462–466, 1993.
- [20] A. L. Petrou and S. P. Perlepes, "Preparation and properties of manganese(II) and manganese(III) complexes possessing ligands with carboxylate and phenolic/phenoxide groups," *Chimika Chronika, New Series*, vol. 23, pp. 155–168, 1994.
- [21] A. L. Petrou and S. P. Perlepes, "Oligonuclear zinc(II) complexes of dianion of hydrocaffeic, caffeic and ferulic acids," *Chimika Chronika, New Series*, vol. 24, pp. 133–146, 1995.
- [22] A. L. Petrou, M. V. Koromantzou, and J. M. Tsangaris, "Coordination complexes of caffeic and ferulic acids with Cu(II), Ni(II), Co(II) and Fe(III)," *Chimika Chronika, New Series*, vol. 22, pp. 189–204, 1993.
- [23] V. Thoma, K. Tampouris, and A. L. Petrou, "Kinetics and mechanism of the reaction between chromium(III) and 3,4-dihydroxy-phenyl-propenoic acid (caffeic acid) in weak acidic aqueous solutions," *Bioinorganic Chemistry and Applications*, vol. 2008, Article ID 624583, 7 pages, 2008.
- [24] K. Zavitsanos, K. Tampouris, and A. L. Petrou, "Reaction of chromium(III) with 3,4-Dihydroxybenzoic acid: kinetics and mechanism in weak acidic aqueous solutions," *Bioinorganic Chemistry and Applications*, vol. 2008, Article ID 212461, 8 pages, 2008.
- [25] J. Xu and R. B. Jordan, "Equilibrium and kinetic studies of the complexing of iron(III) by 1,2-dihydroxybenzene derivatives," *Inorganic Chemistry*, vol. 27, no. 8, pp. 1502–1507, 1988.
- [26] J. Xu and R. B. Jordan, "Kinetics and mechanism of the oxidation of 2,3-dihydroxybenzoic acid by iron(III)," *Inorganic Chemistry*, vol. 27, no. 25, pp. 4563–4566, 1988.
- [27] A. L. Petrou, V. Thoma, and K. Tampouris, "Kinetics and mechanism of the reaction chromium(III) and 2,3-dihydroxybenzoic acid in weak acidic aqueous solutions," *Bioinorganic Chemistry and Applications*, vol. 2010, Article ID 348692, 8 pages, 2010.

Research Article

Use of the 2-Pyridinealdoxime/*N,N'*-Donor Ligand Combination in Cobalt(III) Chemistry: Synthesis and Characterization of Two Cationic Mononuclear Cobalt(III) Complexes

Konstantis F. Konidaris,¹ Catherine P. Raptopoulou,² Vassilis Psycharis,² Spyros P. Perlepes,¹ Evy Manessi-Zoupa,¹ and Theocharis C. Stamatos¹

¹ Department of Chemistry, University of Patras, 26500 Patras, Greece

² Institute of Materials Science, NCSR "Demokritos", 15310 Aghia Paraskevi Attikis, Greece

Correspondence should be addressed to Evy Manessi-Zoupa, emane@upatras.gr and Theocharis C. Stamatos, thstama@chemistry.upatras.gr

Received 31 March 2010; Accepted 27 May 2010

Academic Editor: Elena Milaeva

Copyright © 2010 Konstantis F. Konidaris et al. This is an open access article distributed under the Creative Commons Attribution License, which permits unrestricted use, distribution, and reproduction in any medium, provided the original work is properly cited.

The use of 2-pyridinealdoxime (paoH)/*N,N'*-donor ligand (L-L) "blend" in cobalt chemistry has afforded two cationic mononuclear cobalt(III) complexes of the general type $[\text{Co}(\text{pao})_2(\text{L-L})]^+$, where L-L = 1,10-phenanthroline (phen) and 2,2'-bipyridine (bpy). The $\text{CoCl}_2/\text{paoH}/\text{L-L}$ (1:2:1) reaction system in MeOH gives complexes $[\text{Co}^{\text{III}}(\text{pao})_2(\text{phen})]\text{Cl}\cdot 2\text{H}_2\text{O}$ (1·2H₂O) and $[\text{Co}^{\text{III}}(\text{pao})_2(\text{bpy})]\text{Cl}\cdot 1.5\text{MeOH}$ (2·1.5MeOH). The structures of the complexes were determined by single-crystal X-ray crystallography. The Co^{III} ions are six-coordinate, surrounded by three bidentate chelating ligands, that is, two pao⁻ and one phen or bpy. The deprotonated oxygen atom of the pao⁻ ligand remains uncoordinated and participates in hydrogen bonding with the solvate molecules. IR data of the complexes are discussed in terms of the nature of bonding and the known structures.

1. Introduction

Oximes and their metal complexes are of current interest because of their rich physicochemical properties, reactivity patterns, and potential applications in many important chemical processes in the fields of medicine [1, 2], bioorganic chemistry [3], catalysis [4], and electrochemical and electrooptical sensors [5].

In the treatment of organophosphate insecticide toxicity in man and animals, the use of acetylcholinesterase reactivators in conjunction with atropine has been found to be the most effective treatment [6]. Among various acetylcholinesterase reactivators, 2-pyridinealdoxime (paoH) is routinely used in human and veterinary practices. It is furthermore known that metal complexes of active drugs as ligands can have important pharmaceutical activities because of several factors. In fact, the field of medicinal inorganic chemistry emerged a long time ago [7], and it is based on certain principles that can be summarized as

follows. Complexation with the metal protects the drug against enzymatic degradations because of the inertness of certain metal-ligand linkages. The metal complex can have better hydrophobicity/hydrophilicity properties than the free ligand and, through this, it can improve the transport processes in the tissues. In addition, the metal complex can release the active drug(s) in a specific organ, and its activity can be reinforced by the combination of effects from the ligands and from the metal residue. The application of these principles has already resulted in the design of successful metal-based drugs [8, 9].

Since 1905, when Tschugaeff introduced dimethylglyoxime as a reagent for the analysis of nickel, oxime ligands have played an important role in the continuing progress of coordination chemistry [10]. Furthermore, the ability of the oximate(-1) group ($>\text{C}=\text{N}-\text{O}^-$) to stabilize oxidized forms of metal ions, for example, Ni^{III} or Ni^{IV}, has a vital importance in their role in the areas of technological applications [11]. In contrast to the great number of studies dealing with

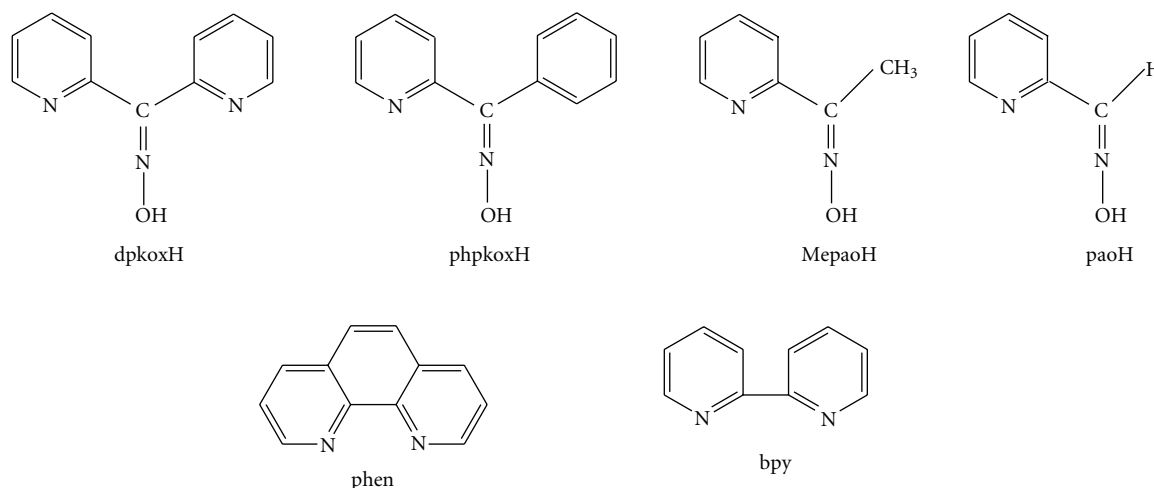


FIGURE 1: Structural formulae and abbreviations of the ligands discussed in the text.

metal complexes of simple oximes and salicylaldoximes [12], relatively little is known about complexes of 2-pyridyloximes [13–15] although this class of compounds could offer unique features in terms of structural and physical properties.

Few years ago our group explored the influence of these ligands on the Co cluster chemistry by reacting cobalt carboxylate salts with neutral 2-pyridyloximes; the main objectives were the access to new structural types of clusters with interesting magnetic and spectroscopic properties and the study of Co-mediated reactions of the oxime group. Reaction schemes involving di-2-pyridyl ketone oxime, dpkoxH (Figure 1), and various Co carboxylate sources led [16] to the first mixed-valence Co(II,III), inverse 12-metallacrown-4 complexes, namely, $[\text{Co}_2^{\text{II}}\text{Co}_2^{\text{III}}(\text{OR})_2(\text{O}_2\text{CR}')_2(\text{dpkox})_4\text{S}_2]\text{X}_2$ ($\text{R} = \text{H}, \text{CH}_3$; $\text{R}' = \text{CH}_3, \text{C}_6\text{H}_5, (\text{CH}_3)_3$; $\text{S} = \text{solvent}$; $\text{X} = \text{ClO}_4, \text{PF}_6$). The use of phenyl 2-pyridyl ketone oxime, phpkoxH (Figure 1), methyl 2-pyridyl ketone oxime, MepaoH (Figure 1), and 2-pyridinealdoxime, paoH (Figure 1) in Co carboxylate chemistry yielded [17] the trinuclear, mixed-valence, carboxylate-free Co(II,III) complexes $[\text{Co}_3(\text{phpkox})_6](\text{PF}_6)_2$, $[\text{Co}_3(\text{Mepao})_6](\text{ClO}_4)_2$, and $[\text{Co}_3(\text{pao})_6](\text{ClO}_4)_2$. The core of these complexes has an open-topology comprising one Co^{II} center and two Co^{III} ions. Recently [18] two of us reported complexes $[\text{Co}_3^{\text{III}}\text{O}(\text{O}_2\text{CPh})_3(\text{pao})_3]_2[\text{Co}_3^{\text{II}}(\text{O}_2\text{CPh})_8]$, $[\text{Co}_3^{\text{III}}\text{O}(\text{O}_2\text{CPh})_3(\text{pao})_3](\text{O}_2\text{CPh})$, $[\text{Co}_3^{\text{III}}\text{O}(\text{O}_2\text{CPh})_3(\text{pao})_3]_2(\text{O}_2\text{CPh})(\text{NO}_3)$, and $[\text{Co}_2^{\text{III}}\text{Co}^{\text{II}}(\text{OH})\text{Cl}_3(\text{pao})_4]$. The above prior results encouraged us to proceed to the amalgamation of 2-pyridyl oximes with N,N'-donor ligands, that is, 1,10-phenanthroline (phen) and 2,2'-bipyridine (bpy) (Figure 1), in cobalt chemistry. The primary aim of this project was the synthesis and structural characterization of a series of cobalt building blocks that could act as “metalloligands” for the construction of one-dimensional heterometallic assemblies with various transition metal ions (e.g., Mn^{III} , Cr^{III} , Fe^{II}) or lanthanides; the latter chains would probably provide interesting magnetic, optical, and spectroscopic properties. A secondary goal was the study of the biological properties of the resulting mixed-ligand complexes. Herein, we concentrate on the synthetic investigation of

the general $\text{CoCl}_2/\text{paoH}/\text{phen}$ or bpy reaction system and describe the preparation and characterization of the cationic mononuclear complexes $[\text{Co}(\text{pao})_2(\text{phen})]\text{Cl}$ and $[\text{Co}(\text{pao})_2(\text{bpy})]\text{Cl}$.

2. Experiments

2.1. Starting Materials and Physical Measurements. All manipulations were performed under aerobic conditions using reagents and solvents as received. Cobalt(II) chloride, 2-pyridinealdoxime (paoH), 1,10-phenanthroline hydrate (phen·H₂O), and 2,2'-bipyridine (bpy) were purchased from Aldrich Co. Elemental analyses (C, H, N) were performed by the University of Ioannina (Greece) Microanalytical Laboratory using an EA 1108 Carlo Erba analyzer. Ir spectra (4000–450 cm^{-1}) were recorded on a Perkin-Elmer 16 PC FT-IR spectrometer with samples prepared as KBr pellets. Solid-state (diffuse reflectance, 28.5–12.5 kK) electronic spectra were recorded on a Varian Cary 100 instrument. Magnetic susceptibility measurements were carried out at 25 °C by the Faraday method using a Cahn-Ventron RM-2 balance standardized with $[\text{HgCo}(\text{NCS})_4]_n$.

2.2. Compound Preparation

2.2.1. Preparation of $[\text{Co}(\text{pao})_2(\text{phen})]\text{Cl}\cdot 2\text{H}_2\text{O}$ ($1\cdot 2\text{H}_2\text{O}$). To a pale yellow, stirred solution of paoH (0.12 g, 1.0 mmol) in MeOH (20 cm^3) was added a colourless solution of phen·H₂O (0.10 g, 0.5 mmol) in the same solvent (5 cm^3). To the resulting, almost colourless solution, a pink solution of CoCl_2 (0.07 g, 0.5 mmol) in MeOH (10 cm^3) was added. The deep orange solution obtained was stirred at ambient temperature for 30 min and allowed to very slowly evaporate at 6–8 °C for one week. Well-formed, X-ray quality crystals of the product slowly appeared. The orange prismatic crystals were collected by filtration, washed with cold MeOH ($2 \times 3 \text{ cm}^3$) and Et₂O ($2 \times 4 \text{ cm}^3$), and dried in air. Yields as high as 70% were obtained (found: C, 51.9; H, 3.8; N, 15.6. $\text{C}_{24}\text{H}_{22}\text{CoN}_6\text{O}_4\text{Cl}$ calcd.: C, 52.1; H, 4.0; N, 15.2%).

TABLE 1: Crystallographic data for complexes **1**·2H₂O and **2**·1.5MeOH.

Parameter	1 ·2H ₂ O	2 ·1.5MeOH
Color (habit)	Red/orange prisms	Red prisms
Crystal size (mm)	0.33 × 0.08 × 0.05	0.50 × 0.35 × 0.30
Chemical formula	C ₂₄ H ₂₂ CoN ₆ O ₄ Cl	C _{23.5} H ₁₉ CoN ₆ O _{3.5} Cl
<i>M</i>	552.86	535.83
Crystal system	Tetragonal	Orthorhombic
Space group	<i>I</i> 4 ₁ / <i>acd</i>	<i>Ic</i> 2 <i>m</i>
Unit cell dimensions		
<i>a</i> (Å)	17.098(5)	13.134(6)
<i>b</i> (Å)	17.098(5)	8.900(4)
<i>c</i> (Å)	31.903(9)	21.293(8)
<i>V</i> (Å ³)	9327(5)	2489(2)
<i>Z</i>	16	4
<i>D</i> _{calc} (g cm ⁻³)	1.575	1.430
<i>μ</i> (mm ⁻¹)	0.896	0.836
Radiation (Å)	MoK _α (0.71073)	MoK _α (0.71073)
Temperature (K)	298	298
Scan mode/speed (° min ⁻¹)	<i>θ</i> -2 <i>θ</i> /2.6	<i>θ</i> -2 <i>θ</i> /3.5
Scan range (°)	2.1 + <i>α</i> ₁ <i>α</i> ₂ separation	2.3 + <i>α</i> ₁ <i>α</i> ₂ separation
<i>θ</i> range (°)	2.1–23.0	1.8–25.0
Reflections collected	3157	3561
Unique reflections	1627 (<i>R</i> _{int} = 0.0276)	2253 (<i>R</i> _{int} = 0.0240)
Reflections used [<i>I</i> > 2 <i>σ</i> (<i>I</i>)]	1237	1882
Parameters refined	164	204
[<i>Δ</i> / <i>σ</i>] _{max}	0.000	0.014
[<i>Δρ</i>] _{max} /[<i>Δρ</i>] _{min} (e Å ⁻³)	0.712/−0.444	0.695/−0.244
GoF (on <i>F</i> ²)	1.101	1.079
<i>R</i> ₁ ^(a) [<i>I</i> > 2 <i>σ</i> (<i>I</i>)]	0.0543	0.0424
<i>wR</i> ₂ ^(b) [<i>I</i> > 2 <i>σ</i> (<i>I</i>)]	0.1453	0.1097

^(a)*R*₁ = Σ(|*F*_o| − |*F*_c|)/Σ(|*F*_o|); ^(b)*wR*₂ = {Σ[*w*(*F*_o² − *F*_c²)²]/Σ[*w*(*F*_o²)²]}^{1/2}, *w* = 1/[*σ*²(*F*_o²) + (*aP*)² + *bP*] where *P* = (max(*F*_o², 0) + 2*F*_c²)/3.

2.2.2. *Preparation of [Co(pao)₂(bpy)]Cl·1.5MeOH (2·1.5MeOH)*. To a pink, stirred solution of CoCl₂ (0.07 g, 0.5 mmol) in MeOH (15 cm³) was added solid paoH (0.12 g, 1.0 mmol). To the resulting deep orange solution a colourless solution of bpy (0.08 g, 0.5 mmol) in the same solvent (5 cm³) was added. The solution was stirred at ambient temperature for 25 min, filtered, and the filtrate was layered with Et₂O/n-hexane (40 cm³, 1 : 1 v/v). Slow mixing gave well-formed, X-ray quality crystals of the product. The reddish orange prismatic crystals were collected by filtration, washed with cold MeOH (2 × 3 cm³) and Et₂O (2 × 3 cm³), and dried in air. Yields as high as 75% were obtained. The crystals were found to lose solvent readily; the dried sample analysed for [Co(pao)₂(bpy)]Cl, that is, **2** (found: C, 53.3; H, 3.4; N, 17.2. C₂₂H₁₈CoN₆O₂Cl calcd.: C, 53.6; H, 3.7; N, 17.1%).

2.3. *X-Ray Crystallographic Studies [1]*. Suitable crystals of **1**·2H₂O were sealed in capillary filled with drops of

the mother liquor, while crystals of **2**·1.5MeOH were mounted in air and covered with epoxy glou. Diffraction measurements of **1**·2H₂O and **2**·1.5MeOH were made on a Crystal Logic dual goniometer diffractometer using graphite-monochromated Mo radiation. Crystal data and full details of the data collection and data processing are listed in Table 1. Unit cell dimensions were determined and refined by using three angular settings of 25 automatically centred reflections in the range 11° < 2*θ* < 23° for both complexes. Three standard reflections, monitored every 97 reflections, showed less than 3% intensity variation and no decay. Lorentz-polarisation corrections were applied for **1**·2H₂O and **2**·1.5MeOH using Crystal Logic software.

The structures were solved by direct methods using SHELXS-97 [19] and refined by full matrix least-squares on *F*² with SHELXL-97 [20]. For both structures, all non-H atoms were refined using anisotropic thermal parameters. Some H-atoms were located by difference maps and refined isotropically. No H-atoms for the solvate molecules of **1**·2H₂O were included in the refinement.

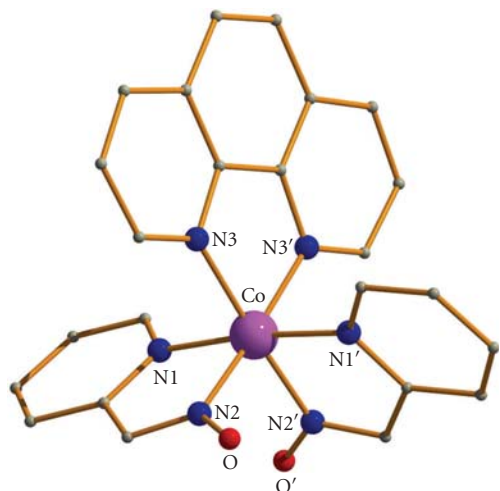


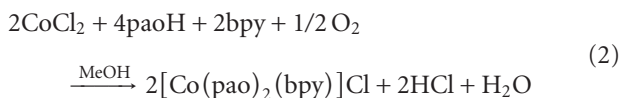
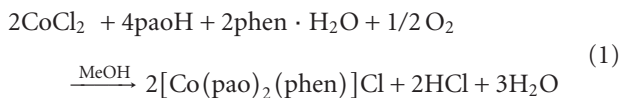
FIGURE 2: Partially labeled plot of the molecular structure of the cation that is present in $1 \cdot 2\text{H}_2\text{O}$. Primes are used for symmetry related atoms. H atoms have been omitted for clarity.

Reference [1] CCDC codes are 771333 and 771334 for complexes $1 \cdot 2\text{H}_2\text{O}$ and $2 \cdot 1.5\text{MeOH}$, respectively.

3. Experiments

3.1. Synthetic Comments. The reaction system that we investigated was the $\text{CoCl}_2/\text{paoH}/\text{phen}$ or bpy one. Treatment of a solution of CoCl_2 with two equivalents of paoH and one equivalent of 1,10-phenanthroline (phen) in MeOH, under aerobic conditions, followed by slow evaporation of the resulting solution allowed orange crystals of the product to be obtained in a form suitable for crystallography. The product was identified as the cationic mononuclear complex $[\text{Co}(\text{pao})_2(\text{phen})]\text{Cl} \cdot 2\text{H}_2\text{O}$ ($1 \cdot 2\text{H}_2\text{O}$). Following a similar reaction scheme and replacing only the corresponding bidentate ligand with 2,2'-bipyridine (bpy), we were able to obtain red crystals suitable for crystallography. The new product was identified as $[\text{Co}(\text{pao})_2(\text{bpy})]\text{Cl} \cdot 1.5\text{MeOH}$ ($2 \cdot 1.5\text{MeOH}$).

The most noticeable feature of this reaction scheme is the deprotonation of the oximate group without the presence of a strong base in the reaction system. Reduction products of the atmospheric oxygen, which is responsible for $\text{Co}^{\text{II}} \rightarrow \text{Co}^{\text{III}}$ oxidation, are possible agents for the former deprotonation. The formation of **1** and **2** can be summarized by the stoichiometric equations (1) and (2), respectively,



The following experimental points should be mentioned at this point. (a) The reactions between CoCl_2 , paoH and $\text{N,N}'$ -donor ligands in MeOH are $[\text{OH}^-]$ -independent.

Addition of one equivalent of $\text{LiOH} \cdot \text{H}_2\text{O}$ in the above described reaction mixtures leads to complexes $1 \cdot 2\text{H}_2\text{O}$ and $2 \cdot 1.5\text{MeOH}$ as well as to unidentified noncrystalline, hydroxo compounds. (b) A number of attempts were made for the isolation of new products by increasing or decreasing the paoH/Co reaction ratio, keeping constant (1 : 1) the phen or $\text{bpy} : \text{Co}$ ratio. Increasing the former ratio, that is, to 3 : 1 or 4 : 1, complexes **1** and **2** remained the main products; however, these were contaminated with variable amounts of the known product $[\text{Co}^{\text{III}}(\text{pao})_3]$ [21] (analytical evidence, unit cell determination of the isolated dark orange crystals). Reducing the above reaction ratio (1 : 1 and/or 0.5/1), paoH -“free” products were isolated containing only bpy or phen and chloride ions. We have not yet found evidence for the existence of the mixed-ligand species $[\text{Co}(\text{pao})(\text{phen})_2]\text{Cl}_2$ and $[\text{Co}(\text{pao})(\text{bpy})_2]\text{Cl}_2$. (c) Both complexes are soluble in water, dimethylformamide, dimethylsulfoxide, and acetonitrile, less soluble in nitromethane and ethanol, and insoluble in benzene, chloroform and dichloromethane.

3.2. Description of Structures. Labeled ORTEP plots of complexes $1 \cdot 2\text{H}_2\text{O}$ and $2 \cdot 1.5\text{MeOH}$ are shown in Figures 2 and 4, respectively. Selected bond distances and angles for complexes $1 \cdot 2\text{H}_2\text{O}$ and $2 \cdot 1.5\text{MeOH}$ are listed in Table 2.

Disregarding the different nature of the $\text{N,N}'$ -donor ligands, compounds $1 \cdot 2\text{H}_2\text{O}$ and $2 \cdot 1.5\text{MeOH}$ display strikingly similar molecular structures. Thus, only the structure of the former will be described in detail.

Complex $1 \cdot 2\text{H}_2\text{O}$ crystallizes in the tetragonal space group $I4_1/acd$. Its structure consists of the mononuclear $[\text{Co}(\text{pao})_2(\text{phen})]^+$ cation, one chloride ion, and two solvate water molecules; the latter three will not be further discussed. The metal ion lies on a crystallographic 2-fold axis. The Co^{III} center is in a six-coordinate ligand environment comprising the two nitrogens from two chelating, anionic pao^- ligands, $[\text{N}(1)/\text{N}(2)$ and their symmetry-related partners] and two aromatic nitrogens from the chelating phen molecule $[\text{N}(3)$ and $\text{N}(3')]$. The metal coordination geometry is well described as distorted octahedral, its chromophore being $\text{Co}^{\text{III}}\text{N}_6$. Two *trans* positions of the octahedron are occupied by the pyridyl nitrogen atoms of the two pao^- ligands $[\text{N}(1)-\text{Co}-\text{N}(1') = 173.8(3)^\circ]$; thus, the two oximate nitrogen atoms $[\text{N}(2), \text{N}(2')]$ are in *cis* position. Angular distortions from perfect octahedral geometry are primarily a consequence of the chelating rings and their restricted bite angles. The $\text{Co}-\text{N}$ bond lengths agree well with values expected for low-spin Co^{III} in octahedral environments [21].

In the crystal lattice of $1 \cdot 2\text{H}_2\text{O}$, the molecules interact through hydrogen bonds forming 1D zig-zag chains (Figure 3). These include the water lattice molecules, the oximate oxygen atom, and the Cl^- counteranion; their dimensions are presented in Table 3.

Complex $2 \cdot 1.5\text{MeOH}$ crystallizes in the orthorhombic space group $Ic2m$; the metal ion lies on a crystallographic twofold axis. One half of the molecule comprises the asymmetric unit of the structure. The three ligands are $\text{N,N}'$ -bidentate chelating. Again the pyridyl nitrogen atoms of the two pao^- ligands are in *trans* positions. A packing diagram of the complex is shown in Figure 5.

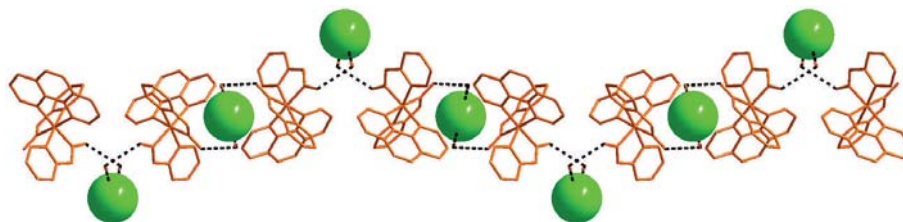


FIGURE 3: A part of the 1D structure of $1 \cdot 2\text{H}_2\text{O}$ due to H-bonding interactions (dashed lines) along the a axis. Chlorides (green) are emphasized using space filling models.

TABLE 2: Selected bond distances (\AA) and angles ($^\circ$) for complexes $1 \cdot 2\text{H}_2\text{O}$ and $2 \cdot 1.5\text{MeOH}$,^a with the estimated standard deviations in parentheses.

	$1 \cdot 2\text{H}_2\text{O}$	$2 \cdot 1.5\text{MeOH}$
<i>Bond distances</i>		
Co–N(1)	1.928(4)	1.937(3)
Co–N(2)	1.904(4)	1.909(4)
Co–N(3)	1.986(4)	1.977(4)
Co–N(1')	1.928(4)	1.937(3)
Co–N(2')	1.904(4)	1.909(4)
Co–N(3')	1.986(4)	1.977(4)
N(2)–O/O(1)	1.294(6)	1.273(5)
N(3)–C(7)	1.322(7)	1.343(6)
N(1)–C(1)	1.343(7)	1.340(6)
N(2)–C(6)	1.298(7)	1.309(7)
<i>Bond angles</i>		
N(3)–Co–N(3')	82.7(2)	82.2(2)
N(1)–Co–N(3)	88.6(2)	93.6(2)
N(1)–Co–N(2)	83.7(2)	83.7(2)
N(2)–Co–N(2')	89.9(3)	89.8(2)
N(1)–Co–N(3')	96.1(2)	90.7(2)
Co–N(2)–O/O(1)	122.7(4)	123.3(3)

^aUnprimed and primed atoms are related by symmetry.

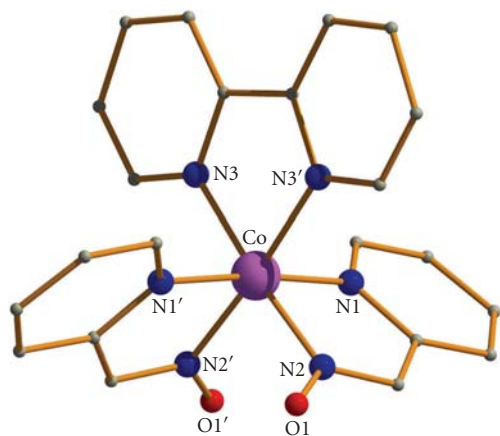


FIGURE 4: Partially labeled plot of the molecular structure of the cation that is present in $2 \cdot 1.5\text{MeOH}$. H atoms have been omitted for clarity. Primes are used for symmetry related atoms.

Since the space group of $1 \cdot 2\text{H}_2\text{O}$ is centrosymmetric and the space group of $2 \cdot 1.5\text{MeOH}$ involves a mirror plane, both complexes are racemic mixtures of their Δ and Λ enantiomorphs.

Complexes **1** and **2** join a small family of structurally characterized homo- [17, 18, 21] and heterometallic [22, 23] Co complexes featuring pao^- as ligand. Many years ago Blackmore and Magee [24, 25] and Grant and Magee [26] studied the reactions between 2-pyridinealdehyde and various Co^{II} sources under a variety of reaction conditions. Structural assignments of the solid products [24, 26] were based on spectroscopic data; no X-ray structures were reported. The authors did not prepare mixed-ligand complexes.

3.3. Physical and Spectroscopic Characterization. Complexes **1** and **2** are diamagnetic, in accordance with their low-spin $3d^6$ character.

TABLE 3: Hydrogen bonding interactions in $1 \cdot 2\text{H}_2\text{O}$.

Interaction D–H···A	D···A (Å)	H···A (Å)	D–H···A (°)	Symmetry operation of A
OW–HWA···O	2.854(7)	1.740(4)	161.7(3)	x, y, z
OW–HWB···Cl	3.124(6)	1.978(2)	163.5(3)	x, y, z

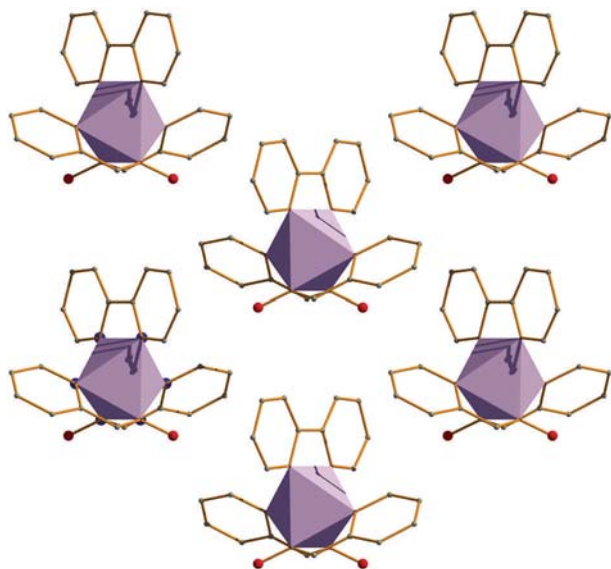


FIGURE 5: Packing diagram of complex $2 \cdot 1.5\text{MeOH}$ along the c axis. The metal coordination spheres are polyhedron designed (purple). The chloride counteranions and the methanol solvate molecules have been omitted.

The solid-state (diffuse reflectance) UV-Vis spectra of the two complexes are almost identical and typical for low-spin $\text{Co}^{\text{III}}\text{N}_6$ chromophores [27]. The low-spin octahedral ground term is $^1A_{1g}$, and there are two relatively low lying spin allowed transitions, with lower lying spin triplet partners, all derived from $(t_{2g})^5(e_g)$. Under this scheme, the bands in the spectra of **1** and **2** at ~ 29.0 , 21.5 , 17.0 , and 13.5 kK are assigned [27] to the $^1A_{1g} \rightarrow ^1T_{2g}$, $^1T_{1g}$, $^3T_{2g}$, and $^3T_{1g}$ transitions, respectively, although a superposition of the highest energy d-d transition and a charge transfer band should not be ruled out.

Two bands, one of medium intensity at $\sim 1015\text{ cm}^{-1}$ assigned to $\nu(\text{N}=\text{O})$ and one strong at 1599 cm^{-1} assigned to $\nu(\text{C}=\text{N})_{\text{-oximate}}$ are common in the IR spectra of the two complexes [21]; the higher-wavenumber band most probably overlaps with an aromatic stretch. The in-plane deformation of the 2-pyridyl ring of the free paoH at 627 cm^{-1} shifts upward on coordination in the spectra of **1** (643 cm^{-1}) and **2** (645 cm^{-1}) [28].

4. Conclusions

The present work extends the body of results that emphasizes the ability of the monoanionic ligand pao[−] to form interesting structural types in 3d metal chemistry. The use of both paoH and phen or bpy in reactions with Co^{II} sources

has led to products **1** and **2**, the first mixed-ligand Co^{III} noncarboxylate complexes involving paoH/pao[−]. Of interest is the nonparticipation of the deprotonated oximate oxygen atom in coordination; this is due to the involvement of the negatively charged oxygen in hydrogen bonding.

Complexes of trivalent 3d metals (e.g., Cr^{III} , Mn^{III} , Fe^{III}) other than Co^{III} with the pao[−]/phen or bpy ligand combinations are not known to date, and it is currently not evident whether the structures of such compounds are dependent on the particular nature of the metal ion. We are studying this matter. Synthetic efforts are also in progress to use **1** and **2** as “metalloligands” for the preparation of heterometallic $\text{Co}^{\text{III}}/\text{M}^{\text{III}}$ complexes ($\text{M} = \text{Fe}, \text{Mn}, \text{lanthanides}$).

Acknowledgments

E. Manessi-Zoupa and K. F. Konidaris thank the Research Committee of the University of Patras for funding this work (C. Karatheodory Grant 2008, No. C.584). This paper is dedicated to Professor Nick Hadjiliadis for his great contributions to Bioinorganic Chemistry and with the authors’ best wishes for his retirement life

References

- [1] J. J. Christensen, D. J. Eatough, and R. M. Izatt, “The synthesis and ion binding of synthetic multidentate macrocyclic compounds,” *Chemical Reviews*, vol. 74, no. 3, pp. 351–384, 1974.
- [2] S. S. Jurisson and J. D. Lydon, “Potential technetium small molecule radiopharmaceuticals,” *Chemical Reviews*, vol. 99, no. 9, pp. 2205–2218, 1999.
- [3] W. A. Volkert and T. J. Huffman, “Therapeutic radiopharmaceuticals,” *Chemical Reviews*, vol. 99, no. 9, pp. 2269–2292, 1999.
- [4] P. Mitchell, “Keilin’s respiratory chain concept and its chemiosmotic consequences,” *Science*, vol. 206, no. 4423, pp. 1148–1159, 1979.
- [5] M. Bakir and J. A. M. McKenzie, “Rhenium(I) di- and tri-carbonyl compounds of polypyridyl-like ligands: electrochemical reactions of fac-[Re(CO)₃(dpk)Cl] (dpk = di-2-pyridyl ketone) with electrophiles and Group I and II metal ions,” *Journal of the Chemical Society, Dalton Transactions*, no. 19, pp. 3571–3578, 1997.
- [6] J. G. Clement, “Efficacy of Pro-PAM (N-methyl-1,6-dihydropyridine-2-carbaldoxime hydrochloride) as a prophylaxis against organophosphate poisoning,” *Toxicology and Applied Pharmacology*, vol. 47, no. 2, pp. 305–311, 1979.
- [7] N. P. Farrell, *Uses of Inorganic Chemistry in Medicine*, The Royal Society of Chemistry, London, UK, 1999.
- [8] J. E. Weder, T. W. Hambley, B. J. Kennedy, P. A. Lay, G. J. Foran, and A. M. Rich, “Determination of the structures of antiinflammatory copper(II) dimers of indomethacin by multipie-scattering analyses of X-ray absorption fine structure data,” *Inorganic Chemistry*, vol. 40, no. 6, pp. 1295–1302, 2001.

- [9] Q. Zhou, T. W. Hambley, B. J. Kennedy et al., "Syntheses and characterization of anti-inflammatory dinuclear and mononuclear zinc indomethacin complexes. Crystal structures of $[\text{Zn}_2(\text{Indomethacin})_4(\text{L})_2]$ ($\text{L} = \text{N,N}$ -dimethylacetamide, pyridine, 1-methyl-2-pyrrolidinone) and $[\text{Zn}(\text{Indomethacin})_2(\text{L}_1)_2]$ ($\text{L}_1 = \text{ethanol, methanol}$)," *Inorganic Chemistry*, vol. 39, no. 17, pp. 3742–3748, 2000.
- [10] P. Chaudhuri, "Homo- and hetero-polymetallic exchange coupled metal-oximates," *Coordination Chemistry Reviews*, vol. 243, no. 1-2, pp. 143–190, 2003.
- [11] H.-J. Krüger, G. Peng, and R. H. Holm, "Low-potential nickel(III,II) complexes: new systems based on tetradentate amidate-thiolate ligands and the influence of ligand structure on potentials in relation to the nickel site in $[\text{NiFe}]$ -hydrogenases," *Inorganic Chemistry*, vol. 30, no. 4, pp. 734–742, 1991.
- [12] C. J. Milios, C. P. Raptopoulou, A. Terzis et al., "Hexanuclear manganese(III) single-molecule magnets," *Angewandte Chemie International Edition*, vol. 43, no. 2, pp. 210–212, 2004.
- [13] C. J. Milios, E. Kefalloniti, C. P. Raptopoulou et al., "2-Pyridinealdoxime [(py)CHNOH] in manganese(II) carboxylate chemistry: mononuclear, dinuclear, tetranuclear and polymeric complexes, and partial transformation of (py)CHNOH to picolinate(-1)," *Polyhedron*, vol. 23, no. 1, pp. 83–95, 2004.
- [14] C. J. Milios, C. P. Raptopoulou, A. Terzis, R. Vicente, A. Escuer, and S. P. Perlepes, "Di-2-pyridyl ketone oxime in 3d-metal carboxylate cluster chemistry: a new family of mixed-valence $\text{Mn}^{\text{II}}\text{Mn}^{\text{III}}$ complexes," *Inorganic Chemistry Communications*, vol. 6, no. 8, pp. 1056–1060, 2003.
- [15] C. J. Milios, Th. C. Stamatatos, and S. P. Perlepes, "The coordination chemistry of pyridyl oximes," *Polyhedron*, vol. 25, no. 1, pp. 134–194, 2006.
- [16] Th. C. Stamatatos, S. Dionyssopoulou, G. Efthymiou et al., "The first cobalt metallacrowns: preparation and characterization of mixed-valence cobalt(II/III), inverse 12-metallacrown-4 complexes," *Inorganic Chemistry*, vol. 44, no. 10, pp. 3374–3376, 2005.
- [17] Th. C. Stamatatos, A. Bell, P. Cooper et al., "Old ligands with new coordination chemistry: linear trinuclear mixed oxidation state cobalt(III/II/III) complexes and their mononuclear "ligand" cobalt(III) complexes featuring 2-pyridyloximates," *Inorganic Chemistry Communications*, vol. 8, no. 6, pp. 533–538, 2005.
- [18] C. P. Raptopoulou and V. Psycharis, "2-Pyridyl aldoxime in cobalt carboxylate chemistry: synthesis and characterization of trinuclear complexes," *Inorganic Chemistry Communications*, vol. 11, no. 10, pp. 1194–1197, 2008.
- [19] G. M. Sheldrick, *SHELXS-97, Structure Solving Program*, University of Göttingen, Göttingen, Germany, 1997.
- [20] G. M. Sheldrick, *SHELXL-97, Crystal Structure Refinement Program*, University of Göttingen, Göttingen, Germany, 1997.
- [21] Th. C. Stamatatos, E. Katsoulakou, A. Terzis, C. P. Raptopoulou, R. E. P. Winpenny, and S. P. Perlepes, "A family of mononuclear $\text{Co}^{\text{III}}/2$ -pyridyloximate complexes and their conversion to trinuclear, mixed-valence linear $\text{Co}^{\text{II/III}}_3$ clusters," *Polyhedron*, vol. 28, no. 9-10, pp. 1638–1645, 2009.
- [22] S. Ross, T. Weyhermüller, E. Bill et al., "Asymmetric heterodinuclear $\text{Fe}^{\text{III}}\text{M}^{\text{II}}$ ($\text{M} = \text{Zn, Cu, Ni, Fe, Mn}$), $\text{Co}^{\text{III}}\text{Fe}^{\text{II}}$ and $\text{Fe}^{\text{II}}\text{Co}^{\text{III}}$ species: synthesis, structure, redox behavior, and magnetism," *European Journal of Inorganic Chemistry*, no. 5, pp. 984–997, 2004.
- [23] S. Ross, T. Weyhermüller, E. Bill, K. Wieghardt, and P. Chaudhuri, "Tris(pyridinealdoximate)metal complexes as ligands for the synthesis of asymmetric heterodinuclear $\text{Cr}^{\text{III}}\text{M}$ species [$\text{M} = \text{Zn(II), Cu(II), Ni(II), Fe(II), Mn(II), Cr(II), Co(III)}$]: a magneto-structural study," *Inorganic Chemistry*, vol. 40, no. 26, pp. 6656–6665, 2001.
- [24] M. W. Blackmore and R. J. Magee, "Studies on the structures of cobalt pyridinealdoximates. I. The preparation and structural investigation of those complexes containing chlorine," *Australian Journal of Chemistry*, vol. 20, pp. 429–438, 1967.
- [25] M. W. Blackmore and R. J. Magee, "An investigation of the slow reaction in aqueous medium between cobalt ions and 2-pyridinealdoxime," *Journal of Inorganic and Nuclear Chemistry*, vol. 31, no. 9, pp. 2859–2869, 1969.
- [26] M. W. Grant and R. J. Magee, "The reaction between cobalt(II) ions and pyridine-2-carbaldehyde oxime in aqueous solution," *Australian Journal of Chemistry*, vol. 27, no. 9, pp. 2475–2482, 1974.
- [27] A. B. P. Lever, *Inorganic Electronic Spectroscopy*, Elsevier, Amsterdam, The Netherlands, 2nd edition, 1984.
- [28] Th. C. Stamatatos, A. Escuer, K. A. Abboud, C. P. Raptopoulou, S. P. Perlepes, and G. Christou, "Unusual structural types in nickel cluster chemistry from the use of pyridyl oximes: Ni_5 , $\text{Ni}_{12}\text{Na}_2$, and Ni_{14} clusters," *Inorganic Chemistry*, vol. 47, no. 24, pp. 11825–11838, 2008.

Research Article

Synthesis, Structure, and Antiproliferative Activity of Three Gallium(III) Azole Complexes

Stergios Zanias,¹ Giannis S. Papaefstathiou,² Catherine P. Raptopoulou,³ Konstantinos T. Papazisis,⁴ Vasiliki Vala,⁴ Dimitra Zambouli,⁴ Alexandros H. Kortsaris,⁴ Dimitrios A. Kyriakidis,^{5,6} and Theodoros F. Zafirooulos¹

¹ Department of Chemistry, University of Patras, 265 04 Patras, Greece

² Laboratory of Inorganic Chemistry, Department of Chemistry, National and Kapodistrian University of Athens, Panepistimiopolis, 157 71 Zografou, Greece

³ Institute of Materials Science, NCSR "Demokritos", 153 10 Aghia Paraskevi Attikis, Greece

⁴ "Theagenion" Cancer Hospital, Al. Simeonides str. 2, 540 07 Thessaloniki, Greece

⁵ Department of Chemistry, Aristotle University of Thessaloniki, 541 24 Thessaloniki, Greece

⁶ The National Hellenic Research Foundation, 48, Vas. Constantinou Ave, 116 35 Athens, Greece

Correspondence should be addressed to Dimitrios A. Kyriakidis, kyr@eie.gr and Theodoros F. Zafirooulos, tzafir@chemistry.upatras.gr

Received 25 March 2010; Accepted 1 May 2010

Academic Editor: Spyros Perlepes

Copyright © 2010 Stergios Zanias et al. This is an open access article distributed under the Creative Commons Attribution License, which permits unrestricted use, distribution, and reproduction in any medium, provided the original work is properly cited.

As part of our interest into the bioinorganic chemistry of gallium, gallium(III) complexes of the azole ligands 2,1,3-benzothiadiazole (btd), 1,2,3-benzotriazole (btaH), and 1-methyl-4,5-diphenylimidazole (L) have been isolated. Reaction of btaH or btd with GaBr₃ or GaCl₃ resulted in the mononuclear complexes [GaBr₃(btaH)₂] (1) and [GaCl₃(btd)₂] (2), respectively, while treatment of GaCl₃ with L resulted in the anionic complex (LH)₂[GaCl₄] (3). All three complexes were characterized by single-crystal X-ray crystallography and IR spectroscopy, while their antiproliferative activities were investigated against a series of human and mouse cancer cell lines.

1. Introduction

The coordination chemistry of gallium(III) has become an area of increasing research activity due to its relevance with both materials science [1–6] and biomedical developments [7–21]. In the area of materials science, for example, complex [Ga₂(saph)₂q₂], where saph²⁻ is the Schiff-base ligand bis(salicylidene-o-aminophenolate)(-2) and q⁻ is 8-quinolate(-1), is a very good candidate as a novel electron-transporting and emitting material for organic light-emitting diodes (OLEDs) [4]. [Gaq₃] is also a promising electroluminescence (EL) material, exhibiting higher power efficiency than the aluminum analogue, [Alq₃] [5, 6]. The biological interest of gallium(III) complexes originates from the incorporation of gallium(III) radionuclides (⁶⁷Ga³⁺, ⁶⁸Ga³⁺) into diagnostic radiopharmaceuticals [7]. In addition, the gallium salts GaCl₃ and Ga(NO₃)₃ as well as few gallium(III)

complexes [8–19] have exhibited antitumour activity, while Ga(NO₃)₃ and some GaCl₃/L complexes (L = various azoles) showed in vitro anti-HIV (HIV = human immunodeficiency virus) activity [20]. The biological activity of gallium(III) complexes has often been attributed to the fact that gallium(III) is the diamagnetic biological mimic of iron(III) [21]. It is worth mentioning that [Gaq₃], which is of current interest in materials science [5, 6], is also being evaluated in clinical trials, along with other Ga(III) complexes, such as gallium maltolate [tris(3-hydroxy-2-methyl-4H-pyran-4-onato)gallium(III)], for anticancer activity [22–24].

Following our interest in the coordination chemistry of gallium(III) [25–31] which is focused on the synthesis, structural characterization, physical/spectroscopic study and evaluation of the biological (antitumour and antiviral) activity of Ga(III) complexes with biologically relevant and nonrelevant ligands, we report herein the synthesis,

structural characterization, and antiproliferative activity of three gallium complexes based on the azole ligands 2,1,3-benzothiadiazole (btd), 1,2,3-benzotriazole (btaH), and 1-methyl-4,5-diphenylimidazole (L).

2. Experimental

2.1. Reagents and Physical Measurements. All manipulations were performed under a dinitrogen atmosphere, using standard inert atmosphere techniques and purified solvents unless otherwise noted. All other chemicals were purchased from commercial sources and used without further purification. L was synthesized as described elsewhere [32]. Microanalyses (C, H, and N) were performed by the University of Ioannina Microanalytical Laboratory using an EA 1108 Carlo Erba analyzer. IR spectra (4000–450 cm^{-1}) were recorded on a Perkin-Elmer 16 PC spectrometer with samples prepared as KBr pellets. Far-IR spectra (500–50 cm^{-1}) were recorded on a Bruker IFS 113v FT spectrometer as polyethylene pellets.

2.2. Compound Preparation

2.2.1. Preparation of $[\text{GaBr}_3(\text{btaH})_2]$ (1). A solution of GaBr_3 (0.3 g, 0.9 mmol) in 3 ml of toluene/diethyl ether (80 : 20, v/v) was added dropwise to a stirred solution of btaH (0.3 g, 2.5 mmol) in toluene (20 ml). The resultant solution was refluxed for about 3 hours and then left undisturbed at room temperature. Upon standing, X-ray quality colorless crystals of **1** formed over a period of 3 days. The crystals were collected by filtration, washed with toluene and dried in vacuum. Yield: 0.31 g (63%); *Anal. Calc.* for $\text{C}_{12}\text{H}_{10}\text{N}_6\text{Br}_3\text{Ga}$: C, 26.32; H, 1.84; N, 15.34. Found: C, 26.28; H, 1.82; N, 15.33%. Selected IR data (cm^{-1}): 3238 m [$\nu(\text{N-H})$], 1222 m [$\nu(\text{N=N})$], 1116 s [$\nu(\text{N-N})$], 291s [$\nu(\text{Ga-Br})$], and 224w [$\nu(\text{Ga-N})$].

2.2.2. Preparation of $[\text{GaCl}_3(\text{btd})_2]$ (2). A solution of GaCl_3 (0.25 g, 1.40 mmol) in 5 ml of toluene/diethyl ether (80 : 20, v/v) was added dropwise to a stirred solution of btd (0.6 g, 4.4 mmol) in toluene/diethyl ether (60 : 40, v/v) (10 ml). The resultant solution was refluxed for about 2 hours and then left undisturbed at -10°C . Upon standing at low temperature for several days, X-ray quality yellowish crystals of **2** formed. The crystals were collected by filtration, washed with diethyl ether and dried in vacuum. Yield: 0.60 g (95%); m.p.: 112°C . *Anal. Calc.* for $\text{C}_{12}\text{H}_8\text{N}_4\text{S}_2\text{Cl}_3\text{Ga}$: C, 32.14; H, 1.80; N, 12.49. Found: C, 32.13; H, 1.78; N, 12.49%. Selected IR data (cm^{-1}): 1612 s and 1528 s [$\nu(\text{C=C})$], 1482 s [$\nu(\text{C=N})$], 961 m and 922 s [$\nu(\text{S-N})$], 382s [$\nu(\text{Ga-Cl})$], and 207 w [$\nu(\text{Ga-N})$].

2.2.3. Preparation of $(\text{LH})_2[\text{GaCl}_4]\text{Cl}$ (3). A solution of GaCl_3 (0.2 g, 1.13 mmol) in 5 ml of toluene/diethyl ether (80 : 20, v/v) was added dropwise to a stirred mixture of L (0.6 g, 2.6 mmol) in diethyl ether (1 ml). The resultant mixture was stirred until a clear yellowish solution was obtained. Slow evaporation of the resultant solution afforded

a microcrystalline solid. The solid was collected by filtration, washed with toluene and diethyl ether, and dried in vacuum. The product was recrystallised three times from toluene to give crystals of **3** suitable for X-ray structural analysis. The crystals were collected by filtration, washed with toluene and dried in vacuum. Yield: 0.18 g (45%); *Anal. Calc.* for $\text{C}_{32}\text{H}_{30}\text{N}_4\text{Cl}_5\text{Ga}$: C, 53.56; H, 4.21; N, 7.81. Found: C, 53.36; H, 4.17; N, 7.78%. Selected IR data (cm^{-1}): 3146–2620 sb [$\nu(\text{N-H})$], 1622 m [$\nu(\text{C=N})$], 1578 w [$\nu(\text{C=C})$], and 369s [$\nu(\text{Ga-Cl})$].

2.3. Single-Crystal X-Ray Crystallography. Crystals of **1** and **2** were mounted in air, while crystals of **3** were mounted in air and covered with epoxy glue. Diffraction measurements for **1** and **2** were made on a Crystal Logic Dual Goniometer diffractometer using graphite-monochromated Mo radiation, while those for **3** were made on a P21 Nicolet diffractometer using graphite-monochromated Cu radiation. Complete crystal data and parameters for data collection and processing are reported in Table 1. Unit cell dimensions were determined and refined by using the angular settings of 25 automatically centred reflections in the ranges $11 < 2\theta < 23^\circ$ for **1** and **2** and $22 < 2\theta < 54^\circ$ for **3**. Three standard reflections monitoring every 97 reflections showed less than 3% variation and no decay. Lorentz, polarization and ψ -scan (only for **1**) corrections were applied using CRYSTAL LOGIC software. The structures were solved by direct methods using SHELXS-86 [33] and refined by full-matrix least squares techniques on F^2 with SHELXL-97 [34]. All hydrogen atoms were located by difference maps and refined isotropically, except those on the methyl groups of **3** which were introduced at calculated positions as riding on bonded atoms. For all the three structures, all nonhydrogen atoms were refined using anisotropic thermal parameters.

2.4. In Vitro Cytotoxic Activity

2.4.1. Test Substances. All test substances (complexes **1**, **2**, and **3**) were diluted in methanol at a concentration of 200 mM. Final concentration of methanol in culture was always less than 0.5%, a concentration that produced no effects on cell growth and proliferation, as was experimentally confirmed.

2.4.2. Cell Lines. Cell lines used were HeLa [35] (human cervical cancer), OAW-42 [36] (human ovarian cancer), HT29 [37] (human colon cancer), MCF-7 [38] (human breast cancer), T47D [39] (human breast cancer), and L929 (929 is a clone isolated [40] from the parental strain L derived from normal subcutaneous areolar and adipose tissues of a mouse [41]). Cells were grown as monolayer cultures in T-75 flasks (Costar), were subcultured twice a week at 37°C in an atmosphere containing 5% CO_2 in air and 100% relative humidity. Culture medium used was Dulbecco's modified Eagle's medium (DMEM, Gibco Glasgow, UK), supplemented with 10% Fetal Bovine Serum (FBS, Gibco, Glasgow, UK), 100 $\mu\text{g}/\text{ml}$ streptomycin and 100 IU/ml penicillin.

2.4.3. Cell Growth and Proliferation Assays. Adherent cells at a logarithmic growth phase were detached by addition of 2–3 ml of a 0.05% trypsin (Gibco, 1:250) –0.02% EDTA mixture and incubation for 2–5 min at 37°C. Cells were plated (100 μ l per well) in 96-well flat-bottom microtiter plates (Costar-Corning, Cambridge) at a density of 5,000 (HeLa and L929) or 10,000 (HT-29, OAW-42, MCF-7 and T47D) cells per well. Cells were left for 24 h at 37°C to resume exponential growth. An equal volume (100 μ l) of either complete culture medium (control wells), or twice the final substance concentration diluted in complete culture medium, was added 24 h later. Six replicate wells for each concentration were used for the sulforhodamine B (SRB) assay and three replicate wells for the bromodeoxyuridine (BrdU) assay. Background control wells ($n = 8$), containing the same volume of complete culture medium, were included in each experiment. Cell growth or DNA-synthesis was evaluated 48 h later by means of the SRB or BrdU assays. All experiments were performed at least twice.

2.4.4. SRB Assay. The SRB assay was carried out by a modification [42] of the previously reported method [43]. In brief, culture medium was aspirated prior to fixation using a microplate-multiwash device (Tri-Continent Scientific, Inc. Grass Valley, CA) and 50 μ l of 10% cold (4°C) TCA were gently added to the wells. Microplates were left for 30 min at 4°C, washed 5 times with deionized water and left to dry at room temperature for at least 24 hr. Subsequently, 70 μ l 0.4% (w/v) sulforhodamine B (Sigma) in 1% acetic acid solution were added to each well and left at room temperature for 20 min. SRB was removed and the plates were washed 5 times with 1% acetic acid before air drying. Bound SRB was solubilized with 200 μ l 10 mM unbuffered Tris-base solution (E. Merck, Darmstadt, Germany) and plates were left on a plate shaker for at least 10 min. Absorbance was read in a 96-well plate reader (Anthos-2001, Anthos labteck instruments, A-5022, Salzburg) at 492 nm subtracting the background measurement at 620 nm. The test optical density (OD) value was defined as the absorbance of each individual well, minus the blank value (“blank” is the mean optical density of the background control wells, $n = 8$). Mean values and CV from six replicate wells were calculated automatically. Results were expressed as the “survival fraction” (sf), derived from the following equation: $sf = OD_x/OD_c$, (where OD_x and OD_c represent the test and the control optical density, resp.).

2.4.5. BrdU Assay. DNA-synthesis was estimated by the BrdU assay [44] using a standard colorimetric ELISA (Boehringer Mannheim). After 47 h exposure to test substances, cells were incubated at 37°C for further 60 min in the presence of 10 μ M BrdU. Subsequently, cells were fixed with an ethanol-containing fixative, an anti-BrdU mouse monoclonal antibody conjugated with peroxidase was added and plates were incubated at 37°C for 60 min. After washing, peroxidase substrate (tetramethylbenzidine) was added, the reaction was stopped 10 min later by 1 M H_2SO_4 and absorbance was read at

450 nm subtracting the background measurement at 620 nm. Results from each triplicate well (OD_{BrdU_x}/OD_{BrdU_c}) were divided by the results of a parallel experiment estimated with the SRB assay (OD_{SRB_x}/OD_{SRB_c}) and they were expressed as the “DNA synthesis fraction” (fDNA) (derived from the following equation: $fDNA = (OD_{BrdU_x} \times OD_{SRB_c}) / (OD_{BrdU_c} \times OD_{SRB_x})$, where OD_x and OD_c represent the test and the control optical density resp.), resulting in an estimation of the DNA synthesis per cell number.

2.4.6. Cell Cycle Analysis by Flow Cytometry. For cell cycle experiments 1.5×10^6 (HeLa and L929) or 2.5×10^6 (HT-29, OAW-42, MCF-7 and T47D) cells were seeded in 75 cm² flasks and left for 24 h in incubator to resume exponential growth. Cells were exposed to test substances (at concentrations that produced 50% inhibition of cell growth—estimated by the SRB assay) and after 48 h they were harvested (using trypsin/EDTA as above), washed in PBS and counted in a hemocytometer chamber; 3×10^6 cells were resuspended in 125 μ l cold “Saline GM” (g/L: glucose 1.1; NaCl 8.0; KCl 0.4; $Na_2HPO_4 \cdot 12H_2O$ 0.39; KH_2PO_4 0.15; and 0.5 mM EDTA) followed by the addition of 375 μ l of 95% nondenatured, ice-cold ethanol [45]. Cells were kept in 4°C for a maximum period of 3 days (short-term storage does not alter results, as was experimentally confirmed) until analysis was performed.

For cell cycle analysis a 10% of standard chicken erythrocyte nuclei were added as a control. The samples were processed in a DNA-preparation Epics Workstation (Coulter, El). By this method the content of cellular DNA is assessed using Propidium Iodide [46, 47]. To avoid an increased signal by staining artifact on double stranded RNA, cells were digested with DNase-free RNase A [48].

Cellular DNA content was measured using an Epics II flow cytometer (Coulter, El). The fluorescent signals from 10,000–20,000 cells were collected and the result was displayed as a frequency-distribution histogram (DNA histogram). The mean channel, cell count, standard deviation (SD), coefficient of variation (CV), DNA index (DI), and cell cycle distribution were calculated for each sample using the Multicycle Cell Cycle Analysis Software (Phoenix Flow Systems Inc.). Care was taken to exclude any doublets or cell debris noise from the assessment.

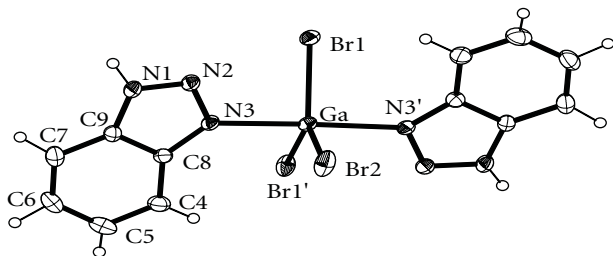
3. Results and Discussion

3.1. Brief Synthetic Comments. Complexes **1** and **2** were prepared by the simple reactions of $GaBr_3$ or $GaCl_3$ and btaH or btd in toluene/diethyl ether under nitrogen employing 1:3 molar ratios, respectively. A similar reaction involving $GaCl_3$ and btaH has yielded $[GaCl_3(btaH)_2]$ [25]. An 1:1 complex of $GaCl_3/btaH$ has also been isolated and structurally characterized [25]. An attempt to isolate the 1:1 $GaBr_3/btaH$ complex was unsuccessful resulting in **1** in a lower yield. Complex **2** is also the only product resulting from the $GaCl_3/btd$ reaction mixtures in various molar ratios. Complex **3** might be regarded as a product of

TABLE 1: Crystallographic data for complexes $[\text{GaBr}_3(\text{btaH})_2]$ (1), $[\text{GaCl}_3(\text{btd})_2]$ (2), and $(\text{LH})_2[\text{GaCl}_4]\text{Cl}$ (3).

	1	2	3
Empirical formula	$\text{C}_{12}\text{H}_{10}\text{N}_6\text{Br}_3\text{Ga}$	$\text{C}_{12}\text{H}_8\text{N}_4\text{S}_2\text{Cl}_3\text{Ga}$	$\text{C}_{32}\text{H}_{30}\text{N}_4\text{Cl}_5\text{Ga}$
Formula weight	547.68	448.42	717.60
Crystal colour, habit	Colourless, prism	Colourless, prism	Colourless, prism
Crystal dimensions (mm)	$0.15 \times 0.25 \times 0.40$	$0.20 \times 0.25 \times 0.40$	$0.15 \times 0.15 \times 0.35$
Crystal system	Monoclinic	Monoclinic	Triclinic
Space group	$I2/a$	$C2/c$	$P-1$
a (Å)	16.797(10)	12.098(11)	10.2358(10)
b (Å)	7.058(4)	7.525(6)	14.9649(16)
c (Å)	14.276(9)	18.968(16)	12.2350(11)
α (°)	90	90	69.235(4)
β (°)	106.60(2)	107.65(3)	86.879(3)
γ (°)	90	90	74.939(4)
V (Å ³)	1621.9(17)	1646(2)	1690.7(3)
Z	4	4	2
D_{calc} (g/cm ⁻³)	2.243	1.810	1.410
$F(000)$	1040	888	732
μ (mm ⁻¹)	9.091	2.411	4.966
Radiation (λ , Å)	0.71073	0.71073	1.54180
Temperature (K)	298	298	298
Scan mode	$\theta-2\theta$	$\theta-2\theta$	$\theta-2\theta$
Scan speed (° min ⁻¹)	3.5	4.2	4.5
Scan range (°)	$2.3 + \alpha_1\alpha_2$ separation	$2.4 + \alpha_1\alpha_2$ separation	$2.25 + \alpha_1\alpha_2$ separation
θ range (°)	2.53–25.00	2.25–24.99	3.67–61.97
hkl ranges	0 to 19 0 to 8 –16 to 16	–14 to 13 –8 to 0 0 to 22	–10 to 9 –14 to 17 0 to 14
Reflections collected	1486	1499	4586
Independent reflections (R_{int})	1430 (0.0250)	1450 (0.0219)	4368 (0.0149)
No of refined parameters	121	118	479
Observed reflections [$I > 2\sigma(I)$]	1293	1341	3740
GOF (on F^2)	1.143	1.062	1.087
Final R indices ^a [$I > 2\sigma(I)$]	$R_1 = 0.0332$ $wR2 = 0.0903$	$R_1 = 0.0301$ $wR2 = 0.0826$	$R_1 = 0.0345$ $wR2 = 0.0830$
R indices ^a (all data)	$R_1 = 0.0375$ $wR2 = 0.0930$	$R_1 = 0.0333$ $wR2 = 0.0852$	$R_1 = 0.0448$ $wR2 = 0.1009$
Largest difference peak and hole (e Å ⁻³)	0.681 and –1.263	0.546 and –0.387	0.418 and –0.493

^a Defined as: $R_1 = \Sigma(|F_o| - |F_c|)/\Sigma(|F_o|)$, $wR2 = \{\Sigma[w(F_o^2 - F_c^2)]/\Sigma[w(F_o^2)]\}^{1/2}$, where $w = 1/[\sigma^2(F_o^2) + (aP)^2 + (bP)]$ with $P = [\max(F_o^2, 0) + 2F_c^2]/3$.

FIGURE 1: A labeled ORTEP plot of $[\text{GaBr}_3(\text{btaH})_2]$ (1) showing 30% probability ellipsoids.

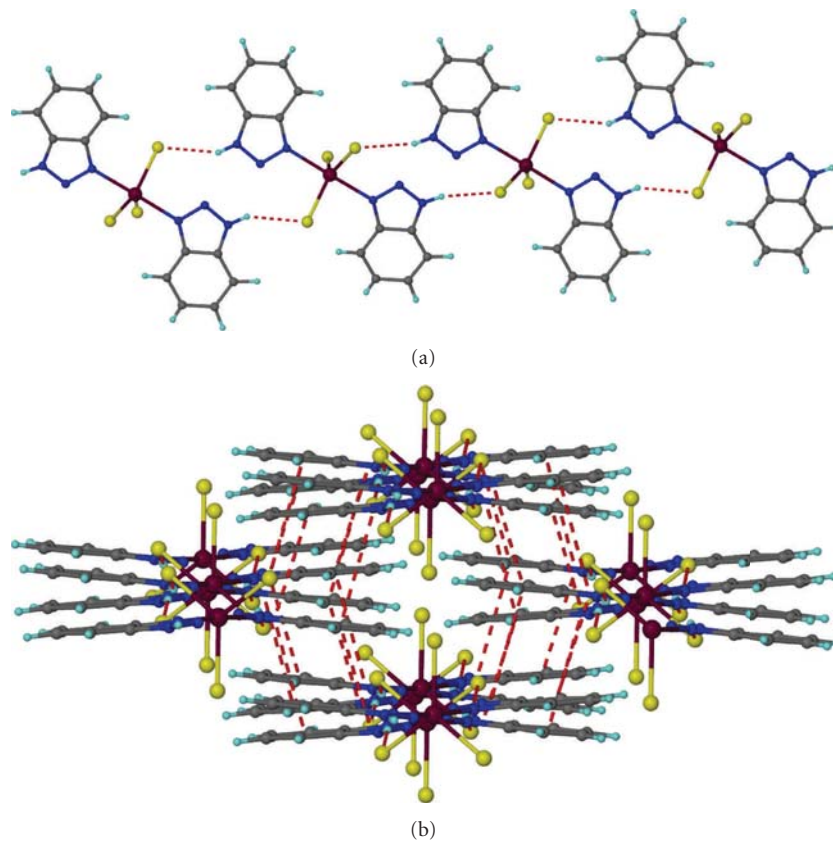


FIGURE 2: The hydrogen-bonded tape of $[\text{GaBr}_3(\text{btaH})_2]$ (1) running parallel to *a* axis (a) and the stacking of the tapes (b).

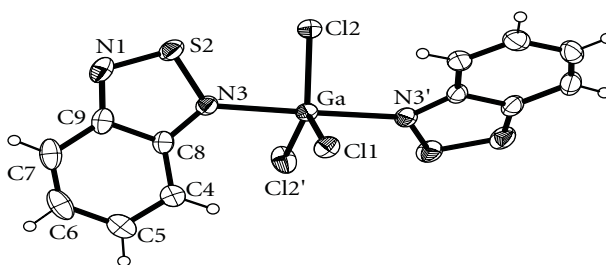


FIGURE 3: A labeled ORTEP plot of $[\text{GaCl}_3(\text{btd})_2]$ (2) showing 30% probability ellipsoids.

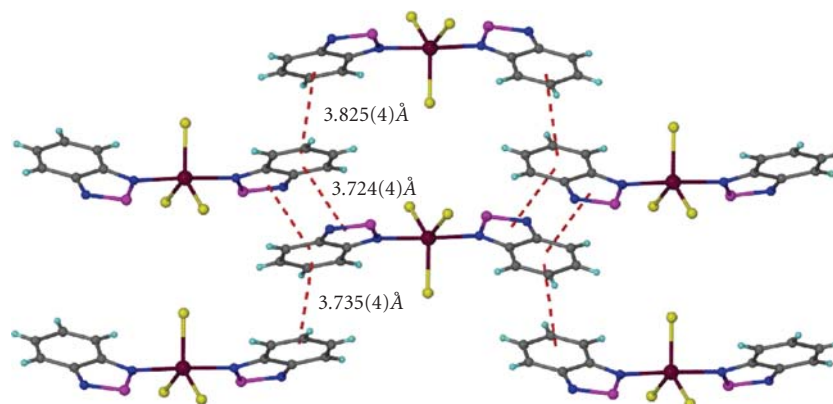


FIGURE 4: The stacking of the $[\text{GaCl}_3(\text{btd})_2]$ molecules in 2.

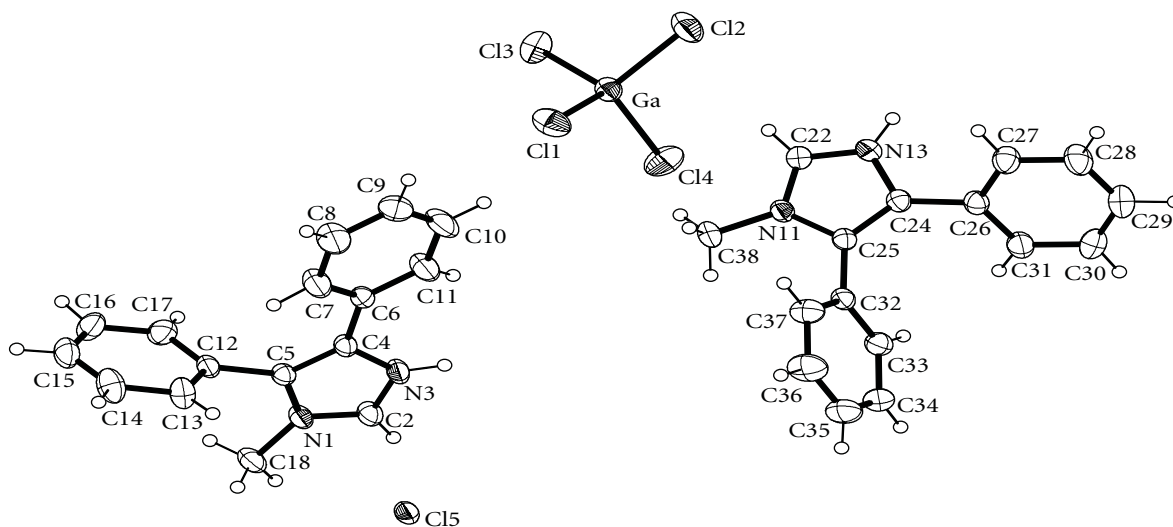


FIGURE 5: A labeled ORTEP plot of the asymmetric unit of $(LH)_2[GaCl_4]Cl$ (**3**), showing 30% probability ellipsoids.

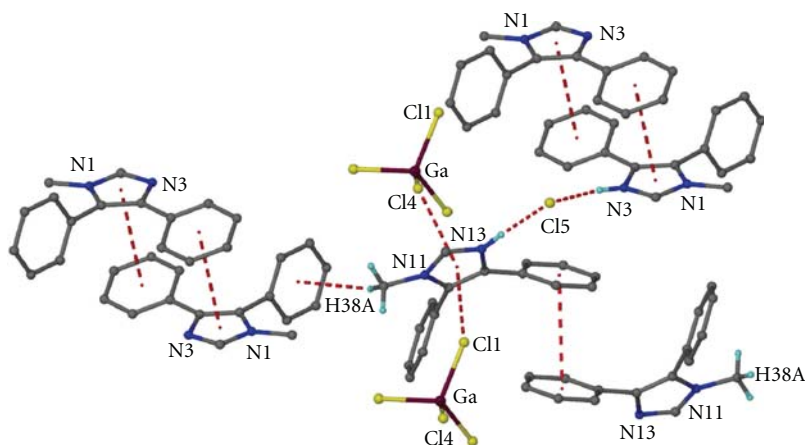


FIGURE 6: The intermixture of the weak interactions between the anions and the cations in **3**. Most of the hydrogen atoms have been omitted for clarity.

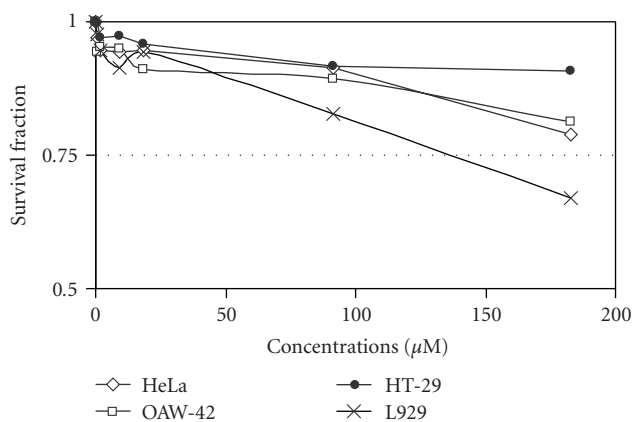


FIGURE 7: Dose-effect plots of complex **1** against a panel of human and mouse cancer cell lines 24 h after the administration of the agents. Cytotoxicity was estimated via SRB assay (each point represents a mean of six replicate wells).

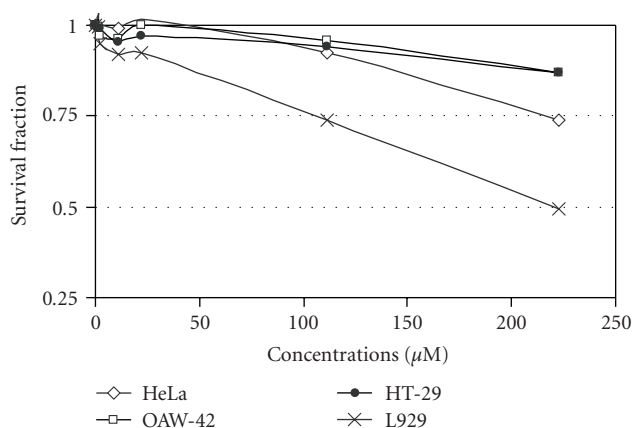


FIGURE 8: Dose-effect plots of complex **2** against a panel of human and mouse cancer cell lines 24 h after the administration of the agents. Cytotoxicity was estimated via SRB assay (each point represents a mean of six replicate wells).

TABLE 2: Selected interatomic distances (\AA) and angles ($^\circ$) for complex **1**.

Ga–N(3)'	2.212(3)	N(3)–N(2)	1.314(5)
Ga–N(3)	2.212(3)	N(3)–C(8)	1.378(6)
Ga–Br(2)	2.3204(17)	N(1)–N(2)	1.323(5)
Ga–Br(1)'	2.3436(11)	N(1)–C(9)	1.344(6)
Ga–Br(1)	2.3436(11)	N(1)–HN1	0.89(7)
N(3)'–Ga–N(3)	176.2(2)	Br(2)–Ga–Br(1)'	123.81(3)
N(3)'–Ga–Br(2)	88.08(10)	N(3)'–Ga–Br(1)	90.13(10)
N(3)–Ga–Br(2)	88.08(10)	N(3)–Ga–Br(1)	92.01(10)
N(3)'–Ga–Br(1)'	92.01(10)	Br(2)–Ga–Br(1)	123.81(3)
N(3)–Ga–Br(1)'	90.13(10)	Br(1)'–Ga–Br(1)	112.39(6)

(')Symmetry code: $-x + 1/2, y, -z + 1$.TABLE 3: Selected interatomic distances (\AA) and angles ($^\circ$) for complex **2**.

Ga–Cl(1)	2.171(2)	N(3)–C(8)	1.357(4)
Ga–Cl(2)'	2.180(1)	N(3)–S(2)	1.631(3)
Ga–Cl(2)	2.180(1)	S(2)–N(1)	1.601(3)
Ga–N(3)	2.201(3)	N(1)–C(9)	1.336(5)
Ga–N(3)'	2.201(3)		
Cl(1)–Ga–Cl(2)'	120.24(4)	Cl(2)'–Ga–N(3)'	88.34(9)
Cl(1)–Ga–Cl(2)	120.24(4)	Cl(2)–Ga–N(3)'	90.45(9)
Cl(2)'–Ga–Cl(2)	119.52(7)	N(3)–Ga–N(3)'	177.58(12)
Cl(1)–Ga–N(3)	91.21(6)	C(8)–N(3)–S(2)	107.52(19)
Cl(2)'–Ga–N(3)	90.45(9)	C(8)–N(3)–Ga	130.00(19)
Cl(2)–Ga–N(3)	88.34(9)	S(2)–N(3)–Ga	122.41(14)
Cl(1)–Ga–N(3)'	91.21(6)	N(1)–S(2)–N(3)	99.20(15)

(')Symmetry code: $-x + 1, y, -z + 1/2$.TABLE 4: Selected interatomic distances (\AA) and angles ($^\circ$) for complex **3**.

Ga–Cl(3)	2.152(1)	C(2)–N(3)	1.309(5)
Ga–Cl(4)	2.166(1)	N(3)–C(4)	1.389(4)
Ga–Cl(1)	2.171(1)	N(11)–C(22)	1.320(5)
Ga–Cl(2)	2.173(1)	N(11)–C(25)	1.392(4)
N(1)–C(2)	1.320(5)	N(11)–C(38)	1.463(4)
N(1)–C(5)	1.393(4)	C(22)–N(13)	1.318(5)
N(1)–C(18)	1.460(4)	N(13)–C(24)	1.383(4)
Cl(3)–Ga–Cl(4)	110.87(5)	Cl(3)–Ga–Cl(2)	110.55(5)
Cl(3)–Ga–Cl(1)	110.17(5)	Cl(4)–Ga–Cl(2)	108.62(5)
Cl(4)–Ga–Cl(1)	109.49(5)	Cl(1)–Ga–Cl(2)	107.05(5)

hydrolysis which is pretty usual in Ga(III) chemistry in water or water containing solutions [30].

3.2. IR Spectra. The IR spectrum of **1** exhibits a medium intensity band at $\sim 3238\text{ cm}^{-1}$, assignable to $\nu(\text{N-H})$. The bands at 1222 and 1116 cm^{-1} are attributed to the $\nu(\text{N=N})$ and $\nu(\text{N-N})$ vibrations, respectively, and are shifted to higher wavenumbers with respect to the spectrum of the free

TABLE 5: Cell cycle distribution of cells before (control) and after 48 h exposure to IC_{50} values of **3** as determined by flow cytometry.

		G1 (%)	S (%)	G2 (%)
HeLa	Control	62.0	26.6	11.4
	3	57.7	35.0	7.3
T47D	Control	57.4	28.4	14.3
	3	58.1	34.3	7.6
HT29	Control	43.5	39.4	17.1
	3	53.2	24.6	22.2
MCF-7	Control	42.0	50.4	7.6
	3	54.1	35.4	10.5
OAW-42	Control	47.8	11.3	40.9
	3	87.2	11.8	1.0
L929	Control	42.0	48.0	10.0
	3	43.0	23.6	33.4

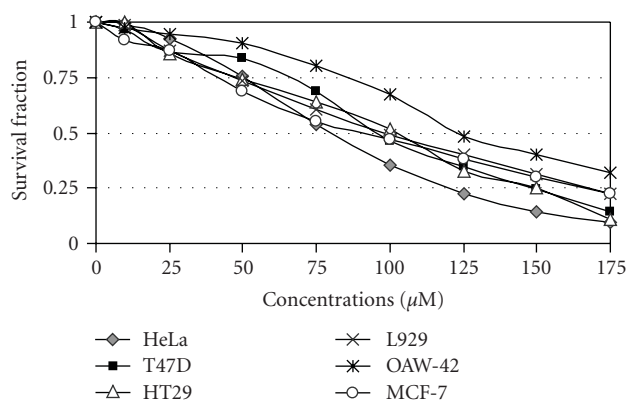


FIGURE 9: Dose-effect plots of complex **3** against a panel of human and mouse cancer cell lines 24 h after the administration of the agents. Cytotoxicity was estimated via SRB assay (each point represents a mean of six replicate wells).

ligand (1208 versus and 1084 m , resp.). The IR spectrum of **2** exhibits three strong intensity bands at 1612 , 1528 and 1482 cm^{-1} assignable to stretching carbon-carbon and carbon-nitrogen vibrations. These bands are not shifted significantly with respect to the spectrum of the free ligand [1608 w , 1518 s and 1476 s]. The bands at 950 and 916 cm^{-1} in the spectrum of **2**, which are assigned to the $\nu(\text{S-N})$ mode, have been shifted to higher wavenumbers in the spectrum of **2** [961 and 922 cm^{-1}]. A set of broad bands in the region of $3146\text{--}2620\text{ cm}^{-1}$ in the spectrum of **3** can be assigned to the $\nu(\text{N-H})$ of the protonated ligand, LH^+ . The $\nu(\text{C=N})$ and $\nu(\text{C=C})$ of the free L at 1602 and 1575 cm^{-1} have shifted to 1622 and 1578 cm^{-1} in the spectrum of **3** due to protonation.

The far-IR spectra of all three complexes are expected to show one Ga–X (X = Cl or Br) stretching mode [25] and these modes appear at 291 s [$\nu(\text{Ga-Br})$ in **1**], 382 s [$\nu(\text{Ga-Cl})$ in **2**], and 369 s [$\nu(\text{Ga-Cl})$ in **3**]. The far-IR spectra of complexes **1** and **2** exhibit one more band at 224 and 207 cm^{-1} , respectively, which are attributed to the $\nu(\text{Ga-N})$ mode [25].

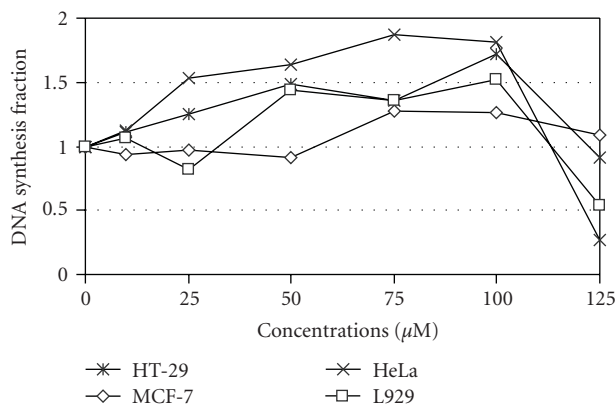


FIGURE 10: DNA synthesis inhibition of human and mouse cancer cell lines 48 h after the administration of complex **3**.

3.3. Description of Structures. An ORTEP diagram of **1** is shown in Figure 1. Selected bond distances and angles are given in Table 2. Complex **1** is isostructural with $[\text{GaCl}_3(\text{btaH})_2]$ [25]. Its structure consists of the monomeric discrete $[\text{GaBr}_3(\text{btaH})_2]$ units. The gallium coordination geometry is trigonalbipyramidal with the bromo ligands defining the equatorial plane. There is a two-fold crystallographic axis along the Ga–Br2 bond. The Ga–N bond length in complex **1** [2.212(3) Å] is longer than that of $[\text{GaCl}_3(\text{btaH})_2]$ [2.169(2) Å]. The dihedral angle between the best planes of the btaH molecules is 10.90 Å and is larger than that of $[\text{GaCl}_3(\text{btaH})_2]$ [7.4°]. The N1 proton is hydrogen bonded to atom Br1 of a neighboring molecule $[\text{N1} \cdots \text{Br1}' (1-x, -y, 1-z) 3.425(4) \text{ \AA}, \text{HN1} \cdots \text{Br1}' 2.64(7) \text{ \AA} \text{ and } \text{N1} - \text{HN1} \cdots \text{Br1}' 149(6)^\circ]$ creating a hydrogen-bonded tape running parallel to the *a* axis (Figure 2). These tapes are held together in the crystal lattice through π - π interactions. Those interactions form between the phenyl groups of the coordinated btaH molecules of neighboring tapes $[\text{centroid} \cdots \text{centroid}' (1-x, 0.5+y, 1.5-z) 3.658(4) \text{ and } 3.906(4) \text{ \AA}]$ (Figure 2).

Complex **2** crystallizes in the monoclinic space group *C2/c*. An ORTEP diagram of **2** is shown in Figure 3, while selected bond distances and angles are listed in Table 3. Its structure consists of monomeric discrete $[\text{GaCl}_3(\text{btd})_2]$ units. The gallium coordination geometry is again trigonalbipyramidal with the choro ligands defining the equatorial plane. There is a two-fold crystallographic axis along the Ga–Cl1 bond. The Ga–Cl bond lengths in complex **2** [2.171(2) and 2.180(1) Å] compare favourably with those of $[\text{GaCl}_3(\text{btaH})_2]$ [2.204(1) and 2.178(2) Å]. The Ga–N bond length in complex **2** [2.201(3) Å] is longer than that of $[\text{GaCl}_3(\text{btaH})_2]$ [2.169(2) Å], but compares well with that of **1** [2.212(3) Å]. The dihedral angle between the best planes of the btd molecules is 52.51 Å and is much larger than that of **1** and $[\text{GaCl}_3(\text{btaH})_2]$ (10.90 and 7.4°, resp.). There appear to be intermolecular stacking interactions between the nearly parallel btd ligands. Those interactions involve both the thiazazole and the phenyl groups of the btd ligands as shown in Figure 4.

An ORTEP diagram of the asymmetric unit of **3** is shown in Figure 5. Selected bond distances and angles are listed in Table 4. The crystal of **3** consists of protonated LH^+ ligand cations, tetrachlorogallate(III) anions and Cl^- anions. The Ga–Cl distances in the tetrahedral $[\text{GaCl}_4]^-$ ion are in the narrow range 2.152(1)–2.173(1) Å with the Cl–Ga–Cl angles varying from 107.1(1)° to 110.9(1)°. These values are similar to those observed for other complexes containing the tetrachlorogallate(-1) ion [13, 29]. The crystal structure of $(\text{LH})_2[\text{GaCl}_4]\text{Cl}$ is dominated by an intermixture of $\text{N}-\text{H} \cdots \text{Cl}$ and $\text{C}_{\text{Me}}-\text{H} \cdots \pi$ hydrogen bonds, $\text{Ga}-\text{Cl} \cdots \pi_{\text{azole}}$ and π - π interactions (Figure 6). The organic moieties LH^+ are connected through $\text{N}-\text{H} \cdots \text{Cl}$ and $\text{C}-\text{H} \cdots \pi_{\text{phenyl}}$ interactions to form a chain; data are as follows $\text{N3} \cdots \text{Cl5}' (2-x, -y, 2-z) 3.088(3) \text{ \AA}, \text{HN3} \cdots \text{Cl5}' 2.24(4) \text{ \AA}$ and $\text{N3}-\text{HN3} \cdots \text{Cl5}' 160(4)^\circ$; $\text{N13} \cdots \text{Cl5}'' (x-1, 1+y, z-1) 3.066(4) \text{ \AA}, \text{HN13} \cdots \text{Cl5}'' 2.19(5) \text{ \AA}$ and $\text{N13}-\text{HN13} \cdots \text{Cl5}'' 177(5)^\circ$; $\text{C38} \cdots \text{Centroid}' (1-x, -y, 2-z) 3.691(5) \text{ \AA}, \text{H38A} \cdots \text{Centroid}' 2.85(1) \text{ \AA}$ and $\text{C38}-\text{H38A} \cdots \text{Centroid}' 147(1)^\circ$. The organic chains are bridged through $\text{Ga}-\text{Cl} \cdots \pi_{\text{azole}}$ interactions to form layers $[\text{Cl1} \cdots \text{Centroid}'' (-x, 1-y, 1-z) 3.455(2) \text{ \AA}$ and $\text{Cl4} \cdots \text{Centroid}''' (1-x, 1-y, 1-z) 3.550(2) \text{ \AA}]$, which are further bridged through π - π interactions in the third dimension $[\text{centroid} \cdots \text{centroid}' (1-x, -y, 2-z) 3.778(3) \text{ and } \text{centroid} \cdots \text{centroid}'''' (-x, 2-y, 1-z) 3.878(3)]$.

3.4. Antiproliferative Activity. Complexes **1** (Figure 7) and **2** (Figure 8) had no significant inhibition on cellular proliferation against HeLa, HT29 and OAW-42 cancer cell lines and a small effect against L929 normal fibroblastic cell line. In contrast, complex **3** inhibited cellular growth of all cell lines, with IC_{50} concentrations varying between 75 and 125 μM (Figure 9).

DNA synthesis was not inhibited in HT29, HeLa, MCF-7 or L929 cell lines when they were exposed to **3** at concentrations up to 100 μM . Higher concentrations exhibited an inhibition of DNA synthesis per cell number only in HeLa and at a lower level in L929 cells (Figure 10).

Treatment with IC_{50} concentrations of **3** for 48h had no effects on cell cycle distribution of HeLa and T47D cells (Table 5). HT29 and MCF-7 were partially arrested at the G1 phase, OAW-42 were arrested at the G1 phase with a percentage of 87.2% and L929 fibroblasts exhibited a partial G2-phase arrest. However, the overall effect of **3** on cell cycle distribution (except with OAW-42 cells) was not significant, an observation in concert with the results of the BrdU assay, where no inhibition of DNA-synthesis was observed.

4. Concluding Comments

In this study, three gallium(III) azole complexes were synthesized and structurally characterized, while their antiproliferative activities were studied. The three different azole ligands were chosen in order to be able to draw structure-properties relations. In two of the complexes (**1** and **2**) the Ga(III) atom is in a trigonal-bipyramidal coordination environment where the terminal azole ligands occupy the axial positions.

The third complex (**3**) consists of $[\text{GaCl}_4]^-$ anions, chlorine anions and protonated imidazole cations. From the three complexes tested only **3** exhibited a potent anti-proliferative activity against all cell lines tested. The order of cell lines in respect to their sensitivity to **3** (at IC_{50} values) is as follows: HeLa > MCF-7 > T47D > L929 > HT29 > OAW-42. Complex **3** does not inhibit DNA synthesis at concentrations that exert antiproliferative activity (IC_{50} s) and does not produce major disturbances in cell cycle distribution (with the exception of OAW-42 cells that, notably, are the most resistant to its anti-proliferative activity).

5. Supplementary Information

CCDC 717554, 717555, and 717553 contain the supplementary crystallographic data for **1**, **2**, and **3**. These data can be obtained free of charge from the Cambridge Crystallographic Data Center via http://www.ccdc.cam.ac.uk/data_request/cif.

Acknowledgments

The authors acknowledge the Research Committee of the University of Patras (Grant “K. Caratheodory”, 2004–2007) for support of this work. G. S. Papaefstathiou thanks the Special Account for Research Grants (SARG) of the National and Kapodistrian University of Athens for support. This work is dedicated to Professor Nick Hadjiliadis for his retirement.

References

- [1] S. Nakamura and G. Fasol, *The Blue Laser Diode*, Springer, New York, NY, USA, 1997.
- [2] F. A. Ponce and D. P. Bour, “Nitride-based semiconductors for blue and green light-emitting devices,” *Nature*, vol. 386, no. 6623, pp. 351–359, 1997.
- [3] Y. Qiu and L. Gao, “Novel synthesis of nanocrystalline gallium nitride powder from gallium(III)-urea complex,” *Chemistry Letters*, vol. 32, no. 8, pp. 774–775, 2003.
- [4] J. Qiao, L. D. Wang, L. Duan, Y. Li, D. Q. Zhang, and Y. Qiu, “Synthesis, crystal structure, and luminescent properties of a binuclear gallium complex with mixed ligands,” *Inorganic Chemistry*, vol. 43, no. 16, pp. 5096–5102, 2004.
- [5] P. E. Burrows, L. S. Sapochak, D. M. McCarty, S. R. Forrest, and M. E. Thompson, “Metal ion dependent luminescence effects in metal tris-quinolate organic heterojunction light emitting devices,” *Applied Physics Letters*, vol. 64, no. 20, pp. 2718–2720, 1994.
- [6] Y. Wang, W. Zhang, Y. Li, L. Ye, and G. Yang, “X-ray crystal structure of gallium tris-(8-hydroxyquinoline): intermolecular $\pi - \pi$ stacking interactions in the solid state,” *Chemistry of Materials*, vol. 11, no. 3, pp. 530–532, 1999.
- [7] S. Jurisson, D. Berning, W. Jia, and M. Da, “Coordination compounds in nuclear medicine,” *Chemical Reviews*, vol. 93, no. 3, pp. 1137–1156, 1993.
- [8] P. Collery and C. Perchery, in *Metal Complexes in Cancer Chemotherapy*, B. K. Keppler, Ed., pp. 249–258, VCH, Weinheim, Germany, 1993.
- [9] T. Pieper, K. Borsky, and B. K. Keppler, *Topics in Biological and Inorganic Chemistry*, vol. 1, p. 177, 1999.
- [10] M. J. Clarke, F. Zhu, and D. R. Frasca, “Non-platinum chemotherapeutic metallopharmaceuticals,” *Chemical Reviews*, vol. 99, no. 9, pp. 2511–2533, 1999.
- [11] M. Thiel, T. Schilling, D. C. Gey, R. Ziegler, P. Collery, and B. K. Keppler, “Relevance of tumor models for anticancer drug development,” in *Contribution to Oncology*, vol. 54, p. 439, 1999.
- [12] L. R. Bernstein, T. Tanner, C. Godfrey, and B. Noll, “Chemistry and pharmacokinetics of gallium maltolate, a compound with high oral gallium bioavailability,” *Metal-Based Drugs*, vol. 7, no. 1, pp. 33–47, 2000.
- [13] V. B. Arion, M. A. Jakupec, M. Galanski, P. Unfried, and B. K. Keppler, “Synthesis, structure, spectroscopic and in vitro antitumour studies of a novel gallium(III) complex with 2-acetylpyridine 4N-dimethylthiosemicarbazone,” *Journal of Inorganic Biochemistry*, vol. 91, no. 1, pp. 298–305, 2002.
- [14] A. V. Rudnev, L. S. Foteeva, C. Kowol et al., “Preclinical characterization of anticancer gallium(III) complexes: solubility, stability, lipophilicity and binding to serum proteins,” *Journal of Inorganic Biochemistry*, vol. 100, no. 11, pp. 1819–1826, 2006.
- [15] A. Dobrov, V. B. Arion, N. Kandler et al., “The first metal-based paullone derivative with high antiproliferative activity in vitro,” *Inorganic Chemistry*, vol. 45, no. 5, pp. 1945–1950, 2006.
- [16] I. Ott and R. Gust, “Non platinum metal complexes as anti-cancer drugs,” *Archiv der Pharmazie*, vol. 340, no. 3, pp. 117–126, 2007.
- [17] C. R. Chitambar, “Gallium compounds as antineoplastic agents,” *Current Opinion in Oncology*, vol. 16, no. 6, pp. 547–552, 2004.
- [18] P. Collery, B. Keppler, C. Madoulet, and B. Desoize, “Gallium in cancer treatment,” *Critical Reviews in Oncology/Hematology*, vol. 42, no. 3, pp. 283–296, 2002.
- [19] M. Frezza, C. N. Verani, D. Chen, and Q. P. Dou, “The therapeutic potential of gallium-based complexes in anti-tumor drug design,” *Letters in Drug Design and Discovery*, vol. 4, no. 5, pp. 311–317, 2007.
- [20] F. Kratz, B. Nuber, J. Weiß, and B. K. Keppler, “Synthesis and characterization of potential antitumour and antiviral gallium(III) complexes of N-heterocycles,” *Polyhedron*, vol. 11, no. 4, pp. 487–498, 1992.
- [21] M. Linas, D. M. Wilson, and J. B. Neilands, “Effect of metal binding on the conformation of enterobactin. A proton and carbon-13 nuclear magnetic resonance study,” *Biochemistry*, vol. 12, no. 20, pp. 3836–3843, 1973.
- [22] M. A. Jakupec, M. Galanski, V. B. Arion, C. G. Hartinger, and B. K. Keppler, “Antitumour metal compounds: more than theme and variations,” *Dalton Transactions*, no. 2, pp. 183–194, 2008.
- [23] C. G. Hartinger and B. K. Keppler, “CE in anticancer metallodrug research—an update,” *Electrophoresis*, vol. 28, no. 19, pp. 3436–3446, 2007.
- [24] M. A. Jakupec and B. K. Keppler, “Gallium in cancer treatment,” *Current Topics in Medicinal Chemistry*, vol. 4, no. 15, pp. 1575–1583, 2004.
- [25] S. Zanas, C. P. Raptopoulou, A. Terzis, and T. F. Zafropoulos, “Gallium (III) chloride-benzotriazole chemistry: variation of product as a function of metal-to-ligand reaction ratio; preparation, structure and properties of a tetrahedral adduct and the first example of a GaX_3L_2 trigonal-bipyramidal complex,” *Inorganic Chemistry Communications*, vol. 2, no. 2, pp. 48–51, 1999.

- [26] G. S. Papaefstathiou, S. Manessi, C. P. Raptopoulou, E. J. Behrman, and T. F. Zafropoulos, "The first metal complex of 5-hydroxyorotic acid: dimethylammonium bis(N,N-dimethylformamide) bis(5-hydroxyorotato(-2))gallate(III)," *Inorganic Chemistry Communications*, vol. 7, no. 1, pp. 69–72, 2004.
- [27] A. Manessi, G. S. Papaefstathiou, C. P. Raptopoulou, A. Terzis, and T. F. Zafropoulos, "Synthetic analogue approach to metalbleomycins: syntheses, structure and properties of mononuclear and tetranuclear gallium(III) complexes of a ligand that resembles the metal-binding site of bleomycin," *Journal of Inorganic Biochemistry*, vol. 98, no. 12, pp. 2052–2062, 2004.
- [28] A. Sofetis, G. S. Papaefstathiou, A. Terzis, C. P. Raptopoulou, and T. F. Zafropoulos, "Preparation, crystal structure and spectroscopic characterization of $[\text{Ga}(\text{OH}) \cdot (\text{SO}_4)(\text{terpy})(\text{H}_2\text{O})] \cdot \text{H}_2\text{O}$ (terpy = 2,2':6',2''-Terpyridine): the first characterized gallium(III) sulfato complex," *Zeitschrift für Naturforschung*, vol. 59, no. 3, pp. 291–297, 2004.
- [29] A. Sofetis, C. P. Raptopoulou, A. Terzis, and T. F. Zafropoulos, "Structural dependence of the gallium(III)/4,4'-dimethyl-2,2'-bipyridine (dmbpy) complexes on the nature of the inorganic anion present: preparation and characterization of $[\text{GaCl}_2(\text{dmbpy})_2][\text{GaCl}_4]$, $[\text{GaCl}_2(\text{dmbpy})_2](\text{ClO}_4)$ and $[\text{Ga}(\text{dmpby})_2(\text{H}_2\text{O})_2](\text{NO}_3)_3$," *Inorganica Chimica Acta*, vol. 359, no. 10, pp. 3389–3395, 2006.
- [30] G. S. Papaefstathiou, A. Manessi, C. P. Raptopoulou, A. Terzis, and T. F. Zafropoulos, "Methanolysis as a route to gallium(III) clusters: synthesis and structural characterization of a decanuclear molecular wheel," *Inorganic Chemistry*, vol. 45, no. 22, pp. 8823–8825, 2006.
- [31] G. S. Papaefstathiou, A. Sofetis, C. P. Raptopoulou, A. Terzis, G. A. Spyroulias, and T. F. Zafropoulos, "2,2'-Bipyridine, 1,10-phenanthroline and 2,2':6',2''-terpyridine in gallium(III) chemistry: complexes containing the $\{\text{Ga}_2^{\text{III}}(\mu\text{-OH})_2\}^{4+}$ core," *Journal of Molecular Structure*, vol. 837, no. 1–3, pp. 5–14, 2007.
- [32] J. McMaster, R. L. Beddoes, D. Collison, D. R. Eardley, M. Helliwell, and C. D. Garner, "A bis(diimidazole)copper complex possessing a reversible $\text{Cu}^{\text{II}}/\text{Cu}^{\text{I}}$ couple with a high redox potential," *Chemistry European Journal*, vol. 2, p. 685, 1996.
- [33] G. M. Sheldrick, *SHELXS-86: Structure Solving Program*, University of Göttingen, Göttingen, Germany, 1986.
- [34] G. M. Sheldrick, *SHELXL-97: Crystal Structure Refinement Program*, University of Göttingen, Göttingen, Germany, 1997.
- [35] G. O. Gey, W. D. Coffman, and M. T. Kubicek, "Tissue culture studies of the proliferative capacity of cervical carcinoma and normal epithelium," *Cancer Research*, vol. 12, p. 513, 1952.
- [36] A. P. Wilson, "Characterization of a cell line derived from the ascites of a patient with papillary serous cystadenocarcinoma of the ovary," *Journal of the National Cancer Institute*, vol. 72, no. 3, pp. 513–521, 1984.
- [37] J. Fogh and G. Trempelln, in *Human Tumor Cells In Vitro*, J. Fogh, Ed., pp. 151–141, Plenum Press, New York, NY, USA, 1975.
- [38] H. D. Soule, L. Vasquez, A. Long, S. Albert, and M. Brennan, "A human cell line from a pleural effusion derived from a breast carcinoma," *Journal of the National Cancer Institute*, vol. 51, no. 5, pp. 1409–1416, 1973.
- [39] I. Keydar, L. Chen, S. Karby, et al., "Establishment and characterization of a cell line of human breast carcinoma origin," *European Journal of Cancer*, vol. 15, pp. 659–670, 1979.
- [40] K. K. Sanford, W. R. Earle, and G. D. Likely, "The growth in vitro of single isolated tissue cells," *Journal of the National Cancer Institute*, vol. 9, no. 3, pp. 229–246, 1984.
- [41] W. R. Earle, E. L. Schilling, T. H. Stark, N. P. Straus, M. F. Brown, and E. Shelton, "Production of malignancy in vitro. IV. The mouse fibroblast cultures and changes seen in the living cells," *Journal of the National Cancer Institute*, vol. 4, pp. 165–212, 1943.
- [42] P. Skehan, R. Storeng, D. Scudiero et al., "New colorimetric cytotoxicity assay for anticancer-drug screening," *Journal of the National Cancer Institute*, vol. 82, no. 13, pp. 1107–1112, 1990.
- [43] K. T. Papazisis, G. D. Geromichalos, K. A. Dimitriadis, and A. H. Kortsaris, "Optimization of the sulforhodamine B colorimetric assay," *Journal of Immunological Methods*, vol. 208, no. 2, pp. 151–158, 1997.
- [44] J.-P. Magaud, I. Sargent, and D. Y. Mason, "Detection of human white cell proliferative responses by immunoenzymatic measurement of bromodeoxyuridine uptake," *Journal of Immunological Methods*, vol. 106, no. 1, pp. 95–100, 1988.
- [45] H. A. Crissman, in *Cell Growth and Apoptosis. A Practical Approach*, G. P. Studzinski, Ed., pp. 22–23, Oxford University Press, New York, NY, USA, 1995.
- [46] H. A. Crissman and J. A. Steinkamp, "Rapid, simultaneous measurement of DNA, protein, and cell volume in single cells from large mammalian cell populations," *Journal of Cell Biology*, vol. 59, no. 3, pp. 766–771, 1973.
- [47] A. Krishan, "Rapid flow cytofluorometric analysis of mammalian cell cycle by propidium iodide staining," *Journal of Cell Biology*, vol. 66, no. 1, pp. 188–193, 1975.
- [48] M. A. Van Dilla, T. T. Trujillo, P. F. Mullaney, and J. R. Coulter, "Cell microfluorometry: a method for rapid fluorescence measurement," *Science*, vol. 163, no. 3872, pp. 1213–1214, 1969.

Research Article

Synthesis, X-Ray Structure, and Characterization of Catena-bis(benzoate)bis{*N,N*-bis(2-hydroxyethyl)glycinate} cadmium(II)

Eugenia Katsoulakou,¹ Konstantis F. Konidaris,¹ Catherine P. Raptopoulou,²
Vassilis Psyharis,² Evy Manessi-Zoupa,¹ and Spyros P. Perlepes¹

¹Department of Chemistry, University of Patras, 265 04 Patras, Greece

²Institute of Materials Science, NCSR "Demokritos", 153 10 Aghia Paraskevi Attikis, Greece

Correspondence should be addressed to Evy Manessi-Zoupa, emane@upatras.gr and
Spyros P. Perlepes, perlepes@patreas.upatras.gr

Received 20 May 2010; Accepted 12 July 2010

Academic Editor: E. R. Milaeva

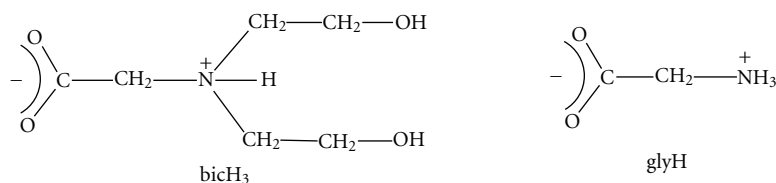
Copyright © 2010 Eugenia Katsoulakou et al. This is an open access article distributed under the Creative Commons Attribution License, which permits unrestricted use, distribution, and reproduction in any medium, provided the original work is properly cited.

The reaction of *N,N*-bis(2-hydroxyethyl)glycine (bicine; bicH₃) with Cd(O₂CPh)₂ · 2H₂O in MeOH yielded the polymeric compound [Cd₂(O₂CPh)₂(bicH₂)₂]_n (**1**). The complex crystallizes in the tetragonal space group *P*4₁2₁2. The lattice constants are *a* = *b* = 12.737(5) and *c* = 18.288(7) Å. The compound contains chains of repeating {Cd₂(O₂CPh)₂(bicH₂)₂} units. One Cd^{II} atom is coordinated by two carboxylate oxygen, four hydroxyl oxygen, and two nitrogen atoms from two symmetry-related 2.21111 (Harris notation) bicH₂⁻ ligands. The other Cd^{II} atom is coordinated by six carboxylate oxygen atoms, four from two bicH₂⁻ ligands and two from the monodentate benzoate groups. Each bicinate(-1) ligand chelates the 8-coordinate, square antiprismatic Cd^{II} atom through one carboxylate oxygen, the nitrogen, and both hydroxyl oxygen atoms and bridges the second, six-coordinate trigonal prismatic Cd^{II} center through its carboxylate oxygen atoms. Compound **1** is the first structurally characterized cadmium(II) complex containing any anionic form of bicine as ligand. IR data of **1** are discussed in terms of the coordination modes of the ligands and the known structure.

1. Introduction

There are many areas illustrating the importance of cadmium coordination and bioinorganic chemistry and the need for further research in this field. The mobilization and immobilization of Cd^{II} in the environment, in the organisms, and in some technical processes can depend significantly on the complexation by chelating organic ligands [1]. For example, anthropogenic chelators released into the environment, humic acids, and several types of ligands produced by microorganisms contribute to the transfer of this metal ion between solid and aqueous phases [2]. Examples of applied cadmium coordination chemistry are found in wastewater treatment and organic separation problems [1, 3]. Cadmium is also important in the interdisciplinary field of Bioinorganic Chemistry. Though Cd^{II}

probably does not have any biological function, the body of a normal human adult usually contains some milligrams of it [4], mainly in metallothioneins, where it is tightly bonded to cysteinyl sulfur atoms [5]. In special cases of cadmium poisoning, the so-called "chelation therapy" can be applied in which synthetic chelators, like EDTA⁴⁻ and 2,3-dimercapto-1-propanol (BAL), are given as antidotes [6]. A number of research groups have been also using ¹¹³Cd NMR spectroscopy as a "spin spy" in the study of Zn^{II}-containing proteins [7]. Systematic comparative studies on the coordination chemistry of Cd^{II} and Zn^{II} with ligands containing donor groups of biological relevance are useful in this topic. The stereochemical adaptability of this d¹⁰ metal ion favours structural variations, and this fact makes Cd^{II} a central "player" in the fields of Crystal Engineering and Metallosupramolecular Chemistry [8, 9].



SCHEME 1: Formulae of *N,N*-bis(2-hydroxyethyl)glycine (bicine; bicH₃) and glycine (glyH) discussed in the paper.

Amongst the ligands that have never been used for the preparation and study of Cd^{II} complexes, neither in the solid state nor in solution, is *N,N*-bis(2-hydroxyethyl)glycine, generally known as bicine (bicH₃, Scheme 1). This is a currently “hot” ligand in Bioinorganic Chemistry. Bicine was first prepared in 1926 by Kiprianov and subsequently became a widely used buffer substance in many biochemical studies [11]. As with its parent compound, the amino acid glycine (glyH) also shown in Scheme 1, the monoanion of bicine, that is, the bicinate (−1) ion (bicH₂[−]), forms metal complexes. The stability constants of many divalent transition metal complexes of bicinate (−1) have been determined, and it has been found that the [M(bicH₂)(H₂O)_x]⁺ species is always the predominant species in solution [12]. It has repeatedly emphasized [13–15] that as a consequence of its strong complexation properties, the use of bicine as a pH buffer in biochemical or medical studies under the assumption that only little (or no) interaction with divalent metal ions occurs is not justified. It has been shown that not only do bicH₃ and related compounds buffer H⁺ concentrations but also the resultant metal complexes buffer H⁺ and metal ion concentrations; therefore the employment of bicH₃ as a buffer requires great care to avoid conflicting data and erroneous conclusions [13–15]. Even though bicinate metal complexes have been studied in solution for years [12–18], mainly through the excellent research of Sigel [12], only few metal complexes have been structurally characterized in the solid state through single-crystal, X-ray crystallography. In those structural studies it was found (see “Results and Discussion”) that the anionic bicH₂[−], bicH^{2−}, and bic^{3−} ligands are versatile and behave in a variety of terminal and bridging modes. Due to this versatility, the anionic forms of bicine are promising ligands for the isolation of polynuclear transition metal complexes (clusters) [19, 20]. Transition metal cluster chemistry is a currently “hot” research field in contemporary inorganic chemistry [21].

In this paper we report the amalgamation of the above-mentioned two research areas by reporting the preparation, structural characterization, and spectroscopic study of the *first* cadmium(II) bicinate complex. This paper can be considered as a continuation of our interest in the coordination chemistry of bicine [11] and in the Cd^{II} carboxylate chemistry [22].

2. Experiments

All manipulations were performed under aerobic conditions using materials and solvents as received. Cd(O₂CPh)₂·2H₂O was prepared by the reaction of Cd(O₂CMe)₂·2H₂O with

an excess of PhCO₂H in CHCl₃ under reflux. C, H, and N analyses were performed with a Carlo Erba EA 108 analyzer. IR spectra (400–450 cm^{−1}) were performed with a Perkin-Elmer PC16 FT-IR spectrometer with samples prepared as KBr pellets.

[Cd₂(O₂CPh)₂(bicH₂)₂]_n (1). Solid bicH₃ (0.120 g, 0.74 mmol) was added to a colourless solution of Cd(O₂CPh)₂·2H₂O (0.289 g, 0.74 mmol) in MeOH (40 cm³); the solid soon dissolved. The solution was refluxed for 20 min and allowed to slowly evaporate at room temperature. Well-formed, X-ray quality colourless crystals of the product appeared within a period of three days. The crystals were collected by vacuum filtration, washed with cold MeOH (2 × 2 cm³) and Et₂O (3 × 5 cm³), and dried in air. The yield was ca. 75%. Found %: C, 39.12; H, 3.97; N, 3.50. Calc % for C₂₆H₃₄N₂O₁₂Cd₂: C, 39.46; H, 4.34; N, 3.54. IR data (KBr, cm^{−1}): 3235 (sb), 3070 (mb), 2972 (m), 2940 (w), 2894 (w), 1606 (s), 1582 (s), 1490 (w), 1445 (w), 1418 (m), 1384 (s), 1334 (m), 1264 (m), 1237 (m), 1174 (w), 1157 (w), 1138 (m), 1069 (s), 1017 (s), 992 (w), 943 (m), 885 (s), 846 (m), 797 (w), 727 (s), 608 (m), 584 (m), 552 (w).

2.1. X-ray Crystallography. X-ray data were collected at 298 K using a Crystal LOGIC dual Goniometer diffractometer with graphite-monochromated Mo-K_α radiation (λ = 0.71073 Å). The appropriate crystal was mounted in air and covered with epoxy glue. Unit cell dimensions were determined and refined by using the angular settings of 25 automatically centered reflections in the range 11 < 2θ < 23°. Intensity data were recorded using a θ–2θ scan. Three standard reflections showed less than 3% variation and no decay. Lorentz polarization and Ψ-scan absorption corrections were applied using Crystal Logic software. The structure was solved by direct methods using SHELXS-97 [23] and refined by full-matrix least-squares techniques on F² with SHELX-97 [24]. Hydrogen atoms were located by difference maps and refined isotropically, except those on O(3), C(6), and C(15) which were introduced at calculated positions as riding on bonded atoms with U equal 1.3 times the U(eq) of the respective atom. All nonhydrogen atoms were refined anisotropically. CCDC 771321 contains the supplementary crystallographic data for this paper. This data can be obtained free of charge at www.ccdc.cam.ac.uk/conts/retrieving.html [or from the Cambridge Crystallographic Data Centre, 12 Union Road, Cambridge CB2 1EZ, UK; Fax: ++44-1223-336 033; E-mail: deposit@ccdc.cam.ac.uk]. Important crystal data and parameters for data collection and refinement are listed in Table 1.

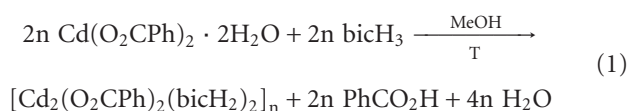
TABLE 1: Crystal data and structure refinement for complex **1**.

Empirical formula	C ₂₆ H ₃₄ Cd ₂ N ₂ O ₁₂
Formula weight	791.35
Crystal size (mm)	0.20 × 0.23 × 0.50
Crystal system	Tetragonal
Space group	P ₄ 12 ₁ 2
Flack parameter <i>x</i>	0.01(3)
θ range for data collection (°)	1.95 ≤ θ ≤ 25.04
<i>a</i> , Å	12.737(5)
<i>b</i> , Å	12.737(5)
<i>c</i> , Å	18.288(7)
α°	90
β°	90
γ°	90
<i>V</i> , Å ³	2967(2)
<i>Z</i>	4
ρ_{calcd} , g cm ⁻³	1.772
μ , mm ⁻¹	1.498
<i>F</i> (000)	1584
	0 ≤ <i>h</i> ≤ 15
Limiting indices, (°)	0 ≤ <i>k</i> ≤ 15
	-21 ≤ <i>l</i> ≤ 21
Reflections collected	5741
Unique reflections	2632 (<i>R</i> _{int} = 0.0454)
Reflections used [<i>I</i> > 2σ(<i>I</i>)]	2448
Parameters	246
<i>GoF</i> (on <i>F</i> ²)	1.047
<i>R</i> 1 ^a	0.0273
<i>wR</i> 2 ^a	0.0674
(Δρ) _{max} /(Δρ) _{min} , e Å ⁻³	0.742/ - 0.570

^a*I* > 2σ(*I*).

3. Results and Discussion

3.1. Synthetic Comments. Treatment of bicH₃ with 1.5 equivalent of Cd(O₂CPh)₂·2H₂O in refluxing MeOH gave a colourless solution from which complex [Cd₂(O₂CPh)₂(bicH₂)₂]_n(**1**) was obtained in 60% yield (based on the ligand). Its formation can be represented by the stoichiometric equation



The “wrong” Cd^{II} to bicH₃ reaction ratio (1.5:1) employed for the preparation of **1** did not prove detrimental to the formation of the product. With the identity of **1** established by single-crystal X-ray crystallography, the “correct” stoichiometry (1:1) was employed and led to the pure compound in 75% yield (see Section 2).

The PhCO₂⁻ group present in the reaction mixture plays a double role. It helps the deprotonation of bicH₃ and participates in the complex as ligand.

TABLE 2: Selected bond lengths (Å) and angles (°) for complex **1**^a.

Cd(1)-O(1)	2.373(2)	Cd(2)-O(11)	2.190(3)
Cd(1)-O(3)	2.375(3)	C(1) ^b -O(1)	1.242(5)
Cd(1)-O(4)	2.557(3)	C(1) ^b -O(2)	1.253(5)
Cd(1)-N(1)	2.465(3)	C(11) ^c -O(11)	1.264(5)
Cd(2)-O(1)	2.550(2)	C(11) ^c -O(12)	1.234(5)
Cd(2)-O(2)	2.311(4)		
O(1)-Cd(1)-O(1')	153.4(1)	O(1)-Cd(2)-O(1'')	156.8(1)
O(1)-Cd(1)-N(1')	119.8(1)	O(1)-Cd(2)-O(2)	52.9(1)
O(3)-Cd(1)-O(3')	87.7(2)	O(2)-Cd(2)-O(2'')	94.2(2)
O(3)-Cd(1)-O(4')	155.3(1)	O(2)-Cd(2)-O(11)	129.6(1)
O(4)-Cd(1)-O(4')	75.3(2)	O(11)-Cd(2)-O(11'')	117.6(2)
O(4)-Cd(1)-N(1')	84.8(1)	O(11)-Cd(2)-O(2'')	93.1(1)
N(1)-Cd(1)-N(1')	147.5(2)	O(1)-C(1) ^b -O(2)	121.2(4)
N(1)-Cd(1)-O(4)	69.3(1)	O(11)-C(11) ^c -O(12)	123.0(4)

^aSymmetry transformations used to generate equivalent atoms: (') *y*, *x*, -*z*; (')' - *y* + 1, -*z* + 1, -*z* + 1/2.^bThis carbon atom (not labeled in Figure 1) belongs to the carboxylate group of the bicinate(-1) ligand.^cThis carbon atom (not labeled in Figure 1) belongs to the carboxylate group of the benzoate ligand.

As a next step we decided to use a large excess of Cd(O₂CPh)₂·2H₂O (Cd^{II}:bicH₃ = 3:1) or to add base (LiOH, Et₃N, Buⁿ₄NOH) in the reaction mixture targeting the double or/and triple deprotonation of bicine. We repeatedly isolated a powder, analyzed as Cd₂(O₂CPh)(bic)(H₂O)₂, but we could not crystallize it; thus this second product has yet to be structurally characterized.

3.2. Description of Structure. Selected interatomic distances and angles for complex **1** are listed in Table 2. The molecular structure of the compound is shown in Figure 1.

The compound contains chains of repeating {Cd₂(O₂CPh)₂(bicH₂)₂} units. Each unit contains two crystallographically independent Cd^{II} atoms [Cd(1), Cd(2)] which lie on crystallographic twofold axes. Cd(1) is coordinated by two carboxylate oxygen atoms [O(1), O(1')], four hydroxyl oxygen atoms [O(3), O(4), O(3'), O(4')] and two nitrogen atoms [N(1), N(1')] from two symmetry-related bicinate(-1), that is, bicH₂⁻, ligands. Cd(2) is coordinated by six carboxylate oxygen atoms; four of them [O(1), O(1''), O(2), O(2'')] belong to two symmetry-related bicH₂⁻ ligands, and two [O(11), O(11'')] come from two symmetry-related monodentate PhCO₂⁻ groups. Each bicH₂⁻ simultaneously chelates Cd(1) through one carboxylate oxygen, the nitrogen, and both hydroxyl oxygen atoms forming three stable, 5-membered chelating rings and bridges Cd(2) through its carboxylate oxygen atoms; thus, one carboxylate oxygen atom [O(1)] of bicH₂⁻ is μ₂. Adopting Harris notation in [10], the crystallographically unique bicH₂⁻ group behaves as a 2.21111 ligand (Scheme 2).

The Cd-O_{carboxylate} bond distances are in the wide range 2.190(3)–2.550(2) Å. The bridging Cd-O(1) distances

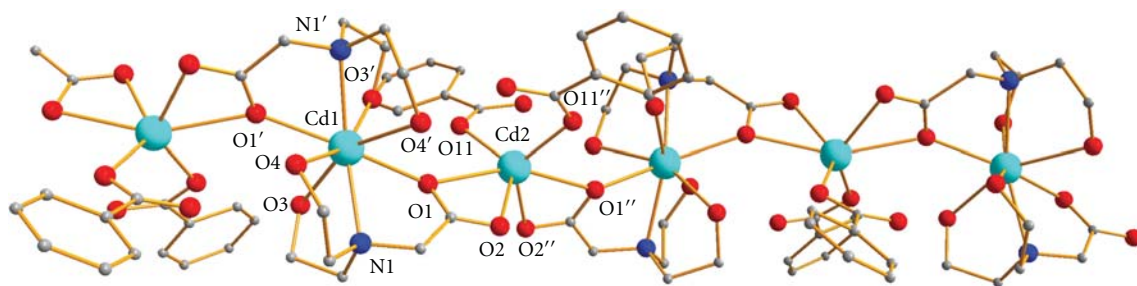
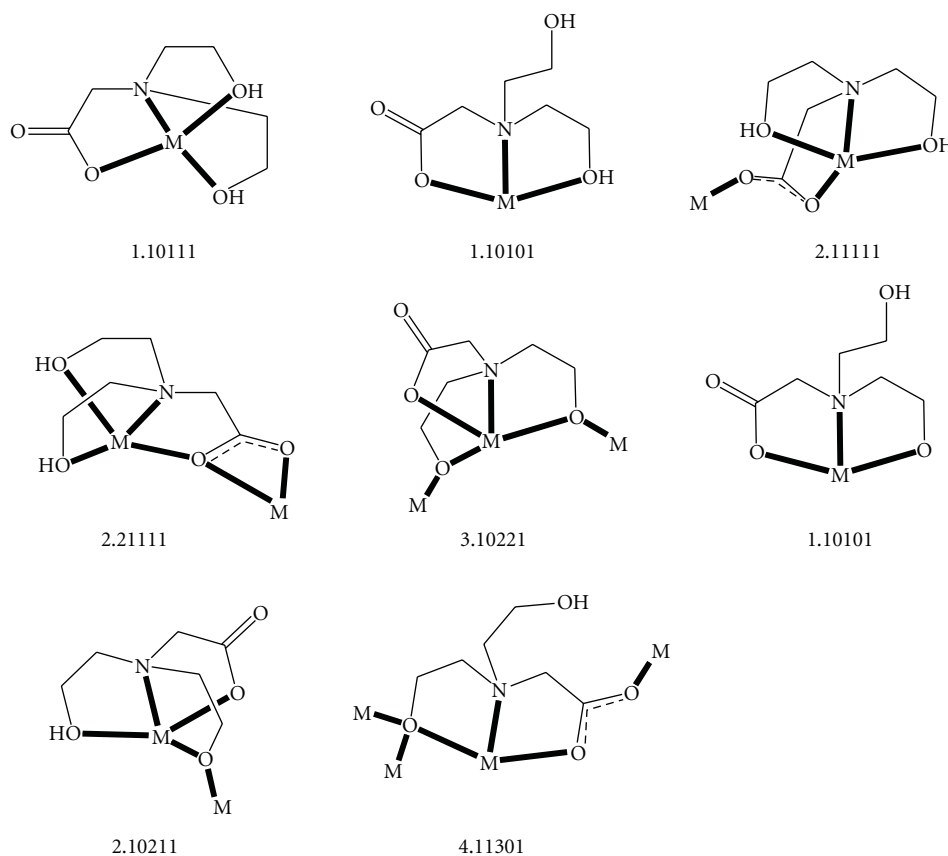


FIGURE 1: Partially labeled plot of a portion of the chain that is present in complex 1. Single and double primes are used for symmetry-related atoms (see footnote of Table 2).



SCHEME 2: The to-date crystallographically established coordination modes of the bicH_2^- , bicH^{2-} , and bic^{3-} ligands and the Harris notation in [10] that describes these modes.

[2.373(2), 2.550(2) Å] are asymmetric. The Cd(2)-O(1) bond distance for the bridging bicinate carboxylate oxygen atom is longer than the distance exhibited by the terminal oxygen atom [O(2)] to the same Cd^{II} atom [2.550(2) versus 2.311(4) Å]. The increase in bond length upon bridging relative to terminal ligation has been observed previously [22] in complexes containing carboxylate ligands with one bridging oxygen atom. Based on theoretical and experimental studies which have indicated that the *syn*-lone pairs of the carboxylate group are more basic than the *anti*-lone pairs [38], one might expect the Cd(2)-O(1) distance to be shorter than the Cd(1)-O(1) distance; however, the reverse relation

holds for **1** (see Table 2). This result, which is in accordance with other Cd^{II} carboxylate complexes [22], suggests that the Cd-O bond lengths involving $\eta^1:\eta^2:\mu_2$ carboxylate groups are mainly influenced by geometrical factors rather than the electronic properties of the carboxylate group. The Cd(2)-O bond lengths agree well with values found for other 6-coordinate cadmium(II) carboxylate complexes [39, 40]. The average value for the Cd(2)-O bond distances [2.350(4) Å] is smaller than that for the Cd(1)-O ones [2.435(3) Å], due to the lower coordination of Cd(2) compared to the coordination number of Cd(1) [6 versus 8]. The intrachain Cd(1) \cdots Cd(2) distance is 4.739(2) Å.

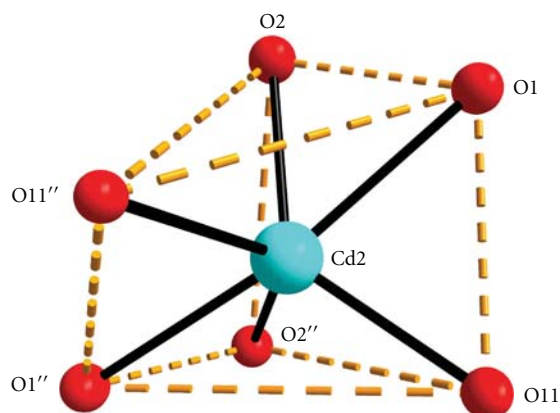


FIGURE 2: The distorted trigonal prismatic geometry of Cd(2) in complex **1**. Double primes are used for symmetry-related atoms (see footnote of Table 2).

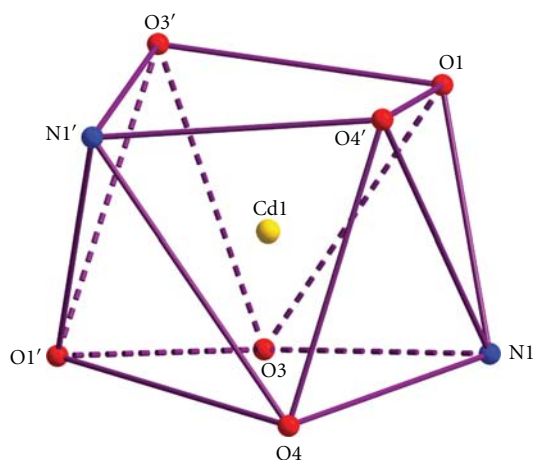


FIGURE 3: The distorted square antiprismatic stereochemistry about Cd(1) in complex **1**. The coordination bonds have not been drawn for clarity. Primes are used for symmetry-related atoms (see footnote of Table 2).

The coordination geometry of Cd(2) can be described as a very distorted trigonal prismatic (Figure 2). The two carboxylate oxygen atoms of bicH_2^- and the benzoate oxygen atom constitute each trigonal face. The angles of triangular faces are in the wide range $32.9\text{--}91.9^\circ$. The two trigonal faces are not parallel, with the planes defined by O(1)-O(2)-O(11'') and O(11'')-O(2'')-O(11) making an angle of 27.6° . The coordination polyhedron of the donor atoms about Cd(1) is best described as a distorted square antiprism (Figure 3). Since even the more stable of the possible 8-coordinate geometries (square antiprismatic, triangular dodecahedral, and cubic) differ slightly in energy from one another, the geometry observed may be largely a reflection of constraints placed on the complex by ligand requirements and packing considerations.

Compound **1** is hydrogen bonded. Metric parameters for the bonds are listed in Table 3. The O-H \cdots O hydrogen bonds are intrachain. Both hydroxyl oxygen atoms [O(3),

O(4)] are involved as donors, while both the coordinated [O(11)] and uncoordinated [O(12)] benzoate oxygen atoms act as acceptors. A weak interchain hydrogen bond, involving one benzoate carbon atom [C(16)] as donor and the terminally ligated carboxylate oxygen atom [O(2)] of a bicH_2^- ligand from a neighbouring chain as acceptor, is responsible for the formation of a 2D network.

Compound **1** joins a family of mononuclear, polynuclear, and polymeric complexes with the mono- (bicH_2^-), di- (bicH^{2-}), and trianionic (bic^{3-}) derivatives of bicine as ligands [11, 19, 20]. The members of this family are listed in Table 4, together with the coordination modes of the bicinate ligands for convenient comparison. The to-date crystallographically established coordination modes of bicH_2^- , bicH^{2-} , and bic^{3-} are shown in Scheme 2. Compound **1** is the first cadmium(II) bicinate complex which has been structurally characterized. The bicH_2^- ligand in **1** adopts the extremely rare coordination mode 2.21111; see Scheme 2. This ligation mode has been observed in the past only in the 1D coordination polymer $\{\text{Mn}_2(\text{bicH}_2)_2(\text{H}_2\text{O})_2\}\text{Br}_2 \cdot 2\text{H}_2\text{O}\}_n$ [36], in which the Mn^{II} ions are 7 coordinate with a slightly distorted pentagonal bipyramidal coordination geometry.

3.3. IR Spectroscopy. IR assignments of selected diagnostic bands for bicH_3 (the free ligand exists in its zwitterionic form in the solid state with the carboxylic group being deprotonated and the tertiary nitrogen atom protonated [41]) and complex **1** are given in Table 5.

The IR spectrum of complex **1** exhibits a medium intensity, broad band at 3070 cm^{-1} , attributable to the O-H stretching vibration of the bicinate(-1) ligand [11, 27, 28]. The broadness and low frequency of this band are both indicative of strong hydrogen bonding [11]. The $\nu(\text{OH})_{\text{bicH}_2^-}$ mode is situated at lower frequencies in the spectrum of **1** than for free bicH_3 (at 3190 and 3090 cm^{-1} [28]); this shift is consistent with the coordination of the -OH groups. The $\nu_{\text{as}}(\text{CO}_2)_{\text{bicH}_2^-}$ and $\nu_{\text{s}}(\text{CO}_2)_{\text{bicH}_2^-}$ bands of **1** appear at 1582 and 1418 cm^{-1} [11]. The corresponding bands of free, zwitterionic bicH_3 are at 1639 and 1401 cm^{-1} [28, 29]. The fact that $\Delta_{\text{complex}} (164\text{ cm}^{-1}) < \Delta_{\text{bicH}_3} (238\text{ cm}^{-1})$, where $\Delta = \nu_{\text{as}}(\text{CO}_2) - \nu_{\text{s}}(\text{CO}_2)$, is in accordance with the crystallographically established chelating-bridging mode ($\eta^1:\eta^2:\mu_2$) of the bicinate(-1) carboxylate group [42]. The strong bands at 1606 and 1384 cm^{-1} in the spectrum of **1** are assigned to the $\nu_{\text{as}}(\text{CO}_2)$ and $\nu_{\text{s}}(\text{CO}_2)$ modes of the benzoate ligands, respectively [42]. The parameter Δ is 222 cm^{-1} significantly larger than that for NaO_2CPh (184 cm^{-1}), as expected for the monodentate mode of benzoate ligation [42].

4. Conclusions and Perspectives

Complex **1** covers a gap in literature, because it is the first structurally characterized cadmium(II) bicinate compound. The bicinate(-1) ligand adopts the extremely rare pentadentate 2.21111 coordination mode, while the two crystallographically independent Cd^{II} centers are found in two different stereochemistries.

TABLE 3: Dimensions of the hydrogen bonds (distances in Å and angles in °) for complex **1**.

D ^a -H...A ^b	D ^a ...A ^b	H...A ^b	< D ^a HA ^b	Symmetry code of A
O(3)-H(30)...O(11)	2.768(4)	1.91(5)	157(5)	$y, x, -z$
O(4)-H(40)...O(12)	2.730(5)	1.99(4)	168(5)	$1-x, 1-y, -1/2+z$
C(16)-H(16)...O(2)	3.088(7)	2.38(5)	128(4)	$-1/2+y, 1/2-x, -1/4+z$

^aD = donor atom^bA = acceptor atom.

TABLE 4: Formulae and coordination modes of the bicinate(-1, -2, -3) groups of the structurally characterized metal complexes containing various forms of bicine as ligands.

Complex ^a	Coordination modes ^b	References
[Cu(bicH ₂) ₂]	1.10101	[25, 26]
[Ni(bicH ₂) ₂]	1.10101	[27]
[CuCl(bicH ₂)]	1.10111	[28]
{[Cu(bicH ₂)](ClO ₄) _n }	2.11111	[29]
[Cu(SCN)(bicH ₂) _n] ^c	1.10111	[30]
[CuBr(bicH ₂)]	1.10111	[31]
[CuBr(bicH ₂)(H ₂ O)]	1.10111	[31]
[Mn ₂ Cl ₂ (bicH ₂) ₂] _n	2.11111	[32]
{[Mn ₂ (bicH ₂) ₂ (H ₂ O) ₂]Br ₂ } _n	2.21111	[33]
[Cu(bicH ₂)(bzimH)](ClO ₄) ^d	1.10111	[34]
[Cu(bicH ₂)(Iq)](ClO ₄) ^e	1.10111	[34]
{[La(bicH ₂) ₂]Cl} _n	1.10111, 2.11111	[35]
[Gd(O ₂ CMe)(bicH ₂)(phen)(H ₂ O)](ClO ₄)	1.10111	[11]
[Fe ₆ (bic) ₆]	3.10221	[19]
[ReCl(bicH ₂){N = NC(O)Ph}(PPh ₃)]	1.10101	[36]
[ReOCl(bicH)(PPh ₃)]	1.10101	[37]
(Et ₂ NH ₂) ₂ [Fe ₆ O ₂ (OH) ₂ (O ₂ CCMe ₃) ₈ (bic) ₂]	3.10221	[20]
[Fe ₁₂ O ₄ (O ₂ CCMe ₃) ₈ (bic) ₄ (bicH) ₄]	3.10221 ^f , 2.10211 ^g , 4.11301 ^g	[20]
[Cd ₂ (O ₂ CPh) ₂ (bicH ₂) ₂] _n	2.21111	This paper

^aSolvate and other lattice molecules have been omitted.^bUsing the Harris notation in [10].^cThe Cu^{II} ions are bridged by the SCN⁻ ligands.^dbzimH: benzimidazole.^eIq: isoquinoline.^fFor the bic³⁻ ligands.^gFor the bicH²⁻ ligands.TABLE 5: Most characteristic and diagnostic IR fundamentals (cm⁻¹) for bicH₃ and complex **1**.

Assignment	bicH ₃	1
ν(OH)	3190 (sb), 3090 (mb)	3070 (mb)
ν(CH)	2904 (m), 2844 (w)	2972 (m), 2940 (w), 2894 (w)
ν _{as} (CO ₂)bicH ₃ /bicH ₂ ⁻	1644 (sb)	1582 (s)
ν _{as} (CO ₂)PhCO ₂ ⁻		1606 (s)
ν _s (CO ₂)bicH ₃ /bicH ₂ ⁻	1394 (s)	1418 (m)
ν _s (CO ₂)PhCO ₂ ⁻		1384 (s)

The results presented here support our belief that the bicH₃/RCO₂⁻ (R = various) ligand “blends” may be effective generators of interesting structural types in

the chemistry of other transition metals. Reactions of CdCl₂, CdBr₂, CdI₂, and Cd(NO₃)₂ with bicH₃ have not been studied to date, and we do believe that the structural types of the products will be dependent on the particular nature of the Cd^{II} source. Analogues of **1** with zinc(II) have not yet been reported, but preliminary results in our laboratories indicate completely different chemistry compared with that of cadmium(II). Synthetic efforts are also in progress to “activate” the potential of bicH²⁻ and bic³⁻ to bridge more than four metal ions.

References

- [1] H. Strasdeit, W. Saak, S. Pohl, W. L. Driessen, and J. Reedijk, “Synthetic and structural studies on the novel nitrogen ligand 2,5,8,10,13,16-Hexaazapentacyclo[8.6.1.1^{2,5}

- .^{09,18}0^{13,17}]octadecane and its reaction products with methanolic cadmium halogenide solutions: $C_1-C_{12}H_{22}N_6$, $[CdX_2(C_1-C_{12}H_{22}N_6)]$ (X=Cl, Br, I), and $[CdI_2(C_{12}H_{23}N_6OCH_3)]$,” *Inorganic Chemistry*, vol. 27, no. 9, pp. 1557–1563, 1988.
- [2] U. Förstner and G.T.W. Wittmann, *Metal Pollution in the Aquatic Environment*, Springer, Berlin, Germany, 1983.
- [3] S. K. Sahni and J. Reedijk, “Coordination chemistry of chelating resins and ion exchangers,” *Coordination Chemistry Reviews*, vol. 59, no. C, pp. 1–139, 1984.
- [4] L. Friberg, C.-G. Elinder, T. Kjellström, and G. F. Nordberg, Eds., *Cadmium and Health: A Toxicological and Epidemiological Appraisal*, vol. 1, CRC, Boca Raton, Fla, USA, 1985.
- [5] J. H. R. Kägi and M. Nordberg, *Metallothionein*, Birkhäuser, Basel, Switzerland, 1979.
- [6] R. E. Gosselin, R. P. Smith, H. C. Hodge, and J. E. Braddock, *Clinical Toxicology of Commercial Products*, Williams and Wilkins, Baltimore, Md, USA, 1984.
- [7] D. L. Reger, J. E. Collins, S. M. Myers, A. L. Rheingold, and L. M. Liable-Sands, “Syntheses of cationic, six-coordinate cadmium(II) complexes containing tris(pyrazolyl)methane ligands. Influence of charge on cadmium-113 NMR chemical shifts,” *Inorganic Chemistry*, vol. 35, no. 17, pp. 4904–4909, 1996.
- [8] Z. Wang, R.-G. Xiong, B. M. Foxman, S. R. Wilson, and W. Lin, “Two- and three-dimensional cadmium coordination polymers based on *N,N*-(2-pyridyl)-(4-pyridylmethyl)amine,” *Inorganic Chemistry*, vol. 38, no. 7, pp. 1523–1528, 1999.
- [9] F. A. Almeida Paz, Y. Z. Khimiyak, A. D. Bond, J. Rocha, and J. Klinowski, “Synthesis and characterization of a novel modular cadmium-organic framework with biphenyl-4,4'-dicarboxylate,” *European Journal of Inorganic Chemistry*, no. 11, pp. 2823–2828, 2002.
- [10] R. A. Coxall, S. G. Harris, D. K. Henderson, S. Parsons, P. A. Tasker, and R. E. P. Winpenny, “Inter-ligand reactions: in situ formation of new polydentate ligands,” *Journal of the Chemical Society, Dalton Transactions*, no. 14, pp. 2349–2356, 2000.
- [11] A. Messimeri, C. P. Raptopoulou, V. Nastopoulos, A. Terzis, S. P. Perlepes, and C. Papadimitriou, “Synthesis and physical studies of lanthanide(III) complexes of *N,N*-bis(2-hydroxyethyl)glycinate (bicinate, $bicH_2^-$): molecular and crystal structure of $[Gd(OM_2CMe)(bicH_2)(phen)(H_2O)](ClO_4) \cdot phen \cdot 3H_2O$ (phen=1,10-phenanthroline),” *Inorganica Chimica Acta*, vol. 336, pp. 8–18, *Inorganica Chimica Acta*.
- [12] H. Sigel, “Quantification of successive intramolecular equilibria in binary metal ion complexes of *N,N*-bis(2-hydroxyethyl)glycinate (Bicinate). A case study,” *Coordination Chemistry Reviews*, vol. 122, no. 1-2, pp. 227–242, 1993.
- [13] C. R. Krishnamoorthy and R. Nakon, “Free metal ion depletion by Good’s buffers. Bicine 1:1 and 2:1 complexes with Mg(II), Ca(II), Co(II), Ni(II), Cu(II) and Zn(II),” *Journal of Coordination Chemistry*, vol. 23, pp. 233–243, 1991.
- [14] N. A. Corfù, B. Song, and J. Liang-nian, “Metal ion/buffer interactions. Stability of binary and ternary metal ion complexes containing the anion of *N,N*-bis(2-hydroxyethyl)glycine (bicine) and adenosine 5'-triphosphate (ATP),” *Inorganica Chimica Acta*, vol. 192, no. 2, pp. 243–251, 1992.
- [15] L.-N. Ji, N. A. Corfù, and H. Sigel, “Stability of ternary metal ion complexes formed by imidazole and the anion of *N,N*-bis(2-hydroxyethyl)glycine (Bicine). Observation of a relatively high stability of the Zn(Bicinate) (imidazole)⁺ complex,” *Inorganica Chimica Acta*, vol. 206, no. 2, pp. 215–220, 1993.
- [16] A. Calderón and A. K. Yatsimirsky, “Formation and phosphodiesterolytic activity of lanthanide(III) *N,N*-bis(2-hydroxyethyl)glycine hydroxo complexes,” *Inorganica Chimica Acta*, vol. 357, no. 12, pp. 3483–3492, 2004.
- [17] M. Taha, M. M. Khalil, and S. A. Mohamed, “Metal ion-buffer interactions. Complex formation of *N,N*-bis(2-hydroxyethyl)glycine (Bicine) with various biologically relevant ligands,” *Journal of Chemical and Engineering Data*, vol. 50, no. 3, pp. 882–887, 2005.
- [18] H. A. Azab, K. M. Abou El-Nour, and S. H. Sorrow, “Metal ion complexes containing dipeptides, tripeptides, and biologically important zwitterionic buffers,” *Journal of Chemical and Engineering Data*, vol. 52, no. 2, pp. 381–390, 2007.
- [19] M. Murugesu, K. A. Abboud, and G. Christou, “Preparation and properties of new Fe₆ and Fe₈ clusters of iron(III) with tripodal ligands,” *Dalton Transactions*, no. 23, pp. 4552–4556, 2003.
- [20] K. Graham, A. Darwish, A. Ferguson, S. Parsons, and M. Murrie, “Synthesis and characterisation of Fe₆ and Fe₁₂ clusters using bicine,” *Polyhedron*, vol. 28, no. 9-10, pp. 1830–1833, 2009.
- [21] A. J. Tasiopoulos and S. P. Perlepes, “Diol-type ligands as central ‘players’ in the chemistry of high-spin molecules and single-molecule magnets,” *Dalton Transactions*, no. 41, pp. 5537–5555, 2008.
- [22] T. C. Stamatatos, E. Katsoulakou, V. Nastopoulos, C. P. Raptopoulou, E. Manessi-Zoupa, and S. P. Perlepes, “Cadmium carboxylate chemistry: preparation, crystal structure, and thermal and spectroscopic characterization of the one-dimensional polymer $[Cd(O_2CMe)(O_2CPh)(H_2O)_2]_n$,” *Zeitschrift für Naturforschung*, vol. 58, no. 11, pp. 1045–1054, 2003.
- [23] G. M. Sheldrick, *SHELXS-97, Structure Solving Program*, University of Göttingen, Göttingen, Germany, 1997.
- [24] G. M. Sheldrick, *SHELXL-97, Crystal Structure Refinement Program*, University of Göttingen, Göttingen, Germany, 1997.
- [25] N. N. Anan’eva, N. I. Samus, T. N. Polynova, M. A. Porai-Koshits, and N. D. Mitrofanova, “Crystal structure of the divalent copper-diethanoglycine complex,” *Journal of Structural Chemistry*, vol. 16, no. 3, pp. 480–481, 1975.
- [26] H. Thakuria and G. Das, “CuO micro plates from a 3D metallo-organic framework (MOF) of a binary copper(II) complex of *N,N*-bis(2-hydroxyethyl)glycine,” *Polyhedron*, vol. 26, no. 1, pp. 149–153, 2007.
- [27] E. B. Chuklanova, T. N. Polynova, M. A. Porai-Koshits, and G. K. Babeshkina, “Crystal structure of bis[*N,N*-di(hydroxyethyl)glycinato]nickel,” *Soviet Journal of Coordination Chemistry*, vol. 7, pp. 459–463, 1981.
- [28] H. Yamaguchi, M. Nagase, Y. Yukawa, Y. Inomata, and T. Takeuchi, “Synthesis, properties, and crystal and molecular structure of chloro[*N,N*-bis(2-hydroxyethyl)glycinato]copper(II),” *Bulletin of the Chemical Society of Japan*, vol. 61, pp. 2763–2766, 1988.
- [29] H. Yamaguchi, Y. Inomata, and T. Takeuchi, “Synthesis, properties, and crystal and molecular structure of *N,N*-bis(2-hydroxyethyl)glycinato copper(II) perchlorate monohydrate,” *Inorganica Chimica Acta*, vol. 161, no. 2, pp. 217–221, 1989.
- [30] H. Yamaguchi, Y. Inomata, and T. Takeuchi, “Synthesis, properties and crystal and molecular structure of isothiocyanato [*N,N*-bis(2-hydroxyethyl)glycinato] copper(II) monohydrate,” *Inorganica Chimica Acta*, vol. 172, no. 1, pp. 105–108, 1990.

- [31] H. Yamaguchi, Y. Inomata, and T. Takeuchi, "Syntheses, properties, and crystal and molecular structures of bromo[*N,N*-bis(2-hydroxyethyl)glycinato]copper(II) and aquabromo[*N,N*-bis(2-hydroxyethyl)glycinato]copper(II)," *Inorganica Chimica Acta*, vol. 181, no. 1, pp. 31–36, 1991.
- [32] Z. Sun, P. K. Gantzel, and D. N. Hendrickson, "One-dimensional polymeric bicinate manganese complex," *Polyhedron*, vol. 16, no. 19, pp. 3267–3271, 1997.
- [33] Z. Sun, P. K. Gantzel, and D. N. Hendrickson, "Zigzag chain of hepta-coordinate manganese complexes," *Polyhedron*, vol. 17, no. 9, pp. 1511–1516, 1998.
- [34] X.-F. He, L.-S. Long, X.-Y. Le, X.-M. Chen, L.-N. Ji, and Z.-Y. Zhou, "Solid and solution studies of ternary copper(II) complexes formed by heteroaromatic N bases and the anion of *N,N*-bis(2-hydroxyethyl)glycine (bicine)," *Inorganica Chimica Acta*, vol. 285, no. 2, pp. 326–331, 1999.
- [35] Y. Inomata, T. Takei, and F. S. Howell, "Synthesis and crystal structure of lanthanide metal complexes with *N,N*-bis(2-hydroxyethyl)glycine," *Inorganica Chimica Acta*, vol. 318, no. 1-2, pp. 201–206, 2001.
- [36] A. M. Kirillov, M. Haukka, M. Fátima, M. F. C. G. Da Silva, and A. J. L. Pombeiro, "Preparation and crystal structures of benzoylhydrazido- and -diazenido-rhenium complexes with N,O-ligands and their catalytic activity towards peroxidative oxidation of cycloalkanes," *European Journal of Inorganic Chemistry*, no. 11, pp. 2071–2080, 2005.
- [37] A. M. Kirillov, M. Haukka, M. V. Kirillova, and A. J. L. Pombeiro, "Single-pot ethane carboxylation catalyzed by new oxorhenium(V) complexes with N,O ligands," *Advanced Synthesis and Catalysis*, vol. 347, no. 10, pp. 1435–1446, 2005.
- [38] K. B. Wiberg and K. E. Laidig, "Barriers to rotation adjacent to double bonds. 3. The C-O barrier in formic acid, methyl formate, acetic acid, and methyl acetate. The origin of ester and amide "resonance"" *Journal of the American Chemical Society*, vol. 109, no. 20, pp. 5935–5943, 1987.
- [39] X.-L. Wang, C. Qin, E.-B. Wang, Z.-M. Su, and Z.-M. Su, "Metal nuclearity modulated four-, six-, and eight-connected entangled frameworks based on mono-, Bi-, and trimetallic cores as nodes," *Chemistry-A European Journal*, vol. 12, no. 10, pp. 2680–2691, 2006.
- [40] Q.-R. Fang, G.-S. Zhu, M. Xue, J.-Y. Sun, and S.-L. Qiu, "Porous coordination polymers with zeolite topologies constructed from 4-connected building units," *Dalton Transactions*, no. 20, pp. 2399–2402, 2006.
- [41] V. Cody, J. Hazel, and D. A. Langs, "*N,N*-bis(2-hydroxyethyl)glycine," *Acta Crystallographica B*, vol. 33, pp. 905–907, 1977.
- [42] G. B. Deacon and R. J. Phillips, "Relationships between the carbon-oxygen stretching frequencies of carboxylato complexes and the type of carboxylate coordination," *Coordination Chemistry Reviews*, vol. 33, pp. 227–250, 1980.

Research Article

Synthesis, Crystal Structures, and DNA Binding Properties of Zinc(II) Complexes with 3-Pyridine Aldoxime

Konstantis F. Konidaris,¹ Rigini Papi,² Eugenia Katsoulakou,¹ Catherine P. Raptopoulou,³ Dimitrios A. Kyriakidis,² and Evy Manessi-Zoupa¹

¹Department of Chemistry, University of Patras, 265 04 Patras, Greece

²Department of Chemistry, Aristotle University of Thessaloniki, 541 24 Thessaloniki, Greece

³Institute of Materials Science, NCSR "Demokritos", 153 10 Aghia Paraskevi Attikis, Greece

Correspondence should be addressed to Evy Manessi-Zoupa, emane@upatras.gr

Received 25 August 2010; Accepted 14 September 2010

Academic Editor: Spyros Perlepes

Copyright © 2010 Konstantis F. Konidaris et al. This is an open access article distributed under the Creative Commons Attribution License, which permits unrestricted use, distribution, and reproduction in any medium, provided the original work is properly cited.

The employment of 3-pyridine aldoxime, (3-py)CHNOH, in Zn^{II} chemistry has afforded two novel compounds: [Zn(acac)₂{(3-py)CHNOH}]·H₂O (**1**·H₂O) [where acac⁻ is the pentane-2,4-dionato(-1) ion] and [Zn₂(O₂CMe)₄{(3-py)CHNOH}₂] (**2**). Complex **1**·H₂O crystallizes in the monoclinic space group *P*2₁/*n*. The Zn^{II} ion is five-coordinated, surrounded by four oxygen atoms of two acac⁻ moieties and by the pyridyl nitrogen atom of the (3-py)CHNOH ligand. Molecules of **1** interact with the water lattice molecules forming a 2D hydrogen-bonding network. Complex **2** crystallizes in the triclinic *P*-1 space group and displays a dinuclear paddle-wheel structure. Each Zn^{II} exhibits a perfect square pyramidal geometry, with four carboxylate oxygen atoms at the basal plane and the pyridyl nitrogen of one monodentate (3-py)CHNOH ligand at the apex. DNA mobility shift assays were performed for the determination of the *in vitro* effect of both complexes on the integrity and the electrophoretic mobility of pDNA.

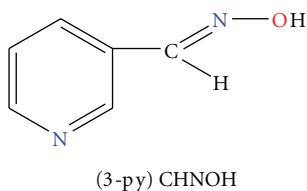
1. Introduction

During the last decades, there has been considerable interest in the interaction of small molecules with DNA [1, 2]. DNA is generally the primary intracellular target of anticancer drugs, so such interactions can cause damage in cancer cells, block their division and consequently result in cell death [3]. Small synthetic binders can interact with DNA through the following three noncovalent modes: intercalation, groove binding, and external static electronic effects [4]. Transition metal complexes are a particularly interesting class of DNA-binders because of their cationic character, well-defined three-dimensional structure, aptitude to perform hydrolysis and redox reactions, as well as extensively developed substitution chemistry that allows easy modulations of their binding and reactive properties [5].

Among the various metal ions studied with nucleic acids and nucleobases, Zn^{II} has occupied a special position [6], mainly due to the following reasons [7]: Zn^{II} is a strong Lewis

acid and exchanges ligands very rapidly; is of low toxicity; it has no redox chemistry, catalyzing only hydrolytic cleavage of DNA. For all the above mentioned reasons, the binding of Zn^{II} complexes with DNA has attracted much attention [8, 9]. It has been reported that the binding properties of the complexes depend on several factors, such as the coordination geometry, the type of the donor-atoms and the planarity of ligands [10].

The ligand used in this work (Scheme 1) belongs to the family of pyridyl oximes. The coordination chemistry of these compounds has been extensively explored over the last two decades, mainly with paramagnetic 3d metal ions towards new molecular materials with interesting magnetic properties [11]. As a consequence, the diamagnetic character of the Zn^{II} ion has led to a "gap" in the literature, concerning the area of the coordination chemistry of oximes. Recently, we have tried to fill this gap by the use of simple pyridyl oximes (the term "simple" means here ligands with only one pyridyl and one oxime group as donors) in Zn^{II} coordination



SCHEME 1: Structural formula and abbreviation of the ligand employed in this work.

chemistry. We reported the largest up to date Zn(II)/oxime cluster [12], as well as the first complexes of Zn^{II} with 3- and 4-pyridine aldoxime [13].

In this study, our efforts were initiated by the synthesis and characterization of new Zn^{II}/3-pyridine aldoxime complexes, while our next objective was to investigate the interaction of these compounds with plasmid DNA. The structural formula of the free ligand is illustrated in Scheme 1.

2. Experiments

2.1. Starting Materials and Physical Measurements. All manipulations were performed under aerobic conditions using reagents and solvents as received. Zinc acetylacetonate, zinc acetate, and 3-pyridinealdoxime were purchased from Aldrich Co. Elemental analyses (C, H, N) were performed by the University of Ioannina (Greece) Microanalytical Laboratory using an EA 1108 Carlo Erba analyzer. IR spectra (4000–450 cm⁻¹) were recorded on a Perkin-Elmer 16 PC FT-IR spectrometer with samples prepared as KBr pellets.

pDNA isolation was performed from a fully grown culture of *Escherichia coli* Top10F⁻ harboring the pBluescript plasmid. The Macherey-Nagel plasmid DNA isolation kit was used. All plastics and glassware used in the experiments were autoclaved for 30 min at 120°C and 130 Kpa.

2.2. Compound Preparation

2.2.1. Preparation of [Zn(acac)₂{(3-py)CHNOH}]·H₂O (1·H₂O). Zn(acac)₂·H₂O (0.210 g, 0.80 mmol) was suspended in MeOH (10 cm³) and then dissolved upon stirring by adding a solution of (3-py)CHNOH (0.195 g, 1.60 mmol) in the same solvent (10 cm³). The resulting colourless solution was stirred at ambient temperature for 30 min and allowed to slowly evaporate at room temperature. Well-formed, X-ray quality colourless crystals of the product appeared within a period of four days. The crystals were collected by vacuum filtration, washed with cold MeOH (2 × 2 cm³) and Et₂O (3 × 5 cm³), and dried in air. The yield was ca. 65%. Found %: C, 47.60; H, 5.84; N, 6.73. Calc % for C₁₆H₂₄N₂O₆Zn: C, 47.36; H, 5.96; N, 6.90. IR data (KBr, cm⁻¹): 3468 (wb), 3196 (wb), 3084 (wb), 2998 (w), 2960 (w), 2914 (w), 2804 (w), 1956 (vw), 1654 (sh), 1586 (s), 1552 (vs), 1400 (s), 1340 (sh), 1316 (sh), 1268 (m), 1190 (m), 1124 (w), 1102 (vw), 1058 (vw), 1020 (w), 986 (m), 928 (w), 890 (vw), 818 (vw), 770 (w), 702 (w), 654 (w), 560 (w), 528 (vw), and 464 (vw).

2.2.2. Preparation of [Zn₂(O₂CMe)₄{(3-py)CHNOH}₂] (2). Zn(O₂CMe)₂·2H₂O (0.110 g, 0.50 mmol) was suspended in Me₂CO (10 cm³) and then dissolved upon stirring by adding a solution of (3-py)CHNOH (0.122 g, 1.00 mmol) in the same solvent (10 cm³). The resulting colourless solution was stirred at ambient temperature for 30 min and then layered with n-hexane (40 cm³). Slow mixing gave well-formed, X-ray quality crystals of the product. The colourless crystals were collected by filtration, washed with cold Me₂CO (2 × 3 cm³) and Et₂O (2 × 3 cm³), and dried in air. The yield was ca. 53%. Found %: C, 39.10; H, 4.01; N, 9.23. Calc % for C₂₀H₂₄N₄O₁₀Zn₂: C, 39.34; H, 3.94; N, 9.17. IR data (KBr, cm⁻¹): 3454 (wb), 3192 (m), 3084 (m), 2996 (m), 2962 (m), 2914 (m), 2808 (w), 1656 (sh), 1586 (vs), 1522 (s), 1400 (vs), 1340 (s), 1316 (s), 1268 (s), 1192 (w), 1124 (w), 1102 (vw), 1058 (vw), 1020 (m), 986 (s), 928 (m), 890 (w), 818 (m), 770 (m), 702 (m), 682 (w), 654 (w), 562 (w), and 418 (vw).

2.3. X-Ray Crystal Structure Determination. Crystals of 1·H₂O (0.22 × 0.34 × 0.45 mm) and 2 (0.12 × 0.14 × 0.24 mm) were mounted in capillary. Diffraction measurements for 1·H₂O were made on a Crystal Logic Dual Goniometer diffractometer using graphite monochromated Mo radiation, and for 2 on a P2₁ Nicolet diffractometer upgraded by Crystal Logic using graphite monochromated Cu radiation. Unit cell dimensions were determined and refined by using the angular settings of 25 automatically centered reflections in the ranges of 11 < 2θ < 23° (for 1·H₂O) and 22 < 2θ < 54° (for 2) and they appear in Table 1. Intensity data were recorded using a θ-2θ scan. Three standard reflections monitored every 97 reflections showed less than 3% variation and no decay. Lorentz, polarization and psi-scan absorption (only for 1·H₂O) corrections were applied using Crystal Logic software. The structures were solved by direct methods using SHELXS-97 [14] and refined by full-matrix least-squares techniques on F² with SHELXL-97 [15]. Further experimental crystallographic details for 1·H₂O: 2θ_{max} = 50°; reflections collected/unique/used, 3449/3284 [R_{int} = 0.0179]/3284; 269 parameters refined; (Δ/σ)_{max} = 0.001; (Δρ)_{max}/(Δρ)_{min} = 0.453/ - 0.457 e/Å³; R1/wR2 (for all data), 0.0371/0.834. Further experimental crystallographic details for 2: 2θ_{max} = 118°; reflections collected/unique/used, 1964/1820 [R_{int} = 0.0538]/1820; 167 parameters refined; (Δ/σ)_{max} = 0.000; (Δρ)_{max}/(Δρ)_{min} = 0.559/ - 0.553 e/Å³; R1/wR2 (for all data), 0.0524/0.1205. Hydrogen atoms were either located by difference maps and were refined isotropically or were introduced at calculated positions as riding on bonded atoms. All nonhydrogen atoms were refined anisotropically. CCDC codes 789660 and 789661 contain the supplementary crystallographic data for this paper. This data can be obtained free of charge at <http://www.ccdc.cam.ac.uk/conts/retrieving.html> [or from the Cambridge Crystallographic Data Centre, 12 Union Road, Cambridge CB2 1EZ, UK; Fax: ++44-1223-336 033; E-mail: deposit@ccdc.cam.ac.uk].

2.4. Effect on pDNA. 0.1 μg of pBluescript were incubated at 25°C in the presence of various concentrations of the

TABLE 1: Crystallographic data for complexes $1 \cdot \text{H}_2\text{O}$ and 2 .

Parameter	$1 \cdot \text{H}_2\text{O}$	2
Formula	$\text{C}_{16}\text{H}_{22}\text{N}_2\text{O}_6\text{Zn}$	$\text{C}_{20}\text{H}_{24}\text{N}_4\text{O}_{10}\text{Zn}_2$
Fw	403.73	611.17
Space group	$P2_1/n$	$P-1$
a (Å)	10.531(4)	7.934(5)
b (Å)	15.779(5)	10.153(6)
c (Å)	11.602(4)	8.392(5)
α (°)	90	70.05(2)
β (°)	101.17(1)	87.34(2)
γ (°)	90	89.07(3)
V (Å ³)	1891.4(11)	634.8(7)
Z	4	1
T (°C)	25	25
Radiation	Mo $K\alpha$	Cu $K\alpha$
ρ_{calcd} (g cm ⁻³)	1.418	1.599
μ (mm ⁻¹)	1.331	2.856
Reflections with $I > 2\sigma(I)$	2865	1585
R_1^a	0.0302	0.0438
wR_2^a	0.0785	0.1125

$$^a w = 1/[\sigma^2(F_o^2) + (\alpha P)^2 + bP] \text{ and } P = (\max F_o^2, 0) + 2F_c^2/3$$

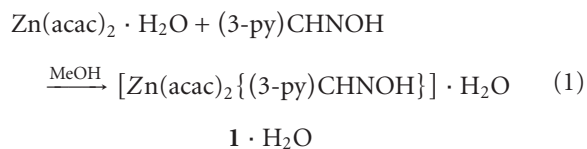
$$R_1 = \Sigma(|F_o| - |F_c|) / \Sigma(|F_o|) \text{ and } wR_2 = \{\Sigma[w(F_o^2 - F_c^2)^2] / \Sigma[w(F_o^2)^2]\}^{1/2}.$$

complexes under study. After 1h at 25°C the reaction was terminated by the addition of loading buffer consisting of 0.25% bromophenol blue, 0.25% xylene cyanol FF and 30% (v/v) glycerol in water. The products resulting from DNA-compound interactions were separated by electrophoresis on agarose gels (1% w/v), which contained 1 $\mu\text{g}/\text{ml}$ ethidium bromide (EtBr) in 40 mM Tris-acetate, pH 7.5, 20 mM sodium acetate, 2 mM Na₂EDTA, at 5 V/cm. Agarose gel electrophoresis was performed in a horizontal gel apparatus (Mini-SubTM DNA Cell, BioRad) for about 4 h. The gels were visualized in the presence of UV light. All assays were duplicated.

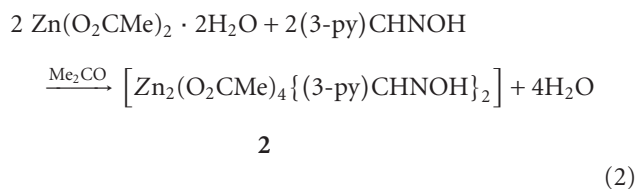
3. Results and Discussion

3.1. Synthetic Comments. Our previous investigation on the reaction between $\text{Zn}(\text{O}_2\text{CPh})_2$ and (3-py)CHNOH led to a trinuclear benzoate cluster [13]. In a subsequent step, we expanded our research to similar or different types of bidentate ligands, such as MeCO_2^- and acac^- , respectively.

Our initial efforts involved the reaction of $\text{Zn}(\text{acac})_2 \cdot \text{H}_2\text{O}$ with one equivalent of (3-py)CHNOH in MeOH, which afforded colourless parallelepiped crystals of $1 \cdot \text{H}_2\text{O}$ upon slow evaporation of the reaction solution. Its formation can be represented by the equation (1)



Treatment of $\text{Zn}(\text{O}_2\text{CMe})_2 \cdot 2\text{H}_2\text{O}$ with two equivalents of (3-py)CHNOH in Me₂CO afforded colourless parallelepiped crystals of 2 upon layering of the reaction solution with n-hexane. The chemically balanced equation for the synthesis of 2 is:



As a next step, we tried to modify the structural identity of $1 \cdot \text{H}_2\text{O}$ by using excess of $\text{Zn}(\text{acac})_2 \cdot \text{H}_2\text{O}$. A probable result would be the isolation of a paddle wheel structure with four bidentate bridging acac^- ligands and two monodentate (3-py)CHNOH ligands, that is, a structure analogous to that of compound 2 . Unfortunately, our efforts did not yield fruits; all the reactions lead to the isolation of solids corresponding to compound $1 \cdot \text{H}_2\text{O}$, emphasizing the reduced (compared to carboxylates) bridging capability of acac^- .

3.2. Description of Structures. Aspects of the molecular and crystal structures of complexes $1 \cdot \text{H}_2\text{O}$ and 2 are shown in Figures 1–4. Selected interatomic distances and angles are listed in Tables 2 and 3, while important hydrogen bonding interactions are presented in Table 4.

Complex $1 \cdot \text{H}_2\text{O}$ crystallizes in the monoclinic space group $P2_1/n$. Its crystal structure consists of mononuclear $[\text{Zn}(\text{acac})_2\{(3\text{-py})\text{CHNOH}\}]$ molecules and H_2O molecules

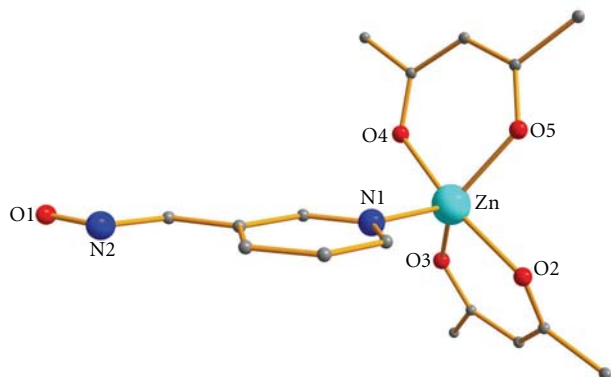


FIGURE 1: Partially labeled plot of the molecular structure of $1 \cdot \text{H}_2\text{O}$. H atoms and the solvate H_2O molecule have been omitted for clarity.

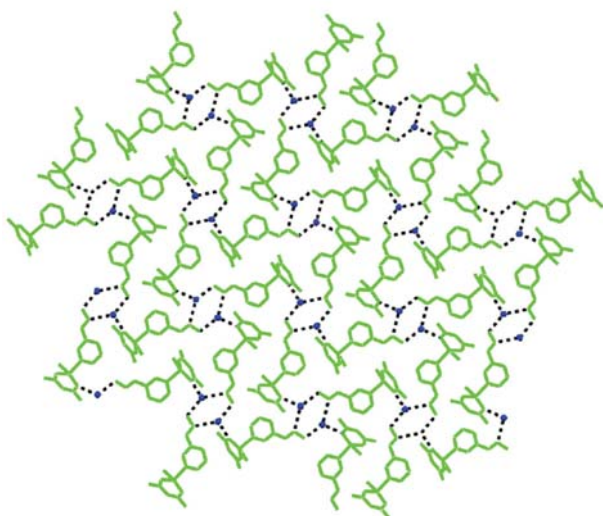


FIGURE 2: A part of the 2D network in the crystal lattice of $1 \cdot \text{H}_2\text{O}$ due to hydrogen bonding interactions (dashed lines). Oxygen atoms of the water lattice molecules are represented by blue spheres.

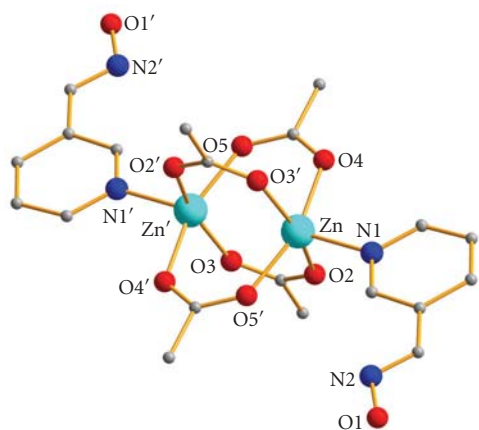


FIGURE 3: Partially labeled plot of the molecular structure of $2 \cdot \text{H}_2\text{O}$. H atoms have been omitted for clarity.

TABLE 2: Selected interatomic distances (\AA) and angles ($^\circ$) for complex $1 \cdot \text{H}_2\text{O}$.

Zn-O(2)	2.055(2)	Zn-O(3)	1.988(2)
Zn-O(4)	2.029(2)	Zn-O(5)	2.000(2)
Zn-N(1)	2.073(2)		
O(3)-Zn-O(5)	137.1(9)	O(4)-Zn-O(2)	169.1(8)
O(3)-Zn-O(4)	88.5(8)	O(3)-Zn-N(1)	113.1(8)
O(5)-Zn-O(4)	89.6(7)	O(5)-Zn-N(1)	109.7(8)
O(3)-Zn-O(2)	89.00(8)	O(4)-Zn-N(1)	94.5(8)
O(5)-Zn-O(2)	85.1(7)	O(2)-Zn-N(1)	96.3(7)

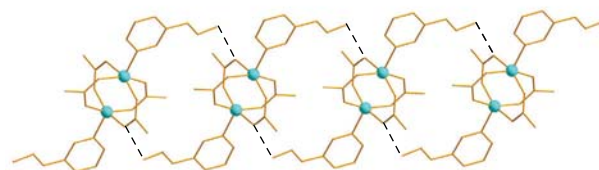


FIGURE 4: A small portion of the ladder-like 1D architectures of 2 due to H-bonding interactions (black dashed lines). The H atoms have been omitted for clarity.

being present in the lattice. The metal center is five-coordinated surrounded by two acetylacetonate (acac^-) and one (3-py)CHNOH ligand. Each of the acac^- moiety acts in a bidentate chelating way, while the (3-py)CHNOH behaves as a monodentate ligand via the nitrogen atom of the pyridine ring. The coordination geometry of the Zn^{II} ion is heavily distorted and thus it can be either described as distorted square pyramidal or as distorted trigonal bipyramidal. Analysis of the shape-determining angles using the approach of Reedijk and coworkers [16] yields a trigonality index, τ , value of 0.53 ($\tau = 0$ and 1 for perfect sp and tbp geometries, respectively). By adopting the square pyramidal geometry, the basal plane is occupied by four acetylacetonate oxygen atoms, while the apical position is taken by the pyridyl nitrogen atom of the oxime ligand. Adopting the trigonal bipyramidal description, the axial positions are occupied by O(2) and O(4) and the equatorial ones by O(3), O(5), and N(1).

In the crystal lattice of $1 \cdot \text{H}_2\text{O}$, the molecules of 1 interact with the water lattice molecules through hydrogen bonds, forming a 2D network (Figure 2, Table 4).

Complex 2 is a new member of $\text{Zn}(\text{II})$ carboxylate complexes with a paddle wheel structure [17–20]. The Zn^{II} ions are bridged by four *syn, syn*- $\eta^1:\eta^1:\mu$ MeCO_2^- ligands and each one has a perfect square pyramidal coordination geometry ($\tau = 0.01$), with the apex provided by the pyridyl nitrogen atom of a monodentate (3-py)CHNOH ligand. The $\text{Zn} \cdots \text{Zn}$ distance is $2.923(2)\text{\AA}$, while each Zn^{II} ion lies 0.386\AA out of its least-squares basal plane towards the pyridyl nitrogen atom. The mean $\text{Zn-O}(\text{carboxylate})$ bond length is approximately 2.044\AA which is typical and unremarkable [21]. There is a crystallographically imposed inversion center in the midpoint of the $\text{Zn} \cdots \text{Zn}$ distance.

TABLE 3: Selected interatomic distances (Å) and angles (°) for complex **2**^a.

Zn-O(2)	2.088(3)	Zn-O(4)	2.016(3)
Zn-O(3')	2.055(3)	Zn-O(5')	2.016(3)
Zn-N(1)	2.049(4)	Zn···Zn'	2.923(2)
O(4)-Zn-O(5')	159.9(1)	N(1)-Zn-O(3')	101.4(1)
O(4)-Zn-N(1)	100.4(1)	O(4)-Zn-O(2)	87.0(1)
O(5')-Zn-N(1)	99.6(1)	O(5')-Zn-O(2)	90.2(1)
O(4)-Zn-O(3')	88.1(2)	N(1)-Zn-O(2)	98.4(1)
O(5')-Zn-O(3')	87.8(1)	O(3')-Zn-O(2)	160.2(1)

^aSymmetry transformations used to generate equivalent atoms: (')-*x*, 1-*y*, -*z*.

TABLE 4: Hydrogen bonding interactions in **1**·H₂O and **2**.

Interaction ^a D-H···A	D···A (Å)	H···A (Å)	D-H···A (°)	Symmetry operation of A
1 ·H ₂ O				
O(1W)-H(1WA)···O(2)	3.002	2.5600	115.0	1/2 - <i>x</i> , -1/2 + <i>y</i> , 1/2 - <i>z</i>
O(1)-H(1O)···O(1W)	2.663	1.970	168.0	1 - <i>x</i> , - <i>y</i> , - <i>z</i>
O(1W)-H(1WB)···N(2)	3.002	2.300	145.0	<i>x</i> , <i>y</i> , <i>z</i>
2				
O(1)-H(1O)···O2	2.712	1.910	166.0	<i>x</i> , <i>y</i> , -1 + <i>z</i>

^aA = acceptor, D = donor.

In the crystal lattice of **2**, the dinuclear molecules interact through hydrogen bonds. Both oxime groups act as donors to carboxylate oxygen atoms, forming double, ladder-like chains along the *c* axis (Table 4, Figure 4).

3.3. IR Spectroscopy. The IR spectra of **1**·H₂O and **2** exhibit weak bands at 3468 and 3454 cm⁻¹, respectively, assignable to the ν(OH) vibration of the coordinated pyridyl oxime ligands [22]. The broadness and relatively low frequency of these bands are both indicative of hydrogen bonding. The medium intensity bands at 1636 and 1124 cm⁻¹ in the spectrum of the free ligand (3-py)CHNOH are assigned to ν(C=N)oxime and ν(N-O)oxime, respectively [23]. In the spectra of the complexes, these bands are observed at approximately the same wavenumbers, confirming the nonparticipation of the oxime group in coordination. The in-plane deformation band of the pyridyl ring of free (3-py)CHNOH (638 cm⁻¹) shifts upwards (654 cm⁻¹) in the spectra of **1**·H₂O and **2**, confirming the crystallography established involvement of the ring-N atom in coordination [24].

The presence of chelating acac⁻ ligands in complex **1**·H₂O is reflected by the presence of two strong intensity bands at 1500–1600 cm⁻¹. The higher frequency band (1586 cm⁻¹) is attributed to ν(C⁻⁻⁻C) coupled with ν(C⁻⁻⁻O), while the lower frequency band (1552 cm⁻¹) is attributed to ν(C⁻⁻⁻O) coupled with ν(C⁻⁻⁻C) [25].

The strong intensity bands at 1522 and 1400 cm⁻¹ in the spectrum of **2** are assigned to the ν_{as}(CO₂) and ν_s(CO₂) modes of the acetate ligands, respectively [26]; the former may also involve a pyridyl stretching character. The

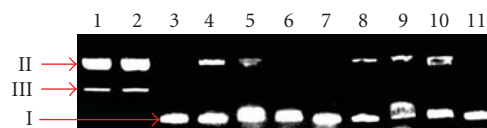


FIGURE 5: Agarose gel electrophoresis pattern of pDNA in the presence of the synthesized complexes and (3-py)CHNOH in various concentrations. Lane 1, DNA + **1**·H₂O (5 mM); lane 2, DNA + **2** (5 mM); lane 3, DNA + (3-py)CHNOH (5 mM); lane 4, DNA + **1**·H₂O (2.5 mM); lane 5, DNA + **2** (2.5 mM); lane 6, DNA + (3-py)CHNOH (2.5 mM); lane 7, DNA + **1**·H₂O (1 mM); lane 8, DNA + **2** (1 mM); lane 9, DNA + **1**·H₂O (0.1 mM); lane 10, DNA + **2** (0.1 mM); lane 11, DNA control.

difference Δ, where Δ = ν_{as}(CO₂) - ν_s(CO₂), is 122 cm⁻¹, less than that for NaO₂CMe (164 cm⁻¹), as expected for bidentate bridging ligation [26].

3.4. Effect on pDNA. DNA mobility shift assays were carried out to investigate the ability of complexes **1**·H₂O and **2**, as well as that of the (3-py)CHNOH free ligand to interact with plasmid DNA. The initial amount of pDNA was incubated with increasing concentrations of the tested compounds. When circular pDNA is subjected to electrophoresis, relatively fast migration will be observed for the supercoiled form (form I). If scission occurs on one strand (nicking), the supercoils will relax to generate a slower-moving open relaxed form (form II) [27]. If both strands are cleaved, a linear form (form III) will be generated and migrate between forms I and II [28].

Figure 5 shows the gel electrophoretic separations of pDNA after incubation with **1**·H₂O, **2** and (3-py)CHNOH

at various concentrations. Both complexes can break the double strand of pDNA and convert it to the relaxed form (II) and in a less extent to its linear form (III), at a concentration of 5 mM (Figure 5, lanes 1 and 2). At lower concentrations, the complexes display a minor effect on the integrity and electrophoretic mobility of pDNA, whereas the latter remains mostly in the supercoiled form (I). The (3-py)CHNOH ligand (Figure 5, lanes 3 and 6) does not display any interaction.

4. Conclusions

Two new complexes of Zn^{II} , with 3-pyridine aldoxime as ligand, have been synthesized and characterized by single-crystal X-ray crystallography, elemental analyses, and IR spectroscopy. In both structures, (3-py)CHNOH acts as a monodentate ligand via the pyridyl nitrogen, while the oxime group does not participate in coordination. This coordination mode is the only one observed in complexes of (3-py)CHNOH with any metal up to date. Complexes **1**·H₂O and **2** are the second and the third structurally characterized Zn(II) complexes of (3-py)CHNOH.

The two complexes affect both the integrity and electrophoretic mobility of pDNA. At the highest tested concentration, **1**·H₂O and **2** are able to totally convert the supercoiled form of pDNA to the relaxed form and in less extent to its linear form. Other types of DNA-binding experiments are currently in progress in order to determine the way of interaction with pDNA. In the future, synthetic efforts with different types of anionic ligands (e.g., NO₃⁻, SO₄²⁻) can lead to a variety of (3-py)CHNOH complexes with potentially interesting DNA-binding properties.

Acknowledgments

E.Manessi-Zoupa and K.F.Konidaris thank the Research Committee of the University of Patras for funding this work (C. Carathéodory Grant 2008, no. C.584). This contribution is devoted to Professor Nick Hadjiliadis on the occasion of his retirement and for his great contributions to Bioinorganic Chemistry.

References

- [1] C. Tan, J. Liu, L. Chen, S. Shi, and L. Ji, "Synthesis, structural characteristics, DNA binding properties and cytotoxicity studies of a series of Ru(III) complexes," *Journal of Inorganic Biochemistry*, vol. 102, no. 8, pp. 1644–1653, 2008.
- [2] Y.-M. Song, Q. Wu, P.-J. Yang, N.-N. Luan, L.-F. Wang, and Y.-M. Liu, "DNA Binding and cleavage activity of Ni(II) complex with all-*trans* retinoic acid," *Journal of Inorganic Biochemistry*, vol. 100, no. 10, pp. 1685–1691, 2006.
- [3] G. Zuber, J. C. Quada Jr., and S. M. Hecht, "Sequence selective cleavage of a DNA octanucleotide by chlorinated bithiazoles and bleomycins," *Journal of the American Chemical Society*, vol. 120, no. 36, pp. 9368–9369, 1998.
- [4] F. R. Keene, J. A. Smith, and J. G. Collins, "Metal complexes as structure-selective binding agents for nucleic acids," *Coordination Chemistry Reviews*, vol. 253, no. 15-16, pp. 2021–2035, 2009.
- [5] L. J. K. Boerner and J. M. Zaleski, "Metal complex-DNA interactions: from transcription inhibition to photoactivated cleavage," *Current Opinion in Chemical Biology*, vol. 9, no. 2, pp. 135–144, 2005.
- [6] B. Lippert, "Multiplicity of metal ion binding patterns to nucleobases," *Coordination Chemistry Reviews*, vol. 200–202, pp. 487–516, 2000.
- [7] E. L. Hegg and J. N. Burstyn, "Toward the development of metal-based synthetic nucleases and peptidases: a rationale and progress report in applying the principles of coordination chemistry," *Coordination Chemistry Reviews*, vol. 173, no. 1, pp. 133–165, 1998.
- [8] X. Sheng, X. Guo, X.-M. Lu et al., "DNA binding, cleavage, and cytotoxic activity of the preorganized dinuclear zinc(II) complex of triazacyclononane derivatives," *Bioconjugate Chemistry*, vol. 19, no. 2, pp. 490–498, 2008.
- [9] H. Zhang, C.-S. Liu, X.-H. Bu, and M. Yang, "Synthesis, crystal structure, cytotoxic activity and DNA-binding properties of the copper (II) and zinc (II) complexes with 1-[3-(2-pyridyl)pyrazol-1-ylmethyl]naphthalene," *Journal of Inorganic Biochemistry*, vol. 99, no. 5, pp. 1119–1125, 2005.
- [10] H. Xu, K.-C. Zheng, Y. Chen et al., "Effects of ligand planarity on the interaction of polypyridyl Ru(II) complexes with DNA," *Dalton Transactions*, pp. 2260–2268, 2003.
- [11] C. J. Milios, T. C. Stamatatos, and S. P. Perlepes, "The coordination chemistry of pyridyl oximes," *Polyhedron*, vol. 25, no. 1, pp. 134–194, 2006.
- [12] K. F. Konidaris, E. Katsoulakou, M. Kaplanis et al., "A tetrahedron in a cube: a dodecanuclear Zn^{II} benzoate cluster from the use of 2-pyridinealdoxime," *Dalton Transactions*, vol. 39, no. 19, pp. 4492–4494, 2010.
- [13] K. F. Konidaris, M. Kaplanis, C. P. Raptopoulou, S. P. Perlepes, E. Manessi-Zoupa, and E. Katsoulakou, "Dinuclear versus trinuclear complex formation in zinc(II) benzoate/pyridyl oxime chemistry depending on the position of the oxime group," *Polyhedron*, vol. 28, no. 15, pp. 3243–3250, 2009.
- [14] G. M. Sheldrick, *SHELXS-97, Structure Solving Program*, University of Göttingen, Göttingen, Germany, 1997.
- [15] G. M. Sheldrick, *SHELXL-97, Crystal Structure Refinement Program*, University of Göttingen, Göttingen, Germany, 1997.
- [16] A. W. Addison, T. N. Rao, J. Reedijk, J. van Rijn, and G. C. Verschoor, "Synthesis, structure, and spectroscopic properties of copper(II) compounds containing nitrogen-sulphur donor ligands; the crystal and molecular structure of aqua[1,7-bis(*N*-methylbenzimidazol-2'-yl)-2,6-dithiaheptane]copper(II) perchlorate," *Journal of the Chemical Society, Dalton Transactions*, no. 7, pp. 1349–1356, 1984.
- [17] H. Kwak, S. H. Lee, S. H. Kim et al., "Substituent effects of pyrazine on construction of crystal structures of Zn(II)-benzoate complexes and their catalytic activities (dinuclear, trinuclear, and pentanuclear to 1-D and 2-D)," *Polyhedron*, vol. 27, no. 17, pp. 3484–3492, 2008.
- [18] A. Karmakar, R. J. Sarma, and J. B. Baruah, "Self-assembly of neutral dinuclear and trinuclear zinc-benzoate complexes," *Inorganic Chemistry Communications*, vol. 9, no. 12, pp. 1169–1172, 2006.
- [19] V. Zelenák, M. Sabo, W. Massa, and J. Černák, "Tetra- μ -benzoato- $\kappa^8 O : O'$ -bis({1-[(3,4-dimethoxyphenyl)methyl]-6, 7-dimethoxyisoquinoline- κN })zinc(II)): the first crystal structure with papaverine as a ligand," *Acta Crystallographica Section C*, vol. 60, no. 2, pp. m85–m87, 2004.
- [20] H. Nəcəfoglul, W. Clegg, and A. J. Scott, "Tetrakis(μ -benzoato)bis[(*N,N*-diethylnicotinamide)zinc(II)]," *Acta Crystallographica E*, vol. 58, pp. m121–m122, 2002.

- [21] Q. Zhou, T. W. Hambley, B. J. Kennedy et al., "Syntheses and characterization of anti-inflammatory dinuclear and mono-nuclear zinc indomethacin complexes. Crystal structures of $[\text{Zn}_2(\text{indomethacin})_4(\text{L})_2]$ ($\text{L} = \text{N,N}$ -dimethylacetamide, pyridine, 1-methyl-2-pyrrolidinone) and $[\text{Zn}(\text{indomethacin})_2(\text{L}_1)_2]$ ($\text{L}_1 = \text{ethanol, methanol}$)," *Inorganic Chemistry*, vol. 39, no. 17, pp. 3742–3748, 2000.
- [22] K. W. Nordquest, D. W. Phelps, W. F. Little, and D. J. Hodgson, "Metal-metal interactions in linear chains. The structure and characterization of bis(pyridine-2-carboxaldoximinato)platinum(II)dihydrate," *Journal of the American Chemical Society*, vol. 98, no. 5, pp. 1104–1107, 1976.
- [23] P. Chaudhuri, M. Winter, U. Flörke, and H.-J. Haupt, "An effectively diamagnetic oximato-bridged asymmetric dinuclear copper(II) complex with a $\text{Cu(II)}-\text{I}$ bond," *Inorganica Chimica Acta*, vol. 232, no. 1-2, pp. 125–130, 1995.
- [24] A. B. P. Lever and E. Mantovani, "The far-infrared and electronic spectra of some bis-ethylenediamine and related complexes of copper(II) and the relevance of these data to tetragonal distortion and bond strengths," *Inorganic Chemistry*, vol. 10, no. 4, pp. 817–826, 1971.
- [25] K. Nakamoto, *Infrared and Raman Spectra of Inorganic and Coordination Compounds*, John Wiley & Sons, New York, NY, USA, 4th edition, 1986.
- [26] G. B. Deacon and R. J. Phillips, "Relationships between the carbon-oxygen stretching frequencies of carboxylato complexes and the type of carboxylate coordination," *Coordination Chemistry Reviews*, vol. 33, pp. 227–250, 1980.
- [27] J. K. Barton and A. L. Raphael, "Photoactivated stereospecific cleavage of double-helical DNA by cobalt(III) complexes," *Journal of the American Chemical Society*, vol. 106, no. 8, pp. 2466–2468, 1984.
- [28] X.-Q. He, Q.-Y. Lin, R.-D. Hu, and X.-H. Lu, "Synthesis, characterization and DNA-binding studies on La(III) and Ce(III) complexes containing ligand of *N*-phenyl-2-pyridinecarboxamide," *Spectrochimica Acta A*, vol. 68, no. 1, pp. 184–190, 2007.